

Catoca kimberlite pipe: Diatreme/crater transition and dynamics of the crater sedimentation

Vladimir Pervov, João Tunga Felix, Francisco João

Departamento de Geologia, Sociedade Mineira de Catoca, República de Angola, vlad.pervov@gmail.com, jotufe@yahoo.com, fjoao10@msn.com

The kimberlite pipes with craters filled with sedimentary rocks are rarely preserved. The best studied and currently mined pipes are Orapa (Gernon et al. 2009) and Mwadui (Stiefenhofer and Farrow 2004). Gentle dip angles of rock stratifications are most typical there, while some steeper angles are considered to be controlled by an on-slope angle of repose (Gernon et al. 2009) or related to syn-eruption subsidence and faulting (Brown et al. 2008). Angola hosts many pipes of this type. For example, among 70 kimberlite bodies discovered within the concession of 350 km² in an area with the Catoca pipe in its center, 50% contain craters with volcanosedimentary infill. Owing to many post-emplacement deformations, the Catoca and some other pipes of the area can be studied to clarify the causes of possible syn-sedimentation subsidence within the crater.

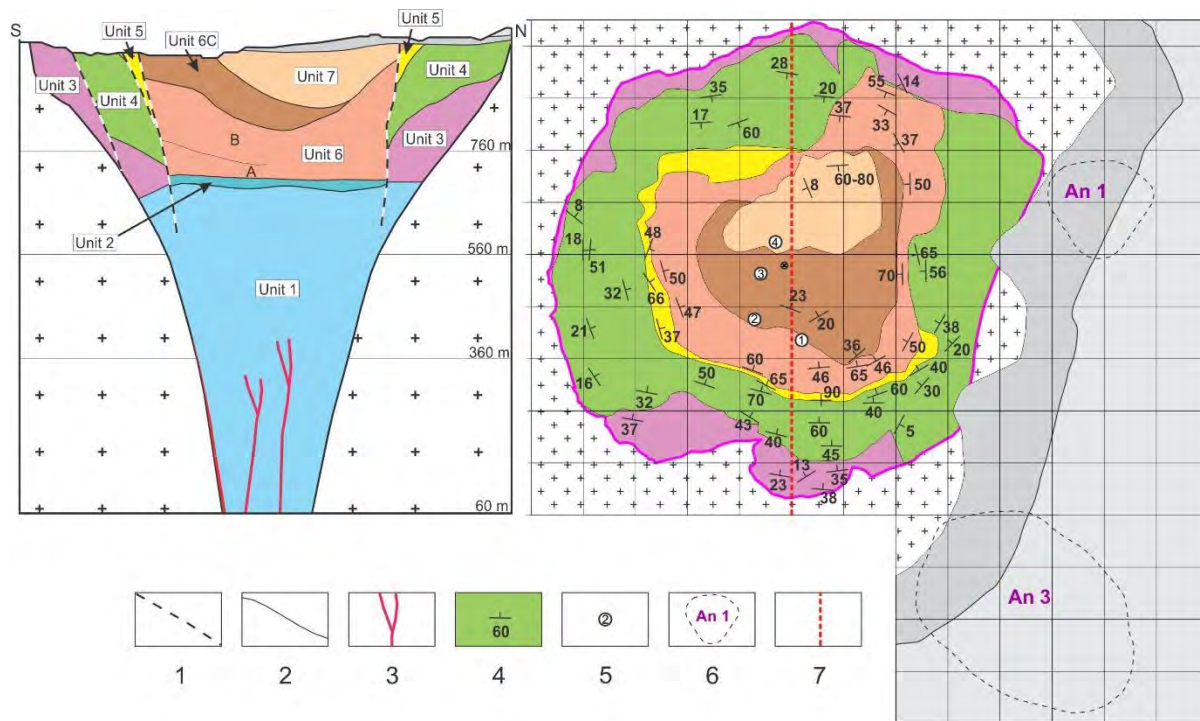


Figure 1: Schematic cross section (2002) and plan (Dec. 2009) of the Catoca kimberlite pipe (the vertical and horizontal scales are similar). See unit description in text. Overlying sediments are shown in grey. Projection of the pipe axis is marked by a crossed circle.

1 – Fault systems, 2 – conformable geological boundaries, 3 – kimberlite dykes, 4 – stratification strike and dip to horizon, 5 – location of boreholes 1 to 4 (see Fig. 2 for lithological columns), 6 – satellite kimberlite pipes, 7 – cross section line.

The Catoca kimberlite pipe is a symmetrical flaring upward body of about 63.6 ha in area on the pipe surface (970 masl = metres above sea level) (Fig. 1). The open pit reached now 820 masl and exploration boreholes – 60 masl. The contact between crater and diatreme zones is sharp and nearly horizontal (705±10 masl). The diatreme zone is composed of massive-textured pyroclastic kimberlite with coherent kimberlite as minor dikes and local diatreme infill (*Unit 1*). The crater zone is more complicated and consists of earlier relict ring of resedimented volcanoclastic kimberlite and banded pyroclastic kimberlite (*Units 3 and 4*) and later central depression of epiclastic kimberlite (*Units 6 and 7*). The ring is separated from the central depression by a circular zone of extensive steeply dipping dislocations with boudinage and numerous bedding-plane and stepped dip-slip faults.

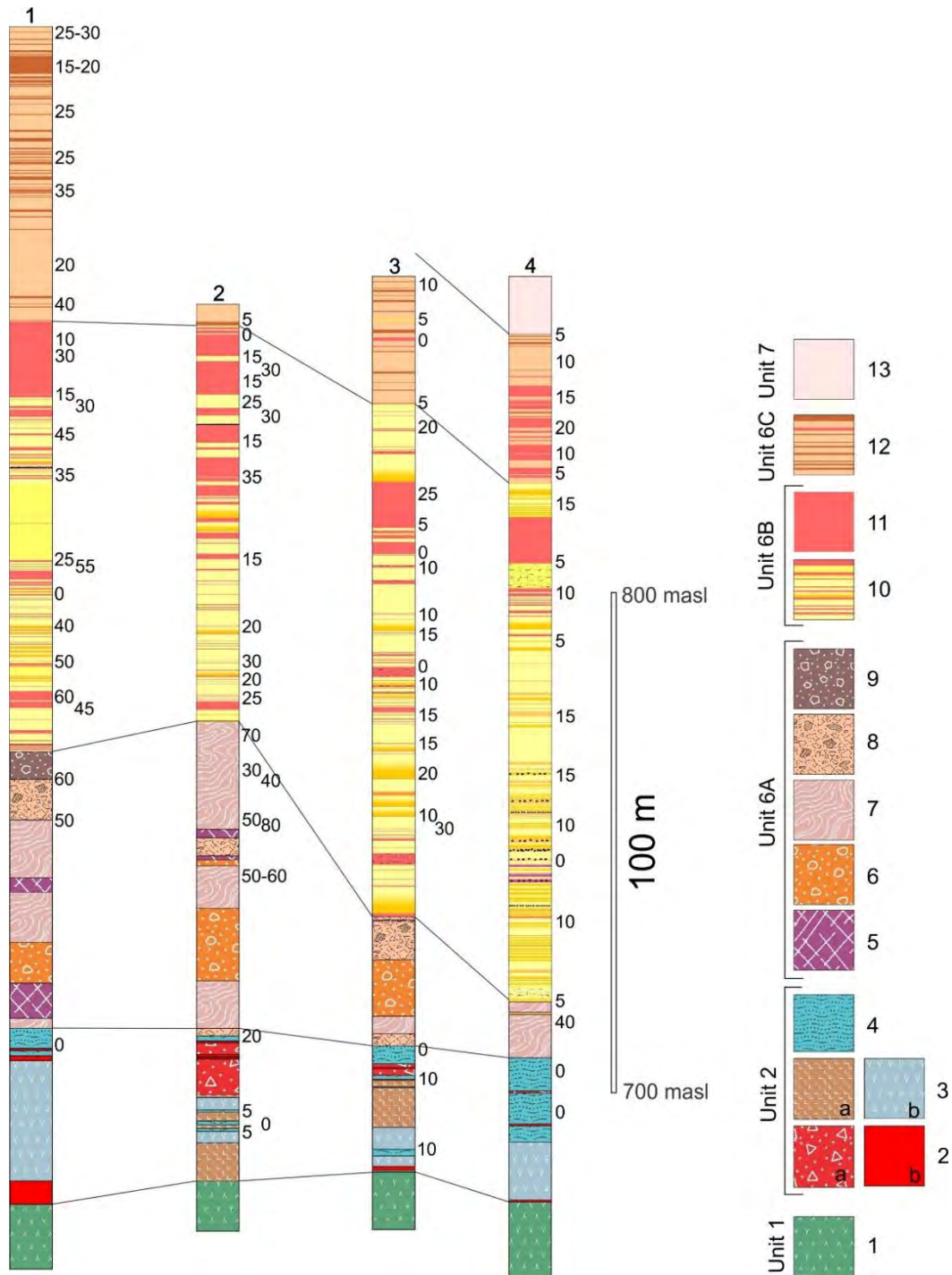


Figure 2: Correlation of borehole profiles (see Fig. 1 for borehole location). Figures at the right hand side of the columns indicate dip angles of stratification to horizon.

1 – Pyroclastic kimberlite, 2a – gneiss breccia with volcanoclastic matrix, 2b – gneiss blocks, 3 – psammitic (a) and psephytic (b) volcanoclastic kimberlite, 4 – pelitic to psammitic volcanoclastic kimberlite, 5 – strongly altered and deformed kimberlite, 6 – complex mixture (conglomerate) of pebble of various kimberlitic rocks (tuffaceous sand- to mudstone to altered pyroclastic kimberlite) and similarly variable matrix, 7 – sand- to mudstone with complicated wrinkled texture and multiple creep microdeformations, 8 – contorted and brecciated sandstone–tuffaceous sandstone–silt- to mudstone locally with kimberlite inclusions, 9 – strongly deformed kimberlite breccia with gneiss clasts, 10 – sandstone and tuffaceous sandstone (yellow and dark yellow, respectively) with bedsets of normally graded 1–2-cm silt-to-mudstone laminae (rose), 11 – thick bedsets of normally graded 1–2-cm silt-to-mudstone laminae, 12 – sandstone with beds of altered resedimented kimberlite (dark brown) and mudstone (rose), 13 – sandstone poorly cemented.

The diatreme to crater transition displays abrupt changes in lithology and rock attitude. The upper diatreme *Unit 2* is 4 to 44 m thick. It consists of frequent intercalation of quartz-free kimberlitic tuffs with variable particle sizes (granule, sand, silt to mud; normally graded beds are characteristic) – 80%, as well as breccias (30–60% xenoliths) and gneiss blocks – totally 20% by thickness (Fig. 2). Analysis of thickness and lithology of Unit 2 based on 23 boreholes showed no distinct centroclinal regularities. The finer grained rock attitude is very gentle to horizontal. We interpret the Unit 2 as a product of waning pyroclastic eruptions with variable intensity intermittently transporting very fine to coarser grains to the surface. Vertical fluid escape channels (probable ways of fines transportation to the surface) were encountered in the upper zone of the underlying pyroclastic kimberlite. Random debris flows provided gneiss clasts and blocks, however, their proportion in the Unit 2 does not exceed the average gneiss content in various rocks of the pipe (<15–20 vol %).

In contrast, volcanosedimentary sequence of the central depression begins with *Unit 6A* of complex structure and composition (Fig. 2). Its thickness is larger in the outer (particularly southern) part of the depression (30–100 m) and significantly decreases (2–15 m) towards the pipe center. This unit probably corresponds to the stage of most intense and rapid downwarping in the central depression with avalanche, slumping, and vast mud–sand flows, with extra-crater sand material generally transported from the south. The Unit 6A passes upward into *Unit 6B* with multiple intercalation of 0.3–1-m-thick beds of tuffaceous sandstone to sandstone and sets of several rhythmic laminae of silt- to mudstone. A 9–15-m-thick mudstone-rich layer occurs in the upper part of the unit. The rocks normally show abundant sedimentary structures (normal grading, parallel and cross-bedding, symmetrical ripple marks, mud cracks, load cast, current marks) indicating their fluvial and shallow lacustrine origin. These rocks deposited when the subsidence became slower. The *Unit 6C*, the uppermost unit of the volcanosedimentary sequence, comprises intercalation of sandstone with tuffaceous gravelstone enriched in strongly altered coarse pseudomorphs after olivine. It may have formed by reworking of the Unit 4 rocks locally exposed at the surface at that time. The *Unit 7* sandstone is devoid of kimberlitic components. It fills the uppermost part of the crater depression and is 105 m thick in its center. Significant deformations in this unit resulting in steep angles and several angular discordances indicate rather active subsidence within the crater even at this late stage of the pipe evolution. All other younger sediments are considered to be overlying and correlated with the *Calonda and Kalahari* deposits.

The Catoca pipe is unique in the abundance and intensity of post-emplacment deformations. The rocks of all crater-filling units (3 to 7) dipping now at high angles show evidence of their primary horizontal deposition. For example, the banded pyroclastic kimberlite of Unit 4 now dipping at about 40°–60° gradually and conformably passes upward into a sequence containing sand- to mudstone layers with equally steep dip angles. Figure 1 demonstrates broad centroclinal dipping at angles particularly high near the circular fault zone. This may indicate significant subsidence of the depression base during sedimentation. However, the formation of the 240-m-deep depression entirely by the gradual sinking from the pipe surface is now hardly explicable. Possibility and causes of significant compaction of pyroclastic material in the diatreme, which is necessary for such a process, should be a subject of comprehensive consideration. We could suggest a specific physical state of the diatreme infill – an olivine-rich low-density aqueous silicate suspension capable of significant compaction. Future studies may prompt the solution to this problem.

References

- Brown RJ, Gernon T, Stiefenhofer J, Field M (2008) Geological constraints on the eruption of the Jwaneng Centre kimberlite pipe, Botswana. *J Volcanol Geoth Res* 174:195–208
- Gernon TM, Field M, Sparks RSJ (2009) Depositional processes in a kimberlite crater: the Upper Cretaceous Orapa South Pipe (Botswana). *Sedimentology* 56:623–643
- Stiefenhofer J, Farrow DJ (2004) Geology of the Mwadui kimberlite, Shinyanga district, Tanzania. *Lithos* 76:139–160

The geology of the Liqhobong Main Pipe kimberlite

Mafusi Rapopo¹, Paul Sobie^{2,3}, Paul Bosma^{1,3}

¹ Liqhobong Mining Development Company, Butha Buthe, Lesotho, mafusie@gmail.com

² MPH Consulting Limited, Toronto, Canada, psobie@mphconsulting.com

³ Firestone Diamonds plc, Cape Town, South Africa, pbosma@firestonediamonds.com

Introduction

The 8.5ha circular Main Pipe is the largest of six known kimberlites comprising the Liqhobong cluster which occurs along a strike of approximately 2.5km. The cluster is part of the larger WNW trending mid-late Cretaceous Lemphane – Robert (L-R) Kimberlite Belt occurring in north-eastern Lesotho. The Liqhobong kimberlites intrude Jurassic Drakensberg lavas and outcrop at ~2650m above sea level. The Drakensberg lavas cover more than two thirds of Lesotho and rise to an altitude of 3500m above sea level with an estimated thickness of 1.5km, and are considered to be related to the breakup of Gondwana (Adelmann and Fiedler, 1996). The regional basement comprises Archean metasediments and metavolcanics of the Kaapvaal Craton.

Geology of the Liqhobong Main Pipe

The Main Pipe is a typical southern African diatreme with steep-sided walls abutting country rock basalt and is comprised of five lithofacies (K1, K2, K4, K5 and K6) distinguished in terms of variations in the matrix hardness, texture, magnetic susceptibility, degree of mantle sampling, dilution and alteration. More than 10km of core in 60 holes has been studied. The pipe's lithofacies are mostly tuffisic (massive volcanoclastic) kimberlite breccias and marginally hypabyssal kimberlite. The deepest core hole was drilled vertically at the centre of the pipe and ended in a tuffisic kimberlite at 650m below surface.

Kimberlite Indicator Minerals (KIMs) occurring as disaggregated xenocrysts are very rare but common as components of peridotite xenoliths. Olivine macrocrysts are conspicuous and more usefully indicative of degree of mantle sampling. All the lithofacies are universally diluted with Drakensberg fragments, and in two cases (K2 and K1)

contain xenolithic evidence for intruding through the basement.

K1, a tuffisic kimberlite breccia (TKB) which comprises approximately ~3% of the indicated resources (to -180m) was exposed during the current mining activity in the NW quadrant of the Pipe. The K1 lithofacies forms a shallow wedge striking NE (Fig. 1), and is recognised by its clayey texture with distinctive highly altered brown basalt and basement xenoliths, moderately abundant olivine macrocrysts, copious carbonate veining and infrequent pelletal lapilli.



Figure 1. The different lithofacies of the Main Liqhobong Kimberlite Pipe. The pipe's surface diameter is ~300m.

K2, the volumetrically most abundant lithofacies to 180m depth, is also a TKB with internal variations in the quantities of crustal xenoliths, olivine macrocrysts, degree of alteration and magnetic susceptibility that makes the unit divisible into two sub-lithofacies (termed TKB1 and TKB2 by previous workers). Both sub-lithofacies are characterised by none to pervasive carbonate segregations and veining (Fig. 2a), dark to dark brown olivine macrocrysts (up to 25%), ≤3% basement clasts, 10-30% basalt clasts and ≤7% peridotite xenoliths. Irregular, distinct localised areas with highly altered basement clasts as well as pockets with highly calcified or chloritised basalt (Fig. 2b) are present. The TKB1 and TKB2 sub-units are commonly

interlayered and distinguished by typical strong magnetic susceptibility, comparatively more altered basalt clasts and lower quantities of pelletal lapilli in the former and weak to nonmagnetic susceptibility and abundant pelletal lapilli in the latter. Rocks transitional between TKB1 and TKB2 are present. It has not yet been established whether diamond grade varies between TKB1 and TKB2.

K5 outcrops in the southwest through to eastern parts of the pipe and constitutes ~12% of the volume in the upper 180m of the pipe, below which it becomes the volumetrically most abundant lithofacies at the expense of K2. The lithofacies is mainly a tuffitic kimberlite breccia (termed TKB3 in the past) with virtually no pelletal lapilli and basement xenoliths, weak to moderate magnetic susceptibility, distinctive small black or dark brown olivine macrocrysts (Fig. 2c) and the most abundant peridotite micro-xenoliths in the Main Pipe. There is minor sub-facies of K5, a more magmaclastic kimberlite (TK1), which has in contrast very minimal crustal dilution, is non-magnetic, and has abundant cream to pale or golden yellow (serpentinised) olivine macrocrysts and phenocryst. The olivine microcryst population in TK1 reaches up to 25%. K5 generally has the highest diamond grade of the Main Pipe's lithofacies.

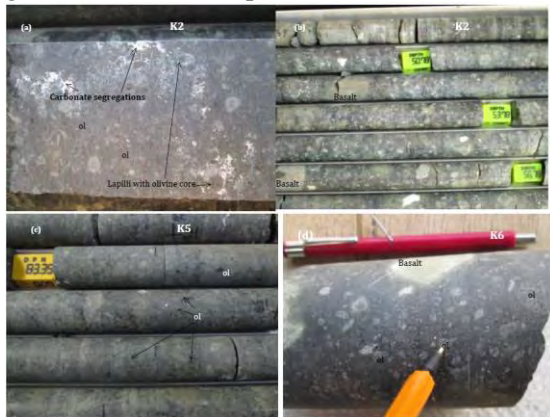


Figure 2. Drillcore samples of the selected lithofacies of the Main Pipe showing (a) carbonate segregations in K2, (b) greenish chloritised basalt clasts in K2, (c) numerous small black olivine macrocrysts in K5 and (d) numerous cream coloured fresh olivine macrocrysts in K6.

K4, a massive volcanoclastic kimberlite breccia constituting about 14% of the indicated resources, is characterised by a non- to weakly magnetic dark competent matrix, virtually no pelletal lapilli, moderately to highly serpentinised olivine macrocrysts and

phenocrysts and infrequent prominent KIM xenocrysts. Although KIM xenocrysts (garnet, Cr-diopside and ilmenite) are broadly infrequent, they are comparatively more abundant in K4 than in any other lithofacies of the Main Pipe.

K6 constituting ~4% of the indicated resources is differentiated by a strongly magnetic competent kimberlite matrix with abundant coarse-grained cream coloured olivine macrocrysts, no pelletal lapilli and no carbonate veining. Not only are the olivine macrocrysts in K6 fresh and uniquely cream in colour, but they are also commonly larger than 5mm in size (Fig. 2d).

Inter-lithofacies relationships

The inter-lithofacies' contacts range from sharp to gradational. K1 abuts onto K2 at a sharp contact inclined from 10 to 30° and in turn hosts K2 autoliths (Fig 3a). K2 has a sub-vertical gradational to indistinct contact with both K5 and K4, and there are some indistinct examples from drillcore where K5 autoliths are apparent in K2.

K4 in turn has a sharp contact with K5, with K5 overlying K4 at an apparent strike/dip angle of 332°/30° in the NE to SE of the Pipe (Fig. 3). K4 autoliths are also found in K5. A somewhat curvilinear slickenside plane with strike/dip angle of 339°/82° is positioned near the K4/K5



Figure 3. Contact relations between (a) K1 and K2 showing an inclined contact as well as K2 autoliths in K1 and (b) K4 and K5 with a clear matrix

competence and colour difference between the two lithofacies on the same bench.

contact and more developed within the more competent K4 lithofacies.

K6 has a gradational contact with K5 in the south of the Pipe marked by a change in the colour and size of olivine macrocrysts and an increase in the magnetic susceptibility. Globular enclaves of K4 are found in K6.

From these sequences, it can be deduced that the intrusive order of emplacement is K4>K6>K5>K2>K1; the first two being largely more magmaclastic kimberlites and the last three being tuffitic kimberlite breccias.

On average, the order of specific gravities is K1<K2<K4<K5<K6, ranging from 2.25 to 2.77g/cm³. The density sequence agrees with the overall abundance of olivine macrocrysts and, with the exception of K6 which has seen minor bulk sampling, mirrors the relative order of diamond grades. With all facies combined, the Main Pipe has an average +1.25mm grade of 23cph.

Discussion

There are numerous mutual similarities between the different lithofacies of the Main Pipe. Country rock basalts are universal in all the lithofacies while basement gneisses and schists are found mainly in K1 and K2 and very occasionally in K4 and K5. The basalt clasts range from fresh to highly altered in K5, K2 and K1, whereas those in K4 and K6 are commonly fresh or minimally chloritised in K4. K2 and K1 lithofacies host generally dark brown to black olivine macrocrysts whereas those in K4 and K6 are cream in colour, unless serpentinitised to golden yellow or greenish colour in K4. Both K2 and K5 have localised zones of basalt brecciation rich in carbonate matrix whereas the basalt breccia in K4 is generally 'dry'. K2 and K5 characteristically exhibit intra-lithofacies variations whereas each of K4 and K6 is fairly homogeneous.

From these observations and relationships, it appears that K5, K2 and K1 are may be genetically related while the older K4 and K6 may also be related.

Conclusions

The gradational K2/K5, K2/K4 and K5/K6 contacts suggest near synchronous intrusions

whereas the sharp K2/K1 and K4/K5 contacts suggest successive magma pulses.

The fairly dark and competent nature of the kimberlite matrix of K4 and K6, their unique cream coloured olivine macrocrysts as well as the presence of comparatively more abundant KIM xenocrysts in K4 suggest different magma sources and different routes to emplacement for K4 and K6 than for K1, K2 and K5.

Both K4 and K6 accounting for less than 15% of the pipe volume are thought to represent earlier melts which either originated from low volume melts or are remnants of earlier pulses slumped into the later comparatively more fluidised K5 intrusion. The absence of K4 and K6 autoliths in the more fluidised K2 favour both K4 and K6 being slumped kimberlites of earlier pulses. The inclined contact between K4 and K5 suggests K4 likely represents a remnant of an earlier pulse. The more magmaclastic nature of K4 and K6, their generally similar olivine macrocrysts populations and kimberlite matrix suggest they could be related.

The overall similarity in the K5, K2 and K1 lithofacies suggest that they represent similar magma sources which were distinguished by the difference in fluid budget. The K5 being younger than K4 and K6 was followed almost synchronously by the intrusion of more fluidised pelletal lapilli-rich K2. K2 and K1 appear to represent the most violent (e.g Brown et al., 2006) and fluidised intrusions, erupted at the mantle-crust interface incorporating basement clasts, with the more tuff-like clayey K1 culminating intrusive activity at the Main Pipe seen at this exposure level of the diatreme. Since the second youngest K2 and oldest K4 lithofacies show gradational contacts, it is more likely that all the lithofacies erupted at closely spaced times.

References

- Adelmann D, and Fiedler K (1996). Sedimentary development of the Upper Ecca and Lower Beaufort Groups (Karoo Supergroup) in the Laingsburg subbasin (SW Karoo Basin, Cape Province/South Africa), *Schriftenreihe der Deutschen Geologischen Gesellschaft* 1: 88-89, Bonn.
- Brown RJ, Tait M, Field M, Sparks RSJ (2006). Progressive enlargement and infill of a kimberlite pipe: K2 pipe, Venetia Kimberlite Field, Limpop Province, South Africa; In *Proceedings of the International Conference, Saskatoon*.



The Petrology and Mineralogy of the Kimberlite Blow in Letšeng-la-Terae: Implication for its Parent Magma Composition

Natalia Stamm and Max W. Schmidt

ETH Zurich, Institute of Geochemistry and Petrology, Zurich, Switzerland, natalia.stamm@erdw.ethz.ch, max.schmidt@erdw.ethz.ch

Introduction

Letšeng-la-Terae, situated in the Maluti Mountains of Lesotho, Southern Africa, is famous for its large high-value, top quality diamonds hosted in two rather low-grade kimberlite bodies (Bowen et al. 2009). Several diatreme facies can be distinguished in the Main and Satellite pipes but fluids altered and overprinted most of the deposits, obfuscating the characteristics of the parent magma. In the vicinity of the two pipes, a kimberlite blow intruded the flood basalts of the Drakensberg. Also the kimberlite blow exhibits various degrees of alteration, captured in different stages of olivine degradation. Nevertheless, an unusual fresh macrocryst-rich sample could be recovered with only slightly serpentinized olivine, fresh groundmass monticellite and symplectitic intergrowth of calcite and apatite, indicating very little syn- and post-emplacement modifications. For this sample we studied mineral, groundmass and bulk compositions with the aim to identify the parent kimberlite melt of Letšeng.

The Xenolithic Suite of the Kimberlite Blow

Mineral compositions of macrocryst and groundmass phases were measured by electron microprobe and LA-ICP-MS. In combination with textural observations, we were able to discriminate between xenolithic and primary phases.

Anhedral, rounded olivine macrocrysts (>1 mm) have homogenous either relatively Fe-rich ($Fe_{<83}$) or Mg-rich ($Fe_{>89}$) cores. Regardless of their core compositions, they all exhibit thin (<50 μm) overgrowth rims of $Fe_{\sim 87}$. This compositionally homogenous overgrowth indicates that the cores of these olivine macrocrysts were in disequilibrium with the host melt. They were hence picked up during ascent, Fe-rich cores fits with the megacryst suite supposed to be formed at the base of the lithosphere (Hops et al. 1992). Olivine with Fe_{89-91} and ~2900 ppm Ni are peridotitic olivines (Fe_{89-92} , 2800–3100 ppm Ni, Herzberg et al. 2013) and Mg-rich olivines with $Fe_{>92}$ represent depleted (harzburgitic/dunitic) mantle (Bernstein et al. 2007). After entrainment, the overgrowth rims crystallized from the kimberlite magma.

Resorbed orthopyroxene macrocrysts are less common than olivine. They are bronzitic in composition (Mg# of 87.5) and are akin to the megacryst suite, together with the Fe-rich olivines. Orthopyroxene cores are rimmed by a reaction corona, which consists of olivine, serpentine, K-richterite, diopside and mica. Assuming that this reaction corona was formed by the disequilibrium between the kimberlite melt and the entrained orthopyroxene, the melt would need to be fairly alkaline to form K-richterite containing 4.1–4.6 wt% Na_2O and 3.9–4.3 wt% K_2O .

The Groundmass Assemblage of the Kimberlite Blow

Subhedral to euhedral olivine microcrysts (<0.5 mm) are homogeneous in composition (Fe_{86-88}). They are primary, crystallized from the kimberlite melt and constitute by far the largest groundmass phase, which has otherwise mineral sizes <100 μm . Olivine crystallization is followed by spinel with initially Cr-rich composition, changing to magnesio-ulvöspinel and finally magnetite. These three stages are manifested in overgrowth of the earlier spinel generation(s) but also by additional nucleation (Fig. 1). Perovskite crystallized together with magnesio-ulvöspinel. Trace element compositions measured in perovskite indicate that this mineral is the main host of rare earth and HFS elements. Groundmass

perovskite and spinel were also used for high-precision U-Pb dating. Perovskite was dated using ID-TIMS, spinel used for initial Pb correction, yielding an emplacement age of the kimberlite blow of 85.5 ± 0.3 (2σ) Ma. Fresh monticellite, Sr-rich carbonate and phlogopite subsequently crystallized from the kimberlite magma, followed by apatite and calcite (Fig. 1). The mineral compositions and observed crystallization sequence suggest that the groundmass phases are primary and best represent the kimberlite melt at near-surface conditions.

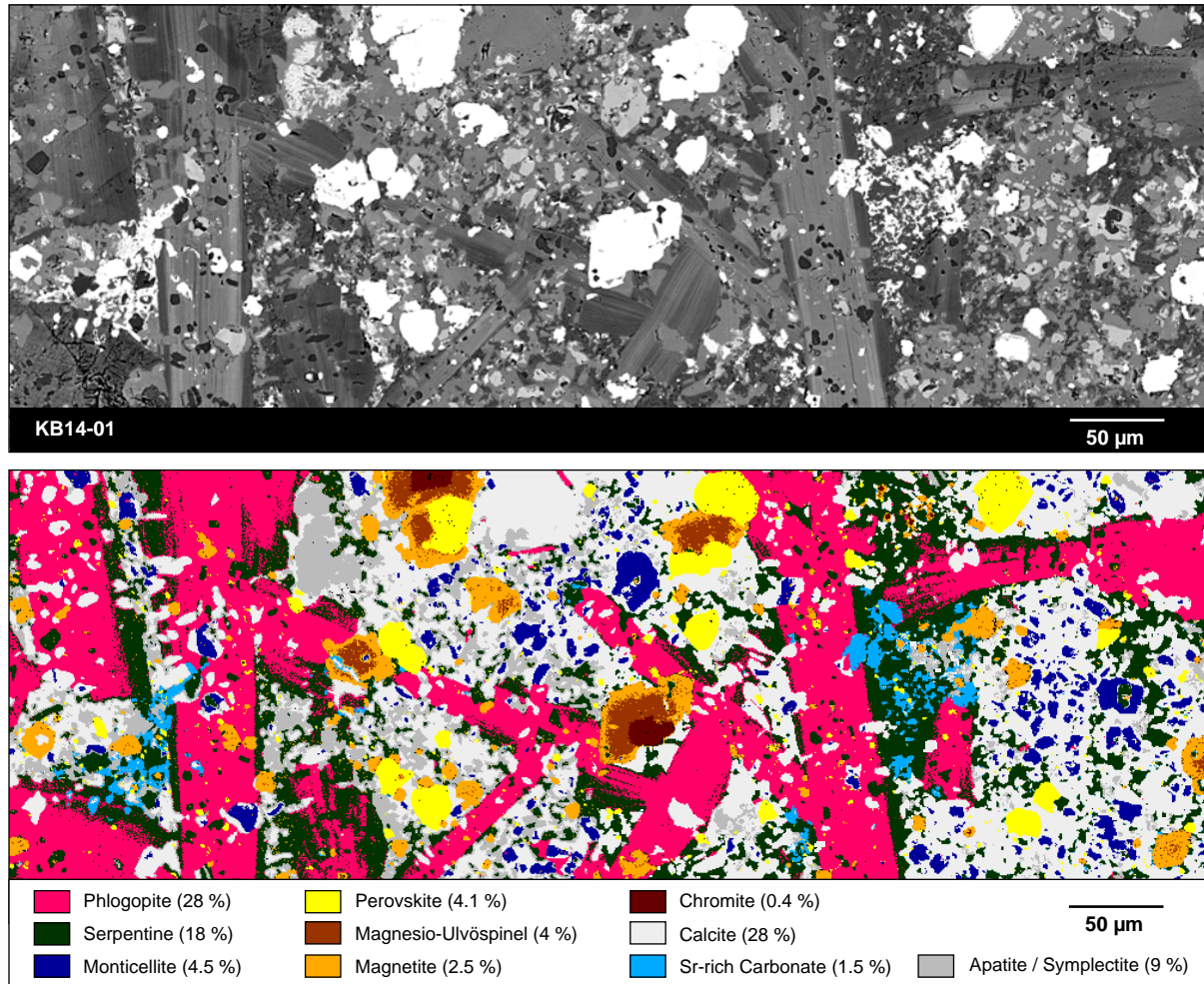


Figure 1: Groundmass characteristics of the kimberlite blow. BSE image showing representative section of the groundmass with corresponding phase map created using the iSpectra toolbox (Liebske 2015). Percentages in the legend indicate the phase abundance present in this particular section. Olivine with grain sizes >0.1 mm is not shown.

Bulk Rock Composition of the Kimberlite Blow

Because the kimberlite blow contains 20–36 vol% xenolithic olivine, orthopyroxene and minor microxenoliths, whole-rock geochemistry does not correspond to the parent magma composition. Nevertheless, to assess heterogeneity, three whole-rock analyses were performed and compared to the groundmass composition. Groundmass was extracted from six thick sections by micro-drilling and analyzed for its bulk composition.

The groundmass bulk has 24–26 wt% SiO_2 , 3.3 wt% TiO_2 , 2.7–2.9 wt% Al_2O_3 , 10–11 wt% FeO_{tot} , 660–1010 ppm Cr, 400–550 ppm Ni, 0.2 wt% MnO, 20–21 wt% MgO, 16–19 wt% CaO, 0.1 wt% Na_2O , 1.9–2.1 wt% K_2O and 1.0–1.3 wt% P_2O_5 . Resulting Mg# of 77.9 ± 0.2 (1σ) and MgO/CaO of 1.1–1.4 are lower than the whole-rock (Mg# of 79.9 ± 1.3 (1σ) and MgO/CaO of 1.7 ± 0.2 (1σ)), which approximates the close-to-primary composition proposed for Group-I kimberlites from South

Africa (Mg# of 84 and MgO/CaO of 1.9, Becker and Le Roex 2006). The low Mg# in combination with low Ni might suggest olivine fractionation along the ascent. However, much higher Ni concentrations are unrealistic in the Letšeng melt and the low Mg and Ni are probably parental. Primitive-mantle normalized trace element patterns (Fig. 2) overlap with proposed close-to-primary Group-I kimberlites (Becker and Le Roex, 2006), except for higher Rb, Ba, K and especially Sr. Isotopic compositions of the kimberlite blow with $^{87}\text{Sr}/^{86}\text{Sr}_{(i)}$ of 0.703602–0.703656, $^{144}\text{Nd}/^{143}\text{Nd}_{(i)}$ of 0.512660 and $^{176}\text{Hf}/^{177}\text{Hf}_{(i)}$ of 0.282671–0.282749 clearly classify Letšeng as Group-I kimberlite; the elevated concentrations of LILE are likely a primary characteristic of Letšeng.

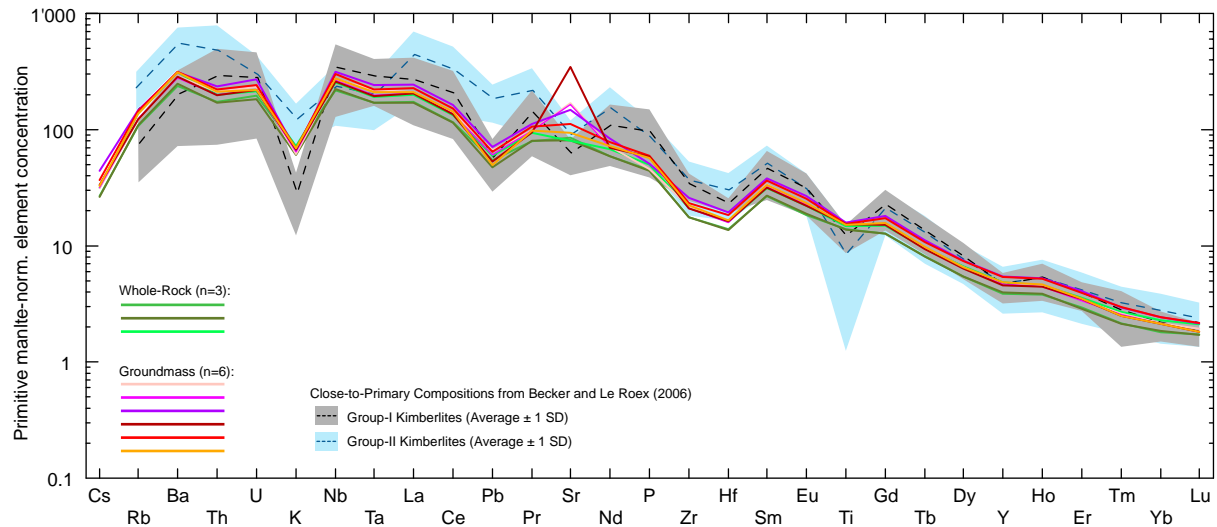


Figure 2: Trace element compositions of the kimberlite blow shown as primitive mantle-normalized element concentrations (normalized after Sun and McDonough, 1989). The three whole-rock and six groundmass analyses are compared with close to primary compositions from Becker and Le Roex, 2006.

The characteristic mineral assemblage with equilibrium olivine microcrysts and the observed major and trace element concentrations complement each other such that the groundmass composition of the kimberlite blow can be regarded as plausible parental melt of the Letšeng kimberlite. However, degassing certainly occurred along the ascent, reducing volatiles and possibly removing some alkalis.

Acknowledgment: We want to express our cordial thanks to Letšeng Diamonds (Pty.) Ltd. for permitting access to the mining area and the possibility of rock sampling.

References

- Becker M, Le Roex AP (2006) Geochemistry of South African On- and Off-craton, Group I and Group II kimberlites: Petrogenesis and Source Region Evolution. *J Petrol* 47(4):673-703
- Bernstein S, Kelemen PB, Hanghoj K (2007) Consistent olivine Mg# in cratonic mantle reflects Archean mantle melting to the exhaustion of orthopyroxene. *Geology* 35(5):459-462
- Bowen DC, Ferraris RD, Palmer CE, Ward JD (2009) On the unusual characteristics of the diamonds from Letšeng-la-Terae kimberlites, Lesotho. *Lithos* 112:767-774
- Herzberg C, Asimow PD, Ionov DA, Vidito C, Jackson MG, Geist D (2013) Nickel and helium evidence for melt above the core-mantle boundary. *Nature* 493(7432):393-398
- Hops JJ, Gurney JJ, Harte B (1992) The Jagersfontein Cr-poor megacryst suite – towards a model for megacryst petrogenesis. *J Volcanol Geoth Res* 50(1-2):143-160
- Liebske C (2015) iSpectra: An Open Source Toolbox For The Analysis of Spectral Images Recorded on Scanning Electron Microscopes. *Microsc Microanal* 21(4):1006-1016
- Sun SS, McDonough WF (1989) Chemical and isotopic systematics of oceanic basalts: Implications for mantle composition and processes. Geological Society, London, Special Publications 42:313-345



The Life Cycle of Diamondiferous Cratons - A Leitmotif with Infinite Regional Variations

Herwart H. Helmstaedt

Queen's University, Kingston ON, Canada, helmstaedt@queensu.ca

Introduction

The evolution of most primary diamond deposits is multi-stage and intricately linked to the tectonic histories of their host cratons and their lithospheric and sublithospheric underpinnings. Yet the integration of the surface geological record of diamondiferous cratons with the complexities observed within the diamond and xenolith populations of their primary igneous hosts (kimberlites, lamproites, etc.) remains a major challenge for both diamond explorers and tectonicians interested in craton formation. A comparison of primary diamond deposits on different cratons shows that whilst processes leading to the formation of such deposits have operated worldwide, the timing of individual diamond-forming events and transport to the surface are craton specific. The recurring theme emerging from such comparisons involves five broad stages, referred to below as life cycle of diamondiferous cratons (Fig. 1). For an economic primary diamond deposit to form and survive to be mineable, the balance between diamond-friendly and diamond-unfriendly events during all stages of this cycle should be in favor of diamond survival. However, judging from the relatively small number of “high-grade” primary diamond mines, this was not the rule. Comparative step-wise craton analyses, integrating detailed geological evolution and geophysical settings with studies of the upper mantle sample from many deposits, bring out similarities and differences and assist in better evaluating the effects of terrane accretion, regional “granite blooms”, rifting and plume events, etc. on the diamond potential of the cratons. This helps to establish more realistic diamond deposit models for area selection and provides important feedback for tectonic models of craton evolution.

| | | |
|----------------|--|--|
| Stage 1 | Earliest subcontinental lithosphere development with depleted roots and harzburgitic P-type diamonds. Proto-continental nuclei. | >3 Ga |
| Stage 2 | Amalgamation of early nuclei and formation of first E-type diamonds. First detrital diamonds appear in sedimentary record and primary igneous rocks. Early roots must survive accretion of Neoproterozoic greenstone terrains, various “granite blooms” and other diamond-unfriendly events. Cratonization , greatest extent of Archean cratons. | ~3 Ga ~2.5 Ga |
| Stage 3 | Post-Archean break-up of Archean cratons , fragments become involved in Proterozoic (and Phanerozoic) orogenic events and supercontinent cycles. Archean craton roots are affected again by various mantle root-friendly or unfriendly tectonic and magmatic events, either diminishing diamond content of lithospheric source rocks or enhancing it by the addition of Proterozoic E-type or, more rarely, by lherzolitic P-type diamonds. | <2.5 Ga |
| Stage 4 | Archean cratons may be intruded by one or more generations of kimberlites or lamproites . Such events may be accompanied or preceded by metasomatic alterations within or below the diamondiferous lithospheric roots. They may also be preceded by growth of late-stage amber or fibrous diamonds (type Ib). Sub-lithospheric diamonds may be picked up by kimberlites at this stage. | kimberlite or lamproite emplacement |
| Stage 5 | Includes all geological factors controlling the preservation of diamondiferous kimberlites or lamproites and the dispersal of indicator minerals. | Post- emplacement |

Figure 1: Generic life cycle of a diamondiferous craton.

Discussion of Stages:

Stage 1 involves the formation of the harzburgitic P-type diamond paragenesis, yielding the bulk of the diamond budget in many mines worldwide, but present in all economic kimberlites and lamproites, even though recognizable in some of the latter only as remnants included in diamond (e.g. Argyle, Ellendale, Bunder). Where dated, it has consistently yielded >3 Ga ages (Gurney et al. 2010), which together with the worldwide association of P-type diamond deposits with > 3.0 Ga protocratons gave rise to the model that such protocratons were coupled to Mesoarchean roots prior to 3 Ga (e.g. Helmstaedt et al. 2010). Nevertheless, the significance of ancient diamond inclusion ages remains controversial, as on the Slave craton, where ca. 3.3 to 3.5 Ga Re-Os isochron ages of sulfide inclusions in Panda and Diavik diamonds (e.g. Westerlund et al. 2006; Aulbach, 2009) were reinterpreted as mixing lines, compatible with Slave subcontinental lithospheric mantle (SCLM) formation at ca. 2.75 Ga (Heaman and Pearson 2010). However, models of craton construction based on these younger SCLM formation ages (e.g. Snyder et al. 2017) are incompatible with the ever increasing evidence for much earlier crust-mantle coupling on most diamondiferous cratons.

Stage 2 begins with the interactions between the proto-continental nuclei, involving various amalgamation and break-up events, and ending with cratonization at the end of the Archean. For the harzburgitic roots, this stage is the beginning of a long survival story, and histories of individual protocratonic nuclei diverge on different cratons and different regions of individual cratons. The oldest E-type diamond-forming events fall into this stage (Kaaivaa, Siberia) and are related to ca. 3.0 to 2.5 Ga accretion of Paleoproterozoic continental nuclei, each underpinned by a potentially P-type diamond bearing lithospheric root, into composite Archean cratons. Interactions between the continental nuclei involved subduction of intervening seafloor, partial melting of hydrated oceanic crust, and widespread formation of tonalite. The geological surface record shows accretion of up to several ages of greenstone sequences, turbidite basins, regional metamorphism, and various granitic intrusive events, some of which form regionally extensive “granite blooms”. The formation of local rift basins may precede or accompany cratonization. On the Kaaivaa craton, lithosphere was thick enough for primary diamond deposits to be emplaced and recycled into ca. 2.9 Ga Witwatersrand deposits (e.g. Smart et al., 2016). On the Slave craton, the oldest cover sequence on the Mesoproterozoic Central Slave superterrane is slightly younger (ca. 2.8 Ga), but it has also yielded detrital diamonds (Jackson, 1997), hinting at the existence of an earlier Slave root. Early roots survived best where the older nuclei remained in the footwall during Neoproterozoic terrane accretion and greenstone belt emplacement (e.g. the eastern part of the Central Slave superterrane was overridden by the Contwoyto terrane; the southern part of the Zimbabwe craton was overthrust by the Northern Marginal Zone of the Limpopo belt). Major “granite blooms” have occurred on most cratons prior to cratonization. Although they had profound effects on crustal differentiation, they generally did not diminish the diamond potential in the lithospheric roots.

Stage 3: Archean cratons reached their greatest extents prior to Proterozoic break-up. After break-up, the tectonic settings of the kimberlitic and lamproitic deposits diverged significantly. Survival of roots depends on size of Archean craton fragments. Future sites of diamondiferous kimberlite remained well within the early Archean nuclei of their respective cratons, while passive rifting occurred at craton margins, whereas those of lamproitic deposits are located near the rifted margins of their respective cratons. Proterozoic convergent tectonism locally underplated eclogites from the craton margin (e.g. Slave craton kimberlites). Eclogites were also added to pre-existing P-type roots under lamproites by an as yet unknown mechanism (e.g. Argyle). Plumes impacting on diamondiferous cratons have a detrimental effect on the diamond potential.

Stage 4: This stage involves the analysis of the geotectonic and structural settings of the country rocks from the craton to local scales at the time of and leading up to kimberlite or lamproite eruption. The question whether plumes have an important role in triggering kimberlite and lamproite magmatism has been debated at length in the literature (e.g. Helmstaedt and Gurney 1997; Jelsma et al. 2009), but from detailed examinations of the structural setting of many kimberlites and lamproites, it is unlikely that their emplacement was directly triggered by plumes. For example, since the latest Precambrian at least

six generations of kimberlites on the Slave craton were intruded while the craton was essentially near sea level. Both of the two most recent plumes known to have impacted the northern margin of the craton, are of Mesoproterozoic (Mackenzie plume, ca. 1270 Ma) and Neoproterozoic (Franklin plume, ca. 720 Ma), the latter predating the oldest kimberlites by at least 100 m.y. On the other hand, a strong case has been made recently for the 75 to 45 Ma Lac de Gras kimberlites, that low-angle subduction along the western continental margin of North America is implicated in having provided fluids for late fibrous diamond formation and triggering of the kimberlite magmatism (Weiss et al. 2015; Currie and Beaumont 2011). However, plumes may have played a role in having metasomatized and fertilized the mantle at some time prior to the kimberlite magmatism. Detailed tectonic analyses in combination with studies of the upper mantle sample are necessary to examine this possibility.

Stage 5: Of crucial importance for a successful diamond exploration program is the post-emplacement history of kimberlites and lamproites. Exploration geologists must identify what geological factors were responsible for the preservation of the diamondiferous host rocks and what processes controlled the dispersal of the indicator minerals.

References

- Aulbach, S., Stachel, T., Creaser, R.A., Heaman, L.M., Shirey, S.B., Muehlenbachs, K., Eichenberg, D., Harris, J.W. (2009) Sulphide survival and diamond genesis during formation and evolution of Archaean subcontinental lithosphere: A comparison between the Slave and Kaapvaal cratons. *Lithos*: 112, 747–757.
- Currie, C.A., and Beaumont, C. (2011) Are diamond-bearing Cretaceous kimberlites related to low-angle subduction beneath western North America? *Earth and Planetary Science Letters*: 303, 59-70.
- Gurney, J.J., Helmstaedt, H.H., Richardson, S.H., Shirey, S.B. (2010) Diamonds through Time. *Economic Geology* 105: 689-712.
- Heaman, L. M., and Pearson, D. G. (2010) Nature and evolution of the Slave Province subcontinental lithospheric mantle. *Canadian Journal of Earth Sciences*: 47, 369-388.
- Helmstaedt, H.H., Gurney, J.J. Richardson, S.H. (2010) Ages of cratonic diamond and lithosphere evolution: constraints on Precambrian tectonics and diamond exploration. *The Canadian Mineralogist*: 48, 1385-1408.
- Helmstaedt, H. H. and Gurney, J. J. (1997) Geodynamic controls of kimberlites - What are the roles of hotspot and plate tectonics? *Russian Geology and Geophysics*: 38, 492-508.
- Jackson, V.A, (1997) Preliminary geology of the Tree River area with descriptive notes, parts of NTS 86 P/1, 2 and 8: Geology Division, Department of Indian Affairs and Northern Development, Yellowknife, N.W.T., EGS Open file 1997-14.
- Jelsma, H., Barnett, W., Richards, S., Lister, G. (2009) Tectonic setting of kimberlites. *Lithos*: 112S, 155–165.
- Smart, K.A., Tappe, S., Stern, R.A., Webb, S.J., and Ashwal, L.D. (2016) Early Archean tectonics and mantle redox recorded in Wiwatersrand diamonds. *Nature Geoscience*: 9, 255-259.
- Snyder, D.B., Humphreys, E., Pearson, D.G. (2017) Construction and destruction of some North American cratons. *Tectonophysics*: 694, 464-485.
- Weiss, Y., McNeill, J., Pearson, D.G., Nowell, G.M., Chris J. Ottley., C.J. (2015) Highly saline fluids from a subducting slab as the source for fluid-rich diamonds. *Nature*: 524, 339-342

Redox state of Archean kyanite/corundum eclogites and garnet pyroxenites from Bellsbank, South Africa

Heidi E. Höfer^{1*}, Gerhard P. Brey¹, Qiao Shu², Christian R. Heckel¹, Prokopy Vasilyev³

¹Institut für Geowissenschaften, Goethe-Universität, Frankfurt, Germany,
hoefer@em.uni-frankfurt.de, brey@em.uni-frankfurt.de, heckchri@web.de

²Dept. Earth Atmospheric Sciences, University of Alberta, Edmonton, Canada, qshu1@ualberta.ca

³John de Laeter Centre, Curtin University, Perth, Australia, prokopy.vasilyev@curtin.edu.au

*presenting author

Introduction

Oxygen fugacity determines the carbon species in eclogites and garnet pyroxenites and, with it, the transport properties of carbon and its role in the Earth's carbon cycle and as a host of diamond. The recently developed oxybarometers allow the estimation of oxygen fugacity of such rocks. One is based on the compositions of coexisting garnet (grt), clinopyroxene (cpx) and coesite (Stagno et al. 2015) and the other on the composition of garnet coexisting with kyanite (ky) and coesite (Vasilyev 2016). The oxygen fugacity of rare orthopyroxene-bearing garnet pyroxenites can be estimated with another oxybarometer based on coexisting garnet, orthopyroxene and olivine (Stagno et al. 2013).

The investigated samples

Aluminous eclogites containing kyanite and/or corundum (cor) from the Bellsbank diamond mine were interpreted as subducted troctolites and layered gabbros (Shu et al. 2016). They consist of grossular-rich garnets (orange brown), jadeite-rich clinopyroxenes (pale green) and pink corundum and/or blue kyanite (Fig. 1a). Garnet compositions are shown in Fig. 2 in a CaO-Cr₂O₃ diagram.

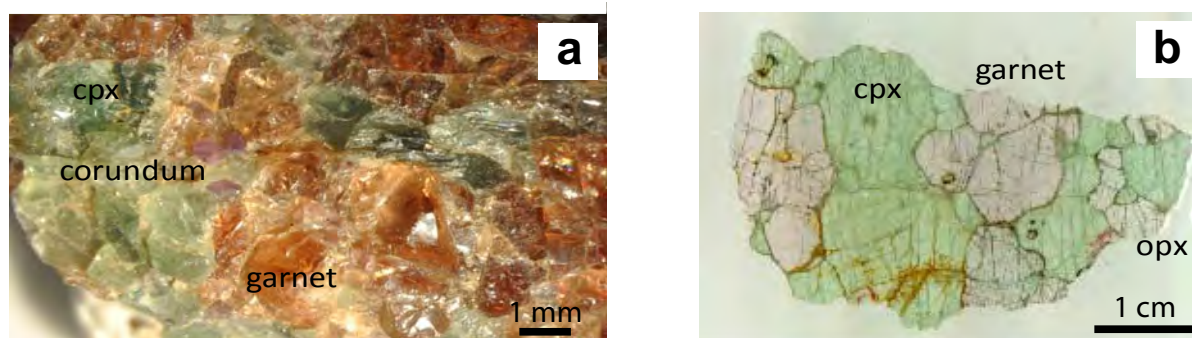


Figure 1: Corundum bearing eclogite xenolith from the Bellsbank diamond mine (a) and a polished thin section of an opx-bearing garnet pyroxenite (b)

These eclogites stem from depths between 150 and 200 km (Fig. 3). Low $\delta^{18}\text{O}$ values below the mantle value indicate high temperature seafloor alteration of the precursor rocks. Depleted LREE patterns witness partial melting between 5 to 30 % in the eclogite stability field after metamorphism. Very unradiogenic $^{87}\text{Sr}/^{86}\text{Sr}$ ratios as low as 0.70076 require a minimum age of 3 Ga of these eclogites. Compared to cumulates of modern oceanic crust, the V and Cr systematics of the reconstructed bulk rocks indicate more reducing conditions during their original magma history. The application of partition coefficients obtained by Mallmann and O'Neill (2009) to these systematics yields a $\Delta\log(f\text{O}_2)$ of -2 compared to the FMQ buffer for the eclogites and of zero for modern day oceanic crust cumulates.

A second type of high-pressure mafic xenoliths from Bellsbank are opx-bearing garnet-pyroxenites (Fig. 1b) that appear transitional to garnet peridotites. They consist of red, pyrope-rich garnets with Cr₂O₃ varying between 1.2 and 6 wt% (Fig. 2), green clinopyroxenes, greyish orthopyroxenes and occasionally olivine. They are from shallower depths between 110 and 140 km (Fig. 3).

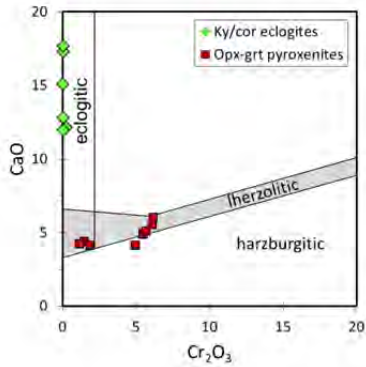


Figure 2: CaO versus Cr₂O₃ (wt%) in garnet

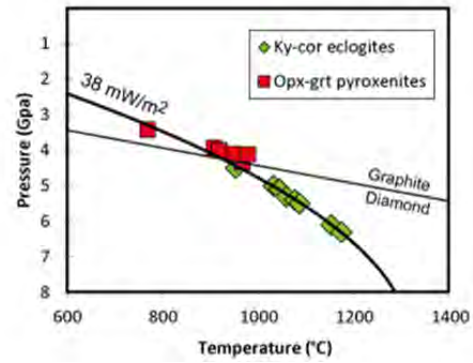


Figure 3: P,T-conditions of Bellsbank ky-cor eclogites (Shu et al. 2016) and opx-grt-pyroxenites. The latter were calculated with the methods of Brey & Köhler (1990) and Harley (1984).

Analytical technique for in situ ferric iron determination

The oxidation state of Fe was determined in garnet by the flank method (Höfer and Brey 2007). The flank method uses the concomitant change of both the intensity and the wavelength of the soft FeL α and FeL β emission lines in the electron microprobe to obtain the Fe³⁺/ Σ Fe ratio (Fig. 4). The comparison with Mössbauer spectroscopy is very favourable with similar errors for both methods (Fig. 5). The error bars indicate that the “limit of detection” for both methods is about 0.02.

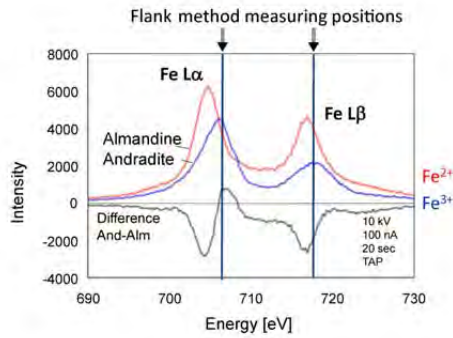


Figure 4: Fe L emission spectra of almandine and andradite and their difference spectrum.

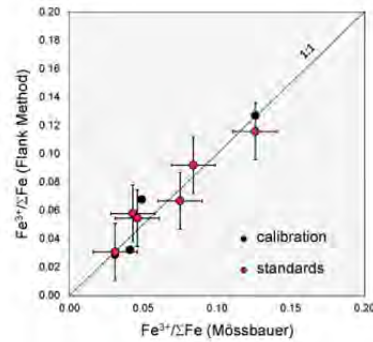


Figure 5: Calibration and comparison of the flank method with Mössbauer spectroscopy

Results and discussion

The Fe³⁺/ Σ Fe values of the ky/cor-bearing eclogites are lower than 0.02 for 5 samples (Table 1). We have used the value of 0.02 to calculate oxygen fugacities for these garnets with very little Fe³⁺. The calculations were done with the oxybarometer of Vasilyev (2016) calibrated for kyanite bearing samples and the results are plotted in Fig. 6. The $\Delta\log(fO_2)$ (FMQ) values are around -2 which are maximum values because of the reduced activity of SiO₂ in our rocks (no coesite) and because the real Fe³⁺/ Σ Fe values are lower than 0.02. The assumption of a SiO₂ activity of 0.5 lowers the calculated oxygen fugacity by about 0.2 log units.

| Ky/cor eclogite | BE1 | BE6 | BE11 | BE13 | BBm | BBs | BBu | BBw |
|--------------------------------|-------|-------|-------|-------|-------|-------|-------|-------|
| Fe ³⁺ / Σ Fe | 0.023 | 0.024 | 0.034 | 0.008 | 0.009 | 0.009 | 0.007 | 0.009 |
| Opx-grt-pyroxenite | 60BB | 61BB | 62BB | 63BB | 64BB | 65BB | | |
| Fe ³⁺ / Σ Fe | 0.057 | 0.093 | 0.022 | 0.029 | 0.020 | 0.038 | | |

Table 1: Fe³⁺/ Σ Fe determined with the flank method

We have applied the oxybarometer of Stagno et al. (2013) for peridotites to the opx-bearing grt-pyroxenites which is applicable to samples with Ca-poor and Cr-rich garnets. The $\text{Fe}^{3+}/\Sigma\text{Fe}$ values of these garnets vary between 0.02 and 0.09 (Table 1) and the calculated $\Delta\log(f\text{O}_2)(\text{FMQ})$ values range between -1 and -4 (Fig. 6). They overlap with those of the ky/cor-bearing eclogites whereby the aluminous eclogites mainly fall into the diamond field and the grt-pyroxenites into the graphite field. Two eclogites from Roberts Victor (Stagno et al. 2015) also plot in the graphite field (Fig. 6). Both graphite and diamond bearing eclogites have been described from Bellsbank and Roberts Victor. It is noteworthy and important that the various versions of oxybarometers for different types of eclogites yield a congruent data set and share the same range of $\Delta\log(f\text{O}_2)(\text{FMQ})$ values derived from garnet peridotites in the Kaapvaal craton as shown in Fig. 6 (after Stagno et al. 2015).

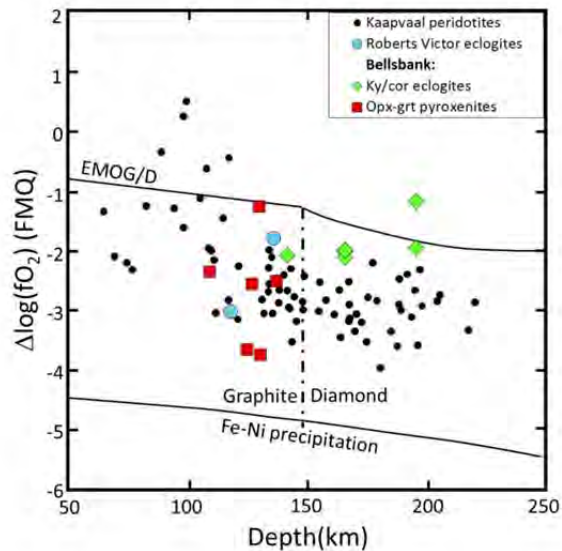


Figure 6: Variation of $\Delta\log f\text{O}_2$ with depth for the studied xenoliths from Bellsbank plotted with Kaapvaal peridotites and Roberts Victor eclogites (Stagno et al. 2013, 2015). The position of the EMOG/D buffer relative to FMQ is given for comparison.

Why do the ky/cor-bearing eclogites contain hardly any Fe^{3+} ? Shu et al. (2016) had estimated a $\Delta\log(f\text{O}_2)(\text{FMQ})$ of -2 for the precursor magmas of these aluminous eclogites which overlaps with the maximum possible value from the present study. The eclogites have a history of high temperature sea floor alteration (low $\Delta^{18}\text{O}$ values), subduction, high pressure metamorphism and partial melting. The earlier low-pressure processes potentially may or may not lead to oxidation at times before the great oxidation event but high-pressure partial melting leads to loss of Fe^{3+} which leaves a more reduced residuum. All these processes most likely led to a net result with lower Fe^{3+} and equilibration at lower oxygen fugacity than in the precursor rocks.

References

- Höfer HE and Brey GP (2007) The iron oxidation state of garnet by electron microprobe: Its determination with the flank method combined with major-element analysis. *Am Min* 92: 873-885
- Mallmann G, O'Neill HStC (2009) The crystal/melt partitioning of V during mantle melting as a function of oxygen fugacity compared with some other elements (Al, P, Ca, Sc, Ti, Cr, Fe, Ga, Y, Zr and Nb). *J Petrol* 50(9):1765–1794
- Shu Q, Brey GP, Hofer H, Zhao Z, Pearson DH (2016) Kyanite/corundum eclogites from the Kaapvaal Craton: subducted troctolites and layered gabbros from the Mid- to Early Archean. *Contrib Mineral Petrol* (2016) 171: 11-24
- Stagno V, Ojwang DO, McCammon CA, Frost DJ (2013) The oxidation state of the mantle and the extraction of carbon from the Earth's interior. *Nature* 493: 84-88
- Stagno V, Frost DJ, McCammon CA, Mohseni H, Fei Y (2015) The oxygen fugacity at which graphite or diamond forms from carbonate-bearing melts in eclogitic rocks. *Contrib Mineral Petrol* (2015) 169:16
- Vasilyev P (2016) The oxidation state of deeply subducted, altered oceanic crust: An experimental study and the evidence from natural samples. PhD thesis Canberra



Construction and destruction of some North American cratons

David Snyder^{1,3}, Gene Humphreys², Graham Pearson³

¹*Geological Survey of Canada (retired), Ottawa, Canada, dbsnyder1867@gmail.com*

²*University of Oregon, Eugene, OR, USA, genehumphreys@gmail.com*

³*University of Alberta, Edmonton, AB, Canada, gdpearso@ualberta.ca*

Introduction

Deep, multi-disciplinary 3-D models based on geophysical and geochemical observations provide important insights into the geological history of cratonic lithosphere and its diamond prospectivity (e.g. Snyder et al., 2015). Each continent's cratons have different types of observations available and this leads to some diversity and complications in straightforward comparison, but the fundamental tools remain the same. South Africa has the earliest body-wave tomography, extensive magnetotelluric (MT) soundings and the most extensive geochemical database from numerous xenolith suites. Australian cratons have quality seismic tomography and MT data, but limited xenolith locations. Russian cratons have mostly geochemical data from xenoliths. North American cratons have all these observations in reasonable abundance and spatial density and will be the focus here.

Each North American craton was affected by each of four main processes to some degree (Snyder et al., 2017). These include (1) the initial building of basic continental cratonic blocks during the Archean, (2) subsequent assembly of cratons into the North American shield during the Proterozoic, (3) coeval or subsequent weakening by metasomatism, and (4) final partial erosion or delamination of the lithospheric base. Similar processes are assumed to have occurred in most, if not all, cratons however significant differences in diamond fertility argue that not all cratons were created alike. Understanding fundamental deep structure of the lithosphere requires, at minimum, a melding of our geochemical (e.g. Aulbach et al., 2013), geodynamical (e.g. Wang et al., 2014), and geophysical (e.g. Humphreys et al., 2015) observations and understanding. Here that is facilitated using multidisciplinary three-dimensional models that overlay different knowledge layers to enhance our understanding of at least the spatial interrelationships (Snyder et al., 2015). What we have found is that variably sparse xenolith samples calibrate geological timing and provide ground truth to continuous geophysically derived physical properties of the mantle. Seismic structures, typically discontinuities, appear to outline fault and shear structures along which cratons were built. Conductivity apparently best maps metasomatism and alteration associated with weakening of the lithosphere, but also its enrichment in metals and carbon.

Tectonics of Construction

Initial ancient (4.0-2.8 Ga) continental lithosphere blocks formed via fractional differentiation of an early Earth semi-stagnant lid into plagioclase-, pyroxene- and olivine-rich layers (Lee et al., 2011). These continental nuclei, several hundred kilometers wide and 90–120-km thick, grew by lateral tectonic accretion of similar, but more juvenile blocks. Seismic observations document wedge-shaped discontinuity surfaces that accommodated horizontal shortening, but no clear seismic evidence currently exists of deeply subducted lithospheric slabs from this period. Isotopic evidence does indicate coeval recycling of near-surface rocks into sub-lithospheric mantle, possibly via pyroxene-rich drips. These composite blocks cooled sufficiently by about 2.6 Ga to possess the strength and buoyancy to survive subsequent collisions and become stabilized cratons. Once subduction started about 2.8 Ga, Archean cratonic blocks eventually interacted and collided along mostly Proterozoic orogenic belts to form a North American continental shield that has largely survived to the present. Today this shield has layered lithosphere that generally gets younger with depth and is 180–220 km thick. Seismic discontinuities beneath many Proterozoic orogenic belts document subduction of intact (oceanic?) lithospheric slabs as is observed in modern subduction zones (Snyder et al., 2015).

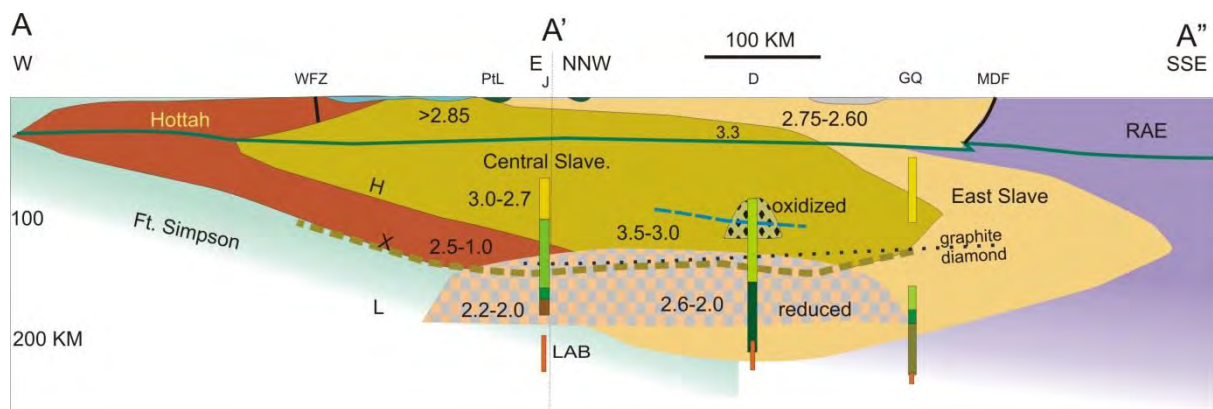


Figure 1. Summary cross section of the Slave craton showing that a Central Slave nucleus grew tectonically outward by wedging apart first the accreting East Slave block at 2.6 Ga, the Rae craton at 2.0-1.9 Ga, and then the Hottah terrane at 1.85 Ga (Snyder et al., 2017). WF and MDF are the Wopmay and MacDonald strike-slip faults. Numbers are rock ages in Ga. The vertical columns labelled J, D, and QG are xenolith suite rock types from Jericho, Diavik/Ekati, and Gahcho Que, respectively. Dashed lines mark seismic discontinuities. LAB is the lithosphere-asthenosphere boundary inferred from geotherms; H, X, and L are discontinuities.

Metasomatism: Prelude to Destruction

Sub-cratonic lithosphere is pervasively metasomatized and locally melted or recrystallized numerous times wherever it has been studied to date via xenoliths (e.g. Aulbach et al., 2013; Heaman and Pearson, 2010) or as inferred from enhanced conductivity. Upwardly migrating small percentage melt intrusions apparently introduce pyroxene-garnet (eclogite) assemblages, often with associated diamonds. Metasomatic fluids are often reducing and significantly weaken the lithosphere. These fluids are apparently rich in carbonates, silica or brine and therefore widely enhance conductivity as shallow as 90–120 km depths. Old, stacked, weakened sub-cratonic lithosphere is variably eroded or underplated by asthenospheric convection. Sparse indicators of lithosphere thickness during the Phanerozoic suggest thicknesses of 150–220 km. Subsidence or uplift indicated by surface basins is modest, only a few kilometers. One prominent exception is the Wyoming craton beneath which the Farallon flat slab was subducted. This process removed the Archean lithospheric base below about 140 km and replaced it with Mesozoic oceanic lithosphere (Humphreys et al., 2015).

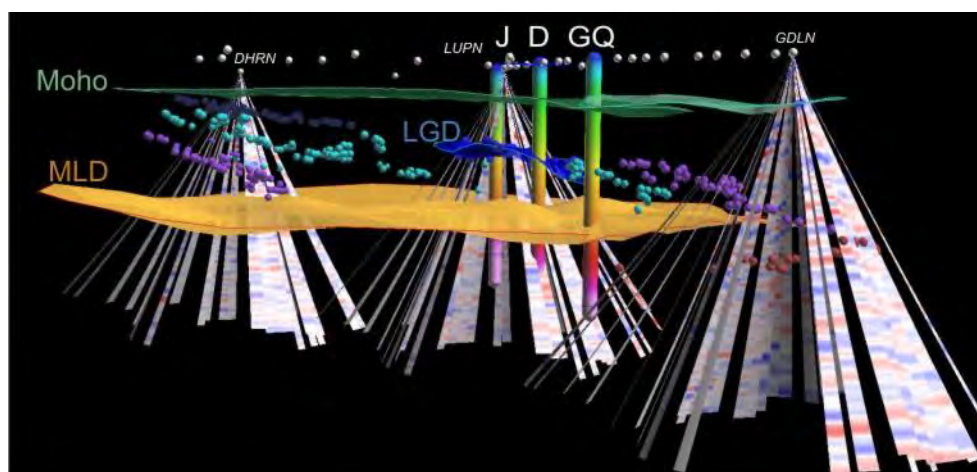


Figure 2. North-looking perspectives of a lithospheric-scale 3-D model of Slave craton structures inferred from seismic discontinuities and xenolith studies (modified from Snyder et al., 2017). Five structural surfaces are observed: a horizontal Moho (green), an undulating (LGD) surface at about 100-km depth (royal blue), a northeast-dipping surface associated with the Hottah terrane (purple), an east-dipping surface associated with the Ft. Simpson slab (blue), and a horizontal mid-lithospheric discontinuity (MLD) at 140-150 km depth (gold). The latter is mapped primarily by its seismic anisotropy, but also coincides with a marked increase in surface

wave velocity. Picks for two other discontinuities are represented by red and violet dots for easier viewing; these wedge-shaped discontinuities partly delimit the central and east Slave blocks at depth. J, D, and GQ are as in previous figure. Cones show 3D Ps receiver functions displayed at three representative seismic stations.

Model Probabilities & Uncertainty

Multi-disciplinary subcontinental lithospheric models present unique challenges if one attempts to move beyond a 'preferred' model and estimate the uncertainty of that model, or alternatively the probability of that or other models being correct. Each variety of seismic observation or MT data or geochemical analysis of xenoliths or xenocrysts has associated differences in analysis uncertainty.

Resolution thresholds and uncertainty within deep multidisciplinary 3-D models based on geophysical observations exist at a minimum of three levels. Seismic waves and potential or electromagnetic field measurements have inherent limitations in resolution related to their dominant wavelengths. Formal uncertainties can be assigned to grid-search type forward models of observable parameter sets. Both of these estimates are typically minor when compared to resolution limits related to the density and shape of a specific observation array used in seismology, electromagnetic, and potential field surveys. Seismic wave source distribution additionally applies in seismology. Comparing results obtained using independent seismic wave phases provides another measure of resolution of particular physical properties. Extremely sparse xenolith suites have systematic uncertainties associated with crystallization temperature and pressure estimates, but provide the only direct correlation of rock type with observed or modelled physical properties. Correlating diverse physical properties in a single 3-D model foremost requires accurate registration, but co-location of anomalies depends on the uncertainties and resolution limits specific to each method. Some physical properties may simply prove unrelated or primarily related to different rock properties and structures. Self-adapting grids, co-kriging and probability estimates increasingly appeal as more practical formulations of uncertainty or resolution in assessing 3-D models than traditional uncertainty criteria. The Canadian Moho map provides one instructive example combining refracted and converted seismic wave co-analysis with gravity modelling. Weaker, deeper lithospheric discontinuities and structures are even more uncertain and lack lateral continuity.

References

- Aulbach, S., Griffin, W.L., Pearson, N.J., O'Reilly, S.Y., 2013. Nature and timing of metasomatism in the stratified mantle lithosphere beneath the central Slave craton (Canada), *Chem. Geol.* 352, 153–169.
- Heaman, L.M., Pearson, D.G., 2010. Nature and evolution of the Slave Province subcontinental lithospheric mantle. *Can. J. Earth Sci.* 47, 369–388.
- Humphreys, E.D., Schmandt, B., Bezada, M.J., Perry-Houts, J., 2015. Recent craton growth by slab stacking beneath Wyoming. *Earth Planet. Sci. Lett.* 429, 170–180.
- Lee, C-T.A., Luffi, P., Chin, E. J., 2011. Building and destroying continental mantle. *Ann.Rev.Earth Planet. Sci.* 39, 59–90.
- Snyder, D.B., Humphreys, G., Pearson, D.G., 2017, Construction and destruction of some North American cratons, *Tectonophysics*, 693; doi.org/10.1016/j.tecto.2016.11.032.
- Snyder, D. B., J. A. Craven, M. Pilkington, & M. J. Hillier, 2015, The 3-dimensional construction of the Rae craton, central Canada, *Geochemistry, Geophysics, Geosystems*, 16, DOI: 10.1002/2015GC005957.
- Wang, H., van Hunen, J., Pearson, D.G., Allen, M.B., 2014. Craton stability and longevity: The roles of composition-dependent rheology and buoyancy. *Earth Planet. Sci. Lett.* 391, 224–233.

Stable isotope data and FTIR analyses of diamonds from Orapa Mine: a clear subduction signature

Ingrid L. Chinn¹, Samantha H. Perritt¹, Johann Stiefenhofer² and Richard A. Stern³

¹ De Beers Exploration, Johannesburg, South Africa, ingrid.chinn@debeersgroup.com,
samantha.perritt@debeersgroup.com

² MinRes, Anglo American Operations Ltd, Johannesburg, South Africa,
johann.stiefenhofer@debeersgroup.com

³ University of Alberta, Edmonton, rstern@ualberta.ca

Introduction

Colour, morphology and Fourier transform infrared (FTIR) data were acquired for over 2000 diamonds from Orapa Mine. The diamonds span a large range in maximum dimension from 0.15-4.75 mm. A subset of 198 diamonds covering the range in colour, morphology, nitrogen content and aggregation state was analysed by secondary-ion mass spectrometry (SIMS) to acquire nitrogen abundance and carbon and nitrogen isotope data. Previous work on inclusion-bearing diamonds from Orapa has highlighted the importance of the eclogitic and websteritic parageneses (Deines et al. 1993), with the latter being characterised by diamonds strongly depleted in ¹³C.

Analytical Methods

Transmission FTIR analyses were conducted on whole stones using a Bruker Vertex 70 spectrometer with Hyperion 2000 microscope from 7500 to 370 cm⁻¹ at a resolution of 4 cm⁻¹. Spectra were baselined manually and processed using an automated Microsoft Excel program based on a program written by D Fisher (De Beers Technologies UK). SIMS analyses were conducted at the Canadian Centre for Isotopic Microanalysis, University of Alberta. Details of analytical conditions and reference materials may be found in Stern et al. (2014) and Hogberg et al. (2016).

Results

Individual diamonds show considerable heterogeneity in nitrogen content and aggregation state, and carbon and nitrogen isotopic composition. Generally, stones that show significant heterogeneity in isotopic composition and/or nitrogen abundance show clear evidence of more than one distinct growth event in cathodoluminescence (CL) images (e.g. Figure 1). In some instances truncation of growth zonation indicates the presence of a resorption boundary associated with a diamond destruction event. Some diamonds appear to show evidence of multiple growth and/or resorption events.

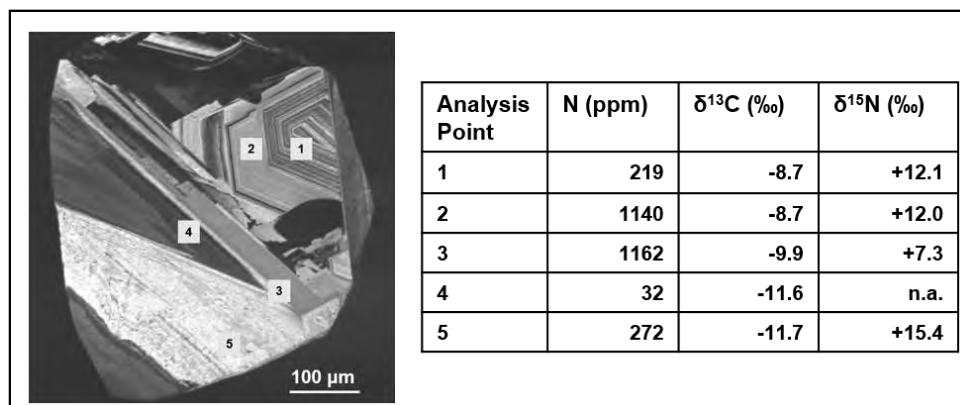


Figure 1: CL image of an Orapa diamond with complex zonation indicative of multiple growth events and at least two resorption boundaries. Locations of SIMS analyses and matching data are shown in the adjacent table.

The range in carbon isotope ($\delta^{13}\text{C}_{\text{VPDB}}$) composition for the diamonds analysed is from -28.6 to -2.1 ‰ and the maximum variation recorded for an individual diamond is 18.0 ‰: from -24.2 ‰ (core) to -6.2 ‰ (rim). The overall range in nitrogen isotope ($\delta^{15}\text{N}_{\text{AIR}}$) composition is from -10.4 to +23.0 ‰ and the maximum variation in a single diamond is 14.7 ‰, from -2.8 to +11.9 ‰. The largest variation in nitrogen content in a single diamond is 3577 atomic ppm, from below 11 to 3588 atomic ppm, where the latter value is the highest nitrogen content recorded by SIMS for these analyses.

Some diamonds with relatively simple zonation (e.g. Figure 2) show a change from cores depleted in ^{13}C , with high nitrogen contents and positive $\delta^{15}\text{N}$ values, to rims with “mantle” $\delta^{13}\text{C}$ values (Cartigny 2005), moderately high nitrogen contents and negative $\delta^{15}\text{N}$ values. The reverse trend is also recognised, consistent with the presence of several growth events recorded by the diamond populations of Orapa.

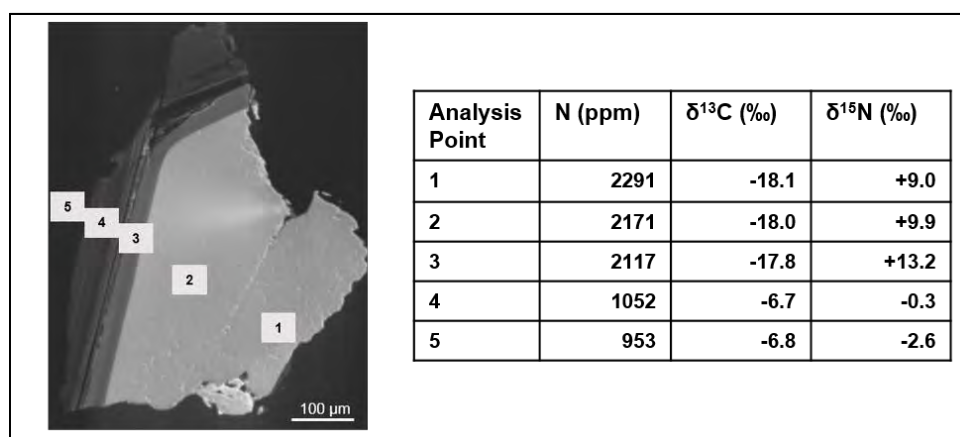


Figure 2: CL image of an Orapa diamond with simple zonation with “mantle” values of $\delta^{13}\text{C}$, $\delta^{15}\text{N}$ and nitrogen content in the rim. Locations of SIMS analyses and matching data are shown in the adjacent table.

A “mantle” signature is seen in a group of diamonds with restricted $\delta^{13}\text{C}$ values from -8 to -2 ‰, $\delta^{15}\text{N}$ values from -5 to +5 ‰, and nitrogen contents of ~600 to 1800 ppm. The carbon isotope compositions of this group correspond to one of the two modes recognised for Orapa inclusion-bearing diamonds by Deines et al. (1993). They reported a well-defined mode between -15 and -13 ‰ for eclogitic diamonds. In the current data this mode is shifted to lower values between -20 and -18 ‰.

A plot of nitrogen content versus $\delta^{13}\text{C}$ (Figure 3) shows a significant proportion (22%) of the 508 coupled SIMS analyses displaying strongly negative $\delta^{13}\text{C}$ values and high nitrogen contents, falling well outside the limit sector curve defined for diamonds worldwide (Cartigny et al. 2001). The anomalous diamonds are also characterised by positive $\delta^{15}\text{N}$ values (Figure 3) consistent with a crustal/sedimentary derivation (Thomazo et al. 2009). A few similar anomalous diamonds have been reported previously (Hogberg et al. 2016 and references therein) including a diamondite from Orapa and websteritic diamondites from unknown southern African sources (Mikhail et al. 2014).

Discussion

Given the extreme heterogeneity in isotopic compositions and nitrogen content recorded in individual diamonds and supported by CL images, the need for detailed and spatially controlled stable isotopic analyses of representative samples is clearly demonstrated if the complex origins of diamonds such as these from Orapa are to be fully understood. Diamond growth complexity must also be taken into account when isotopic ratios of inclusions are used to generate diamond growth ages, as a large proportion of diamonds clearly grew episodically, and in some cases over an extended period of time, e.g. 2 Ga, (Timmerman et al. 2017). Unfortunately, most diamonds for which carbon isotope data have been published are inclusion-bearing, and in isotopic composition are not necessarily representative of the run-of-mine populations, resulting in a bias that has missed the presence of the subduction isotopic signature recognised here. Whole stone FTIR analyses and bulk isotopic analyses

which form the bulk of global diamond analyses are likely to have resulted in average isotopic values and nitrogen contents that precluded recognition of diamonds that grew from subducted sedimentary material. The data presented here show that diamonds reflecting sedimentary subduction signatures in terms of both carbon and nitrogen isotopic compositions can comprise a significant proportion of the diamond populations at an operational mine, highlighting the economic importance of subduction and the global carbon cycle.

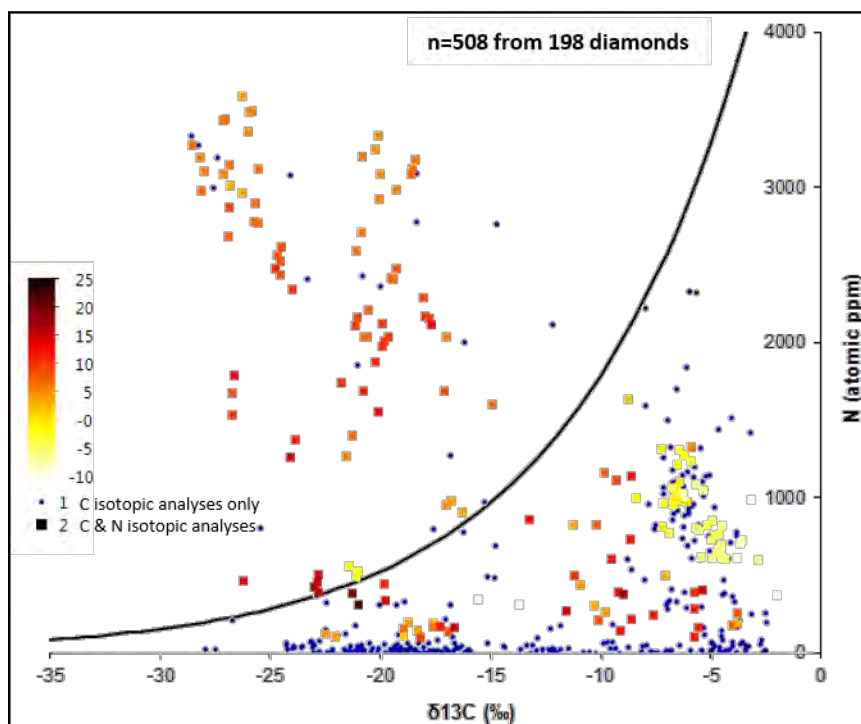


Figure 3: Nitrogen content versus carbon isotopic composition for Orapa diamonds. Selected SIMS analyses for which there was sufficient nitrogen to obtain nitrogen isotopic compositions (large symbols) are colour coded for $\delta^{15}\text{N}$ values as per the legend. The black line represents the limit sector curve of Cartigny et al. (2001).

References

- Cartigny P, Harris JW, Javoy M (2001) Diamond genesis, mantle fractionations and mantle nitrogen content: a study of $\delta^{13}\text{C}$ -N concentrations in diamonds. *Earth Planet. Sci. Lett.* 185:85-98
- Cartigny P (2005) Stable Isotopes and the Origin of Diamond. *Elements* 1:79-84
- Deines P, Harris JW, Gurney JJ (1993) Depth-related carbon isotope and nitrogen concentration variability in the mantle below the Orapa kimberlite, Botswana, Africa. *Geochim. Cosmochim. Acta* 57:2781-2796
- Hogberg K, Stachel, T, Stern RA (2016) Carbon and nitrogen isotope systematics in diamond: Different sensitivities to isotopic fractionation or a decoupled origin? *Lithos* 265:16-30
- Mikhail S, Verchovsky AB, Howell D, Hutchinson MT, Southworth R, Thomson AR, Warburton P, Jones AP, Milledge HJ (2014) Constraining the internal variability of the stable isotopes of carbon and nitrogen within mantle diamonds. *Chem. Geol.* 366:14-23
- Stern RA, Palot M, Howell D, Stachel T, Pearson DG, Cartigny P, Oh A. (2014) Methods and reference materials for SIMS diamond C- and N-isotope analysis. Canadian Centre for Isotopic Microanalysis, Research Report 14-01. University of Alberta, Education and Research Archive. <http://hdl.handle.net/10402/era.38738>.
- Thomazo C, Pinti DI, Busigny V, Ader M, Hashizume K, Philippot P (2009) Biological activity and the Earth's surface evolution: Insights from carbon, sulfur, nitrogen and iron stable isotopes in the rock record. *C. R. Palevol* 8:665-678
- Timmerman S, Koornneef JM, Chinn IL, Davies GR (2017) Dated eclogitic diamond growth zones reveal variable recycling of crustal carbon through time. *Earth Planet. Sci. Lett.* 463:178-188



Mineralogy, Geochemistry, and Petrogenesis of Paleoproterozoic Alkaline Magmas in the Yilgarn Craton, Western Australia

Eunjoo Choi¹, Marco Fiorentini¹, Andrea Giuliani², Anthony Kemp¹, Franco Pirajno¹, Stephen Foley³

¹*School of Earth and Environment, Centre for Exploration Targeting, ARC Centre of Excellence for Core to Crust Fluid Systems, The University of Western Australia*

²*KiDs (Kimberlites and Diamonds), School of Earth Sciences, The University of Melbourne*

³*Department of Earth and Planetary Sciences, ARC Centre of Excellence for Core to Crust Fluid Systems and GEMOC, Macquarie University*

Introduction

The Yilgarn Craton in Western Australia is a world-class metallogenic Archean craton hosting considerable metal resources, including komatiite-associated Ni-sulfides and orogenic Au. Interest in the geodynamic evolution of the crust and upper mantle in the craton has increased greatly over the last decade through various studies, which mainly relied on regional scale geophysical datasets, and geochemical, isotopic and geochronological information of subalkaline magmas felsic, mafic and ultramafic magmas (e.g. Blewett et al. 2010; Mole et al. 2013). These previous studies have helped establish the four-dimensional evolution of the lithospheric mantle under the Yilgarn Craton. However, these studies only provide limited information about the composition of the underlying lithospheric-asthenospheric mantle which remains poorly defined from a geochemical and isotopic point of view.

The study of the poorly characterised alkaline magmas (kimberlites, lamprophyres and carbonatites) that are distributed throughout the eastern part of the Yilgarn Craton as well as along its northern margins can address this knowledge gap and provide invaluable information about the nature of the lithosphere and asthenosphere. The aim of this study is to establish the mineralogical, geochemical and petrogenetic features of the alkaline magmas as probes to unravel the composition of the upper mantle under the Yilgarn Craton.

Alkaline Rocks in the Yilgarn Craton

The Yilgarn Craton contains various types of alkaline magmas, including kimberlites, carbonatites and two types of lamprophyres - ultramafic lamprophyres (UML) and calc-alkaline lamprophyres (CAL) - in the eastern area and northern margins of the craton. The spatial distribution of the alkaline rocks in the craton can be subdivided into two groups: off-craton and on-craton. The off-craton alkaline rocks comprise UML and kimberlites on the northern boundary of the craton with ages of 1324 ± 4 and 1900 - 1700 Ma (Shee et al. 1999) and the Norseman UML on the south-eastern boundary with an age of 849 Ma (Robey et al. 1989). The alkaline rocks within the Yilgarn Craton are older than the off-craton alkaline rocks, with ages of more than 2000 Ma. The age of kimberlites, UML and carbonatites in the centre of the eastern part of the craton is 2025 ± 10 Ma (Graham et al. 2004). Most CAL have not been dated except for those in Kambalda with an unpublished U-Pb zircon age of 2684 ± 6 Ma cited in Perring et al. (1989).

The alkaline rocks of the Yilgarn Craton mainly show a volcanic texture comprising phenocrysts of mafic minerals (e.g. olivines, phlogopites, and amphiboles) and felsic matrix phases (e.g. feldspars and quartzs). Phlogopites and amphiboles are common minerals in the Yilgarn alkaline rocks, and occur as macrocrysts (> 0.3 mm), microcrysts (0.3 - 0.1 mm), phenocrysts and groundmass crystals. CAL contain both minerals and clinopyroxenes as variable phases from groundmass to macrocrysts with a matrix of albites, K-feldspars, quartzs, titanites, and apatites. UML generally consist of macrocrysts and microcrysts of phlogopites, and are characterized by primary carbonate minerals (calcites and

dolomites) as a groundmass phase with clinopyroxenes, phlogopites, apatites, magnetites and ilmenites and less feldspar than CAL. Yilgarn carbonatites contain phlogopites and apatites as variable sizes (up to ~0.7 mm) with olivine and magnetite microcrysts, including a groundmass phase of primary calcites and dolomites, and fine-grained pyrochlore and barite (< 20 µm). Kimberlites have an rounded huge olivines (up to ~0.6 mm), including phlogopite, pyroxene, ilmenite, magnetite and monazite groundmasses.

Bulk-rock major element and PGE compositions

Results of whole rock analysis of the Yilgarn alkaline rocks exhibit different geochemical characteristics of major and platinum group elements (PGE) for the different the alkaline rock types. CAL show distinct geochemistry and have higher SiO₂ contents ranging from 50.6 to 59.3 wt.% with lower contents of Fe₂O₃ (5.5 - 8.4 wt.%) and MgO (4.2 – 9.2 wt.%) compared to the other alkaline rocks. Both kimberlites and UML have low SiO₂ contents (27.1 – 47.7 and 20.4 – 42.7 wt. % respectively), while TiO₂ contents in kimberlites are generally lower than those of the UML (0.5 – 3.9 vs. 2.4 – 8.3 wt.%).

Primitive-mantle normalized PGE patterns of CAL show strong fractionation with relative depletion in Os, Is and Ru (IPGE), enrichment in Rh, Pt, and Pd (PPGE) and high (Pd/Ir)_N from 11.64 to 24.58, reflecting a less primitive PGE component (McDonald et al. 1995). In contrast, other alkaline rocks such as carbonatites, UML and kimberlites are characterized by much less fractionation of PPGE from IPGE with low (Pd/Ir)_N values (< 10.60). These characteristics of CAL are similar to off-craton alkaline rocks and alkali volcanics, while UML and kimberlites show similar PGE patterns of on-craton kimberlites reported by McDonald et al. (1995). This may indicate that the source of CAL was shallower in the upper mantle than the other alkaline rocks of the Yilgarn Craton.

Mineral Chemistry

Phlogopites exhibit variable features, depending on the alkaline rock types. Macrocryst phlogopites in UML are characterized by compositional zoning patterns. X-ray mapping of the phlogopite macrocrysts show cores with high Si, Mg and Fe and low Ti and Cr concentrations that are overgrown by two distinct rims which are enriched in Mg, Al and Ba compared to the cores (Figure 1). The low Ti-Cr-Al feature of the cores is similar to that in mantle-derived xenocryst phlogopites of south African kimberlites (Giuliani et al. 2016). The inner rim is enriched in Ti, whereas the outer rim contains high BaO contents up to 2.8 wt.%. Phlogopites in kimberlites are dominantly unzoned, and have lower FeO contents and higher MgO contents than groundmass phlogopites in other alkaline rocks. In carbonatites, phlogopite are either zoned with a xenocrystic core with similar composition to the cores in UML phlogopites and a tetraferriphlogopite rim, or unzoned with tetraferriphlogopite composition (Al = 0.00 - 0.19, Fe = 2.57 – 3.13).

Amphiboles occurring in CAL are dominantly Mg-hastingsite, displaying complex zoning patterns. The cores of macrocrysts and microcrysts are characterized by higher FeO (10.9 - 15.3 wt.%) and Al₂O₃ (9.5 - 13.4 wt.%) than rims, whereas the rims have higher Si (upto 7.62 a.f.u.). Groundmass amphiboles are zoned or unzoned. The zoned groundmass amphiboles have similar features to macrocrysts and microcrysts in that the cores are enriched in FeO (11.4-15.5 wt.%), and Al₂O₃ (10.2-13.4 wt.%), whereas the rims (and unzoned) amphiboles contain higher Si.

The major element geochemistry of phlogopites and amphiboles in the Yilgarn Craton shows distinct zoning patterns and compositional changes from macrocrysts to groundmass, outlining the compositional fractionation of the alkaline magmas. Further researches on these major and trace element chemistry of phlogopites, amphiboles and other minerals such as olivines, clinopyroxenes and apatites will be conducted to understand the petrogenesis of the various types of alkaline magmas and to trace the compositional and geodynamic evolution of the lithospheric mantle under the Yilgarn Craton.

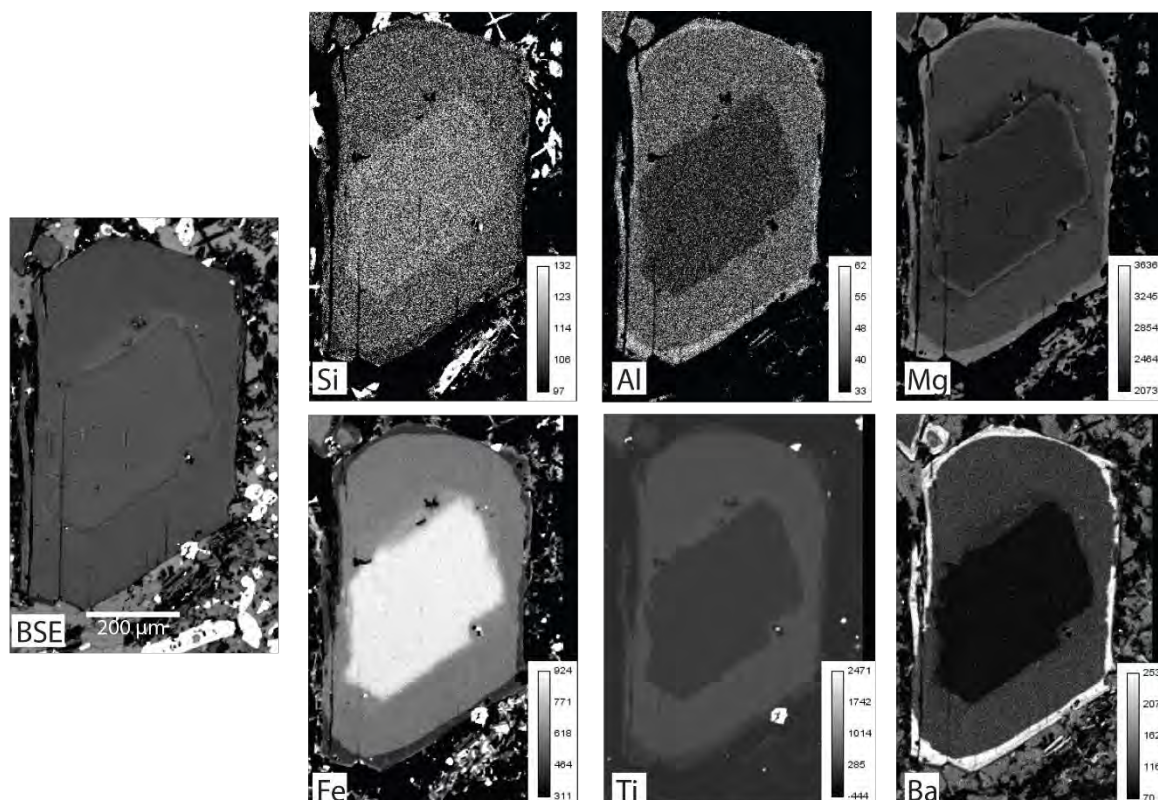


Figure 1: Back-scattered electron (BSE) image and EPMA elemental distribution maps of phlogopite in ultramafic lamprophyres (UML) in the Yilgarn Craton. The coloured scales on the right bottom of each panel indicate the relative concentration of each element

References

- Blewett RS, Henson PA, Roy IG, Champion DC, Cassidy KF (2010) Scale-integrated architecture of a world-class gold mineral system: the Archaean eastern Yilgarn Craton, Western Australia *Precambrian Research* 183:230-250
- Giuliani A, Phillips D, Kamenetsky VS, Goemann K (2016) Constraints on kimberlite ascent mechanisms revealed by phlogopite compositions in kimberlites and mantle xenoliths *Lithos* 240:189-201
- Graham S, Lambert D, Shee S (2004) The petrogenesis of carbonatite, melnoite and kimberlite from the Eastern Goldfields Province, Yilgarn Craton *Lithos* 76:519-533
doi:10.1016/j.lithos.2004.03.031
- McDonald I, De Wit M, Smith C, Bizzi L, Viljoen K (1995) The geochemistry of the platinum-group elements in Brazilian and southern African kimberlites *Geochimica et Cosmochimica Acta* 59:2883-2903
- Mole DR et al. (2013) Crustal evolution, intra-cratonic architecture and the metallogeny of an Archaean craton *Geological Society, London, Special Publications* 393:23-80
doi:10.1144/sp393.8
- Perring CS, Rock NM, Golding SD, Roberts DE (1989) Criteria for the recognition of metamorphosed or altered lamprophyres: a case study from the Archaean of Kambalda, Western Australia *Precambrian Research* 43:215-237
- Robey J, Bristow J, Marx M, Joyce J, Danchin R, Arnott F (1989) Alkaline ultrabasic dikes near Norseman, Western Australia *Kimberlites and Related Rocks* 1:383-391
- Shee SR, Vercoe SC, Wyatt BA, Hwang PH, Campbell AN, Colgan EA Discovery and geology of the Nabby kimberlite province, Western Australia. In: *Proceedings of the VIIth International Kimberlite Conference, 1999*. pp 764-787

Relation between micro- and macro-diamonds: Myth, myopia or both?

Stephen E. Haggerty

Florida International University MIAMI, FL 33199, USA, haggerty@fiu.edu

Introduction

The origin of micro-diamonds (<0.5 mm) has been a topic of long standing debate and uncertainty. Once entirely of academic interest, the presence and determination of micro-diamonds has received increasing attention over the past two decades to the point that these barely visible diamonds are now center stage to kimberlite exploration and modern evaluation programs. The underlying assumption in this progression is that micro-diamonds are a measure of, and directly related to, the presence and abundance of macro-diamonds, thus providing an inexpensive method of potential grade determination. And as such, micros have become a requirement (an industry norm) to investment. Among several important questions are whether micros and macros shared a common C-source, and whether both experienced the same P-T-t conditions and origin in the mantle, which reduces fundamentally to: Did the two populations ever co-exist? The answers individually and collectively provide an assessment of the overall reliability of a micro to macro relationship. The relation of size vs abundance is ideally modelled as being uniformly log-normal (Rombouts, 1994, 1995), but in fact micros are linear, macros are quadratic, and the two are separated by a discontinuity (Chapman & Boxer, 1984; Deaken & Boxer, 1989), as illustrated in Fig. 1 (Lock & Barton, 2007); the extrapolation of abundant micros to sizes of value cannot, therefore, be tacitly assumed (Coopersmith et al., 2002). The vast majority of kimberlites contain micro-diamonds but there are few studies relating these to macros, (drawn upon below from e.g. McCandless et al., 1994; Patterson & Levinson, 1995; Johnson et al., 2012; Melton et al., 2013).

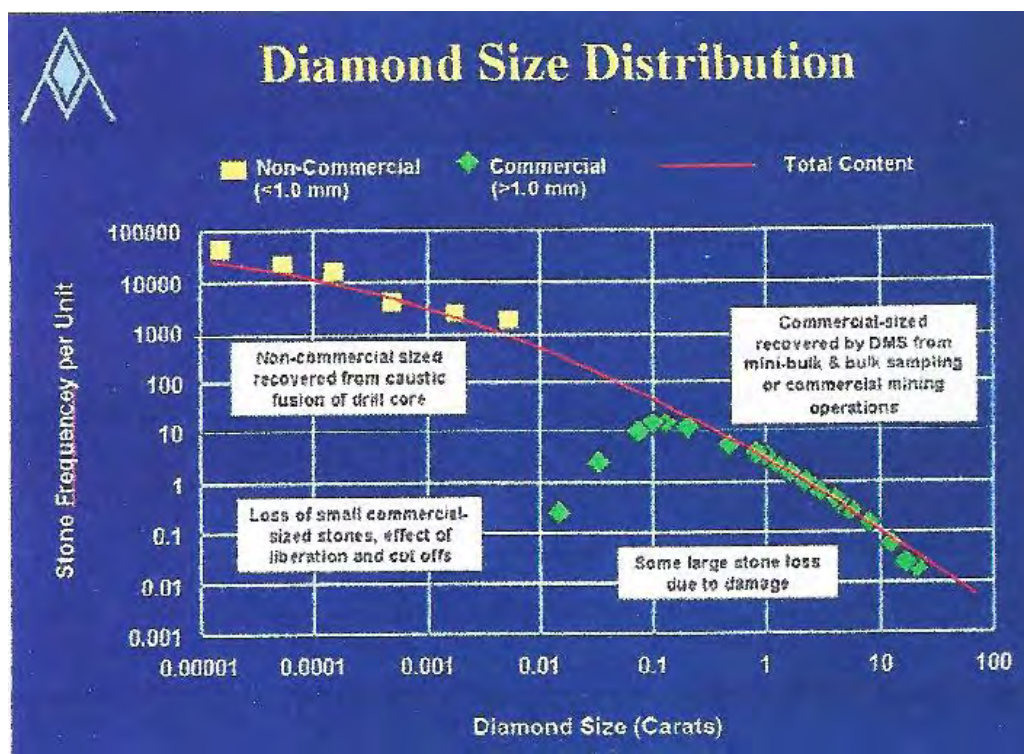


Fig. 1 Typical relation between micros (yellow squares) and macros (green diamonds).

Are Micros and Macros related?

Micro-diamonds generally have the following features: typically octahedra and *free* of mineral inclusions, growth ornamentation, etch and corrosion features; and *abundance* is overwhelmingly greater than macros.

First order objections to this relationship are:

1. Given the lateral and vertical heterogeneities in the mantle, the inferred distribution of rock types in the subcontinental lithosphere, the transition zone and the lower mantle, it is reasonable to expect that the distribution of carbon is highly variable, and that the abundance of diamond and the population of sizes must be equally heterogeneous.
2. This heterogeneity must also apply to the mechanisms of nucleation, growth, and dissolution in which populations of micros and macros are assuredly variable rather than cohesive.
3. Sampling at depth and along the eruptive conduit is chaotic with assured mixing of rocks, both diamond and non-diamond bearing that lack discrimination in population sizes or in sampling efficiency; and if intrinsic relations once existed these were surely lost on explosive eruption.
4. This is manifest in the fact that all kimberlites are multiple intrusions with highly variable diamond contents between intrusions and within the same intrusive body. Hence, a strict correlation between micros and macros is highly unlikely.
5. Harzburgites and eclogites are the major hosts to diamonds, the latter being typically higher in diamond content and with significantly larger diamonds. Thus, if micros are intrinsically related to macros it follows that peridotitic suites ought to be deficient in micros. And because the diamond populations are mixed, the end result in the kimberlite must also be mixed. With diminished micros in one rock type and potentially large and abundant diamonds in another the relation between micros and macros must inevitably be incoherent.
6. Modelled ideally as oxidation of CH₄ or reduction of CO₂ the diamond yield should be equal, but macros and micros are unequal in size and abundance further implying that the two populations are genetically unrelated.
7. Micros are typically Type Ib octahedra or Type II, whereas macros are Type Ia octahedra commonly corroded to dodecahedra or tetrahexahedra. These differences clearly indicate that the two populations cannot have co-existed under the same P-T-t environments in the mantle.
8. C-isotopes and H-contents are equivocal possibly because of mixed populations of micros and diamond fragments that are small but are not micros *sensu stricto*.
9. The broad-based continuum from micro- to macro-diamonds is separated by the “*Chapman & Boxer Discrepancy Zone*.”(Fig. 1), and ignores the ultra-ultra-fine population at one extreme that is never recovered analytically, and mega-stones at the other that are rarely encountered. Further complications are shown in the comprehensive treatment by Hutchinson (2012) in Fig. 2.
10. With a huge disparity in the surface to volume ratio, micros and macros cannot be of the same age, or have resided over the same period of time in an environment of constant C, or in a setting affected by the same corrosive mantle fluids (Haggerty, 1986). In essence, if micros and macros are coeval then what inhibited growth of the former, and why is it that only the latter are affected by dissolution?
11. There is also a huge disparity in methodology: Micros are determined on ~200 kg of kimberlite by acid dissolution or caustic fusion; Macros are concentrated from ~20,000 T in bulk sampling programs by mechanical and X-ray means on crushed kimberlite + xenoliths + crustal enclaves. That there should be any relationship between the two diamond populations stretches credulity.
12. Having micros “protected in xenoliths” from kimberlite attack (Robinson et al., 1989), or progressive release in the conduit are unlikely because it’s slow corrosion not combustion. Moreover, the mantle is a massive body of P and E diamond-bearing host rocks *hundreds of cubic km* in extent---- not a mélange of disruptive xenoliths!

Genesis of Micros & Macros

Given the existence of lower mantle (bridgemanite) and TZ-diamonds (ringwoodite and majorite), young intrusive-age Type Ib micros are from >660 km and permissively from plume-bearing D'' carbon in proto-kimberlites; micro-diamonds formed from *large* numbers of nucleation centers in the upward

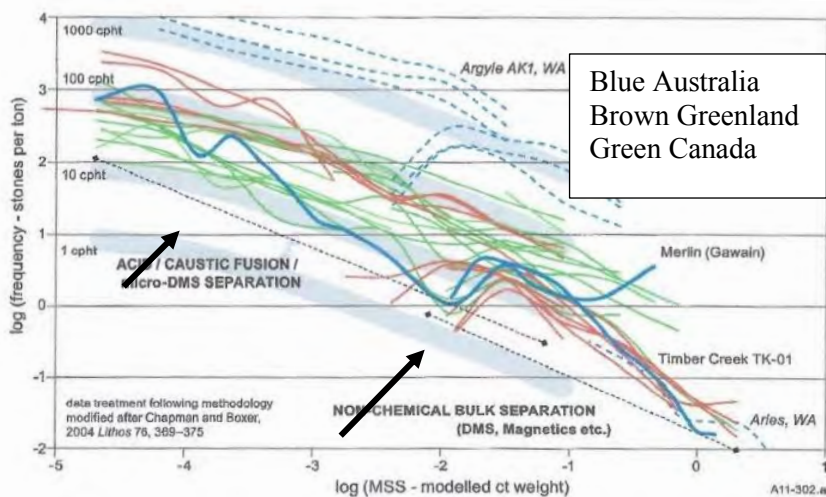


Fig. 2. Log cpht vs log mean stone size.

moving plume. By contrast, ancient Type Ia macros (2.8-3.2 Ga) are from primordial mantle carbon, with crystallization by thermochemical cracking of fluid/gas species under variable fO_2 from *small* numbers of diamond nucleation sites; slow and intermittent growth, dissolution by hyperactive metasomatic fluids, and with resident annealing over long periods of time under high P-T conditions.

Conclusions

Micros and macros are seemingly unrelated so any inferred relation is mythical and the widespread lognormal association, so common in nature (Lampert et al., 2001), is myopic (*by definition: shortsighted, unimaginative, and unrealistic*). Possible exceptions are: (i) diamonds are uniformly small; (ii) breakage is extensive; (iii) micros and fragments of macros are mixed; and (iv) if C from the partial solution of Type Ia macros becomes the source of C in Type Ib micros, a continuum might be expected if both are retained in a single intrusive body-----a most unlikely scenario!

References

- Chapman JG and Boxer GL (2004) *Lithos* 76, 369-375.
 Coopersmith H, Pell J, Scott-Smith B (2002) Kimberlite Emplacement Workshop. Saskatoon. Unpaged.
 Deakin AS and Boxer GL (1989) *Geol. Soc. Australia Spec. Paper* 14, 1117-1122.
 Haggerty, SE (1986) *Nature* 320, 34-38.
 Hutchinson MT (2012) *Proc. 10th IKC India* 2, 257-280.
 Johnson CN, Stachel T, Muehlenbachs K, Stern RA, Armstrong JP (2012) *Lithos* 148, 86-97.
 Lampert E, Stachel WA Abbt M (2001) *BioScience* 51, 341-352.
 Lock N and Barton E (2007) *Geol. Soc. South Africa. Kimberley Symposium*. Unpaged.
 McCandless TE, Waldman MA, Gurney JJ (1994) *Proc. 5th IKC Brazil* 2, 78-97.
 Melton GL, Stachel T, Stern RA, Carlson J, Harris JW (2013) *Lithos* 110-119.
 Pattison DRM, Levinson AA (1996) *Applied Geochemistry* 10, 725-738.
 Robinson DN, et al. (1989) *Geol. Soc. Australia Spec. Pub.* 14, 990-1000.
 Rombouts L (1994) *Proc. 5th IKC, Brazil.* 2, 203-214.
 Rombouts L (1997) *Russian Geology & Geophysics.* 38, 599-611.



The Victor Diamond Mine (Superior Craton, Canada) – A new paradigm for exploration in unconventional settings

Thomas Stachel¹, Anetta Banas², Sonja Aulbach^{1,3}, Karen V. Smit^{1,4}, Pamela Wescott¹,
Ingrid Chinn⁵, David Fisher⁶ and Julie Kong⁷

¹ University of Alberta, Edmonton, Canada, tstachel@ualberta.ca

² APEX Geoscience Ltd., Edmonton, Canada, abanas@apexgeoscience.com

³ Goethe-Universität, Frankfurt, Germany, s.aulbach@em.uni-frankfurt.de

⁴ Gemological Institute of America, New York, USA, ksmit@gia.edu

⁵ De Beers Exploration, Southdale, South Africa, Ingrid.Chinn@debeersgroup.com

⁶ De Beers Technologies UK, Maidenhead, UK, David.Fisher@debeersgroup.com

⁷ De Beers Canada, Toronto, Canada, Julie.Kong@debeersgroup.com

Introduction

The James Bay area on the Superior Craton is host to kimberlites of Mesoproterozoic (~1.1 Ga; Kyle Lake kimberlites) and Jurassic age (~180-170 Ma; Attawapiskat kimberlites; Januszczak et al. 2013). De Beers' Victor Mine is part of the Attawapiskat kimberlite field and derives a diamond production of superb quality from a geologically discrete phase (Victor Main) within the North pipe and from the SW pipe. At 1.1 Ga the area was affected by a thermal event that likely represents the northern extension of the major Midcontinent Rift, impacting the Superior Craton from the South. This thermal event is documented in an elevated geotherm (40-41 mW/m² reference geotherm of Hasterok and Chapman 2011) derived from mantle xenocrysts in Kyle Lake kimberlites, reflecting a small diamond window in the lithospheric mantle between 140-180 km depth (Smit et al. 2014). For the Jurassic Attawapiskat kimberlites, xenocrysts indicate a "cool" cratonic geotherm (39 mW/m²) associated with a large diamond window (120-200 km; Smit et al. 2014).

James Bay area diamond populations

An infra-red spectroscopic study of nitrogen concentrations and aggregation states in diamonds from Mesoproterozoic (T1) and Jurassic (U2) kimberlites revealed distinct diamond populations (Fig. 1; Smit et al. 2014). Diamonds in the older T1 kimberlite are characterized by low nitrogen concentrations (typically <80 at.ppm) and high aggregation states (all >70 %B; median: 87 %B). Diamonds in the Jurassic U2 kimberlite, however, typically show high nitrogen contents (median 290 at.ppm) at low aggregation states (median: 12 %B). Our data for Victor diamonds display this Jurassic signature of high nitrogen contents (median: 460 at.ppm) and low aggregation states (median: 20 %B) even more prominently (Fig. 1). As aggregation of nitrogen into B centres is an irreversible process, the distinct diamond populations sampled by Mesoproterozoic and Jurassic kimberlites imply diamond destruction, presumably in the course of the 1.1 Ga Midcontinent Rift event, followed by renewed diamond formation. This conclusion is supported by distinct carbon isotopic signatures for the two age groups, with diamonds in the Mesoproterozoic T1 kimberlite showing a narrow mode in $\delta^{13}\text{C}$ at -3.5 to -2.5 ‰ (median: -3.3 ‰, Fig. 2) which is shifted to -6.0 to -5.0 ‰ (median: -5.3 ‰) for the Jurassic U2 and Victor kimberlites.

Age of Diamond Formation

Geologically "young" diamond formation beneath the Western Superior Craton, postdating the Midcontinent Rift event, is entirely consistent with the outcomes of our Re-Os dating study based on 20 sulfide inclusions released from 19 Victor diamonds, which produced a robust model-3 isochron age of 718 ±49 Ma (Aulbach et al., this volume). This diamond age agrees with models for lithosphere-scale dissipation of thermal events that indicate thermal relaxation over ~0.4 Ga (95 % decay for 200 km thick lithosphere; Vitorello and Pollack 1980). Our ~720 Ma age also overlaps with the break-up of the Rodinia supercontinent, which may have triggered the mobilisation of carbon-bearing fluids or melts.

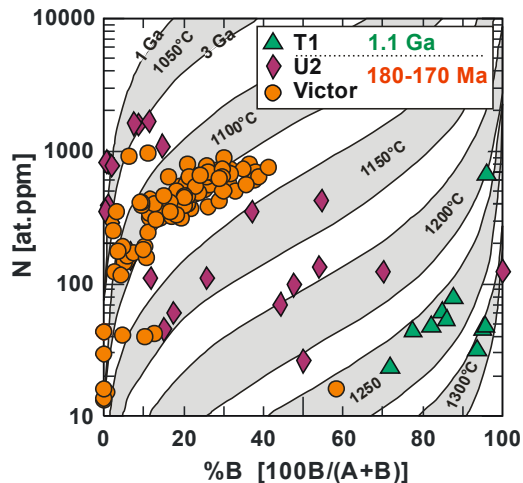


Figure 1: Nitrogen content versus nitrogen aggregation state (as relative percentage of nitrogen in fully aggregated B-centers) for diamonds from Mesoproterozoic (T1) and Jurassic kimberlites (U2, Victor) in the James Bay area.

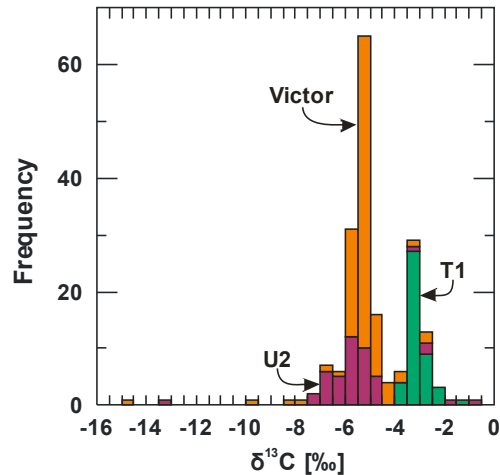


Figure 2: Carbon isotopic composition of diamonds from Mesoproterozoic (T1) and Jurassic kimberlites (U2, Victor). Values for T1 and U2 are averages of multiple SIMS analyses per diamond (from Smit et al. 2014), Victor diamonds represent bulk analyses.

Diamond Substrates in the Lithospheric Mantle beneath Attawapiskat

We studied the paragenesis and the major and trace element composition of mineral inclusions in 116 diamonds from Victor. Based on 99 diamonds with classified silicate and sulphide inclusions, 87% of Victor diamonds belong to the peridotitic and 13% to the eclogitic suite. The peridotitic inclusion assemblage consists principally of garnet (63%) and olivine (14%), with minor (<10% each) orthopyroxene, clinopyroxene and sulphides. Mg-chromite inclusions are completely absent. Considering only diamonds with peridotitic inclusions for which a specific paragenesis could be derived (n=65), 97% belong to the lherzolitic and 3% to the wehrlitic paragenesis, whilst harzburgitic inclusions are completely absent (shown for garnet inclusions in Fig. 3). Chemically, the lherzolitic association represents moderately depleted cratonic peridotites, with olivine Mg-numbers (91.3 ± 0.2 , Fig. 4) below world wide average. Sinusoidal REE_N patterns for garnet inclusions imply an absence of melt metasomatism. The eclogitic inclusion suite (n=18) is dominated by garnet, SiO₂ (presumably primary

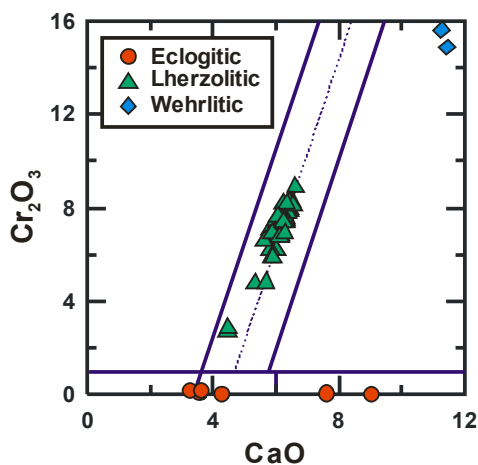


Figure 3: Cr-Ca plot for garnet showing the overwhelmingly lherzolitic paragenesis of inclusions in Victor diamonds. Note that the Victor lherzolitic garnets overlap the division (thin dashed line) between diamond-associated G9A and graphite-associated G9B garnets of Grütter and Menzies. (2003).

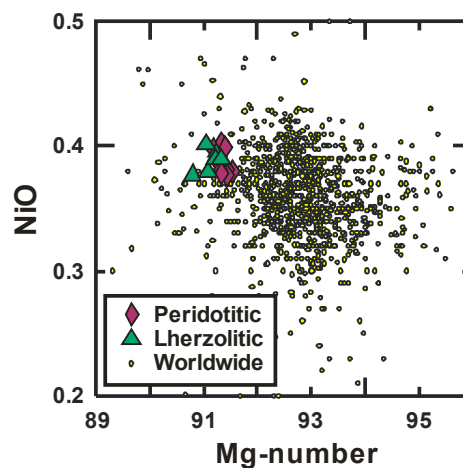


Figure 4: NiO versus Mg-number for olivine inclusions in Victor diamonds. Olivines without co-existing garnet or clinopyroxene inclusions cannot be further classified and are labelled “peridotitic”. Peridotitic olivine inclusions from diamonds worldwide are shown for comparison.

coesite) and sulphide inclusions, with single occurrences of clinopyroxene, kyanite and a mica-ilmenite intergrowth. For six of the 13 eclogitic diamonds, inclusions were recovered from fibrous coats.

Geothermobarometry

Nitrogen-in-diamond based thermometry (Leahy and Taylor 1997) for Victor inclusion-bearing diamonds indicates a narrow interval in mantle residence temperatures (1142 ± 24 °C) bracketing the average for diamonds worldwide (~ 1150 °C). Projection of these temperatures onto the Attawapiskat paleogeotherm reveals diamond sampling from a thin layer at 163 ± 4 km depth. Temperature estimates based on five clinopyroxene inclusions yield 1120 ± 20 °C at an assumed pressure of 50 kbar (thermometer of Nimis and Taylor 2000; none of the inclusions pass the compositional filters of Ziberna et al. 2016 for pressure calculations). Projection of clinopyroxene-derived temperatures onto the local paleogeotherm results in a depth of sampling of 158 ± 4 km. Using Ni-in-garnet thermometry (Canil 1999), the peak mantle entrainment for the Victor Main high grade unit occurred at about 153 ± 10 km depth (Januszczak et al. 2013; their Fig. 8), implying fortuitously efficient sampling of this well-defined diamondiferous layer.

Conclusions

Guided by Clifford's Rule and paragenetic diamond associations defined via inclusion studies (e.g., Gurney 1984), exploration focusses on harzburgitic and eclogitic diamond substrates associated with Archean cratons. The Victor Mine, however, exploits a 720 million year old lherzolitic diamond population derived from a section of sub-cratonic lithospheric mantle that experienced a diamond destructive thermal event 1.1 Ga ago. This establishes Victor as an unconventional diamond deposit. As its key outcome, our study implies that future exploration programs in unconventional settings should pay close attention to diamond facies lherzolitic garnets during indicator mineral assessment.

References

- Canil D (1999) The Ni-in-garnet geothermometer: calibration at natural abundances. *Contributions to Mineralogy and Petrology* 136:240-246
- Grütter H, Menzies A (2003) Mutually consistent classification schemes for mantle-derived garnet and chromite, for use by diamond explorers. In: 8th International Kimberlite Conference, Victoria (Canada), Extended Abstracts (CD), pp 1-5
- Gurney JJ (1984) A correlation between garnets and diamonds in kimberlites. In: Glover JE, Harris PG (eds) *Kimberlite occurrence and origin: a basis for conceptual models in exploration*, Vol 8. *Publications Geol Dept & Univ Extension, Univ West Aust, Perth*, pp 143-166
- Hasterok D, Chapman DS (2011) Heat production and geotherms for the continental lithosphere. *Earth and Planetary Science Letters* 307(1-2):59-70
- Januszczak N, Sellar MH, Kurszlaukis S, Murphy C, Delgaty J, Tappe S, Ali K, Zhu J, Ellemers P (2013) A multidisciplinary approach to the Attawapiskat Kimberlite Field, Canada: Accelerating the discovery-to-production pipeline. In: Pearson DG et al. (eds) *Proceedings of the 10th International Kimberlite Conference*, Vol 2, Springer India, New Delhi, pp 157-171
- Leahy K, Taylor WR (1997) The influence of the Glennie domain deep structure on the diamonds in Saskatchewan kimberlites. *Russian Geology and Geophysics* 38(2):481-491
- Nimis P, Taylor WR (2000) Single clinopyroxene thermobarometry for garnet peridotites. Part I. Calibration and testing of a Cr-in-cpx barometer and an enstatite-in-cpx thermometer. *Contributions to Mineralogy and Petrology* 139(5):541-554
- Smit KV, Stachel T, Stern RA (2014) Diamonds in the Attawapiskat area of the Superior craton (Canada): evidence for a major diamond-forming event younger than 1.1 Ga. *Contributions to Mineralogy and Petrology* 167(1):1-16
- Vitarello I, Pollack HN (1980) On the variation of continental heat flow with age and the thermal evolution of continents. *Journal of Geophysical Research: Solid Earth* 85(B2):983-995
- Ziberna L, Nimis P, Kuzmin D, Malkovets VG (2016) Error sources in single-clinopyroxene thermobarometry and a mantle geotherm for the Novinka kimberlite, Yakutia. *Am Miner* 101:2222-2232

Innovative Kimberlite Dike Mining Technologies

Stefan Schwank¹ and Lars Roesler²

¹BAUER Maschinen GmbH, Schrobenhausen, Germany, Stefan.Schwank@bauer.de

²BAUER Technologies South Africa, Johannesburg, South Africa, Lars.Roesler@bauer.de

Introduction

Mining narrow kimberlite dikes to great depths always has been a challenge for diamond miners. Up to now dikes are mined manually by small scale drill and blast operation, supported by hydraulic jack hammers and small excavators. Mining dikes require high manpower utilization at overall low production rates and significant safety hazards. In inclined dikes mining conditions are even worse.

BAUER Mining Technology

Development of the cutter technology for diaphragm and cut-off walls for civil engineering applications started at BAUER in 1984 with a newly developed trench cutter for a cut-off wall project in Bavaria, Germany. Based on this first experience, BAUER has continuously developed the trench cutter system over the last 30 years and nowadays has more than 300 units working around the world.



- Cutter frame
- Steering plates
- Submersible pump
- Suction box with reamer/crusher plates
- Cutter wheels with shock absorbers



Figure 1: left: Key components of a BAUER trench cutter - right: Cutter arrangement for 150 depth.

Two counter rotating cutter wheels (with a foot print of 3,2 m x 1 to 4 m) equipped with pick teeth attached to a heavy cutter frame, are cutting and crushing the rock to maximum 80 mm in particle size. Trench Cutter excavations are performed under bentonite slurry (in civil engineering) or water support (in mining) and the cuttings are pumped to surface for recovery in a separation plant.

The cleaned slurry or water is pumped back to the cutter in a closed cycle to minimise consumption. Rocks with a strength of up to 200 MPa have been cut by the BAUER trench cutters. For deep shafts and due to the increased safety requirements in dam construction, cutter systems can now reach a depth of 250m.

Kimberlite Dike Mining

The relative small size of the ore body over great length and only little outcrop at surface makes it difficult to mine kimberlite dikes economically. Open-pit mining often comes to an end soon due to the high stripping ratio. Underground mining is expensive for the development time and costs and the tight working condition.

The well proven trench cutter and grab systems of BAUER, are very much suitable to mine these kimberlite dikes mechanically from surface. These hands free diamond mining systems includes primary crushing and with the ore being pumped to the separation plant, leads to a better recovery rate and at the same time avoids several stages of re-handling.

The width of the dike as well as the strength of the kimberlite determines the size of the excavation tool. For wider trenches or instable host rock conditions, paste back of pillar or of the entire dike, will provide sufficient support for safe working conditions. Very hard ore bodies above approx. 80 MPa uniaxial compressive strength, can be pre-blasted to mine the dikes economically. The success of pre-blasting however depends on the accuracy of blast and expansion hole drilling, especially in inclined dikes and available expertise in blasting. The BAUER systems are suitable for inclined dikes with not more than 20 degrees from vertical. In such a case, the compressive strength of the ore should be lower than the host rock and the cutter or grab will follow the inclined dike. A special guide frame system is available to start cutter mining with the same inclination as the dike.

Optionally a new cutter head is developed with gripper system to the sidewalls of the trench and high hydraulic forces applied on the cutter head for improved load on bit and thus increased cutter performance in very hard ore.

Kimberlite Dike Mining by Cutter



Most of the kimberlite orebodies in eastern Sierra Leone are kimberlite dikes. Jointly the idea was born with our client to use trench cutter equipment as mining tool for these dikes to greater depth. Despite the remote location, it was decided to carry out trial mining with a cutter BC 33 (figure 2). The cutter width chosen was 800 mm, based on the client's assumption of a dike width between 800 and 1000 mm. Trial excavation in kimberlite was undertaken to 40 m depth.

Kimberlite Large Scale Trial Mining

BAUER and BHP Billiton together with NUNA Logistics successfully tested the cutter system in a large scale trial mining exercise in the Misery pit of the EKATI mine in the Northwest Territories of Canada.

A trench cutter BC 40, still available in the area from the cut-off wall installation on the DIAVIK diamond mine, was mobilized to the EKATI mine (figure 3). Cutter and separation plant BE 500 were rigged-up at the bottom of the pit, sitting directly on kimberlite ore. Different cutter wheels with different teeth arrangements were tested intensively with parameters being varied such as rotation speed, load on bit and pump speed to find the optimum performance. All ore was pumped to the separation plant and collected in big bags for analysis of size distribution, diamond content, potential diamond breakage and so on.

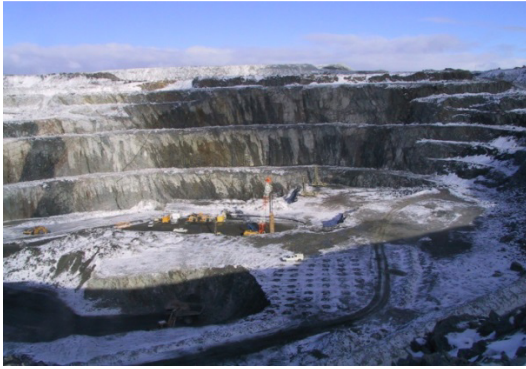


Figure 3: BC 40 in Misery pit, EKATI mine

Diamond Recovery

Further trials with BAUER cutter were conducted with DeBeers of South Africa to prove the safe recovery of diamonds from on-shore alluvial deposits. BAUER's test pit in Schrobenhausen, Germany, was filled with clay, sand, gravels and cobbles. Red tracers with same specific gravity as diamonds and artificial diamonds were placed within the material at specified locations. Utilizing a standard cutter BC 30 and a standard BE 250 separation plant, the material recovered was screened manually which turned out to be difficult due to the huge amount of material. All except one of the red tracers could be recovered. Overall the tests confirmed that a BAUER cutter can recover even diamonds with a specific gravity of 3.51 kg/dm³.

Diamond Breakage

A previous client studied diamond breakage as a result of RC drilling, conventional mining and using the BAUER cutter system. To respect the confidentiality of the client, the Kimberlite deposit and diamond parcel names have been removed, however the results remain intact. The results indicated that the two RC drilling parcels tested had a higher proportion of freshly damaged stones (40% and 36%) of the diamond population (respectively) than the run of mine parcel (27%) and the two BAUER Cutter parcels using the Bauer cutter at 28%. The results suggest that diamond breakage using the BAUER cutter system is consistent with breakage expected in traditional mining methods.

Conclusion – BAUER Cutter Mining - A Selective Sustainable Mining Technology

The advantages of the BAUER Cutter Mining system are:

- Mechanized, hands free mining of Kimberlite dikes (reduced workforce / higher HSE)
- mining of 'uneconomic' small orebodies
- time to mine is extremely short due to standard equipment used
- selective mining with minimum dilution of ore (reduced environmental impact)
- primary crushing incorporated in the system
- equipment can be used on several orebodies or mine sites.

Mining has always been at the centre of various interests. Economic viability, environmental impact and social acceptance are key factors that have to be balanced to achieve a sustainable mining solution. Dike and vein mining with cutter and grab technology is an excellent example for how to achieve these goals and can not only be applied in kimberlite but also in other commodities like coal and gold veins or uranium dikes.

References

Schwank S, 2015. Cutter mining – cross-over technology from civil engineering to mining, in *Proceedings Third International Future Mining Conference*, pp 95–100 (AusIMM; Melbourne).



Evidence for a > 200 km thick diamond-bearing root beneath the Central Mackenzie Valley, Northwest Territories, Canada? Diamond indicator mineral geochemistry from the Horn Plateau and Trout Lake regions

S.P. Poitras¹, D.G. Pearson¹, T. Stachel¹ and S. Cairns²

¹ Department of Earth & Atmospheric Sciences, University of Alberta, Edmonton, Canada, spoitras@ualberta.ca, gdpearso@ualberta.ca, tstachel@ualberta.ca

² Northwest Territories Geological Survey, Yellowknife, Canada, scott_cairns@gov.nt.ca

Introduction

The Horn Plateau and Trout Lake Candidate Protected Areas are located in the Central Mackenzie Valley of the Northwest Territories, Canada. This region, between the western margin of the Slave Craton and the eastern edge of the Cordillera, occupies a portion of the Phanerozoic Western Canadian Sedimentary Basin. Below the > 1 km sequence of Phanerozoic platform rocks lie Precambrian rocks, known from a few deep oil exploration wells. The Precambrian rocks of the Central Mackenzie Valley are believed to be a complex series of magmatic arcs and terranes making up the 2.2-1.8 Ga Wopmay Orogen that formed by subduction of Paleoproterozoic lithosphere below the western Slave Craton. Both LITHOPROBE (Cook et al. 1982) and more recent regional-scale surface wave seismic studies (Schaefer and Lebedev 2014) indicate the likely presence of thick, cold lithospheric mantle extending into the diamond stability field. The Slave-Northern Cordillera Lithospheric Evolution (SNORCLE) transect line 1 also indicates a relatively deep lithosphere-asthenosphere boundary at ~180 km within the region (Cook and Erdmer 2005 and references therein). These studies support the idea that a thick cold subcontinental lithospheric mantle – favourable for diamond exploration – existed prior to rifting of the late-Precambrian supercontinent Rodinia and may still exist at depth, underpinning an area of several hundreds of km² within the Central Mackenzie Valley. Although this region is not a traditional Archean “cratonic” setting – a widely accepted pre-requisite for the occurrence of diamondiferous kimberlites (Janse 1994) – many discoveries of primary diamond occurrences in North America were made in similar settings (e.g. Buffalo Head Hills, northwestern Alberta) suggesting the diamond potential in this region should be further examined.

The Central Mackenzie Valley south of Great Bear Lake, has seen relatively little diamond exploration. Diapros Canada Ltd. first recovered kimberlite indicator minerals (KIM) in the late 1970s in the northwestern Northwest Territories. Currently only Olivut Resources Ltd. is conducting an exploration program in the Central Mackenzie Valley region and have reported the discovery of at least twenty-nine kimberlites (two diamondiferous) since the commencement of their HOAM Project in 1993 (Pitman 2014). The reported KIM chemistry of discovered kimberlites (Pitman 2014), however, differs from that obtained during regional stream sediment and till sampling (Mills 2008, Pronk 2008), suggesting the possible presence of additional, potentially diamondiferous sources. Here we present new major, minor, trace element and isotopic geochemistry on regional Central Mackenzie Valley KIM discovered to date, with the aim of obtaining geotherm, depth of mantle sampling constraints and diamond potential estimates.

Samples

The Horn Plateau region (25,233 km²) lies east and north of the Mackenzie River, > 180 km to the west-southwest of Yellowknife, while the Trout Lake region (10,680 km²) lies > 330 km southwest of Yellowknife, north of the 60th parallel and south of the junction of the Mackenzie and Liard Rivers. In total, ~ 3600 (Horn Plateau) and ~ 640 (Trout Lake) KIM were picked from the 0.25-2.0 mm size fractions, from stream sediments in the Horn Plateau region and till in the Trout Lake region. For the

Horn Plateau, peridotitic garnets dominate the KIM inventory (46 %), followed by ilmenite (26 %), with decreasing individual proportions (< 15 %) of chromite, olivine, chrome-diopside and eclogitic garnet. Trout Lake KIM are also dominated by peridotitic garnet (45 %), followed by chromite (22 %), chrome-diopside (21 %), olivine (10 %) and 1 % of both ilmenite and eclogitic garnet.

Analytical Results

A sub-sample of ~ 3100 (Horn Plateau) and ~ 570 (Trout Lake) KIM grains were analysed by electron microprobe. To this major and minor element data we applied traditional methods of estimating and understanding the diamond potential of the KIM from the two regions, based on the comparison to diamond inclusions from worldwide sources. The Cr-Ca contents of the peridotitic (> 1 wt. % Cr₂O₃) garnets analysed from the two regions suggest significantly different compositions of lithosphere sampled and transported to the surface by kimberlite. From the ~ 1600 Horn Plateau garnet grains collected, lherzolitic garnets (G9) dominate (67 %), followed by high-TiO₂ peridotitic garnets (G11, 17 %) and harzburgitic garnets (G10, 14 %) using the Grütter et al. (2004) classification. Additionally, a relatively large population of the garnets are Cr₂O₃-rich (up to 15 wt. %), suggesting derivation from deep and highly depleted lithosphere extending into the diamond stability field. Conversely, the Trout Lake garnet chemistry is dominated by lherzolitic garnets (G9, 83 %), followed by high-TiO₂ peridotitic garnets (G11, 8 %), wherlitic garnets (G12, 7 %) and no harzburgitic garnets (G10), suggesting kimberlite sampling of a relatively less depleted lithosphere (Grütter et al. 2004).

Paleo-geotherms for each of the two regions were determined using clinopyroxene thermobarometry (Nimis and Taylor 2000), assuming that the grains were locally derived and sampled penecontemporaneously from their mantle sources. The geotherm constrains the depth of lithosphere being sampled and allows the placement of various geochemical groups (e.g. fertile and depleted peridotites) within a lithospheric mantle stratigraphic framework. The well-constrained Horn Plateau geotherm (57 grains) suggests that at the time of volcanic activity it was underlain by a 215 km thick lithosphere; the geothermal gradient is identical to the central Slave Craton, although the mode of sampling occurs at slightly shallower depths (125-175 km). The poorly-constrained Trout Lake geotherm (4 grains) indicates a paleo-geothermal gradient with a substantially shallower base of the lithosphere (175 km) and a mode of sampling between 80-120 km depth, outside the diamond stability field.

A sub-sample of 840 peridotitic garnets and 61 mantle olivine grains from the Horn Plateau were selected for trace element characterization by laser ablation inductively-coupled plasma mass spectrometry (LA-ICP-MS). Similarly, a sub-sample of 168 peridotitic garnets and 42 mantle olivine grains from the Trout Lake region were analysed. The chondrite-normalized rare-earth element (REE_N) patterns of the majority of the peridotitic garnet grains are sinusoidal, typical of diamond inclusions, suggesting these garnet grains may have interacted with diamond forming fluids (Stachel and Harris 2008). Nickel concentrations were used to determine the temperature of equilibration of individual peridotitic (lherzolitic and harzburgitic) garnet grains; the majority of the garnets from the Horn Plateau indicate equilibration temperatures between 850-1150 °C, while those from the Trout Lake region have a smaller range, between 850-1000 °C (averages of Griffin et al. 1989 and Canil 1999). Extrapolation of these data to the two “regional” geotherms indicates significant sampling of garnet-peridotites in the diamond stability field for the Horn Plateau, whilst the small diamond window in the mantle beneath Trout Lake was sampled less extensively. These results are supported by temperature estimates based on the Al-in-olivine geothermometer (Bussweiler et al. 2017) for olivine derived from garnet-peridotite (Al analysed via LA-ICP-MS).

Horn Plateau kimberlitic ilmenite crystals from the 1.0-2.0 mm size fraction (n = 22) were selected for analysis of Hf isotope compositions to derive an age bracket for the emplacement of their source kimberlites. As there were only five kimberlitic ilmenites (0.25-0.5 mm size fraction) recovered from the Trout Lake region, an additional sixty-five rutile grains from this region were analysed by LA-ICP-MS for U-Pb isotopic ratios to help constrain source kimberlite emplacement age. From the Trout

Lake rutile analysed, seven grains (from five samples) had potential U-Pb kimberlitic ages, between ~ 415-110 Ma, consistent with eruption through the Cretaceous to Devonian aged sedimentary rocks found within this region; similar ages are reported for kimberlites elsewhere in the western North American Craton, but they are distinct from the kimberlite ages of the Central Slave Craton. Only five Trout Lake rutile grains have ages similar to the Central Slave (2.8-2.5 Ga), while the remainder (n = 53) have ages between 2.2-1.6 Ga, similar to the Wopmay Orogen. These first constraints on the eruption age(s) of the Central Mackenzie Valley kimberlites, based on rutile U-Pb dating and ilmenite Hf isotope compositions, indicate the potential for three KIM sources for the Horn Plateau region, while possibly two (or more) sources exist for the KIMs supplied to the Trout Lake region.

Discussion

The Horn Plateau KIM are derived from a source underpinned by a cold, deep (> 200 km) diamondiferous root. The geotherm and mantle sampling pattern along with the high proportion of G10 garnets for the Horn Plateau are similar to the Central Slave Craton. However, our initial geochronology results are not consistent with the Central Slave kimberlites representing the source of the KIM in this region but instead indicate the potential for new local kimberlite sources of previously undocumented ages. Our results provide a better understanding of where diamond exploration efforts should be focused in the Central Mackenzie Valley.

References

- Bussweiler Y, Brey GP, Pearson DG, Stachel T, Stern RA, Hardman MF, Kjarsgaard BA, Jackson SE (2017) The aluminum-in-olivine thermometer for mantle peridotites—Experimental versus empirical calibration and potential applications. *Lithos* 272:301-14
- Canil D (1999) The Ni-in-garnet geothermometer: calibration at natural abundances. *Contributions to Mineralogy and Petrology* 136:240-6
- Cook A, van der Velden AJ, Hall KW, Roberts BJ (1982) Frozen subduction in Canada's Northwest Territories: Lithoprobe deep lithospheric reflection profiling of the western Canadian Shield. *Tectonics* 77:1-24
- Cook A, Erdmer P (2005) An 1800 km cross section of the lithosphere through the northwestern North American plate: lessons from 4.0 billion years of Earth's history. *Canadian Journal of Earth Sciences* 42:1295-1311
- Griffin WL, Cousens DR, Ryan CG, Sie SH, Suter GF (1989) Ni in chrome pyrope garnets: a new geothermometer. *Contributions to Mineralogy and Petrology* 103:199-202
- Grütter HS, Gurney JJ, Menzies AH, Winter F (2004) An updated classification scheme for mantle-derived garnet, for use by diamond explorers. *Lithos* 77:841-57
- Janse AJA (1994) Is Clifford's rule still valid? Affirmative examples from around the world. In: Meyer HOA, Leonardos OH (eds) *Diamonds: characterization, genesis and exploration*, CPRM Special Publication, Brasilia, pp 215-235
- Mills AJ (2008) Phase II Non-renewable Resource Assessment : analysis and interpretation of regional stream sediment and water sampling results for the Edézhíé Candidate Protected Area, Northwest Territories, Canada, parts of NTS 85E, F, K, L. NWT Open File 2008-03, pp 1-91
- Nimis P, Taylor WR (2000) Single clinopyroxene thermobarometry for garnet peridotites. Part I. Calibration and testing of a Cr-in-Cpx barometer and an enstatite-in-Cpx thermometer. *Contributions to Mineralogy and Petrology* 139:541-54
- Pitman PW (2014) Technical Report On The HOAM Project, Northwest Territories, Canada NTS Map Sheets 85L, 85M, 95A, 95G, 95H, 95I, 95J, 95O, 95P, 96A and 96B. Olivut Resources Ltd. pp 1-55
- Pronk A (2008) NWT Open File 2008-08 Samba K 'e Candidate Protected Area Phase 1 Non-renewable Resource Assessment – Minerals. NWT Open File 2008-08, pp 1-33
- Schaeffer AJ, Lebedev S (2014) Imaging the North American continent using waveform inversion of global and USArray data. *Earth and Planetary Science Letters* 402:26-41
- Stachel T, Harris J (2008) The origin of cratonic diamonds - Constraints from mineral inclusions. *Ore Geology Reviews* 34:5-32

Origin of coarse-granular and equigranular eclogites from V. Grib kimberlite pipe, Arkhangelsk region, NW Russia

E.V. Shchukina^{1,3}, A.M. Agashev¹, N.G. Soloshenko², M.V. Streletskaya², D.A. Zedgenizov^{1,3}, V.S. Shchukin⁴, N.P. Pokhilenko^{1,3}.

¹Sobolev Institute of Geology and Mineralogy SB RAS, Novosibirsk, Russia, helenaashchukina@gmail.com, shchukinalena@igm.nsc.ru, agashev@igm.nsc.ru, zed@igm.nsc.ru, chief@igm.nsc.ru

²Zavaritsky Institute of Geology and Geochemistry UB RAS, Yekaterinburg, Russia, nats_igg@mail.ru, soloshenko@igg.uran.ru, isotop-igg@mail.ru

³Novosibirsk State University, Novosibirsk, Russia, helenaashchukina@gmail.com, zedgenizov@inbox.ru

⁴Proex Service Ltd., Arkhangelsk, Russia, vlad.shchukin@mail.ru

Introduction

The 372 Ma V. Grib kimberlite pipe (Shevchenko et al., 2004) is located in the central part of Arkhangelsk Diamondiferous Province (ADP) in 135 km NE of the Arkhangelsk city and in 35 km NE of the Lomonosov diamond deposit. As observed from the garnet xenocrysts study from the heavy mineral concentrate (Shchukina et al., 2016), eclogites comprise 10 – 12 % of the mantle population of V. Grib pipe kimberlite. V. Grib pipe eclogite xenoliths could be divided into two main groups based on the textural varieties and mineral composition: coarse-granular (CG) and equigranular (EG) zircon-bearing eclogites. Herein, we present the results of the first comprehensive study of the eclogite xenoliths from the diamondiferous V. Grib kimberlite pipe. This study aims to define the protolith for each of the eclogite samples based on the isotopic, major- and trace-element data.

Analytical Results

CG eclogites are distinguished by large (0.5 – 1.3 cm) fractured bright orange garnet and partly altered dark-green clinopyroxene grains with accessory phases + Phl ± Ilm ± Ru. EG eclogites are composed of minerals (Gar + Cpx + Ilm + Ru + Zr) with a grain size of < 0.2 cm. Al^{VI}/Al^{IV} ratios > 2 in the clinopyroxenes for all eclogites indicates their equilibration at high-pressure conditions (Aoki and Shiba, 1973). CG eclogites are divided into A, B and C groups according to Taylor and Neal (1989) classification. The average Na₂O_{cpx} content increase in the following sequence (wt. %): EG (2.1), Group A (2.4), Group B (4.0), Group C (7.3). The average MgO_{grt} and MgO_{WR} contents increase in the following sequence (wt. %): EG (6.1 and 9.0), Group C (10.8 and 9.6), Group B (12.5 and 11.5), Group A (18.3 and 17.2). P-T estimations indicate that xenoliths were taken by kimberlites

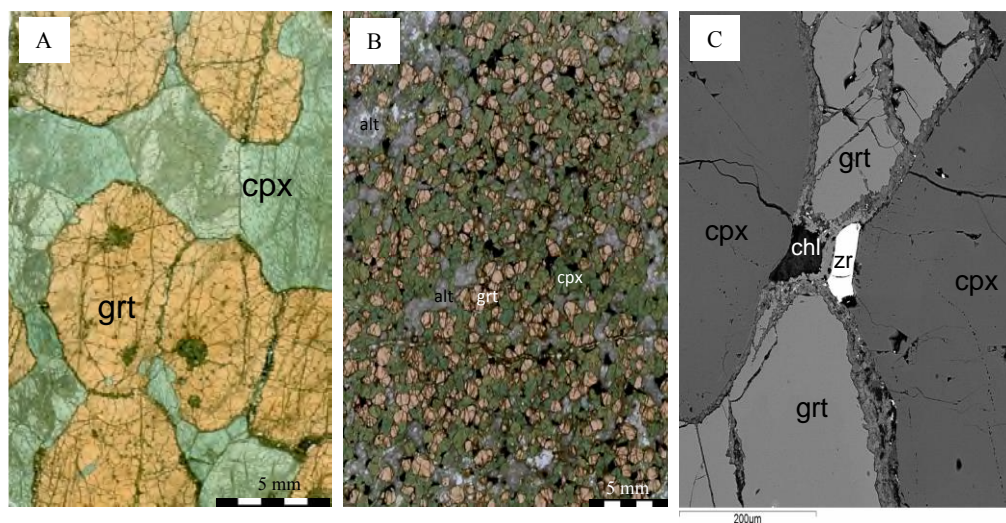


Figure 1. Photos of thin sections of coarse-granular (A) and equigranular (B, C) eclogites from the V. Grib kimberlite pipe. Cpx – clinopyroxene, grt – garnet, zr – zircon, chl – chlorite, alt – altered.

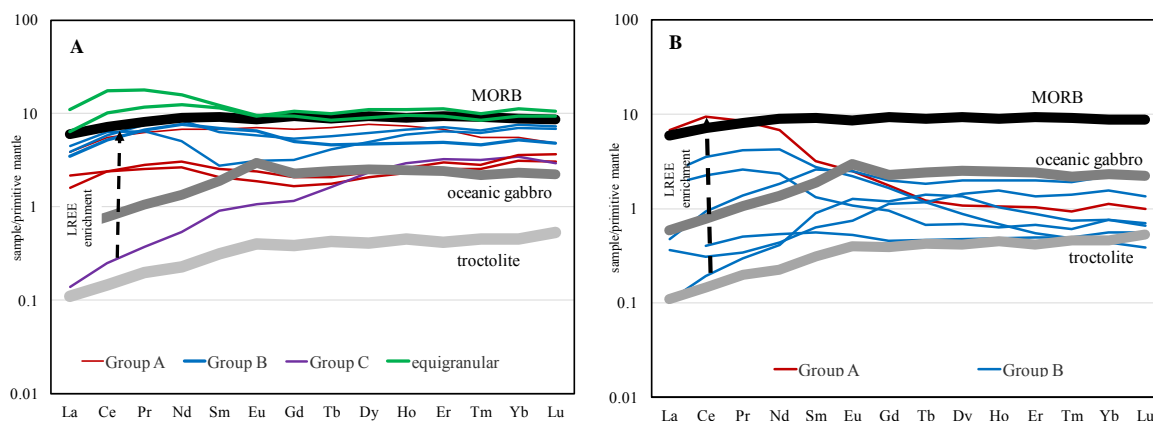


Figure 2. PM-normalized (McDonough & Sun, 1995) reconstructed whole-rock REE profiles of V.Grib pipe CG and EG eclogites. A – eclogites with upper-crustal protholites, B – eclogites with low-crustal protholites. MORB (Le Roux et al., 2002), gabbro and troctolite (Godard et al., 2009).

from the depth of graphite stability field of lithospheric mantle section in case of EG eclogites (~ 120 km) and from diamond stability field in case of CG eclogites (~130 – 240 km). We considered that protoliths for all studied eclogites are of oceanic affinities and remnants of different layers of the oceanic crust. CG eclogites with higher WR HREE predominantly represent upper-oceanic crustal protoliths whereas protoliths for CG eclogites with lower WR HREE could be of gabbro-troctolite series of the lower oceanic crust (fig. 2). High-MgO eclogites of Group A could represent MgO-rich portions in oceanic crustal rocks: picritic/MgO basaltic portions in the upper oceanic crust and/or troctolite/peridotite portion in the lower oceanic crust. EG eclogites retained the geochemical characteristics of MORB and could be the relicts of the oceanic crust which did not undergo partial melting, i.e. products of recrystallization as a result of the evolution of the P–T parameters. However, CG and EG eclogites have different history that is evidenced from the age determination: by Sr and Nd isotope composition of garnet and clinopyroxene for six of CG eclogites samples and by U-Pb and Lu-Hf zircon (19 grains) age for one of EG eclogites. Similarities in Nd isotope composition and 2-point Sm-Nd isochron ages suggest the similar history of CG suite of eclogites: they were taken from the deep levels of lithospheric mantle that were heated by pre-kimberlite thermal event (396 ± 24 Ma) that leads to re-equilibration of Sm-Nd isotope system between garnet and clinopyroxene. Nd DM model age calculated from reconstructed whole-rock composition gives the ranges of age 2.8 Ga, 2.0, 1.8 and 1.2 Ga. Sr isotope composition of clinopyroxenes gives an isochron age of 2.84 Ga. The age of the most of zircons from V. Grib pipe EG eclogite ranges within 1.8–1.9 Ga and the age of 1.2 Ga was obtained from the rim in one zircon grain. $\epsilon_{\text{Hf}(T)}$ values varies from -1.90 to +1.16. Hafnium DM model ages are in range of 2.26 – 2.36 Ga. The calculated two-stage crustal extraction age is 0.23 – 0.32 Ga older than DM model age.

Discussion and conclusions

Archean age obtained from CG eclogites correspond to the age of subduction-related Salma eclogites that outcrops in the Meso-Neoproterozoic Belomorian eclogite province of Kola peninsula. The main subduction event and eclogite-facies metamorphism of the Salma association occurred within the time interval from ~2.87 to ~2.82 Ga (Mints et al., 2014). Late Archean age (2.7 Ga) was also obtained from the V.Grib pipe granulitic zircons that corresponds to major events recorded in upper-crustal rocks of the north-eastern Baltic Shield (Koreshkova et al., 2014). Nevertheless, three of V. Grib pipe CG eclogites samples have Proterozoic Sm/Nd DM model ages of 2.0, 1.8 and 1.2 Ga that correspond to the age of the most of V. Grib pipe EG eclogites zircons. The ages of 2.72 – 2.70 Ga, ~ 2.4 Ga and 1.9 Ga were also obtained from the Salma and Gridino eclogites assemblage of the Belomorian province and indicated the periods of post-eclogite history with mantle plumes invoked (Mints et al, 2014). And, the 1.7 Ga is regarded as the time of exhumation of the Belomorian province eclogite assemblage to mid-to-lower crust under the erosion or younger thermal event (Mints et al, 2014). The Proterozoic ages were also established for the tonalite–trondhjemite–granodiorite (TTG) orthogneiss

and granitoids (1.8–2.0 Ga) representing the lower crust in the area of V. Grib kimberlite pipe (Samsonov et al., 2009) as well as for some granulitic zircons from V. Grib pipe (1.8 – 1.9 Ga; Koreshkova et al., 2014). The age range of 1.8 – 1.9 Ga corresponds to the period of the formation of the orogenic zones upon collision in many cratons worldwide (e.g. Akitkan orogen in Siberia, Russia; Wopmay in NW Canada), including the time of collision of the Karelian and Kola Cratons (Zhao et al., 2002). Data obtained from V. Grib pipe CG and EG eclogites can indicate two major subducted events in the lithospheric mantle of the ADP region: 1) the Archean (2.8 Ga) subduction corresponds to the time of formation of the Meso-Neoproterozoic Belomorian eclogite province in the northeastern Fennoscandian Shield as well as to crustal rock formation of the north-eastern Baltic Shield; 2) the Proterozoic (1.8 – 1.9 Ga) subduction that corresponds to the time of collision of the Karelian and Kola Cratons.

This work was supported by the Russian Science Foundation under Grant No. 16-17-10067.

References

- Aoki, K.-I, Shiba, I (1973) Pyroxenes from lherzolite inclusions of Itiome-gata, Japan. *Lithos*, 6, 41 – 51.
- Godard, M, Awaji, S, Hansen, H, Hellebrand, E, Brunelli, D, Johnson, K., Yamasaki, T, Maeda, J, Abratis, M, Christie, D, Kato, Y, Mariet, C, Rosner, M (2009) Geochemistry of a long in-situ section of intrusive slow-spread oceanic lithosphere: Results from IODP Site U1309 (Atlantis Massif, 30°N Mid-Atlantic-Ridge) *Earth and Planetary Science Letters* 279, 110–122.
- Koreshkova, MYu., Downes, H, Glebovitsky, VA, Rodionov, NV, Antonov, AV., Sergeev, SA (2014) Zircon trace element characteristics and ages in granulite xenoliths; a key to understanding the age and origin of the lower crust, Arkhangelsk kimberlite province, Russia. *Contrib Mineral Petrol* 167:973.
- Le Roux, PS, le Roux, AP, Schilling, JG (2002) Crystallization processes beneath the southern Mid-Atlantic Ridge (40 – 55 ° S), evidence for high-pressure initiation of crystallization. *Contribution to mineralogy and petrology* 142, 582 – 602.
- McDonough, WF, Sun, SS (1995) The composition of the Earth. *Chem Geol* 120, 223–253.
- Mints, MV, Dokukina, KA, Konilov, AN (2014) The Meso-Neoproterozoic Belomorian eclogite province: Tectonic position and geodynamic evolution. *Gondwana Research* 25, 561–584.
- Samsonov, AV, Nosova, AA, Tretyachenko, VV, Larchenko, VA, Larionova, YuO (2009) Collisional Sutures in the Early Precambrian Crust as a Factor Responsible for Localization of Diamondiferous Kimberlites in the Northern East European Platform *Doklady Earth Sciences*, 425 (2), 226–230.
- Shchukina, EV, Agashev, AM, Pokhilenko, NP (2016) Metasomatic origin of garnet xenocrysts from the V. Grib kimberlite pipe, Arkhangelsk region, NW Russia. *Geoscience Frontiers* <http://dx.doi.org/10.1016/j.gsf.2016.08.005>
- Shevchenko, SS, Lokhov, KI, Sergeev, SA (2004) Isotope studies in VSEGEI. Prospects of application of results for predicting and search of diamond deposits, in *Proceedings of Scientific Practical Conference on Efficiency of Prediction and Search for Diamond Deposits: Past, Present, and Future*, St. Petersburg, pp. 383–387.
- Taylor, LA, Neal, CR (1989) Eclogites with oceanic crustal and mantle signatures from the Bellsbank kimberlite, South Africa, Part I: mineralogy, petrography, and whole rock chemistry. *J Geol* 97, 551–567.
- Zhao, G, Cawood, PA, Wilde, SA, Sun, M (2002) Review of global 2.1 – 1.8 Ga orogens: implications for a pre – Rodinia supercontinent. *Earth – Science review* 59 (1 – 4), 125 – 162.



DiaMap: New applications for processing IR spectra of fluid-rich diamonds and mapping diamonds containing isolated nitrogen (Type Ib) and boron (Type IIb)

Daniel Howell¹, Yaakov Weiss², Karen V. Smit³, Lorne Loudin³, Fabrizio Nestola¹

¹ *Università di Padova, I-35131 Padova, Italy. dan@ddl.diamonds, fabrizio.nestola@unipd.it*

² *Lamont-Doherty Earth Observatory of Columbia University, Palisades, NY, USA. yweiss@ldeo.columbia.edu*

³ *Gemological Institute of America, New York City, NY, USA. ksmit@gia.edu, lloudin@gia.edu*

Introduction

Since infrared (IR) spectroscopy was first used to characterise diamonds in the 1930's (Robertson et al., 1934), it has become a commonly used, non-destructive tool in diamond research. Not only does it provide information on various nitrogen-related defects, it can also be used to characterize fluid micro-inclusions in diamonds (Navon et al., 1988), providing key information on different C-O-H-bearing mantle fluid types, and water and carbonate cycling in the Earth's deep interior.

IR studies of diamonds are typically limited to single point analyses, while linear transects of multiple points have also been used to show core to rim variations in nitrogen content and aggregation state, and fluid micro-inclusions composition. Technological developments over the past 15 years, however, have made the application of IR-mapping feasible. DiaMap freeware was developed to take advantage of these new applications (Howell et al., 2012). It allows automated and easy processing of the abundant IR spectra obtained from the IR-mapping of a single diamond, and provides spatial quantitative information of nitrogen- and hydrogen-related defects. IR-mapping of cuboid and fibrous diamonds showed that our traditional understanding from monocrystalline diamonds on the nitrogen aggregation rates and platelet development does not apply to all diamond growth types (Howell et al., 2012). Moreover, since nitrogen aggregation in diamonds is temperature and time dependent, diamond IR-mapping is advantageous for understanding the geological history of natural diamond. Here we report new applications of DiaMap software, allowing easy and quantitative determination of the mineralogy and type of fluids in micro-inclusion-bearing diamonds (DiaMap_Fluid) and automated deconvolution of IR spectral maps collected across plates of Type Ib and IIb diamonds (DiaMap_Ib and IIb).

DiaMap_Fluid

High-density fluids (HDFs) encapsulated in micro-inclusions within diamonds vary between four major compositional types: saline, silicic, and high-Mg and low-Mg carbonatitic. IR spectroscopy is the only method that provides the relative concentrations of water and secondary phases of the mineral assemblage in the microinclusions (i.e., carbonates, silicates and apatite) that grew from trapped HDFs. Constraining the relative abundances of these phases provides information on the amount of water and carbonate in different HDF types, and was proven as a semi-quantitative method to determine carbonatitic to silicic compositions (Weiss et al., 2010). However this was accomplished by manual subtraction of diamond intrinsic absorption and nitrogen absorption, followed by deconvolution of the IR absorbance due to various phases in the micro-inclusions; a long and slow process to be conducted routinely in the study of fluid-rich diamonds.

The complete automation of deconvoluting fluid inclusion-rich diamond IR spectra is complex for the following reasons: (1) a 'one size fits all' approach to baselining and subtracting the various components in the spectrum is almost impossible given the chemical variability observed; (2) automation offers little to no user refinement, and the need to discern the quality of the data output undermines the time saved by automating it. We therefore developed a semi-automated approach – DiaMap_Fluid – for fast subtraction and deconvolution processing of a fluid inclusion-rich diamond IR spectrum. This software allows for user refinement during each stage of spectral processing,

making it a much faster user process, while also greatly enhancing precision in the data output from a single spectrum compared with manual processing by different individuals.

We have applied the DiaMap_Fluid program to 38 fluid inclusion-rich diamonds, from localities in Africa (Finsch, Kankan, DeBeers-Pool, Koingnass), Canada (Ekati) and Russia (Udachnaya, Aykhal). The samples have been studied by quantitative methods including electron microprobe and laser ablation ICPMS (Weiss et al., 2008; 2010), allowing the FTIR data on the water (OH), carbonate and silicate components of the microinclusions to be compared with their bulk chemistry. The results provide the phase concentrations (in ppm by weight) in the diamonds, and show that on a ternary plot of carbonate – water – silicates + apatite (Figure 1), the four HDF end-members fall in fairly distinct groupings. This makes FTIR analyses using the DiaMap_Fluid software a very simple method for determining phase concentrations and broadly discerning the chemistry of HDF in fluid-rich diamonds.

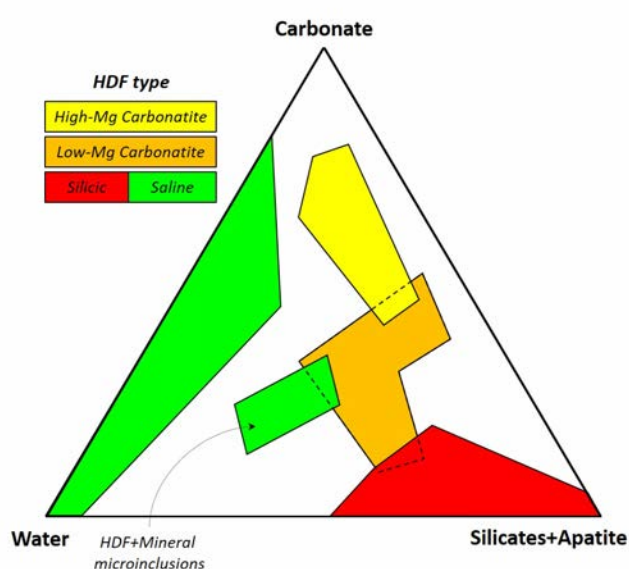


Figure 1: Carbonate – water – silicates + apatite ternary plot showing the relative amount of daughter phases in microinclusions of different HDF types. The fields for HDF in 38 diamonds (high-Mg carbonatite – 13; low-Mg carbonatite – 5; saline – 11; silicic – 9) show minimal overlap, allowing easy and fast characteristics of HDF type in diamonds using the IR analyses and the DiaMap_Fluid software. The small saline field plots away from the water – carbonate axis due to a large proportion of micro-minerals relative to HDF micro-inclusions, in 2 diamonds studied.

DiaMap_Type_Ib

The mapping of isolated nitrogen (N_S) in any natural or synthetic diamond is a relatively simple process compared to the complexities of mantle fluids, and as such has been feasible for some time (Babich & Fiegelson, 2009). Isolated nitrogen produces vibrational peaks at both 1344 cm^{-1} and 1130 cm^{-1} that are correlated with each other. Since the 1344 cm^{-1} peak is sharper, with a clearer peakshape to fit at low concentrations compared to the broad 1130 cm^{-1} peak, we decided to employ this peak to calculate N_S in DiaMap_Ib. Given the two peaks are correlated, data can still be compared between our new datasets and previous datasets that employ the 1130 cm^{-1} calibration.

DiaMap_Ib was used to map N_S in a suite of 15 natural Neoproterozoic Ib diamonds from the Zimmi alluvial deposits in West Africa (Smit et al., 2016). IR absorption was analysed at $100\text{ }\mu\text{m}$ intervals across each double-sided plate, with a high spectral resolution of 1 cm^{-1} to resolve the sharp 1344 cm^{-1} peak. In the 15 samples that were spectroscopically analysed, N_S averages between 12 and 54 ppm, though areas of higher N_S (up to 150 ppm) are observed in the FTIR maps. Comparison between DiaMap_Ib output with N concentrations measured by SIMS show excellent agreement. Fancy brownish-yellow to greenish-yellow colours observed in Zimmi Ib diamonds result mainly from N_S , although deformation-related defects may also contribute to body colour. Maps of N_S concentration in these diamonds are being used to better understand the relationship between N_S and colour distribution, since previous studies have suggested no direct correlation. In the suite as a whole, average N_S (calculated from all the spectra in the FTIR maps) does not correlate to the most vivid colours. For individual diamonds, FTIR mapping will help us understand how N_S concentration affects colour concentration between core and rim, and how N_S impacts the formation of other defects (e.g., NV centres) during exhumation-related deformation (Smit et al., 2016).

DiaMap_Type_IIB

The study of boron in natural diamonds has been very limited due to their high value. Uncompensated boron (i.e., the amount of boron that is in excess of nitrogen) is IR active and can produce several features that have been calibrated for their concentration (Collins, 2010). The primary B peak is $\sim 2800\text{ cm}^{-1}$ ($0.035 \pm 0.0028 \times H_{2800}$ ppm) with a secondary feature at $\sim 2458\text{ cm}^{-1}$ ($0.105 \pm 0.008 \times H_{2458}$ ppm). Boron concentration in natural diamonds is commonly <1 ppm, however in synthetic diamonds, B concentrations can be orders of magnitude higher (>50 ppm; Collins, 2010). As B concentration increases, the 2800 cm^{-1} peak broadens significantly and is no longer quantifiable, but an additional peak appears in the one phonon region $\sim 1290\text{ cm}^{-1}$ ($1.00 \pm 0.15 \times H_{1290}$ ppm; Collins, 2010). As broadening of the primary peak occurs, normalising and subtraction of a Type IIa spectrum by the usual fitting procedure becomes impossible and can only be achieved using calculations involving a sample's thickness. FTIR mapping of B concentration in Type IIb diamonds is important for understanding growth sector dependencies for B incorporation.

Since Type IIb mapping has never previously been achieved, we developed DiaMap_IIB. This routine utilises either the 2800 cm^{-1} or 1290 cm^{-1} peak, depending on whether the primary peak is saturated or not. Mapping of two synthetic samples (provided by New Diamond Technologies) has shown that B is preferentially incorporated into the $\{111\}$ growth sectors, relative to the $\{100\}$ sectors, with an enrichment factor of >30 (~ 0.5 ppm in $\{100\}$ vs ~ 17 ppm in $\{111\}$; Figure 2). In addition to the large inter-sectorial variations, more subtle intra-sectorial variations exist within the $\{100\}$ sectors. This suggests additional factors affect impurity uptake beyond just the difference in bonding opportunities on different crystal faces.

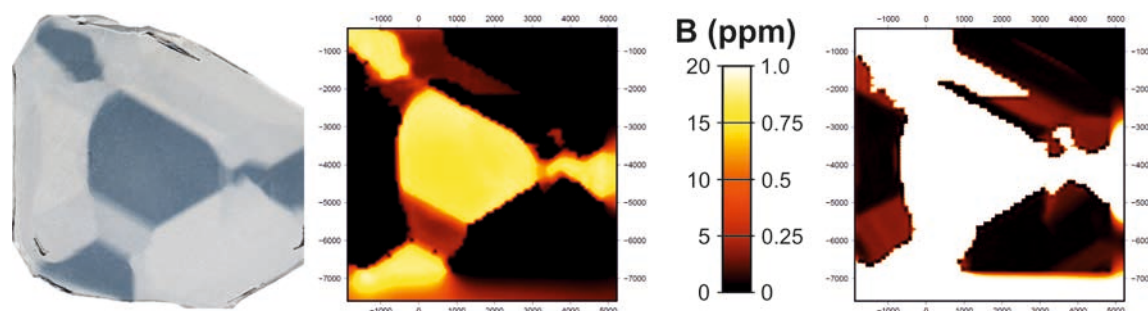


Figure 2: A regular light photograph of a synthetic Type IIb diamond, along with two maps showing boron concentrations (in ppm) generated from the FTIR mapping. The difference between the two maps is the scale bar. In the map on the left, the colour scale runs from 0 – 20 ppm, showing the large concentration difference between growth sectors. In the map on the right, the colour scale only runs from 0 – 1 ppm, highlighting subtle variations within the low concentration $\{100\}$ sectors, while the $\{111\}$ sectors are just shown in white.

References

- Babich YV, Fiegelson BN, 2009. Spatial distribution of the nitrogen defects in synthetic diamond monocrystals: data of IR mapping. *Geochemistry International*, 47, 94.
- Collins A, 2010. Determination of the boron concentration in diamond using optical spectroscopy. *Proceedings 61st Diamond Conference*, Warwick.
- Howell D, O'Neill CJ, Grant KJ, Griffin WL, Pearson NJ, O'Reilly SY 2012. FTIR mapping: distribution of impurities in different types of diamond growth. *Diamond & Related Materials*, 29, 29.
- Navon O, Hutcheon ID, Rossman GR, Wasserburg GJ, 1988. *Nature*, 335, 784.
- Robertson R, Fox JJ, Martin AE, 1934. Two types of diamond. *Phil. Trans. Roy. Soc. Lond.*, 232, 463.
- Smit KV, Shirey SB, Wang W, 2016. Type Ib diamond formation and preservation in the West African lithospheric mantle: Re-Os age constraints. *Precambrian Research*, 286, 152.
- Weiss Y, Kiflawi I, Navon O, 2010. IR spectroscopy: quantitative determination of the mineralogy & bulk composition of fluid microinclusions in diamonds. *Chemical Geology*, 275, 26.
- Weiss Y, Griffin WL, Elhlou S, Navon O, 2008. Comparison between LA-ICP-MS and EMPA analysis of trace elements in diamonds. *Chemical Geology*, 252, 158.

The Liqhobong kimberlite cluster: a perspective on the distinct geology, emplacement, dilution and diamond grades for each intrusion

Mafusi Rapopo¹, Paul Sobie²

¹ Liqhobong Mining Development Company, Butha Buthe, Lesotho, mafusie@gmail.com

² MPH Consulting Limited, Toronto, Canada, psobie@mphconsulting.com

Introduction

The Cretaceous Liqhobong kimberlite cluster comprises at least six known diamondiferous Group 1 kimberlite bodies; namely the circular Main Pipe (8.5 ha), ovoid Satellite Pipe (1.6 ha), Discovery Blow (0.15 ha), Blow (0.1 ha), the Main Dike adjoining the blows and pipes, and one other recently exposed dike. The kimberlites intrude Jurassic Drakensberg lavas and outcrop at ~2650 masl in rugged Maluti Mountain terrain, and are emplaced along a strike of about 2.5km. The cluster represents at least three episodes of structurally controlled kimberlite intrusion; the first which comprised the dike(s?) and the two blows (the blows being dike enlargements emplaced 1km apart) and later the two separate emplacements of the Main and Satellite Pipes.

Relative emplacement of the pipes, blows and dikes

The two pipes and blows are spread over 1.75km with the adjacent Satellite and Main Pipes being 300m apart and both lying NW of the blows (Fig. 1). Both pipes show typical Southern African diatreme kimberlite morphologies with steep-sided walls. A precursor 'Main Dike', intruded by both pipes, trends 300° and is characterised by two to four parallel vertical dikes that are 10 to 60cm wide and separated by a few centimetres of country rock. The other dike trends in the same WNW direction as the Main Dike.



Figure 1. The respective locations of the kimberlites of the Liqhobong cluster.

This newly identified dike is ~45cm wide and was exposed during the current Cut 1 waste stripping at the Main Pipe. Its intrusive relationship within the cluster is unknown at present, however it outcrops ~20m away from the easternmost margin of the Main Pipe and some 120 metres to the south of the Main Dike.

Distinct lithofacies' infill and dilution of the pipes and blows

A local magnetic geophysical survey and interpretation (performed in 1997) points to several other pipe-like features within the mining lease, as well as the position of possible other dikes. It was noted that only limited sections of the Main Pipe display a magnetic response; the bulk of the pipe showing no susceptibility contrast in relation to the country rock. The Satellite Pipe was not surveyed as it was undergoing artisanal production and LMDC ("Liqhobong Mining Development Company") bulk sampling at the time. The Blows on the other hand have very distinctive magnetic anomalies.

Data available for the known Liqhobong kimberlites' classification include surface exposures and >10km of core in 60 drillholes from the Main Pipe, 1.4km in 22 drillholes from the Satellite Pipe, one drillhole from the Blow, eleven drillholes from the Discovery Blow, as well as 790m in 5 drillholes that intersected the Main Dike over short intervals.

Both of the Main and Satellite Pipes are filled with mostly tuffisitic (massive volcanoclastic) kimberlite breccias and marginally with hypabyssal kimberlite. A comparatively more diversified infill is characteristic of the Main Pipe. The dominant infill lithofacies of the Main Pipe, K2 and K5, are massive tuffisitic breccias with distinct black to dark brownish olivine macrocrysts and conspicuous pelletal lapilli (sensu Brown *et al.*, 2009), carbonate veining and, uniquely, basement clasts in K2

(Fig. 2a-b). The two subordinate volcanoclastic kimberlite breccia (VKB) lithofacies, K4 and K6, represent the older pulses and account for less than 15% of the Main Pipe's volume. K6 has distinctive abundant fresh cream coloured olivine macrocrysts whereas K4 has abundant moderate to highly serpentinised darkish green to golden yellow olivine macrocrysts (Fig. 2c), as well as prominent kimberlite indicator mineral ("KIMs") xenocrysts. The macrocryst populations in both K4 and K6 are generally more like that of the Satellite Pipe and the Blows.

The Satellite Pipe and both Blows have conspicuous peridotitic garnet, Cr-diopside, ilmenite, phlogopite xenocrysts, olivine macrocrysts and mantle xenoliths and in decreasing order of abundance range from the Blow, Discovery Blow to the Satellite Pipe. The Satellite Pipe's olivine macrocrysts are mostly cream in colour but have developed moderate to intense serpentinisation (Fig. 2d). The olivine macrocrysts in both Blows are cream to crystal green coloured and mostly fresh (Fig. 2e). Pyrope garnet in both Blows has commonly developed a kelyphitic rim. In general, both the Blow and Discovery Blow are compositionally similar except that the Discovery Blow has comparatively fewer quantities of KIMs xenocrysts. Both Blows commonly display military green tinged alteration of the kimberlite matrix.

Country rock dilution in both the Main and Satellite Pipes ranges up to 30% whereas both Blows generally have less than 10% dilution.

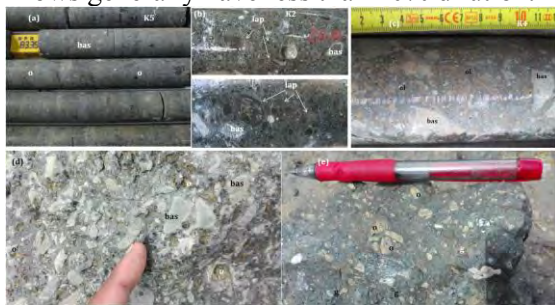


Figure 2. Samples of the Main and Satellite Pipes and Blows at the Liqhobong Property; (a) is K5, (b) is K2 and (c) is K4 - all from the Main Pipe. Sample (d) is from the Satellite Pipe and (e) is from the Blow kimberlite. (bas=basalt, o=olivine, g=garnet, lap=lapilli).

Mode of emplacement of the different kimberlites

All of the Liqhobong kimberlites contain basalt \pm basement, mantle peridotite \pm eclogite xenoliths and mantle xenocrysts and despite having intruded through the Karoo sedimentary rocks which underlie the country rock basalt, host no sedimentary xenoliths.

Both pipes show multifaceted volcanoclastic intrusions exhibiting subvertical to inclined internal contacts. The intrusion characteristics pertinent to the Main Pipe are the evidence of thorough vertical mixing (Fig. 3a), the development of pelletal lapilli in K2 (one of the major lithofacies) and comparatively more abundant development of carbonate veining and segregations, followed by more diversified infills ranging from hypabyssal to massive tuffisic (volcanoclastic) breccias. The Main Pipe exhibits less mantle sampling than the smaller Satellite Pipe and Blows.

The mined out Satellite Pipe's two major lithofacies, S1 and S3/S4, are distinguished by compositional variations, with the dominant S1 MVK more dilute with country rock. Although not always present, S3/S4 exhibits flow alignment wherein clasts are elongated in a common direction, as well as clast segregation evidenced by interlayering of country rock-rich and virtually undiluted kimberlite layers (Fig. 3b). The Satellite Pipe had a large basalt raft (~30m) internal within S1, whereas the Main Pipe has mostly dispersed zones of basalt breccia with the largest megaxenolith exposed thus far measuring ~19m in the K4 lithofacies.

Both Blows are characterised by no lapilli development and virtually no carbonate veining. The presence of kimberlite 'bubbles', typically cored by a small lithic clast (Fig. 3c-d), is observed in both Blows with especially well-established bubbles visible in the Discovery Blow (Fig. 3d). The Blow has similar, but less developed kimberlite bubbles (Fig. 3c). Such 'bubbles' are filled with dark coloured kimberlite matrix, olivine phenocrysts and rare olivine macrocrysts; they do not resemble lapilli.

The Liqhobong Pipes and Blows share a common structural-controlled aspect to their emplacement; all are emplaced along the WNW striking 'Main' Dike which is parallel to the major pervasive jointing in the country rock. The two pipes most likely represent separate

events and are each emplaced in the locus of a network of intersections of at least three pairs of pervasive joints. Each pipe hosts a distinctive macrocrystic kimberlite dike intersected at depth by drill core, which is distinct from the Main dike observed at surface, but which orientation has not been accurately determined. The two Blows are emplaced as enlargements of the 'Main Dike' at their respective positions. The other recently discovered dike is oriented parallel to the Main Dike, and although in its immediate environs no pervasive jointing has been exposed yet, is also parallel to the regional major jointing in the basalt.



Figure 3. The different emplacement mechanisms of (a) Main Pipe showing thorough mixing of clasts, (b) Satellite Pipe showing compositional 'banding', (c) Blow showing poorly-developed kimberlite 'bubble' and (d) Discovery Blow showing well-develop kimberlite bubbles.

Diamond sampling

The Satellite and Main Pipes run of mine production has yielded grades of 68.7cpht and 25cpht respectively with the Main Pipe producing better average stone size and value. There has not been formal bulk sampling or production of the Blows and Dikes. However, the 1996 microdiamond analyses of the Blow, Discovery Blow and 'Main' Dike suggested preliminary +1mm grades of 340, 55 and 37cpht respectively.

Discussion

The similarity in the nature of olivine macrocrysts between the two Blows, the Satellite Pipe and (the earlier) K4 and K6 facies of the Main Pipe, suggests a probable relationship of the associated kimberlite melts and/or sampling of identical mantle. The dispersal and concentration of such near 'identical' mantle was likely governed by the volume of magma influx, structurally

controlled accommodation space and the fluids' budget. Generally, the Main and Satellite Pipes are more diluted with country rock than the Blows. Both Blows are dike enlargements and therefore possibly intruded through a narrow fissure and consequently incorporated smaller amounts of country rock. Also, the Blows' magmas seemed to have been comparatively dry, as witnessed by the 'dry' bubbles therein.

Judging by the similarity in the nature of olivine macrocrysts in K5, K2 and K1 of the Main Pipe, it appears that these lithofacies represent similar or related magmas and sampled identical mantle and one that differs from that sampled by all other Liqhobong kimberlite intrusions. The presence of pelletal lapilli in K2, accompanied by modest carbonate veining, suggest a more fluidised environment than in K5.

Conclusion

The observed diversity in the mode of emplacement, mantle sampling and associated diamond grades of kimberlites so closely spaced at Liqhobong suggests a period of aggressive kimberlite intrusion. All evidence suggests the emplacement of the Liqhobong kimberlites was controlled primarily by pre-existing structures (United Nations, 1984) and secondarily by the nature of the intruding kimberlite including the fluid budget and accommodation space. The differential fluid budget amongst the Liqhobong kimberlites is testified by the differing degree of serpentinisation of olivine macrocrysts and phenocrysts, the absence or presence of carbonate veining and segregations, by the presence of brecciated basalt or kimberlite, and by the presence or absence of pelletal lapilli.

References

- Brown RJ, Tait M, Field M, Sparks RSJ (2009). Geology of a complex kimberlite pipe (K2 pipe, Venetia Mine, South Africa): insights into conduit processes during explosive ultrabasic eruptions. *Bull Volcanol* 71:95-112
- United Nations (1984) Geology and mineral resources of Lesotho – exploration for diamonds (phase I) and exploration for minerals (Phase II). Technical Report.

Geochronology and mantle source characteristics of kimberlites and related rocks from the Rae Craton, Melville Peninsula, Nunavut, Canada

Chiranjeeb Sarkar^{1*}, Bruce A. Kjarsgaard², D. Graham Pearson¹, Larry M. Heaman¹, John P. Armstrong³

¹ Department of Earth and Atmospheric Sciences, University of Alberta, 1-26 Earth Sciences Building, Edmonton, Alberta, Canada T6G 2E3

² Geological Survey of Canada, 601 Booth Street, Ottawa, Ontario, Canada, K1A 0E8

³ Lucara Diamond, Vancouver, Canada V6C 3E8

Introduction

Kimberlites of the Qilalugaq cluster were first discovered in 2003 by BHP Billiton approximately 10 km NE of the hamlet of Repulse Bay on the Rae Isthmus, southern Melville Peninsula, Nunavut, NE Canada. The Aviat kimberlite cluster was discovered by Stornoway Diamonds in 2002, approximately 60 km WSW of Igloolik on the Melville Peninsula (Fig 1). Subsequent detailed exploration program on these kimberlites revealed that kimberlites in both of these clusters are diamondiferous. The grade of Aviat kimberlites (80-160 carat per hundred ton) is significantly higher than those of the Qilalugaq cluster (14-40 carat per hundred ton). In this study, we present the first U-Pb perovskite (CaTiO_3) geochronology of several kimberlite bodies to determine their emplacement ages along with the tracer isotope data to evaluate the evolution and nature of the mantle sources. We have also carried out new mineralogical and petrographic characterisation of these kimberlites to comment on their nomenclature and degree of alteration.

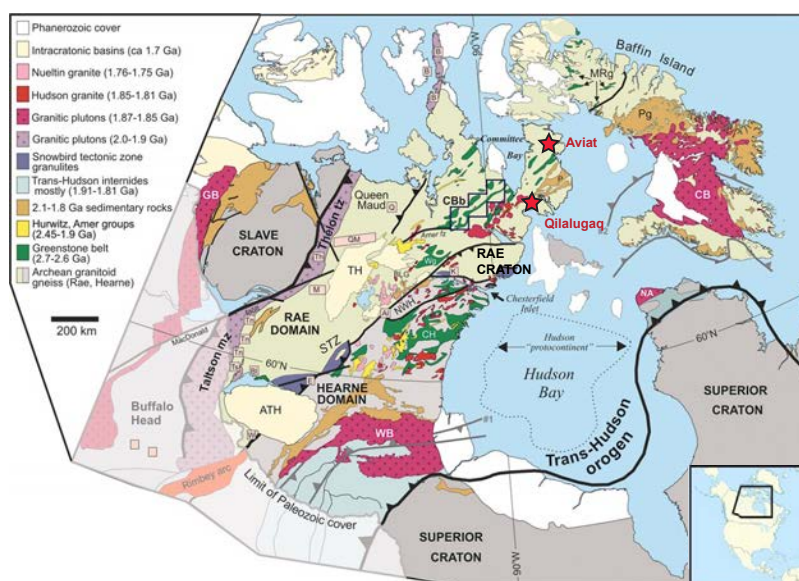


Fig 1: Simplified geological map of the Canadian Shield (modified after Berman, et al. (2005)). Location of Aviat and Qilalugaq kimberlite clusters shown by red stars.

Kimberlites and sampling

Both the Aviat and Qilalugaq kimberlite clusters intruded Archean tonalite-granodiorite gneisses, metasedimentary and metavolcanic rocks of the Rae craton (Dredge 2002). The Aviat cluster comprises 3 kimberlite pipes (AV1, AV4 and AV9) and five sheet-like bodies (AV2, AV3, AV5, AV8 and AV267; (Armstrong, et al. 2008)). All Aviat kimberlites occur within a 10 km long and 3

km wide corridor. The Aviat pipes mostly consist of coherent (hypabyssal) kimberlite (HK) to tuffisitic kimberlite breccia (TKB) while the sheet-like structures are dominated by HK and hypabyssal kimberlite breccia (HKB). The Qilalugaq cluster, located ~300 km to the south of Aviat, also consists of numerous kimberlite bodies including the Q1-4 complex that comprises four coalescing phases (A28, A48, A61 and A88) and several isolated kimberlite pipes (A34, A42, A59, A76, A94, A95, A152). Several dyke-like structures (Naujaat 1 to Naujaat 8) of variable width (1.5 m to 4.5 m) were also discovered (Kupsch and Armstrong 2013). The dominant phase in most of the Qilalugaq pipes and the dykes is a massive volcanoclastic kimberlite (MVK) that can be classified as TKB, which commonly transitions toward HK with depth. They all show variable degrees of country rock dilution with the dykes being diluted more than the pipes. Qilalugaq kimberlites contain peridotitic xenoliths with multi-modal Re-depletion ages ranging from Archean (3.0-2.7 Ga), Paleoproterozoic (2.1–1.7 Ga) and “Recent” (<1 Ga), suggesting the kimberlites intruded through a complex layered lithosphere (Liu, et al. 2016).

Samples were collected from both kimberlite clusters in the summer of 2012, from the pits and trenches remaining after the earlier exploration. Some drill core samples were also used for petrographic and mineralogical study. Relatively hard and unaltered HK were chosen for perovskite recovery following a standard heavy mineral separation.

Petrography and Mineralogy

The Aviat pipes and sheets examined are all hypabyssal (coherent) rocks and are broadly similar from a mineralogical perspective. Large olivine grains are set in a groundmass of olivine, apatite, perovskite, spinel (chromite zoned to Ti-magnetite), ilmenite, calcite and poikilitic, zoned phlogopite. All olivine grains are variably replaced by calcite and/or serpentine. However, the Aviat sheets are distinctive in that apatite, perovskite and calcite are less abundant, and there is a higher proportion of groundmass ilmenite and spinel as compared to samples from the Aviat pipes. In the sheets, rutile +/- dolomite is also observed as secondary mineral(s). The Qilalugaq and Naujaat samples are quite variably altered; the Naujaat dykes being extensively carbonatized (>60% dolomite, +/-calcite), or silicified (45-60 wt% SiO₂). In the Naujaat samples, the olivine is completely replaced; only groundmass apatite, spinel and phlogopite are preserved, with secondary rutile and dolomite. Hypabyssal (coherent) samples from A34, A88 and A94 are similar, with olivine (replaced by serpentine and/or carbonate) set in a groundmass of apatite, spinel (chromite zoned to Ti-magnetite), phlogopite, calcite (+/-dolomite), +/-perovskite. All of the samples noted above from Aviat, Qilalugaq and Naujaat classify as being kimberlite, using the criteria of Woolley, et al. (1996). However, hypabyssal samples from Qilalugaq A61 consist of olivine set in a groundmass of apatite, perovskite, spinel, tetraferriphlogopite, calcite, augite and Ti-andradite (schorlomite-melanite) garnet; the latter two minerals consistent with these samples being ultramafic lamprophyres or orangeites, but not Gp I (archetypal) kimberlites. Mineral chemistry studies are currently being undertaken to refine the classification of these rocks.

Results and Discussion

ID-TIMS U-Pb analyses of seven perovskite fractions from both Aviat and Qilalugaq kimberlites indicate their early Cambrian age. While the major pipes from both clusters were emplaced between 531 and 536 Ma, the sheet-like kimberlite bodies at Aviat are ~30 Ma younger, emplaced between 503 and 507 Ma. Perovskite U-Pb results from the Naujaat dykes, gave a Proterozoic date, but is considered unreliable due to their unusually high common Pb correction. In general, Cambrian kimberlites are uncommon worldwide. The ~530 Ma Venetia kimberlite in South Africa is perhaps the best known. However, there are several kimberlite clusters of Late Neoproterozoic to Eocambrian age that have been reported from North America and some of these have economic diamond potential. These include Pelly Bay from Rae craton (Kienlen, et al. 2008; Liu, et al. 2016), Snap Lake and Gahcho Kué from SE Slave craton (Heaman, et al. 2004), Renard and Wemindji from the Superior craton (Tappe, et al. 2016), Chicken Park and George Creek from the Wyoming craton (Heaman, et al. 2004). Several other kimberlites (Labrador Sea Province, Lac Beaver kimberlite) and related rocks

(ultramafic lamprophyres and carbonatites from Labrador and west Greenland) of similar age have been reported from eastern North America and western Greenland (Heaman, et al. 2004; Tappe, et al. 2014). This region of north-eastern North America and western Greenland has been termed the Eocambrian/Cambrian Labrador Sea Province and the magmatism here has been suggested to be associated to Eocambrian rifting along the northeastern margin of Laurentia and opening of the Iapetus Ocean (Heaman, et al. 2004).

Sr-Nd tracer isotopes were also obtained on the same perovskite fractions used for U-Pb dating from Qilalugaq and Aviat. The main kimberlite pipes at Qilalugaq (A61 and A94) and Aviat (AV1) have overlapping, relatively restricted $^{87}\text{Sr}/^{86}\text{Sr}_i$, varying between 0.70405 and 0.70465. The Sr isotopic signature of these pipes are slightly more radiogenic than typical Cretaceous age Group I kimberlites from South Africa (Nowell, et al. 2004) but are very similar to other Canadian kimberlites, such as Lac de Gras, Kirkland Lake, Somerset Island, and Fort à la Corne (e.g., Tappe, et al. (2013)). In contrast, the sheet-like bodies (AV2 and AV6) have considerably more radiogenic signatures ($^{87}\text{Sr}/^{86}\text{Sr}_i = 0.70948\text{-}0.70969$). Initial ϵNd values from Qilalugaq kimberlites define a very narrow range of +4.2 and +4.7, consistent with the restricted $^{87}\text{Sr}/^{86}\text{Sr}_i$ values. In contrast, those from Aviat kimberlites cluster around chondritic values (-1.5 to +1.5). The homogeneous Sr-Nd isotopic nature of the main kimberlites from Aviat and Qilalugaq and their position on a mantle array in ϵNd vs $^{87}\text{Sr}/^{86}\text{Sr}$ space suggest their derivation from the asthenosphere or transition zone. However, the more radiogenic signature recorded by the perovskites from sheet-like intrusions at Aviat are unlikely to be due to any contamination/alteration, as perovskite is much more robust to the effects of crustal contamination. Hence, these younger kimberlites may be derived from a Subcontinental Lithospheric Mantle source, similar to that recorded in high-T peridotite xenoliths entrained in the nearby Somerset Island kimberlites (Schmidberger and Francis 2001).

References

- Armstrong J, Stublely M, Chang F (2008) Geology and exploration history of the Aviat kimberlite cluster, northern Rae craton, Melville Peninsula, Nunavut, Canada. In: 9th international kimberlite conference, Frankfurt, Germany, Extended Abstract, vol 266.
- Berman RG, Sanborn-Barrie M, Stern RA, Carson CJ (2005) Tectonometamorphism at ca. 2.35 and 1.85 Ga in the Rae domain, western Churchill Province, Nunavut, Canada: insights from structural, metamorphic and in situ geochronological analysis of the southwestern Committee Bay Belt. *The Canadian Mineralogist* 43(1):409-442
- Dredge LA (2002) Quaternary geology of southern Melville Peninsula, Nunavut: surface deposits, glacial history, environmental geology, and till geochemistry. Geological Survey of Canada,
- Heaman LM, Kjarsgaard BA, Creaser RA (2004) The temporal evolution of North American kimberlites. *Lithos* 76(1):377-397
- Kienlen B, Blackmore E, Curry N, Gill G, Kolebaba M, Lyon R, Ozyer C, Pratt Z, Vanderspiegel R (2008) The Amarak project in Canada's new Pelly Bay diamond district. In: 9th International Kimberlite Conference Extended Abstract, vol., p 00334
- Kupsch B, Armstrong J (2013) Exploration and Geology of the Qilalugaq Kimberlites, Rae Isthmus, Nunavut, Canada. In: Proceedings of 10th International Kimberlite Conference, vol. Springer, pp 67-78
- Liu J, Riches AJ, Pearson DG, Luo Y, Kienlen B, Kjarsgaard BA, Stachel T, Armstrong JP (2016) Age and evolution of the deep continental root beneath the central Rae craton, northern Canada. *Precambrian Research* 272:168-184
- Nowell G, Pearson D, Bell D, Carlson R, Smith C, Kempton P, Noble S (2004) Hf isotope systematics of kimberlites and their megacrysts: new constraints on their source regions. *Journal of Petrology* 45(8):1583-1612
- Schmidberger S, Francis D (2001) Constraints on the trace element composition of the Archean mantle root beneath Somerset Island, Arctic Canada. *Journal of Petrology* 42(6):1095-1117
- Tappe S, Brand NB, Stracke A, van Acken D, Liu C-Z, Strauss H, Wu F-Y, Lugué A, Mitchell RH (2016) Plates or plumes in the origin of kimberlites: U/Pb perovskite and Sr-Nd-Hf-Os-CO isotope constraints from the Superior craton (Canada). *Chemical Geology*
- Tappe S, Graham Pearson D, Kjarsgaard BA, Nowell G, Dowall D (2013) Mantle transition zone input to kimberlite magmatism near a subduction zone: Origin of anomalous Nd-Hf isotope systematics at Lac de Gras, Canada. *Earth and Planetary Science Letters* 371-372(0):235-251
- Tappe S, Kjarsgaard BA, Kurszlauskis S, Nowell GM, Phillips D (2014) Petrology and Nd-Hf isotope geochemistry of the Neoproterozoic Amon kimberlite sills, Baffin Island (Canada): evidence for deep mantle magmatic activity linked to supercontinent cycles. *Journal of Petrology* 55(10):2003-2042
- Woolley AR, Bergman SC, Edgar AD, Le Bas MJ, Mitchell RH, Rock NM, Scott Smith B (1996) Classification of lamprophyres, lamproites, kimberlites, and the kalsilitic, melilitic, and leucitic rocks. *Canadian Mineralogist* 34:175-186



Ages of mantle metasomatism from U-Th-He systematics of diamond-forming C-O-H fluids

Yaakov Weiss, Cornelia Class, Steven L. Goldstein and Gisela Winckler

Lamont-Doherty Earth Observatory of Columbia University, New York, United States, yweiss@ldeo.columbia.edu

Introduction

Carbon and water-rich (C-O-H) mantle fluids play a major role in metasomatism of the deep sub-continental lithospheric mantle (SCLM). Yet the origin and composition of the fluids involved and, in particular, the timing of metasomatic fluid-rock interaction, is still poorly constrained. 'Fibrous' diamonds form over short time intervals during metasomatism by percolating C-O-H fluids in the SCLM. Fibrous diamonds commonly encapsulate C-O-H fluids as μm -scale high-density fluid (HDF) inclusions, which can be directly sampled. Due to the physical strength and chemically inert nature of their diamond host, these HDF inclusions remain pristine for billions of years even when brought to Earth's surface. They thus offer a unique opportunity to investigate metasomatic events involving C-O-H mantle fluids and the SCLM through Earth's history. But until now no technique has been able to provide direct and reliable age constraints on HDFs.

Here we explore the radioactive U-Th-He system in HDF microinclusions-bearing fibrous diamonds as a tool for providing meaningful radiometric ages of C-O-H mantle fluids, and to constrain the timing of metasomatic events in the SCLM. The HDFs in 'fibrous' diamonds exhibit high helium concentrations up to $\sim 10^{-5}$ ccSTP/g, and are enriched in incompatible elements (including U and Th). Nonetheless, only few such diamonds have been analyzed until now for their He contents and $^3\text{He}/^4\text{He}$ ratios, despite the great opportunities they provide for investigating deep mantle volatiles. We have developed an in-vacuum crushing technique for determining the He concentrations and $^3\text{He}/^4\text{He}$ ratios in the trapped HDFs. Combined with EPMA and LA-ICP-MS analyses of major and trace element abundances of HDFs in the same diamonds, we determine the amount of U, Th and He in the fluids themselves, as opposed to their concentrations in the bulk diamonds. Below we present preliminary data and show that HDF type and $^3\text{He}/^4\text{He}$ ratios are related. In addition, diamonds from the Kimberley cluster and the Finsch mine, South Africa, reveal 3 metasomatic events in the southwestern Kaapvaal SCLM during the last ~ 1 Gyr, each by a different metasomatic agent. The youngest episode indicates direct relationships between metasomatism by highly saline fluids, fibrous diamond formation and late-Mesozoic kimberlite eruptions.

Helium contents and $^3\text{He}/^4\text{He}$ ratios in different C-O-H mantle fluid-types

HDFs in fibrous diamonds vary in major-element compositions between four major types: silicic, saline, and high-Mg and low-Mg carbonatitic. Moreover, they display two main trace-element patterns, one with high field strength element (HFSE) depletions and large ion lithophile element (LILE) enrichments, similar to calcalkaline magmas and continental rocks, the other with lower LILE abundances and 'smoother' overall trace-element patterns, similar to oceanic basalts. Thus, HDFs record a large range of compositions and sources for the metasomatic C-O-H mantle fluids. Recently, Weiss et al. (2015) reported the first conclusive trace-element and Sr isotope evidence for seawater-altered subducting slabs as the source of deep C-O-H-bearing mantle fluids having saline compositions, and that these fluids are parental to carbonatitic and silicic melts formed *in-situ* within the lithosphere.

We report He contents and $^3\text{He}/^4\text{He}$ ratios of HDFs in 15 fibrous diamonds, previously analyzed for their major-element compositions. Excluding three diamonds having non-saline HDFs with radiogenic $^3\text{He}/^4\text{He}$ signatures (see discussion below), the saline HDFs have the lowest $^3\text{He}/^4\text{He}$ ratios (Fig. 1a). Our preliminary

He analyses on 6 diamonds carrying saline HDFs strengthen the connection between saline-type deep C-O-H fluids and recycled subducted surface material, based on their low $^3\text{He}/^4\text{He} \approx 3.5 R_A$ (where R_A is the atmospheric ratio of 1.39×10^{-6}). Also, $^3\text{He}/^4\text{He}$ ratios of HDFs and the amount of K_2O (in wt.%) and carbonate component (expressed as $(\text{MgO}+\text{FeO}+\text{CaO})/\text{SiO}_2/\text{Cl}$; Fig. 1b) correlate. This may reflect the involvement of subduction-related saline fluids in the formation of silicic and carbonatitic HDFs within the lithosphere, as concluded by Weiss et al. (2015). The South African silicic and carbonatitic diamonds have more radiogenic $^3\text{He}/^4\text{He}$ ratios compared to saline diamonds from the same kimberlite pipes, and much lower $^3\text{He}/^4\text{He}$ compared to silicic and carbonatitic diamonds from Botswana and Guinea (Fig. 1). This could suggest a complex evolution of diamond source fluids. Alternatively, the varying $^3\text{He}/^4\text{He}$ signatures of different C-O-H fluid compositions could represent different metasomatic events at different times over the history of local continental mantle.

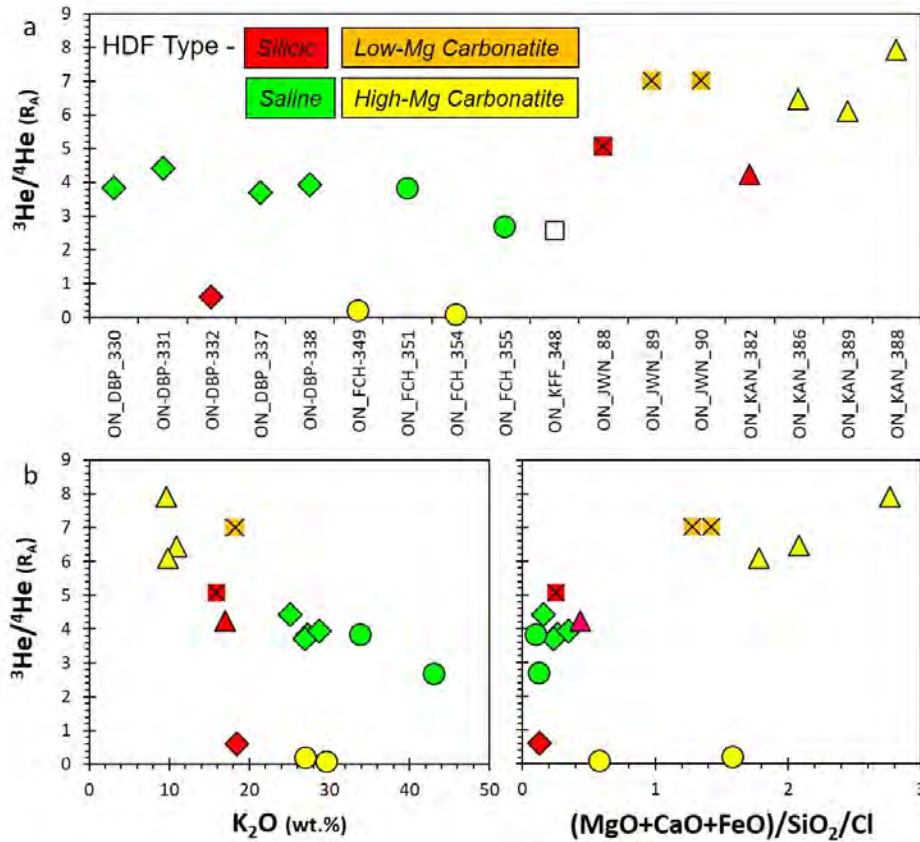


Figure 1: $^3\text{He}/^4\text{He}$ ratio (in R_A) of different HDF compositional types. (a) $^3\text{He}/^4\text{He}$ (R_A) of 17 diamonds from DeBeers-Pool (DBP), Finsch (FCH) and Koffiefontein (KFF; HDF type not yet determined), South Africa; Jwaneng (JWN), Botswana; Kanakan (KAN), Guinea. Data for the 2 low-Mg carbonatitic diamonds from Jwaneng are from Schrauser and Navon (1994) and Burgess et al. (1998). (b) $^3\text{He}/^4\text{He}$ (R_A) against K_2O (in wt.%) and against $(\text{MgO}+\text{FeO}+\text{CaO})/\text{SiO}_2/\text{Cl}$, expressing the amount of carbonate in the HDF.

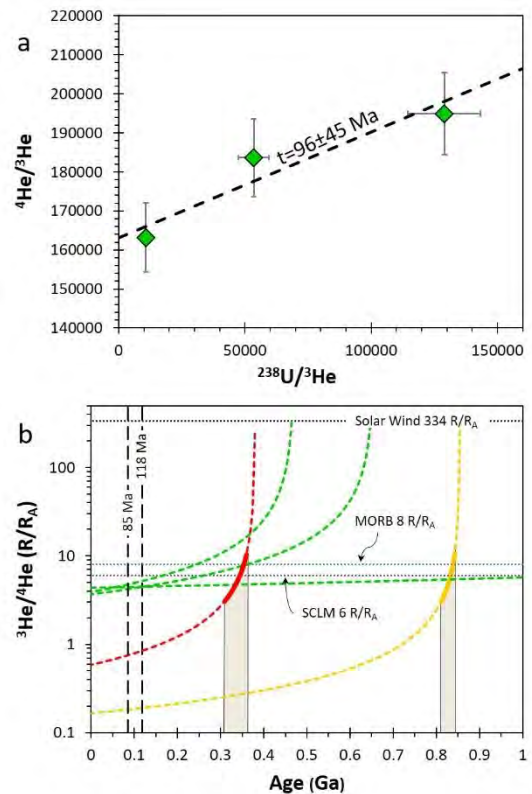
A billion years of metasomatic alteration of the Kaapvaal SCLM encapsulated in fibrous diamonds

The different kimberlites in the DeBeers-Pool cluster and the Finsch kimberlite are close in space and age and sample the southwestern part of the Kaapvaal SCLM. One Finsch and four DeBeers-Pool diamonds have high and uniform microinclusion densities, and an inner fragment of each diamond could be separated and analyzed for He. This prevents possible effects of implantation of ^4He from the surrounding host rock, or the loss of ^4He due to α -recoil from the outer $<20 \mu\text{m}$ of the diamond. U-Th-He ages were calculated for

these diamonds. The saline HDFs in 3 of the DeBeers-Pool diamonds have very similar major and trace element compositions and low-aggregated states of nitrogen (IaA-type IR spectrum), suggesting their formation during a single metasomatic event by C-O-H fluids close in time to kimberlite eruption (Extended Abstract No. 11IKC-004461). Plotting these diamonds on a $^4\text{He}/^3\text{He}$ vs. $^{238}\text{U}/^3\text{He}$ defines an isochron with an age of 96 ± 45 Myr (Fig. 2a). This result represents the first radiometric age reported for fibrous diamonds and the C-O-H mantle fluids they carry. In addition, 1 diamond from the DeBeers-Pool has silicic microinclusion compositions while 2 from Finsch carry carbonatitic HDFs. These diamonds display more radiogenic $^3\text{He}/^4\text{He}$ ratios of 0.59 and 0.17 R_A (Figure 1a), and associated aggregated nitrogen IaAB-type IR spectra with 25% and 32% B-centers, respectively, suggesting their formation during earlier and different metasomatic events.

Using the U, Th, ^4He and ^3He contents of these diamonds, and the equation for ^4He production by U and Th decay, we calculate $^3\text{He}/^4\text{He}$ ratios as a function of time. Assuming that the HDFs initial R/R_A values varied between 3-11, representing common values for MORB, the SCLM and subducted components, the silicic and carbonatitic HDFs represent two older metasomatic events that took place in the Kaapvaal SCLM at ~ 350 and ~ 850 Myr (Figure 2b). Thus, our new data reveal 3 episodes of chemical changes in the Kaapvaal SCLM during the last ~ 1 Gyr, each by a different metasomatic agent. The youngest episode indicates direct relationships between highly-saline fluid metasomatism, fibrous diamond formation and late-Mesozoic kimberlite eruptions, while the older silicic and carbonatitic metasomatic events may be related to the regional Namaqua-Natal Orogeny (~ 1 Gyr), Damara Orogeny (~ 500 Myr) or the Karoo magmatism (~ 200 Myr).

Figure 2: (a) A $^4\text{He}/^3\text{He}$ vs. $^{238}\text{U}/^3\text{He}$ isochron diagram for 3 saline HDF-bearing diamonds from the DeBeers-Pool giving a diamond formation and metasomatism age of 96 ± 45 Myr (calculated based on the least squares fitting of a straight line with correlated errors). Error bars account for a possible $\pm 15\%$ on the U concentrations, $\pm 2\%$ on the ^4He and $\pm 5\%$ on the ^3He content. (b) $^3\text{He}/^4\text{He}$ model ages for DeBeers-Pool and Finsch fibrous diamonds. The diagram illustrates $^3\text{He}/^4\text{He}$ ratios as a function of age for the different diamonds (dotted lines), calculated based on the measured $^3\text{He}/^4\text{He}$ and the ^4He , ^3He , U, and Th concentrations in these diamonds. Importantly, saline fluids (green – same diamonds as in 2a) controlled the metasomatism in the Kaapvaal craton before late-Mesozoic kimberlite eruption (at 85 Myr), and that at least two additional metasomatic events by silicic (red - DeBeers-Pool) and carbonatitic (yellow - Finsch) C-O-H fluids took place in the Kaapvaal SCLM during the last 1 Gyr. If we assume an initial $^3\text{He}/^4\text{He}$ in the range of 3-11 R_A (thick red and yellow lines), then these metasomatic events occurred at ~ 350 and ~ 850 Myr.



References

- Weiss Y, McNeill J, Pearson DG, Nowell GM, Ottley CJ (2015) Highly saline fluids from a subducting slab as the source for fluid-rich diamonds. *Nature* 524:339-342.
- Burgess, R., Johnson, L.H., Matthey, D.P., Harris, J.W., Turner, G., 1998. He, Ar and C isotopes in coated and polycrystalline diamond. *Chemical Geology* 146, 205–217.
- Schrauder, M., Navon, O., 1994. Hydrous and carbonatitic mantle fluids in fibrous diamonds from Jwaneng, Botswana. *Geochimica et Cosmochimica Acta* 58, 761–771.



Thermo-chemical conditions of Mesozoic metasomatism at the southwestern Kaapvaal SCLM

Yaakov Weiss¹, Oded Navon², Steven L. Goldstein¹ and Jeff W. Harris³

¹ Lamont-Doherty Earth Observatory of Columbia University, New York, United States,

yweiss@ldeo.columbia.edu, steveg@ldeo.columbia.edu

² The Hebrew University of Jerusalem, Jerusalem, Israel, oded.navon@mail.huji.ac.il

⁴ University of Glasgow, Glasgow, United Kingdom, Jeff.Harris@glasgow.ac.uk

Introduction

The SCLM of the southwestern part of the Kaapvaal Craton in South Africa has been studied intensively. Mantle derived xenoliths and xenocrysts from this area document intensive Archean melt extraction, followed by a complex metasomatic history. The timing of metasomatism coincides with Archean subduction events during and after amalgamation of the Craton, and with Proterozoic and early Phanerozoic orogenies. ‘Young’ metasomatism is attributed to Mesozoic magmatism, by both Karoo flood basalts (175-185 Myr) and the eruptions of Group II (mainly at 125±10 Myr) and Group I (at 85±5 Myr) kimberlites. Along with chemical modifications, mantle metasomatism is responsible for both thermal perturbation and changes in the oxygen fugacity (fO_2) of the SCLM; where mantle xenoliths and xenocrysts are likely to record mainly the changes resulting from the last metasomatic event. Temperature variations recorded by xenoliths are commonly interpreted as the result of Cretaceous metasomatism, occurring between the Group II and Group I kimberlite episodes, while metasomatic fO_2 increases from core-to-rim in some xenolithic garnets are estimated to take place within <1 Ma of kimberlite eruptions.

Here, we focus on the recent metasomatic events that took place at the southwestern Kaapvaal SCLM. However rather than investigating the chemical changes of lithospheric rocks and inferring the metasomatic agent involved, we look directly at the fluids and melts responsible for alteration, by analyzing the composition of μm size inclusions in boart diamonds. We report nitrogen aggregation and the major- and trace-element data for a suite of eight microinclusion-bearing diamonds DeBeers-Pool kimberlites (i.e. four kimberlites around Kimberley, South Africa). Combining our results with data on mineral inclusions in monocrystalline diamonds and garnet-bearing peridotite xenoliths from DeBeers-Pool and related kimberlites in the southwestern Kaapvaal region, we discuss the source and evolution of the metasomatic agent, the possible timing of alteration and young diamond growth, and the impact of Mesozoic metasomatism and volcanism on the thermal and redox state of the lithosphere.

Results

Seven of the diamonds are rich in saline high density fluids (HDFs, Fig. 1a), carry peridotitic mineral microinclusions and are characterized by a nitrogen IaA Type IR spectrum. Their trace-element patterns show high alkalis (K, Rb and Cs), Ba and LREEs compared to Th, U, Nb and Ta and are characterized by negative anomalies of Ti, Zr, Hf and Y relative to REEs of similar compatibility. Major and trace element compositions show intra- and inter-diamond relationships. The molar (K+Na)/Cl ratio varies between 1.01±0.09 (1 σ) and 1.55±0.31, and correlates with a general increase of MgO, SiO₂ and Na₂O (and CaO, Al₂O₃ and P₂O₃ to some extent). Trace-element patterns and ratios vary with Cl and MgO (and carbonate). In general, with decreasing Cl and increasing MgO, the La/Pr ratio increases and Eu/Sm and Ba/Nb ratios decrease; Sr/Rb, Th/Rb and Zr/Hf ratios increase and the Eu/Ti ratio decrease, due to higher Sr, Th, Zr and Ti concentrations. The change, from saline towards somewhat more saline-carbonatitic compositions appears between diamonds in which no mineral microinclusions were found and diamonds containing both HDFs and mineral microinclusions, and likely represent increasing fluid-rock interaction. Another diamond that trapped silicic HDFs exhibits an IaAB-Type spectrum with 25% of the nitrogen in B-centers and

The P-T field as determined by geothermobarometry of mineral microinclusions in the saline HDF-bearing diamonds overlap with equilibration temperatures of touching inclusion-pairs in monocrystalline diamonds from the same sources, and are altogether lower, on average, by 150–250°C compared to the observed P-T gradient of xenoliths from both Group II and Group I kimberlites (Fig. 2a). A significant temperature difference persists, even when a possible underestimation of ~60°C is accounted for in the diamond inclusions, due to differences between the Grt-Opx thermometer (used for the inclusions) and the two-pyroxene thermometer (used for the xenoliths). If mantle-derived xenoliths from the southwestern Kaapvaal lithosphere record a snapshot of thermal advection during the last event of metasomatism and/or kimberlite eruption, then the P-T conditions of the xenoliths, the non-touching mineral microinclusions, and the touching inclusion pairs, should all plot along a similar P-T gradient. However, this is not the case. Moreover, we observe a gap between the fO_2 conditions of peridotitic xenoliths and saline metasomatism (Fig. 2b). This implies that the redox state recorded by peridotitic xenoliths from the southwestern Kaapvaal lithosphere does not represent interaction with saline HDFs, but rather is a reflection of the pre-existing lithospheric fO_2 conditions. To reconcile the temperature and oxygen fugacity discrepancy between xenoliths and inclusions in diamond, we suggest that xenoliths did not equilibrate during the last saline metasomatic event and/or kimberlite eruption. Thus the P-T- fO_2 gradients they record represent pre-existing lithospheric conditions, likely expressing the last major thermal event in the Kaapvaal craton (i.e. the Karoo magmatism at ~200 Myr). Local and small volume eruptions of Mesozoic kimberlites had limited thermal influence on the lithosphere, while the last metasomatic event by saline fluids led to local SCLM cooling and shifted the redox state of the impacted SCLM to more oxidized conditions upon fluid-rock interaction.

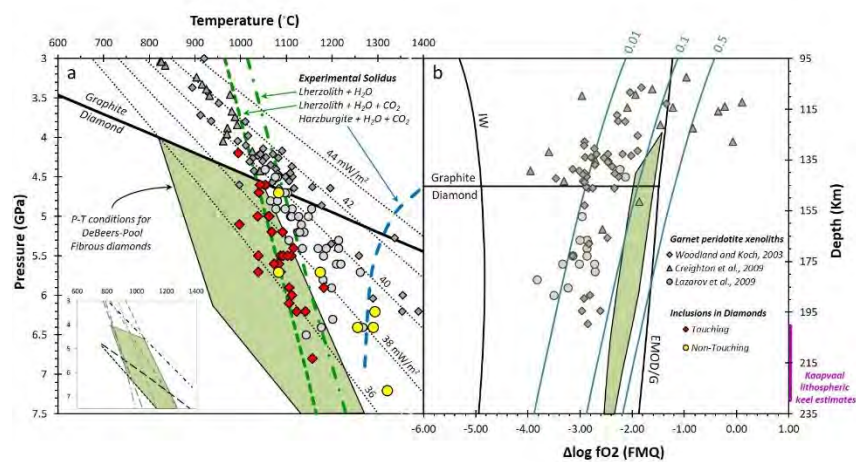


Figure 2: Temperature-pressure- fO_2 conditions of inclusions in diamond and xenoliths from the southwestern Kaapvaal Craton. (a) possible P-T conditions of saline metasomatism (green area); the inset shows the different Ol-Grt-Cpx-Opx thermometers and barometers used to define these conditions. Also shown are P-T conditions of mineral inclusions in DeBeers-Pool diamonds; 36–44 mW/m^2 continental geotherms; the graphite–diamond transition; the solidus for lherzolite+ H_2O+CO_2 ,

lherzolite+ H_2O , and the solidus for harzburgite+ H_2O+CO_2 . (b) fO_2 variations of saline HDFs as a function of pressure (green area). Also shown are the iron–wüstite buffer reaction (IW); graphite–diamond transition reaction and enstatite+magnesite=olivine+graphite/diamond reaction (EMOG/EMOD); the maximum- fO_2 stability of carbonate-bearing melts (blue lines with molar fraction of CO_2 on top; Stagno and Frost, 2010).

References

- Stagno V, Frost DJ (2010) Carbon speciation in the asthenosphere: Experimental measurements of the redox conditions at which carbonate-bearing melts coexist with graphite or diamond in peridotite assemblages. *Earth and Planetary Science Letters* 300:72-84.
- Weiss Y, McNeill J, Pearson DG, Nowell GM, Ottley CJ (2015) Highly saline fluids from a subducting slab as the source for fluid-rich diamonds. *Nature* 524:339-342.



50 Myr kimberlite magmatism in the Fort à la Corne field, Sask craton, recorded by zircon megacrysts

Q. Shu^{1*}, D.G. Pearson¹, B. A. Kjargaard² and G. Read³

¹Dept. of Earth and Atmospheric Sciences, University of Alberta, Edmonton, Canada T6G 2E3,

²Geological Survey of Canada, 601 Booth Street, Ottawa, Ontario, Canada, K1A 0E8.

³Shore Gold Inc., 300 - 224 4th Ave South, Saskatoon, Saskatchewan, Canada, S7K 5M5.

*qshu1@ualberta.ca

Introduction

Zircon megacrysts from kimberlites appear to have a direct relationship to the magmatic activity that lead to the eruption of their host kimberlites because i) they yield kimberlite eruption ages (Davis, 1977) and ii) their trace element patterns and concentrations significantly differ from crustal zircons, most significantly by the absence of a negative Eu anomaly (Belousova et al., 2002). These are also the features of a large suite of zircon megacrysts from heavy mineral concentrates separated during diamond evaluation of the Orion South kimberlites of Fort à la Corne, central Saskatchewan that erupted through the Sask craton.

Here we seek to use this large suite of kimberlite-derived zircons to evaluate i) the potential age range of kimberlite activity within a single kimberlite cluster and ii) examine via tracer Hf isotopes evidence for any temporal evolution of the megacryst source magma.

U-Pb and Hf isotope results

We analysed 106 zircon megacrysts from 3 distinct kimberlite phases; i) the Pense kimberlite ii) Early Joli Fou (EJF), kimberlite and iii) Late Joli Fou (LJF) kimberlite from the Fort à la Corne field by LA-ICPMS for trace elements and U-Pb and Hf isotope ratios. The U-Pb ages have a total range of 95-150 Ma, defining a spread of ~ 55 Myr, with a single kimberlitic zircon giving an age of 1.86 Ga, coincident with the Transhudson orogeny. The data define a main age cluster from 95 to 108 Ma (75% of zircons: Fig.1), overlapping with ages obtained from U-Pb dating of groundmass perovskite (Kjargaard et al., 2017), which should record the low-pressure crystallization of kimberlite along with its primary geochemical and isotopic signature. Such U-Pb perovskite ages from Fort à la Corne yield a main peak in the age of volcanism between 92.5 and 103.2 Ma, in agreement with our main zircon U-Pb age peak, with a precursor event at 115 Ma (Kjargaard et al., 2017). This age range for the majority of FALC kimberlite magmatism is in agreement with earlier ages of 96 and 98 Ma determined with the Rb-Sr isotope system on phlogopite by Lehnert-Thiel et al. (1992) and Hegner et al. (1995), respectively. The close temporal relationship between groundmass crystallisation ages and zircon megacryst ages suggests a genetic relationship between the zircons and the host kimberlites for a large proportion (~ 73% using Gaussian mixture modeling – Fig. 1) of zircons. However, prior to this peak in Cretaceous kimberlite magmatism, the zircon age spectrum (Fig.1) clearly indicates that at least 5 periods of older magmatism affected the basal lithospheric mantle of the Sask craton at 110-120Ma (9%), 124-127Ma (5%), 132-139 Ma (8%), 143-150 Ma (2%) and 1860 Ma (1%). The older 3 age clusters have not been recorded as crystallization ages in any of the erupted units of the FALC cluster so far, hence the zircon megacryst ages appear to be yielding information about kimberlite-related activity that may have stalled in the lithospheric mantle, without erupted equivalents, that were later sampled by the more voluminous phase of activity in late mid-Cretaceous times.

The Hf isotope systematics vary systematically between the different age populations (Fig.2). The youngest zircons (95 to 108 Ma) show a large range in initial Hf isotope compositions with $\epsilon\text{Hf}(t)$ values from -0.5 to +7.3. Older zircons grew from magmas with significantly more radiogenic $\epsilon\text{Hf}(t)$, up to +11.7. The 110-120 Ma zircons have $\epsilon\text{Hf}(t)$ from +3.5 to +11; the 124-127 Ma zircons possess

the most radiogenic Hf isotope composition with $\epsilon\text{Hf}(t)$ from +7.7 to +11.7; the 132-139 Ma zircons have similarly radiogenic $\epsilon\text{Hf}(t)$ from +9.8 to +11 while the 143-150 Ma zircons yield very constant $\epsilon\text{Hf}(t)$ values from +6.6 to +6.9. The single Proterozoic zircon (1.86 Ga) also originated from a source with a depleted mantle signature ($\epsilon\text{Hf}(t)$: $+3.9 \pm 0.7$).

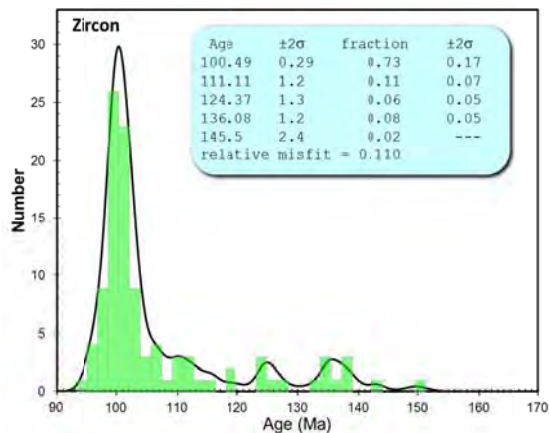


Fig. 1 The probability distribution of U-Pb ages of zircons from the kimberlites erupted in the Fort à la Corne field, central Saskatchewan through the Sask craton. Inset is a Gaussian mixture model of possible age components in the data derived from ISOPLOT.

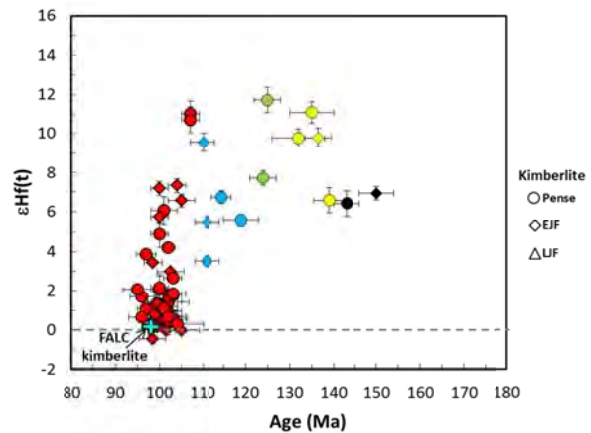


Fig. 2 U-Pb ages versus $\epsilon\text{Hf}(t)$ of zircons from the 3 separate kimberlite phases (Pense, EIJ, LJJ) in the Fort à la Corne field, compared with kimberlite eruption age (U-Pb age from perovskite: Kjarsgaard et al., 2017, where available for U-Pb zircon age). Uncertainties are 95% confidence. The colour coding is based on distinct age groupings in Fig.3

Discussion

Our study on kimberlitic zircons shows that long-lived kimberlitic magmatism affected the lithospheric mantle of the Sask craton from 1860 to 95 Ma in at least 5 main age clusters some of which have not been found as erupted kimberlites at the craton surface so far (Fig.3). The ages of about 75% of the zircons overlap with the time of their host kimberlite magma emplacement as defined by U-Pb perovskite and Rb-Sr mica dating. This indicates a direct relation of the zircons to the kimberlite magma, i.e. that they were crystallized from a magma closely related in time and space to the surface expression of kimberlite magma. Perovskites from kimberlites in the Fort à la Corne field defined the main period of kimberlite magmatism over a timespan from 115 – 93 Ma in the central Sask craton, while our study on kimberlitic zircon megacrysts from the same kimberlite cluster indicates 4 more periods of pre-cursor magmatism besides the main period in the mid-Cretaceous (Fig.3). Around 25% of the zircon population yield much older ages than the host kimberlite eruption ages as determined by groundmass perovskite and phlogopite and indicate a significant period of kimberlite activity in one cluster, over a 55 Myr period. The extended period of kimberlite activity in the FALC cluster is in line with protracted, yet punctuated periods of kimberlite magmatism seen in other clusters and fields (e.g., Lac de Gras, Sarkar et al., 2015; Chidliak, Heaman et al., 2015) and even within individual eruptive bodies, such as Renard (Ranger et al., 2017). Interestingly, the oldest of the Mesozoic zircon ages at FALC overlap the main phase of kimberlite activity recorded in the Chidliak cluster, Baffin Island and is, to date, the westernmost expression of this Jurassic/Early Cretaceous kimberlite activity that spans N. America.

Most kimberlite bodies in the Fort à la Corne field are composed of more than one pulse of magma that transported zircons with very different Hf isotope compositions. For example, five eruptive events occurred from ~103-99 Ma at the Star kimberlite, and seven eruptive events occurred from ~103-95 Ma at the Orion South kimberlite (Kjarsgaard et al., 2017). Our youngest zircons (95 to 108 Ma) show a continuous vertical trend of Hf isotope composition with $\epsilon\text{Hf}(t)$ from -0.5 to +7.3 (Fig.2), with the majority clustering around 0 to +2. We speculate that the younger parental magmas

originate from a magma source region similar to OIB, beneath the lithosphere. The generation of the more radiogenic Hf isotope compositions likely reflects varying interaction with depleted cratonic mantle. The older zircons show more radiogenic Hf isotope composition with $\epsilon\text{Hf}(t)$ from +4 to +12 (Fig.2). Apparently, the contribution of a depleted mantle source plays a vital role in generating the magmas that crystallized the older zircons. The older parental kimberlite magmas, lacking the OIB-source signature, point to the depleted lithospheric source region and may have suffered thermal death in the lithosphere, explaining the lack of erupted kimberlites of these ages in the greater Sask craton.

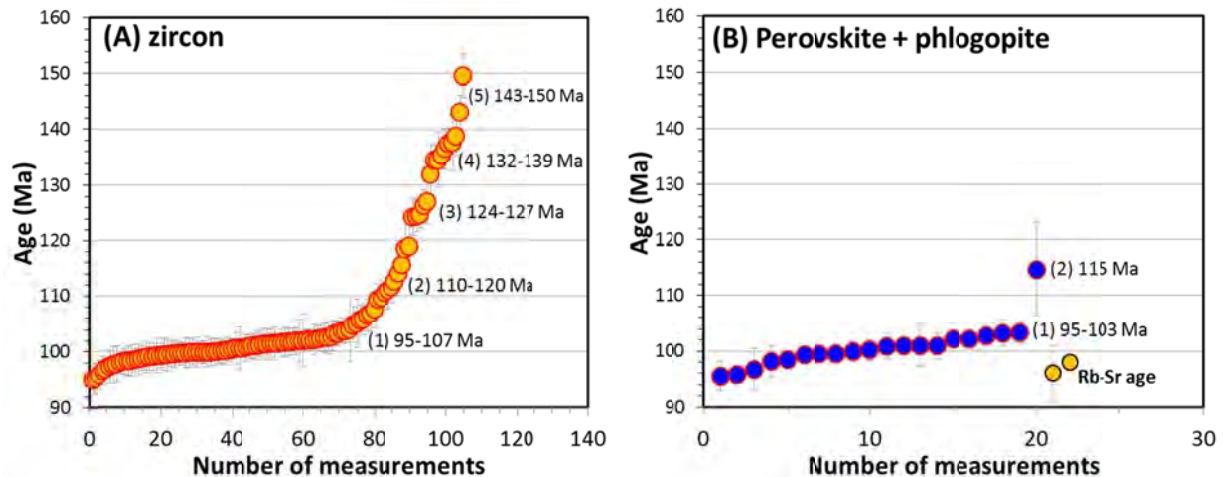


Fig. 3 Comparison of kimberlite and zircon megacryst ages from the Fort à la Corne field: (A) U-Pb mantle zircon age; (B) U-Pb perovskite (blue circles) (Kjarsgaard et al., 2017) and Rb-Sr model age from phlogopite (yellow circles; Lehnert-Thiel et al., 1992 ; Hegner et al., 1995).

References

- Belousova E, Griffin WL, O'Reilly SY, Fisher NI (2002) Igneous zircon: trace element composition as an indicator of source rock type. *Contrib. Mineral. Petrol.* 143: 602–622.
- Davis GL (1977) The ages and uranium contents of zircons from kimberlites and associated rocks. *Carnegie Inst. Wash. Yearbook* 76: 631–635.
- Heaman LM, Pell, JA, Grutter H, Creaser RA (2015) U–Pb geochronology and Sr/Nd isotope compositions of groundmass perovskite from the newly discovered Jurassic Chidliak kimberlite field, Baffin Island, Canada. *Earth Planet. Sci. Lett.* 415: 183-199.
- Hegner E, Roddick JC, Fortier SM, Hulbert L (1995) Nd, Sr, Pb, Ar and O isotopic systematics of Sturgeon Lake kimberlite, Saskatchewan, Canada: constraints on emplacement age, alteration and source composition. *Con. Min. Pet.*, 120: 212-222.
- Kjarsgaard BA, Heaman LM, Sarkar C, Pearson DG (2017) The North America mid-Cretaceous kimberlite corridor: Wet, edge driven decompression melting of an OIB-type deep mantle source. *Geochemistry, Geophysics, Geosystems* (in review).
- Lehnert-Thiel K, Loewer R, Orr RG, Robertshaw P (1992) Diamond-bearing kimberlites in Saskatchewan, Canada: The Fort à la Corne case history. *Exp. Min. Geol.* 1: 391-403.
- Ranger IM, Heaman LM, Pearson DG, Laroulandie C, Lepine I, Zhuk V (2017) Punctuated, long-lived emplacement history of kimberlites from the Renard cluster, Superior Province, Canada indicated by new high precision U-Pb groundmass perovskite dating. 11th International Kimberlite Conference Extended Abstract No. 11IKC- 4493.
- Sarkar C, Heaman LM, Pearson DG (2015) Duration and periodicity of kimberlite volcanic activity in the Lac de Gras kimberlite field, Canada and some recommendations for kimberlite geochronology. *Lithos*, 218-219: 155-166.



Metasomatic diamond formation revealed by X-Ray CT scanning of diamondiferous eclogites from southern Africa

J. J. Gurney^{1,2}, R. L. Kahle², B. Kahle², S. H. Richardson², A. du Plessis³

1. Mineral Services, 42 Morningside, N'dabeni, Cape Town 7701, john.gurney@msgroup.net

2. Department of Geological Sciences, University of Cape Town, Rondebosch, Cape Town 7701

3. CT Scanner Facility, Stellenbosch University, PO Sauer Building, Bosman Road, Stellenbosch 7602

In terms of understanding the origins of diamond, it is now widely accepted that they form at depth mainly, though not exclusively, in the continental lithospheric roots of ancient cratons. There they reside until sampled and conveyed to the Earth's surface, most frequently in a rapidly emplaced kimberlite eruption. Current wisdom holds that most diamonds formed early in the history of their craton hosts, and so are themselves ancient. Diamonds are observed in association with both peridotite and eclogite populations at specific localities and may be dominated by peridotitic diamonds (e.g. Kimberley mines), or by eclogitic diamonds (e.g. Orapa). In this study, attention has been focused only on eclogitic diamonds. The collection consists of a suite of diamondiferous eclogite xenoliths, ranging in size from sub-centimetre to approximately 4 cm in the longest dimension. All of these samples have at least one diamond visible on the surface of the xenolith. The samples are sourced from the Excelsior (11) and Newlands (5) mines, both near Barkly West (Northern Cape, South Africa), with two additional samples from Orapa (Botswana). Excelsior and Newlands are small occurrences (mainly thin dykes) of Group II kimberlite. Both kimberlite occurrences are on cratonic lithosphere ~170 km thick. Orapa, in contrast, is the largest mined kimberlite in the world. The pipe is on the N. side of the Kalahari craton, where the lithosphere is ~180 km thick. (McKenzie & Priestley, 2008).

Visual inspection of the samples suggests that the diamonds are located in fluid pathways. The diamonds occur in both altered garnet (gt) and altered clinopyroxene (cpx). There appears to be a dominance of cpx hosting, even though gt is considerably more abundant than cpx. The samples have been subjected to X-ray tomography analysis, in order to create three-dimensional (3-D) images of the surfaces and the interiors of the samples (Figs 1 & 2). The 3-D images reveal that the samples contain abundant, in some cases pervasive, secondary veining that is clearly younger than the eclogite. In all but one case, diamonds occur along veins, but most of the veining is unrelated to the spatial positioning of diamond in the samples (Fig 1). In some instances, early veining through a host-mineral has annealed or partially annealed (Fig 2), suggesting a range in timing of at least some of the several metasomatic events that have affected the rock. Our findings (Fig 3) can be summarised as:

- Diamonds may be associated with either cpx or gt; they may be enclosed entirely within one mineral phase, or lie along grain boundaries between different minerals (Fig 1).
- Samples contain between ~1% and ~9% diamond (± 47 diamonds). At Newlands and Excelsior generally these crystals are unresorbed octahedra. In contrast the diamonds in the Orapa xenoliths are resorbed wherever situated.
- In all but one of the eclogites, the diamonds lie in clear metasomatic pathways or planes (Figs 1 & 2 and cartoon (Fig 3)). These structures may retain evidence of fluid flow, in the form of secondary phases; may have been re-opened late in the history of the sample, perhaps during kimberlite eruption; or may have been completely annealed (Fig 1 and cartoon (Fig 3)). In one case, the diamonds appear to be more uniformly distributed throughout the xenolith.
- Of the xenoliths that contain more than a single diamond, some contain one population of diamonds. However, in many of the centimetre-scale xenoliths, more than one population of diamonds can be recognised based on morphology and/or size.
- Primary metasomatic high-absorption phases identified by SEM scanning are Fe-Cu-Ni sulphides and rutile; they may follow the diamond planes, or lie along clear planes that are completely independent, and differently oriented, to the diamond planes (Figs 1 & 2 and cartoon (Fig 3)). In one case, a sulphide inclusion is observed in a diamond (implying that the sulphide pre-dated the diamond or formed at the same time). In one case, a plane of sulphides is deflected around the diamond plane. This can be interpreted either as the sulphide-bearing fluid being deflected around a pre-existing diamond, or that a diamond grew after the sulphides and led to deformation of the plane.

- Secondary minerals include barite, found in association with diamonds and in some cases along metasomatic channels as noted by Schulze et al. (1996) in a diamond eclogite from Roberts Victor.

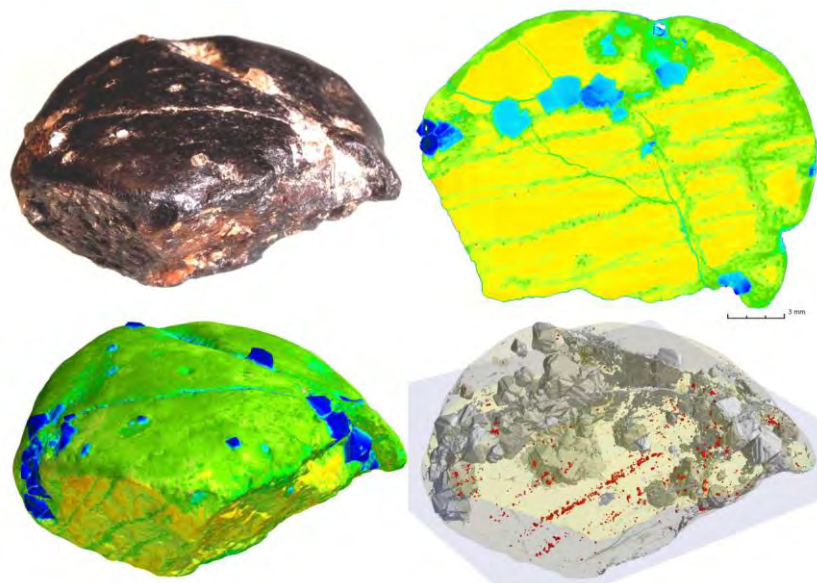


Figure 1: X-ray CT results for sample EX22 (Excelsior). Clockwise from top left: (i) photograph of sample showing visible diamonds on surface; (ii) cross section through X-ray CT results (blue = diamond, yellow = garnet, green = alteration material, red = high absorption phases interpreted to be sulphides); (iii) 3-D volume rendered transparent to highlight diamonds (grey) and sulphides (red), which lie on clear, though unrelated, planes; (iv) 3-D volume from X-ray C-T results (compare with photograph above) with identical colour palette to ii.

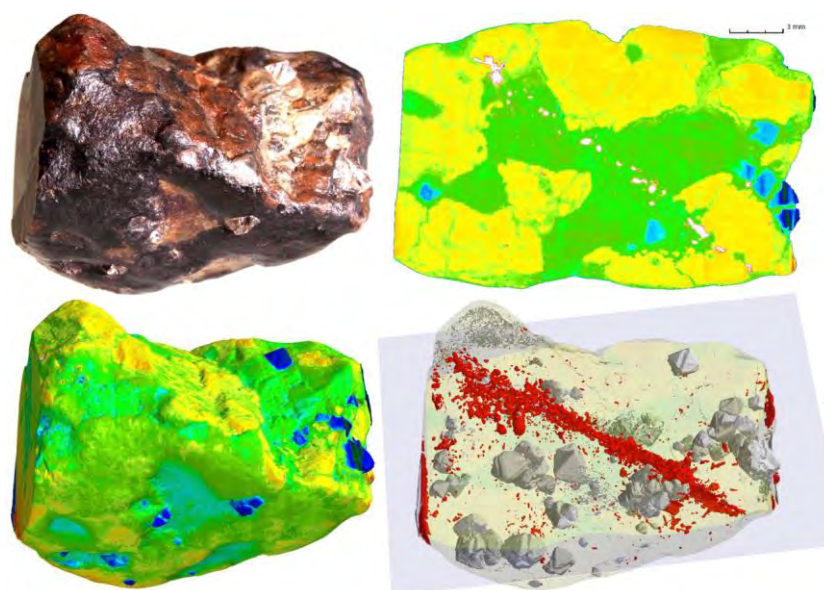


Figure 2: X-ray CT results for sample EX23 (Excelsior). Clockwise from top left: (i) photograph of sample showing visible diamonds on surface; (ii) cross section through X-ray CT results (blue = diamond, yellow = garnet, green = cpx and alteration material, red = high absorption phases interpreted to be sulphides); (iii) 3-D volume rendered transparent to highlight diamonds (grey) and sulphides (red); (iv) 3-D volume from X-ray C-T results (compare with photograph above) with identical colour palette to ii. Note the annealing of the sulphide-bearing vein.

Conclusions

Diamond grade in mantle eclogites can be orders of magnitude higher than found in any kimberlite or lamproite. Metasomatism is a common process in mantle eclogites. Metasomatism plays an important role in eclogitic diamond formation in the lithospheric mantle. Evidence has been provided that in the

studied eclogites both non-diamondiferous, but “diamond friendly” and “diamond unfriendly” metasomatic events can be traced along with the mineralised veins, of which there may also be more than one. SEM scans have identified Fe-C-Ni sulphide rutile and secondary barite in both diamondiferous and non-diamondiferous examples. Several studies have previously described similar features to those reported here in Siberian diamondiferous eclogites (e.g. Anand et al., 2003; Spetsius and Taylor, 2003; Taylor et al., 2003; Howarth et al., 2014)

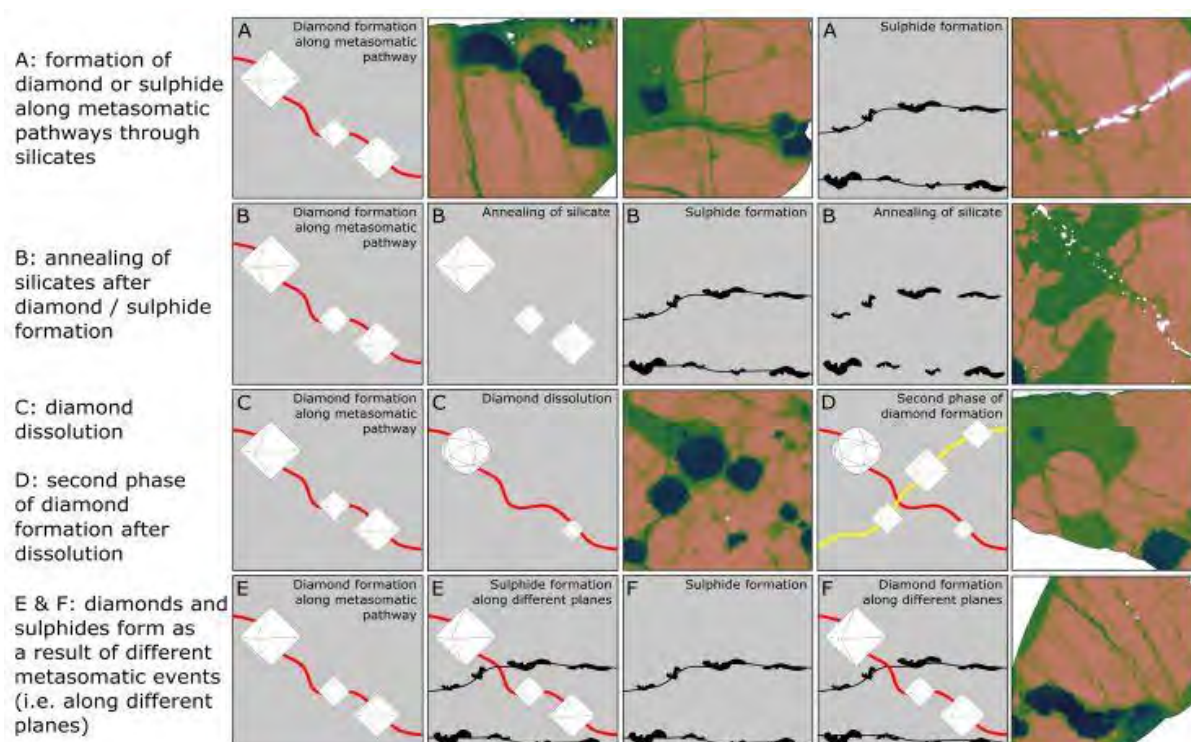


Figure 3: Cartoon summarising our interpretation of X-ray CT results. Examples of X-ray CT cross-sections have the following colour palette: blue = diamond; red = gt; green = cpx and alteration material; white = high absorption phases interpreted to be sulphides.

References

- Anand, M., Taylor L.A., Carlson W.D., Taylor, D-H & Sobolev N.V., 2003. Diamond genesis revealed by x-ray tomography of diamondiferous eclogites. 8th International Kimberlite Conference, Canada, Extended abstract.
- Howarth, G.H., Sobolev, N.V., Pernet-Fisher, J.F., Barry, P.H., Penumadu, D., Puplampu, S., Ketcham, R.A., Maisano, J.A., Taylor, D. & Taylor, L.A. 2014. The secondary origin of diamonds: multi-modal radiation tomography of diamondiferous mantle eclogites. *International Geology Review* Vol 56, No. 9, 1172-1180.
- McKenzie, D. and Priestley, K., 2008. The influence of lithospheric thickness variations on continental evolution. *Lithos*, 102(1), pp.1-11.
- Schulze, D.J., Wiese, D & Steude, J., 1996. Abundance and distribution of diamonds in eclogite revealed by volume visualization of CT X-ray scans. *J. Geol.* 104, 109-113.
- Sobolev, V.N., Taylor, L.A., Snyder, G.A. & Sobolev, N.V., 1994. Diamondiferous eclogites from the Udachnaya kimberlite pipe, Yakutia. *Internat. Geol. Rev.* 36, 42-64.
- Spetsius, Z.V., Taylor, L.A., 2003. Kimberlite xenoliths as evidence for subducted oceanic crust in the formation of the Siberian craton. *Proceedings of 3d Intern. Workshop: Plumes and problem of deep sources of alkaline magmatism.* Irkutsk, 3-15.
- Taylor, L.A., Taylor, D-H, Anand, M., Metchum, R., Carlson, W., Pokhilenko, N.P., & Sobolev, N.V., 2003. Diamondiferous peridotites: Tomography as a precursor to dissections. *Amer. Geophys. Union Fall Mtg.*, abstract.

Monticellite in Group-I kimberlites: Implications for evolution of parental melts and post-emplacement CO₂ degassing

Adam Abersteiner¹, Vadim S. Kamenetsky¹, D. Graham Pearson², Maya Kamenetsky¹,
Karsten Goemann³, Kathy Ehrig⁴

¹ School of Physical Sciences, University of Tasmania, Australia, adam.abersteiner@utas.edu.au,
dima.kamenetsky@utas.edu.au, Maya.Kamenetsky@utas.edu.au

² Department of Earth and Atmospheric Sciences, University of Alberta, Canada, gdpearso@ualberta.ca

³ Central Science Laboratory, University of Tasmania, Australia, Karsten.Goemann@utas.edu.au

⁴ BHP Billiton, Australia, Kathy.J.Ehrig@bhpbilliton.com

Introduction

Reconstructing the composition and evolution of kimberlite magmas is challenging because kimberlite rocks are no longer considered to be representative of their parental melts because of: i) entrainment and assimilation of mantle and crustal material, ii) volatile (e.g., CO₂, H₂O) exsolution and degassing, and iii) kimberlite rocks are almost always altered by deuteric and/or hydrothermal/meteoric fluids.

In order to constrain the petrogenesis of Group-I (or archetypal) kimberlite melts, we examine monticellite which occurs as a magmatic and/or deuteric mineral in the groundmass of kimberlites, exclusively within minimally altered samples in highly variable amounts, rarely up to 80 vol. % (Mitchell, 1986). In this contribution, we present a detailed petrographic and geochemical study of monticellite and monticellite-hosted inclusions from the Leslie (Slave Craton, Canada) and Pipe 1 (Karelian Craton, Finland) kimberlites to demonstrate the influence of monticellite crystallisation on kimberlite melt evolution and CO₂ degassing.

Petrography

Samples LDC7 and FLP1 were examined by optical and scanning electron microscopy (SEM). Both samples are representative of Group-I (or archetypal) hypabyssal facies kimberlite and exhibit similar groundmass textures and mineralogy. Olivine is abundant (~40 – 50 vol.%), occurring as anhedral-to-rounded (up to 10 mm) and euhedral phenocrystic grains (<0.1 - >0.5 mm) which exhibit limited alteration to serpentine and carbonate (i.e. calcite). The groundmass is characterised by (in order of relative abundance) monticellite, calcite, phlogopite/kinoshitalite, brucite, spinel (Cr-spinel, MUM, Mg-magnetite, pleonaste), apatite, perovskite and Fe-Ni-Cu-sulphides along with abundant alteration phases (i.e. brucite and interstitial serpentine and calcite).

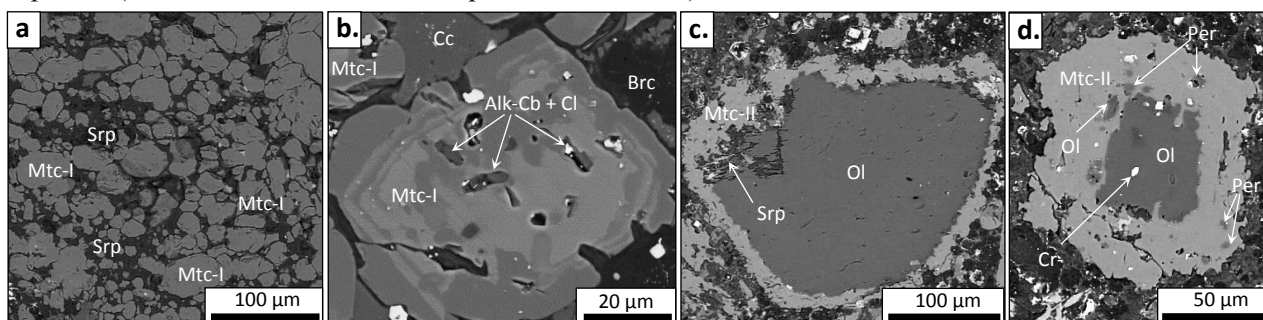


Figure 1. Back-scattered electron (BSE) SEM images of: (a, b) Discrete monticellite-I (Mtc-I) grains in the groundmass of sample FLP1. (b) A concentrically zoned Mtc-I grain oscillating between lighter (more Fe-rich) and darker (less Fe-rich) areas. This grain also contains several multiphase inclusions consisting of alkali-carbonates (Alk-Cb) and chlorides (Cl). (c, d) Olivine (Ol) partially replaced by monticellite-II (Mtc-II) in sample LDC7. Mtc-II commonly host abundant primary inclusions of periclase (Per). Srp: serpentine, Brc: brucite, Cc: calcite, Cr-Spl: Cr-spinel.

Monticellite is a dominant groundmass mineral in samples LDC7 (~25 vol.%) and FLP1 (~40 – 45 vol.%) occurring as two distinct morphological types: i) Mtc-I: subhedral-to-euhedral microphenocrysts ranging from 10 – 150 μm (Figs. 1a and b). Monticellite grains are generally uniformly distributed throughout the groundmass but also form densely packed clusters (Fig. 2a). The majority of monticellite grains exhibit compositional heterogeneity and zoning is usually patchy and diffuse, which is characterised by minor variations in Fe-content. ii) Mtc-II: forms pseudomorphs after olivine (Figs. 1c and d). Pseudomorphic monticellite sometimes completely replaces smaller olivine grains (<50 – 100 μm). These completely replaced olivine grains are distinguished from discrete groundmass grains (i.e. Mtc-I) by the presence of small relic inclusions (<20 μm ; Fig. 1d) of olivine and Cr-spinel, and the absence of zoning.

Inclusions

Monomineralic inclusions are typically round-to-euhedral in shape and range in size between 1 – 12 μm and are comprised of (in order of decreasing abundance) periclase (Figs. 1d and 2), perovskite, phlogopite, Fe-Mg-Al-oxides (Mg-magnetite, pleonaste). To our knowledge, this is the first confirmation of periclase occurring in kimberlites.

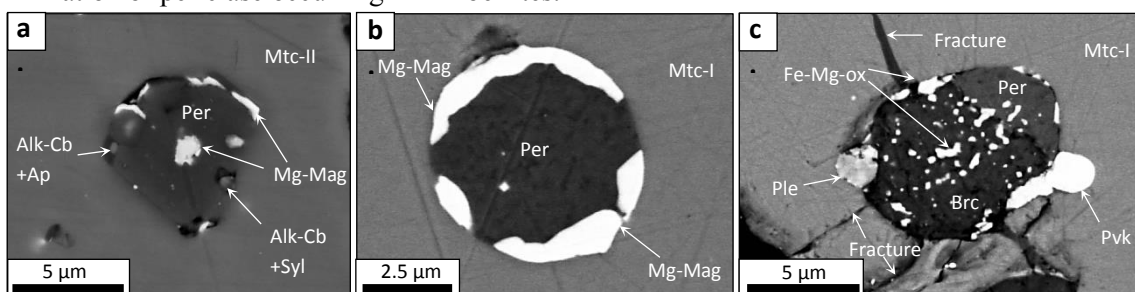


Figure 2. Back-scattered electron (BSE) SEM images of: (a) Periclase inclusions in Mtc-II (Mtc) replacing olivine in sample LDC7. These inclusions are commonly accompanied by a ‘coating’ along the inclusion peripheries of Mg-magnetite (Mg-mag) and occasionally other phases such as alkali-carbonates (Alk-Cb), apatite (Ap), and sylvite (Syl). (b, c) Periclase inclusions in groundmass Mtc-I grains in sample FLP1. (b) Similar to LDC7, this inclusion contains a ‘coating’ of Mg-magnetite along the inclusion peripheries; (c) An inclusion of periclase transected by multiple fractures, exposing it to post-entrapment alteration. Periclase and brucite (Brc) co-exist, where periclase has been partially altered to mixtures of brucite and disseminated Fe-Mg-oxides (Fe-Mg-Ox). This inclusion demonstrates the incomplete transformation of periclase to brucite. Ple: Pleonaste, Pvk: perovskite .

Multiphase (i.e. melt) inclusions are abundant in Mtc-II and to a lesser extent in Mtc-I and are sometimes associated with periclase inclusions (Fig. 2a). Multiphase inclusions in monticellite exhibit a variety of shapes, ranging from rounded-to-elongate and amoeboid and are 1 – 15 μm in size (Fig. 3). These inclusions are extremely heterogeneous in composition and contain between two and six phases which are represented in order of abundance by calcite, alkali (Na, K, Sr, Ba and some F-bearing \pm V) carbonates, dolomite, periclase, Mg-Fe-Al-spinel, F-rich apatite, forsteritic olivine, sylvite/halite, perovskite, phlogopite and Ni-Fe-sulphides.

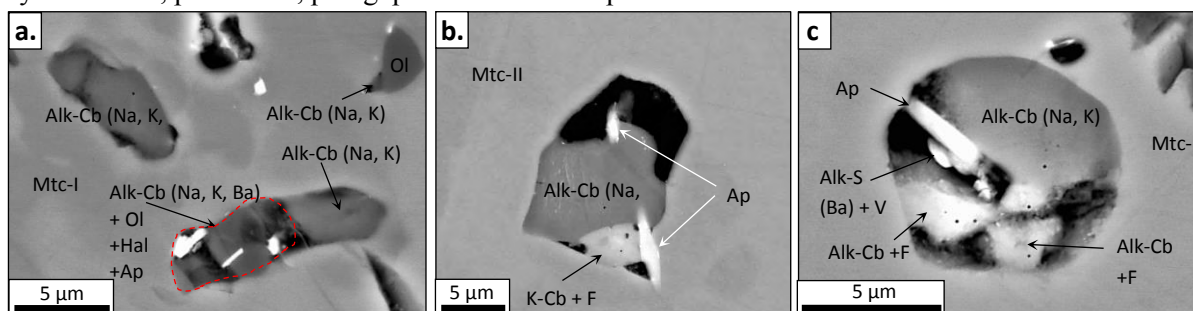


Figure 3. Back-scattered electron (BSE) SEM images of representative multiphase inclusions in monticellite (Mtc). These inclusions contain daughter crystals of alkali-carbonates (Alk-Cb) including fluorine (F) bearing varieties, alkali-sulphur-bearing phase (Alk-S) that contain vanadium (V), halite (Hal), apatite (Ap) and olivine (Ol).

Discussion

The preservation of Mtc-II suggests that monticellite crystallisation occurred *in-situ* after magma was emplacement and that the groundmass was not significantly disrupted by any physical processes such as mechanical rounding/abrasion, explosivity or brecciation. Previous studies of melt inclusions in olivine and magmatic minerals from various kimberlites worldwide (Golovin et al., 2007; Kamenetsky et al., 2012; Abersteiner et al., 2016), olivine and ilmenite in kimberlitic polymict breccias (Giuliani et al., 2012) and in mantle xenolith-hosted minerals (Soltys et al., 2016) report similar alkali-carbonate dominated, Si-Cl-P-bearing phase assemblages to the ones observed in our samples. We suggest that the melt inclusions in groundmass kimberlite minerals represent the entrapment of a variably differentiated kimberlite melt. Based on our analyses of melt inclusions, monticellite likely crystallised from a Ca-Mg and alkali (Na, K, Ba, Sr) enriched, P-Cl-bearing, carbonate-silicate melt.

Petrographic and textural data indicates that olivine replacement by Mtc-II resulted from olivine reacting with the carbonate component of the kimberlite melt. A plausible scenario for this replacement of olivine could be attributed to a specific decarbonation reaction (i.e. release of CO₂).

Reaction 1: $(Fe, Mg)_2SiO_4 + CaCO_3 \rightleftharpoons Ca(Fe, Mg)SiO_4 + (Fe, Mg)O + CO_2$
Olivine (forsterite) + Carbonate (melt) \rightleftharpoons Monticellite + Periclase + Carbon Dioxide (vapour)

This reaction is supported by the preservation of abundant primary inclusions of periclase and to a lesser extent Fe-Mg-oxides in monticellite. Based on the preservation of primary periclase inclusions, we infer that periclase also existed in the groundmass, but was subsequently altered by post-magmatic processes to brucite and Fe-Mg-oxides.

Degassing of CO₂ in the latter stages of kimberlite magma emplacement into the crust could be largely driven by the observed reaction between olivine and the carbonate melt. For this reaction to proceed, CO₂ should be removed (i.e. degassed), which will cause further reaction and additional monticellite, periclase/Fe-Mg-oxides production and CO₂ degassing in response to this chemical system change (*Le Chatelier's principle*). Our study demonstrates that these proposed decarbonation reactions may be a commonly overlooked process in the crystallisation of monticellite and exsolution of CO₂, which may in turn contribute to the explosive eruption and brecciation processes that occur during kimberlite magma emplacement and pipe formation.

References

- Abersteiner A, Giuliani A, Kamenetsky VS, Phillips D (2016) Petrographic and melt-inclusion constraints on the petrogenesis of a magmaclast from the Venetia kimberlite cluster, South Africa. *Chem Geol*: <http://dx.doi.org/10.1016/j.chemgeo.2016.08.029>.
- Golovin AV, Sharygin VV, Pokhilenko NP (2007) Melt inclusions in olivine phenocrysts in unaltered kimberlites from the Udachnaya–East pipe, Yakutia: Some aspects of kimberlite magma evolution during late crystallization stages. *Petrology* 15:168–183.
- Giuliani A, Kamenetsky VS, Phillips D, Kendrick MA, Wyatt BA, Goemann K (2012) Nature of alkali-carbonate fluids in the sub-continental lithospheric mantle. *Geology* 40:967-970.
- Kamenetsky, VS, Kamenetsky, MB, Golovin, AV., Sharygin, VV, Maas, R (2012) Ultrafresh salty kimberlite of the Udachnaya-East pipe (Yakutia, Russia): A petrological oddity or fortuitous discovery? *Lithos* 152, 173-186.
- Mitchell RH, 1986. *Kimberlites: Mineralogy, Geochemistry and Petrology*. Plenum Publishing Company, New York.
- Soltys A, Giuliani A, Phillips D, Kamenetsky VS, Maas R, Woodhead J, Rodemann T (2016) In-situ assimilation of mantle minerals by kimberlitic magmas — Direct evidence from a garnet wehrlite xenolith entrained in the Bultfontein kimberlite (Kimberley, South Africa). *Lithos* 256-257:182-196.

Formation of unusual yellow Orapa diamonds

Suzette Timmerman¹, Ingrid L. Chinn², David Fisher³, Gareth R. Davies¹

¹Vrije Universiteit, Amsterdam, Netherlands, suzette.timmerman@anu.edu.au, g.r.davies@vu.nl

²De Beers Exploration, Southdale, South Africa, ingrid.chinn@debeersgroup.com

³De Beers Technologies, Maidenhead, United Kingdom, david.fisher@debeersgroup.com

Introduction

Complex growth structures in monocrystalline diamonds accompanied by changes in N and/or $\delta^{13}\text{C}$ reflect episodic growth and changes in the C-H-O-S rich diamond-forming media. Determining the nature of different types of diamond growth is important to build an understanding of the conditions of diamond formation in the mantle. Recent changes to processing at Orapa have significantly increased the yield of unusual yellow diamonds. These diamonds have an uneven yellow colour owing in part to the presence of relict unaggregated nitrogen defects (C defects) rather than the N3 defect that gives rise to the more common “Cape yellow” colour. They represent a previously undocumented eclogitic diamond-formation event at a mine dominated by eclogitic diamonds. The diamonds studied were sizeable; of $\frac{3}{4}$ to 1 carat, underlining the economic importance of understanding the formation of these particular diamonds. To this end, we present a detailed FTIR, carbon isotope and inclusion major element study of 20 of these unusual eclogitic diamonds from Orapa.

Results

In general, all the diamonds have an uneven yellow to orange colour and an irregular morphology, with trigons present on some faces. The internal growth structure of central plates, as revealed by DiamondViewTM fluorescence imaging, shows complex intergrowth of zones with green fluorescence and non-fluorescent to blue zones. Growth sector zonation was identified in the green fluorescent zones that are directly related to the yellow colour in normal transmitted light (Fig. 1). The non-fluorescent to blue zones correspond with colourless zones in transmitted light. Most diamonds show a clear resorption boundary (Fig. 1b) between the green fluorescent zones and non-fluorescent to blue fluorescent zones. More examples of the growth structure of these Orapa diamonds can be found in the supplementary information of Timmerman et al. (2017).

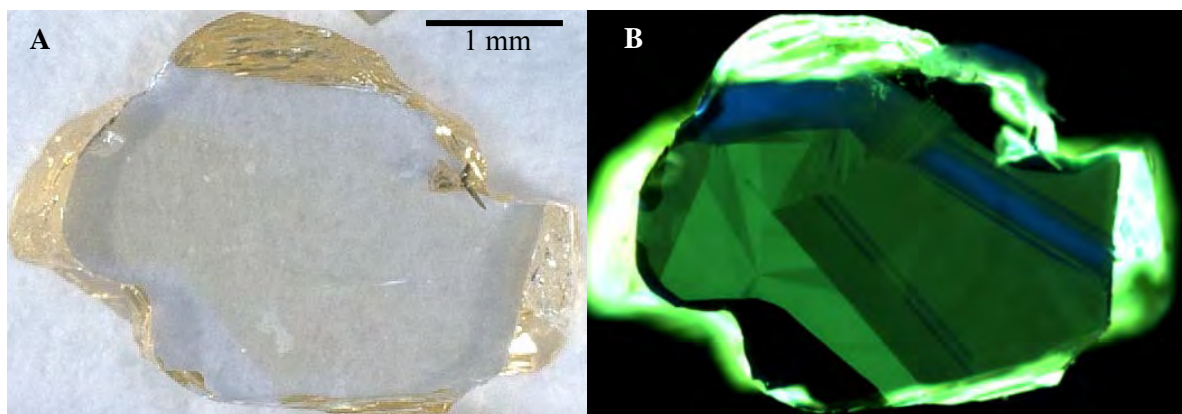


Figure 1: A) Normal transmitted light image, and B) DiamondViewTM image of diamond OR19. The yellow section in transmitted light corresponds to the green luminescence in DiamondView.

FTIR spectra show that all growth zones are characterized by low nitrogen concentrations (<125 ppm) and a hydrogen peak at 3107 cm^{-1} (Fig. 2). Some spectra contain platelet peaks, marking the start of aggregation from A to B centres. Relict unaggregated nitrogen defects are present in the yellow growth zones. The nitrogen peak at 1344 cm^{-1} of single substitutional nitrogen is very low corresponding to 0.2 to 1.1 ppm (Fig. 2) and absorption at 1332 cm^{-1} is partially caused by N^+ . The single phonon region

does not generally fit well to the usual C, A and N⁺ components and the nature of the defects causing the additional absorption is presently unknown.

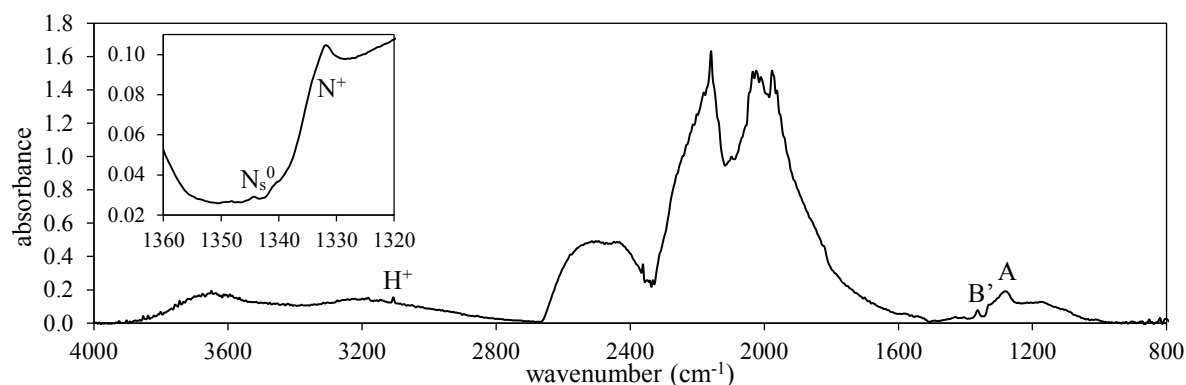


Figure 2: FTIR spectrum of diamond OR07, showing the small nitrogen A-centre peak relative to the diamond absorbance, and the platelet peak at 1363 cm⁻¹ (B'). The inset shows the presence of the N peaks at 1344 and 1332 cm⁻¹.

The $\delta^{13}\text{C}$ values of these Orapa diamonds show a limited range of -5.7 to -10.6 ‰. Yellow and colourless zones exhibit a similar variation in carbon isotope composition of -5.7 to -10.6 ‰ and -6.8 to -10.4 ‰ respectively (Fig. 3a). One heavier composition of -2.9 ‰ was found for the blue fluorescent inner zone of diamond OR12. Most diamonds show no significant change in their carbon isotope composition throughout the diamond (Fig. 3a). Similar to the limited variation in carbon isotope composition and nitrogen content, the major element compositions of the mineral inclusions show limited variability. Mineral inclusions all occur in colourless zones and none were observed in zones with yellow body colour. Garnet inclusions show a range in calcium content of 3.46 – 6.89 wt%, with one calcium-poor outlier (1.73 wt%; Fig. 3b). Both calcium and iron decrease with increasing magnesium content and the data form a single population in bi-variant diagrams suggesting that there is only one garnet population. Clinopyroxenes show limited variation in Mg[#] and Cr[#], apart from 3 clinopyroxenes in diamond OR18. Based on the fluorescence images four non-touching garnet-clinopyroxene pairs were considered to be in equilibrium and yielded temperatures of 1105-1191 °C at an assumed pressure of 5 GPa, calculated with the Fe-Mg exchange thermometer of Krogh (1988). These temperatures are ~100 °C higher than the temperatures of ±1000-1100 °C previously reported for eclogitic diamonds from Orapa (Deines and Harris 2004).

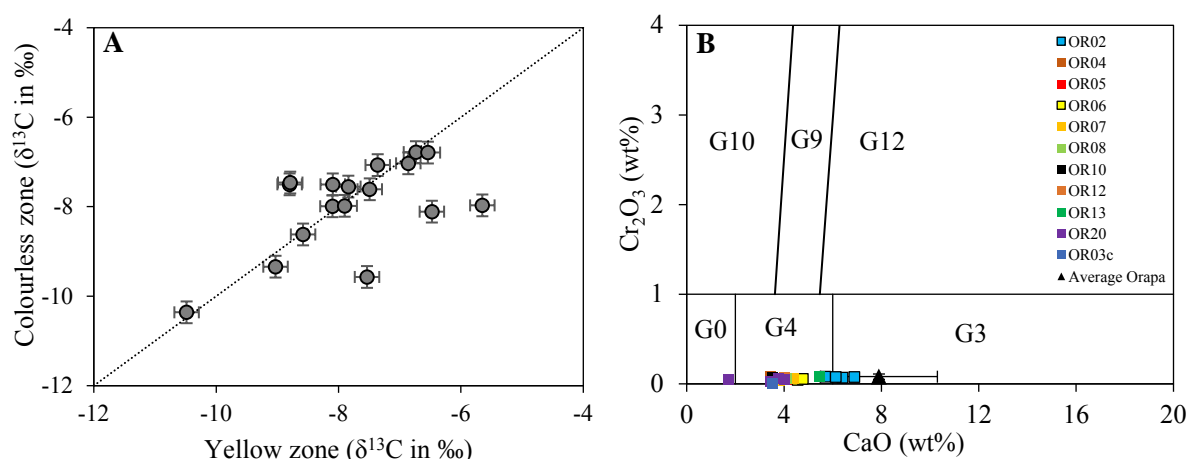


Figure 3: A) Carbon isotope compositions for yellow and colourless zones of the studied Orapa diamonds. B) Limited variation in major element composition of garnet inclusions in the Orapa diamonds, with on average lower calcium contents compared to the average eclogitic population reported by Deines et al. (1993). Classification diagram after Grütter et al. (2004).

Discussion

Despite a distinct difference in growth structure and fluorescence between yellow and colourless zones, the nitrogen concentration and carbon isotope composition are indistinguishable. The restricted range in N and $\delta^{13}\text{C}$ within the diamonds suggests that the different zones formed from similar fluids. Furthermore the presence of only one compositional population of eclogitic silicate inclusions in all 20 studied diamonds shows that the colourless zones formed from similar fluids. The source of the fluid and conditions of growth can be further constrained based on the nitrogen contents and composition of the inclusions. Nitrogen aggregates from single nitrogen to nitrogen pairs to four nitrogen around a vacancy, and is dependent on time, temperature and nitrogen concentration (Taylor et al. 1996). The relict unaggregated nitrogen defects present in the studied diamonds therefore suggest young diamond formation, formation in a cool environment, and/or low aggregation rates due to the low nitrogen concentration. A dating study of silicate inclusions derived from the colourless outer zones of these same unusual yellow Orapa diamonds yielded isochron ages of 140 ± 93 , 1096 ± 230 , and 1699 ± 340 Ma (Timmerman et al. 2017). This implies that some of the yellow inner zones are likely to be ≥ 1699 Ma and indicates that the diamonds did not have an unusually short mantle residence time. The equilibration temperatures of $1105\text{--}1191^\circ\text{C}$ for four non-touching garnet-clinopyroxene pairs suggest that the unaggregated nitrogen defects are not associated with diamond formation at unusually low temperatures. It is possible, however, that diamond formation took place during a thermal perturbation associated with hot upwelling mantle material resulting in a higher equilibrium temperature recorded in the mineral inclusions. Subsequent cooling to ambient mantle conditions would result in a lower average residence temperature. The unaggregated nitrogen defects are more likely a consequence of the difficulty of aggregation at low N concentrations. In addition, the lack of aggregated nitrogen may be explained by the formation of hydrogen-nitrogen complexes instead of nitrogen aggregates.

The distinct characteristics of these diamonds compared to other diamonds from Orapa suggest they were formed in a different environment and growth event to the majority of Orapa diamonds. The $^{87}\text{Sr}/^{86}\text{Sr}$ composition of the silicate inclusions in the colourless zones of the diamonds showed large variations ($0.7033\text{--}0.7084$; Timmerman et al. 2017), and coupled to the limited range in $\delta^{13}\text{C}$ it was suggested to be caused by mixing fluids from a depleted mantle and a post-Archaeon subducted sediment source (Timmerman et al. 2017). In summary, the similarity of all twenty diamonds in terms of morphology, growth structure and the limited range in nitrogen concentration, aggregation state, inclusion major element composition, formation temperature, and carbon isotope composition indicate that these complexly zoned diamonds formed from fluids mixed from depleted mantle and post-Archaeon subducted sediment sources that have restricted carbon isotope compositions.

References

- Deines P, Harris JW (2004) New insights into the occurrence of ^{13}C -depleted carbon in the mantle from two closely associated kimberlites: Letlhakane and Orapa, Botswana. *Lithos* 77(1):125-142
- Deines P, Harris JW, Gurney JJ (1993) Depth-related carbon isotope and nitrogen concentration variability in the mantle below the Orapa kimberlite, Botswana, Africa. *Geochimica et Cosmochimica Acta* 57(12):2781-2796
- Grütter HS, Gurney JJ, Menzies AH, Winter F (2004) An updated classification scheme for mantle-derived garnet, for use by diamond explorers. *Lithos* 77(1):841-857
- Krogh EJ (1988) The garnet-clinopyroxene Fe-Mg geothermometer—a reinterpretation of existing experimental data. *Contributions to Mineralogy and Petrology* 99(1):44-48
- Taylor WR, Canil D, Milledge HJ (1996) Kinetics of Ib to IaA nitrogen aggregation in diamond. *Geochimica et Cosmochimica Acta* 60(23):4725-4733
- Timmerman S, Koornneef JM, Chinn IL, Davies GR (2017) Dated eclogitic diamond growth zones reveal variable recycling of crustal carbon through time. *Earth and Planetary Science Letters* 463:178-188



Relation between fluid end-members and noble gases in South African diamonds

Suzette Timmerman¹, Masahiko Honda¹, David Phillips², A. Lynton Jaques¹, Jeff W. Harris³

¹Australian National University, Canberra, Australia, suzette.timmerman@anu.edu.au,
masahiko.honda@anu.edu.au, lynton.jaques@anu.edu.au

²University of Melbourne, Parkville, VIC, Australia, dphillip@unimelb.edu.au

³University of Glasgow, Glasgow, United Kingdom, jeff.harris@glasgow.ac.uk

Introduction

Fibrous diamond growth zones can contain abundant high density fluid inclusions (HDFs) and these provide the most direct information on the source and composition of diamond-forming fluids. Four different fluid end-members have been defined; silicic, low-Mg carbonatitic, high-Mg carbonatitic, and saline (Weiss et al. 2015 and references therein). Continuous arrays exist between the silicic and low-Mg carbonatitic end-member and between the saline and high-Mg carbonatitic end-member. Different processes have been proposed to explain the two major element compositional arrays, but the origin of and relation between the various fluid end-members is still debated. In this study we provide new constraints on the evolution and origin of these diamond-forming fluids by combining noble gas systematics with $\delta^{13}\text{C}$, N concentrations, and fluid inclusion compositions. The rationale is that as noble gases are primarily concentrated in the HDFs in diamonds (Burgess et al. 2009; Johnson et al. 2000), there could potentially be a relationship between the noble gas and fluid inclusion compositions. To this end, we have studied 24 growth zones from 14 diamonds from the Finsch (n=4), De Beers Pool (n=7), and Koffiefontein (n=3) mines, located along a west to east transect on the Kimberley Block in South Africa. Noble gases from fluid inclusions were extracted by crushing.

Results

Twelve of the studied diamonds are opaque and have fibrous growth zones, whilst the other two (from the Finsch mine) have a milky appearance in normal reflected light with few fluid inclusions. The carbon isotope compositions for the fibrous opaque diamonds range from -2.8 to -8.6‰, whereas the milky diamonds have $\delta^{13}\text{C}$ values up to -1.6‰. The majority of the fibrous diamonds are 100% IaA and have nitrogen concentrations ranging from 310 to 800 ppm. The milky diamonds from Finsch contain 30-40 ppm (diamond 03) and 800-1000 ppm (diamond 04), with diamond 04 having a strong hydrogen peak and clear aggregation to IaB (up to 40%). There is no relation between $\delta^{13}\text{C}$ -N and the noble gas isotopic composition, although in general, higher noble gas concentrations are found in the fibrous diamonds with higher nitrogen concentrations. The majority of the studied diamonds (n=11) fall along the high-Mg carbonatitic to saline compositional array, whereas three diamonds fall on the silicic to low-Mg carbonatitic compositional array. ^4He concentrations range from 0.3-65.1 $\times 10^{-6}$ ccSTP/g, with saline diamonds from De Beers Pool having higher concentrations (3.4-65.1 $\times 10^{-6}$) than Finsch (0.4-4.1 $\times 10^{-6}$) and Koffiefontein (0.3-2.5 $\times 10^{-6}$; see Figure 1a). Similarly for ^{40}Ar , the concentrations of De Beers Pool samples (1.3-78.2 $\times 10^{-7}$) are in general higher than those of the Koffiefontein samples (0.3-4.1 $\times 10^{-7}$). $^{40}\text{Ar}^*/^4\text{He}$ ratios are lower for diamonds near the saline end-member (<0.12) than for silicic diamonds (≥ 0.6 ; Fig. 1b; 1.1-4.4 for Jwaneng diamonds; Burgess et al. 1998). The silicic-carbonatitic diamonds have low $^{40}\text{Ar}/^{36}\text{Ar}$ ratios of 390-1940, whereas saline diamonds have $^{40}\text{Ar}/^{36}\text{Ar}$ ratios up to 30,200 (Fig. 1c). ^{22}Ne , ^{84}Kr and ^{132}Xe yielded concentrations of 0.9-16.0 $\times 10^{-11}$, 0.4-28.2 $\times 10^{-11}$ and 0.4-111 $\times 10^{-12}$ cc/g respectively. R/Ra values in this study range from 1.1 to 6.7 and the majority is similar to values in Panda diamonds (R/Ra: 3.0-6.4) studied via step-heating by Burgess et al. (2009): these show generally higher R/Ra and ^4He concentrations for saline diamonds (Fig. 1d).

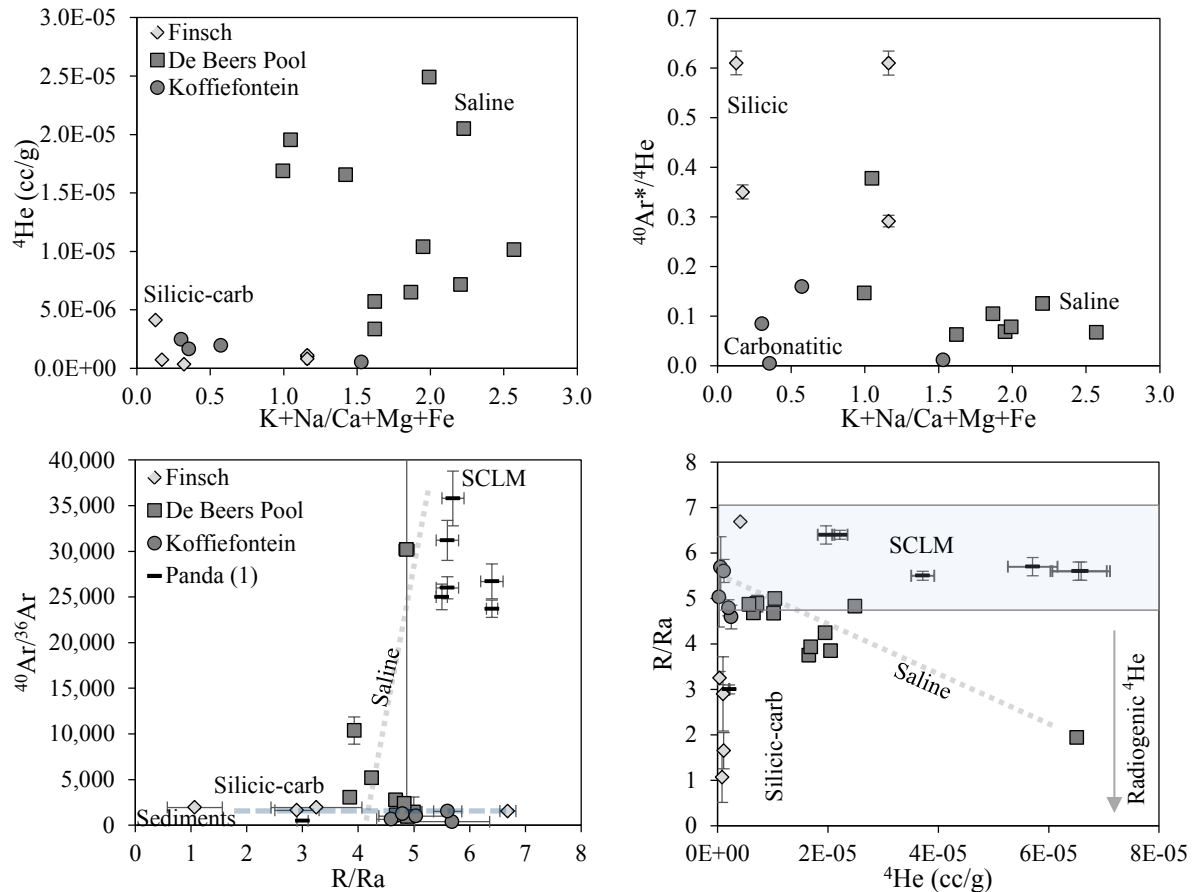


Figure 1: Relationship between the fluid composition and the noble gas compositions and concentrations. The salinity of the fluid composition is expressed as potassium plus sodium relative to calcium plus magnesium plus iron. A) ^4He concentrations versus salinity showing saline diamonds from De Beers Pool have higher helium concentrations. B) $^{40}\text{Ar}^*/^4\text{He}$ versus the salinity of the diamonds. C) $^{40}\text{Ar}/^{36}\text{Ar}$ versus R/Ra ($^3\text{He}/^4\text{He}_{\text{sample}}/^3\text{He}/^4\text{He}_{\text{air}}$) show some saline diamonds have sub-continental lithospheric mantle (SCLM) compositions. (1) Panda diamonds are from Burgess et al. (2009). The dashed line shows the range in saline diamonds. D) R/Ra versus ^4He concentration showing saline diamonds have higher concentrations but a more limited R/Ra range, similar to the SCLM (R/Ra of 5.9 \pm 1.2; Day et al., 2005).

Discussion

Different sources and processes have been suggested to explain the two arrays and evolution of the diamond-forming fluid end-members. As the SCLM is not a closed system, possible sources include accreted mantle from convergent margins, subducted oceanic lithosphere plus sediments, asthenospheric mantle by underplating, and $\text{H}_2\text{O}-\text{CO}_2$ fluids (e.g. kimberlites). The low $^{40}\text{Ar}/^{36}\text{Ar}$ and R/Ra observed in the low-Mg carbonatitic HDF-bearing diamonds are very similar to the ratios of the atmosphere (296 and 1 respectively), sea-water (296; 1), oceanic crust (516; 0.04) and its sediments (374; n/a; Allègre et al. 1987). The observed low $^{40}\text{Ar}^*/^4\text{He}$ ratios can be explained by the loss of K relative to U, Th during dehydration of the subducting slab. The noble gas characteristics of the carbonatitic HDFs are, however, also comparable to carbonatitic and kimberlitic magmas ($^3\text{He}/^4\text{He}$ ratios of 1×10^{-8} to 1.06×10^{-5} and $^{40}\text{Ar}/^{36}\text{Ar}$ ratios of 302 to 5000; Sasada et al. 1997 and references therein) and is supported by a limited range in halogen ratios (Burgess et al. 2009). Silicic HDF-bearing diamonds have been related to eclogitic rocks (Weiss et al. 2015 and references therein) and this also appears consistent with their noble gas characteristics. The variable high $^{40}\text{Ar}^*/^4\text{He}$ ratios (this study; Jwaneng diamonds from Burgess et al. 1998) and variable R/Ra are likely related to the variation in U/He and K/U ratios in eclogites. The saline HDF-bearing diamonds in this study show some correlation between R/Ra and ^4He concentration (Fig. 1d), suggesting a dependency on radiogenic ^4He ingrowth over time. The $^{40}\text{Ar}/^{36}\text{Ar}$ ratios reach 35800 (this study; Burgess et al. 2009). The He and Ar isotope systematics of the saline diamonds are similar to the SCLM (4.7-7.1 R/Ra ;

Day et al. 2005). The R/Ra could also be explained by a HIMU source (4.2-6.7 R/Ra; Barfod et al. 1999) and is supported by relatively high Cl contents and Cl/K (Stroncik and Haase 2004) in samples from HIMU sources, and a correlation of $^{40}\text{Ar}/^{36}\text{Ar}$ with Cl/ ^{36}Ar ratios (Johnson et al. 2000) in diamonds. The relatively low $^{40}\text{Ar}/^{36}\text{Ar}$ ratios of HIMU sources (<16300; Barfod et al. 1999) are similar to the $^{40}\text{Ar}/^{36}\text{Ar}$ ratios of most saline diamonds in this study. The high $^{40}\text{Ar}/^{36}\text{Ar}$ of Panda saline diamonds (Burgess et al. 2009) suggests that saline fluids are influenced by the SCLM and possibly originate from a mix of a HIMU and SCLM source.

Different processes have been proposed to explain the continuous arrays between fluid end-members. The difference in $^{40}\text{Ar}/^{36}\text{Ar}$, $^{40}\text{Ar}^*/^4\text{He}$ ratios, and R/Ra values between saline and silicic HDFs may be explained with an immiscibility process by fractionation of K from U-Th (K more into saline fluid) and fractionation of light from heavy noble gases, but similar trace element patterns (Weiss et al. 2015 and references therein) suggest there is no significantly large U-Th/K fractionation. Fractional crystallisation of minerals such as carbonates has been proposed to explain the changes in major element composition. Changing isotopic compositions by crystallisation of minerals, however, seems unlikely on a short timescale. The simplest process to explain the correlations is by mixing the various end-member fluids from different sources. The volatility of noble gases will assist rapid mixing. Another possible process is metasomatic interactions with the wall rock in the SCLM. Carbonatitic fluids with low gas concentrations change composition readily when small volumes percolate through the mantle (eclogitic or peridotitic lithologies).

In summary, the combined fluid–noble gas results from this study provide important new insights into the origin of diamond-forming fluids. The noble gas characteristics of low-Mg carbonatitic HDFs are similar to the various components in a subducting slab and carbonatites/kimberlites. Saline fluids have noble gas compositions which most closely resemble a peridotitic host lithology in the SCLM or a mix of HIMU and SCLM. The noble gases of silicic fluids appear similar to eclogitic lithologies. From a noble gas perspective, the two compositional arrays between silicic and low-Mg carbonatitic and between saline and high-Mg carbonatitic fluids are best explained by mixing between the different sources or by a parental carbonatitic fluid interacting with the SCLM (eclogitic or peridotitic lithology).

References

- Allègre CJ, Staudacher T, Sarda P (1987) Rare gas systematics: formation of the atmosphere, evolution and structure of the Earth's mantle. *Earth and Planetary Science Letters* 81(2-3):127-150
- Barfod DN, Ballentine CJ, Halliday AN, Fitton JG (1999) Noble gases in the Cameroon line and the He, Ne, and Ar isotopic compositions of high μ (HIMU) mantle. *Journal of Geophysical Research: Solid Earth* 104(B12):29509-29527
- Burgess R, Johnson LH, Matthey DP, Harris JW, Turner G (1998) He, Ar and C isotopes in coated and polycrystalline diamonds. *Chemical Geology* 146(3):205-217
- Burgess R, Cartigny P, Harrison D, Hobson EL, Harris JW, (2009) Volatile composition of microinclusions in diamonds from the Panda kimberlite, Canada: implications for chemical and isotopic heterogeneity in the mantle. *Geochimica et Cosmochimica Acta* 73(6):1779-1794
- Day JM, Hilton DR, Pearson DG, Macpherson CG, Kjarsgaard BA, Janney PE (2005) Absence of a high time-integrated $^3\text{He}/(\text{U}+\text{Th})$ source in the mantle beneath continents. *Geology* 33(9):733-736
- Johnson LH, Burgess R, Turner G, Milledge HJ, Harris JW (2000) Noble gas and halogen geochemistry of mantle fluids: comparison of African and Canadian diamonds. *Geochimica et Cosmochimica Acta* 64(4):717-732
- Sasada T, Hiyagon H, Bell K, Ebihara M (1997) Mantle-derived noble gases in carbonatites. *Geochimica et cosmochimica acta* 61(19):4219-4228.
- Stroncik NA, Haase KM (2004) Chlorine in oceanic intraplate basalts: Constraints on mantle sources and recycling processes. *Geology* 32(11):945-948
- Weiss Y, McNeill J, Pearson DG, Nowell GM, Ottley CJ (2015) Highly saline fluids from a subducting slab as the source for fluid-rich diamonds. *Nature* 524(7565):339-342



The Walgidee Hills zoned lamproite intrusion, West Kimberley Province, Western Australia

A.L. Jaques

Research School of Earth Sciences, Australian National University, Canberra, ACT, Australia

Email lynton.jaques@anu.edu.au

Introduction

Walgidee Hills is the largest (~2.5 km in diameter) and, at 17.5 Ma, the youngest lamproite in the Miocene West Kimberley lamproite province which lies at the southwest margin of the Kimberley Craton of Western Australia (Jaques et al. 1986). The Walgidee Hills intrusion is the type location for several K-, Ba- and Ti-rich minerals characteristic of lamproite, including priderite (K,Ba)(Ti,Fe³⁺)₈O₁₆, wadeite (K₂ZrSi₃O₉), jeppeite (K,Ba)₂(Ti,Fe)₆O₁₃, and noonkanbahite (BaKNaTi₂Si₄O₁₄; Wade and Prider 1939; Jaques 2016). Previous reconnaissance studies have shown that Walgidee Hills is concentrically zoned in terms of grain size, mineralogy, and mineral and rock composition, ranging from olivine-, MgO-, and Ni-rich lamproite through to coarse grained lamproite with low MgO and Ni contents at the centre of the intrusion (Jaques et al. 1986). This abstract summarises results of a detailed integrated study of the petrology and geochemistry of Walgidee Hills.

Geology and Petrography

Geological mapping and company exploration drilling at the margins of the Walgidee Hills intrusion has shown that a thin (≤ 25 m) layer of porphyritic olivine lamproite and tuff with abundant country rock fragments occurs at the outer margin of and beneath the main magmatic lamproite forming the intrusion. The Walgidee Hills intrusion is zoned from porphyritic olivine (altered) lamproite at the margin of the intrusion through medium grained lamproite comprised of olivine (altered), diopside, Ti-phlogopite, leucite (altered but with very rare surviving grains) and Ti-potassic richterite with accessory priderite, perovskite, apatite, and wadeite to coarse grained and pegmatitic lamproite rich in K-Ti richterite, priderite, jeppeite, perovskite, apatite, wadeite and noonkanbahite at the centre of the body (Jaques et al. 1986). The pronounced coarsening in grain size of the Walgidee Hills lamproite is illustrated by perovskite which increases from < 50 μm in the porphyritic olivine lamproite up to ~ 2.5 cm in the pegmatitic lamproite. Similarly, priderite increases in size across the body from < 100 μm near the margins to 4 cm in the pegmatitic lamproite at the centre. Lithological zoning from the margins to the centre of the intrusion and textural relationships within samples suggests that the paragenetic sequence is: olivine – chromian spinel – diopside – perovskite – leucite – phlogopite – apatite – priderite – wadeite – titanian potassium richterite – sanidine – jeppeite – noonkanbahite.

Mineral zoning

Modest compositional zoning is evident from outer to inner zone rocks and from cores to rims of individual grains of Cr spinel, phlogopite (to lower Mg, Al and higher Fe) and, to a lesser extent, in Ti K-richterite (to higher Fe, Na), priderite (to lower Cr) and perovskite. However, zoning of individual grains is mostly confined to the fine-grained porphyritic olivine lamproite at the margins of the intrusion, and most individual grains in coarser grained rocks show only limited zoning, consistent with slow cooling of most of the Walgidee Hills intrusion. Spinels are almost entirely restricted to the porphyritic olivine lamproite and range in composition from titanian magnesiochromite with 3–8 wt % TiO₂, < 5 wt % Al₂O₃, and 5–11 wt % MgO to titanian chromites with lower MgO (< 5 wt %) and higher Fe and Cr₂O₃ contents. These spinels are considerably more evolved than those found in the olivine lamproites of the Ellendale Field (Stachel and Brey 1993; Jaques 2016). Phlogopite is characterised by high TiO₂ (up to 10 wt %) and modest Al₂O₃ (up to 9 wt %). It follows a trend to lower Al contents with decreasing Mg/(Mg+Fe) (increasing FeO), typical of lamproites (Mitchell and Bergman 1991) and similar to the coarser groundmass phlogopite in the Ellendale olivine lamproites and more Mg-rich phlogopite in the diopside–K-richterite–phlogopite–leucite lamproites (Jaques et al.

1986; Stachel et al. 1994). The K-richterite has high TiO₂ (3–7 wt %) and low Na₂O (2–7 wt %) contents and shows an increase Ti (and lesser increase in Na and Na/(Na+K)) and a decrease in Al with decreasing Mg/(Mg+Fe). Walgidee Hills perovskites contain significant Sr, Nb and LREE, and have highly fractionated REE patterns strongly enriched in LREE (Jaques 2016). The perovskites define an evolutionary trend of enrichment in Na, Sr, Y, Nb, U and REE, and depletion in Cr, Fe, and Th towards the centre of the body. Early crystallised perovskite has significant Cr₂O₃ contents (up to 1.2 wt %) and LREE (La/Yb_N =1100–2500) whereas late crystallising perovskite at the centre of the intrusion has higher U, Y, and HREE but shows a decrease in LREE relative to HREE in earlier crystallised perovskite LREE (La/Yb_N <1000, decreasing to <500) due to extended crystallisation of LREE-enriched perovskite and apatite (Jaques 2016).

Geochemical zoning

Whole rock analyses show a decrease in MgO, Ni and Cr, and increase in Fe, Ti, Y, Zr, Nb, Hf, Rb, REE, and Th abundances inwards towards the most evolved rocks at the centre of the intrusion (Fig. 1). The zoning is well displayed by the MgO and Ni contours over the eastern part of the intrusion based on sampling of grid drilling (Jaques et al. 1986). The porphyritic olivine lamproite at the outer margin is characterised by moderate to high MgO and Ni contents (14–18% MgO, 500–600 ppm Ni) and passes inwards through more MgO- and Ni-rich (18–22 wt% MgO, 600–700 ppm Ni) medium grained lamproite into the MgO- and Ni-poor pegmatitic lamproites (~ 4–10 wt % MgO, < 200 ppm Ni, < 100 ppm Cr) at the centre.

Samples on a north–south transect shows the increase in TiO₂, Y, Zr and Nb towards the centre of the intrusion, and the decrease in MgO, Ni and Cr (Fig. 1). Increases towards the centre of the body are evident in Fe (total), P₂O₅, Sr, and Ba contents and also, to a lesser extent, K₂O, Rb, Pb, Th and U. A greater dispersion of some of the LIL elements (e.g. K, Rb, Ba, U) is thought to be due to the effects of low temperature alteration. The Walgidee Hills lamproites exhibit a strong near-linear correlation of Ni and Cr and an inverse correlation of TiO₂, K₂O, and most LIL elements (e.g. Rb, Sr, LREE, Th) and high field strength cations (e.g. Y, Zr, Nb, Hf) with MgO, similar to that observed in the West Kimberley lamproites generally (Jaques et al. 1984, 1986). The Walgidee Hills lamproites have parallel highly fractionated REE patterns strongly enriched in LREE (La_{CN} ~ 520–1450 x, Lu ~ 3.8–10 x) with the lowest REE abundances found in the most MgO-rich lamproites and the highest REE abundances in the pegmatitic lamproites.

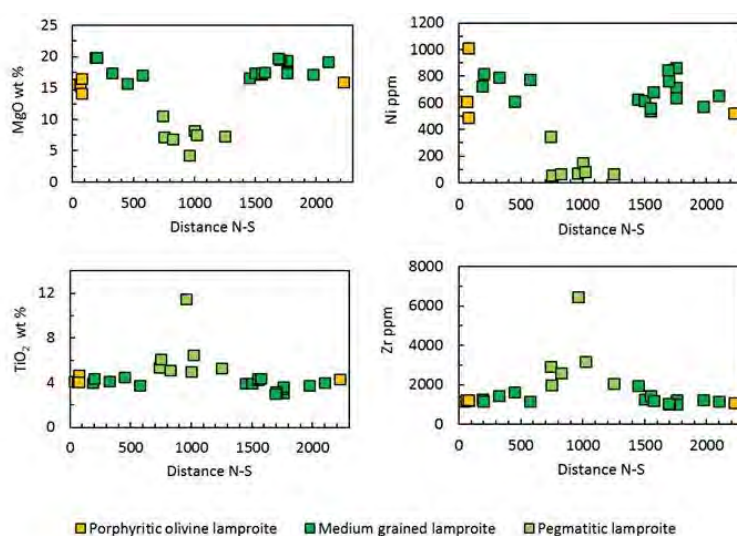


Figure 1. Geochemical variation in rock geochemistry shown by selected major and trace elements within the Walgidee Hills intrusion.

There is a strong correlation of major and trace elements with MgO which, coupled with the presence of macrocrystic olivine, suggests that the geochemical variation is controlled in part by accumulation and fractionation of olivine. The porphyritic olivine lamproite at the margin of the intrusion has a relatively uniform composition (SiO₂ 43.1±0.8, TiO₂ 4.2±0.1, Al₂O₃ 5.7±0.3 Fe as Fe₂O₃ 7.5±0.2, MnO 0.10, MgO 15.7±1.0, CaO 4.1±0.4, Na₂O 0.40±0.1, K₂O 6.3±1.3, P₂O₅ 1.0±0.5 wt %, Cr 770±80, Ni 550±50 ppm) and might approximate the parent magma composition for the Walgidee Hills intrusion. Preliminary modelling suggests that the more MgO-rich lamproites (~20% MgO) can be approximated by incorporation of ~10–12 wt % of mantle olivine whereas the more evolved coarse grained lamproites at the centre of the body are the result of slow cooling and extended fractional crystallisation.

Conclusions

Walgidee Hills is unusual in terms of the relatively large volume of lamproite magma erupted in the ~2.5 km diameter body where slow cooling allowed extended fractionation and the crystallisation of coarse grained to pegmatitic lamproites with abundant K-Ba-titanate minerals, apatite and wadeite, minerals normally found in the evolved groundmass of finer grained lamproites. The most MgO-rich of the Walgidee Hills lamproites ranges up to the most MgO-poor (22–24 wt %) olivine lamproites found in the two largest pipes (Ellendale 4 and 9) of the Ellendale Field which also show (limited) evidence of petrographic and geochemical zoning (coarsening of the groundmass, minor geochemical variation) within their former lava lakes (Jaques et al. 1986; Stachel et al. 1994). The parent magma composition for the Ellendale lamproites is estimated to have been more primitive than that of Walgidee Hills containing ~ 22 wt % MgO and ~ 1,000 ppm Ni (Foley 1993).

Diamond exploration has yielded mineral concentrates containing mantle fragments dominated by Cr-Al spinel with rare Cr-pyrope (G9) garnet and traces of diamond indicating that the Walgidee Hills lamproite was likely derived from partial melting of mantle within the diamond stability field. Walgidee Hills, like the other Noonkanbah field lamproites, is slightly less geochemically enriched than the Ellendale lamproites, but trace element and Sr, Nd and Pb isotope compositions indicate a similar origin involving small degrees of partial melting of a formerly depleted mantle source that has undergone long term (> 2 Ga) geochemical enrichment (Jaques et al. 1984, 1986; Nelson et al. 1986).

References

- Foley SF (1993) An experimental study of olivine lamproite: First results from the diamond stability field: *Geochim Cosmochim Acta* 57:483-489
- Jaques AL (2016) Major and trace element variations in oxide and titanate phases in the West Kimberley lamproites, Western Australia. *Miner Petrol* 110:159-197
- Jaques AL, Lewis JD, Smith CB, Gregory GP, Feguson J, Chappell BW, McCulloch MT (1984) The diamond-bearing ultrapotassic (lamproitic) rocks of the West Kimberley region, Western Australia. In Kornprobst J et al (eds) *Kimberlites I: Kimberlites and related rocks*, Elsevier, pp. 225-254
- Jaques AL, Lewis JD, Smith CB (1986) The kimberlites and lamproites of Western Australia. *Bull Geol Surv W Aust* 132: 268 pp
- Mitchell RH, Bergman SC (1991) *Petrology of Lamproites*. New York: Plenum, 447 pp.
- Nelson DR, McCulloch MT, Sun SS (1986) The origins of ultrapotassic rocks as inferred from Sr, Nd and Pb isotopes. *Geochim Cosmochim Acta* 50:231-245
- Stachel T, Brey G (1993) Spinels in the Ellendale olivine lamproites (Western Australia): significance for diamond distribution and emplacement history. *Neues Jahrbuch Miner Abh* 165: 155-167
- Stachel T, Lorenz V, Smith CB, Jaques AL (1994) Volcanology and geochemistry of the Ellendale Lamproite Field, (Western Australia). In Meyer HOA, Leonardos OH (eds) *Kimberlites, related rocks, and mantle xenoliths*. CPRM-Special Publ 1/91:177-194
- Wade A, Prider RT (1940) The leucite-bearing rocks of the West Kimberley area, Western Australia. *Quart J Geol Soc Lond* 96:39-98

New insights into volatile-rich mantle metasomatism at the Bultfontein diamond mine, Kimberley, South Africa

Charlotte G. Jackson¹ and Sally A. Gibson¹

¹University of Cambridge, Cambridge, United Kingdom, cj340@cam.ac.uk, sally@esc.cam.ac.uk

Introduction

Metasomatised regions of the sub-continental lithospheric mantle potentially represent a large volatile reservoir. Nevertheless, the mechanisms involved in the storage and upward transport of volatiles (such as C and S) from the convecting mantle and/or subducting slabs, are poorly understood. We have carried out a systematic micro-analytical study on a suite of sulfide-rich mantle peridotites from the Kaapvaal Craton. The studied xenoliths are from the Bultfontein diamond mine, Kimberley and exhibit a range of trace-element enrichment processes, from solely cryptic to modally metasomatised (Kramers et al. 1983). We have chosen this suite because the olivines have the same mantle normalised REE pattern with varying levels of enrichment. We investigate the possibility that the suite represents the progressive stages of reactive percolation of a volatile-rich small-fraction metasomatic agent during ascent through the subcratonic lithospheric mantle.

Petrographic description

Our study focusses on two key xenoliths that appear to represent the two endmembers of reactive percolation of a metasomatic agent: one is a cryptically metasomatised harzburgite that has had no modal mineralogical change (BD1676) and the other represents the modally metasomatised endmember (BD3067).

BD1676 has 60% olivine, 35% orthopyroxene and 5% fingerprint spinel/augite intergrowths, i.e. a decompression product of garnet. BD3067 contains large (6 mm) porphyroclastic olivines in a matrix of small polygonal olivine neoblasts. The spectacular feature of this xenolith is a large, trichotomous branching clinopyroxene-rich vein, measuring 45 mm at its widest point in hand specimen. This vein is shown in the QEMSCAN image in Figure 1. Branch terminations and regions of clinopyroxene crystallisation away from the main vein are associated with phlogopite crystallisation. There are also large zircons, up to 5mm diameter, within the vein. Additionally, large interstitial Fe-Ni sulfides occur amongst the olivine neoblasts.



Figure 1: QEMSCAN image of xenolith BD3067

Analytical Results

Olivine

The olivine in cryptically metasomatised BD1676 has a forsterite content typical of sub-cratonic mantle (F₀₉₂-F₀₉₃). In contrast, both the porphyroclasts and neoblasts in BD3067 have had significant Fe-enrichment (F₀₈₈). The latter are also enriched in MnO (0.13- 0.19 wt. %) relative to the olivines in BD1676 (MnO= 0.09-0.13 wt.%). Both olivine populations in BD3067 are homogeneous in all the major elements but the largest porphyroclasts show Ni-variation in core to rim profiles (Figure 2). The olivines in BD3067 are all Ni-depleted (0.18-0.22 wt. % NiO) compared to those from BD1676 (>0.4 wt. % NiO). In BD3067, only the largest crystals (>4 mm diameter) are unequilibrated. Experimental work has shown that the diffusion coefficients for Fe-Mg, Mn and Ni are very similar at all conditions tested (*T* and *fO*₂, and *P*; Petry et al. 2004; Holzappel et al. 2007). The olivines are all otherwise

homogeneous in Fe, Mg and Mn, we therefore conclude that differing diffusivities of the elements in olivine is not responsible for the Ni variation.

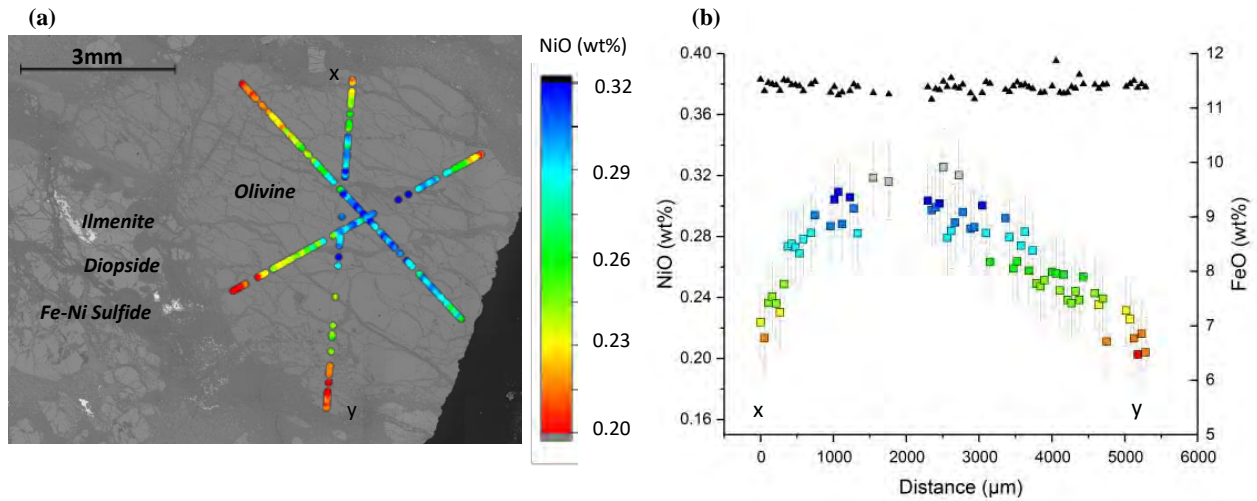


Figure 2: NiO variation in a large unequilibrated olivine from BD3067. (a) BSE image with NiO profiles overlain. (b) Example of profiles marked x-y in (a) that shows the asymmetry in core-rim variation of NiO. Black triangles show the FeO concentration along the same profile.

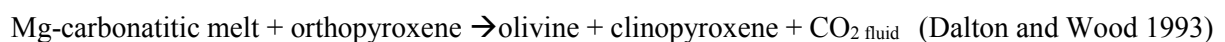
The Ni/Fe ratio in the olivines ranges from 0.016-0.019. This is very low for mantle olivines, but is within the range of the olivines found as inclusions in diamonds (Tomlinson et al., 2005). These workers attributed the anomalously low Ni/Fe ratios to olivine crystallisation in the presence of Ni-rich sulfides. The latter are one of the most common mineral phases found as inclusions in peridotitic diamonds and, since Ni partitions preferentially into sulfides over olivine, the olivine crystallising in the presence of sulfides is expected to have a lower Ni content.

Sulfides

Modally metasomatised xenolith BD3067 contains a high modal proportion of Fe-Ni sulfides. They are interstitial and associated with phlogopite and carbonate. These features imply that these are metasomatic sulfides rather than primary mantle sulfides. The sulfides are heavily serpentinised and extremely heterogeneous in terms of their compositions. The Ni-rich regions of the sulfides have >35 wt% NiS and are in equilibrium with the Ni-depleted olivines ($K_D = 30$; Fleet and MacRae 1988).

Interpretations

The absence of orthopyroxene in the modally metasomatised xenolith BD3067 implies that the precursor peridotite (harzburgite) may have reacted with a silica-undersaturated melt. We suggest that the suite of xenoliths represents the progression of the reaction:



Recent experimental work by Gervasoni et al. (2017) has confirmed that a wehrlitic assemblage is produced by the reaction of a carbonatitic melt and fertile peridotite and that the ratio of pyroxene to olivine is reflective of the melt:rock ratio. High Mg# in the clinopyroxenes (90-93) support this interpretation.

The presence of metasomatic Fe-Ni sulfides in BD3067 implies that the Bultfontein mantle has experienced an interaction with a sulfur-rich fluid. We suggest that preferential partitioning of Ni into the sulfide caused the observed Ni-depletion of olivine in the host mantle, (Figure 3). While the olivine neoblasts have reached Ni equilibrium with the sulfides the largest porphyroclasts have not. Our calculations of Ni diffusivity in olivine suggest that the S-rich infiltration event occurred within 1 Myr of the eruption of the 84 Ma Bultfontein kimberlite (Figure 4). It is unclear whether the S-rich

metasomatism was in conjunction with the carbonatitic metasomatism, or at a later stage. Our findings are consistent with Giuliani et al. (2013) who identified multiple stages of kimberlite melt evolution, two of which include an alkali-carbonate melt and an immiscible sulfide liquid, at Bulfontein.

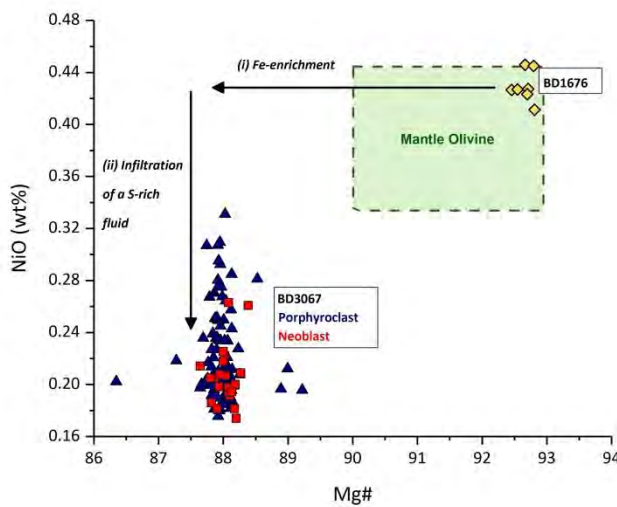


Figure 3: Olivine Mg# vs. NiO showing the effect of (i) Fe-enrichment by a metasomatic agent and (ii) the infiltration of a sulfur-rich fluid.

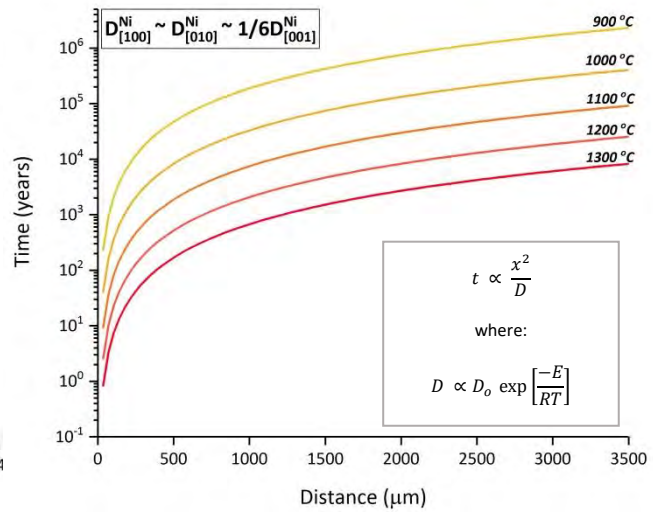


Figure 4: Diffusion timescales for Ni in olivine in the slowest direction [100] and [010] over a range of temperatures. The fastest direction [001] is roughly equal to 6 times the slowest diffusion timescales (Petry et al. 2004)

Conclusions

The Bulfontein xenoliths offer a rare insight into the mantle enrichment processes that accompany kimberlite activity. We conclude that at least two different phases of volatile-rich mantle metasomatism affected the southern Kaapvaal craton immediately prior to kimberlite emplacement at 84 Ma. These involve (i) reactive percolation of a silica-undersaturated carbonatitic melt that transformed primary enstatite to diopside and the formation of olivine neoblasts; and (ii) the infiltration of a S-rich fluid. Furthermore, the abundance of metasomatic Ni-sulfides at Bulfontein highlights the prevalence of sulfur transport through the sub-cratonic mantle, and the capacity of ancient sub-continental lithosphere to store volatiles.

References

- Dalton JA, Wood BJ (1993) The compositions of primary carbonate melts and their evolution through wallrock reaction in the mantle. *Earth Planet Sci Lett* 119:511–525. doi: 10.1016/0012-821X(93)90059-I
- Fleet ME, MacRae ND (1988) Partition of Ni between olivine and sulfide: equilibria with sulfide-oxide liquids. *Contrib Mineral Petrol* 100:462–469. doi: 10.1007/BF00371375
- Gervasoni F, Klemme S, Rohrbach A, et al (2017) Experimental constraints on mantle metasomatism caused by silicate and carbonate melts. *Lithos* 282–283:173–186. doi: 10.1016/j.lithos.2017.03.004
- Giuliani A, Kamenetsky VS, Kendrick MA, et al (2013) Oxide, sulphide and carbonate minerals in a mantle polymict breccia: Metasomatism by proto-kimberlite magmas, and relationship to the kimberlite megacrystic suite. *Chem Geol* 353:4–18. doi: 10.1016/j.chemgeo.2012.09.025
- Holzappel C, Chakraborty S, Rubie DC, Frost DJ (2007) Effect of pressure on Fe–Mg, Ni and Mn diffusion in $(\text{Fe}_x\text{Mg}_{1-x})_2\text{SiO}_4$ olivine. *Phys Earth Planet Inter* 162:186–198. doi: 10.1016/j.pepi.2007.04.009
- Kramers JD, Roddick JCM, Dawson JB (1983) Trace element and isotope studies on veined, metasomatic and “MARID” xenoliths from Bulfontein, South Africa. *Earth Planet Sci Lett* 65:90–106. doi: 10.1016/0012-821X(83)90192-9
- Petry C, Chakraborty S, Palme H (2004) Experimental determination of Ni diffusion coefficients in olivine and their dependence on temperature, composition, oxygen fugacity, and crystallographic orientation. *Geochim Cosmochim Acta* 68:4179–4188. doi: 10.1016/j.gca.2004.02.024



Melting of hydrous-carbonated eclogite at 4–6 GPa and 900–1200°C: implications for the sources of diamond-forming fluids.

Oded Elazar¹, Ronit Kessel^{1,2} and Oded Navon^{1,3}

¹The Institute of Earth Sciences, The Hebrew University of Jerusalem, Israel, oded.elazar@mail.huji.ac.il

²ronit.kessel@mail.huji.ac.il, ³oded.navon@mail.huji.ac.il

Introduction

Eclogites play a significant role in geodynamic processes, transferring large amounts of basaltic material and volatiles (chiefly CO₂ and H₂O species) into the earth's mantle via subduction. They are also linked to formation of high density fluid inclusions in diamonds (HDF's). Previous studies on eclogite melting focused on two end member systems: either carbonated or hydrous eclogites. Here we focus on a hydrous carbonated eclogitic system in order to define the position of its solidus and determine the fluid and melt compositions at 4-6 GPa and 900-1200°C. In contrast to procedures commonly adopted in the past, we rely on direct measurements of the liquid phase (melt/fluid/supercritical liquid) compositions in determining the solidus location instead of relying on solid mineral compositions and/or textural criteria. The variations in the chemistry of the liquid phase enable us to discuss the role of eclogites in the sources and formation of HDFs found in diamond inclusions.

Analytical Results

All experiments contained garnet and clinopyroxene, representing an eclogitic assemblage and are in equilibrium with a H₂O and CO₂-rich fluid or melt. At 4-5 GPa and 900°C a large amount of H₂O and CO₂ in the liquid phase indicates the presence of an aqueous-carbonated fluid in equilibrium with the eclogite solid assemblage. A stepwise decrease in the H₂O and CO₂ contents of the liquid between 1000-1100°C is coupled with a stepwise increase in other oxides suggesting that the solidus is located at these conditions. At 6 GPa a smooth decrease in H₂O and CO₂ contents of the liquid phase with increasing temperature is observed. This smooth change indicates the existence of a supercritical fluid and the existence of a second critical end-point for the eclogite+H₂O+CO₂ system at ~5.5 GPa and ~1050°C.

Table 1: Determined liquid composition coexisting in equilibrium with eclogite as obtained in this study.

| P (GPa) | 4 | 4 | 4 | 4 | 5 | 5 | 5 | 5 | 6 | 6 | 6 | 6 |
|---|-------|-------|-------|-------|-------|-------|-------|-------|-------|------|-------|-------|
| T | 900 | 1000 | 1100 | 1200 | 900 | 1000 | 1100 | 1200 | 900 | 1000 | 1100 | 1200 |
| SiO ₂ ^a | 81.09 | 43.84 | 47.53 | 44.43 | 68.52 | 39.64 | 39.84 | 42.76 | 69.25 | 50.6 | 48.83 | 36.35 |
| TiO ₂ | 0.41 | 2.42 | 2.45 | 2.94 | 0.76 | 1.79 | 2.84 | 3.16 | 0.63 | 1.63 | 2.33 | 2.58 |
| Al ₂ O ₃ | 4.79 | 3.31 | 6.2 | 6.82 | 1.33 | 3.71 | 5.26 | 9.1 | 2.23 | 2.54 | 3.21 | 4.96 |
| FeO | 0.53 | 10.5 | 9.95 | 11.97 | 9.24 | 12.92 | 14.47 | 12.42 | 4.3 | 6.43 | 7.48 | 14.28 |
| MgO | 0.58 | 10.41 | 9.93 | 12.01 | 5.54 | 9.89 | 15.09 | 12.69 | 3.69 | 7.15 | 8.22 | 15.25 |
| CaO | 4.07 | 19.43 | 19.03 | 18.14 | 9.56 | 24.28 | 19.25 | 17.25 | 13.53 | 27.5 | 27.12 | 17.03 |
| Na ₂ O | 6.73 | 8.93 | 4.56 | 3.39 | 3.1 | 7.03 | 3.27 | 2.32 | 4.73 | 3.22 | 2.37 | 8.93 |
| K ₂ O | 1.8 | 1.15 | 0.3 | 0.27 | 1.94 | 0.72 | NA | 0.22 | 1.61 | 0.91 | 0.41 | 0.59 |
| Cr ₂ O ₃ | 0.005 | 0.03 | 0.05 | 0.04 | 0.02 | 0.02 | NA | 0.08 | 0.03 | 0.02 | 0.01 | 0.03 |
| H ₂ O _{mole fraction} ^b | 66.78 | 60.63 | 40.65 | 30.32 | 66.93 | 60.96 | 42.14 | 29.9 | 66.8 | 56.7 | 49.3 | 53.2 |
| H ₂ O+CO ₂ _{mole fraction} | 82.45 | 83.48 | 57.96 | 44.65 | 89.06 | 85.95 | 60.08 | 44.03 | 91.2 | 78 | 68.5 | 78.3 |

a. Calculated CO₂ and H₂O free basis normalized to 100%.

b. Mole fractions of H₂O and H₂O+CO₂ were calculated using the hydrous-carbonated fluid/melt compositions.

At 4-6 GPa and 900°C, the hydrous carbonated fluids we found are silica-rich and mostly consist of H₂O and CO₂ with very little carbonate content. They are not represented in the naturally occurring HDFs, but are similar in composition to recent thermodynamical computations done by Sverjensky and Haung (2015). They calculated, using a thermodynamic model, a hypothetical composition of a siliceous fluid after reaction with eclogite at 5 GPa and 900°C and predicted that such a fluid can contain significant amounts of CO₂ (47 wt% relative to ~34 wt% in this study).

At 4-6 GPa and 1000-1100°C the composition of the fluids reported here fall generally between those of silicic and low-Mg HDFs. The Al₂O₃, CaO, MgO and FeO content of the fluid increases with rise in temperature, while the Na₂O content remains relatively constant. At 1200°C, the composition of the determined melts is close to the bulk composition of the system (F=70%). As such, this composition is not representative of natural systems.

The fluid and near solidus melt compositions reported in this study indicate that the hydrous carbonated eclogite system is a possible source rock for HDFs whose composition is intermediate between low-Mg carbonatitic and silicic endmembers. We suggest that the silicic-carbonatitic array is not the result of continuous melting of an eclogite source, but rather, of variations in the H₂O/CO₂ ratio of the fluid.

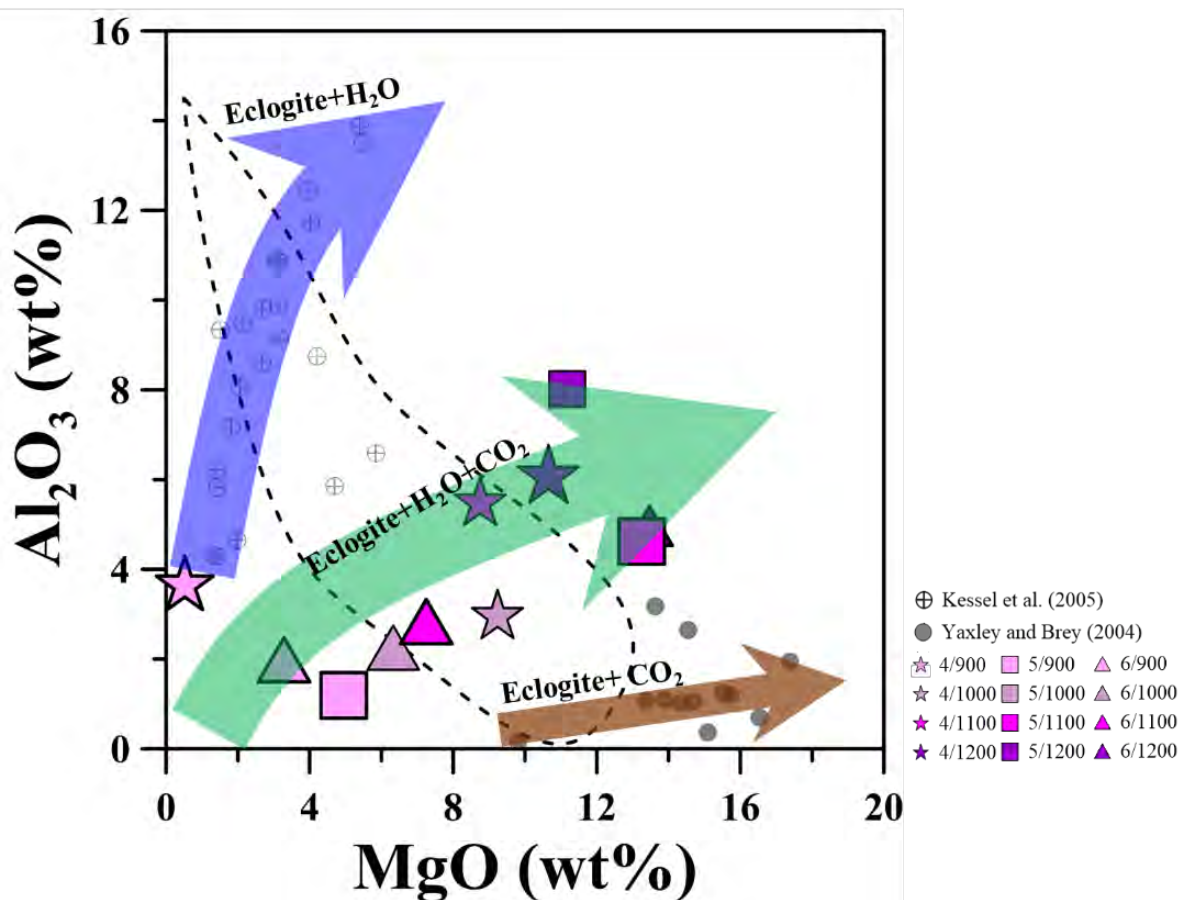


Fig 1: Al₂O₃ vs MgO variation diagram with liquid compositions from Kessel et al. (2005), Yaxley and Brey (2004) and this study (Water and CO₂-free compositions, corrected for lack of K₂O). Near solidus compositions in the eclogite+H₂O and eclogite+H₂O+CO₂ plot within the array charted by the low-Mg carbonatitic to silicic array (Wiess et al, 2009) suggesting that incipient melting of heterogeneous eclogitic sources as a possible mechanism for the production of the various HDF compositions.

References

Kessel R, Ulmer P, Pettke T, Schmidt MW, Thompson AB (2005) The water–basalt system at 4 to 6 GPa: phase relations and second critical endpoint in a K-free eclogite at 700 to 1400°C. *Earth and Planetary Science Letters* 237(3):873-892

- Sverjensky DA, Huang F (2015). Diamond formation due to a pH drop during fluid–rock interactions. *Nature communications* (6).
- Yaxley, GM, Brey GP (2004). Phase relations of carbonate-bearing eclogite assemblages from 2.5 to 5.5 GPa: implications for petrogenesis of carbonatites. *Contributions to Mineralogy and Petrology* 146(5):606-619.
- Weiss Y, Kessel R, Griffin W.L, Kiflawi I, Klein-BenDavid O, Bell D.R, Harris J.W., Navon, O (2009) A new model for the evolution of diamond-forming fluids: Evidence from microinclusion-bearing diamonds from Kankan, Guinea. *Lithos*, 112, pp 660-674.

Conodont Geothermometry in Pyroclastic Kimberlite: Constraints on emplacement temperatures and cooling histories

Pell¹, J., Russell², J.K. and Zhang³, S.

¹ *Peregrine Diamonds Ltd, Vancouver, Canada, jennifer@pdiam.com*

² *Department of Earth, Ocean & Atmospheric Sciences, University of British Columbia, Vancouver, Canada*

³ *Canada-Nunavut Geoscience Office, Iqaluit, Canada*

Introduction

Conodonts are phosphatic marine microfossils commonly preserved in Paleozoic carbonate rocks; they experience progressive, cumulative and irreversible colour changes upon heating and the changes have been experimentally calibrated as a colour alteration index (CAI). CAI values are time and temperature dependent, and permit us to estimate the maximum temperatures to which conodont-bearing rocks have been heated assuming a given time frame. Paleozoic carbonate xenoliths are entrained in resedimented kimberlite (RVK), pyroclastic (PK) and welded or agglutinated deposits (ACK) in many of the kimberlites from Chidliak, Baffin Island. The conodonts within the xenoliths have CAI values ranging from 1.5 to 8 (Zhang and Pell, 2014), which correlate strongly to the type of pipe infill (Figure 1). Thermal models for cooling of these pipes and synchronous heating of conodont-bearing xenoliths indicate short time-spans for these events (Pell et al., 2015). In this study, we present data for CAI traverses across carbonate blocks up to 13.9 m in core length which show variations in CAI and allow us to further constrain the emplacement temperatures (T_E 's) and cooling histories of the Chidliak kimberlite pipes.

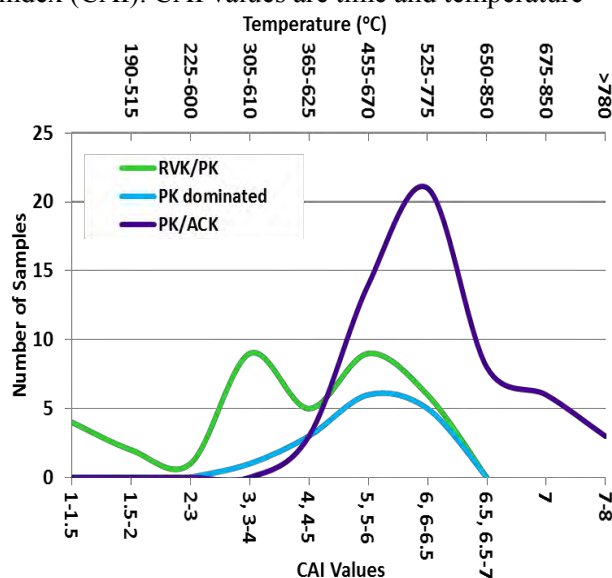


Figure 1. CAI values and corresponding temperature ranges for conodonts from carbonate xenoliths entrained in Chidliak kimberlites by dominant type of pipe infill.

Observations

Within some of the larger carbonate xenoliths, CAI values are zoned. The best example is a 13.9 m xenolith located near the margin of kimberlite CH-46, a pipe with PK/ACK infill. This xenolith shows distinct concentric zoning, with lower CAI values in the core and higher ones towards its outer margins. The base of the xenolith, which is closer to the centre of the pipe, shows the highest CAI value and matches values for conodonts from a smaller adjacent xenolith (Figure 2). Based on the calibration presented in Pell et al. (2015), the CAI values in the core of this xenolith of 4-5, those surrounding the core of 5-6 and those at the base and in the adjacent small xenolith of 6.5-7 correspond to T 's of 365-625°C, 455-670 °C and 650-850 °C, respectively. Another xenolith, 5.8 m in core length, also shows lower CAI values in its core (4) than towards its rims (5-6), while a third, 6.8 m xenolith, also may have similar zoning, but no conodonts were recovered from the material collected from the xenolith rims (possibly destroyed by high temperatures).

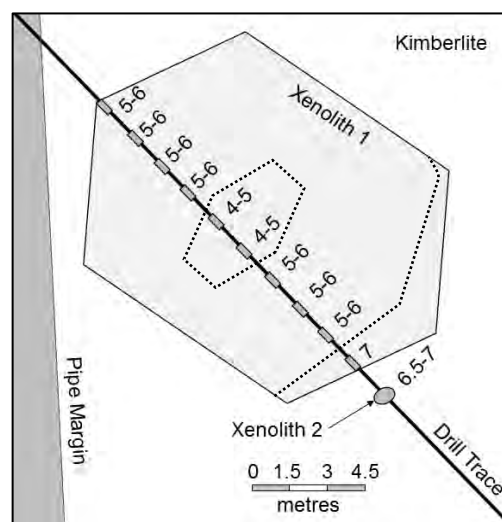


Figure 2. CAI traverse across a 13.9 m xenolith located proximal to the pipe margin in CH-46. Xenoliths shown in grey with CAI data points darker. Dotted lines are schematic CAI zone boundaries.

Two xenoliths, 2.6 and 2.9 m in core length, show a slight increase in CAI from top to base. One is from a PK-dominated pipe and records CAI values of 3-4 on the upper margin of the xenolith, 4 in the core and 4-5 on the lower margin. The second is from a PK/ACK infilled pipe and records CAI values of 6 throughout most of the xenolith, with CAI of 6-6.5 at its basal margin. Two xenoliths, 0.6 and 2.8 m in core length, both contained in PK, showed no variation in CAI (recording values of 5-6 throughout). Two xenoliths from kimberlite CH-45 are anomalous: a 2 m xenolith shows higher CAI at its top than its base (6.5 and 5-6 respectively) and a 3.5 m xenolith has higher CAI values in its core (6.5-7) than those from its margins (5-6). CH-45 has two main types of infill; one is PK/RVK and contains the xenoliths and the other is a carbonate xenolith-free coherent kimberlite.

Models

A conductive cooling model was constructed for a 50 m diameter pipe with an emplacement temperature (T_E) of 1000°C and an ambient T of 25°C for the host rock. Within 1 year the T at the pipe margin, and the peak temperature for the proximal wall rocks, is ~475°C. After a decade the pipe has a peak T of ~400°C and the country rocks are heated by ~100°C degrees up to 50 m from the contact. (Figure 3).

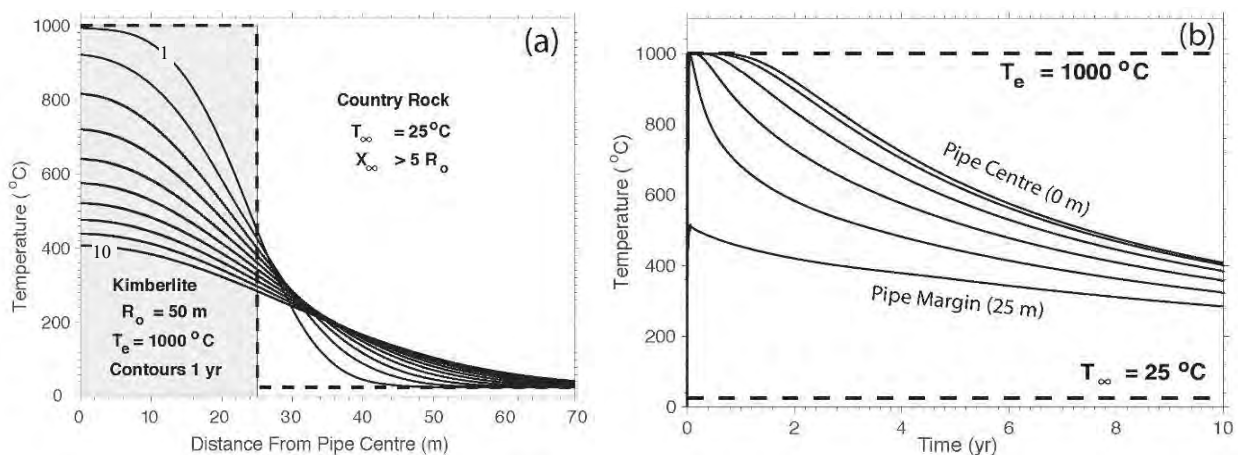
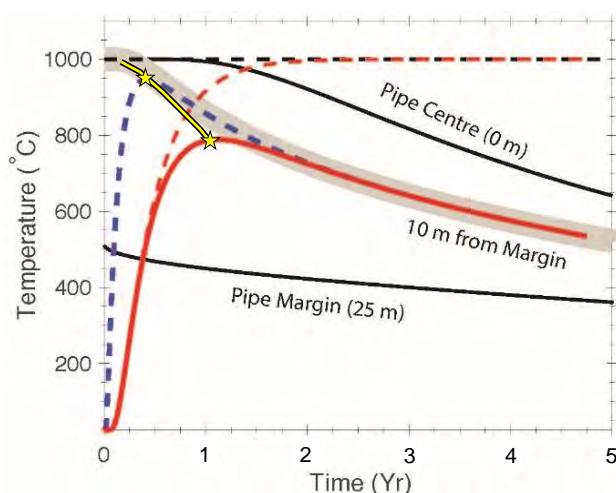


Figure 3. Conductive cooling model for a 50 m diameter pipe, modelled after CH-46. Simulation uses an initial T of 1000°C. (a) shows the temperature distributions from centre of kimberlite pipe (0 m) into the country rock (25 - 70 m) over a ten year period, using 1 year contours. (b) The same model simulation expressed as cooling curves (T vs t) for different positions in the pipe, contoured for increasing distances (5 m increments) from the pipe centre (0 m) until the margin of the pipe (25m). In 10 years the pipe centre is at ~400°C whilst the margin is at ~300°C. These curves are relevant to heating of the individual xenoliths as they define the TRANSIENT ambient T felt by the xenolith as it heats up.

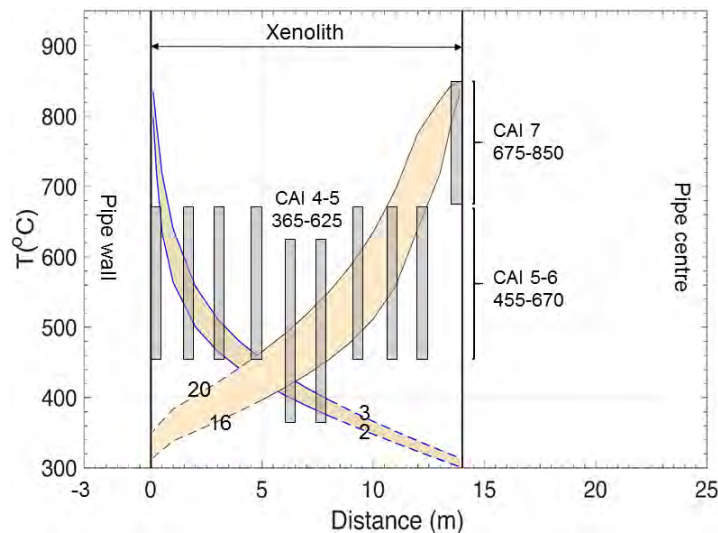
Figure 4. Heating of 14 m diameter xenolith ($T_{ORIGINAL}=25$ °C) 10 m from the wall of a 50 m diameter pipe ($T_E=1000$ °C) as it cools over 5 years is depicted. The solid black lines denote the cooling paths for the centre of the pipe and the margin (see Figure 3). Yellow stars and joining line denote the array of peak T s experienced across the xenolith.



We have modelled the heating of a 14 m diameter xenolith (T initial of 25°C) located 10 m from the margin of a 50 m diameter pipe (T_E of 1000°C) (heavy grey line; Figure 4). If the pipe remained at its T_E , the xenolith core would be heated along the dashed red line and, ultimately, would reach the pipe T_E of 1000°C. However, the pipe is cooling as the xenolith heats up. Thus, the core of the xenolith would be heated along the path described by the solid red line; heating up until it intersects the heavy grey line which denotes the transient cooling path of this part of the kimberlite pipe. Thereafter, the xenolith cools in tandem with the pipe. The blue dashed line denotes the thermal

history of the same xenolith at 3 m from its rim (rather than the core). This demonstrates that the rim of the xenolith heats faster and to higher T 's than its core and therefore different parts of the xenolith will record different peak T s. If this xenolith was in the middle of the pipe, both core and rim could reach similar (high) peak T s that would be close to the T_E of the pipe. Conversely, if this xenolith was at the margin of the pipe, the xenolith rim and core would lock in lower T s. It is implicit that smaller xenoliths will be heated rapidly enough to record similar T s in rim and core, whilst large xenoliths may record quite different T s in their rims and cores.

We applied our model to explain the CAI zoning seen within the large xenolith depicted in Fig. 2. We modelled the peak temperatures reached within this xenolith from rim to core. The heating is



asymmetric because the large xenolith is situated very close to one margin of the pipe; that side of the xenolith (left in Fig. 5) is only exposed to 2 to 3 m of kimberlite. The other side (right) has a significant width of kimberlite available to heat it. Fig. 5 shows the best match to the actual data, which was obtained using a T_E of 850°C for the host kimberlite. Lower pipe temperatures are incapable of matching the CAI values observed. Higher temperatures cannot be ruled out, but also do not match the CAI values as well as the model at 850°C does.

Figure 5. Model for asymmetric heating of the large (~14 m) xenolith shown in Fig. 2 in its actual position within the kimberlite. Grey bars are located where the CAI data was collected and they show the temperature range for the CAIs observed. The curves represent the arrays of peak T s attained by the xenolith in its respective position (i.e. the line joining the yellow stars on Fig. 4) for the width of kimberlite against xenolith contacts (2 to 3 m on the left side, 16 to 20 m on the right).

Discussion

Four main types of CAI distribution in xenoliths was observed at Chidliak: 1) xenoliths that show the same CAI throughout; 2) xenoliths with lower CAI values in their cores than at their rims; 3) xenoliths that have CAIs that increase from one side to the opposite; and, 4) an unusual xenolith with higher CAI recorded in its core than at its rims. Our simple model shows that xenoliths that are unzoned or that display regular zoning, such as the xenolith depicted in Fig. 2 can be explained by in-place conductive heating of a xenolith by its host kimberlite. Our model, however, would not be applicable to situations where there the xenolith had experienced a more complex thermal history such as being entrained in a kimberlite magma during transport and subsequently being incorporated into a PK deposit, or to xenoliths emplaced within a thermally layered pipe infill (eg. interlayered PK/RVK or PK/CK) in which case heat transfer could be dominated by advection. The xenoliths with CAIs increasing from one side to the other have either experienced uneven heating, possibly in thermally layered pipe infill, or may be parts of larger, normally zoned xenoliths that have been broken prior to their current positioning. The one xenolith with higher CAI values in its apparent core requires an alternate explanation.

References

- Pell, J., Russell, J.K. and Zhang, S., 2015. Kimberlite emplacement temperatures from condont geothermometry. *Earth and Planetary Science Letters* 411, 131-141.
- Zhang, S. and Pell, J., 2014. Conodonts recovered from the carbonate xenoliths in the kimberlites confirm the Paleozoic cover on the Hall Peninsula, Nunavut. *Can. J. of Earth Sci.* 51, 142-155.



Chalcophile elements in the mantle

Allison T. Greaney¹ and Roberta L. Rudnick¹

¹*Department of Earth Science, University of California Santa Barbara, Santa Barbara, CA 93106*
greaney@umail.ucsb.edu, rudnick@geol.ucsb.edu

Introduction

The elements V, Ga, Ge, As, Mo, Ag, Cd, In, Sn, Sb, W, Tl, Pb, and Bi show variable geochemical behavior between Earth's different reservoirs. All of these elements, with the exception of V, W and Ga, have been shown experimentally or observationally to partition into sulfides to varying extents in the bulk silicate earth (Li and Audetat, 2012; Kiseeva and Wood, 2015). However, these elements can also exhibit siderophile (V, Ga, Ge, As, Mo, Ag, Sn, Sb, W) and lithophile (V, Ga, Ge, As, Mo, Cd, In, Sn, Sb, W, Tl, Pb) behavior based on studies of mantle peridotites (Witt-Eickschen et al., 2009), and mantle-derived magmas (Greaney et al., 2017; Patten et al., 2013; Yi et al., 1995; Jochum et al., 1993; Jochum and Hofmann, 1997; McDonough and Sun, 1995). Many of these studies infer geochemical behavior based on element ratios in the whole rock or glass and do not directly measure the abundance of these variably chalcophile elements in sulfides themselves.

By measuring the abundances of variably chalcophile elements in situ, their mineralogical hosts and partitioning behavior can be directly determined. These data serve as a comparison to experimental data and will allow for greater accuracy in determining the behavior of these elements during partial melting and fractional crystallization. Additionally, we aim to determine more accurate BSE abundances for the highly volatile elements (Cd, In, Sn, Tl) than those calculated by element ratios in basalts and komatiites from McDonough and Sun (1995).

We have analyzed preserved sulfides in lherzolite and harzburgite xenoliths from the North China Craton for the aforementioned elements. While most peridotite xenoliths have lost their sulfides due to metasomatism or alteration during/post-eruption (Lorand, 1990; Liu et al., 2010), the xenolithic peridotites hosted in the Hannuoba basalts from the Trans-North China Orogen preserve them surprisingly well. The sulfides are predominately pentlandite with associated MSS1, pyrrhotite, and chalcopyrite. Textural and chemical evidence suggests that there are multiple generations of sulfides between the samples. The distinctly metasomatised samples (noted by distinct LREE patterns and incomplete Sm-Nd and Rb-Sr mass balance) fall off a Re-Os isochron, however Re and Os have not been significantly disturbed by metasomatism in most samples (Gao et al., 2002).

Using LA-ICP-MS, we analyzed 48 sulfides and many olivine, clinopyroxene, orthopyroxene, and spinel from eight peridotites. Whole rock data was collected using standard addition solution ICP-MS.

Mineralogical Hosts

The LA-ICP-MS data are shown in Fig. 1 where elements are ordered based on their median primitive-mantle-normalized abundance in sulfides. All of the elements are more enriched in the sulfides than the silicates and spinel, except for Ga and V, which substitute for Al and Fe or Cr, respectively. Despite this, mass balance reveals that silicates are the dominant hosts for all of the elements studied here except for Ag and Bi, which are primarily hosted in sulfides, and Mo, Sn, and W, for which mass balance consistently falls short (up to 90% missing, indicating that they may be hosted along grain boundaries or in an unidentified phase). A predominate silicate host is somewhat in agreement with the results of Witt-Eickschen et al. (2009), however sulfides still contribute a significant proportion of the mass balance (> 20%) for the elements As, Cd, In, and Pb. Molybdenum seems to be significantly affected by metasomatic processes, where it is likely carried in fluids in its soluble, hexavalent state and subsequently reduced and deposited in secondary sulfides. The metasomatised sample DMP-60 shows an overabundance of Mo relative to the melt depletion trend (Fig. 2) and the sulfides within this sample contain an order of magnitude more Mo (mean $[Mo]_{\text{metasomatised}} = 650$ ppm) than in other un-altered samples (mean $[Mo]_{\text{primary}} = 56$ ppm).

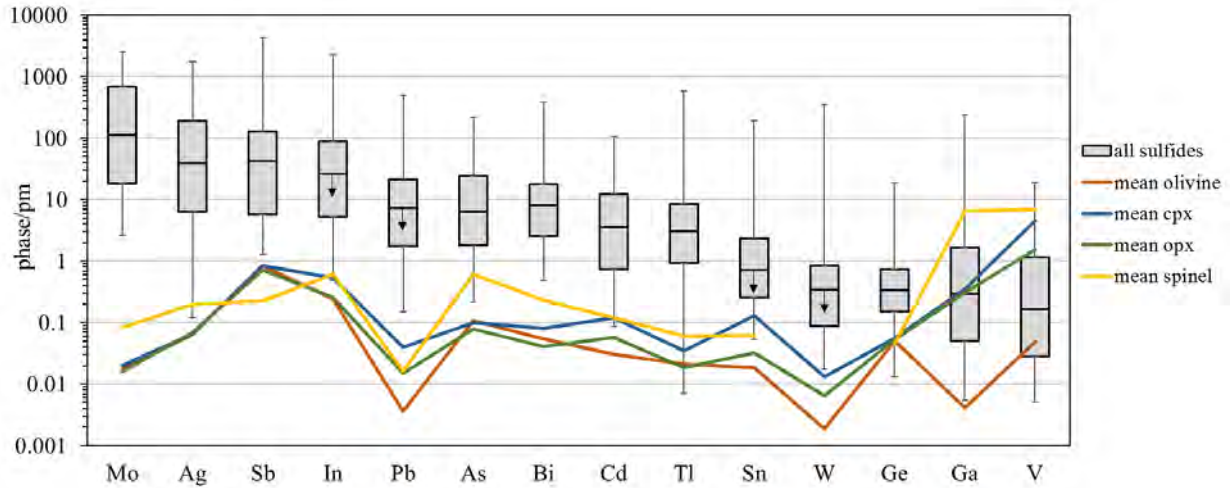


Figure 1. Primitive mantle-normalized LA-ICP-MS data of all phases with the sulfide data represented by box and whisker plots (error bars plot the max. and min. values measured). Elements are ordered by their median concentration in the sulfide with Mo having the highest median abundance in sulfide and V having the lowest. Several sulfides contained less than the detection limit (~ 0.01 ppm) of Sb, In, Sn, and W. These sulfides were not included in the analysis, so the plotted data are skewed to slightly higher values (hence the arrows).

Bulk Silicate Earth Abundances

Melt depletion trends are observed for a subset of elements (Fig. 2).

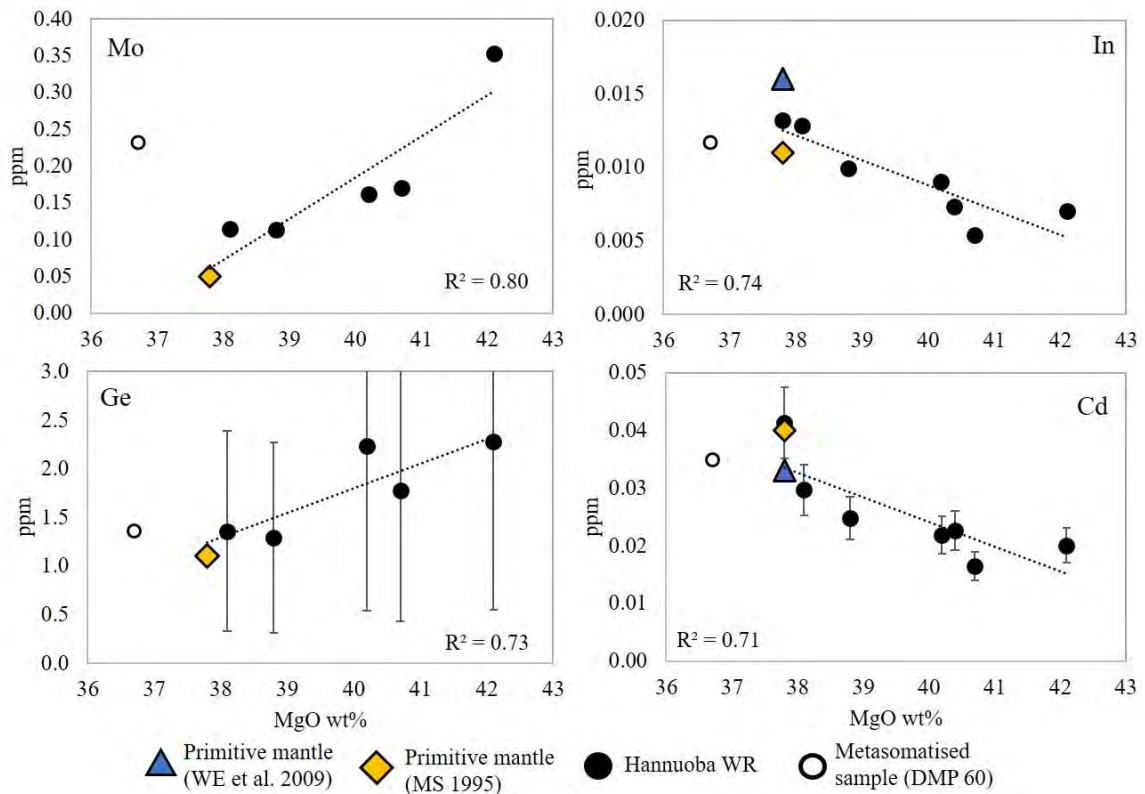


Figure 2. Melt depletion trends for Mo, Ge, In, and Cd; the regressions are through the DMP samples (excluding DMP 60). The large error bars on Ge reflect a high, unstable background signal created after a synthetic Ge-glass was run on the ICP-MS. The 2σ error bars for Mo and In are within the data point.

The refractory element Mo and moderately volatile element Ge show compatible behavior during mantle melting with estimated primitive mantle values of Mo = 62 ppb (± 50) and Ge = 1240 ppb (± 280). This estimate for [Mo] is slightly higher than the basalt-derived estimates of McDonough and Sun

(1995) (50 ppb) and Palme and O'Neill (2014) (47 ppb), however there is a large error associated with the Mo regression, given the scatter in the data. This higher mantle estimate supports the observations of Liang et al. (2017) who found that Mo is enriched in peridotites relative to previous estimates, suggesting that Mo may be slightly more compatible in the mantle than initially thought, or that Mo may be selectively enriched from mantle metasomatism. Both Mo compatibility and metasomatic enrichment are observed in this study. Liang et al. propose that Mo may be retained in mantle sulfides, which is seemingly supported by this data given Mo's high abundance in the sulfides measured here (1.8 to 2000 ppm). However, sulfides are exhausted during mantle melting and Mo mass balance is incomplete in these samples, so another unknown phase may be needed to explain Mo's compatibility.

The volatile elements Cd and In are incompatible during mantle melting, with primitive mantle values estimated at Cd = 32 ppb (\pm 5.1) and In = 12 ppb (\pm 1.4), in good agreement with values calculated by Witt Eickschen et al. (2009) and McDonough and Sun (1995), respectively. The data collected for the remaining elements V, Ga, As, Ag, Sn, Sb, W, Tl, Pb, and Bi form rough melt depletion trends against MgO or Al₂O₃, but there is too much scatter for a BSE estimate to be reliably calculated.

References

- Gao S., Rudnick R.L., Carlson R.W., McDonough W.F., Liu Y. (2002) Re-Os evidence for replacement of ancient mantle lithosphere beneath the North China craton, *EPSL* **198** 307-322
- Greaney A.T., Rudnick R.L., Helz R.T., Gaschnig R.M., Piccoli P.M., Ash R.D. (2017) The behavior of chalcophile elements during magmatic differentiation as observed in Kilauea Iki lava lake, Hawaii, *Geochim. Cosmochim. Acta*, in press
- Kiseeva E.S. and Wood B.J. (2015) The effects of composition and temperature on chalcophile and lithophile element partitioning into magmatic sulphides, *EPSL*. **424**, 280-294
- Jochum K.P., Hofmann A.W., Seufert H.M. (1993) Tin in mantle-derived rocks: Constraints on Earth evolution, *Geochim. Cosmochim. Acta* **57**, 3585-3595
- Jochum K.P. and Hofmann A.W. (1997) Constraints on earth evolution from antimony in mantle-derived rocks, *Chem. Geol.* **139**, 39-49
- Li Y. and Audétat A. (2012) Partitioning of V, Mn, Co, Ni, Cu, Zn, As, Mo, Ag, Sn, Sb, W, Au, Pb, and Bi between sulfide phases and hydrous basanite melt at upper mantle conditions, *EPSL*. **335-336**, 327-340
- Liu J., Rudnick R.L., Walker R.J., Gao S., Wu F., Piccoli P.M. (2010) Processes controlling highly siderophile element fractionations in xenolithic peridotites and their influence on Os isotopes, *EPSL* **297**, 287-297
- Lorand J.P. (1990) Are spinel lherzolite xenoliths representative of the abundance of sulfur in the upper mantle? *Geochim. Cosmochim. Acta* **54**, 1487-1492
- Liang Y., Halliday A.N., Siebert C., Fitton G., Burton K.W., Wang K., Harvey J. (2017) Molybdenum isotope fractionation in the mantle, *Geochim. Cosmochim. Acta* **199**, 91-111
- McDonough W.F. and Sun S.s (1995) The composition of the Earth, *Chem. Geol.* **120**, 223-253
- Palme H. and O'Neill H.S.C. (2014) Cosmochemical Estimates of Mantle Composition, *Treatise on Geochemistry*, 2nd Edition
- Patten C., Barnes S., Mathez E.A., Jenner F.E. (2013) Partition coefficients of chalcophile elements between sulfide and silicate melts and the early crystallization history of sulfide liquid: LA-ICP-MS analysis of MORB sulfide droplets, *Chem. Geol.* **358**, 170-188
- Witt-Eickschen G., Palme H., O'Neill H.S.C., Allen C.M. (2009) The geochemistry of the volatile trace elements As, Cd, Ga, In, and Sn in the Earth's mantle: New evidence from in situ analyses of mantle xenoliths, *Geochim. Cosmochim. Acta* **73**, 1755-1778
- Yi W., Halliday A.N., Alt J.C., Lee D., Rehkamper M., Garcia M.O., Langmuir C.H., Su Y. (2000) Cadmium, indium, tin, tellurium, and sulfur in oceanic basalts: Implications for chalcophile element fractionation in the Earth, *Jour. Geophys. Res.* **105**, 18,927-18,948



A tale of two pipes: Using whole rock geochemistry to see through alteration and contamination at the CH-6 & CH-7 kimberlites, Chidliak kimberlite province, Baffin Island, Nunavut.

Pell¹, J., Grütter¹, H.S., and Williams², N.

¹ Peregrine Diamonds Ltd, Vancouver, BC, Canada, jennifer@pdiam.com

² High Power Exploration, Vancouver, BC, Canada.

Introduction

Major and trace element whole rock geochemistry is a simple and inexpensive tool that can be applied to monitor the similarities or differences between kimberlites. Here, we present major and trace element data for archetypal carbonate-serpentine-monticellite kimberlites from the Hall Peninsula on Baffin Island, Nunavut, Canada with a focus on the CH-6 and CH-7 pipes (181 and 428 samples respectively) on Peregrine Diamonds' 100% held Chidliak project. We also analyzed 44 samples of country rock gneisses and six samples of sedimentary carbonate xenoliths. The goals of this study were to see if whole rock geochemistry could be used to distinguish completely altered kimberlite from completely altered country rock and to differentiate kimberlite units/grade domains within a pipe, especially when the kimberlite had been weathered or altered.

The CH-6 kimberlite is infilled by two main geological units which are distinguished megascopically by the respective presence or paucity of Paleozoic carbonate xenoliths. KIM-L varies from pyroclastic kimberlite (PK) to apparently coherent kimberlite (ACK); when weathered it is denoted as wKIM-L. A high-grade zone (KIM-L-HG) has been defined based on microdiamond content. KIM-C is a comparatively homogeneous coherent kimberlite (CK). A minor unit, KIM-HK, occurs as carbonate xenolith-free CK horizons in KIM-L. Carbonate, serpentine \pm monticellite and, to a lesser extent, phlogopite are the dominant matrix minerals throughout CH-6. Six main geological units have been recognized at CH-7, each with distinct physical characteristics. KIM-1 is coarse-grained CK, KIM-6 is a gneiss xenolith-bearing CK, whereas KIM-2, KIM-3 and KIM-4 are PK. KIM-5 is texturally variable (PK, ACK) and locally lateritized; it also has a high-grade sub-unit (KIM-5-(H)). KIM-2 and KIM-6 have a serpentine-dominated groundmass/matrix, KIM-3 is carbonate-dominated, KIM-1 contains monticellite-carbonate-serpentine and the other units have a carbonate \pm serpentine matrix. Phlogopite is present locally, but not as prevalent as in CH-6. In both pipes, crustal dilution is 5 volume % or less on average and the upper 40 – 50m are very weathered. Also, in both pipes, a number of samples cannot be readily assigned to a lithologic unit using conventional logging and petrology, due to weathering and alteration among other things and are currently classified as “RFW” (requires further work.).

Data Analysis and Interpretation

Initial analysis of the data began eliminating elements from the dataset where most of the results were below detection limit and then testing the remaining elements for mobility: Ca, K, Rb, Sr, Ba and Na are mobile and depleted during near-surface alteration/weathering; incompatible, high field strength elements (Nb-Ta, U-Th, Zr-Hf, REEs-Y) as well as Ti, Al, Ga, Cu, Cr, Fe, Mn, P and V are immobile and conserved. Simple bivariate plots of conserved elements have little value for discrimination of kimberlites at Chidliak, despite their discriminatory attributes noted for the Attawapiskat kimberlites (Fig. 1). Ratio-ratio plots that utilized incompatible, immobile elements were used in an attempt to differentiate the known geological units and readily showed distinctly different, albeit overlapping, compositional attributes for the different kimberlite units that were logged at CH-7. The same approach failed to clearly and unambiguously describe geological units or known grade domains at CH-6; instead they showed remarkably similar compositions throughout CH-6 (Fig. 2). However, simple plots such as Al/Ti vs Nb/Ga or Ti/Ga vs Nb/Ga proved to be extremely useful in discriminating completely clay-altered and unrecognizable kimberlite from similarly unrecognizable country rocks (not illustrated).

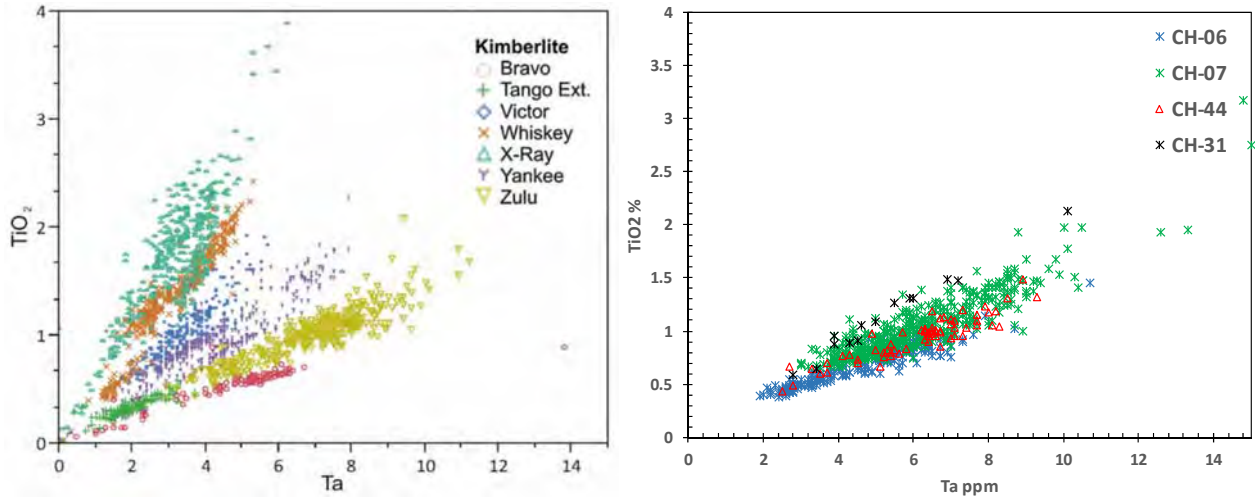


Figure 1: Simple bivariate element plots show clear differences between Attawapiskat kimberlites (plot on left, from Januszczak et al., 2013), but have proved ineffective to distinguish between kimberlites at Chidliak (plot on right).

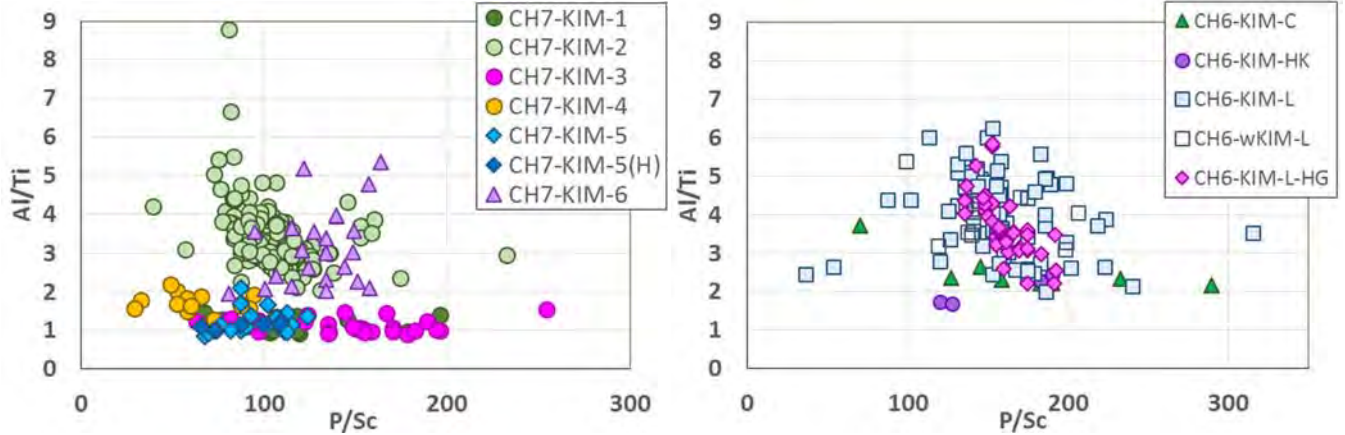


Figure 2: Element ratio-ratio plots for CH-7 (left) and CH-6 (right). At CH-7 there is some differentiation between units, particularly separating the serpentine-dominated (KIM-2 and KIM-6) from the low Al/Ti carbonate-rich units. The low Al/Ti lithologies do not occur at CH-6.

Multivariate techniques were employed to take the study to the next level. Principal component analysis (PCA) was remarkably efficient at identifying those elements that best define primary kimberlite magma compositions, and identify element associations related to mantle and crustal contamination. Outcomes of this part of the study were: 1) Si, Mg, Fe, Ni, Co & Zn show similar behaviour, interpreted to reflect olivine abundance and so tracks mantle contamination; 2) Al and Ga reflect the groundmass serpentine content (see Fig. 2) and, at CH-6, K-Rb & Sr are related to the abundance of matrix/groundmass phlogopite rather than being controlled by country rock gneisses contamination; and 3) the primary magma compositions are best described at both localities by Ti, Nb-Ta, Cr, REEs-Y, U-Th, & Sc. Additionally Mn, Ba & K-Rb-Sr at CH-6 and Cu, V, P & Zr at CH-7 relate to primary magma compositions.

A number of unsupervised and supervised classification techniques available in MATLAB® were applied to (i) the limited element suite that describes the CH-7 primary kimberlite magma, and (ii) to a wider suite of 39 elements (though excluding LOI, Total C and elements mobilised during weathering). The best results were obtained when a multivariate analysis of variance (MANOVA) was applied to generate a linear discriminant analysis (LDA) to find the canonical variables that best isolate units from the 39-element log-centred ratio transformed (LCRT) data, with the transformed data classified using a linear discriminant supervised classifier. In this case, self-recognition accuracy of 97% was obtained (Fig. 3). The self-recognition accuracy is 94.8% when these routines are applied to the more limited

primary magma element suite for CH-7. The self-recognition results inspire confidence in using these techniques to help classify the “RFW” samples from CH-7.

At CH-6, we went directly to the last step, MANOVA on LCRT data (42 elements, retaining Ba-K-Rb-Sr, the phlogopite component, which had not been used at CH-7 because they were mobile, and eliminating Pb) and then ran the supervised classifiers. The results for CH-6 were not as satisfactory, for the LDA classifier, with only 76.8% self-recognition of units on the full element suite and 75.4% on the primary magma element suite. However, a RUSBoosted Trees supervised classifier returned 88.4% self recognition of units on the full element suite. At CH-6, the number of samples in each unit is strongly biased (89 in KIM-L, 8 in KIM-C); the RUSBoosted Tree classifier returned the best results since it compensates for unbalanced class sizes by under-sampling the over-represented classes. The best results for the primary magma element suite (77.5%) were obtained using a Simple Tree classifier, which is not adequate to allow confident classification of the CH-6 “RFW” samples.

Discussion

Multivariate analyses, particularly linear discriminant analyses, of whole rock geochemical datasets predominantly using the immobile elements, has proven in this, and other studies (e.g. Grunsky and Kjarsgaard, 2008) to be a useful tool in differentiating kimberlite units where clear differences exist. It therefore can be used to help classify weathered and altered rocks particularly when subjective techniques such as petrography are not capable of doing so. However, these techniques were not as successful in differentiating units where differences are subtle and undersampling of some units is an issue. It is likely that better results would be obtained from data sets where all units had roughly equal numbers of samples.

For the CH-6 and CH-7 kimberlites at Chidliak, significant geochemical variability was found to be dominated by the crustal or mantle contaminants, and geochemical variability was only subtly related to kimberlite magmas *sensu stricto* (e.g. Nb, LREEs). The best unit discrimination was obtained when all elements, except those most mobile during weathering, were considered, essentially treating the kimberlite as the sum of its complete history and composition, not simply considering its magmatic component.

References

Grunsky, E.C. and Kjarsgaard, B.A., 2008. Classification of distinct eruptive phases of the diamondiferous Star kimberlite, Saskatchewan, Canada based on statistical treatment of whole rock geochemical data. *Applied Geochemistry* 23, 3321-3336.

Januszczak, N., Seller, M.H., Kurszlaukis, S., Murphy, C., Delgaty, J., Tappe, S., Ali, K., Zhu, J. and Ellmers, P., 2013. A multidisciplinary approach to the Attawapiskat Kimberlite Field, Canada: Accelerating the discovery-to-production pipeline. In D.G. Pearson et al. (eds), *Proceedings of 10th International Kimberlite Conference, V2, Special Issue of the Journal of the Geological Society of India*, 157-171.

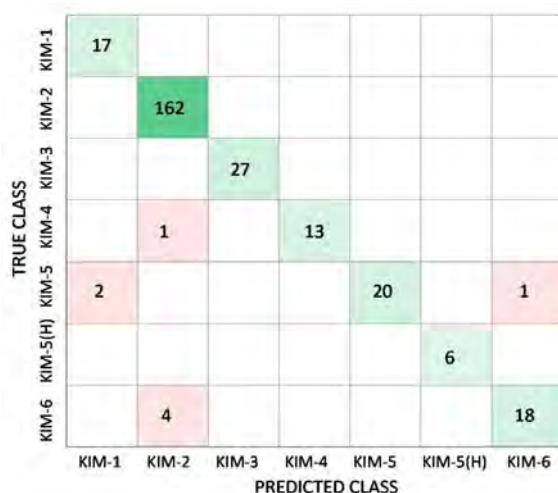


Figure 3: Confusion matrix for the LDA geochemical classification of CH-7 kimberlite. Numbers in the boxes are numbers of samples in each class.



Ultramafic Lamprophyre from the Wajrakarur Kimberlite Field of Southern India and its Petrogenetic Significance

Ashish Dongre¹, Fanus Viljoen², M. Malandkar³ and Petrus Le Roux⁴

¹Department of Geology, Savitribai Phule Pune University, Pune 411007, India

²Department of Geology, University of Johannesburg, Auckland Park 2006, South Africa

³Department of Geology, Institute of Science, Aurangabad 431004, India

⁴Department of Geology, University of Cape Town, Rondebosch 7700, India

Introduction

Wajrakarur kimberlite field (WKF) of southern India contains more than 45 intrusions of diamond host rocks. They have been identified as kimberlites, orangeites/ olivine lamproites and ultramafic lamprophyres during previous studies. All the so far reported kimberlites and related rocks show ~1100 Ma age except Timmasamudram kimberlite which gave ~90 Ma age (e.g. Chalapathi Rao et al., 2013; Chalapathi Rao et al., 2016).

Present detailed study from one of the pipe of Lattavaram cluster of WKF utilizes mineralogical genetic, radiogenic isotopic composition and whole rock geochemical approach on one of the previously known kimberlite pipe to show its affinity towards ultramafic lamprophyre (UML) and to further discuss the genetic and geodynamic significance. The rock contains abundant elongated crystals of clinopyroxene in groundmass, olivine phenocrysts that are mostly serpentinised, microphenocrysts of phlogopite restricted to groundmass, and amphiboles, spinels and carbonates. However the additional presence of Ti-rich garnets (Schorlomite) in groundmass mineralogically confirms it to be aillikite (e.g. Tappe et al., 2005). It is considered that the present aillikite also belongs to the Mesoproterozoic (i.e. 1100 Ma) age spectrum of kimberlite and related rocks of WKF.

Constituent mineral compositions

Microphenocrysts of phlogopite are widespread in the present pipe that coexists with clinopyroxenes and schorlomite in groundmass. In phlogopites Ti content is high and ranging from 3.9 to 6.4 wt.% TiO₂ whereas Al₂O₃ shows constant range varying between 9-11 wt.%. High BaO content is up to 4.4 wt.% and correlates positively with Al₂O₃. The fluorine content is also high having concentrations up to 3.05 wt.%. These phlogopites differ from kimberlite and orangeites in terms of Al and Ti enrichment and coexists with other aluminous phases in groundmass.

Clinopyroxene occurs only in groundmass and present in two paragenesis, one as elongate crystals of less than 40 μ at the base of serpentine and another as subhedral resorbed crystals associated with amphiboles. They mostly show diopside composition rich in CaO (18.8 to 23.48 wt.%) and MgO (15.17 to 16.98 wt.%) and poor in FeO (3.87 to 7.9 wt.%). Diopsides here show Al and Ti enriched trend typical of ultramafic lamprophyres. Atomic Al/Ti ratios is ~2 similar to aillikite clinopyroxenes from type area of Aillik Bay, Greenland (Tappe et al., 2008). Groundmass clinopyroxenes from recently reported Timmasamudram kimberlite of WKF (e.g. Dongre et al., 2017) are also plotted for comparison that are mostly showing composition similar to worldwide orangeite and lamproite and indicate a different composition.

Amphiboles are free from inclusion and any zoning and occur as subhedral grains at the margins of olivine crystals and also as discrete grains in groundmass. All the amphiboles are ranging in composition from potassium richterite to titanian potassium richterite having TiO₂ content 2 to 4 wt.%. They show higher and approximately constant Na/K ratio with varying Ti and composition away from the MARID field and similar to Torngat and Aillik Bay UMLs (e.g. Tappe et al., 2006)

and are unlike of amphiboles from lamproites and orangeites. The Al_2O_3 content varies up to 1.2 wt.% and crystals typically co-exists in groundmass with other aluminous phases such as clinopyroxene, phlogopite and schorlomite.

Cr_2O_3 content in groundmass spinels reaches up to 46 wt.% and Al_2O_3 is mostly below 5 wt.%. Spinel rich in Cr, Al mostly follow the titanomagnetite trend i.e. trend 2 (Mitchell, 1986) whereas rim composition rich in Mg (up to 16.7 wt.% MgO) and poor in Cr, Al follows magnesian ulvöspinel compositional trend.

Geochemistry and conclusion

The rock shows ultramafic nature with SiO_2 depletion (41-43 wt.%) and MgO enrichment (~19 wt.%). All samples have high incompatible element abundances when normalized to primitive mantle values (Sun and McDonough, 1995) and show very low HREE contents i.e. 1 x PM for Lu as well as fractionated LREE/HREE contents (La/Yb_n is ranging from 40-98). They show major depletions at K, Sr, Hf and Ti which are the characteristic of aillikites worldwide. Depletions at K in aillikites are relatively smaller when compared to kimberlites.

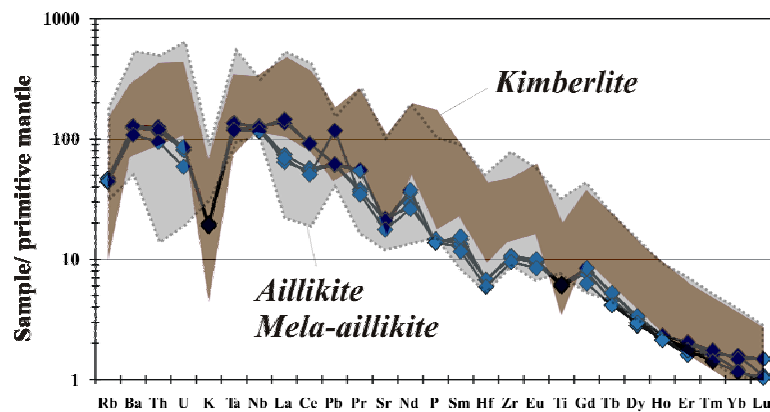


Figure 1: Primitive mantle normalized multi-element diagram for samples under study. Field for aillikite and mela-aillikite composition is based on data from Tappe et al. (2006, 2008) and Donnelly et al. (2011), and for kimberlites is from Becker and Le Roex (2006) given for comparison.

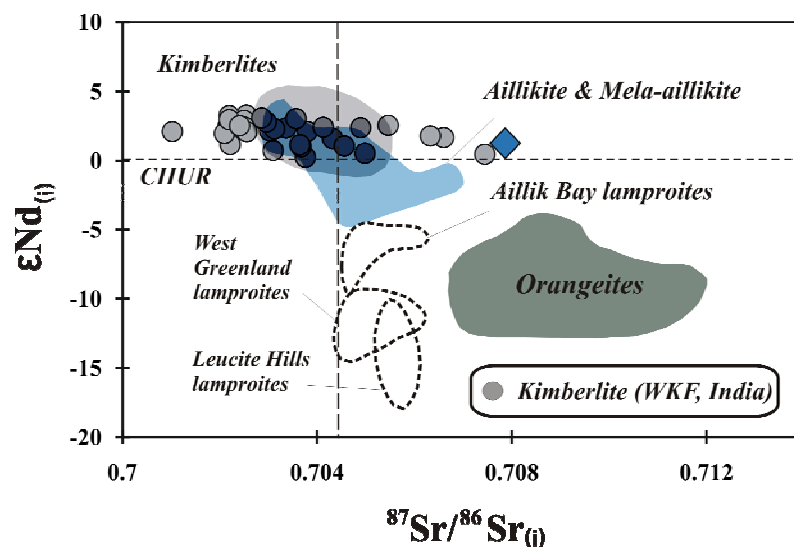


Figure 2: Initial $\epsilon\text{Nd}_{(t)}$ vs $^{87}\text{Sr}/^{86}\text{Sr}_{(t)}$ for aillikite under study. Compositional fields for aillikite and mela-aillikite are from Tappe et al. (2008) and references therein and from Donnelly et al. (2011). Unpublished data for Wajrakarur kimberlites, Southern India is given for comparison.

The aillikite dyke here shows isotopically depleted nature ($^{87}\text{Sr}/^{86}\text{Sr}_i = 0.70786$ and $\epsilon\text{Nd}_i = +1.25$) similar to kimberlites of WKF ($^{87}\text{Sr}/^{86}\text{Sr}_i = 0.70102\text{--}0.70744$, $\epsilon\text{Nd}_i = +0.23$ to $+3.28$). However initial $^{87}\text{Sr}/^{86}\text{Sr}$ values are on higher side and resembles upper limit of WKF kimberlites and close to recently reported aillikites from Kaapvaal craton, South Africa ($^{87}\text{Sr}/^{86}\text{Sr}_i = 0.70670$) (Donnelly et al., 2011).

Mineralogical, geochemical data and similar isotopic compositions of aillikite reported here and synchronous kimberlites from WKF indicates its origin from same tectono-magmatic event and from similar mantle source region with a different metasomatic assemblage and also indicates magma generation in the presence of CO_2 like those in the case of kimberlites.

References

- Becker M, Le Roex AP (2006) Geochemistry of South African on and off craton Group I and II kimberlites: petrogenesis and source region evaluation. *J Pet* 47: 673-703
- Chalapathi Rao NV, Dongre A, Wu FY, Lehmann B (2016) A Late Cretaceous (ca. 90 Ma) kimberlite event in southern India: Implication for sub-continental lithospheric mantle evolution and diamond exploration. *Gond Res* 35: 378-389
- Chalapathi Rao NV, Wu FY, Mitchell RH, Li QL, Lehmann B (2013) Mesoproterozoic U–Pb ages, trace element and Sr–Nd isotopic composition of perovskite from kimberlites of the Eastern Dharwar craton, southern India: Distinct mantle sources and a widespread 1.1 Ga tectonomagmatic event. *Chem Geol* 353: 48-64
- Dongre A, Chalapathi Rao NV, Viljoen KS, Lehmann B (2017) Petrology, genesis and geodynamic implication of the Mesoproterozoic–Late Cretaceous Timmasamudram kimberlite cluster, Wajrakarur field, Eastern Dharwar Craton, southern India. *Geosci Front* 8 (3): 541-553
- Donnelly CL, Griffin WL, O'Reilly SY, Pearson NJ, Shee SR (2011) The kimberlites and related rocks of the Kuruman kimberlite Province, Kaapvaal craton, South Africa. *Contrib Min Petrol* 161: 351-371
- Mitchell RH (1986) *Kimberlites: Mineralogy, geochemistry and petrology*. New York: Plenum
- Tappe S, Foley SF, Jenner GA, Kjarsgaard BA (2005) Integrating ultramafic lamprophyres into the IUGS classification of igneous rocks: Rationale and implications. *J Petrol* 46: 1890-1900
- Tappe S, Foley SF, Jenner GA, Heaman LM, Kjarsgaard BA, Romer RL, Stracke A, Joyce N, Hoefs J (2006) Genesis of ultramafic lamprophyres and carbonatites at Aillik Bay, Labrador: a consequence of incipient lithospheric thinning beneath the North Atlantic craton. *J Petrol* 47: 1261-1315
- Tappe S, Foley SF, Kjarsgaard BA, Romer RL, Heaman LM, Starcke A, Jenner GA (2008) Between carbonatite and lamproite- Diamondiferous Torngat ultramafic lamprophyres formed by carbonate fluxed melting of cratonic MARID type metasomes. *Geochim Cosmochim Acta* 72: 3258-3286

Cr-rich Megacrysts of Clinopyroxene and Garnet from Lac de Gras Kimberlites, Slave Craton, Canada – Implications for the Origin of Clinopyroxene and Garnet in Cratonic Peridotites

Yannick Bussweiler¹, D. Graham Pearson¹, Thomas Stachel¹, Bruce A. Kjarsgaard²

¹ University of Alberta, Edmonton, Canada, bussweil@ualberta.ca

² Geological Survey of Canada, Ottawa, Canada

Introduction

In kimberlites, megacrysts are large crystals (> 1 cm) of garnet, clinopyroxene, ilmenite, olivine, phlogopite, orthopyroxene, or zircon (Nixon and Boyd 1973; Mitchell 1986). Megacrysts can be subdivided into a Cr-poor and a Cr-rich suite, but compositional thresholds between the two have varied in different studies (Moore and Belousova 2005; Kopylova et al. 2009). In contrast to the more common Cr-poor suite (Harte 1983), megacrysts of the Cr-rich suite are enriched in Cr and depleted in Fe and Ti and thus are chemically indistinguishable from their peridotite equivalents (Eggler et al. 1979). Traditionally, megacrysts are assumed to crystallize from a fractionating magma near the base of the lithosphere at 150-200 km depth (Harte 1983). In this model, the Cr-poor suite is thought to crystallize first at high melt/rock ratios, whereas Cr-rich megacrysts are the product of progressing chemical interaction with the surrounding peridotite at low melt/rock ratios. The exact nature of the proposed megacryst magma and its relationship to the host kimberlite is an ongoing matter of debate (Mitchell 1986; Bell and Moore 2004; Moore and Belousova 2005). A cognate relationship between megacrysts

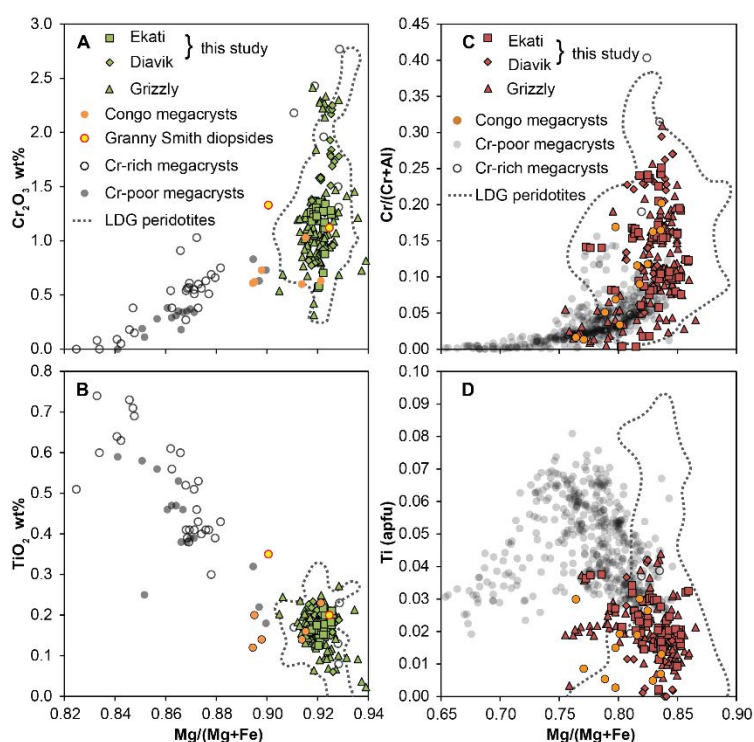


Figure 1: Major and minor element (EPMA) compositions of LDG megacrysts of Cr-diopside clinopyroxene (A,B) Cr-pyrope garnet (C,D) compared to reference data from megacrysts worldwide and phases from peridotites from Lac de Gras (LDG).

and kimberlites has been questioned by isotopic studies that show disequilibrium (e.g., Hops et al. 1992; Davies et al. 2001), although other studies find greater similarity (Nowell et al. 2004; Malarkey et al. 2010). More recently, the Cr-rich suite has been interpreted to originate from multi-stage metasomatic processes, based on studies on Cr-rich megacrysts from the Jericho kimberlite, northern Slave Craton (Kopylova et al. 2009), and from the Democratic Republic of Congo (DRC) (Pivin et al. 2009). Here, we report on Cr-rich megacrysts of clinopyroxene and garnet from the Diavik and Ekati diamond mines, Lac de Gras, central Slave Craton, Canada. The Cr-rich megacrysts are interpreted to have formed from precursor kimberlite melts that stalled in the mantle and were then sampled by later kimberlites.

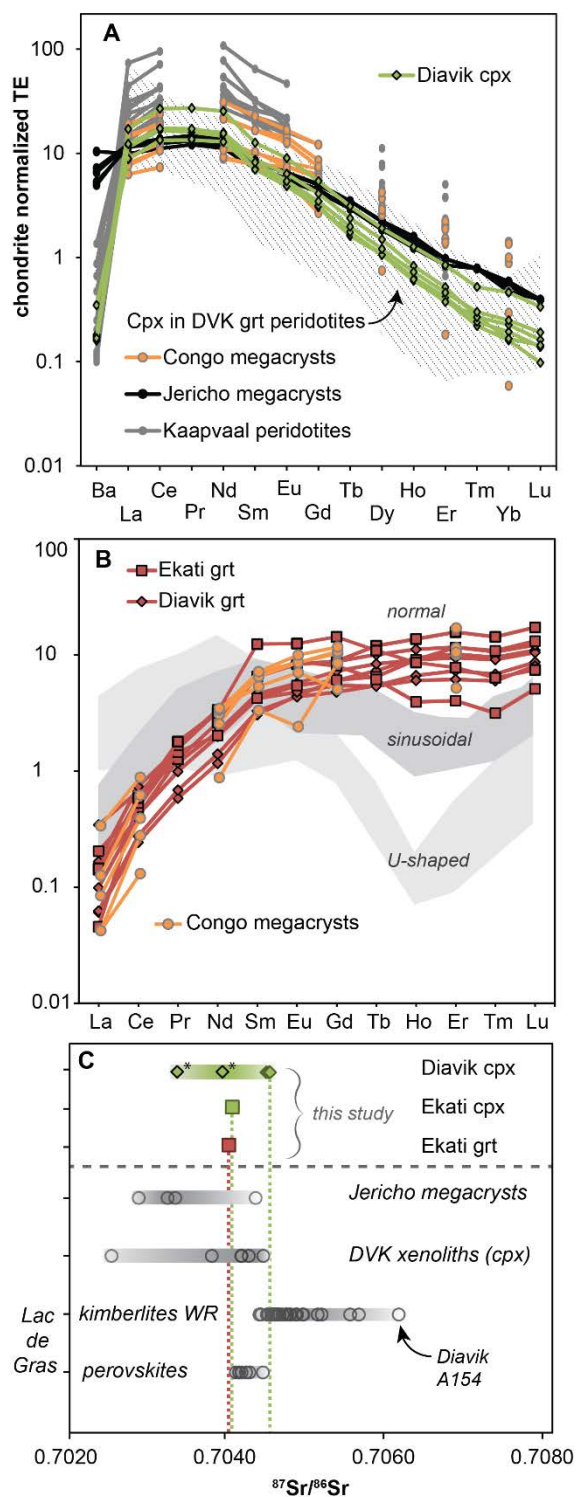


Figure 2: Trace element (LA-ICP-MS) compositions of Cr-diopsides (A) and Cr-pyropes (B) and Sr isotope (SIMS) ratios (C) compared to reference data from megacrysts worldwide, phases from peridotite xenoliths and kimberlites from Lac de Gras.

flow is more percolative, diopsides (and pyropes) distributed throughout cratonic lherzolites may form (e.g., Simon et al. 2003). The megacrysts may be re-sampled by later kimberlites that successfully ascend to the surface. Polymineralic inclusions commonly observed in the LDG megacryst samples (Bussweiler et al. 2016) are formed during this later entrainment.

Results

No significant compositional differences between megacryst samples from the Diavik and Ekati occurrences were found in major and trace elements, and Sr isotopes (Figs. 1, 2). The samples are thus collectively referred to as Lac de Gras (LDG) samples. They plot at the Cr-rich and high-Mg# end of the global megacryst trend (Fig. 1). There is consistent overlap with LDG lherzolitic phases (Aulbach et al. 2007), but also with Cr-rich megacrysts from other locations, e.g., the Jericho kimberlite (Kopylova et al. 2009) or kimberlites in the DRC (Pivin et al. 2009). In terms of trace element signatures, there is no distinction between the LDG samples, the worldwide Cr-rich megacryst suite, and clinopyroxene and garnet from LDG lherzolites (Figs. 2a, b). Their Sr isotope signatures overlap with those of typical mantle phases and are less radiogenic than the host kimberlite, but also overlap with Sr isotope data of primitive groundmass perovskite in LDG kimberlites (Figure 2c) (Sarkar et al. 2015). Thus, we suggest that the LDG samples described here are associated with the Cr-rich megacryst suite, and may have grown from sources that are isotopically similar to LDG kimberlites (Tappe et al. 2013).

Discussion

A plausible model combining the crystallization of the Cr-rich megacryst suite and the localized introduction of lherzolitic clinopyroxene and garnet into the surrounding mantle could involve the process of percolative fractional crystallization (Harte et al. 1993). Reaction between kimberlite-like melts, associated with a failed kimberlite, and a lithospheric mantle column is illustrated schematically in Fig. 3. This failed kimberlite may be responsible for the formation of polymict mantle breccias (Giuliani et al. 2013), possibly accompanied by crystallization of Cr-poor megacrysts (e.g., ilmenite, garnet, olivine). The crystallization of Cr-rich megacrysts (predominantly Cr-diopside and Cr-pyrope) could occur along channel walls, where they could grow to large sizes. Further away from the channel, where the

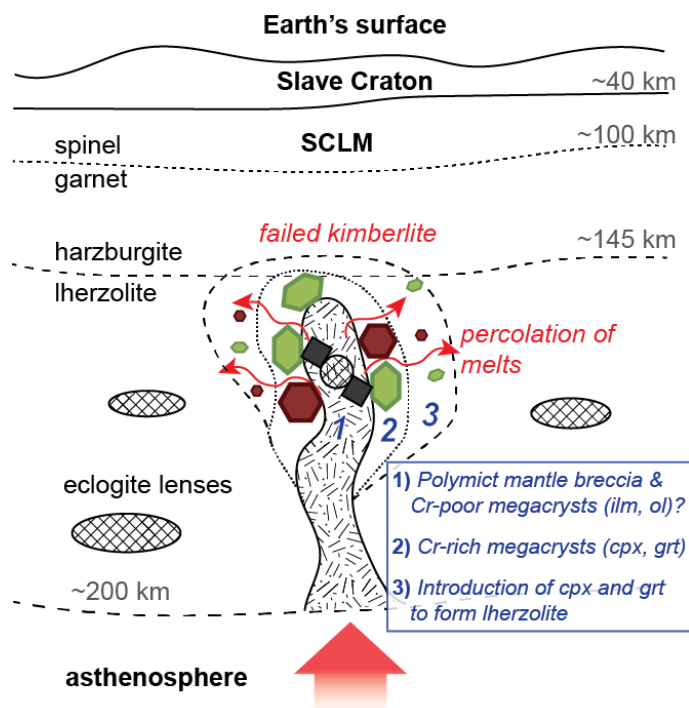


Figure 3: Schematic cartoon showing the formation of Cr-rich megacrysts from a failed precursor kimberlite melt that percolates into and crystallizes in the surrounding lithospheric mantle.

References

- Aulbach S, Griffin WL, Pearson NJ, et al (2007) Lithosphere formation in the central Slave Craton (Canada): plume subcretion or lithosphere accretion? *Contrib to Mineral Petrol* 154:409–427.
- Bell DR, Moore RO (2004) Deep chemical structure of the southern African mantle from kimberlite megacrysts. *South African J Geol* 107:59–80.
- Davies G, Spriggs A, Nixon P (2001) A non-cognate origin for the Gibeon kimberlite megacryst suite, Namibia: implications for the origin of Namibian kimberlites. *J Petrol* 42:159–172.
- Eggler DH, McCallum ME, Smith CB (1979) Megacryst assemblages in kimberlite from northern Colorado and southern Wyoming: Petrology, geothermometry-barometry and areal distribution. *Boyd Meyer* 2:213–226.
- Giuliani A, Kamenetsky VS, Kendrick MA, et al (2013) Oxide, sulphide and carbonate minerals in a mantle polymict breccia: Metasomatism by proto-kimberlite magmas, and relationship to the kimberlite megacrystic suite. *Chem Geol* 353:4–18.
- Harte B (1983) Mantle peridotites and processes - the kimberlite sample. In: Hawkesworth CJ, Norry MJ (eds) *Continental Basalt and Mantle Xenoliths*. Shiva, Nantwich, pp 46–91
- Harte B, Hunter RH, Kinny PD (1993) Melt geometry, movement and crystallization, in relation to mantle dykes, veins and metasomatism. *Phil Trans R Soc Lond* 342:1–21.
- Hops JJ, Gurney JJ, Harte B (1992) The jagersfontein Cr-poor megacryst suite — towards a model for megacryst petrogenesis. *J Volcanol Geotherm Res* 50:143–160.
- Kopylova MG, Nowell GM, Pearson DG, Markovic G (2009) Crystallization of megacrysts from protokimberlitic fluids: Geochemical evidence from high-Cr megacrysts in the Jericho kimberlite. *Lithos* 112:284–295.
- Malarkey J, Pearson DG, Kjarsgaard BA, et al (2010) From source to crust: Tracing magmatic evolution in a kimberlite and a melilitite using microsample geochemistry. *Earth Planet Sci Lett* 299:80–90.
- Mitchell RH (1986) *Kimberlites: Mineralogy, Geochemistry and Petrology*. Plenum Press, New York
- Moore A, Belousova E (2005) Crystallization of Cr-poor and Cr-rich megacryst suites from the host kimberlite magma: implications for mantle structure and the generation of kimberlite magmas. *Contrib to Mineral Petrol* 149:462–481.
- Nixon PH, Boyd FR (1973) The discrete nodule association in kimberlites from northern Lesotho. *Lesotho kimberlites Maseru, Lesotho Natl Dev Corp* 97–75.
- Nowell GM, Pearson DG, Bell DR, et al (2004) Hf isotope systematics of kimberlites and their megacrysts: New constraints on their source regions. *J Petrol* 45:1583–1612.
- Pivin M, Féménias O, Demaiffe D (2009) Metasomatic mantle origin for Mbuji-Mayi and Kundelungu garnet and clinopyroxene megacrysts (Democratic Republic of Congo). *Lithos* 112:951–960.
- Sarkar C, Heaman LM, Pearson DG (2015) Duration and periodicity of kimberlite volcanic activity in the Lac de Gras kimberlite field, Canada and some recommendations for kimberlite geochronology. *Lithos* 218–219:155–166.
- Simon NSC, Irvine GJ, Davies GR, et al (2003) The origin of garnet and clinopyroxene in “depleted” Kaapvaal peridotites. *Lithos* 71:289–322.
- Tappe S, Graham Pearson D, Kjarsgaard BA, et al (2013) Mantle transition zone input to kimberlite magmatism near a subduction zone: Origin of anomalous Nd-Hf isotope systematics at Lac de Gras, Canada. *Earth Planet Sci Lett* 371–372:235–251.



Evolution of Calcite-Bearing Kimberlites by Melt-Rock Reaction – Evidence from Polymineralic Inclusions within Clinopyroxene and Garnet Megacrysts from Lac de Gras Kimberlites, Canada

Yannick Bussweiler¹, Rebecca S. Stone¹, D. Graham Pearson¹, Robert W. Luth¹,
Thomas Stachel¹, Bruce A. Kjarsgaard², Andrew Menzies³

¹ University of Alberta, Edmonton, Canada, bussweil@ualberta.ca

² Geological Survey of Canada, Ottawa, Canada

³ Universidad Católica del Norte, Antofagasta, Chile

Introduction

Polymineralic inclusions are fully crystallized melt inclusions commonly found in megacrysts from kimberlites. Since the 1970s, such inclusions have been reported to occur in a variety of phases from different locations. Haggerty and Boyd (1975) first documented inclusions in olivine megacrysts from the Monastery kimberlite, South Africa, and interpreted them as an early kimberlite melt with an immiscible sulphide liquid. Schulze (1985) described inclusions in clinopyroxene and garnet megacrysts from Kentucky, USA, and suggested that they represent the megacryst magma from which the host crystals formed. Van Acherbergh et al. (2002) interpreted inclusions in Cr-diopsides from Lac de Gras, Slave Craton, Canada, as trapped primary carbonatitic melt, that may have differentiated towards more silicic melts (van Acherbergh et al. 2004; Araújo et al. 2009). A striking commonality of these reports is that the inclusions are carbonate-rich and typically contain high modal proportions of calcite. However, from high-pressure, high-temperature experiments it is well established that carbonates at mantle depths, and by extension carbonate-rich melts in the mantle, must be Mg-rich, i.e., dolomite or magnesite (Wyllie and Huang 1975; Brey et al. 1983; Dalton and Presnall 1998). The presence of calcite within polymineralic inclusions was previously interpreted to be a result of unmixing and quenching in the final stages of kimberlite emplacement (van Acherbergh et al. 2002). Here we document carbonate-rich polymineralic inclusions in clinopyroxene and garnet megacrysts from the Diavik and Ekati diamond mines, Lac de Gras, Canada. The inclusions provide mineralogical and chemical evidence for an origin of kimberlite involving the reaction of a siliceous dolomitic magma with diopside-bearing mantle assemblages to produce a melt that crystallizes a calcite-dominated assemblage in the crust (Bussweiler et al. 2016).

Results

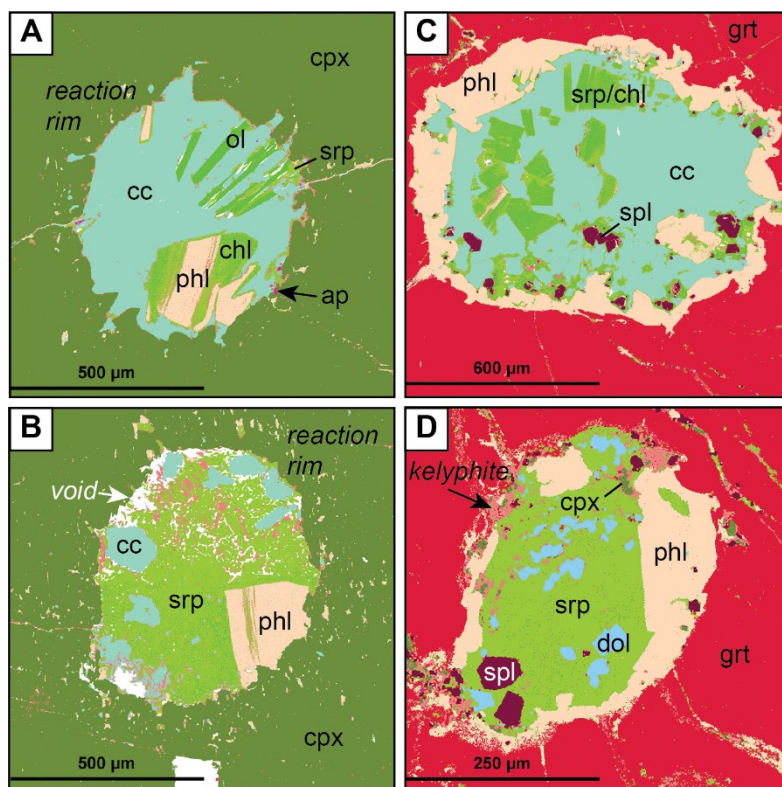


Figure 1: QEMSCAN images of polymineralic inclusions in clinopyroxene (Cr-diopside) and garnet (Cr-pyrope) megacrysts from Lac de Gras kimberlites.

Polymineralic inclusions in Cr-diopside megacrysts commonly contain the phases calcite, phlogopite, serpentine/chlorite, olivine, and chromite/spinel (Fig. 1a,b). The inclusions are surrounded by reaction rims, similar to spongy rims, and trails of fluid inclusions (CO₂-rich) extend from the polymineralic inclusions. Phases within polymineralic inclusions in garnet (Cr-pyrope) megacrysts are the same as those in clinopyroxenes, but further include Al-rich cpx, Al-spinel, and Ni-sulfide (Fig. 1c,d). Importantly, carbonates within polymineralic inclusions in garnet can be more Mg-rich (dolomite and Mg-calcite). Polymineralic inclusions in garnet are commonly surrounded by kelyphite-like rims. The mineral chemistry of the inclusion phases

olivine, phlogopite, chromite/spinel, and serpentine (EPMA) is overall consistent with that of early magmatic kimberlite mineral phases, but indicates extensive reaction with the host minerals; compared to equivalent phases in kimberlites, the inclusion phases are enriched in Cr, Al, and Mn. Trace element signatures of phlogopite within the inclusions (LA-ICP-MS) constrain their crystallization from the melt inclusions at lithospheric mantle depths. The textural evidence for disequilibrium between polymineralic inclusions and their host crystals is supported by Sr isotopes (SIMS). For the complete dataset the reader is referred to Bussweiler et al. (2016).

Discussion

Bulk compositions of the inclusions (Fig. 2) were reconstructed using modal proportions obtained by QEMSCAN (Fig. 1), and mineral compositions measured by EPMA. Reconstructed bulk compositions of the inclusions bear a general resemblance to experimentally derived partial melts of carbonated peridotites and to previous estimates of primary kimberlite magmas, but indicate assimilation of mantle minerals (e.g., orthopyroxene) including the host minerals clinopyroxene and garnet (Fig. 2). Thus, we propose that the polymineralic inclusions represent snapshots of kimberlite melt reacting with the lithospheric mantle during ascent. Importantly, inclusions in Cr-diopside record direct evidence for a decarbonation reaction of the form: dolomitic melt + diopside → forsterite + calcite + CO₂, which is expected to begin at pressures <2.5 GPa (Stone and Luth 2016). This reaction may play an important role, along with other decarbonation reactions (e.g., Abersteiner et al. 2017), in the *en-route* transformation of an upward moving dolomitic silico-carbonatite melt into the calcite-bearing kimberlite observed at the surface.

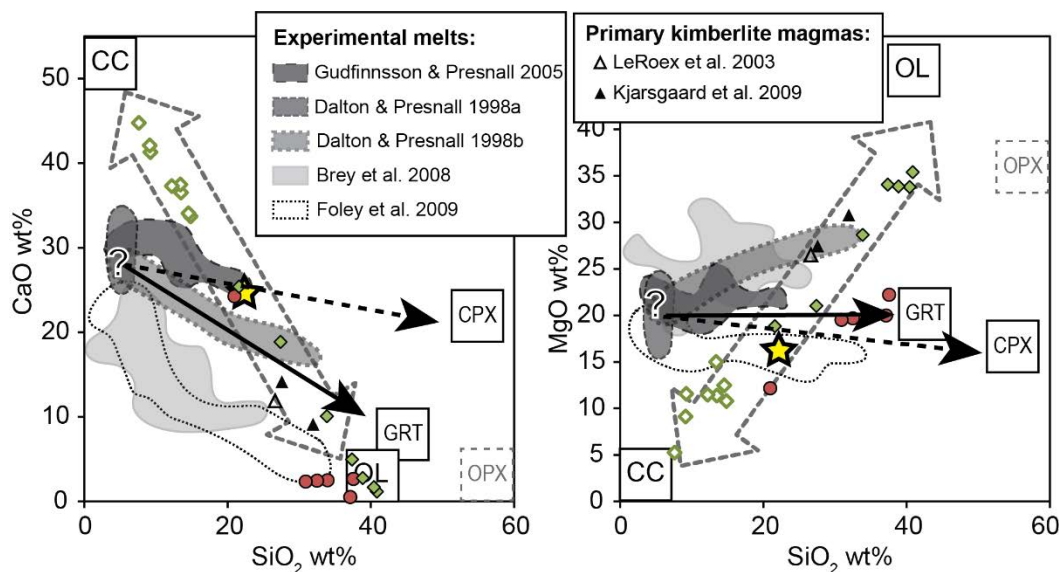


Figure 2: Reconstructed bulk compositions of polymineralic inclusions (green diamonds = in Cr diopsides; red circles = in Cr-pyropes) plot along a linear array (dashed, gray, double-arrow field) due to sectioning effects. An average composition (star symbol) can be related to partial melts of carbonated peridotite produced in high-P-T experiments by reaction with the host phases (cpx, grt) and orthopyroxene (opx).

References

- Abersteiner A, Kamenetsky VS, Pearson DG, et al (2017) Monticellite in Group-I kimberlites: Implications for evolution of parental melts and post-emplacement CO₂ degassing. *Lithos In Press*
- Araújo DP, Griffin WL, O'Reilly SY (2009) Mantle melts, metasomatism and diamond formation: Insights from melt inclusions in xenoliths from Diavik, Slave Craton. *Lithos* 112:675–682.
- Brey G, Brice WR, Ellis DJ, et al (1983) Pyroxene-carbonate reactions in the upper mantle. *Earth Planet Sci Lett* 62:63–74.
- Bussweiler Y, Stone RS, Pearson DG, et al (2016) The evolution of calcite-bearing kimberlites by melt-rock reaction: evidence from polymineralic inclusions within clinopyroxene and garnet megacrysts from Lac de Gras kimberlites, Canada. *Contrib to Mineral Petrol* 171:65.
- Dalton J, Presnall D (1998) Carbonatitic melts along the solidus of model lherzolite in the system CaO-MgO-Al₂O₃-SiO₂-CO₂ from 3 to 7 GPa. *Contrib to Mineral Petrol* 131:123–135.
- Haggerty SE, Boyd FR (1975) Kimberlite inclusions in an olivine megacryst from Monastery. In: De Beers Kimberlite Symposium I. Cambridge,
- Schulze D (1985) Evidence for primary kimberlitic liquids in megacrysts from kimberlites in Kentucky, USA. *J Geol* 93:75–79.
- Stone RS, Luth RW (2016) Orthopyroxene survival in deep carbonatite melts: implications for kimberlites. *Contrib to Mineral Petrol* 171:63.
- van Achterbergh E, Griffin WL, Ryan CG, et al (2002) Subduction signature for quenched carbonatites from the deep lithosphere. *Geology* 30:743.
- van Achterbergh E, Griffin WL, Ryan CG, et al (2004) Melt inclusions from the deep Slave lithosphere: implications for the origin and evolution of mantle-derived carbonatite and kimberlite. *Lithos* 76:461–474.
- Wyllie PJ, Huang WL (1975) Peridotite, kimberlite, and carbonatite explained in the system CaO-MgO-SiO₂-CO₂. *Geology* 621–624.



Provenance History of Detrital Diamond Deposits, West Coast of Namaqualand, South Africa

David Phillips¹, Jeff W. Harris² and Mike C.J. de Wit³

¹The University of Melbourne, Parkville, Australia, dphillip@unimelb.edu.au.

²University of Glasgow, Glasgow, Scotland, Jeff.Harris@glasgow.ac.uk.

³Tsodilo Resources Ltd, Toronto, Canada, mdewit@tsodiloresources.com.

Introduction

The West Coast of Namaqualand in South Africa hosts extensive detrital diamond deposits, but considerable debate exists as to the provenance of these diamonds. Some researchers have suggested that the diamonds were sourced from the erosion of >115 Ma orangeites located along the western part of the Kaapvaal craton and transported by the palaeo-‘Karoo’ river system, to be deposited in the Atlantic ocean near the current outlet of the Olifants river (e.g., de Wit, 1993). Other workers have argued that the majority of Namaqualand diamonds originated from recent erosion of Permo-Carboniferous Dwyka glacial deposits (ca.300 Ma), with their ultimate source being pre-Karoo kimberlites in the interior of the Kaapvaal craton (e.g., Moore and Moore, 2004).

In the current study, we analysed clinopyroxene inclusions extracted from a suite of detrital diamonds from coastal deposits along the Namaqualand coast in an effort to constrain the provenance of these diamonds.

Previous Work

Previous ⁴⁰Ar/³⁹Ar analyses of clinopyroxene inclusions extracted from diamonds sourced from the Orapa kimberlite produced a range of apparent ages from the time of kimberlite eruption to ~100 Ma older than this event (Phillips and Harris, 2008). As the ages were significantly younger than inferred diamond formation ages (>1.0 Ga), the ⁴⁰Ar/³⁹Ar results were interpreted to indicate significant argon diffusion to the diamond/inclusion interface zone prior to kimberlite emplacement, with >90% of radiogenic argon lost during inclusion extraction. Therefore, although this approach does not constrain the time of diamond formation, it provides a novel means of estimating (maximum) kimberlite eruption ages and is useful for constraining the provenance of detrital diamond deposits (Phillips and Harris 2009).

In a subsequent study, we analysed clinopyroxene inclusions from detrital diamonds collected from the west coast of Namibia and Namaqualand, using the ⁴⁰Ar/³⁹Ar laser probe dating method (Phillips and Harris, 2009). These analyses yielded maximum ages for the time of emplacement of source kimberlites/orangeites, mostly younger than ca.300 Ma. These data were used to infer diamond provenance from <300 Ma kimberlites/orangeites located on the Kaapvaal craton. However, these results were too imprecise to ascertain whether the diamonds were sourced from ca.85 Ma Group I kimberlites, >110 Ma orangeites, or possibly from both (or other) sources.

Results

In the current study, clinopyroxene inclusions were extracted from 35 Namaqualand detrital diamonds. ⁴⁰Ar/³⁹Ar ages were then determined using a new generation multi-collector ARGUSVI mass spectrometer system capable of ultra-high precision analyses (e.g. Phillips and Matchan, 2013; Phillips et al. 2017). Large inclusions were step-heated in two increments, whereas smaller inclusions (<200 µm) were fused in single analyses. Of the specimens analysed, 30 of 35 produced measurable signals, giving apparent ages ranging from 121.5 ± 3.3 Ma to 668.7 ± 4.9 Ma (2σ). Only six clinopyroxene inclusions yielded (maximum) apparent ages older than 300 Ma, with the majority (22 of 30) being <260 Ma. No clinopyroxene inclusions produced ages <100 Ma.

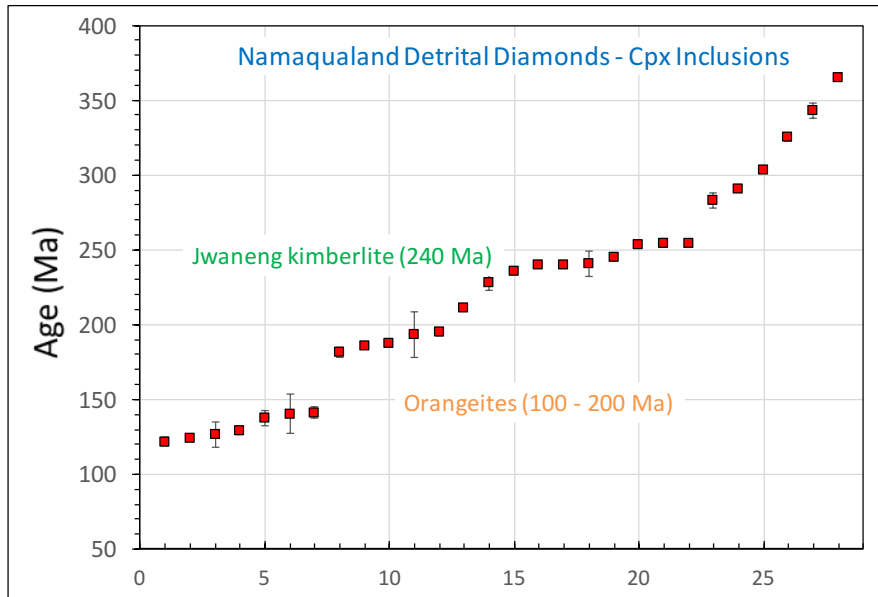


Figure 1. $^{40}\text{Ar}/^{39}\text{Ar}$ apparent ages determined on clinopyroxene inclusions extracted from detrital diamonds sources from Namaqualand coastal deposits (error bars are $\pm 2\sigma$). These ages represent maximum estimates for the time of source kimberlite/orangeite eruption due to the retention of up to ~10% of pre-eruption argon by the inclusions (see Phillips and Harris, 2009 for details).

Conclusions

The $^{40}\text{Ar}/^{39}\text{Ar}$ clinopyroxene results confirm that the vast majority of Namaqualand diamonds were sourced from post-Dwyka kimberlites/orangeites. These could include Late Cretaceous Group I kimberlites (80 – 90 Ma), Cretaceous/Jurassic orangeites (110 – 200 Ma) and/or early Triassic kimberlites (e.g. ~240 Ma Jwaneng kimberlite). However, it is noteworthy that none of the inclusions yielded ages typical of most Group I kimberlites (80 – 90 Ma). Although these ages are necessarily maxima, the data imply dominant diamond provenance from Cretaceous/Jurassic orangeites rather than Cretaceous Group I kimberlites. This conclusion accords with palaeo-drainage reconstructions in the area, which indicate a change in drainage in the mid-Cretaceous from a southwesterly directed palaeo-‘Karoo’ fluvial system to the current westerly directed Orange river drainage basin (de Wit, 1993).

References

- De Wit MCJ (1993) Cainozoic evolution of drainage systems in the north-western Cape. Unpubl PhD thesis, Univ Cape Town 371pp.
- Moore JM, Moore AE (2004) The roles of primary kimberlitic and secondary Dwyka glacial sources in the development of alluvial and marine diamond deposits in Southern Africa. *J African Earth Sci* 38:115–134.
- Phillips D, Harris JW (2008) Provenance studies from $^{40}\text{Ar}/^{39}\text{Ar}$ dating of mineral inclusions in diamonds: Methodological tests on the Orapa kimberlite, Botswana. *Earth Planet Sci Lett* 274(1-2):169-178.
- Phillips D, Harris JW (2009) Diamond provenance studies from $^{40}\text{Ar}/^{39}\text{Ar}$ dating of clinopyroxene inclusions: An example from the west coast of Namibia. *Lithos* 112S:793-805
- Phillips D, Matchan EL (2013) Ultra-high precision $^{40}\text{Ar}/^{39}\text{Ar}$ ages for Fish Canyon Tuff and Alder Creek Rhyolite sanidine: New dating standards required? *Geochim Cosmochim Acta* 121:229-239.
- Phillips D, Matchan EL, Honda M, Kuiper KF (2017) Astronomical calibration of $^{40}\text{Ar}/^{39}\text{Ar}$ reference minerals using high-precision, multi-collector (ARGUSVI) mass spectrometry. *Geochim Cosmochim Acta* 196:351-369.



A Comparison of Geochronology Methods Applied to Kimberlites and Related Rocks from the Karelian Craton, Finland

David Phillips¹, Darwin Zhong¹, Erin L. Matchan¹, Roland Maas¹, Henrietta Farr¹,
Hugh O'Brien² and Andrea Giuliani¹

¹The University of Melbourne, Parkville, Australia, dphillip@unimelb.edu.au.

²Geological Survey of Finland, Bentonimiehenkuja, Finland, hugh.obrien@gtk.fi.

Introduction

A range of geochronology techniques have been applied to kimberlites and related rocks, including the Rb-Sr phlogopite, U-Pb perovskite, U-Pb zircon, ⁴⁰Ar/³⁹Ar phlogopite and Fission Track apatite methods. These approaches all have specific advantages and disadvantages, with the Rb-Sr phlogopite and U-Pb perovskite methods being the most commonly used for kimberlite geochronology.

In this study, we compare the Rb-Sr phlogopite, U-Pb perovskite and ⁴⁰Ar/³⁹Ar phlogopite/kinoshitalite dating methods, applied to kimberlites and orangeites from the Karelian craton, Finland. This region includes the Kaavi-Kuopio Group I kimberlite province, located along the southwestern margin of the craton, the Kuusamo Group I kimberlites in the north-central part of the craton, and orangeites and related alkaline rocks of the Lentiira-Kuhmo-Kostomuksha area in the centre of the craton straddling the eastern Finland – Russia border.

Previous Work

Previously published ²⁰⁶U/²³⁸Pb perovskite ages for the Kuusamo Group I Kattaisenvaara and Kalettomanpuro kimberlites are 759 ± 15 Ma and 756.8 ± 2.1 Ma, respectively (O'Brien and Bradley 2008). ²⁰⁶U/²³⁸Pb perovskite results for the Kaavi-Kuopio kimberlites give an age range of 589 – 626 Ma (O'Brien et al. 2005). ⁴⁰Ar/³⁹Ar analyses of phlogopite from the Seitaperä (Pipe 16, two samples) and Lentiira orangeites (Lentiira-Kuhmo cluster) yielded weighted mean ages of 1202 ± 3 Ma, 1199 ± 3 Ma and 1204 ± 4 Ma, respectively (O'Brien et al. 2007). These results are broadly similar to Rb-Sr data reported for orangeite samples from the Kostomuksha cluster (Belyatsii et al. 1997; Nikitina et al. 1999), which give a recalculated age of 1232 ± 10 Ma (2σ; MSWD = 35) (O'Brien et al. 2007).

Methods

Handpicked phlogopite and kinoshitalite micas were washed in water, 2M HCl, and dissolved in HF-HNO₃. Sample solutions were equilibrated with a ⁸⁵Rb-⁸⁴Sr tracer, with Rb and Sr extracted on Eichrom Sr resin and cation resin columns. Isotopic analyses were carried out on a Nu Plasma MC-ICPMS (University of Melbourne). ⁸⁷Rb/⁸⁶Sr ratios determined by isotope dilution have an external precision of ±0.5% (2σ). Isochron ages were calculated using the ISOPLOT software from the Berkeley Geochronology Centre (www.bgc.org.au). The decay constant of ⁸⁷Rb is 1.397E-11/yr.

Phlogopite and kinoshitalite grains were irradiated in the Oregon State University reactor, together with the monitor Fish Canyon Tuff sanidine (28.126 Ma; Phillips et al. 2017). Single grain ⁴⁰Ar/³⁹Ar step-heating analyses were conducted on a multi-collector ARGUSVI mass spectrometer (University of Melbourne). Ages were calculated using the atmospheric ratio of 298.56 ± 0.31 (Lee et al. 2016) and the decay constants of Steiger and Jäger (1977). Plateau ages were calculated using ISOPLOT.

Results

Rb-Sr and ⁴⁰Ar/³⁹Ar analyses of phlogopite and kinoshitalite from representative samples of Kuusamo kimberlites produced indistinguishable ages of 747 ± 4 Ma and 747.8 ± 1.0 Ma (2σ), respectively (Figs. 1, 2), broadly similar to previous U-Pb perovskite results from the same localities.

Rb-Sr analysis of three leach aliquots from a Kostomoksha orangeite dyke (KOS OL) give an isochron age of 1180 ± 5 Ma (Fig. 1). $^{40}\text{Ar}/^{39}\text{Ar}$ analyses of single phlogopite grains from the same sample produced slightly discordant age spectra, with most ages in the range 1200 – 1210 Ma. $^{40}\text{Ar}/^{39}\text{Ar}$ analyses of phlogopite from other orangeites in the nearby Lentiira-Kuhmo cluster produced more consistent results, although only one sample produced a plateau age – 1204.4 ± 1.2 Ma (2σ) (Fig. 3). No perovskite was recovered from the orangeite localities.

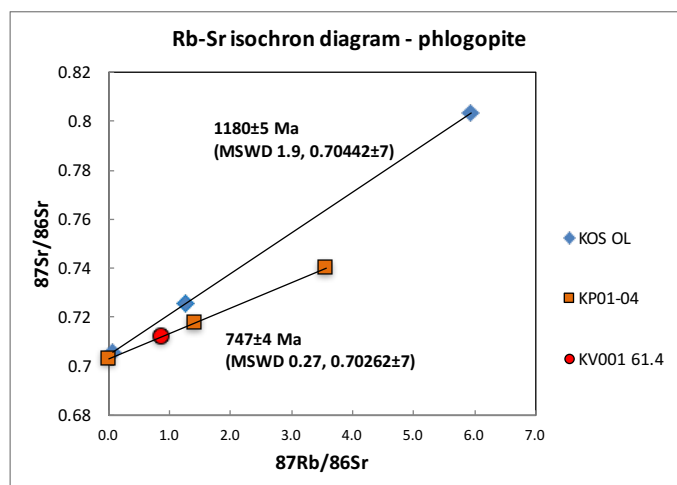


Figure 1. Rb-Sr isochron plots for leached separates of kinoshitalite from two Kusammo Group I kimberlite (Kalettomanpuro - sample KP01-04; Kattaisenvara – sample KV001-61.4m; orange and red symbols, respectively) and from a Kostomoksha orangeite (sample Kos-Ol; blue symbols). (uncertainties are $\pm 2\sigma$).

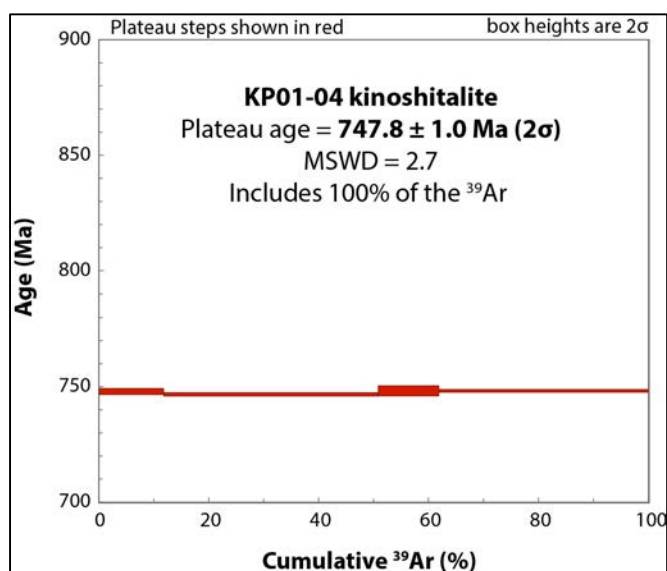


Figure 2. $^{40}\text{Ar}/^{39}\text{Ar}$ step-heating age spectrum for kinoshitalite extracted from the Kalettomanpuro Group I kimberlite (sample KP01-04), Kuusamo cluster. This sample shows a plateau age of 747.8 ± 1.0 Ma (2σ).

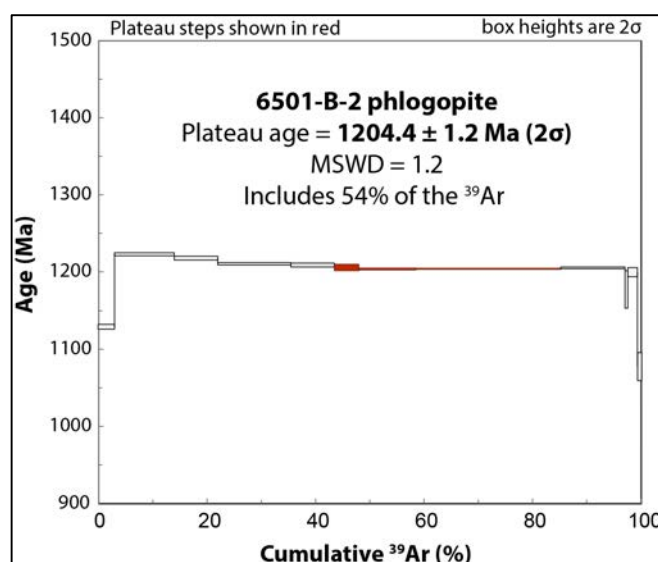


Figure 2. $^{40}\text{Ar}/^{39}\text{Ar}$ step-heating age spectrum for phlogopite extracted from the Seitaperä orangeite intrusion in the Kuhmo region (sample 6501-B-2). This age spectrum shows discordance in the low temperature steps, with the higher temperature steps yielding an plateau age of $1204.4 \pm 1.2 \text{ Ma}$ (2σ).

Discussion

The concordance of the Rb-Sr and $^{40}\text{Ar}/^{39}\text{Ar}$ results (748 Ma) obtained on the Kuusamo kimberlite samples provides confidence in the age of these localities. However the results are distinctly younger than the most precise $^{238}\text{U}/^{206}\text{Pb}$ perovskite age reported for the Kuusamo cluster Kalettomanpuro kimberlite ($756.8 \pm 2.1 \text{ Ma}$; O'Brien and Bradley, 2008). In contrast, the Rb-Sr and $^{40}\text{Ar}/^{39}\text{Ar}$ ages reported for the Lentiira-Kuhmo-Kostomuksha orangeites are less consistent, with Rb-Sr ages ($1180 \pm 5 \text{ Ma}$, $1232 \pm 10 \text{ Ma}$) bracketing $^{40}\text{Ar}/^{39}\text{Ar}$ results (1200 – 1210 Ma). Unfortunately, U-Pb perovskite data could not be obtained from these localities. Although the current results provide the most precise estimates for the time of kimberlite/orangeite magmatism in Finland, this study illustrates the importance of using multiple geochronology methods for precise and accurate determination of kimberlite and orangeite emplacement events.

References

- Belyatskii BV, Nikitina LP, Savva V, Levskii LK (1997) Isotopic signatures of lamproite dikes on the Eastern Baltic Shield. *Geochemistry International* 35: 575–579.
- Lee J-Y, Marti K, Severinghaus JP, Kawamura K, Yoo H-S, Lee JB and Kim JS (2006) A redetermination of the isotopic abundances of atmospheric Ar. *Geochim Cosmochim Acta* 70: 6.
- Nikitina LP, Levsky, LK, Lohkov, KI et al. (1999) Proterozoic alkaline-ultramafic magmatism in the eastern part of the Baltic Shield. *Petrology* 7: 246–266.
- O'Brien HE, Peltonen P, Vartiainen H (2005) Kimberlites, carbonatites, and alkaline rocks. In: Lehtinen, M., et al (Ed). *Precambrian Geology of Finland—Key to the Evolution of the Fennoscandian Shield*. Developments in Precambrian Geology 14. Elsevier, Amsterdam: pp. 605–644.
- O'Brien H, Phillips D, Spencer R (2007) Isotopic ages of Lentiira-Kuhmo-Kostomuksha olivine lamproite— group II, kimberlites. *Bull Geol Soc Finland* 79: 203–215.
- O'Brien H, Bradley J (2008) New kimberlite discoveries in Kuusamo, northern Finland. In: Extended Abstracts, Proc. 9th International Kimberlite Conf. Frankfurt. 9IKC-A-00346: 3.
- Phillips D., Matchan E.L., Honda M., Kuiper K.F. (2017) Astronomical calibration of $^{40}\text{Ar}/^{39}\text{Ar}$ reference minerals using high-precision, multi-collector (ARGUSVI) mass spectrometry. *Geochim Cosmochim Acta* 196: 351–369.
- Steiger R., Jäger E. (1977) Subcommittee on geochronology: convention on the use of decay constants in geo- and cosmochronology. *Earth Planet Sci Lett* 36: 359–362.

New constraints on the origins of MARID and PIC rocks based on mineral and bulk-rock geochemical data: Implications for mantle metasomatism and alkaline magmatism

Angus Fitzpayne^{1*}, Andrea Giuliani^{1,2}, Janet Hergt¹, David Phillips¹, Philip Janney³

¹*KiDs (Kimberlites and Diamonds), School of Earth Sciences, The University of Melbourne, Parkville, 3010 Victoria, Australia (*afitzpayne@student.unimelb.edu.au)*

²*ARC Centre of Excellence for Core to Crust Fluid Systems and GEMOC, Department of Earth and Planetary Sciences, Macquarie University, North Ryde, 2019 New South Wales, Australia*

³*Department of Geological Sciences, University of Cape Town, Rondebosch 7701, South Africa*

Introduction

Metasomatism has been implicated as the key process in refertilising mantle domains as a precursor to alkaline magmatism. MARID (Mica-Amphibole-Rutile-Ilmenite-Diopside) and PIC (Phlogopite-Ilmenite-Clinopyroxene) xenoliths represent end-member compositions produced by processes of melt/fluid enrichment in the mantle. These rocks have been interpreted as either the products of intense metasomatic alteration of peridotites or as magmatic cumulates in the lithospheric mantle. Irrespective of their formation mechanism(s), the compositions and sources of their parental fluids/melts and the role of MARID-PIC rocks in the genesis of alkaline magmas in intraplate settings remain unclear. To provide new constraints on these outstanding questions, we have studied the petrography and mineral major and trace element chemistry of 26 MARID and PIC xenoliths from southern African kimberlites and orangeites in the Kimberley and Barkly West areas.

Results

Major Elements

Mineral major element compositions are distinct in MARID and PIC rocks. MARID clinopyroxene and phlogopite grains are depleted in Al_2O_3 (<0.8 wt% and 8-12 wt%, respectively) and enriched in FeO_T (2.9-6.2 wt% and 5.3-10.2 wt%, respectively) relative to PIC minerals (clinopyroxene: 1.3-2.5 wt% Al_2O_3 , 2.9-3.6 wt% FeO_T ; phlogopite: 10.7-12.6 wt% Al_2O_3 , 3.7-4.8 wt% FeO_T). As such, the compositions of PIC minerals bear several similarities to peridotitic minerals (Fig. 1).

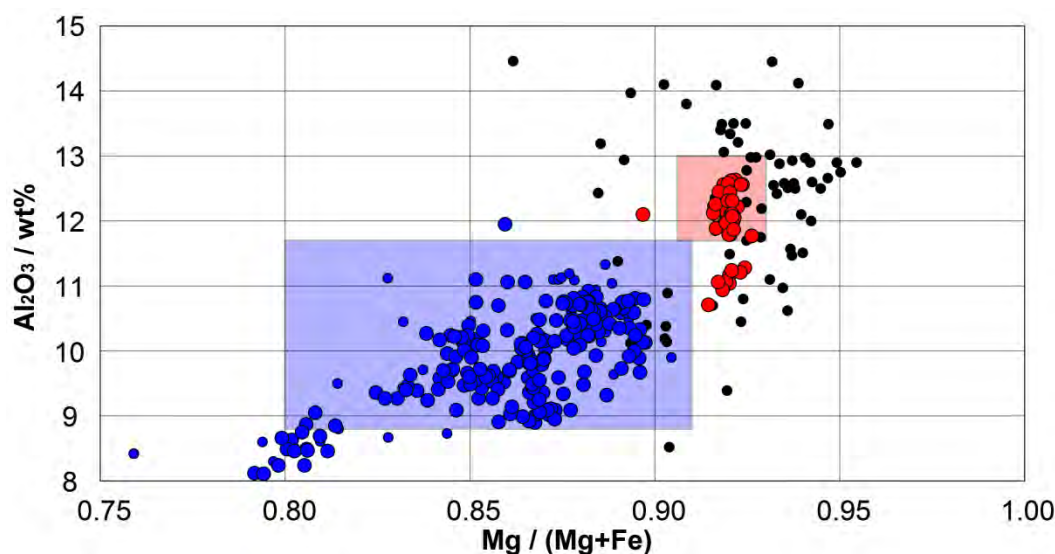


Figure 1: Plot showing phlogopite Al_2O_3 vs $\text{Mg}/(\text{Mg}+\text{Fe})$ in MARID and PIC rocks in this study (large blue and red circles, respectively); for comparison, literature MARID (small blue circles) and peridotite (small black circles) data have also been plotted. Blue and red fields represent MARID and PIC phlogopite ranges from Grégoire et al. (2002), respectively.

Comparisons between the compositions of MARID minerals and their peridotitic counterparts also indicate the possibility that MARID xenoliths form part of the metasomatic continuum that can be observed in peridotite xenoliths (Erlank et al., 1987; Fig. 2).

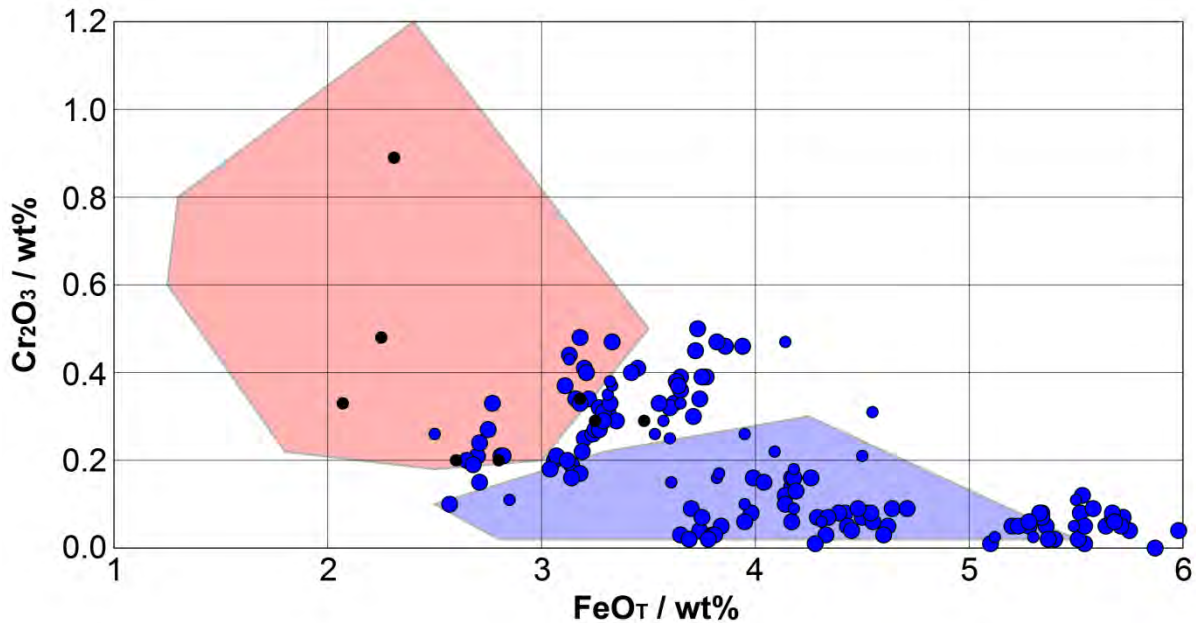


Figure 2: K-richterite Cr_2O_3 vs FeO_T in MARID rocks in this study (large blue circles), literature MARID data (small blue circles), and literature peridotite data (small black circles). Red and blue fields from Erlank et al. (1987), indicating previous ranges of peridotite and MARID K-richterite compositions, respectively.

Trace Elements

Mineral trace element characteristics, such as clinopyroxene rare earth element (REE) patterns, may also be used to distinguish MARID and PIC rocks (chondrite-normalised Ce/Yb 16-60 and 9-21, respectively). Moreover, similar trace element patterns to MARID clinopyroxene can be observed in peridotitic and eclogitic clinopyroxene samples from many locations within and external to southern Africa (Fig. 3), including several off-craton localities (e.g. Kerguelen islands: Grégoire et al., 2000; Namaqua-Natal mobile belt: Le Roex and Class, 2016).

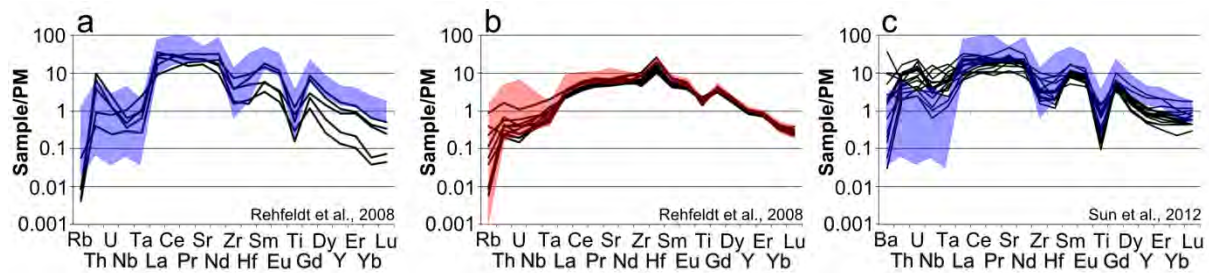


Figure 3: Primitive mantle normalised trace element diagrams for clinopyroxene from dunite, wehrlite (a) and websterite (b) xenoliths from the Kimberley kimberlites (data from Rehfeldt et al., 2008), and harzburgite xenoliths from the North China craton (c; data from Sun et al., 2012). Blue and red fields indicate ranges of MARID and PIC clinopyroxenes analysed in this study, respectively. Normalising values from McDonough and Sun (1995).

Bulk Rock reconstructions

Bulk rock reconstructions were performed employing mineral modal abundances and average mineral major and trace element compositions. The average reconstructed MARID composition resembles published whole-MARID analyses (e.g., Grégoire et al., 2002). Some trace elements (e.g., REEs) are less abundant in the reconstructions, owing to the effective removal of secondary trace element-

enriched components such as apatite (occurring in veins, for example) that are unrelated to the primary MARID paragenesis.

Discussion

The major element compositions of phlogopite and clinopyroxene grains in PICs are similar to those in metasomatised peridotites entrained by southern African kimberlites. Furthermore, all silicate MARID minerals exhibit broader compositional ranges than previously reported, which also partly overlap those in peridotites (Fig. 2). The overlap in compositions necessitates reevaluation of a genetic link between MARID/PIC rocks and metasomatised peridotites. Similarities in the trace element compositions of MARID and peridotitic clinopyroxene from other on- and off-craton localities also indicate that the infiltration of MARID-like fluids may be a ubiquitous metasomatic process in the lithospheric mantle (Fig. 3). The variation in the lithospheric mantle setting/age/thickness hosting these clinopyroxenes suggests that MARID rocks cannot be genetically linked to kimberlite magmas; they are more likely to be formed by interactions with more typical mantle fluids that are mobilised during regional tectono-magmatic events.

The bulk-rock reconstructions of MARID and PIC samples presented here exhibit positive HFSE anomalies, which resemble bulk-rock analyses of MARID and PIC xenoliths performed by Grégoire et al. (2002), and are unusual in mantle-derived rocks. Bulk-rock geochemical enrichments indicate that the metasomatic fluid responsible for MARID genesis must be a HFSE-LILE-enriched silicate melt, which could denote a group II kimberlite (orangeite) melt. However, available age constraints indicate MARID genesis prior to orangeite magmatism, suggesting MARIDs are more likely to be the source of such alkaline rocks (Giuliani et al., 2015). A comparison of MARID bulk-rock and average mineral compositions with published data on alkaline volcanic rocks implicates melting of the silicate components of MARID rocks in the creation of the major and trace element characteristics of alkaline magmas belonging to the lamproite clan (e.g., lamproites, orangeites).

References

- Erlank, A., Waters, F., Hawkesworth, C., Haggerty, S., Allsopp, H., Rickard, R., & Menzies, M. (1987). Evidence for mantle metasomatism in peridotite nodules from the Kimberley pipes, South Africa. *Mantle metasomatism*, 221-311.
- Giuliani, A., Phillips, D., Woodhead, J. D., Kamenetsky, V. S., Fiorentini, M. L., Maas, R., Soltys, A., Armstrong, R. A. (2015). Did diamond-bearing orangeites originate from MARID-veined peridotites in the lithospheric mantle? *Nature Communications*, 6, 6837.
- Grégoire, M., Moine, B., O'Reilly, S. Y., Cottin, J., & Giret, A. (2000). Trace element residence and partitioning in mantle xenoliths metasomatized by highly alkaline, silicate- and carbonate-rich melts (Kerguelen Islands, Indian Ocean). *Journal of Petrology*, 41(4), 477-509.
- Grégoire, M., Bell, D., & Le Roex, A. (2002). Trace element geochemistry of phlogopite-rich mafic mantle xenoliths: their classification and their relationship to phlogopite-bearing peridotites and kimberlites revisited. *Contributions to Mineralogy and Petrology*, 142(5), 603-625.
- le Roex, A., & Class, C. (2016). Metasomatic enrichment of Proterozoic mantle south of the Kaapvaal Craton, South Africa: origin of sinusoidal REE patterns in clinopyroxene and garnet. *Contributions to Mineralogy and Petrology*, 171(2), 1-24.
- McDonough, W. F., Sun, S-s. (1995). The composition of the Earth. *Chemical Geology*, 120, 223-253.
- Rehfeldt, T., Foley, S. F., Jacob, D. E., Carlson, R. W., & Lowry, D. (2008). Contrasting types of metasomatism in dunite, wehrlite and websterite xenoliths from Kimberley, South Africa. *Geochimica et Cosmochimica Acta*, 72(23), 5722-5756.
- Sun, J., Liu, C.-Z., Wu, F.-Y., Yang, Y.-H., & Chu, Z.-Y. (2012). Metasomatic origin of clinopyroxene in Archean mantle xenoliths from Hebi, North China Craton: Trace-element and Sr-isotope constraints. *Chemical Geology*, 328, 123-136.

Multiple metasomatic events recorded in MARID xenoliths

Angus Fitzpayne^{1*}, Andrea Giuliani^{1,2}, David Phillips¹, Janet Hergt¹, James Farquhar³,
Russell N. Drysdale⁴

¹*KiDs (Kimberlites and Diamonds), School of Earth Sciences, The University of Melbourne, Parkville, 3010 Victoria, Australia (*afitzpayne@student.unimelb.edu.au)*

²*ARC Centre of Excellence for Core to Crust Fluid Systems and GEMOC, Department of Earth and Planetary Sciences, Macquarie University, North Ryde, 2019 New South Wales, Australia*

³*Department of Geology and ESSIC, University of Maryland, College Park, Maryland 20742, USA*

⁴*School of Geography, The University of Melbourne, Parkville, 3010 Victoria, Australia*

Introduction

MARID (Mica-Amphibole-Rutile-Ilmenite-Diopside) and PIC (Phlogopite-Ilmenite-Clinopyroxene) xenoliths are interpreted as extremely metasomatised mantle rocks, based on their high abundances of alkali metals and volatile components. MARID xenoliths are often traversed by compositionally distinct carbonate- and serpentine-rich veins, and exhibit other signs of metasomatic overprinting (e.g., chemical zonation of the main mineral constituents). To characterise the compositions and origins of metasomatic fluids that have overprinted MARID and PIC xenoliths, we have examined the petrography and mineral chemistry of vein assemblages and the compositional zoning of MARID-PIC phases in 28 xenoliths from southern African kimberlites and orangeites from the Kimberley and Barkly West areas. For one sample, detailed C-O-Sr isotopic work on clinopyroxene, calcite, sulfides and sulfates in carbonate-rich veins was undertaken in order to clarify the origin(s) of the metasomatic fluid.

Petrography

Carbonate- and serpentine-rich veins in MARID rocks contain small (<100 μm), euhedral grains of clinopyroxene, phlogopite and ilmenite, as well as minerals (e.g., apatite, Cr-spinel) that are not associated with the primary MARID paragenesis (Fig. 1a). Primary MARID phases are often zoned when in contact with these veins. Similar veins are not observed in PIC rocks, which instead display rare serpentine pools containing small (<50 μm) grains of magnetite, as well as less common ilmenite, rutile, titanite and Cr-spinel. “Spongy” rims surrounding both MARID and PIC clinopyroxene grains (Fig. 1b) display a mineral inclusion assemblage similar to the groundmass mineralogy of kimberlites.

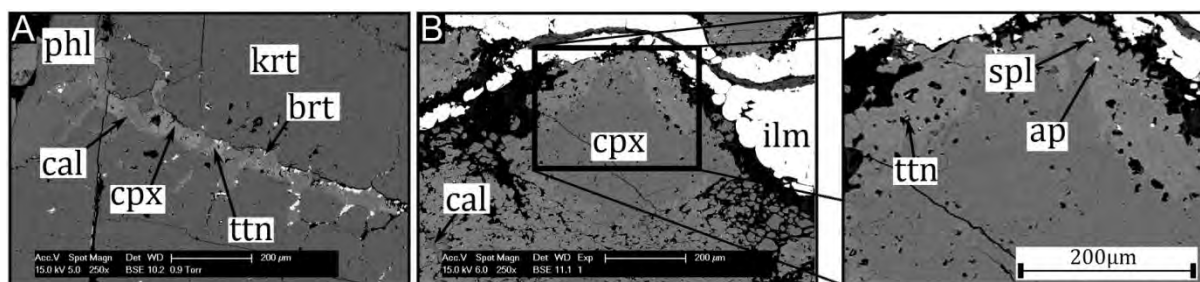


Figure 1: SEM back-scattered electron images of: A) calcite (cal) vein, containing “secondary” (i.e. non-MARID) clinopyroxene (cpx), titanite (ttn), and barite (brt), traversing matrix phlogopite (phl) and K-richite (krt) in MARID sample BLFX26; B) zoned cpx, adjacent to ilmenite (ilm) in PIC sample AJE540, while patchy cc occurs between small cpx; cpx rim contains inclusions (inset) of ttn, apatite (ap), and spinel (spl).

Mineral chemistry

“Secondary” (i.e. non-MARID) clinopyroxene grains display higher TiO_2 contents than “primary” MARID grains (0.8 ± 0.5 wt% and 0.10 ± 0.05 wt% respectively). “Spongy” clinopyroxene rims in MARID and PIC rocks also exhibit CaO enrichment and Al_2O_3 - Na_2O depletions relative to their

cores. “Secondary” clinopyroxene grains in MARID rocks exhibit distinct trace element patterns, resembling either primary MARID or PIC clinopyroxene (Fig. 2a, b). Clinopyroxene spongy rims are REE-depleted relative to their cores in MARID samples, whereas those in PIC rocks are relatively REE-enriched (Fig 2c, d). “Secondary” phlogopite grains also have higher TiO₂ contents with respect to “primary” MARID grains (2.9 ± 1.3 wt% and 1.4 ± 0.9 wt%, respectively). Two types of ilmenite occur in MARID xenoliths: “primary MARID” ilmenite in textural equilibrium with other MARID phases (36.0 wt% FeO_T, 9.1 wt% MgO, 51.7 wt% TiO₂), and “PIC-like” ilmenite (27.0 wt% FeO_T, 14.1 wt% MgO, 55.8 wt% TiO₂), which occurs in veins or as thin rims around rutile grains.

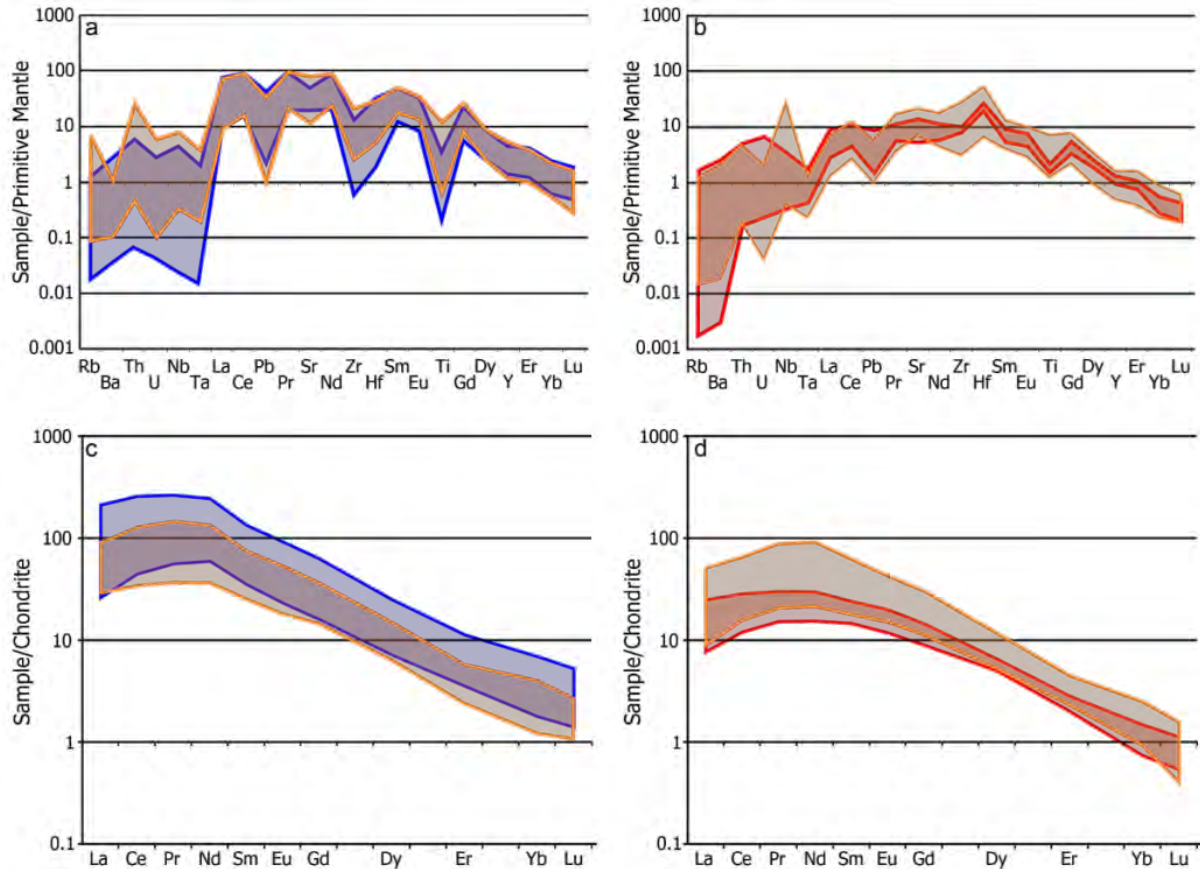


Figure 2: a,b) Primitive mantle-normalised trace element diagram showing MARID (blue field) and PIC primary clinopyroxene (red field) ranges from this study, relative to MARID- and PIC-like secondary clinopyroxenes in MARID rocks (orange fields); c,d) CI-chondrite normalised REE diagram for MARID (blue field) and PIC (red field) primary clinopyroxene ranges from this study, compared to spongy clinopyroxene rims around MARID and PIC clinopyroxene in this study (orange); all normalising values from McDonough and Sun (1995).

Radiogenic Isotopes

Sample XM1-331, derived from the Bultfontein kimberlite, hosts abundant carbonate-rich veins containing euhedral clinopyroxene and phlogopite, and lesser barite and sulfides. Strontium isotope compositions were collected *in situ* by LA-MC-ICPMS for primary clinopyroxene, K-richterite and phlogopite, and secondary clinopyroxene and carbonates. Primary MARID phases are in isotopic equilibrium with one another, but their isotopic compositions (i.e. primary clinopyroxene $^{87}\text{Sr}/^{86}\text{Sr}_i = 0.70811$) differ from those of the vein phases (i.e. vein clinopyroxene $^{87}\text{Sr}/^{86}\text{Sr}_i = 0.70581$).

Stable Isotopes

Oxygen isotope compositions of secondary carbonates from MARID sample XM1-331 are higher, and carbon isotope compositions are lower, compared with bulk carbonates in the kimberlite host

($\delta^{18}\text{O}_{\text{VSMOW}} = +17.22 \text{ ‰}$ and $+11.73 \text{ ‰}$, respectively; $\delta^{13}\text{C}_{\text{VPDB}} = -9.18 \text{ ‰}$ and -4.28 ‰ , respectively). Sulfur isotope analyses of bulk rock sulfide and a barite separate from sample XM1-331 provide $\delta^{34}\text{S}$ values = -0.81 ‰ and $+4.69 \text{ ‰}$, respectively.

Discussion

No MARID phases occur as secondary minerals in PIC xenoliths, whereas some PIC-like clinopyroxene and ilmenite occur in veins in MARID samples, indicating that PIC mineral precipitation in the Kimberley area likely post-dated MARID formation. Some phases, such as clinopyroxene, in veins transecting MARID rocks display discrete compositional zones on a micron scale; such subtle zoning can only be preserved under mantle conditions for up to a few ky. The preservation of geochemical heterogeneities (as mineral zonation, as well as primary vs vein mineral compositions), in addition to Sr isotope disequilibrium between MARID and vein minerals in sample XM1/331, suggest that metasomatism occurred shortly before entrainment and transport to surface by kimberlite magmas.

The $^{87}\text{Sr}/^{86}\text{Sr}_i$ of primary and secondary generations of MARID minerals indicate that, although MARID rocks may be generated from an enriched mantle source, subsequent phases of metasomatism are caused by mantle fluids with less radiogenic Sr. Coupled C-O isotope compositions suggest that vein carbonates could be sourced from mantle that has been enriched with recycled crustal material. Assuming sulfur isotopic equilibrium, barite and sulfides in MARID veins crystallised at 850-900°C (Miyoshi et al., 1984), consistent with the thermal regime of MARID formation (based on Ca-in-opx thermometry from Konzett et al., 2014). It can therefore be concluded that sulfur-rich fluids interacted with MARIDs during their residence in the lithospheric mantle, and not during transport to, or emplacement into, the crust.

While it appears that secondary metasomatic features in MARID rocks may be temporally linked to kimberlite magmatism, the C-O-Sr isotopic composition of vein material in sample XM1/331 is clearly unlike the host kimberlite. Therefore, we favour fluid derivation from a mantle source containing recycled material, the remobilisation of which was triggered by the thermal anomaly associated with kimberlite magmatism.

References

- Konzett, J., Krenn, K., Rubatto, D., Hauzenberger, C., & Stalder, R. (2014). The formation of saline mantle fluids by open-system crystallization of hydrous silicate-rich vein assemblages – Evidence from fluid inclusions and their host phases in MARID xenoliths from the central Kaapvaal Craton, South Africa. *Geochimica et Cosmochimica Acta*, 147, 1-25.
- McDonough, W. F., Sun, S-s. (1995). The composition of the Earth. *Chemical Geology*, 120, 223-253.
- Miyoshi, T., Sakai, H., & Chiba, H. (1984). Experimental study of sulfur isotope fractionation factors between sulfate and sulfide in high temperature melts. *Geochemical Journal*, 18(2), 75-84.



New insights into volcanic processes and diamond grades from deep mining at Argyle

Murray J. Rayner¹, Stephen W. Moss^{2,3}, A. Lynton Jaques⁴, Volker Lorenz⁵, Grant L. Boxer⁶, Chris B. Smith⁷, and Kimberley Webb²

¹ Argyle Diamonds, Rio Tinto, Perth, Australia, murray.rayner@riotinto.com

² Mineral Services Canada, Vancouver, Canada, kimberley.webb@mineralservices.com

³ Terram Vero Consulting Inc., Vancouver, Canada, smoss@terramvero.com

⁴ Australian National University, Canberra, Australia, lynton.jaques@anu.edu.au

⁵ University of Würzburg, Würzburg, Germany, vlorenz@geologie.uni-wuerzburg.de

⁶ Consultant Geologist, Perth, Australia, boxerg@inet.net.au

⁷ University of Bristol, Bristol, United Kingdom, chris_b_smith@bopenworld.com

Introduction

The Argyle mine in the east Kimberley region of Western Australia is one of the world's largest diamond deposits, and has produced some 835 million carats (cts) since mining began in 1983. At its peak in the period 1993–1998 Argyle produced more than 40 million cts per annum. The Argyle AK1 pipe is one of the world's highest grade mines with production averaging ~3–4 cts/tonne. Information obtained during deep open pit mining over the past 28 years, extensive drilling programs, and underground mining since 2013 has provided the basis for a re-examination of the geology and volcanology of the AK1 lamproite pipe, requiring some revisions to earlier accounts.

Geology

Comprehensive 3-D modelling shows AK1 is a composite body comprising four coalesced, steep-sided diatremes that are aligned along a NNE-trending fault and taper to narrow feeder zones at depth. The body is in-filled by deposits of volcanoclastic olivine lamproite and cut by late olivine lamproite dikes (Boxer et al. 1989; Jaques et al. 1989). Following emplacement, AK1 was tilted 30° to the north and cut by the sinistral NNW–SSE Gap fault system, and by the dextral E-W Razor Ridge fault, resulting in N-S elongation of the body (Rayner et al. 2017).

The largest domain in AK1 is the so-called southern diatreme (Fig. 1), which comprises two coalesced diatremes at depth and features a zone of distinctly higher grade at its southern end from the pre-mining post-eruption surface to 900 m below surface. Previous studies have shown that the Argyle diamond population is characterized by a small diamond size with a log-normal distribution and high stone frequency, with large variations in diamond grade (along with some small value variations) within the pipe due to differences in stone frequency (Hall and Smith 1985). The apparent consistency of the diamond population in the southern diatreme at Argyle was complemented historically by assumptions of a simple internal geology model.

However, recent mining within the block cave mine at depth has displayed grade and quality fluctuations which appear to be in conflict with the historical simplistic single source lamproite model within the southern diatreme. Here, we report results from recent studies and reconciliation work aimed at defining the volcanological controls on diamond grade within the ore body. These results suggest a more complex internal geology in the southern diatreme, and point to the occurrence of at least four distinct lamproite lithofacies (Fig. 2), with two of these having unique diamond contents.

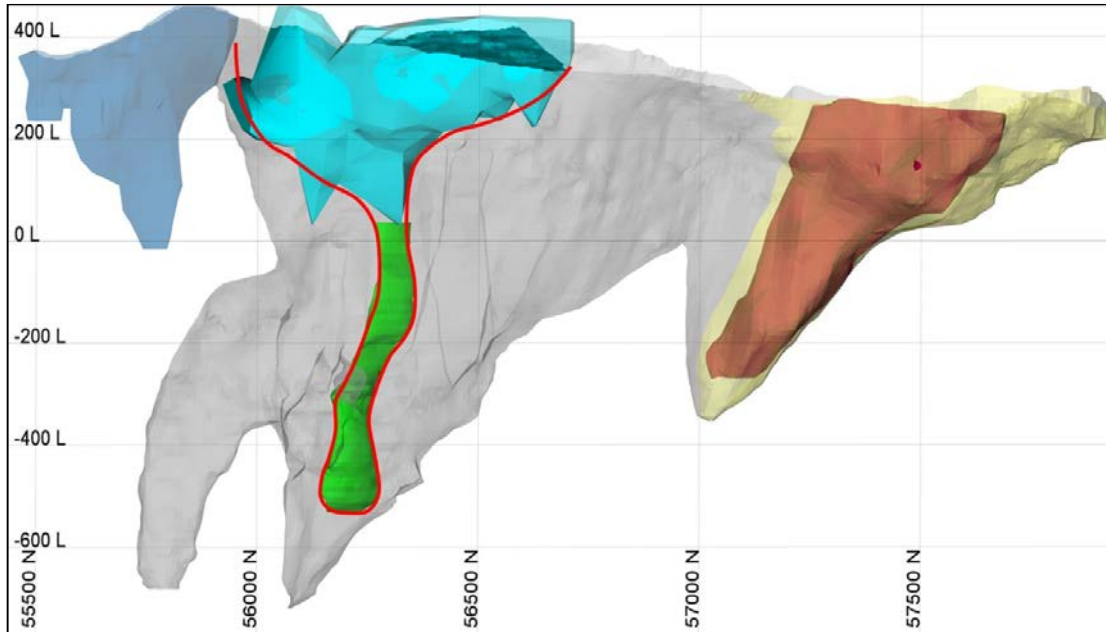


Figure 1: Long-section of the Argyle AK1 pipe facing west showing the high grade domain at the south end of the southern diatreme (light blue), the newly-identified high grade domain (green), and interpreted conduit-like geometry (red outline) of the combined deep and shallow high grade zones. Also displayed are the north sandy (yellow), non sandy (red), southern tail (dark blue) and south sandy low (grey) domains; the latter comprises undifferentiated Lamp1a, Lamp2 and Lamp4 lithofacies. Scale in metres.

Lamp1a comprises thinly-bedded quartz-rich volcanoclastic (altered) olivine lamproite, and is distinct because of a) fine-scale (1 - 15 cm) bedding, and b) pale grey quartz-rich matrix. Beds contain free olivine (8 - 15% of the rock) and characteristic blocky to irregular juvenile pyroclasts (typically 10 - 25%) ranging up to 20 mm in size with variably vesiculated, formerly glassy to very fine grained pale/dark brown or black groundmass. This is a common lithofacies throughout much of the southern diatreme.

Lamp1h (from the newly-recognised high grade domain) is similar to Lamp1a but has distinctly less detrital quartz and a much higher proportion of free (altered) olivine. Lamp2 is a massive, quartz-rich volcanoclastic lamproite with distinctive wispy and irregular-shaped formerly glassy pyroclasts. This lithofacies is found in both the north and south of the southern diatreme but predominantly in its northern section and at depth. Lamp4 comprises juvenile lapilli-rich, quartz-poor, and crudely-bedded volcanoclastic lamproite. It has

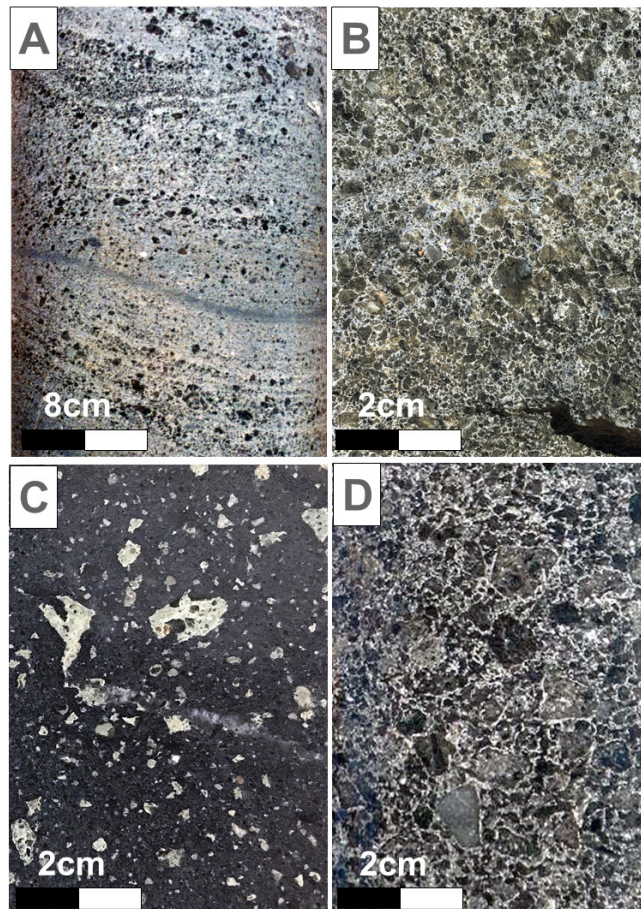


Figure 2: Main lamproite lithofacies from southern diatreme of AK1: a) Lamp1a; b) Lamp1h; c) Lamp2; and d) Lamp4

been mapped in the central and eastern portions of the southern diatreme.

Key textural differences between the lamproite lithofacies in the southern diatreme include the relative proportions of juvenile lapilli, olivine and detrital quartz. These differences are interpreted to reflect: a) the proportion of mantle-derived olivine; b) the degree to which olivine has been liberated from the lamproite host melt; c) the speed of melt cooling; d) the organization of pyroclastic components, and e) the amount of dilution by quartz grains.

Lamproite Grades

Grade variations realized during mining are shown to be the result of changes in the relative proportions of the lamproite lithofacies being mined: high grades are associated with volcanoclastic lamproite that is olivine-rich and has low dilution (i.e. Lamp1h), while lower grades are linked to olivine-poor and highly diluted volcanoclastic lamproites (i.e. Lamp2). High grade (> 10 ct/t) volcanoclastic lamproite at the south end of the southern diatreme provides a basis for linking the high grade zones at the original mining surface with those encountered at depth during block cave mining and deep underground drilling (Fig. 1). The resulting geometry of the combined high grade zone of AK1 resembles that of a volcanic feeder or conduit, and requires modifications to previous emplacement interpretations (Rayner et al. 2017).

Conclusions

A complex series of volcanoclastic lamproites that have been displaced by post-eruption faulting events have been unraveled to form a new view of the previously more simplistic volcanological model for Argyle. This new view provides a firmer basis for understanding both the volcanological history and the controls on diamond grade within the Argyle pipe.

References

- Boxer GL, Lorenz V, Smith CB (1989) The geology and the volcanology of the Argyle (AK1) lamproite diatreme, Western Australia. In: Ross J et al (eds), Kimberlites and related rocks, vol 1: Their composition, occurrence, origin and emplacement. Geol Soc Aust Spec Publ 14:140-152
- Hall AE, Smith CB (1985) Lamproite diamonds - are they different? In: Glover JE, Harris PG (eds), Kimberlite occurrence and origin: a basis for conceptual models in exploration, Geology Department and University Extension, University of Western Australia, Publ No 8, 167-212
- Jaques AL, Haggerty SE, Lucas H, Boxer GL (1989) Mineralogy and petrology of the Argyle (AK1) lamproite pipe, Western Australia. In Ross J et al (eds), Kimberlites and related rocks, vol 1: Their composition, occurrence, origin and emplacement. Geol Soc Aust Spec Publ 14:153-169
- Rayner MJ, Jaques AL, Boxer GL, Smith CB, Lorenz V, Moss SW, Webb K, Ford D (2017) The geology of the Argyle (AK1) diamond deposit, Western Australia. Soc Econ Geol Spec Publ (in press)



Diamond exploration and prospectivity of Western Australia

M. T. Hutchison^{1,2}

¹ Geological Survey of Western Australia, Perth, WA, Australia, mark.hutchison@dmp.wa.gov.au

² Trigon GeoServices Ltd., Las Vegas, NV, United States, mth@trigon-gs.com

Introduction

Western Australia (WA) hosts 696 000 km² of exposed, onshore, exclusively Archean rocks and 439 000 km² of Paleoproterozoic rocks. In total, pre-1.6 Ga rocks comprise around 45% of the onshore area of the State, constituting the West Australian Craton (WAC; Yilgarn and the Pilbara Cratons) and the western part of the North Australian Craton (NAC). Seismic tomography demonstrates that considerable remaining portions of the State are also underlain by thick mantle lithosphere (Kennett et al., 2013), hosting the conditions under which diamonds form. Subsequently, most of the State is prospective for diamonds and numerous diamondiferous lamproite and kimberlite fields are known. Emplacement of diamond-bearing rocks spans much of geological time, from the c. 1868 Ma Brockman Creek kimberlite in the Pilbara (White, 2000) to the c. 17 Ma Walgidee Hills lamproite, Noonkanbah field, West Kimberley (Phillips et al, 2012). According to Kimberley Process statistics, Australia is estimated to have produced approximately 11% of global rough diamond production by weight in 2015, ranking it fourth in the world after the Russian Federation, Botswana and the Democratic Republic of Congo. These production figures are accounted for by two mines, both in WA. However, due to the closure of the Ellendale mine in 2015, responsible for a large proportion of the world's fancy yellow production, only one currently producing mine remains in Australia (at the AK1 olivine lamproite at Argyle, NAC). In order to assess the effectiveness of prior exploration and draw attention to under-explored prospective areas, a thorough compilation and interpretation of WA diamond exploration data has been conducted.

Methodology

Despite its position in world-wide diamond production, the size, terrain, infrastructure and climate of Western Australia has resulted in many areas being underexplored. Some 68% of the State's onshore areas lie over 20 km from a known diamond exploration sample site. Yet continuous diamond exploration since the 1970s has resulted in abundant data, including 4200 company reports citing diamond as a commodity of interest. In construction of a Diamond Exploration Database (DED) focus has been applied on the primary method of exploration, that is, physical sampling. The DED for Western Australia incorporates the locations of over 88 000 diamond exploration samples, the overwhelming majority (~ 90%) being taken for separation of diamonds or other minerals indicating diamond potential. Associated with these samples are over 30 000 good quality chemical analyses of mineral separate grains. Furthermore, locations of 523 discrete in-situ bodies which in principal have a diamond potential (kimberlites, lamproites, ultramafic lamprophyres and carbonatites), have been compiled, with 114 confirmed to be diamondiferous. As a companion to the in-situ occurrences, 127 emplacement age determinations from 63 bodies are compiled with detailed geochronological information.

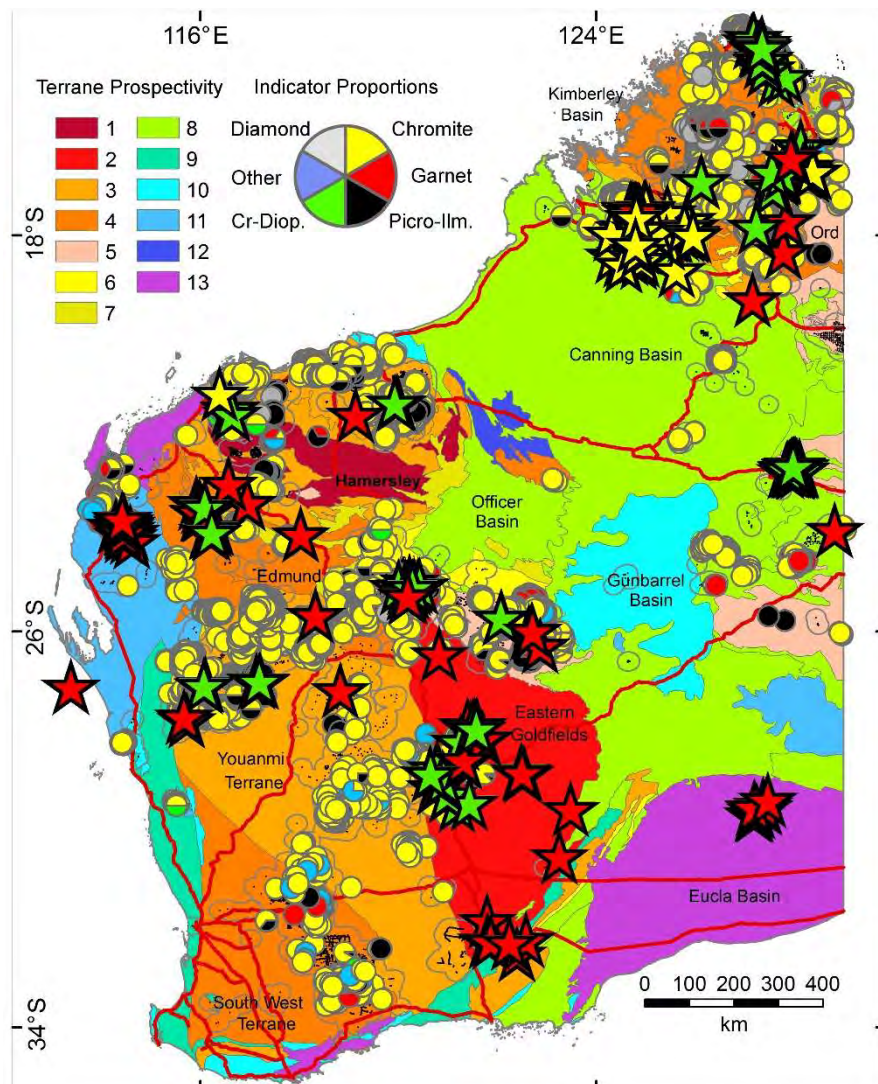
To assess prospectivity, the State has been subdivided into 67 onshore tectonic units in 4 geographic areas. The extent and results of sampling, in conjunction with the age of surface rocks relative to ages of diamond-prospective rocks, and the underlying mantle structure have been analysed in order to produce a prospectivity map. Methodology follows that of Hutchison (2013) for the Northern Territory (NT). The resulting map presents a 13-level ranking of attractiveness for future diamond exploration.

Mineral Sampling Results

Indicator distributions and sampling methodologies show that programs recovering 0.3–0.4 mm grains from high-energy trap sites are most successful. Diamond occurred in 3.5% of indicator mineral samples, whereas non-diamond indicators were identified by visual inspection in 28% of samples. The large majority are spinels, relatively durable in the harsh Western Australian weathering environment.

In addition to chromite, diopside, garnet, ilmenite, monticellite, orthopyroxene, olivine, perovskite, phlogopite, pseudobrookite and tourmaline with indicator chemistries have all been recovered. False positives occur amongst grains which are identified only visually. However, 80% (over 25 000) of good-quality mineral compositional analyses are classified as genuine indicators. Ninety-one percent of indicator spinels are mantle-derived chromites and clinopyroxenes largely show garnet peridotite affinity. Twenty five per cent of peridotitic garnets are G10s (following Grütter et al., 2004). Amongst ilmenites, 93% with indicator chemistry fall within the kimberlite field (following Wyatt et al. 2004).

Figure 1: Diamond prospectivity of Western Australia. Geological subdivisions are ranked for prospectivity in the context of mantle structure, the age of surface rocks, the extent of sample coverage and recovery of visually-determined indicators. Ranking follows the key, with 1 being the most prospective area. In-situ bodies are shown by stars: green – kimberlite; yellow – lamproite; red – ultramafic lamprophyre / carbonatite. Sample sites are shown by small black dots with a 20 km radius indicating explored areas. Larger circles indicate sites of recovery of visually-determined indicator minerals with colours in the key. Principal roads are marked in red. Diamond and chromite distinguish themselves as the most robust and hence commonly-recovered indicator minerals. Much of WA is under-explored with prospective areas in the NAC and particularly the WAC.



Yellow and pink diamonds contribute 5% and 1% of the State-wide regional sampling populations; colours reflected in production from the Argyle and Ellendale mines. Of original growth forms octahedral forms are most abundant (45%), in contrast to the NT where cubes dominate (Hutchison, 2013). This suggests relatively higher formation temperature and mature, deeper and more prospective diamond growth settings than farther east-northeast in the NT. However, 41% are dodecahedral or tetrahedral and 53% of octahedral stones show surface etching and resorption. Considerable proportions of diamonds have been distressed, either at formation depths or during emplacement, consistent with the chemical incompatibility between diamond and some WA diamond host rocks, particularly leucite lamproites.

Geographic Variations and Regional Prospectivity Ranking

Indicator mineral occurrences and in-situ bodies with diamond potential (Figure 1) largely occupy the

north (NAC) and west (WAC) of the State. These areas correspond to thick mantle lithosphere (Kennett et al., 2013) establishing the conditions for diamond growth. Clusters in Figure 1 particularly correlate with areas of significant changes in mantle thickness reflecting structures favourable for diamond emplacement. Similar features also extend into under-sampled areas, the most notable being the far-west Kimberley, the extension of thickened lithosphere south of the Kimberley into the Proterozoic basement of the Arunta, the boundary between the Capricorn Orogen and the Archean to Proterozoic Hamersley Basin, and the east and central-west Yilgarn in the WAC.

With the exception of thinner mantle under the Pilbara, the cratonic regions of WA and the NT are underlain by particularly thick mantle lithosphere (220–240 km; Kennett et al., 2013). However, geothermobarometry from Merlin kimberlites in the NT (Hutchison, 2013) shows that some mantle minerals derive from considerably shallower depths (~ 160 km). The spectra of indicator chemistry throughout WA demonstrates the same effect, that mantle material has been derived from depths not necessarily at the base of the lithosphere. Garnets show clear geographic subdivision with the lherzolitic trend being more Ca-depleted in WAC samples compared to the NAC. Although the main trend is not as prominently bordering the G10 field as from the Merlin field of the eastern NAC in the Northern Territory (NT; Hutchison, 2013), WAC samples show a much broader scatter into strongly diamond-prospective G10 and G10D compositions. For WA ilmenites, NAC samples extend the western NT-border samples further into Mg-enriched compositions consistent with kimberlites. However, consistent with findings for garnets, ilmenites from the WAC (particularly the Hamersley Basin and Eastern Goldfields) show the most diamond-prospective trend. As the prospectivity model assesses mineralogy in addition to regional mantle structure, variations in source depth are accounted for. Figure 1 shows the results of ranking terranes with areas colour-coded according to prospectivity. The NAC, location of WA's diamond mines, scores well. However, partly because of under-sampling combined with good indicator recovery, results point to parts of the WAC being more prospective. Most notable are the Hamersley Basin, Eastern Goldfields Superterrane and the Goodin Inlier of the Yilgarn Craton.

Conclusions

Despite prolific diamond exploration, Western Australia is considerably under-explored and the ageing Argyle mine and recent closure of operations at Ellendale warrant a re-evaluation of diamond potential. Indicator mineral chemistries reflect mantle sources with respectable diamond tenor, consistent with diamond and visually-determined indicator recovery, known diamondiferous source rocks and mining in parts of the State. However, analysis of exploration data also draws attention to under-explored areas particularly in the WAC. As kimberlite and lamproite emplacements span 2 500 Ma, there are significant opportunities for diamond-affinity rocks being present near surface even within the large, under-explored sedimentary basins overlying thick mantle lithosphere evident through much of the State. Results of prospectivity analysis make a compelling case for renewed diamond exploration.

References

- Grütter HS, Gurney JJ, Menzies AH, Winter F (2004) An updated classification scheme for mantle-derived garnet, for use by diamond explorers. *Lithos* 77: 841–857
- Hutchison MT (2013) Diamond Exploration and Regional Prospectivity of the Northern Territory of Australia. In: Pearson DG et al. (eds) *Proceedings of the 10th International Kimberlite Conference, Volume 2, Special Issue of the Journal of the Geological Society of India*, pp 257–280
- Kennett BLN, Fichtner A, Fishwick S, Yoshizawa K (2013) Australian Seismological Reference Model (AuSREM): mantle component. *Geophysical Journal International* 192: 871–887
- Phillips D, Clarke W, Jaques AL (2012) New ⁴⁰Ar/³⁹Ar ages for the West Kimberley lamproites and implications for Australian plate geodynamics. 10 IKC Ext. Abs. Bangalore, India: 10IKC-104
- White B (2000) The geochronology and thermochronology of the Brockman Creek 01, Melita and Melita 02 kimberlites, Western Australia. Unpubl. Hons. Res. Rep., Univ. Melbourne
- Wyatt BA, Baumgartner M, Anckar E, Grütter H (2004) Compositional classification of "kimberlitic" and "non-kimberlitic" ilmenite. *Lithos* 77: 819–840



The suitability of microdiamonds for local (blocked) resource estimation – opportunities and challenges

J. Stiefenhofer¹, M.L. Thurston², D.E. Bush³

¹MinRes, Corporate Division, Anglo American Operations Ltd, Johannesburg, South Africa,
johann.stiefenhofer@debeersgroup.com

²Technical and Sustainability, De Beers Group Services (Pty) Ltd, Johannesburg, South Africa,
malcolm.thurston@debeersgroup.com

³Z-Star Mineral Resource Consultants, Cape Town, South Africa,
david.bush@zstar.co.za

Introduction

The suitability of microdiamonds for kimberlite and related-rock resource evaluation has been the subject of robust debate for many years. These debates have centred round the suitability of microdiamonds for global and zonal average grade calculations. The impact of mantle processes and geology on microdiamond-based estimation methods has already been addressed (Stiefenhofer et al., 2016), as well as key features of the microdiamond estimation process (Stiefenhofer et al., in prep.). In this paper the debate is taken a step further and the suitability of microdiamonds for use in local block estimates was investigated through analysis of key geostatistical properties.

Any variable, or function thereof, randomly distributed in space with a value at every point and a set of spatial coordinates, is considered a regionalised variable, micro-diamonds included. Our investigation focussed on the essential parameters which characterise a regionalised variable, and without which geostatistical applications would not be possible. These include the spatial attributes and structure, i.e. variography, of micro-diamonds, sample support size limitations, and consistency of the diamond size frequency in space.

Study results

Tests were undertaken to verify the relationship between micro-diamond sample support and stone grade variance, more specifically relating to point sampling. This required the calculation of non-adjacent sample covariance. The output was compared against a hand-calculated sample support up-scaling exercise using the real sample data, as well as the block dispersion variance following the kriging of a single 50x50x15m block using the same variogram input parameters. It should be noted that the sampling protocols are completely different for microdiamond sampling (point samples) compared to macrodiamond samples (continuous line sampling). The level of internal geological heterogeneity in the kimberlite is critical – higher variability will require more samples to reduce the variance of statistical parameters to acceptable levels. Following a continuous sampling exercise at Jwaneng Mine Centre Pipe, the data revealed a predictable decrease

in variance with increasing sample support (sample length), as shown in Figure 1. Analysis also confirmed a stable size frequency distribution (SFD) with increasing depth in the Centre Pipe, as well as at other locations (Figure 2).

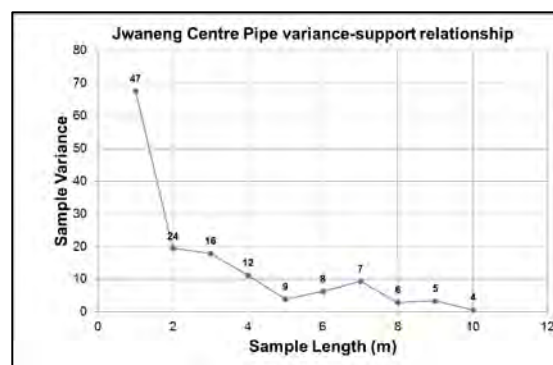


Figure 1: Variance-support relationship for microdiamond sampling within the Jwaneng Centre Pipe. Labels refer to the number of samples down the particular drillhole.

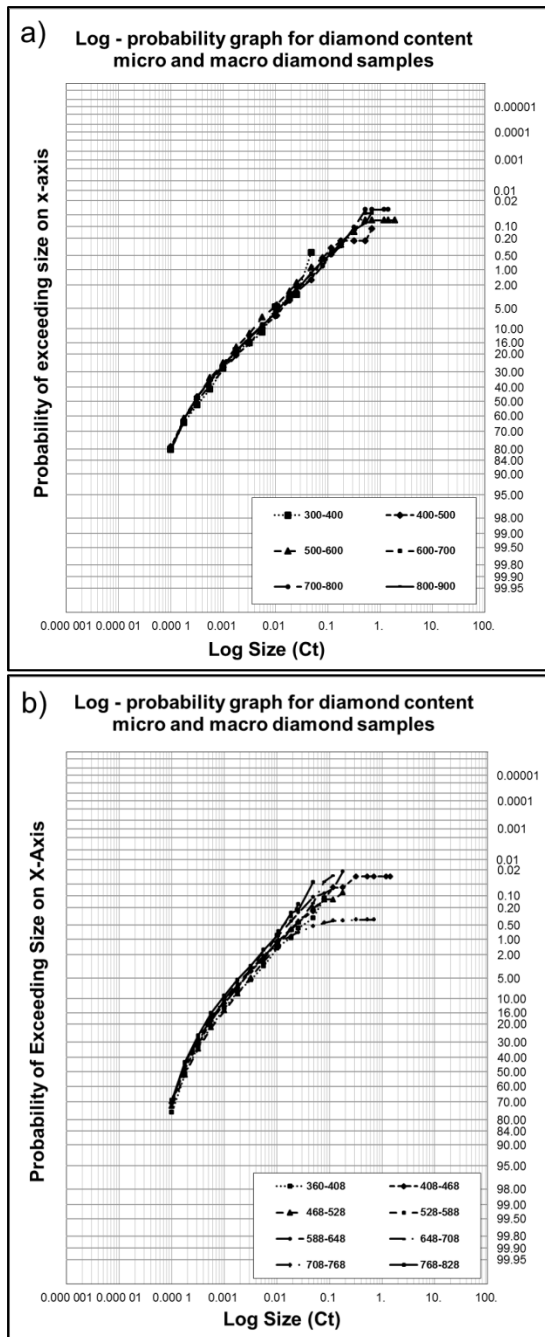


Figure 2: SFD's at 100m depth intervals for the Centre Pipe Volcaniclastic Kimberlite (a) and at 60m depth intervals for the Venetia K1 Dark Volcaniclastic Kimberlite (b). The variability observed at the upper (coarse) end of the curves is due to sample support constraints.

Successful variance-support analysis is a function of optimal micro-diamond sample support size which is in turn related to the stone density of the kimberlite under investigation. It is important to optimise the sample support size prior to any resource evaluation sampling. Data from such

optimised micro-diamond sampling campaigns yield clear spatial structure, consistent with that of a regionalised variable. Studies conducted across four different kimberlite clusters (Snap Lake, Venetia K1, Orapa and Jwaneng) and eleven different lithologies revealed nugget effect proportions ranging from 21-65% and variogram ranges from 67-220m. An example is shown in Figure 3.

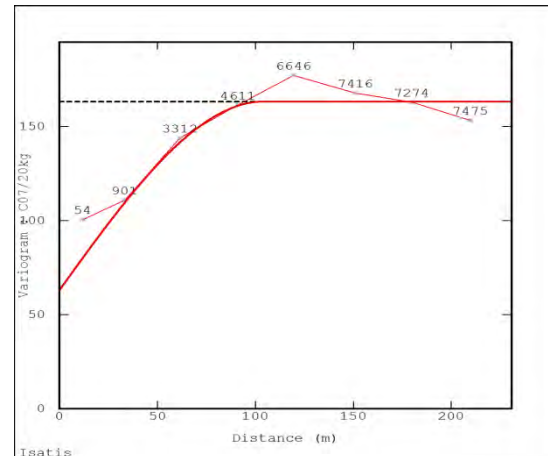


Figure 3: Omnidirectional variogram for the Southern Dark Volcaniclastic Kimberlite (SDVK) unit in the Orapa AK1 South Lobe. The range is 104m and the number labels refer to the number of pairs in the lags of the experimental semivariogram.

Z-star Mineral Resource Consultants have generated several “digital kimberlite” simulations using high-density micro-diamond point samples. The output was validated against the input data which consisted of real microdiamond samples (actual data). Thereafter, both micro and macrodiamond data sets were generated from the simulations and used to generate local estimates on a 50x50x16m block grid. The macrodiamond output was compared against real macrodiamond data obtained from large diameter drilling (actual data). As expected the large diameter data exhibited a better correlation to actual compared to the microdiamond data, although both correlations are significant (Figure 4). These exercises were performed for both high- and low-grade kimberlites. It was also possible to optimise the micro-diamond sampling such that a resource of an indicated level of confidence could be obtained.

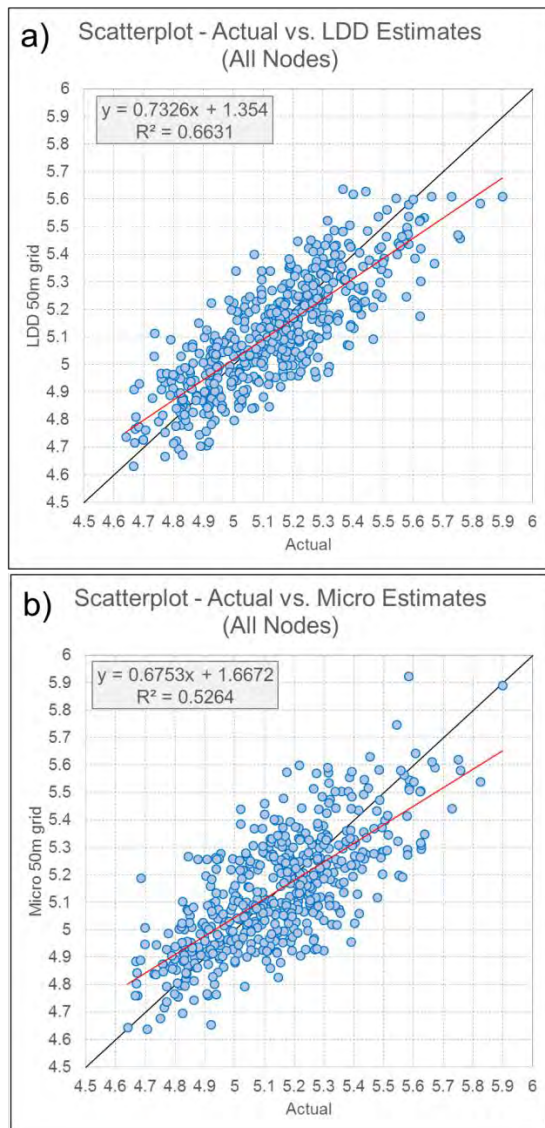


Figure 4: Actual block value vs. LDD (a) and actual block value vs. micro-diamond estimates (b). Both correlations are significant. An LDD sample contains on average 2,016 stones (96 micro-diamond samples) compared to only 21 stones in a single microdiamond sample. Actual and estimated block grades have been converted from stones/20kg to carats/m³.

Conclusions

Our analysis yielded no reason why micro-diamonds should not be considered for local block resource estimation, provided some precautions are adhered to. These are:

- A valid and robust geological understanding of the pipe emplacement and lithologies;
- The required degree of confidence in the resource estimate must be agreed

upon prior to any sampling. This should include the maximum variance which can be tolerated in the anticipated monthly or quarterly cash-flows;

- The sample support size and indeed also the sampling layout must be optimised for both the kimberlite under investigation and the level of risk acceptable to all stakeholders;
- Provision for some macro-diamond sampling to assess the integrity of the size frequency distribution beyond micro-diamonds and into the commercial diamond sizes; and
- Demonstrable stability in diamond size frequency, both across the pipe as well as at depth. A robust geological model will contribute significantly towards this goal. Failure to achieve this will result in a failed resource estimate.

Acknowledgements

The authors would like to thank the De Beers Group of Companies, Debswana and Anglo American Corporation for permission to publish this work. Mr. Cuan Lohrentz is acknowledged for his assistance in the computational aspects of the simulation studies.

References

- Stiefenhofer J, Thurston ML, Rose DM, Chinn IL, Ferreira JJ (2016) Principles relating to the use of micro-diamonds for resource estimation: 1 – The impact of mantle and kimberlite processes. *CIM Journal* 7(4) <http://dx.doi.org/10.15834/cimj.2016.26>
- Stiefenhofer J, Thurston ML, Rose DM, Bush DE (in prep.) Principles relating to the use of micro-diamonds for resource estimation: 2 – Case studies to illustrate micro-macro diamond estimates.



Mantle Composition, Age and Geotherm beneath the Darby Kimberlite field, West Central Rae Craton

Garrett A. Harris¹, D. Graham Pearson¹, Jingao Liu², Matthew F. Hardman¹ and David Kelsch³

¹ University of Alberta, Edmonton, Canada, gaharris@ualberta.ca, gdpearso@ualberta.ca, mhardman@ualberta.ca

² China University of Geosciences, Beijing, China, jingao@cugb.edu.cn

³ Bluestone Resources Inc., Vancouver, Canada, dkelsch@telusplanet.net

Introduction

The Rae craton in Canada's North contains several kimberlite fields and has been the subject of episodic diamond exploration, with proven diamond-bearing deposits. However, relatively little is known about the deep mantle lithosphere that underpins the architecturally complex crust of this craton. The Darby Kimberlite field, located ~ 200 km southwest of the community of Kugaaruk, Nunavut, provides an opportunity to study the mantle beneath the western portion of the central Rae craton via erupted mantle xenoliths. The Darby kimberlite field contains nine bodies, of which at least eight are kimberlitic. The bodies erupted at circa 540 Ma (Rb-Sr phlogopite). Five of the kimberlites have proven to be diamondiferous including the 12 hectare 'Iceberg' kimberlite (Counts 2008).

Samples

Mantle xenoliths were collected from kimberlite float above proven kimberlite targets across the property. Most of the surface kimberlite is highly altered and hence the peridotite xenoliths they contain are generally serpentized or deeply-weathered. A total of 33 mantle xenoliths exceeding one cm in maximum dimension (14 peridotites and 19 "eclogites") were selected for mineral chemistry and bulk analysis. After the xenoliths were removed from the kimberlite, the remaining kimberlite was crushed for kimberlite indicator mineral separation to allow for a larger suite of kimberlite indicator minerals (KIMs) to be analyzed. Because of the small numbers of mantle xenoliths recovered the KIM suite permits a more statistically valid determination of the mantle mineralogy and lithological variation beneath the Darby kimberlite field.

Results

Peridotites: Fresh olivine within the peridotite xenoliths is scarce. Olivine in 11 peridotitic samples have a median Mg# of 92.5, indistinguishable from the median value of 92.6 that is typical of cratonic peridotites world-wide (Pearson and Wittig 2014). Four of the 14 peridotitic xenoliths contain fresh garnet. Of these, garnet in one sample is classified as harzburgitic (G10), giving a minimum pressure of 4.7 GPa using the P₃₈ geobarometer (38 mW/m² model geothermal gradient), while garnets from three peridotites are classified as lherzolitic (G9) using the Grütter et al. (2004) classification scheme. Of the garnets picked from the kimberlite concentrate, 52 grains (18 %) are peridotitic. Of these, 98 % are lherzolitic, in two distinct groups (31% "on-craton" i.e., lower Ca/Cr, 67 % "off-craton" i.e., higher Ca/Cr) and 2 % wehrlite (G12). Two of the garnet-bearing peridotites display "sinusoidal" garnet rare earth element patterns which are often associated with rocks that have interacted with a diamond forming fluid (Stachel and Harris 2008), and of these the harzburgitic (G10) garnet has the strongest "sinusoidal" pattern. The other two garnet peridotites have garnets that are light rare earth element depleted with La < C1 chondrite and heavy rare earth element enriched (~ 10 x C1 chondrite), typical of lherzolitic garnets from cratonic peridotites (Stachel and Harris 2008).

Eclogites: The garnets from 19 "eclogite" samples are relatively Ca-poor and range from pyrope to almandine on a Mg-Ca-Fe ternary. From these eclogite xenoliths 53 % are classified as pyroxenitic (G4) and 47% eclogitic (G3). The majority of the garnet concentrate (239 grains or 82 %) contained

less than 1 wt. % Cr₂O₃, and of these 5 % fall into the unclassified (G0) field, 32 % in the pyroxenitic (G4) field, and 63 % in the eclogitic (G3) field. Garnets from the eclogitic xenoliths have low TiO₂ and low Na₂O, plotting away from the eclogitic diamond inclusion field of Gurney and Zweistra (1995). Therefore, these eclogites are most likely from shallow depths outside the diamond stability field. Traditionally, to classify these eclogitic garnets as having a mantle or crustal origin, the approach of Schulze (2003) has been employed, which utilizes Ca# and Mg# as variables. This approach classified all of our xenoliths as being mantle-derived, and assigns 82 % of our eclogitic concentrate as mantle-derived. The majority of the eclogites are primarily biminerally with respect to garnet and clinopyroxene (~ 60:40 modal abundance, respectively, ± trace rutile); however, one sample was identified petrographically as a plagioclase-bearing garnet-pyroxenite. This petrographic assessment classified this xenolith as crustal in origin, in conflict with the Schulze (2003) classification. The Hardman et al. (submitted) graphical classification scheme reduces the failure rate of crustal garnets by employing log-normalised Pearce element ratios of Ti. The method correctly classifies the plagioclase pyroxenite in our dataset as crustal and reduces the number of classified “mantle-derived” xenoliths from 100 to 47 %, and “mantle-derived” concentrate garnets from 82 % to 19 %. The Hardman et al. (submitted) graphical method defines fields where 66 % and 95 % of the scheme training data fail or are misclassified. Most of our xenolith garnet data falls within the 66 % failure envelope suggesting that crust or mantle classifications of such data are less certain. It is inferred that they are derived from very close to the crust-mantle boundary. Of 11 “eclogitic” xenoliths with fresh clinopyroxene, nine are classified as garnet-pyroxenites containing low jadeite clinopyroxene, thus most of the “eclogites” studied at Darby should be referred to as pyroxenitic.

Geotherm: Darby peridotite xenoliths were too altered to perform multiphase thermobarometry. Instead, clinopyroxenes, selected based on compositional filters of Nimis and Taylor (2000) from kimberlite heavy mineral concentrate yield a 37-39 mW/m² preliminary geotherm for the West Central Rae lithosphere and indicate a lithospheric thickness of ~ 200 km. Using averaged Ni-in-garnet temperatures calculated from Griffin et al. (1989) and Canil (1999), four garnet peridotites and 49 peridotitic garnets from concentrate yield two distinct modes in mantle sampling depths. A cluster of samples from the higher Ca/Cr Iherzolitic garnets equilibrated at 765 to 920 °C and a group of peridotitic garnets (50 % of xenoliths and 28 % of concentrate) from the lower Ca/Cr Iherzolitic garnets (94 %) have anomalously high Ti concentrations and very high Ni, yielding unreasonable T_{Ni} values of >> 1400 °C. In addition, the aluminum-in-olivine thermometer of Bussweiler et al. (2017) was applied to olivine from concentrate and xenoliths based on applying the Al – V based “garnet facies” compositional filters outlined by Bussweiler et al. (2017). This yielded two distinct mantle sampling depths from 785 to 1005 °C, in broad agreement with the Ni-in-garnet sampling mode and 1140 to 1390 °C, suggesting deep mantle sampling of thermally disturbed lithosphere close to the lithosphere-asthenosphere boundary. The Ni-in-garnet and Al-in-olivine temperatures show that the Darby kimberlite field is sampling a large depth region across the geotherm.

Age of lithospheric mantle: Osmium isotope analyses of the Darby peridotites reveal that they are highly unradiogenic. Whole-rock Re-depletion ages range from Mesoarchean to Paleoproterozoic. The pyroxenite xenoliths have very radiogenic Os isotope compositions and provide the first age information from pyroxenites/“eclogites” beneath the Rae craton. Their resulting Archean whole rock T_{MA} ages are consistent with a Mesoarchean age of the western Central Rae lithosphere, older than the lithosphere beneath the Repulse Bay block in the East section of the Rae craton (Liu et al. 2016).

Conclusions

The highly depleted olivine compositions, thick cold lithosphere, and Archean ages of the Darby peridotite xenoliths clearly indicate the presence of thick cold cratonic lithospheric mantle beneath the western segment of the central Rae craton circa 540 Ma. The Archean model ages of most of the pyroxenites support this, notwithstanding the fact that some of these rocks could be sampling either crust or mantle lithologies very close to the crust-mantle boundary. The anomalously high abundance of pyroxenite in xenoliths and in garnet concentrate at Darby (58 % of xenoliths and 82 % of

concentrate: every field location yielded such xenoliths) is at odds with the abundance of eclogite/pyroxenite thought to be present in cratonic lithospheric mantle from xenocryst studies (~ one to ~ five %; Schulze, 1989; Dawson and Stephens, 1975). However, a significant portion of these rocks could originate from the lower crust, or from a pyroxenite-enriched layer in the very shallow mantle, close to the Moho. If the amount of pyroxenite is an accurate reflection of the deeper crust or shallow lithosphere beneath Darby, the high abundance of these may be related to the proximity of the field to the proposed suture between the Committee Block and the Queen Maud Block to the far West of the Rae craton. In terms of diamond potential, the low pressure nature of the abundant pyroxenitic component sampled by Darby kimberlites is non-prospective. However, the recovery of a harzburgitic (G10) garnet-bearing xenolith in a small sample of mantle xenoliths is encouraging evidence of diamond-facies peridotitic mantle being sampled. Furthermore, garnet T_{Ni} and olivine T_{Al} suggest a fairly wide diamond window is being sampled. The presence of very high T_{Ni} in some peridotitic garnets and Al-in-olivine temps approaching 1400 °C, along with the abundant higher Ca/Cr Iherzolitic garnets are indicative of late thermal disturbance of the lowermost lithosphere, close to kimberlite eruption. This heating event may have reduced the diamond tenor of the lithosphere. Further studies are on-going to better evaluate the diamond potential of the Darby cratonic mantle.

References

- Bussweiler Y, Brey GP, Pearson DG, Stachel T, Stern RA, Hardman MF, Kjarsgaard BA, Jackson SE (2017) The aluminum-in-olivine thermometer for mantle peridotites — Experimental versus empirical calibration and potential applications. *Lithos* 272–273:301–314
- Canil D (1999) The Ni-in-garnet geothermometer: calibration at natural abundances. *Contrib Mineral Petrol* 136:240-246
- Counts B (July 31, 2008) Indicator Minerals' Darby Project Yields More Kimberlite; Partner Increases Budget. In: Market Wired. Indicator Minerals Inc. Available via PRESS RELEASE <http://www.marketwired.com/press-release/indicator-minerals-darby-project-yields-more-kimberlite-partner-increases-budget-tsx-venture-ime-884912.htm>. Accessed May 15, 2017
- Dawson JB, Stephens WE (1975) Statistical Classification of Garnets from kimberlite and Associated Xenoliths. *The Journal of Geology* 83(5):589-607
- Griffin WL, Cousens DR, Ryan CG, Sie SH, Suter GF (1989) Ni in chrome pyrope garnets: a new geothermometer. *Contributions to Mineralogy and Petrology* 103(2):199-202
- Grütter HS, Gurney JJ, Menzies AH, Winter F (2004) An updated classification scheme for mantle-derived garnet, for use by diamond explorers. *Lithos* 77:841-857
- Gurney JJ, Zweistra, P (1995) The interpretation of the major element compositions of mantle minerals in diamond exploration. *Journal of Geochemical Exploration* 53:293-309
- Hardman MF, Pearson DG, Stachel T, Sweeney RJ (submitted) Statistical approaches to the discrimination of crust- and mantle-derived low-Cr garnet -- major-element-based methods and their application in diamond exploration. *Journal of Geochemical Exploration*
- Liu J, Riches AJV, Pearson DG, Luo Y, Kienlen B, Kjarsgaard BA, Stachel T, Armstrong JP (2016) Age and evolution of the deep continental root beneath the central Rae craton, northern Canada. *Precambrian Research* 272:168-184
- Nimis P, Taylor WR (2000) Single clinopyroxene Thermobarometry for garnet peridotites Part 1. Calibration and testing of Cr-in-Cpx barometer and an enstatite-in-Cpx thermometer. *Contrib Mineral Petrol* 139:541-554
- Pearson DG, Wittig N (2014) 3.6 - The formation and evolution of the subcontinental mantle lithosphere - evidence from mantle xenoliths. In: *Treatise of Geochemistry* 2nd edition, Elsevier, Oxford, pp 255–292
- Schulze DJ (1989) Constraints on the abundance of eclogite in the upper mantle. *Journal of Geophysical Research* 94(B4):4205-4212
- Schulze DJ (2003) A classification scheme for mantle-derived garnets in kimberlite: a tool for investigating the mantle and exploring for diamonds. *Lithos* 71(2–4):195–213
- Stachel T, Harris JW (2008) The origin of cratonic diamonds - Constraints from mineral inclusions. *Ore Geology Reviews* 34(1–2): 5–32



Oxidation state of majoritic inclusions in diamond

Kiseeva E.S.¹, Vasiukov D.M.^{2,3}, Wood B.J.¹, Stachel T.⁴, McCammon C.A.³, Chumakov A.⁵, Harris J.W.⁶, Dubrovinsky L.S.³

¹ – Department of Earth Sciences, University of Oxford, UK, kate.kiseeva@earth.ox.ac.uk, berniew@earth.ox.ac.uk

² – Laboratory of Crystallography, University of Bayreuth, Germany, vasyukov@physics.msu.ru

³ – Bayerisches Geoinstitut, Universität Bayreuth, Germany, catherine.mccammon@uni-bayreuth.de, Leonid.Dubrovinsky@uni-bayreuth.de

⁴ – Department of Earth and Atmospheric Sciences, University of Alberta, Canada, tstachel@ualberta.ca

⁵ – ESRF-The European Synchrotron, Grenoble, France, chumakov@esrf.fr

⁶ – School of Geographical and Earth Sciences, University of Glasgow, UK, Jeff.Harris@glasgow.ac.uk

Introduction

Inclusions in diamond are the only currently known samples from the mantle transition zone and the lower mantle. Majoritic garnet is a rare inclusion (to date only ~150-200 crystals have been reported), but its Si content is indicative of its depth of re-equilibration and it therefore has the potential to provide a depth profile of composition and properties such as oxidation state in the transition zone.

In this study, we use a novel technique – the Synchrotron Mössbauer Source (SMS) (beamline ID18 at ESRF) to determine the ferric-ferrous ratios of 13 small (30 to 100 micrometers in diameter) majoritic inclusions in diamonds from Jagersfontein. The inclusions were initially studied by X-ray diffraction at the Extreme Conditions Beamline (ECB), P02.2, at the PETRA III synchrotron, Hamburg and confirmed as predominantly monophase garnet single crystals or (in very few cases) as aggregates of single crystals. There is good agreement between determinations of Fe³⁺/Fe_{tot} using Mössbauer spectroscopy and single crystal X-ray refinement as well as calculations based on composition assuming stoichiometry.

Results and discussion

The major element compositions of studied inclusions are listed in Table 1.

| Sample | SiO ₂ | TiO ₂ | Al ₂ O ₃ | Cr ₂ O ₃ | FeO _{tot} | MnO | MgO | CaO | Na ₂ O | K ₂ O | P ₂ O ₅ | Total | Pressure , GPa | Fe ³⁺ /ΣFe |
|--------|------------------|------------------|--------------------------------|--------------------------------|--------------------|------|-------|-------|-------------------|------------------|-------------------------------|--------|----------------|-----------------------|
| JF-01A | 42.67 | 0.13 | 19.95 | 0.24 | 12.58 | 0.42 | 17.51 | 6.14 | 0.15 | | 0.02 | 99.81 | 8.10 | 0.12(2) |
| JF-09A | 42.38 | 0.09 | 21.03 | 0.08 | 14.08 | 0.40 | 16.19 | 6.11 | 0.20 | 0.01 | 0.02 | 100.59 | 7.88 | 0.11(3) |
| JF-22A | 48.69 | 0.50 | 9.65 | 0.22 | 11.74 | 0.36 | 21.74 | 5.73 | 0.65 | 0.01 | 0.09 | 99.37 | 17.88 | 0.27(3) |
| JF-37A | 42.46 | 0.17 | 20.64 | 0.14 | 12.95 | 0.38 | 16.88 | 6.46 | 0.14 | 0.01 | 0.02 | 100.24 | 7.74 | 0.08(5) |
| JF-37B | 42.36 | 0.19 | 20.68 | 0.12 | 12.93 | 0.37 | 16.82 | 6.40 | 0.14 | 0.01 | 0.01 | 100.03 | 7.71 | 0.12(3) |
| JF-39A | 45.20 | 0.31 | 15.01 | 0.24 | 10.76 | 0.24 | 20.29 | 5.67 | 0.37 | 0.01 | 0.03 | 98.13 | 13.47 | 0.20(1) |
| JF-42A | 43.40 | 0.54 | 17.38 | 0.03 | 12.89 | 0.36 | 13.35 | 11.16 | 0.54 | 0.02 | 0.01 | 99.67 | 13.04 | 0.17(3) |
| JF-44B | 44.12 | 0.32 | 17.87 | 0.31 | 11.75 | 0.30 | 17.73 | 7.97 | 0.18 | 0.01 | 0.02 | 100.58 | 10.15 | 0.15(3) |
| JF-50A | 42.53 | 0.09 | 21.00 | 0.15 | 13.18 | 0.36 | 17.72 | 4.87 | 0.19 | 0.01 | 0.02 | 100.11 | 7.94 | 0.08(1) |
| JF-55A | 47.94 | 0.41 | 11.91 | 0.34 | 9.44 | 0.25 | 21.99 | 7.41 | 0.43 | 0.02 | 0.02 | 100.15 | 15.56 | 0.30(3) |
| JF-58A | 43.31 | 0.28 | 18.09 | 0.19 | 14.69 | 0.41 | 18.20 | 4.62 | 0.27 | 0.01 | 0.03 | 100.08 | 10.30 | 0.15(2) |
| JF-58B | 43.67 | 0.28 | 18.41 | 0.17 | 14.63 | 0.40 | 18.42 | 4.62 | 0.26 | 0.01 | 0.03 | 100.90 | 9.92 | 0.27(5) |
| JF-84A | 44.25 | 0.41 | 17.27 | 0.30 | 11.69 | 0.31 | 18.81 | 6.36 | 0.30 | 0.01 | 0.02 | 99.72 | 11.50 | 0.15(4) |

Table 1. Major element compositions, pressure and ferric iron contents of analysed majoritic garnet inclusions (Tappert et al., 2005; Beyer and Frost, 2017).

The garnet inclusions we have studied are, in common with most other majorite inclusions, pyroxenitic in composition in that they follow the peridotite “trend” on a plot of M²⁺ versus (M⁴⁺+M⁵⁺) (see Kiseeva et al., 2013 for details), but are low in Cr₂O₃ (0.03-0.34 wt%) and Mg# (0.65-0.81) and high in CaO (4.62-11.2 wt%) (Table 1, Fig. 1).

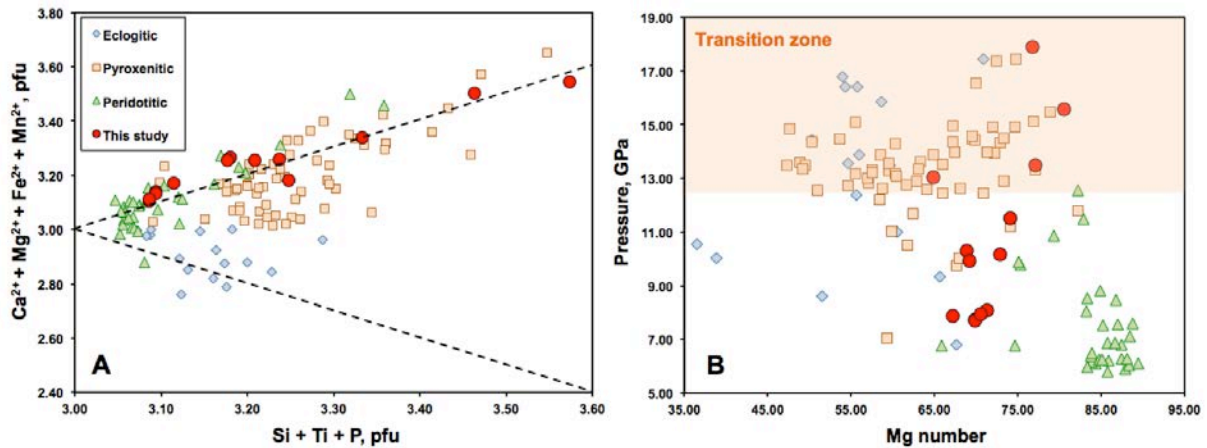


Figure 1. Majoritic garnet inclusions in diamonds worldwide (literature data from Kiseeva et al., 2013). Inclusions studied here from the Jagersfontein kimberlite are shown by red circles. In order to compare compositions with those of previous studies, all iron has been calculated as Fe^{2+} . (A) Divalent cations plotted against Si, Ti and P. (B) Pressure according to Beyer and Frost (2017) geobarometer plotted against Mg number.

Our measurements show an increase in $\text{Fe}^{3+}/(\text{Fe}^{2+} + \text{Fe}^{3+})$ with increasing amount of majorite substitution and hence pressure (Fig. 2). Assuming the presence of pyroxene in the pyroxenitic diamond substrates, garnet compositions yield pressures of formation of 7.7-17.9 GPa using the Beyer and Frost majorite geobarometer (Beyer and Frost, 2017). These are minimum pressures, however, because equilibrium with pyroxene has not been demonstrated. Figure 2 shows that $\text{Fe}^{3+}/(\text{Fe}^{2+} + \text{Fe}^{3+})$ is extremely well correlated with calculated pressure, increasing from 0.08 at 7.7 GPa to values between 0.30 at 16 GPa and 0.27 at 18 GPa. Note that at least 4 of these 13 garnets were formed at (minimum) pressures of 13 to 18 GPa and, therefore crystallised in the transition zone (410-660 km depth). It is also interesting to note that our measured $\text{Fe}^{3+}/(\text{Fe}^{2+} + \text{Fe}^{3+})$ values define a clear extension of the trend apparent in the data from peridotite xenoliths crystallised at lower pressures and that Fe from the transition zone garnets is at least twice as oxidised as in any garnet from xenoliths of subcratonic lithospheric mantle.

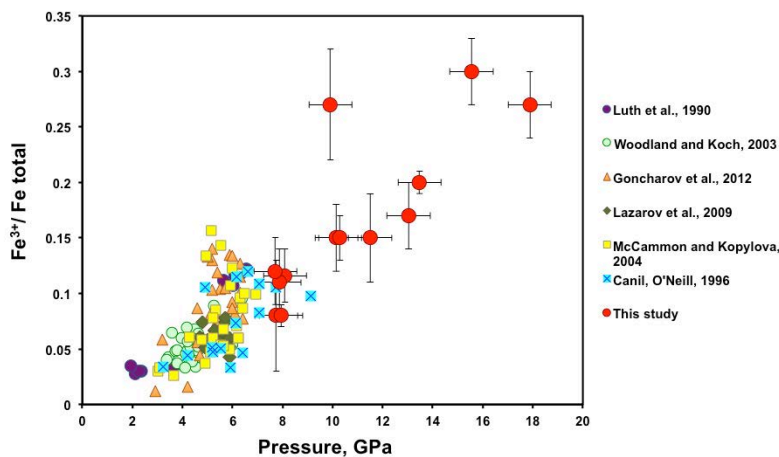
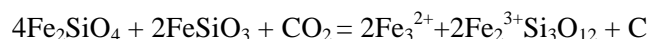


Figure 2. Ferric iron contents of majoritic garnets from Jagersfontein diamonds compared to lithospheric garnets from peridotite xenoliths. All ferric iron contents determined by Mössbauer spectroscopy. Data from Luth et al., 1990; Canil and O'Neill, 1996; Woodland and Koch, 2003; McCammon and Kopylova, 2004; Lazarov et al., 2009 and Goncharov et al., 2012.

The $\text{Fe}^{3+}/\text{Fe}^{2+}$ ratio of mantle minerals has been commonly used to determine the oxidation state of the mantle. According to experimental data and thermodynamic calculations, with increasing depth, $f\text{O}_2$ should decrease at constant $\text{Fe}^{3+}/\text{Fe}^{2+}$ ratio (Wood et al., 1990), driving carbonate into the diamond

stability field. Carbonate would therefore be unstable and should oxidise Fe²⁺ into Fe³⁺, with the latter dissolving into garnet according to reactions such as:



This reaction implies that garnet in equilibrium with carbon (in the form of diamond) should have elevated Fe³⁺/Fe²⁺ ratios, consistent with our new observations. To our knowledge, these are the first data bearing on the oxidation state of majoritic garnets derived from the mantle transition zone.

Our results show that the mantle transition zone is highly heterogeneous and suggest that the diamond-forming process is intimately linked with the oxidation state of garnet according to reactions such as proposed above.

References

- Beyer, C., Frost, D.J. (2017) The depth of sub-lithospheric diamond formation and the redistribution of carbon in the deep mantle. *Earth and Planetary Science Letters*, 461: 30-39.
- Canil, D., O'Neill, H.S.C. (1996) Distribution of ferric iron in some upper-mantle assemblages. *Journal of Petrology*, 37(3): 609-635.
- Goncharov, A.G., Ionov, D.A., Doucet, L.S., Pokhilenko, L.N. (2012) Thermal state, oxygen fugacity and C-O-H fluid speciation in cratonic lithospheric mantle: New data on peridotite xenoliths from the Udachnaya kimberlite, Siberia. *Earth and Planetary Science Letters*, 357: 99-110.
- Kiseeva, E.S. et al. (2013) Metapyroxenite in the mantle transition zone revealed from majorite inclusions in diamonds. *Geology*.
- Lazarov, M., Woodland, A.B., Brey, G.P. (2009) Thermal state and redox conditions of the Kaapvaal mantle: A study of xenoliths from the Finsch mine, South Africa. *Lithos*, 112: 913-923.
- Luth, R.W., Virgo, D., Boyd, F.R., Wood, B.J. (1990) Ferric iron in mantle-derived garnets - implications for thermobarometry and for the oxidation state of the mantle. *Contributions to Mineralogy and Petrology*, 104(1): 56-72.
- McCammon, C., Kopylova, M.G. (2004) A redox profile of the Slave mantle and oxygen fugacity control in the cratonic mantle. *Contributions to Mineralogy and Petrology*, 148(1): 55-68.
- Tappert, R. et al. (2005) Diamonds from Jagersfontein (South Africa): messengers from the sublithospheric mantle. *Contributions to Mineralogy and Petrology*, 150(5): 505-522.
- Wood, B.J., Bryndzia, L.T., Johnson, K.E. (1990) Mantle oxidation state and Its relationship to tectonic environment and fluid speciation. *Science*, 248(4953): 337-345.
- Woodland, A.B., Koch, M. (2003) Variation in oxygen fugacity with depth in the upper mantle beneath the Kaapvaal craton, Southern Africa. *Earth and Planetary Science Letters*, 214(1-2): 295-310.



Age of the Lithospheric Mantle Beneath the Karowe Diamond Mine

Matthew Wudrick¹, D. Graham Pearson¹, Thomas Stachel¹, John Armstrong², Sarah J. Woodland¹, Theetso Motsamai¹

¹University of Alberta, Edmonton, Canada, mwudrick@ualberta.ca, dgpearson@ualberta.ca, tstachel@ualberta.ca, sjwoodlan@ualberta.ca, motsamai@ualberta.ca

²Lucara Diamond Corp., Vancouver, Canada, johna@namdo.com

Introduction

The Karowe Diamond Mine has been developed by Lucara Diamond Corp following evaluation of the AK6 kimberlite pipe in north-central Botswana. The AK6 pipe erupted through the early Proterozoic (~1.8 Ga) Magondi Belt on the western edge of the Zimbabwe craton. The pipe formed as a part of the cretaceous Orapa Kimberlite Cluster, and is situated approximately 25 kilometers south of the Orapa mine, and 25 kilometers west of the Letlhakane mine. The Karowe Mine is characterised by the recovery of numerous large, Type IIa diamonds, including the 1,111 carat Lesedi La Rona. A study of mantle xenoliths from Karowe has been undertaken to characterise the level of depletion and any cryptic metasomatic alteration. Re-Os dating has also been performed to determine the age of the lithospheric mantle sampled by the kimberlite, and to determine the extent of lithospheric overprinting or new lithosphere formation caused by the Magondi event.

Sample Description and Petrography

A suite of 19 peridotite xenoliths were selected for analysis from a selection gathered from the mine's coarse tailings. The samples were analysed for mineral chemistry (EPMA and LA-ICP-MS), bulk rock major elements (XRF), and Re-Os plus platinum group elements. Mineral assemblages include clinopyroxene, present as bright green chromium diopside, orthopyroxene, olivine and either spinel or garnet. All samples are lherzolitic in composition. 14 samples are spinel lherzolites and five are garnet lherzolites. Three of the garnet lherzolites also have amphibole in the form of pargasite present, likely due to metasomatic infiltration. All samples can be described as coarse equant with granuloblastic textures, based on the classification of Harte (1977). Despite the close spatial occurrence of Karowe to Orapa, Orapa's mantle xenolith population is dominated by eclogites (McDonald & Viljoen, 2006) while Karowe yields abundant peridotites, with relatively few eclogites recovered so far. A garnet pyroxenite xenolith component, defined here as containing Al-augite rather than omphacite as clinopyroxene, is also evident and more abundant than eclogites.

Clinopyroxene is found dispersed throughout the peridotite samples, and can be intergrown with other phases. Secondary clinopyroxene associated with veining was observed in only one sample. In garnet-bearing samples, clinopyroxene often forms clusters, involving pargasite if present. Phlogopite is absent in the sample found. Few, small sulfide clusters can be found in the garnet-bearing samples. The peridotite xenoliths have orthopyroxene contents averaging ~ 30 vol%, comparing well with Kaapvaal Craton xenoliths.

Mineral Chemistry

The forsterite (Fo) contents of olivine - a measure of melt depletion - range from Fo₉₁ to Fo₉₃. This range in Fo content overlaps the mean Fo of peridotites from the Kaapvaal craton at Fo_{92.6} (Pearson & Wittig, 2008). Samples with higher Fo content contain less clinopyroxene, consistent with an origin during higher degrees of melt-depletion. Samples with lower Fo content tend to be garnet-bearing, with an average of Fo_{91.5}.

Ni-in-garnet thermometry was calculated, based on an average of Canil (1999) and Griffin et al. (1989), using the Ni content obtained from LA-ICP-MS analysis of garnet plus the Ni content of the coexisting olivine from each sample. This gives temperatures that range within 60°C, from 790°C to 850°C.

In the 10 peridotites analysed for Os isotopes so far, the concentrations of osmium range widely, from 0.32 to 6.35 ppb. This range brackets the average cratonic mantle value of ~3.8 ppb Os (Pearson et al., 2003; Aulbach et al. 2016). The concentration of osmium does not correlate with Os isotopic ratios. The Os isotope data is multi-modal in nature. The unradiogenic $^{187}\text{Os}/^{188}\text{Os}$ values range from 0.109 to 0.114. This range overlaps the mode of values from elsewhere in the Kaapvaal and Kalahari cratons (Pearson et al., 2004). Samples with radiogenic $^{187}\text{Os}/^{188}\text{Os}$ (0.1260 to 0.1295) overlap modern convecting mantle values. These highly radiogenic values come from samples that have relatively high modal abundances of clinopyroxene.

T_{RD} ages relative to E-chondrite show a peak at 2.6 Ga and are as low as 2.0 Ga.

Discussion

The xenoliths sampled from the mantle at Karowe come predominantly from the shallow mantle, the spinel facies, and only a few samples extend into the garnet facies. Garnet-bearing peridotites have a minimum pressure of 19-23 kbar, based on Cr_2O_3 and CaO content (Grütter et al., 2006). In contrast, peridotite-derived xenocrysts show much deeper sampling of the mantle, which is consistent with the diamondiferous nature of the Karowe pipe (Motsamai, in prep.).

The T_{RD} model ages for the lithospheric mantle beneath Karowe range widely. The population peaks at the oldest ages (2.6 Ga), which are derived from peridotites with the highest Fo contents and with the lowest modal abundance of diopside. This Neoproterozoic age peak at Karowe agrees well with the main mode of Re depletion ages for peridotites from the Kaapvaal craton (Pearson & Wittig, 2008), and also coincides with the peak in ages from base-metal poor, highly depleted peridotites from the nearby Letlhakane Mine (Luguet et al., 2015) and from the Murowa Mine on the southern edge of the Zimbabwe Craton (Pearson et al., in press).

The younger, circa 2 to 2.3 Ga Re depletion ages seen at Karowe are not found in peridotites from Letlhakane and are sparse at Murowa. These Paleoproterozoic ages overlap with the formation age of the Bushveld Intrusive Complex at ~2.0 Ga (Olsson et al., 2010). The two peridotites with the most radiogenic Os and highest abundances of clinopyroxene yield Phanerozoic model ages. This likely reflects metasomatic disturbance closely related to kimberlite activity in the Cretaceous, with associated introduction of metasomatic diopside and radiogenic Os hosted in sulfides.

Our preliminary conclusion is that the lithospheric mantle beneath both the Karowe Mine - and the Orapa Kimberlite Field in general - is typical depleted Archean cratonic lithospheric mantle, formed in the Neoproterozoic. Similar to the conclusion reached by Stiefenhofer et al. (1997) at Letlhakane, these Archean ages imply thrusting of the Magondi belt over pre-existing Zimbabwe Craton lithospheric mantle. This cratonic mantle, however, has a strong metasomatic overprint that could be related to either the large-scale Bushveld intrusive event, or to metasomatic fluids associated with the ~1.8 Ga formation of the Magondi Belt. We note that the range in ages presented here, especially the relatively frequent occurrence of peridotites with 2 Ga model ages, is similar to the age spectrum seen in peridotites from the Premier mine, which also produces large Type IIa gem diamonds.

References

- Aulbach, S., Mungall, J. E., & Pearson, D. G. (2016). Distribution and processing of highly siderophile elements in cratonic mantle lithosphere. *Reviews in Mineralogy and Geochemistry*, 81(1), 239-304.

- Canil, D. (1999). The Ni-in-garnet geothermometer: calibration at natural abundances. *Contributions to Mineralogy and Petrology*, 136(3), 240-246.
- Griffin, W. L., Cousens, D. R., Ryan, C. G., Sie, S. H., & Suter, G. F. (1989). Ni in chrome pyrope garnets: a new geothermometer. *Contributions to Mineralogy and Petrology*, 103(2), 199-202.
- Grütter, H., Latti, D., & Menzies, A. (2006). Cr-saturation arrays in concentrate garnet compositions from kimberlite and their use in mantle barometry. *Journal of Petrology*, 47(4), 801-820.
- Harte, B. (1977). Rock nomenclature with particular relation to deformation and recrystallisation textures in olivine-bearing xenoliths. *The Journal of Geology*, 85(3), 279-288.
- Luguet, A., Behrens, M., Pearson, D. G., König, S., & Herwartz, D. (2015). Significance of the whole rock Re–Os ages in cryptically and modally metasomatised cratonic peridotites: Constraints from HSE–Se–Te systematics. *Geochimica et Cosmochimica Acta*, 164, 441-463.
- McDonald, I., & Viljoen, K. S. (2006). Platinum-group element geochemistry of mantle eclogites: a reconnaissance study of xenoliths from the Orapa kimberlite, Botswana. *Applied Earth Science*, 115(3), 81-93.
- Motsamai, T. (In Prep.) (Unpublished doctoral thesis). University of Alberta, Edmonton, Canada
- Olsson, J. R., Söderlund, U., Klausen, M. B., & Ernst, R. E. (2010). U–Pb baddeleyite ages linking major Archean dyke swarms to volcanic-rift forming events in the Kaapvaal craton (South Africa), and a precise age for the Bushveld Complex. *Precambrian Research*, 183(3), 490-500.
- Pearson, D. G., Canil, D., & Shirey, S. B. (2003). Mantle samples included in volcanic rocks: xenoliths and diamonds. *Treatise on geochemistry*, 2, 568.
- Pearson, D. G., Irvine, G. J., Ionov, D. A., Boyd, F. R., & Dreibus, G. E. (2004). Re–Os isotope systematics and platinum group element fractionation during mantle melt extraction: a study of massif and xenolith peridotite suites. *Chemical Geology*, 208(1), 29-59.
- Pearson, D. G., & Wittig, N. (2008). Formation of Archaean continental lithosphere and its diamonds: the root of the problem. *Journal of the Geological Society*, 165(5), 895-914.
- Pearson, D. G., & Wittig, N. (2014). 3.6-The Formation and Evolution of Cratonic Mantle Lithosphere–Evidence from Mantle Xenoliths.
- Pearson, D. G., Liu, J., Smith, C. B., Mather, K. A., Krebs, M. Y., Bulanova, G. P., & Kobussen, A. (in press). Characteristics and origin of the mantle root beneath the Murowa diamond mine: Implications for craton and diamond formation. Chapter X: Special Publication of the Society of Economic Geologists
- Stiefenhofer, J., Viljoen, K. S., & Marsh, J. S. (1997). Petrology and geochemistry of peridotite xenoliths from the Letlhakane kimberlites, Botswana. *Contributions to Mineralogy and Petrology*, 127(1), 147-158.



Primitive melt composition of the Bultfontein Kimberlite (South Africa).

Ashton Soltys¹, Andrea Giuliani^{1,2}, David Phillips¹

¹ *KiDs (Kimberlites and Diamonds), School of Earth Sciences, The University of Melbourne, Parkville, 3010 Victoria, Australia*

soltysa@student.unimelb.edu.au

² *ARC Centre of Excellence for Core to Crust Fluid Systems and GEMOC, Department of Earth and Planetary Sciences, Macquarie University, North Ryde, 2019 NSW, Australia*

Introduction

The compositions of kimberlite melts at depth remain elusive. This can be attributed to the unquantified effects of multiple complex processes (e.g., alteration, assimilation, and incorporation of xenogenic material) which modify kimberlites pre-, syn- and post-emplacement. In turn, our inability to accurately constrain the composition and physical properties of kimberlite melts prevents a comprehensive understanding of their petrogenesis.

Method and Approach

To improve constraints on the compositions of kimberlite melts, we have adopted a new approach to reconstruct primitive melt compositions, which combines detailed modal analysis, including discerning xenocrystic from magmatic phases, and determination of mineral compositions. The accuracy of this reconstruction process is validated by the similarity between reconstructed and measured whole-rock values. To this reconstructed whole-rock composition we apply a series of corrections and assumptions to account for the effects of post-emplacement alteration (dominantly serpentinisation) as well as the inclusion and assimilation of mantle material. This reconstruction method involves a number of different stages which are outlined below.

Stage 1: Whole-rock reconstruction.

Stage 2: Correction for pseudomorphic serpentinisation of monticellite, assuming a constant volume replacement process occurring in an open system (e.g., Sparks et al. 2009). We model this generation of pseudomorphic serpentine as having a completely deuteric origin because monticellite is enclosed in carbonates with magmatic textures and composition.

Stage 3: Formation of matrix serpentine from deuteric (*Model I*), external (*Models II to IV*) or mixed fluids (*Model V*). In addition to modeling different fluid sources, the replaced phases (*Models III to V*) vary between models. In *Model A* serpentine is considered a primary deuteric phase (e.g., Mitchell 2013), whereas in *Model B* matrix serpentine is considered a secondary phase (e.g., Afanasyev et al. 2014). *Models C* and *D* involve replacement of various combinations of alkali-carbonate phases based on the suggestions of Kamenetsky et al. (2014). Finally, *Model E* considers serpentine is derived from 30% deuteric and 70% external fluids, where serpentine replaced carbonates (calcite and dolomite). This is our preferred model, and is based on detailed petrographic observations of sample BK (Giuliani et al., 2016).

Stage 4: Removal of xenocrystic components (i.e., olivine and phlogopite).

Stage 5: Correction for orthopyroxene assimilation, where the amount of orthopyroxene is estimated based on the amount of xenocrystic olivine in sample BK and the ratios of olivine to orthopyroxene in mantle xenoliths from the Kaapvaal craton.

Stage 6: Correction for clinopyroxene and garnet assimilation. The amount of clinopyroxene and garnet is estimated in the same way as orthopyroxene. In light of poor constraints on the extent of assimilation

of these phases, we model complete (C), and partial (P) assimilation of clinopyroxene and garnet (i.e., 60% and 40%, respectively – arbitrary values).

Results

The primitive melt reconstructed at from *Model E* (our preferred model) contains 22.2 wt.% SiO₂, 23.5 wt.% MgO, 23.8 wt.% CaO, ~1.8 wt.% H₂O, ~12.7 wt.% CO₂, 3.5 wt.% P₂O₅, 1.6 wt.% TiO₂, 1.2 wt.% Al₂O₃ and 0.8 wt.% K₂O, and has a Mg# value of 83.2 (see Table 1). When compared with *Model A* (i.e., all serpentine considered as dunitic), *Model E* contains significantly less SiO₂, and MgO, and more CaO and CO₂. This primitive melt composition (*Model E*) is also poorer in SiO₂, MgO and H₂O, but enriched in CaO and CO₂ compared with most previous reconstructions of primitive kimberlite melts based on southern African or Canadian samples (Table 1). The reconstructed primitive melt reported here is remarkably similar to the reconstructed primitive melt parental to the Majuagaa kimberlite, Greenland (Neilson and Sand, 2008).

These results suggest primitive kimberlites are transitional silicate-carbonate melts (i.e., melts with 18-32 wt.% SiO₂ + Al₂O₃), which become progressively enriched in SiO₂, MgO and to a lesser extent Al₂O₃ and Cr₂O₃ through the assimilation of lithospheric mantle material. Importantly, these results are seemingly not consistent with the suggestion that kimberlites are produced as SiO₂-free ‘carbonatitic’ melts that are converted to kimberlitic compositions by extensive assimilation.

| | XRF | Stage 1 | Stage 6 | | Total change‡ | | 1 | 2 | 3 | 4 | 5 |
|--------------------------------|-------|---------|----------------|----------------|----------------|----------------|-------|-------|-------|-------|-------|
| | | | <i>Model A</i> | <i>Model E</i> | <i>Model A</i> | <i>Model E</i> | | | | | |
| SiO ₂ | 30.66 | 30.83 | 26.02 | 22.18 | -4.81 | -8.65 | 26.50 | 25.60 | 31.79 | 26.70 | 17.47 |
| TiO ₂ | 1.54 | 1.18 | 1.55 | 1.56 | 0.37 | 0.38 | 2.20 | 3.35 | 0.72 | 1.73 | 4.99 |
| Al ₂ O ₃ | 1.83 | 1.32 | 1.19 | 1.18 | -0.13 | -0.14 | 2.20 | 3.31 | 3.08 | 1.57 | 2.27 |
| Cr ₂ O ₃ | 0.18 | 0.15 | 0.12 | 0.12 | -0.03 | -0.03 | n.d. | 0.24 | n.d. | 0.36 | 0.28 |
| FeO _t | 9.35 | 9.23 | 8.97 | 8.44 | -0.26 | -0.79 | 8.00 | 10.30 | 8.28 | 7.58 | 10.61 |
| MnO | 0.18 | 0.11 | 0.10 | 0.09 | -0.01 | -0.02 | n.d. | 0.21 | 0.19 | 0.18 | 0.24 |
| MgO | 31.42 | 31.21 | 25.50 | 23.47 | -5.71 | -7.74 | 26.50 | 27.20 | 30.77 | 28.25 | 23.98 |
| NiO | | 0.13 | 0.05 | 0.05 | -0.08 | -0.08 | 0.01 | 0.01 | n.d. | n.d. | 0.02 |
| CaO | 10.93 | 12.16 | 18.69 | 23.79 | 6.53 | 11.63 | 12.00 | 15.30 | 9.23 | 12.90 | 17.27 |
| Na ₂ O | 0.19 | 0.09 | 0.14 | 0.08 | 0.05 | -0.01 | n.d. | 0.28 | 0.10 | 0.10 | 0.13 |
| K ₂ O | 1.07 | 0.89 | 0.86 | 0.81 | -0.03 | -0.08 | 1.50 | 0.70 | 1.03 | 1.26 | 0.32 |
| P ₂ O ₅ | 1.82 | 2.66 | 3.55 | 3.54 | 0.89 | 0.88 | n.d. | 1.83 | 0.97 | 0.40 | 0.81 |
| BaO | 0.17 | 0.05 | 0.06 | 0.06 | 0.01 | 0.01 | n.d. | 0.01 | n.d. | n.d. | 0.16 |
| F | | 0.15 | 0.19 | 0.17 | 0.04 | 0.02 | n.d. | n.d. | n.d. | n.d. | n.d. |
| LOI | 9.20 | | | | 0.00 | 0.00 | | | | | |
| H ₂ O | | 2.48 | 3.18 | 1.76 | 0.70 | -0.72 | 12.30 | 6.20 | 8.72 | 9.07 | n.d. |
| CO ₂ | | 7.36 | 9.82 | 12.71 | 2.46 | 5.35 | 7.00 | 4.77 | 5.13 | 9.88 | n.d. |
| Sum | 98.5 | 100.0 | 100.0 | 100.0 | | | | | | | |
| Mg# | 85.7 | 85.8 | 83.5 | 83.2 | -2.26 | -2.56 | 86 | 82.5 | 86.9 | 86.9 | 80.1 |

Table 1: Measured and reconstructed whole-rock and primitive melt compositions. The following previous reconstructions of primitive kimberlite melts/magmas are shown for comparison: (1) Kimberley - Primary magma (le Roex et al. 2003); (2) Wesselton - Primitive melt (Shee 1985); (3) Lac de Gras - Low Ti Parental magma (Kjarsgaard et al. 2009); (4) Jerico - Primitive melt (before orthopyroxene assimilation - Kopylova et al. 2009); (5) Majuagaa - Parental melt (Neilson and Sand, 2008). ‡Total change represents the difference between reconstructed whole-rock value (i.e., Stage 1) and primitive melt (i.e., Stage 6).

Comparison between this primitive melt composition and experimentally produced low-degree melts of carbonated peridotite suggests the Bultfontein kimberlite could have been produced by ~0.5% melting of a lherzolitic source at 6.0-8.6 GPa (i.e., ~190-285 km) and 1420-1500 °C. The apparent lack

of excess heat required for melt generation combined with the low-degree of melting is inconsistent with conventional views of plume-induced magmatism. Therefore, alternative processes of melt generation such as volatile flux melting or decompression melting should be considered.

Production of kimberlite melts by decompression melting of ‘normal’ shallow asthenospheric mantle is unlikely unless the source was previously enriched in CO₂, K₂O, H₂O, and P₂O₅ via metasomatism. This could be achieved by long-term metasomatic redox pre-conditioning by carbonate-silicate melts (e.g., Yaxley et al. 2017). Alternatively, kimberlite melt generation may be triggered by volatile fluxing, when rising volatiles (i.e. fluids) interact with the source region (e.g., Bailey 1980; Tappe et al. 2013). These fluids would likely have high CO₂/H₂O ratios, and may also carry significant amounts of K₂O, H₂O and P₂O₅.

References

- Afanasyev A, Melnik O, Porritt L, Schumacher JC, Sparks, RSJ, (2014). Hydrothermal alteration of kimberlite by convective flows of external water. *Contributions to Mineralogy and Petrology*, 168 (1), 1-17.
- Bailey DK, (1980). Volatile flux, geotherms, and the generation of the kimberlite-carbonatite-alkaline magma spectrum. *Mineralogical Magazine*, 43 (330), 695-699.
- Giuliani A, Soltys A, Phillips D, Kamenetsky VS, Maas R, Goemann K, Woodhead JD, Drysdale RN, Griffin WL, (2016). The final stages of kimberlite petrogenesis: Petrography, mineral chemistry, melt inclusions and Sr-C-O isotope geochemistry of the Bultfontein kimberlite (Kimberley, South Africa). *Chemical Geology*.
- Kamenetsky VS, Golovin AV, Maas R, Giuliani A, Kamenetsky MB, Weiss Y, (2014). Towards a new model for kimberlite petrogenesis: Evidence from unaltered kimberlites and mantle minerals. *Earth-Science Reviews*, 139, 145-167.
- Kjarsgaard BA, Pearson DG, Tappe S, Nowell GM, Dowall DP, (2009). Geochemistry of hypabyssal kimberlites from Lac de Gras, Canada: comparisons to a global database and applications to the parent magma problem. *Lithos*, 112, 236-248.
- Kopylova MG, Matveev S, Raudsepp M, (2007). Searching for parental kimberlite melt. *Geochimica et Cosmochimica Acta*, 71 (14), 3616-3629.
- le Roex AP, Bell DR, Davis P, (2003). Petrogenesis of Group I Kimberlites from Kimberley, South Africa: Evidence from Bulk-rock Geochemistry. *Journal of Petrology*, 44 (12), 2261-2286.
- Nielsen TF, Sand KK, (2008). The Majuagaa kimberlite dike, Maniitsoq region, West Greenland: constraints on an Mg-rich silicocarbonatitic melt composition from groundmass mineralogy and bulk compositions. *The Canadian Mineralogist*, 46 (4), 1043-1061.
- Sparks RSJ, Brooker RA, Field M, Kavanagh J, Schumacher JC, Walter MJ, White J, (2009). The nature of erupting kimberlite melts. *Lithos*, 112, 429-438.
- Tappe S, Pearson DG, Kjarsgaard BA, Nowell G, Dowall D, (2013). Mantle transition zone input to kimberlite magmatism near a subduction zone: origin of anomalous Nd–Hf isotope systematics at Lac de Gras, Canada. *Earth and Planetary Science Letters*, 371, 235-251.
- Yaxley GM, Berry AJ, Rosenthal A, Woodland AB, Paterson D, (2017). Redox preconditioning deep cratonic lithosphere for kimberlite genesis-evidence from the central Slave Craton. *Scientific reports*, 7(1), 30.



Apatite from the Kimberley Kimberlites (South Africa): Petrography and Mineral Chemistry

Ashton Soltys¹, Andrea Giuliani^{1,2}, David Phillips¹

¹ *KiDs (Kimberlites and Diamonds), School of Earth Sciences, The University of Melbourne, Parkville, 3010
Victoria, Australia*

soltysa@student.unimelb.edu.au

² *ARC Centre of Excellence for Core to Crust Fluid Systems and GEMOC, Department of Earth and Planetary
Sciences, Macquarie University, North Ryde, 2019 NSW, Australia*

Introduction

Apatite ($\text{Ca}_5(\text{PO}_4)_3(\text{F}, \text{Cl}, \text{OH})$) is a common accessory phase in a variety of igneous, metamorphic, and sedimentary rocks on Earth, as well as a diverse range of extra-terrestrial bodies (e.g., the Moon, Mars, and meteorites). Apatite is a robust mineral that is commonly used in thermochronology and geochronology studies, for tracing magmatic evolution (e.g., Chakhmouradian et al., 2017), and as a discrimination tool for exploration purposes (e.g., Mao et al., 2016).

Apatite is a near ubiquitous, late-stage, groundmass phase in archetypal kimberlites worldwide (e.g., Mitchell, 1986). In addition, it is a magmatic phase that does not contain xenocrystic components, unlike many other apparently magmatic phases in kimberlites (e.g., spinel, olivine, ilmenite, mica). Despite this, major element data for apatite in kimberlitic apatite is sparse (e.g., Chakhmouradian et al., 2002; Mitchell, 1986), in contrast with the numerous analyses published for other kimberlitic minerals, such as olivine, spinel, and mica (e.g., Mitchell, 1986; Roeder and Schulze, 2008, and references therein). In this contribution, we report the petrography and major-minor element chemistry of apatite from the Kimberley kimberlites (South Africa). The studied samples are derived from the Kimberley Mine, De Beers, Wesselton (units W2 and W3 – Shee, 1985), Wesselton water tunnel sills, and Benfontein. The samples range in texture from “evolved” aphanitic kimberlites (i.e., without olivine macrocrysts - Benfontein) to highly macrocrystic kimberlites (i.e., ~30 vol.% olivine macrocrysts - Wesselton (W3) and Kimberley Mine).

Apatite Petrography

Apatite from the Kimberley kimberlites occurs in two textural settings: (1) discrete subhedral-euhedral hexagonal prisms, which range from ~1-100 μm in size, with most grains ~20-50 μm in length and characterised by hopper-like crystal forms; and (2) aggregates of elongate (up to 400 μm in length) acicular apatite with radial growth forms that are confined to carbonate-rich or carbonate-serpentine segregations. These textural descriptions are consistent with previous petrographic reports of apatite in kimberlites (e.g., Mitchell, 1986; Malarkey et al., 2010), and both textural types commonly occur within the same thin section.

Most apatite grains appear unzoned in back-scattered electron (BSE) images, except for apatite from the Kimberley Mine which have a thin (<5 μm) overgrowth of Na-rich apatite (~3.5 wt.% Na_2O based on semi-quantitative SEM-EDS measurement). Acicular apatite in radial aggregates associated with carbonate-rich segregations of the Wesselton water tunnel sills show zonation under cathodoluminescence (CL); however, no compositional variation was detected by EMP analysis, consistent with the lack of change in BSE response, and findings from previous studies of various other rock types (e.g., carbonatites, porphyries, skarns – Mao et al., 2016)

Apatite Composition

Average compositions of apatite from the Kimberley kimberlites are reported in Table 1. Measured grains can effectively be considered as solid solutions between fluorapatite (2.2 ± 0.4 wt.% F) and hydroxyapatite (0.70 ± 0.20 wt.% H_2O), with a negligible chlorapatite component (Cl was below the

detection limits of EMP measurements in most instances). Apatite from serpentine-rich segregations in the De Beers kimberlite have the highest H₂O contents (1.0 ± 0.1 wt.%). The studied apatite grains contain relatively homogeneous CaO (55.0 ± 1.0 wt.%) and P₂O₅ (38.9 ± 0.7 wt.%) contents. Minor impurities include variable SiO₂ (0.77 ± 0.48 wt.%) and SrO (2.1 ± 1.4 wt.%) contents, as well as subordinate concentrations of Na₂O (≤0.4 wt.%), FeO (≤0.5 wt.%), and LREE oxides (≤0.3 wt.% Ce₂O₃) in some samples. These compositions are broadly consistent with the limited published data available (e.g., Mitchell, 1986).

| | (1), n=7 | | (2), n=14 | | (3), n=13 | | (4), n=24 | | (5), n=8 | | (6), n=19 | |
|--------------------------------|--------------|-------------|--------------|-------------|--------------|-------------|--------------|-------------|--------------|-------------|--------------|-------------|
| | Mean | 1σ | Mean | 1σ | Mean | 1σ | Mean | 1σ | Mean | 1σ | Mean | 1σ |
| SiO ₂ | 0.70 | 0.18 | 0.30 | 0.17 | 0.60 | 0.12 | 0.47 | 0.10 | 1.51 | 0.40 | 1.36 | 0.15 |
| TiO ₂ | 0.02 | 0.01 | 0.03 | 0.06 | 0.02 | 0.01 | 0.02 | 0.03 | 0.00 | 0.00 | 0.01 | 0.02 |
| Fe ₂ O ₃ | 0.26 | 0.07 | 0.13 | 0.05 | 0.21 | 0.06 | 0.28 | 0.07 | 0.06 | 0.05 | 0.16 | 0.08 |
| MgO | 0.12 | 0.13 | 0.02 | 0.02 | 0.04 | 0.03 | 0.03 | 0.04 | 0.04 | 0.02 | 0.07 | 0.02 |
| CaO | 53.58 | 0.56 | 55.75 | 0.62 | 56.05 | 0.38 | 53.98 | 0.75 | 55.16 | 0.15 | 55.47 | 0.41 |
| Na ₂ O | 0.24 | 0.07 | 0.13 | 0.11 | 0.05 | 0.02 | 0.19 | 0.10 | 0.11 | 0.05 | 0.08 | 0.02 |
| P ₂ O ₅ | 38.03 | 0.45 | 39.50 | 0.45 | 39.50 | 0.37 | 38.52 | 0.56 | 38.74 | 0.65 | 38.91 | 0.43 |
| SrO | 3.46 | 0.27 | 1.68 | 0.67 | 1.18 | 0.12 | 3.73 | 0.80 | 1.40 | 0.11 | 0.61 | 0.07 |
| La ₂ O ₃ | 0.04 | 0.04 | 0.02 | 0.03 | 0.08 | 0.05 | 0.04 | 0.04 | 0.05 | 0.05 | 0.16 | 0.05 |
| Ce ₂ O ₃ | 0.00 | 0.00 | 0.02 | 0.03 | 0.03 | 0.03 | 0.00 | 0.01 | 0.03 | 0.04 | 0.22 | 0.06 |
| SO ₃ | 0.06 | 0.03 | 0.07 | 0.03 | 0.03 | 0.02 | 0.05 | 0.03 | 0.04 | 0.04 | 0.04 | 0.03 |
| F | 2.65 | 0.34 | 1.56 | 0.23 | 2.55 | 0.22 | 2.33 | 0.22 | 2.16 | 0.23 | 2.01 | 0.18 |
| Cl | 0.00 | 0.00 | 0.02 | 0.04 | 0.01 | 0.01 | 0.01 | 0.01 | 0.02 | 0.02 | 0.03 | 0.01 |
| H ₂ O(c) | 0.45 | 0.16 | 1.00 | 0.11 | 0.54 | 0.10 | 0.61 | 0.10 | 0.72 | 0.11 | 0.78 | 0.08 |
| O=F | 1.11 | 0.14 | 0.66 | 0.09 | 1.08 | 0.09 | 0.98 | 0.09 | 0.91 | 0.10 | 0.85 | 0.08 |
| O=Cl | 0.00 | 0.00 | 0.00 | 0.01 | 0.00 | 0.00 | 0.00 | 0.00 | 0.00 | 0.00 | 0.01 | 0.00 |
| Total | 98.58 | 0.48 | 99.61 | 0.71 | 99.86 | 0.53 | 99.32 | 0.63 | 99.17 | 0.48 | 99.10 | 0.57 |

Table 1: Average compositions of apatite from the Kimberley Kimberlites: (1) Kimberley Mine; (2) De Beers; (3) Wesselton (W2); (4) Wesselton (W3); (5) Wesselton water tunnel sills; (6) Benfontein.

Apatite from more “evolved” aphanitic carbonate-rich dykes and sills (i.e., Benfontein and Wesselton Water Tunnel Sills) are generally enriched in SiO₂ (and LREE in the case of Benfontein), and generally poorer in Na₂O and SrO, compared with apatite in macrocrystic kimberlites (i.e., Kimberley Mine and Wesselton) (Fig. 1; Table. 1). In addition, bi-variate major-minor element plots can be used to discriminate between different kimberlite samples and, probably, intrusions (e.g., Fig. 1). Apatite compositions exhibit more variation between intrusions than either spinel or olivine from the Kimberley kimberlites (our unpublished results). This may be attributed to the fact that apatite is a relatively late-stage phase in kimberlites (compared with olivine or spinel) and therefore may be more sensitive to the effects of magmatic differentiation.

Although the current apatite grains show variation between intrusions across the Kimberley kimberlites, when compared with other rock types, kimberlitic apatite grains exhibit relatively narrow compositional ranges. For instance, kimberlitic apatite grains contain lower SrO and SiO₂ than those in South African orangeites (e.g., Mitchell, 1995, and references therein), and significantly less BaO and TiO₂ compared to apatite in Western Australian lamproites (Edgar, 1989). In addition, the low Cl concentrations of kimberlitic apatite overlap those of apatite in carbonatites (Piccoli and Candella, 2002, and references therein); however, kimberlitic apatite does not show the same excess of F in the anion site, potentially suggesting lower CO₃²⁻ concentrations in kimberlitic apatite. In addition, kimberlitic apatite grains generally contain less MnO, Na₂O, and S than carbonatitic apatite. These differences in apatite composition appear to reflect variations in bulk-rock composition between these magma types (i.e., carbonatites contain more MnO, Na₂O, CO₂ and S than kimberlites).

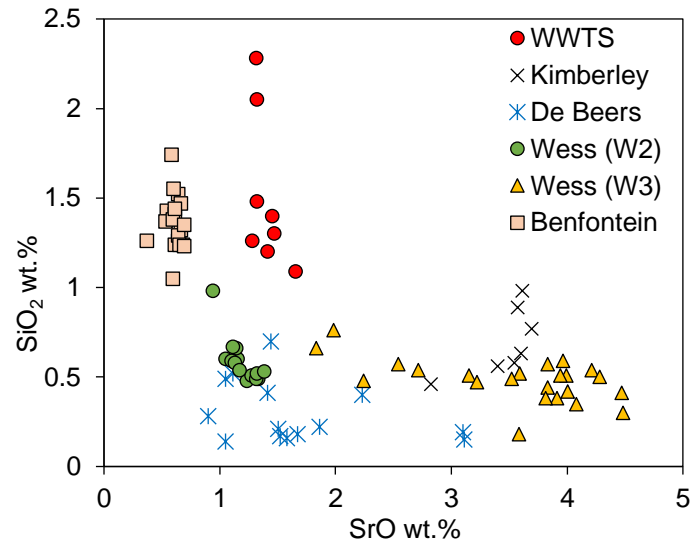


Figure 1: SiO₂ vs. SrO variations for apatite grains from the Kimberley Kimberlites.

References

- Chakhmouradian AR, Reguir EP, Mitchell RH (2002). Strontium-apatite: New occurrences, and the extent of Sr-for-Ca substitution in apatite-group minerals. *The Canadian Mineralogist*, 40(1), 121-136.
- Chakhmouradian AR, Reguir EP, Zaitsev AN, Couëslan C, Xu C, Kynický J, Mumin AH, Yang P (2017). Apatite in carbonatitic rocks: Compositional variation, zoning, element partitioning and petrogenetic significance. *Lithos*.
- Edgar AD (1989). Barium- and strontium-enriched apatites in lamproites from West Kimberley, Western Australia. *American Mineralogist*, 74(7-8), 889-895.
- Malarkey J, Pearson DG, Kjarsgaard BA, Davidson JP, Nowell GM, Ottley CJ, Stammer J (2010). From source to crust: tracing magmatic evolution in a kimberlite and a melilitite using microsample geochemistry. *Earth and Planetary Science Letters*, 299(1), 80-90.
- Mao M, Rukhlov AS, Rowins SM, Spence J, Coogan LA (2016). Apatite trace element compositions: A robust new tool for mineral exploration. *Economic Geology*, 111(5), 1187-1222.
- Mitchell RH (1986). *Kimberlites: mineralogy, geochemistry, and petrology*. Plenum Press, New York.
- Mitchell RH (1995). *Kimberlite, Orangeites and Related Rocks*. Plenum Press, New York. 410pp
- Piccoli PM, Candela PA (2002). Apatite in igneous systems. *Reviews in Mineralogy and Geochemistry*, 48(1), 255-292.
- Roeder PL, Schulze DJ (2008). Crystallization of groundmass spinel in kimberlite. *Journal of Petrology*, 49(8), 1473-1495.
- Shee SR, (1985). *The Petrogenesis of the Wesselton Mine Kimberlites, Kimberley, Cape Province, R.S.A.* (Ph.D) Department of Geochemistry. University of Cape Town, South Africa.

Significance of halogens (F, Cl) in kimberlite melts: Insights from mineralogy and melt inclusions in the Roger pipe (Ekati, Canada)

Adam Abersteiner¹, Vadim S. Kamenetsky¹, Maya Kamenetsky¹, Karsten Goemann³, Kathy Ehrig⁴, Thomas Rodemann³

¹ School of Physical Sciences, University of Tasmania, Australia, adam.abersteiner@utas.edu.au, dima.kamenetsky@utas.edu.au, Maya.Kamenetsky@utas.edu.au

² Central Science Laboratory, University of Tasmania, Australia, Karsten.Goemann@utas.edu.au, Thomas.Rodemann@utas.edu.au

³BHP Billiton Olympic Dam, Adelaide, Australia, Kathy.J.Ehrig@bhpbilliton.com

Introduction

The abundance and distribution of halogens (F, Cl) are rarely recorded in kimberlites and therefore their petrogenetic significance is poorly constrained. Halogens are usually present in kimberlite rocks in the structure of phlogopite and apatite, but their original concentrations are never fully retained due to the effects of alteration. Fluorine and chlorine in magmatic systems are influential on melt viscosity, phase equilibria and the mobility of metals (Kamenetsky et al., 2007; Tropper and Manning, 2007; Brey et al., 2009). Therefore, elucidating the halogen content of kimberlite magmas is fundamental in understanding parental melt compositions, rheology and ultimately their petrogenesis.

In this study, we examine a sample of hypabyssal kimberlite from the Roger pipe (Ekati, Canada). A remarkable feature of the Roger kimberlite is the presence of F-bearing minerals (i.e. bultfonteinite: $\text{Ca}_4(\text{Si}_2\text{O}_7)(\text{F},\text{OH})_2$ and fluorite) replacing olivine. In order to constrain the evolution of kimberlite melts and the origin of halogens in the Roger kimberlite, we focus on documenting the petrography and geochemistry of halogen-bearing minerals and characterise melt inclusions hosted within olivine and magmatic groundmass minerals.

Petrography and Geochemistry

The studied sample is characterised by porphyritic textures defined by euhedral-to-anhedral olivine set in a fine-grained groundmass consisting largely of interstitial serpentine, carbonate (i.e. calcite) and to a lesser extent garnet (andradite-schlorlomite). The groundmass mineralogy is typical of hypabyssal Group-I (or archetypal) kimberlites (Mitchell, 1986, 2008) and contains abundant monticellite (~20 vol.%) along with subordinate amounts of phlogopite, apatite, Fe-Mg-Al-Cr-spinel (i.e. magnesian ulvöspinel-magnetite (MUM), Mg-magnetite, pleonaste, Cr-spinel), perovskite and Ni ± Fe-sulphides.

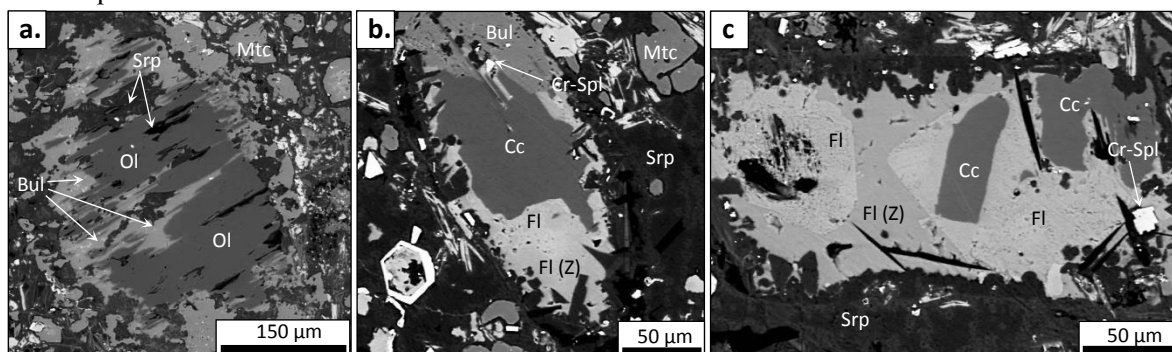


Figure 1. Back-scattered electron (BSE) SEM images of (a – c) Olivine (Ol) showing varying degrees of replacement by fluorite (Fl), bultfonteinite (Bul), serpentine (Srp) and calcite (Cc). (b, c) Pseudomorphic fluorite is zoned where darker fluorite areas are characterised by O-enrichment (Fl (Z)) and lighter fluorite areas contain minor-O (Table 1). Mtc: monticellite, Cr-Spl: Cr-spinel.

Bultfonteinite and fluorite are common replacement minerals after olivine which also overprint secondary calcite replacing olivine (Fig. 1) as well occurring as rare interstitial segregations (up to ~125 μm) throughout the groundmass. Bultfonteinite is homogeneous in composition, whereas fluorite is usually irregularly zoned along crystal faces in contact with the groundmass (i.e. rims) which is characterised by F-depletion and O-enrichment (Fig. 1c; Table 1). This abundance of F-rich minerals in the Roger kimberlite is illustrated by F-content (2263 and 2688 ppm). These results are consistent with previous analyses (1534 – 2532 ppm F; Nowicki et al., 2008) of the Roger kimberlite.

| | Bultfonteinite | | | | Fluorite | | | | |
|------------------------|----------------|-------|-------|-------|--------------|-------|-------|-------|-------|
| | 1 | 2 | 3 | 4 | 4-R | 5-R | 13-C | 8-C | |
| SiO₂ | 28.11 | 28.27 | 29.13 | 28.06 | Si | 0.27 | 0.23 | 0.03 | 0.09 |
| FeO | 0.51 | 0.14 | 0.15 | 0.64 | Fe | 0.18 | 0.12 | 0.05 | 0.14 |
| MgO | 0.28 | <0.02 | <0.01 | 0.20 | Mg | 0.04 | 0.06 | <0.01 | <0.01 |
| CaO | 52.41 | 53.07 | 51.57 | 52.30 | Ca | 48.14 | 47.87 | 50.62 | 50.1 |
| SO₃ | 0.44 | <0.01 | 0.01 | 0.52 | Sr | 0.23 | 0.32 | 0.22 | 0.31 |
| F | 8.87 | 9.26 | 9.20 | 9.36 | Na | 0.10 | 0.10 | 0.07 | <0.02 |
| H₂O | 12.91 | 12.77 | 12.90 | 12.78 | F | 43.76 | 43.03 | 47.20 | 47.00 |
| -O=F | 3.73 | 3.90 | 3.87 | 3.94 | O | 7.21 | 7.75 | 0.95 | 1.46 |
| Total | 99.79 | 99.61 | 99.10 | 99.91 | Total | 99.93 | 99.48 | 99.14 | 99.11 |

Table 1. Representative mineral analyses of bultfonteinite and fluorite replacing olivine in oxide and element wt.% respectively. R = rim, C = core.

Inclusions

In order to examine the composition and evolution of the kimberlite melt prior to post-magmatic processes, we analysed melt inclusions in olivine, Cr-spinel, monticellite and apatite using a scanning electron microscope (SEM). Inclusions in Cr-spinel, monticellite and apatite contain polycrystalline assemblages, are randomly distributed throughout their host grain and located away from any fracture system, and are therefore considered to be primary. In contrast, olivine hosted inclusions are located along internal healed fractures and are therefore interpreted to be secondary, as defined by Roedder (1984). Melt inclusions contain heterogeneous daughter phase assemblages (Fig. 2) composed of alkali/alkali-earth (Na, K, Ba, Sr)-enriched Ca-Mg-carbonates \pm F/V, Na-K-chlorides and sulphates, phosphates, spinel, silicates (e.g. olivine, phlogopite, (clino)humite) and sulphides. In addition, melt inclusions also contain other ‘exotic’ phases which include Ba-K \pm W \pm V \pm Mo-bearing phases, alkali-REE-phosphates and scheelite.

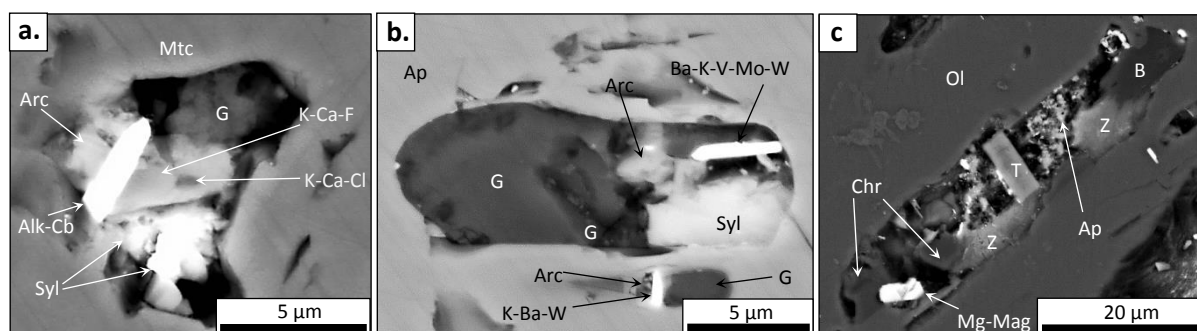


Figure 2. Back-scattered electron (BSE) SEM images of multiphase inclusions in: (a) monticellite (Mtc), (b) apatite (Ap) and (c) olivine. These multiphase inclusions host daughter phases of: gregoryite (G: $(\text{Na}_2, \text{K}_2, \text{Ca})\text{CO}_3$), alkali-carbonate (Alk-Cb), arcanite (Arc: K_2SO_4), zemkorite (Z: $(\text{Na}, \text{K})_2\text{Ca}(\text{CO}_3)_2$), tetraferriphlogopite (T: $\text{KMg}_3(\text{Fe}^{3+}\text{Si}_3\text{O}_{10})(\text{OH})_2$), sylvite (Syl), Mg-magnetite (Mg-Mag), bradleyite (B: $\text{Na}_3\text{Mg}(\text{PO}_4)(\text{CO}_3)$), apatite (Ap), clinohumite (Chr), Ba-K-V-Mo-W-phase (Ba-K-V-Mo-W), K-Ca-F-bearing phase (K-Ca-F), K-Ca-Cl-bearing phase (K-Ca-Cl) and K-Ba-W-bearing phase.

The Roger kimberlite is unique amongst other Ekati kimberlites, as it contains the highest F-content (up to 2688 ppm) and large amounts of F-rich minerals (i.e. bultfonteinite, fluorite) replacing olivine. The compositions and textures of bultfonteinite and fluorite in the Roger kimberlite are consistent with a secondary origin. The formation of interstitial andradite-schroteromite garnet is indicative of hydrothermal precipitation from a Ca-bearing hydrothermal serpentinising fluid (Stripp et al., 2006; Buse et al., 2010). In addition, based on the occurrence of bultfonteinite and fluorite, it is inferred that this alteration fluid was also F-bearing. Buse et al. (2010) constrained the temperature range for secondary hydrogarnet and bultfonteinite formation in basalt xenoliths from the B/K9 kimberlite (Botswana) to occur between 350 – 250 °C, which is a similar temperature range to when serpentinisation occurs (Evans, 2004; Stripp et al., 2006; Mitchell, 2008). Therefore, it is likely the observed alteration assemblages in our sample formed at similar low-temperature conditions.

Comparisons between halogens and other trace elements of similar compatibility (i.e. F/Nd and Cl/U) in the Roger kimberlite and their respective estimated primitive mantle abundances show that halogens should be a more significant component in kimberlites than typically measured. We propose that fluorine in the Roger kimberlite was magmatic and was redistributed during hydrothermal alteration by Ca-bearing serpentinising fluids to produce the observed bultfonteinite/fluorite assemblages. The absence of alkali, halogen and other highly incompatible trace element bearing phases from the Roger groundmass and other kimberlites worldwide is attributed to alkalis and chlorine accommodated in water soluble phases (i.e. alkalis in carbonates, sulphates and phosphates, and Cl in chlorides). The scarcity of these components in the kimberlite groundmass is attributed to the near ubiquitous effects of syn- and post-magmatic alteration.

Based the compositions and daughter mineral assemblages in primary melt inclusions and reconstructed halogen abundances, we suggest that Cr-spinel, monticellite and apatite crystallised from a variably differentiated Si-P-Cl-F-bearing carbonate melt enriched in alkalis/alkali-earths and highly incompatible trace elements. This presence of halogens in the parental kimberlite melt may bear unrecognised implications for melt liquidus temperatures, rheological properties and composition.

References

- Brey GP, Bulatov VK, Gurnis AV (2009) Influence of water and fluorine on melting of carbonated peridotite at 6 and 10 GPa. *Lithos* 112:249-259.
- Buse B, Schumacher J, Sparks RSJ, Field M, (2010) Growth of bultfonteinite and hydrogarnet in metasomatized basalt xenoliths in the B/K9 kimberlite, Damtshaa, Botswana: insights into hydrothermal metamorphism in kimberlite pipes. *Contrib Mineral Petrol* 160:533-550.
- Evans B (2004) The Serpentinite Multisystem Revisited: Chrysotile Is Metastable. *Int Geol Rev* 46: 479-506.
- Kamenetsky, VS, Kamenetsky, MB, Sharygin, VV, Golovin, AV (2007) Carbonatechloride enrichment in fresh kimberlites of the Udachnaya-East pipe, Siberia: a clue to physical properties of kimberlite magmas? *Geophys. Res. Lett.* 34.
- Mitchell RH (1986) *Kimberlites: Mineralogy, Geochemistry and Petrology*. Plenum Publishing Company, New York, 442 pp.
- Mitchell RH (2008) Petrology of hypabyssal kimberlites: Relevance to primary magma compositions. *J Volcanol. Geotherm Res* 174:1-8.
- Nowicki T, Porritt L, Crawford, B, Kjarsgaard B (2008) Geochemical trends in kimberlites of the Ekati property, Northwest Territories, Canada: Insights on volcanic and resedimentation processes. *J Volcanol Geotherm Res* 174:117-127.
- Stripp GR, Field M, Schumacher JC, Sparks RSJ, Cressey G (2006) Post-emplacement serpentinization and related hydrothermal metamorphism in a kimberlite from Venetia, South Africa *J Metamorph Geol* 24:515-534.
- Tropper P, Manning CE (2007) The solubility of fluorite in H₂O and H₂O–NaCl at high pressure and temperature. *Chem Geol* 242:299-306.



Punctuated, long-lived emplacement history of kimberlites from the Renard cluster, Superior Province, Canada indicated by new high precision U-Pb groundmass perovskite dating

I.M. Ranger¹, L.M. Heaman¹, D.G. Pearson¹, C. Laroulandie², I. Lépine² and V. Zhuk²

¹ *University of Alberta, Edmonton, Canada, iranger@ualberta.ca, larry.heaman@ualberta.ca, graham.pearson@ualberta.ca*

² *Stornoway Diamond Corporation, North Vancouver, Canada, claroulandie@stornowaydiamonds.com, ilepine@stornowaydiamonds.com, vzhuk@stornowaydiamonds.com*

Introduction

A number of Neoproterozoic (~680-550 Ma) kimberlites and related intrusions have been identified in eastern North America and southwest Greenland (e.g. Tappe et al., 2016). In eastern Canada these intrusions are known to occur in at least three clusters (Figure 1); the ca. 610-550 Ma ultramafic lamprophyre intrusions from the Torngat Mountains to Aillik Bay in Labrador (e.g. Tappe et al., 2008 and references therein), the ca. 629 Ma Wemindji kimberlite sills near James Bay (Letendre et al., 2003) and the ca. 656-551 Ma Otish kimberlite field in north-central Québec (Moorhead et al., 2003; Birkett et al., 2004; Fitzgerald et al., 2009; Tappe et al., 2016). An intriguing aspect of this magmatism that has been alluded to previously (e.g. Heaman et al., 2004) is that it broadly coincides with the timing of the breakup of the Rodinia supercontinent and the opening of the Iapetus Ocean (ca. 760-550 Ma; Cawood et al., 2001). However, in detail the connection between kimberlite magmatism and the rifting history of northeast Rodinia remains unclear.

In this study we have conducted a detailed multi-sample ID-TIMS U-Pb perovskite age investigation of Renard kimberlite pipes in the diamondiferous Renard cluster, located within the Otish mountains region of north-central Québec. One of the main challenges at Renard is establishing the exact emplacement age and intrusion history of these kimberlites. For example, published U-Pb perovskite dates for hypabyssal kimberlite from within the same pipe (e.g. Renard 2) yield a range of ages from 640.5±2.8 Ma to 655.8±6.0 Ma (Fitzgerald et al., 2009; Tappe et al., 2016).

Geologic Setting and Previous Geochronology

The diamondiferous Renard cluster comprises a core of nine kimberlite bodies (Renard 1 to 10 with Renard 65 combined), two dyke systems (Lynx and Hibou) and several anomaly dykes which erupted through Archean crust of the eastern Superior Province. Most of the kimberlite bodies follow a ~2 km long NNW-trending alignment and the surface area of individual pipes vary between 0.3 and 3.1 ha (Farrow and Hopkins, 2015). The internal geology of Renard 2 and Renard 3 were described by Fitzgerald et al. (2009) and Muntener and Scott Smith (2013), respectively, with the remaining kimberlite bodies described by Farrow and Hopkins (2015).

The Renard kimberlites are considered to be Group I kimberlites and consist of hypabyssal kimberlite (e.g. dykes) and one or more pipe-infilling units ranging from coherent to transitional to massive volcanoclastic kimberlite in each pipe (Kimberley-type pyroclastic kimberlite previously termed tuffisitic kimberlite) (Scott Smith et al., 2013; Farrow and Hopkins, 2015). For example, Fitzgerald et al. (2009) characterised the blue massive volcanoclastic kimberlite in Renard 2 as phlogopite kimberlite and the brown coherent kimberlite as monticellite phlogopite kimberlite. In addition, cm- to tens of meters thick hypabyssal kimberlite occur throughout the Renard pipes as dykes, irregular intrusions or possibly autoliths. These hypabyssal kimberlites also occur within the marginal breccia and/or cracked country rock. Fitzgerald et al. (2009) described the hypabyssal kimberlite intrusions in Renard 2. They range in primary groundmass mineralogy, primarily with varying amounts of phlogopite to monticellite.

A number of U-Pb perovskite dates by both TIMS and SIMS have been reported for Renard kimberlites. The first published U-Pb TIMS groundmass perovskite date of 631.6 ± 3.5 Ma was reported for a Renard 1 hypabyssal kimberlite (Birkett et al., 2004). A slightly older U-Pb TIMS composite emplacement age of 640.5 ± 2.8 Ma from Renard 2 and 3 was reported by Fitzgerald et al. (2009). Recent U-Pb perovskite age determinations by SIMS from hypabyssal kimberlite in Renard 2 (655.8 ± 6.0 Ma) and Renard 3 (653.8 ± 5.9 Ma) (Tappe et al., 2016) expanded the previously known range of kimberlite magmatism in the Renard cluster to ca. 656-632 Ma. These studies highlight a significant discrepancy between the U-Pb perovskite TIMS and SIMS dating results for the same pipe. Unfortunately the sampling details of hypabyssal kimberlites in Renard 1-3 were not described in the previous studies, even though the complexity of these bodies requires this detail in order to understand the significance of the ages. In addition, the Otish field includes the much younger 550.9 ± 3.5 Ma Lac Beaver hypabyssal kimberlite located ~90 km south of the Renard cluster (Figure 1; Moorhead et al., 2003).

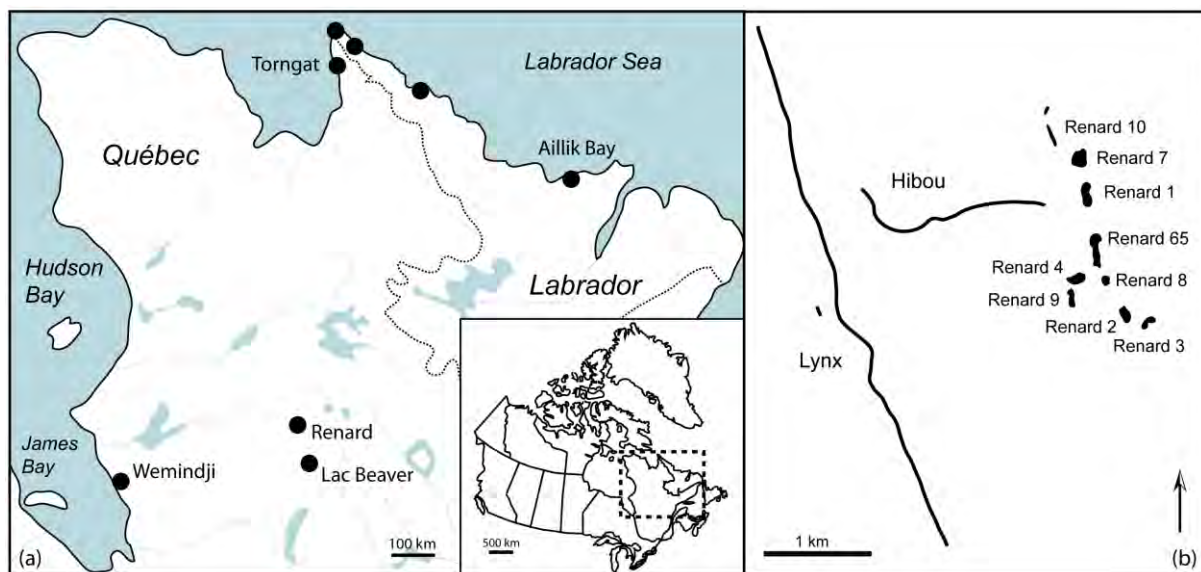


Figure 1. Simplified sketch of (a) the locations of kimberlite clusters and related intrusions in eastern Canada and (b) the Renard kimberlite cluster outlining Renard 1-10 and the Lynx and Hibou dyke systems in north-central Québec. Modified from a Natural Resources Canada reference map (2001), Tappe et al. (2008), and Farrow and Hopkins (2015).

Results and Discussion

This study provides new high-precision ($\pm 1-3$ Ma; 2σ) ID-TIMS U-Pb groundmass perovskite dates for the Renard cluster. A more detailed investigation of the ages of the main pipe-infilling units versus hypabyssal kimberlite uncovered a novel result that offers an explanation for understanding complicated kimberlite geochronology where multiple U-Pb perovskite dates for a single pipe exist. There is clear evidence for multiple episodes of hypabyssal kimberlite magmatism at Renard, with a geologically significant range in emplacement dates. Interestingly this protracted kimberlite intrusion history is recorded even within some individual pipes.

For example, eight new U-Pb dates from Renard 2 indicate that the hypabyssal kimberlite has emplacement dates that span at least ~20 Myr from approximately ~652-632 Ma. Some hypabyssal kimberlites were emplaced both prior to and post the ~643 Ma emplacement of the coherent to massive volcanoclastic kimberlite main pipe-infilling units. These new age results demonstrate that hypabyssal kimberlite magmatism in the Renard 2 pipe took place at punctuated intervals over a protracted period of time. The findings of this study demonstrate that a single radiometric date obtained on hypabyssal kimberlite from one pipe may not be representative of the age of the main pipe-infilling units.

New high precision ID-TIMS U-Pb perovskite dates from the Renard kimberlite cluster indicate that the majority of this magmatism occurred much earlier than the kimberlite and ultramafic lamprophyre magmatism recorded in southwest Greenland and Labrador (ca. 610-550 Ma) (e.g. Tappe et al., 2008 and references therein). Furthermore, the timing of the majority of Renard kimberlite magmatism is distinct from the two proposed periods of Rodinia rifting (e.g. ca. 760-700 Ma and ca. 620-550 Ma, Cawood et al., 2001) and at least ~35 m.y. earlier than estimates for the birth of the Iapetus Ocean (Kamo et al., 1989).

References

- Birkett TC, McCandless TE, Hood CT (2004) Petrology of the Renard igneous bodies: host rocks for diamond in the northern Otish Mountains region, Quebec. *Lithos* 76:475-490
- Cawood PA, McCausland PJA, Dunning GR (2001) Opening Iapetus: constraints from the Laurentian margin in Newfoundland. *GSA Bulletin* 113(4):443-453
- Farrow D, Hopkins R (2015) Mineral resource update for the Renard Diamond Project, Québec, Canada. National Instrument (NI) 43-101 Technical Report:139p
- Fitzgerald CE, Hetman CM, Lepine I, Skelton DS, McCandless TE (2009) The internal geology and emplacement history of the Renard 2 kimberlite, Superior Province, Quebec, Canada. *Lithos* 112S:513-528
- Heaman LM, Kjarsgaard BA, Creaser RA (2004) The temporal evolution of North American kimberlites. *Lithos* 76:377-397
- Kamo SL, Gower CF, Krogh TE (1989) Birthdate for the Iapetus Ocean? A precise U-Pb zircon and baddeleyite age for the Long Range dikes, southeast Labrador. *Geology* 17:602-605
- Moorhead J, Beaumier M, Girard R, Heaman L (2003) Distribution, structural controls and ages of kimberlite fields in the Superior Province of Quebec. 8th International Kimberlite Conference Extended Abstract FLA-0275:5p
- Muntener C, Scott Smith BH (2013) Economic geology of Renard 3, Québec, Canada: a diamondiferous, multi-phase pipe infilled with hypabyssal and tuffisitic kimberlite. In: Pearson DG et al (eds) Proceedings of 10th International Kimberlite Conference, Volume 2, Special Issue of the Journal of the Geological Society of India, Springer, New Delhi, pp 241-256
- Natural Resources Canada (2001) Lakes and Rivers of Canada. <http://www.nrcan.gc.ca/earth-sciences/geography/atlas-canada/reference-maps/16846>
- Scott Smith BH, Nowicki TE, Russell JK, Webb KJ, Mitchell RH, Hetman CM, Harder M, Skinner EMW, Robey JvA (2013) Kimberlite terminology and classification. In: Pearson DG et al (eds) Proceedings of 10th International Kimberlite Conference, Volume 2, Special Issue of the Journal of the Geological Society of India, Springer, New Delhi, pp 1-17
- Tappe S, Brand NB, Stracke A, van Acken D, Liu C-Z, Strauss H, Wu F-Y, Luguet A, Mitchell RH (2016) Plates or plumes in the origin of kimberlites: U/Pb perovskite and Sr-Nd-Hf-Os-C-O isotope constraints from the Superior craton (Canada). *Chem Geol*, In Press: <http://dx.doi.org/10.1016/j.chemgeo.2016.08.019>
- Tappe S, Foley SF, Kjarsgaard BA, Romer RL, Heaman LM, Stracke A, Jenner GA (2008) Between carbonatite and lamproite - diamondiferous Torngat ultramafic lamprophyres formed by carbonate-fluxed melting of cratonic MARID-type metasomes. *Geochim Cosmochim Acta* 72:3258-3286



IaB diamond and its geological implications

Tingting Gu, Wuyi Wang

Gemological Institute of America, 50 W 47th Street, New York City, NY 10036, USA

Introduction

Nitrogen is one of the most common impurities in diamonds, and its aggregation styles in diamonds have been used as criteria for diamond classification. Among all diamond types, Ia is the most common type in nature, including type IaA, IaAB and IaB. However, pure IaB (with 100% B aggregation) diamonds are rather rare. Some of them are found in diamond suites that are related with super deep origin (Buffalo Hills, Eureka, Sao Luis, Rio Soriso, Kankan, Jagersfontein Kimberlite, etc.) or oldest diamondiferous rocks (Wawa), others can be found occasionally in alluvial diamonds (Arenapolis, Boa Vista, Namibia) or at the base of lithosphere with deformation features (Argyle). The origin and formation of those diamonds are mainly mysterious. The nitrogen concentration of those diamonds can be very low (less than 200 ppm, i.g., Eureka, Sao Luis, Buffalo Hills), and they can mix with type IIa diamonds in the same stone with large size. Experimental data shown that C center in diamonds can be gradually changed to A center and to B center (Evans & Qi, 1982) by high-temperature annealing, with parallel formation of the platelet in {001} planes. Therefore, the occurrence of B center and low nitrogen concentration has often been interpreted as a sign of high temperature and probably longer geological time for the host diamond. However, for many pure IaB diamonds, the platelet defects can be degraded completely (Buffalo Hills), which have been termed as irregular diamonds (Woods & Collins, 1986), indicating that they could have undergone unusual geological event during the diamond forming process. Previous studies proposed that platelet degradation in these diamonds results in formation of octahedral voidites and dislocation loops lying in the {001} planes (Evans et al., 1995). Those voidites could provide a milky/hazy appearance to the IaB diamonds and contain mantle-derived fluids but their physical and chemical properties are still controversial.

To understand the formation and geological implications of type IaB diamonds, we systematically studied their defects and deformation features by FTIR, cathodoluminescence, photo-luminescence spectroscopy, and examined their inclusions by Raman spectroscopy. We obtained evidence of the sublithospheric origin of a majority of IaB diamonds, and their interaction with deep hydrocarbon and carbonate fluids, which might be important to interpret the recycling of nitrogen in deep Earth.

Results

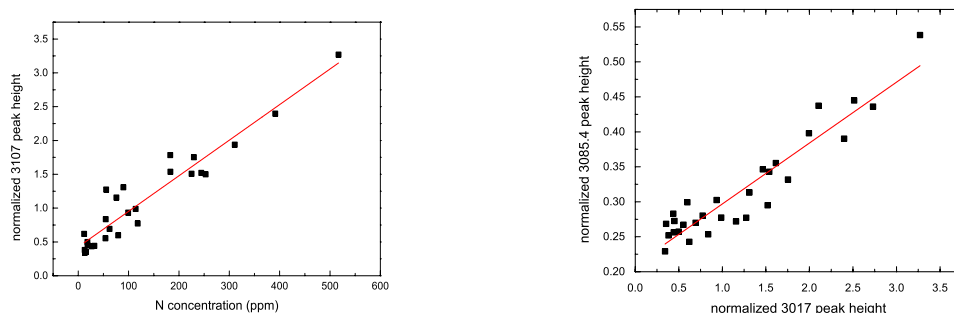


Figure 1 (Left) Nitrogen concentration determined by FTIR as a function of hydrogen concentration constrained by normalized 3107 peak height. (Right) Normalized 3107 peak height as a function of 3085.4 peak height. (Peak height at 3107 cm^{-1} and 3085.4 cm^{-1} have been normalized by diamonds peak at 2460 cm^{-1})

We examined about 69 IaB diamonds ranging from 0.2 ct to ~100 ct, and most of them (97%) shown the degradation of the platelet peaks, while 38 diamonds show micro inclusions detectable by Raman

spectroscopy. Nitrogen concentration ranges from 4 ppm to 516 ppm determined by FTIR spectra. Hydrogen peaks at 3107 cm^{-1} have been detected, which shows a linear correlation with nitrogen concentration (Fig. 1). We observed the peak at 3085.4 cm^{-1} featured by IaB diamonds with milky appearance or cloudy inclusions; in contrast, this peak is missing among more than 90% of IaB diamonds without detectable cloudy inclusions. We normalized the peak height at 3107 cm^{-1} and 3085.4 cm^{-1} to diamond peak at 2460 cm^{-1} , and observed a linear correlation of the two peaks (Fig. 1). However, no correlation of the peak height at 3085.4 cm^{-1} and 3107 cm^{-1} has been observed for the greyish or violet type IaAB diamonds. Therefore, the peak at 3085.4 cm^{-1} could be a typical optical feature for the milky IaB diamond, which might be related with the VN3H defects (Goss et al., 2014) and B aggregation.

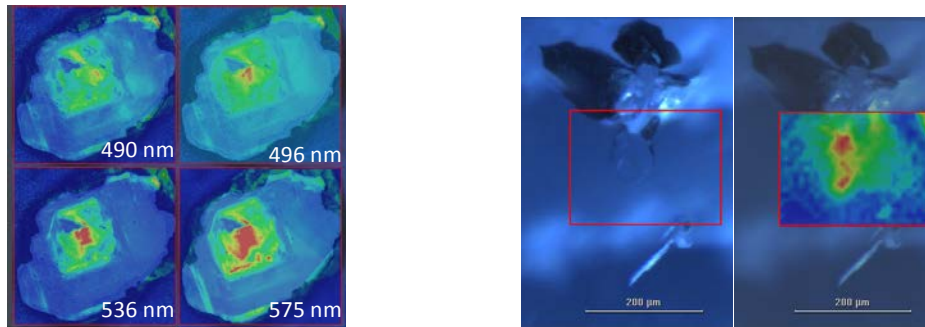


Figure 2 (Left) Diamond defect maps of photo-luminescence (PL) spectra taken with 455 and 532 nm excitations at liquid-nitrogen temperature. (Right) PL mapping of the 536 nm defect around the fracture area alongside a walstromite inclusion.

From cathodoluminescence (CL) images of the IaB diamonds, we found about half of them show dislocation networks and deformation features, indicating they have been brought up from deep Earth and experienced plastic deformation under high-pressure conditions. Photo-luminescence spectra have been taken at liquid-nitrogen temperature. Among 69 stones we examined, we observed ~90% IaB milky diamonds contain 536 nm defect, in contrast with IaB diamonds with no distinct cloudy features among which less than 30% showing 536 nm defects. In a IaB diamond with cloudy zone in the center, we observed 490 nm, 496 nm, 536 nm, and 575 nm defects in the cloudy center compared with the relatively clean surrounding area (Fig. 2). The 536 nm defect has also been observed in the discoid fracture alongside a walstromite inclusion, which might be caused by high temperature plastic deformation (Fig. 2). Therefore, presence of 536 nm defects in most milky IaB diamonds may indicate a certain dislocation style associated with high temperature.

By examining systematically the mineral inclusions in those diamonds, we found more than three quarters of them are from sublithosphere, indicated by inclusions that might be fragments of transition zone and lower mantle. Walstromite, larnite, titanite, coesite, Ca-perovskite assemblages have been found for more than half of the IaB diamonds, which indicates they originate as deep as the transition zone area. The equilibrium of the Ca-silicate inclusions imply that the initial Ca-silicate inclusions were trapped by diamond growth at conditions near to the CaSiO_3 -walstromite \rightarrow larnite (β - Ca_2SiO_4)+ CaSi_2O_5 -titanite equilibrium phase boundary, which begins above 10 GPa and 1773 K (Anzolini et al., 2016). Besides, we observed ferropericlase in several IaB diamonds, coexisting with walstromite and Ca-perovskite, indicating a superdeep origin of its host diamonds. We also found jeffbenite (TAPP) in three typical IaB diamonds, either as separate phase or coexisting with enstatite pyroxene and walstromite. The well preserved rhombus shape of the jeffbenite inclusion (Fig. 3) indicates that it could be a syngeneic inclusion with the host diamond forming in the lower mantle as bridgmanite while retrograde to current phase. In addition, spinel phase which has been considered as retrogressed calcium ferrite (CF) structured phases with high Al content at upper lower mantle (Walter et al., 2011) was observed coexisting with enstatite pyroxene phase in several milky IaB diamonds with relatively high hydrogen concentration. Interestingly, we found calcite and dolomite inclusions in six IaB diamonds coexisting with walstromite or as separate phases, with calcite phase in a well-crystallized rhombus shape suggesting their syngeneic character. The coexisting walstromite

phase indicates their deep origin and implies that a carbonate-rich fluid has been involved during the diamond forming process in the transition zone. Moreover, methane has been detected coexisting with carbonate phases in a IaB diamond with low nitrogen concentration (4 ppm). In this typical diamond, calcite, dolomite, magnetite, ferroperricite, spinel, nepheline and corundum have been detected by Raman spectroscopy. Methane has been detected in the fluid jacket in several inclusions (Fig. 3). Coexisting of methane and carbonate phases could confirm the former experimental evidence of the production of methane through the reaction $\text{CaCO}_3 + \text{H}_2\text{O} + \text{FeO} \rightarrow \text{CH}_4 + \text{CaO} + \text{Fe}_3\text{O}_4$ under mantle conditions (Scott et al., 2004).

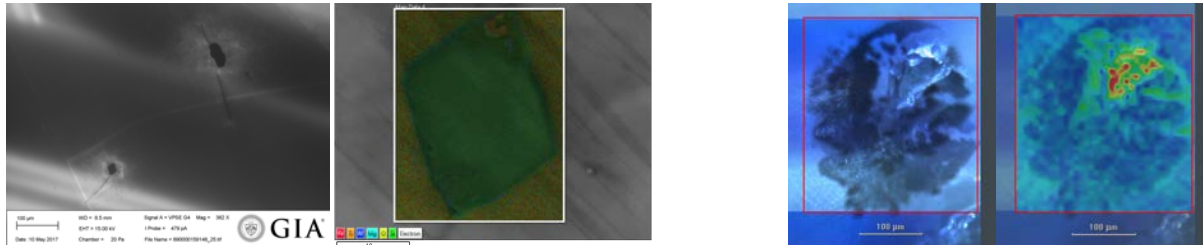


Figure 3 (Left) CL image of a diamond with jeffbenite (TAPP) phase on the surface and the chemical mapping of the smaller one with rhombus shape. (Right) Raman mapping of the methane peak at $\sim 2913 \text{ cm}^{-1}$ in a diamond inclusion with spinel and nepheline.

Discussions

Combined with FTIR, Raman spectroscopy and the luminescence optical features, formation of IaB diamonds may take place in the transition zone and lower mantle region where large size pure IaB diamonds (5 ct up to 100 ct) can form. Absence of the platelet peak and presence of the 536 nm defect for most milky IaB diamonds indicates they have experienced high temperature during their residence in the deep Earth, which could take a long geological time suggested by the full aggregation of B center. The FTIR features of the IaB diamonds suggests a N-H rich fluid has been involved during the diamond formation process, which could reach as deep as the lower mantle in ancient geological time. Compared with nitrogen free sublithospheric diamonds (such as IIa diamonds with metallic inclusions, Evan et al., 2016), inclusions in the pure IaB diamonds suggests they could form from C-O-H system that might be more compatible with nitrogen.

References

- Anzolini C, Angel RJ, Merlini M, Derzsi M, Tokár K, Milani S, Krebs MY, Brenker FE, Nestola F, Harris JW (2016) Depth of formation of CaSiO_3 -walstromite included in super-deep diamonds. *Lithos*, 1-10
- Evans T, Kiflawi I, Luyten W (1995) Conversion of platelets into dislocation loops and voidite formation in Type IaB diamonds. *Proceedings: Mathematical and Physical Sciences* 499(1936): 295-313
- Evans T, Qi Z (1982) The Kinetics of the Aggregation of Nitrogen Atoms in Diamond. *Proceedings of the Royal Society A: Mathematical, Physical and Engineering Sciences* 381, 159-178
- Smith EM, Shirey SB, Nestola F, Bullock ES, Wang J, Richardson SH, Wang W (2016) Large gem diamonds from metallic liquid in Earth's deep mantle. *Science* 354 (6318): 1403-1405
- Goss JP, Briddon PR, Hill V, Jones R, Rayson MJ (2014) Identification of the structure of the 3107 cm^{-1} H-related defect in diamond. *J. Phys.: Condens. Matter* 26, 145801
- Scott HP, Hemley RJ, Mao H (2004) Generation of methane in the Earth's mantle: in situ high pressure-temperature measurements of carbonate reduction, *Proceedings of the National Academy of Sciences* 101(39): 14023-14026
- Walter MJ, Kohn SC, Araujo D, Bulanova GP, Smith CB, Gaillou E, Wang J, Steele A, Shirey SB (2011) Deep Mantle Cycling of Oceanic Crust: Evidence from Diamonds and Their Mineral Inclusions. *Science* 334, 54-57
- Woods GS, Collins AT (1986) Platelets and the infrared absorption of type Ia diamonds. *Proceedings of the Royal Society of London A* 407, 2109-2238



The Nxaunxau kimberlites of northwest Botswana

De Wit MCJ, Hiyoveni RT, Kahari M, Bruchs J
Tsodilo Resources Ltd, Toronto, Ontario, Canada

Introduction

The Nxaunxau kimberlites in northwest Botswana are part of the Xaudum kimberlite province that extends into northeast Namibia. The province comprises 45 known kimberlites of which 31, the Nxaunxau bodies, occur in Botswana, and the others, seven in the Kaudom South cluster, four near Sikereti and two in the Gura cluster, occur in Namibia (De Wit, 2013).

Exploration history

The Xaudum kimberlite province straddles the Botswana/Namibian border just south of the Caprivi strip and roughly 250 km northwest of Maun. All the known kimberlites in this province, apart from the two Gura bodies, are situated within the easterly directed Xaudum drainage. The first kimberlites of this province, the Sikereti bodies, were found in 1979 in Namibia by De Beers using soil sampling. These four kimberlites were classified as Group-1 diatremes and both tuffisitic (TKB) and magmatic (aphanitic and macrocrystic varieties) rock-types are present. No macrodiamonds were produced from the bulk sampling and only three microdiamonds were recovered from one of the kimberlites (Winter and Rikhotso, 1998). The Ashton Mining/Reunion Mining joint venture discovered 18 of the kimberlites in Botswana, close to Nxaunxau, in 1998. These were found using the Botswana government aeromagnetic data that was started in 1998 on 250 m spaced north-south orientated flight lines with the sensor some 70 m above the ground. From 2002 onwards exploration by Tsodilo Resources Ltd discovered an additional 13 kimberlites and increased the number of discoveries in the Nxaunxau cluster to 31, with the last kimberlite being drilled in 2011. All of these also belong to the Group-1 variety. In 2004 and 2005 eight more kimberlites were discovered north of the Sikereti pipes in Namibia by Motapa Diamonds and are referred to as the Kaudom South cluster. Around 70 km south of the Sikereti kimberlites, around 2000, Mount Burgess found two small kimberlites, Gura 1 and Nxa-on, and one para-kimberlite called Rabbit. Judging from the geographical distribution of the 45 kimberlites, it is suggested that the Nxaunxau, Kaudom South and Sikereti clusters form part of one field of 43 occurrences: here referred to as the Xaudum kimberlite province. The Gura 1 and Nxa-on kimberlites, some distance to the south, probably form a separate cluster, and the Rabbit para-kimberlite may be a different event altogether. The continued interest in the region is based on yet unresolved kimberlitic mineral anomalies in Namibia, containing both high-interest garnets and diamonds, occurring proximal to these kimberlites. In addition, deep penetrating magnetotelluric surveys, carried out in the area between 2005 and 2006, showed that northwest Ngamiland is underlain by resistive lithosphere which appears to be part of the Congo Craton (Khoza, 2013). This was further confirmed by Tsodilo which drilled basement rocks of Archean ages in the immediate vicinity (www.tsodiloresources.com).

Regional geology

On a local scale the Nxaunxau kimberlites have intruded Neoproterozoic carbonates of the Ah-a Hills Formation, which are covered by remnants of Mulden Group phyllites/psammities of Cambrian age, and Karoo Supergroup sediments, and are intruded by Karoo dolerites. Lower Karoo sediments are preserved in deep valleys. Continued exploration has shown that the meta-sediments of the Damara orogeny have been thrust over the southern edge of the Congo Craton basement. The kimberlites are also spatially associated with the NW-SE trending Botswana dyke swarm of Jurassic age, although pre-Karoo dolerites are also present in the area. These cover sequences provided a wide variety of the crustal xenoliths within the kimberlite with commonly Damara carbonate and Karoo Supergroup tillites, shales, sandstones and dolerite. Xenoliths of the possibly basal Kalahari Group sediments have been described within the Nxaunxau kimberlites (De Wit, 2013) and the Sikereti bodies (Balfour, 1985). The Nxaunxau kimberlites are covered by Kalahari Group sediments of up to 30 m in thickness.

Age of kimberlite event

A kimberlite event has been dated at 83.2 ± 1.2 Ma, based on U-Pb dating of perovskite from three of the kimberlites: K20, K21 and K22 (Batumike et al., 2007). This was confirmed by Leong (2014) who obtained U-Pb perovskite ages for kimberlites K20, K21, K22 and K25 from samples of greater than 100 m depths. Some of the grains were large as 100-200 μm and fresh. Although thin bands of phlogopite in K8 appeared enough for $^{40}\text{Ar}/^{39}\text{Ar}$ dating method, the U-Pb perovskite dating gave the most robust and precise age of 84 ± 4 Ma (Leong, 2014).

This relatively young age is supported by the presence of crustal xenoliths of Kalahari basal conglomerate and calcretes. It therefore also suggests that the base of the Kalahari in north-west Botswana is at least Late Cretaceous in age.

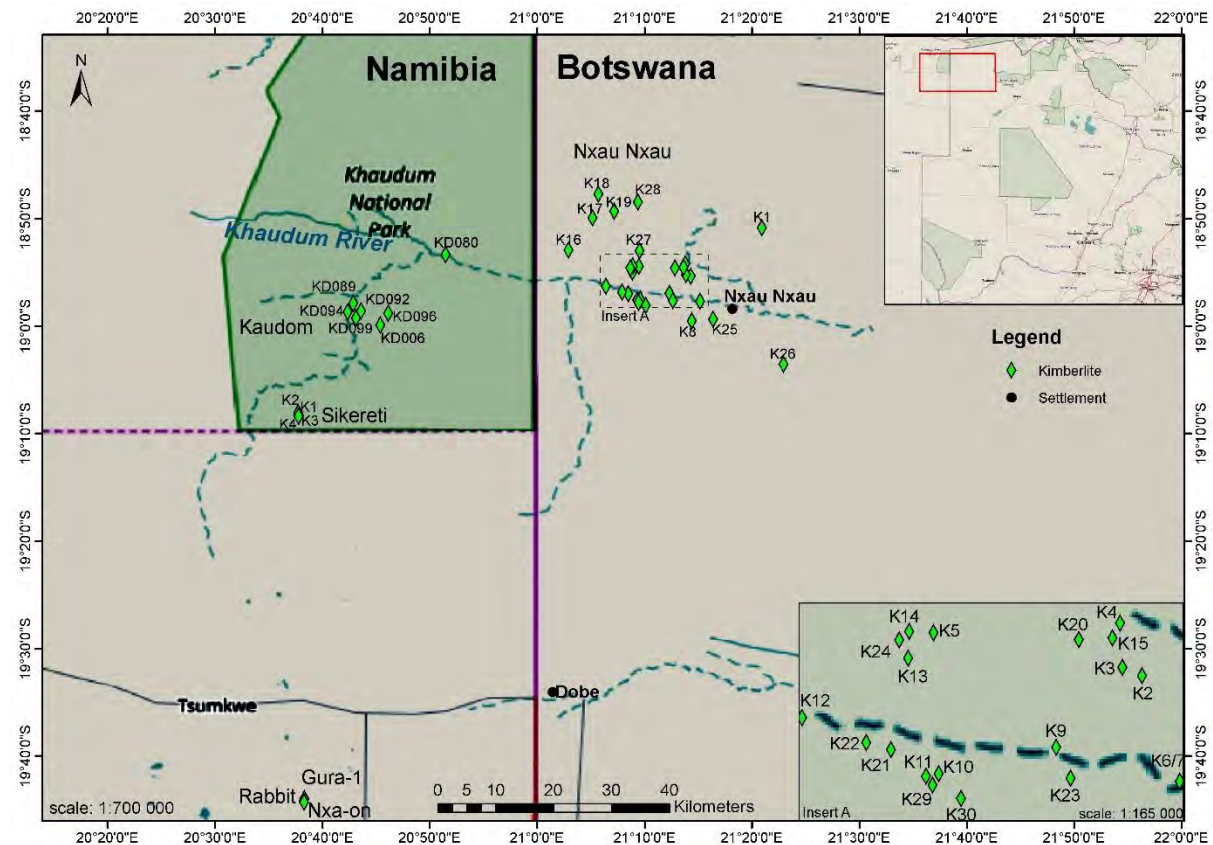


Figure 1. Local locality map for the Khaudum kimberlite province straddling the Namibian/Botswana border.

Petrography

From a petrographic point of view the Nxaunxau kimberlites range from volcanoclastic (re-sedimented and pyroclastic kimberlite) to coherent (hypabyssal) kimberlite. Serpentinized olivines, ilmenite and phlogopites form the main macro constituents of the kimberlite set in a groundmass of perovskites, atoll textured spinels, calcite and serpentine. Although this province has been shown to be diamondiferous with micro-diamonds recovered from four of six Nxaunxau kimberlites tested, its low counts, and the garnet mineral chemistry, which indicate that these are mainly of lherzolitic paragenesis dominated by G9 and G5 varieties, supports the conclusion that from an economic point of view these kimberlites have so far not warranted any further evaluation.

The Nxaunxau kimberlites are highly altered; displaying an assortment of textures and diverse mineralogy ranging from volcanoclastic to coherent. The volcanoclastic kimberlite is highly fragmented and contains abundant angular xenoliths, such as dolerite, limestone, shale and biotite amphibolites, rounded magma clasts, including peletal lapilli, and abundant macrocrysts, ilmenite and garnet, irregularly distributed throughout the rock (Hiyoveni, 2015). The matrix is highly altered to clay minerals and calcite and some of the samples contain spinels, atoll textured titanomagnetite and highly

altered perovskites. The coherent kimberlites have inequigranular texture and are typically macrocrystic. Some of the samples display segregationary texture with pools of interstitial calcite between olivine phenocrysts (Leong, 2014). Olivine macrocrysts are abundant with rare ilmenite macrocrysts. Matric minerals are fine-grained and serpentinised or altered to calcite. Common groundmass minerals include perovskite and titanomagnetite and Leong (2014) observed very rare apatite in a sample from K21.

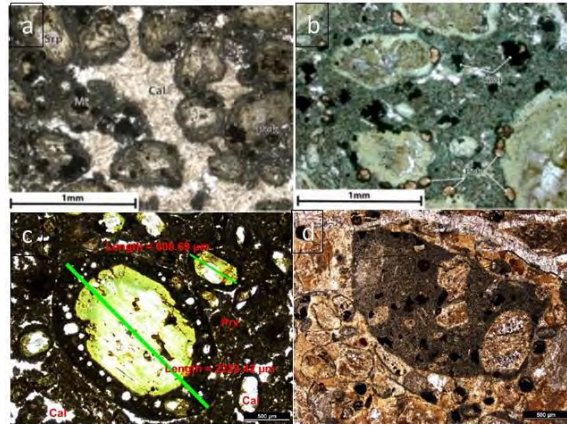


Figure 1. a) Macrocrystic coherent kimberlite with segregationary texture. b) Coherent kimberlite with olivine macrocrysts and perovskite grains. c) Volcaniclastic kimberlite with peletal lapilli. d) Volcaniclastic kimberlite with magma clasts with altered olivine inclusions.

The kimberlites proximal to the Botswana Karoo dolerite dyke swarm were generally the volcaniclastic types and seem to contain a much higher abundance of crystals xenoliths than those located further from dykes.

References

- Balfour DJ, Hegenberger W, Medlycott AS and Wilson KJ (1985) Kimberlites near Sikereti, north-eastern South West Africa/Namibia. *Communs Geol. Surv. SW Africa/Namibia*, 1, 69-77.
- Batumike J, Belousova EA and Griffin WL (2007) U-Pb dating of perovskite Nxau Nxau kimberlite, Botswana. *Gemoc Report Tsodilo-2007/1*, pp 13
- De Wit MCJ (2013) The Xaudum kimberlite province straddling the southern margin of the Angolan Craton. Abstract 24th Colloquium of African Geology, 8th – 14th January 2013, Ethiopia, pp 1
- Hiyoveni RT (2015) Characterization of (K29, K30) Nxaunxau kimberlites. Unpubl. BSc thesis. University of Botswana, Botswana, pp 47
- Khoza TD, Jones AG, Muller MR, Evans RL, Miensopust MP and Webb SJ (2013) Lithospheric structure of an Archean craton and adjacent mobile belt revealed from 2-D and 3-D inversion of magnetotelluric data: Example from southern Congo craton in northern Namibia. *J. Geophys. Res: Solid Earth*, vol. 118, 1-20
- Leong HX (2014) Petrology of the Nxau Nxau Kimberlites, northwest Botswana. Unpubl. MSc thesis. University of Melbourne, Australia, pp 78
- Winter F and Rikhotso CT (1998) Final report on CDM Exploration activities in north-eastern Namibia. *Open File Geol. Surv. Namibia*, Report No. KR/98/0476, pp 51



Geochemistry of Eclogite Xenoliths from Kimberlite Pipe Udachnaya: Section of Archean Oceanic crust sampled?

A.M. Agashev, L.N. Pokhilenko, N.P. Pokhilenko

V.S. Sobolev Institute of Geology & Mineralogy SB RAS, Novosibirsk 630090, Russia (* correspondence: agashev@igm.nsc.ru)

Introduction

Eclogites are important component of lithospheric mantle beneath Archean cratons. They found as xenoliths in all kimberlites worldwide usually comprising minor (1-5%) part, but in some cases can dominate the xenoliths population. As the most of kimberlitic eclogites are Archean in age (Pearson et al, 1995; Jacob 2004) study of their composition is very useful tool to constrain the Archean geodynamics and cratons formation. Among the xenoliths population in kimberlites eclogites more often contain diamonds than other type of mantle rocks and hence could be the main diamond reservoir of the earth. Here we report the new results on eclogites from Siberian Udachnaya kimberlite pipe. A suite of 17 unique big (1 to 20 kg) and fresh eclogite xenoliths including two diamondiferous have been studied for their whole-rock and minerals major and trace elements composition.

Results

Whole rock major elements composition of the Udachnaya eclogite xenoliths suite have a great variability in their MgO contents (9-19 wt%). Based on major elements composition Udachnaya eclogites can be subdivided in two subsets, high magnesian (Mg# 68.8-81.9) and low magnesian (Mg# 56.8-59). High variations also shown by Al₂O₃ (10.17- 18.74 wt %) and Na₂O (0.64-3.09 wt%) concentrations and high Mg# samples tend to contain less of those oxides than low Mg# samples with some exceptions. Two eclogitic groups are clearly different in style of inter-elements correlations. FeO and CaO contents are positively correlate with MgO in low Mg# group of eclogites but negatively in high Mg# group. The same relations present between Al₂O₃ contents of eclogite groups with their Mg#. Compared to present day MORB composition eclogite samples have similar contents of most elements with some depletion in TiO₂ and P₂O₅ and enrichment in MgO and K₂O. Concentrations of TiO₂ are varies in range of 0.2 -1.2 wt % in both groups and do no correlates with their Mg#. Loss of ignition (LOI) values detected in eclogites is in the range of 0.44-1.78 wt% that indicates a little or no secondary alteration experienced by samples at near surface environment. Only one sample has LOI value of 3.58 wt%.

In terms of trace elements composition Udachnaya eclogites are variable enriched over PM in

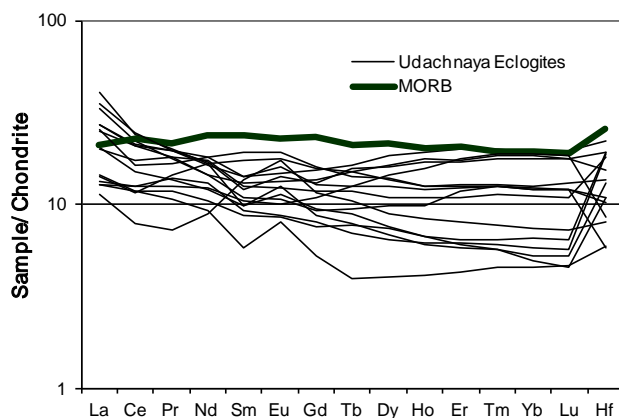


Figure 1. Chondrite normalized REE patterns of Udachnaya eclogites

incompatible elements with most pronounced enrichment in LILE elements (Rb, Ba, K, Sr) contents. Concentrations of incompatible HFSE (Nb, Ta, and REE are comparable to present day MORB values. Middle REE and Zr are lower than that of MORB. Heavy REE elements concentration varies from values comparable to present day MORB to significantly lower. Although the two groups of eclogites are overlapped in their HREE contents the high Mg# group has subset of samples with very low concentrations of HREE (Yb n 2.38-1.48 ppm) that outside the range of low Mg# group (6.83-2.72 ppm). Most of the samples show positive Eu anomaly irrespectable of groups (Fig.1). Excess of Eu expressed as Eu# ($Eu_n/(Sm_n$

+Gd_n/2)) positively correlate with Sr concentrations of the rocks. The positive Eu anomaly is positively correlate with Mg# in low Mg group but do not correlate in high Mg group. Most of eclogites of both groups show positive Sr and Nb anomalies and negative Ti anomalies. The most pronounced difference in trace elements pattern between groups is the Zr anomaly which is negative in low Mg group of samples but not evident or positive in high Mg groups. Concentration of the very incompatible elements (Kd mineral/melt close to zero) La,Ce, Nb, Ta, Th and U are positively correlates with P₂O₅ contents in WR composition and between each other. The same feature was documented for deformed peridotite xenoliths from Udachnaya (Agashev et al, 2013).

Discussion and Conclusion

To evaluate the degree of metasomatic enrichment we calculate the WR composition of eclogites from composition of Cpx and Gar and their modes. Calculated WR composition contain only 0-20% of Rb and Ba of measured WR and 1-30% of Nb, Th and U (Fig). Budget of LREE in calculated WR composition are in range of 20-50% as they are compatible in Cpx. Calculated WR composition contains from 60 to 100 % of MREE, Zr and Hf. Negative Zr anomaly is present in lowMg# eclogites reconstructed composition and absent in High Mg# rocks. Positive Sr anomaly is preserved in calculated WR composition of both groups indicating that it is not of metasomatic origin. Approximately 100% of heavy REE, Ni, Co, and Sc budget of WR composition are concentrated in Gar and Cpx. The most of hardly incompatible elements reside in garnet rims. It is unclear when that garnet rims was formed. The nature of metasomatic agent is impossible to evaluate from concentration. Simple subtraction of calculated WR composition from measured gives composition that is comparable to measured composition in terms of incompatible elements and significantly different from host kimberlite composition. Therefore simple addition of kimberlite melt is not a suitable explanation of metasomatic enrichment observed in measured WR composition of eclogites.

Major elements composition of eclogites does not significantly change by metasomatic overprint that allow to use measured WR composition to constrain the protholith composition. For comparison of major elements compositions we selects two section of modern oceanic crust particularly IODP site U1309 of Atlantis Massif (Godard et al, 2009) and Hess Deep rift of Pacific Ocean (Gillis et al, 2013). As an example of Archean oceanic crust section we take the well

documented and geochemically characterized rocks of Ivisaartog greenstone belt (Polat et al, 2008). In term of MgO-CaO relations Udachnaya eclogites show identical trends to that of modern oceanic crust (Godard et al, 2009; Gillis et al, 2013) from troctolite through gabbroic rocks to basalts (Fig. 2). The same relation is evident in composition of Archean section of oceanic crust in Ivisaartoq greenstone belt (Greenland). However, modern oceanic crust contains less FeO than Udachnaya eclogites and Archean oceanic crust from Greenland. That could be consequence of higher Fe contents of Archean mantle and/or lower redox condition under which Fe was preferably incorporated in silicate minerals but presently it form oxides and oxide gabbro layers. Probably the amount of oxide gabbros is underestimated in average lower oceanic crust composition. The gabbroic suite from Atlantis massif contain to low FeO to be in equilibrium with the mantle (Coogan, 2014).

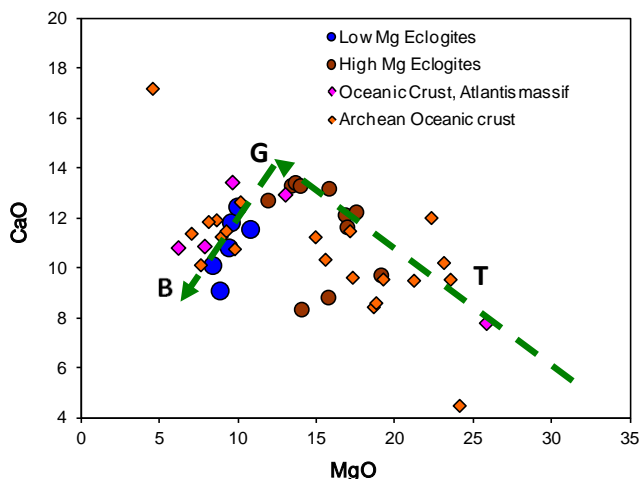
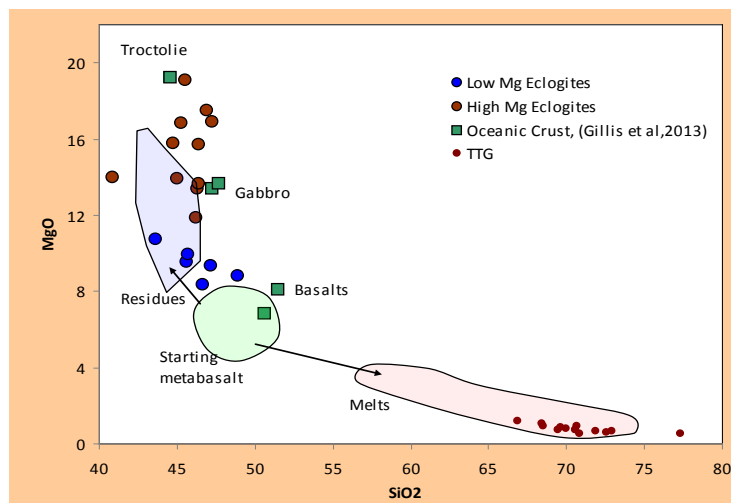


Figure 2. MgO-CaO relations in Udachnaya Eclogites compared to modern and Archean oceanic crust. Line with arrow indicate crystallisation trend (Gillis et al, 2013)

Effect of partial melting:

Mantle eclogite are often considered to be complementary residues to TTG complexes that occurs in archean cratonic areas (Rudnic 1995). This melting process according the experimental data

lives SiO₂ poor and MgO rich residues compared to starting material of basaltic composition (Rapp and Watson 1995). To evaluate the effect of partial melting we compare eclogites major elements composition to experimental data of metabasalt partial melting (Rapp and Watson 1995) and composition of present day oceanic crust. The low Mg# eclogites show negative correlations between MgO and SiO₂ that could be expected from partial melting. However high MgO eclogites have a range of MgO contents at nearly constant SiO₂ that comparable to variation of these elements observed in present day lower oceanic crust gabbro-troctolite rocks composition of (Godard 2009). Udachnaya eclogites have range of Sm/Nd ratio from 0.25 to 0.5 (MORB is 0.32) which positive covariates with Nd content that contradict to all geochemical lows. This trend could not be a result of dehydration, melt extraction nor of metasomatic enrichment as all that processes will give positive correlation. This feature is also precludes the origin of eclogites as cumulates because fractional crystallization of basic melt in the mantle will produce positive correlation between Nd and Sm/Nd ratio. Rather this feature could reflect heterogeneity of oceanic crust composition and milling/mixing of different lithologies of oceanic crust especially its lower section that consists of sm scaled layers of



different rocks during subduction. Mixing with peridotite component is also possible.

Based on study results following conclusion can be made. WR Major element composition and HREE contents of Udachnaya eclogites indicate the oceanic crustal protholith. Low Mg# eclogites could represent upper oceanic crust. High Mg# eclogites could be a mixture of different rocks composing layered lower oceanic crust. High Mg# eclogites do not experienced significant partial melting during subduction.

Figure 3. Diagram comparing composition of Udachnaya eclogites with oceanic crust section of Gillis et al, 2013) and experimental data on metabasalt melting that produce eclogitic residues (Rapp and Watson 1995).

References

- Agashev, A.M., Ionov, D.A., Pokhilenko, N.P., Golovin, A.V., Cherepanova, Yu., Sharygin, I.S., 2013. Metasomatism in the lithospheric mantle roots: constraints from WR and minerals chemical composition of deformed peridotite xenoliths from kimberlite pipe Udachnaya. *Lithos* 160–161, 201–215.
- Gillis, K.M., Snow, J.E., Klaus, A., Abe, N., et al., 2013. Primitive layered gabbros from fast spreading lower oceanic crust. *Nature* 505, 204–207
- Jacob DE (2004) Nature and origin of eclogite xenoliths from kimberlites. *Lithos* 77:295–316
- Godard M, Awaji S, Hansen H, et al. Hellebrand E., Brunelli D., Johnson K., Yamasaki T., Maeda J., Abratis M., Christie D., Kato Y., Mariet C., Rosner M. (2009) Geochemistry of a long in-situ section of intrusive slow-spread oceanic lithosphere: Results from IODP Site U1309 (Atlantis Massif, 30°N Mid-Atlantic Ridge). *Earth and Planetary Science Letters* 279: 110–122.
- Pearson, D.G., Snyder, G.A., Shirey, S.B., Taylor, L.A., Carlson, R.W., Sobolev, N.V., 1995. Archaean Re–Os age for Siberian eclogites and constraints on Archaean tectonics. *Nature* 374, 711 – 713.
- Polat, A., Frei, R., Appel, P.W.U., Dilek, Y., Fryer, B., Ordóñez-Calderón, J.C., Yang, Z., 2008. The origin and compositions of Mesoproterozoic oceanic crust: evidence from the 3075 Ma Ivisartoq greenstone belt, SW Greenland. *Lithos* 100, 293–321.
- Rudnick R (1995) Making continental crust. *Nature* 378:571–577
- Rapp RP, Watson EB (1995) Dehydration melting of metabasalt at 8–32 kbar: implication for continental growth and crust-mantle recycling. *J Petrol* 36:891–93

Geochemistry of Mirny field kimberlites, Siberia

Agashev A.M.,¹ Nakai S.,² Serov I.V.,³ Tolstov A.V.,¹ Garanin K.V.,³ Kovalchuk O.E.³

¹ V.S. Sobolev Institute of Geology & Mineralogy, Novosibirsk 630090, Russia (* correspondence: agashev@igm.nsc.ru)

² Earthquake Research Institute, The University of Tokyo, Tokyo, Japan

³ ALROSA Co Ltd., Mirny, Russia

Introduction

Kimberlites are known as incompatible elements and volatile enriched mantle originated rocks which contains a diamond. Geochemical composition of kimberlites is very heterogenic as between closely located pipes and even within one kimberlite body (Agashev et al, 2000). However, kimberlites composing one kimberlite field could be genetically related and formed by single tectono-magmatic episode from the one source. In this study we attempt to find the regularities in variations of geochemical composition of kimberlites within one kimberlite field which could arise from their genetic relationship. Mirny kimberlite field is located in the central part of Siberian craton in the southernmost part of Siberian kimberlite province. Tectonic position of the field is within the Botuobinskaya anticlinal structure, which divides the Tunguss and Vilyui synclises. Mirny field consists of six kimberlite pipes, 2 independent dykes, one satellite pipe and several dikes connected with pipes. Four kimberlite pipes are economical diamond mines. Hence, Mirny kimberlite field is a good object to systematic study the compositional variations of kimberlites composing the field.

Chemical composition

Kimberlites of Mirny field are enriched in incompatible trace elements having a solid/liquid distribution coefficient in mantle silicates of approximately zero (Ba, Sr, Nb, Ta, Zr, Hf, Th, U and LREE). At the same time they are enriched in trace elements compatible to ultramafic mineralogy such as Cr, Ni, Sc, and V and these features are typical for kimberlites. The concentrations of incompatible elements normalized to the PM composition (Fig. 2) have negative anomalies for Rb, K, Zr and positive for Nb, Th or Ba, Nd and Sm. This type of distribution was shown to be common for Gr I kimberlites (Smith et al 1985) and plume-related OIB. The degree of enrichment in incompatible elements is variable between particular pipes and concentrations of LIL elements are most variable. (Fig. 2). Variation in concentrations of LREE and HFS elements in Mirny field kimberlites are much less comparative to that of LILE. On the plot of Ba/Nb and La/Nb ratios, Mirny field kimberlites show great scatter in their Ba/Nb along the composition of main mantle reservoirs (Hoffman 1997) from values lower than that of HIMU OIB and up to values of EM OIB (Fig. 3).

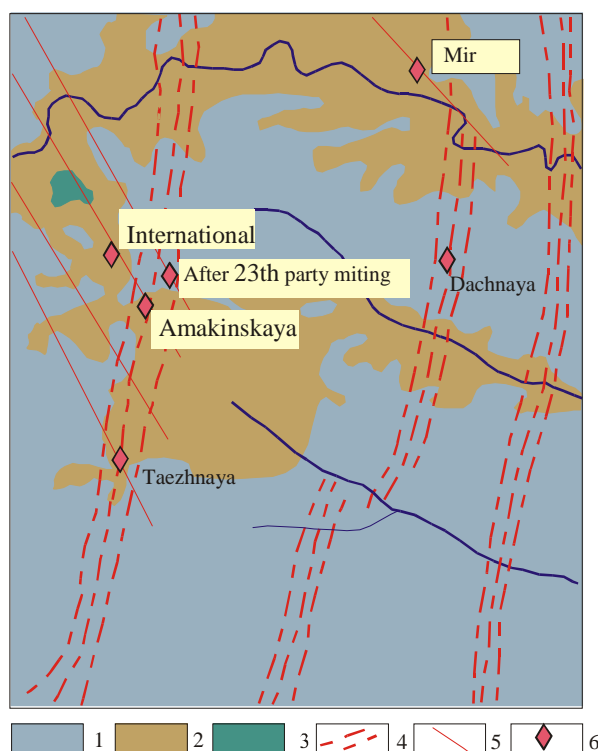


Figure 1. Schematic map of the Mirny kimberlite field 1. Lower Jurassic continental sediments. 2. Lower Paleozoic terrigenous-carboniferous rocks. 3. Basalts. 4. Regional faults. 5. feathering faults. 6. Kimberlite pipes

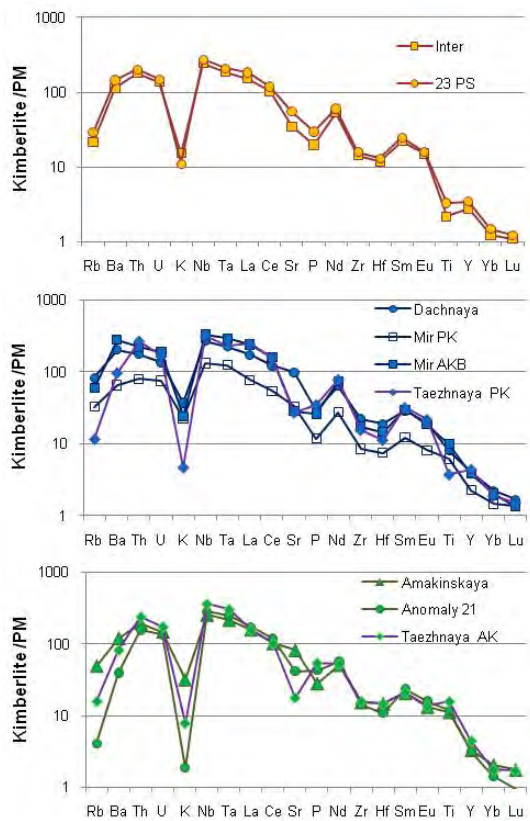


Figure 2. Primitive Mantle (PM) normalized trace elements patterns of Mirny field kimberlites. PM values after MackDonough and Sun (1995).

the word biggest diamond deposits consists of two main varieties of kimberlites (PK and AKB), which systematically differs in their geochemical composition. AKB is enriched in all incompatible elements comparative to PK. Kimberlite of Dachnaya and Taezhnaya pipes are compositionally very similar to AKB of Mir pipe.

Kimberlites of Amakinskaya pipe, Anomaly 21 dyke and AK of Taezhnaya contain high amount of low Cr megacrysts, low diamond grade and are enriched in TiO_2 , Fe_2O_3 and HFSE relative to light and middle REE.

Sr-Nd isotopes

Initial Nd isotope ratios calculated back to time of Mirny field kimberlite emplacement ($t=360$ ma) show variable depletion relative CHUR model being 4 up to 6 of ϵNd_t units, suggesting asthenospheric source for incompatible elements in kimberlites. On their Sr and Nd these kimberlites could be classified as group I, as the most of Siberian middle-Paleozoic kimberlites (Agashev et al, 2001). Sr isotope ratios are significantly variable, indicating complex source history and possible influence of postmagmatic alteration.

Discussion

Geochemical variations in kimberlite composition within one field could be explained by combination of factors and first of all it is small scale heterogeneity of source. Kimberlite source region which located at the base of lithospheric mantle (Agashev et al, 2000, 2008) have a complex history. Magmas ascending from asthenosphere beneath could form the veined heterogeneously enriched source through fractional crystallization and metasomatism of adjacent peridotites. High temperature

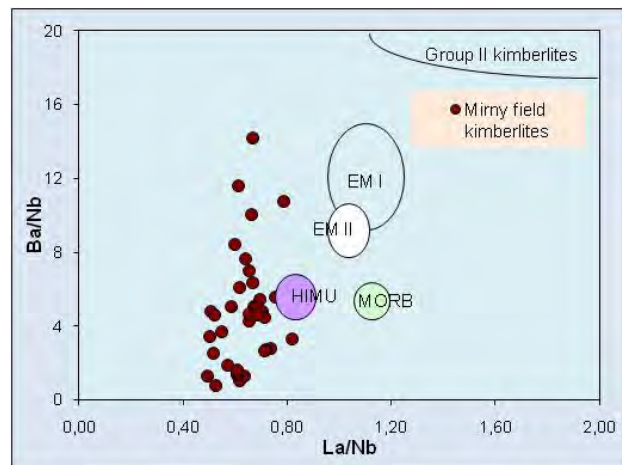


Figure 3. La/Nb vs Ba/Nb ratios diagram for Mirny field kimberlites. Compositional fields for MORB and OIB after Hofmann 1997.

Based on the chemical composition and mineralogy kimberlites of Mirny field could be subdivided into 3 groups. First group is kimberlites of Inter and 23PC, which have low TiO_2 and Fe_2O_3 contents and very similar to each other geochemical composition. They contain a little of ilmenite and other minerals of low Cr megacrysts suite and are very rich in diamond.

Second group includes Mir, Dachnaya and Taezhnaya pipes. The Mir kimberlite pipe is one of the word biggest diamond deposits consists of two main varieties of kimberlites (PK and AKB), which systematically differs in their geochemical composition. AKB is enriched in all incompatible elements comparative to PK. Kimberlite of Dachnaya and Taezhnaya pipes are compositionally very similar to AKB of Mir pipe.

Kimberlites of Amakinskaya pipe, Anomaly 21 dyke and AK of Taezhnaya contain high amount of low Cr megacrysts, low diamond grade and are enriched in TiO_2 , Fe_2O_3 and HFSE relative to light and middle REE.

Sr-Nd isotopes

Initial Nd isotope ratios calculated back to time of Mirny field kimberlite emplacement ($t=360$ ma) show variable depletion relative CHUR model being 4 up to 6 of ϵNd_t units, suggesting asthenospheric source for incompatible elements in kimberlites. On their Sr and Nd these kimberlites could be classified as group I, as the most of Siberian middle-Paleozoic kimberlites (Agashev et al, 2001). Sr isotope ratios are significantly variable, indicating complex source history and possible influence of postmagmatic alteration.

Discussion

Geochemical variations in kimberlite composition within one field could be explained by combination of factors and first of all it is small scale heterogeneity of source. Kimberlite source region which located at the base of lithospheric mantle (Agashev et al, 2000, 2008) have a complex history. Magmas ascending from asthenosphere beneath could form the veined heterogeneously enriched source through fractional crystallization and metasomatism of adjacent peridotites. High temperature

silicate metasomatism directly by asthenospheric magmas and precipitations of megacrysts suite is not favorable for diamond survival, but low-temperature metasomatism by residual volatile enriched melt probably favorable for diamond survival and grows. Parts of the source enriched in low-Cr megacrysts suite could be responsible for low diamond grade, Ti and Fe rich kimberlites like Amakinskaya pipe. Melts for diamond rich kimberlites of Inter and 23PC pipes could be formed from part of source experienced low-temperature metasomatism by residual CO₂-rich melt. In melting of high volume kimberlite magma of Mir pipe probably diverse parts of source were involved and several batches of magma were formed.

The research was supported by the Russian Foundation for Basic Research, grants no. 15-05-07758 and no. 16-05-00811 and by state assignment project (project No. 0330-2016-0006).

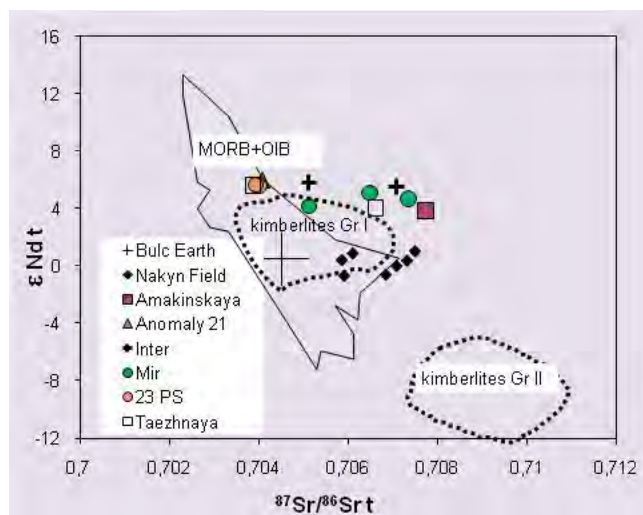


Figure 4. Sr and Nd isotope composition of Mirny field kimberlites. Compositional fields for MORB and OIB after Hofmann (1997). Nakyn field kimberlites after Agashev et al (2001). Kimberlites Group I and II after Smith (1983).

References

- Agashev A.M., Orihashi Y., Watanabe T., Pokhilenko N.P and Serenko V.P. (2000). Sr and Nd isotope and geochemical features of Siberian Platform kimberlites. *Russian Geology and Geophysics*, v41, p.90-99.
- Agashev A.M. Watanabe T. Bydaev D.A. Pokhilenko N.P. Fomin A.S. Maehara K. Maeda J. Geochemistry of kimberlites from the Nakyn field, Siberia: Evidence for unique source composition // *Geology*. - 2001. - Vol. 29. - № 3. - P. 267-270
- Agashev A.M. Pokhilenko N.P. Takazawa E. McDonald J.A. Vavilov M.A. Watanabe T. Sobolev N.V. Primary melting sequence of a deep (>250 km) lithospheric mantle as recorded in the geochemistry of kimberlite-carbonatite assemblages, Snap Lake dyke system, Canada // *Chemical Geology*. - 2008. - Vol. 255. - № 3-4. - P. 317-328.
- Hofmann, A.W., 1997, Mantle geochemistry: the message from oceanic volcanism: *Nature*, v. 385, p. 219-229.
- McDonough, W.F., and Sun, S.-s., 1995, The composition of the Earth: *Chemical Geology*, v120, p. 223-253.
- Smith, C.B., (1983), Pb, Sr and Nd isotopic evidence for sources of southern African Cretaceous kimberlites: *Nature*, v304, p. 51-54.

3-D Geological Model of the BK16 kimberlite pipe located within the Orapa Kimberlite Field (OKF) in Botswana

Mike C.J. de Wit, Macdonald Kahari, Alistair B. Jeffcoate, R. Theo Hiyoveni, Iuma Martinez, James Bruchs

Tsodilo Resources Ltd, Toronto, Ontario, Canada. mdewit@tsodiloresources.com, mac@tsodiloresources.com, alistair.jeffcoate@tsodiloresources.com, imartinez@tsodiloresources.com, jbruchs@tsodiloresources.com

INTRODUCTION

BK16 is one of the known diamondiferous kimberlites of the Orapa Kimberlite Field (“OKF”) in Botswana of at least 83 known kimberlites, and which Tsodilo Resources Ltd (“Tsodilo”) is currently evaluating for its economic potential (Fig. 1). AK01 (the Orapa Mine) was dated at 93.1 Ma (Allsopp et al., 1989), and it is presumed that all the kimberlite intrusions of the OKF are of similar post-Karoo age. Of the 83 known kimberlites of the OKF two (2) are currently being mined AK01 (of which AK02 and AK07 were part) (Orapa Mine, Debswana) and AK06 (Karowe Mine, Lucara Diamond Corporation). Other kimberlites in the area that have been mined but are currently on care and maintenance are BK09 and BK12 (Damtshaa Mine, Debswana), BK11 (Firestone Diamonds) and the DK01 and DK02 (Letlhakane Mine, Debswana). However, construction of a new treatment plant is currently underway to retreat the dumps at Letlhakane. Finally BK01 and BK15 are part of the mine plan for the Damtshaa mine to be exploited in the future. The Karowe mine is renowned for its large stones and has produced such notable diamonds as the 1,109 carat 'Lesedi La Rona' and the 813 carat 'Constellation'. The OKF lies on the northern edge of the Central Kalahari Karoo Basin, where the Karoo Supergroup dips very gently to the SSW and laps on to the pre-Karoo high consisting of Archaean and Palaeoproterozoic basement parts of which outcrop within the Makgadikgadi Depression.

The diamondiferous BK16 kimberlite pipe is approximately 5.9 hectares in size at surface, and contains Type IIa diamonds (Tsodilo, 2016). A core drilling campaign in 2015 totalling 3,050 m from 20 holes identified five (5) phases of kimberlite emplacement that make up the BK16 kimberlite pipe (see below). A geological model based on this program and historical drill information, 51 line kilometers of high resolution ground magnetic survey, and a detailed gravity survey of 441 survey stations was completed.

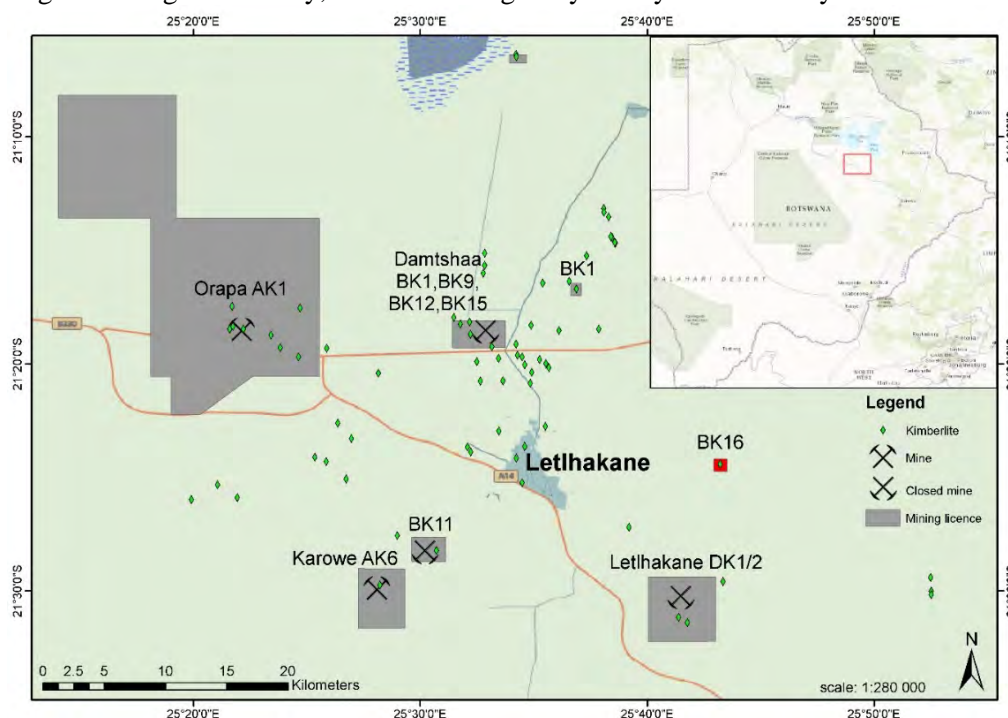


Figure 1. Location of BK16 in relation to the other kimberlites and mines within the OKF.

BK16 GEOLOGY

Five (5) different and distinct phases of kimberlite were recognised at BK16 from the recent geological logging and petrography of selected samples (Robey, 2015), these phases of kimberlite are as follows:

Kimberlite phases:

1. CB = Country Rock Contact Breccia. CB is highly diluted by country rock xenoliths and is thought to represent the embryonic phase of kimberlite emplacement. Bulk Density = 2.52 g/cm³.
2. VK2 = Volcaniclastic Kimberlite (Phase 2). VK2 phase is almost black when fresh and occupies the eastern part of the pipe. It has a magmaclastic texture and is a highly serpentinised volcaniclastic kimberlite with variable amounts of relatively unaltered basalt xenoliths. Bulk Density = 2.51 g/cm³, although when weathered is reduced to 2.31 g/cm³ (on average).
3. VK3 = Volcaniclastic Kimberlite (Phase 3). VK3 is generally a grey kimberlite when fresh and forms the western part of the pipe. It is a distinctively speckled volcaniclastic kimberlite due to common but relatively small (<10 cm) totally altered grey basalt xenoliths. Bulk Density = 2.54 g/cm³, although when weathered is reduced to 2.28 g/cm³ (on average).
4. VKxxx = Volcaniclastic Kimberlite. VKxxx is a basalt xenolith dominated (up to 88 % by volume) volcaniclastic kimberlite, and occurs dominantly in the central upper part of the pipe. Bulk Density = 2.51 g/cm³.
5. CK1 = Coherent Kimberlite. CK1 is a minor part of the intrusion and is a coherent kimberlite that was drilled in the southeast part of the pipe. It is a macrocrystic opaque-rich, and monticellite-phlogopite rich kimberlite phase. CK1 is interpreted as an early stage kimberlite dyke. Bulk Density = 2.40 g/cm³.

The average kimberlite density is 2.48 g/cm³.

Along with these kimberlite phases there is an overlying younger Kalahari overburden of approximately 25 m, consisting of calcrete and silcrete developed in the Kalahari sands and some limited loose sands at the surface. The country rock of the kimberlite is made up of Karoo age basalts of the Stormberg Lava Group down to between 90 and 120m followed by Ntsane sandstones down to some 170 m and Lower Karoo mudstones from 170 to a minimum depth of 270 m.

BK16 3D GEOLOGICAL MODEL

The data from the 20 drill core holes alongside that from the 27 historical boreholes were combined and incorporated into a three-dimensional (3-D) geological model using Gocad software. This geological model includes BK16's different phases and areas of dilution (Fig. 2). This recent Gocad model greatly refined the initial conceptual model reported in a company press release in December 2014 (Tsodilo, 2014).

From this refined model along with a retrospective study of the historical bulk sampling data that includes relative positions of these samples in relation to the zones defined by the geological model, it was possible to establish the following:

1. Of the five key kimberlite phases VK2 and VK3 are the most significant volumetrically and represent some 95% of the volume of the pipe down to 300 m.
2. The area of the pipe measures 5.9 hectares (ha) at surface, which is a substantial increase from previous estimates of 3.5 ha. A similar increase in surface size was found during exploration of AK06 (Karowe Mine), which increased from 3.3 ha determined in the early 1970s to 9.5 ha when modern exploration techniques were applied in 2003 (Lynn et al., 2014).

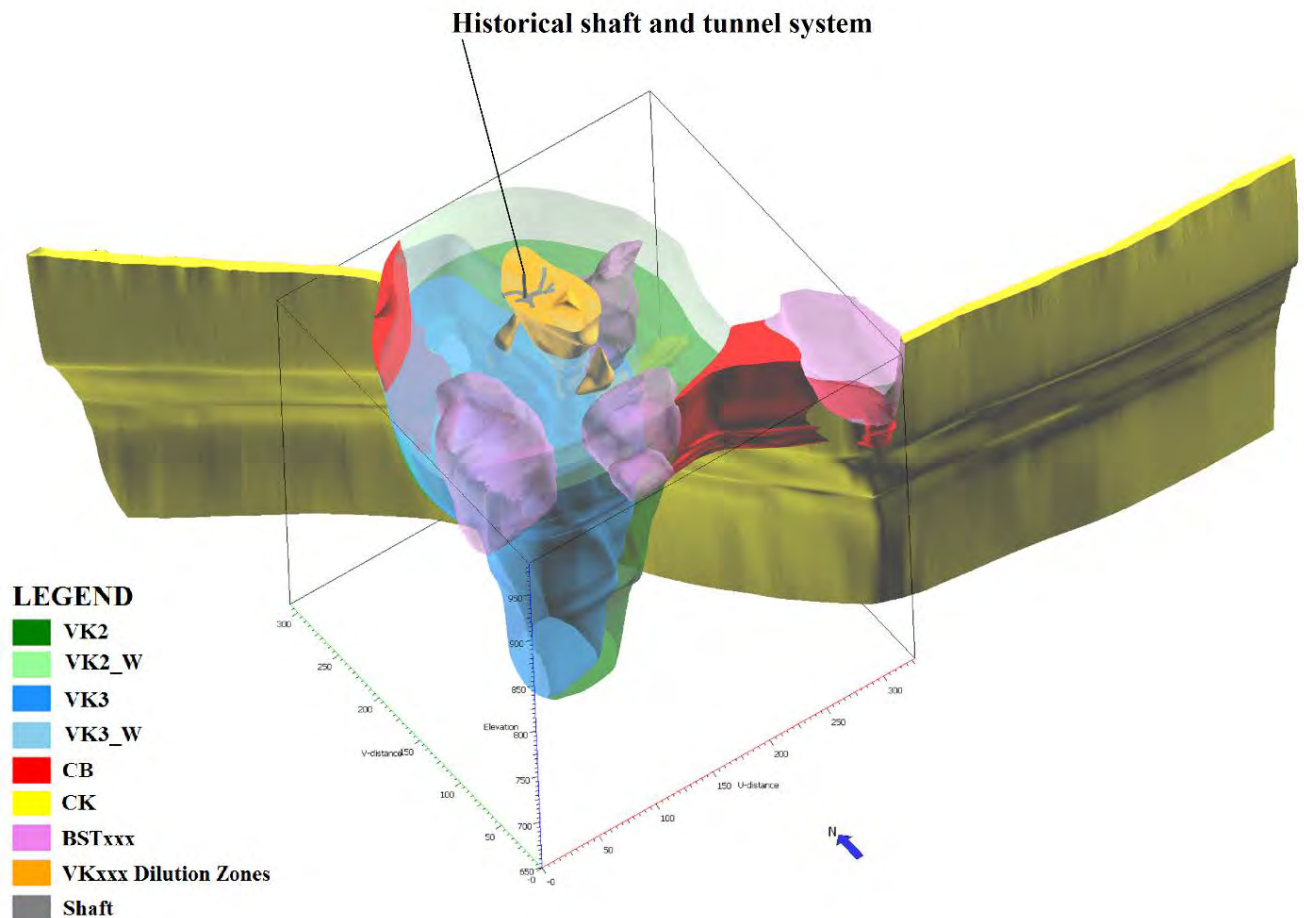


Figure 2. BK16 Geological model below the Kalahari cover overburden, created using Gocad software. It highlights the different kimberlite phases and areas of VKxxx dilution zones (often referred to as basalt breccia). Also shown are the shaft and tunnel systems and their location relative to these VKxxx zones.

References

- Allsopp HL, Bristow JW, Smith CB, Brown R, Gleadow AJW, Kramers JD, Garvie OG (1989) A summary of radiometric dating methods applicable to kimberlites and re-lated rocks. *Kimberlites and Related Rocks*, vol. 1, Their composition, occurrence, origin and emplacement. *Spec.Publ.-Geol. Soc. Aust.*, vol. 14, pp. 343–357.
- Lynn M, Nowicki T, Valenta M, Robinson B, Gallagher M, Bolton R, Sexton J (2014) Karowe Diamond Mine Botswana NI 43-101 Independent Technical Report (Amended). Prepared on Behalf of Lucara Diamond Corp.
- Robey JvA (2015) Petrography of selected samples taking of BK16 core during the April 2015 logging exercise - Bosoto Pty (Ltd). Internal Report by Rockwise Consulting CC.
- Tsodilo Resources Limited Press Release, Dcember 15th (2014) Conceptual Geological Model for BK16. http://www.tsodiloresources.com/i/pdf/2014-12-15_NR-59uXmN.pdf
- Tsodilo Resources Limited Press Release, May 31st (2016) Tsodilo Resources Limited Confirms the Presence of Rare and Valuable Type Ila Diamonds in BK16. http://www.tsodiloresources.com/i/pdf/2016-05-31_NR.pdf

Mineralogy of the baotite-bearing Gundrapalli lamproite, Nalgonda district, Telangana, India

Gurmeet Kaur¹ and Roger H. Mitchell²

¹ Panjab University, Chandigarh, India, gurmeet28374@yahoo.co.in

² Lakehead University, Thunder Bay, Ontario, Canada, rmitchel@lakeheadu.ca

Introduction

Ultrapotassic magmatism is quite prevalent in the Eastern Dharwar Complex of south India. Numerous new finds of lamproite dykes from and around the Palaeo-Mesoproterozoic Cuddapah basin gives an opportunity to understand the nature of the subcontinental lithospheric mantle in southern India. We present the mineralogy of a newly discovered lamproite dyke at Gundrapalli village (Nalgonda district) northwest of Cuddapah basin (Figure 1 inset). The lamproite dyke at Gundrapalli village, intruded into the Paleoproterozoic biotite granite unit of Peninsular Gneissic Complex form part of eastern Dharwar Complex. (Figure 1; Kumar et al., 2013, Ahmed et al., 2012).

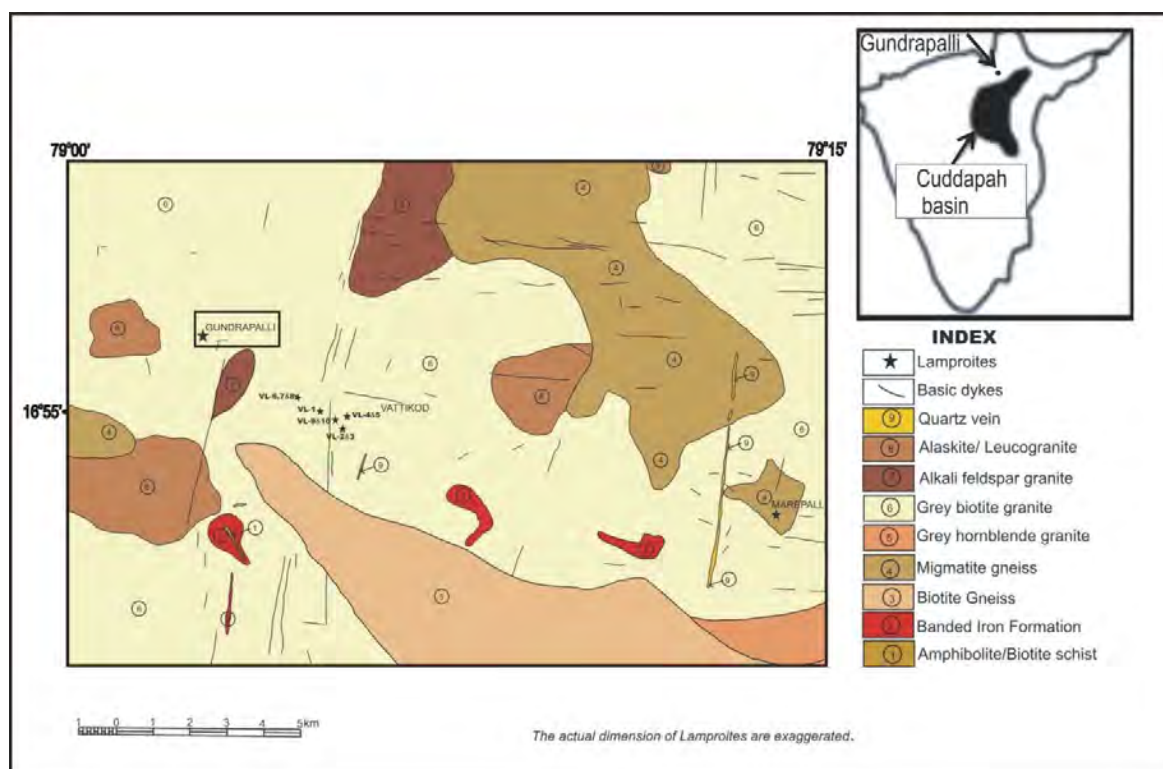


Figure 1: The location of Gundrapalli dyke (northwest of Cuddapah basin; Inset map) and other lamproite dykes of Vattikod in the vicinity of Gundrapalli in Nalgonda district, Telangana, India (after Kumar et al., 2013; Gurmeet Kaur et al., 2016).

Mineralogy of Gundrapalli dyke

The Gundrapalli dyke consists of a mineral assemblage whose compositions are comparable to those of lamproites in terms of the presence of: phlogopite (Ti-rich, Al-poor); amphiboles (potassic-richterite, potassic-arfvedsonite, magnesio-riebeckite, Ti-rich potassic-magnesio-arfvedsonite, potassic-magnesio-arfvedsonite, katophorite and potassic-ferri-katophorite); Al-poor pyroxene; K-feldspars (leucite/sanidine), spinel (chromite-magnesiochromite), apatite (fluorine-rich), titanite, rutile, baritocalcite, calcite, ilmenite, hydro-zircon, baotite, strontianite, allanite, quartz and pyrite. The absence of Ba-Ti-Zr minerals such as wadeite, priderite have been compensated for by the

presence of baotite, rutile, barite, hydrozircon. The presence of secondary phases such as allanite, hydro-zircon, chlorite, quartz and cryptocrystalline SiO₂, implies that the dyke has undergone varied degrees of deuteric alteration. We classify the dyke on the basis of its typomorphic major mineralogy as pseudoleucite-phlogopite-amphibole-lamproite.

We report the presence of the rarely occurring mineral, baotite from this lamproite. This is also the first report of mineral baotite from a lamproite from India. Baotite, a Cl-rich barium-titanium-silicate mineral has been earlier reported from a few carbonatites and lamproites, in addition to some alkali granites and pegmatites. Generally, baotites from different rock types have composition varying between the end member Ba₄Ti₈Si₄O₂₈Cl and end member Ba₄Ti₂Fe²⁺₂Nb₄Si₄O₂₈Cl.

The presence of baotite and fluorine rich apatite is of great importance as a similar mineralogy for lamproites has been reported from the Kvaløya lamproite dyke, intruded into Paleoproterozoic granite, part of the West Troms Basement Complex, on the island Kvaløya, northern Norway. There is striking similarity between the baotite found in Kvaløya and Gundrapalli. Baotites in both rocks form as aggregates with radiating structures instead of well-defined crystals and are closely associated with rutile, amphiboles and (also titanite in case of Gundrapalli) which raise the question of their being of magmatic origin (Figure 2A, B). Another striking similarity between the two dyke rocks is presence of zoned apatites with an early magmatic phase in the core and the REE-rich apatite overgrowths on the cores indicating reactions with the late magmatic fluid.

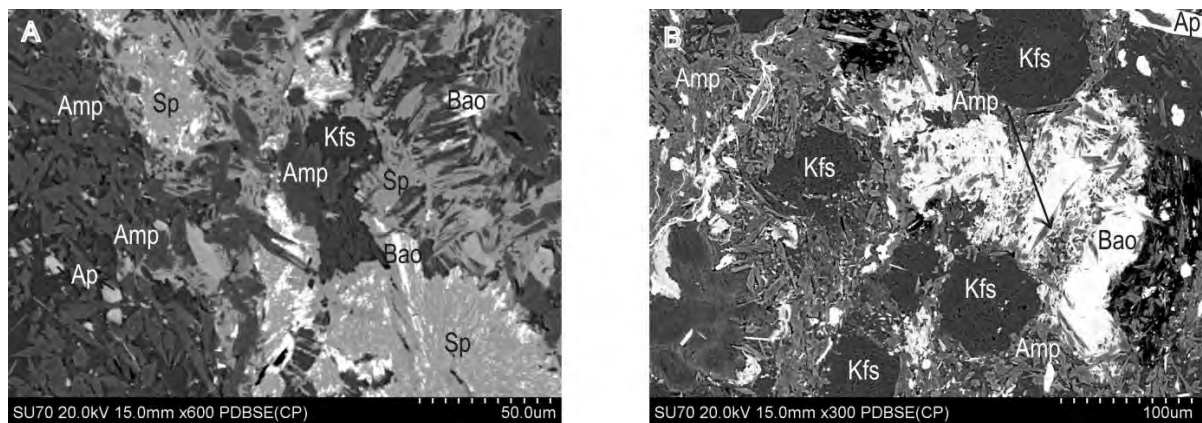


Figure 2A: Baotite in association with titanite (Sp). Also seen are groundmass minerals amphiboles, K-feldspar and apatite (BSE image). **Figure 2B:** Baotite in association with amphiboles. K-feldspar, amphiboles, apatite and barite form groundmass material (BSE image).

Baotites from both the Norwegian and Indian lamproites are Nb-free types with the composition Ba₄Ti₈Si₄O₂₈Cl (Table 1). The high Cl-content of baotite in Gundrapalli, as also in case of Kvaløya, indicates partitioning of Cl into baotite in the presence of a Cl-bearing F-rich hydrous fluid.

Table 1:

| Oxides (wt%) | 1 | 2 | 3 | 4 | 5 | 6 | 7 (n=38) | Std. Dev. |
|--------------------------------|-------|-------|-------|-------|-------|-------|----------|-----------|
| SiO ₂ | 15.86 | 15.87 | 15.26 | 15.52 | 15.90 | 15.92 | 15.70 | 0.21 |
| TiO ₂ | 40.52 | 39.87 | 39.56 | 39.77 | 40.09 | 39.32 | 41.91 | 0.23 |
| Al ₂ O ₃ | n.d. | n.d. | n.d. | n.d. | n.d. | n.d. | 0.32 | 0.03 |
| FeO* | 0.88 | 1.38 | 1.33 | 1.41 | 1.38 | 1.65 | n.d. | |
| CaO | 2.30 | 2.12 | 3.02 | 0.40 | 2.93 | 1.65 | 0.06 | 0.09 |
| BaO | 38.34 | 38.11 | 37.89 | 40.71 | 38.71 | 39.40 | 39.20 | 0.24 |
| SrO | n.d. | n.d. | n.d. | n.d. | n.d. | n.d. | 0.17 | 0.05 |
| K ₂ O | n.d. | n.d. | n.d. | n.d. | n.d. | n.d. | 0.16 | 0.07 |

| | | | | | | | | |
|---|--------|--------|--------|--------|--------|--------|--------|------|
| Nb ₂ O ₅ | 1.20 | 1.25 | 1.28 | 1.01 | 0.82 | 1.10 | 0.35 | 0.17 |
| Cl | 2.11 | 2.20 | 2.19 | 2.24 | 1.97 | 2.17 | 2.43 | 0.04 |
| Total | 101.21 | 100.80 | 100.53 | 101.06 | 101.80 | 101.21 | 100.30 | |
| O=Cl | 0.48 | 0.50 | 0.49 | 0.51 | 0.44 | 0.49 | 0.55 | |
| Total | 100.73 | 100.30 | 100.04 | 100.55 | 101.36 | 100.72 | 99.75 | |
| <i>Structural formula calculated on the basis of 16 cations</i> | | | | | | | | |
| Si | 3.90 | 3.92 | 3.95 | 3.91 | 3.86 | 3.94 | 3.96 | |
| Ti | 7.49 | 7.41 | 7.24 | 7.54 | 7.32 | 7.33 | 7.94 | |
| Al | 0.00 | 0.00 | 0.00 | 0.00 | 0.00 | 0.00 | 0.10 | |
| Fe | 0.18 | 0.29 | 0.27 | 0.30 | 0.28 | 0.34 | 0.00 | |
| Ca | 0.61 | 0.56 | 0.79 | 0.11 | 0.76 | 0.44 | 0.02 | |
| Ba | 3.69 | 3.69 | 3.61 | 4.02 | 3.68 | 3.83 | 3.87 | |
| Sr | 0.00 | 0.00 | 0.00 | 0.00 | 0.00 | 0.00 | 0.02 | |
| K | 0.00 | 0.00 | 0.00 | 0.00 | 0.00 | 0.00 | 0.05 | |
| Nb | 0.13 | 0.14 | 0.14 | 0.12 | 0.09 | 0.12 | 0.04 | |
| Cl | 0.88 | 0.92 | 0.90 | 0.96 | 0.81 | 0.91 | 1.04 | |

n.d. –not detected; FeO*total Fe expressed as FeO

Table 1 : Representative compositions (wt. %) of baotites (1-6) from Gundrapalli lamproite and average composition of baotite (7) from the Kvaløya lamproite (n=38). Data for Kvaløya lamproite taken from Kullerud et al., 2012.

Conclusions

The Gundrapalli dyke, occurs in vicinity of other lamproites within the Vatikod lamproite field (Gurmeet Kaur et al., 2016) and is classified as **pseudoleucite-phlogopite-amphibole-lamproite**. Baotite has been identified for the first time from an Indian lamproite. The presence of Ti- and Ba-rich phases such as baotite, rutile, allanite, titanite together with quartz suggest high aSi, aTi, aBa, in equilibrium with a high-F, Cl-bearing hydrous fluids. The lamproite magmas are generally enriched in F and Cl and are characteristic of lamproite rocks (Mitchell and Bergman, 1991). The presence of above F and Cl phases indicate that the high F, Cl fluids were operational during the formation of Gundrapalli lamproite.

References

- Ahmed S, Kumar A (2012) Search for Kimberlite/lamproite in Paluvayi block in Nalgonda district, Andhra Pradesh. Geological Survey of India report on www.portal.gsi.gov.in.
- Gurmeet Kaur, Mitchell RH, Ahmed S (2016) Typomorphic mineralogy of the Vattikod lamproites from Mesoproterozoic Ramadugu Lamproite Field, Nalgonda District, Telangana, India: A plausible manifestation of subduction-related alkaline magmatism in the Eastern Ghats Mobile Belt? 35th IGC abstract id 3482.
- Kullerud K, Zozulya D, Ravna E (2012) Formation of baotite-a Cl-rich silicate-together with fluorapatite and F-rich hydrous silicates in the Kvaløya lamproite dyke, North Norway. *Mineralogy and Petrology* 105: 145-156.
- Kumar A, Ahmed S, Priya R, Sridhar M (2013) Discovery of lamproites near Vattikod area, NW margin of the Cuddapah basin, Eastern Dharwar craton, southern India. *Journal of the Geological Society of India* 82: 307–312.
- Mitchell RH, Bergman SC (1991) *Petrology of Lamproites*. Plenum Press, New York, 447pp.

Discrete Ti-Al±Ca metasomatism at ~53 kbar in chromite-garnet peridotites from Newlands kimberlite, South Africa

H. S. Grütter¹ and A. H. Menzies²

¹ Peregrine Diamonds Ltd., Vancouver, BC, Canada, herman@pdiam.com

² Universidad Católica del Norte, Antofagasta, Chile, amenzies@ucn.cl

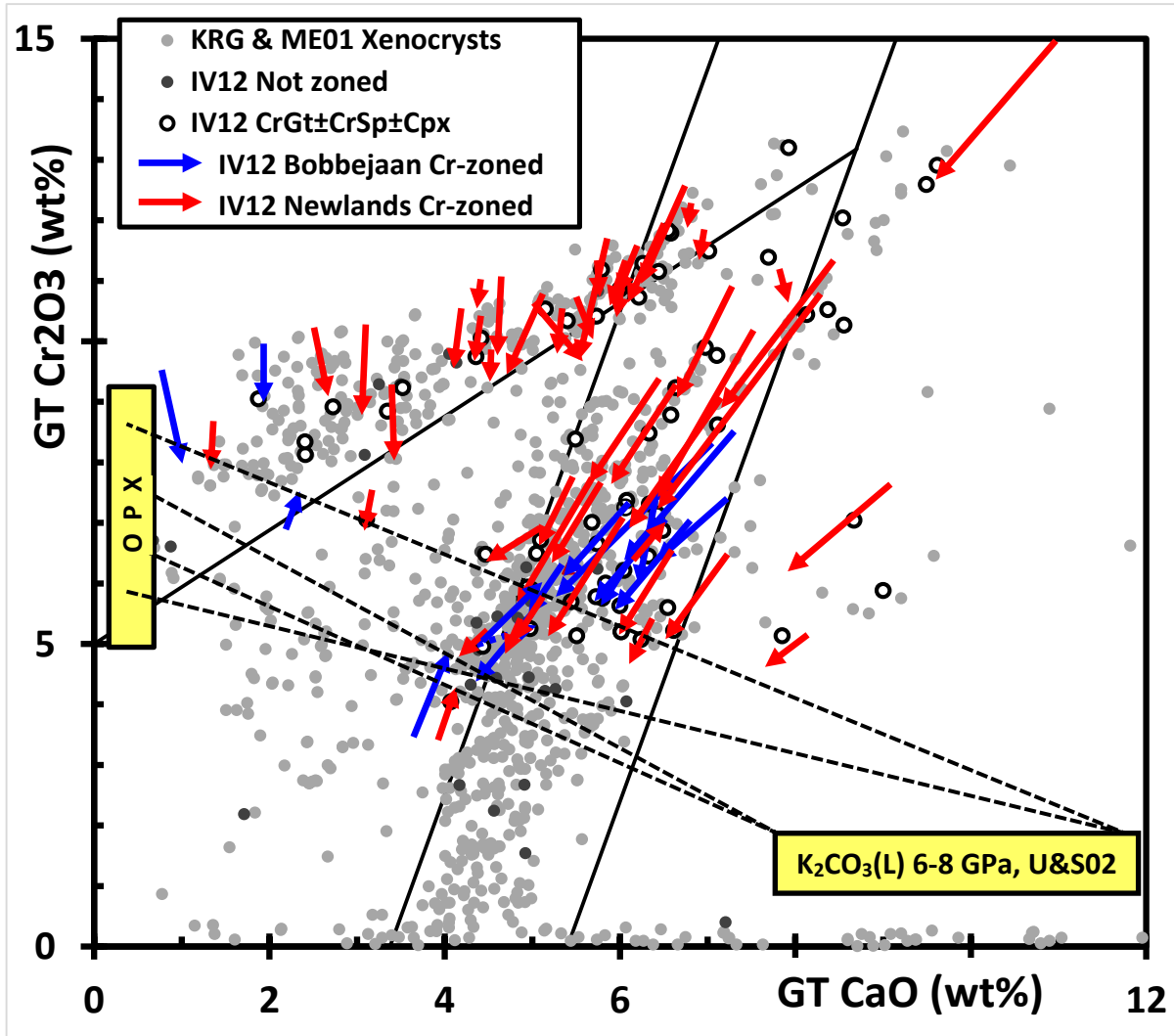


Figure 1: Cr₂O₃-CaO diagram showing Newlands garnet compositions (dots, circles) and core to rim Cr-zonation (arrows) of garnets from Newlands (red) and Bellsbank-Bobbejaan (blue). Down-Cr₂O₃ vs. up-Cr₂O₃ zonation vectors constrain an Opx-modulated interaction with carbonate melt (yellow boxes, dashed tielines).

Introduction

Peridotite xenoliths containing equilibrated, coexisting chromite+garnet assemblages are of special interest to mantle researchers because their low-variance assemblage(s) constrain critical P-T-X relationships among Olivine (Ol), orthopyroxene (Opx), clinopyroxene (Cpx), Cr-pyropo garnet (CrGt), chromite (CrSp) ± diamond ± graphite (Dia/Gph) (e.g. Grütter et al, 2006; Zibera et al, 2013). A veritable treasure trove of such CrSp+CrGt±Dia assemblages from the ~114 Ma Newlands kimberlite and the ~118 Ma Bellsbank-Bobbejaan fissure were described in Ph.D. theses by Menzies (2001 [ME01]) and Ivanic (2007 [IV07]), and substantive portions of these valuable data sets are now published (Menzies et al., 1999 [ME99]; Ivanic et al., 2012 [IV12]). Cr-pyropo compositions in the IV12 data set cover a significant CaO range and show striking Cr-zoned trends (Fig. 1) that IV12 interpret as resulting from metamorphic re-equilibration during a postulated 10-20 kbar

decompression event. A down-pressure evolution is one feasible explanation for down-Cr₂O₃ garnet zonation, *though not for up-Cr₂O₃ garnet zonation*, because high-Cr CrSp grains and serpentinized former peridotitic phases occur in intimate contact/intergrowths with the Cr-zoned garnets. We examined the unique IV12 data set to potentially derive a Ti-correction factor for our Cr/Ca-in-pyrope barometer (Grütter et al, 2006), though instead found tieline evidence of a discrete ~ 53 kbar, Ti-Al±Ca (carbonatitic) melt-metasomatic interaction modulated by peridotitic Opx that we hold accountable for the Cr-zoned garnet compositions (Fig. 1). Some of our findings are detailed below.

Metasomatic TiO₂ in garnet

Peridotitic CrGt±CrSp±Cpx micro-xenoliths and xenocrysts selected from coarse concentrate and respectively investigated by ME01 and IV12 show subtle, though distinct, differences in TiO₂ content: Two-thirds of ME01 CrGt's have TiO₂ ≤ 0.05 wt%, typical of unmetasomatised depleted peridotite, while two-thirds of IV12 CrGt's have TiO₂ > 0.05 wt%, indicative of cryptic, metasomatic TiO₂ enrichment (Figure 2). Ti-, Y-, Zr- and REE-enriched zones at CrGt exteriors are a well-known feature related to Fe-Ti melt-metasomatism in high-temperature “sheared” peridotite xenoliths (Griffin et al, 1996 and references there-in). However, none of the 79 Cr-zoned specimens investigated by IV12 contain a low-Ti CrGt core mantled by a higher-Ti exterior zone. IV12 Cr-zoned garnets instead contain mostly 0.1 to 0.7 wt% TiO₂ in their cores, and contain effectively uniform TiO₂ content from cores to rims (Figure 2); several samples show a subtle 0.02 to 0.04 wt% TiO₂ decrease rimward. Consistent, equilibrated Ti partition for CrGt/CrSp is observed for 47 of 53 touching CrGt+CrSp±Cpx (sub)-assemblages analysed by IV12, with Ti-CrSp compositions overlapping those of metasomatised peridotite xenoliths from the Kimberley area: elevated CrGt TiO₂ at Newlands is metasomatic !

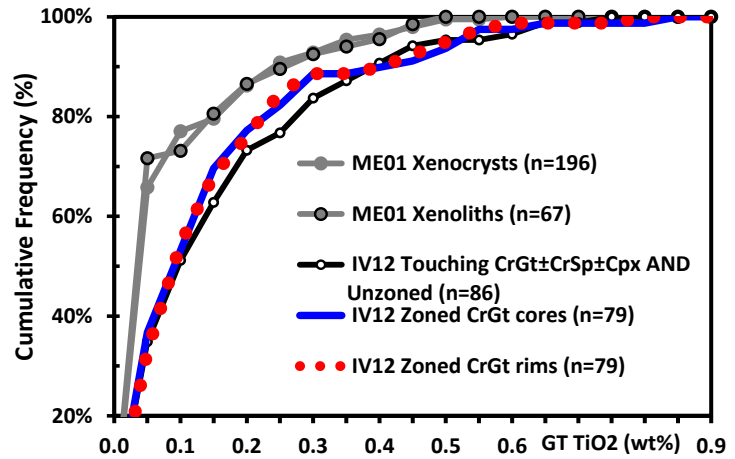


Figure 2: Comparative GT TiO₂ contents for xenocrysts, micro-xenoliths and Cr-zoned garnets from Newlands (and Bobbejaan). Note essentially constant, *not-zoned* TiO₂ from cores to rims of IV12's Cr-zoned garnets, even at 0.1 to 0.7 wt% GT TiO₂.

An alkali-carbonatite metasome

We interpret the equilibrated, elevated, not-zoned and sample-specific Ti attributes in the Newlands & Bobbejaan Cr-zoned garnets as resulting from garnet growth in a metasomatically infiltrated peridotitic “closed” system characterised by internal buffering at low (< 1 ?) metasome/rock ratios. Based in part on the tieline evidence shown in Figure 1, we envisage the metasome to be similar to the Group-2 kimberlite-type alkali-carbonatitic liquids that Ulmer and Sweeney (2002 [U&S02]) experimentally equilibrated with garnet harzburgite mineralogy at 4.0 – 9.5 GPa and 1200 to 1500°C. The U&S02 alkali-carbonatitic liquids equilibrated with additional Cpx (i.e. garnet lherzolite) at lower temperatures, and contain somewhat more SiO₂, Al₂O₃ and TiO₂ than obtained by Sokol et al (2016 [SO16]) for alkali-carbonatitic liquids in H₂O-absent sandwich experiments designed to simulate the interaction of “dry” carbonatite with peridotite (see Table 1).

| Reference | Composition | SiO ₂ | TiO ₂ | Al ₂ O ₃ | Cr ₂ O ₃ | FeO | MnO | NiO | MgO | CaO | Na ₂ O | K ₂ O | Sum | CO ₂ | H ₂ O |
|-----------|-------------|------------------|------------------|--------------------------------|--------------------------------|-----|-----|-----|------|------|-------------------|------------------|------|-----------------|------------------|
| U&S02 | Liq / GPll | 24.4 | 1.7 | 3.3 | 0.2 | 6.8 | 0.2 | - | 21.6 | 9.5 | 1.1 | 5.3 | 74.0 | 15.3 | 10.7 |
| SO16 | Liq / HC | 2.3 | 0.6 | 0.6 | 0.0 | 4.7 | 0.2 | 0.2 | 12.3 | 13.2 | 1.9 | 16.4 | 55.2 | 47.7 | - |
| SO16 | Liq / LC | 4.0 | 0.5 | 1.2 | 0.1 | 6.0 | 0.2 | 0.0 | 12.0 | 13.4 | 1.8 | 13.3 | 52.4 | 47.4 | - |
| SO16 | HC HZB | 45.8 | - | 2.7 | 1.1 | 7.7 | 0.1 | 0.3 | 41.5 | 0.6 | - | - | 99.7 | | |
| SO16 | LC LHZ | 45.8 | 0.2 | 4.1 | 0.5 | 7.5 | 0.1 | 0.4 | 37.7 | 3.2 | 0.3 | - | 99.7 | | |

Table 1: Average alkali-carbonatite liquid compositions equilibrated with typical harzburgite (HC) or lherzolite (LC) by Ulmer and Sweeney (2000 [U&S02]) or Sokol et al. (2016 [SO16]).

Al₂O₃, Cr₂O₃ and CaO in garnet

The core-to-rim zonation of garnet Cr₂O₃ content shown on Figure 1 reflects changing garnet Cr/(Cr+Al), in response to changing bulk Cr/(Cr+Al). A quick calculation shows some 5 modal% *completely new* garnet can be grown at progressively changing Cr/(Cr+Al) by progressively adding 0.9 wt% Al₂O₃ to a depleted peridotite. Since the U&S02 alkali-carbonatitic liquids in the peridotite-H₂O-CO₂ system contain significant Al₂O₃ (~3.3 wt%, Table 1) at very low Cr/(Cr+Al), the nett Al₂O₃ balance to grow the Newlands down-Cr zoned garnets *from scratch* would be completely satisfied by interacting 1 part U&S02 melt with ~3.6 parts peridotite. Up-Cr₂O₃ garnet growth occurs where initial garnets have Cr/(Cr+Al) lower than a tieline between Opx and percolating U&S02 melt (see Fig. 1).

Most harzburgitic garnets impacted by natural (or experimental) metasomatism show substantive increases in CaO from core-to-rim (e.g. Griffin et al, 1999). We ascribe the unique near-constant CaO observed by IV12 in harzburgitic garnets (Fig. 1) to low metasome/rock ratios and attendant effective internal buffering of CaO in garnet harzburgite-magnesite-U&S02 melt assemblages. IV12 uniquely also record garnet CaO content *decreasing* across the lherzolite field (Fig. 1), which we ascribe to metasomatically increased Na₂O in Cpx coexisting with CrGt (see Sobolev et al., 1997).

Pressures and temperatures

Single-Cpx thermobarometry shows a ~ 38 mW/m² geotherm for Newlands, with no evidence of near-adiabatic high temperatures, nor thermal disturbances at high P&T. Cr/Ca-in-pyrope barometry (Grütter et al, 2006) gives real P₃₈ of 26 to 53 kbar for IV12 CrGt+CrSp samples, and 44 to 53 kbar for the ten diamond-bearing CrGt+CrSp samples described by ME01. The P-T data are consistent with undetectable heat transfer during U&S02 melt interaction with opx-bearing peridotite across the pressure range 53 to 26 kbar. These P-T data support the internally buffered systems at low metasome/rock ratios that we implicate in the genesis of the Newlands Cr-zoned garnets.

References

- Griffin WL, Shee SR, Ryan CG, Win TT, Wyatt BA (1999) Harzburgite to lherzolite and back again: metasomatic processes in ultramafic xenoliths from the Wesselton kimberlite, Kimberley, South Africa. *Contrib Mineral Petrol* 134: 232-250
- Griffin WL, Smith D, Ryan CG, O'Reilly SY, Win TT (1996) Trace-element zoning in mantle minerals: metasomatism and thermal events in the upper mantle. *Can Mineral* 34:1179-1193.
- Grütter H, Latti D, Menzies A (2006) Cr-saturation arrays in concentrate garnet compositions from kimberlite and their use in mantle barometry. *J Petrol* 47:801-820.
- Ivanic T (2007) The chromite-garnet peridotite assemblages and their role in the evolution of the mantle lithosphere, PhD Thesis, University of Edinburgh, 249 pp. [IV07]
- Ivanic TJ, Harte B, Gurney JJ (2012) Metamorphic re-equilibration and metasomatism of highly chromian, garnet-rich peridotitic xenoliths from South African kimberlites. *Contrib Mineral Petrol* 164:505–520. [IV12]
- Menzies AH (2001) A detailed investigation into diamond-bearing xenoliths from Newlands kimberlite, South Africa. PhD Thesis, University of Cape Town [ME01]
- Menzies AH, Shirey SB, Carlson RW, Gurney JJ (1999) Re–Os systematics of Newlands peridotite xenoliths: implications for diamond and lithosphere formation. *Proceedings of the 7th International Kimberlite Conference*. Red Roof Design, Cape Town, V2, pp. 566–583. [ME99]
- Sobolev VN, Taylor LA, Snyder GA, Sobolev NV, Pokhilenko NP, Kharkiv AD (1997) A unique metasomatised peridotite from the Mir kimberlite, Siberia. *Russian Geol. Geophys.* 38: 218–228
- Sokol AG, Kruk AN, Chebotarev DA, Palyanov YN (2016) Carbonatite melt–peridotite interaction at 5.5–7.0 GPa: Implications for metasomatism in lithospheric mantle. *Lithos* 248–251: 66–79.
- Ulmer P and Sweeney RJ (2002) Generation and differentiation of group II kimberlites: Constraints from high-pressure experiments to 10 GPa. *Geochim Cosmochim Acta* 66: 2139–2153. [U&S02]
- Ziberna L, Klemme S, Nimis P (2013) Garnet and spinel in fertile and depleted mantle: insights from thermodynamic modelling, *Contrib Mineral Petrol* 166: 411-421.

Tracing kimberlitic indicators to their kimberlite source at Chidliak, Nunavut, Canada, re-visited: the unexpected accuracy of a simplified Mahalanobis-distance approach

H. S. Grütter, C. E. Fitzgerald and J. A. Pell

*Peregrine Diamonds Ltd., Vancouver, BC, Canada,
herman@pdiam.com, cathy@pdiam.com, jennifer@pdiam.com*

Introduction

Peregrine Diamonds has previously reported on the evolution and refinement of efforts to trace kimberlitic indicators recovered from till sampling campaigns to their kimberlite source(s) at the Chidliak project on Baffin Island, Canada (see Neilson et al., 2012; Pell et al., 2013). Our earlier work capitalized on the comparative abundance of fresh peridotitic ± eclogitic garnets in till samples, and leveraged Mn-thermometry applied to Cr-pyrope compositions (after Grütter and Tuer, 2009) to reveal distinct Temperature-TiO₂ profiles (TTiPs) that match equally distinct TTiPs in up-ice kimberlite sources (see Fig. 1 for TTiP explanation and Fig. 2 for an example from northern Chidliak). Simple visual comparison of TTiPs has served to conclusively “fingerprint” and resolve several sources, but we have encountered ambiguous TTiP-source interpretations in settings where:

- Similar TTiPs occur in closely spaced known sources (e.g. Fig. 7 of Neilson et al., 2012);
- One or more known source(s) contain log-orders more indicators per kilogram of kimberlite, and consequently “swamp” the TTiP signal from nearby source(s) that have low indicator counts;
- A high sample density reveals many till samples with a near-uniform “bulk-average” TTiP, resulting in ambiguous interpretations of potentially unique sources (e.g. Fig. 5 of Neilson et al., 2012). This “problem” is particularly conducive to analysis by Mahalanobis-distance techniques due to an anchoring effect provided by the common “bulk-average” (or mean) TTiP.

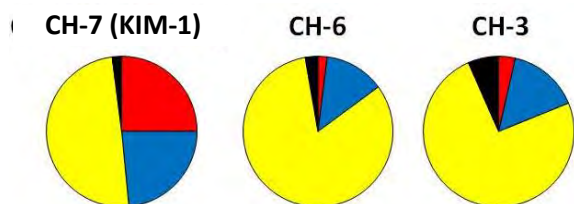


Figure 1 (above): Pie-charts showing temperature-TiO₂ profiles (TTiP’s) for Cr-pyrope populations from the CH-7 (KIM-1), CH-6 and CH-3 kimberlites. Mn-in-pyrope thermometry classes are: graphite-facies (T-Mn < 900°C, yellow), shallow diamond-facies (T-Mn 900 to 1100°C, blue), deep diamond-facies (T-Mn > 1100°C, red), and high TiO₂ (G1 and G11 garnets with TiO₂ > 0.6 wt%, black). The Mahalanobis-distance technique espoused in this work easily differentiates the CH-6 TTiP from the CH-3 TTiP, even though they appear visually similar.

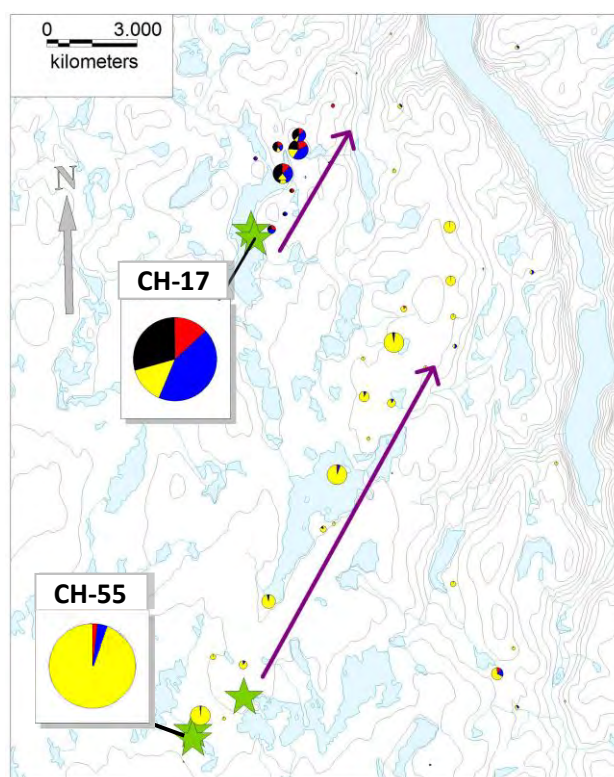


Figure 2 (at right): Temperature-TiO₂ profiles of kimberlites CH-17 and CH-55 are very distinct, and remain distinct in till samples defining northeastward down-ice glacial dispersion (after Fig. 3 of Neilson et al., 2012).

The Mahalanobis distance

We have compiled an intuitive definition from several sources, and describe the Mahalanobis distance (MD) as “a unitless descriptive statistic that measures the relative distance of a datum from a common point (i.e. a standardized residual relative to a mean). It is used to gauge the similarity in attributes of a given sample to the mean of the same attributes in a population. Mahalanobis is scale-invariant and differs from Euclidean distance as it accounts for correlations within multi-variate data”. A graphical representation is shown in Fig. 3.

In practise, we isolate all Cr-pyrope data from the area of interest, and for each (till) sample we calculate

$$MD = T\text{TiP}_{(\text{area_mean})} - T\text{TiP}_{(\text{sample})},$$

subject to $n \geq 5$ Cr-pyrope analyses per sample. We exclude sample X-Y coordinate data from our TTiP-based MD calculation, even though generic MD applications often promote X-Y coordinates or nearest-neighbour attributes to be factored into MD calculations (i.e. cluster analysis). Our MD calculation quantifies two questions:

- How different is the TTiP of this (till) sample from the mean TTiP in this area ?
- Which samples in this area have a similar MD and could belong to the same TTiP population ?

An example outcome: The CH-6 area

Outcomes of our MD calculations are typically examined at the ~ 4 to 12 km scale that Cr-pyrope garnets spread away from a (presumed) kimberlite source; the related detail is difficult to reproduce in the format of this long abstract. We show the outcome of MD calculations in the area of the CH-6, CH-20, CH-10 and CH-22 kimberlites as an example (Figure 4). The following notes apply:

- Forty-three of 85 till samples collected in the CH-6 area are represented by five or more analysed Cr-pyrope garnets. Our MD calculations are based on the 1,338 Cr-pyrope analyses from these 43 samples because we consider them statistically representative of the area of interest.
- 511 Cr-pyrope analyses from 17 of 43 samples define a dominant near-mean MD population (within 0.46 standardized units). Figure 4a) shows the TTiP for Cr-pyropes from these samples comprises $89.4 \pm 2.6\%$ graphite-facies temperatures (yellow), $9.8 \pm 2.8\%$ shallow diamond-facies temperatures (blue) and - significantly - no high-TiO₂ grains. The near-mean population occurs in a western spatial subset of Cr-pyropes occurring down-ice of CH-6 (see Fig. 4a).
- 517 Cr-pyrope analyses from 7 of 43 samples define another significant MD population, though with off-mean MD values (at 0.53 to 1.7 standardized units). Figure 4b) shows the TTiP for Cr-pyropes from these samples comprises $81.2 \pm 7.0\%$ graphite-facies temperatures (yellow), $16.7 \pm 6.5\%$ shallow diamond-facies temperatures (blue) and - significantly - 2% high-TiO₂ grains (black). Application of the MD technique has clearly differentiated the subtly different TTiP attributes of this population; that this population occurs in a distinct spatial subset down-ice of CH-6 (see Fig. 4b) provides empirical validation that the MD technique can capably resolve relative differences in the 2% to 7% range.
- 310 Cr-pyrope analyses from 19 of 43 samples define a second population with off-mean MD values (at 0.53 to 1.3 standardized units). Figure 4c) shows the TTiP for Cr-pyropes from these samples comprises $90.7 \pm 11.5\%$ graphite-facies temperatures (yellow), $8.4 \pm 11.3\%$ shallow diamond-facies temperatures (blue) and - significantly - no high-TiO₂ grains. This population defines a lower-abundance and eastern spatial subset of Cr-pyropes occurring down-ice of CH-6. Low-incidence grains scattered in the west could possibly be related to the dominant near-mean population (compare Fig. 4a with Fig. 4c).

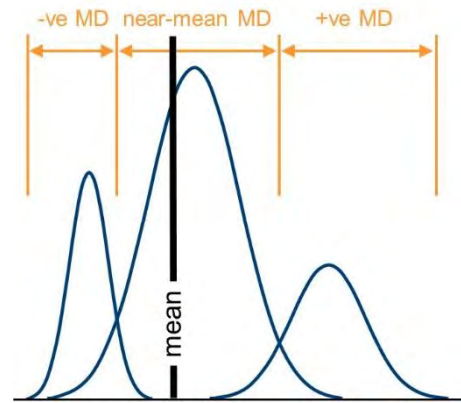
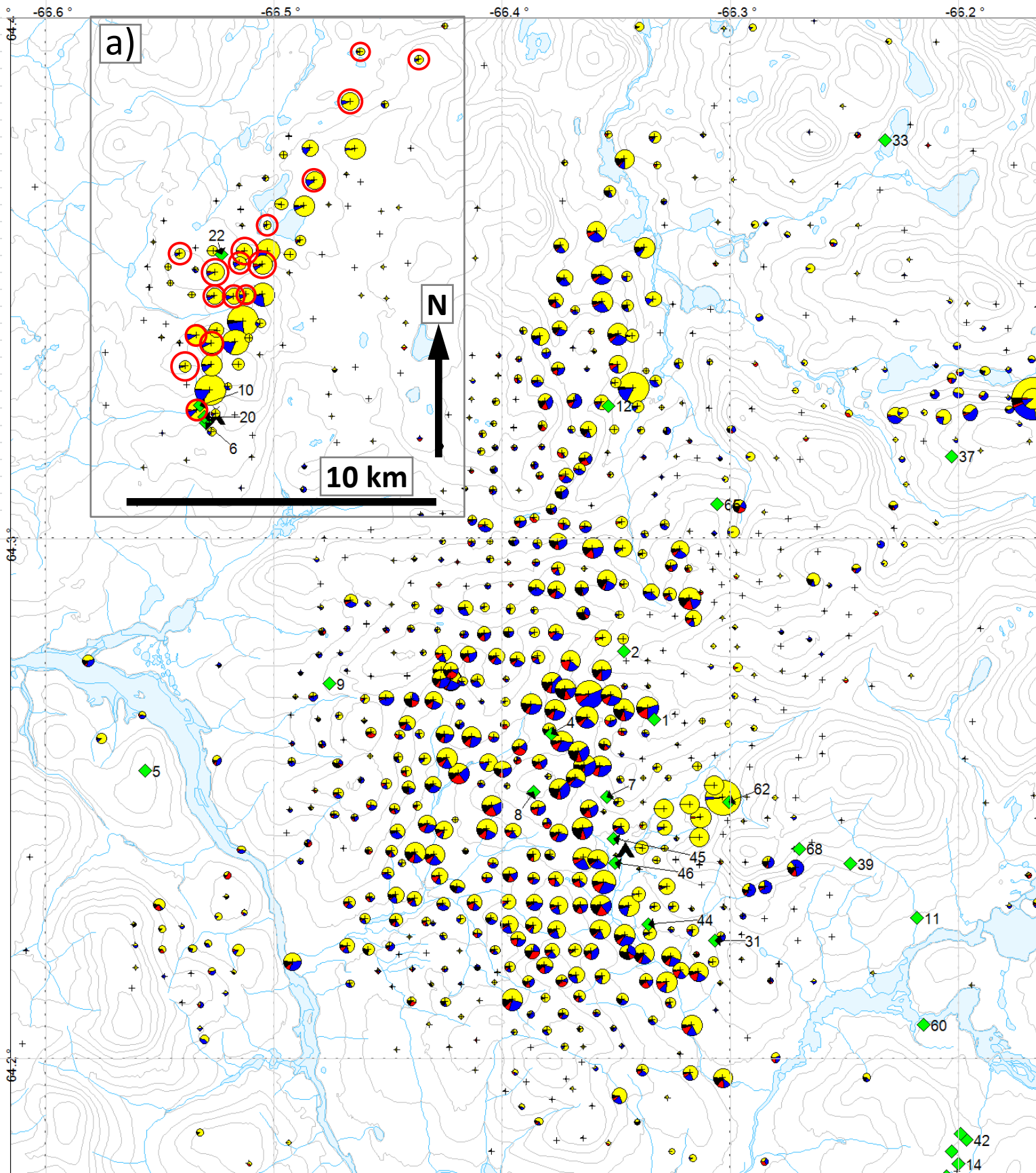


Figure 3: In this hypothetical example, the mean of three populations marks Mahalanobis-distance (MD) = 0, relative to which a range of (standardized) negative, near-mean or positive MD's distinguish each population. We calculate a single MD across all four attributes that specify the TTiP for a Cr-pyrope population.



Conference, Bangalore, Extended Abstract
 Pell J, Grütter H, Neilson S, Lockhart G, Dempsey S, Grenon H (2013) Exploration and discovery of the Chidliak kimberlite province, Baffin Island, Nunavut: Canada's newest diamond district. Pearson DG et al. (eds.), Proc 10th Int Kimb Conf, J Geol Sgc India Spec Pub V2: 209-227.



Type IIb diamonds originate from the sublithospheric mantle

Evan. M. Smith and Wuyi Wang

Gemological Institute of America, New York, USA, evan.smith@gia.edu

Introduction

Type IIb diamonds, those defined as having trace amounts of substitutional boron, are prized for their blue colors. The famous Hope diamond is a perfect example. Besides their boron content, these rare diamonds are also characterized by their general lack of nitrogen. Little is known about how type IIb diamonds form, but they are especially intriguing because boron is often regarded as a crustal element whose presence in mantle-derived diamonds is unexpected.

Despite interest in type IIb diamonds as a potential geochemical tracer of mantle processes, minimal research progress has been made to date. They are simply so rare and their color so highly valued that sample access is problematic. Even when access to type IIb diamonds is granted, these diamonds are typically free of mineral or fluid inclusions that might illuminate their geological significance (e.g. Gaillou et al. 2012; King et al. 1998).

Methods

To investigate the geology of type IIb diamonds, we leveraged the day-to-day diamond grading operations of the Gemological Institute of America. Diamonds passing through GIA's New York laboratory were systematically screened to identify type IIb diamonds with inclusions. Over the course of about a year, more than twenty prospective diamonds were encountered. Each prospective diamond was then carefully examined and inclusions were analyzed using laser Raman spectroscopy in order to identify included mineral phases in-situ, nondestructively. Polished diamonds are well suited to Raman analysis because they are covered on all sides by high quality windows that permit optical access to most of internal space within the diamond. Most inclusions could be characterized this way, relatively quickly and without disrupting the flow of diamond grading. This approach allowed the examination of multiple examples of what are otherwise exceedingly rare and inaccessible diamonds.

Results and Discussion

The most common inclusion identified in the type IIb diamonds examined was CaSiO₃-walstromite, interpreted as an inversion product from CaSiO₃-perovskite. Some of these inclusions also contained larnite (Ca₂SiO₄), and less frequently CaSi₂O₅-titanite, wollastonite, and perovskite (CaTiO₃). The second most common inclusion type was pyroxene, with some inclusions also containing jeffbenite (TAPP), spinel and olivine. These inclusions are interpreted as retrogressed bridgmanite (MgSiO₃-perovskite). An important additional inclusion phase found in three diamonds is coesite, interpreted as inverted stishovite. These assemblages suggest derivation from a basic, possibly Ca-rich, host rock paragenesis from the lower mantle.

As shown in figure 1, the silicate inclusions are often surrounded by graphitic decompression fractures and lobate sprays of tiny satellite inclusions in healed fractures emanating from the main inclusion. These satellite inclusions probably formed during decompression, as the inclusion ruptured the host diamond and some of the inclusion expanded out into the fracture, followed by healing of the crack. Such behaviour requires significant inclusion volume expansion, consistent with a deep, sublithospheric origin for the inclusions. Equivalent inclusion textures have been described previously from sublithospheric diamonds (Smith et al. 2016).

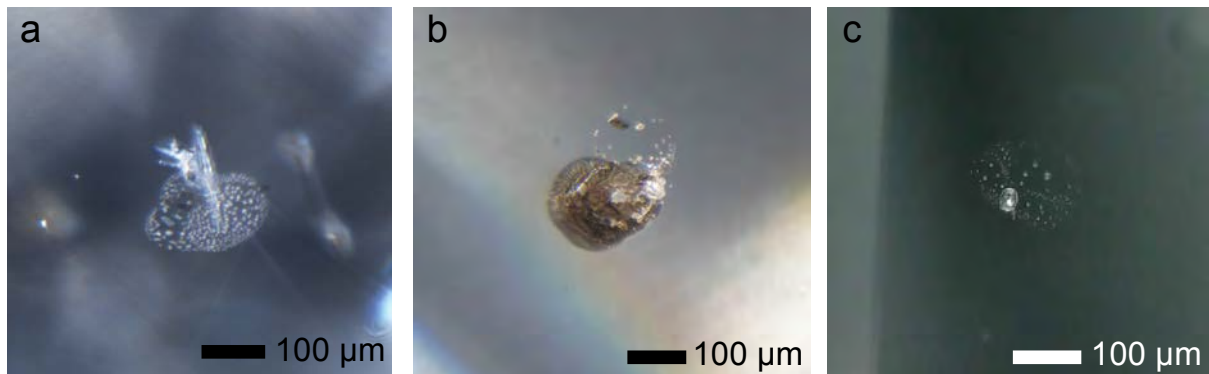


Figure 1: Examples of high-pressure silicate inclusions residing inside several cut and polished type IIb diamonds. a, b) Inclusions of colorless transparent calcium-silicate phases, dominated by CaSiO_3 -walstromite, interpreted as former CaSiO_3 -perovskite. c) Inclusion of orthopyroxene, interpreted as former bridgmanite.

The implication that type IIb diamonds originate from the sublithospheric mantle is surprising, but follows suit with the recent findings that many large, predominantly type IIa diamonds like the 3106 carat Cullinan (CLIPPIR diamonds) likely come from the mantle transition zone and also contain silicate inclusions of basic affinity (Smith et al. 2016). These findings show that some of the most prized of all diamonds are also invaluable samples of the deep Earth.

References

- Gaillou E, Post JE, Rost D, Butler JE (2012) Boron in natural type IIb blue diamonds: Chemical and spectroscopic measurements. *Am Mineral* 97(1):1-18
- King JM, Moses TM, Shigley JE, Welbourn CM, Lawson SC, Cooper M (1998) Characterizing natural-color type IIb blue diamonds. *Gems & Gemology* 34(4):246-268
- Smith EM, Shirey SB, Nestola F, Bullock ES, Wang J, Richardson SH, Wang W (2016) Large gem diamonds from metallic liquid in Earth's deep mantle. *Science* 354(6318):1403-1405 doi:10.1126/science.aal1303

Petrography and geochronology of the Nxau Nxau kimberlites, north-west Botswana

Henrietta Farr¹, David Phillips¹ and Mike de Wit^{2, 3}

¹ KiDs (Kimberlites and Diamonds), School of Earth Sciences, The University of Melbourne, Parkville, 3010, Victoria, Australia

² Tsodilo Resources Ltd, Toronto, Ontario, Canada

³ Delrand Resources Pty Ltd., Toronto, Ontario, Canada

Introduction

The Nxau Nxau kimberlite cluster is part of the Xaudum province on the south-eastern margin of the Congo craton, which straddles the border between Namibia and Botswana. This kimberlite province is geographically isolated from other known kimberlites and occurs in an area previously thought to be part of the Damara mobile belt. The kimberlites were emplaced within the outer limits of the Okavango Mafic Dyke Swarm which was emplaced as part of the early Jurassic Karoo magmatism, although some dykes are Proterozoic in age (Jourdan et al. 2004). Nineteen kimberlites were discovered in 1997 with another 9 discovered in 2005-06 by Tsodilo Resources. Exploration interest in this area gathered momentum after ~20% of garnets analysed by Rio Tinto Namibia Pty Ltd. from 1994 to 1996 exhibited subcalcic G10 compositions (Hoal et al. 2000).

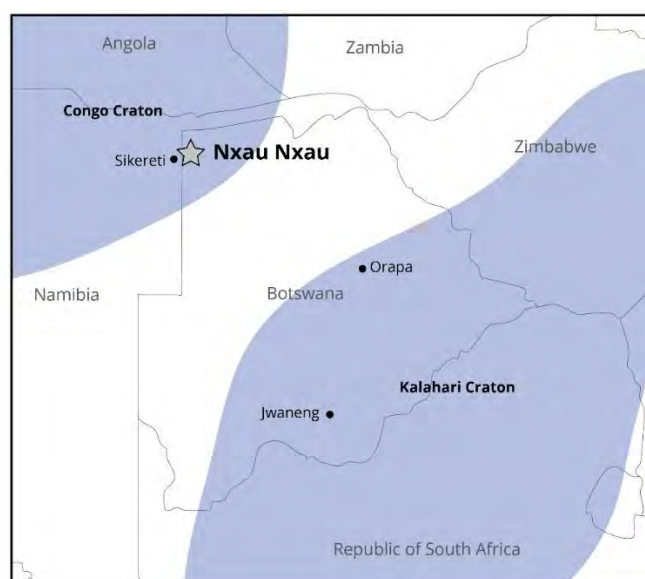


Figure 1: Map showing the location of the Nxau Nxau kimberlite field in relation to the Congo and Kalahari Cratons. The locations of the Sikereti, Orapa and Jwaneng kimberlites are also shown.

Petrography

A variety of volcanoclastic and hypabyssal units were observed in the Nxau Nxau samples. Samples from kimberlites in close proximity to the dykes are predominantly volcanoclastic and contain a higher proportion of crustal xenoliths. The hypabyssal samples can be broadly described as coherent macrocrystic olivine, calcite kimberlites, with serpentinised and calcitised olivine typically up to 1mm in size. Titanomagnetite and perovskite (<100µm) are the dominant groundmass phases with apatite and phlogopite being less common. Phlogopite is most abundant in sample B8/1 but generally uncommon. Later veins of kimberlite cross-cut some of the hypabyssal samples with an earlier generation of kimberlite present in one drillhole (2164A1).

As evident from cross-cutting relationships and xenoliths present within the kimberlites, the kimberlites intruded rocks of the Karoo Supergroup (late Carboniferous – early Jurassic) (Smith 1984), the Damara Supergroup (late Precambrian) and basement granites and gneisses that have been dated at 2.9-2.5Ga (Batumike et al. 2009). Karoo dolerite and Nosib quartzite are the dominant crustal xenoliths present with lesser amphibolite occurrences.

Geochemistry & Geochronology

Five samples from four bodies containing sufficient fresh perovskite were analysed for strontium isotopes using *in situ* LA-ICPMS methods. Four of the samples analysed define a narrow $^{87}\text{Sr}/^{86}\text{Sr}_i$ range around 0.7036. The most altered sample (C15/3) gave a significantly higher $^{87}\text{Sr}/^{86}\text{Sr}_i$ value of 0.7042. These results are consistent with values characteristic of archetypal (Group I) kimberlites (Woodhead et al. 2009). A sixth sample (2164A1) contained extensively altered perovskite which was unable to be analysed.

The same five samples were dated using *in-situ* U-Pb LA-ICPMS methods, giving a weighted average age of 84 ± 4 Ma. Phlogopite from one kimberlite was also analysed by $^{40}\text{Ar}/^{39}\text{Ar}$ and Rb-Sr dating yielding an $^{40}\text{Ar}/^{39}\text{Ar}$ inverse isochron age of 86.5 ± 8.6 Ma (Fig. 2) and a two-point Rb-Sr age of 87.1 ± 3.1 Ma. All ages are within error of one another.

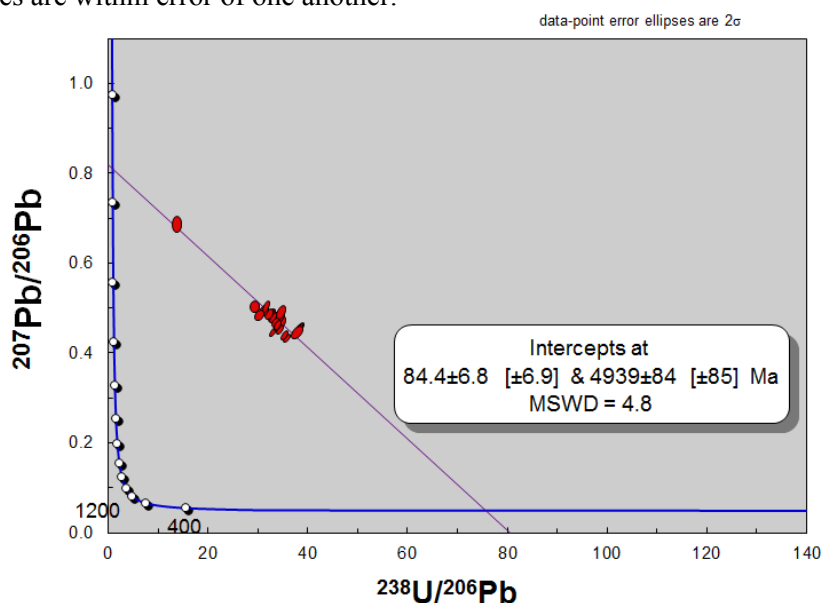


Figure 2: Tera-Wasserburg concordia diagram for sample 21181A4, ellipses show 2σ

Table 1: Summary of kimberlites ages. U-Pb perovskite ages have been corrected for common lead using the measured abundances of $^{207}\text{Pb}/^{206}\text{Pb}$ and $^{238}\text{U}/^{206}\text{Pb}$ (Tera and Wasserburg 1972). Several other methods of constraining common lead were tested with some giving higher precision; however, the TW intercept proved the most consistent and was deemed the most accurate.

| Sample | Age (Ma) | Method | Analysis |
|-----------|--------------|--|--|
| 21181A4 | 84.4 ± 7 | U-Pb perovskite | LA-ICP-MS 23 spots |
| A36/3 | 84.0 ± 9 | U-Pb perovskite | LA-ICP-MS 24 spots |
| B8/1 | 82.5 ± 1 | $^{40}\text{Ar}/^{39}\text{Ar}$ phlogopite | Total gas (3 steps) from single grain |
| | 86.5 ± 9 | $^{40}\text{Ar}/^{39}\text{Ar}$ phlogopite | Inverse isochron (3 steps) from single grain |
| | 87.1 ± 3 | Rb-Sr phlogopite | Two leached fractions |
| C15/3 | 79.0 ± 6 | U-Pb perovskite | LA-ICP-MS 20 spots |
| 1821C16/3 | 82.2 ± 8 | U-Pb perovskite | LA-ICP-MS 26 spots |

Discussion

All three dating techniques applied are in agreement that the Nxau Nxau kimberlite field was emplaced at ~84 Ma. In this study it is considered that U-Pb perovskite dating gives the most robust and precise results due to extraneous argon and argon loss affecting phlogopite analyses. Therefore, the weighted average of the U-Pb ages (84 ± 4 Ma) is proposed as the best estimate for the time of emplacement of the Nxau Nxau kimberlites. These kimberlites represent the first known expression of Cretaceous alkaline magmatism in this area and join a large number of other kimberlites emplaced during the Cretaceous from ~70-90 Ma. The emplacement of kimberlites in the Cretaceous is considered to be related to the break-up of Gondwana and relevant tectonic stresses. In the case of these kimberlites, a significant reorganisation of global tectonic stresses with the cessation of intra-continental movements within Africa at 84 Ma (Chron 34) may have been a trigger for kimberlite magmatism (Nürnberg and Müller 1991).

The cross-cutting kimberlite (seen in sample 2164A1) was unable to be dated, however, the pervasive alteration suggests that it is significantly older than 84 Ma. Perovskite in this kimberlite is petrographically similar to that of kimberlites in the Kuruman Province, South Africa. From this it is suggested that the older Nxau Nxau kimberlite may fall within the 1000-1200Ma or 1600-1800Ma periods of alkaline magmatism.

References

- Batumike JM, Griffin WL, O'Reilly SY, Belousova EA, Pawlitschek M (2009) Crustal evolution in the central Congo-Kasai Craton, Luebo, D.R. Congo: Insights from zircon U–Pb ages, Hf-isotope and trace-element data *Precambrian Research* 170:107-115 doi:<http://dx.doi.org/10.1016/j.precamres.2008.12.001>
- Hoal K, Hoal B, Griffin W, Armstrong R (2000) Characterization of the age and nature of the lithosphere in the Tsumkwe region, Namibia *Communications of the geological survey of Namibia* 12:21-28
- Jourdan F et al. (2004) The Karoo triple junction questioned: evidence from Jurassic and Proterozoic $^{40}\text{Ar}/^{39}\text{Ar}$ ages and geochemistry of the giant Okavango dyke swarm (Botswana) *Earth and Planetary Science Letters* 222:989-1006 doi:<http://dx.doi.org/10.1016/j.epsl.2004.03.017>
- Nürnberg D, Müller RD (1991) The tectonic evolution of the South Atlantic from Late Jurassic to present *Tectonophysics* 191:27-53
- Smith RA (1984) The lithostratigraphy of the Karoo Supergroup in Botswana. Geological Survey Department with the authority of Ministry of Mineral Resources and Water Affairs, Republic of Botswana,
- Tera F, Wasserburg G (1972) U-Th-Pb systematics in three Apollo 14 basalts and the problem of initial Pb in lunar rocks *Earth and Planetary Science Letters* 14:281-304
- Woodhead J, Hergt J, Phillips D, Paton C (2009) African kimberlites revisited: In situ Sr-isotope analysis of groundmass perovskite *Lithos* 112S:311-317



Tracing mantle metasomatism using combined stable (S, O, N) and radiogenic (Sr, Nd, Hf, Pb) isotope geochemistry: case studies from mantle xenoliths of the Kimberley kimberlites

Andrea Giuliani^{1,2}, David Phillips², Roland Maas³, Jon D. Woodhead³, Chris Harris⁴, Marco Fiorentini⁵, James Farquhar⁶, Emilie Thomassot^{7,8}, Chen Cheng⁸, Angus Fitzpayne²

¹ ARC Centre of Excellence for Core to Crust Fluid Systems (CCFS) and GEMOC, Department of Earth and Planetary Sciences, Macquarie University, Australia
andrea.giuliani@mq.edu.au, andrea.giuliani@unimelb.edu.au

² KiDs (Kimberlites and Diamonds), School of Earth Sciences, The University of Melbourne, Australia

³ Melbourne Isotope Geochemistry, School of Earth Sciences, The University of Melbourne, Australia

⁴ Department of Geological Sciences, University of Cape Town, South Africa

⁵ Centre for Exploration Targeting, ARC Centre of Excellence for Core to Crust Fluid Systems (CCFS), School of Earth and Environment, The University of Western Australia, Australia

⁶ Department of Geology and ESSIC, University of Maryland, College Park, USA

⁷ Centre de Recherches Pétrographiques et Géochimiques, CNRS, Université de Lorraine, France

⁸ Institute de Physique du Globe de Paris, France

Introduction

Mantle fluids continuously (or intermittently) transfer chemical species across reservoirs, thus modifying the composition of different mantle domains. To improve understanding of mantle evolution, it is therefore important to establish criteria to constrain the origin and evolution of mantle fluids. The sub-cratonic lithospheric mantle is a long-lived (>3 Ga) reservoir, which has experienced multiple episodes of metasomatic enrichment. Metasomatised mantle xenoliths entrained by kimberlite magmas during ascent through craton interiors therefore provide ideal candidates to investigate mantle fluids.

Samples, methods and results

Here we document the results of a multi-isotope study of mantle xenoliths from the Boshof Road dumps, which host historical waste material from mining of the ~84 Ma Bultfontein Kimberlite (Kimberley, South Africa). The sample suite includes phlogopite-rich peridotites hosting clinopyroxene and/or LIMA (lindsleyite-mathiasite) titanates, wehrlites, MARID rocks and a mantle polymict breccia (Table 1). Five samples include variably fresh sulfide grains, whose S isotope ratios were measured by bulk-rock and *in situ* SIMS methods. The O isotope composition of mineral separates from each xenolith, plus two additional (modally) unmetasomatised peridotites (Table 1) were analysed using the laser fluorination technique. The N isotope systematics of phlogopite were examined using a seal-tube combustion technique combined with conventional static mass spectrometry. The Sr-Nd-Hf-Pb isotope composition of clinopyroxene, K-richite and LIMA were measured using MC-ICPMS with a combination of *in situ* (Sr only) and solution-mode methods.

The oxygen isotope composition of olivine grains is remarkably consistent among the examined samples, including modally unmetasomatised samples, and overlaps with that of olivine in mantle peridotites worldwide ($\delta^{18}\text{O} = 5.18 \pm 0.14$, 1sd; Matthey et al., 1994). Conversely, the $\delta^{18}\text{O}$ values of clinopyroxene grains, a typical metasomatic phase in the sub-cratonic mantle, in the peridotite samples range to below typical mantle values (5.57 ± 0.18 , 1sd; Matthey et al., 1994) (Fig. 1). The $\delta^{34}\text{S}$ values of sulfide grains in four peridotites and a polymict breccia vary between ~-1 and -6‰, with most values being between -2 and -5‰ (Fig. 1; Giuliani et al., 2016). Phlogopite $\delta^{15}\text{N}$ compositions are between +4.4 and +6.2‰ (five

peridotites, one MARID), which is significantly different from the mantle signature of $-5 \pm 2\%$ inferred from studies of diamonds and oceanic basalts (e.g., Cartigny and Marty, 2013).

Table 1. Petrographic features, T, P and age constraints for studied mantle xenoliths

| sample name | lithology | equilibrium T (°C) | equilibrium P (GPa) | Age of metasomatism (Ma) | isotopic systems examined |
|-------------|---------------------------------------|--------------------|---------------------|--------------------------|---------------------------|
| XM1/355 | garnet harzburgite | 1060-1100 | 4.7-4.9 | no metasomatism | O |
| XM1/422 | spinel harzburgite | 680-710 | 2.7-2.8 | no metasomatism | O |
| XM1/371 | Phl-rich wehrlite | 1120-1160 | 5.0-5.1 | no constraints | O, S, N, Sr, Nd, Hf, Pb |
| BLFX-2 | garnet wehrlite | 1040-1080 | 4.2-4.4 | no constraints | O, Sr, Nd, Hf, Pb |
| XM1/142 | Phl-rich Spl harzburgite | 750-860 | 3.0-3.5 | 82 ± 3^a | O, S, N, Sr, Nd, Hf, Pb |
| XM1/341 | LIMA-bearing Phl-rich Spl lherzolite | 830-910 | 3.4-3.8 | 177 ± 12^b | O, S, N, Sr, Nd, Hf, Pb |
| XM1/345 | LIMA-bearing Phl-rich Spl harzburgite | 750-850 | 3.0-3.4 | 178 ± 29^b | O, S, N, Sr |
| XM1/362 | LIMA-bearing Phl-rich Spl lherzolite | 770-830 | 3.1-3.4 | 190 ± 24^b | O, S, N, Sr, Nd, Hf, Pb |
| XM1/331 | MARID | - | - | 129.8 ± 2.0^c | O, Sr, Nd, Hf, Pb |
| XM1/498 | Cpx-free MARID | - | - | $80-90^d$ | O, N, Sr, Nd, Hf |
| BLFX-3 | Cpx-free MARID | - | - | no constraints | O, Sr, Nd, Hf, Pb |
| DU-1 | polymict breccia | 850-900 | 3.4-3.7 | $\sim 80-90^e$ | S |

^a zircon U/Pb age (Konzett et al., 2000); ^b LIMA U/Pb age (Giuliani et al., 2014b); ^c maximum zircon U/Pb age (Giuliani et al., 2015); ^d zircon U/Pb age (Konzett et al., 1998); ^e metasomatism coeval with kimberlite magmatism in the Kimberley area (Giuliani et al., 2014a)

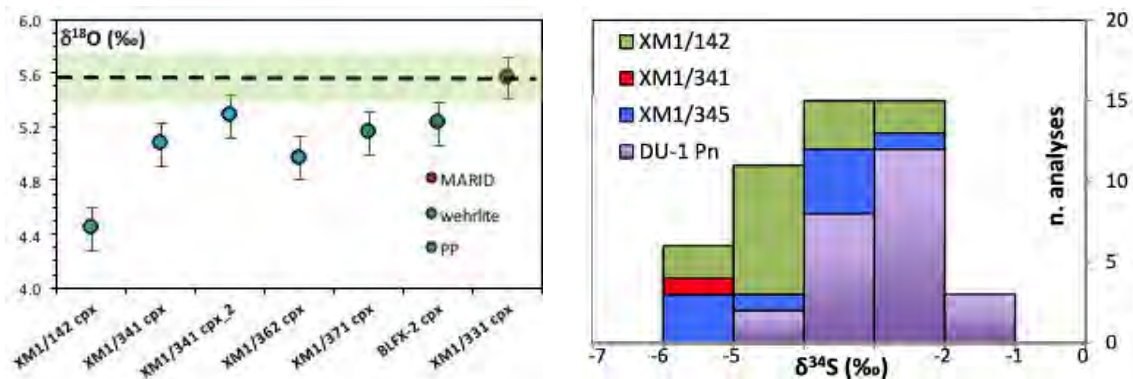


Figure 1. Left panel: Oxygen isotope composition of clinopyroxene grains; the green band represents the mantle range ($\delta^{18}\text{O} = 5.57 \pm 0.18$, 1sd; Matthey et al., 1994). Right panel: In-situ S isotope analyses of pentlandite (Pn) grains.

The Sr-Nd-Hf isotope composition of metasomatic phases vary considerably between xenolith types. Clinopyroxene in the two wehrlite samples exhibit similar values ($\epsilon\text{Nd}_{84\text{Ma}} = 3.2-3.7$, $\epsilon\text{Hf}_{84\text{Ma}} = 2.0-2.1$) in the range of southern African Cretaceous archetypal kimberlites. Metasomatic phases in the phlogopite-rich xenoliths, including two MARID samples, show a large compositional range from values ($\epsilon\text{Nd}_{84\text{Ma}} = -8$ to -13 , $\epsilon\text{Hf}_{84\text{Ma}} = -13$ to -17) typical of metasomatised lithospheric mantle magmas (e.g., lamproites, orangeites) to compositions below the Nd-Hf mantle array (i.e. $\Delta\epsilon\text{Hf}_{84\text{Ma}} = -10$ to -12 and $\epsilon\text{Nd}_{84\text{Ma}} = -3$ to -5), and similar to those of southern African transitional kimberlites.

LIMA minerals exhibit variable initial Sr isotope ratios ($^{87}\text{Sr}/^{86}\text{Sr} \sim 0.705$ to ~ 0.713) at every scale (from between samples to within a single grain). In each sample, two or three generations of LIMA minerals can

be distinguished based on trace element and Sr isotope variations. However, U/Pb dating of LIMA grains indicates a single episode of LIMA formation at ~180-185 Ma for each xenolith (Giuliani et al., 2014b).

Discussion

The S isotope systematics are inconsistent with the metasomatic agent(s) that introduced sulfides into the Bultfontein mantle being sourced in the depleted asthenospheric mantle, whose $\delta^{34}\text{S}$ is ~ -1.4‰ (Labidi et al., 2013). $\delta^{34}\text{S}$ values as low as -6‰ require input from recycled crustal material, perhaps sulfide-bearing sediments. The interpretation that subducted material occurred in the source of the metasomatic fluids is strengthened by the O and N isotope data for clinopyroxene and phlogopite, respectively. Furthermore, sulfide S and phlogopite N isotope compositions are remarkably homogeneous across the sample suite despite the variable style, P-T conditions and age of metasomatism (Table 1). This might indicate that metasomatic mantle fluids beneath Kimberley tapped a relatively homogeneous (sub-lithospheric?) source over a time-span extending from ~180 Ma (i.e. Karoo) to ~80-90 Ma (i.e. kimberlite emplacement age). This view is at odds with the diverse range of recorded Sr-Nd-Hf compositions, which instead suggest contributions from different sources including the asthenospheric (see the wehrlites) and lithospheric mantle (see some of the phlogopite-rich xenoliths). This apparent contradiction could be reconciled by accounting for the progressive evolution of the fluid(s) source with attendant radiogenic ingrowth; and if the Sr-Nd-Hf (and O) isotope compositions were affected by interaction with lithospheric wall rocks to a larger and more variable extent than the N-S isotope systems. The variable Sr isotope compositions of coeval LIMA grains might further highlight the fundamental contribution of lithospheric protoliths and/or wall rocks to the radiogenic isotope compositions of some metasomatic phases.

References

- Cartigny P, Marty B (2013) Nitrogen Isotopes and Mantle Geodynamics: The Emergence of Life and the Atmosphere-Crust-Mantle Connection. *Elements* 9(5):359-366
- Giuliani A, Fiorentini ML, Martin LAJ, Farquhar J, Phillips D, Griffin WL, LaFlamme C (2016) Sulfur isotope composition of metasomatised mantle xenoliths from the Bultfontein kimberlite (Kimberley, South Africa): Contribution from subducted sediments and the effect of sulfide alteration on S isotope systematics. *Earth and Planetary Science Letters* 445:114-124
- Giuliani A, Phillips D, Kamenetsky VS, Kendrick MA, Wyatt BA, Goemann K, Hutchinson G (2014a) Petrogenesis of Mantle Polymict Breccias: Insights into Mantle Processes Coeval with Kimberlite Magmatism. *Journal of Petrology* 55(4):831-858
- Giuliani A, Phillips D, Maas R, Woodhead JD, Kendrick MA, Greig A, Armstrong RA, Chew D, Kamenetsky VS, Fiorentini ML (2014b) LIMA U–Pb ages link lithospheric mantle metasomatism to Karoo magmatism beneath the Kimberley region, South Africa. *Earth and Planetary Science Letters* 40:132-147
- Giuliani A, Phillips D, Woodhead JD, Kamenetsky VS, Fiorentini ML, Maas R, Soltys A, Armstrong RA (2015) Did diamond-bearing orangeites originate from MARID-veined peridotites in the lithospheric mantle? *Nature Communications* 6:6837
- Konzett J, Armstrong RA, Günther D (2000) Modal metasomatism in the Kaapvaal craton lithosphere: constraints on timing and genesis from U–Pb zircon dating of metasomatized peridotites and MARID-type xenoliths. *Contributions to Mineralogy and Petrology* 139(6):704-719
- Konzett J, Armstrong RA, Sweeney RJ, Compston W (1998) The timing of MARID metasomatism in the Kaapvaal mantle: An ion probe study of zircons from MARID xenoliths. *Earth and Planetary Science Letters* 160:133-145
- Labidi J, Cartigny P, Moreira M (2013) Non-chondritic sulphur isotope composition of the terrestrial mantle. *Nature* 501(7466):208-211
- Mattey D, Lowry D, Macpherson C (1994) Oxygen isotope composition of mantle peridotite. *Earth and Planetary Science Letters* 128:231-241



[Petrogenetic evidence and FTIR constraints on the origin of diamonds in xenoliths from Yubileynaya and Komsomolskaya pipes, Yakutia]

[Z.V. Spetsius¹, I.N. Bogush¹, W.L. Griffin², S.Y. O'Reilly² and A.S. Ivanov]

[¹Geo-Scientific Investigation Enterprise, ALROSA PJSC, Mirny, 678170, Russia, spetsiuszv@alrosa.ru

²ARC Centre of Excellence for Core to Crust Fluid Systems (CCFS/GEMOC), Macquarie University, NSW 2109, Australia, bill.griffin@mq.edu.au]

[Introduction]

[Mantle eclogites make up an important component in mantle xenolith suites and are transported to the surface by kimberlite magmas; diamondiferous eclogites represent one of the main diamond reservoirs on Earth. Although peridotitic xenoliths are dominant in kimberlites and P-type diamonds are more abundant than E-type, recovered diamondiferous eclogite xenoliths are significantly more abundant world-wide than are diamondiferous peridotites and are present in all industrial kimberlite deposits of the Yakutian province (Kostrovizky et al., 2015). Despite the relative rarity of eclogitic xenoliths sampled by kimberlites, they offer key constraints on the formation of thickened Archean cratonic lithosphere, as well as the extent of modification resulting from interaction with melt or fluids in mantle environments and during kimberlite transport (e.g., Pearson et al., 2003). Studies of eclogites are important for refining models of global crust–mantle evolution and provide constraints on the origin of diamondiferous mantle as eclogites represent significant diamond reservoirs in some portions of SCLM of Siberian Craton (e.g., Spetsius et al., 2008).

The late Devonian Komsomolskaya and Yubileynaya pipes are located in the center of the Yakutian province, within the Alakit-Marhinsky kimberlite field. The diamond grade of Yubileynaya kimberlites (0.90 ct/t) is higher than Komsomolskaya (0.36 ct/t) but the diamond value of the latter is twice as high. The aim of this study is to petrologically characterize the Yubileynaya and Komsomolskaya xenoliths and their diamonds in order to place robust constraints on the differences in origin of diamonds within the SCLM beneath these pipes. Examination of these diamondiferous eclogites can also have important implications for understanding of diamond genesis and lithosphere evolution within the Siberian Platform, in general. These xenoliths present the opportunity to investigate a unique collection of diamond-bearing xenoliths that will permit constraints on their source materials and on diamond-forming processes. Here, we present major- and trace-element data on garnet and clinopyroxene minerals along.

[Samples and Methods]

35 diamondiferous xenoliths from the Komsomolskaya and Yubileynaya pipes of Yakutia comprise bimineraleclogites, rare kyanite eclogites and some garnet megacrysts. Most xenoliths contain two or more diamond crystals (0.5-8.0 mm) with predominantly octahedral or transitional forms (Fig.1). Coated diamonds were found in two xenoliths from the Yubileynaya pipe. The distribution of crystals in xenoliths is irregular and does not coincide with the specimen surfaces. Mineral inclusions are rare and represented by sulfides, garnet, clinopyroxene and very rare rutile. Fine-grained interstitial metasomatic mineral assemblages and partial melting phases have also been identified in these xenoliths; this is a characteristic feature of most of the specimens, and a specific feature of diamondiferous eclogites. Samples from Yubileynaya are more intensively metasomatised and altered.

Major element compositions of garnets and clinopyroxenes in the xenoliths were determined with a Superprobe JXA-8800R electron microprobe at the "ALROSA" OJS Company (Mirny, Yakutia). Natural minerals and synthetic were used as standards. Analytical conditions included an accelerating voltage of 15 keV, a beam current of 20 nA, beam size of 5 µm, and 20 seconds counting time for all elements. All analyses underwent a full ZAF correction.

The trace elements have been measured by laser Ablation ICP-MS (LAM) in the Geochemical Analysis Unit at Macquarie University, with NIST 610 glass as external standard and Ca as internal standard; pit diameters were 40–50 μm and partly at Virginia Polytechnic and State University, and details are given in (Pernet-Fisher et al, 2014).

The morphology of about 300 crystals from eclogite xenoliths of both pipes diamonds was studied, and selected diamonds Komsomolskaya (102) and Yubileynaya (167) were analyzed by micro-Fourier transform infrared (FTIR) spectroscopy to determine both nitrogen content (N_{FTIR}) and nitrogen aggregation state. IR spectra were obtained over the range of 370–4200 cm^{-1} with the use of Vertex 70 FTIR spectrometer and Hyperion 2000 microscope. The spectra resolution was 2 cm^{-1} . Errors in nitrogen content (N_{FTIR}) and nitrogen aggregation state are estimated to be better than 20% and 5% respectively.

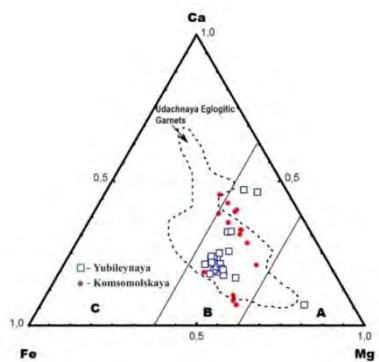
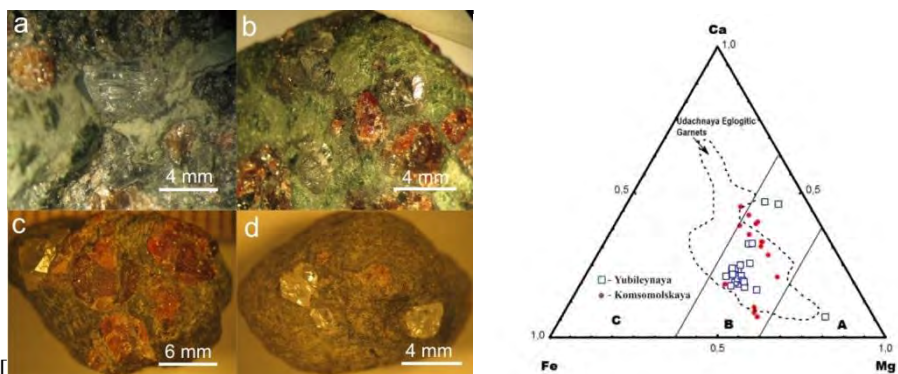


Figure 1: Examples of diamondiferous xenoliths from the Komsomolskaya (a, b) and Yubileynaya (c, d) pipes.

Figure 2: Compositions of garnets of Yubileynaya and Komsomolskaya diamondiferous xenoliths.

[Analytical Results

Investigations of 35 xenoliths with diamonds from Yubileynaya and Komsomolskaya pipes allowed to confirm the petrology of these unique rocks and provide new results on the properties of diamonds. Data on major- and trace elements in minerals of 35 diamondiferous xenoliths from the Komsomolskaya and Yubileynaya kimberlites are summarized. Garnets and clinopyroxenes typically plot within the Group B eclogite classification field (Fig. 2). One sample from the Yubileynaya pipe is a high-magnesian chromian harzburgite-dunite garnet megacryst ($\text{Cr}_2\text{O}_3 = 9.85 \text{ wt}\%$) that contains inclusions of octahedral diamond. Two samples from Komsomolskaya pipe correspond to Group C eclogite (one of these contains minor amounts of kyanite). Minerals in eclogites from this study display no zonation in their chemistry; as such, the major-element compositions can be used to estimate the equilibration temperatures of these samples. We adopted the thermometer of Ellis and Green (1979), which is based on Mg-Fe^{2+} exchange between clinopyroxene and garnet. The results suggest equilibration at 1000–1225 $^\circ\text{C}$ at 4 GPa and integrated residence temperatures of $\sim 1160\text{--}1200$ $^\circ\text{C}$ for diamond growth with slightly lower temperatures for Yubileynaya eclogites.

Garnets in Yubileynaya eclogites are generally characterized by low Cr_2O_3 (<0.2 wt%) and TiO_2 (0.15–0.45 wt%) at a near-constant MgO of 11.2–13.4 wt%; in contrast CaO and FeO contents show large variations, respectively (7.2–17.7 wt%) and (4.4–16.4 wt%) defining two different groups (Fig. 2). Eclogitic garnets of this pipe also define two obviously different groups with low and high LREE (Fig. 3). Komsomolskaya eclogitic garnets have variable Cr_2O_3 extending up to 1.2 wt%, low TiO_2 (0.10–0.39 wt%), and a range of FeO (9.0–17 wt%) and CaO (3.6–17.2 wt%) contents. Garnets of Group B and C eclogites from Komsomolskaya pipe generally have $\text{Mg}\# > 60$ and convex-upward REE profiles. Most clinopyroxenes and some garnets in xenoliths from both pipes display LREE and MREE enrichments, consistent with cryptic metasomatism. The REE variation in garnets and clinopyroxenes suggests that some of the xenoliths were formed by subduction. The presence of Eu-anomalies suggests a plagioclase-rich cumulate protolith for some eclogites. Subducted oceanic crust is suggested by garnets of some xenoliths from both pipes.

FTIR data display differences in total nitrogen content and aggregation state in diamonds of xenoliths from these two pipes. About 80% of the crystals from xenoliths of Yubileynaya pipe have high total contents of nitrogen (600–1500 at.ppm) with low aggregation state (20–30%) and 20% of crystals have total nitrogen content < 500 at.ppm with high aggregation states (30–80%). Two obvious trends are

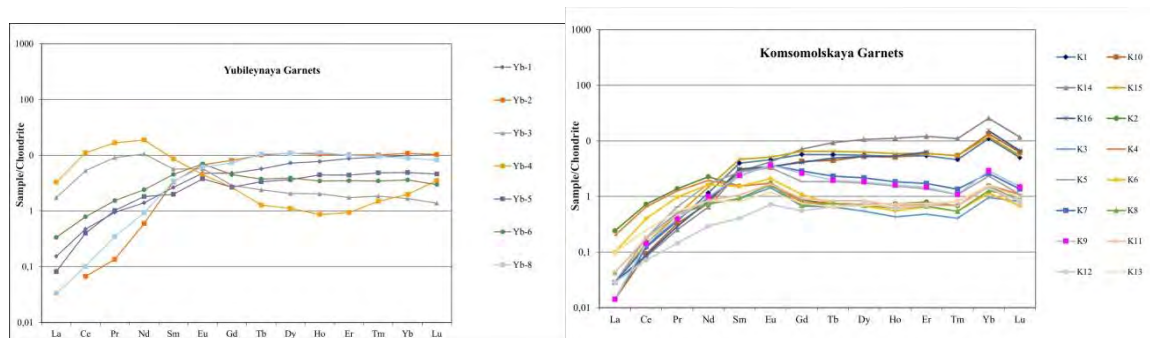


Figure 3: Chondrite-normalized REE abundances of Yubileynaya and Komsomolskaya xenolith garnets. All normalization factors from McDonough and Sun (1995).

evident on the plot of total nitrogen vs aggregation state that confirms the presence of two diamond populations in xenoliths from this pipe. Crystals in xenoliths from Komsomolskaya pipe have moderate nitrogen contents (200-900 at.ppm) and predominantly 20-50% aggregation. Diamonds with different nitrogen aggregation state occur in individual xenoliths from both pipes. FTIR data confirm the multistage growth of the diamonds.

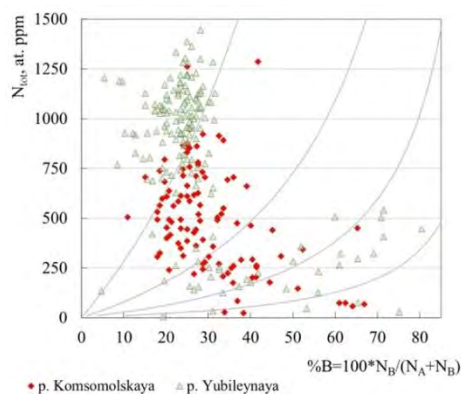


Figure 4. Distribution of total nitrogen and aggregation state in diamonds from Yubileynaya and Komsomolskaya eclogitic xenoliths.

Conclusions

The distribution of diamonds in the xenoliths, the presence of diamonds with different nitrogen aggregation state in the same xenolith and other evidence suggest multistage diamond growth from metasomatic fluids. Diamonds in eclogites may precipitate directly from water-rich melts/fluids. In addition, metasomatic fluids that may themselves originate from subducted crust potentially play an important role in the modification of primary mantle eclogites and may be linked to diamond formation.]

References

- [Ellis DJ, Green DH (1979) An experimental study of the effect of Ca upon garnet-clinopyroxene Fe-Mg exchange equilibria. *Contrib Mineral Petrol* 71:13-22.
- Kostrovizky SI, Spetsius ZV, Yakovlev DA, Fon-der-Flaas GS, Suvorova LF, Bogush IN (2015) Atlas of primary diamond deposits of Yakutian kimberlite province. Mirny, OOO MGT, 480 p. (in Russian).
- McDonough WF, and S.-S. Sun (1995) The composition of the Earth, *Chem. Geol.*, 120, 223-253.
- Pearson DG, Canil D, Shirey SB (2003) Mantle samples included in volcanic rocks: xenoliths and diamonds. *Treatise Geochem* 2:171-275.
- Pernet-Fisher JF, Howarth GH, Liu Y, Barry PH, Carmody L, Valley JW, Bodnar RJ, Spetsius ZV, Taylor LA (2014) Komsomolskaya diamondiferous eclogites: Evidence for oceanic crustal protoliths. *Contrib Mineral Petrol* 167(3):1-17.]

Impact–Cosmic–Metasomatic Origin of Microdiamonds from Kumdy–Kol Deposit, Kokchetav Massiv, N. Kazakhstan

L. I. Tretiakova¹ and A. M. Lyukhin²

¹St. Petersburg Branch Russian Mineralogical Society, RUSSIA, ltretia@gmail.com

²Institute of remote ore prognosis, Moscow, RUSSIA, alex.lyukhin@gmail.com

Introduction

Any collision extraterrestrial body and the Earth had left behind the “signature” on the Earth’s surface. We are examining a lot of signatures of an event caused Kumdy-Kol diamond-bearing deposit formation, best-known as “metamorphic” diamond locality among numerous UHP terrains around the world. We are offering new impact-cosmic-metasomatic genesis of this deposit and diamond origin provoked by impact event followed prograde and retrograde metamorphism with metasomatic alterations of collision area rocks that have been caused of diamond nucleation, growth and preserve.

Brief geology of Kumdy-Kol diamond-bearing deposit

Kumdy-Kol diamond-bearing deposit located within ring structure ~ 4 km diameter, in the form and size compares with small impact crater (Fig. 1). It is important impact event signature.

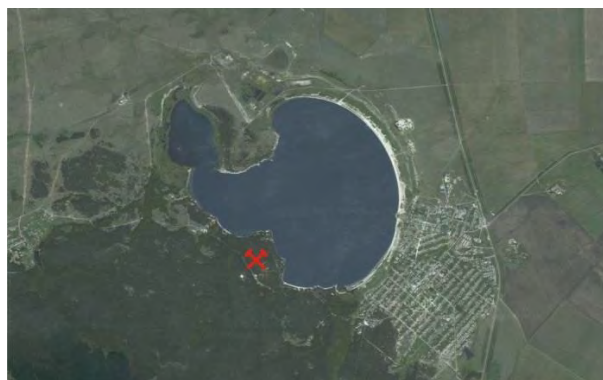


Figure1: Cosmic image of Kumdy-Kol deposit area [<http://map.google.ru/>].

Diamond-bearing domain had been formed on the peak of UHP metamorphism provoked by comet impact under oblique angle on the Earth surface. As a result, steep falling system of tectonic dislocations, which breakage and fracture zones filling out of impact and host rock breccia with blastomylonitic and blastocataclastic textures have been created. Diamond-bearing domain has complicated lenticular-bloc structure (1300 x 40-200 m size) and lens out with deep about 300 m. Compositions of diamond-bearing rocks are dominate garnet-biotite gneisses and discontinuous lenses of carbonate, quart, garnet-pyroxene rocks, amphibolised eclogites, that alternated with lenses of diamondless not altered garnet-biotite gneisses and granite. Diamond-bearing rocks are characterize strong metasomatic alteration with the strongest contrast revealed in a gneissose substrate. Ages of these rocks are: Grt-Bi gneisses – Proterozoic, diamond-bearing rocks–Cambrian, granites Later Cambrian – Ordovician. Spatial diamond distributions have not precise lithological lines. [Tretiakova, Lyukhin, 2016 and references there in].

Feasible scenario of impact event

Comet core was consisted from chondritic matter with abundance of carbon and possible nano-diamonds, having abnormal value of noble gases (He, Ne, Ar, Xe) + IDPs (SiC, graphite and diamonds with high

contents of noble gases) + carbonaceous matter presolar grains, including diamond and graphite, SiC, Si₃N₄, Al₂O₃, MgAl₂O₄, CaAl₁₂O₁₉, TiO₂, Mg(Cr,Al)₂O₄, silicates, TiC, Fe-Ni metal, noble gases and trace elements [Clayton, Nittler, 2004]. These evaporated comet substance under high pressure was injected into previously metamorphic host rocks appeared to be impact-cosmogenic source of diamond seeds and/or nanodiamonds. Water-vapor comet cloud with H₂O, C, CH, CH₄, CN, HCN gases and fine dispersed comet core, survived during comet passing through Earth dense air, mixed with vapor and melting target rocks and produced complicated carbon saturated fluid–melt [DeNiem, 2002] that was a source of epitaxial diamond growth (CVD) on carbonaceous matter seeds imported by a comet.

Signatures of impact metamorphism

Collision of huge velocity comet and the Earth had been caused of rapid shock wave compression (pressure peak > 50 GPa) and multiple complex mineral transformation, among them: 1. Presence of UHP minerals: diamond↔lonsdaleite, coesite, omphacite. The formation of hexagonal diamond (lonsdaleite) is interpreted as a direct transformation (solid to solid) of cubic diamond by a kinetic mechanism due to the shear stress and enhanced temperature induced by the rapid shock wave compression [He, 2002], Microdiamond (~10 - 50 μm size), graphite and coesite crystals distributed within the grains of all rock-forming minerals and also associated with fractures in rocks and minerals; 2. Delivering by comet moissanite (SiC) and graphite spherulites; meteoritic matter: magnetite, hematite, iocite, troilite, α-Fe, Ni-Fe; 3. Annealed metallic globules having various fanciful forms (globules, small dump-bells, drops, spherules and so on) in host rock and rock-forming minerals; 4. Dislocation and birefringence in diamonds, planar structure in quartz, inclusions UHP minerals in rock-forming minerals.

Signatures of progressive metamorphism

1. Mineral association: dolomite + diopside + garnet ±diamond observed in dolomite marble; 2. High concentrations: Na, Ti in garnets, K, Na in clinopyroxenes, K in amphiboles, Al, Si in titanite, Al in phengite [Zwang et al., 1997]; 3. Cation's exchange in shock-activated phases by displacement: $2Al^{3+} \rightarrow [(Mg, Fe)^{2+}+Ti]$ or $(Ca+Al) \rightarrow (Na+Ti)$ in garnets, $Si \rightarrow (Mg^{2+} +Na +Al^{3+})$ in clinopyroxenes, and so on; 4. Solid phase transformations: K-feldspar and phengite exsolution in diopside; coesite lamella in titanite and diopside, quartz lamella in eclogitic clinopyroxene, and so on; 5. HP and low P mineral inclusions in zoned garnets and zircons.

Signatures of regressive metamorphism

Sharp drop pressure and slowly decrease temperature after impact created conditions of regressive metamorphism. Fluid/melt also acted on intensive metasomatic alteration of diamond-bearing rocks. Metasomatic changes characterize by presence graphite rims on diamond crystals; quartz pseudomorphs after coesite; biotite–K–feldspar and plagioclase–amphibole symplectite-like intergrowth around clinopyroxenes and garnets; a replacement garnet by biotite are the marker of amphibolite metamorphic phase (~ 650-680°C, <10 GPa); solid to solid phase transformation dolomite to calcite and chlorite-actinolite in matrix of host rocks are markers of greenschist (~ 420°C, ~2–3 GPa) metamorphic phase.

Inclusions in diamonds

Polycrystalline nano-inclusions in diamonds represented by oxides Si, Ti, Fe, Cr with trace element impurities: Mg, Ca, Al, K, Na, S, P, Pb, Nb, Cl, Zn, Ni [Dobrzhinetskaya et al., 2003], and also Si-P-K-containing glasses and K-Si-COH fluid inclusions [Hwang, 2006]; mineral inclusions also captured by diamonds-bearing garnets and zircons in both progressive and regressive metamorphic stages. Inclusion compositions have similarity to extraterrestrial matter.

Carbon, Helium, Nitrogen, Hydrogen and Nickel in diamonds

Carbon represents by graphite, diamond↔lonsdaleite, chaoite, α- and β-carbines, X-ray amorphous skeletal forms. Diamonds have different forms: cubes (dominated), distorted forms, skeletal and spheroid crystals,

octahedra, twins. Core and rim differ on morphology, C and N isotope compositions in cube forms. Symplectite-like diamond-graphite intergrowth, coated diamonds with graphite rim and graphite crystals are observed. Diamond carbon isotope composition of $\delta^{13}\text{C}$ (-8.9 to -27 ‰) compare with $\delta^{13}\text{C}$ (-5 to -31 ‰) in meteorites; diamonds from gneisses have lighter $\delta^{13}\text{C}$ relatively to those of pyroxene-carbonate and garnet-pyroxene rocks that suggest to discrete carbon sources. Values $\delta^{13}\text{C}$ of graphite are lighter than those in diamonds that do not supported the hypothesis of transformation graphite to diamond for this deposit. Carbon matter composition compared with those presolar nanodiamonds.

$^3\text{He}/^4\text{He}$ isotopic ratio (7×10^{-1} to 8×10^{-9} ‰) of diamonds [Shykolukov et al., 1996] is significantly higher than $^3\text{He}/^4\text{He}$ ratio of IDP ($> 10^{-4}$ ‰), the Earth's atmosphere (1.4×10^{-6}), Solar wind (4.3×10^{-4}), MORB (1.1×10^{-5}), OBI (0.7×10^{-4}). ^3He occur in diamond lattice and inclusions, it means that ^3He was trapped by diamonds during its formation outside the Solar System, more likely ^3He is primordial galactic component. ^4He , Ne, Ar, Xe also present in these diamonds.

High N (up to 10000 ppm), high enriched $\delta^{15}\text{N}$ ($+5.3$ to $+25$ ‰), high H in diamonds compare with value coma comet gases (CN, HCN), diamonds from chondrites and presolar diamond grains. N aggregation state are Ib+IaA (Ib $>$ IaA). Presence of Ni-N centers in diamonds identified by PLS. So, diamond crystallization occurred by CVD growth process on carbonaceous matter seeds from over saturated carbon fluid/melt. Small diamond sizes, low N aggregation state and diamond preservations suggest to short-term diamond grown process.

References

- Clayton DD, Nittler LR (2004) Astrophysics with presolar stardust. *Annual Review of Astronomy and Astrophysics* 42: 39–78
- DeNiem D (2002) Multiple stages of condensation in impact-produced vapor clouds. In: Koeberl C, MacLeod KG (eds). *Catastrophic events and mass extinctions: impacts and beyond*. Boulder Colorado. Geological Society America, Special Paper 356: 631–644
- Dobrzhinetskaya L F, Green HW, Bozhilov K N, Mitchel TE, Dickerson RM (2003) Crystallization environment of Kazakhstan microdiamond: from nanometric inclusions and mineral associations. *Journal Metamorphic Geology* 21(5):425 – 437
- He H, Sekine T, Kobayashi T. (2002) Direct transformation of cubic diamond to hexagonal diamond. *Applied Physics Letter* 81(4): 610–612
- Hwang S-L, Chu H-T, Yui T-F, Shen P, Schertl H-P, Liou JG, Sobolev NV (2006) Nanometer-size P/K-rich silica glass (former melt) inclusions in microdiamond from the gneisses of Kokchetav and Erzgebirge massifs. *Earth Planetary Science Letter* 243: 94–106
- Shukoljukov Ju A , Pleshakov A M , Semjonova L.F , Fisenko A.A , Lavrova A D , Pustjakova A Ju (1996) He isotopic composition in diamond-bearing metamorphic rocks of N. Kazakhtan. *Geokhimiya* (1): 22–35 (in Russian)
- Tretiakova LI, Lyukhin AM (2016) Impact-cosmic-metasomatic origin of microdiamonds from Kumdy-Kol deposit, northern Kazakhstan. *Otechestvennaya geologiya* (2):69-77 (in Russia)
- Zhang RY, Liou JG, Ernst WG, Coleman RG, Sobolev NV, Shatsky VS (1997) Metamorphic evolution of diamond-bearing and associated rocks from the Kokchetav Massif, northern Kazakhstan. *Journal Metamorphic Geology* 15(4): 479 – 496

History of Natural Diamond Formation Based on Defect Characteristics Detected by Spectroscopic Methods

L.I. Tretiakova¹, A.M. Lyukhin²

¹St. Petersburg Branch Russian Mineralogical Society, RUSSIA, ltretia@gmail.com

²Institute of remote ore prognosis, Moscow, RUSSIA, alex.lyukhin@gmail.com

Introduction

The history of natural gem diamond formation that genetically related with impact events followed by shock, progressive and regressive metamorphism of target rock areas has been deduced by data obtained by complex nondestructive spectroscopic methods: Raman spectroscopy, PLS, CLS, IRS and also mineralogical and literature data. About 200 representative natural gem diamonds have been picked out from investigated thousands samples: colorless, yellow, brown colors, 0.03 – 1.60 carat weight, zoning with cubic internal morphology of crystal centers graduated to cubo-octahedral and octahedral forward to intermediate and rim zones, mineral inclusions in central zones were represented by tiny inclusions of graphite, α -Fe, Ni-Fe, sulfides etc., intermediate – by peridotitic, eclogitic and UHP minerals, often surrounded by discoid fractures and melt inclusions; rim zones – association of secondary minerals and gas/fluid inclusions. Diamond zones were differentiated by C and N isotopic compositions and also N content and N aggregation state. All diamond crystals had dislocations, plastic deformation, discoid fractures around inclusions and birefringence.

UHP-HT features of natural diamonds

1. The presence of $sp^1 \rightarrow sp^2 \leftrightarrow sp^3$ carbon phase transformations (Fig.1), including diamond \leftrightarrow lonsdaleite transformation that has been completed in nanoseconds under a shock wave compression of cubic diamond [He, 2002]. Lonsdaleite line maximum in Raman spectra is the 1324.4 cm^{-1} (552.2 nm).

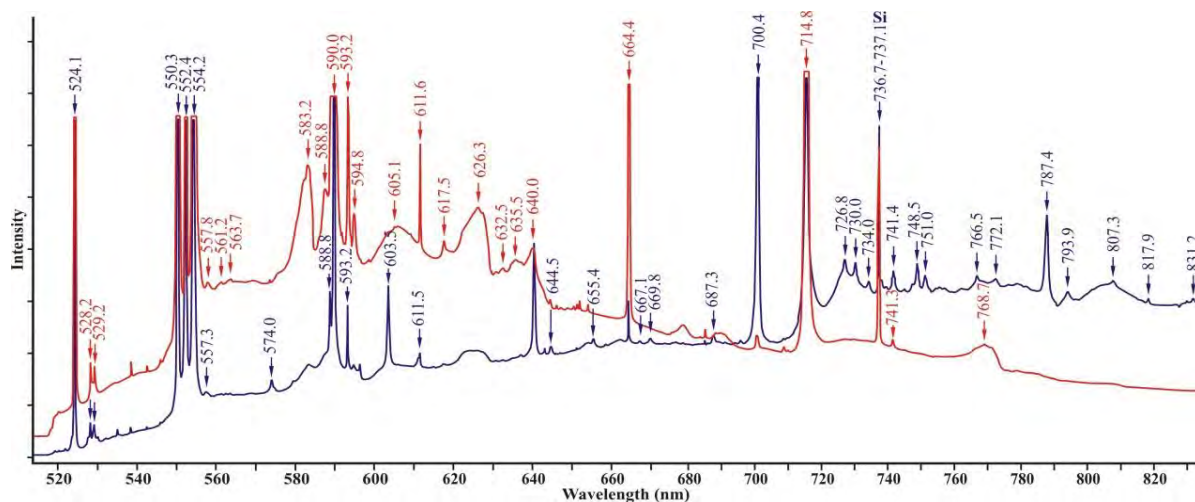


Fig. 1. PLS (λ_{exc} 514.5 nm) IaAB (regular) diamond. Strong lines in range 550.3-552.4 nm – $sp^2 \leftrightarrow sp^3$ carbon phase transformations [Zaitsev, 2001]; 554.2-554.7 nm – $sp^1 \rightarrow sp^2 \rightarrow sp^3$ primary carbon matter transformations by shock wave [Miyamoto, 1993]; 583.2-594.8 nm – superposition of II order Raman lines and radiation defects; 524.1, 664.4, 714.8 nm lines identified radiation damage [Zaitsev, 2001]; 605.1- 640-700.4, 787.4, 793.9 nm - Ni-N defects, 669.8 - Co-N defect [Yelisseyev., Kanda, 2007]; 528.2 nm – Si--defects, 736.7-737.1 – [Si—V]– defect [Clark et al., 1995]. These defects formed at different PT conditions and preserved in natural diamonds have different temperature formations: $sp^1 \rightarrow sp^2 \rightarrow sp^3$ carbon phase transformations >2500 K, Ni-N ~2500–1600 K, Co-N ~1850–1750 K, [Si-V]– ~2200 –1200–800 K, and radiation damage ~1000 - 800 K.

2. Raman line in studied natural diamonds represented intensive positive or negative asymmetric line with maximum 1332.5 cm^{-1} , and FWHM in the range 3.2 cm^{-1} to 9 cm^{-1} (as a result of HPHT environment conditions) and $\gg 4.5 \text{ cm}^{-1}$ to very large width (HPHT + radiation damage conditions).
3. UHP mineral inclusions in diamonds: diamond \leftrightarrow lonsdaleite, coesite, SiC and its various modifications, majorite, ringwoodite, TAPP, perovskite and etc. Protogenetic central nano-inclusions, appeared to be diamond seeds, its mineral compositions are carbon phases with He, Ar, Ne, Xe, H₂, N₂, CO₂, CO, H₂O, CH₄ gases, REEs, Fe, Cu, Cr, Au, Ag and etc.; Ni, Fe, Co, Cu, Zn sulfides etc.; Fe-Cr, Fe-Cr-Ti, Fe-Cr-Ni, FeC, oxides Mg, Ti, Pb, Ba. All nano-inclusions are minerals extraterrestrial origin [Rubin, 1997].
4. Variety of crystal structure defects, dislocations, plastic deformations, discoid fractures around inclusions, birefringence, mosaic structures.

Carbon, nitrogen, hydrogen, noble gas sources in natural diamonds

Nano-diamonds from chondritic meteorites, micro-meteorites, IDPs indicating that they formed outside our solar system and reflecting the conditions in interstellar space, solar nebula and host meteorites [Huss, 2005]. They were the sources of carbon, nitrogen, hydrogen, noble gases in earth's diamonds. ^{13}C value in kimberlitic diamond varied in the range (-41% to $+5.0\%$) [Cartigny, 2005]. Value $\delta^{13}\text{C}$ eclogitic and micro-diamonds are nearly to value $\delta^{13}\text{C}$ (-31 to -38%) similar to extraterrestrial nano-diamonds. Variety of C modifications and its isotope compositions allow to assume a derivation of different diamond groups from various or mixed carbon sources reflected host rocks (target + impactor) composition. Most part C- and N- containing phases in carbonaceous chondrites are organic matter, which is characterized by high D/H ratio, value δD ($+300$ to $+1600\%$) [Remusat, 2015].

Dawson (1980) wrote: —Nitrogen exists in platelets and segregated nodes within diamond which is the only site of upper-mantle nitrogen known at present. Whereas some evidence, albeit scanty, exists for a source of carbon and phosphorus, the initial source of the nitrogen and other rare gases within diamond must remain an enigma". There is only one answer of this enigma: C, N, H, noble gases have extraterrestrial nature. N is widely distributed in Universe and present in diamonds and matrix of chondritic meteorites, micro-meteorites, IDPs, asteroids, comets as variety molecules, including organic. Interstellar organic matter has anomalies of H and N isotope, that suggesting of its derivation in presolar molecular clouds or protoplanet disk. [Remusat, 2015]. Values $\delta^{15}\text{N}$ (-25 to $+20\%$) are in kimberlite diamonds and $\delta^{15}\text{N}$ ($+5.3$ to $+25\%$) in micro-diamonds from Kumdyy-Kol deposit.

Signatures of noble gases He, Ne, Ar, Kr, Xe in meteoritic and comet matter preserved in natural diamonds. ^3He is original galactic component have been trapped outside our Solar System [Huss, 2005]. Value $^3\text{He}/^4\text{He}$ in natural diamonds varied in the range (7×10^{-1} – $8 \times 10^{-9}\%$) [Shukoljukov et al., 1996]. ^4He , Ne, Ar и Xe have radiogenic origin, ^{40}Ar and ^{21}Ne joined to diamond seeds during their formation in the space. Noble gases can identify by PL spectra: He $\sim 523, 536.6, \sim 562$, Ne⁺ – 716, 719.5 Xe⁺ – 811.6, 793.3, D (H⁺) – 555.0 nm lines [Zaitsev, 2001].

Transition metals - Ni, Co, Cr, Ti, Fe - and Si in natural diamonds

Transition metal defects were observed by PLS in studied diamonds mixed type 1b + IaAB (regular and irregular) with various N and H concentrations:

(Co-N) – the 519.7–521.1–523.4, 542.5, 544.1, 623.5 nm and Co-C – 669.4 nm systems [Tretiakova 2010] Temperature formation of these defects in the range ~ 1850 – 1750 K.

(Ni-N) defects – the S1, S2, S3, 535.2, 694.3–692.4, 603.6, 640.5, 700.6, 787.6, 795.3 nm are complex interstitial defects with various number N atoms [Yelisseyev, Kanda, 2007] were formed at temperature range ~ 2200 до ~ 1600 K.

Cr³⁺ center characterized of R₁ 693.7 nm and R₂ 692.2 nm lines in PLS.

Ti-defects the 973.2 and 991.8–1014 (replica) nm, the 991.8 nm center (Ti-Ti bonds) were observed in natural IIa type diamonds in PLS at first time by authors. Formations temperature of the 973.2 and 993.2–1014.1 nm defects ~ 1900 – 1800 K and 1600 K, respectively.

Fe. Most of natural diamonds are magnetic susceptibility, that due iron presence as Fe-magnetic impurity in nano- and submicron diamonds and fluid inclusions, which size \sim equal or less λ_{light} , doing them invisible under optic research; α -Fe, Fe₃C и Fe_xN phases/inclusions are known in meteorites and “central inclusions” in natural diamonds.

Si-defects – 528.2 nm, [Si-V]⁰⁻ – ~ 946–948 nm, and [Si-V]⁻ = 736.7–737.1 nm that formed at ~2200 – 1200–800 K.

Conclusion

All of above are evidences of impact events that were provoked diamond generation from carbon matter, delivered by meteoroids and followed diamond growth at shifting HPHT (sharp drop pressure and gradually decreased temperature) conditions corresponding of shock, progressive and regressive metamorphism with metasomatic alterations of impact area rocks.

So, natural diamonds generated and grown in solution-melts due to collision any meteoroid and the Earth followed by shock, progressive and regressive metamorphism in target rock areas. Protogenetic central inclusions in diamond represented by meteoritic minerals and appear to be diamond seeds, early diamond growth started at HPHT conditions by growth scheme HPHT synthetic diamonds; subsequent growth under lower PT conditions came by CVD growth scheme. Sources of C, N, H, noble gases had cosmic origin.

Simultaneous presence in PLS of single natural diamond (Fig.1) defects, formed and preserved at different PT conditions, demonstrate their different temperature formations $sp^1 \rightarrow sp^2 \rightarrow sp^3$ carbon phase transformations >2500 K, Ni-N ~2500–1600 K, Co-N ~1850–1750 K, Si ~2200 – 1200–800 K, radiation damage ~1000 - 800 K defects and suggest long diamond history during gradually changing HPHT conditions.

Diamond varieties (from gem stones to carbonado) occurred in one diamond deposit due conditions that took place during these events. Kimberlite pipes and dykes were formed under closer to vertical diamondiferous asteroid impacts to the Earth [Lyukhin, 2008]. At oblique impact diamondiferous asteroid, diamond dispersed on extended territories and later concentrated in placers. Deposits of “metamorphic” diamonds formed under oblique impacts as well. Every kimberlite pipe, every placer and metamorphic deposit of natural diamonds are especially individual under all its parameters.

References

- Cartigny P (2005) Stable isotopes and the origin of diamond. *Element* (1):79-84
- Clark C D, Kanda H, Kiflawi I, Sittas G (1995) Silicon defects in diamond. *Physical Review B* 51(23): 16681–16688
- He H, Sekine T, Kobayashi T (2002) Direct transformation of cubic diamond to hexagonal diamond. *Applied Physics Letter* 81(4): 610–612
- Huss GR (2005) Meteoritic nanodiamonds: messengers from the stars. *Elements* (1): 97–100
- Lyukhin A (2008) The Hypothesis of Impact Origin of Diamonds and Kimberlites. 9-th International Kimberlite Conference, Frankfurt, Germany: Extended. Abstract 9IKC-080
- Miyamoto M, Takase T, Mitsuda Y (1993) Raman spectra of various diamonds. *Mineralogical Journal, Japan* 16(5):246–257
- Remusat L (2015) Organic in primitive meteorites. *EMU Planetary Mineralogy* (15): 33-65
- Rubin AE (1997) Mineralogy of meteorite groups. *Meteoritics & Planetary Science* (32):231–247
- Shukoljukov Ju A, Pleshakov AM, Semjonova LF, Fisenko AA, Lavrova AD, Pustjakova AJu (1996) He isotopic composition in diamond-bearing metamorphic rocks of N. Kazakhtan. *Geokhimiya* (1):22–35 (in Russian)
- Tretiakova L (2010) Spectroscopic features due to Ni- and Co related defects in gem-quality natural diamonds. 20-th General Meeting, IMA, Hungary. Budapest 2010. *Acta mineralogical-petrographica abstract series* (6):33
- Yelisseyev A, Kanda H (2007) Optical Centers Related to 3d Transition Metals in Diamond. *MY Tokio: New Diamond and Frontier Carbon Technology* 17(3):127–178
- Zaitsev AM (2001) *Optical properties of diamond*. Berlin: Springer, pp 502



Three phases of diamond growth spanning >2.0 Ga beneath Letlhakane established by Re-Os and Sm-Nd systematics of individual eclogitic sulphide, garnet and clinopyroxene inclusions

M.U. Gress^a, D.G. Pearson^b, S. Timmerman^a, I.L. Chinn^c,
J.M. Koornneef^a, G.R. Davies^a

^a *Vrije Universiteit, De Boelelaan 1085, 1081 HV Amsterdam, The Netherlands, m.u.gress@vu.nl, suzette.timmerman@anu.edu.au, j.m.koornneef@vu.nl, g.r.davies@vu.nl*

^b *University of Alberta, Edmonton T6G 2E3, Canada, gdpearso@ualberta.ca*

^c *De Beers Exploration, Johannesburg, South Africa, ingrid.chinn@debeersgroup.com*

Introduction

The diamondiferous Letlhakane kimberlites are part of the Orapa kimberlite cluster (~ 93.1 Ma) in north-eastern Botswana, located on the edge of the Zimbabwe Craton, close to the Proterozoic Magondi Mobile Belt. Here we report the first Re-Os ages of six individual eclogitic sulphide inclusions from Letlhakane diamonds along with their carbon isotope and FTIR data from the corresponding growth zones of the host diamonds. For the first time, Re-Os data will be compared to Sm-Nd ages of individual eclogitic silicate inclusions recovered from the same diamonds. All inclusions are considered as recording information synchronous to their corresponding diamond growth zone because at mantle temperatures (> 1000°C) experimental data suggests isotopic equilibration during inclusion precipitation/ recrystallization due to rapid elemental diffusion between minerals and diamond forming fluids.

Analytical Results

The analysed inclusion set encompasses pairs of individual sulphides from two diamonds (LK040, LK113) and sulphide inclusions from two separate diamonds along with their matrix composition and rhenium, osmium, iridium and platinum concentrations. Sm-Nd isochron ages at Letlhakane were obtained by compiling recently published Sm-Nd data from nine individual eclogitic inclusions that indicate three distinct diamond forming events at 2.3 ± 0.02 , 1.0 ± 0.14 and 0.25 ± 0.04 Ga (Timmerman et al., 2017) with newly acquired data e.g., two garnets of LK113. Ongoing work will analyse additional individual eclogitic inclusions for Sm-Nd to extend the data set.

Individual diamond growth zones have variable C-isotope compositions ($\delta^{13}\text{C}$: -38.5 to -3.8‰), nitrogen aggregation (8 to 90% IaB) and nitrogen content (22 to 821 ppm N) extending the range of C-isotope data compared to that previously reported on bulk stones (Deines & Harris, 2004). Cathodoluminescence images of central plates from the sulphide-bearing samples LK040 and LK113 reveal a core-rim zonation. The two sulphides of LK040 were situated together with a cpx inclusion in the rim. The two sulphides within LK113 occurred together with two garnet inclusions in the core. Individual garnet inclusions were classified by their Cr_2O_3 vs CaO content (Fig. 1) with categories G4 and G5 (e.g., LK113, LK338 lying on the 1.0 Ga Sm-Nd isochron mentioned above) within error of the sodium threshold ($\text{Na}_2\text{O} > 0.07$ wt.%) between eclogitic, websteritic and pyroxenitic inclusions (Grütter et al. 2004).

Sulphides from the rim zone of LK040 define an 'isochron' of 0.92 ± 0.23 Ga. Sulphides from the core zone of LK113 have clear imposed diamond morphology and indicate diamond formation at 0.93 ± 0.36 Ga (Fig. 2). Both 'isochrons' have high, but different initial Os ratios of 1.31 ± 0.24 and 0.69 ± 0.44 , respectively. Corresponding T_{MA} ages of the sulphides range from 1.06 to 2.3 ± 0.1 Ga, their Re and Os concentrations (200-2500 ppb and 14-134 ppb, respectively) are low compared to high Os peridotitic inclusions and due to the small sample size (3.0 – 35.7 µg), account for the relatively large errors in the ages. C1-normalized iridium and platinum compositions from the analysed sulphide inclusions display enrichment in Ir (3.4 to 33 ppb) and Pt (2.3 to 28.1 ppb) in comparison to eclogitic xenolith data from Orapa that are depleted relative to chondrite (McDonald & Viljoen 2006).

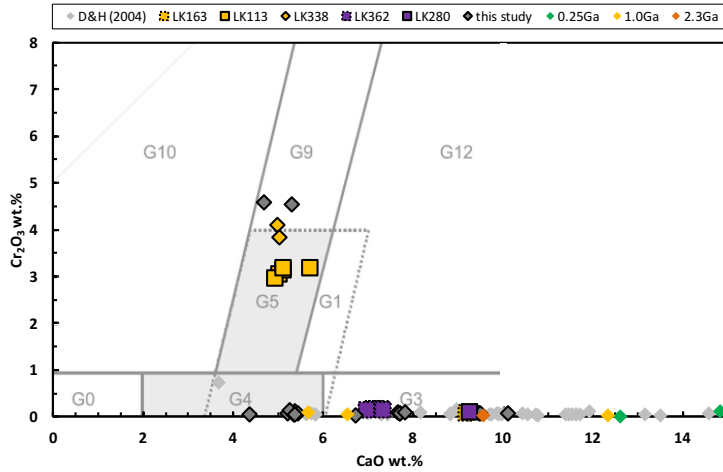


Fig. 1: Garnet classification scheme of individual inclusions from Letlhakane with categories after Grütter et al. (2004). Reference data from Deines & Harris (2004) as grey symbols without borders; Coloured symbols without borders from inclusions on isochrons after Timmerman et al. (2017); Coloured symbols with borders from this study; Grey symbols with border not yet analysed for Sm-Nd. The inclusions plot in the fields for high- and low-Ca eclogitic garnets (G3, G4); pyroxenitic, websteritic and eclogitic garnets (G5) and lherzolitic garnets (G9).

Discussion

The 2-point Re-Os isochrons are within error of previously reported ages from the adjacent (~40 km) Orapa mine (1.0 Ga) based on sulphide inclusions from different diamonds (Shirey et al., 2004), and compare well with a two-point isochron of individual eclogitic inclusions (1096 ± 230 Ma) reported by Timmerman et al. (2017) as well as with a 990 ± 50 Ma isochron for composite (n=730) eclogitic silicate inclusions by Richardson et al. (1990).

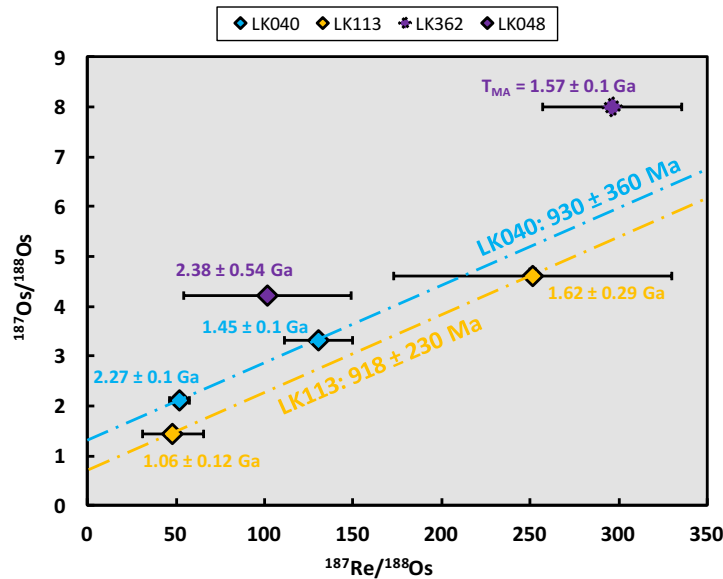


Fig. 2: Re-Os isochron data of individual eclogitic inclusions from Letlhakane (LK) with calculated mantle model ages. The two isochrons are each defined by two sulphide inclusions.

data, however, initial ratios determined for the Sm-Nd isochrons in this study (Fig. 3) are close to bulk Earth (ϵ_{Nd} : -0.5 to +6.2) and much less variable than the Re-Os system, due to smaller parent-daughter isotope fractionations and the larger decay constant of ^{147}Sm .

Following the approach of Timmerman et al. (2017) we group inclusions from different diamonds based on a combination of the nitrogen aggregation state (%IaB) of the corresponding diamond growth zone and Sr-isotopes of the inclusion. Although not all these criteria have yet been applied in the present study, silicate inclusions of LK113, LK163, and LK338 fall on the 998 ± 140 Ma isochron of Timmermann et al (2017). A clinopyroxene of LK338 from a different growth zone and of LK079 falls on the 2.3 Ga isochron; and the clinopyroxene of LK131 falls onto the 245 ± 38 Ma isochron.

Although the sulphides of LK040 and LK113 are in the same growth zone in their host diamonds, their T_{MA} ages (1.06 to 2.3 ± 0.1 Ga) are highly variable. This highlights that using model ages in sulphides with low to medium Os contents (e.g., eclogitic sulphides) can be problematic, due to the high variability of initial Os isotope ratios. This variability indicates why it is essential, for Re-Os diamond dating, to use sulfides from the same diamond/growth zone – clearly there is no single isochron that would fit all the sulfide data in Fig. 2.

The same problem may occur when obtaining Sm-Nd age information from diamonds containing single or pairs of silicate inclusions (i.e., how to establish that inclusions are co-genetic). In contrast to the Re-Os

The garnet of LK280 does not plot on a previously defined isochron. The addition of garnets of LK113 and LK163 to the 1.0 Ga isochron improves the fit and precision of the age to 1081 ± 67 Ma. This Sm-Nd isochron age is within error of the 918 ± 230 Ma Re-Os isochron age of the sulphides from the same diamond. Hence a ~ 1 Ga diamond-forming event in the lithosphere beneath the Orapa/Letlhakane region is firmly established and is further evidence of a more wide-spread, circa 1 Ga diamond-forming event over the Kaapvaal craton, e.g., at Koffienfontein or Premier (Pearson et al., 1998, Richardson 1986).

The clinopyroxene of LK040 fits on both the 0.25 and 1.0 Ga Sm-Nd isochron. Given the high chromium content of LK040 and clinopyroxene and garnets of LK113 and LK338, all these inclusions (including LK040) likely grew at 1.0 Ga. These preliminary data indicate that different inclusion populations (plotting in G3, G4, G5; Fig. 1) all formed at 1.0 Ga, suggesting that diamond formation occurred at the same time in different parts of the sub-continental lithospheric mantle, via metasomatic processes where carbon-bearing fluids infiltrate different host rock lithologies.

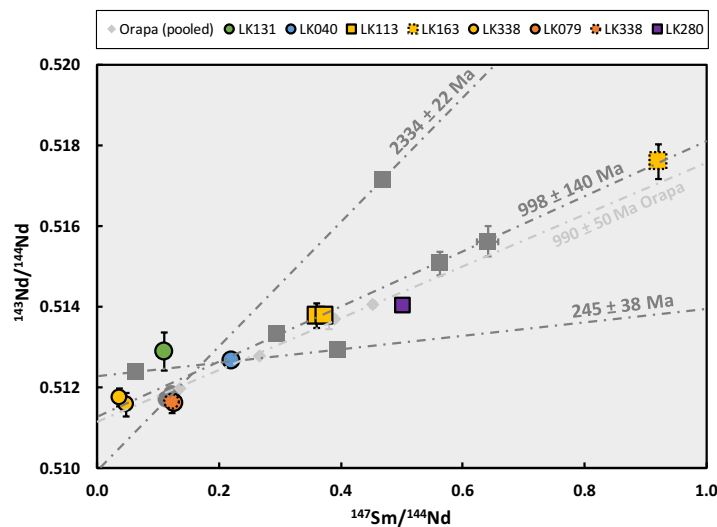


Fig. 3: Compilation of Sm-Nd isochrons of silicate inclusions from Letlhakane (LK) and Orapa. Square markers represent individual garnets, circles individual clinopyroxene inclusions. Colour codes: dark grey symbols define isochron ages of 2334 ± 22 Ma, 998 ± 140 Ma and 245 ± 38 Ma for Letlhakane after Timmerman et al. (2017); Light grey symbols represent groups of pooled eclogitic inclusions ($n=720$) from Orapa on a 990 ± 50 Ma isochron after Richardson et al. (1990); Coloured symbols with borders represent newly acquired data from this study.

This is the first time that both sulphide and silicate inclusions from a single growth zone in diamonds have been measured. The Re-Os and Sm-Nd isotope systems of individual silicate and sulphide inclusions record the same time of diamond formation. The entire inclusion dataset demonstrates a phase of Neoproterozoic/ Paleoproterozoic diamond formation as well as Mesoproterozoic and Mesozoic diamond growth, in punctuated events spanning > 2.0 Ga.

References

- Deines P, Harris JW (2004) New insights into the occurrence of ^{13}C -depleted carbon in the mantle from two closely associated kimberlites: Letlhakane and Orapa, Botswana *Lithos* 77:125-142
- Grütter HS, Gurney JJ, Menzies AH, Winter F (2004) An updated classification scheme for mantle-derived garnet, for use by diamond explorers *Lithos* 77:841-857
- McDonald I, Viljoen K (2006) Platinum-group element geochemistry of mantle eclogites: a reconnaissance study of xenoliths from the Orapa kimberlite, Botswana *Applied Earth Science* 115:81-93
- Pearson DG, Shirey SB, Harris JW, Carlson R (1998) A Re-Os isotope study of sulfide diamond inclusions from the Koffienfontein kimberlite, S. Africa: constraints on diamond crystallisation ages and mantle Re-Os systematics *Earth Planet Sci Lett* 160:311-326
- Richardson SH (1986) Latter-day origin of diamonds of eclogitic paragenesis *Nature* 322:623-626
- Richardson SH, Erlank A, Harris JW, Hart S (1990) Eclogitic diamonds of Proterozoic age from Cretaceous kimberlites *Nature* 346:54-56
- Shirey SB, Richardson SH, Harris JW (2004) Integrated models of diamond formation and craton evolution *Lithos* 77:923-944
- Timmerman S, Koornneef JM, Chinn IL, Davies GR (2017) Dated eclogitic diamond growth zones reveal variable recycling of crustal carbon through time *Earth and Planetary Science Letters* 463:178-188

Variation in diamond growth events recorded in Botswanan diamonds

M.U. Gress^a, S. Timmerman^a, Q van den Heuvel^a, E. Schulten^a,

I.L. Chinn^b, G.R. Davies^a

^a Vrije Universiteit, De Boelelaan 1085, 1081 HV Amsterdam, The Netherlands, m.u.gress@vu.nl, suzette.timmerman@anu.edu.au, j.m.koornneef@vu.nl, g.r.davies@vu.nl

^b De Beers Exploration, Johannesburg, South Africa, ingrid.chinn@debeersgroup.com

Introduction

The number of diamond-forming events recorded in the mantle beneath an individual diamond mine and the scale of these events, remains unknown, limiting the understanding of the geological processes that ultimately control diamond formation. In a first step towards constraining these parameters we report a study of diamond populations from the Orapa kimberlite cluster in central Botswana (Damtshaa, Letlhakane and Orapa mines) and the Jwaneng mine in southern Botswana, ~400 km to the southwest.

This study was conducted as part of an inclusion-bearing diamond collection campaign. Over a 4-year period run of mine production was examined from a total of 8 kimberlite pipes, with diamonds ranging in size from 0.12 to just under 1 ct.

Analytical Results

In total over 332 000 diamonds were characterised for their inclusion content. Inclusions were defined as a recognisable mineral (> 10 µm) for counting purposes. The inclusion abundance (Fig. 1) varies between diamond size fractions but on average Damtshaa has 2.1 to 4.9%, Letlhakane, 1.5 to 5.5%, Orapa 2.8 to 5.4% and Jwaneng 2.0 to 4.5% inclusion-bearing diamonds.

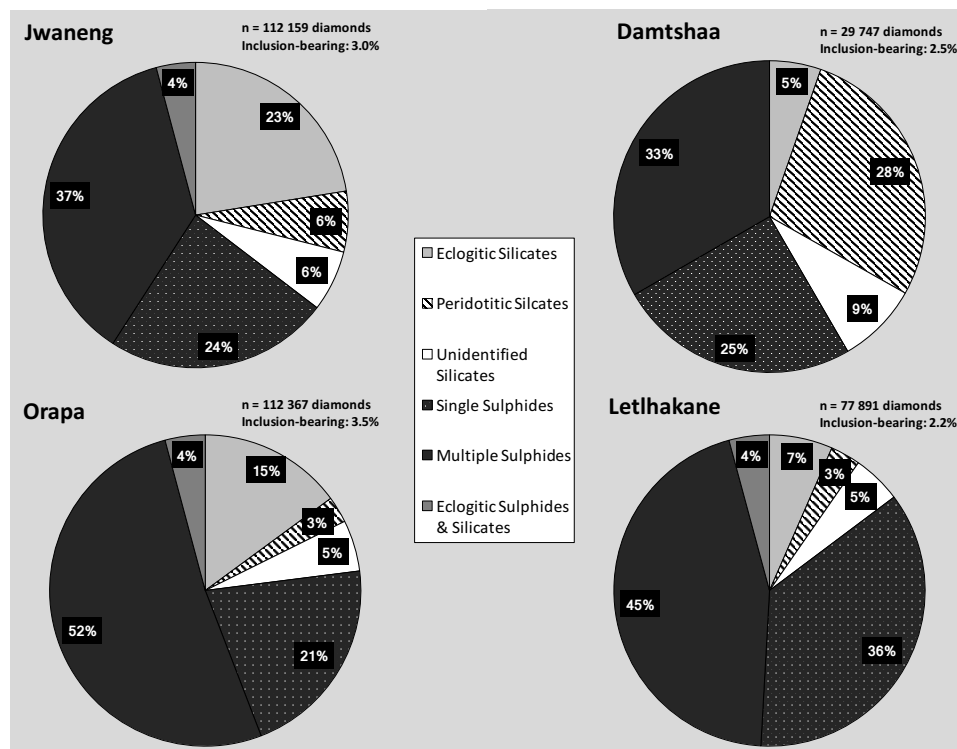


Fig.1: Average inclusion abundance for Jwaneng, Damtshaa, Orapa and Letlhakane diamond mines for 332 000 diamonds from 0.12 to 1 ct.

Eclogitic inclusions dominate the inclusion population at Letlhakane (80%), Jwaneng (83%) and Orapa (86%), while Damtshaa (20%) has a notably lower eclogitic inclusion abundance.

All diamond populations record colour variations with Orapa for example being characterised by several populations with different yellow-orange colours. A representative set of diamonds was selected from each mine for bulk diamond FTIR analyses (~1900 stones). All localities record marked variation in nitrogen abundance (10 to 1200 at.ppm) and nitrogen aggregation state (0-100 %N as B).

A set of inclusion-bearing diamonds were examined to determine their detailed growth history by cathodoluminescence (CL) imaging of central plates. To date > 145 diamonds have been characterised and FTIR traverses conducted. More than 70% record complex growth histories with up to 9 recognisable growth zones and multiple resorption events. Diamond growth zones were measured for C-isotope ratios from diamonds recording both simple and complex growth zonation. Carbon isotope ratios vary markedly; for example, $\delta^{13}\text{C}$ values range from -38.5 to -3.8 ‰ in Letlhakane and from -9.1 to -3.5 ‰ in Jwaneng, although larger ranges have been recorded in previous studies from Jwaneng (Cartigny et al. 1998; Deines et al. 1997).

As with the bulk diamond data, the diamond plates recorded marked variation in nitrogen content (< 10 to 1400 at.ppm) and nitrogen aggregation (0-100 %N as B). FTIR core to rim traverses reveal marked variability. Individual plates can be relatively homogeneous with N-content within ± 50 at.ppm, while others record marked changes in nitrogen content and aggregation states (Fig. 2) at the boundaries between individual growth zones (changes in N-content up to 500 ppm and N-aggregation from 5 to 95 %N as B). Isotherms calculated for mantle residence times based on recently published diamond formation ages (0.25, 1.0, 2.3 Ga) at Letlhakane show varying conditions for diamond precipitation for the diamonds with complex growth (Timmerman et al. 2017).

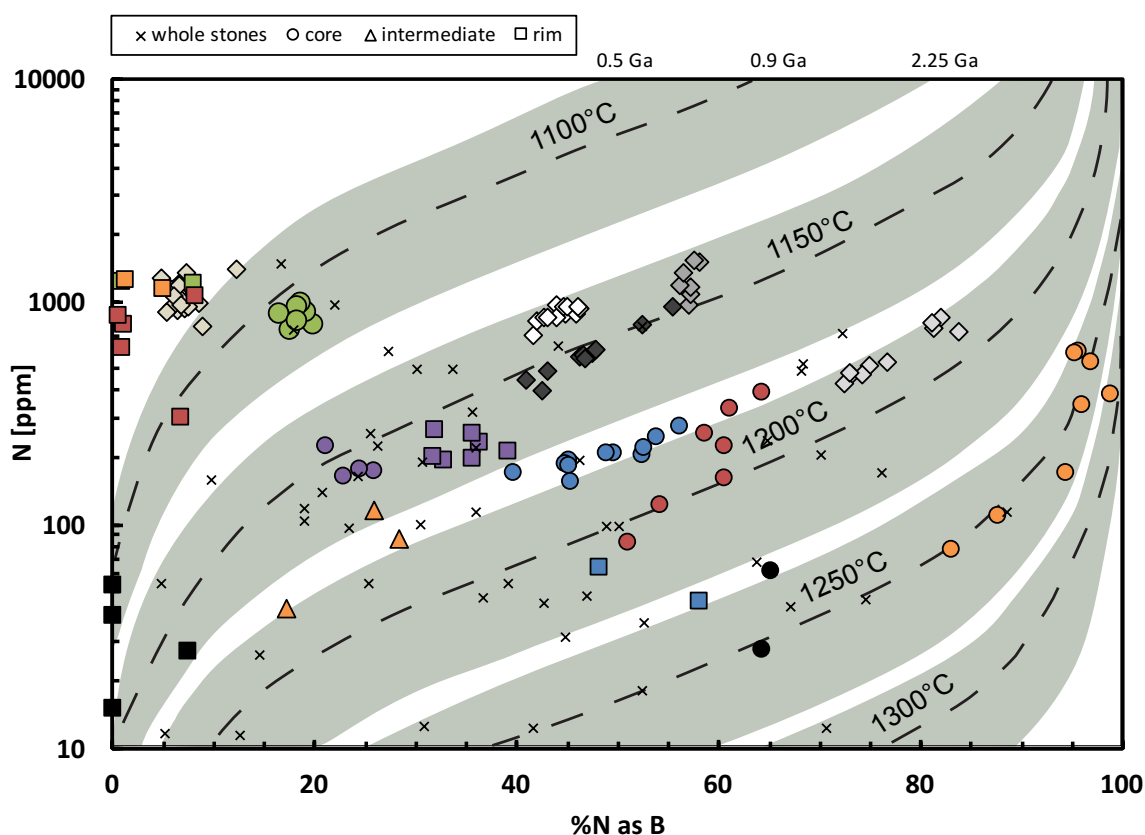


Fig. 2: Comparison of nitrogen content [ppm] vs nitrogen aggregation [%B] of FTIR data from Letlhakane of bulk stones (x) with traverses on individual plates subdivided into homogeneous growth (rhombus); and complex growth: core (circle), intermediate (triangle) and rim (rectangle). The different colours mark individual samples, isotherms are calculated for 0.5, 0.9 (dotted line) and 2.25 Ga mantle residence time accounting for diamond formation at 1.0 and 2.33 Ga and kimberlite eruption 93.1 my ago.

The integrated datasets establish that Orapa, Letlhakane and Jwaneng record multiple diamond growth events and have a limited number of unique characteristic growth events at each locality. This raises the question whether different diamond-forming events record evolution of diamond-forming fluids over time or are distinct events with new fluid input. On-going inclusion dating studies are designed to answer this question.

References

- Cartigny P, Harris JW, Javoy M (1998) Eclogitic Diamond Formation at Jwaneng: No Room for a Recycled Component *Science* 280:1421-1424 doi:10.1126/science.280.5368.1421
- Deines P, Harris J, Gurney J (1997) Carbon isotope ratios, nitrogen content and aggregation state, and inclusion chemistry of diamonds from Jwaneng, Botswana *Geochimica et Cosmochimica Acta* 61:3993-4005
- Timmerman S, Koornneef JM, Chinn IL, Davies GR (2017) Dated eclogitic diamond growth zones reveal variable recycling of crustal carbon through time *Earth and Planetary Science Letters* 463:178-188



Genesis of diamond inclusions: An integrated cathodoluminescence (CL) and Electron backscatter diffraction (EBSD) study on eclogitic and peridotitic inclusions and their diamond host.

**Q. Van den Heuvel^a, M.U. Gress^a, S. Matveev^b, M.R. Drury^b, I.L. Chinn^c,
G.R. Davies^a**

^a *Vrije Universiteit, De Boelelaan 1085, 1081 HV Amsterdam, The Netherlands,
m.u.gress@vu.nl; g.r.davies@vu.nl*

^b *Universiteit Utrecht, Heidelberglaan 8, 3584 CS Utrecht, The Netherland,
s.matveev@uu.nl, m.r.drury@uu.nl*

^c *De Beers Exploration, Johannesburg, South Africa,
ingrid.chinn@debeersgroup.com*

Introduction

Diamond inclusions are potentially fundamental to understanding the formation conditions of diamond and Earth's long-term volatile cycles. In order to fully understand the implications of the mineralogical and compositional information recorded by inclusions and their host diamonds it is vital to know whether the inclusions are proto-, syn-, or epigenetic and the extent to which they have equilibrated with the diamond-forming media. In the latter context Nestola et al., (2017) have recently proposed the use of the term synchronous to cover the situation where a protogenetic phase records the time of diamond growth due to achieving equilibration with the diamond-forming media. In previous studies, the widespread assumption was made that the majority of diamond inclusions were syngenetic, based upon visual observation of cubo-octahedral morphology imposed on the inclusion (e.g., Harris & Gurney, 1979) and crystallographic controlled relationships between host diamond and inclusions (e.g., Harris & Gurney, 1979; Wiggers de Vries et al 2010). Recent work, however, has questioned this assumption and reported that the crystallographic relationships between inclusions and the host diamond are highly complex (Agrosi et al., 2016) with the lack of crystallographic controlled relationships between inclusions and diamonds used to question the significance of imposed diamond morphology (Nestola et al., 2014).

Analytical Results

This study presents an integrated electron backscatter diffraction (EBSD) and cathodoluminescence (CL) study of 9 diamonds containing 20 pyropes, 2 diopsides, 1 forsterite and 1 rutile from the Jwaneng and Letlhakane kimberlite clusters, Botswana. A new method was developed to image diamond growth zonation using CL and analyze the crystallographic orientation of the host diamond and the inclusions with EBSD. Diamonds were cut into plates and sequentially polished to uncover the inclusions on the plate's surface, revealing inclusions at different levels in the diamond. Imaging was performed on a JEOL JXA-8530F field emission electron probe (EMP) fitted with a panchromatic JEOL CL detector at the University of Utrecht. Imaging was done with an acceleration voltage of 10 kV and a beam current of 5pA. CL imaging at different depths was performed in order to produce a 3D view of diamond growth zones around the inclusions. Standard diamond polishing techniques proved too aggressive for silicate inclusions as they were damaged to such a degree that EBSD measurements on the inclusions were impossible. The inclusions were milled with a Ga⁺ focused ion beam (FIB) at a 12° angle to clean the surface for EBSD measurements. Crystallographic orientations of diamond and the inclusions were determined using EBSD using a Helios Nanolab G3 UC. Compositions of extracted inclusions were initially determined on unpolished samples following

the techniques of Timmerman et al. (2015) using EMP. Subsequently, inclusions were mounted in epoxy and polished to obtain core to rim compositional traverses.

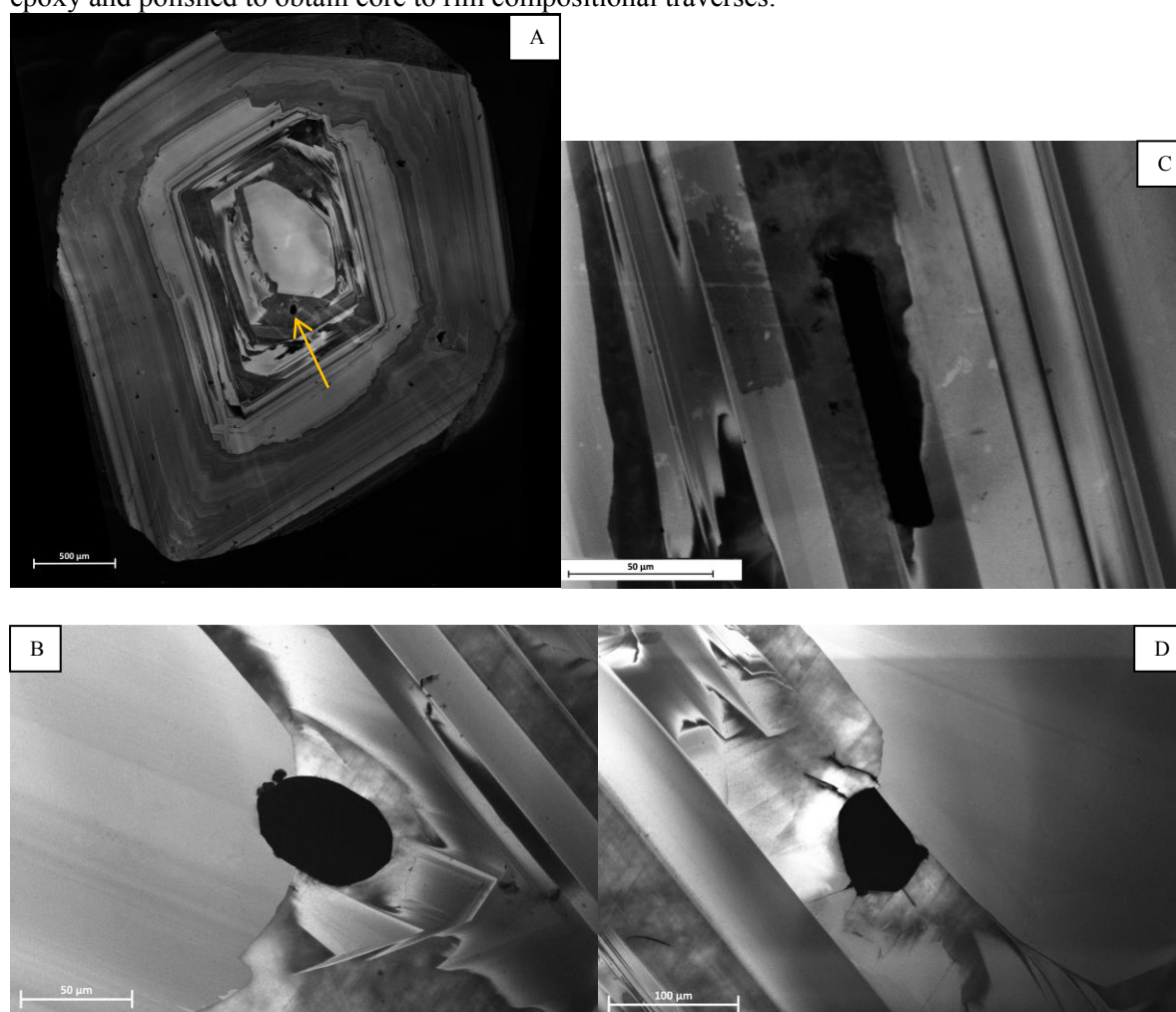


Figure 1: CL images of a central diamond plate of JW 203. **A:** Composite CL image of showing complex growth and resorption history. The core shows cubo-octahedral growth followed by a shift to a more octahedral growth. Orange arrow indicates position of an isolated garnet inclusion. **B:** close up of image A after further polishing. At greater depth the isolated garnet inclusions in image A is seen to be partly within the central core. **C:** Garnet inclusion parallel to diamond growth zones. **D:** garnet with straight face in the NE corner that nucleated on a diamond resorption surface.

Discussion

Of the 26 inclusions, 9 have an imposed cubo-octahedral morphology. Of these inclusions, 6 have faces orientated parallel to diamond growth zones (Fig. 1c) and/or appear to have nucleated on a diamond growth surface, implying syngensis (Fig. 1d). In contrast other diamonds record resorption such that inclusions now cut through diamond growth zones making the inclusion protogenetic to later growth (Fig. 1c). In most cases, diamond growth around inclusions is not well defined due to CL haloes (Fig. 2B). A detailed TEM crystallographic and compositional study has been conducted on a transect away from an inclusion to better understand the mechanisms that control formation of the CL halo. Some inclusions cut diamond growth, suggesting syngensis (Fig 2a & B).

Combined EBSD and CL data reveal that there is no direct correlation between the crystal orientation of silicate inclusions and the host diamond (i.e., no epitaxial growth), even when the mineral phases are of the same symmetry group.

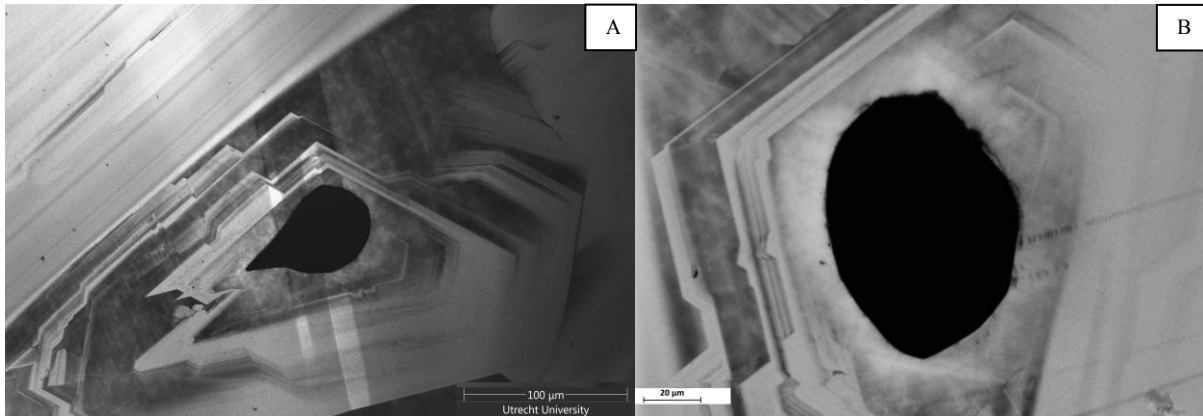


Figure 2: CL images of a central plates of JW 012. **A:** garnet inclusion with a shape controlled by diamond growth zones. Lighter grey tracks are areas of FIB milling. **B:** clinopyroxene partly surrounded by CL halo.

EBSD analyses on the diamonds themselves showed no angular deviations despite having multiple growth and resorption zones, implying epitaxial growth of diamond. In contrast no consistent epitaxial relationships were found between diamond and the 26 inclusions (1 crystallographic plane of a clinopyroxene was found parallel to $\{112\}$ of the host diamond).

EBSD analysis of two different diamonds with inclusion clusters in different growth zones, $\sim 400 \mu\text{m}$ apart, revealed the same chemical composition and orientation for 3 inclusions, potentially implying they originated from a common larger inclusion that is protogenetic in relation to the later grown diamond.

In summary, the relationships between silicate inclusions and their host diamond reveal a multi-stage growth history of diamond such that individual inclusions in a single diamond may show both syngenetic and protogenetic relationships to the growth zone in which they are trapped.

References

- Agrosi, G., Nestola, F., Tempesta, G., Bruno, M., Scandale, E., & Harris, J. (2016). X-ray topographic study of a diamond from Udachnaya: Implications for the genetic nature of inclusions. *Lithos*, 248-251, 153–159.
- Harris, J. W. & Gurney, J. J. (1979). Inclusions in diamond. In ed J.E. Field. *The Properties of Diamond*, 555-591, Academic Press.
- Nestola, F., Jung, H. & Taylor, L. A. (2017). Mineral inclusions in diamonds may be synchronous but not syngenetic. *Nature Communications* **8**, 14168.
- Nestola, F., Nimis, P., Angel, R. J., Milani, S., Bruno, M., Prencipe, M., & Harris, J. W. (2014). Olivine with diamond-imposed morphology included in diamonds. Syngeneses or protogeneses?, *Int. Geol. Rev.* **56**, 1658-1667.
- Timmerman, S. Matveev, S., Gress, M.U. & Davies, G.R. (2015). A methodology for wavelength dispersive electron probe microanalysis of unpolished silicate minerals. *Journal of Geochemical Exploration* 159, 243-251.
- Wiggers de Vries, D. F., Drury, M. R., de Winter, D. A. M., Bulanova, G. P., Pearson, D. G., & Davies, G. R. (2010). Three-dimensional cathodoluminescence imaging and electron backscatter diffraction: tools for studying the genetic nature of diamond inclusions. *Contributions to Mineralogy and Petrology*, 161, 565–579.



Robust New Statistical Approaches to the Discrimination of Mantle- and Crust-derived Low-Cr garnets using Major and Trace Element Data

Matthew F. Hardman¹, D. Graham Pearson¹, Thomas Stachel¹ and Russell J. Sweeney²

¹University of Alberta, Edmonton, Canada, mhardman@ualberta.ca, gdpearso@ualberta.ca, tstachel@ualberta.ca

²RJ Sweeney Consulting, Eastbourne, United Kingdom, russelljsweeney@gmail.com

Introduction

Diamond exploration focuses on geochemical analysis of indicator minerals that are much more abundant than diamond itself. While exploration practices using peridotitic xenocrysts are robust and widely-used, similar methodologies are underdeveloped for eclogitic indicator minerals. Low-Cr garnets from mantle eclogites overlap compositionally with those of many lower-crustal lithologies transported by kimberlite. Misclassification of such crustal garnets may create “false positive” mantle signatures, possibly leading to a misdirection of exploration effort.

Dataset

We have produced new major and trace element geochemical data for paired garnet and clinopyroxene from 564 kimberlite-hosted, crust- and mantle-derived samples from cratons worldwide. Sample character was determined based on xenolith petrography: crustal samples are plagioclase-bearing and primarily garnet-granulites while mantle samples are a mixture of eclogite and pyroxenite. Garnets contain < 1.00 wt. % Cr₂O₃ in all instances. Trace elements were analyzed by sector-field laser ablation inductively-coupled plasma mass spectrometry (LA-ICP-MS) and include Sr, Zr, Y, Nb, Ba, Hf and the REE (rare earth elements). The combined major and trace element data set allows us to compare error rates between new trace element-based and existing major element-based schemes, and derive new combined major- and trace-element-based schemes.

Background

The garnet classification scheme of Schulze (2003), utilizing Mg# and Ca#, was designed to separate garnets of crustal and mantle origin. Our new dataset reveals, however, that some 66 % of cratonic garnet-granulites misclassify as mantle-derived in this classification scheme. This is problematic for locations where garnet-granulite-derived and other low-Cr crustal garnets are abundant. Hardman et al. (submitted) present new garnet major element-based graphical and statistical schemes and evaluate the usefulness of logistic regression and linear discriminant analysis in detail. They demonstrate how these methods may be applied to exploration datasets from different environments to yield the lowest classification error rate. These new major-element-based methods involve the minor elements Na and/or Ti, thereby placing more stringent requirements on the quality of garnet analyses (i.e., increased accuracy in classification comes at an analytical cost). While error rates can be substantially reduced in these new schemes, some garnets remain indistinguishable, a result in keeping with the findings of Krippner et al. (2014).

The behaviour and exchange of trace elements in garnet (including REE) may differ from that of the major elements. For instance, a temperature and pressure dependency for REE and Y exchange between garnet and omphacite has been proposed (Sun and Liang 2015). As such, trace elements may add an additional dimension to constraining the origin or source lithology of garnets. To-date, no substantial studies have been carried-out into crust versus mantle discrimination using trace elements in garnet. This study aims to evaluate the potential of trace elements, in concert with major elements, to enhance garnet source rock discrimination.

Results and Discussion

Median chondrite-normalized ($_N$) REE patterns (\pm one median absolute deviation) for crust and mantle garnets (Figure 1) are parallel for the MREE $_N$ -HREE $_N$ (Sm to Lu), with crustal garnets having up to $> 5\times$ higher concentrations. The median pattern for crustal garnets also is much steeper in the LREE $_N$ (La to Nd; Figure 1), with slightly lower median concentrations of La and Ce compared to mantle garnets. The shallower LREE $_N$ slope of mantle garnets likely reflects mantle metasomatism and is a potential first-order discriminant of mantle versus crustal origin. The lower La and Ce abundances in crustal garnets may be a response to the frequent occurrence of LREE-enriched accessory phases in crustal rocks.

A much decreased resolving power becomes apparent upon inspection of the full suite of individual REE $_N$ patterns. A bivariate plot comparing LREE $_N$ slope (Sm_N/Ce_N) and HREE abundance (Yb_N) for the full suite of garnets reveals a significant population overlap (Figure 2).

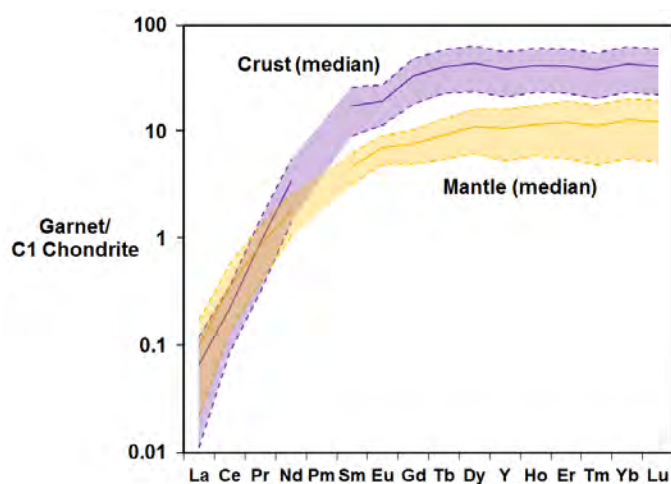


Figure 1: C1 chondrite (McDonough and Sun 1995) normalized REE abundances in low-Cr garnets. Solid lines indicate median concentrations for crust (purple) and mantle (yellow) garnets. Envelopes correspond to one median absolute deviation (MAD). Pm was not analyzed. Y is included with the MREE based on its matching ionic radius and charge.

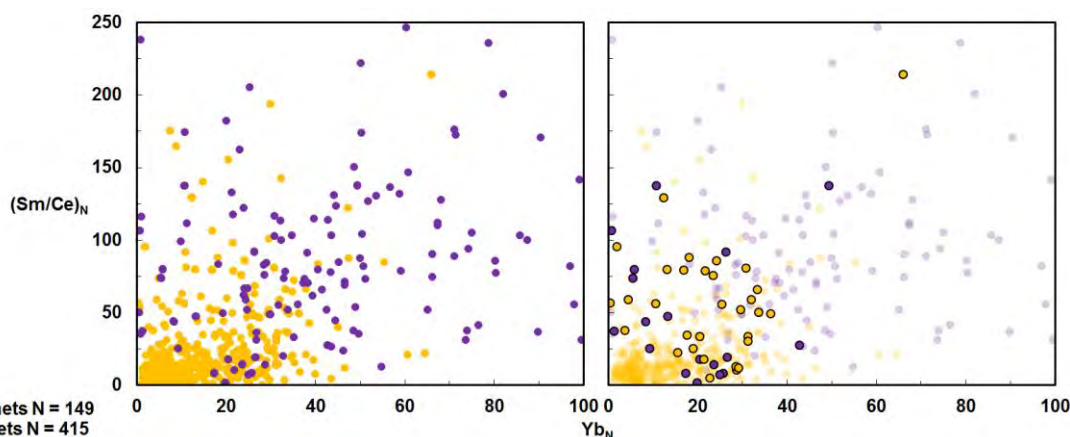


Figure 2: Bivariate plot of Sm_N/Ce_N versus Yb_N , representing LREE $_N$ slope and HREE $_N$ abundance. To better investigate problematic samples, the more solid-coloured yellow and purple points in the rightmost plot are those which misclassify using the Hardman et al. (submitted) graphical method.

To more closely investigate the nature of samples that misclassify using major elements schemes, the compiled trace element dataset ($N = 564$) is tested against the Schulze (2003) Ca# versus Mg# method and the Hardman et al. (submitted) $\ln \frac{\text{Mg}}{\text{Fe}^*\text{Si}}$ versus $\ln \frac{\text{Ti}}{\text{Si}}$ graphical method. The Schulze (2003) method results in a 17.1 % classification error, while the Hardman et al. (submitted) graphical method results

in only a 9.4 % classification error. Samples that misclassify using the Hardman et al. (submitted) graphical method are highlighted in the rightmost plot in Figure 2. It is observed that in almost all cases their LREE_N slopes and HREE_N abundances are transitional between crustal and mantle garnets (i.e. employing REE cannot significantly improve the resolving power of major element based classification schemes).

Other trace element discriminators being explored are Zr and Y, which both appear to be systematically more enriched in crustal versus mantle garnets. Discriminants using these elements combined with REE ratios will be explored using linear discriminant analysis and logistic regression techniques.

Conclusions

It is clear that any low-Cr garnet classification schemes must be trained and tested with databases containing cratonic garnet-granulite compositions, which provide the toughest discrimination challenge. As a result of expanding training datasets to include such garnets, the multivariate major-element statistics-based classification schemes proposed by Hardman et al. (submitted) are the most robust schemes to date. Here we attempted to improve the discrimination power of these approaches by adding trace elements to the mix of elements. While clear differences exist in the median REE_N patterns of crust and mantle garnets (different slopes in LREE_N and distinctly different HREE_N abundances), examination of the full sample suite shows that discrimination of many garnets is not possible using REE alone. Samples which misclassify using advanced major element based techniques typically also have REE_N patterns that are inconsistent with the median pattern (\pm one median absolute deviation) of their population (crust or mantle). We are currently evaluating other trace elements (including Zr) for their potential to enhance the resolving power of REE-based classifications. However, based on our preliminary results for REE, the usefulness of trace elements as a discriminatory tool likely does not justify the increased time and cost associated with their analysis. Major element-based multivariate approaches, such as linear discriminant analysis and/or logistic regression, using robust data normalization procedures appear to be the most efficient and successful way forward in mantle versus crust garnet classification.

References

- Hardman MF, Pearson DG, Stachel T, Sweeney RJ. Statistical approaches to the discrimination of crust- and mantle-derived low-Cr garnet – major-element-based methods and their application in diamond exploration. Submitted to Journal of Geochemical Exploration
- Krippner A, Meinhold G, Morton AC, von Eynatten H (2014) Evaluation of garnet discrimination diagrams using geochemical data of garnets derived from various host rocks. *Sedimentary Geology* 306: 36-52
- McDonough WF, Sun S-s (1995) The composition of the Earth. *Chemical Geology* 120: 223-253
- Schulze DJ (2003) A classification scheme for mantle-derived garnets in kimberlite: a tool for investigating the mantle and exploring for diamonds. *Lithos* 71: 195-213
- Sun C, Liang Y (2015) A REE-in-garnet-clinopyroxene thermobarometer for eclogites, granulites and garnet peridotites. *Chemical Geology* 393-394: 79-92



Microbial response to the presence of buried kimberlite pipes in the Attawapiskat region, northern Ontario; Bacteria-kimberlite interactions

Laura Donkervoort¹ Stewart Hamilton² Dale Sutherland³ and Gordon Southam⁴

¹ *The University of Western Ontario, London, Canada, ldonkervoort@srk.com*

² *Ontario Geological Survey, Sudbury, Canada, stew.hamilton@ontario.ca*

³ *Activation Laboratories Ltd., Ancaster, Canada, dalesutherland@actlabsint.com*

⁴ *The University of Queensland, St. Lucia, Australia, g.southam@uq.edu.au*

Introduction

Bacteria are active in surface and near surface environments and are the dominant group of organisms in the subsurface (Stevens and McKinley 1995; Stevens et al. 1993). In both environments they are important catalysts of geochemical reactions where they can play a significant role in altering the permeability of geologic systems by dissolving and precipitating minerals, thus controlling fluid flow (Southam and Saunders 2005). The bacterial communities that can generate the most energy under a particular set of geochemical conditions will be enriched and will in turn alter their geochemical environment. Kimberlite exploration has traditionally involved the use of indicator minerals and geophysics. However, geochemical conditions ‘produced’ by kimberlite-water interactions have been identified as a potential tool in diamond exploration (Hattori and Hamilton 2008 refs). In these systems, bacteria-water-rock interactions (Wanger et al 2008) can enhance mineral weathering contributing to this geochemical signal.

Analytical Results

Jurassic kimberlites in the Attawapiskat region of the James Bay Lowlands, Canada, are intruded into Paleozoic carbonate rocks and covered by Holocene marine silts and extensive peat. These buried kimberlite pipes ‘produce’ geochemical conditions, e.g., increased pH and decreased Eh, in overlying peat (Sadler et al 2011) that have selected for bacterial populations that are best able to grow and, which, in turn affect the geochemistry, producing a linked biogeochemical signal. The dispersion halo is characterized by abiotic-inorganic (Sadler et al 2011) & organic markers and biotic, biogeochemical markers that are shown to complement the aqueous geochemical indicators of buried kimberlites i.e., increased pH and decreased Eh, in near surface samples of peat.

A microbiological study of peat conducted over the Zulu kimberlite located in the Attawapiskat area demonstrated that limestone and sub-cropping kimberlite influenced the diversity and populations of microorganisms living in the overlying peat. Results of bacterial enumeration combined with biodiversity analysis demonstrate increased anaerobic populations and lower biodiversity directly above the kimberlite pipe, suggesting that the release of geochemical nutrients via water kimberlite interactions have selected for a subset of the overall bacterial population. Overall, the bacterial counts were higher across the Zulu transect when compared the control transect (Figure 1). The aerobic heterotrophs show a pattern of greater populations corresponding to the kimberlite edges, similar to the classic, ‘rabbit ear’ or edge effect pattern identified in the complementary, geochemical survey (Sadler et al., 2011). In contrast, the anaerobic heterotrophs revealed a pattern of greater populations in samples directly overlying the kimberlite body. Ratioing anaerobes:aerobes, in order to account for heterogeneity of the substrate and variations in nutrient availability demonstrated an enrichment in anaerobic bacteria directly over the kimberlite as an apical pattern. Spatiotemporal Geochemical Hydrocarbons (Actlabs, SGH) demonstrated that the Zulu kimberlite was found to possess a wide range of high molecular weight organic compounds that intuitively, influenced the diversity and populations of the heterotrophic microorganisms living in the overlying peat. The observed SGH “halo” anomaly likely represents a strong REDOX cell, consistent with the methane production described by Sader et al. (2013).

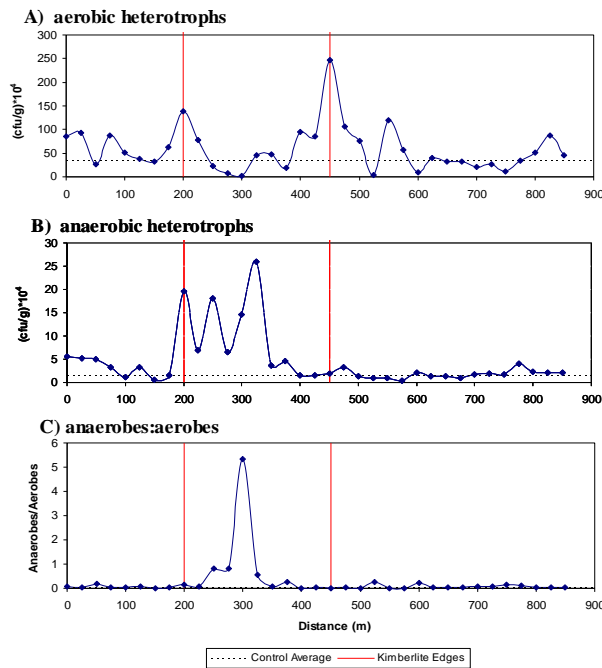


Figure 1 - Viable heterotrophic spread plate counts (cfu/g), cultured from peat collected along the Zulu transect. (A) aerobic heterotrophs; (B) anaerobic heterotrophs; (C) ratio of anaerobic:aerobic heterotrophs. The dotted line indicates the average control population.

Using anaerobic microcosm experiments designed to replicate field conditions, and imaging with scanning electron microscopy, the Zulu kimberlite was shown to support significant bacterial growth. A sample of kimberlite collected from the Zulu occurrence was capable of supporting a lithotrophic (rock-eating) community of microorganisms (Figures 2 and 3). These natural, kimberlite associated bacteria, grew in a sterile distilled water-kimberlite system, demonstrating that the bacteria directly interacted with kimberlite and that kimberlite contains all of the essential nutrients required to support the growth of bacteria. After 2 months incubation, bacteria had colonized the entire surface of the kimberlite producing an evenly distributed bacterial population of 3.2×10^5 bacteria/cm² plus larger bacterial microcolonies highlighting active growth on select mineral substrates (Figure 2, inset).

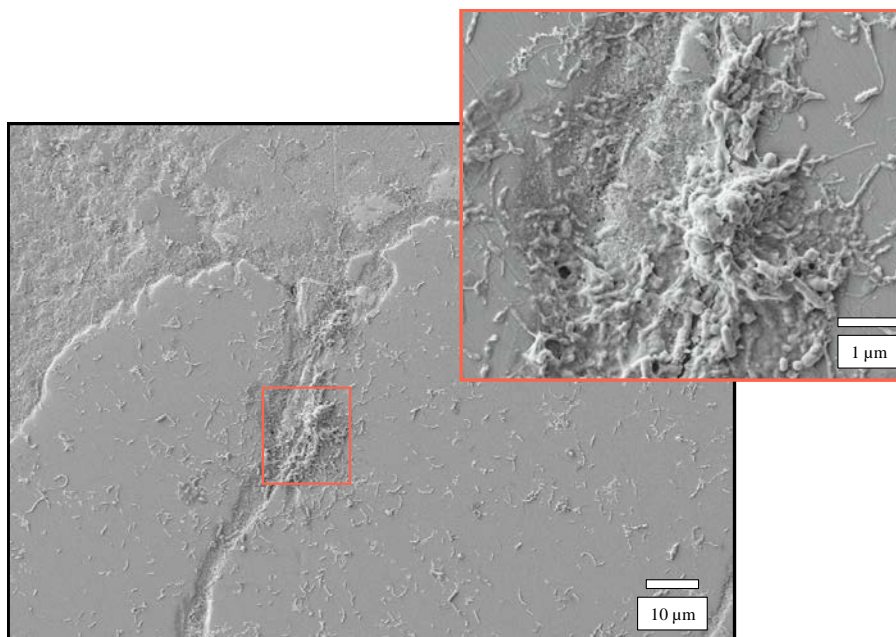


Figure 2 - SEM micrographs showing colonization/growth patterns and population density after 2 months; highlighting the bacterial monolayer and a microcolony (inset).

High resolution scanning electron microscopy revealed that growth occurred via the development of complex biofilms consisting of a network of pilus-like appendages that connect cells to one another and to the kimberlite surface. These structures provide enhanced attachment to solid reactants in this system, thereby overcoming the spatial barrier created during secondary mineral precipitation and may act as catalysts for low-temperature serpentinization via these putative nanowires, pulling electrons directly from the kimberlite (olivine) surface (compare reactions 1 and 2).

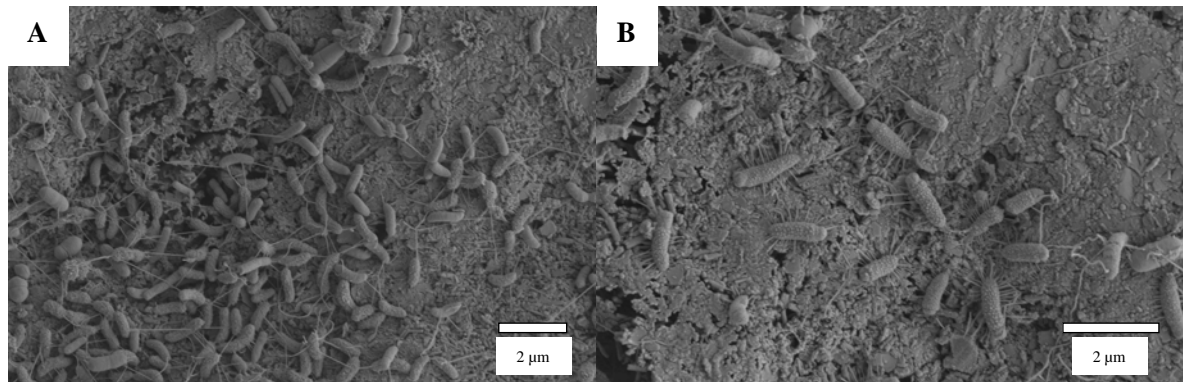
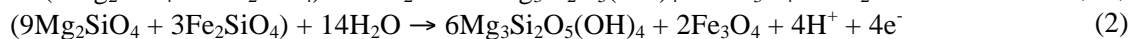
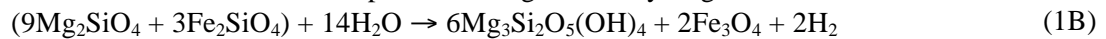
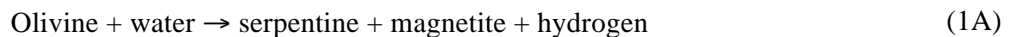


Figure 3 - (A) pilus-like appendages connect cells within the biofilm grown on the kimberlite surface (B) close up image showing a network of cell-cell and extensive cell-mineral connections.



Kimberlite provides all of the nutrients necessary to support the growth of bacteria, enhancing kimberlite dissolution. Growth of these bacteria contributed to a weathering front extending up to 100 µm into the kimberlite matrix demonstrating that kimberlite can be weathered *in situ* with the aid of bacteria.

References

- Hattori K, Hamilton SM (2008) Geochemistry of peat over kimberlites in the Attawapiskat area, James Bay Lowlands, northern Canada. *Appl Geochem* 23:3767-3782.
- Sader JA, Hattori KH, Kong JM, Hamilton SM, Brauneder K (2011) Geochemical responses in peat groundwater over Attawapiskat kimberlites, James Bay Lowlands, Canada and their application to diamond exploration. *Geochem: Explor Environ Anal* 11:193-210.
- Sader JA, Hattori KH, Brauneder K, Hamilton SM (2013) The influence of buried kimberlite on methane production in overlying sediment, Attawapiskat region, James Bay Lowlands, Ontario. *Chem Geol* 360–361:173-185.
- Southam G, Saunders JA (2005) The geomicrobiology of ore deposits. *Econ Geol* 100:1067-1084.
- Stevens TO, McKinley JP (1995) Lithoautotrophic microbial ecosystems in deep basalt aquifers. *Science* 270:450-454.
- Stevens TO, McKinley JP, Fredrickson JK (1993) Bacteria associated with deep, alkaline, anaerobic groundwaters in southeast Washington. *Micro Ecol* 25:35-50.
- Wanger G, Onstott TC, Southam G (2008) Stars of the terrestrial deep subsurface: A novel ‘star-shaped’ bacterial morphotype from a South African platinum mine. *Geobiol* 6:325-330.



The genesis and evolution of subcontinental lithospheric mantle beneath Botswana and N. South Africa.

G.R. Davies^a, Q. van der Meer^b, M. Klaver^c, A.M. Borst^d, B. Davidheiser^e, T.J. Meulemans^f, S. de Jong^g, C.S. Nooitgedacht^h, C.M. de Heijⁱ

^a Vrije Universiteit, De Boelelaan 1085, 1081 HV Amsterdam, The Netherlands, g.r.davies@vu.nl;

^bqvandermeer@gmail.com; ^cmartijn.klaver@bristol.ac.uk; ^damb43@st-andrews.ac.uk;

^eBrett.Davidheiserkroll@colorado.edu; ^ftmeulem@gmail.com; ^gsharon90_8@hotmail.com;

^hcas_nooitgedacht@outlook.com; ⁱcarlijndeheij@gmail.com.

Introduction

The processes that led to the formation and stabilisation of sub continental lithospheric mantle (SCLM) remain a matter of debate (e.g., Pearson & Wittig, 2014; Aulbach et al., 2017). Resolving this question is required to determine how the SCLM is subsequently modified over time and to establish possible links between specific events within the mantle and diamond formation. This project reports on a project designed to obtain an integrated view of the SCLM beneath the north-west portion of the Kalahari Craton. The region was chosen specifically to assess the effects of amalgamation of the Kaapvaal and Zimbabwe Cratons and the subsequent formation of the Mesopalaeproterozoic Magondi-Gweta and Choma-Kaloma Terranes. Over the last decade peridotite xenoliths have been sampled from open pits and drill cores from the Jwaneng, Orapa and Letlhakane (Botswana ~92 Ma) and Venetia (Limpopo Mobile Belt, northern South Africa ~530 Ma) diamond mines with the aim of determining the timing and processes responsible for the formation and subsequent modification of the SCLM. Samples were subjected to detailed petrological studies and selected samples to whole rock major and trace element and Re-Os isotope analysis and mineral major and trace element and coupled Sr-Nd-Hf isotope analysis.

Results & Discussion

Lithological abundances were quantified from the observation of 400 to > 1000 xenoliths at each location. Garnet lherzolite (clinopyroxene visible in hand specimen) dominate all assemblages with variable abundance of harzburgites and dunites (10-20%) and subordinate amounts of pyroxenites-websterites (<10%) and metasomites dominantly formed of amphibole and/or phlogopite (<5%). With the notable exception of Letlhakane, the preservation state of xenoliths recovered from open pits is poor with olivine only locally preserved. It is, however, possible to determine the original modal mineralogy. Xenoliths recovered from drill cores from up to 1200 m below the surface generally have much better preservation such that mineral zonation can be evaluated by electron microprobe.

As reported from elsewhere in the Kalahari Craton, high temperature harzburgites and lherzolites ($T > 1150^{\circ}\text{C}$), are usually deformed and have olivine with forsterite contents (Fo) between 88-92. In contrast low temperature garnet harzburgites/lherzolites ($T < 1150^{\circ}\text{C}$), have Fo between 92-93.5. Based on olivine abundance and composition the majority of the SCLM appears to have undergone extensive melt depletion: 30-50%. The xenolith suites from the different mines record different degrees of Si/orthopyroxene enrichment with for example Letlhakane having up to 40% orthopyroxene (Fig. 1). There are, however, significant regional variations recorded in the degree of Si-enrichment but as yet no consistent variation with depth among the low temperature peridotites.

Calculated whole rock trace element contents of low temperature peridotites, such as low HREE, coupled with the high Fo olivine imply the low temperature harzburgites/lherzolites originated as residua formed by up to 50% predominantly in the absence of garnet. This conclusion contrasts with

the widespread occurrence of clinopyroxene +/- amphibole and/or phlogopite, phases that record trace element enrichment. The majority of the clinopyroxene, amphibole and phlogopite in the garnet lherzolites is not in trace element and Nd-Hf isotope equilibrium with coexisting garnet implying metasomatic addition shortly before eruption of the host kimberlite with coupled Nd-Hf isotope ratios implying the involvement of metasomatic melts comparable to the host kimberlites. The exception to this observation are websterites and wehrlites that have coupled Nd-Hf isotope systematics indicating formation in the Proterozoic. The majority of the low temperature peridotites with petrographic evidence of significant clinopyroxene, amphibole and phlogopite addition have a within plate signature trace element signature (e.g., low La/Nb, Th/Nb) associated with clinopyroxene addition. Harzburgitic samples, in contrast, locally preserve a clear subduction related metasomatic signature (e.g., high La/Nb, Th/Nb).

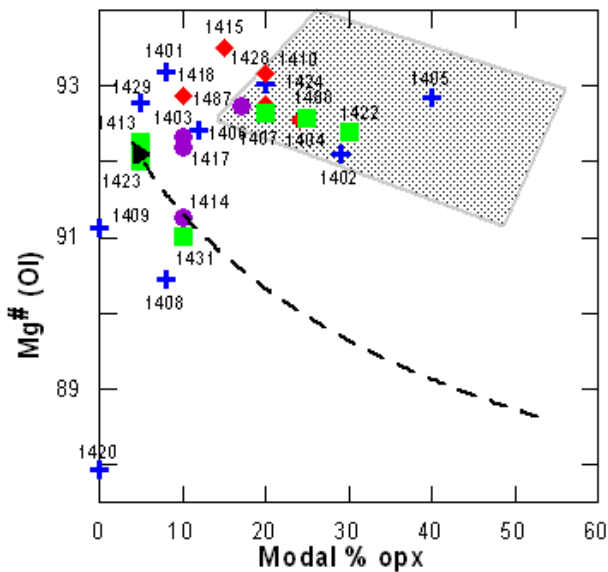


Figure 1: Olivine Mg# versus modal orthopyroxene content for Letlhakane samples. Black arrow is oceanic melting trend; grey field represents typical Kaapvaal xenoliths assuming 100 % olivine and opx assemblages (Boyd, 1989). SiO₂ enrichment leads to orthopyroxene addition, i.e. points move to the right of the oceanic melting trend. Blue cross: garnet free peridotites, Red diamond: garnet harzburgites, Green square: garnet lherzolites, Purple circle; amphibole garnet lherzolites.

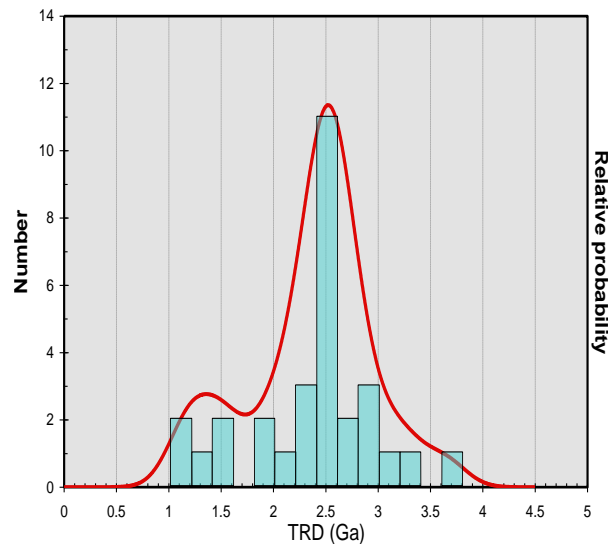


Figure 2: Relative probability plots for rhenium depletion ages of all analysed samples, including Carlson, 1999 (n=30). An error of 0.2 Ga is used for calculation of the Gaussian probability curve for all rhenium depletion ages.

Os isotope whole rock data were performed on samples across the region. Rhenium depletion ages range from 1 to 3 Ga with the majority in the region of 2.5-2.7 Ga implying major melt depletion of the peridotitic precursors associated with stabilisation/amalgamation of the craton and Limpopo Belt formation. A finding comparable to previously reported data (e.g., Irvine et al. 2001; Luguet et al., 2015). Major differences between mantle depletion and Re depletion ages, however, imply that many samples have undergone significant redistribution of Re and/or Os. This process is best illustrated in the 530 Ma Venetian suite, which is characterised by significant Si-enrichment. Samples without petrographic and geochemical evidence of clinopyroxene addition immediately prior kimberlite eruption record a coherent isochronous relationship that defines an age of 3.28 ± 0.17 Ga, an age indistinguishable from the mantle depletion ages of the samples but significantly older than T_{RD} ages (van der Meer et al. in press; Fig. 2). Samples defining the “isochron” are derived from ~50 to ~170 km depth, suggesting coeval melt depletion of the majority of the Venetia lithospheric mantle column. Remaining samples have elevated Re/Os due to Re addition during kimberlite magmatism but have otherwise undergone a similar evolution as the samples that define the “isochron” and have

overlapping $^{187}\text{Os}/^{188}\text{Os}$ at eruption age: $^{187}\text{Os}/^{188}\text{Os}_{\text{SEA}}$. A subset of samples have low Os concentrations, unradiogenic $^{187}\text{Os}/^{188}\text{Os}_{\text{SEA}}$ and were effectively Re-free prior to kimberlite magmatism. The combination of Re-Os mobility, preservation of an isochronous relationship, place firm constraints on the formation and subsequent evolution of Venetia lithosphere. Melt depletion and remobilisation of Re and Os must have occurred within error of the 3.28 Ga mean T_{MA} age, potentially related to Si-enrichment. Perhaps most importantly, the refractory peridotites contain significant Re despite recording >40 % melt extraction suggesting that melting does not remove all Re from peridotites and that T_{RD} ages can significantly underestimate the time of melt depletion. The overlap of the ~2.6 Ga T_{RD} ages with the time of Limpopo Orogeny is therefore interpreted as purely fortuitous and has no geological significance.

Throughout the region Nd-Hf-Sr isotope relationships recorded by minerals in the peridotites are highly variable. Harzburgitic samples preserve evidence of initial Archaean depletion ($\epsilon_{\text{Hf}} > 300$) followed by metasomatism that produced LREE enrichment in the late Archaean, mid and late Proterozoic. These events were followed by widespread clinopyroxene, amphibole and phlogopite formation, in some cases associated with kimberlite related magmatism. Clinopyroxene, amphibole, phlogopite and garnet are often in, or close to, isotopic equilibrium at the time of kimberlite eruption with initial ratios that imply equilibration with the host kimberlites or related magmas. In contrast, websterites and pyroxenites record evidence of late Proterozoic formation yielding relatively coherent Hf and Os T_{MA} ages. In summary, the regional SCLM records evidence of melting/metasomatic events at ~3.2, >2.0, ~1.5 and 1.0 Ga, ages that coincide with diamond formation and can be linked to regional tectono-magmatic events (Richardson et al 2004; Koornneef et al., 2016; Timmerman et al. 2017).

References

- Aulbach, S., Massuyeau, M., Gaillard, F. (2017). Origins of cratonic mantle discontinuities: A view from petrology, geochemistry and thermodynamic models. *Lithos* 268–271, 364–382.
- Boyd, F.R., 1989. Compositional distinction between oceanic and cratonic lithosphere. *Earth and Planetary Science Letters*, 96(1-2): 15-26.
- Carlson, R., Pearson, D., Boyd, F., Shirey, S., Irvine, G., Menzies, A. and Gurney, J. (1999) Re–Os systematics of lithospheric peridotites: implications for lithosphere formation and preservation, *The JB Dawson Volume—Proceedings of the Seventh International Kimberlite Conference*, Cape Town. Red Roof Design, Cape Town, pp. 99-108.
- Irvine, G.J., Pearson, D.G. and Carlson, R.W. (2001). Lithospheric mantle evolution of the Kaapvaal Craton: A Re-Os study of peridotite xenoliths from Lesotho Kimberlites. *Geophysical Research Letters*, 28(13): 2505-2508.
- Koornneef, J., Gress, M.U., Harris, J.W. Davies, G.R. (2016). Archaean diamond growth beneath Venetia established by Sm-Nd systematics of individual garnet inclusions. *Goldschmidt abstract* 1588.
- Luget, A., Behrens, M., Pearson, D.G., Stephan König, S., Herwartz, D. (2015). Significance of the whole rock Re–Os ages in cryptically and modally metasomatised cratonic peridotites: Constraints from HSE–Se–Te systematics. *Geochimica et Cosmochimica Acta*, 164, 441–463.
- Timmerman, S., Koornneef, J.M., Chinn, I.L., Davies, G.R. (2017). Dated diamond growth zones reveal variable recycling of crustal carbon through time. *Earth and Planetary Science Letters*, 463, 178-188.
- Pearson, D. G., & Wittig, N. (2014). The Formation and Evolution of Cratonic Mantle Lithosphere—Evidence from Mantle Xenoliths. In *Treatise on Geochemistry* (eds. H. D. Holland and K. K. Turekian). Elsevier, p. 255–292.
- Richardson, S.H., Shirey, S.B., Harris, J.W., 2004. Episodic diamond genesis at Jwaneng, Botswana, and implications for Kaapvaal craton evolution. *Lithos* 77, 143-154.
- van der Meer, Q.H.A., Klaver, M., Reisberg, L., Riches, A.J.V., Davies, G.R. (2017). Preservation of an Archaean whole rock Re-Os isochron for the Venetia lithospheric mantle: evidence for rapid crustal recycling and lithosphere stabilisation at 3.3 Ga. *Geochimica Cosmochimica Acta*. Proof stage.

Melt evolution of the Finsch orangeite, South Africa

Henrietta Farr¹, Andrea Giuliani^{1,2} and David Phillips¹

¹ *KiDs (Kimberlites and Diamonds), School of Earth Sciences, The University of Melbourne, Australia*

² *ARC Centre of Excellence for Core to Crust Fluid Systems and GEMOC, Department of Earth and Planetary Sciences, Macquarie University, Australia*

Introduction

The Finsch diatreme is a diamondiferous orangeite with eight mapped units F1 – F8 (Fig. 1) ranging from diatreme facies volcanoclastic to hypabyssal intrusions. The F5 and F6 varieties occur as part of a precursor pipe termed the “southwest precursor” (SWPC), which is considered to have been emplaced just below the surface. The nature of the SWPC and its relationship to the main pipe remain enigmatic. Evolutionary trends in orangeites have previously been linked to variations in the abundance of olivine macrocrysts, a trend which also appears to influence the diamond grade in kimberlites. Point counting previously done by Fraser & Hawkesworth (1992) indicated that the F5/6 units have up to twice the volume of macrocrystal olivine compared with F2/4; however, this does not take into account the proportion of magmatic and xenocrystic olivine.

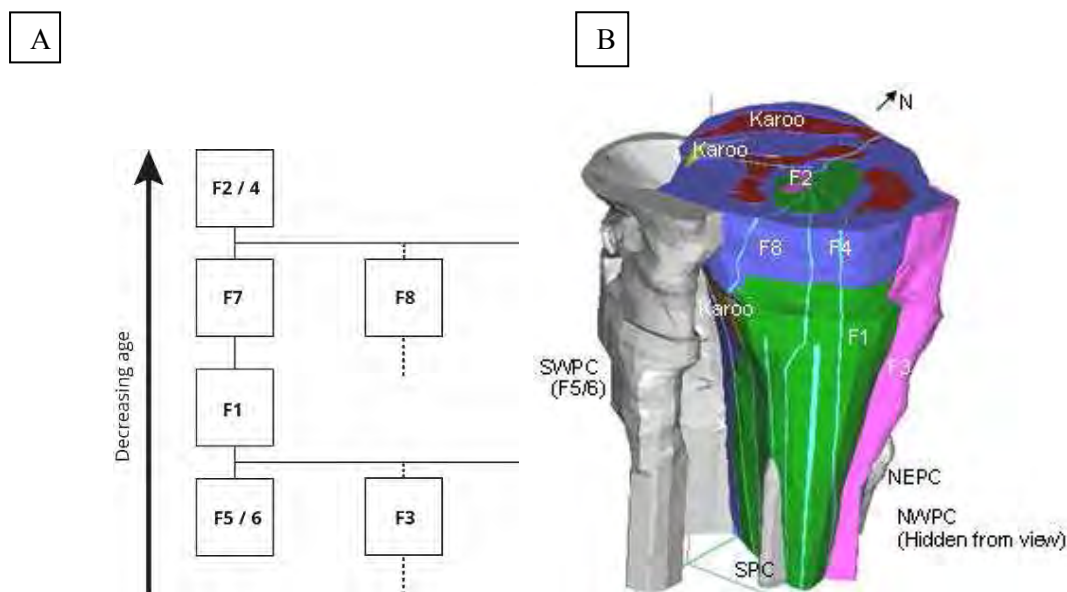


Figure 1: A) Proposed emplacement order of units in the Finsch diatreme modified from Clement 1982 and Fraser & Hawkesworth 1992. B) 3-dimensional model from Rowlands 2008.

Samples from the F2, F6 and F8 units were examined for this study with F2 and F8 representing the “main pipe” and F6 the precursor. Additionally, as F2 occurs in the middle of the main pipe with late stage dykes radiating from this unit, it is thought that F2 represents the final stage of formation of the Finsch diatreme. F6 and F2 represent the earliest and latest significant magmatic activity at Finsch, respectively.

Petrography

Samples from the F2 (main pipe) and F6 units (SWPC) are both coherent orangeites. The mineralogy of F2 samples is dominated by phlogopite, olivine and diopside, whereas the F6 samples contain no diopside but abundant serpentine and carbonates and display a prominent segregatory texture.

Compositionally distinct olivine populations occur in the two units. Samples from F6 contain significant amounts of magmatic olivine as overgrowths (up to 200 μm thick) on xenocrystic cores, with rare grains composed of >50% magmatic rim by volume. Olivine is commonly partially serpentinised with uncommon carbonate replacement for more altered grains. Mica from the F6 samples is extremely fine-grained and shows little Al depletion and Fe enrichment towards the rim. The F2 samples contain abundant, partially resorbed but otherwise unaltered xenocrystic olivine in direct contact with the predominantly phlogopite, diopside groundmass. Phlogopite in F2 samples is zoned, exhibiting extreme FeO_{tot} enrichment (up to 25 wt%) towards pure tetraferriphlogopite in the rims.

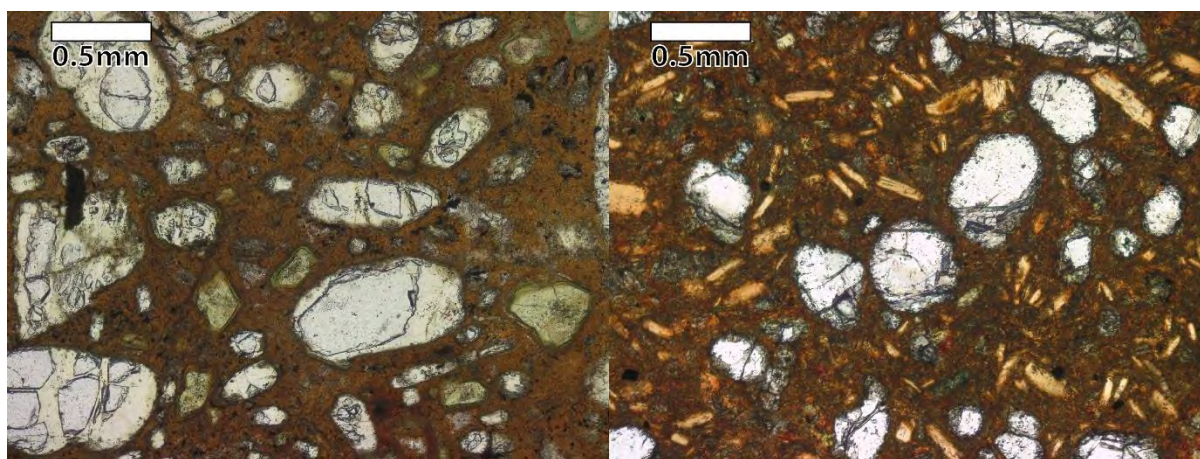


Figure 2: Photomicrographs of F6 (left) and F2 (right)

Discussion

The F5/6 precursor kimberlite has been generally interpreted as being hypabyssal in nature, however, more detailed analysis of the textures present suggests that these more coherent samples resulted from agglutination and sintering of the kimberlite upon emplacement (Rowlands 2008). This is consistent with emplacement at surface as a diatreme.

Despite the many differences in texture, the most striking difference between F6 and F2 is the lack of magmatic olivine in the latter. Although magmatic olivine in unit F2 may have been completely resorbed, it seems unlikely that it was present in similar quantities to F6 (rims up to 200 μm in thickness) if at all. Additionally, significant differences in the alteration style of the olivine suggests that the late-stage fluids may have been distinct in chemical and physical characteristics for each unit.

This new data will be compared with existing whole rock and mineral chemistry from samples from the other Finsch units to highlight broader compositional and evolutionary trends. The effects of fractional crystallisation of olivine and other minerals will be re-evaluated within the framework provided by this textural and compositional information. Possible mechanisms involved in the evolution of the magma include varying degrees of partial melting of the same source and magmatic differentiation.

References

- Clement CR (1982) A comparative geological study of some major kimberlite pipes in the Northern Cape and Orange Free State. PhD Thesis, University of Cape Town
- Fraser KJ (1987) Petrogenesis of Kimberlites from South Africa and Lamproites from Western Australia and North America. PhD Thesis, The Open University
- Fraser KJ, Hawkesworth CJ (1992) The petrogenesis of group 2 ultrapotassic kimberlites from Finsch Mine, South Africa *Lithos* 28:327-345 doi:[http://dx.doi.org/10.1016/0024-4937\(92\)90013-O](http://dx.doi.org/10.1016/0024-4937(92)90013-O)

Rowlands T (2008) Proposed Emplacement Model for the Finsch Precursor Kimberlites. Masters Thesis, University of the Witwatersrand



[Oxygen isotopes of garnets in diamondiferous eclogites from the Udachnaya pipe, Yakutia: Evidence for their origin]

[Z.V. Spetsius¹, L.A. Taylor², J.W. Valley³, M.J. Spicuzza³, W.L. Griffin⁴ and A.S. Ivanov¹]

¹*Geo-Scientific Investigation Enterprise, ALROSA PJSC, Mirny, 678170, Russia, spetsiuszv@alrosa.ru*

²*Department of Earth and Planetary Sciences, University of Tennessee, Knoxville, USA, lataylor@utk.edu*

³*Department of Geoscience, University of Wisconsin, Madison, WI 53706, USA, valley@geology.wisc.edu*

⁴*ARC Centre of Excellence (CCFS/GEMOC), Macquarie University, Australia, bill.griffin@mq.edu.au*

[Introduction]

[The Udachnaya pipe is one of the most unique primary deposits in the Siberian Platform and is characterized by a high content of diamonds and their high quality. It is the deepest open-pit mine in the world and well-known for its numerous eclogite xenoliths of different varieties (A, B & C Groups), including a wide selection of diamondiferous eclogites. At that moment from kimberlites of this pipe were recovered more than 300 xenoliths with diamonds. The relatively numerous diamondiferous eclogites from the Udachnaya have been well-characterized (e.g., Sobolev et al., 1994); however, oxygen isotope analyses of minerals from these samples are not abundant (Spetsius et al., 2009).

Mantle eclogites make up an important component in mantle xenolith suites and diamondiferous eclogites represent one of the main diamond reservoirs. Studies of eclogites are important for refining models of global crust-mantle evolution and provide constraints on the origin of diamondiferous mantle as eclogites represent significant diamond reservoirs in some portions of SCLM of Siberian Craton (e.g., Spetsius et al., 2008). Here, we present major- and trace-element data for eclogitic minerals along with oxygen-isotope data for garnets from 30 new samples and some xenoliths of old collection eclogites with diamonds.

Samples and Methods

Studied collection of 60 diamondiferous xenoliths from the Udachnaya pipe of Yakutia comprise by bimineraleclogites, rare kyanite eclogites and some corundum eclogites. Most xenoliths contain two or more diamond crystals (0.2-1.0 mm) with predominantly octahedral or transient forms (Fig. 1). The amount of diamonds in separate samples could be up to 260 crystals with the predominating of small crystals (<1.0 mm). Cubic diamonds were found in six xenoliths. The distribution of crystals in xenoliths is irregular and does not coincide with the specimen surfaces. Mineral inclusions are rare and represented by sulfides, garnet, clinopyroxene and rare rutile. Fine-grained interstitial metasomatic mineral assemblages and partial melting phases have been identified in all xenoliths; this is a characteristic specific feature of diamondiferous eclogites (Spetsius, Taylor, 2008).

Major element compositions of eclogite minerals were determined with a Superprobe JXA-8800R electron microprobe at the "ALROSA" OJS Company. Natural minerals and synthetic were used as standards. Analytical conditions included an accelerating voltage of 15 keV, a beam current of 20 nA, beam size of 5 μm , and 20 seconds counting time for all elements. All analyses underwent a full ZAF correction. The trace elements have been measured by laser Ablation ICP-MS (LAM) at the Macquarie University, with NIST 610 glass as external standard and Ca as internal standard; pit diameters were 40–50 μm .

Oxygen-isotopes were measured on the garnet separates using a laser fluorination technique at the University of Wisconsin, Madison. Prior to analysis, the samples were cleaned with isopropanol and methylene chloride to remove any contaminants. The oxygen-isotope analyses were performed on garnet mineral separates, approximately 1-2 mg per run, using a 32 W CO₂ laser, BrF₅, and a dual-inlet Finnigan MAT 251 mass spectrometer (Valley et al., 1995). All $\delta^{18}\text{O}$ values are reported with respect to V-SMOW. Over the course of oxygen-isotope analysis, standard UWG-2 gave a mean of 5.77 ± 0.14 ‰ (2 sd). Replicate analyses were performed on several samples including those that had initial oxygen-isotope values outside of the normal mantle range of 4.7-5.9 ‰.

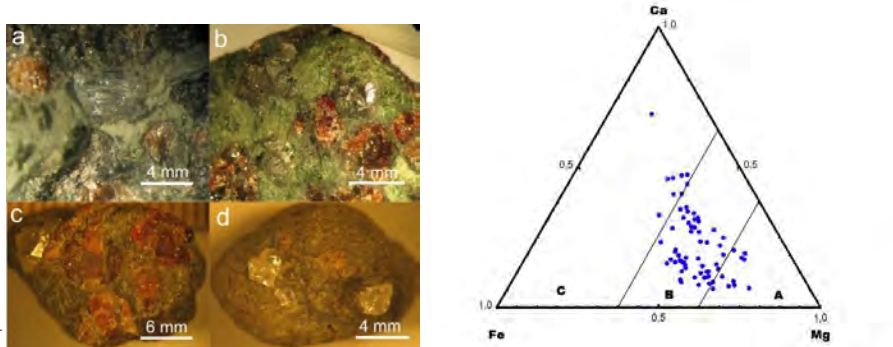


Figure 1: Diamondiferous eclogites from the Udachnaya pipe. (a - sample Ue-11 with the step-faced octahedron crystal, b - sample Ue-12 containing more than 10 octahedral crystals, c - sample Ue-28 containing octahedron with two inclusions of sulfides, d - sample Ue-33 corundum eclogite containing 6 octahedral crystals).

Figure 2: Compositions of diamondiferous eclogites garnets from the Udachnaya on Ca-Fe-Mg ternary plot.

[Analytical Results

Garnets from eclogitic xenoliths have a wide variation in Fe-, Mg- and Ca-content (Spetsius and Taylor, 2008). Studied garnets are relatively low in Cr_2O_3 (< 0.2 wt. %) and plot predominantly within the Group B eclogite field and six garnets from kyanite and corundum eclogites have occupied the field of C-group eclogites (Fig. 2). Garnets of two eclogites with corundum differ by higher Ca# (up to 17.2 wt. % CaO) and they have high Mg#. Twelve high-magnesian garnets with MgO content up to 20 wt.% answer the field of B-group eclogites. Minerals in eclogites from this study display no zonation in their chemistry; as such, the major-element compositions can be used to estimate the equilibration temperatures of these samples. Clinopyroxene-garnet thermobarometry which is based on Mg-Fe^{2+} exchange suggests equilibration at 1000–1325 °C at 4 GPa according to the thermometer of Ellis and Green (1979).

The rare earths elements (REE) and other trace elements have been obtained for the garnets and clinopyroxenes. Eclogitic garnets form obvious two different groups of TRE profiles with low and high LREE (Fig. 3). Most clinopyroxenes and some garnets in xenoliths display LREE and MREE enrichments, consistent with minor amounts of cryptic metasomatism. The presence of Eu-anomalies suggests a plagioclase-rich cumulate protolith for some eclogites. The distribution of REE for Group C and partly B eclogites overlap with typical oceanic basalts; the presences of distinct Eu anomalies suggest that their protoliths had undergone significant plagioclase fractionation/accumulation. Most clinopyroxenes and about 40% of the garnets display LREE and MREE enrichments, consistent with possible cryptic metasomatism. The lack of obvious mineral zoning preserved in these samples suggests that any cryptic metasomatism must have occurred over relatively large time scales, likely predating entrainment into the host kimberlite.

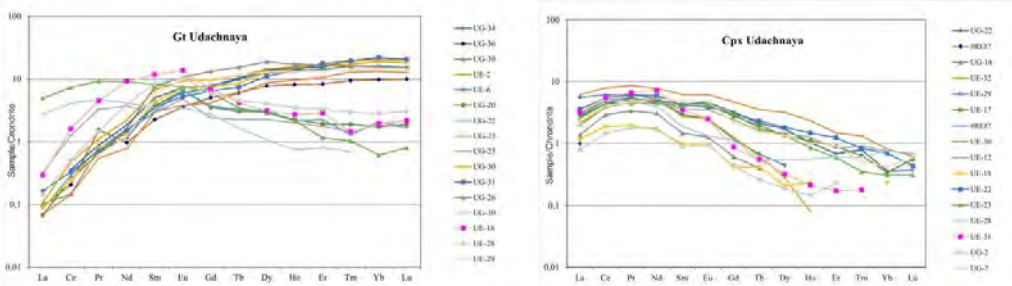


Figure 3: Chondrite-normalized REE abundances of Udachnaya eclogite garnets and clinopyroxenes. All normalization factors from McDonough and Sun (1995).

The garnet oxygen isotope data can be divided into two distinct groups of eclogites. The majority of the samples lie within the range of average mantle $\delta^{18}\text{O}$ values (5.5 ± 0.45 ‰), and remaining group ($\approx 40\%$) have $\delta^{18}\text{O}$ values above 6.0 ‰. This second group includes all garnets of Group C eclogites and part of the Group B garnets, with high contents of MgO (>14.0 wt. %) and low CaO <7.5 wt. %.

There is fixed not a very strong inverse relationship of $\delta^{18}\text{O}$ values with Mg# of garnets. It should be pointed that all high magnesium Group A garnets answer mantle range. We have presented on a diagram (Fig. 4) a comparison the results of oxygen isotope data for Udachnaya eclogitic garnets with analogous data for garnets of Nyurbinskaya diamondiferous xenoliths that show very obvious similarity. The unusual range of high $\delta^{18}\text{O}$ values for these xenolithic garnets is accompanied by evidence for strong late-stage metasomatism. Thereby, the possibility exists that mantle metasomatic fluids may also possess crustal signatures, as a result of ancient subduction. This wide range and abundance of high $\delta^{18}\text{O}$ values of garnets in diamondiferous xenoliths from Udachnaya and Nyurbinskaya pipes, outside of mantle values that combined with crustal evidences from several of the other Yakutian kimberlites (Spetsius et al., 2014; Pernet-Fisher et al., 2014), confirm the intense evolution of the lithospheric mantle beneath the Siberian Platform.

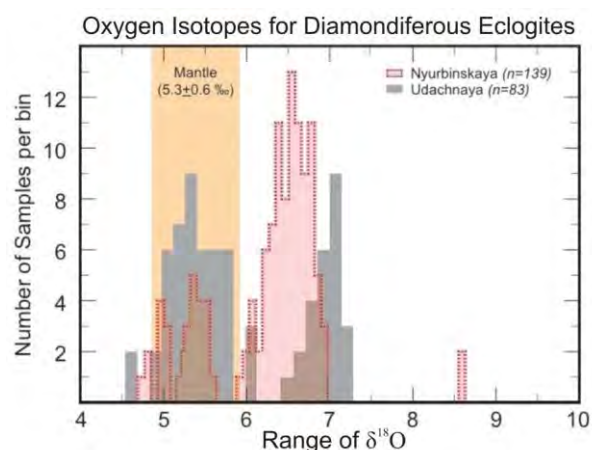


Figure 4: Distribution of $\delta^{18}\text{O}$ in garnets of diamondiferous eclogitic xenoliths from the Udachnaya pipe in comparison with $\delta^{18}\text{O}$ for garnets of Nyurbinskaya diamondiferous xenoliths (Spetsius et al., 2008).

Conclusions

In summary, we confirm that approximately half of diamondiferous eclogites from the Udachnaya pipe represent protoliths from subducted oceanic crust, with the possibility of a portion of the eclogites as mantle restites. The distribution of diamonds in the xenoliths, the presence of diamonds with different morphology in the same xenolith and other evidence suggest multistage diamond growth from metasomatic fluids that could be a generated during subduction.]

References

- [Ellis DJ, Green DH (1979) An experimental study of the effect of Ca upon garnet-clinopyroxene Fe-Mg exchange equilibria. *Contrib Mineral Petrol* 71:13-22.
- Pernet-Fisher JF, Howarth GH, Liu Y, Barry PH, Carmody L, Valley JW, Bodnar RJ, Spetsius ZV, Taylor LA (2014) Komsomolskaya diamondiferous eclogites: Evidence for oceanic crustal protoliths. *Contrib Mineral Petrol* 167(3):1-17.
- McDonough WF, and S.-S. Sun (1995) The composition of the Earth, *Chem. Geol.*, 120, 223-253.
- Sobolev VN, Taylor LA, Snyder GA, Sobolev NV (1994) Diamondiferous eclogites from the Udachnaya kimberlites pipe, Yakutia, *Inter Geol Rev* 36: 42–64.
- Spetsius ZV, Taylor LA, Valley J., De Angelis MT, Spicuzza M., Ivanov AS, and Banzeruk VI (2008) Diamondiferous xenoliths from crustal subduction: garnet oxygen isotopes from the Nyurbinskaya pipe, Yakutia. *Eur Jour Mineral* 20:375-385.
- Spetsius ZV, Taylor LA (2008) *Diamonds of Siberia: Photographic evidence for their origin*. Tranquility Base Press, Lenoir City, Tennessee, USA, 278p.
- Spetsius ZV, Wiggers de Vries DF and Davies GR (2009) Combined C-isotope and Geochemical Evidence for a Recycled Origin for Diamondiferous Eclogite Xenoliths from Kimberlites of Yakutia. *Lithos* 1125:1032–1042
- Valley JW, Kitchen N, Kohn MJ, Niendorf CR, Spicuzza MJ (1995) UWG-2, a garnet standard for oxygen isotope ratios: strategies for high precision and accuracy with laser heating. *Geochim. Cosmochim. Acta* 59: 5223-5231.]



ONTARIO'S NEWEST KIMBERLITE CLUSTER – THE PAGWACHUAN CLUSTER

**John Delgaty, Alexandrina Fulop, Michael Seller, Michael Hartley, Lee Zayonce,
Nicole Januszczak and Stephan Kurszlauskis**

De Beers Group of Companies – Canada Exploration

Introduction

The Pagwachuan kimberlite cluster is located ~55km southeast of the community of Geraldton on the southern Archean Superior Craton in Northwestern Ontario, Canada. A total of five kimberlites were discovered during the period of late 2015 to early 2016 after sediment sampling, structural mapping, glacial mapping, airborne geophysics and core drilling. Initial exploration in the Pagwachuan Lake area took place during two periods of the early 1960's and the mid 1980's where regional sediment samples yielded kimberlitic indicator mineral grains (KIMs). Samples collected in 2002 near the samples containing kimberlitic grains did not repeat the earlier results. Targeting and desktop review by De Beers in 2011 triggered a renewed interest in the area due to its geological setting, the presence of proximal surface textures on garnets and ilmenites from till samples and the presence of chrome diopsides with mineral chemistry that suggests they are derived from within the diamond window. A small field work program in 2012 repeated the KIM grains. Detailed glacial mapping, ice flow reconstruction and focused till sampling (tightly spaced fences) in 2014 identified multiple mineral dispersal trains with up-ice cut-offs. Till samples at the head of the mineral dispersal trains contained abundant KIMs with remnants of kimberlite preserved on the grains. Mineral chemistry of the kimberlite indicator mineral grains from samples showed lherzolitic and harzburgitic garnets as well as multiple and distinct populations of ilmenite suggestive of multiple kimberlite sources in the area.

Bedrock and Structural Geology

The Pagwachuan kimberlite pipes are located within the Quetico Terrane of the Western Superior Province. The kimberlites are emplaced into a strain flattened, fold thrust belt of deformed and metamorphosed basement rocks of Neoproterozoic (~2.7 Ga) age. The terrane represents an east-west trending belt of greenstones and arc-related (meta) sedimentary rocks that have reached amphibolite and granulite facies resulting in partial melting along with the intrusion of numerous syn- to post-tectonic feldspathic granites and pegmatites (Percival et al., 2006). This was followed by a phase of Paleoproterozoic orogenesis which culminated in the collision of the Superior Craton with neighboring micro continents (e.g. Hearne-Rae and Nain) during the Trans-Hudson Orogen at ~2.0-1.8 Ga. Further periods of active margin orogenesis during the Neoproterozoic and Phanerozoic are likely to have transmitted tectonic stresses resulting in intraplate reactivation and disturbances to isotopic systems along major crustal structures across the region. This is supported by low temperature apatite fission track thermochronometry data from the southern and western Superior Province (Kohn et al., 2005). The area around the central Quetico belt is conducive for kimberlite emplacement due to the presence of thick lithosphere, high strain tectonic corridors of the Trans-Superior Tectonic Zone and the presence of an array of upper crustal reactivation structures such as faults, shears and dykes possibly connected to a lower crustal plumbing pathway. Highly faulted internal architecture of NW-SE, NE-SW and E-W trending intersecting lineaments form complexly overprinted structural wedges which may disperse ascending melts and produce dyke-related bodies and smaller feeder pipes during emplacement events. Drilling results show that some of the kimberlite bodies are plunging suggesting emplacement may be guided by fold-thrust structures of the complexly deformed metasedimentary accretionary sequences. Other known occurrences located ~50km south of the cluster consist of carbonatites, diamond bearing kimberlite dykes and para-lamproites.

Glacial Geology and Mineral Dispersal

The Pagwachuan area has a flat to rolling topography dominated largely by ground moraine till and lesser amounts of bedrock knobs, eskers, outwash plains and lacustrine plains. Approximately 60% of the Pagwachuan area is covered by silty to sandy till veneer which is conducive for sampling. The Nakina end moraine is present in the northeast part and consists of fine sand, followed by lesser amounts of coarser outwash sand and gravel. The area was influenced by glacial Lake Barlow, post glacial Lake Minong and ice-marginal Lake Nakina (Temiskaming Interstadial period 9000 - 8500 BP) as evidenced by varved silts and clays existing in isolated pockets throughout the north part of the area. The lakes were short lived and did not influence grain dispersal. Mapping of ice flow indicators, verification of surficial material types, identification of tills and reconstructing former ice flows helped in the identification and behaviour of mineral dispersal trains and provided constraints for outlining areas for detailed geophysical surveys. Four ice advances during the Mid-Late Wisconsinan (28,000-9500 BP) confirmed by measuring striations on bedrock in the field flowed towards the south-southwest (200° - oldest), west (271°), southwest (216°) and west-southwest (249° - youngest). Based on drilling, the Pagwachuan kimberlites are covered in 10-35m of glacial drift consisting of 3 types of tills: 1) the oldest Sandy till dominated by Precambrian clasts and lesser amounts of Paleozoic clasts, 2) the sandy-silty Bankfield till dominated by Precambrian clasts and lesser amounts of Paleozoic clasts and 3) the youngest silty-sandy Matheson till dominated by Paleozoic clasts and lesser amounts of Precambrian clasts. The fine silt-clay rich Cochrane till is absent in the Pagwachuan area. Till recognition was made possible by the analysis of grain size, carbonate content, clast lithology and till chemistry. Mineral dispersal trains emanating from the kimberlites show a very dominant NE-SW trend and a lesser but notable ENE-WSW trend. The fan shaped trains range in length from 1 to 20km and this variation in length within the cluster may be a function of one or a combination of the size of the kimberlites, variable thickness in drift cover and mineralogical abundance within the kimberlites.

Airborne and Ground Geophysics

During the spring of 2015, the Ontario Geological Survey released a geophysical airborne magnetic dataset known as the Lac des Mille, Lacs-Nagagami area survey. The survey covered ~22,500km², with line spacing of 200m and 100m mean terrain clearance. It produced a number of high grade magnetic anomalies which were subsequently staked. During the summer of 2015 De Beers commissioned a high resolution heliborne magnetic and frequency domain electromagnetic (DIGHEM/Resolve) survey, the Pendant Creek survey, over a cluster of high grade anomalies and over the heads of mineral trains in the Pagwachuan Lake area. This 347km² survey with 50m line spacing and 35m mean terrain clearance confirmed the interest level of the anomalies picked from the Lac des Mille magnetic survey and yielded additional high interest targets. The Pagwachuan kimberlites were discovered by drilling discrete magnetic highs with associated weak electromagnetic responses. Ground magnetic surveys were conducted over the kimberlites to confirm the 2D size of the kimberlite. Ground gravity surveys were completed over three of the kimberlites to identify any new facies not seen in the magnetic and electromagnetic surveys, but did not increase the 2D size of the pipes. Results from petrophysics on the kimberlite core and the host rock confirmed the contrasts seen in the geophysical surveys. All five kimberlites exhibit high magnetic susceptibilities compared to the host rock resulting in anomalous amplitude magnetic signatures. Three of the five kimberlites tested have lower densities than the host rock, these bodies manifest as gravity low signatures in follow-up ground gravity surveys. Inversion modeling of the detailed ground magnetics over the kimberlites resulted in modelled subcropping sizes for the pipes ranging from 0.5 to 2.5 ha.

Core Drilling

During late 2015, core drilling discovered the first kimberlite in the Pagwachuan Lake area. One HQ diameter core hole was drilled into the center of each magnetic high anomaly of interest to a depth of approximately 400m. Five kimberlites were discovered: Arriba, Bronco, Caliente, Domino and El Nino. Of the five kimberlites drilled, the Arriba kimberlite is the largest with a 2D size of 2.5ha and

the Caliente kimberlite is the smallest at 0.5ha. Four of the five kimberlite discovery holes ended prematurely in country rock thereby suggesting the deposits have complex shapes not common to typical kimberlite pipes. It is also speculated that the pipes are structurally controlled and may be plunging but this is not fully supported by the geophysics.

Kimberlite Petrology and Age of Emplacement

The Pagwachuan kimberlites are multi-phased with up to three different facies identified through drill core, thin section and whole rock chemistry investigations. Overall, typical crater-facies volcanoclastic kimberlites suggesting phreatomagmatic explosions are identified in Arriba and Bronco pipes. The Caliente, Domino and El Nino pipes comprise kimberlites which combine apparent coherent textures with emplacement style of fragmental rocks suggesting both magmatic and phreatomagmatic eruptions. Interestingly, the coherent textured-kimberlites indicate high temperature metasomatic reaction with contained felsic country rocks, atypical for pyroclastic rocks. The Arriba and Bronco kimberlites are comprised of different volcanoclastic kimberlites emplaced by combined, primary pyroclastic and resedimentation processes. Debris flows are interlayered with grain flows and fallout or base surge deposits are typically identified in Arriba. The Arriba kimberlites demonstrate differences in olivine abundance, primary carbonate and mantle component, typically eclogite xenoliths and ilmenite. The Bronco kimberlites indicate mostly resedimentation, entraining exceptionally large and abundant crustal blocks and locally grain flows which concentrate abnormally high abundant ilmenite. The Caliente, Domino and El Nino kimberlites are typically low abundant fine grained olivine and almost devoid of indicator minerals. The rocks testify to spatters, lava lakes and even intrusions, but also to highly energetic explosive events. Crustal contamination of different mafic and felsic compositions impacts on the mineralogy and chemistry of the kimberlites. The Caliente kimberlites typically show strong metasomatic reactions with felsic crustal rocks which obliterate most of the primary composition. Rubidium strontium (Rb-Sr) dating of the phlogopite from the Arriba, Bronco, Caliente and Domino kimberlites yields an average age of 252.9 ± 2.4 Ma (Late Permian). Uranium lead (U-Pb) dating of the perovskite from the Caliente and Domino kimberlites yields an average age of $220 \text{ Ma} \pm 7.8 \text{ Ma}$ (Early to Middle Triassic) (De Beers data, 2016-2017).

Mineral Chemistry Characteristics and Diamonds

Core samples for each of the Pagwachuan kimberlites were processed to quantify the abundance and composition of mantle derived indicators present (i.e. garnet, clinopyroxene, spinel and ilmenite). The general trend of recovered indicators for all kimberlites is of garnet (46%) > clinopyroxene (25%) > ilmenite (20%) > spinel (8%). The predominant size fraction of the recovered indicators is +0.5mm (47%) followed by +0.15mm (29%) and lastly +0.3mm (23%). However, variations in grain recoveries and proportions of indicators from the various size fractions do occur between kimberlites. The principal compositional features of the garnet populations recovered from the Pagwachuan kimberlites are a high proportion of megacrystics (53% G1) followed by lherzolitic (28% G9) and Ti-metasomatised (5% G11) compositions (classification scheme after Grütter et al., 2004). The remaining garnet compositions consist of low proportions of eclogitic (4% G3), pyroxenitic (3% G4, G5), harzburgitic (2% G10), and wherlitic (2% G12) garnets. The presence of diamond-facies like compositions is rare (<0.5% of all garnets recovered) with most derived from the eclogitic, pyroxenitic and then harzburgitic compositions. Mantle barometry using the Cr/Ca-in-pyrope barometer of Grütter et al., (2006) shows a maximum P_{38} of 57 kbar indicating sampling of thick lithosphere, however, very few garnets fall above the 43 kbar “graphite diamond constraint” (GDC) which indicates sampling within the diamond stability field. The Arriba and Domino kimberlites were sampled for micro diamonds. Arriba returned one 0.104mm broken and highly resorbed dodecahedron diamond that is colourless, translucent, and has possible graphite inclusions. Domino returned one 0.074mm broken and translucent octahedron diamond that is colourless, and has macle twinning.

Conclusion

Geophysics and sediment sampling are effective exploration methods in the discovery of the Pagwachuan kimberlites. The multi-phased Pagwachuan kimberlites located in the Quetico terrane are structurally controlled, have sampled thick lithosphere and are diamond bearing. Unfortunately, they are considered to be uneconomic due to their small sizes, complex shapes, unique but low interest petrology and poor microdiamond recoveries. They however represent the first discovery of a Late Permian to Early Triassic aged kimberlite cluster in Ontario.

Acknowledgement

The authors would like to thank De Beers Exploration and De Beers Canada for support and permission to publish this work. G. Van Der Linde, S. Joy and R. Caesar are thanked for providing geochronology services.

References

- Grütter HS, Gurney JJ, Menzies AH, Winter F (2004) An updated classification scheme for mantle-derived garnet, for use by diamond explorers. *Lithos* 77: 841–857
- Grütter H, Latti D, Menzies A (2006) Cr-Saturation arrays in concentrate garnet compositions from kimberlite and their use in mantle barometry. *Journal of Petrology* 47: 801–820
- Kohn BP, Gleadow AJW, Brown RW, Gallagher K, Lorencak M, Noble WP (2005) Visualizing thermotectonic and denudation histories using apatite fission track thermochronology. *Reviews in Mineralogy & Geochemistry* 58: 527-565
- Percival JA, Sanborn-Barrie M, Skulski, T, Stott GM, Helmstaedt H, White DJ (2006) Tectonic evolution of the western Superior Province from NATMAP and lithoprobe studies. *Canadian Journal of Earth Sciences* 43: 1085-1121



Insights into the petrogenesis of the West Kimberley lamproites from trace elements in olivine

A.L. Jaques¹ and S.F. Foley²

1. Research School of Earth Sciences, Australian National University, Canberra, ACT, Australia, lynton.jaques@anu.edu.au.

2. ARC Centre of Excellence for Core to Crust Fluid Systems (CCFS) and Department of Earth and Planetary Sciences, Macquarie University, NSW, Australia, stephen.foley@mq.edu.au

Introduction

Minor and trace element abundances in olivine can provide important information on the origin and evolution of a range of mantle-derived magmas (e.g. Foley et al., 2013). Mantle olivine may record a residue of partial melting, and the impact of metasomatism over time. Magmatic olivines can record the crystallisation history of the magma and help to identify the rock assemblages present in the source region.

We report minor and trace element analyses of olivine from the Miocene (17–22 Ma) olivine lamproites and olivine-bearing leucite lamproites of the West Kimberley province of Western Australia with the aim of assessing the extent to which the trace element inventories of olivine provide information on 1) the nature of the mantle sampled by the lamproites, 2) the mantle processes, including metasomatism, that may have affected the mantle source region of the lamproites, and 3) magmatic processes involved in lamproite formation and evolution.

Petrography

The West Kimberley lamproite province lies at the southwest margin of the Kimberley Craton of Western Australia extending from the Proterozoic King Leopold Orogen bordering the craton across the Fitzroy Trough in the northern Canning Basin. It comprises some 180 individual bodies occurring as volcanic pipes, plugs, sills and dykes clustered in three main fields (Jaques et al. 1984, 1986). The Ellendale field in the north is dominated by olivine lamproite pipes, many of which carry diamonds at low concentrations with Ellendale pipes 4 and 9 being mined in the period 2002–2009. The two other main fields (Noonkanbah and Calwynyardah) as well as the smaller clusters and isolated lamproite intrusions are dominated by leucite lamproites occurring as pipes, plugs, sills and dykes.

Magmatic olivine occurs as sub- to euhedral phenocrysts and microphenocrysts in olivine-diopside-leucite lamproites with as little as 7 wt % MgO through to the diamondiferous Ellendale olivine lamproites with up to 32 wt % MgO (Jaques et al. 1984, 1986; Stachel et al. 1994). The olivine lamproites are characterised by abundant mantle olivine in the form of dunite micro-xenoliths and xenocrysts (both characterised by solid-state deformation), and anhedral macrocrysts of uncertain origin. In addition to the micro-xenoliths of dunite, sparse small xenoliths of harzburgite containing minor Cr-Al spinel in symplectic intergrowths with Cr-diopside (inferred to be a re-equilibrated former garnet) are found in Ellendale 7 (Jaques et al. 1984).

Analytical Results

Major and minor elements were obtained by Cameca SX-100 EPMA operating at 15 kV and 30 nA employing a range of natural and synthetic standards and full ZAF corrections. Abundances of Li, Na, Al, Si, P, K, Ca, Sc, Ti, V, Cr, Mn, Co, Ni, Cu, Zn, Sr, Y, Zr, and Nb were determined by LA-ICP-MS at the Australian National University using Si values determined by EPMA as an internal standard and NIST SRM 612 as reference standard. Data were processed using the Iolite software package (Paton et al. 2011).

The *mantle olivines* have a limited compositional range ($Mg_{90-92.5}$) with most being of uniform composition apart from narrow ($< 100 \mu m$) rims (Fig. 1a). Mantle olivines with $Mg < 91$ invariably have more Mg-rich rims (Mg_{91-93}) whereas the more Mg-rich mantle olivines either have no discernable zoning or normal or reverse zoning. The mantle olivines are all characterised by high Ni (2700–3300 ppm), uniform Mn (600–1100 ppm), and low Ca (≤ 420 ppm). All have low Li (1.2–2.9 ppm), Na (< 190 ppm), Al (≤ 130 ppm), Sc (< 5 ppm), Ti (≤ 160 ppm), and V (3–9 ppm), modest Cr (90–430 ppm) and Co (130–150 ppm), and extremely low Sr (< 0.25 ppm), Zr (< 0.025 ppm) and Nb (< 0.01 ppm). Macrocrystal olivines have very similar Mg ($Mg_{90.2-92.9}$) and trace element abundances implying that most are also of mantle origin although a few with lower Ni and higher Mn contents lie outside the mantle cluster and on the magmatic trend (Fig. 1b): these may be early phenocrysts. Olivine in the harzburgite xenolith ($Mg_{92.4}$) shows strong depletion in lithophile elements, at the low end of the range of mantle olivine values (e.g. 4 ppm Na, 10 ppm Al, 60 ppm Ca, 4 ppm Ti, 45 ppm Cr) but similar Ni, Co and Ni to the other mantle olivines. Olivine inclusions in diamonds from Ellendale (Griffin et al., 1988) show a much wider range in Mg ($Mg_{93.5-88.3}$) but, with the exception of the Fe-rich olivine, have Cr, Mn and Ni contents comparable with mantle olivines (Fig. 1a).

The abundances of Al, Mn and V suggest that most of the West Kimberley mantle olivines are derived from garnet peridotite but a few of the macrocrysts are likely derived from spinel peridotite based on the discrimination diagrams of De Hoog et al. (2010) and Bussweiler et al. (2017). Estimated equilibration temperatures based on Al in olivine (Bussweiler et al. 2017) for the mantle olivines (Fig. 1c) lie in the range ~ 900 – $1270^\circ C$ (at an assumed pressure of 5 GPa; Fig. 1c). The mantle olivines display a trend of increasing Ti (and Zr) with decrease in Mg# in olivine (Fig. 1d).

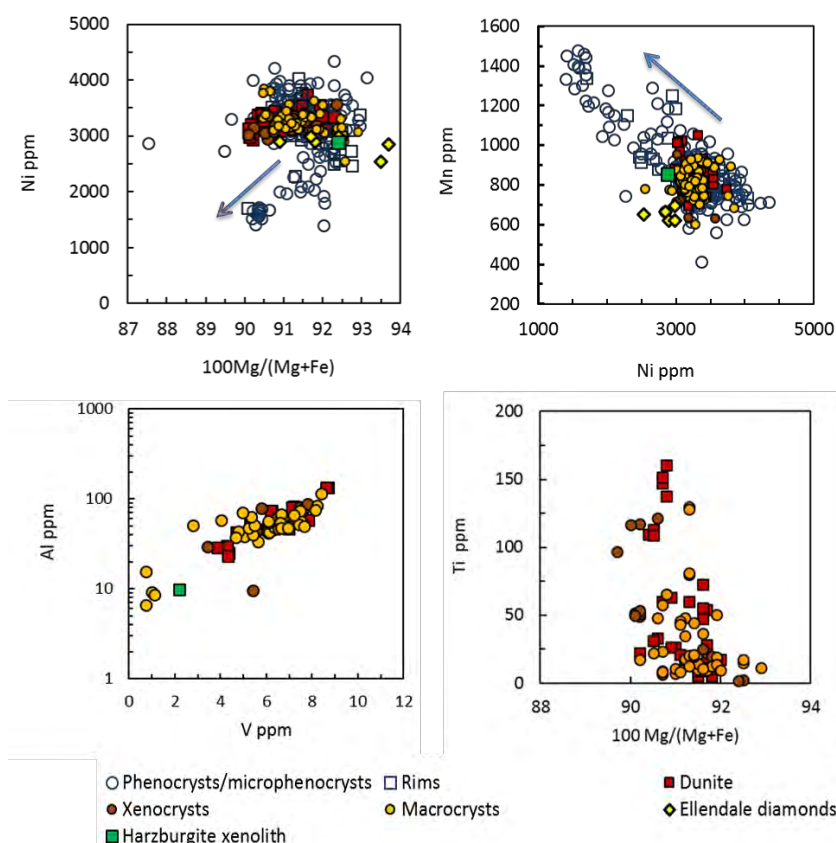


Figure 1. Minor and trace element variation in the West Kimberley olivines: a) 100Mg/(Mg+Fe) versus Ni (ppm, EPMA data); b) Mn versus Ni (ppm, EPMA data); c) V versus Al abundances (ppm) in dunite, xenolith, and macrocyst olivine (LA-ICP-MS data); d) Ti versus Zr abundances (ppm) in dunite, xenolith, and macrocyst olivine (LA-ICP-MS data). Arrows indicate direction of magmatic trends.

The *magmatic olivines* have a wider range in Mg ($Mg_{87.5-93}$) and most trace element abundances than the mantle olivines. The magmatic olivines show a decrease in Cr and Ni, and an increase in Mn abundances with falling Mg# (Fig. 1a, b), consistent with fractional crystallisation. Fractionation trends range from 4300 ppm to 1400 ppm for Ni and from 550 to 1500 ppm for Mn. The microphenocrysts in the olivine-diopside-leucite lamproites commonly have high Ni, Mn and Ca contents. Rims on the mantle olivines have an identical compositional range to the phenocrysts and microphenocrysts, confirming their magmatic origins. Trace element abundances generally overlap the compositions of the mantle olivines but show a greater range in Cr (20–1050 ppm) and extend to higher abundances of Li (to 6 ppm), Na (to 260 ppm), Al (to 150 ppm), Ca (to 1230 ppm), Ti (to 190 ppm), Sr (to 1 ppm), Y (to 40 ppb), Zr (to 1.2 ppm), and Nb (to 350 ppb). Abundances of many elements (e.g. Na, Al, Ca, Ti, Co, Mn) increase with decrease in Mg# and Ni, consistent with melt fractionation.

The mantle olivine Mg-values and trace element abundances are typical of moderately refractory sub-cratonic mantle of garnet (and minor spinel) peridotite equilibrated at ~900–1270°C (at 5 GPa). Variations in major and trace elements in olivine are inferred to reflect variable degrees of depletion during partial melting of the mantle. However, olivines with higher Fe, Ti, Sr, Zr and Nb may record metasomatism of previously more refractory mantle.

The West Kimberley lamproites are believed to have been derived from formerly depleted mantle peridotite that has undergone ancient (>2 Ga) geochemical enrichment that likely involved addition of a subducted sedimentary component based on their K/Rb, K/Ba, Ba/La and Th/U ratios and Sr, Nd and Pb isotope compositions (Jaques et al. 1984; Nelson et al. 1986). However, the low Li contents of the West Kimberley olivines are typical of cratonic mantle, and unlike those in potassic magmas from orogenic regions (up to 45 ppm; Foley et al. 2013). These observations can be reconciled if Li added to the mantle from subducted sediment in the past has been largely lost by diffusion over time.

References

- Bussweiler Y, Brey GP, Pearson DG, Stachel T, Stern RA, Hardman MF, Kjarsgaard BA, Jackson SE (2017) The aluminum-in-olivine thermometer for mantle peridotites - Experimental versus empirical calibration and potential applications. *Lithos*, 272–273:301-314
- De Hoog JCM, Gall L, Cornell DH (2010) Trace-element geochemistry of mantle olivine and application to mantle petrogenesis and geothermobarometry. *Chemical Geology* 270:196-215
- Foley SF, Prelevic D, Rehfeldt T, Jacob DE (2013) Minor and trace elements in olivines as probes into early igneous and mantle melting processes. *Earth Planet Sci Letts* 363:181-191
- Griffin WL, Jaques AL, Cousens D, Ryan C, Sie S, Suter G (1988) Conditions of diamond growth: a proton microprobe study of inclusions in West Australian diamonds. *Contrib Mineral Petrol* 99:143-158
- Jaques AL, Lewis JD, Smith CB, Gregory GP, Feguson J, Chappell BW, McCulloch MT (1984) The diamond-bearing ultrapotassic (lamproitic) rocks of the West Kimberley region, Western Australia. In Kornprobst J et al (eds) *Kimberlites I: Kimberlites and related rocks*, Elsevier, pp. 225-254
- Jaques AL, Lewis JD, Smith CB (1986) The kimberlites and lamproites of Western Australia. *Geological Survey West Australia Bulletin* 132:268 p.
- Nelson DR, McCulloch MT, Sun S-S (1986) The origins of ultrapotassic rocks as inferred from Sr, Nd and Pb isotopes. *Geochim Cosmochim Acta* 50, pp. 231-245
- Paton C, Hellstrom J, Bence P, Woodhead J, Hergt J (2011) Iolite: Freeware for the visualization and processing of mass spectrometric data. *J Anal At Spectrom* 26:2508-2518
- Stachel T, Lorenz V, Smith CB, Jaques AL (1994) Volcanology and geochemistry of the Ellendale Lamproite Field, (Western Australia). In Meyer HOA, Leonardos OH (eds) *Kimberlites, related rocks, and mantle xenoliths*. CPRM-Special Publ 1(91):177-194



Features of apatite in kimberlites from Ekati Diamond Mine and Snap Lake, Northwest Territories, Canada: modelling of kimberlite composition

R. Milligan¹, Y. Fedortchouk¹, P. X. Normandeau², A. Fulop³, M. Robertson⁴

¹Department of Earth Sciences, Dalhousie University, Halifax, Canada, rachel.milligan@dal.ca, yana@dal.ca

²Northwest Territories Geological Survey, Yellowknife, Canada, philippe_normandeau@gov.nt.ca

³DeBeers Canada, Toronto, Canada, alexandrina.fulop@debeersgroup.com

⁴Department of Physics, Acadia University, Wolfville, Canada, michael.robertson@acadiau.ca

Introduction

Volatile proportions (H₂O, CO₂, F, Cl) and timing of fluid exsolution have important implications for kimberlite melt compositions, evolution and eruptive processes. The timing of fluid exsolution from kimberlite melts can affect the resorption and preservation of diamonds carried to the surface (Fedortchouk et al. 2010).

Apatite, Ca₅(PO₄)₃(F,Cl,OH), is a common groundmass mineral in kimberlites, crystallizing together with serpentine and carbonates (Malarkey et al. 2010) and is often used as an indicator of volatile behaviour in igneous rocks (Miles et al. 2013; Piccoli and Candela 1994). Apatite is a major host of halogens, rare earth elements (REE's) and Sr, whose concentrations are sensitive to magma fractionation and the presence and composition of fluid during magma crystallization and post-magmatic hydrothermal alteration. This study uses groundmass apatite to evaluate the volatile history of kimberlites with various eruption styles using kimberlite pipes from Ekati Mine and Snap Lake mine kimberlite dyke. We show textural and compositional variations of apatite in neighbouring kimberlite bodies and the mineralogical in Snap Lake dyke. Concentrations of REE and other trace elements combined with experimentally derived partitioning coefficients of these elements from the literature between apatite and silicate melt, carbonate melt and aqueous fluid help us to examine the composition of each studied kimberlite magma.

| Kimberlite | Abundance | Size (µm) | Habit | Zonation |
|-----------------------------|--------------|-----------|-----------|-------------|
| Leslie (CK) | abundant | 5-60 | euhedral | patchy |
| Grizzly (CK) | intermediate | < 10 | subhedral | core-rim |
| Panda (RVK) | intermediate | 20-100 | subhedral | oscillatory |
| Beartooth (RVK) | v. low | | | |
| Misery (VK) | v. low | | | |
| Koala (VK) | intermediate | 10-150 | anhedral | core-rim |
| Snap Lake (phlogopite-poor) | abundant | 10-100 | Type 1, 2 | core-rim |
| Snap Lake (phlogopite-rich) | abundant | 20-50 | Type 3 | concentric |

Table 1: Features of apatite in six Ekati Mine kimberlites and in Snap Lake dyke. (Type 1,2,3 refer to the apatite types in Snap Lake, CK – coherent kimberlite, RVK – resedimented volcanoclastic kimberlite).

Samples and Methods

This study used two thin-sections from each of the six Ekati Mine kimberlites (Koala, Panda, Leslie, Misery, Grizzly and Beartooth). Different geological features (Table 1) and diamond populations (Fedortchouk et al. 2010) of these kimberlites suggest different volatile and eruption histories. 32 thin-sections from Snap Lake kimberlite dyke represent six mineralogical zones ranging from fresh phlogopite-poor to altered and highly-altered phlogopite-rich kimberlite. We used scanning electron microscopy (SEM) and cathodoluminescence (CL) to examine growth and resorption zonation in apatite; wavelength dispersive spectroscopy (WDS) for microprobe analyzes of major and minor

elements, and laser ablation inductively coupled plasma mass spectrometry (ICP-MS) for trace element analyzes. REE patterns of apatite discriminate between xenocrystal apatite from country rock and kimberlitic apatite.

Apatite Types

Apatite grains are present in four of the six Ekati kimberlites: Leslie, Panda, Grizzly and Koala. Leslie has abundant euhedral apatite with many monticellite inclusions, patchy zonation (Fig. 1a) and high content of LREE and Sr (Fig. 2a). Apatite in Panda is subhedral with complex oscillatory zonation rich in LREE (Figs. 1b, 2a). In Grizzly, resorbed apatite xenocrysts with low LREE and Sr are surrounded by resorbed kimberlitic apatite with high REE and Sr (Figs. 1c, 2a). Apatite in Koala are abundantly preserved, xenocrystic (Fig. 2a) and have inherited core-rim zonation (Fig. 1d).

In Snap Lake kimberlite dyke, three textures of apatite were observed and classified as separate “Types”. They all have similar REE and trace element patterns, with exchange of Sr in the case of lower REE concentrations. Snap Lake apatite grains show less fractionated LREE-HREE patterns than Leslie and Panda apatites (Fig. 2). Fresh, phlogopite-poor kimberlite lithofacies have abundant radial aggregates of acicular or columnar apatite crystals (Type 1, Fig. 1e) with strong zoning revealed in CL and the lowest concentration of REE in Snap Lake. This is accompanied by prismatic zoned apatite in carbonate veins (Type 2). Altered, phlogopite-rich kimberlite have prismatic euhedral apatite with well-formed growth zoning (Type 3, Fig. 1f), and higher content of REE, U, HFSE and Ti (Fig. 2b).

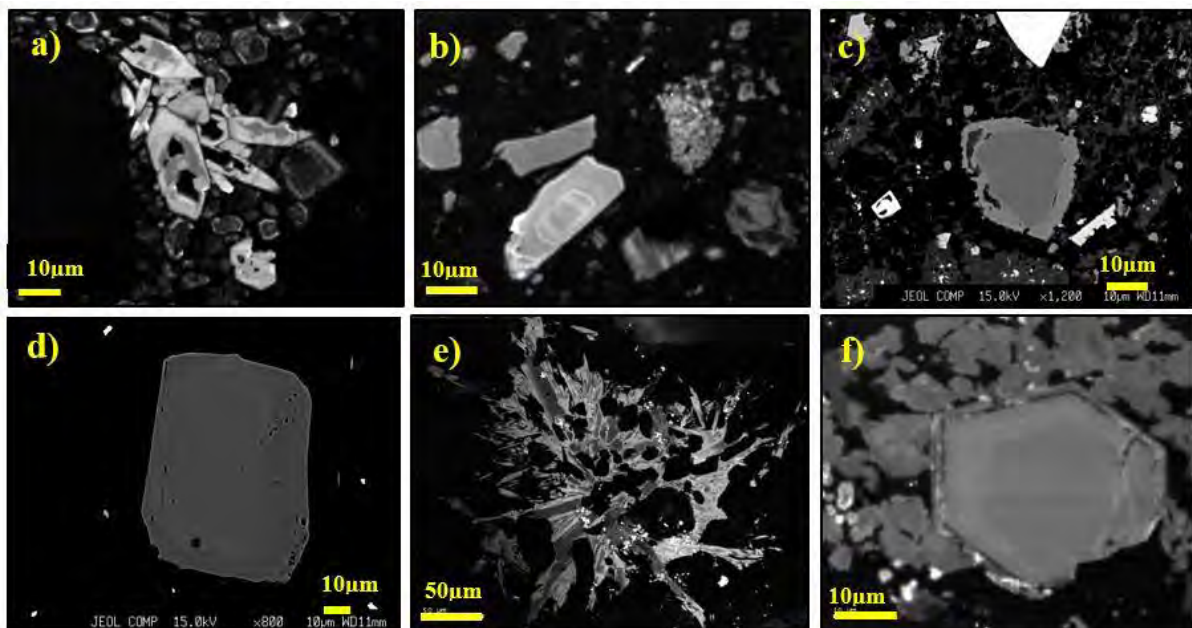


Figure 1: Apatite textures from Ekati kimberlites a) Leslie, CL image, b) Panda, CL image, c) Grizzly, BSE image, d) Koala, BSE image, e) Snap Lake Type 1, CL image, and f) Snap lake Type 3, CL image.

Apatite as an indicator mineral

Our data shows variation in both: preservation of xenocrystal apatite from country rock and crystallization of kimberlitic apatite in the six neighbouring kimberlites from Ekati Mine. Xenocrystal apatite is well-preserved in Koala and partially preserved in Grizzly. If present initially, it was completely dissolved by Leslie, Panda, Misery and Beartooth magmas, and in Snap Lake. Apatite was most stable in Koala and only slightly rounded by dissolution. In Grizzly, rounded resorbed xenocrystal cores were overrown by the rims of kimberlitic apatite, which also show resorption. Fig. 2a shows that the most distinct changes in the composition of crustal-derived apatite which resided in kimberlite magma are increase of LREE relative to MREE, HREE and Sr (Fig. 2a). This could allow the use of apatite as a kimberlite indicator mineral during prospecting.

Crystallization of apatite from kimberlite magma is controlled by reaching phosphorous saturation and only occurred in Leslie, Panda and Grizzly (as rims on xenocrysts). Preservation of xenocrystal apatite in Koala could explain lower phosphorous content in the magma, insufficient for the crystallization of kimberlitic apatite. However, in Misery and Beartooth, phosphorous saturation was not reached. Phosphorous saturation required for apatite saturation also depends on temperature and melt composition (SiO_2 , CaO ; Watson, 1980; Tollari et al. 2008). Apatite crystallization could reflect variation in assimilation of crustal xenoliths by different kimberlite magmas, which alter both P_2O_5 and SiO_2 in the melt, triggering or impeding the crystallization of apatite. In Snap Lake, all apatite is kimberlitic (Fig. 2b), crystallizing either from the melt or from deuteric kimberlite fluids. Identical composition of radial aggregates of acicular apatite Type 1 and apatite Type 2, found in post-magmatic veins that cut through olivine macrocrysts, point to their common post-magmatic origin. Euhedral zoned Type 3 apatite found in phlogopite-rich lithologies shows similar REE patterns, but has higher REE content and much lower Sr/La ratio than Type 1 and 2. Its Sr/La ratio is similar to apatite from Ekati samples. The higher H_2O activity in phlogopite-rich lithologies could be responsible for earlier apatite saturation (Tollari et al. 2008). We obtain partition coefficients (D) for REE and other trace elements for apatite using our LA-ICPMS data and bulk rock compositions for the same kimberlites from the literature (Nowicki et al. 2004) and compare them to experimentally determined D values for silicate melt and carbonate melt from the literature (Prowatke and Klemme, 2006). Our data for Leslie, Grizzly, and Panda best agree with apatite crystallization from a silicate melt.

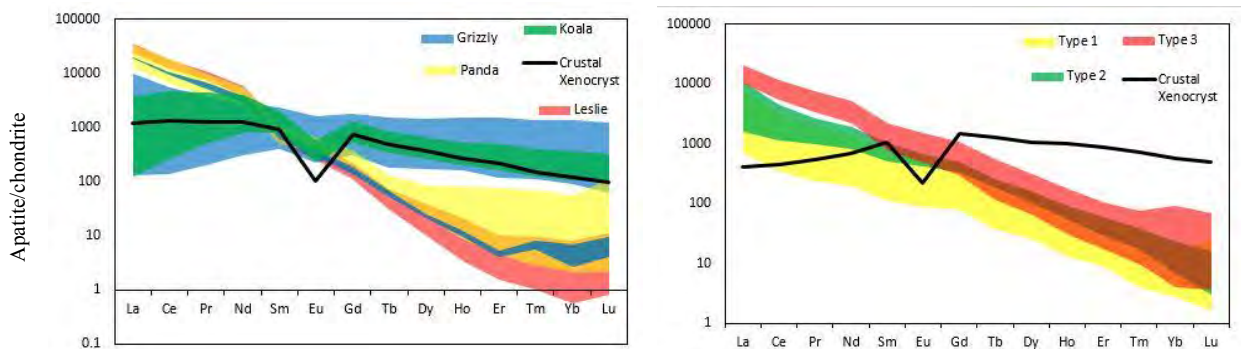


Figure 2: Chondrite normalised REE patterns of apatite from a) Ekati kimberlites, and b) Snap Lake. Crustal xenocrysts determined from textural relationships (xenolith inclusions).

References

- Fedortchouk Y, Matveev S, Carlson JA (2010) H_2O and CO_2 in kimberlitic fluid as recorded by diamonds and olivines in several Ekati Diamond Mine kimberlites, Northwest Territories, Canada. *Earth Planet Sc Lett* **289**:549-559.
- Malarkey J, Pearson DG, Kjarsgaard BA et al (2010) From source to crust: tracing magmatic evolution in a kimberlite and a melilitite using microsample geochemistry. *Earth Planet Sc Lett* **299**: 80-90.
- Miles AJ, Graham CM, Hawkesworth CJ et al (2013) Evidence for distinct stages of magma history recorded by the compositions of accessory apatite and zircon. *Contrib Mineral Petr* **166**: 1-19.
- Nowicki T, Crawford B, Dyck D et al (2004) The geology of kimberlite pipes of the Ekati property, Northwest Territories, Canada. *Lithos* **76**: 1-27.
- Piccoli PM, Candela PA (1994) Apatite in felsic rocks: a model for the estimation of initial halogen concentrations in the Bishop Tuff (Long Valley) and tuolumne intrusive suite (Sierra Nevada Batholith) magmas. *Am J Sci* **297**: 92-135.
- Prowatke S, Klemme S (2006) Trace element partitioning between apatite and silicate melts. *Geochim Cosmochim Ac* **70**: 4513-4527.
- Tollari N, Baker DR, Barnes S-J (2008) Experimental effects of pressure and fluorine on apatite saturation in mafic magmas, with reference to layered intrusions and massif anorthosites. *Contrib Mineral Petr* **156**: 161-175.
- Watson EB (1980) Apatite and phosphorous in mantle source regions: an experimental study of apatite/melt equilibria at pressures to 25kbar. *Earth Planet Sc Lett* **51**: 322-335.

A tale of three lamproites, their diamonds and settings – Bunder, Majhgawan and Argyle

Chris B. Smith¹, Galina Bulanova¹, Venkatasubramanian Meenakshisundaram² and Lynton Jaques³

¹University of Bristol, United Kingdom, chris_b_smith@btopenworld.com, galina_bulanova@hotmail.com

²Rio Tinto Exploration India Private Limited, Bangalore, India, venkat@riotinto.com

³Australian National University, Canberra, Australia, lynton.jaques@anu.edu.au

Bunder pipes (Madhya Pradesh, India), Majhgawan (Madhya Pradesh, India) and Argyle (Western Australia) (Fig. 1) are Mesoproterozoic diamondiferous diatremes with affinities to lamproite, as characterised by their ultrapotassic nature, high content of Sr, Zr, Nb, La and Ba and LREE, former glassy matrix, and the presence of characteristic minerals such as priderite, potassic richterite, Ti-rich tetraferriphlogopite and leucite (Argyle; Jaques et al., 1986), tetraferriphlogopite (Bunder and Majhgawan; Masun et al., 2009; Farreduddin and Mitchell, 2012). Lamproites are regarded as lithospheric mantle-derived melts (Mitchell and Bergman, 1991). However, Sr and Nd isotopic compositions suggest a greater input from the asthenospheric mantle in the case of the Indian pipes (Das et al., in press.), and the presence of microilmenite megacrysts at Bunder (Masun et al., 2009) and Mahjgawan (Mukherjee et al., 1997) suggests derivation from the low velocity zone at the base of the lithospheric mantle, a feature associated with Group I kimberlites rather than lamproite (Mitchell and Bergman, 1991). Such conflicting features led Chalapathi Rao (2015) to suggest that Majhgawan (and hence also Bunder) are transitional between kimberlite and lamproite.

All three occurrences lie within or adjacent to Proterozoic orogenic belts representing former tectonic collision zones between cratons. Bunder and Majhgawan lie on the edge of the Archean Bundelkhand Craton next to the Central Indian Tectonic Zone (“CITZ”) and tap diamonds sourced from the underlying peridotitic mantle (Fig. 1a). These two Indian lamproites lie on the ENE trending Asmara seismic lineament (interpreted as a fault in the crystalline basement (Helmstaedt, in press; Prasad and Rao, 2006). The CITZ is seismically active and marks the major Precambrian (1.6-1.5 and 1.1-1.0 Ga) zone of collision of the Bundelkhand and Bastar Cratons during formation of the Rodinia supercontinent. Argyle lies within the strongly faulted Paleoproterozoic Halls Creek Orogen (“HCO”) adjacent to the Kimberley Craton (Fig. 1b). The HCO marks the Paleoproterozoic collision of the Archean Kimberley and North Australian Cratons. The HCO remained tectonically active during the Proterozoic and has been further deformed by later NE-SW faulting (Betts et al., 2015; Helmstaedt, in press; Tyler et al., 2012). Argyle diamonds are predominately eclogitic, possibly derived from subducted North Australian Craton crust (Fig. 1b). It is suggested these highly fractured, tectonically active, collision zones facilitated and enhanced interaction of asthenosphere-derived, alkali-rich fluids with overlying lithospheric mantle, giving rise after partial lithospheric mantle melting to the chemically enriched nature of resultant magmas with lamproite affinities.

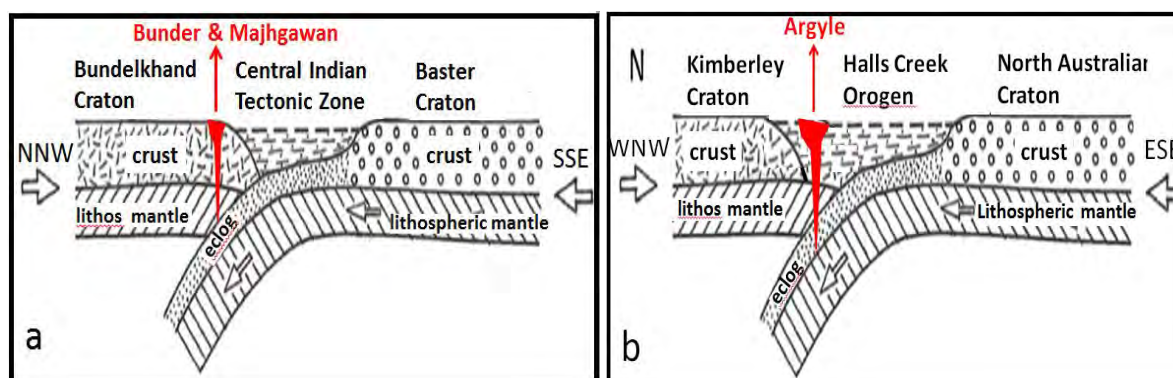


Fig. 1: a) Bunder X-section (based on Mandal et al., 2013), b) Argyle X-section (based on Tyler et al., 2012); images are interpreted from seismic tomography, with suggested pipe locations superimposed upon them.

The three occurrences have significant diamond content. The Atri pipe at Bunder has an inferred resource of 37 million tonne, containing 27.4 million cts. Majhgawan and surrounding alluvials at Panna are one of the world's oldest mined diamond deposits, with production dating back to the 13th century. Argyle has been the world's largest diamond producing pipe, realising some 825 million cts since 1983. The diamonds from these three pipes, considered to be formed from fluids in cracks within lithospheric mantle peridotite and eclogite, show signs of stress with common development of plastic deformation and associated brown colour (Fig. 2 due to resultant vacancy cluster defects).

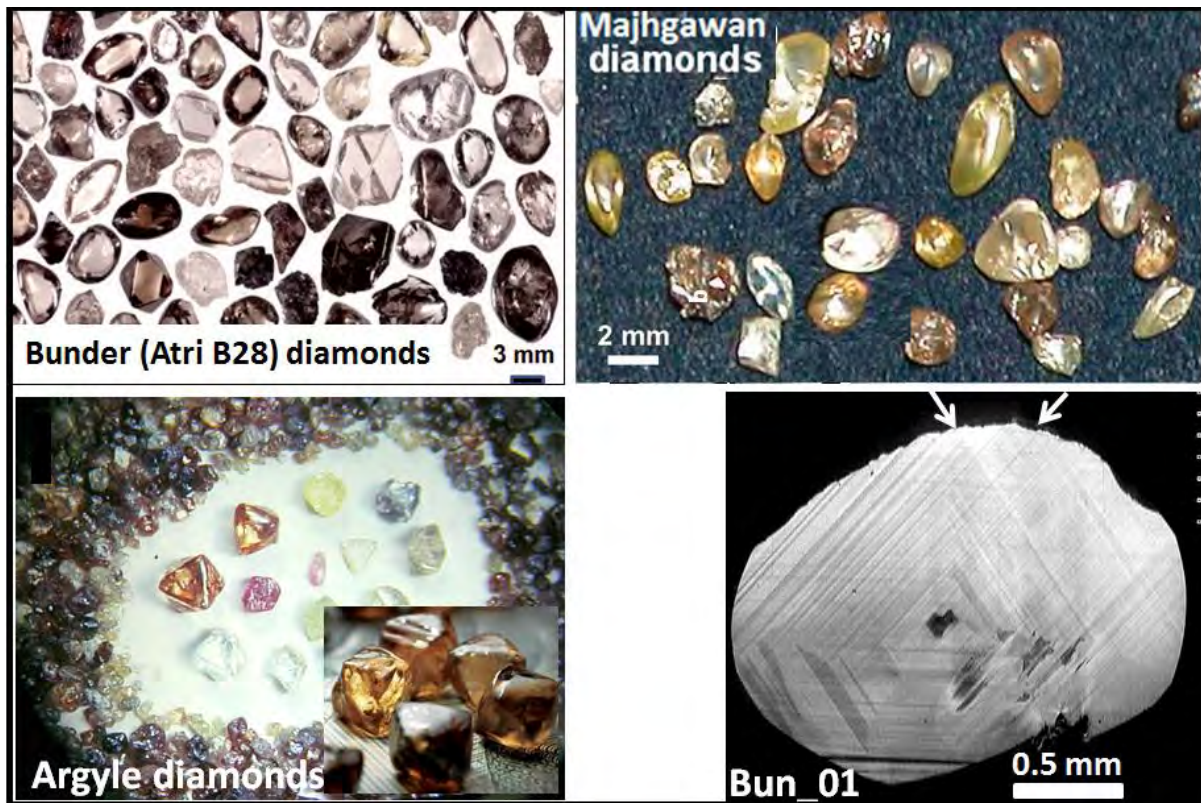


Fig. 2: Images of diamonds from Bunder, Majhgawan and Argyle. Note prominent brown colours. Bunder diamond Bun_01 shows prominent plastic deformation in two directions indicated by white arrows.

Such brown colour is found in diamonds of both peridotitic and eclogitic mantle hosts (Bulanova et al., in press). Bunder diamonds carry predominantly peridotitic inclusions of olivine ($\sim\text{Fo}_{92}$) and high Cr magnesiochromite suggestive of a harzburgitic domain, with a minor eclogitic component indicated by a kyanite inclusion (Smith et al., in press.). Majhgawan has inclusions of olivine, diopside, garnet and spinel (Fareeduddin and Mitchell, 2012). At Argyle, diamonds with eclogitic inclusions predominate (>90%) over peridotitic stones. The eclogitic diamonds have predominantly light C-isotopic compositions, contain mineral inclusions with high $\delta^{18}\text{O}$ values, and are inferred to have formed from subducted crustal carbon (Stachel et al., in press). Diamonds, also mainly brown in colour, have been recovered from peridotite xenoliths at Argyle (Jaques et al., 1990).

FTIR data indicate that Argyle diamonds have highly aggregated N. Temperatures calculated from N aggregation and mineral inclusions give main ranges of 1120-1250°C for Argyle peridotitic diamonds and 1240-1300 for eclogitic stones (Bulanova et al., in press.; Jaques et al. in press.; Stachel et al., in press.) This contrasts with the more moderately aggregated N in Bunder diamonds with indicated temperatures of 1140-1200°C (Smith et al., in press).

Conclusions

We therefore suggest a link between stress conditions in tectonic collision zones and adjacent craton margins and development both of diamonds, often brown and plastically deformed, and of host rocks of lamproite affinity. Such faulted and fractured terrains facilitate movement of fluids and magmas

and thus provide a craton margin diamond exploration target, alternative to traditional search for classical kimberlites in more central, structurally less disturbed, interior craton settings.

References

- Betts PG, Armit RJ, Stewart J, Aitken RAA, Ailleres L, Donchak P, Hutton L, Withnall L, and Giles D, (2015) Australia and Nuna. In: Li ZX, Evans DAD, Murphy JB, Eds., Supercontinent Cycles Through Earth History, Geological Society of London Special Publications, v. 424., pp. 47-81.
- Bulanova GP, Speich L, Smith CB, Gaillou L, Kohn SC, Wibberley E, Chapman JG, Howell D, Davy AT (in press) The unique nature of Argyle fancy diamonds: internal structure, paragenesis and reasons for color. In: Geoscience and Exploration of Rio Tinto's diamond deposits. Society of Economic Geologists, Inc., Special Publication.
- Chalapathi Rao NV (2005) A petrological and geochemical reappraisal of the Mesoproterozoic diamondiferous Majhgawan pipe of central India: evidence for transitional kimberlite – orangeite (group II kimberlite) – lamproite rock type. *Mineralogy and Petrology* v. 84, pp. 69–106.
- Das H, Kobussen AF, Webb K, Phillips D, Maas R, Soltys A, Howell D (in press) The Bunder diamond project, India: geology, petrography, geochemistry and age of the diamondiferous Atri pipes. In: Geoscience and Exploration of Rio Tinto's diamond deposits. Society of Economic Geologists, Inc., Special Publication.
- Fareeduddin, Mitchell RM (2012) Diamonds and their source rocks in India. Geological Society of India, Bangalore, 434 p.
- Jaques AL, Lewis JD, Smith CB (1986) The kimberlites and lamproites of Western Australia. *Geol. Surv. Western Australia, Bull.* 132, 268 p.
- Jaques AL, O'Neill HStC, Smith CB, Moon J, Chappell BW (1990) Diamondiferous peridotite xenoliths from the Argyle (AK1) lamproite pipe, Western Australia. *Contrib Mineral Petrol* 104:255-276
- Jaques AL, Luguét A, Smith CB, Pearson DG, Yaxley GM, and Kobussen A, (in press) Nature of the mantle beneath the Argyle AK1 lamproite 1 pipe: constraints from mantle xenoliths, diamonds and lamproite geochemistry. In: Geoscience and Exploration of Rio Tinto's diamond deposits. Society of Economic Geologists, Inc., Special Publication.
- Helmstaedt H., in press. Tectonic and structural controls on diamondiferous kimberlite and lamproite and their bearing on area selection for diamond exploration. In: Geoscience and Exploration of Rio Tinto's diamond deposits. Society of Economic Geologists, Inc., Special Publication.
- Mandal B, Sen MK, Rao VJ (2013) New seismic images of the Central Indian Suture Zone and their tectonic implications. *Tectonics*, v. 32, pp. 908–921
- Masun K, Sthapak AV, Singh A, Vaidya A, Krishna C, (2009) Exploration history and geology of the diamondiferous ultramafic Saptarshi intrusions, Madhya Pradesh, India. 9th IKC Proceedings, *Lithos* 112S: 142–154
- Mitchell RH, Bergman SC (1991) *Petrology of Lamproites*. Plenum Press, New York, 447 p.
- Mukherjee A, Rao KS, Bandyopadhyay D, Roy G (1997) Chemistry of garnet & ilmenite from Majhgawan diamondiferous pipe, Panna District, vis-a-vis diamond potential and preservation. *Journ. Geol. Soc. India*, v.50, pp.441-448
- Prasad BR, and Vijaya Rao V (2006) Deep seismic reflection study over the Vindhyan of Rajasthan: Implications for geophysical setting of the basin. *Journal of Earth System Science*, v. 115, pp. 135-147.
- Smith CB, Bulanova GP, Kobussen A, Burnham A, Chapman J, Davy AT, Sinha KK (in prep.). Diamonds from the Bunder lamproites and implications for the nature of the underlying mantle. In: Geoscience and Exploration of Rio Tinto's diamond deposits. Society of Economic Geologists, Inc., Special Publication.
- Stachel T, Harris JW, Hunt L, Muehlenbachs K, Kobussen A, EIMF (in press) Argyle Diamonds - How subduction along the Kimberley Craton edge generated the world's biggest Diamond Deposit. In: Geoscience and Exploration of Rio Tinto's diamond deposits. Society of Economic Geologists, Inc., Special Publication.
- Tyler IM, Hocking RM, Haines P (2012) Geological evolution of the Kimberley region of Western Australia: Episodes, v. 35, p. 298-306.

Kimberlite emplacement and mantle sampling through time at A154N kimberlite volcano, Diavik Diamond Mine

Moss, S.¹; Kobussen, A.²; Powell, W.²; Pollock, K.³; Cutts, J.⁴

¹ *Terram Vero Consulting Inc., Vancouver, Canada, smoss@terramvero.com*

² *Rio Tinto Exploration, Melbourne, Australia, alan.kobussen@riotinto.com, will.powell@riotinto.com*

³ *Diavik Diamond Mines Inc., Yellowknife, Canada, kpollock@riotinto.com*

⁴ *The University of British Columbia, Vancouver, Canada, jcutts@eos.ubc.ca*

Introduction

The Diavik Diamond Mine in the NWT of Canada (Fig. 1A, B) has produced in excess of 100 million carats from 3 kimberlite pipes since mining commenced in 2002, and geology work to support mining has generated new insights into the nature of kimberlite pipes at Lac de Gras to depths >700 m below surface. Here, we present new findings from deep (>400 m below surface) mining, sampling and drilling work on the A154N kimberlite volcano. The drilling and mining has revealed additional geological domains, and contact relationships apparent among the eight domains (Dueys, PK1-N, VRVK-1N, PK2-N, PK3-N, MRVK2-N, PK4-N, CK-N) allow for a sequential organization of emplacement events. Updated 3D internal geological models and pipe shapes for A154N are also presented which expand upon understandings of Lac de Gras kimberlite pipe morphology.

Representative populations of mantle minerals extracted from the various geological units corresponding to discrete kimberlite magmas at A154N are analyzed for major and trace elements, and provide insights into the nature of the mantle sampled through time in a single kimberlite volcano.

These findings require a revision of previous geological and emplacement models and provide a window into how the sub-continental lithospheric mantle (SCLM) below Diavik was sampled by kimberlite magmas through time.

Updated A154N architecture

Contact relationships apparent among the geological domains allow for a sequential organization of emplacement events, and identify as many as four temporally-discrete contributions of kimberlite magma within or surrounding A154N: (1) Dueys; (2) PK1-N; (3) PK3-N; (4) CK-N. Pipe excavation and deposit emplacements within A154N were preceded by emplacement of coherent kimberlite within a pre-existing structure known as “Dueys” striking at 030° (Dueys; Fig. 1C). The updated internal geology features two volcanic packages, each comprising massive, mud-poor, poorly-sorted pyroclastic deposits with minimal country rock clasts overlain by mud-rich, moderately- to well-sorted volcanoclastic deposits (i.e. PK1-N/MRVK1-N and PK3-N/MRVK2-N; Fig. 1C). Late stage coherent

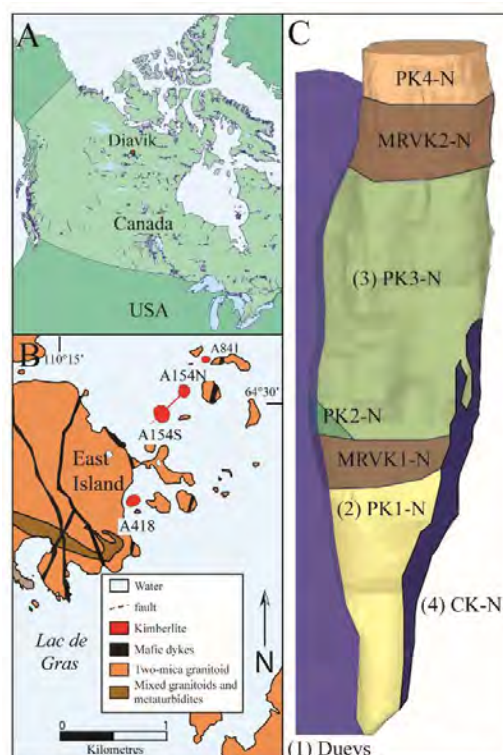


Figure 1: a) Location of Diavik within Northwest Territories of Canada; b) the kimberlite bodies at Diavik, superimposed on geological mapping of Lac de Gras area from Stuble (1998); c) schematic showing updated geological model of A154N comprising a precursor dyke (Dueys), and seven different geological domains. The relative timing of five temporally-discrete contributions of magma within or adjacent to A154N are shown with numbers 1 to 4. Modified from Moss et al. (2009).

kimberlite cross-cuts the deeper pyroclastic and volcanoclastic deposits (CK-N; Fig. 1). This layer-cake architecture is interpreted to represent two successive cycles of explosive eruption from within A154N followed by active and passive sedimentation from a presumed crater-rim, and the whole package of deposits are both preceded (i.e. Dueys) and followed (i.e. CK-N) by intrusions of coherent kimberlite. The top of A154N is infilled by an externally-sourced graded deposit of pyroclastic kimberlite (PK4-N) captured by and preserved within a maar crater as described by Moss et al. (2008; 2009).

Mineral chemistry

To support an investigation of how the SCLM was sampled through time at a single kimberlite volcano, a statistically significant and representative subset of garnet and clinopyroxene grains were extracted from each domain in A154N for mineral chemistry analysis. Major and trace element analyses were carried out on >600 garnet xenocrysts, using electron microprobe and laser ablation inductively coupled plasma–mass spectrometry, respectively. Garnet grains were classified based on their compositions according to Grütter et al. (2004). We utilized the empirical Ni-in-garnet thermometer as described by Ryan et al. (1996) to calculate equilibration temperatures for peridotitic garnets. Equilibration pressures for garnets were estimated by applying a “kinked” geotherm comprising 38 mW/km and 40 mW/km geotherms from Hasterok and Chapman (2011) to grains with calculated temperatures above and below 950°C, respectively. Chrome diopside compositions were used to estimate pressure and temperature conditions of formation using the thermobarometric methods of Nimis and Taylor (2000). Calculated garnet and chrome diopside pressures were translated to equivalent depths using an assumed density profile comprising 80% lithospheric mantle ($\rho = 3.30 \text{ g/cm}^3$) and 20% lithospheric crust ($\rho = 2.65 \text{ g/cm}^3$).

Calculated depths from cpx grains indicate that garnet lherzolite from the SCLM sampled by the kimberlite magmas feeding A154N ranged from depths of 100 km to 200 km depth. More than 75% of the grains among all domains are sourced from the 110-160 km depth range, and a relatively even distribution of the remaining grains are sourced from >160 km. Calculated depths indicate that kimberlite magmas emplaced in A154N sampled progressively deeper mantle through time (Fig. 2).

Garnets from two samples analyzed for minor elements and REE to date also show >75% of the grains are sourced from 110-160km, and a similar increase in sampling depth with time (Fig. 3). Lherzolic and harzburgitic garnets are present in similar abundances from 130 to 160 km in PK1-N. The earlier PK1-N mantle sample shows a distinctively higher relative proportion of harzburgite than that of the subsequently emplaced PK3-N which fills the majority of A154N. These results also collectively show a restricted depth range from which the majority of mantle peridotite was sampled for two key pipe-filling deposits.

The Zr, TiO₂, Y and Ga compositions of peridotitic garnets are evaluated over the range of estimated depths to test models of the SCLM underlying the central Slave terrane. Preliminary results show an increase in Y, Zr and TiO₂ corresponding to depths of approximately 160km.

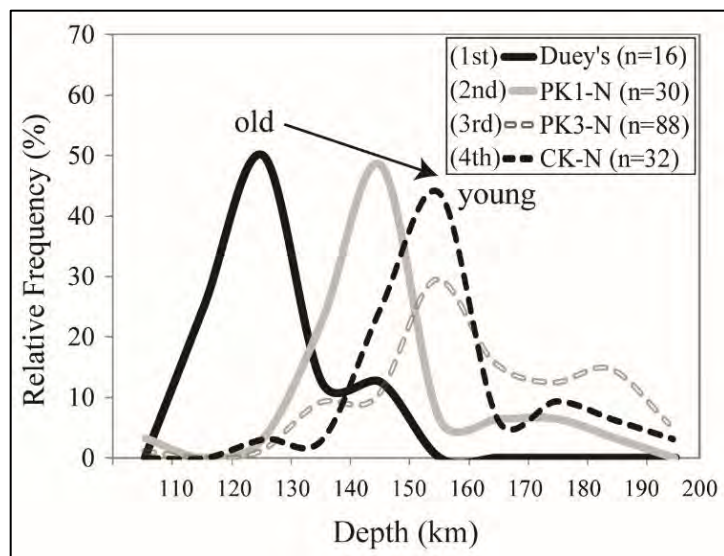


Figure 2: Relative abundances of calculated source depths of clinopyroxene among magmatic and pyroclastic deposits at A154N. The known relative timing indicates magmas emplaced at surface entrained successively deeper mantle through time.

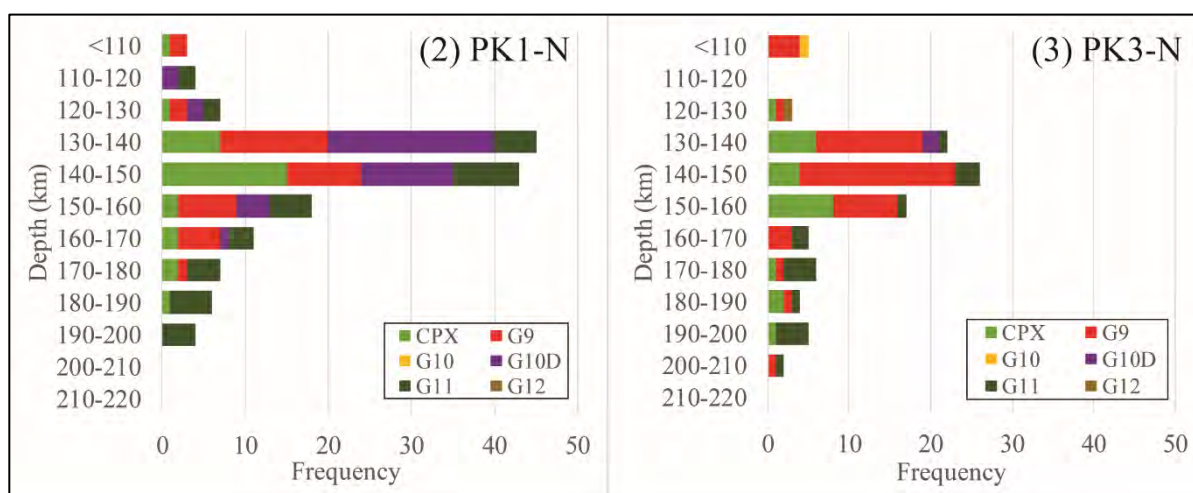


Figure 3: Calculated source depths for clinopyroxene and peridotitic garnets. Thermobarometry techniques described by Nimis and Taylor (2000) and Ryan et al. (1996) were applied to PK1-N and PK3-N, and converted to equivalent depths. Parentheses indicate relative timing of emplacement of kimberlite source magmas within A154N. Peridotitic garnets classified using Grütter et al. (2004): G9 = lherzolitic garnet; G10 = harzburgitic garnet; G10D = harzburgitic garnet consistent with inclusions in diamond; G11 = High-Ti peridotitic garnet; G12 = wehrlitic garnet.

Raman spectroscopy techniques are used to calculate pressures of formation for inclusions in diamonds from select units, and results test the hypothesis that, in contrast to the garnet lherzolite sample, the diamonds in each kimberlite magma emplaced at A154N are sourced from a common depth horizon.

These findings both complement and contradict aspects of current models for mantle stratigraphy of the central Slave SCLM (e.g. Griffin, et al. 1999), and have potential implications upon the application of mantle mineral chemistry in exploring for and evaluating kimberlite bodies.

References

- Griffin W, Doyle B, Ryan C, Pearson N, O'Reilly S, Davies R, Kivi K, Van Achtebergh E, Natapov L (1999) Layered mantle lithosphere in the Lac de Gras area, Slave craton: composition, structure and origin. *Journal of Petrology* 40(5):705-727
- Grütter HS, Gurney JJ, Menzies AH, Winter F (2004) An updated classification scheme for mantle-derived garnet, for use by diamond explorers. *Lithos* 77(1-4):841-857
doi:10.1016/j.lithos.2004.04.012
- Hasterok D, Chapman D (2011) Heat production and geotherms for the continental lithosphere. *Earth and Planetary Science Letters* 307(1):59-70
- Moss S, Russell JK, Andrews GDM (2008) Progressive infilling of a kimberlite pipe at Diavik, Northwest Territories, Canada: Insights from volcanic facies architecture, textures, and granulometry. *Journal of Volcanology and Geothermal Research* 174(1-3):103-116
doi:10.1016/j.jvolgeores.2007.12.020
- Moss S, Russell JK, Brett RC, Andrews GDM (2009) Spatial and temporal evolution of kimberlite magma at A154N, Diavik, Northwest Territories, Canada. *Lithos* 112, Supplement 1(0):541-552
doi:10.1016/j.lithos.2009.03.025
- Ryan CG, Griffin WL, Pearson NJ (1996) Garnet geotherms: Pressure-temperature data from Cr-pyroxene garnet xenocrysts in volcanic rocks. *Journal of Geophysical Research: Solid Earth* 101(B3):5611-5625
- Stubley MP (1998) Bedrock Geology of the East Island Area, Lac de Gras, unpublished internal report prepared for Diavik Diamond Mines Inc.

Natural diamond growth conditions recorded by their internal structures.

Galina P. Bulanova¹, Chris B. Smith¹, Simon C. Kohn¹ and Laura Speich¹

¹ University of Bristol, Bristol, UK, galina_bulanova@hotmail.com; chris_b_smith@btopenworld.com; simon.kohn@bristol.ac.uk; laura.speich@bristol.ac.uk

Introduction

Kimberlite and lamproite-hosted diamonds originate in a variety of lithospheric and sublithospheric mantle environments. They are thought to form by the reactions between fluids (derived from the asthenosphere or subduction processes) with mantle peridotite or eclogite over time from Archean to Proterozoic. We describe conditions under which such processes evolve (free or restricted space for growth, stable or dynamic systems, presence or absence of stress), as recorded by diamond growth structures and defects in the crystals observed by optical methods in polished central plates of diamonds. We analyse conditions of diamond formation in different mantle settings and investigate the dissimilarities in growth history of the diamonds and the spatial distribution of nitrogen (N) content and model temperatures calculated from aggregation.

Samples and analytical methods

The internal structures of 250 octahedral or dodecahedral lithospheric macro-diamonds from Russian (Mir, Udachnaya, Aikhal), Zimbabwean (Murowa, Sese), Canadian (Diavik) kimberlites, and from Australian (Argyle) and Indian lamproites (Bunder) were studied. Additionally, 70 sublithospheric (SL) diamonds of more complex resorbed shape from Juina-5, Collier-4 kimberlites, Machado River alluvials (Brazil), and 30 diamonds of un-conventional lamprophyric origin from the Dachine komatiite (French Guyana, Smith et al., 2016) were investigated. All analytical work was done at the University of Bristol. The diamonds were polished along two parallel dodecahedral planes for production of central plates to reveal internal structures. Cathodoluminescence images were taken using a scanning electron microscope (SEM). Core-rim diamond traverses for nitrogen (N) content and aggregation were performed using a Thermo iN10MX infrared microscope. Mineral inclusion compositions were determined by electron microprobe analysis.

Results

Most peridotitic (P) and eclogitic (E) diamonds from kimberlites have simple octahedral zonation (Fig 1a, b). Rarely, sectorial or cubic initial growth occurs, changing into octahedra in later stages.

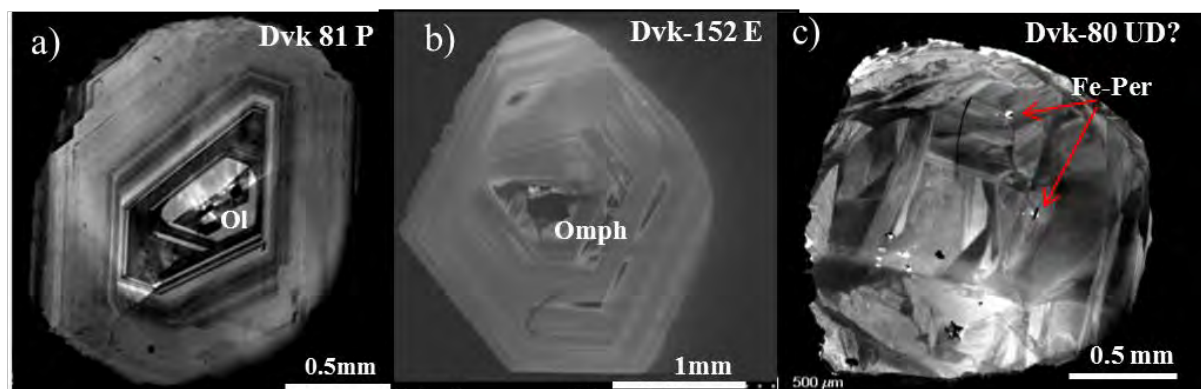


Figure 1: Internal zonation of diamonds from kimberlites (Diavik): a). Sharp octahedral zonation and external resorption of P diamond; b). Weak octahedral zonation in eclogitic crystal; c). Blocky texture of SL diamond.

E diamonds from Argyle lamproites grew with narrow octahedral zones with minor internal resorption (Fig. 2a). Small Argyle P diamonds have sharp octahedral zonation (Fig 2b), but some of the larger, strongly resorbed P stones display sectorial growth as well (Fig. 2c).

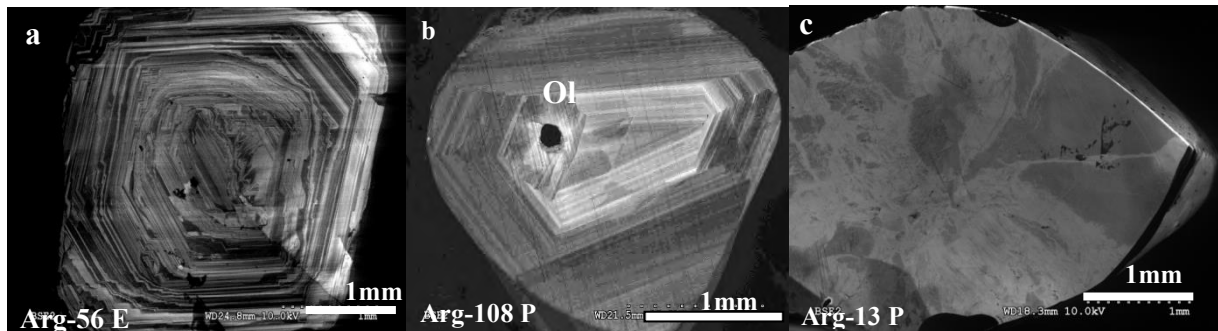


Figure 2: Internal morphology of diamonds from Argyle lamproites (explanations are given in the text)

Sublithospheric stones (Fig 3a, b and 1a) and Dachine diamonds (Fig. 3c) are characterised by very weak or lack of zonation, by complex internal structures, blocky textures, stress and internal cracks.

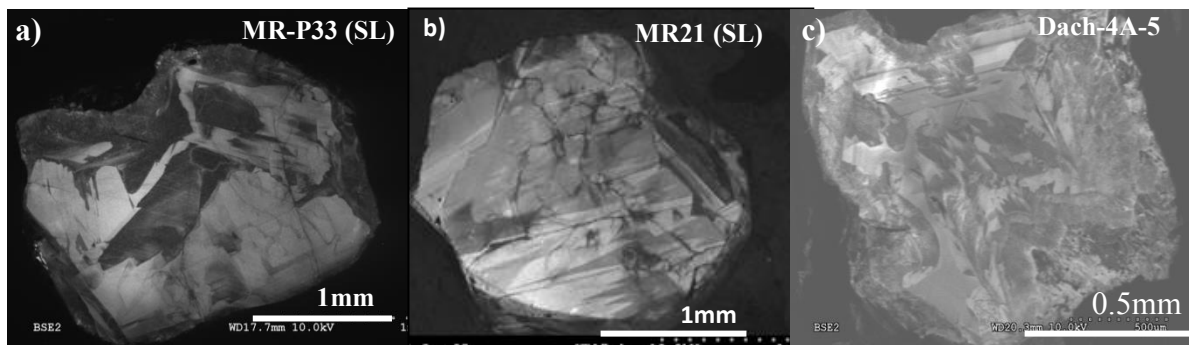


Figure 3: Internal structure of SL (a, b), and unconventional (c) diamonds (see text for descriptions).

Argyle eclogitic stones and sublithospheric diamonds are the most defective, displaying brittle and plastic deformation, resorption and re-growth features. Thus the central zone of Arg pink-3 crystal is a broken diamond (Fig. 4a), giving an example of brittle deformation (see arrow in Fig.) taking place during crystal formation. Arg pink-2 eclogitic diamond shows octahedral zonation with simultaneous minor internal resorption/regrowth shown by arrows in Fig. 4b. Occurrence of internal twinning during growth of P diamond is displayed in Fig 4c.

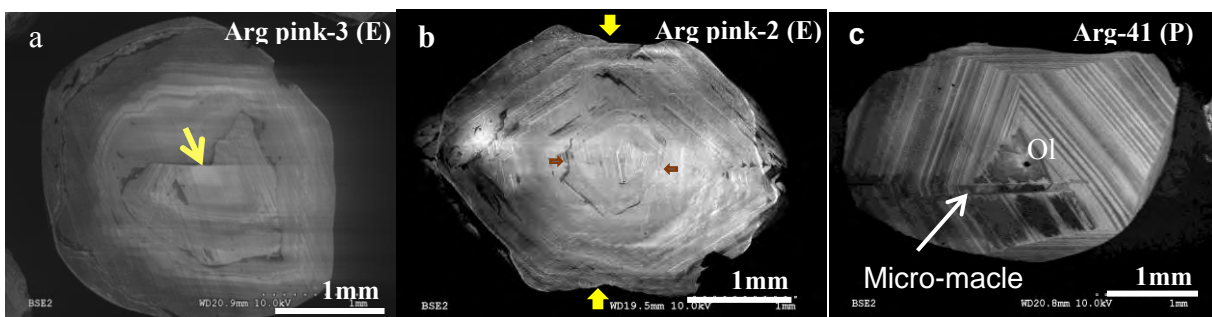


Figure 4: Internal breakages, resorption-regrowth and twinning in Argyle diamonds (Bulanova et al, 2017).

In agreement with previous observations, N concentration is greater in the core growth zones, relative to the rims of lithospheric P and E diamonds. However, this is not always the case (Fig 5), as different patterns can include (i) concentric octahedral zones with changing or oscillating N concentrations (Sese 1-58.8, Dvk 143, Mur-265); (ii) non-concentric heterogeneity, particularly in core zones (Mir-1164). Model temperatures can be calculated from such data sets, and for zoned diamonds additional

constraints on thermal history can be deduced (Kohn et al., 2016). Most sublithospheric stones are type II (N free) diamonds.

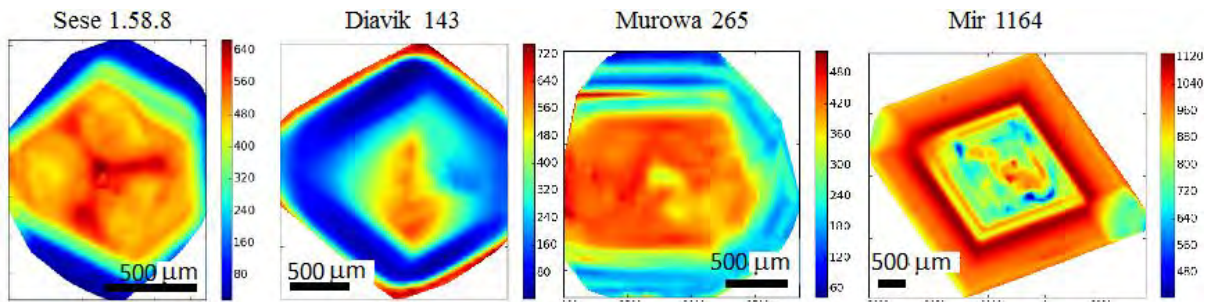


Figure 5: Distribution of N in typical lithospheric diamonds in FTIR maps. The scale bar represents ppm N.

Discussion and Conclusions

We conclude that P and E lithospheric diamonds have mainly octahedral zonation, sometimes with sectorial, cubic or cubo-octahedral growth during initial stages of origin (Fig. 5). The majority of SL and Dachine diamonds show lack of zoning but are blocky, brecciated and deformed (Fig. 5).

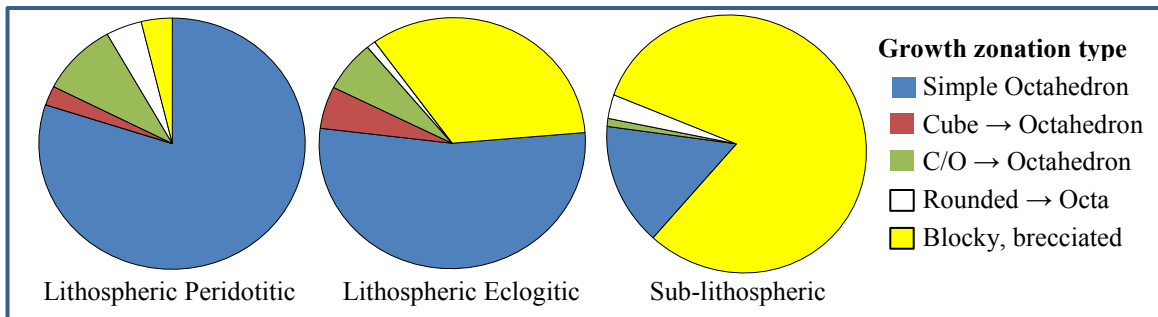


Figure 6: Comparison of growth zonation type abundances in the 350 studied diamonds

Therefore, internal structures in diamonds from different tectonic settings vary, recording variable formation conditions. Octahedral zonation in lithospheric P and E diamonds formed by layer by layer growth from fluids/melts of low to moderate degree of carbon supersaturation (Sunagawa, 1984), under relatively stable conditions in sufficient space where idiomorphic crystals can originate (Chernov, 1984). SL, Dachine, and Argyle E diamonds grew as metasomatic crystals during subduction processes from fluids of moderate to high degrees of carbon supersaturation, and in restricted spaces, such as veins and cracks. Geothermometry, based on N contents, aggregation state, and age relationships of the diamonds, shows that most lithospheric stones have temperatures corresponding with a $\sim 40\text{mW/m}^2$ model geotherm and a lithospheric keel depth of $\sim 180\text{-}200$ km. SL diamonds grew at depths ranging down to the Transition Zone and Lower Mantle.

References

- Bulanova GP, Speich L, Smith CB, Gaillou E, Kohn SC, Wibberley E, Chapman JG, Howell D, Davy AT (2016) The unique nature of Argyle fancy diamonds: internal structure, paragenesis and reasons for color. In: *Geoscience and Exploration of Rio Tinto's diamond deposits*. Society of Economic Geologists, Inc., Special Publication (in press).
- Chernov AA (1984) *Modern crystallography III.*, Springer, New York, Tokyo. 517pp.
- Kohn SC, Speich L, Smith CB, Bulanova GP (2016) FTIR thermochronometry of natural diamonds: a closer look. *Lithos* 265: 148-158
- Smith CB, Walter MJ, Bulanova G, Mikhail S, Burnham A, Gobbo L, Kohn S (2016) Diamonds from Dachine, French Guiana: A unique record of early Proterozoic subduction. *Lithos* 265: 82–95.
- Sunagawa I (1984) Morphology of natural and synthetic diamond crystals. In: Sunagawa, I., *Materials Science of the Earth's interior*. Terra Scientific Publishing, Tokyo, 303–330.



The nitrogen budget of subducted crust

A.D. Burnham¹, S. Mikhail², G.P. Bulanova³ and C.B. Smith³

¹Research School of Earth Sciences, Australian National University, Acton ACT 2601, Australia

antony.burnham@anu.edu.au

²School of Geography and Earth Sciences, University of St Andrews, St Andrews, KY16 9AJ, Great Britain

³School of Earth Sciences, University of Bristol, Bristol, BS8 1RJ, Great Britain

Background

Nitrogen is a volatile, atmophile element whose terrestrial cycle has not been adequately constrained. Nitrogen speciation in fluids is complex, controlled by oxygen fugacity, pH, temperature and pressure (Mikhail et al., 2017); moreover, microanalysis of N can be challenging.

One indicator that N is subducted back into the mantle is that N concentrations in diamonds from an eclogitic paragenesis are generally higher than those in peridotitic diamonds. However, it has to date been unclear whether N can be hosted in significant concentrations by other minerals in eclogites. The mostly likely method for N to be present in silicates is as the ammonium (NH₄⁺) ion. The charge and size of this ion indicate that it is likely to have similar chemistry to Rb, and therefore should be most abundant in K-rich minerals. In diamonds from Argyle, Western Australia, the concentrations of K₂O in omphacite can be as high as 1.4 %, which, in addition to the high modal abundance of omphacite, makes this mineral likely to be the most significant host of NH₄⁺ in the subducted slab. We aim to present ion probe measurements of N from Argyle diamond inclusions to evaluate the range of possible N fluxes to the mantle.

Omphacite inclusions were analysed by EPMA for major element composition and using the SHRIMP-RG ion probe for N contents. The SHRIMP-RG measurements used the ¹⁴N⁺/²⁸Si²⁺ ratio, referenced to synthetic buddingtonite (NH₄AlSi₃O₈). A small subset of inclusions were observed *in situ* and the N content of the diamond adjacent to the inclusion was measured by SHRIMP to determine $D_N^{\text{omphacite/diamond}}$.

Table 1. Compositions of omphacite inclusions from Argyle diamonds, as determined by EPMA.

| | A70 | A110 | A112 | A116 | A145 | ARG103 |
|--------------------------------|--------|--------|--------|--------|--------|--------|
| SiO ₂ | 56.01 | 56.20 | 54.22 | 56.76 | 55.84 | 55.09 |
| TiO ₂ | 0.61 | 0.51 | 0.73 | 0.46 | 0.69 | 0.51 |
| Al ₂ O ₃ | 13.04 | 13.76 | 8.20 | 17.22 | 12.98 | 10.01 |
| Cr ₂ O ₃ | <0.04 | <0.04 | <0.04 | <0.04 | <0.04 | <0.04 |
| FeO | 4.88 | 3.30 | 7.74 | 4.23 | 6.23 | 5.62 |
| MnO | 0.04 | 0.03 | 0.09 | 0.04 | 0.06 | 0.08 |
| MgO | 7.00 | 7.69 | 9.62 | 4.61 | 6.63 | 8.72 |
| CaO | 10.93 | 11.25 | 14.75 | 8.26 | 10.11 | 13.08 |
| Na ₂ O | 6.97 | 6.74 | 4.11 | 8.68 | 7.41 | 4.81 |
| K ₂ O | 0.72 | 1.23 | 0.69 | 0.33 | 0.73 | 1.12 |
| P ₂ O ₅ | <0.05 | <0.05 | <0.05 | <0.05 | 0.07 | n.a. |
| NiO | <0.04 | <0.04 | <0.04 | <0.04 | <0.04 | <0.04 |
| Total | 100.22 | 100.70 | 100.14 | 100.58 | 100.76 | 99.06 |

N concentrations will be presented in due course.

Reference

Mikhail S, Barry PH and Sverjensky DA (2017) The relationship between mantle pH and the deep nitrogen cycle. *Geochim. Cosmochim. Acta* 209: 149-160



The mantle of Scotland viewed through the Glen Gollaidh aillikite

M. T. Hutchison¹, J. W. Hughes², J. W. Faithfull³

¹ *Trigon GeoServices Ltd., Las Vegas, NV, USA, mth@trigon-gs.com*

² *Department of Earth Sciences, University of Durham, Durham, UK, joshua.w.hughes@durham.ac.uk*

³ *Hunterian Museum, University of Glasgow, Glasgow, UK, John.Faithfull@glasgow.ac.uk*

Introduction

Smith et al. (2008) and Faithfull (2012) describe a carbonate-rich olivine macrocrystal dyke in Sutherland, Scotland. The 1 m wide dyke, named after its location in Glen Gollaidh, outcrops at 58.3675°N 4.6975°W, to the west of Ben Hope. Stream-bed outcrops can be seen at two further locations <75 m west northwest along the Allt Strath Feinne-Bheinn and a fourth lies 250 m east southeast along the ca. 100° strike (Hughes, 2012).

Primary minerals consist of olivine (fresh and serpentinised), calcite, phlogopite (tetraferriphlogopite rims), clinopyroxene (cpx), apatite, chromite, magnetite, and accessory perovskite, rutile, Ca–Ti–(REE) and Zr oxides. The presence of primary cpx precludes identification as kimberlite. However, mineralogy and bulk chemistry (Hughes, 2012) are consistent with a classification as aillikite (after Tappe et al. 2005). Mineralogy is variable with parts of the dyke transitioning to carbonatite (> 50% carbonate), in a similar fashion to aillikite / carbonatite associations in West Greenland (Hutchison and Frei, 2009). Larger olivines and orthopyroxene (opx) xenocrysts and abundant serpentinised spinel lherzolite xenoliths (≤3 cm) reflect a mantle component. Weathered surfaces show the very competent, sandpaper textured orange-brown knobbly appearance ubiquitous in North Atlantic Craton (NAC) aillikites (Hutchison and Frei, 2009).

Age determination

Five batches of groundmass phlogopite separates were dated at the SUERC Argon Isotope Facility, East Kilbride, UK. ⁴⁰Ar/³⁹Ar geochronology gives a late Devonian emplacement age of 363 Ma (±2 Ma 2σ; MSWD 1.63, n = 17). Caledonian metamorphism associated with the Moine Thrust largely ceased at 429 Ma (Goodenough et al. 2011) although some minor alkali intrusives and fenitised rocks along the Great Glen are as young as ca. 390 Ma (Macdonald and Fettes, 2007). The Glen Gollaidh emplacement age is ca. 50 Ma after the final closure of the Iapetus and pre-dates the intra-plate alkali magmatism that affected southern Scotland from ca. 350 Ma. Aillikites have not otherwise been recorded in the UK and with an age determination, the Glen Gollaidh dyke provides an opportunity to study the mantle component of the Scottish part of the NAC in the specific context of the late Devonian.

Mantle mineralogy

A single 9.8 kg sample was disaggregated to <1 mm in two batches by high-voltage pulse fragmentation (SelFrag AS) with all fines retained. All 6.05 kg of 0.25–1.0 mm grains, and 500g of 0.18–0.25 mm were liquid density separated (S.G. 2.96; SRC, Saskatchewan) with a purpose-designed flowsheet built to retain any microdiamonds. After mineral picking, 38 g of sample was archived and the total remaining sample was treated by caustic fusion. While all fifteen quality-control tracer diamonds were recovered, the aillikite was found to be barren of diamond to the minimum size of 0.075 mm tested. Inspection of heavy mineral concentrates recovered abundant chromites, Cr-diopsides (in both size fractions) and four olivine grains (> 0.25 mm). No perovskite, picro-ilmenite or garnet was identified.

Major element chemistry was determined by Cameca SX100 electron microprobe (15 keV, 10 and 100 nA; Univ. Edinburgh) with minerals classified following references in Hutchison and Frei (2009). The large majority of picked spinels are Mg, Al chromites with compositions coinciding with chromites in kimberlites, within the garnet peridotite field (based on Ti and Cr content; Grütter and Apter, 1998) and describing the spinel Trend 2 based on divalent / trivalent cations. Cr content (<47.2% Cr₂O₃) is not

high enough to be consistent with the diamond stability field. Cpx compositions range from 2.6–6.6 wt% Al₂O₃ and 19.9–23.9 wt% CaO encompassing, at one place, most of the ‘remarkable range’ (Upton et al. 2011) exhibited by Scottish mantle-derived cpx compared to world-wide xenolith localities. Based on Cr and Al content, the majority of Cr-diopsides are consistent with spinel lherzolite compositions (CLS) although a significant proportion (30%) also plot in the garnet peridotite (CGP) field with Cr₂O₃ content up to 1.56%. Olivines are Mg-rich (Fo₈₉ – Fo₉₁) and, with Ni contents (confirmed by trace element measurements) in excess of 3000 ppm, are more similar to those from Type Ia kimberlites than aillikites found elsewhere in the North Atlantic Craton, in West Greenland (Hutchison and Frei, 2009).

Concentrations for 27 trace elements were determined by laser ablation inductively coupled plasma-mass spectrometry (ICP-MS; 47–137 µm, 5 and 10 Hz; ANU, Canberra). Cr-diopsides express four distinct rare-earth element (REE) trends. Of 41 grains, the most common trend (63%) shows a LREE enrichment up to 50x chondrite, to chondritic values amongst the HREE. Trends are similar to those from Rinibar cpx (north of Glen Gollaidh; Upton et al. 2011). A further 22% of grains show the opposite trend: La and Ce are slightly enriched (some with Ce enriched over La relative to chondrite), Nd and Sm have chondritic values and HREE are up to 10x chondrite. Five grains (12%) show a flat REE trend consistently close to 10x chondritic and similar to trends from Streap Com’Laidh and Fidra cpx (south of Glen Gollaidh; Upton et al. 2011). A single outlier shows a sinuous trend, LREE enriched and with a minimum at Dy (0.49 ppm) resembling the average Rinibar samples of Hughes et al. (2015).

Mantle conditions

The Glen Gollaidh dyke is hosted within the Neoproterozoic sedimentary rocks of the Moine Supergroup. However, it occurs ca. 4 km east of the Moine Thrust, marking the westernmost extent of the Caledonian metamorphism in Britain. Mantle mineralogy and the proximity to the Moine Thrust leads to the conclusion that the dyke overlies buried Lewisian sub-continental lithospheric mantle, the crustal counterpart of which dominates outcrops in Scotland lying to the west of the Moine Thrust. The Lewisian comprises a part of the reworked North Atlantic Craton (NAC) mobile belt, most of which is preserved to the north west in the previously adjoining Greenlandic component, there termed the Nagssugtoqidian Orogen. The Glen Gollaidh dyke lies almost exactly half way between Loch Roag and Rinibar mantle peridotite suites, both of which are concluded by Hughes et al. (2015) to evidence an underlying keel of NAC which is not present ca. 175 km south at Streap Com’Laidh.

The absence of garnet, relatively low Cr-content chromite and spinel lherzolite Cr-diopside compositions are consistent with the failure of the small sample tested to yield diamonds. The cratonic root underlying the Glen Gollaidh aillikite during the late Devonian was apparently too thin to lie within the diamond stability field, consistent with xenoliths from alkali basalts elsewhere in Scotland (Upton et al. 2011). Examples of diamond-hosting rocks with spinel rather than garnet lherzolites are known (Archangelsk, Russia; Capita and Lehmann, 2000) but they are very rare. The small sample size tested for diamonds does not definitively prove that the body is non-diamondiferous but the negative result for both garnet and diamond makes the commercial prospects of the dyke itself very unlikely.

Despite the dominant affinities with spinel lherzolites, LREE-enriched clinopyroxene is consistent with crystallisation with garnet as are a significant portion of grains’ major element compositions. Opx has been identified in lherzolite xenoliths but in the absence of opx chemistry, the opx-cpx solvus thermometer (Bertrand and Mercier, 1985) provides minimum temperature estimates. Cr-diopside compositions require at least 22 kbar (65 km) to give an average minimum temperature of 961°C. Given the spread of data, this is the smallest pressure which results in cool enough temperatures for some cpx compositions to coincide with even a warm (42 mWm⁻²) geotherm. More robust geothermobarometry is warranted. However, calculations place some mantle components from the dyke close to the spinel-garnet transition (although firmly within the graphite stability field) and consistent with the conclusions from independent mineral chemistry. Despite the absence of diamond, mineral chemistry potentially places the dyke as hosting some of the deepest mantle components recovered in the UK. The Glen

Gollaidh aillikite apparently sat at the edge of diamond-prospective mantle suggesting diamond potential a short distance to the west within the Lewisian and also what is now East Greenland.

Isotopic and bulk rock trace element data suggest a highly enriched lithospheric source (Faithfull, 2012). On the Isle of Lewis, the Loch Roag monchiquite dyke (Menzies et al. 1989) has a similar enriched trace-element signature. High LREE enrichment can imply partial melting in equilibration with garnet. Alternatively, the apparent absence of garnet supports small degrees of melting of shallower, previously metasomatised mantle, favoured by Upton et al. (2011). It is apparent from other studies (e.g. Upton et al. 2011; Hughes et al, 2015) that the Scottish mantle has experienced an unusually complex history of fragmentation, amalgamation and sporadic metasomatism. This conclusion is very much borne out at Glen Gollaidh, particularly in the considerable variability in spinel and clinopyroxene compositions. Likely the variability reflects a large depth range sampled within the mantle contributing to the Glen Gollaidh aillikite, and its late Devonian age after the conclusion of the upheavals associated with the closure of the Iapetus and accumulation of Laurussia (Macdonald and Fettes, 2007).

Study of the Glen Gollaidh aillikite provides closer understanding of the limits of diamond prospective areas at the peripheries of the NAC, likely a relatively short distance to the north and west. Furthermore, the considerable variability of mantle geochemistry at Glen Gollaidh represents a microcosm of North Atlantic Craton evolution supporting a complex multi-component evolution and justifying further work.

Acknowledgements Brian Upton (Univ. Edinburgh; guidance), Dan Barfod (SUERC; geochron.), Chris Hayward (Univ. Edinburgh; electron probe), Hugh O'Neill, Greg Yaxley, Jung-Woo Park (ANU; ICP support), Wayne Taylor (ICP standards), Alex Weh (Selfrag), Cristiana Mirceau (SRC; sample processing), and Heather Gow (site access) are gratefully acknowledged.

References

- Bertrand P, Mercier J-CC (1985) The mutual solubility of coexisting ortho- and clinopyroxene: toward an absolute geothermometer for the natural system? *Earth Planet Sci Lett* 76:109–122
- Capita AA, Lehmann B (2000) The new Archangelsk diamond province, NW Russia. *Erzmetall* 53:357–363
- Faithfull JW (2012) Gem sapphire and diamond potential in NW Scotland. *Trans Inst Min Met B* 120:64
- Goodenough KM, Millar I, Strachan RA, Krabbendam M, Evans JA (2011) Timing of regional deformation and development of the Moine Thrust Zone in the Scottish Caledonides: constraints from U–Pb geochronology of alkaline intrusions. *J Geol Soc London* 168:99–144
- Grütter HS, Apter DB (1998) Kimberlite- and lamproite-borne chromite phenocrysts with “diamond inclusion”-type chemistries. 7th Int Kimb Conf Ext Abstr, pp 280–282
- Hughes HSR, McDonald I, Faithfull JW, Upton BGJ, Downes H (2015) Trace-element abundances in the shallow lithospheric mantle of the North Atlantic Craton margin: Implications for melting and metasomatism beneath Northern Scotland. *Mineral Mag* 79:877–907
- Hughes JW (2012) The First Reported Occurrence of Aillikite from the United Kingdom: Potential for the GLSDP? MSci thesis, Cardiff University
- Hutchison MT, Frei D (2009) Kimberlite and related rocks from Garnet Lake, West Greenland, including their mantle constituents, diamond occurrence, age and provenance. *Lithos* 112S:318–333
- Macdonald R and Fettes DJ (2007) The tectonomagmatic evolution of Scotland. *Trans Royal Soc Edinburgh: Earth Sci* 97:213–295
- Menzies MA, Halliday AN, Hunter RH, MacIntyre RM, Upton BJB (1989) The age, composition and significance of a xenolith-bearing monchiquite dike, Lewis, Scotland. *Geol Soc Australia Spec Publ.* 14:843–852
- Smith CG, Faithfull JW, Jackson B (2008) Gemstone prospectivity in Scotland. In: Walton G (ed) *The proceedings of the 14th Extractive Industry Conference*. EIG Conferences, pp 9–11
- Tappe S, Foley SF, Jenner GA, Kjarsgaard BA (2005) Integrating ultramafic lamprophyres into the IUGS Classification of Igneous Rocks: Rationale and implications. *J Petrol* 46:1893–1900
- Upton BGJ, Downes H, Kirstein LA, Bonadiman C, Hill PG, Ntaflos T (2011) The lithospheric mantle and lower crust–mantle relationships under Scotland: a xenolithic perspective. *J Geol Soc London* 168:873–885

Geology of the Snap Lake kimberlite dyke, Northwest Territories, Canada, and its metasomatic interaction with granite

Alexandrina Fulop¹, Maya Kopylova², Pamela Ellemers¹, Charlene Squibb³

1. De Beers Canada; 300-1601 Airport Rd., Calgary, Alberta, T2E 6Z8; Alexandrina.Fulop@debeersgroup.com; Pamela.Ellemers@debeersgroup.com
2. University of British Columbia, 2207 Main Mall, Vancouver, British Columbia, V6T1Z4. mkopylov@eoasubc.ca
3. De Beers Canada; 300, 5120 49 Street, Yellowknife, Northwest Territories X1A1P8. Charlene.Squibb@debeersgroup.com

Introduction

Carbonate-rich intrusions in contact with felsic rocks theoretically should show metasomatism due to their contrasting compositions. In reality, though, metasomatism is rarely reported on kimberlite contacts. We present the first documented case of a metasomatically-produced mineralogical zonation in a kimberlite, the Snap Lake dyke. Our detailed petrographic, mineralogical and geochemical study is based on more than 100 logged drill core, 400 thin sections, >400 whole rock and microprobe analyses, detailed profiles through the contacts, powder and single-crystal X-ray diffractometry, and microdiamond data.

The Snap Lake kimberlite dyke dated at 523 +/- 6.9 Ma is located in the south-central Slave Craton of northern Canada and intrudes granitoids and basic amphibolite-bearing metavolcanic rocks. The Snap Lake dyke is comprised of volumetrically prevalent hypabyssal xenolith-poor kimberlite (HK) and two types of kimberlite breccia enriched in granite and metavolcanic xenoliths. Fresh hypabyssal kimberlite (HK1) in the center of the thick dyke transitions to altered kimberlite (HK6) at the contact with granite through consecutive zones (HK2-6) parallel to the dyke walls (Fig. 1a). The same progression of alteration zones several centimeters wide develops around granite xenoliths (Fig. 1a). In thin dykes only the HK6 kimberlite facies is present. Kimberlite in alteration zones HK2-6 is richer in granite xenoliths (10-50 vol.%) than fresh kimberlite HK1 (0-5%). The progressive changes in the kimberlite mineralogy and texture towards dyke margins are not observed where the dyke intrudes metavolcanics (Fig. 1b).

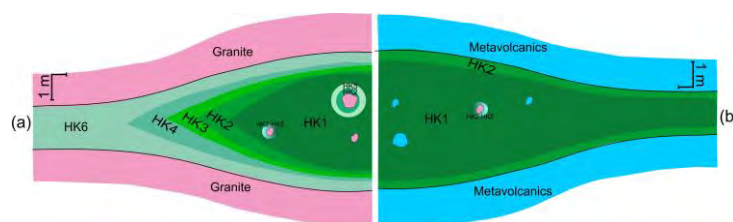


Figure 1: Zonation of alteration in the Snap Lake kimberlite dyke in contact with granite and metavolcanic rocks.

Petrography and bulk rock composition of the Snap Lake kimberlite

HK1 is comprised of olivine macrocrysts and microcrysts, and phlogopite macrocrysts set in a groundmass of monticellite, phlogopite, spinel, perovskite, and apatite crystals with interstitial lizardite and carbonate (Fig. 2a, b). Fresh olivine macrocrysts Fo 91-92% and perovskite are identified exclusively in HK1. The groundmass carbonate in rare samples with fresh olivine is represented by calcite with up to 0.2 wt% SrO; in all other samples the groundmass carbonate is dolomite. The spinel-group mineral is titanian magnesiochromite throughout the entire dyke. The total amount of phlogopite increases from HK1 to HK4 at the expense of serpentine, olivine, and monticellite, and then decreases from HK4 to HK6 as it is progressively replaced by multiphase phyllosilicates. The phlogopite changes its shape from elongate poikilitic with inclusions of monticellite and spinel in

HK1, to short prismatic tabular in HK3 (Fig. 2a, b). Morphology and texture of phlogopite types correlate well with their compositions, with poikilitic phlogopite being richer in Ba and more severely zoned than tabular grains. The most altered HK6 is an equigranular rock made of tabular grains of a cryptocrystalline multiphase phyllosilicate composed of phlogopite + lizardite + chlorite + talc, but optically resembling phlogopite (Fig. 2c, d).

The Snap Lake kimberlite is petrographically classified as Group I. Geochemically, it is similar to Group II kimberlite reflecting the abnormally high abundance of mica for a Group I kimberlite (Fig.

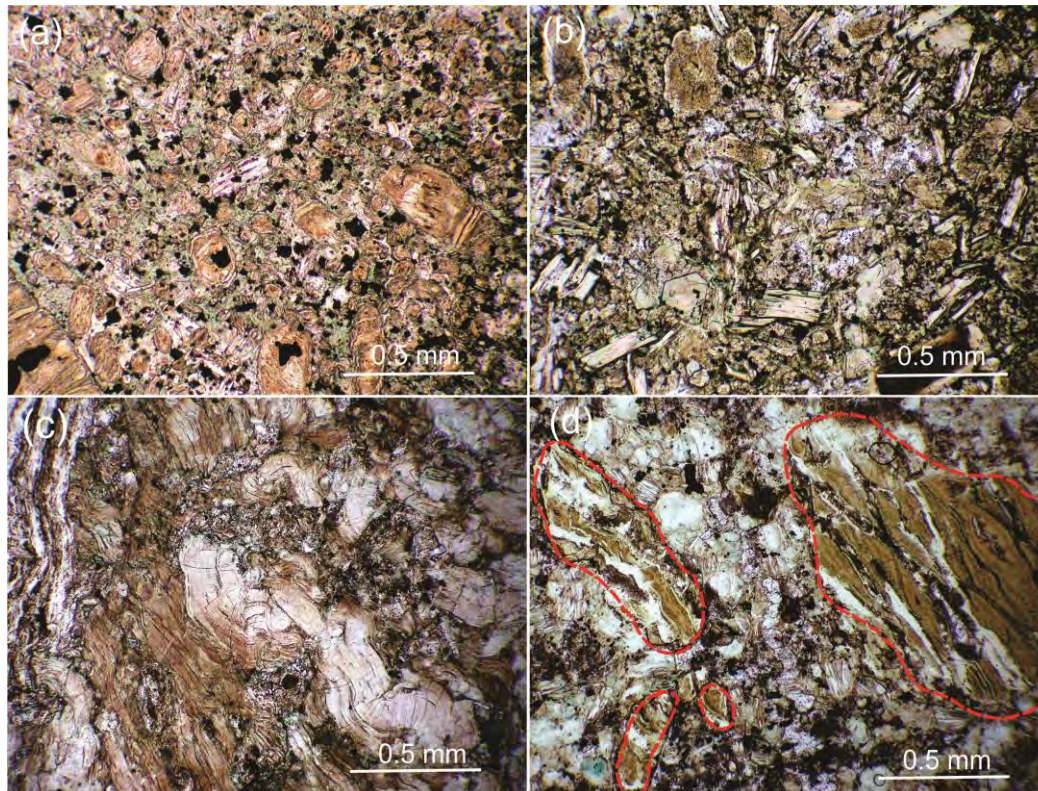


Figure 2: Photos of thin sections: (a) HK1; (b) HK3; (c) multiphase phyllosilicates and (d) olivine digested by smectites in HK6.

3a). The Snap Lake kimberlite is the only known kimberlite with extremely low bulk CaO and P₂O₅ contents. Mineralogical and petrographic contrasts between the identified HK zones are accompanied by subtle and gradual changes in the bulk rock composition. HK1 shows the lowest K₂O and SiO₂, and the highest Fe_{Total} and MgO. In contrast, HK2-6 are enriched in K₂O and SiO₂ due to the reaction with granite (Fig. 3b). The overall similarity in diamond content and size frequency distribution between HK1-2 and HK3-6 rocks is consistent with their crystallization from a single batch of magma.

Several post-emplacement processes modified the kimberlite. An early process was a reaction of olivine and monticellite with deuteritic H₂O and CO₂, which led to serpentinization, replacement of calcite by dolomite, alteration of perovskite and decomposition of apatite. The Calcite + Olivine assemblage is not stable in the presence of hydrous CO₂ and transforms to hydrous silicate + dolomite at T ~ 500°C and 100 MPa (Tracy, Frost, 1991). Dolomitization of calcite is thus expected in all kimberlites where exsolved magmatic CO₂+H₂O have enough time to react with the rocks. Leaching of Ca under CO₂-rich acidic fluid regime is also observed in alteration of perovskite and its replacement by monazite and rutile. The subsequent metasomatism was a rare process unique to the Snap Lake dyke, the interaction of kimberlite and fluids with the host granite. The unusual bulk chemistry and a protracted, predominantly subsolidus recrystallization of the Snap Lake kimberlite is

controlled by this interaction. Since formation of phlogopite in Group 1 kimberlites on a scale comparable to that of Snap Lake has not been reported in kimberlites, the Ba-poor K-rich Snap Lake

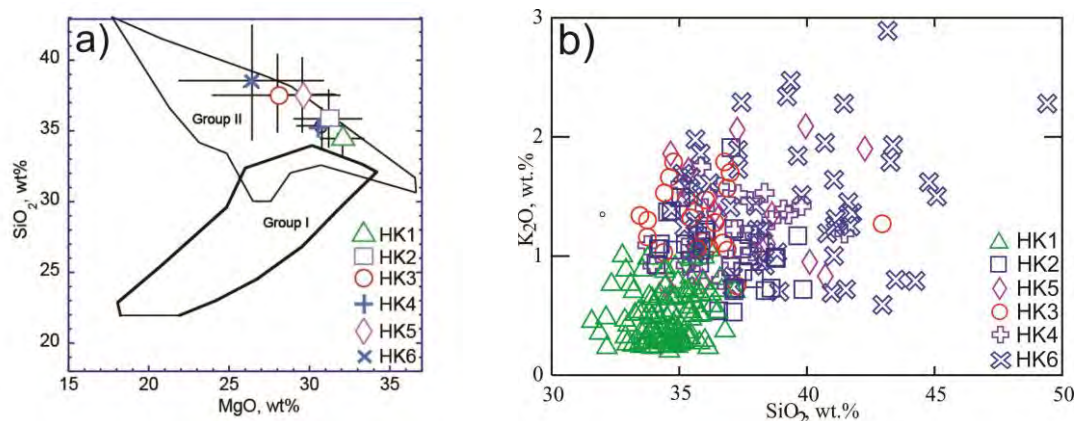


Figure 3: Bulk rock composition of Snap Lake kimberlite. a): SiO₂ vs. MgO (wt.%) of averaged compositions of fresh HK1 and altered kimberlites HK2-6 in comparison with global fields for Group I and Group II kimberlites. b). K₂O vs. SiO₂ (wt.%) for Snap Lake fresh HK1 and altered kimberlites HK2-6.

phlogopite, both poikilitic and tabular, cannot be solely deuteric. In our opinion, the crystallization of abundant Ti- and K-rich phlogopite and other phyllosilicates may have been caused by the ingress of K and Si from the granite, which relates to xenoliths assimilation and later metasomatism.

Comparison of bulk compositions of fresh HK1 and altered HK2-6, compositions of phlogopites and geochemical profiles through the granite-kimberlite contacts suggest that Mg, Fe, Ca, Ni and Sr moved locally from the kimberlite into the granite, while K and Si were introduced into the kimberlite. The alteration chemistry fully agrees with the theoretical T-dependent element mobilities and the composition of the contact silicate rocks. Potassic alteration in skarns is expected in contact with granites, but should be absent at contact with mafic rocks. In full correspondence with these patterns, we see the weak subsolidus secondary alteration of the kimberlite when it intrudes mafic metavolcanics, but an intense alteration at the granite-kimberlite contacts. Potassic alteration and wide skarn zones form in contact with quartzo-feldspathic rocks only at higher temperatures, above 450°C; temperatures of a shallow kimberlite melt thus permit the high-temperature mobility of K and Si.

Conclusions

Snap Lake kimberlite emplaced from a single magma batch. The altered margins of the Snap Lake dyke could be considered a rare example of contact metasomatism superimposed on the carbonate-rich intrusive protolith. One can think of the Snap Lake kimberlite as of an “endofenite”, i.e. a rock complementary to fenites, but replacing the igneous rock itself. The Snap Lake alteration highlights the high potential of carbonate-rich intrusions like carbonatites and kimberlites, to produce metasomatic columns when juxtaposed against felsic rocks at high temperature. Kimberlite geologists involved in resource modelling should especially be aware of susceptibility of carbonate-rich rocks to granite-induced metasomatism that deceptively look like separate emplacement phases.

References

- Tracy RJ, Frost BR (1991) Phase equilibria and thermobarometry of calcareous, ultramafic and mafic rocks and iron formations. In: Kerrick, D. M. & Ribbe, P. H. (ed) Contact metamorphism, *Reviews in Mineralogy*, 26, Mineralogical Society of America, pp 207 – 289

Origin of mantle-derived carbonate nodules from the Bultfontein kimberlite

Geoffrey H. Howarth¹, Andy Moore², and Chris Harris¹

¹University of Cape Town, Cape Town, South Africa, geoffrey.howarth@uct.ac.za, chris.harris@uct.ac.za

²Rhodes University, Grahamstown, South Africa, andy.moore.bots@googlemail.com

Introduction

In order to account for CO₂-rich, Si-undersaturated magmas such as carbonatites and kimberlites, it has long been suggested that a carbonate-bearing peridotite mantle source must be present in the upper mantle. Experimental evidence suggests that if carbonate was present within kimberlite-derived mantle xenoliths, it would dissociate and degass and should not survive transport from the sub-continental lithospheric mantle (SCLM) to the surface (Canil, 1990). However, several studies have described the presence of fine-grained (10-20 μm) mantle-derived carbonate within xenoliths (e.g., Berg, 1986). This suggests that in some cases carbonate may survive rapid transport to the surface during kimberlite ascent. Here, we present textural descriptions along with major and trace element, O-C stable isotope, and Sr-Nd-Pb radiogenic isotope data for coarse (>1 cm) carbonate nodules from the Bultfontein kimberlite, South Africa.



Figure 1. Photograph of carbonate nodules within a hypabyssal kimberlite block from the Bultfontein kimberlite. Note the distinct green reaction margins. Scale is in cm.

Results

The Bultfontein carbonate nodules (Figure 1) are polycrystalline calcite, coarse-grained (~4 mm), and are observed up to 10 cm (Figure 2). They are characterized by reaction margins with quench-related textures, including: radiating clusters of microlitic grains, a glass phase, and spherulites contained within the glass (Figure 2c). Furthermore, olivine grains spatially associated with the carbonate nodules are completely altered relative to the fresh grains away from the margins. Six of the carbonate nodules were powdered and analysed for Sr-Nd-Pb-O-C isotopes and solution ICP-MS trace element analyses at the University of Cape Town. Strontium and Ba concentrations are 225-490

ppm and 1.4-17.7 ppm, respectively. The REE are LREE enriched with relatively low concentrations 0.01 (HREE) to 1 (LREE) relative to chondrite (Figure 3). They have $\delta^{13}\text{C}$ and $\delta^{18}\text{O}$ of -6.0 to -6.3 ‰ and 15.7 to 16.9 ‰, respectively. The $(^{87}\text{Sr}/^{86}\text{Sr})_i$ values have little variation with a range of 0.7047-0.7048 (Figure 4). In contrast, a large range in ϵNd was observed from -3 to -25 (Figure 4). Lead isotopes also show a large range with $^{208}\text{Pb}/^{204}\text{Pb}$ (36.5-38.5), $^{207}\text{Pb}/^{204}\text{Pb}$ (15.4-15.6), and $^{206}\text{Pb}/^{204}\text{Pb}$ (16.7-18.9).

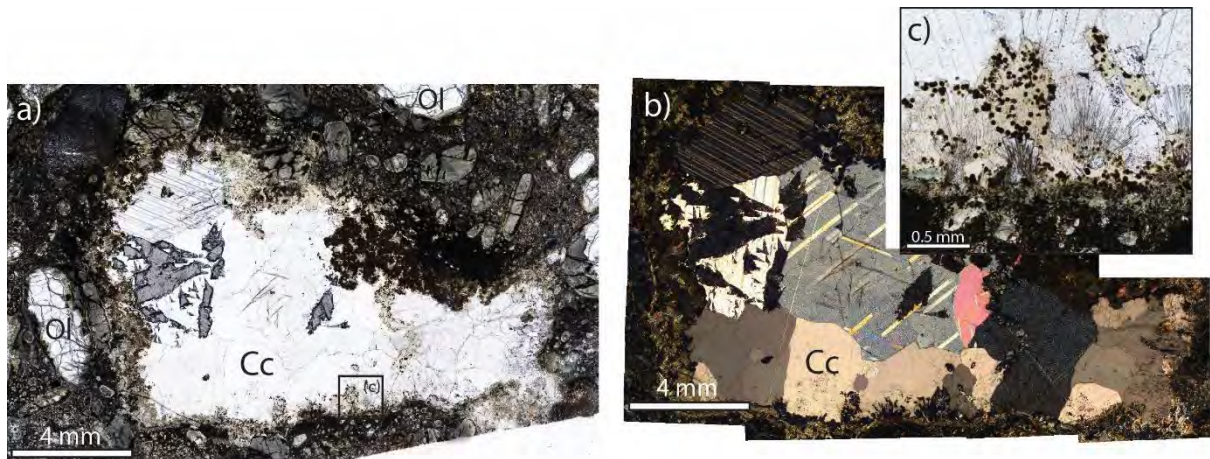


Figure 2. a) Plain polarized light (PPL) and b) cross-polarized light (XPL) photomicrographs illustrating the textures of a representative carbonate nodule from the Bultfontein kimberlite, South Africa. c) Inset: PPL image of the region marked in (a) illustrating the reaction textures surrounding carbonate nodules.

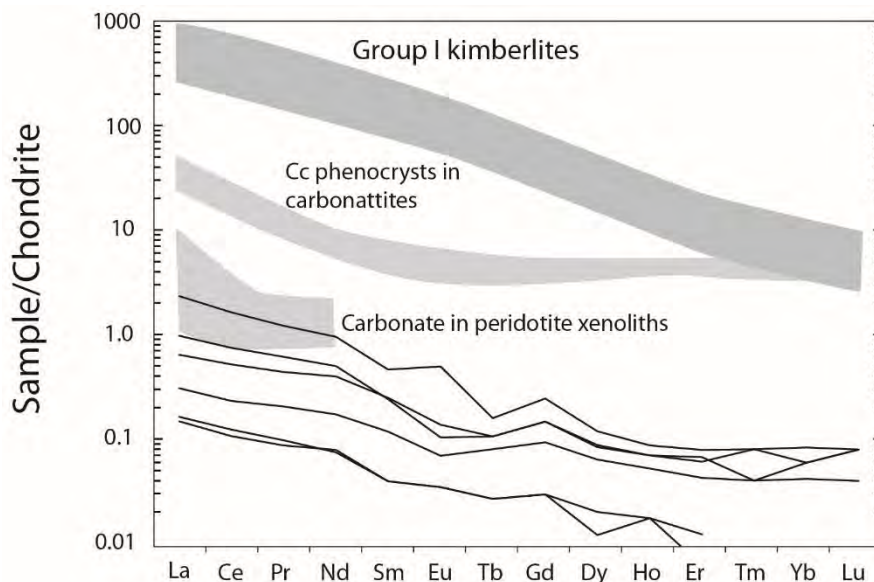


Figure 3. Chondrite normalized REE patterns for the Benfontein carbonate nodules. Field for Group I kimberlites is after Becker and le Roex (2006). The calcite (Cc) phenocryst field is after LREE enriched phenocrysts from the Spitskop carbonatites (Ionov and Harmer, 2002). The field for carbonate in peridotite xenoliths is for mantle xenoliths in alkali basalts (Ionov, 1998).

Discussion

The distinct reaction margins and coarse-grained texture (relative to surrounding groundmass minerals) of the Bultfontein carbonate nodules indicate that they are not late-stage crystallization products but rather represent xenoliths entrained at some stage during kimberlite ascent from the SCLM. The $\delta^{13}\text{C}$ and $(^{87}\text{Sr}/^{86}\text{Sr})_i$ and are consistent with formation within the mantle and not a crustal component. The REE concentrations are significantly lower than typical kimberlites

(Figure 3) suggesting that these carbonates do not represent late-stage residual carbonatitic melts associated with kimberlite melt evolution. The REE concentrations overlap with those reported for carbonates from peridotite mantle xenoliths recovered from alkali basalts (Figure 3). The very low $^{143}\text{Nd}/^{144}\text{Nd}$ ratios similarly suggest that these xenoliths are not related to the kimberlite magmas. Additionally the absence of correlation between $^{87}\text{Sr}/^{86}\text{Sr}$ with $^{143}\text{Nd}/^{144}\text{Nd}$ suggests that the very low ϵ_{Nd} is not a result of crustal assimilation, but likely represents an ancient lithospheric mantle source.

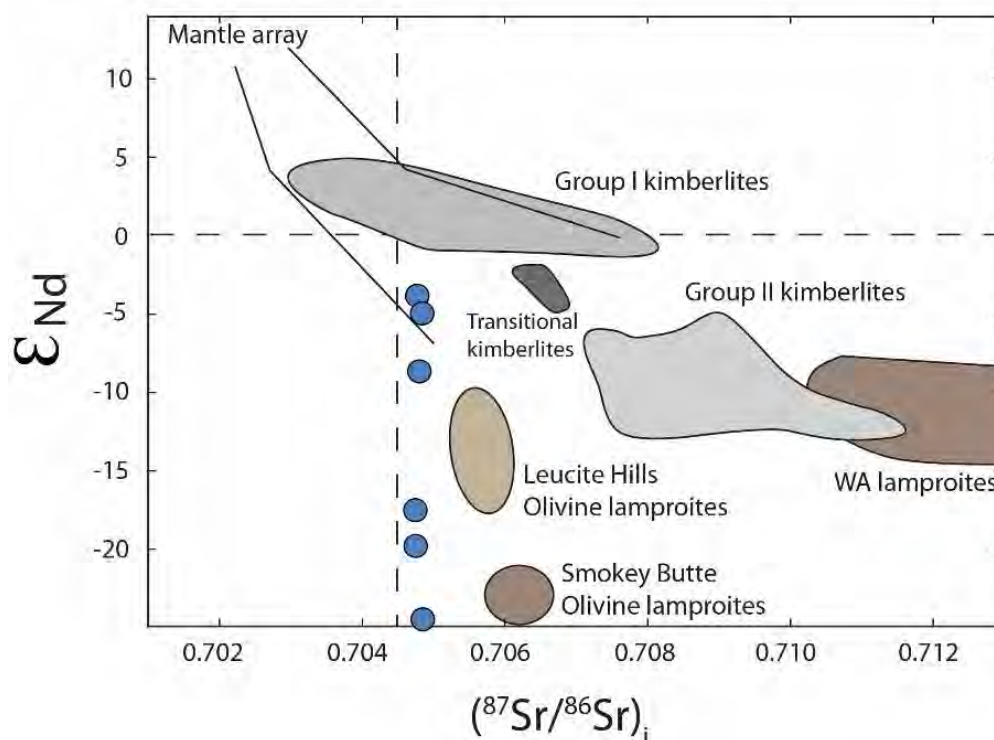


Figure 3. $(^{87}\text{Sr}/^{86}\text{Sr})_i$ versus ϵNd for the Bultfontein carbonate nodules illustrating the large range in ϵNd at constant $(^{87}\text{Sr}/^{86}\text{Sr})_i$. Group I and II kimberlite fields are after Nowell et al. (2004). Lamproite fields are after Fraser et al. (1985).

Conclusions

Carbonate nodules from the Bultfontein kimberlite represent mantle xenoliths likely derived from an ancient lithospheric mantle source. They do not appear to be related to the host kimberlite. These types of xenoliths have not been previously identified in kimberlite magmas and may represent a distinct coarse-grained carbonate-rich mantle lithology within the SCLM.

References

- Becker, M., & Le Roex, A. P. (2006). Geochemistry of South African on- and off-craton, Group I and Group II kimberlites: petrogenesis and source region evolution. *Journal of Petrology*, 47(4), 673-703.
- Berg, G. W. (1986). Evidence for carbonate in the mantle. *Nature*, 324(6092), 50-51.
- Canil, D., & Scarfe, C. M. (1990). Phase relations in peridotite + CO_2 systems to 12 GPa: implications for the origin of kimberlite and carbonate stability in the Earth's upper mantle. *Journal of Geophysical Research: Solid Earth*, 95(B10), 15805-15816.
- Fraser, K. J., Hawkesworth, C. J., Erlank, A. J., Mitchell, R. H., & Scott-Smith, B. H. (1985). Sr, Nd and Pb isotope and minor element geochemistry of lamproites and kimberlites. *Earth and Planetary Science Letters*, 76(1-2), 57-70.
- Ionov, D., & Harmer, R. E. (2002). Trace element distribution in calcite-dolomite carbonatites from Spitskop: inferences for differentiation of carbonatite magmas and the origin of carbonates in mantle xenoliths. *Earth and Planetary Science Letters*, 198(3), 495-510.
- Ionov, D. (1998). Trace element composition of mantle-derived carbonates and coexisting phases in peridotite xenoliths from alkali basalts. *Journal of Petrology*, 39(11-12), 1931-1941.
- Nowell, G. M., Pearson, D. G., Bell, D. R., Carlson, R. W., Smith, C. B., Kempton, P. D., & Noble, S. R. (2004). Hf isotope systematics of kimberlites and their megacrysts: new constraints on their source regions. *Journal of Petrology*, 45(8), 1583-1612.



Solid molecular nitrogen (N₂) inclusions in Juina diamonds: exsolution at the base of the transition zone

Oded Navon¹, Richard Wirth², Christian Schmidt², Brooke Matat Jablon¹, Anja Schreiber² and Simon Emmanuel¹

1) Institute of Earth Sciences, The Hebrew University, Jerusalem, Israel, oded.navon@mail.huji.ac.il, bmjablon@gmail.com, simon.Emmanuel@mail.huji.ac.il.

2) GFZ German Research Centre for Geosciences, Potsdam, Germany, wirth@gfz-potsdam.de, christian.schmidt@gfz-potsdam.de, schreib@gfz-potsdam.de.

Introduction

Diamonds originating from the transition zone or lower mantle were previously identified based on the chemistry of their silicate or oxide mineral inclusions. Here we present data for such a super-deep origin based on the internal pressure of nitrogen in sub-micrometer inclusions in diamonds from São Luiz, Juina Province, Brazil. The Juina area is known for the high percentage of super-deep diamonds (>300 km), many of these diamonds carry no detectable nitrogen or little nitrogen in a highly aggregated stage (most or all resides in B-centers). The diamonds we examined are nitrogen-rich and expand the known compositional range of super-deep diamonds. We will describe the diamonds and their nitrogen and discuss probable scenarios for their formation and ascent.

Results

The diamonds are opaque. Polish slabs show zoning that is not concentric, with dark, cloudy, inclusion-rich zones and more transparent ones. Secondary electron images show many small inclusions in the cloudy zones. Secondary electron imaging reveal microinclusions (30-300, Average 150 nm). TEM reveals an additional population of nano-inclusions, ~20-30 nm in size (Fig. 1). Chemical analysis of shallow subsurface inclusions with EPMA shows no oxygen or heavier atoms. Infrared spectroscopy of inclusion-rich zones in four diamonds revealed high concentrations of fully aggregated nitrogen (470-1060, average of 900 ppm, all in B centers) and almost no platelets. Hydrogen concentrations (the VN₃H centers) are high.

Raman spectroscopy conducted on three diamonds yielded a spectrum of solid, cubic δ -N₂ at 10.9±0.2 GPa. Figure 2a shows the two lines: a sharp peak at ~2354 cm⁻¹ and a weaker one at ~2367 cm⁻¹. The location of these two peaks, their relative intensity and the separation between the two peaks are fully compatible with assignment to the weaker ν_1 and the more intense ν_2 vibrational modes of δ -N₂ as measured in earlier studies. The positions of both peaks closely fit those of δ -N₂ at a pressure of 10.9±0.2 GPa (Figure 2b; Schneider et al., 1992). The corresponding density is ~1900 kg/m³. Using the number density and size of the inclusions measured by SEM and TEM, we estimated the nitrogen content of microinclusions at ~100 ppm, while the smaller, but more ubiquitous nano-inclusions carry ~350 ppm N₂ by weight.

EELS also detected nitrogen and a diffraction pattern of one nano-inclusion yielded a tetragonal phase, which resembles γ -N₂ with a density of 1400 kg/m³ (internal pressure = 2.7 GPa). In this case, the corresponding pressure at room temperature lies outside the stability field of the γ -N₂ phase, which is limited to T<100K. Using AFM, we also observed up-warping of small areas (~150 nm in size) on the polished surface of one diamond. The ~2 nm rise can be explained by a shallow subsurface microinclusion, pressurized internally to more than 10 GPa

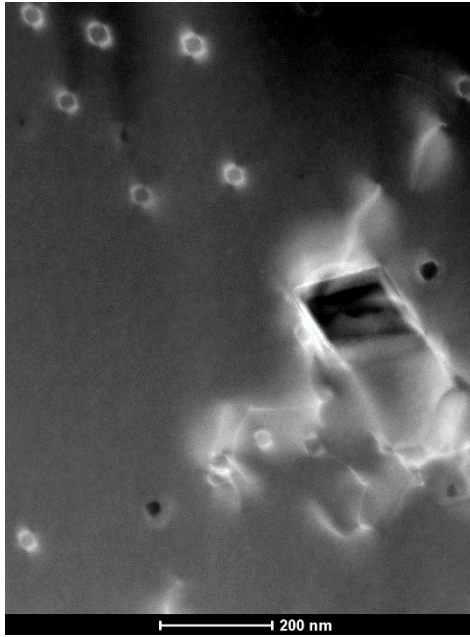


Fig. 1. TEM bright-field images of diamond ON-SLZ-392. The large microinclusion (120 nm) is surrounded by dislocations, together with many small nanoinclusions (~20 nm). All the inclusions are octahedral in shape and aligned parallel to the diamond's major crystallographic axes. The microinclusion is exposed to the polished surface, as are some of the nanoinclusions (dark ones), but many are still closed and under pressure, as indicated by the strain contrast at their sides.

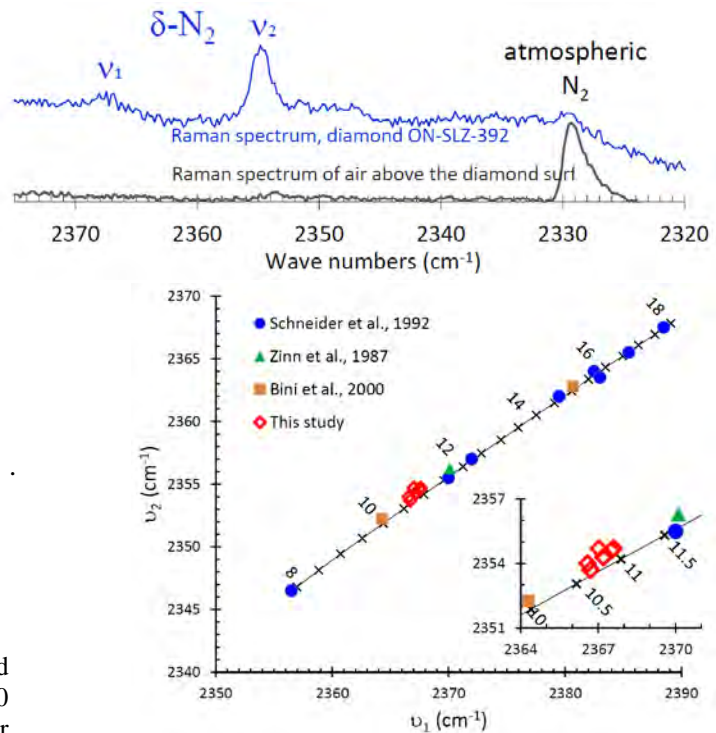


Fig. 2. a. Spectrum of inclusion-rich zone in diamond ON-SLZ-392 shows the two characteristic peaks of $\delta\text{-N}_2$ and compared with a spectrum of atmospheric nitrogen. b. The position of the two peaks (open red diamonds) compared with high pressure measurements (solid symbols) and the best fit line for the results (Schneider et al., 1992, black crosses and line). All spectra yield similar pressure of 10.9 ± 0.2 GPa.

Discussion

We adopt the clear fit of the Raman data with $\delta\text{-N}_2$ over the structural data of the single inclusion obtained by TEM and conclude that the inclusions carry $\delta\text{-N}_2$ at pressure of 10.9 ± 0.2 GPa at room temperature. Most of the nitrogen of the diamond resides in B centers (~900 ppm) but the micro- and nanoinclusions also carry an appreciable amount of ~100 and 350 ppm, respectively. Similar inclusions were described more than 20 years ago by Loyten et al. (1994) and recently by Rudloff-Grund et al. (2016) and Kagi et al. (2016), but none reported a clear evidence for the nature of the included phase. At mantle temperatures, the nitrogen in the inclusions was in a fluid state. Using available equations of state for fluid nitrogen and diamond, we calculated the pressures and temperatures of mechanical equilibrium of the inclusions and their diamond host at the mantle geotherm. The inclusions originated at the deepest part of the transition zone at pressures of ~22 GPa (630 km) and temperatures of ~1640°C. Further support for such deep source comes from the identification of a deep transition zone or lower mantle assemblage of ferroperricite, clinopyroxene and olivine in Juina diamonds that carry similar nanoinclusions (Kagi et al., 2016).

We suggest that the formation of both micro- and nanoinclusions are the result of exsolution of nitrogen from B centers and from platelets during their degradation. Evans et al. (1995) and Kiflawi and Bruley (2000) observed nitrogen-bearing "voidites" (that are identical to our nanoinclusions) within or very close to dislocation loops left after destruction of platelets in platelet-bearing diamonds that were heated to 2650-2750°C. Using the kinetics of their experiments and the activation energy for the migration of B centers that is equal or larger than that for the formation of B centers, we constrained the rate of

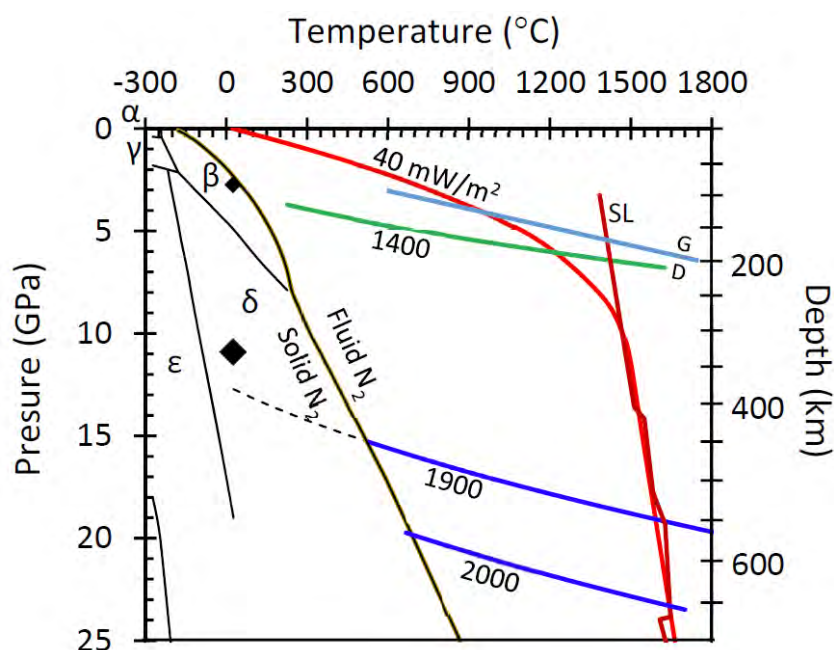


Fig. 3. Phase diagram for molecular nitrogen, the PT conditions of the inclusions and the mantle geotherm. α , β , γ , δ and ϵ : the stability fields of the various phases of molecular N_2 . Large black diamond – the pressure measured using Raman spectroscopy (10.9 GPa at room T). The small black diamond – The PT conditions for the tetragonal phase measured using TEM. Red and brown lines – the geotherm (adiabat from Stixrude and Lithgow-Bertelloni, 2007). Blue and green lines – isochores for 2000, 1900 and 1400 kg/m^3 . The density at room T and 10.9 GPa is 1900 kg/m^3 . Since the diamond expands during ascent, the initial density must have been higher, intermediate between 1900 and 2000 kg/m^3 , intersecting the geotherm at 22 GPa, 1640°C.

growth of the nano- and microinclusions. The high concentrations of nitrogen and the need for a short growth period (of the order of a few million years) advocates growth in a subducting environment.

We favor a scenario where the diamonds formed deep in the transition zone in a down-flowing mantle current associated with subduction. The nitrogen aggregated to form B centers, platelets were degraded and most of the dislocation loops disappeared or served as site for the microinclusions. At the high temperatures at the base of the transition zone, nitrogen exsolved to form the microinclusions and then the nano-inclusions. The diamonds were then trapped and transported up in a plume or a melt. Growth of the inclusions ceased quickly as temperatures decreased during ascent. The diamonds traveled to the base of the lithosphere, and were later transported to the surface by a kimberlitic melt. Cooling at the surface led to solidification of the nitrogen that remained under high pressure, the highest pressure ever measured in any mineral inclusion.

References

- Kagi H, Zedgenizov DA, Ohfuji H, Ishibashi H (2016) Micro- and nano-inclusions in a superdeep diamond from São Luiz, Brazil. *Geochem Internat*, 54:834-838.
- Kiflawi I, Bruley J, Luyten W, van Tendeloo G (1998) 'Natural' and 'man-made' platelets in type-Ia diamonds. *Phil Mag B*, 78:299-314.
- Luyten W, van Tendeloo GV, Fallon PJ, Woods GS (1994) Electron microscopy and energy-loss spectroscopy of voidites in pure type IaB diamonds. *Phil Mag A* 69:767-778.
- Rudloff-Grund J, Brenker FE, Marquardt K, et al. (2016) Nitrogen nano-inclusions in milky diamonds from Juina area, Mato Grosso State, Brazil. *Lithos*, 265:57-67.
- Schneider H, Häfner W, Wokaun A, Olijnyk H (1992) Room temperature Raman scattering studies of external and internal modes of solid nitrogen at pressures of 8-54 GPa. *J Chem Phys* 96:8046-8053.
- Stixrude L and Lithgow-Bertelloni C (2007) Influence of phase transformations on lateral heterogeneity and dynamics in Earth's mantle. *Earth Planet Sci Lett* 263:45-55.

Diamond brecciation and annealing accompanying major metasomatism in eclogite xenoliths from the Sask Craton, Canada

Janina Czas¹, Thomas Stachel¹, D. Graham Pearson¹, Richard A. Stern¹, George H. Read²

¹ University of Alberta, Canada, jczas@ualberta.ca, tstachel@ualberta.ca, gdpearso@ualberta.ca, rstern@ualberta.ca

² Shore Gold Inc., Saskatoon, Canada, GRead@shoregold.com

Introduction

The Fort à la Corne (FALC) kimberlite field on the Archean Sask Craton (Collerson et al. 1990) is located in Western Canada within the Paleoproterozoic (~1.8 Ga) Trans Hudson Orogen (THO; Rayner et al. 2005). During the THO, the Superior and the Churchill provinces were amalgamated, creating the North American Craton (Hoffman 1988). Diamonds have been discovered in 75% (Harvey et al. 2009) of the Cretaceous FALC kimberlites (Leckie et al. 1997), which sampled principally Trans Hudson age (~1.9 Ga) lithospheric mantle beneath the Archean Sask Craton (Czas et al. submitted). In the absence of Archean lithospheric mantle, the FALC kimberlites provide an opportunity to study the composition of the lithospheric mantle, its metasomatic history and the mode of diamond formation of an unconventional diamond deposit.

Samples and methods

We studied eclogite xenoliths (diamondiferous n=23; diamond-free n=30) from FALC, including a unique sample crosscut by a diamond vein, for their major element (EPMA), trace element (LA-ICPMS), nitrogen, and stable isotope ($\delta^{18}\text{O}$, $\delta^{13}\text{C}$, $\delta^{15}\text{N}$; SIMS), compositions to assess their metasomatic history and possible relationships between metasomatism and diamond formation.

Diamond-free eclogites

All diamond-free eclogites consist of garnet and clinopyroxene, with accessory rutile or apatite being present in less than 10% of the samples. Clinopyroxene is omphacitic ($\text{Na}/(\text{Na}+\text{Ca}) \geq 0.2$; Clark and Papike 1968), indicating an eclogitic rather than pyroxenitic assemblage. Even though the mineral chemistry spans a wide compositional range among xenoliths (garnet Mg# varies from 33 – 82 and

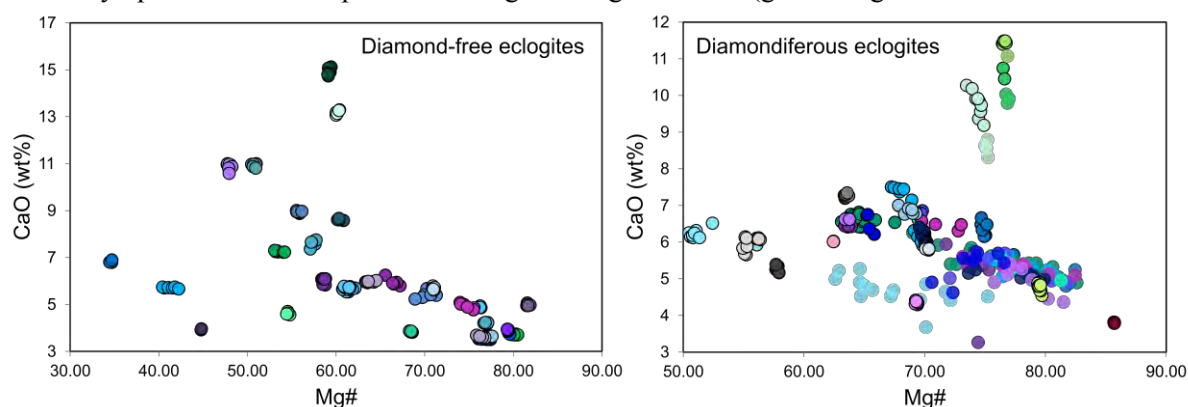


Figure 1: Major element variations in garnets from diamond-free and diamondiferous eclogites. At least two analytical spots were placed on each garnet grain, up to three grains were analysed per sample; colours indicate garnet analyses from individual samples. Garnet analyses from diamond free eclogites show a broad range, yet intra-sample variants are small. Garnets associated with diamonds often show significant variations within xenoliths and have been plotted as unaltered remnants (black rims) and metasomatized garnet (coloured rims).

CaO content from 3.5 – 15.1 wt%), it is typically homogenous within samples (Figure 1), with the exception of spongy-textured, jadeite-poor clinopyroxene related to partial melting and metasomatism (Carswell 1975; Su et al. 2011) that occurs in thin veins and rims surrounding relict omphacite. Garnet oxygen isotope compositions show a broad range from $\delta^{18}\text{O} = +3.6 \pm 0.3 \text{ ‰}$ to $+7.9 \pm 0.3 \text{ ‰}$. Temperatures calculated from Mg-Fe exchange between garnet and clinopyroxene (Krogh 1988) and projected onto the Sask Craton geotherm ($\sim 38\text{mW/m}^2$ reference geotherm of Hasterok and Chapman 2011) range widely, from 740 to 1300 °C, indicating the presence of eclogite through most of the lithospheric mantle.

Diamondiferous eclogites

Clinopyroxene is commonly absent in the small diamondiferous microxenoliths and garnet often represents the only identified silicate mineral. Compositionally, the garnets from diamondiferous eclogites have high Mg# (50 to 86) and low to moderate CaO contents (3.3 to 11.5 wt%). Temperatures (Krogh 1988) are restricted to higher values (1180 – 1390 °C), indicating a deep derivation. The majority of garnets exhibit complex irregular textures in back-scattered electron (BSE) images (Figure 2A), corresponding to large variations in Mg# (up to 25; Figure 1) and CaO content (up to 3.1 wt%). Similar but less pronounced trends of increasing pyrope content have been reported for rims around eclogitic garnet and were attributed to late stage kimberlite infiltration. This prominent melt-metasomatic overprint is also reflected in LREE enrichment in the garnets of up to one order of magnitude within one sample and a shift in $\delta^{18}\text{O}$ dominantly towards mantle-like ($+5.4$ to $+5.7 \text{ ‰}$; Ickert et al. 2013) compositions, showing that intense mantle metasomatism may

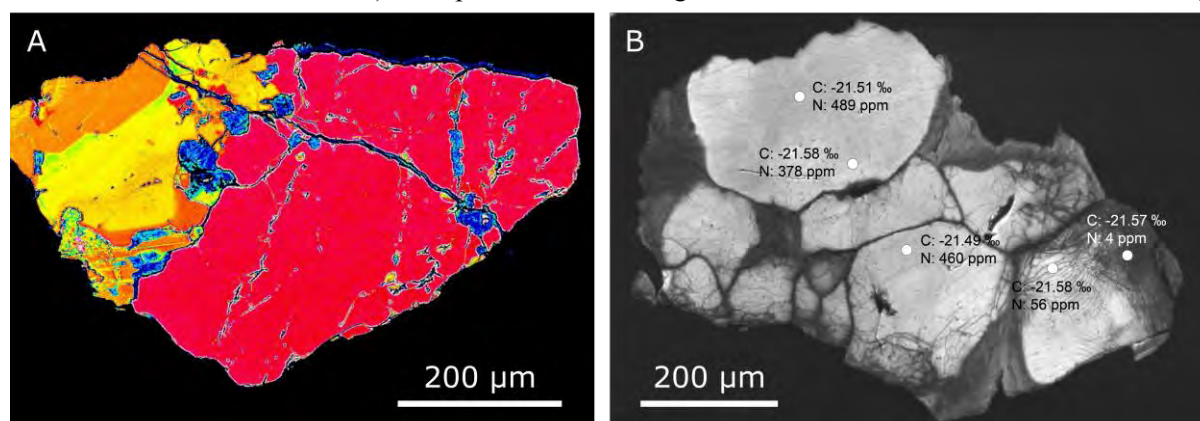


Figure 2: **A.** Backscattered-electron image showing intra-grain chemical variability within a single garnet from a diamondiferous eclogite. Mg# varies between 51 (read area) and 71 (yellow area). **B.** Cathodoluminescence image of a brecciated diamond (primary diamond light grey) with secondary low-N diamond in annealed fractures (dark grey). Spot analyses of carbon isotope values and N concentrations are indicated.

homogenise oxygen isotope compositions rather than diversify them (cf Huang et al. 2012). Cathodoluminescence (CL) imaging of diamonds within intensely metasomatised FALC eclogite xenoliths reveals complex internal textures such as irregular thin bands and rims, exhibiting very low N abundances (Figure 2B). These unusual textures appear to represent diamond brecciation followed by annealing. The very close agreement in carbon isotopic composition between original nitrogen-rich diamonds and secondary nitrogen-poor fracture fillings and overgrowths suggests that annealing was based on carbon already present in the rock, involving, for instance, a diamond dissolution – re-precipitation process.

Discussion

Eclogites in the FALC lithospheric mantle are distributed throughout the lithospheric mantle section underpinning the Sask craton. A major metasomatic event is evident that (1) primarily affected diamondiferous eclogites, (2) occurred shortly before kimberlite entrainment, as compositional heterogeneity within individual garnets is still preserved, (3) produced deviatoric stress resulting in

diamond brecciation, and (4) took place within the diamond stability field as annealing through secondary diamond occurred. This process created strong elemental compositional gradients while acting to homogenise oxygen isotopic compositions, as expected from melt-rock interaction mass balance models (e.g., Riches et al. 2016). A likely process could involve the intrusion and stagnation of a melt related to kimberlite magmatism near the base of the lithosphere, a process similar to the formation of polymict mantle breccias (Lawless et al. 1979; Giuliani et al. 2014).

References

- Carswell DA (1975) Primary and secondary phlogopites and clinopyroxenes in garnet lherzolite xenoliths. *Phys Chem Earth* 9:417–429. doi: 10.1016/0079-1946(75)90031-2
- Clark JR, Papike JJ (1968) Crystal-chemical characterization of omphacites. *Am Mineral* 53:840–868.
- Collerson KD, Lewry JF, Bickford ME, Van Schmus WR (1990) Crustal evolution of the buried Precambrian of southern Saskatchewan: Implications for diamond exploration. In: Beck LS, Harper CT (eds) *Modern Exploration Techniques: Saskatchewan Geological Society*. pp 150–165
- Czas J, Pearson DG, Stachel T, Read GH, Kjarsgaard BA (submitted) Is there an Archean lithospheric mantle root beneath the Sask Craton, Canada?
- Giuliani A, Phillips D, Kamenetsky VS, et al (2014) Petrogenesis of Mantle Polymict Breccias: Insights into Mantle Processes Coeval with Kimberlite Magmatism. *J Petrol* 55:831–858. doi: 10.1093/petrology/egu008
- Harvey S, Kjarsgaard B, McClintock M, et al (2009) Geology and evaluation strategy of the Star and Orion South kimberlites, Fort à la Corne, Canada. *Lithos* 112:47–60. doi: 10.1016/j.lithos.2009.04.040
- Hasterok D, Chapman DS (2011) Heat production and geotherms for the continental lithosphere. *Earth Planet Sci Lett* 307:59–70. doi: 10.1016/j.epsl.2011.04.034
- Hoffman PF (1988) United Plates of America, the Birth of a Craton: Early Proterozoic Assembly and Growth of Laurentia. *Annu Rev Earth Planet Sci* 16:543–603.
- Huang JX, Gréau Y, Griffin WL, et al (2012) Multi-stage origin of Roberts Victor eclogites: Progressive metasomatism and its isotopic effects. *Lithos* 142–143:161–181. doi: 10.1016/j.lithos.2012.03.002
- Ickert RB, Stachel T, Stern RA, Harris JW (2013) Diamond from recycled crustal carbon documented by coupled $\delta^{18}\text{O}$ - $\delta^{13}\text{C}$ measurements of diamonds and their inclusions. *Earth Planet Sci Lett* 364:85–97. doi: 10.1016/j.epsl.2013.01.008
- Krogh EJ (1988) The garnet-clinopyroxene Fe-Mg geothermometer - a reinterpretation of existing experimental data. *Contrib to Mineral Petrol* 99:44–48. doi: 10.1007/BF00399364
- Lawless PJ, Gurney JJ, Dawson JB (1979) Polymict Peridotites from the Bultfontein and de Beers Mines, Kimberly, South Africa. In: Boyd FR, Meyer HOA (eds) *The Mantle Sample: Inclusions in Kimberlites and Other Volcanics*. American Geophysical Union, Washington, DC, pp 144–155
- Leckie DA, Kjarsgaard BA, Bloch J, et al (1997) Emplacement and reworking of Cretaceous, diamond-bearing, crater facies kimberlite of central Saskatchewan, Canada. *Geol Soc Am Bull* 109:1000–1020. doi: 10.1130/0016-7606(1997)109<1000:EAROCD>2.3.CO;2
- Rayner NM, Stern R a, Bickford ME (2005) Tectonic implications of new SHRIMP and TIMS U–Pb geochronology of rocks from the Sask Craton, Peter Lake Domain, and Hearne margin, Trans-Hudson Orogen, Saskatchewan. *Can J Earth Sci* 42:635–657. doi: 10.1139/e04-045
- Riches AJV, Ickert RB, Pearson DG, et al (2016) In situ oxygen-isotope, major-, and trace-element constraints on the metasomatic modification and crustal origin of a diamondiferous eclogite from Roberts Victor, Kaapvaal Craton. *Geochim Cosmochim Acta* 174:345–359. doi: 10.1016/j.gca.2015.11.028
- Su BX, Zhang HF, Sakyi PA, et al (2011) The origin of spongy texture in minerals of mantle xenoliths from the Western Qinling, central China. *Contrib to Mineral Petrol* 161:465–482. doi: 10.1007/s00410-010-0543-x

Contrasting thermal structure, melt depletion and metasomatism of mantle lithosphere beneath two Proterozoic terranes west of the Kaapvaal Craton, southern Africa

Ellwin T. Shiimi¹ & Philip E. Janney¹

¹Department of Geological Sciences, University of Cape Town, Rondebosch, South Africa

Introduction

The Archean Kaapvaal Craton of southern Africa is bounded to the west and south by two Proterozoic terranes (Fig. 1): the Rehoboth Province (RP) and Namaqua-Natal Province (NNP). Mineral major and trace element data were obtained for garnet bearing peridotite xenoliths exhumed from four Late Cretaceous Group 1 kimberlites (71-83 Ma; Davis et al., 1976; Davies et al., 2001; Griffin et al., 2014) located near the RP-NNP border. These are Rietfontein and Louwrensia (one of the Gibeon cluster kimberlite pipes) in the southern RP, and Hoedkop and Pofadder in the northwestern NNP (Figure 1). Forty-four peridotite xenoliths were investigated from these four localities in order to compare the thermal and metasomatic characteristics of the mantle lithosphere beneath these terranes with each other and with the Kaapvaal Craton. Major element mineral data have been published for peridotites from the Louwrensia and Hoedkop localities (Boyd et al., 2004; Janney et al., 2010), but not for those from Rietfontein or Pofadder. New clinopyroxene and garnet trace element data were obtained for all samples by laser ablation ICP-MS at UCT. For both major and trace element data, there were no significant compositional differences observed between cores and rims of the grains analysed.

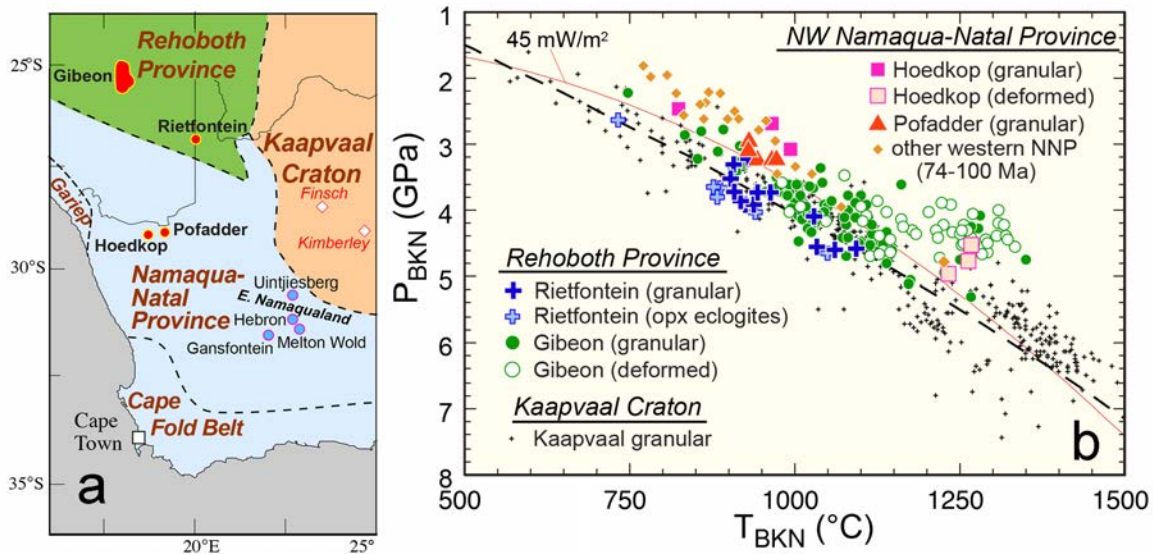


Figure 1. (a) Location map of the RP, western NNP and western Kaapvaal Craton in southern Africa, showing the xenolith localities investigated in this study (red). Also shown are the locations of other off-craton xenolith localities in the western NNP. (b) T_{BKN} - P_{BKN} plot for garnet peridotites from the RP, western NNP and Kaapvaal craton. The dashed curve is the “Kalahari geotherm” of Rudnick & Nyblade (1999) and the thin red curve is the 45 mWm^{-2} geotherm of Pollack and Chapman (1977), which effectively separates the bulk of the granular RP peridotites from the higher temperature peridotites from the western NNP.

Thermobarometry results and discussion

Based on the combined T_{BKN} - P_{BKN} thermobarometer of Brey and Köhler (1990), the majority of xenoliths from the RP display pressures and temperatures that overlap with granular peridotites from the Kaapvaal craton. Like cratonic peridotites, these granular off-craton peridotites lie between the 40 and 45 mWm^{-2} conductive geotherms of Pollack and Chapman (1977) and most fall along the Kalahari

paleogeotherm of Rudnick and Nyblade (1999). This appears to be a regional feature of the RP, and is consistent with values for opx-bearing eclogites from the Rietfontein kimberlite pipe (Appleyard et al., 2007) and other peridotites from Gibeon kimberlite field (Mitchell, 1984; Franz et al., 1996a; Boyd et al., 2004). In contrast, granular peridotites from Pofadder and Hoedkop record higher temperatures (by 50-100°C) for any given pressure and lie between the 45 and 50 mWm⁻² geotherms, similar to other garnet peridotites from late Cretaceous kimberlites in the western NNP (Janney et al., 2010). However, these higher temperatures in the NNP do not appear to be a long-term feature of the regional lithosphere, as data for garnet peridotites from an older kimberlite also in the western NNP, Melton Wold (~150 Ma; Griffin et al., 2014), also coincide with the Kaapvaal/Kalahari geotherm. This suggests that the western NNP has been affected by a regional thermal disturbance that did not affect xenoliths from the RP prior to their entrainment (Bell et al., 2003).

The similarities in geothermal gradients between the RP and the western NNP (prior to 100 Ma, as indicated by Melton Wold) and the Kaapvaal Craton suggests that at one time they may have had a similar thickness (Bell et al., 2003; Boyd et al., 2004; Janney et al., 2010). Seismological constraints currently indicate that the RP and western NNP are 30 to 50 km thinner than typical Kaapvaal craton lithosphere (e.g., Chevrot & Zhao, 2007). Significant lithospheric thinning, contemporaneous with or following late Cretaceous kimberlite magmatism, thus appears to have occurred, and would most likely have occurred via melt-lithosphere interaction/thermal erosion due to the lack of evidence for regional extension (e.g., Boyd et al., 2004; Kobussen et al., 2008; 2009; Janney et al., 2010).

Geochemistry results

All garnets studied from the 4 localities have relatively low Cr₂O₃/Al₂O₃ values, in addition to being calcic, and fall in the lherzolitic (G9) compositional field on plots of CaO vs Cr₂O₃ implying a lower degree of melt extraction than typical garnet from cratonic peridotites. There is a large degree of overlap in major element composition between data for the garnet studied and that for peridotitic garnet from Kimberley, although a significant population from Kimberley are also subcalcic. Assuming the concentration of HREE and Y in garnet to be unmodified subsequent to the last partial melting allows further assessment of melt depletion. Garnets from Rietfontein (RP) peridotites are characterised by “normal” REE patterns with high values and flat patterns in the MREE-HREE and strong depletions in the LREE, as well as relatively high average Y contents of 21 ±12 ppm. The majority of garnets from Louwrensia have similar garnets with normal REE patterns and high average Y content of 22 ±10 ppm, but a minority have sinusoidal REE patterns (with relatively low Tb to Er abundances) and low Y contents of 10±2 ppm, similar to typical Kaapvaal peridotite garnets with Y contents of 7-10 ppm. These latter values suggest unusually high degrees of melting for off-craton settings, but peridotite garnets with similar compositions have also been described from other Gibeon kimberlite localities (Luchs et al., 2013). Garnets from Hoedkop (NNP) have normal REE patterns but with slightly lower than typical MREE-HREE contents as well as low average Y contents of 11±4 ppm. Garnets from Pofadder (NNP) are unusual in having relatively linear, positively sloping normal REE patterns, show moderate chondrite normalised HREE contents along with average Y content of 15 ±3 ppm suggesting relatively mild degrees of melting.

Clinopyroxenes from Rietfontein, Louwrensia and Hoedkop all have similar LREE-enriched, HREE depleted patterns with maximum enrichments in Ce, Pr or Nd. Pofadder cpx is distinct in having unusual linear REE patterns with maximum enrichments in La and strong depletions in the heaviest REE, as well as unusually strong depletions in the HFSE Zr, Hf and Ti.

Metasomatism

Minerals from the RP and western NNP peridotites have incompatible element enrichments indicative of significant metasomatism. Peridotites from the RP preserve evidence for moderate metasomatic enrichment in the highly incompatible trace elements such as LILE and LREE, with good internal mineral equilibrium for most trace elements. A few Louwrensia peridotites and one Hoedkop peridotite have garnets with sinusoidal REE patterns indicating strong depletion of all REE by extensive partial melting followed by re-enrichment of the middle REE. The most likely metasomatic agent(s) in Louwrensia and Rietfontein are kimberlitic melts. In the western NNP, Hoedkop and

particularly Pofadder peridotites show greater garnet-cpx disequilibrium and greater fractionation between the REE, HFSE and LILE suggesting a possible role for volatile-rich metasomatic agents such as carbonatite or hydrous melts. The latter is also suggested by mineral reactions requiring infiltration of a K-bearing hydrous fluid into the Hoedkop peridotites. Pofadder peridotites show evidence for intense metasomatism characterised by extreme enrichment in incompatible trace elements (high LREE/HREE ratios). The striking resemblances in primitive mantle normalised trace element patterns between clinopyroxene from Pofadder peridotites and Cr-rich megacrysts studies (e.g., Janney & Bell, abs. 4630, this volume) suggest that the Pofadder clinopyroxene may have crystallized directly from the magma parental to these megacrysts (presumably kimberlite).

References

- Appleyard, C.M., Bell, D.R., and le Roex, a. P. (2007), Petrology and geochemistry of eclogite xenoliths from the Rietfontein kimberlite, Northern Cape, South Africa: *Contributions to Mineralogy and Petrology* **154**(3):309–333
- Bell, D.R., Schmitz, M.D., and Janney, P.E. (2003) Mesozoic thermal evolution of the southern African mantle lithosphere: *Lithos* **71**(2–4):273–287
- Boyd, F.R., Pearson, D.G., Hoal, K.O., Hoal, B.G., Nixon, P.H., Kingston, M.J., and Mertzman, S. a., 2004, Garnet lherzolites from Louwrensia, Namibia: bulk composition and P/T relations: *Lithos* **77**(1–4):573–592
- Brey, G.P., and Köhler, T. (1990) Geothermobarometry in four-phase lherzolites II. New thermobarometers, and practical assessment of existing thermobarometers: *Journal of Petrology* **31**(6):1353–1378
- Chevrot, S., and Zhao, L., 2007, Multiscale finite-frequency Rayleigh wave tomography of the Kaapvaal craton: *Geophysical Journal International* **169** (1), 201–215.
- Davies, G. R., Spriggs, A. J. & Nixon, P. H. (2001). A non-cognate origin for the Gibeon kimberlite megacryst suite, Namibia: Implications for the origin of Namibian Kimberlites. *Journal of Petrology* **42**, 159–172.
- Davis, G., Krogh, T. & Erlank, A. J. (1976). The ages of zircons from kimberlites from South Africa. *Carnegie Institution Yearbook* **75**, 821–824.
- Franz, L., Brey, G.P., and Okrusch, M. (1996b) Steady state geotherm, thermal disturbances, and tectonic development of the lower lithosphere underneath the Gibeon Kimberlite Province, Namibia.: *Contributions to Mineralogy and Petrology* **126**(1–2):181–198.
- Griffin, W. L., Batumike, J. M., Greau, Y., Pearson, N. J., Shee, S. R. & O'Reilly, S. Y. (2014). Emplacement ages and sources of kimberlites and related rocks in southern Africa: U-Pb ages and Sr-Nd isotopes of groundmass perovskite. *Contributions to Mineralogy and Petrology* **168**, 1032.
- Janney, P.E., Shirey, S.B., Carlson, R.W., Pearson, D.G., Bell, D.R., Le Roex, a. P., Ishikawa, a., Nixon, P.H., and Boyd, F.R. (2010) Age, Composition and Thermal Characteristics of South African Off-Craton Mantle Lithosphere: Evidence for a Multi-Stage History: *Journal of Petrology* **51**(9):1849–1890
- Kobussen, A.F., Griffin, W.L., and O'Reilly, S.Y. (2009) Cretaceous thermo-chemical modification of the Kaapvaal cratonic lithosphere, South Africa: *Lithos* **112S**:886–895
- Kobussen, A.F., Griffin, W.L., O'Reilly, S.Y., and Shee, S.R., 2008, Ghosts of lithospheres past: Imaging an evolving lithospheric mantle in southern Africa: *Geology*, **36** (7)515–518
- Luchs, T., Brey, G.P., Gerdes, a., and Höfer, H.E., (2013) The lithospheric mantle underneath the Gibeon Kimberlite field (Namibia): A mix of old and young components—Evidence from Lu–Hf and Sm–Nd isotope systematics: *Precambrian Research* **231**:263–276
- Mitchell, R.H. (1984) Garnet lherzolites from the Hanaus-I and Louwrensia kimberlites of Namibia.: *Contributions to Mineralogy and Petrology* **86**(2):178–188.
- Pearson, D.G., and Wittig, N. (2008), Review Formation of Archaean continental lithosphere and its diamonds : the root of the problem: *Journal of the Geological Society London* **165**:895–914.
- Pollack, H.N., and Chapman, D.S. (1977) On the regional variation of heat flow, geotherms and lithospheric thickness: *Tectonophysics* **38**: 279–296.
- Rudnick, R., and Nyblade, A. (1999) The thickness and heat production of Archean lithosphere: constraints from xenolith thermobarometry and surface heat flow: Mantle Petrology: Field Observations and High Pressure Experimentation: A Tribute to Francis R. (Joe) Boyd (6):3–12



A new look at diamonds from the Koffiefontein Mine

Nicole A. Meyer¹, Thomas Stachel¹, D. Graham Pearson¹, and Jeff W. Harris^{1,2}

¹University of Alberta, Edmonton, Canada, nameyer@ualberta.ca, tstachel@ualberta.ca,
gdpearso@ualberta.ca

²University of Glasgow, Glasgow, United Kingdom, Jeff.Harris@glasgow.ac.uk

Introduction

The Koffiefontein kimberlite is one of the classical diamond mines on the Kaapvaal Craton and best known for being the first locality where sublithospheric inclusions in diamond were recovered (Moore et al. 1986). Koffiefontein diamonds were the first to be dated using Re-Os decay in sulphides and gave two age populations with E-type sulphides having late Archean (~2.7 Ga) and Proterozoic populations (~1.1 Ga), while a single peridotitic diamond gave an age within error of the age of kimberlite eruption (Pearson et al. 1998). Koffiefontein diamonds and their inclusions were last studied in the 1980s and, based on major advances in micro-analytical techniques, here we revisit this mine to provide improved inclusion-based geothermobarometry.

Sample Set

Our new sample set contains a variety of octahedra, dodecahedroids, macles, and irregular stones. The majority (85 %) of the crystals are colourless. Diamonds with peridotitic inclusions have a median nitrogen concentration of 67 at. ppm (range of 0 to 1580 at. ppm), eclogitic stones having a higher median at 175 at. ppm (range of 0 to 778 at. ppm). Within the new suite, 68 diamonds with peridotitic inclusions have been studied and a total of 156 olivine, Cr-rich pyrope garnet, enstatite, and diopside inclusions liberated. The peridotitic inclusion suite from Koffiefontein is dominated by a highly-depleted harzburgitic component. Most of the harzburgitic garnets (90 %) contain ≤ 3.00 wt. % CaO and strong melt-depletion is also seen in olivine data, with Mg-numbers ranging between 93 and 95. Only ~15 % of the peridotitic inclusion suite is lherzolitic based on the presence of clinopyroxene inclusions or garnet inclusions that classify as G9.

Geothermobarometry

We used xenolith data from the Koffiefontein study of Cardoso (1980) to apply the more modern Ca-in-opx thermometer of Brey and Köhler (1990) in combination with the orthopyroxene-garnet barometer of Nickel and Green (1985, with Al in M1 calculated after Carlswell & Gibb 1987), to estimate the paleogeotherm for the lithosphere beneath Koffiefontein. A 38 mW/m² reference geotherm (Hasterok and Chapman 2011) provides the best fit through our data (Figure 1).

For inclusions in diamond, the single-grain clinopyroxene thermometer and barometer (Nimis and Taylor 2000) was used where possible, otherwise temperature was estimated from Ca-in-opx (lherzolite, Brey and Köhler 1990) or garnet-orthopyroxene pairs (harzburgite, Harley 1984) and combined with garnet-orthopyroxene based barometry (NG85*, Nickel and Green 1985, with Al in M1 calculated after Carlswell & Gibb 1987) to obtain P-T estimates. With one exception, the inclusion pairs were non-touching and, therefore, generally yield the conditions likely to approximate to those of diamond formation. Harzburgitic inclusions derive from close to the base of the lithosphere (1160-1285 °C and 60-71 kbar, five inclusion sets; and 1151 °C and 53 kbar, touching pair) whilst much rarer lherzolitic inclusions last equilibrated in the upper portion of diamond stable lithosphere (985-1158 °C and 48-52 kbar, three inclusion sets; one outlier at 24 kbar, above the graphite-diamond transition). The thermometer of Harley (1984) has been shown to underestimate calculated temperature above 1000 °C (Brey and Köhler 1990), thus the harzburgitic samples (Figure 1, blue circles) may lie closer to the 38 mW/m² reference geotherm. Adding inclusion assemblages from five diamonds studied by Cardoso (1980) to our data set yields consistent results. Both harzburgitic and lherzolitic associations fall along

the xenolith-based 38 mW/m² reference geotherm, implying that thermal conditions beneath Koffiefontein remained fairly constant over billions of years and that diamond formation occurred in a lithosphere about 220 km thick.

To expand our geothermobarometry data beyond rare garnet-bearing associations, we conducted high-precision trace element analyses of Al in olivine inclusions via EPMA. This technique allows for non-destructive, trace element analysis of olivine inclusions as small as 20 µm in diameter. Using long count times (300 seconds on peak and each background) and a 200 nA beam current, detection limits of 8 ppm for Al were achieved. Based on these Al analyses, temperatures were calculated using the updated Al-in-olivine thermometer of Bussweiler et al. (2017) projected onto a 38 mW/m² reference geotherm. Using a set of 30 olivine inclusions, temperatures of 970-1340 °C were obtained (with one outlier at 760 °C, above the graphite-diamond transition).

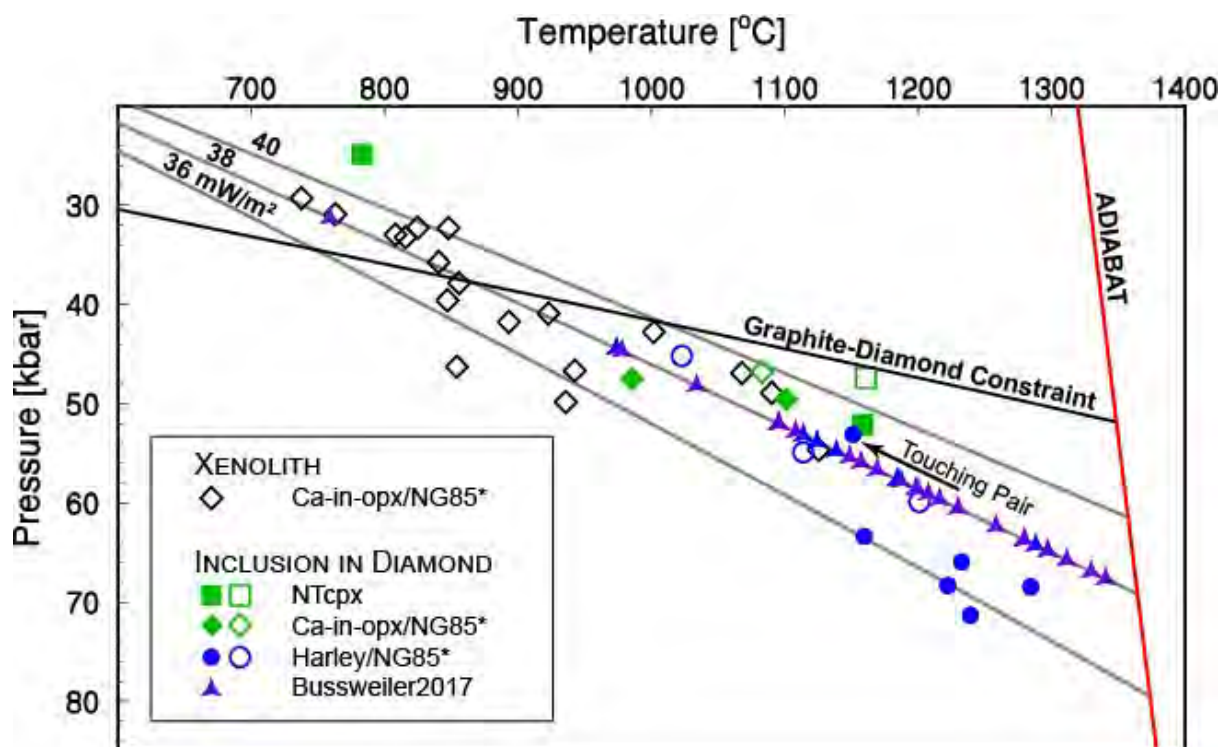


Figure 1: Pressure and temperature estimates applying modern geothermobarometers to xenolith (Cardoso 1980) and inclusion in diamond data (Cardoso 1980 and this study). Xenolith data define a 38 mW/m² reference geotherm (Hasterok and Chapman 2011). Inclusions in diamond follow the same reference geotherm but derive from much greater depth. Geothermobarometers utilised are explained in the text. Filled symbols denote data from this study and open symbols from the Cardoso (1980) study. Xenolith data is in black, with inclusion in diamond data coloured: green = lherzolithic, blue = harzburgitic, and purple = unclassified peridotitic. Graphite-diamond transition curve of Day (2012).

Conclusions

A re-investigation of existing data from Cardoso (1980) and new data on inclusions in diamond (this study) confirms the ultra-depleted nature of the Koffiefontein subcontinental lithospheric mantle, providing new insights into spatial (vertical) variations in diamond-host lithologies and into the nature of how the Koffiefontein kimberlite sampled the diamond-stability field during magma ascent. Our new geothermobarometric data indicate a cool 38 mW/m² geotherm for the Koffiefontein pipe, lower than the generally accepted average for group 1 kimberlites on the Kaapvaal craton (Grütter et al. 2006). From the expanded geothermobarometry data set, the main depth region of sampling for Koffiefontein diamonds lies between about 160-210 km. The vertical distribution of diamond-bearing lithologies

bears a strong resemblance to the lithological layering in the Kaapvaal cratonic lithosphere first proposed by Boyd et al. (1993), in which a zone of low-Ca, high Cr depleted harzburgite is concentrated in the lower section of the cratonic mantle.

References

- Boyd FR, Pearson DG, Nixon PH, Mertzman SA (1993) Low-calcium garnet harzburgites from Southern Africa: their relations to craton structure and diamond crystallization. *Contrib to Mineral Petrol* 113:352–366.
- Brey GP, Köhler T (1990) Geothermobarometry in four-phase lherzolites 2. New thermobarometers, and practical assessment of existing thermobarometers. *J Petrol* 31:1353–1378.
- Bussweiler Y, Brey GP, Pearson DG, et al (2017) The aluminum-in-olivine thermometer for mantle peridotites — Experimental versus empirical calibration and potential applications. *Lithos* 272–273:301–314.
- Cardoso P (1980) A study of mantle inclusions in the Koffiefontein kimberlite pipe, South Africa. University of Cape Town.
- Carswell DA, Gibb FGF (1987) Evaluation of mineral thermometers and barometers applicable to garnet lherzolite assemblages. *Contrib to Mineral Petrol* 95:499–511.
- Day HW (2012) A revised diamond-graphite transition curve. *Am Mineral* 97:52–62.
- Harley SL (1984) An experimental study of the partitioning of Fe and Mg between garnet and orthopyroxene. *Contrib to Mineral Petrol* 86:359–373.
- Hasterok D, Chapman DS (2011) Heat production and geotherms for the continental lithosphere. *Earth Planet Sci Lett* 307:59–70.
- Grütter HS, Latti D, Menzies A (2006) Cr-saturation arrays in concentrate garnet compositions from kimberlite and their use in mantle barometry. *J Petrol* 47:801–820.
- Moore RO, Otter ML, Rickard, RS, Harris, JW, Gurney, JJ (1986) The occurrence of moissanite and ferro-periclase as inclusions in diamond. 4th International Kimberlite Conference, Perth, Extended Abstracts; Geological Society of Australia. 16:409–411.
- Nickel KG, Green DH (1985) Empirical geothermobarometry for garnet peridotites and implications for the nature of the lithosphere, kimberlites and diamonds. *Earth Planet Sci Lett* 73:158–170.
- Nimis P, Taylor WR (2000) Single clinopyroxene thermobarometry for garnet peridotites. Part I. Calibration and testing of a Cr-in-Cpx barometer and an enstatite-in-Cpx thermometer. *Contrib to Mineral Petrol* 139:541–554.
- Pearson DG, Shirey SB, Harris JW, Carlson RW (1998) Sulphide inclusions in diamonds from the Koffiefontein kimberlite, S Africa: Constraints on diamond ages and mantle Re-Os systematics. *Earth Planet Sci Lett* 160:311–326.



Discovery of an orangeite magmatic event in the central Kalahari: Implications for the origin of southern African kimberlites

Marylou Vinès¹, Sebastian Tappe^{1,*}, Andreas Stracke², Allan Wilson³, Andrew Rogers⁴

¹University of Johannesburg, South Africa, *sebastian@uj.ac.za

²Westfälische Wilhelms-Universität Münster, Germany, stracke.andreas@uni-muenster.de

³University of the Witwatersrand, South Africa, allan.wilson@wits.ac.za

⁴Petra Diamonds South Africa (Pty) Ltd, andrew.rogers@petradiamonds.com

Introduction

Southern Africa hosts more than 1,600 kimberlite bodies, and over 75% of these fall within a 250 to 50 Ma age range. These Mesozoic-Cenozoic kimberlites have Group-1 and Group-2 compositional affinities, with occurrences of both groups providing significant primary diamond deposits. While Group-1 kimberlites represent a relatively homogenous type of CO₂- and H₂O-rich ultramafic magma in cratonic regions worldwide (Kjarsgaard et al., 2009), Group-2 kimberlites are compositionally more diverse potassic rocks that are confined to the Kaapvaal craton with emplacement ages between 200-110 Ma (Mitchell, 1995). Most models proposed for the origin of Group-1 kimberlites suggest sublithospheric depleted upper mantle sources (Tappe et al., 2017), whereas the compositions of Group-2 kimberlites require long-term enriched sources (Smith et al., 1985; Becker and Le Roex, 2006), with cratonic mantle lithosphere providing a suitable substrate to generate these H₂O-rich potassic magmas. The complexity of Group-2 kimberlites is consistent with the heterogeneous nature of the Kaapvaal craton root (Giuliani et al., 2015), and some authors emphasized strong petrogenetic links to olivine lamproites and ultramafic lamprophyres from cratons worldwide (Tappe et al., 2008). Group-2 kimberlites may therefore be interpreted as the magmatic expression of metasomatized mantle lithosphere beneath the Kaapvaal craton. Within such a model each craton produces its own compositional ‘flavour’ of ultramafic potassic magmatism due to the differences in composition, style, and timing of lithospheric mantle enrichment. The re-introduction of the term ‘orangeite’ for Group-2 kimberlite (Mitchell, 1995) reinforced the fact that these often diamond-bearing rocks differ significantly from archetypal kimberlites and, thus, they should be treated separately within models that seek to explain volatile-rich mantle-derived magmatism on thick continental shields.

KX36 Pipe - a newly discovered kimberlite occurrence in the central Kalahari of Botswana

The KX36 kimberlite pipe was discovered in 2008 during geophysical surveying of the central Kalahari in Botswana (Rogers et al., 2013). The pipe represents a ~5 ha large magmatic body that is covered by 80 m of Kalahari Group sedimentary overburden. The KX36 kimberlite pipe cuts through 400 m of Karoo Supergroup basaltic lava, and the kimberlite magma has locally entrained up to 10-20 vol% of basalt wall-rock, as well as some minor granitoid basement. On the basis of stratigraphy, the KX36 kimberlite pipe was emplaced between 180 and 50 Ma. The nearest known kimberlite occurrences are the Gope cluster some 60 km to the NW and the highly economic Orapa field some 250 km to the NNE of KX36, with kimberlite pipe emplacement ages between 115 and 80 Ma (Griffin et al., 2014). However, our first U/Pb perovskite age results for two magmatic kimberlite units within the KX36 pipe indicate magma emplacement at the NW margin of the Kaapvaal craton between 160 and 140 Ma. The robustness of these preliminary results is currently tested by additional analyses, also including an alternative analytical method.

Petrography and mineralogy

Two main units, ‘black’ and ‘green’ kimberlite, can be distinguished within the KX36 pipe down to ~500 m depth. Both units represent coherent magmatic kimberlite, and the green variety appears to be a hydrothermally altered and more crustally contaminated variant of the fresh black kimberlite. The black kimberlite is highly macrocrystic with individual olivine crystals approaching 15 mm across (up

to 30 vol%). Phlogopite macrocrysts up to 3 mm across are common (up to 5 vol%). Their rims typically enclose minute groundmass spinel crystals. The groundmass of the black kimberlite variety consists of variable proportions of phlogopite flakes (20-120 μm), carbonate and serpentine. Accessory groundmass phases comprise atoll-textured spinel and perovskite (<60 μm), and very rare Mg-rich ilmenite.

A sizable (20 cm across) micaceous autolith was recovered from KX36 kimberlite drill core. The fresh autolith is inequigranular and dominated by olivine, phlogopite and clinopyroxene, with minor spinel, Mn-rich ilmenite, calcite, serpentine, apatite and Ti-rich andradite garnet. Macrocrystic olivine has high forsterite content of Fo_{92} . Phlogopite has high TiO_2 content (1-4 wt%) and evolves by Al-depletion toward tetraferriphlogopite. Clinopyroxene is close to diopside end-member composition with minor amounts of Ti and Al. Spinel crystals occur in interstices and as inclusions in phlogopite and clinopyroxene. They have magnesian chromite composition with high Cr# of up to 93 and low TiO_2 content (<6 wt%). Interstitial magmatic garnet has Ti-andradite composition with up to 1 wt% ZrO_2 . These mineralogical features suggest that the parent magma was of orangeite affinity.

Bulk rock major- and trace element compositions

Although the fresh black kimberlite variety of the KX36 pipe macroscopically resembles archetypal kimberlite, several mineralogical and geochemical features suggest a petrogenetic affinity to Group-2 kimberlite. For example, the transitional nature of the KX36 kimberlite between archetypal kimberlite and orangeite is illustrated by the elevated K contents at constant and low Ti concentration levels. This trend culminates at the micaceous autolith (Fig.1). Primitive mantle normalized incompatible element patterns show a significant slope for the LILE (Cs, Rb, Ba), unfractionated low concentrations for the HFSE (Th, U, Nb, Ta), and highly fractionated LREE/HREE. These patterns strongly resemble the trace element distributions of orangeites (Fig.2). The trace element pattern of the micaceous autolith is highly fractionated and bears resemblance to primitive continental arc volcanic rocks. Such a geochemical signature is typically found in subduction zone settings.

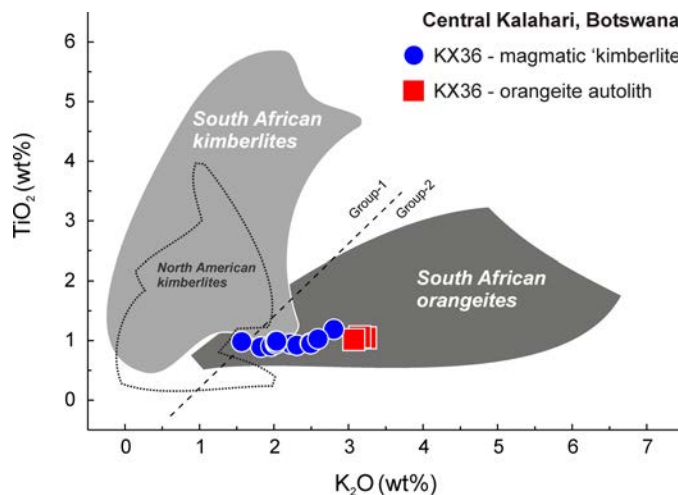


Figure 1: TiO_2 vs. K_2O for fresh uncontaminated (C.I. <1.25) magmatic KX36 kimberlite and an entrained micaceous autolith (fields for comparison from: Smith et al., 1985; Becker and Le Roex, 2006; Coe et al., 2008; Tappe et al., 2017).

Preliminary conclusion

Our study provides first evidence for the occurrence of kimberlite magmatism of Group-2 affinity in the central Kalahari basin. This discovery increases the geographic extent of ultramafic potassic magmatism in southern Africa by more than 300 km toward the NW Kaapvaal craton edge. As previously suggested for orangeite magmatism in other parts of the Kaapvaal craton (cf., Coe et al., 2008), the combination of a high-LILE and low-HFSE geochemical fingerprint at the NW craton margin is best explained by involvement of strongly K-metasomatized mantle lithosphere. The distinctive trace element signature can be linked to prior subduction-driven collision events during the Proterozoic evolution of the Kaapvaal craton and surrounding orogenic belts.

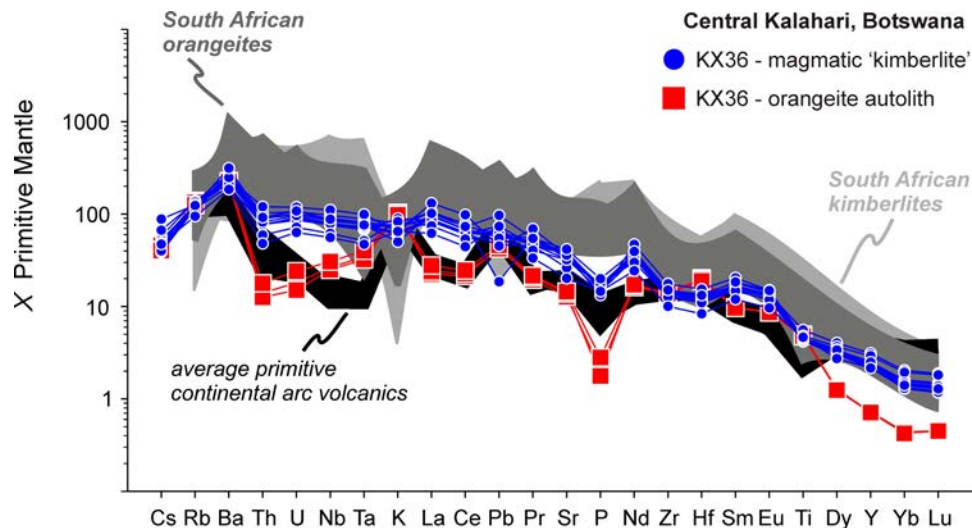


Figure 2: Normalized incompatible element patterns for fresh uncontaminated (C.I. <1.25) magmatic KX36 kimberlite and an entrained micaceous autolith (fields for comparison from: Becker and Le Roex, 2006; <http://georoc.mpch-mainz.gwdg.de/georoc/>).

Acknowledgments

This PhD study is conducted with support of the CIMERA DST-NRF Centre of Excellence at the University of Johannesburg. We thank 11-IKC for financial support to present this work at the conference.

References

- Becker M, Le Roex AP (2006) Geochemistry of South African on- and off-craton, Group I and Group II kimberlites: Petrogenesis and source region evolution. *J Petrol* 47: 673-703
- Coe N, Le Roex AP, Gurney JJ, Pearson DG, Nowell GM (2008) Petrogenesis of the Swartruggens and Star Group II kimberlite dyke swarms, South Africa: Constraints from whole rock geochemistry. *Contrib Mineral Petrol* 156: 627-652
- Giuliani A, Phillips D, Woodhead JD, Kamenetsky VS, Fiorentini ML, Maas R, Soltys A, Armstrong RA (2015) Did diamond-bearing orangeites originate from MARID-veined peridotites in the lithospheric mantle? *Nat Commun* 6: 1-10
- Griffin WL, Batumike JM, Greau Y, Pearson NJ, Shee SR, O'Reilly SY (2014) Emplacement ages and sources of kimberlites and related rocks in southern Africa: U-Pb ages and Sr-Nd isotopes of groundmass perovskite. *Contrib Mineral Petrol* 168: 1-13
- Kjarsgaard BA, Pearson DG, Tappe S, Nowell GM, Dowall D (2009) Geochemistry of hypabyssal kimberlites from Lac de Gras, Canada: Comparisons to a global database and applications to the parent magma problem. *Lithos* 112: 236-248
- Mitchell RH (1995) Kimberlites, orangeites, and related rocks. Plenum Press, New York
- Rogers AJ, Hough TG, Davidson JM (2013) KX36 - rediscovering the diamond exploration potential of the central Kalahari in Botswana. *The Journal of The Southern African Institute of Mining and Metallurgy* 113: 539-545
- Smith CB, Gurney JJ, Skinner EMW, Clement CR, Ebrahim N (1985) Geochemical character of Southern African kimberlites: A new approach based on isotopic constraints. *Transactions of the Geological Society of South Africa* 88: 267-280
- Tappe S, Foley SF, Kjarsgaard BA, Romer RL, Heaman LM, Stracke A, Jenner GA (2008) Between carbonatite and lamproite: Diamondiferous Torngat ultramafic lamprophyres formed by carbonate-fluxed melting of cratonic MARID-type metasomes. *Geochim Cosmochim Acta* 72: 3258-3286
- Tappe S, Romer RL, Stracke A, Steinfeldt A, Smart KA, Muehlenbachs K, Torsvik TH (2017) Sources and mobility of carbonate melts beneath cratons, with implications for deep carbon cycling, metasomatism and rift initiation. *Earth and Planetary Science Letters* 466: 152-167



Yellow and white diamonds from Qilalugaq kimberlites: Two generations of diamond growth

Anetta Banas¹, Thomas Stachel², Karen V. Smit³, Ken Armstrong⁴

¹ APEX Geoscience Ltd., Edmonton, Canada, abanas@apexgeoscience.com

² University of Alberta, Edmonton, Canada, tstachel@ualberta.ca

³ Gemological Institute of America, New York, USA, ksmit@gia.edu

⁴ North Arrow Minerals Inc., Vancouver, Canada, karmstrong@northarrowminerals.com

Introduction

A population of intense yellow diamonds has been identified at the Q1-4 kimberlite on the Naujaat (formerly the Qilalugaq) Project. The Qilalugaq Kimberlite Field is located near the hamlet of Naujaat (Repulse Bay), Nunavut, Canada. It consists of 16 kimberlites: 8 kimberlite pipes and 8 laterally extensive kimberlite dykes. The kimberlites were emplaced at ca. 546 Ma (Kupsch and Armstrong, 2013). The Q1-4 kimberlite, the largest (12.5 Ha) within the cluster, is interpreted as a multi-phased, complex-shaped kimberlite pipe. An Inferred Mineral Resource of 48.8 million tonnes at a grade of 53.6 cppt (total recovery) containing 26.1 million carats has been reported for Q1-4 (Kupsch and Farrow, 2013).

Background

In 2014, a bulk sample was collected from the Q1-4 kimberlite to provide additional information on the diamond content of the pipe and to establish whether or not a population of yellow diamonds recovered in earlier sampling persists into the larger diamond sizes. Approximately 384 carats of diamonds larger than 1.1 mm (DTC+1) were recovered from the 1,353.3 tonne bulk sample. The results from the bulk sample confirmed that a population of yellow diamonds is present at Q1-4 and that the yellow diamonds are present into the grainer and carater diamond sizes (North Arrow, 2015a). The yellow diamonds comprise approximately 9.0% by stone count and 21.5% by carat weight of the total diamond parcel. The yellow diamonds display a range of hues, tones and saturation levels, ranging from dark/intense (orangy) yellow to very pale yellow (Figure 1). Dark/intense yellow diamonds make up 3.2% by stone count and 6.5% by carat weight of the total parcel. The proportion of yellow diamonds increases, both by stone count and carat weight, in the larger size classes (North Arrow, 2015a).

Diamond Samples

A parcel of rough diamonds containing 56 stones <1.1 mm (DTC-1) and 10 stones ~1.8 mm (DTC+5) in size was analysed by FTIR (Fourier Transform Infrared) spectroscopy to determine nitrogen contents and aggregation states. The DTC-1 diamond parcel contained 32 yellow diamonds of varying colour intensity and 24 white diamonds (Figure 1). All 10 DTC+5 diamonds were yellow with varying degrees of colour intensity. Subsequently, an additional 10 diamonds, cut and polished from rough diamonds ranging in size from 0.125 to 4.41 carats, were analysed by FTIR. Nine of the polished diamonds were of saturated orangy yellow colour and one diamond had an intense yellow colour. Four of the polished diamonds were also analysed by VIS-NIR spectroscopy.



Figure 1. Colour distribution of the DTC-1 diamond parcel. From left to right: green-yellow, intense yellow, pale yellow, very pale yellow and white.

Results

The yellow diamonds are largely characterized by cuboid shapes, have a limited range of nitrogen contents between 360 and 748 atomic ppm and contain single substitutional nitrogen (C centres or Nc) ranging from 2.9 -233 atomic ppm (Figure 2A). These diamonds are classified as intermediate Type Ib-IaA. VIS-NIR spectroscopy documents a complete absence of N3 centres in four polished yellow diamonds, confirming their Type Ib-IaA classification. Total nitrogen contents and the proportion of nitrogen in C centres are consistent across the examined size range and consequently, yellow diamonds from all size fractions are considered to be part of one diamond population. C centres cause absorption between 300 and 700nm in the visible light range, resulting in yellow colours that are often described as “canary” or saturated yellow in the gem trade. For this sample set a broad correlation exists between the concentration of nitrogen in the C-centre and the intensity of the yellow colour where a higher Nc concentration results in a more vivid yellow to orange yellow colour.

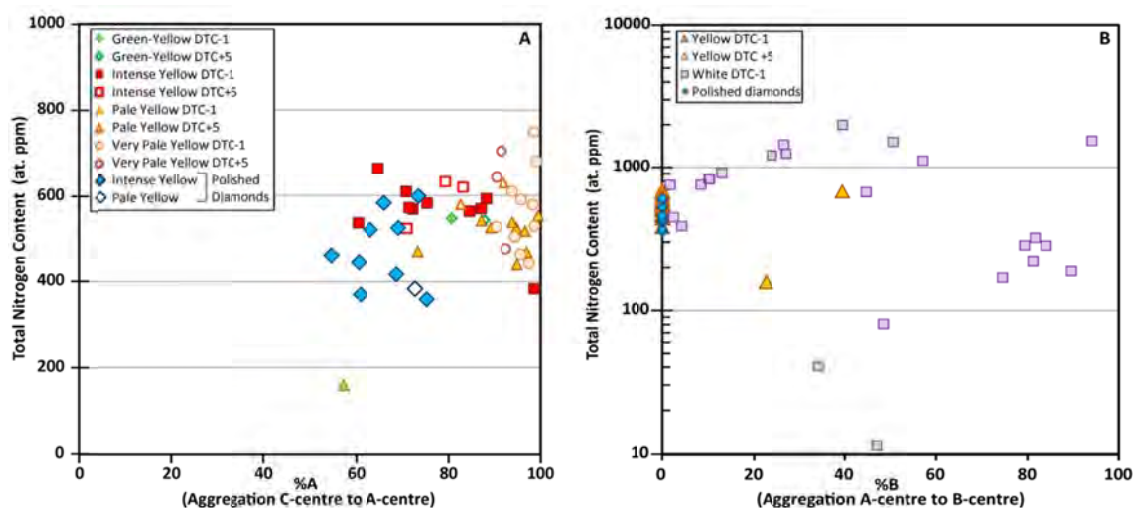


Figure 2. Nitrogen aggregation characteristics for diamonds from Q1-4: **A**) %A ($100 * A/(A+C)$) aggregation vs total nitrogen content (atomic ppm) for Type Ib-IaA yellow diamonds and **B**) %B ($100 * A/(A+B)$) aggregation vs total nitrogen content (atomic ppm) for all diamonds.

The white (colourless) diamonds are mainly characterized by octahedral and dodecahedral (resorbed octahedral) shapes. They have a broad range in total nitrogen contents ranging from 11 – 1994 atomic ppm. The white diamonds can be classified as Type IaAB based on the presence of fully aggregated nitrogen in B-centres ranging from 2-94 %B (Figure 2B).

Implications for Diamond Formation

The relative concentration of A-centres in Type Ib-IaA diamonds and the relative concentration of B-centres in IaAB diamonds can be used to provide constraints on the mantle residence time or the time-averaged residence temperature of the diamonds if one or the other is known (Taylor et al., 1996; Leahy and Taylor 1997). Since no constraints on residence time are available (i.e. no diamond ages) for the Qilalugaq area a temperature constraint based on the geotherm was used to estimate mantle residence times for the diamonds. A 38-40mW/m² geotherm has been modelled based on clinopyroxene from garnet peridotite (Kupsch and Armstrong, 2013).

For the yellow diamonds the modelling indicates possible mantle residence times in the range of thousands of years up to a few 10's of millions of years. The maximum modelled mantle residence time for the Type Ib-IaA diamonds is 30 Ma.

Given that a typical cratonic geotherm has been calculated for the Qilalugaq area, the temperature distribution of the Q1-4 Type IaAB diamonds should approximately correspond to that of cratonic

diamonds worldwide. Worldwide cratonic diamonds have a T_{Nitrogen} (temperature calculated from nitrogen aggregation) distribution of $1150 \pm 70^\circ\text{C}$ (Stachel, 2014). Applying the maximum 30 Ma mantle residence time calculated for the Type Ib-IaA diamonds to the Type IaAB diamonds gives a T_{Nitrogen} distribution of $1240 \pm 70^\circ\text{C}$. This would indicate mantle storage under exceptionally hot conditions. For a 1 Ga mantle residence time, Q1-4 Type IaAB diamonds have a T_{N} distribution of $1150 \pm 60^\circ\text{C}$, in perfect accordance with the worldwide distribution indicating that the white diamonds represent an older generation of diamond formation in the Qilalugaq area.

Conclusions

The majority (~98%) of diamonds worldwide are classified as Type Ia and range between IaA and IaB. Natural Type Ib diamonds are exceptionally rare, estimated to make up less than 0.1% of natural diamonds globally (Harlow, 1998). The studied yellow diamonds from the Q1-4 contain unaggregated nitrogen, a defining characteristic of natural Type Ib diamonds with the highly coveted canary yellow color. The high proportion of Type Ib diamonds recovered from Q1-4 is extremely unusual (North Arrow, 2015b).

Based on the spectroscopic data, the yellow and white diamonds from Q1-4 are interpreted as two discrete populations. The lack of overlap in the mantle residence time estimates for yellow and white Qilalugaq diamonds implies that these two populations were formed during temporally distinct diamond forming events. The white diamonds share the nitrogen characteristics of typically Archean to Paleoproterozoic diamond populations worldwide. In contrast, the yellow diamonds likely formed in temporal proximity to host kimberlite magmatism. Fancy yellow colors can have a positive impact on diamond valuation; therefore, understanding the characteristics and distribution of the yellow diamond population is critical to further the evaluation of the economic potential of the Q1-4 kimberlite.

References

- Harlow, G. E. (1998) *The Nature of Diamonds*. American Museum of Natural History. 278p.
- Kupsch, B., Armstrong, J. (2013) Exploration and Geology of the Qilalugaq Kimberlites, Rae Isthmus, Nunavut, Canada. In: D.G. Pearson et al (eds.) *Proceedings of the 10th International Kimberlite Conference Volume 2, Special Issue of the Journal of the Geological Society of India*, P. 67-78.
- Kupsch, B., Farrow, D. (2013) Qilalugaq Diamond Project Nunavut, Canada, NI 43-101 Technical Report Mineral Resource. Prepared for North Arrow Minerals Inc. www.Sedar.com 73p.
- Leahy, K., Taylor, W.R., (1997) The influence of the Glennie domain deep structure on the diamonds in Saskatchewan kimberlites. *Russian Geology and Geophysics* 38 (2), 481–491.
- North Arrow Minerals Inc. (2015a) North Arrow Reports Final Diamond Recoveries From the Qilalugaq Bulk Sample. Press Release May 5, 2015. www.Sedar.com 2p.
- North Arrow Minerals Inc. (2015b) North Arrow Reports Yellow Diamonds From Q1-4 Kimberlite are Rare Natural Type Ib Diamonds Press Release April 21, 2015. www.Sedar.com 2p.
- Stachel, T. (2014) Diamonds. In: Groat, L. (ed) *Geology of Gem Deposits Edition 2*, Mineralogical Association of Canada Short Course, V44, 1-28.
- Taylor, W.R., Canil, D., Milledge, H.J. (1996) Kinetics of Ib to IaA nitrogen aggregation in diamond. *Geochim. Cosmochim. Acta* 60, 4725–4733.



Geodynamic and geophysical consequences of stealth(y) mantle metasomatism: craton evolution and metallogeny

Suzanne Y. O'Reilly¹, William L. Griffin¹ and Norman J. Pearson¹

¹ARC Centre of Excellence for Core to Crust Fluid Systems (CCFS) and GEMOC, Earth and Planetary Sciences, Macquarie University, NSW 2109, Australia; sue.oreilly@mq.edu.au; bill.griffin@mq.edu.au; norman.pearson@mq.edu.au

Introduction

The metasomatised lithospheric mantle is a palimpsest, recording the multiple events that have affected that domain since it formed. Interpreting this complex record and tracking specific episodes and processes is a key to reconstructing lithosphere evolution through time, and the nature of volatile fluxes from the deep Earth. Convergence between datasets of Hf isostopic model ages for zircons (e.g., Belousova et al., 2010) and Re-Os model ages for mantle sulfides (Griffin et al., 2014), reinforced by other geochemical and tectonic criteria, indicate that over 75% of the subcontinental lithospheric mantle (SCLM) and its overlying crust (now mostly lower crust) formed at 3.0-3.5 Ga, probably in global overturn events that marked a change in Earth's fundamental geodynamic behaviour (Griffin et al., 2014).

Pristine Archean lithospheric mantle, the roots of the Archean cratons up to >300km deep, is not only *more* depleted (low in basaltic melt components) than younger lithospheric mantle, it is *differently* depleted. Proterozoic and Phanerozoic lithospheric mantle (xenoliths and orogenic massifs), as well as abyssal peridotites, ophiolitic peridotites, all have one important feature in common: as Al decreases, Fe (and Cr) contents show only a very narrow range (8 ± 1 wt% FeO). In contrast, Archon peridotites have lower Fe at low Al contents, and may show a weak positive correlation between Fe (and Cr) and Al, suggesting that no Cr-Al phase (i.e. spinel or garnet) was present on the liquidus during the melting that produced Archean lithosphere. Garnet-peridotite suite rocks in cratonic mantle are thus now interpreted as products of the metasomatic introduction of garnet and clinopyroxene into original depleted harzburgite, thus "refertilising" the depleted residue. Therefore, the "oceanic melting trend" of Boyd (1989) is now interpreted as a refertilisation trend, with the compositional trend arrow reversed (Griffin et al., 2009). The cratonic roots in contact with the asthenosphere, and their vertical margins in contact with repeated fluid and melt fluxes, are the most strongly modified domains through time, so cratonic root compositions show a general increase in fertility with increasing depth.

Integration of geochemical and geophysical datasets, groundtruthed with petrophysical measurements and modelling for different mineral compositions and modes, has enabled geologically realistic interpretations of global (and regional) tomographic results, identifying the vertical and horizontal extent of original Archean cratonic mantle and their refertilised domains (Figure 1).

Stealth Metasomatism and its Geophysical Significance

Metasomatism (and associated refertilisation) affects not only the geochemical characteristics of the lithospheric mantle, but also its physical *parameters* (and hence geophysical signatures) including density, seismic response and thermal and electrical characteristics. The concept of "*stealth*" *metasomatism* has been introduced to highlight the "deceptive" addition to lithospheric mantle rock-types of new phases (e.g. garnet and/or clinopyroxene) indistinguishable mineralogically from common mantle-peridotite phase assemblages.

Recognition of *stealth metasomatism* reflects the increasing awareness of the importance of refertilisation of ancient refractory mantle regions by metasomatic fluid fronts in modifying mantle domains. Understanding the timing and nature of *stealth metasomatism* is critical to understanding the geochemical and geodynamic evolution of the lithospheric mantle domains and assessing their metallogenic fertility.

Primitive Archean lithospheric mantle is highly magnesian (~49% MgO) with lower density (~3.31 g/cm³) than fertile mantle (~3.37 g/cm³). The resulting contrasts in *seismic response* become measurable if metasomatised regions are on the scale of tens to hundreds of km. Metasomatic refertilisation of the cratonic lithospheric mantle not only increases its density, but also strongly affects its rheology. The recognition that the cratonic lithospheric mantle may in general consist of a very depleted upper layer, becoming more metasomatised (evidenced by garnet peridotites) at depth, provides a solution to some important discrepancies between geophysical data and numerical models. A deep cratonic root made up mainly of garnet peridotites would imply a lower geoid and a much greater elevation than is observed for the Kaapvaal craton, and a mismatch in Vp/Vs ratios (Afonso et al., 2010), but a layered model in with refertilization increasing with depth, yields numerical models that fit the geophysical data.

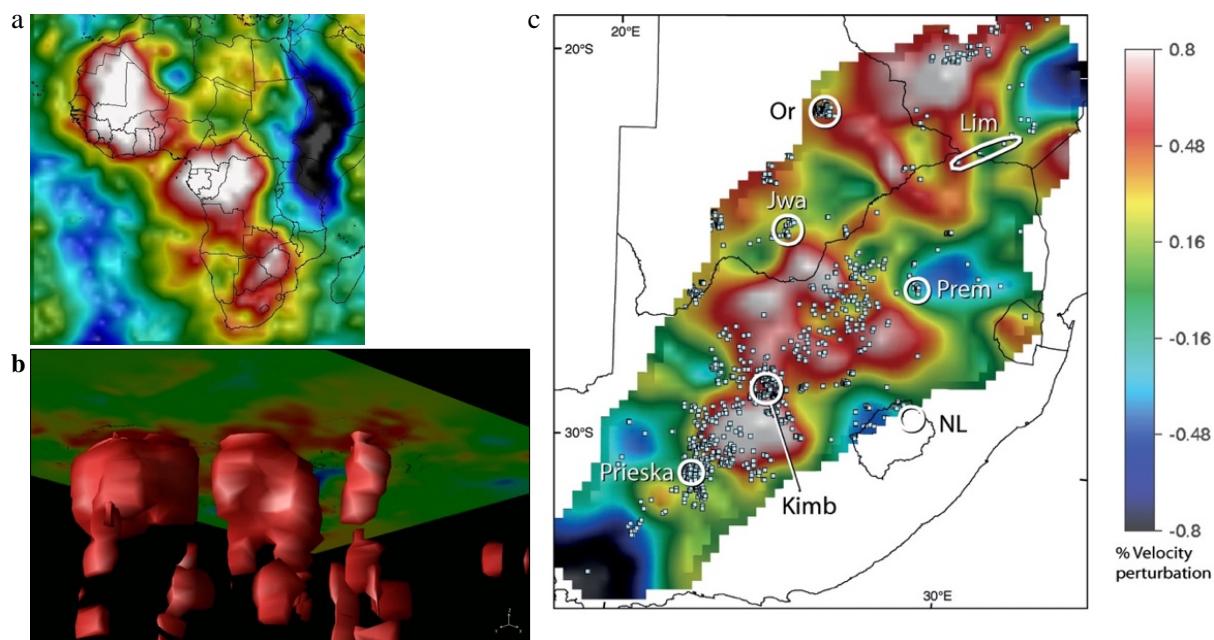


Figure 1: Vs tomography (100-150 km) of the lithospheric mantle. Red to white colours indicate high Vs; blue colours low Vs (modified from Griffin et al., 2013 and Begg et al., 2009). **(a)** Africa, showing distribution of the boundaries of high-velocity cratonic blocks with metasomatised (red) margins. **(b)** modelled high-Vs irregular volume of cratonic roots to ~350 km beneath each craton. **(c)** Detailed seismic tomography for Kaapvaal craton with kimberlites clustered at margins of high-velocity volumes. White circles show major kimberlite provinces.

Thermal changes are caused by advective transfer of heat by relatively hot metasomatising fluids and by the influx of heat-producing elements (K, U, Th) that accompanies some types of metasomatism. Radioactive decay of these elements can raise the local heat flow by 50-70% over normal reduced mantle heat flow. The origins of significantly contrasting *electromagnetic (MT) responses* in the lithospheric mantle have not yet been satisfactorily identified. Fluid-related recrystallisation demonstrated in microstructural studies may result in significant H contents in mantle minerals and may affect electrical conductivity. The key to understanding the electromagnetic signals from the mantle lies in identifying the nature of fluids and their distribution and thus is closely connected with a full understanding of metasomatic processes, grain sizes and fabrics, and fluid compositions and movement mechanisms in the mantle. Comparisons of high-resolution MT traverses with geochemical mapping traverses show a correlation of higher conductivity with more strongly metasomatised domains.

Implications for metallogeny

Magma-related ore systems form economic deposits that underpin our human civilisation. The magmas related to metallic element redistribution derive from the asthenosphere, then traverse and interact to

varying degrees with the subcontinental lithospheric mantle. The evolution of the original Archean lithospheric mantle has been the single largest influence on the formation of most of Earth's ore deposits (Griffin et al., 2013):

- the high degree of buoyancy of this ancient SCLM relative to the asthenosphere, results in the persistence today of low-density, rheologically coherent Archean domains and commonly, the preservation of old crustal (or at least lower-crustal) domains;
- the enduring (and volumetrically dominating) Archean lithospheric mantle domains are a reservoir for metasomatic enrichment over their long history, creating a potentially metallogenically-fertile mantle impregnated with critical elements (e.g., Au, Cu, Ni and PGEs (Zhang et al., 2008);
- the formation of Archean cratons provided an architectural mantle-scape of regions with contrasting rheology, composition and thickness. These cohesive Archean domains direct magma and fluid pathways around their margins and along old sutures between blocks, and may act as both sinks and sources for ore-forming elements depending on the geodynamic evolutionary stage;
- if the first stabilisation of lithospheric mantle at 3.0-3.5 Ga signalled the end of a mantle overturn regime (either uniquely, or intermittently with subduction), then this is when long-lived tectonic regimes conducive to mineralising systems (e.g. back-arc basins, passive margins, cratonic boundaries) became available Begg et al., (2010).

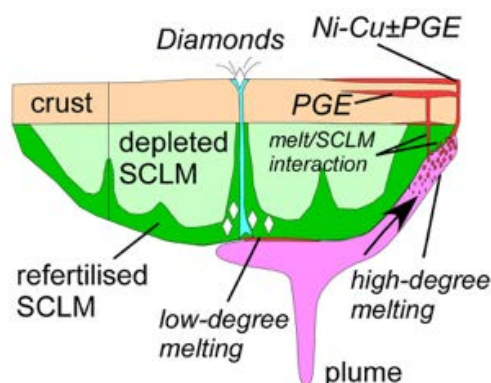


Figure 2: Interactions between magmas and the base and edges of cratonic roots. Plume magmatism triggers kimberlite formation and flows to areas of thinner SCLM where melting is focused. Variable interaction of melts with crust and SCLM influences Ni-Cu and PGE deposit genesis. Lithosphere-scale discontinuities and zones of weakness can focus the locus of kimberlite eruption.

References

- Afonso JC, Ranalli G, Fernandez M, et al. (2010) On the Vp/Vs-Mg# correlation in mantle peridotites: Implications for identification of thermal and compositional anomalies in the upper mantle. *Earth Planet Sci Lett* 289: 606-618
- Begg GC, Griffin WL, Natapov LM, et al. (2009) The lithospheric architecture of Africa: Seismic tomography, mantle petrology and tectonic evolution. *Geosphere* 5: 23-50
- Begg GC, Hronsky JAM, Arndt NT, et al. (2010) Lithospheric, cratonic, and geodynamic setting of Ni-Cu-PGE sulfide deposits. *Econ. Geology* 105: 1057-1070
- Belousova EA, Kostitsyn YA, Griffin WL, et al. (2010) The growth of the continental crust: Constraints from zircon Hf-isotope data. *Lithos* 119: 457-466
- Boyd FR (1989) Composition and distinction between oceanic and cratonic lithosphere. *Earth Planet. Sci. Lett.*, 96: 15-26
- Griffin, W., O'Reilly, S.Y., Afonso, J.C., Begg, G.C., 2009. The composition and evolution of lithospheric mantle: A re-evaluation and its tectonic implications. *J. Petrology* 50(9): 1185-1204
- Griffin WL, Begg GK, O'Reilly SY (2013) Continental-root control on the genesis of magmatic ore deposits. *Nature Geoscience* 6: 905-910
- Griffin WL, Belousova EA, O'Neill C, et al. (2014) The world turns over: Hadean-Archean crust-mantle evolution. *Lithos* 189: 2-15
- O'Reilly SY, Zhang M, Griffin WL, Begg G, Hronsky J, 2009. Ultradeep continental roots and oceanic remnants: a solution to the geochemical "mantle reservoir" problem? *Lithos* 112(2): 1043-1054
- Zhang M, Wang K-L, O'Reilly SY, Hronsky J, Griffin WL (2008) Flood basalts and metallogeny: The lithospheric mantle connection. *Earth Science Reviews* 86: 145-174



Super-reducing conditions in ancient and modern volcanic systems: implications for the carbon budget of the deep lithosphere

William L. Griffin¹, Sarah E.M. Gain¹, Jinxiang Huang¹, Yoann Greau¹, Vered Toledo² and Suzanne Y. O'Reilly¹

¹ARC Centre of Excellence for Core to Crust Fluid Systems (CCFS) and GEMOC, Earth and Planetary Sciences, Macquarie University, NSW 2109, Australia; bill.griffin@mq.edu.au; sarah.gain@mq.edu.au;

jinxiang.huang@mq.edu.au; yoann.greau@mq.edu.au; sue.oreilly@mq.edu.au

²Shefa Yamim (A.T.M.) Ltd., Netanya 4210602, Israel gold101@netvision.net.il

Introduction

Estimates of the oxygen fugacity (fO_2) of the cratonic subcontinental lithospheric mantle (SCLM) range from above the quartz-fayalite-magnetite (QFM) buffer to just above the iron-wüstite (IW) buffer, and generally decrease with depth. While several lines of evidence suggest that the sublithospheric mantle may be constrained by the IW buffer (the presence of metallic Fe), there also is evidence that at least localized volumes of significantly lower fO_2 must exist within the SCLM, and perhaps within the deeper mantle. In this contribution, we describe a remarkable example of super-reducing conditions in an off-craton volcanic setting (Griffin et al., 2016a), and discuss its implications for other tectonic settings, and for the transfer of carbon and hydrogen from the deeper mantle.

Super-reducing conditions in a Cretaceous volcanic system, Mt Carmel, Israel

Aggregates of hopper-formed crystals of Ti-rich corundum are abundant in Upper Cretaceous basaltic pyroclastic rocks (vent breccias, tuffs) exposed on Mt Carmel near Haifa, Israel. Melt pockets trapped within and between corundum crystals contain mineral assemblages (SiC (moissanite), TiC, Fe-Ti-Zr silicides/phosphides and native V) that require $P \geq 1$ GPa, $T = 1500-1100$ °C and extremely low fO_2 (ΔIW -10 to -12) (Griffin et al., 2016a). Mineral parageneses suggest that the corundum and the low- fO_2 assemblages developed through interaction of basaltic magmas with mantle-derived (CH_4+H_2) at high fluid/melt ratios, leading to progressive lowering of fO_2 .

A schematic illustration of the process is shown in Figure 1; this model envisions a magma chamber being flushed by a steady supply of $CH_4 \pm H_2$, but other configurations are possible. The material described here comes from at least 8 different volcanoes, with eruptions spread over ca 10 Ma, providing snapshots of similar magmatic systems erupted at different stages of their evolution, and has been used to reconstruct the evolution of a single synthetic system. The early oxidation of CH_4 may have led to the precipitation of abundant, commonly vesicular, wüstite found as ejecta in the pyroclastics; this suggests fO_2 at or below the QFM buffer. The CO_2 released by this reaction may in turn have driven the precipitation of abundant high-Mg calcite, also found in the ejecta; this could continue to fO_2 as low as the EMOD/G buffer. The progressive lowering of fO_2 to the IW buffer is marked by the appearance of a suite of mutually immiscible melts: native Fe, Fe-oxide/silicate melt and Ti-oxide/silicate melt. This reaction appears to have removed most of the FeO from the system; none of the silicate phases in the trapped melts (see below) have significant contents of Fe. The removal of the Fe-FeO buffer would allow fO_2 to decline (rapidly?) to the levels ($\Delta IW = -6$ to -8) where SiC could precipitate. This would desilicate the melt (now dominated by CaO- Al_2O_3 -MgO), driving it into the field where corundum is on the liquidus. The hopper form of the corundum aggregates implies Al_2O_3 -supersaturation, causing the rapid growth of corundum, and the trapping of melt pockets, some of which contain silicide melts that precipitated abundant TiC. The desilication process apparently continued to near-completion, leading, in some cases, to a coarse-grained assemblage of hibonite ($CaAl_{12}O_{19}$) + grossite ($CaAl_6O_{10}$) + MgAl spinel + fluorite + native V, at $fO_2 \leq \Delta IW -11$. Many of the larger corundum aggregates are cut by breccia veins of amorphous (commonly vesicular) carbon, and this material also

occurs in parallel-sided veinlets down to the sub-micron (TEM) scale, emphasising the important role of carbon in the evolution of these systems.

Not a unique occurrence

Similar mineral assemblages (+ diamond) occur in the “ophiolitic” peridotites of the Yarlong-Zangbo and Bangong-Nujuang suture zones (southern Tibet; Xu et al., 2009; Zhang et al., 2016; Griffin et al., 2016b; F. Xiong et al., 2017) and the Polar Urals (Yang et al. 2016). In each of these cases, as in the Mt Carmel example, most of the more highly reduced phases, including nitrides, silicides and

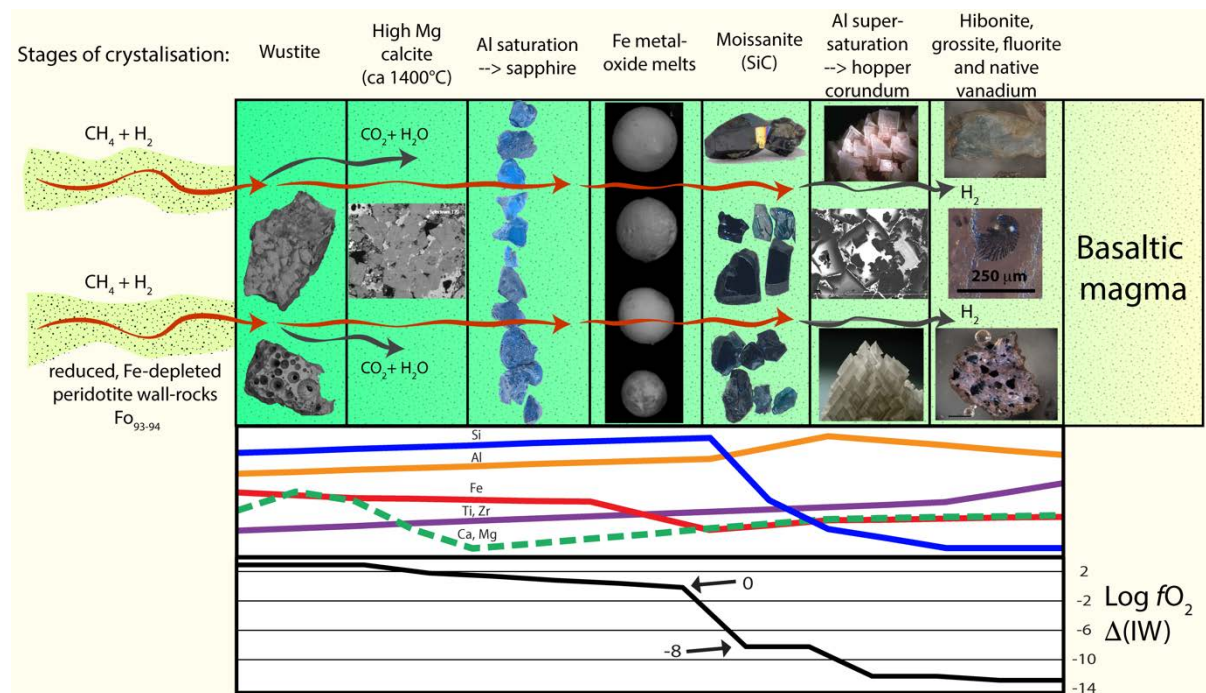


Figure 1. Model for the evolution of the Mt Carmel corundum-SiC system(s), as a progressive interaction between mantle-derived volatiles ($\text{CH}_4 \pm \text{H}_2$) and a basaltic magma. The evolution of the melt composition and the $f\text{O}_2$ of the system is illustrated schematically in the lower panels; the curves for elemental abundance are not to scale. The most important aspects are the drop in Fe (especially FeO) at the IW buffer, the rapid desilication of the melt following the onset of SiC crystallization, and the extremely low $f\text{O}_2$ required by the presence of abundant native V in the hibonite-grossite assemblage. The incongruent melting of anorthite suggests $P \geq 9\text{kb}$, while phase relationships in immiscible silicide melts indicate $T = 1500\text{-}1200^\circ\text{C}$.

carbides, are found as inclusions in grains of Ti-rich corundum. The main difference between the “ophiolitic” and the Mt Carmel occurrences is that some carbon in the former occurs as diamond (in breccias of amorphous carbon; Yang et al. 2014; Zhang et al. 2016). Q. Xiong et al. (2017) therefore have suggested that the “ophiolitic” occurrences reflect crystallization in late-magmatic systems related to the rapid emplacement of the host peridotites to shallow depths (McGowan et al., 2015; Griffin 2016b). Similar processes probably are occurring today beneath the Kamchatka volcanic arc, where mafic pyroclastic volcanic rocks carry diamond, SiC and Ti-rich corundum (Gordeev et al., 2014).

The streaming of low- $f\text{O}_2$ fluids from the deep upper mantle thus may accompany many types of deep-seated volcanism, especially in tectonic situations (continental collision zones, deep subduction zones, major transform faults) that allow the rapid ascent and focussing of deep-seated magmas. If the $f\text{O}_2$ of the deep upper mantle is controlled by the IW buffer, then C-O-H fluids will be dominated by $\text{CH}_4 + \text{H}_2$, like those trapped in metal-bearing Type II diamonds (Smith et al., 2016). The rapid transport of such fluids to shallower depths as components of deep-seated magmas (including kimberlites) is thus inferred to produce local, perhaps transient, volumes of low- $f\text{O}_2$ assemblages.

SiC is a key indicator for these processes; it is widespread in Siberian kimberlites, and the small number of reports from S. African kimberlites could simply reflect different approaches to the study and processing of kimberlites. However, in both cratons, SiC occurs as inclusions in diamond, and we have separated SiC from Roberts Victor eclogites, apparently associated with the metasomatism that generated diamonds in these rocks. The most common inclusion in SiC from all of these localities is silicon metal, with morphologies suggesting trapping as a liquid, which subsequently commonly exsolved FeSi₂ and related phases; these are high-temperature phases (1400-1500 °C) and thus are not related to late serpentinization. The extremely low fO_2 required for the formation of SiC strongly suggests the presence of H₂, which could be generated by the partial oxidation of CH₄ and the deposition of diamond (i.e. SiO₂ + 3CH₄ → SiC + C + 3H₂ + CO₂). The isotopically light carbon ($\delta^{13}C = -25$ to -33) of the SiC in the Mt Carmel samples (and kimberlitic SiC worldwide) is similar to that in the Tibetan diamonds and some Transition-Zone diamonds, and may reflect the composition of abiogenic methane in the deep upper mantle.

Other implications

Redox melting in the presence of abundant CH₄±H₂, rather than simply carbon, may be more efficient; it may also involve the desilication of wall rocks and their melts, and the production of Al-rich lithologies such as corundum eclogites with negative Eu anomalies. We suggest that all of these processes would accompany the arrival at the SCLM of kimberlites or other melts generated in the deep upper mantle or Transition Zone, and may have contributed significantly to the carbon budget of the lower lithosphere through time.

The recognition that CH₄±H₂ may accompany melts rising from a deeper, metal-saturated mantle also suggests an explanation for the zones of high conductivity that mark the tracks of mantle-derived magmatic systems (from kimberlites to Bushvelds). The oxidation of CH₄ in rising fluids could propagate networks of microveinlets of amorphous carbon (even if later recrystallized to other forms), which might provide the fine-scale connectivity of conductive material in some mantle domains implied by the striking MT images now becoming more widely available.

References

- Gordeev EI, Karpov GA, Anikin LP, et al. (2014) Diamonds in lavas of the Tolbachik fissure eruption in Kamchatka. *Doklady Earth Sciences* 454: 47-49.
- Griffin WL, Gain SEM, Adams DT, et al. (2016) First terrestrial occurrence of tistarite (Ti₂O₃): Ultra-low oxygen fugacity in the upper mantle beneath Mt Carmel, Israel. *Geology* 44: 815-818.
- Griffin WL, Afonso JC, Belousova EA, et al. (2016) Mantle Recycling: Transition-Zone metamorphism of Tibetan ophiolitic peridotites and its tectonic implications. *Journal of Petrology* 57: 655-684.
- McGowan NM, Griffin WL, González-Jiménez JM, et al. (2015) Tibetan chromitites: excavating the slab graveyard. *Geology* 43: 179-182.
- Xiong F, Yan, J-S, Dilek Y, et al. (2017) Origin and significance of diamonds and other exotic minerals in the Dingqing ophiolite peridotites, eastern Bangong-Nujiang suture zone, Tibet. *Lithosphere* (in press).
- Xiong Q, Griffin WL, Huang J-X, et al. (2017) Super-reduced mineral assemblages in “ophiolitic” chromitites and peridotites: The view from Mt Carmel. *Eur. Jour. of Mineralogy* (in press)
- Xu XZ, Yang JS, Chen SY, et al. (2009) Unusual mantle mineral group from chromitite orebody Cr-11 in Luobusa ophiolite of Yarlung-Zangbo suture zone, Tibet. *Jour. Earth Sci.* 20: 284–302.
- Yang J-S, Robinson PT, Dilek Y (2014) Diamonds in ophiolites. *Elements* 10: 127-130.
- Yang J-S, Meng F, Xu X-Z, et al. (2015). Diamonds, native elements and metal alloys from chromitites of the Ray-Iz ophiolite of the Polar Urals. *Gondwana Research* 27: 459-485.
- Zhang RY, Yang J-S, Ernst WG, et al. (2016) Discovery of in situ super-reducing, ultrahigh-pressure phases in the Luobusa ophiolitic chromitites, Tibet: New insights into the deep upper mantle and mantle transition zone. *American Mineralogist* 101: 1285-1294.



Inclusions in perovskite-magnetite-silicate rocks from Afrikanda, Russia: Clues to the early history of carbonatites?

N. J. Potter¹, V. S. Kamenetsky¹, A. R. Chakhmouradian², K. Goemann³

¹ *School of Physical Sciences, University of Tasmania, Australia, pottern@utas.edu.au, dima.kamenetsky@utas.edu.au*

² *Department of Geological Sciences, University of Manitoba, Canada, chakhmou@cc.umanitoba.ca*

³ *Central Science Laboratory, University of Tasmania, Australia, Karsten.Goemann@utas.edu.au*

Introduction

The Devonian Kola Alkaline Province (KAP) hosts more than twenty alkaline-ultramafic rock complexes and is one of the largest carbonatite and alkaline magmatic provinces in the world. The Afrikanda massif is characterised by a large perovskite deposit and has been evaluated as a potential REE resource (Zaitsev et al., 2015). Afrikanda is composed of texturally and modally diverse olivinites and clinopyroxenites with a coarse-grained core grading through to fine-grained at the margin, cross-cut by dikes of carbonatitic and foiditic rocks (Chakhmouradian and Zaitsev, 2004). Early crystallizing perovskite is typically an accessory phase in silica-undersaturated magmas and related rocks, yet is highly abundant throughout the Afrikanda complex. Our aim is to determine the processes involved in this unusual accumulation of perovskite.

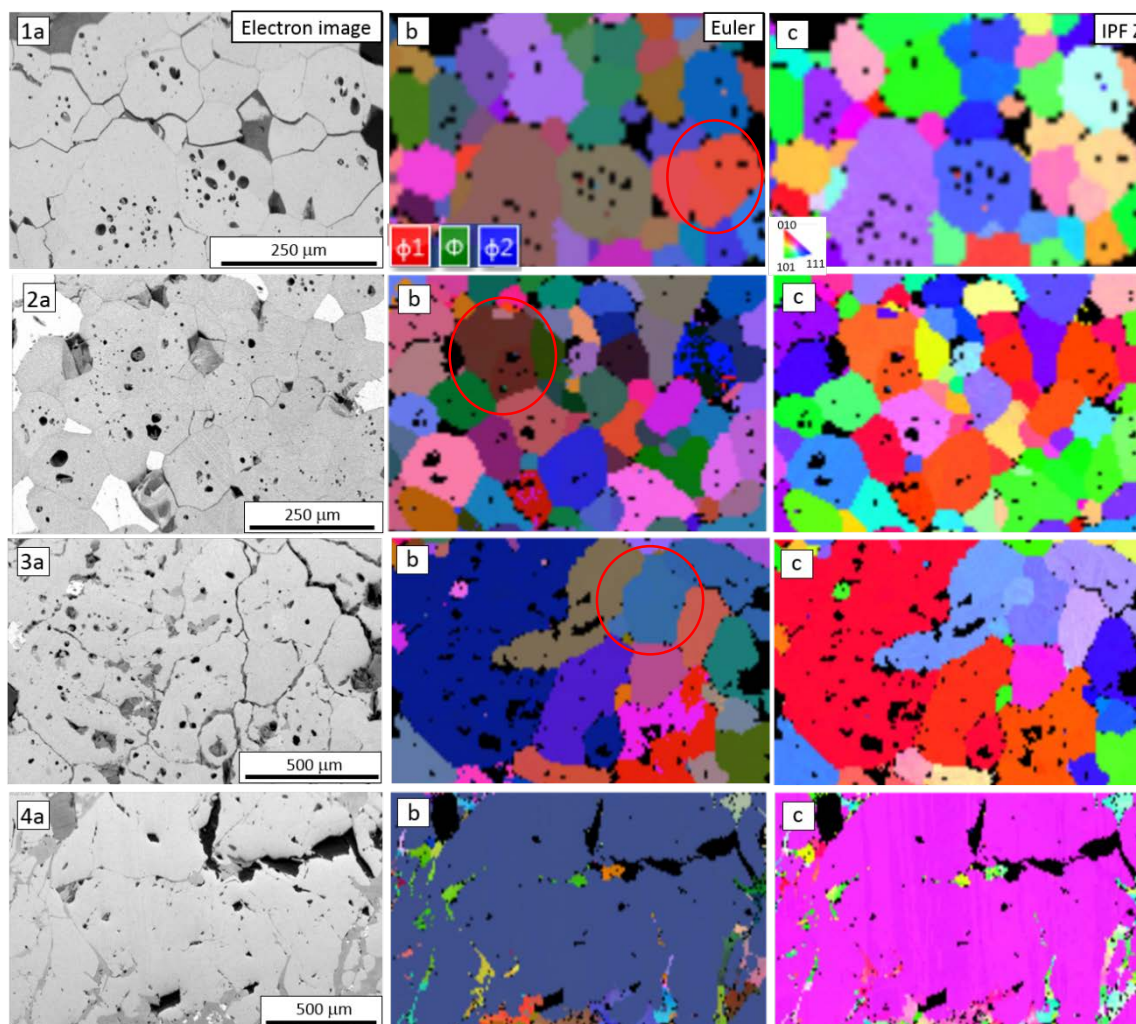
Perovskite textures

Olivinites and clinopyroxenites from Afrikanda were examined by scanning electron microscopy (SEM) and electron backscattered diffraction (EBSD) to analyse textures, geochemistry and inclusions in perovskite. EBSD was used to identify the crystallographic orientation of perovskite grains and to examine the textural variation between samples. Perovskite (CaTiO_3) can constitute up to 60 vol. % of a sample and contain variable REE, Nb, Sr and Th contents (up to 9.5 wt.% total). The EBSD analysis enabled the identification of four textural types of perovskite (Fig 1-4). The olivinites exhibit type one (T1), while the clinopyroxenites display several types (T2-4).

T1 is characterised by euhedral perovskite crystals (50 - 200 μm), occurring together to form a polygonal crystal mosaic with widespread 120° triple-junctions (Fig. 1a). The crystals have no detectable zoning and a high abundance of multiphase inclusions. In the electron and Euler images (Fig. 1a, b) each perovskite crystal appears to be an individual grain, however in the Z direction (Fig. 1c) some of these grains are revealed as a composite of several subgrains with slight variations in orientation.

T2 is similar to T1 with an interlocked mosaic, prevalent 120° triple-junctions and an abundance of multiphase inclusions (Fig. 2a). However, the perovskite grains (50 - 270 μm) are subhedral to anhedral and the extent of zoning is variable across each sample; with some homogeneous areas and others with patchy zoning that crosses grain boundaries. Also some grains have rims of variable thickness displaying subtle oscillatory zoning. The presence of subgrains is also observed in T2 (Fig. 2b, c).

Perovskite in T3 are larger anhedral (200 μm - 1 mm) grains and form an intricate crystal mosaic with irregular grain boundaries (Fig. 3a). Zoning is discontinuous, patchy and may cross grain boundaries, and some grains show weakly developed zonation on grain margins. Multiphase inclusions are only abundant in some perovskite grains. Titanite occurs as irregular patches between minerals and as thin rims around most perovskite grains. Perovskite grain margins in contact with titanite are enriched in trace elements. Perovskite grain boundaries are difficult to identify using the electron image (Fig. 3a), but the grains are clearly visible in the EBSD image (Fig. 3b). EBSD reveals that T3 perovskite have significantly larger grain size than T1 and T2, and that subgrains are still observed (Fig. 3b, c).



Figures 1-4: Display texture types T1 to T4, respectively. (a) Electron images of areas mapped, (b) Euler angle map using colours to denote the variety of crystal orientations in space using Euler angles: ϕ_1 -red ϕ -green, ϕ_2 -blue, (c) Inverse pole figure (IPF Z) map in the Z direction showing varying crystal orientations in different colours. Red circles show grains that are composed of subgrains with different crystallographic orientations in the Z direction.

T4 perovskite is massive with highly irregular, patchy zoning, rare multiphase inclusions and interstitial titanite, calcite and loparite-(Ce) (Fig. 4a). These perovskite contain the highest concentrations of trace elements.

Multiphase inclusions

Multiphase inclusions are most abundant in T1 perovskite from olivinites and are not observed in other rock-forming minerals. The inclusions are variable in size and abundance, and preferentially occur in the cores of the perovskite grains. A total of 81 inclusions were analysed using SEM

| Silicates | | Carbonates | |
|-------------------------|----|--|----|
| sodalite | 18 | nyerereite | 23 |
| clinopyroxene | 15 | calcite | 15 |
| melilite | 12 | shortite | 15 |
| wollastonite | 12 | Na-Ca-Sr-carbonate | 4 |
| forsterite | 10 | Oxides | |
| diopside | 9 | magnetite | 27 |
| humite | 8 | Phosphates | |
| titanite | 4 | fluorapatite | 18 |
| nepheline | 4 | apatite | 9 |
| andradite | 4 | Sulphides | |
| monticellite | 2 | pyrrhotite | 6 |
| Water-bearing silicates | | chalcopyrite | 4 |
| biotite | 42 | rasvumite | 4 |
| pectolite | 29 | Table 1: Tallied occurrence of daughter phases in perovskite-hosted inclusions from olivinites. | |
| cuspidine | 20 | | |
| phlogopite | 16 | | |
| chlorite | 5 | | |
| magnesiostastingsite | 2 | | |

and Raman spectroscopy. These inclusions exhibit rounded to negative crystallographic shapes and range from 5 to 30 μm , with an average of 10 μm . There is no relationship between perovskite grain size and the abundance of inclusions. We identified more than 35 minerals in the inclusions (Table 1) with the phase assemblage differing significantly between and within perovskite grains and variable modal abundances of each component (Figs. 5a-c).

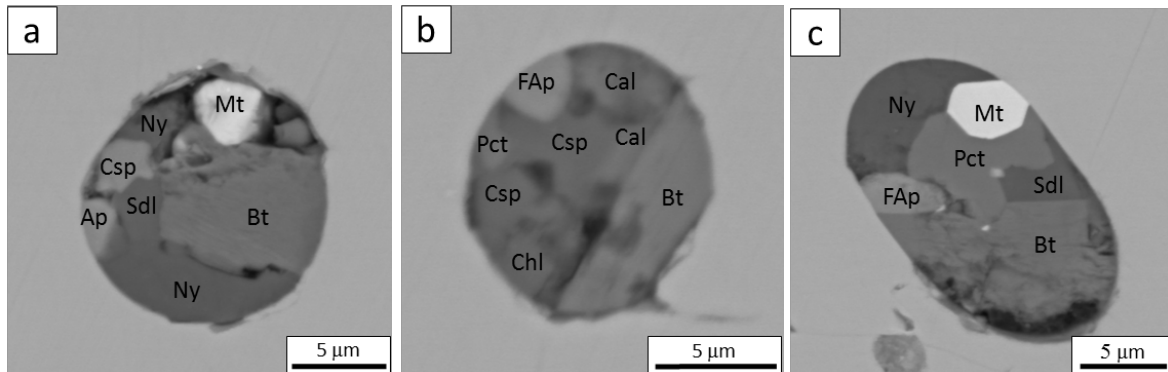


Figure 5: Back-scattered electron (BSE) SEM images of representative multiphase inclusions in perovskite, containing apatite (Ap), biotite (Bt), calcite (Cal), clinocllore (Chl), cuspidine (Csp), fluorapatite (FAP), magnetite (Mt), nyerereite (Ny), pectolite (Pct), sodalite (Sdl).

Discussion

The textures show the systematic transformation of perovskite from a mosaic of individual perovskite grains to massive perovskite with interstitial titanite and an associated high concentration of trace elements. The observed progression of perovskite textures and compositions in the samples are key to interpreting the multistage evolution of the accumulating perovskite and the development of massive textures.

The range of minerals in the inclusions and the contrast in mineral assemblage of adjacent inclusions is unusual. These inclusions are likely to be primary and were trapped during perovskite growth. Evidence is based on their rounded shape, distribution of inclusions within the interior of grains and lack of alignment with fractures. The absence of glass suggests that the mineral constituents of inclusions were mostly trapped in solid state. The variety of inclusion compositions within the same grain could be a result of a heterogeneous multiphase environment. If they are primary inclusions the coexistence of silicate- and carbonate-dominated assemblages in the inclusions of oxide-dominated rocks are unlikely to represent the parental medium but could provide insight into the composition of the environment that crystallised perovskite.

References

- Chakhmouradian AR, Zaitsev AN (2004) Afrikanda: an association of ultramafic, alkaline and alkali-silica rich carbonatitic rocks from mantle-derived melts. In: Wall F, Zaitsev AN (ed) *Phoscorites and Carbonatites from Mantle to Mine: The Key Example of the Kola Alkaline Province*, Mineralogical Society, London, pp 247-291
- Zaitsev AN, Williams CT, Jeffries TE, Strekopytov S, Moutte J, Ivashchenkova OV, Spratt J, Petrov SV, Wall F, Selmann R, Borozdin AP (2015) Rare earth elements in phoscorites and carbonatites of the Devonian Kola Alkaline Province, Russia: Examples from Kovdor, Khibina, Vuoriyarvi and Turij Mys complexes. *Ore Geology Reviews* 64:477-498



Continuity of Kimberley-type pyroclastic kimberlite phases within Renard 2 over 1,000 m depth – Insights to the geological and emplacement model, Superior Craton, Canada

Zhuk, V.¹, Lépine, I.¹, and Laroulandie, C.¹

¹Stornoway Diamond Corporation, North Vancouver, Canada

vzhuk@stornowaydiamonds.com, ilepine@stornowaydiamonds.com, claroulandie@stornowaydiamonds.com

Introduction

The Renard 2 kimberlite pipe is the largest body within a cluster of nine diamondiferous pipes emplaced approximately 640 Ma into Archean granitoid and gneissic rocks of the eastern portion of the Superior Craton, Canada (Fitzgerald et al, 2009). Located in the Otish Region of northern Québec, Renard 2, a mid-sized pipe with a surface expression of approximately 2.3 hectares, currently forms the bulk of feed to Stornoway Diamond Corporation's newly commissioned Renard Mine. Kimberlite pipes within the Renard cluster are all characterized by similar Kimberley-type pyroclastic kimberlite (KPK; formerly termed TK or tuffisitic kimberlites). Renard 2 is a diatreme- to root-zone kimberlite consisting of two main KPK pipe-infills (Kimb2a and Kimb2b) characterised by distinct diamond grades and determined as emplacement products from distinct and separate batches of magma. In addition, a third phase, Kimb2c, classified as hypabyssal kimberlite, occurs in the form of irregular intrusions and late stage cross cutting dykes. This phase is found within and along contacts of Kimb2a and Kimb2b, as well as along wall rock contacts, and contributes an average of 17% by volume to the modelled kimberlite pipe. A marginal country rock breccia, CRB, envelopes the KPK units, and smooths the external pipe shape.

Culminating with a deep directional drilling campaign in 2014, detailed petrological, dilution, geochemical and diamond grade data derived from >45 km of diamond drilling confirmed vertical continuity of the two KPK phases on Renard 2, through more than 1,000 m, and provided for an updated robust geological model to a depth of 865 meters (Figure 1) (Lépine and Farrow, 2017) as well as new perspective into the emplacement.

Geology and Petrology

The Renard 2 main pipe-infills, Kimb2a and Kimb2b, exhibit contrasting primary features: olivine abundances and populations, country rock xenolith abundances and populations as well as groundmass mineralogy. Kimb2a is volumetrically the most significant phase infilling the pipe, accounting for 70% of total kimberlite by volume. It consists of olivine, pyroclasts and country rock xenoliths that are poorly sorted, typically loosely packed and less commonly clast supported, and set within a highly altered interclast matrix. Olivine macrocrysts comprise 5-15 modal % of the rock and are typically medium-grained to rarely coarse-grained. Primary groundmass minerals within pyroclasts include phlogopite, spinel and perovskite. This unit commonly contains 40-65, and up to 95 modal % fresh to moderately altered granitoid and gneissic country rock xenoliths. These are set within a non-crystalline matrix that comprises clays, serpentine and microlitic clinopyroxene. Kimb2a can be classified mineralogically as a phlogopite kimberlite.

Kimb2b accounts for 30% of total kimberlite by volume and reveals very similar mostly coherent, to limited pyroclastic, textures throughout the entire geological model, with olivine, country rock xenoliths and rare pyroclasts that are unsorted and set within a crystalline to semi-crystalline groundmass. Olivine macrocrysts comprise 10-25 modal % of the rock and are medium- to coarse-grained with common very coarse-grained crystals. The Kimb2b groundmass consists of primary minerals of phlogopite, spinel, perovskite, carbonate and rare monticellite, and late stage minerals of serpentine, clays and microcrystic clinopyroxene. This unit commonly contains 20-50 modal %

moderately to strongly altered gneissic and less abundant granitoid country rock xenoliths. Kimb2b can be classified mineralogically as a monticellite-phlogopite kimberlite.

Hypabyssal kimberlite Kimb2c occurs in Renard 2 in the form of late-stage HK dykes and irregular intrusions. Kimb2c phases present within Kimb2a and Kimb2b form up to 14% and 25% of their volumes, correspondingly. The various HK intrusions include a spectrum of primary groundmass mineral assemblages, ranging from monticellite dominated to phlogopite dominated, each additionally consisting of common carbonate, spinel and perovskite.

The kimberlite in Renard 2 is surrounded by extensive marginal country rock breccia. This CRB has a maximum width of approximately 100 m near surface and extends the full depth of the body on the north side of the pipe. Importantly, the Kimb2c hypabyssal dykes (although not modelled in 3D) are also present within the CRB unit, and form up to 10% of its volume contributing to diamond grade of the CRB.

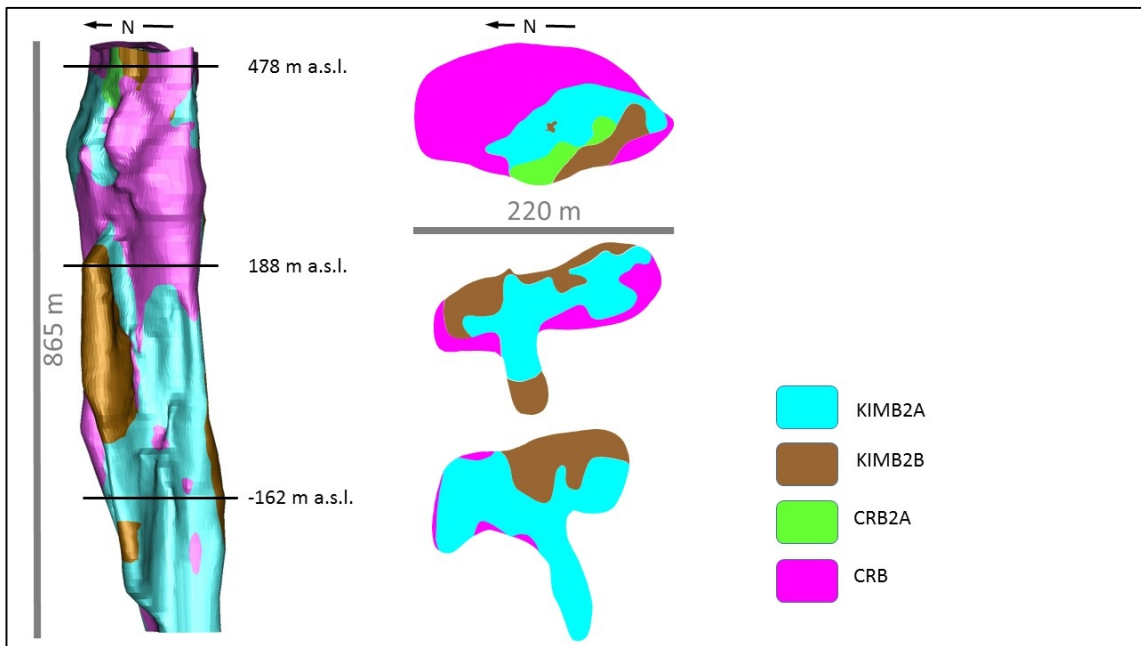


Figure 1: Renard 2 kimberlite 3D geological model (left) with the Kimb2a and Kimb2b major kimberlite infills and the enveloping CRB, and plan views (right) at vertical levels of 478 m a.s.l., 188 m a.s.l., and -162 m a.s.l. (above sea level).

Detailed petrological, petrographic, and internal dilution data derived from >45 km of diamond drilling (161 holes) confirmed vertical continuity of both KPK phases, Kimb2a and Kimb2b, through more than 1,000 m.

Geochemistry

Geochemical signatures for Kimb2a and Kimb2b were sampled through a series of 50 m horizontal slices from the surface to depth of 865 meters below surface.

Whole rock analyses, including C, S and LOI, and Ni identify distinctive geochemical differences between the Kimb2a and Kimb2b phases but demonstrate continuity by phase with depth. There is also a consistent pattern of increasing SiO₂, Al₂O₃, Na₂O and K₂O with increasing levels of country rock dilution: lower in Kimb2b and higher in Kimb2a, but the average dilution itself remains consistent with increasing depth.

The LREE elements are elevated in the less diluted Kimb2b (and in Kimb2c), which reflects the more primitive rock composition associated with kimberlite. HREE values tend to overlap between the phases with more elevated values appearing in the heaviest REE (Er, Yb and Lu) in Kimb2a.

The incompatible elements Cs, Rb, K, Hf, Zr and Y are generally elevated in Kimb2b or Kimb2a, respectively, in comparison to Kimb2c. Incompatible elements Ta, Nb, and Ti are increasingly depleted in Kimb2b and Kimb2a, respectively, compared to Kimb2c but again remain consistent with depth.

First series transition elements Ti, Cr, Co and Ni are depleted in the more dilute Kimb2a and Kimb2b samples compared to Kimb2c. Manganese appears depleted in Kimb2a, but not Kimb2b, when compared to Kimb2c, and all are consistent with depth.

The geochemical signatures for Kimb2a and Kimb2b from each 50 m horizontal slice are proved consistent individually and on a level by level basis from the surface to depth of 865 meters below surface, corresponding to the current extent of the 3D geological model.

Diamond Content

To test for continuity of diamond content within each phase of kimberlite, and with depth in the Renard 2 body, sampling for microdiamonds and macrodiamonds was undertaken on 50 m levels from surface to the base of the modelled body at 1,000 m below surface (-352 m a. s. l.). Within each 50 m level, approximately 200 kg from each of Kimb2a and Kimb2b was collected from drill core and treated for microdiamond recovery. A total of 4,141 kg of Kimb2a and 3,844 kg of Kimb2b were analyzed by standard caustic dissolution. Totals of 1,496 diamonds and 3,117 diamonds larger than 0.106mm square mesh were recovered from Kimb2a and Kimb2b respectively. When combined with overall diluted macrodiamond sampling of Kimb2a and Kimb2b, the undiluted diamond size frequency distribution plots in each of the 50 m depth slices demonstrate good grade continuity with increasing depth. The modelled undiluted adjusted grades were 83cph and 181cph for Kimb2a and Kimb2b, correspondingly (Farrow and Hopkins, 2015).

Discussion and Conclusion

Petrology, internal country rock dilution, geochemistry, and diamond content studies of the two main KPK pipe-infills at Renard 2 (Kimb2a and Kimb2b) confirm vertical continuity of the Kimberley-type pyroclastic kimberlite phases through more than 1,000 m.

The findings of this work provide new insight into the geological and emplacement model, with a diatreme-zone vertically continuous through over 1 km; a rare and notable feature for Canadian kimberlites.

References

- Fitzgerald CE, Hetman CM, Lépine I, Skelton DS, McCandless TE (2009) The internal geology and emplacement history of the Renard 2 kimberlite, Superior Province, Quebec, Canada. *Lithos* 112S 513-528
- Lépine I and Farrow D J (2017) 3D geological modelling of the Renard 2 Pipe, Québec, Canada: from exploration to extraction. 11th International Kimberlite Conference Extended Abstract No. 11IKC-4545, 2017, Gaborone, Botswana.
- Farrow D and Hopkins R (2015) Mineral Resource Update for the Renard Diamond Project, Quebec, Canada. National Instrument (NI) 43-101 Technical Report: 139p.

Oxygen fugacity as a control on the distribution of diamond in the sub-cratonic lithospheric mantle

Patrick Y. Goodarzi¹, Andrew J. Berry¹, D. Graham Pearson², Gregory M. Yaxley¹ and Matt Newville³

¹Australian National University, Canberra, Australia, patrick.goodarzi@anu.edu.au, andrew.berry@anu.edu.au, greg.yaxley@anu.edu.au

²University of Alberta, Edmonton, Canada, graham.pearson@ualberta.ca

³University of Chicago, Chicago, USA, newville@cars.uchicago.edu

Oxygen fugacity and metasomatism

For diamond to exist in the lithospheric mantle the ambient oxygen fugacity (fO_2) must be sufficiently reduced for diamond to be the stable phase of carbon. Garnet peridotite xenoliths record the fO_2 at which they equilibrated prior to kimberlite eruption by the oxidation state of Fe ($Fe^{3+}/\Sigma Fe$) in garnet. It has been asserted that, at pressures above the graphite-diamond transition, the lithospheric mantle beneath diamond-bearing kimberlites (e.g. Diavik, Finsch, Udachnaya) was adequately reduced for diamond to be stable. Metasomatism of lithospheric mantle by fluid or melt is, however, thought to perturb fO_2 to more oxidising conditions, potentially sufficient to destabilise diamond (Hanger et al. 2015). Metasomatism of this nature is most discernibly recorded by enrichment of high-field strength elements (HFSE) coupled with “normal” chondrite-normalised rare earth element (REE_N) patterns in garnet, but the relationship with fO_2 change remains poorly understood. Studies of this type have been limited predominantly to peridotite samples from economically diamondiferous kimberlites. Here we present fO_2 results for garnet-peridotite xenoliths from two non-diamondiferous kimberlites.

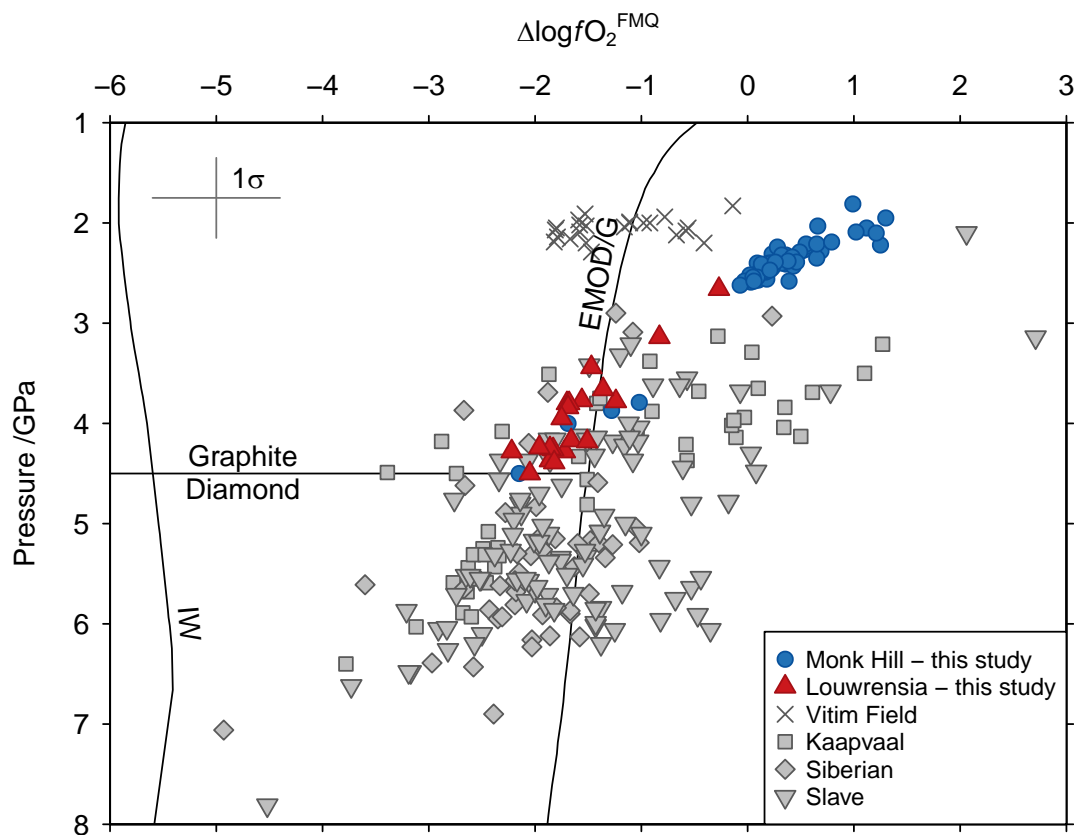


Figure 1: Pressure vs. $\Delta \log fO_2^{FMQ}$ for xenoliths from Monk Hill and Louwrensia. A global dataset of garnet-bearing xenoliths is shown for comparison. The iron-wüstite buffer (IW) and the enstatite-magnesite-olivine-diamond/graphite reaction (EMOD/G) were calculated along a geotherm derived from Kaapvaal xenoliths.

Samples

(1) The Louwrensia kimberlite is one of over 70 non-diamondiferous pipes within the off-cratonic Gibeon kimberlite field of south-central Namibia. Twenty-three lherzolite samples have been well characterized in previous studies (Boyd et al. 2004; Pearson et al. 2004) and were found to derive from pressures between 2.7 and 4.8 GPa. The geothermal gradient defined by these samples indicates that the lithosphere at the time of eruption was comparable in thickness to that of the nearby diamond-bearing Kaapvaal craton (Mather et al. 2011).

(2) The Monk Hill kimberlite is one of a cluster of non-diamondiferous pipes within the Adelaide Fold Belt of South Australia. Thirty-six lherzolite samples were derived from pressures between 1.8 and 4.6 GPa (Tappert et al. 2011).

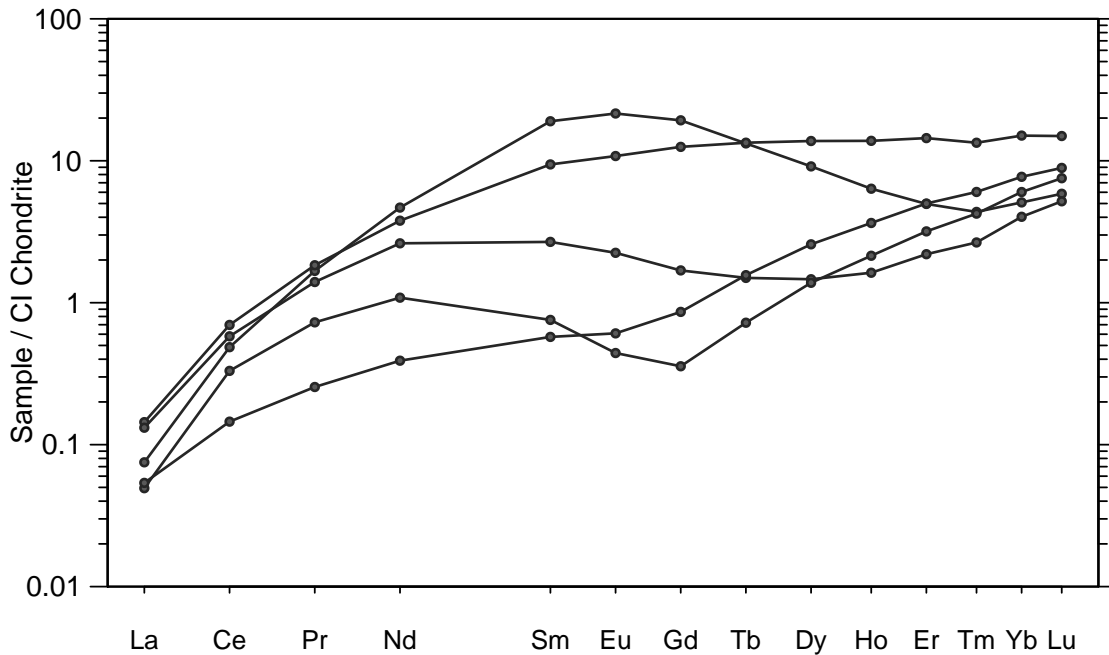


Figure 2: Chondrite-normalised REE concentrations in garnet from five Louwrensia samples, representative of the observed diversity.

Fe K-edge XANES and results

Determining $\text{Fe}^{3+}/\sum\text{Fe}$ of garnet for large numbers of samples was previously challenging due to long acquisition times (Mössbauer spectroscopy) or onerous analytical procedures (the electron microprobe “flank method”). Here, $\text{Fe}^{3+}/\sum\text{Fe}$ of garnet was determined by Fe K-edge X-ray Absorption Near Edge Structure (XANES) spectroscopy following the approach of Berry et al. (2010), Yaxley et al. (2012), and Hanger et al. (2015), by which $\text{Fe}^{3+}/\sum\text{Fe}$ can be determined with micron spatial resolution in less than 10 minutes. $\text{Fe}^{3+}/\sum\text{Fe}$ was quantified using the intensity of the *post-edge minimum* – a spectral feature that correlates well with known $\text{Fe}^{3+}/\sum\text{Fe}$ in peridotitic garnet standards ($R^2 = 0.93$) – and was reproducible to a precision of 0.002 (1σ , $n = 8$). The resultant $f\text{O}_2$ was computed using the recent garnet-oxybarometer calibration of Miller et al. (2016). $\Delta\log f\text{O}_2^{\text{[FMQ]}}$ (where FMQ is the fayalite-magnetite-quartz buffer) ranged between -0.27 and -2.22 for the Louwrensia samples, and between 1.3 and -2.15 for those from Monk Hill. These results are the first determination of the $f\text{O}_2$ of the lithospheric mantle beneath the Australian craton and circum-cratonic Kaapvaal. Both are consistent with $f\text{O}_2$ -depth profiles from the Kaapvaal, Slave, and Siberian cratons (Fig. 1), and comparison with samples from other kimberlites in the Kaapvaal region highlights the consistent ambient $f\text{O}_2$ in this part of the lithosphere over the 50 Mya interval between the eruption of Finsch (120 Ma) and Louwrensia (70 Ma).

The fO_2 s determined for both sample suites are sufficiently reduced for diamond to be stable at an appropriate lithospheric thickness. The absence of diamonds in these pipes is therefore explained by the kimberlite not sampling the diamond stability window.

Trace element concentrations in garnet and clinopyroxene were determined by LA-ICP-MS. REE_N patterns in garnet from the Louwrensia samples exhibit diverse shapes, from normal to sinusoidal to sloped (Fig. 2). Garnets are enriched in Ti and Zr in samples derived from >4 GPa, which corroborates the idea that metasomatism of this kind occurs within a restricted depth horizon (Yaxley et al. 2012), despite the apparent absence of a concomitant change in fO_2 . In contrast, Monk Hill samples show little deviation from normal patterns but are not HFSE enriched, and are thought to derive from too low pressures to have experienced the same style of metasomatism. REE_N was parameterised following the method of O'Neill (2016) and a comparison with results from a global dataset will be presented.

References

- Berry AJ, Yaxley GM, Woodland AB, Foran GJ (2010) A XANES calibration for determining the oxidation state of iron in mantle garnet. *Chemical Geology* 278:31-37
- Boyd FR, Pearson DG, Hoal KO, Hoal BG, Nixon PH, Kingston MJ, Mertzman SA (2004) Garnet lherzolites from Louwrensia, Namibia: bulk composition and P/T relations. *Lithos* 77:573-592
- Hanger BJ, Yaxley GM, Berry AJ, Kamenetsky VS (2015) Relationships between oxygen fugacity and metasomatism in the Kaapvaal subcratonic mantle, represented by garnet peridotite xenoliths in the Wesselton kimberlite, South Africa. *Lithos* 212-215:443-452
- Mather KA, Pearson DG, McKenzie D, Kjarsgaard BA, Priestly K (2011) Constraints on the depth and thermal history of cratonic lithosphere from peridotite xenoliths, xenocrysts and seismology. *Lithos* 125:729-742
- Miller WGR, Holland TJB, Gibson SA (2016) Garnet and spinel oxybarometers: new internally consistent multi-equilibria models with applications to the oxidation state of the lithospheric mantle. *Journal of Petrology* 57(6):1199-1222
- Pearson DG, Irvine GJ, Ionov DA, Boyd FR, Dreibus GE (2004) Re-Os isotope systematics and platinum group element fractionation during mantle melt extraction: a study of massif and xenolith peridotite suits. *Chemical Geology* 208:29-59
- O'Neill HSt.C (2016) The smoothness and shapes of chondrite-normalised rare earth element patterns in basalts. *Journal of Petrology* 57(8):1463-1508
- Tappert R, Foden J, Muehlenbachs K, Wills K (2011) Garnet peridotite xenoliths and xenocrysts from the Monk Hill kimberlite, South Australia: Insights into the lithospheric mantle beneath the Adelaide Fold Belt. *Journal of Petrology* 52(10):1965-1986
- Yaxley GM, Berry AJ, Kamenetsky VS, Woodland AB, Golovin AV (2012) An oxygen fugacity profile through the Siberian craton – Fe K-edge XANES determinations of $Fe^{3+}/\Sigma Fe$ in garnets from the Udachnaya East kimberlite. *Lithos* 140-141:142-151

Evolution of kimberlite magmatism on the dynamic Earth

Sebastian Tappe¹, Katie Smart², Richard Stern³, Malcolm Massuyeau¹, Mike de Wit⁴

¹University of Johannesburg, South Africa, sebastian@uj.ac.za, mmassuyeau@uj.ac.za

²University of the Witwatersrand, South Africa, katie.smart2@wits.ac.za

³University of Alberta, Canada, rstern@ualberta.ca

⁴University of Pretoria, South Africa / Tsodilo Resources Ltd., mdewit@tsodiloresources.com

Introduction

Plate tectonics and magmatism are consequences of heat loss from a planet's interior. Earth was significantly hotter in the distant past and has been cooling for most of its history. One of the strongest lines of evidence for the secular cooling of Earth is the changing composition of mantle-derived melts. Archean basalts are typically more MgO-rich compared with their modern analogs due to higher degrees of partial melting at higher mantle potential temperatures. The hottest magmas on Earth, komatiites, are largely restricted to the Archean and Early Proterozoic, demonstrating that mantle temperatures were up to 400°C higher than today. Conversely, some igneous rock types appear to have been formed more frequently during the latter half of Earth's history. The temporal distribution of global carbonatites and kimberlites is strikingly skewed toward the more recent Earth history (Fig.1), and it appears that deep mantle melting under volatile-rich conditions was particularly frequent during the Mesozoic-Cenozoic and rare during the Precambrian. Although this pattern may be influenced by preservation, it can be inferred from petrology that the 'delayed' appearance of terrestrial carbonatite and kimberlite magmatism is a strong function of secular mantle cooling (Tappe et al., 2014).

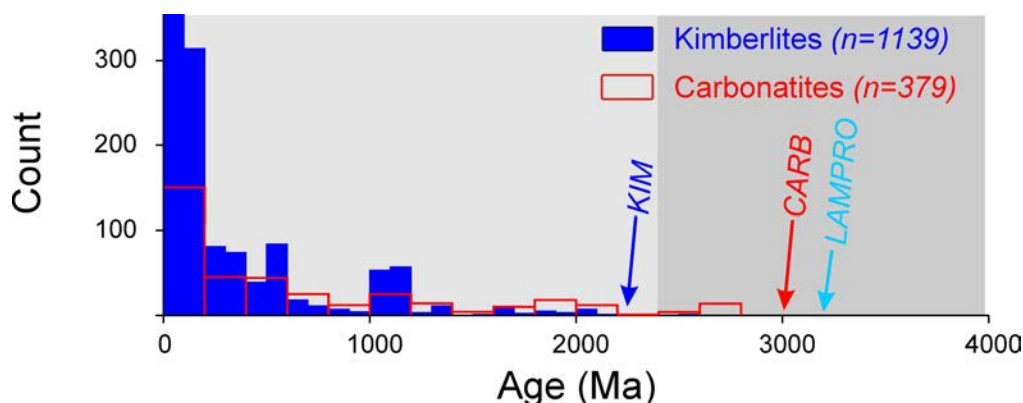


Figure 1: Histogram of emplacement ages for global kimberlites and carbonatites (data: Tappe et al., 2014).

Triggers of kimberlite magmatism

Kimberlites are arguably the least understood melting products of the Earth's mantle. Kimberlite magmatism occurred on every continent in most cratonic domains, and the pulsed nature over the past 2 Gyr (Fig.1) has provided ample room for speculation about magma origins and tectonic trigger mechanisms. Some models advocate magma derivation from mantle plume sources, whereas others only require the heat from hotspots to cause melting in thick overriding tectonic plates (e.g., Heaman and Kjarsgaard, 2000). Alternative models invoke far-field effects of rifting (e.g., Jelsma et al., 2009) with lateral fracture zone propagation that enables kimberlitic melts to 'drain' beneath cratonic roots. Some kimberlite magmatic activity can be linked to the effects of complex subduction systems on the mantle dynamics beneath continental lithosphere far away from plate margins (e.g., Tappe et al., 2013). Hence, not all kimberlites are created equal and a variety of trigger mechanisms and combinations thereof can explain this global phenomenon (Tappe et al., 2017a).

How and when do kimberlites form?

The most critical petrologic variables enabling the formation of kimberlite melts are the availability of oxidized CHO volatile species such as CO₂ and H₂O (Yaxley et al., 2017), as well as the operation of an incipient melting regime over a wide temperature interval within the Earth's mantle. Only melting near the solidus of peridotite at high pressures can produce high-MgO melts with significantly elevated trace element concentrations. These conditions are met only beneath thick continental lithosphere in a thermal boundary layer that is part of the convecting upper mantle. Ultimate melt origin from this mantle reservoir is supported by moderately depleted to slightly enriched Nd-Hf isotope systematics of kimberlites through time (Fig.2a). Although kimberlite melt formation may be ubiquitous in this boundary layer where variable CHO volatile mixtures control melting of peridotite in the absence of heat anomalies, the extraction of low-volume melts to Earth's surface requires tectonic trigger mechanisms such as changes in the speed and direction of lithospheric plate motion (Tappe et al., 2017a). Importantly, CO₂- and H₂O-fluxed deep cratonic keels, forming parts of larger drifting tectonic plates, existed by 3 Ga or even before (Smart et al., 2016), which means that kimberlite melts could have formed as early as the Mesoproterozoic.

Temporal evolution of kimberlite magmatism and secular mantle cooling

The temporal distribution of kimberlite magmatism is strikingly skewed toward more recent Earth history (Fig.1), with deep volatile-rich mantle melting being particularly frequent during the Mesozoic and scarce during the Precambrian. One of the earliest major global kimberlite magmatic pulses occurred during the Mesoproterozoic at ca. 1.1 Ga, and Stern et al. (2016) argued that more frequent kimberlite magmatism after 1 Ga reflects build-up of H₂O and CO₂ in the convecting mantle due to onset of deep subduction. However, if an increase in H₂O content of the upper mantle after 1 Ga due to subduction recycling caused enhanced kimberlite magmatism, why then does the frequency of global kimberlite eruptions pulse and why did the earliest kimberlites form during the Paleoproterozoic at ca. 2 Ga? Furthermore, why do kimberlites not erupt today (Fig.2b)?

The pulsed nature of global kimberlite magmatism has been noted in particular for the Mesozoic-Cenozoic activity that was linked to the breakup stages of the Gondwana-Pangea supercontinent cycle (Jelsma et al., 2009). Likewise, Tappe et al. (2014) noted a significant gap in global kimberlite magmatic activity at 1,000-850 Ma. This gap coincides with the stable Rodinia supercontinent configuration, and periods of pronounced kimberlite magmatic activity at 1,250-1,050 Ma and 800-550 Ma overlap with its assembly and breakup, respectively. These examples provide evidence that the relatively short time windows in global kimberlite volcanism do not necessarily reflect restrictions in the formation of these melts at mantle depths, but rather successful 'drainage' events intimately linked to tectonic plate motions. One of the key questions is why the earliest kimberlites on Earth formed during the Paleoproterozoic at ca. 2 Ga, and not already at 3 Ga or earlier if the petrologic prerequisites of kimberlite melt formation were established by that time.

Prior to 3 Ga, mantle melting occurred mainly within the major melting regime, due to the much warmer thermal conditions during the Early Archean with ambient mantle potential temperatures of >1,500°C. Theoretical and observational constraints from the rock record suggest that the ambient mantle potential temperature started to cool significantly between 3 and 2.5 Ga (Herzberg et al., 2010). By 2 Ga, mantle potential temperature was probably <1,400°C. Secular cooling of Earth's mantle increasingly established CHO-volatile driven incipient melting regimes beneath the stabilizing continents (Tappe et al., 2014). In other words, after 3 Ga and more prominently after 2 Ga, low-degree partial melting of peridotitic mantle in the presence of CO₂ and H₂O between 150-250 km depth produced ubiquitous trace element enriched, high-MgO carbonated silicate liquids of kimberlitic affinity. While the pulsed nature of this new form of terrestrial magmatism appears to be controlled by supercontinent cycles, the general increase in the frequency of kimberlite magmatic activity from the Paleoproterozoic to the Mesozoic-Cenozoic may be an expression of the increasing thermal maturity of the interface between deep continental roots and the cooling convecting mantle,

approaching the modern day potential temperature of 1,280°C. Although burial and unroofing of continental shields certainly played a role in the age pattern of global kimberlite magmatism (Fig.1), it is doubtful that preservation biased the overall distribution. Clearly, much fewer kimberlites erupted between today and 50 Ma ago compared with the striking Mesozoic-Cenozoic kimberlite ‘bloom’ between 200 and 50 Ma. Also, no relationship exists between the erosion-modified surface areas of diamondiferous kimberlite bodies and their emplacement ages (Fig.2b) providing evidence against a strong preservation bias of the global kimberlite record. Assuming that the ‘delayed’ appearance of kimberlites is real, then secular mantle cooling in combination with supercontinent cyclicity provides a simple solution to the latter-day origin and pulsed nature of deep volatile-rich magmatism.

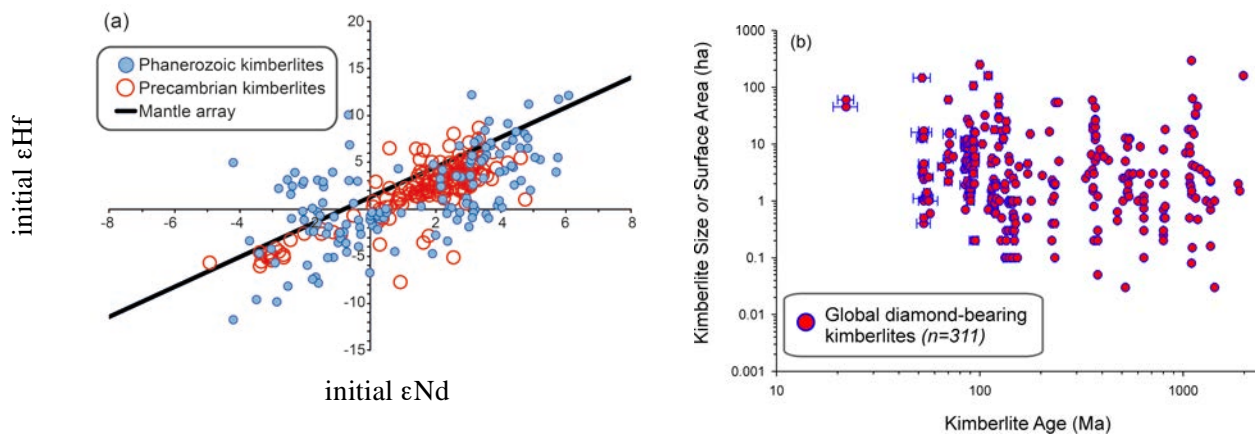


Figure 2: (a) Nd-Hf isotope systematics of global kimberlites (data compilation from Tappe et al., 2017b). (b) Surface area versus emplacement age of global diamondiferous kimberlite bodies (>1 CPHT; modified from de Wit, 2014).

References

- de Wit M (2014) World-class diamond deposits. Unpublished PDAC presentation, Toronto
- Heaman LM, Kjarsgaard BA (2000) Timing of eastern North American kimberlite magmatism: Continental extension of the Great Meteor hotspot track? *Earth and Planetary Science Letters* 178(3-4): 253-268
- Herzberg C, Condie K, Korenaga J (2010) Thermal history of the Earth and its petrological expression. *Earth and Planetary Science Letters* 292(1-2): 79-88
- Jelsma H, Barnett W, Richards S, Lister G (2009) Tectonic setting of kimberlites. *Lithos* 112:155-165
- Smart KA, Tappe S, Stern RA, Webb SJ, Ashwal LD (2016) Early Archaean tectonics and mantle redox recorded in Witwatersrand diamonds. *Nature Geoscience* 9: 255-259
- Stern RJ, Leybourne MI, Tsujimori T (2016) Kimberlites and the start of plate tectonics. *Geology* 44(10): 799-802
- Tappe S, Pearson DG, Kjarsgaard BA, Nowell GM, Dowall D (2013) Mantle transition zone input to kimberlite magmatism near a subduction zone: Origin of anomalous Nd-Hf isotope systematics at Lac de Gras, Canada. *Earth and Planetary Science Letters* 371-372: 235-251
- Tappe S, Kjarsgaard BA, Kurszlaukis S, Nowell GM, Phillips D (2014) Petrology and Nd-Hf isotope geochemistry of the Neoproterozoic Amon kimberlite sills, Baffin Island (Canada): Evidence for deep mantle magmatic activity linked to supercontinent cycles. *J Petrol* 55(10): 2003-2042
- Tappe S, Brand NB, Stracke A, van Acken D, Liu C-Z, Strauss H, Wu F-Y, Luguët A, Mitchell RH (2017a) Plates or plumes in the origin of kimberlites: U/Pb perovskite and Sr-Nd-Hf-Os-C-O isotope constraints from the Superior craton (Canada). *Chemical Geology*, 10.1016/j.chemgeo.2016.08.019, in press
- Tappe S, Romer RL, Stracke A, Steenfelt A, Smart KA, Muehlenbachs K, Torsvik TH (2017b) Sources and mobility of carbonate melts beneath cratons, with implications for deep carbon cycling, metasomatism and rift initiation. *Earth and Planetary Science Letters* 466: 152-167
- Yaxley GM, Berry AJ, Rosenthal A, Woodland AB, Paterson D (2017) Redox preconditioning deep cratonic lithosphere for kimberlite genesis. *Scientific Reports* 7 (30): 1-10



The origin of Type II diamonds: Insights from contrasting mineral inclusions in Cullinan Type I and Type II stones

N.M. Korolev^{1,2}, M. Kopylova¹, Y. Bussweiler³, D.G. Pearson³, J. Gurney⁴, A.E. Moore⁵, J. Davidson⁶

¹ University of British Columbia, Vancouver, BC, Canada, nkorolev@eoas.ubc.ca, mkopylov@eos.ubc.ca

² Institute of Precambrian Geology and Geochronology RAS, St. Petersburg, Russia

³ University of Alberta, Edmonton, Alberta, Canada, bussweil@ualberta.ca, gdpearso@ualberta.ca

⁴ University of Cape Town, Cape Town, South Africa, john.gurney@msgroup.net

⁵ Rhodes University, Grahamstown, South Africa, andy.moore.bots@googlemail.com

⁶ Petra Diamonds, Bryanston, South Africa, jim@petradiamonds.com

We investigated the differences in mineralogical characteristics and mineral inclusions in Type I and Type II diamonds from the Cullinan mine. Diamonds for the study were selected from the run-of-the-mine production from Clivage, Breakage, Gem Quality and Melee classes, with 0.01-0.07 ct diamonds comprising 87% of the 341 samples. Of the studied stones, 75 are Type II diamonds with N contents below 20 ppm, as identified by FTIR analysis. Most stones are represented by single crystals or fragments, the proportion of macles and aggregates is less than 14%. Approximately 70% of all stones and 59% of Type II diamonds have dodecahedral habit, hence the majority of diamonds fall into resorption categories 1 and 2. Octahedrons comprise 15% (Type I) to 32% (Type II) of the collection. There are no correlations between the diamond type and the morphology. Color was evaluated visually by a binocular microscope. All diamonds are white, and only 46 diamonds display brown color of different shades, ten of them are Type II. Other colors were not recognized. Very weak blue UV fluorescence is detected in 6 samples out of 75 Type II diamonds (8%), whereas 138 out of 266 Type I stones (40%) show weak blue - turquoise fluorescence.

Raman and EPMA measurements defined a variety of primary mineral inclusions, i.e. garnet, majorite, clinopyroxene, orthopyroxene, olivine, CaSiO₃ phases, coesite, spinel and kyanite. All inclusions (n=332 from 202 diamonds) can be subdivided into four parageneses, lithospheric peridotitic (1) and eclogitic (2), mixed (3) (peridotitic-eclogitic) and sublithospheric mafic (4) (Table 1). There is also a small group of diamonds with an undetermined paragenesis in both types of diamond represented by Fe and Fe-Ni sulphides. One Type I diamond contains a unique super-deep inclusion, the unreverted CaSiO₃ phase with the perovskite lattice structure, found in nature for the first time.

Table 1. Parageneses and mineral association from the studied Cullinan mine diamonds.

| Parageneses | Mineral association | Type-I (n diamonds) | Type-II (n diamonds) |
|------------------------|---------------------------------|------------------------|-------------------------|
| Sublithospheric mafic | Mj | 5 | 5 |
| | Mj + Omp | 2 | 1 |
| | Mj + Co + Ky | - | 1 |
| | Mj + Prp-Alm | 1 | - |
| | CaSiO ₃ (Wo and Prv) | 2 | 2 |
| Total: | | 10 (6%) | 9 (22%) |
| Lithospheric eclogitic | Grt + Cpx | 14 | - |
| | Grt + (Co) | 32 (1) | - |
| | Cpx + (Co) | 70 | 7 (2) |
| | Co + (Ky) | 10 | 6 (1) |
| | En + Co | - | 1 |
| Total: | | 126 (79%) | 14 (33%) |

| | | | |
|---------------------------------|-----------------|-----------------|-----------------|
| Lithospheric peridotitic | Grt + Fo + (En) | 2 | 2 (1) |
| | Cr-Aug + (En) | - | 3 (1) |
| | Fo | 17 | 13 |
| | En | 4 | - |
| | Spl | - | 1 |
| Total: | | 23 (14%) | 19 (45%) |
| Lithospheric mixed | Fo + Co | 1 (1%) | - |
| Total: | | 160 | 42 |

The overwhelming majority of peridotitic inclusions are of lherzolitic paragenesis, as evidenced by the chemical composition of garnets, the average Mg# of olivines (92.2 - very close to the average for lherzolitic olivine diamond inclusions worldwide of 92.0) and the low Al₂O₃ contents in enstatites (below 1.0 wt.%). The eclogitic inclusions are very diverse, with ranges of garnet composition Prp 28.3-72.8, Alm 19.3-43.2, Grs 1.6-46.1 and ranges of omphacite composition Jd 12.5-59.2, Aeg 0-9.0, Wo+En+Fs 40.8-79.6. These observations suggest that the studied minerals represent both A and B types of eclogite, and only one Type I diamond contains grossular and diopside inclusions similar to the grosspyrite association (type C eclogite). Rare associations such as Mj + Co + Ky and Mj + Prp-Alm that combine inclusions incompatible by the depth of origin, highlight that some diamonds could grow sequentially in different PT-ranges.

Since there are several types of mineral parageneses in Cullinan diamonds, we used different ways to evaluate PT-parameters of mineral associations. The temperatures were evaluated using an Al-in-Ol thermometer (Bussweiler et al., 2017) (17 samples), an Opx-Cpx thermometer (Taylor, 1998) with a Opx-Grt barometer (Nickel, Green, 1985) (1 sample) and a single crystal Cpx thermometer (Nimis, Taylor, 2000) (1 sample) for peridotitic inclusions and a Grt-Cpx thermometer (Nakamura, 2009) for eclogitic inclusions (14 samples). Approximately two thirds of the lithospheric inclusions can be projected onto the local geotherm approximated by a 40 mW/m² geotherm (Hasterok and Chapman, 2011) and show PT-parameters consistent with the lithospheric conductive thermal regime; 1090-1400°C and 45-63 kb. One third of the diamonds yield very high Al-in-Ol and Cpx-Gar temperatures, above the upper error limit of potential temperatures for non-plume convecting upper mantle adiabats (1327±40°C, Katsura et al., 2010); these super-adiabatic temperatures are common for peridotite xenoliths in kimberlites. These diamonds are interpreted to have formed in a mantle region with potential temperatures from ~ 1327 to 1440°C, labeled as a dark field on Fig. 1. The high potential temperatures suggested by this Cullinan inclusion cluster suggest that we are seeing a unique snapshot of diamond formation at plume-like temperatures, at 1200 Ma, the time of the Cullinan kimberlite emplacement. For the lithospheric diamonds, the PT-conditions of origin for inclusions of eclogitic and peridotitic parageneses are identical. To calculate the pressure of majorite origin, the new improved majorite geobarometer was chosen (Wijbrans et al., 2016). The majorite barometry yields pressures of 93-138 kb (17 samples) when projected onto 1327 and 1440°C adiabats. The sublithospheric mafic diamonds are thus sourced from the transition zone, based on the stability of Ca-Si perovskite (below 500 km) and 300-460 km based on the inferred depth of majorite origin. The pressure estimates for sublithospheric Type II diamonds are identical to those of Type I diamonds (Fig. 1).

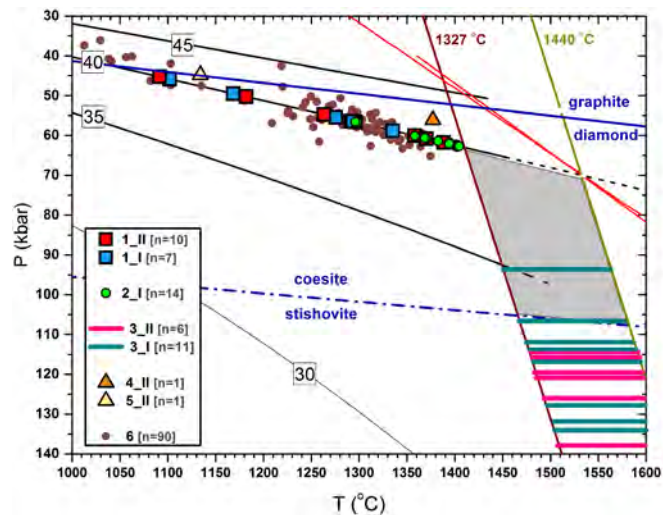


Fig. 1. Pressure-temperature estimates for studied Cullinan diamond inclusions using the following thermometers and barometers: 1 – Al-in-Ol thermometer (Bussweiler et al., 2017); 2 - Grt-Cpx thermometer (Nakamura, 2009); 3 - Mj geobarometer (Wijbrans et al., 2016); 4 - Single-Cpx geothermobarometer (Nimis, Taylor, 2000); 5 - Opx-Grt barometer (Nickel, Green, 1985) and Opx-Cpx thermometer (Taylor, 1998); 6 – Peridotitic xenoliths from Premier pipe (Viljoen et al., 2009). The legend contains sample numbers with “_II” and “_I” labelling type-II and type-I diamonds, respectively. Red univariant P-T lines calculated from Nakamura, 2009) and Al-in-Ol thermometer (Bussweiler et al., 2017) are for inclusions with the highest PT-parameters. An intersection of the lines with the local geotherm defines the 1440°C potential temperature. Dark field is a probable area of origin for eclogitic diamonds with high Cpx-Gar temperatures and peridotitic diamonds with high Al-in-Ol temperatures. The field is limited by the ambient 1327°C adiabat, the 1440°C adiabat, the 40 mW/m² geotherm (Hasterok and Chapman, 2011) and the coesite-stishovite phase boundary, since only coesite inclusions are common in the studied diamonds.

We conclude that the peridotitic paragenesis predominates in Type II diamonds, whereas 79% of the Type I stones are sourced from eclogites. The result confirms a well-known fact that E-type diamonds contain more nitrogen than P-type diamonds. This may reflect natural N heterogeneity of the parent diamondiferous rocks, but may also be controlled by the external diamond-forming fluid. Another contrast in the parageneses of Type I and Type II diamonds relates to the higher incidence of sublithospheric inclusions in the Type II stones, 22% against 6% in Type I diamonds. Type II diamonds are more commonly derived from the transition zone, where low N contents in Cullinan sublithospheric diamonds may be linked to the presence of Fe or FeC (Smith and Kopylova, 2014). We conclude that Type II diamonds are diverse in paragenesis and consequently in origin, as originally emphasised by Moore (2009).

The study was funded by the Dr. Eduard Gübelin Association through the 2015 Dr. Eduard Gübelin research scholarship to N. Korolev.

References

- Bussweiler Y, Brey GP, Pearson DG, Stachel T, Stern RA, Hardman MF, Kjarsgaard BA, Jackson SE (2017) The Aluminum-in-Olivine Thermometer for Mantle Peridotites-Experimental versus Empirical Calibration and Potential Applications. *Lithos* 272-273:301-314
- Moore AE (2009) Type II diamonds: flamboyant megacrysts. *S. Afr. J. Geol.* 112: 23-38
- Smith EM, Kopylova MG (2014) Implications of metallic iron for diamonds and nitrogen in the sublithospheric mantle. *Can J Earth Sci* 51(5):510-516
- Viljoen F, Dobbe R, Smit B (2009) Geochemical processes in peridotite xenoliths from the Premier diamond mine, South Africa: evidence for the depletion and refertilisation of subcratonic lithosphere. *Lithos* 112:1133-1142
- Wijbrans CH, Rohrbach A, Klemme S (2016) An experimental investigation of the stability of majoritic garnet in the Earth’s mantle and an improved majorite geobarometer. *Contrib Mineral Petrol* 171(5):1-20



Mineral inclusions in diamonds from Karowe Mine, Botswana: examining the mantle sources of a diamond population containing exceptionally large crystals.

Theetso Motsamai¹, Jeff W. Harris², Thomas Stachel¹, D. Graham Pearson¹, John Armstrong³

¹ University of Alberta, Edmonton, Canada, motsamai@ualberta.ca, tstachel@ualberta.ca, gdpearson@ualberta.ca

² University of Glasgow, Glasgow, UK, Jeff.harris@glasgow.ac.uk

³ Lucara Diamond Corporation, Vancouver, Canada, JohnA@namdo.com

Introduction

Mineral inclusions in diamonds play a critical role in understanding the relationship between diamonds and mantle lithologies. Here we report the first major and trace element study of mineral inclusions in diamonds from the Karowe Mine (Orapa kimberlite cluster) in north-east Botswana, above the western edge of the Zimbabwe Craton. Our objective is to evaluate the mantle sources associated with a coarse diamond population containing very large gem-quality stones. From a total of 107 diamonds, 134 silicate, 14 oxide and 22 sulphide inclusions were recovered. Assigning the inclusions to principal suites, 55% of the diamonds classify as eclogitic (59 diamonds) and 43% peridotitic (46 diamonds). The remaining 2% consist of one sub-lithospheric diamond, containing a non-touching inclusion pair of majoritic garnet and omphacitic clinopyroxene, and a diamond of likely websteritic association.

Analytical Results

The 35 eclogitic garnets recovered classify into two groups on the basis of CaO content (Fig. 1): high-Ca garnets contain 7.04 to 16.10 wt% CaO and have ranges in Na₂O and TiO₂ between 0.13 to 0.55 wt% and 0.44 to 1.71 wt%, respectively. The low-Ca garnets range from 3.78 to 5.99 wt% CaO with Na₂O and TiO₂ contents vary between 0.07 and 0.24 wt% and 0.46 to 0.66 wt%, respectively. A total of 39 eclogitic clinopyroxene inclusions span the compositional range from (low-Cr) diopside-augite (n=16) to omphacite (n=24), based on their jadeite component (cut-off value of 0.2 for their molar $2\text{Na}/(2\text{Na}+\text{Mg}+\text{Ca}+\text{Fe})$). They contain variable Al₂O₃ (1.79-15.47 wt%), Na₂O (2.03-6.48 wt%), TiO₂ (0.15-0.84 wt%) and low Cr₂O₃ (<0.27 wt%). A cation plot of Al vs Na shows common excess of Al over Na indicative of the presence of a Tschermarks component. In addition to the major eclogitic inclusions, three kyanites were recovered, two colourless and one deep blue. The latter coexisted with an orange garnet and had elevated levels of TiO₂ (0.31 wt%), Cr₂O₃ (0.17 wt%), FeO (0.34 wt%) and MgO (0.18wt%) compared to the two colourless kyanites where these oxides totalled <0.1wt%. The associated garnet contained 7.04 wt% CaO, which is too low for derivation for typical grosspyrite (value of >0.5 at molar calculation (Ca/Ca+Mg+Fe)). In 3 diamonds three pure SiO₂ inclusions were found and are assumed to represent primary coesite. They were separately associated with garnet, clinopyroxene and sulphide. The garnet belongs to the low-Ca group, the clinopyroxene to the low-Cr diopside-augite class and the sulphide has a low Cr content indicative of an eclogitic origin.

In the peridotitic suite, 38 olivine inclusions have Mg# 92.26 to 94.18 with a mean of 93.09 and a median of 93.11. On the basis of coexisting garnets or Mg-chromites (worldwide, with one exception, associated with lherzolitic inclusions), eight are harzburgitic. Based on their generally similar Mg# (mean of 93.02 and median of 93.10), the remaining olivines likely also are mainly of harzburgitic paragenesis. NiO contents in olivine vary between 0.25 and 0.39 wt% (mean of 0.37 and median of 0.36 wt%). Garnet inclusions are harzburgitic (n=8; Fig. 1) and lherzolitic (n=1), with Cr₂O₃ contents ranging between 5.65 and 14.70 wt% and CaO varying between 0.91 and 5.68 wt%. Four garnets have very low CaO contents (0.91-1.79 wt%), indicative of potentially dunitic sources. One of these low-Ca garnets is very rich in Cr₂O₃ (14.70 wt%; Fig. 1). All harzburgitic garnets record very low TiO₂ contents (<0.05 wt%) compared to a single lherzolitic garnet which has elevated TiO₂ (0.24 wt%).

The Cr₂O₃ contents of the 11 Mg-chromites were analysed, two coexisting with olivines, range between 61.83 and 67.28 wt% and TiO₂ varies between 0.06 and 1.12 wt%. All the chromites recorded more than 65.16 wt% Cr₂O₃ and less than 0.40 wt% TiO₂ content, except one with Cr₂O₃ of 61.83 wt% and a high TiO₂ at 1.12 wt%. The six orthopyroxene inclusions recovered have a narrow Mg# range (93.56-94.53; mean 94.00 and median of 94.04), CaO contents between 0.31 and 0.62 wt% and Al₂O₃ contents 0.53 to 0.98 wt%. Two of the orthopyroxenes coexist with garnets, one harzburgitic and one lherzolitic. Of the remaining four inclusions (one co-existing with olivine), two can be assigned to the harzburgitic paragenesis based on their high Mg# and low CaO content (see Fig. 14 of Stachel & Harris, 2008), the other two may be either lherzolitic or harzburgitic. The single Cr-diopside inclusion recovered has an Mg# of 93.11, a Cr₂O₃ content of 0.54 wt%, Na₂O at 0.29 wt% and Al₂O₃ at 0.67 wt%.

The majoritic garnet in the sub-lithospheric diamond has 3.23 Si atoms per formula unit ([O]=12), accompanied by high Na₂O (0.76 wt%) and TiO₂ (1.43 wt%), and low CaO (4.60 wt%). The chemical composition of the accompanying clinopyroxene is omphacitic. A single orthopyroxene inclusion shows an exceptionally low Mg# (56.67), a very high CaO content (1.43 wt%) and elevated Al₂O₃ (0.93 wt%) and Cr₂O₃ (0.20 wt%) concentrations. Based on these characteristics the inclusion is tentatively assigned to the websteritic suite, but based on its very high CaO content could also be of sublithospheric origin.

Of the 22 sulphide inclusions recovered, 20 belong to the eclogitic suite based on low Cr contents (<0.03 at.%) and associated inclusion minerals. Only 5 inclusions consisted of monosulphide solid solution (mss), 2 associated with pentlandite and chalcopyrite respectively; 14 were pyrrhotites, of which three coexisted with pentlandite, chalcopyrite and pyrite separately and one with a pyrite-chalcopyrite assembly; 3 were pentlandites, one being associated with a Ni-Fe alloy. The mss has Ni contents of 7.33-13.79 at.%, and the pyrrhotites have a range in Ni from 0.12- 5.21 at.%. The alloy has a composition of 69.00 at.% Ni, 29.38 at.% Fe and 1.51 at.% Co. The two peridotitic sulphides are mss and contain 0.37 at.% Cr; they were both recovered from the same diamond along with an olivine.

Trace element concentrations were analysed for 12 garnets and 12 clinopyroxenes from the eclogitic suite. The low-Ca (n=3) garnets exhibit steep positive slopes within the LREE_N and less positive ones at MREE_N-HREE_N, the latter at about 11 to 13 times chondritic abundances. Six of the high-Ca garnets show steep positive slopes within the LREE_N, but flat distributions between MREE_N and HREE_N. The remaining three garnets are similar, except that they are slightly enriched in LREE_N. Of the 12 REE_N patterns for eclogitic clinopyroxenes, nine are characterized by a slight positive slope among the LREE_N and a slight steady decline within MREE_N-HREE_N from 10 to about 0.2 to 3 chondritic abundances. Two of the remaining clinopyroxenes have humped patterns, peaking in the LREE_N at about 12 to 99 times chondritic abundances, but thereafter, their slopes are similar to the ones noted above. The last pattern has typical LREE_N but is depleted in the HREE_N. This sample is the only one to show a positive Eu anomaly. Four garnet-clinopyroxene pairs from four diamonds were used to reconstruct eclogite bulk rock REE_N patterns (Fig. 2). They show broadly N-MORB like patterns with

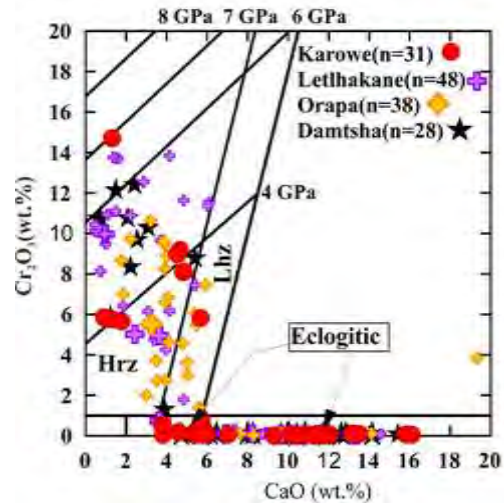


Figure 1: Cr₂O₃ vs CaO diagram for garnets from Karowe and other mines in Orapa cluster (Deines & Harris, 2004; Stachel et al., 2004; Deines et al., 2009). Cr-in-garnets isobars are from Grütter et al., 2006.

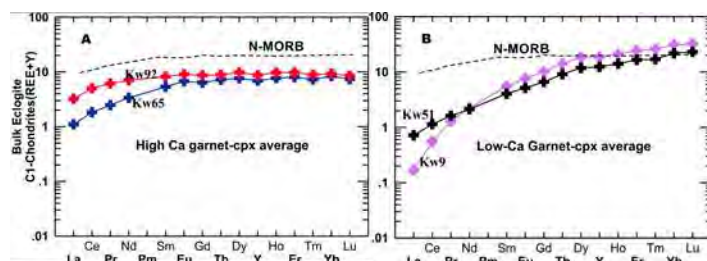


Figure 2: Reconstructed whole-rock REE_N for eclogitic bulk rocks associated with high- and low-Ca garnets (assuming grt:cpx=1:1). N-MORB composition is from Sun & McDonough, 1989.

reconstruct eclogite bulk rock REE_N patterns (Fig. 2). They show broadly N-MORB like patterns with

overall REE depletion for high-Ca garnet associated bulk rocks and prominent LREE_N depletion for the low-Ca associated bulk rocks. Furthermore, five harzburgitic and one lherzolitic garnet were analysed. The harzburgitic garnets show distinctly sinusoidal REE_N patterns with strongly variable overall REE contents. The single analysed lherzolitic garnet has a normal REE_N pattern with flat MREE_N-HREE_N at about 3 times chondritic abundance. The majoritic garnet shows a steep negative slope from LREE_N (~100× chondritic) to HREE_N (at about chondritic abundance)

Geothermobarometry

Non-touching garnet-orthopyroxene inclusion pairs (n=2) indicate peridotitic diamond formation at 1060 °C / 48.9 kbar and 1090 °C / 51.5 kbar, i.e. along a 38 mW/m² geothermal gradient. This value is slightly below the ~40 mW/m² paleogeotherm derived from mantle xenoliths at Letlhakane (Stiefenhofer et al., 1997). Cr-in-garnet barometry (Grütter et al., 2006) indicates peridotitic diamond formation up to a (minimum) depth of up to 220 km (Fig. 1). Based on Ca-in-opx thermometry, the presumed single websteritic pyroxene last equilibrated at 1380 °C, which suggests derivation from a thermally perturbed lithospheric source or from below the lithospheric mantle. Based on Si excess, the majoritic garnet inclusion derives from a depth of about 361 km.

Discussion and Conclusions

With few exceptions, the chemical composition of the eclogitic and peridotitic inclusions in Karowe diamonds compares well to previous studies on inclusion-bearing diamonds from other kimberlites in the Orapa cluster (Orapa, Damtshaa and Letlhakane mines). Among the eclogitic garnets, one sample records the highest TiO₂ concentration (1.71 wt%) yet observed in the Orapa cluster and the same garnet is also enriched in LREE and Zr (130 ppm). This indicates a higher metasomatic activity for Karowe eclogitic diamond sources. In the peridotitic garnets, one Karowe inclusion shows a much higher Cr₂O₃ content (14.70 wt%) than previously observed in the Orapa cluster, suggesting a very thick and highly depleted cratonic lithosphere at the time of diamond formation. Harzburgitic garnets are characterised by LREE_N depletion, in contrast to LREE_N enriched patterns for the bulk of Orapa harzburgitic garnets (Stachel et al., 2004). The sublithospheric inclusion suite reported here, consisting of a majoritic garnet and possibly a Ca-rich orthopyroxene, is unique within the Orapa cluster and may provide a key link to the presence of exceptionally large diamonds at Karowe (Smith et al. 2017).

References

- Deines, P., & Harris, J. W. (2004). New insights into the occurrence of 13 C-depleted carbon in the mantle from two closely associated kimberlites: Letlhakane and Orapa, Botswana. *Lithos*, 77(1), 125-142.
- Deines, P., Stachel, T., & Harris, J. W. (2009). Systematic regional variations in diamond carbon isotopic composition and inclusion chemistry beneath the Orapa kimberlite cluster, in Botswana. *Lithos*, 112, 776-784.
- Grütter, H.S., Latti, D. & Menzies, A. (2006). Cr-saturation arrays in concentrate garnet compositions from kimberlite and their use in mantle barometry. *Journal of Petrology*, 47, 801-820.
- Stachel, T., & Harris, J. W. (2008). The origin of cratonic diamonds—constraints from mineral inclusions. *Ore Geology Reviews*, 34(1), 5-32.
- Stachel, T., Viljoen, K. S., McDade, P., & Harris, J. W. (2004). Diamondiferous lithospheric roots along the western margin of the kalahari craton—the peridotitic inclusion suite in diamonds from Orapa and Jwaneng. *Contributions to Mineralogy & Petrology*, 147(1), 32-47.
- Smith, E.M., Shirey, S.B., Nestola, F., Bullock, E.S., Wang, J.H., Richardson, S.H. & Wang, W.Y., 2016. Large gem diamonds from metallic liquid in Earth's deep mantle. *Science*, 354, 1403-1405..
- Stiefenhofer, J., Viljoen, K.S., Marsh, J.S., 1997. Petrology and geochemistry of peridotite xenoliths from the Letlhakane kimberlites, Botswana. *Contributions to Mineralogy and Petrology*, 127, 147-158.
- Sun, S., & McDonough, W. (1989). Chemical and isotopic systematics of oceanic basalts: Implications for mantle composition and processes. Geological Society, London, Special Publications, 42(1), 313-345



3D Geological Modelling of the Renard 2 Pipe, Québec, Canada: From Exploration to Extraction

I. Lepine¹ and D.J. Farrow²

1 Stornoway Diamond Corporation, North Vancouver, Canada, ilepine@stornowaydiamonds.com

2 GeoStrat Consulting Services Inc., North Vancouver, Canada, darrell.farrow@geotrat.ca

Introduction

The Renard 2 pipe is one of nine diamondiferous pipes situated in the Renard kimberlite cluster in northern Québec, Canada and is the main body presently being extracted at the Renard Diamond Mine. Located in the south-eastern portion of the Superior Province, the Renard 2 pipe was emplaced ~ 640 Ma (Fitzgerald et al., 2009) into Archean gneiss and granitic rocks.

Renard 2 has been the subject of numerous diamond drilling campaigns since its discovery in 2001. The first three dimensional (3D) model of this pipe was completed in 2006. A change in modeling philosophy and subsequent targeted drilling in 2009 resulted in a significant increase to the pipe size, depth and contained mineral resource (Muntener and Scott Smith, 2013). The new 2009 3D model was updated in 2015 following a program of deep directional drilling.

Geology

The Renard 2 kimberlite pipe consists of two main pipe infills, Kimb2a and Kimb2b which are classified as Kimberley-type pyroclastic kimberlite (KPK). A marginal country rock breccia (CRB) interpreted as part of the kimberlite emplacement event surrounds the kimberlitic units. Extensive intrusive coherent kimberlite (Kimb2c) occurs as late stage, cross cutting dykes and irregular intrusions within Kimb2a, Kimb2b and CRB. Renard 2 is interpreted as a diatreme-zone kimberlite with local irregularities in the upper portion but an overall smooth and tapering shape when the emplacement envelope is considered. It is slightly elongated on its north-south axis and has a sub-circular surface expression of 2.3 hectares.

3D Modelling

The first 3D model completed in 2006 consisted of only the kimberlitic units modelled as one shape. The second model completed in 2008 comprised three geological domains, Kimb2a, Kimb2b and CRB, modelled separately (Figures 1 - 3) to a depth of 540 m. Two separate unconnected areas of coherent kimberlite were modelled, but their genesis was not understood at the time.

In 2009 a new approach to 3D modeling was adopted whereby the entire kimberlite pipe event was modelled and then divided into five main geological domains: Kimb2a, Kimb2b, CRB, CRB2a and CCR (Figures 1 - 3). Due to the spatial distribution of the Kimb2c, it was not possible to model these numerous drill intersections and consequently the Kimb2c was included within each geological domain. Where Kimb2c is in contact between two geological units, it was modelled with the more coherent kimberlitic unit, i.e., if a Kimb2c intersection was in contact with Kimb2b and Kimb2a, it was modeled in the Kimb2b domain.

This new approach of modelling the entire kimberlite, including the emplacement envelope and projecting the modelled pipe shape to depth, allowed more focused targeting of deep drilling where kimberlite had not yet been discovered. This targeted drilling resulted in an increase in the Indicated Resource of 5.3 million m³.

In 2015, the 2009 model was updated following a program of deep directional drilling and extended the base of the pipe shape from 710 m to a depth of 865 m below surface (Figures 1 - 3). The total

volume of the Indicated Resource was estimated at 12.3 million m³, an increase of 5.6 million m³ (Farrow and Hopkins, 2015).

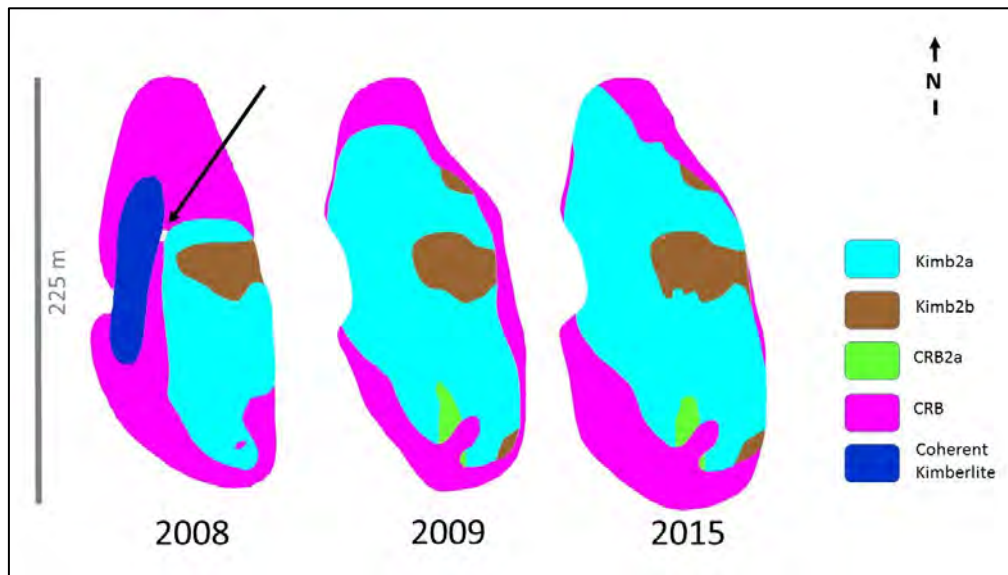


Figure 1: Plan view at 308 m above sea level (a.s.l.) comparing the 2008, 2009 and 2015 geological models. Note the gap in the 2008 model between the coherent kimberlite and the Kimb2a domain created by individually modeling each domain (arrow).

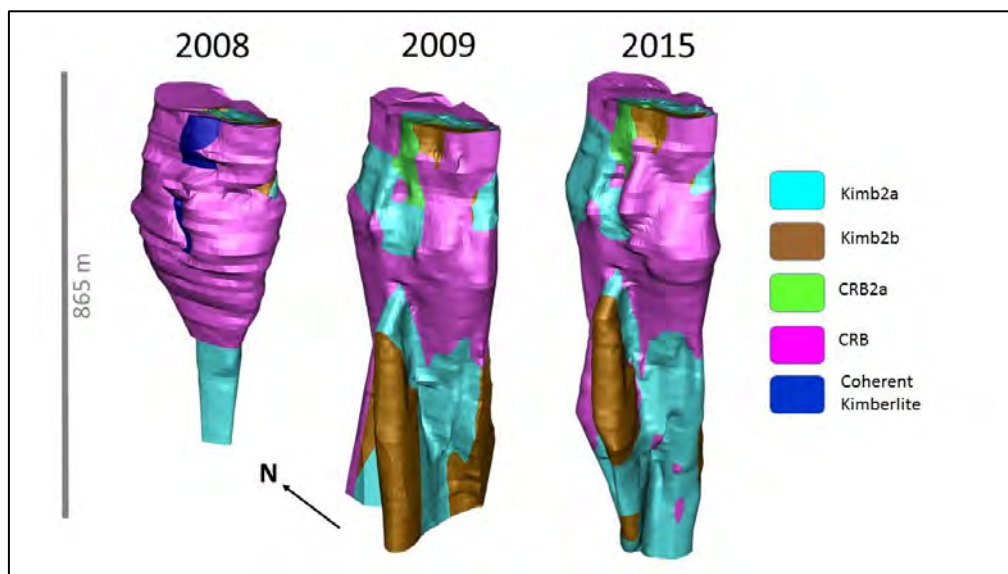


Figure 2: Comparison of 2008, 2009 and 2015 Renard 2 3D geological models (depth of 575 m, 710 and 865 m from surface, respectively). The emplacement envelope (CCR) is not shown for clarity.

Modelling and Drilling Density

The initial modeling approach used only the main kimberlite units and led to a large amount of drilling in the upper portion of the pipe in order to determine the geology and morphology of the kimberlite. The new approach, adopted in 2009, used a series of holes drilled horizontally from the underground exploration sampling level to constrain the shape of the pipe on this level. This shape was successively adjusted to accommodate contacts in drill holes at other depths. Modeling in this way highlighted that the upper portion of the pipe did not change in shape much, and had therefore been over drilled.

For the basic definition of the kimberlite pipe shape, the best drilling approach is to generate a series of pierce points at regularly spaced intervals, rather than on section as is a customary approach in exploration drilling. Defining the pipe shape on one level and using this to guide the modeling, requires significantly less drilling. Removal of a significant proportion of holes drilled on Renard 2 would have resulted in the same pipe shape.

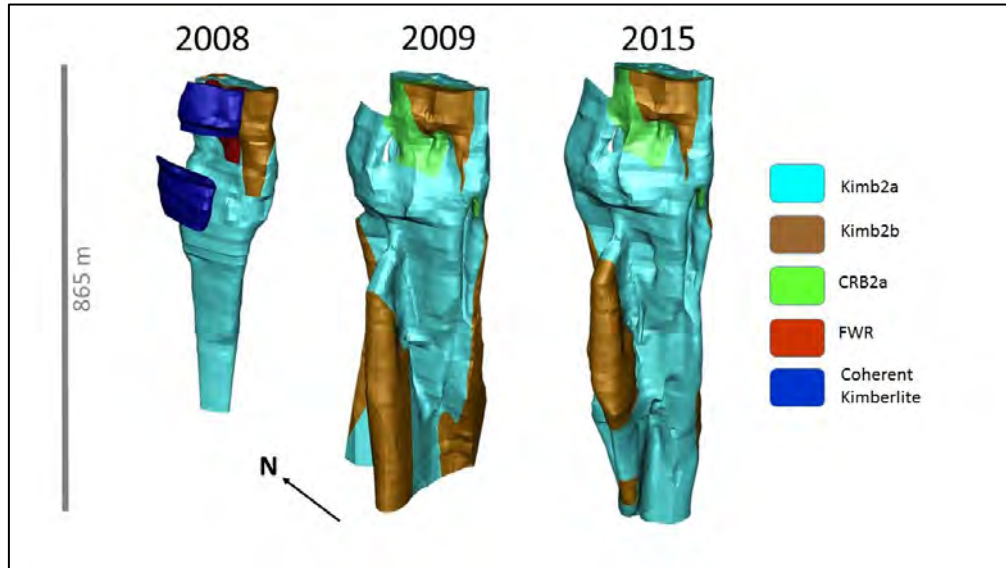


Figure 3: Comparison of 2008, 2009 and 2015 Renard 2 3D geological models excluding the CRB. Note the individually modeled coherent kimberlite units in the 2008 model. In the 2008 model, FWR stands for further work required.

Mining

The Renard 2 pipe is presently the focus of open pit mining and at the end of 2016, five 10 m benches had been completed in the open pit. Underground development has commenced on the 160 m mining depth level (or 355 m a.s.l). The open pit and underground mapping of the pipe shape corresponds well to the 2015 3D model and no major contact changes have as of yet been observed. Country rock/kimberlite contacts have been encountered within 1 m of the modeled contacts. Open pit mining has revealed a large Kimb2c dyke in the CRB domain which was not possible to model from drilling intersections.

Conclusions

Modeling individual kimberlite units separately resulted in a significant underestimation of the kimberlite body and over drilling of the upper portion of the pipe. A systematic approach, consisting of modeling the entire kimberlite emplacement event allows for more focused targeting of delineation drilling and minimises the number of drill holes required to obtain a robust 3D geological model that can be used for resource modeling and feasibility studies.

References

- Fitzgerald CE, Hetman CM, Lépine I, Skelton DS, McCandless TE (2009) The internal geology and emplacement history of the Renard 2 kimberlite, Superior Province, Quebec, Canada. *Lithos* 112S, pp 513-528
- Muntener C and Scott Smith BH (2013) Economic Geology of Renard 3, Québec, Canada: A Diamondiferous, Multi-Phase Pipe Infilled with Hypabyssal and Tuffisitic Kimberlite. *Proceedings of the 10th International Kimberlite Conference, Springer India, Vol 2, pp 241-256*



Origin of upper mantle eclogites from the Catoca pipe (N.-E. Angola)

N.M. Korolev^{1,2}, L.P. Nikitina^{2,3}, A.E. Melnik^{4,2}, V.N. Zinchenko⁵

¹ University of British Columbia, Vancouver, BC, Canada, nkorolev@eoas.ubc.ca

² Institute of Precambrian Geology and Geochronology RAS, St. Petersburg, Russia

³ St. Petersburg State University, St. Petersburg, Russia, lpnikitina2011@yandex.ru

⁴ Saint-Petersburg Mining University, St. Petersburg, Russia, aleks@melnik.co

⁵ Geological Department of SM Catoca, Catoca, Angola, vladimir.zin@mail.ru

The abstract studies mineralogical, petrological and geochemical evidences on genesis and alteration of mantle eclogites xenoliths (21 samples) from Catoca kimberlite pipe (Kasai Craton, N.-E. Angola). Three types of eclogite have been distinguished: high-alumina (high-Al₂O₃), low-magnesian (low-MgO) and high-magnesian (high-MgO) eclogites. Eclogites of each group are characterized by its own unique set of features. High-Al₂O₃ eclogites consist of high-Na omphacite (Jd 51-67) and garnet (Prp30-33 Alm28-29 Grs37-41). There are small quantities of kyanite in each sample (up to 15 vol.%). Low-MgO eclogites are bimineralic, composition of garnet: Prp35-53 Alm28-45 Grs16-28; composition of omphacite: Jd 32-57. High-MgO eclogites are also bimineralic and consist of minerals with a high MgO content, composition of garnet: Prp68-70 Alm21-23 Grs5-8; composition of omphacite: Jd 19-25. Rutile is the most common accessory mineral. High-Al₂O₃ and low-MgO eclogites have a granoblastic texture. High-MgO eclogites have mainly porphyroblastic-like texture combined with either banded or implicitly shale and massive structure.

We used almost all known tools of classical thermobarometry to estimate the PT-parameters of mantle eclogites. In the case of low-MgO some of high-Al₂O₃ eclogites geothermometers (Ellis, Green, 1979; Powell, 1985; Ai, 1994; Krogh, 2000; Nakamura, 2006, 2009) have shown a good agreement in the range of 1000-1200°C at pressures of 40-50 kbar. PT-parameters of high-Al₂O₃ and high-MgO eclogites vary in the significant range 900-1360°C, 35-60 kbar. Thus, to compare all samples together we have chosen the same for all groups of eclogites set of tools. The equilibration temperatures of the eclogite xenoliths were evaluated using a garnet-clinopyroxene geothermometer (Nakamura, 2006). To calculate the pressure of the xenoliths, a geotherm with the heat flow capacity of 40mW/m² was chosen (Hasterok, Chapman, 2011). The relevance of the selection is based on the indirect mineralogical and geochemical criteria (Mg# and Mg/Si in the reconstructed bulk rock, Cr contents in rock-forming minerals). The choice of the geotherm accounted for the fact that almost all of the current estimates of P and T parameters for the mantle beneath ancient Archaean cratons (including Kasai Craton) are close to it. In addition, the Catoca unaltered garnet lherzolite xenolith points lie on the geotherm with the heat flow capacity of 40mW/m².

Different groups of the eclogites represent different levels (with insignificant overlaps) of the Kasai Craton lithospheric mantle. The upper part of the mantle profile 110-170 km (P=35-50 kb, T=900-1200°C) is represented by high-Al₂O₃ and low-MgO eclogites. High-MgO eclogites were taken from depths corresponding to an area of diamond stability: 170-210 km, P=52-60 kb, T=1220-1360°C. The lower boundary of the lithospheric mantle beneath the Kasai Craton according to global seismic tomography is estimated at the depth of 300–400km (O'Reilly et al., 2009; Begg et al., 2009). Thus, our data shows that mantle eclogites from the Catoca pipe represent only about 2/3-1/2 of the lithospheric mantle (110-210 km).

Origin of mantle eclogites, geochemical evidences.

High-Al₂O₃ eclogites. REE_N patterns (Fig. 1), Y, Zr, Li contents and Zr/Sm, Zr/Hf, La/Sm ratios (Fig. 2b) and other geochemical markers of reconstructed whole rock of high-Al₂O₃ eclogites reveal greatest similarity with ophiolitic gabbro and modern oceanic gabbro. Weak Eu-peak together with an increased concentration of Sr in garnets are also an indicator of a plagioclase-bearing protolith.

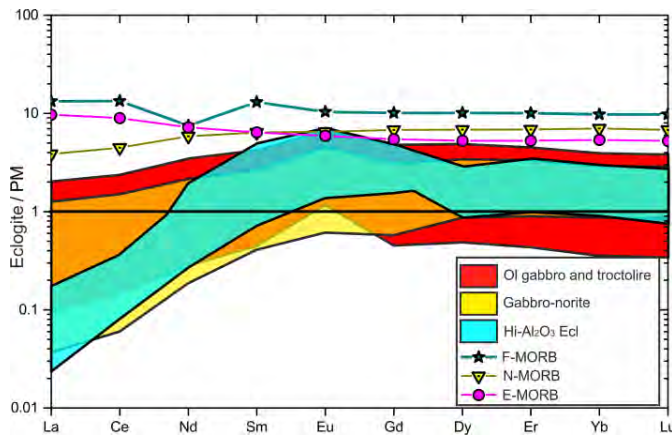


Fig. 1. Rare Earth element patterns of the reconstructed bulk composition of high- Al_2O_3 eclogites and hypothetical protolith (gabbro and troctolite, gabbro-norite, F-MORB, N-MORB, E-MORB).

Low-MgO eclogites. REE_N patterns, Y, Zr, Li contents, Zr/Sm, Zr/Hf, La/Sm ratios as well as other geochemical markers and depleted LREE_N of the reconstructed whole rock of lo-MgO eclogites may indicate that these eclogites were formed during transformation of N-MORB (possible with a boninite component) restite. The geochemical modelling results of melting at 1100-1200°C, 30-40 kbar support the introduced assumption. According with the geochemical modelling results a melting degree of eclogitic protolith/eclogites could reach 25-50%. Figure 2 demonstrates the similarity of the compositions of restites and mantle eclogites in relation to key indicators Zr/Sm, Zr/Hf, La/Lu.

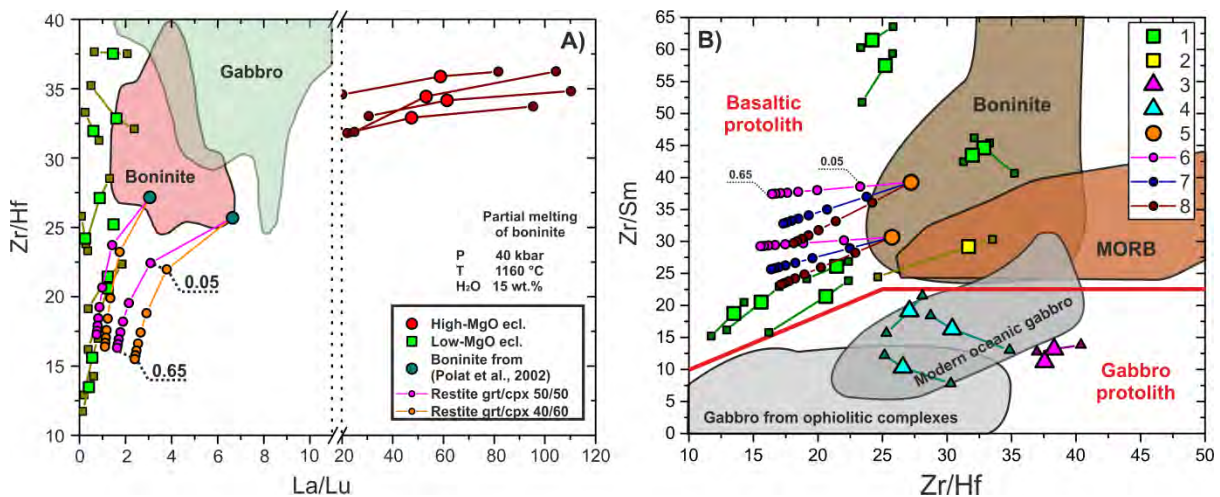


Fig. 2. A) The Zr/Hf vs. La/Lu diagram for the reconstructed bulk compositions of mantle eclogites. Signs on the trend of partial melting of boninites (orange and purple lines) indicates restite. The degree of partial melting increases from 0.05 to 0.65 in increments of 0.1. B) The Zr/Sm vs. Zr/Hf diagram for the reconstructed bulk compositions of mantle eclogites. 1 – Low-MgO eclogites, 2 – altered low-MgO eclogite, 3 and 4 - High- Al_2O_3 eclogites, 5 – boninites, 6-8 – Trends of partial melting of boninites (6 – 40grt/60cpx, 7 – 50grt/50cpx, 8 – 60grt/40cpx) with the degree of partial melting from 0.05 to 0.65.

Values of $^{187}\text{Sr}/^{186}\text{Sr}$ (0.7056-0.7071, n=4), positive ϵ_{Nd} (1.8-2.6, n=9), high values of $^{187}\text{Re}/^{188}\text{Os}$ (80 and 135) and $^{187}\text{Os}/^{188}\text{Os}$ (1.311 and 1.9709), high radiogenic ^{187}Os isotopic composition ($\gamma_{\text{Os}}=129$ and 147) in single eclogites support their subduction origin.

High-MgO eclogites. A large body of mineralogical and geochemical data shows that at least part of high-MgO eclogites could be recrystallized at mantle conditions. Clinopyroxene and garnet from high-MgO eclogites are enriched in Ba, Sr, LREE and other trace elements relative to the counterpart minerals from a peridotite and other eclogite types from the Catoca pipe. Some samples contain fine grained garnet as well as rare coarse grains (~ 5mm). Proto-cores were found in some coarse grains. Chemical composition of the proto-core garnet (major and trace elements) appreciably differs from the recrystallized fine grained garnet. Comparison of the different garnet composition (unaltered and

altered garnet from low-MgO eclogite, proto-cores and recrystallized fine grained garnet from high-MgO eclogite and unaltered garnet from fresh peridotite xenolith) is shown in the figure 3.

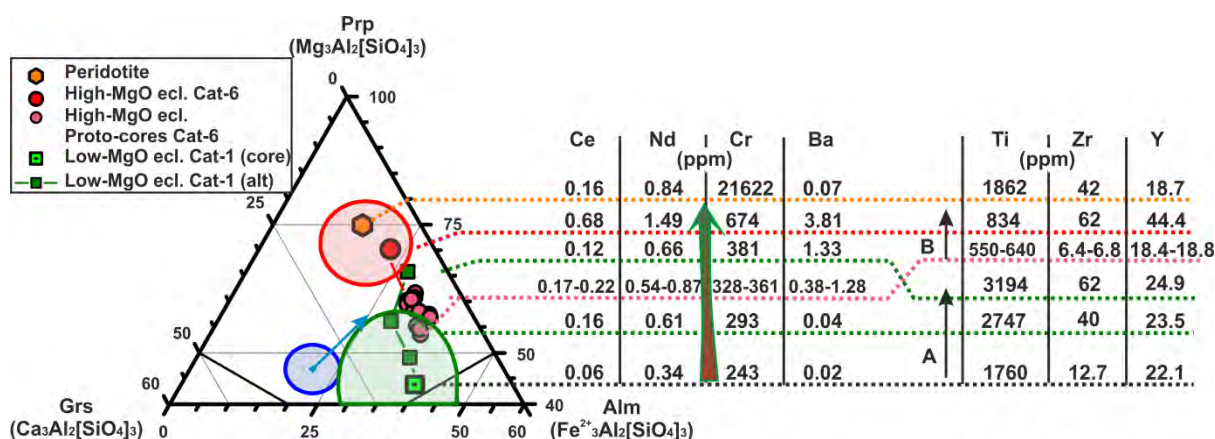


Fig. 3. Comparison of chemical composition of garnet proto-cores from high-MgO eclogite with different type of garnet from mantle xenoliths from Catoca pipe. Red area shows compositions of garnets from high-MgO eclogites and peridotite; Green area shows compositions of garnets from low-MgO eclogites; Blue area shows the composition of garnets from high-Al₂O₃ eclogites.

As shown by our study, processes of recrystallization of the mantle eclogites and specific “metasomatic” processes leading to a high-niobium rutile formation have already appeared. The average Nb₂O₅ content 7-11 wt.% in the rutiles from the high-MgO eclogites was determined. There are some areas (no more than 10–15 microns) with composition of Nb₂O₅ up to 20–25 wt.% and Ta₂O₅ up to 4 wt.% within the rims of the rutile grains (Korolev et al., 2014).

The reported study was funded by the Russian Foundation of Basic Research (RFBR), research projects № 16-35-00321 mol_a and 16-35-60092 mol_a_dk.

References

- Ai Y (1994) A revision of the garnet-clinopyroxene Fe+2-Mg exchange geothermometer. *Contrib Mineral Petrol* 115:467-473
- Begg GC, Griffin WL, Natapov LM, O'Reilly SY, Grand SP, O'Neill CJ, Hronsky JMA, Poudium Djomani Y., Swain CL, Deen T, Bowden P (2009) The lithospheric architecture of Africa: tomography, mantle petrology and tectonic evolution. *Geosphere* 5:23-50
- Ellis DJ, Green DH (1979) An Experimental Study of the Effect of Ca Upon Garnet-Clinopyroxene Fe-Mg Exchange Equilibria. *Contrib Mineral Petrol* 71:13-22
- Hasterok D, Chapman DS (2011) Heat production and geotherms for the continental lithosphere. *Earth Planet Sci Lett* 307:59-70
- Korolev NM, Marin YB, Nikitina LP, Zinchenko VN, Chissupa HM (2014) High-Nb rutile from upper mantle eclogite xenoliths of the diamond-bearing kimberlite pipe Catoca (Angola). *Dokl Earth Sci* 454(1):50-53
- Krogh Ravna EJ (2000) The garnet-clinopyroxene Fe²⁺-Mg geothermometer: an updated calibration. *J Metamorph Geol* 18(2):211-219
- Nakamura D (2009) A new formulation of garnet-clinopyroxene geothermometer based on accumulation and statistical analysis of a large experimental data set. *J Metamorph Geol* 27:495-508
- O'Reilly SY, Zhang M, Griffin WL, Begg G, Hronsky J (2009) Ultradeep continental roots and their oceanic remnants: a solution to the geochemical “mantle reservoir” problem? *Lithos* 112(Suppl 2):1043-1054.
- Powell R (1985) Regression diagnostics and robust regression in geothermometer/geobarometer calibration: the garnet-clinopyroxene geothermometer revisited. *J Metamorph Geol* 3(3):231-243



The Renard 2 Coherent Kimberlitic Units, Québec Canada – Spatial Distribution and Economic Implications

I. Lépine¹ and V. Zhuk¹

¹*Stornoway Diamond Corporation, North Vancouver, Canada,
ilepine@stornowaydiamonds.com, vzhuk@stornowaydiamonds.com*

Introduction

Situated in the Otish Region of northern Québec, Canada, the Renard cluster consists of nine diamondiferous kimberlite pipes and associated kimberlite dykes. Renard 2, the principal body currently being mined by Stornoway Diamond Corporation at the Renard Mine, was emplaced approximately 640 Ma into Archean granitic and gneissic rocks of the south-eastern portion of the Superior Province and is interpreted as a diatreme-zone kimberlite (Fitzgerald et al., 2009). It has an overall regular three dimensional (3D) shape and is slightly elongated north-south with a sub-circular outline at surface of approximately 2.3 hectares.

Renard 2 consists of two main pipe-infills, Kimb2a and Kimb2b, with contrasting primary textures and diamond content. Both units are classified as Kimberley-type pyroclastic kimberlite (KPK; formerly known as tuffisitic kimberlite) similar to “typical” South African-style kimberlites (Fitzgerald et al., 2009; Zhuk et al., 2017). A marginal country rock breccia, CRB, interpreted as part of the pipe emplacement event, surrounds the kimberlitic units. Finally, a third intrusive coherent kimberlite phase, Kimb2c, occurs as cross cutting discontinuous late stage dykes and irregular intrusions, ranging from a few cm up to 15 m in thickness. Kimb2c occurs throughout the Kimb2a and Kimb2b phases, along pipe contacts and within the CRB, representing approximately 17 % of kimberlite logged in drill core. Extensive drilling (over 45 km cumulative, and to depth of 1,000 m) allowed creation of a 3D geological model that was later divided into a series of 50 m thick horizontal depth slices (or levels) allowing detailed studies including geology, volume, internal dilution, geochemistry and diamond content per level. This resulted in a more comprehensive understanding of the spatial distribution of Kimb2c and enabled use of a single diamond content estimate for this phase in the resource model.

Geology

The Kimb2c phase is characterised by a spectrum of primary groundmass mineral assemblages, ranging from monticellite-bearing carbonate-dominated to phlogopite-dominated, each of which consists of common serpentine, spinel and perovskite. It is typically characterised by medium to coarse grained, partially to completely serpentinised/carbonatised olivine (47-51 modal %). Olivine macrocrysts and phenocrysts comprise 25 and 24 modal % of the Kimb2c, respectively. In general, Kimb2c contains between 7 and 13 modal % country rock xenoliths which are typically less than 5 cm in size, irregular in shape and highly altered. Garnet, picroilmenite, chrome diopside and chromite are the most commonly observed indicator minerals. Detailed petrographic observations suggest that Kimb2c may potentially be divided into three subunits (Kimb2c-1, Kimb2c-2 and Kimb2c-3) on the basis of subtle differences in the amount, size and crystal habit of the groundmass phlogopite, with Kimb2c-1 being dominant throughout the pipe and the other two subunits being volumetrically insignificant. More work would be needed to confirm this hypothesis as phlogopite variations alone are not a solid enough line of evidence to prove that these subunits represent different kimberlites. Kimb2c, including each of the possible subunits, are distributed throughout all geological units in the pipe.

Volume

The complex spatial distribution of Kimb2c intersections encountered in the drill holes and underground exploration development made separate 3D modelling of this unit unfeasible, a decision supported by recent open pit mining activities. As such, Kimb2c was included in each of the 3D geological domains (Lépine and Farrow, 2017). Volumetric proportions of Kimb2c were established on a proportionate length basis using geological logging of surface and underground drill holes as well as underground workings. Volume distribution of the Kimb2c was compared spatially within the overall 3D model, within and between the different geological units, on an overall level by level basis using the 50m horizontal depth slices, and on a level by level basis using geological units. Based on this work, approximately 14% Kimb2c is observed in Kimb2a, 25% in Kimb2b and 10% in the CRB representing an average bulk contribution of 17% (Figure 1).

Internal Dilution

Kimb2c country rock xenolith content (i.e. internal dilution) measured from drill core and underground exposures on a metre by metre basis using 0.5 cm resolution was used to create statistically relevant 3D models of dilution. Individual measurements from the Kimb2c units show that internal dilution varies from 0 to 85 modal % (average 12%). Results were evaluated within the overall 3D model, within and between the different geological units, and on a 50m horizontal depth slice basis using both a bulk approach and individual geological units. In spite of the relatively large range of internal dilution, there are no significant observed trends over the 850 m vertical extent of the geological model for each geological unit (Figure 1). On a level by level basis, the internal dilution of the Kimb2c ranges from 5 to 41 modal % (average of 11%) in Kimb2a, between 5 and 25 modal % (average 14%) in Kimb2b and between 8 and 54 modal % (average 17%) in the CRB domains.

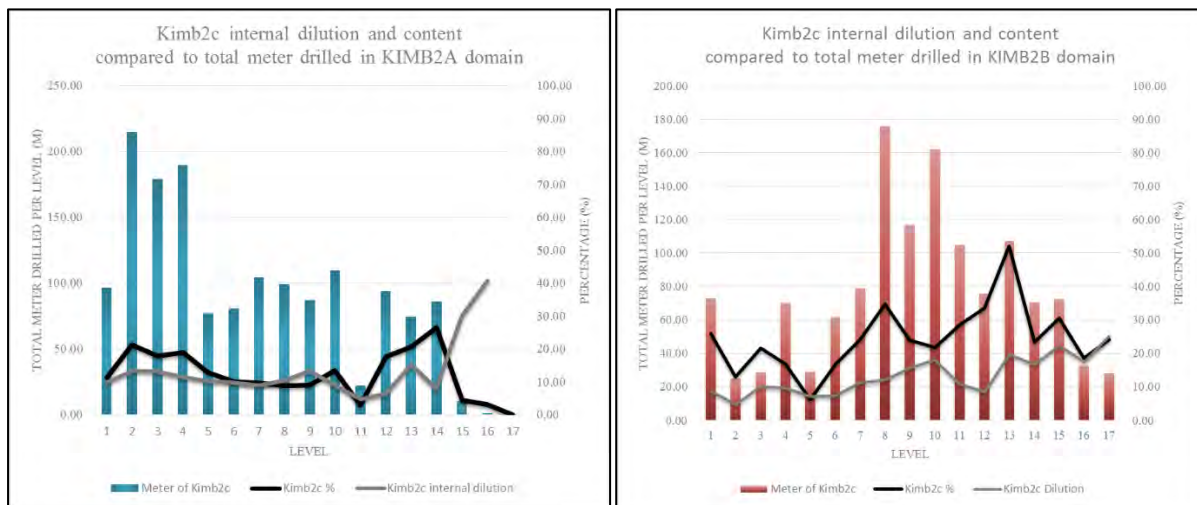


Figure 1: Kimb2c content and internal dilution percentage per 50m level for the KIMB2A domain (on the left) and the KIMB2B domain (on the right) with regards to the total meter of Kimb2c drilled in each domain.

Geochemistry

Compared to Kimb2a and Kimb2b, the Kimb2c samples are relatively enriched in Ta, Nb, and Ti. Kimb2c geochemical samples have a relatively low contamination index of ≤ 1.5 (Clement, 1982). Whole rock, REE and incompatible trace element signatures of Kimb2c within each of the geological units (Kimb2a, Kimb2b and CRB) are remarkably similar, and consistent throughout all depth levels of Renard 2. A closer look at the possible Kimb2c subunits may suggest a potential difference between Kimb2c-1 and Kimb2c-2/3, based mainly on the contamination index, with Kimb2c-1 demonstrating greater contamination index ranging between 1.15 – 1.5 (compared to 0.98 to 1.27 for Kimb2c-2/3) and also slightly higher contents of Fe_2O_3 , MgO, CaO, TiO_2 and Cr_2O_3 . However, the sample dataset for subunits Kimb2c-2/3 is too small to comfortably distinguish between subunits.

Diamond Content

Samples of Kimb2c were submitted for both microdiamond (caustic dissolution) and macrodiamond (dense media separation - DMS) recovery. A total of 2,850 diamonds larger than 0.106mm square mesh were recovered from 126 individual samples of Kimb2c ranging in size from 2.8 to 76.9 kg and averaging 12 modal % internal dilution. A total of 7.4 tonnes of Kimb2c in 22 different samples were submitted for DMS processing at an average measured internal dilution of 11.5 modal %. The composite as recovered +1DTC total diamond content was 296cpht.

Diamond size frequency distribution (SFD) plots on a stones per hundred tonnes per unit interval (SPHTUI) basis, using both the micro- and macrodiamond data for Kimb2c in each of the 50m depth slices, demonstrates grade continuity with depth and the interpretation of a single diamond source population for Kimb2c. Visual assessment of the diamond characteristics from individual Kimb2c samples show a strong degree of similarity also supporting a single diamond source.

Kimb2c grade models derived from micro- and macrodiamond data are consistent between samples and on a level by level basis, and robust when combined. The best fit +1-23DTC carat grade model, adjusted downwards to reflect the loss of smaller stones associated with commercial recoveries, is 294 cpht. This Kimb2c diamond content is supported by larger tonnage geologically mixed DMS samples where Kimb2c grade has been back-calculated based on volumetric contributions, and demonstrates the economic implications of understanding late stage Kimb2c intrusions during the creation of a resource model.

Discussion and Conclusion

Increasing the dataset of geochemical samples to attempt further discriminations between the different Kimb2c subunits may be warranted based on possible differences between Kimb2c-1 and Kimb2c-2/3 that may be present in the original dataset. However, our work clearly demonstrates that the geology, volume, percentage of internal dilution, geochemistry, diamond grade and diamond characteristics of Kimb2c are all very similar and consistent from the top of the pipe to 1,000 m below surface, suggesting that the Kimb2c intrusions, although varying petrographically in groundmass phlogopite, sampled the same diamondiferous part of the mantle and followed similar emplacement processes. These data therefore support the use of a single diamond grade for Kimb2c in the resource model and contribute to a more comprehensive emplacement model of the Renard 2 kimberlite pipe.

References

- Clement CR (1982) A comparative geological study of some major kimberlite pipes in the Northern Cape and Orange Free State. Unpublished Ph.D. thesis, University of Cape Town, 431p
- Fitzgerald CE, Hetman CM, Lépine I, Skelton DS, McCandless TE (2009) The internal geology and emplacement history of the Renard 2 kimberlite, Superior Province, Quebec, Canada. *Lithos* 112S 513-528
- Lépine I and Farrow D J (2017) 3D geological modelling of the Renard 2 Pipe, Québec, Canada: from exploration to extraction. 11th International Kimberlite Conference Extended Abstract No. 11IKC-4545, 2017, Gaborone, Botswana.
- Zhuk V, Lépine I and Laroulandie C (2017) Continuity of Kimberley-type pyroclastic kimberlite phases within Renard 2 over 1,000 m depth – Insights to the geological and emplacement model, Superior Craton, Canada. 11th International Kimberlite Conference Extended Abstract No. 11IKC-4540, 2017, Gaborone, Botswana.



Depth of formation of super-deep diamonds

Anzolini C.^{1,*}, Nestola F.¹ and Harris J.W.²

¹University of Padova, Padova, Italy, chiara.anzolini@phd.unipd.it, fabrizio.nestola@unipd.it

²University of Glasgow, Glasgow, United Kingdom, Jeff.Harris@glasgow.ac.uk

Introduction

Diamonds and the mineral inclusions that they trap during growth provide a unique window on the deep Earth. A small portion (~6%) of diamonds (Stachel and Harris 2008) are interpreted to crystallize between 300 and 800 km depth (Harte 2010) because some of the inclusions entrapped are considered to be the products of retrograde transformation from lower-mantle or transition-zone precursors. However, in many cases undisputed evidence of these purported high-pressure precursors as inclusions in diamonds is lacking, and, consequently, their real depth of origin has been proven only in rare cases (e.g. Brenker et al. 2002; Pearson et al. 2014). Most so-called “super-deep diamonds” contain mainly walsstromite-structured CaSiO_3 (CaSiO_3 -walsstromite), ferropericlase ($(\text{Fe,Mg})\text{O}$), enstatite (MgSiO_3) and jeffbenite ($(\text{Mg,Fe})_3\text{Al}_2\text{Si}_3\text{O}_{12}$), and it is through the study of these mineral phases that the depth of formation of super-deep diamonds can be retrieved.

CaSiO_3 -walsstromite is a dominant Ca-bearing phase in super-deep diamonds (Joswig et al. 1999) and it has been suggested that it is the product of back transformation from CaSiO_3 -perovskite, which is stable only below ~600 km depth. Nevertheless, its real depth of origin is controversial. Single-inclusion elastic barometry, a method recently improved by Angel et al. (2014, 2015), allows us to estimate the pressure and temperature conditions of entrapment for an inclusion within a diamond by knowing its residual pressure (P_{inc}), measured at ambient conditions, and the thermoelastic parameters of the mineral inclusion and the diamond host. The P_{inc} sustained by an inclusion can be determined mainly in two ways: 1) by comparing the unit-cell volume of the inclusion before and after release from its host; 2) by comparing the Raman spectrum of the inclusion still trapped within the diamond and the Raman spectrum of the same mineral phase at room pressure. The first method requires inclusions large enough to be analyzed by single-crystal X-ray diffraction, but large inclusions are more likely to fracture the surrounding host during exhumation and therefore their internal pressure is largely released. The second method allows the analysis of tiny inclusions with no fractures in the diamond host, which commonly preserve higher internal pressures, and, at the same time, the original integrity of the host-inclusion system is maintained.

This work aims to obtain the depths of formation of diamonds containing CaSiO_3 -walsstromite inclusions by non-destructive methods. At present, we have studied 6 super-deep diamonds by a combination of in situ single-crystal X-ray diffraction and micro-Raman spectroscopy. High-pressure micro-Raman investigations were carried out to obtain a calibration curve to determine the P_{inc} of a CaSiO_3 -walsstromite inclusion by means of Raman spectroscopy without breaking the diamond. We additionally calculated the Raman spectrum of CaSiO_3 -walsstromite by ab initio methods both under hydrostatic and non-hydrostatic stress conditions to avoid misinterpretation of the results caused by the possible presence of deviatoric stresses causing anomalous shift of CaSiO_3 -walsstromite Raman peaks. Lastly, we applied single-inclusion elastic barometry to estimate the entrapment pressure of a CaSiO_3 -walsstromite-diamond pair.

Experimental Methods

X-ray data were collected in situ on the inclusions using a Rigaku Oxford Diffraction *SuperNova* goniometer, equipped with a Dectris *Pilatus 200 K* area detector and with a *Mova* X-ray microsource. A $\text{MoK}\alpha$ radiation was operated at 50 kV and 0.8 mA. The sample to detector distance was 68 mm. Data reduction was performed using CrysAlis software (Rigaku Oxford Diffraction), which corrected for L_p

effects and absorption. Raman measurements were carried out in situ with a Thermo Scientific™ DXR Raman Microscope using a green argon ion laser (532 nm) as excitation source at the Department of Geosciences, University of Padova. The analyses were performed using a 50× objective with $\sim 2.5 \text{ cm}^{-1}$ spectral resolution and $1.1 \text{ }\mu\text{m}$ spatial resolution at 10 mW of power. The synthetic CaSiO_3 -walstromite crystal selected for the Raman investigation was synthesized at 9 GPa and 2000 K in a multi-anvil press. First, a Raman spectrum was collected at room conditions; for the high-pressure measurements a diamond-anvil cell was loaded with the crystal of CaSiO_3 -walstromite, a piece of ruby as internal pressure standard and a 4:1 mixture of methanol:ethanol as pressure- transmitting medium. The Raman spectra were collected at the University of Roma Tre with a micro-Raman spectrometer equipped with a green argon ion laser (532 nm) focused through a 20× LWD objective. The spatial resolution of the sample surface was $\sim 1 \text{ }\mu\text{m}$ and the spectral resolution was 0.3 cm^{-1} . Spectral fitting was carried out using the Thermo Scientific™ OMNIC™ Spectra Software. The ab initio calculation of the vibrational frequencies and intensities of the Raman-active modes was performed by using the CRYSTAL14 software (Dovesi et al. 2013).

Analytical Results

At ambient pressure the main Raman peaks of CaSiO_3 -walstromite were observed at 656, 977 and 1037 cm^{-1} (hereafter called Peak 1, 2 and 3, respectively). With increasing pressure, all Raman peaks shifted continuously toward higher wavenumbers. In particular, Peaks 1 and 2 showed almost linear trends. The pressure-dependence of the three main Raman bands was fitted with a weighted linear regression and the resulting pressure coefficients were: $dv/dP = 3.22(5) \text{ cm}^{-1} \text{ GPa}^{-1}$ for Peak 1, $dv/dP = 5.16(9) \text{ cm}^{-1} \text{ GPa}^{-1}$ for Peak 2 and $dv/dP = 6.5(1) \text{ cm}^{-1} \text{ GPa}^{-1}$ for Peak 3 (Figure 1a). Our calculated Raman spectra under hydrostatic stress are comparable with the experimental frequencies. Again, all Raman frequencies systematically increase with increasing pressure. The pressure-dependence of the three main Raman bands was fitted with a weighted linear regression and the resulting pressure coefficients were: $dv/dP = 3.32 \text{ cm}^{-1} \text{ GPa}^{-1}$ for Peak 1, $dv/dP = 4.68 \text{ cm}^{-1} \text{ GPa}^{-1}$ for Peak 2 and $dv/dP = 5.89 \text{ cm}^{-1} \text{ GPa}^{-1}$ for Peak 3 (Figure 1b). The ab initio calculated peak shifts under non-hydrostatic stresses show patterns similar to those under hydrostatic pressure. Also, the pressure-dependencies of the three main peaks under non-hydrostatic stresses are comparable to those calculated under hydrostatic pressure. However, Peak 2 is the least sensitive to the application of differential stresses, and therefore it is the most reliable peak to be used as a calibrant to calculate the P_{inc} of a CaSiO_3 -walstromite inclusion. Therefore, we used its pressure coefficient to calculate the P_{inc} of an inclusion still trapped within a diamond which shows the highest Raman peak shifts ever reported in the literature (main Raman peaks at 669, 999 and 1061 cm^{-1}) and we obtained a value of $4.26(7) \text{ GPa}$.

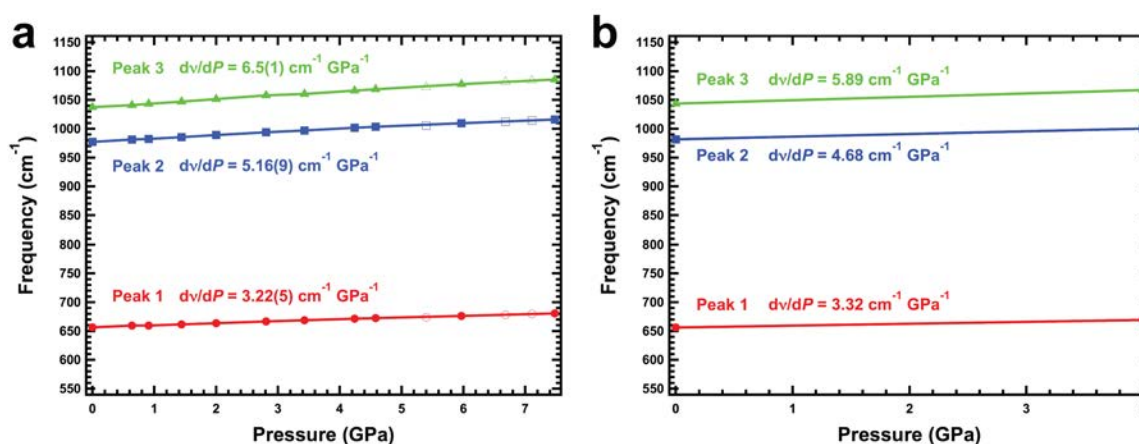


Figure 1: a) Experimental and b) calculated pressure dependencies of the main Raman peaks of CaSiO_3 -walstromite under hydrostatic conditions. In a) compression and decompression are represented by solid and open symbols, respectively. The error bars lie within the symbols.

Ten CaSiO_3 -walsstromite inclusions were individually investigated by single-crystal X-ray diffraction. All of the inclusions have unit-cell volumes less than the room pressure volume of CaSiO_3 -walsstromite ($\sim 376 \text{ \AA}^3$), confirming the Raman results that these inclusions retain a remnant pressure. We have determined their residual pressures, which range from ~ 0.17 to ~ 1.8 GPa, by using the thermoelastic parameters for CaSiO_3 -walsstromite reported in Anzolini et al. (2016). The presence of fractures around these inclusions explains why they exhibit lower pressure than the residual pressure of 4.26(7) GPa obtained previously by using the Raman calibration curve.

The calculation of the pressure of formation for the CaSiO_3 -walsstromite – diamond pair was performed with the software EoSFit7c. We used thermal expansion and compressibility data for CaSiO_3 -walsstromite reported in Anzolini et al. (2016), thermoelastic properties for diamond from the review of Angel et al. (2015) and the residual pressure of 4.26(7) GPa. Assuming a temperature range between 1200 K and 2000 K for CaSiO_3 -walsstromite formation, we obtained entrapment pressures ranging from 8.10 to 9.27 GPa, corresponding to 240-280 km depth (Figure 2, from Anzolini et al. 2017).

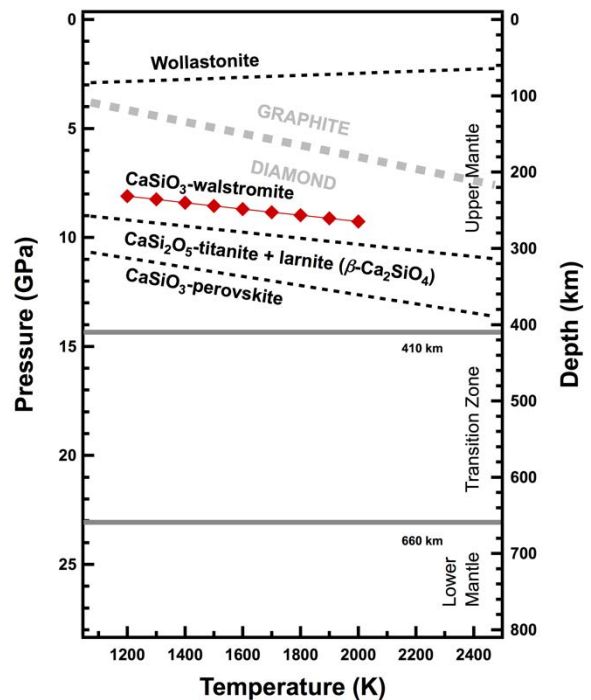


Figure 2: Phase diagram of the CaSiO_3 system. Entrapment pressures from which our sample may have originated are represented with red symbols.

References

- Angel RJ, Mazzucchelli ML, Alvaro M, Nimis P, Nestola F (2014) Geobarometry from host-inclusion systems: The role of elastic relaxation. *Am Mineral* 99:2146-2149
- Angel RJ, Alvaro M, Nestola F, Mazzucchelli ML (2015) Diamond thermoelastic properties and implications for determining the pressure of formation of diamond-inclusion systems. *Russ Geol Geophys* 56:211-220
- Anzolini C, Angel RJ, Merlini M, Derzsi M, Tokár K, Milani S, Krebs MY, Brenker FE, Nestola F, Harris JW (2016) Depth of formation of CaSiO_3 -walsstromite included in super-deep diamonds. *Lithos* 265:138-147
- Anzolini C, Prencipe M, Alvaro M, Romano C, Vona A, Lorenzon S, Smith EM, Brenker FE, Nestola F (2017) Depth of formation of super-deep diamonds: Raman barometry of CaSiO_3 -walsstromite inclusions. *Am Mineral* submitted
- Brenker FE, Stachel T, Harris JW (2002) Exhumation of lower mantle inclusions in diamond: A TEM investigation of retrograde phase transitions, reactions and exsolution. *Earth Planet Sci Lett* 198:1-9
- Dovesi R, Saunders V, Roetti C, Orlando R, Zicovich-Wilson C, Pascale F, Civalleri B, Doll K, Harrison N, Bush I CRYSTAL14 User's Manual; University of Torino: Torino, 2014
- Harte B (2010) Diamond formation in the deep mantle: the record of mineral inclusions and their distribution in relation to mantle dehydration zones. *Mineralogical Magazine* 74:189-215
- Joswig W, Stachel T, Harris JW, Baur WH, Brey GP (1999) New Ca-silicate inclusions in diamonds – tracers from the lower mantle. *Earth Planet Sci Lett* 173:1-6
- Pearson D, Brenker F, Nestola F, McNeill J, Nasdala L, Hutchison M, Matveev S, Mather K, Silversmit G, Schmitz S (2014) Hydrous mantle transition zone indicated by ringwoodite included within diamond. *Nature* 507:221-224
- Stachel T, Harris J (2008) The origin of cratonic diamonds – constraints from mineral inclusions. *Ore Geology Reviews* 34:5-32



Hydration of the lithospheric mantle in the northern Slave craton (Canada): constraints from combined FTIR and EBSD measurements on peridotite xenoliths

Qin Wang^{1*}, Haojie Yan¹, Maya G. Kopylova²

¹ Nanjing University, Nanjing, China, qwang@nju.edu.cn, 438463628@qq.com

² University of British Columbia, Vancouver, Canada, mkopylov@eoas.ubc.ca

Introduction

Water contents of nominally anhydrous mantle minerals have significant influence on the mantle strength and change with magmatism and metasomatism. Measurements of water content in olivine from the cratonic mantle are therefore an important tool for deciphering deep mantle processes, both rheological and geochemical. Due to the fast eruption rate of kimberlites, peridotite xenoliths from kimberlites are the best samples to study the distribution of in-situ water contents in the cratonic lithospheric mantle.

Using a new method that combines Fourier transform infrared spectroscopy (FTIR) and electron backscatter diffraction (EBSD) analysis, we measured water contents and crystal preferred orientation (CPO) of olivine in peridotite xenoliths from the middle Jurassic MuskoX kimberlite pipe (northern Slave craton, Canada). The results reveal contrasting water contents and fabrics of olivine in spinel peridotites and garnet peridotites, which highlight the importance of magmatism and metasomatism on deformation mechanisms of the mantle.

Methods

Infrared spectroscopy determines concentrations of OH-groups in olivine based on the infrared light absorption coefficients, which differ depending on crystallographic directions in anisotropic minerals. Ideally, water contents in olivine should be analyzed on oriented grains using polarized infrared light. However, this method requires mineral separation and orientation. Based on results of Bell et al. (2003), an ellipsoid of water absorption coefficient (W) is established using W values along crystallographic directions [100], [010] and [001] (Figure 1a). Then based on the EBSD-derived orientation of an olivine grain, the specific water absorption coefficient along a certain direction (W_s) in the ellipsoid is determined. Finally, water content of the olivine grain is calculated using the Beer-Lambert equation.

Orientations of olivine and orthopyroxene were measured by the manually EBSD indexing using JEOL JSM-6490 electron microprobe equipped with an HKL Nordlys-S EBSD detector. The EBSD measurements were carried out at accelerating voltage of 20 kV, a working distance of 15–30 mm with 70° tilt angle of a thin section (Figure 1b). Although it is difficult to determine the lineation and foliation of peridotite xenoliths, orthopyroxene generally develops the CPO with concentration of [001] axes parallel to the lineation and that of [100] axes normal to the foliation (Wang et al., 2013). Therefore we rotated the EBSD data to obtain the CPO of orthopyroxene, and then plotted pole figures of olivine.

Water contents of olivine were measured by the Bruker Vertex 70V FTIR spectrometry using polarized light. All thin sections were analyzed with the polarization direction of infrared light parallel to the long axis of the thin section (0°//X1 direction). In addition, 3 garnet peridotite samples also have the FTIR analysis with the polarization direction of infrared light 90° to the long axis of thin section (90°//Y1 direction) (Figure 1c). For coarse olivine grains, there is no difference in water contents of olivine from core to rim. The results demonstrate reliability of this new method and homogenous water distribution in olivine in microscale (Table 1). All experiments were carried out at the State Key Laboratory for Mineral Deposits Research, Nanjing University.

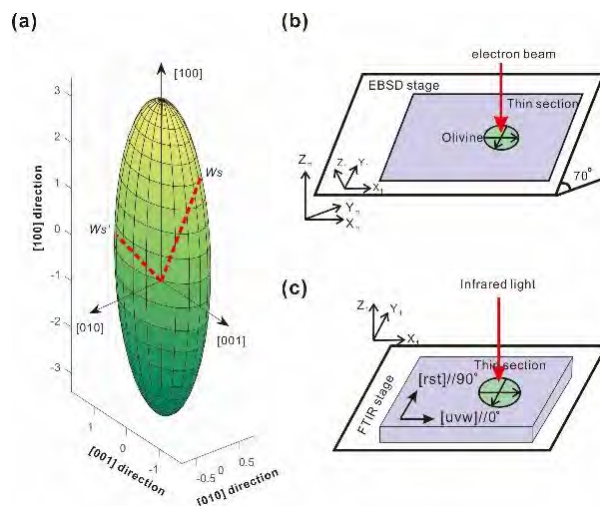


Figure 1: (a) Ellipsoid of water absorption coefficient of olivine, and coordinate systems in (b) EBSD and (c) FTIR experiments.

Analytical Results

Olivine infrared spectra (Figure 2) are similar to previously published spectra for olivine (Bell et al., 2003). The dominance absorption in different polarization directions is between 3650 and 3450 cm^{-1} , with absorption peaks at 3572 cm^{-1} and 3525 cm^{-1} . To avoid effects of serpentinization, spectra with absorption peaks at 3650–3790 cm^{-1} were not included.

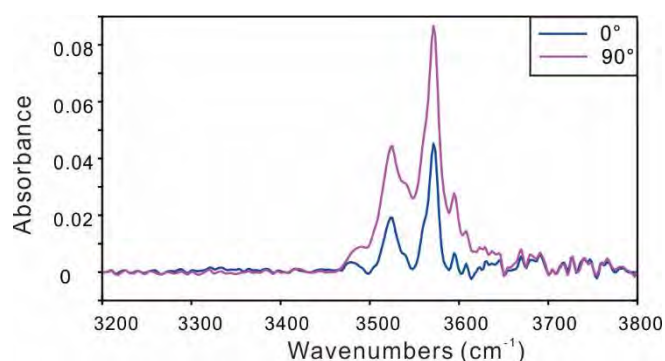


Figure 2: Polarized infrared spectra of olivine grains with polarization direction of 0° and 90°.

Four garnet peridotites show porphyroclastic sheared texture and contain phlogopite, whereas three spinel peridotites have granoblastic coarse texture and one sample MOX7-62-3 contains hornblende. Olivine from 4 garnet peridotite samples has the average Mg# of 90.5 and average water content of 82 ± 5 ppm, and develops the B-type fabric due to dominance of the [001](010) slip system. In contrast, olivine from spinel peridotites shows the average Mg# of 92 and average water content of 33 ± 6 ppm, and the E-type fabric due to dominant activation of [100](001) slip system (Table 1 and Figure 3).

Our results suggest higher water concentration in the deeper part (>100 km) of the northern Slave craton. Wang (2010) summarized that the average water contents in olivine from cratonic kimberlite nodules is 17 ± 13 ppm H_2O for the unpolarized light and the Paterson's calibration, i.e., ~ 60 ppm H_2O for the polarized light using the Bell et al. (2003) calibration. Therefore, olivine in coarse-grained spinel peridotites from the Muskoix kimberlite pipe kept very dry after the initial large degree of partial melting, whereas olivine in the sheared garnet peridotites has been hydrated above the average cratonic mantle. The calculated equilibrium P-T conditions for garnet peridotites are 1210 ± 20 °C and 6.0 ± 0.3 GPa. This indicates hydrogen-enhanced strain localization in garnet peridotites near the lithosphere-aesthenosphere boundary (LAB), which is contrary to water-poor olivine from the LAB beneath the

Kaapvaal craton (Preslier et al., 2010). Hydration of the lithospheric mantle beneath the deep northern Slave craton may record mantle metasomatism after formation of the cratonic root, which resulted in a weakened LAB and pre-condition of the Jurassic mantle to the formation of kimberlite melts.

| Sample No. | Lithology | Grain number (N) | Water content in section a | Water content in section b | | Average water content | Mg# | Olivine fabric |
|--|-------------------|------------------|----------------------------|----------------------------|---------------------|-----------------------|-------|----------------|
| Polarization direction of infrared light | | | 0°//X ₁ | 0°//X ₁ | 90°//Y ₁ | | | |
| MOX1-45-5 | Garnet peridotite | 86 | 89±17 (N=44) | 93±17 (N=21) | 92±18 (N=21) | 91±17 | 90.11 | [001](010) |
| MOX25-124-8 | Garnet peridotite | 117 | 81±11 (N=45) | 81±17 (N=36) | 81±16 (N=36) | 81±14 | 90.58 | [001](010) |
| MOX28-320-1 | Garnet peridotite | 82 | 83±11 (N=34) | 75±12 (N=24) | 76±10 (N=24) | 76±12 | 89.28 | [001](010) |
| MOX24-125-0A | Garnet peridotite | 38 | 76±17 | | | | 91.85 | [001](010) |
| MOX3-78-8A | Spinel peridotite | 34 | 25±9 | | | | 93.4 | [100](001) |
| MOX7-62-3 | Spinel peridotite | 49 | 40±14 | | | | 91.82 | [100](001) |
| MOX7-97-6 | Spinel peridotite | 26 | 34±8 | | | | 90.68 | [100](001) |

Table 1: Water contents in ppm H₂O, Mg# and fabric of olivine from the Muscox peridotite xenoliths

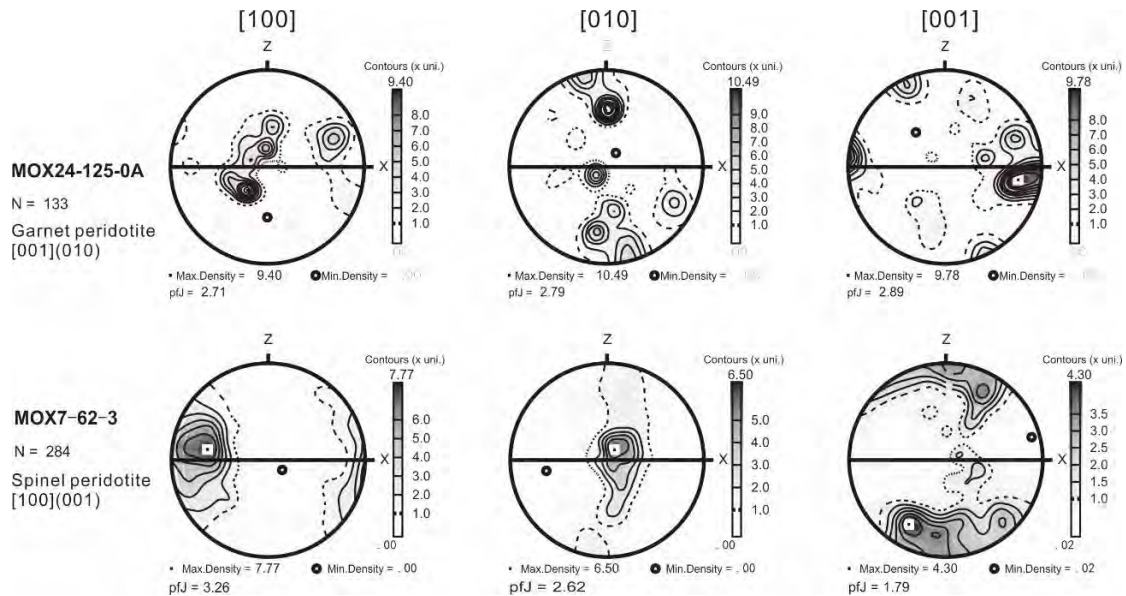


Figure 3: Lower hemisphere projection for pole figures of olivine from typical peridotite xenoliths. X is parallel to the lineation, Z is normal to foliation, N is measured grain number.

References

- Bell DR, Rossman GR, Maldener J, Endosch D, Rauch, F (2003) Hydroxide in olivine: a quantitative determination of the absolute amount and calibration of the IR spectrum. *J Geophys Res* 108: 2105. doi:10.1029/2001JB000679
- Paterson MS (1982) The determination of hydroxyl by infrared absorption in quartz, silicate glasses and similar materials. *Bull Mineral* 105: 20–29
- Peslier AH, Woodland AB, Bell DR, Lazarov M (2010) Olivine water contents in the continental lithosphere and the longevity of cratons. *Nature* 467: 78-82
- Wang Q (2010) A review of water contents and ductile deformation mechanisms of olivine: implications for the lithosphere–asthenosphere boundary of continents. *Lithos*, 120: 30-41
- Wang Q, Xia QK, O'Reilly SY, et al (2013) Pressure- and stress-induced fabric transition in olivine from peridotites in the Western Gneiss Region (Norway): implications for mantle seismic anisotropy. *J Metamorph Geol* 31: 91-111



Experimental milling of olivine: Implications for ascent and eruption of kimberlite

Thomas J. Jones¹ & J. K. Russell²

¹*Department of Earth Sciences, Durham University, South Road, Durham, DH1 3LE, UK, t.j.jones@durham.ac.uk; tomjj7@gmail.com*

²*Department of Earth, Ocean & Atmospheric Sciences, University of British Columbia, Vancouver, British Columbia, V6T 1Z4, Canada, jkr2002@gmail.com*

Introduction

Kimberlite magmas entrain, transport and erupt large volumes of mantle-derived olivine grains. Characteristically, the olivine crystals found in kimberlite are rounded and ellipsoidal in shape. The origin of their ellipsoidal morphologies remains somewhat enigmatic given their origin from disaggregation of lithospheric mantle rocks. Explanations include rounding by magmatic corrosion and dissolution (Kamenetsky et al. 2008; Pilbeam et al. 2013) or mechanical milling (Arndt et al. 2006; Arndt et al. 2010; Russell et al. 2012; Jones et al. 2014; Brett et al. 2015). Here, we focus on mechanical processes that operate during turbulent mantle ascent, facilitating reshaping and resurfacing of olivine.

During transport orthopyroxene and other mantle minerals are assimilated by the kimberlite magma. One effect of the assimilation is to raise the melt's SiO₂ content, thereby causing a reduction in CO₂ solubility and the spontaneous exsolution of a CO₂-dominated fluid phase (Brooker et al. 2011; Russell et al. 2012; Moussallam et al. 2015). This assimilation-driven exsolution of a fluid phase provides a continuous decrease in density, an increase in buoyancy, and an accelerating ascent. Additionally, there is strong evidence that, during kimberlite magma ascent through the mantle lithosphere, substantial mechanical modification of the suspended cargo occurs (Jones et al. 2014; Brett et al. 2015). Brett et al. (2015) hypothesized that the ascending dyke segregates into a turbulent gas-rich head where particle-particle interactions dominate followed by a trailing tail of less gas-charged magma. This ascending dyke continually modifies its cargo from initial disaggregation to ultimately, eruption. Here, we present data from a series of novel, scaled, analogue attrition experiments that inform on the rates, efficiency and timings of mechanical modification possible during transport through the mantle lithosphere.

Methods and scaling

Our experiments consist of a particle bed that contains disaggregated olivine crystals derived from mantle dunite. Before loading the particle feed, olivine grains were sieved to a restricted size range (500 µm – 1mm) and washed with deionised water to remove any adhering particles. The particle bed in which the sample is loaded rests on a distributor plate that is connected to a compressed air supply allowing a controlled gas feed of 85 Lmin⁻¹ (Fig. 1). Above the bed lies a 1.2 m high tube where particles can rise and interact within a gas suspension. Lastly, the attrition tube is connected to a fine mesh screen and passed through a water collection trap to ensure that all the experimental run products are recovered, even micron size fragments. The attrition experiments were performed at nine different durations from 0.5 to 32 hours to replicate various mantle transport times. After each experiment the remaining coarse grain size fraction (> 63 µm) was removed from the distributor plate and sieved using a set of standard Tyler sieves. Then, all of the experimental rig components were flushed with deionised water to collect any ultra-fine particles. This water suspension along with any material collected in the water collection pail (Fig. 1) was measured for grain size using a Malvern Instruments Mastersizer 2000; a laser diffraction analyser capable of measuring particles suspended in water.

Our experiments build on previous work from the Engineering Sciences that has shown that particle attrition is highly dependent on a minimum of four governing parameters: the particle concentration suspended in the jet; the feed particle size distribution; the particle/gas velocity; and the particle residence time. Attrition is promoted by high particle concentrations, poorly sorted feed distributions, high differential velocities, and long residence times (Bemrose and Bridgwater 1987; Jones et al.

2017). For us to compare our analogue results to nature and evaluate the attrition potential during kimberlite ascent, for example, we provide a dimensional analysis. Our experimental conditions are such that they fall within the same range of Reynolds numbers (Re ; Equation 1) and Dimensionless particle concentrations (ϕ ; Equation 2) expected in the natural system:

$$Re = \rho u D / \mu \quad [\text{Eqn. 1}]$$

$$\phi = v_0 / v_f \quad [\text{Eqn. 2}]$$

where ρ is the gas density, u the gas velocity, D the crack width or tube diameter, μ the gas dynamic viscosity, v_0 the volume of the particles and v_f the volume of the fluidized system. In detail, we calculate the minimum and maximum Re and ϕ predicted for the gas-rich fluidized head of the propagating dyke using crack widths $0.1 < 2.5$ m and ascent velocities $0.25 < 8$ ms^{-1} . For all these parameters, we find both our experiments and natural kimberlite ascent lie within the same dimensionless turbulent, particle-laden regime. Hence, this allows us to compare our experimental results to timescales and processes that operate within the gas-rich head of an ascending kimberlite dyke.

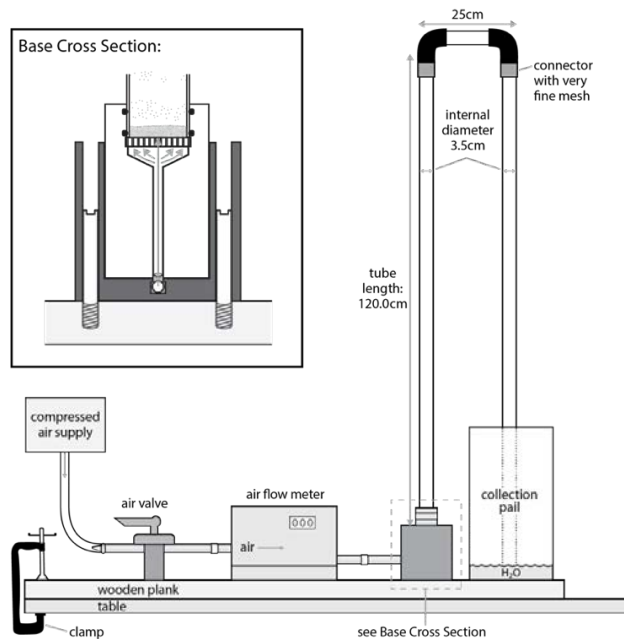


Figure 1: Diagram of the experimental attrition rig designed for this study.

Results and Analysis

In all experiments the gas feed and associated bulk gas flow velocities of 1.13 ms^{-1} were sufficient to fluidize the olivine particles and sustain a turbulent flow regime. The initial packed bed height of 12.5 mm increased to ~ 140 mm resulting in particles rapidly being transported within a particle-laden suspension. For all experiments the abundance of input feed material (500 μm – 1 mm) reduces during an experiment (Fig. 2a). This reduction in feed or parent particles is non-linear and faster at short attrition times. The reduction in parent particles can be attributed to the production of smaller (< 500 μm) daughter particles formed through fragmentation and abrasion (Fig. 2a). We find that the rate of fines production (defined as the mass of daughter particles, m_d normalised to the feed mass, m_0) is best described as:

$$m_d / m_0 = a(1 - e^{-bt}) \quad [\text{Eqn. 3}]$$

where a is the infinite time limit, b is the attrition rate constant and t , the residence time. Experimental and modelled values for olivine attrition are shown in Fig. 2b.

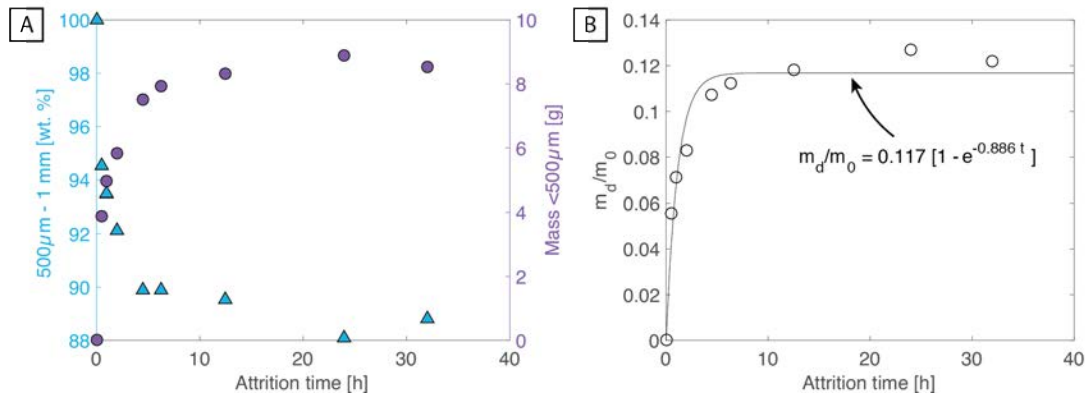


Figure 2: (a) Mass loss of feed (blue triangles) and mass gain in fines (purple circles) as a function of residence time. (b) Fines production model (Eqn. 3) for olivine attrition in a fluidized bed at $Re = 2690$ and $\phi = 0.090$.

Implications

The experimental results have several implications for conceptual models of kimberlite ascent. They demonstrate that at short times (minutes to hours) olivine within a fluidized bed can be reshaped and resized efficiently. The dimensional similitude between our experiments and ascending kimberlite magmas supports a model whereby the shapes, sizes, and surface properties of the olivine cargo in kimberlite are derived by attrition processes operating in the fluidized ascending magma. During transport, attrition rapidly re-shapes, re-sizes and re-surfaces mantle olivine grains whilst continually creating a fine-grained sub-population. The fine chips of olivine have large surface area to volume ratios that accelerate chemical dissolution reactions, thereby removing the evidence of milling processes and facilitating the simultaneous modification of the melt composition. Such particles are susceptible to high rates of chemical dissolution; hence, rarely preserved in kimberlite. To fully understand the transportation of mantle cargo, particle interactions in the form of mechanical attrition, must be built into ascent models.

References

- Arndt NT, Boullier A-M, Clément J-P, et al (2006) What olivine, the neglected mineral, tells us about kimberlite petrogenesis. *eEarth Discuss* 1:37–50.
- Arndt NT, Guitreau M, Boullier A-M, et al (2010) Olivine, and the origin of kimberlite. *J Petrol* 51:573–602.
- Bemrose CR, Bridgwater J (1987) A review of attrition and attrition test methods. *Powder Technol* 49:97–126.
- Brett RC, Russell JK, Andrews GDM, Jones TJ (2015) The ascent of kimberlite: Insights from olivine. *Earth Planet Sci Lett* 424:119–131. doi: <http://dx.doi.org/10.1016/j.epsl.2015.05.024>
- Brooker RA, Sparks RSJ, Kavanagh JL, Field M (2011) The volatile content of hypabyssal kimberlite magmas: some constraints from experiments on natural rock compositions. *Bull Volcanol* 73:959–981.
- Jones TJ, Russell JK, Lim CJ, et al (2017) Pumice attrition in an air-jet. *Powder Technol* 308:298–305. doi: 10.1016/j.powtec.2016.11.051
- Jones TJ, Russell JK, Porritt LA, Brown RJ (2014) Morphology and surface features of olivine in kimberlite: implications for ascent processes. *Solid Earth* 5:313.
- Kamenetsky VS, Kamenetsky MB, Sobolev A V, et al (2008) Olivine in the Udachnaya-East kimberlite (Yakutia, Russia): types, compositions and origins. *J Petrol* 49:823–839.
- Moussallam Y, Morizet Y, Massuyeau M, et al (2015) CO₂ solubility in kimberlite melts. *Chem Geol* 418:198–205.
- Pilbeam LH, Nielsen TFD, Waight TE (2013) Digestion fractional crystallization (DFC): an important process in the genesis of kimberlites. Evidence from olivine in the Majuagaa kimberlite, southern West Greenland. *J Petrol* 54:1399–1425.
- Russell JK, Porritt LA, Lavallée Y, Dingwell DB (2012) Kimberlite ascent by assimilation-fuelled buoyancy. *Nature* 481:352–356.



Kimberlitic olivine attrition: Fingerprinting environments and timescales

Thomas J. Jones¹ & J. K. Russell²

¹*Department of Earth Sciences, Durham University, South Road, Durham, DH1 3LE, UK, t.j.jones@durham.ac.uk; tomjj7@gmail.com*

²*Department of Earth, Ocean & Atmospheric Sciences, University of British Columbia, Vancouver, British Columbia, V6T 1Z4, Canada, jkr2002@gmail.com*

Introduction

Attrition results in the size reduction and rounding of particles and occurs in a wide variety of geological environments. From the Engineering Sciences, we identify two modes of attrition (Bemrose and Bridgwater 1987; Xiao et al. 2014; Jones et al. 2017): (1) fragmentation and (2) abrasion. Fragmentation (1) is described as particle fracturing where the original particles, often referred to as the parent particles, break-down to form a group of similarly-sized daughter particles. A ‘critical’ collision which achieves fragmentation typically occurs through direct impact with other particles or with a hard surface at, or above, a threshold velocity. Abrasion (2) describes a less energetic process wherein the rough edges or asperities of the parent particles are rounded off to leave the parent particles with smoother surfaces and morphologies. An additional by-product of abrasion processes is the production of very fine particles. There are several factors that control the rate of attrition and they can be broadly divided into two groups: particle properties and environmental factors. Particle properties include, but are not limited to, size, shape, surface texture, particle size distribution, hardness and internal defects/flaws. Environmental factors affecting rates of attrition include: particle residence times, particle concentrations, temperature, pressure, and differential velocities (i.e. between colliding particles or between particles and confining wall). Attrition is most successful when velocities are high, particle concentrations are high, particle shapes are irregular, residence times are long and particle size distributions are poorly sorted.

Particle attrition affecting kimberlitic minerals potentially operates in several different environments between the lithospheric mantle and the Earth’s surface. Attrition of kimberlitic indicator minerals during sedimentological transport within glacial and fluvial deposits has been studied and used in exploration to assess distance to the source kimberlite pipe (McCandless 1990; Afanas’ev et al. 2008). More recent work has evaluated the potential for, and consequences of, attrition of mantle cargo attending the transport, fragmentation, and emplacement/eruption of kimberlite magma. Specifically, Jones et al. (2014) and Brett et al. (2015) suggested that the shapes and surfaces of mantle-derived xenocrystic minerals could be a strong indicator of turbulent ascent of kimberlite magmas through the lithospheric mantle and within subsurface feeder dykes. Within any geological environment, the nature of particle-particle interactions can be highly variable, however, at a first-order attrition operates with two contrasting styles: (1) high velocity, transient particle-particle or particle-wall interactions and (2) lower energy sustained abrasive contacts. Here, these two attrition styles are investigated with contrasting experiments performed in a fluidized bed and a tumbling mill respectively.

Methods

All experiments were performed on crushed dunite that was sieved to a restricted, narrow range of grain sizes which constituted the feed for each experiment. Specific operating conditions for the experiments performed in the fluidized attrition tube (Fig. 1a) and in the tumbling mill (Fig. 1b) are listed in Table 1. At the end of each experiment all the material was recovered and flushed with deionised water to collect all of the ultra-fine particles. Grain size distributions were measured by dry sieving of all particles measuring > 63 µm using a standard stack of Tyler sieves and then by laser particle size analysis on particles < 63 µm. We allowed a 63 – 125 µm overlapping grain size range.

| Description | Fluidized Attrition Tube | Tumbling Mill |
|------------------------|--------------------------|-----------------------|
| Mass of Feed | 70 g | 120 g |
| Feed grain size range | 125 – 500 μm | 1 – 2 mm |
| Experiment Duration | 0.5 – 32 hours | 1 – 30 days |
| Material bulk velocity | 1.13 ms^{-1} | 0.27 ms^{-1} |

Table 1: Experimental operating conditions.

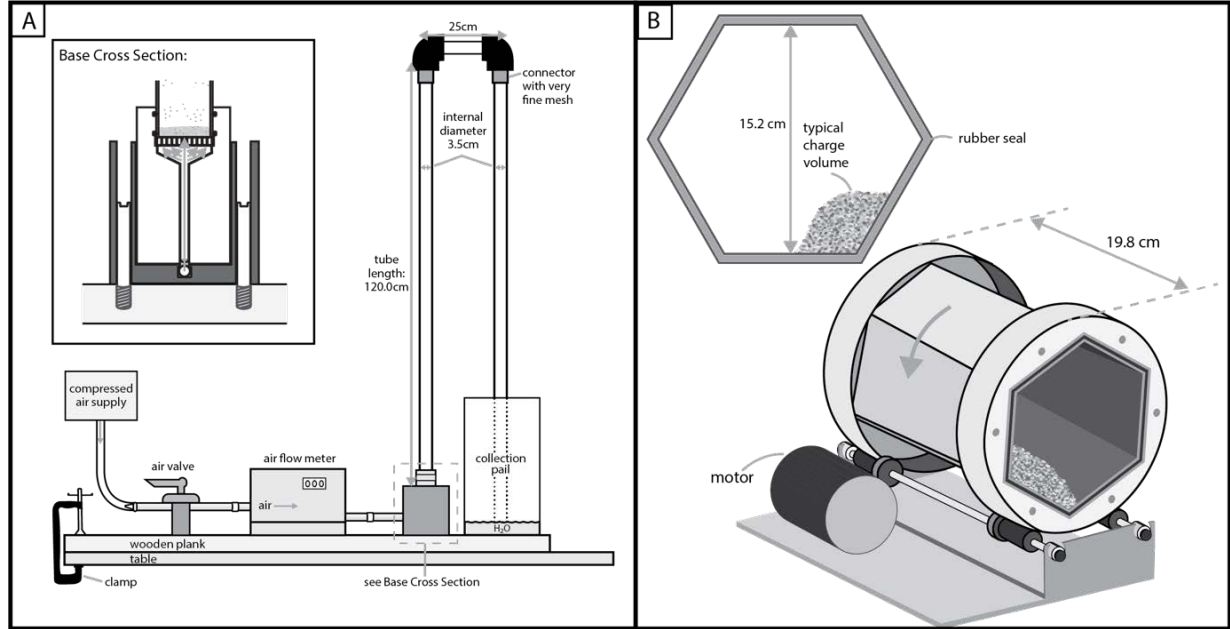


Figure 1: Diagram of (a) fluidized attrition tube and (b) tumbling mill used in this study.

Results and Analysis

In both the attrition tube and the tumbling mill the olivine feed was systematically reduced in grain size as a function of residence time. Furthermore, this reduction in feed or parent particles is non-linear in time, such that attrition is faster at short times and slower at longer times (Fig. 2). The reduction in the parent feed can be attributed to the production of smaller daughter particles formed by both fragmentation and abrasion. We find that the rate of fines production (defined as the mass of daughter particles, m_d normalised to the feed mass, m_0) is best described as:

$$m_d/m_0 = a(1 - e^{-bt}) \text{ [Eqn. 1]}$$

where a is the infinite time limit, b is the attrition rate constant and t , the residence time reported in hours (Jones et al. 2017). Modelled values for olivine attrition within a fluidized bed and tumbling mill are shown in Figures 2a and b respectively.

We note that both the infinite time limit and the attrition rate constant are higher for the fluidized bed relative to the tumbling mill. Firstly, this suggests that the attrition tube can produce more stable daughter products relative to the parent feed. It is likely that this is a direct consequence of the higher energy environment (\sim higher velocity) that the olivine particles experience within the attrition tube. Higher energy fragmentation environments lead to a finer stable grain size (Jones & Russell, *accepted pending revisions*). Secondly, the attrition rate is an order of magnitude faster in the fluidized bed. Daughter fragments start to reach a near stable size after \sim 5 hours of attrition rather than \sim 80 hours as observed in the lower energy tumbling mill. Faster early attrition is due to rapid fragmentation of residual particle defects/flaws and easy abrasion of highly irregular external morphologies, producing abundant ultra-fine chips. Furthermore, this can be visualised through scanning electron microscopy of individual particles. We observe the highly irregular particle

exteriors of the feed to become smoothed during attrition. Abrupt ridges and fracture planes are rounded and surfaces become coated in ultra-fine chips with increased residence time.

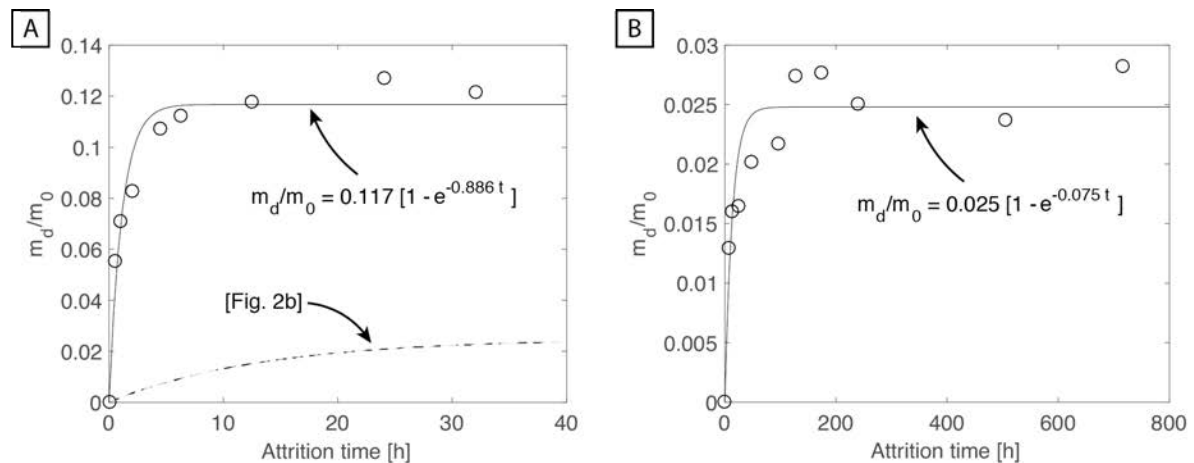


Figure 2: Fines production model (Equation 1) for (a) fluidized attrition tube and (b) tumbling mill used in this study. Note the change in axis scale between the different plots.

Implications and Future Work

Our results elucidate the effects of transport conditions and durations on specific olivine crystal size populations. We show that two very different energy environments, which are relevant to a wide range of natural systems, support particle attrition. The rates and extents of attrition for a similar feed are shown to be strongly controlled by the environment and residence time. This allows for a preliminary assessment of the attrition potential of a system depending on the environment that is considered. For example, olivine transported post-eruption in a river bed will experience little grain size modification compared to turbulent sub-surface transport. Once the attrition environment is known, our fines production model can help estimate the residence time/ transport distance a particle population has experienced. Future work will involve quantitative shape analysis on the experimental products and more experiments at different velocities (e.g. higher energies).

References

- Afanas' ev VP, Nikolenko EI, Tychkov NS, et al (2008) Mechanical abrasion of kimberlite indicator minerals: experimental investigations. *Russ Geol Geophys* 49:91–97.
- Bemrose CR, Bridgwater J (1987) A review of attrition and attrition test methods. *Powder Technol* 49:97–126.
- Brett RC, Russell JK, Andrews GDM, Jones TJ (2015) The ascent of kimberlite: Insights from olivine. *Earth Planet Sci Lett* 424:119–131. doi: <http://dx.doi.org/10.1016/j.epsl.2015.05.024>
- Jones TJ, Russell JK, Lim CJ, et al (2017) Pumice attrition in an air-jet. *Powder Technol* 308:298–305. doi: 10.1016/j.powtec.2016.11.051
- Jones TJ, Russell JK, Porritt LA, Brown RJ (2014) Morphology and surface features of olivine in kimberlite: implications for ascent processes. *Solid Earth* 5:313.
- Jones TJ, Russell JK (Accepted Pending Revisions) Ash production by attrition in volcanic conduits and plumes. *Scientific Reports*.
- McCandless TE (1990) Kimberlite xenocryst wear in high-energy fluvial systems: Experimental studies. *J Geochemical Explor* 37:323–331.
- Xiao G, Grace JR, Lim CJ (2014) Evolution of Limestone Particle Size Distribution in an Air-Jet Attrition Apparatus. *Ind Eng Chem Res* 53:15845–15851.



Potential for Offsetting Diamond Mine Carbon Emissions through Mineral Carbonation of Processed Kimberlite

Evelyn M. Mervine¹, Gregory M. Dipple², Ian M. Power², Siobhan A. Wilson³, Gordon Southam⁴, Colette Southam⁵, Juerg M. Matter⁶, Peter B. Kelemen⁷, Johann Stiefenhofer⁸, and Zandile Miya¹

¹ *The De Beers Group of Companies, Johannesburg, South Africa, Evelyn.Mervine@debeersgroup.com, Zandile.Miya@debeersgroup.com*

² *The University of British Columbia, Vancouver, Canada, gdipple@eoas.ubc.ca, ipower@eoas.ubc.ca*

³ *Monash University, Melbourne, Australia, sasha.wilson@monash.edu.au*

⁴ *University of Queensland, Brisbane, Australia, g.southam@uq.edu.au*

⁵ *Bond University, Brisbane, Australia, csoutham@bond.edu.au*

⁶ *University of Southampton, Southampton, United Kingdom, J.Matter@southampton.ac.uk*

⁷ *Columbia University, New York City, USA, peterk@ldeo.columbia.edu*

⁸ *Anglo American Operations Ltd., Johannesburg, South Africa, Johann.Stiefenhofer@debeersgroup.com*

Introduction

There is enormous untapped potential for offsetting diamond mine carbon emissions through mineral carbonation of processed kimberlite. Mineral carbonation, also referred to as carbon mineralization, is the storage of carbon dioxide in stable carbonate minerals (e.g. Power et al., 2013, 2014). The formation of secondary carbonate alteration minerals, many of which form at low temperatures and pressures and sequester substantial quantities of atmospheric carbon, is a well-recognized pathway for storing carbon in mafic and ultramafic rocks, such as basalts and peridotites (e.g. Matter and Kelemen, 2009; Power et al., 2009). Limited studies have been conducted on kimberlites, but it is expected that atmospheric carbon is also sequestered in these rocks through both natural (e.g. in situ alteration of kimberlite pipes) and artificially enhanced (e.g. accelerated carbonation rates in processed kimberlite) formation of secondary carbonates. Understanding the various origins (e.g. primary magmatic vs. high temperature hydrothermal vs. low temperature secondary) of carbonates in kimberlite pipes and in processed kimberlite is critical in order to understand the carbonation rates and enhanced carbonation potential of kimberlite. Furthermore, it is important to be able to trace the sources of incorporated carbon (e.g. atmospheric carbon vs. recycled magmatic or bedrock carbon).

Although on-going low temperature carbonation reactions have been observed in kimberlite pipes (for example, in the Attawapiskat region of Canada, e.g. Sader et al., 2007) and it is well-recognized that processed kimberlite is highly suitable for sequestration (for example, by the Carmex Project, Bodéan et al., 2014), only a handful of studies have previously investigated carbonation at specific diamond mines. Furthermore, these studies have focused on two mining operations (Diavik and Ekati) in the Canadian Arctic, with detailed work only having been carried out at Diavik (e.g. Rollo and Jamieson, 2006; Wilson et al., 2009, 2011). Carbonation of processed kimberlite at Diavik is rapid: two orders of magnitude faster than the natural rate (Wilson et al., 2011), even under unfavorable conditions (i.e. subaqueous storage in an arctic climate). Deliberate acceleration of carbonation of the processed kimberlite produced annually at Diavik has the potential to offset up to 10x the mine's carbon emissions (Wilson et al., 2011).

The goal of this study is to present additional information on the mineral carbonation potential of kimberlite mines. Detailed mineralogical characterization studies to assess carbonation potential have

been undertaken on processed kimberlite samples from the De Beers mine site Venetia in South Africa, as well as from the De Beers mine sites Victor, Gahcho Kué, and Snap Lake in Canada.

Analytical Results

Qualitative mineralogical composition data for fresh (recently-deposited, rather than historical) fine processed kimberlite samples from five diamond mines in South Africa and Canada are listed in Table 1. The mineral contents were estimated from the relative intensity of peaks using powder X-Ray diffraction data. These processed kimberlite samples have considerable diversity in mineral content, which reflects variable conditions of kimberlite magmatism and emplacement, as well as subsequent alteration processes. The samples also have variable mineral surface area, which is indicated in the table as Brunauer–Emmett–Teller (BET) surface area (Brunauer et al., 1938).

| Minerals | Venetia | Diavik | Victor | Gahcho Kué | Snap Lake |
|---|---------|--------|--------|------------|-----------|
| Tectosilicates | | | | | |
| K-feldspar | | | | m | m |
| Plagioclase | | m | | t | M |
| Quartz | m | t | t | t | m |
| Phyllosilicates | | | | | |
| Chlorite | | | t | m | M |
| Mica | M | m | t | M | M |
| Serpentine | M | M | M | M | M |
| Smectite | M | m | | M | t |
| Talc | | | | M | m |
| Inosilicates | | | | | |
| Amphibole | m | | | t | |
| Clinopyroxene | M | t | t | | |
| Orthopyroxene | | | t | | |
| Orthosilicates | | | | | |
| Garnet | | t | | | |
| Olivine | t | M | M | | |
| (Hydr)oxides | | | | | |
| Brucite | | | t | | |
| Spinel | t | | t | | |
| Carbonates | | | | | |
| Calcite | m | m | M | m | m |
| Dolomite | | | M | t | m |
| Magnesite | | | t | | |
| Siderite | | | t | | |
| BET surface area (m²/g) | 13.8 | 48.0 | 21.4 | 46.2 | 24.7 |

Table 1: Detailed mineralogical composition of the De Beers processed kimberlite samples, compared with previous results from Diavik (Wilson et al., 2009). Note that M = major, m = minor, and t = trace.

Discussion and Conclusions

Because kimberlites display considerably mineralogical diversity, detailed characterization of processed kimberlite samples is essential in order to assess the mineral carbonation potential of specific diamond mine sites, as well as the technologies that could potentially be employed to enhance carbonation. Despite their mineralogical diversity, all of the processed kimberlite samples presented in this study contain abundant minerals with carbonation potential. Minerals of particular interest for reactivity with carbon dioxide include serpentine, olivine, brucite, talc, smectite, and chlorite. The major minerals, such as serpentine, provide the bulk of the carbonation potential. However, the presence of minor and trace minerals is also important, particularly for minerals such as brucite and talc that are easily carbonated under low pressure and temperature conditions. The surface areas of the processed kimberlite also vary. The samples with the highest surface areas are likely to be easiest to carbonate. Overall, the new mineralogical results from De Beers mine sites concur with the previous research at

Diavik that enhanced mineral carbonation of processed kimberlite has the potential to offset up to 10x the carbon emissions of a diamond mine.

Previous research (e.g. Power et al., 2013, 2014) has demonstrated that carbonation rates in ultramafic mine wastes are highly variable and controlled by factors such as: (1.) the nature of ore, gangue, and alteration mineralogy; (2.) mineral processing and mine design; (3.) tailings handling and storage; (4.) local climate; and (5.) biology. Additional research, particularly on historical tailings, is required to assess what factors are limiting carbonation reactions at the De Beers mine sites assessed in this study. Once the factors limiting carbonation have been identified, then technologies to accelerate carbonation can be identified and tested, first at the laboratory-scale and then at pilot scales on the mine sites.

Tapping into the full carbonation potential of processed kimberlite is not likely to be economically or practically achievable at diamond mines in the near future. However, carbonating even a small percentage of processed kimberlite could lead to substantial carbon offsets or even carbon neutral mining operations and will likely be feasible, using existing technologies, in the near future. Laboratory-scale studies (e.g. Power et al., 2013, 2014) indicate that carbonation rates of ultramafic mine tailings can be increased by orders of magnitude by targeting rate-limited reactions, such as CO₂ supply and mineral dissolution. Technologies that could be employed to enhance carbonation include CO₂ injection and biotechnologies, such as bioreactors. In addition, making simple, low-cost physical changes to processed kimberlite storage, such as depositing thinner layers of tailings, could also enhance carbonation rates.

References

- Bodénan, F., Bourgeois, F., Petiot, C., Augé, T., Bonfils, B., Julcour-Lebigue, C., Guyot, F., Boukary, A., Tremosa, J., Lassin, A., Gaucher, E.C., and Chiquet, P. (2014) Ex situ mineral carbonation for CO₂ mitigation: Evaluation of mining waste resources, aqueous carbonation processability, and life cycle assessment (Carmex project). *Minerals Engineering* 59: 52-63.
- Brunauer, S., Emmett, P. H., and Teller, E. (1938) Adsorption of Gases in Multimolecular Layers. *Journal of the American Chemical Society* 60: 309–319.
- Matter, J. M. and Kelemen, P. B. (2009) Permanent storage of carbon dioxide in geological reservoirs by mineral carbonation. *Nature Geoscience* 2: 837-841.
- Power, I.M., Wilson, S.A., Thom, J.M., Dipple, G.M., Gabites, J.E. and Southam, G. (2009) The hydromagnesite playas of Atlin, British Columbia, Canada: A biogeochemical model for CO₂ sequestration. *Chemical Geology* 260: 286-300.
- Power, I.M., Harrison, A.L., Dipple, G.M., Wilson, S.A., Kelemen, P.B., Hitch, M. and Southam, G. (2013) Carbon mineralization: From natural analogues to engineered systems, in: DePaolo, D.J., Cole, D.R., Navrotsky, A., Bourg, I.C. (Eds.), *Geochemistry of Geologic CO₂ Sequestration*. The Mineralogical Society of America, Chantilly, Virginia, U.S.A., pp. 305-360.
- Power, I.M., McCutcheon, J., Harrison, A.L., Wilson, S.A., Dipple, G.M., Kelly, S., Southam, C. and Southam, G. (2014) Strategizing carbon-neutral mines: A case for pilot projects. *Minerals* 4, 399-436.
- Rollo, H. A. and Jamieson, H. E. (2006) Interaction of diamond mine waste and surface water in the Canadian Arctic. *Applied Geochemistry* 21: 1522-1538.
- Sader, J. A., Leybourne, M. I., McClenaghan, M. B., and Hamilton, S. M. (2007) Low-temperature serpentinization processes and kimberlite groundwater signatures in the Kirkland Lake and Lake Timiskiming kimberlite fields, Ontario, Canada: implications for diamond exploration. *Geochemistry: Exploration, Environment, Analysis* 7: 3-21.
- Wilson, S.A., Dipple, G.M., Power, I.M., Barker, S.L.L., Fallon, S.J. and Southam, G. (2011) Subarctic weathering of mineral wastes provides a sink for atmospheric CO₂. *Environmental Science & Technology* 45: 7727-7736.
- Wilson, S., Raudsepp, M., Dipple, G.M. (2009) Quantifying carbon fixation in trace minerals from processed kimberlite: A comparative study of quantitative methods using X-ray powder diffraction data with applications to the Diavik Diamond Mine, Northwest Territories, Canada. *Applied Geochemistry* 24: 2312-2331.

The diamond size frequency and size quality distributions in the Argyle AK1 lamproite.

Andrew T. Davy¹, Murray J. Rayner² and Richard W. Platell³

¹ Rio Tinto Plc, London, United Kingdom, (andy.davy@riotinto.com)

² Argyle Diamonds, Perth, Western Australia (murray.rayner@riotinto.com)

³ Independent Consultant, Perth, Western Australia (rplatell@bigpond.net.au)

Introduction

The Argyle AK1 diamond mine in the east Kimberley region of Western Australia commenced production as an open cast operation in December 1985. In January 2013, mining switched to an underground block cave in the central section of the ore body. During 31 years of operation, ore treatment rates have ranged from 3.5 million tonnes per annum (M tpa) to 11 M tpa and, more recently, to 6 M tpa producing, on average, 27 M carats of lower quality and finer-tending diamonds per annum. No other primary diamond deposit has ever produced so many diamonds over its life or on an annual basis.

Unique features of the Argyle lamproite are the high grade and the fine diamond size frequency distribution (SFD). Early in the mine's life, Rio Tinto recognised that the micro-diamond stone counts from five metre sections of NQ drill core (about 20 kgs of lamproite) could be transformed into equivalent macro-diamond grade estimates, thereby reducing significantly the drilling and sample processing costs more usually associated with diamond ore body evaluation (Deakin & Boxer, 1989).

The robustness of this grade estimation method (be it at Argyle or for other primary source rocks) is dependent upon the in-situ diamond SFD (from 0.150 mm to 20 mm) remaining consistent. At Argyle, the diamond SFDs in the upper regions of the ore body were found to be subtly different in each of the four main ore domains, meaning that the algorithms for transforming micro-diamond stone frequencies into macro-diamond grade estimates had to be adjusted for each domain.

In 2015, changes in the diamond size quality distribution (SQD) recovered from the deeper block cave prompted Rio Tinto to conduct a thorough review of the earlier geological and volcanological models. This petrographic review revealed a series of volcanoclastic lamproites in the central section of the southern diatreme (Rayner et al, this volume) with similar diamond SFDs but differing SQDs.

Variations in the In-Situ Diamond Size/Frequency Distribution (+0.21 mm to +1.70 mm)

The 1999-2000 deep drilling programme revealed that the AK1 deposit comprised a number of diatremes or feeders containing different lamproites (Figure 1).

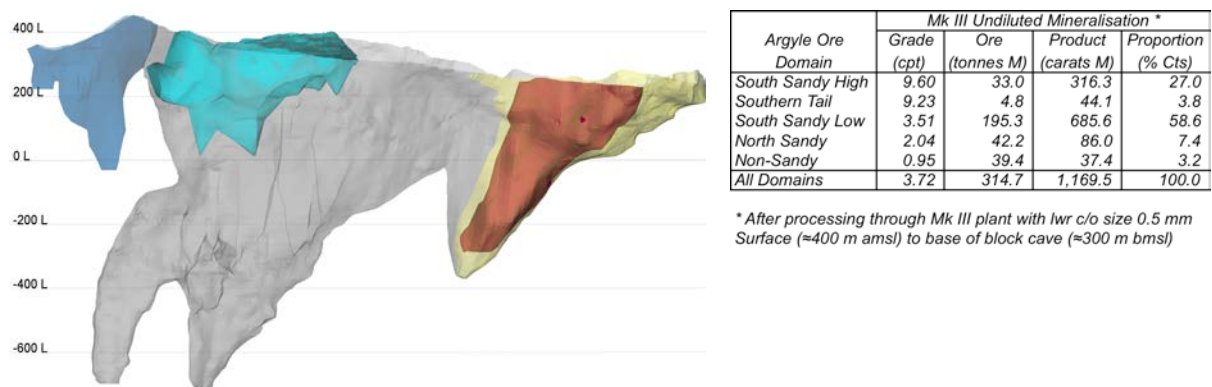


Figure 1. 3D model of the Argyle AK1 lamproite showing ore domains as follows: from L to R, Southern Tail (dark blue), South Sandy High (light blue), South Sandy Low (grey), North Sandy (yellow), Non-Sandy (red). Accompanying table lists mineralisation based on 2016 ore body model, mostly now mined out.

The diamond size frequency distributions for each diatreme were checked for consistency and found to differ. These same differences were recognised in the production SFD and correlated with changes in the relative proportions of ore that were processed from each domain.

Drill cores and hand specimens of lamproite were dissolved to give the in-situ diamond content for samples from different locations and diatremes in the AK1 deposit (Table 1). A sub-sampling exercise conducted in the South Sandy High ore domain in 1986 revealed variations in the SFD on a local basis (Davy, 1988). More than 200 x 20 kg samples were processed in this exercise.

| Sample | Sample Weight (tonnes) | Diamonds -2.36+0.21 mm * | | | Δ from SSL & SSH (%) | In-Situ Samp Grade >0.85 mm (carats/tonne) |
|----------------------------------|---------------------------|--------------------------|--------------------|-----------------------|--------------------------------|--|
| | | Count (stones) | Weight (carats) | MSS (carats/stone) | | |
| South Sandy High Sample MD3 1986 | 1.016 | 6,981 | 13.13 | 0.00188 | 83% | 10.39 |
| Southern Tail 2003 | 4.938 | 42,841 | 80.45 | 0.00188 | 83% | 13.71 |
| South Sandy High Sample MD1 1986 | 0.840 | 7,078 | 14.51 | 0.00205 | 90% | 14.88 |
| Non-Sandy 2003 | 4.803 | 3,410 | 7.00 | 0.00205 | 91% | 1.38 |
| UG2 2012 | 33.311 | 77,189 | 166.74 | 0.00216 | 96% | 4.43 |
| UG2 >10 cpt 2012 | 0.856 | 9,586 | 21.04 | 0.00219 | 96% | 20.46 |
| North Sandy 2003 | 12.697 | 22,760 | 49.85 | 0.00219 | 97% | 3.63 |
| South Sandy Low (SSL) 2007 | 35.509 | 90,271 | 203.41 | 0.00225 | 100% | 5.28 |
| South Sandy (SSH + SSL) 2007 | 86.247 | 265,447 | 601.96 | 0.00227 | 101% | 6.58 |
| South Sandy High (SSH) 2007 | 10.574 | 67,014 | 152.50 | 0.00228 | 101% | 14.41 |
| South Sandy High MD2 1986 | 0.800 | 4,968 | 11.60 | 0.00233 | 103% | 12.00 |

* samples contain >20 stones in -2.36+1.70 mm size class

Table 1: Micro-diamond sample data for the five ore domains obtained by dissolution of lamproite with a lower cut-off size of 106 microns. Stones counts are for the size range +0.21 mm to +1.70 mm. Samples designated MD were from the 1986 programme. MSS = mean stone size.

Comparisons between the mean stone sizes for the four domains and the South Sandy Low domain over three log cycles (in carat terms) of size revealed that the Southern Tail SFD was 17% finer, the Non-Sandy SFD was 9% finer, the North Sandy SFD was 3% finer and the South Sandy High SFD was 1% coarser. Comparisons between the mean stone sizes for the three sub-samples of the South Sandy High domain and the South Sandy High domain (all samples) revealed that the Sub-sample MD3 SFD was 17% finer, Sub-sample MD1 SFD was 10% finer, Sub-sample MD2 SFD was 3% coarser and Sub-sample UG2 SFD was 4% finer than the Upper SSH.

It was not unexpected that the domains (in some cases equivalent to diatremes, Rayner et al, this volume) contained different diamond size frequency distributions, but it was important from an ore body evaluation perspective. Rio Tinto's experience at Argyle provides a benchmark for the industry; it suggests that the relationship between the micro- and macro-diamond stone counts will be unique for each diatreme, domain or geological unit (i.e. for each emplacement event). In the case of Argyle, the southern diatreme comprised the South Sandy High and the South Sandy Low domains which were contemporaneous and contained similar diamond SFDs. As a result of this similarity, Rio Tinto was able to develop a method for estimating the macro-diamond grade of 86% (by carat content) of the Argyle AK1 deposit using micro-diamond stone counts from 20 kg samples of spatially representative NQ drill core, cheaper by an order for magnitude than conventional LDC grade sampling (Deakin & Boxer, 1989).

The results from the three MD samples suggest that, even within a single geological unit, the diamond SFD can vary and hence that macro-diamond sample grades estimated from micro-diamond stone counts will have +/- limits due to both sample size and local variability effects (Davy, 1988).

Roffey et al (2017) have compared the macro-diamond SFDs from sampling and production. The consistency of the macro-diamond SFD across the main South Sandy High and Low domains at Argyle was reflected in the recovered (i.e. production) SFD which has been remarkably consistent throughout the life of the mine.

Variations in the Diamond Size/Quality Distributions (>1 DTC sieve size)

The diamond size quality distribution (SQD) in the South Sandy Low ore domain has been consistent also for many years. Changes in the SQD were observed when ore sourced from the Southern Tail and the Non-Sandy domains was treated, the former contained proportionately more lower quality diamonds and the latter contained proportionately more better quality diamonds.

Little has been published on the quality distributions of diamonds from operating mines. Gurney et al (2004) presented shape and colour distributions on the smaller diamonds from 12 kimberlites on the Ekati block. Argyle production from 2015 comprised 13% Gem, 41% Near-Gem, and 46% Bottom-End material¹, but these proportions are not consistent from size to size (Figure 2); the gem quality stones increased from 9% in the 3 Grainers (0.66 to 0.89 Cts) to 24% in the 8 Cts size class. This observation has significant implications for the accuracy of modeled price estimates based on assumptions that the quality distribution in the finer size classes from smaller parcels of diamonds can be used to estimate the quality distributions and hence prices of diamonds in the coarser size classes.

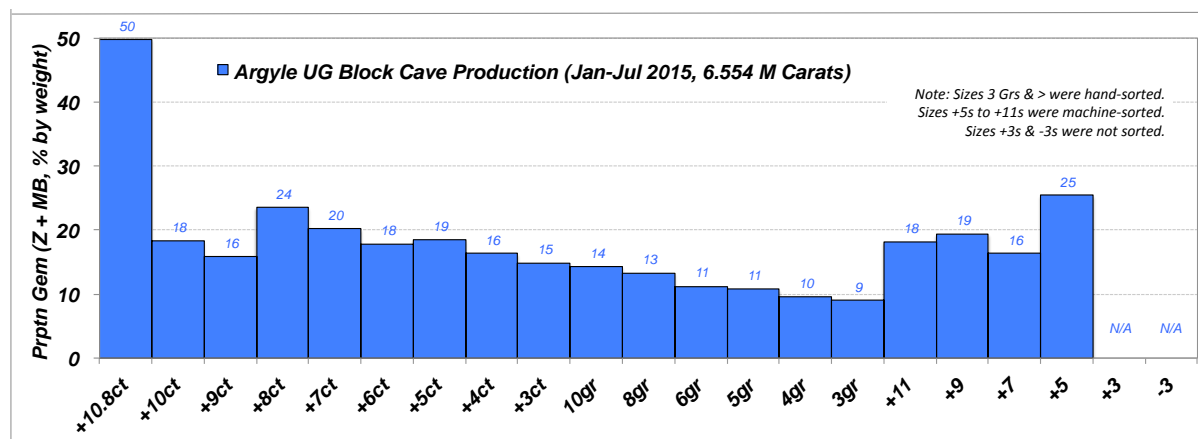


Figure 2: Proportion of gem quality diamonds (sawables, makeables, fancy makeables, white, yellow and brown) in ROM production from the underground block cave, South Sandy Low ore domain.

Discussion and Conclusions

It has taken almost 30 years for the internal structure and characteristics of the Argyle deposit to emerge. This situation is not uncommon on large, world-class ore bodies. There can be a tendency to assume that the status quo will continue between diatremes or with increasing depth from surface. Recognising changes in the diamond SFD and SQD is challenging because large parcels of diamonds are required in order to confirm and quantify the effects of these changes. Rio Tinto's experience at Argyle is not dissimilar to the situation it has encountered at Diavik and Murowa. For those companies new to diamond mining and for the resource geologists involved in the evaluation of primary diamond deposits (gathering Ore Body Knowledge), Rio Tinto's learnings on the variability of the SFD and SQD at Argyle should provide a reality check and a reason to reflect on the robustness of their global resource estimates.

References

- Davy AT, The ADM Micro-Diamond Programme 1986-87, 1988, Argyle Diamond Mines Confidential Internal Report, pp 197.
- Deakin AS, Boxer GL, 1989: Argyle AK1 diamond size distribution: the use of fine diamonds to predict the occurrence of commercial size diamonds. Proceedings of the Fourth International Kimberlite Conference, Perth, Geological Society of Australia Spec. Pub. No. 14, pp. 1117-1122.
- Gurney JJ, Hildebrand PR, Carlson JA, Fedortchouk Y, Dyck DR, 2004, The Morphological Characteristics of Diamonds from the Ekati Property, Northwest Territories, Canada. Elsevier, 8th International Kimberlite Conference, Selected Papers, Volume 2, pp 21-38.
- Rayner MJ, Moss SW, Jacques AL, Lorenz V, Boxer GL, Smith CB, and Webb K, 2017, New Insights into Volcanic Processes and Diamond Grades from Deep Mining at Argyle (ibid).
- Roffey S, Rayner MJ, Davy AT, Platell RW, Evaluation of the Argyle Lamproite, 2017, SEG Special Publication (in press).

¹ Explanatory notes on the diamond sizing process and Rio Tinto's diamond quality sorting matrix are provided in Appendices 1 & 2 respectively.



The magnitude of termites to the future of kimberlite exploration in Botswana

Leon R.M. Daniels, Tshireletso A. Dira and Onesimo Kufandikamwe

Pangolin Diamonds (Pty) Limited, Tatitown, Botswana

ldaniels@pangolindiamonds.com, tdira@pangolindiamonds.com, okufandikamwe@pangolindiamonds.com

Introduction

The majority of the diamond mines in Botswana (Orapa, Jwaneng, Letlhakane, Damsthaa, Lerala and BK11) were discovered as a direct consequence of soil sampling for indicator minerals such as garnet and microilmenite. Over the past sixty years the application of soil sampling for indicator minerals as a primary exploration tool has diminished while aeromagnetic surveys have increased in popularity. The rate of kimberlite discovery in Botswana over the past fifteen years has declined significantly. The obvious magnetic kimberlites have been discovered. The future of new kimberlite discoveries, mainly poorly magnetic to non-magnetic, is once again dependent on soil sampling for kimberlite indicator minerals. The only mechanism to transport indicators from source to surface through the Kalahari Formation overburden is through termite bioturbation.

Soil Sampling History in Botswana

Initial soil sampling programmes conducted by De Beers and Central African Selection Trust (CAST) in Botswana (then Bechuanaland) during the mid to late 1950's were confined to stream sediments in areas where drainage was developed. Concentrates were generated using gold pans. This method was quite ineffective and possibly resulted in Jwaneng being missed in a soil sampling programme conducted in 1962 (Lamont, 2011). A "semi-continuous scoop" sampling method was developed to sample interfluvial areas and eventually into the Kalahari sandveld. The gold pan was abandoned as a concentrating tool and a gravitating screen, commonly used by diamond diggers, was introduced to concentrate soil samples between 2mm and 0.5mm in size. This new method of soil sampling and concentrating of soil samples ultimately led to the discovery of the Orapa kimberlite field (Lamont, 2011). After the discovery of Orapa in 1967, diamond prospecting in Botswana extended progressively deeper into the Kalahari sandveld. The activity of termites to transport material through bioturbation from depth to surface was recognised as a key component in soil sampling for kimberlite indicators in areas where there was significant sand cover (Lamont, 2011). After the discovery of Jwaneng in 1973 it was observed that termite structures extended to a depth of at least 70 metres below surface (Lock, 1985). The indicator counts at surface of kimberlite discoveries after Jwaneng (e.g. Lerala and KX36) were low counts, scarcely above background (Rogers et al, 2013).

Termites

It is essential to have an in depth understanding of the transport mechanism of kimberlite indicators from the kimberlite to the present day surface of the Kalahari Formation which is via termite bioturbation. Termites require moisture for their saliva as well as for their fungi farms. The termites obtain their required moisture from the water table. In order to access the water table the termites have to excavate access paths from their nests. When termites encounter a kimberlite at or above the water table interface, fragments of kimberlite and indicator minerals resistant to weathering are occasionally transported to surface where they are included in exploration soil samples. While indicators may be included in the construction of termite nests, the majority of the indicators are discarded at vent holes, some distance from the nests.

The concentration of indicators at surface is dependent on a number of factors, some of which are directly dependent on the physical characteristics and capabilities as well as behavioural patterns of the particular termite species dominant in the exploration area. While termites have been recorded to

access kimberlites to depths of at least 70 metres and possibly deeper than 80 metres, several species found in Botswana are limited to shallower depth penetration. The size of the mandibles of specific species also has a significant effect on the size of the indicators found at surface. Mandibles of termite species in Botswana vary from 3mm to 0.5mm in size which in turn have definitive restrictions on the size of indicators to be transported to surface (Figure 1, (Uys, 2002)).

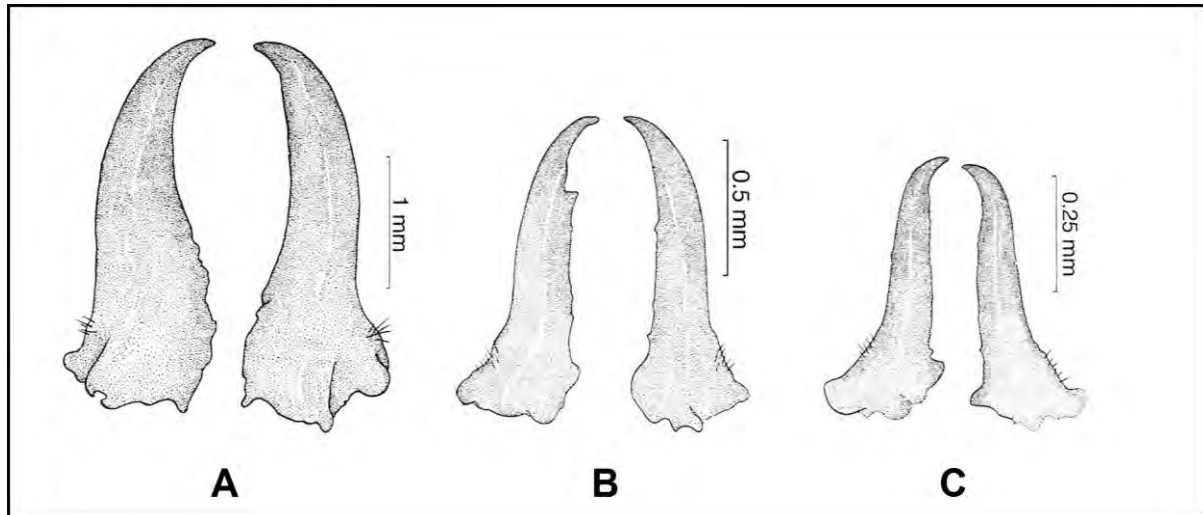


Figure 1: Soldier mandible sizes of (A) *Macrotermes natalensis*, (B) *Odontotermes latericius* and *Microtermes havilandi* (After Uys, 2002).

Several species may be active within an area and up to four species may colonise the same nest (Uys, 2002). A survey conducted in southeastern Botswana found six species of termites active within an area of 0.8 hectare (Dangerfield et al. (1992). Some species build their nest structures above the ground, e.g the iconic nests of *Macrotermes michaelseni* while others construct their nests underground, e.g. *Odontotermes latericius* (Dangerfield et al., 1992, Uys, 2002). Darlington (1982) recorded passage densities as high as 1.9m of passage and 21.4 storage pits per square metre in the main foraging zone of *Macrotermes michaelseni* termites, which is 10 – 35m from a single nest. The estimated total length of passages was just under 6000 metres and 72,000 storage pits within an area of 0.8 hectares. Turner et al (2006) reported as much as 190 kg of wet soil being added to a single termite nest in one rainy season. The excavated material from the access routes is transported from the water table to surface in a “bucket system”, particles being passed from termite to termite. Not all indicators will reach surface as particles are abandoned between the kimberlite and the surface. The transportation of indicators to surface has been an ongoing process throughout the deposition of the Kalahari Formation and continues today. Some species of termites are active all year round, others have seasonal activities associated with the breeding of alates. In general, termite activity is minimal during the dry, winter season.

The Future

In the absence of kimberlites with distinctive aeromagnetic signatures, the discovery of future diamond mines in Botswana will be closely associated with an in depth understanding of the relationship between indicator size and concentration in surface soils and the seasonal behaviour, depth penetration capabilities, bucket system transport efficiencies and mandible size of the termite species within the exploration area. The size distribution of indicators at surface is closely linked to the mandible size of the dominant species of termite in the area. For example, if the dominant species within the exploration area is one of the eight *Microtermes* species with a mandible size of 0.5mm, it is unlikely that a significant number of indicators will be found in excess of 0.5mm in diameter. Small indicators (~0.5mm) have often been interpreted as “distal from source” and indicative of significant transport from source. Standard screen sizes used in Botswana diamond soil sample programmes (0.425 – 2mm) may not capture sufficient indicators in a *Microtermes* dominant area to create an

anomalous concentration. Termites, due to the bucket system of grain transport, will be less efficient in transporting indicators to surface the greater the depth of the Kalahari Formation. It is possible that a significant “anomaly” consists of a single indicator. In the past single indicators have been interpreted as “background”. Seasonal activity may have a significant impact on soil sample results. When termites are very active they are likely to bring a greater amount of material to surface, e.g. when they need an increased amount of water during the alate breeding season. Conducting a soil sample programme during this period of high termite activity may result in sporadic anomalous counts of indicators in a soil sample. Sampling the same area a few months later may result in a completely negative sample. Indicators, due to their higher density (>3.4 g/cc) than the quartz grains (2.7 g/cc) making up the vast majority component of the Kalahari sand, are likely to sink into the sand profile soon after being discarded at surface by the termites. The distribution of indicators at surface may not be spatially closely associated with the nest, but may be tens of metres distant if it has been discarded at a vent hole. Volumetrically, far more kimberlite fragments than kimberlite indicator minerals are likely to be excavated by termites and discarded at surface. Trace element sampling analysing for LREE’s and HREE’s anomalous in kimberlites relative to the intruded sub-Kalahari bedrock may be considered as a follow-up programme when indicators are recovered from soil samples.

In conclusion, areas in Botswana where indicators recovered from soil samples and have been described as distal from source or “background” will require re-evaluation. Without detailed termite studies the rate of discovery will continue to decline. However, a kimberlite exploration programme integrating an in depth knowledge of the dominant termite species in the exploration area with adapted exploration techniques has significant potential to unlock a new wave of discoveries in the sandveld region of Botswana. The magnitude of termites to the future of kimberlite exploration in Botswana should not be underestimated.

References

- Dangerfield, JM, Veenendaal, EM, Riddoch, BJ, Black H (1992) Termites and land use in south-east Botswana: Variety and abundance of termite surface features. *Botswana Notes and Records* 24:165-179.
- Darlington, JPEC (1982) The underground passage and storage pits used in foraging by a nest of the termite *Macrotermes michaelseni* in Kajiado, Kenya. *J Zool* 198:237-247.
- Lamont, G (2011) The Quest for Diamonds in The Bechuanaland Protectorate and Botswana. In: De Wit, MCJ, Köstlin, EO, Liddle, RS (eds) *Prospecting in Africa* De Beers Consolidated Mines Limited pp 171-201.
- Lock, N (1985) Kimberlite exploration in the Kalahariregion of southern Botswana with emphasis on the Jwaneng kimberlite province. In: Raines GL et al (eds) *Prospecting in areas of desert terrain*. Institute of Mining and Metallurgy, London, pp183-190.
- Rogers, AJ, Hough, TG, Davidson, JM (2013) KX36-rediscovering the diamond exploration potential of the central Kalahari in Botswana. *J S Afr Inst Min Metall* 113:539-545.
- Turner, S, Marais, E, Vinte, M, Mudengi, A, Park, W (2006) Termites, water and soils. *Agricola*, 16: 40-45.
- Uys, V (2002). A guide to the Termite Genera of Southern Africa. Plant Protection Research Institute Handbook No. 15, Agricultural Research Council, Pretoria, pp 116

Models of reflection of kimberlite pipes of North-East of Botswana in eolian haloes of dispersion

V. Ustinov¹, B. Mosigi², I. Kukui¹, E. Nikolaeva¹, J. Campbell²,
Yu. Stegnitskiy¹, M. Antashchuk¹

¹ ALROSA, Saint-Petersburg, Russia, UstinovVN@alrosa.ru, KukuyIM@alrosa.ru

² Botswana Diamonds, London, UK, Bmosigi@gmail.com, James@botswanadiamonds.co.uk

The Late Cretaceous kimberlite pipes of the Orapa field (Figure 1) breaking through the Lower Jurassic basalts of Stormberg Group manifest themselves in haloes of dispersion of kimberlite indicator minerals (KIMs) enclosed in talus, proluvial, biogenic (in termite mounds), eolian and other sediments.

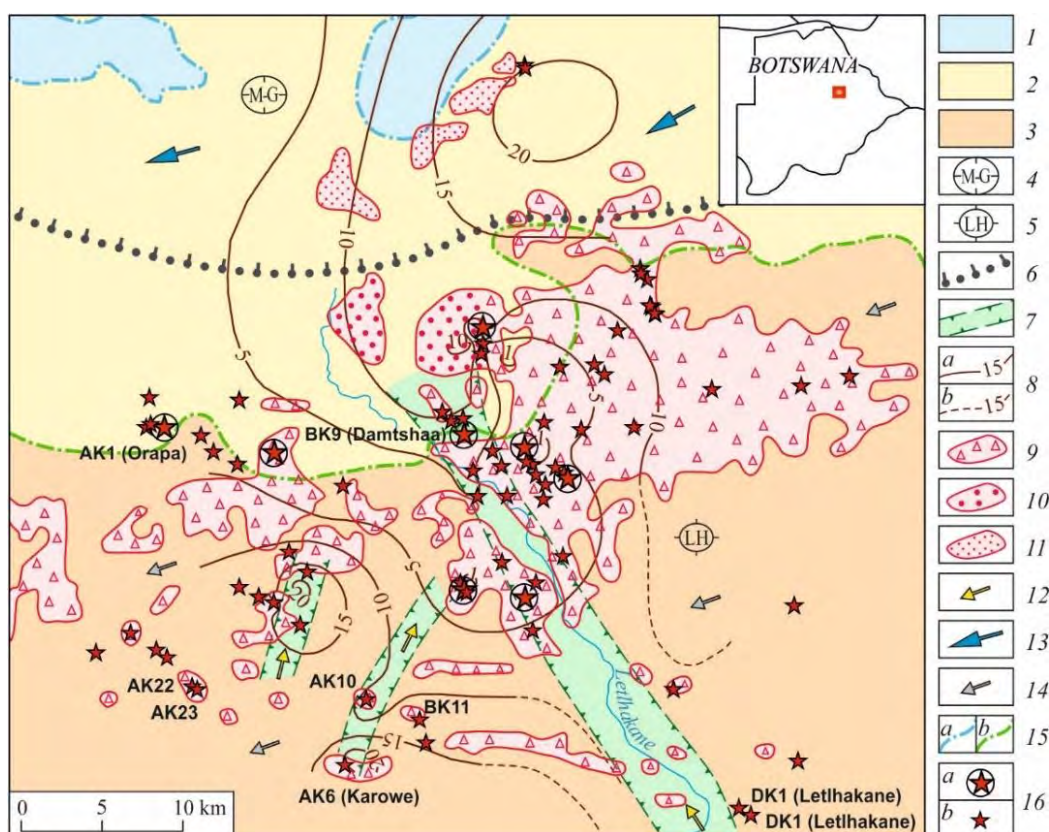


Figure 1: Eolian haloes of dispersion of KIMs in the area of Orapa kimberlite field.

1-7 – forms and elements of the Neogene-Quaternary relief: megaforms (1 – subhorizontal low accumulative plain, 2 – gently-sloping denudation-accumulative plain, 3 – slightly elevated denudation-accumulative plain); macroforms (4 – depression: Makgadikgadi, M-G; 5 – elevation: Lethakane, LH); 6 – boundaries of macroforms; mesoforms (7 – river valleys and paleovalleys); 8 – isopaches of the Neogene-Quaternary sediments of Kalahari Group (*a* – reliable, *b* – supposed); 9-11 – eolian haloes of dispersion of KIMs formed due to wind reworking of: 9 – talus and proluvial sediments, 10 – deltaic, 11 – continental and basinal of different genesis; 12-14 – directions of transportation of kimberlite minerals: 12 – water streams, 13 – wind, 14 – waves; 15 – standing levels of an inland basin (*a* – minimal, *b* – maximal); 16 – the Early Cretaceous kimberlite pipes (*a* – diatrema shaped, *b* – pear shaped and pipes-embryos).

The most widely developed in the area are eolian sands of the Kalahari Group, overlying pipes and forming the surface of relief. In the Orapa field they contain pyropes and picroilmenites almost on the entire territory. These are of different degrees of abrasion (I - unabraded, II - slightly, III -

moderately, IV – extensively, V - very extensively abraded). The combination of kimberlite minerals that come from different sources, situated on short, moderate or long distances often occurs in eolian haloes of dispersion.

KIMs of high (IV-V) degrees of abrasion which are transitory create a general mineralogical blanket (up to 10 gr./20 l) within the Orapa field and adjacent territories. They were accumulated in geomorphological traps (depressions, valleys, ancient shorelines etc.), where they form a higher contents of minerals (20-30 gr./20 l or more). On the examples of known kimberlite pipes (AK10, AK22, AK23 and others), which are overlain by sands of the Kalahari group up to 20 meters thickness, the eolian haloes of dispersion of short travel are characterized by the presence of KIMs mainly of I-II degrees of abrasion, and are situated close to kimberlite bodies. A change in the morphological features and degrees of abrasion of pyropes and microilmenites has been traced with the distance from the primary sources (Figure 2).

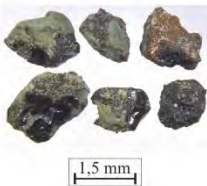


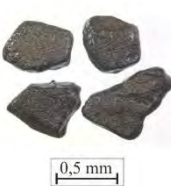

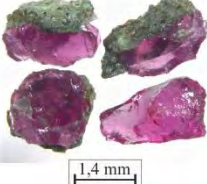
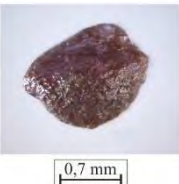
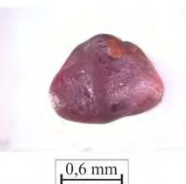


| Above the pipe | 100-200 m | 300-400 m | 500-600 m | 700-800 m |
|---|---|---|--|---|
| I | I-II | II | II-III | III |
|  1,5 mm |  0,6 mm |  0,5 mm |  0,5 mm |  0,4 mm |
|  1,4 mm |  0,7 mm |  0,6 mm |  0,5 mm |  0,5 mm |

Figure 2: Change in the morphological features and degrees of abrasion (I-III) of microilmenite and pyrope grains at different distances from AK10 pipe.

The eolian haloes of short travel covering gentle slopes of plains often have sizes of 500 x 1000 m and are of oval or conical shape. Haloes are characterized by a reduction of the contents of unabraded and slightly abraded grains (+2 mm, -2+1 mm and -1+0,35 mm) from hundreds and thousands gr./20 l above the pipe to 5 gr./20 l of -1+0,35 mm size at a distance of up to 1 km. A sharp reduction of contents (up to 10 gr./20 l) at a distance of 100-200 m from the source is a typical feature (Figure 3). At a distance of 500-600 m slightly abraded microilmenites were found only in fine size (-0,35 mm). Pyropes of I and II degrees in fraction +1 mm are recorded in the surface sediments above the body, at a distance of 100 m they are established only in -0,35 mm size.

Some of the eolian haloes are enclosed in the low-contrast negative forms of relief which occur above the kimberlite pipes. KIMs in the surface sediments were abraded and broken up under the influence of wind and temporary water flows almost above the sources. Grains of III degree of abrasion can be found along with kimberlite minerals of I-II degrees.

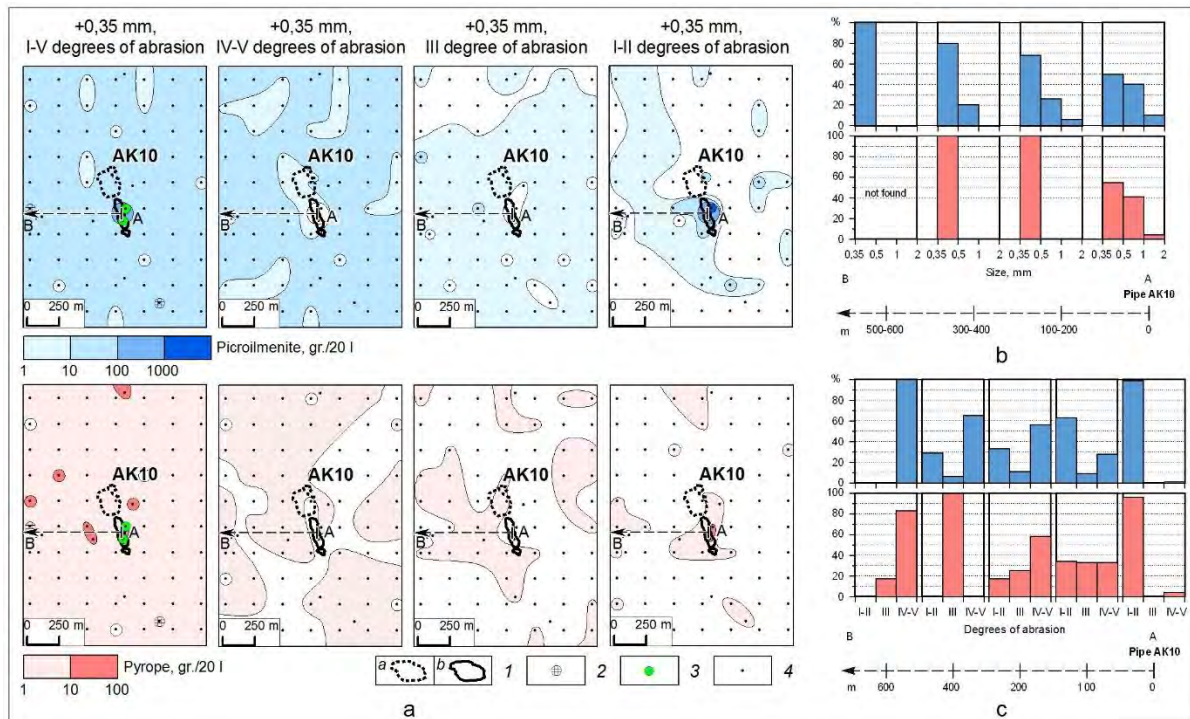


Figure 3: Haloes of dispersion of pyropes (red) and picroilmenites (blue) in area of AK10 pipe (a), distribution of kimberlite minerals according to size (b) and to degree of mechanical abrasion (c) on profile AB in area of AK10 kimberlite pipe.

1 – contour of kimberlite pipe in enclosing rocks (basalts): *a* – under basalts, *b* – on the surface of basalts; 2 – occurrences of chrome-spinels; 3 – occurrences of chrome-diopsides, 4 – heavy concentrate samples.

As a result of studies, models of reflection of kimberlite bodies in eolian haloes of dispersion of KIMs were created on the basis of analysis of contents, fractional composition and typomorphic features of minerals. It has been established that it is necessary to take into account pyropes and picroilmenites only of I-II degrees of abrasion in fraction +0,35 mm for the contrast delineation of haloes of short travel. It is shown that during prospecting works it is advisable to compile the mineral maps of KIMs distribution (separately for pyropes and picroilmenites) in the surface sediments by the degree of abrasion and grain size. It is important to note that even single grains of unabraded KIMs or those with a slight degree of abrasion found in eolian sediments have important prospecting value, and may indicate the proximity of the primary source.



Applied Geological Techniques for the Evaluation of Kimberlitic Tailings Mineral Resources: the case of Orapa and Letlhakane mines, Botswana

Strength Mkonto¹ and Martin A Roberts².

¹Debswana, Orapa Mine, smkonto@debswana.bw

²Anglo American plc, martin.roberts@angloamerican.com

Introduction

As primary kimberlite and secondary (alluvial and eluvial) diamond deposits become depleted, and new discoveries become increasingly elusive, diamond mine houses have turned to tailings mineral resources (TMR), as a way of prolonging the life-of mines. TMR diamond resources have the advantages of easy accessibility, low cost mining and crushing, and unique finer diamond size frequency distribution (SFD). Tremendous growth in the global diamond price and demand in the last few decades, have heightened the focus on TMR deposits. In addition, the technological advancement in diamond processing technology, have also increased the interest in exploiting this type of diamond deposits. To facilitate the conversion of the tailings deposits into resources for exploitation, there has been increasing need for new geological knowledge relating to TMR geology and evaluation techniques.

Debswana have developed innovative methods for optimizing the sampling and evaluation of TMRs. These have aided the successful execution of TMR evaluation campaigns at Orapa and Letlhakane mines. This presentation demonstrates that applied geo-techniques deriving knowledge from kimberlite deposit evaluation and sediment analysis, can be applied to effective sample optimization and sampling evaluation of TMRs.

Origins of TMRs

The TMR deposits are formed as coarse residue from the Dense Medium Separation (DMS) during treatment of kimberlitic ore. The original processing plants were inefficient either during comminution, screening, DMS concentration, and recovery, resulting in sub-optimal diamond recovery, and therefore loss of diamonds to the tailings. The TMR deposits were modified by mining and treatment processes of blasting, blending, stock-piling, crushing, screening, DMS concentration, tailings conveyance and spreading, and prolonged exposure to weathering elements, once they are deposited as TMR dumps. The TMRs are therefore complex deposits characterized by unique geology (mineralogical composition and diamond distribution), that often are not comparable to the original kimberlite source. The coarseness of the TMRs are dependant on the original DMS plant screen cut-offs sizes applied in separating the DMS feed from the slimes and slurry, screening efficiency, and kimberlite resistance to weathering.

TMR Geo-chronological Model

In order to optimize the TMR sampling and evaluation plan, knowledge of the TMR formation and deposition mechanisms is required. The geo-chronological model outlines how the TMR deposit was grown over time, including an indication of the kimberlite ore source and the treatment window when the particular TMR zone was grown. Modern mine planning systematically plan for the TMR dumps to ensure preservation of the TMRs for future potential exploitation. This entails conducting ground preparation prior to dumping, conveyance layouts, determining dump heights, advancement rates and directions. This ensures the TMR is preserved from waste contamination. The TMR geo-chronological model allows for correlation of the TMR geology to the original mined kimberlite ore source and grade. In addition, the TMR geo-chronological zones could be correlated to the treatment window when the ore was processed. The residual diamond grade could therefore, be inferred on the basis of the run-of-

mine ore grade treated through the plants and the processing plant recovery efficiency at the time when the ore was treated.

Sample Optimization

An accurate TMR growth model (geo-chronological model) is a key input to the sample optimization and forms the basis of determining the optimum sampling grid spacing, individual sample sizes, sample support, and sample lift intervals. In addition, the TMR features such as the angle of repose and internal layering are influenced by particle mechanics and dynamics. As the individual particles roll, creep and slump forming the angle of repose, there is particle segregation and sorting, that affect the diamond grade and size frequency distribution within the TMR.

A systematic approach was adopted during the sample optimization study. A geo-chronological model was constructed taking into consideration the angle of repose of the deposit. The model was used to establish the critical distance spacing of vertical drill-holes that is required in order to seamlessly and uniquely sample a different time zone of the deposit. The critical distance spacing of vertical drill-holes was related to the height of the deposit and the angle of repose, and was calculated using trigonometry.

The sample optimization determined the appropriate sampling techniques and tools, the expected diamond recoveries per sample, the predicted diamond size frequency distribution, the optimal individual sample size, the optimal sample intervals, the sample grid dimensions, sample quality standards, and sample plant treatment efficiency parameter targets for diamond liberation, screening, concentration, and recovery, and diamond bottom cut-off sizes to be applied in evaluation campaigns.

Granulometry and historical production efficiency factors were used to derive a desktop TMR residual grade. The average TMR base elevation was calculated and set as a constant datum for aligning the samples. The angle of repose of the TMR deposit was also calculated based on the dump profile. The analysis of the TMR elevation along the growth timeline was conducted in order to determine the critical sample drill-hole spacing required for time-line overlap of adjacent drill-holes, and the number of sample lift intervals required. The sample configuration was then determined to ensure adequate sample support. The outcome of the above approach was a sample configuration aligned to the direction of the TMR growth. This made it possible to estimate the anticipated total sample tonnes and the total sample carats, based on drill-hole configuration, sample sizes and global TMR estimated grade and density. The number of drill-holes and samples that would deliver the confidence criteria for an indicated resource category (both grade and revenue) were determined through simulation. In addition,

Geological Analysis and Interpretations

A number of applied geo-techniques were utilized in analysing and interpreting the TMR geological units for internal geology modeling. The primary data was obtained from drilling using a BG36C Auger drill rig with a 1.5m diameter bucket. Auger drilling was undertaken using 15m sampling lift height, on optimized 60 x 60m 5-spot grid for Lethlakane and 100 x 100 m 5 spot grid for Orapa mine. Each sample size (lift) weighed between 48 to 60 tonnes, depending on the moisture content and level of weathering. The primary purpose of the sampling was for recovery of diamond grade SFD for resource estimation and for geological analysis. Geological analysis of the recovered samples was conducted using both qualitative and quantitative methods. Qualitative methods involved physical observation geological sample logging. Residual kimberlite features in the TMR were analysed for mineralogy, grain size, colour, intensity of weathering, and composition of xenoliths (mantle and crustal rocks). Quantitative analytical methods included particle size distribution (PSD) and constituent analyses. The PSD of each sample were derived from sieving the samples through a successive suite of sieves, which ranged from +32mm to -1mm aperture. A PSD ratio analysis based on Cum sum +8mm / Cum sum-8mm fractions, was used to differentiate between TMR coarse unit (HZ2) and TMR finer unit (HZ1). Recovered sub-samples above +4mm and above, were each analysed for constituent composition. This involved identifying the different constituent rock types by weight of each sample. The limitation on the quantitative data set was the bias introduced by preferential weathering of weaker minerals and their

reconstitution into the finer sieves sizes. On the other hand, the harder minerals were preferential enriched in the corser fractions. The mineral constituent data was useful in the interpretation of the diamond grade data, where dilution was correlated with grade data. The PSD was used in the interpretation of SFD grade data, as coarser diamond SFD was expected in coarse samples.

Metallurgical settling tests analysis data from TMR samples mapped the olivine alteration trends within the TMR. No serpentine was found in older deeply weathered TMR (HZ1), but serpentine was abundant in the newer less weathered competent TMR (HZ2), with values ranging between 1.1 to 11.2 % in the -5 micron fraction. The smectite (montmorillonite) distribution results were inconclusive, as no definite trends (correlation) existed between smectite content and the level of weathering exhibited in the older HZ1 and newer HZ2 units. The density results showed relatively higher density values obtained from less weathered and more competent newer HZ2, compared to lower values obtained from the older highly weathered HZ1. The diamond liberation (diamond lock-up) analysis based on comparisons of diamond recoveries from samples treated without recrushing and audit samples treated with additional recrushing, showed higher diamond lock-up in competent newer HZ2 and lower diamond lock-up in highly weathered and less competent HZ1. The following diamond lock-up profiles were established from the 3 Orapa TMR units: HZ1 (<10%), HZ1/HZ2 (10 to 20%), and HZ2 (>20 to 32%). The diamond lock-up profiles were used as further validation of the interpreted TMR geo-zones. The strong correlation between the different data sets (quantitative (PSD), metallurgical data (settling tests), density, qualitative data (observation logs), and liberation data (diamond lock-up profiles) provided confidence in differentiating TMR geological units for internal 3D geological modeling.

3-Dimensional Geological Models

Based on the interpreted TMR geological units, 3-D geology models were developed. The Letlhakane mine TMR geology model example is presented below:

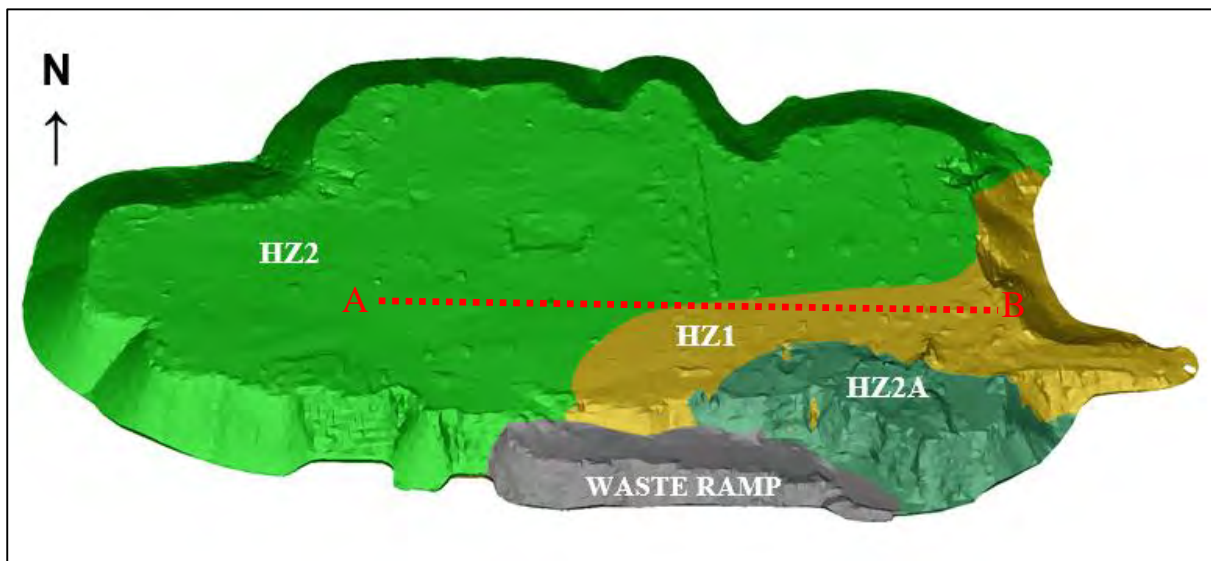


Figure 1: Final 3-Dimensional Geological model of the Letlhakane mine TMR

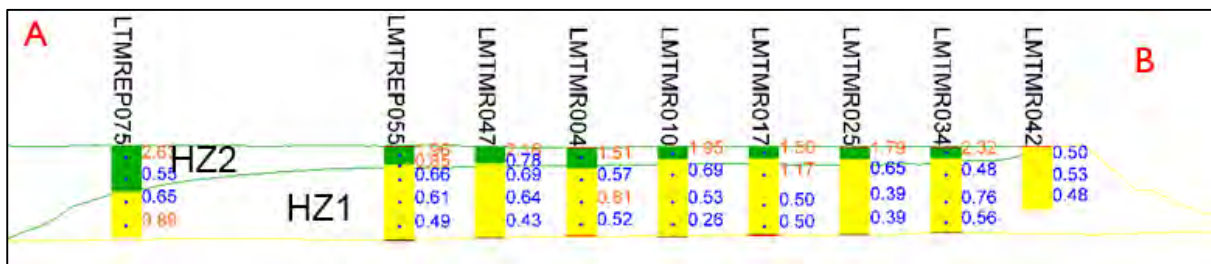


Figure 3: Section A- B showing strong correlation between PSD Ratio data and the Letlhakane mine TMR geological model



Varied emplacement within adjacent kimberlite vents, Jwaneng Mine, Botswana

Martin A. Roberts¹, K. (Major) Mmualefe²

¹ Anglo American Corporation, London, UK, martinandrew.roberts@angloamerican.com

² Debswana, Gaborone, Botswana, k.mmualefe@debswana.bw

Introduction

The Jwaneng kimberlite occurrence comprise a series of adjacent kimberlite pipes (235 ±4 Ma, Kinney et al. 1989) within the Jwaneng kimberlite cluster in Southern Botswana. Recent drilling (totaling 57km of kimberlite intersection) within the Jwaneng Resource Extension Projects (2004-2013) has aided the review of the geological and emplacement models to a depth of 1000m. Three adjacent pipes: South, Centre and North pipes dominate the Jwaneng occurrence which represented a combined 54 ha area at surface at the time of discovery in 1972. Additional minor kimberlite bodies have been discovered during the stripping of overlying Kalahari sediments through progressive expansion of the Jwaneng open pit. Field relationships observed during early mining, demonstrated that South Pipe was partially truncated by Centre Pipe, with North Pipe showing no intersection with adjacent pipes. The age interpretation is that South Pipe preceded Centre Pipe which preceded North Pipe. The geology of Jwaneng has been previously described by Webb et al (2003) and Brown et al (2008) based on field evidence within the pit and earlier drilling programs.

Characteristics across the pipes

All the pipes erupted through the same pre-existing country rock geology which at surface was the Beaufort Group (Karoo) terrestrial sediments consisting of fluvial mudstones, siltstones and sandstones that were potentially underlain by minor Waterberg arkoses and poorly developed conglomerates no longer preserved. Below this is the thick sequence of Transvaal sediments with quartzitic shales overlying dolomites. Although the Karoo and Waterberg are no longer preserved in-situ today, the Karoo mudstones are well preserved as large blocks and smaller fragments within the kimberlite pipes. The shape of the mudstone fragments are often fluidal and this may suggest that the mudstones were wet at the time of the kimberlite emplacement. All three pipes are associated with steep (~80 degrees) and relatively smooth and sharp kimberlite/wall-rock contacts. Before the onset of mining, the upper portions of the pipes were dominated by reworked volcanoclastic sediments with shallow dipping bedding structures. This is underlain by the main pipe infill which is typically dominated by broadly massive volcanoclastic kimberlite (MVK) which is largely well mixed and with relatively few clasts >10cm, with bedded pyroclastic and volcanoclastic units only preserved in the North Pipe. Common internal features across the three pipes include a sequence of rim units associated with local wall rock breccia and volcanoclastic units showing steeply inclined bedding and associated shearing. Large Karoo mudstone blocks are common within these units and are typically rotated and have moved downwards along the pipe margin (in places >900m below their in-situ stratigraphic level). The internal core units which volumetrically dominate the pipes, are associated with relatively low levels of country rock dilution (typically <10% measured in fragments above 5mm). The resultant geometry of the pipes and infill characteristics (including the presence of PK and RVK and the absence of tuffisitic kimberlite) fall within the Class 3 kimberlites described by Skinner and Marsh (2004) and have strong similarities to the Lac de Gras style kimberlite pipes in Canada (Scott Smith 2008).

Specific features of South Pipe

The South Pipe is dominated by broadly massive to weakly bedded volcanoclastic kimberlite (VK) units. Although bedding is locally observed, the bedding is typically not traceable between drill holes or extensive mining faces. The bedding appears disrupted in many areas and the bedded zones are often bounded by joints showing slickenside movement (post emplacement). The core domain is dominated by the VK unit at higher levels which transitions into the newly described 'autholith-rich' VK unit

(AVK). The rim domain is dominated at higher levels by the quartz-rich volcanoclastic kimberlite (QVK) which is identified by elevated levels of free quartz grains. It occurs on the margins of the pipe, is steeply dipping, often sheared and includes fragments of crystal tuffs and occasionally coal clasts. The source of the free quartz is believed to be from Karoo sandstones and Waterberg arkoses present at surface during the eruption of the South Pipe kimberlite.

Specific features of Centre Pipe

The unique feature when compared to the other pipes is the presence of a large wedge of quartzitic shale and dolomite breccia (>80% average dilution) on the south western portion of the pipe. At depth (~1000m), these breccias include kimberlite breccia which contains >50% country rock fragments. The contact between the breccias and the rest of the pipe infill is sharp and dilution drops within a few metres to levels typically <15%. The internal nature of the breccias including the jigsaw locking of many of the fragments, together with the very steep and sharp nature of the breccia/VK contact, is consistent with a collapse mechanism during the explosive venting of magma at depth (as opposed to breccias formed by collapsing of wall rock into a deep open crater). The process that formed these breccias may be seen as analogous to a block caving mechanism whereby, after the expansion event associated with the magmatic explosions and the removal of magma from depth, the country rock mass is no longer supported and collapses downwards. The collapse front then propagates upwards from the depth level of the explosive excavations. Within this package of breccias, kimberlite infilling is locally observed (post breccia formation). The kimberlite contains abundant fragments of the local host country rock breccia and has coherent magmatic textures in core specimens. Petrography (Skinner, pers. comm. 2012) has confirmed that this kimberlite breccia infill is largely an intrusive event and not fragmental. Locally, however, fragmental textures (including the presence of highly rounded locally derived clasts) are observed in contact with the country rock and further away from the contact, magmatic textures are observed. These macro observations are similarly confirmed by the petrographic descriptions by Skinner, pers. comm. (2012). The interpretation of these features is that initial intrusion of late stage kimberlite melt interacted with limited water ingress within the breccias. This produced steaming discharge, fragmenting the kimberlite melt and aggressively rounding the trapped clasts during the gaseous discharge. Once the limited supply of water was removed through the gas discharge, the remaining kimberlite intruded and inflated the breccia unit. Previous spinel chemistry studies (Stiefenhofer pers. comm. 2007) and a recent study from Phase 2 samples (Mmualefe, pers. comm, 2014) have demonstrated that the kimberlite within the dolomite breccias (part of the KBW_DM facies), appear to be subtly distinct from the VK (Volcanoclastic Kimberlite). Local late-stage macrocrystic dykes (typically <1m in width) are observed in the south western quadrant of the Centre Pipe in particular.

Specific features of North Pipe

The North Pipe consists of 3 broad zones: the upper core, the lower core and the rim zones. The upper core zone includes the mined out oxidized kimberlite (OK) and reworked volcanoclastic kimberlite (RVK(N)) units. Both of these units are classified as volcanoclastic kimberlites with the OK displaying high levels of oxidation and associated weathering. The RVK(N) unit was the dominant unit in the upper core domain of North Pipe and the spinel chemistry indicates that this unit is thought to be petrologically distinct from the PK and VK units in the lower core domain (Stiefenhofer, pers. comm. 2007). As it completely overlies the lower core domain it is believed to be the final volcanic expression of the North Pipe. The rim zone is dominated by volcanoclastic kimberlite (VK) that has been reworked with minor sandstone breccia units on the margins. Although this VK unit has many similarities to the VK units in Centre and South Pipes, it often displays a finer grain size, higher ash content and locally displays well developed/preserved bedding and laminations. The bedding is typically steeply dipping (>45 degrees) and locally, adjacent to the pipe margins, steepens to >60 degrees. A particularly fine-grained ash-dominated VK was identified in several drill holes and represents a unit that is dominated by ashy VK interbedded with 'normal' VK. The lower North core domain is dominated by pyroclastic kimberlite (PK) which is unique within the context of the Jwaneng kimberlite pipes. The pyroclastic kimberlite is identified by its hard, dark competent physical appearance together with the relatively high

levels of tightly packed juvenile fragments, abundant olivine macrocrysts and phenocrysts and relatively low levels of lithic dilution and ash. The PK is moderately to well bedded and often clast supported in comparison to the poorly sorted and matrix supported VK unit. Three principal varieties of PK were identified by Webb et al. (2003) and were modelled into the two units: PKa and PKbc units. The primary distinction is that the PKa unit shows lower levels of lithic dilution, is very dark, has higher olivine and mantle xenocryst abundances and the presence of highly baked mudstone/shale clasts with associated metasomatism resulting in needle like gypsum/calcite growth (indicating higher emplacement temperatures). The PKbc in contrast is lighter in colour, has higher levels of lithic fragments and is typically less well sorted (with an associated increase in clay content). The PKbc unit shows strong bedding identified by zones of higher lithic content (sometimes coarse, clast supported beds) that typically grade upwards into cleaner PK (which are occasionally overlain by thin ashy beds). The base of these PKbc units which are relatively lithic rich and often have sub-rounded to well-rounded lithic clasts that become rare away from the base of these units. Recent drilling post 2007 has indicated that the PKa and PKbc are often interbedded and suggest a coeval and cyclical relationship that extends to depth. They have now been incorporated into a single geological unit dominating the core of North Pipe.

Proposed contrasting emplacement models for South/Centre and North pipes

The emplacement model proposed for South and Centre pipe includes major vent clearing phases removing more than 70% of country rock volume possibly initiated by phreatomagmatic activity (as suggested by rare accretionary lapilli, and presence of water bearing Karoo sediments), followed by downward propagation of the pipe. The massive VK units rapidly formed during the collapse of ejected material from the explosion columns and associated tuff rings were significantly reworked within the vent during continued eruptive events. Steeply dipping and internally sheared rim units (which incorporate the highest abundance of preserved pre-eruption surface sediments) were formed by incremental downward propagation relative to the core units during repeated discharge events at depth. The volumetrically significant breccia units in Centre Pipe formed by the caving of the pipe wall rock during eruptions at depth and were subsequently inflated by the injection of later kimberlite magma into the breccias with small scale, localized explosive (groundwater assisted) kimberlite fragmentation. The North pipe with its characteristic pyroclastic unit dominating the core of the pipe, is thought to have formed under reduced explosive energy conditions (after the initial vent forming and clearing phase) as seen by lower levels of explosive fragmentation and the sequence of largely fining-upwards primary pyroclastic beds that are locally interbedded with minor ashy beds and which represent a phase of crater infilling produced by multiple discrete eruptive blasts. The lower energy eruptive environment has resulted in enhanced preservation of primary emplacement features within North Pipe and may indicate reduced groundwater sourcing during eruptions (due to depressed water table), a lower primary volatile content or reduced magma feed rates.

References

- Brown RJ, Gernon TM, Stiefenhofer J, Field M (2008) Geological constraints on the eruption of the Jwaneng Centre kimberlite pipe, Botswana. *Journal of Volcanology and Geothermal Research* 174:195-208
- Kinney PD, Compston W, Bristow JW, Williams IS (1989) Archean mantle xenocrysts in a Permian kimberlite: two generations of kimberlitic zircon in Jwaneng DK2, southern Botswana. In: Ross N (ed) *Kimberlites and related rocks*, Geol. Soc. Australia, pp 833–842
- Webb KJ, Stiefenhofer J, Field M (2004) Overview of the geology and emplacement of the Jwaneng DK2 kimberlite, Southern Botswana. 8th International Kimberlite Conference, Long Abstract.
- Skinner EMW, Marsh JS (2004) Distinct kimberlite classes with contrasting eruption processes. *Lithos* 76:183–200.

Slope stability challenges and solutions for mining Kimberlite resources hosted in structurally complex country rock: Dip slope mining at Jwaneng Mine, Botswana

Oakantse Mogorosi¹, Kabo Gabanakgosi¹, Otsile M. Barei¹ and Thokweng Thokweng¹.
[¹Debswana Diamond Company]

Introduction

The Jwaneng Diamond Mine diatremes have intruded the late Archean to early Proterozoic mixed siliciclastic – carbonate sediments of the Transvaal Supergroup. The structural geology of the country rock at Jwaneng Mine indicates that the area has been subjected to at least three deformational events. The first deformation (D1) is NW-SE directed compression which resulted in NE trending open folds (F1) and low angle thrust faults that tend to dissipate into bedding. The second deformation (D2) is N-S shortening that resulted in sinistral, oblique shearing along the pre-existing radial cleavage developed around the F1 folds coupled with development of antithetic structures and NW-trending folds, (F2). The third deformational event, D3 is an NE-SW extensional deformation leading to development of normal faulting along pre-existing F1 cleavage creating a series of wedge shaped fault-bounded blocks. The normal faulting was coupled with rotation of blocks towards the N resulting high dip value on the eastern slopes daylighting in to Jwaneng mine open pit. (Creus, et al., 2017) in prep

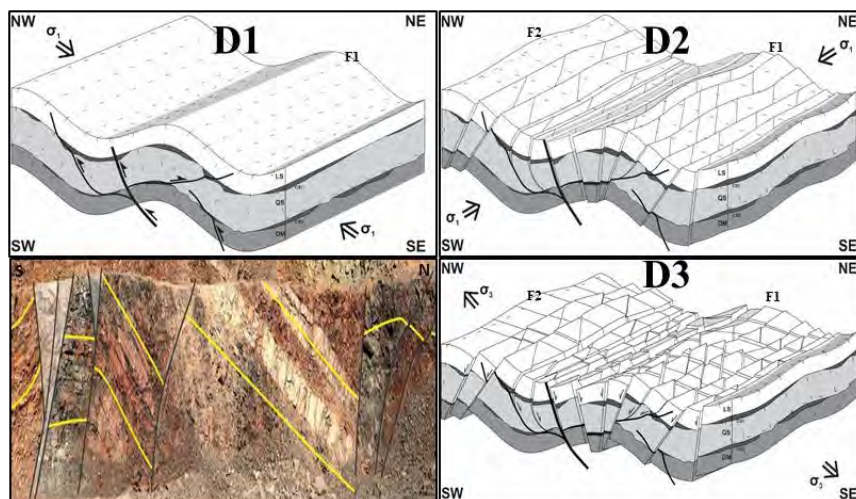


Figure 1: a) An early compression D1 resulting in NE-SW trending folds; b) SW-NE compression D2 resulting in NW trending folds (F2) and interference folding; c) N-S extension resulting in normal faulting wedge shaped blocks; d) combined effect of all deformational events. (Creus, et al., 2017)

The steeply dipping bedding planes presents slope stability challenges particularly for the eastern side of the pit where the strike direction of the planes is parallel to the pit slope strike. Single to multiple bench instabilities have over the years been experienced for the eastern side of the pit primarily driven by undercutting of the bedding planes. Consequences of slope failures can range from injury of personnel, damage to equipment, loss of production and possibly force majeure. In this paper we present a solution, determined through extensive data collection and analysis methodologies, aimed at to reducing the afore-mentioned detrimental consequences.



Figure 2: Planar failures on the Jwaneng mine eastern slopes mined with conventional vertical batters

Implementation of the dip slope mining solution

Planar instability experienced in the eastern slopes is primarily driven by bedding planes dipping steeper than the bedding friction angle. Extensive laboratory testing carried out over time for the shales in Jwaneng mine indicated a friction angle of 37° (Contreras, 2010). In order to capture for localised variation, data from extensive mapping of exposed faces coupled with downhole geophysics (optical and acoustic televiewer) was used to develop a localised fabric model representing bedding surfaces using the 3D implicit modelling Leapfrog™ software. An example of a surface waveform has been illustrated in Figure 3 below.

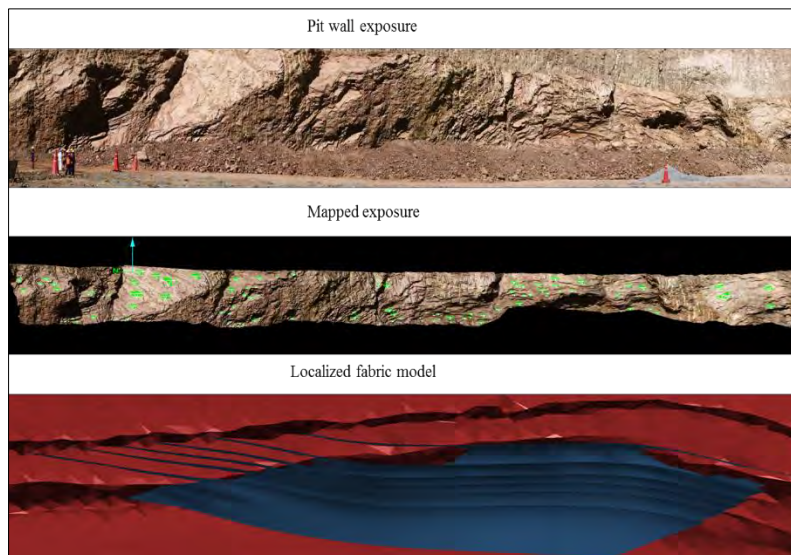


Figure 3: Development of localised fabric based on mapped pit faces

Jwaneng Mine ordinarily adopts vertical batter berm configuration. This conventional configuration leads to instabilities influenced by steep bedding in certain areas. A mining method new to the operation locally referred to as dip slope mining then had to be considered for such areas. The basic principle for this mining method involves mining of benches along the dip of the bedding therefore avoiding undercutting of the planes which is the primary cause of the instability. The criteria for determining bench configuration is based on kinematic feasibility which considers the following and is summarised by Figure 4 below;

- Dip of bedding versus friction angle (37°)

- Bedding strike versus design slope strike (within approximately $\pm 20^\circ$) (Wyllie & Mah, 2004)

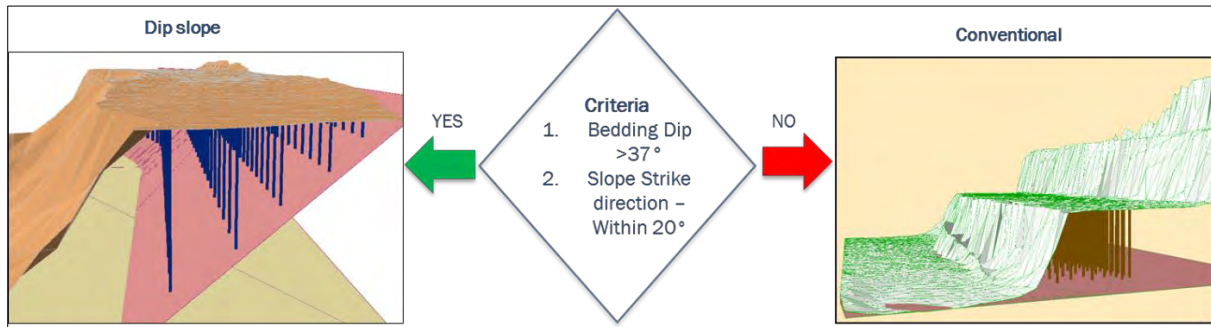


Figure 4: Application of the dip slope mining criteria for bench design configurations

When a mining block has been determined to meet the dip slope mining criteria, a 3D surface inclined at an appropriate angle is created on GEOVIA GEMSTM software. The inclined surface represents a target plane to which blastholes are designed to as shown by Figure 4 above and eventually mined to. Stringent controls are applied to the drilling and blasting processes to ensure preservation of targeted bedding plane. The implementation of this methodology has led to successful elimination of the initially experienced instabilities due to the undercutting of steep bedding. Figure 5 below shows a comparison of the pit wall conditions before and after implementation of the dip slope mining method.



Figure 5: Pit wall conditions before and after implementation of dip slope mining

Conclusions

The dip slope mining solution proved highly effective in drastically reducing the stability challenges that were experienced in the eastern Cut 8 slopes.

References

- Contreras, L. F., 2010. *Jwaneng Mine – Cut 8 Slope Geotechnical Design*. SRK Report No 401886, Johannesburg, South Africa: SRK Consulting (South Africa) (Pty) Ltd..
- Creus, P. et al., 2017. *Structural Analysis and 3D Implicit Modelling of Jwaneng Mine: Insights in to Deformation of the Transvaal Supergroup in SE Botswana*. s.l.:s.n.
- Wyllie, D. C. & Mah, C. W., 2004. *Rock Slope Engineering: Civil and Mining*. 4th ed. London: Spon Press.

Neoproterozoic Zimmi diamond formation through infiltration of recycled methane into sulphide-bearing Archaean eclogite

Karen V. Smit¹, Steven B. Shirey², Erik H. Hauri², Jianhua Wang², Thomas Stachel³
and Richard A. Stern³

¹ Gemological Institute of America, New York City, NY, USA, ksmit@gia.edu

² Department of Terrestrial Magnetism, Carnegie Institution for Science, Washington, DC USA, sshirey@carnegiescience.edu, ehauri@carnegiescience.edu, jwang@carnegiescience.edu

³ Canadian Centre for Isotopic Microanalysis, University of Alberta, Edmonton, AB, Canada, tstachel@ualberta.ca, rstern@ualberta.ca

Introduction

Sulphide-bearing alluvial diamonds from Zimmi on the Man Shield (West African Craton) have provided an unparalleled opportunity to evaluate eclogitic diamond formation processes. Through high precision analyses of multiple isotopes (Re-Os , $\delta^{13}\text{C}$, $\delta^{33}\text{S}$, $\delta^{34}\text{S}$, $\delta^{36}\text{S}$) we are able to determine: 1) the timing of Zimmi eclogitic diamond formation and whether there is any link with local tectonic processes, 2) the genetic relationship between eclogitic sulphide inclusions and diamond-forming fluids (i.e., whether these sulphides were pre-existing or rather co-precipitated from the carbon-bearing fluids), 3) the implications for the interpretation of isotopic diamond ages, and 4) the redox speciation of fluids likely released during Neoproterozoic subduction, and whether they participated in diamond formation through redox processes or isochemical cooling.

Neoproterozoic ages for Zimmi eclogitic diamonds

Ten pyrrhotite-rich eclogitic sulphides encapsulated in three Zimmi diamonds have Re-Os isotopic compositions that plot along three 650 Ma age arrays (Figure 1; Smit et al., 2016). Each of the three diamonds records identical absolute ages, with distinct initial $^{187}\text{Os}/^{188}\text{Os}$ between 1.5 and 2.2. These three 650 Ma diamond ages overlap with the timing of continental assembly through subduction recorded in the Rokelide orogen along the southwestern margin of the West African craton (700-550 Ma; Lytwyn et al., 2006).

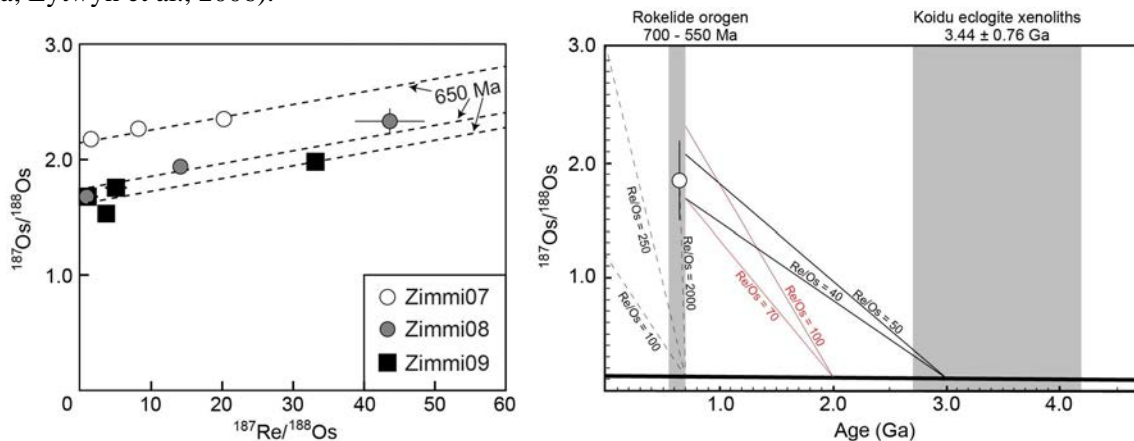


Figure 1: Ten pyrrhotite-rich eclogitic sulphides in three different Zimmi diamonds record identical Re-Os absolute ages of 650 Ma. Initial $^{187}\text{Os}/^{188}\text{Os}$ ratios of 1.5 to 2.2 are too radiogenic to be derived from Neoproterozoic oceanic crust, but could evolve from enriched Archaean reservoirs in the lithosphere that have Re/Os around 40-50.

Evidence from Re-Os for pre-existing sulphides

All ten sulphides have radiogenic Os isotopic compositions that are not supported by their low Re/Os ratios, requiring some Re loss prior to or at the time of diamond formation. This confirms that the

sulphides and diamond-source fluids/melts cannot share a single-stage origin. Furthermore, initial $^{187}\text{Os}/^{188}\text{Os}$ ratios for the age arrays in three diamonds are all very radiogenic ($^{187}\text{Os}/^{188}\text{Os}$ between 1.5 to 2.2), relative to the chondritic mantle at 650 Ma (0.124; Figure 1), indicating that unlike the diamond-forming fluids, the sulphides did not originate in Neoproterozoic oceanic crust. Rather, the radiogenic $^{187}\text{Os}/^{188}\text{Os}$ initial ratios indicate the sulphides' residence in an enriched lithospheric reservoir. In the West African lithospheric mantle, such enriched reservoirs could be represented by Archaean eclogites, such as those from the Koidu kimberlite (Barth et al., 2002). With Re/Os ratios around 40-50 such eclogites could evolve to radiogenic $^{187}\text{Os}/^{188}\text{Os}$ recorded in Zimmi sulphides over 2 billion years (Figure 1).

Evidence from multiple sulphur isotopes for an Archaean sulphur source

An Archaean source of sulphur for the inclusions in Neoproterozoic Zimmi diamonds was tested through in situ multiple sulphur isotope analyses by NanoSIMS (Hauri et al., 2016), using methods similar to those described for the 1280 ion microprobe (Whitehouse et al., 2013). Preliminary data on three sulphide inclusions in three different diamonds, have a wide range of $\delta^{34}\text{S}$ values, between -1 and -6 ‰, all outside of the typical mantle value and consistent with a crustal sulphur reservoir. All three sulphides have $\delta^{33}\text{S}$ and $\delta^{36}\text{S}$ values that deviate from the arrays that define mass dependent fractionation ($\delta^{33}\text{S} = 0.5167 \times \delta^{34}\text{S}$ and $\delta^{36}\text{S} = 1.9 \times \delta^{34}\text{S}$). Expressed as $\Delta^{33}\text{S}$ and $\Delta^{36}\text{S}$, these deviations are due to mass independent fractionation (MIF), a process commonly understood to only occur in the Archaean oxygen-deprived atmosphere (Farquhar et al., 2000). Zimmi sulphides have $\Delta^{33}\text{S}$ between +0.3 and +1.7 ‰ and $\Delta^{36}\text{S}$ between -0.7 and -2.5 ‰ that plot along the array for Archaean metasediments (Figure 2). Importantly, MIF of sulphur isotopes in Zimmi sulphides indicate that sulphur could not have been solely derived from Neoproterozoic oceanic crust. Rather, these MIF signatures support the Re-Os evidence for sulphur residence in an Archaean enriched reservoir prior to encapsulation in diamond.

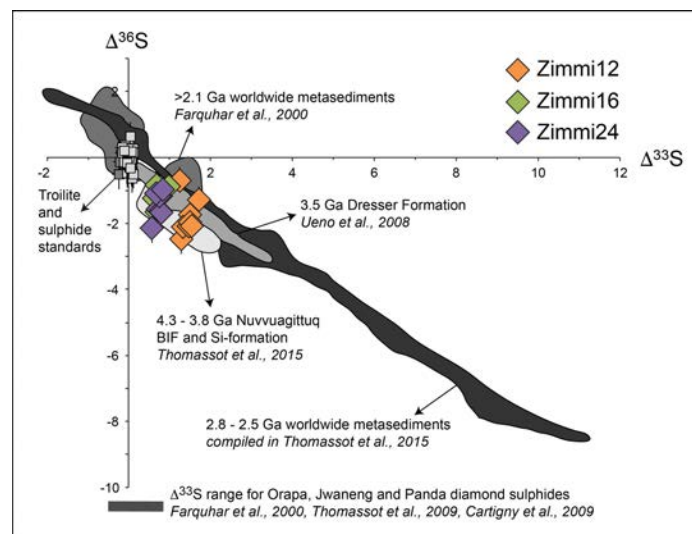


Figure 2: Preliminary NanoSIMS sulphur isotope data for three Zimmi sulphide inclusions compared to Archaean metasediments from the literature. MIF sulphur isotopes only originate during the Archaean, suggesting that carbon and sulphur in Zimmi diamonds and their inclusions do not share a common origin in Neoproterozoic oceanic crust. Error bars for Zimmi sulphides are similar to the symbol size.

Recycled carbon source for diamond-forming fluids

Carbon isotopic compositions for 5 diamonds from Zimmi range between -6.5 and -24.5 ‰. $\delta^{13}\text{C}$ values below -10 ‰ are outside the range for mantle carbon and require derivation from subducted oceanic crust. The presence of recycled carbon in Zimmi diamonds is consistent with the timing of diamond formation derived from the Re-Os isotope data and Neoproterozoic subduction in the West

African Craton. $\delta^{13}\text{C}$ values for Zimmi diamonds that overlap with the mantle value could represent carbon derived from the convecting mantle, however a recycled origin for these mantle-like values cannot be excluded as they could be indicative of abiogenic carbon contributions from the oceanic crust.

Diamond precipitation during oxidation of methane

In eclogitic assemblages, diamond formation processes through either redox buffering or cooling of carbon-bearing fluids are not well constrained. In one Zimmi diamond, a core-to-rim trend of gradually decreasing $\delta^{13}\text{C}$ (-23.4 to -24.5 ‰) and N-content is indicative of formation from reduced $\text{CH}_4\pm\text{C}_2\text{H}_6$ fluids, likely derived from oceanic crust recycled during Neoproterozoic subduction. Unlike mixed $\text{CH}_4\text{-CO}_2$ fluids near the H_2O -maximum, isochemical cooling of such reduced fluids is only efficient during ascent (Stachel and Luth, 2015) and therefore cannot explain smooth compositional trends within individual diamonds residing at constant pressure (documented here). Consequently, this Zimmi eclogitic diamond likely formed through redox buffering of reduced subduction-related fluids, infiltrating into sulphide-bearing eclogite.

Growth conditions for Zimmi eclogitic diamonds

Neoproterozoic Zimmi eclogitic diamonds formed during infiltration of carbon-bearing fluids that can be temporally linked to local subduction that introduced oceanic crust and its carbon budget into the lithospheric keel. The wide range in $\delta^{13}\text{C}$ values recorded by five diamonds indicate multiple carbon sources in the oceanic crust that include $\text{CH}_4\text{-C}_2\text{H}_6$ with $\delta^{13}\text{C}$ around -24 ‰. At least one Zimmi diamond formed during oxidation of this reduced recycled carbon when it infiltrated into the Archaean lithosphere. Our Re-Os, $\Delta^{33}\text{S}$ and $\Delta^{36}\text{S}$ data require that, unlike carbon, sulphur was not solely derived from Neoproterozoic sources. Rather, at least some of the sulphur in Zimmi sulphide inclusions resided in the enriched Archaean lithosphere prior to encapsulation in Neoproterozoic diamonds. This unequivocally demonstrates that multiple pre-existing sulphides can record diamond ages if their Re-Os isotopes diffuse and re-equilibrate during diamond formation. This is expected during eclogitic diamond formation since PT conditions for worldwide eclogitic diamond inclusions indicate formation in partially molten conditions above 1100 °C (Stachel and Luth, 2015), significantly above the closure temperature for Re-Os exchange in pyrrhotite (400 °C; Brenan et al., 2000).

References

- Barth, M, Rudnick, RL, Carlson, RW, Horn, I, McDonough, WF (2002) Re-Os and U-Pb geochronological constraints on the eclogite-tonalite connection in the Archean Man Shield, West Africa. *Precamb Res*, 118, 267–283
- Brenan, JM, Cherniak, DJ, Rose, LA (2000) Diffusion of osmium in pyrrhotite and pyrite: implications for closure of the Re-Os isotopic system. *EPSL*, 180, 399-413
- Farquhar, J, Bao, H, Thiemens, M (2000) Atmospheric Influence for Earth's Earliest Sulfur Cycle. *Science*, 289, 756-758
- Hauri, EH, Papineau D, Wang, J, Hillion, F (2016) High-precision analysis of multiple sulfur isotopes using NanoSIMS. *Chem Geol*, 420, 148-161
- Lytwyn, J, Burke, K, Culver, S (2006) The nature and location of the suture zone in the Rokelide orogen, Sierra Leone: geochemical evidence. *Journal of African Earth Science*, 46, 439–454
- Smit, KV, Shirey SB, Wang, W (2016) Type Ib diamond formation and preservation in the West African lithospheric mantle: Re-Os age constraints from sulphide inclusions in Zimmi diamonds. *Precamb Res*, 286, 152-166
- Stachel, T, Luth RW (2015) Diamond formation – Where, when and how? *Lithos*, 220-223, 200-220
- Whitehouse, MJ (2013) Multiple sulfur isotope determination by SIMS: Evaluation of reference sulfides for $\Delta^{33}\text{S}$ with observations and a case study on the determination of $\Delta^{36}\text{S}$. *Geostand. Geoanal. Res.* 37, 19-33



Relationships between the Diamond Trading Company (DTC) round aperture Diamond Sieve (DS) plates.

PJ Lawless¹ and David Farrow²

¹*Dr Paddy Lawless and Associates CC), Johannesburg, Gauteng, South Africa;
paddy@plawless.co.za*

²*Stornoway Diamond Corporation, North Vancouver, British Columbia, Canada;
DFarrow@Stornowaydiamonds.com*

Introduction

The relationships between the various round aperture DTC, formerly Central Selling Organisation (CSO) diamond sieves have been an enigma for many years and despite many enquiries and efforts, sensible mathematical relationships could not be established for the relationship(s) between the diameters of the apertures of the round DTC diamond sieve plates.

Results

Separate replies from two long-serving CSO/DTC members alleged that these apertures were based on the sizes of buck and/or bird shot pellets. This allegation was investigated and it was found that out of the 19 DTC sieve plates often used, i.e. 23, 21, 19, 17, 15, 14, 13, 12, 11, 10, 9, 8, 7, 6, 5, 4, 3, 2 and 1 there were 13 double matches with various shot sizes to within 0.002 inches and 4 double matches to within 0.004 inches. The DTC permitted tolerance for DS plates is +/- 0.002 inches.

Two of the larger buck shot pellet sizes, #4 and 'F', could have been equivalent to the 18 and 16 DTC DS which currently do not exist. Another two buck shot sizes, #000 and #2, could also have been equivalent to the 22 and 20 DTC DS but these sieves also do not currently exist. The #1 DTC DS has an equivalent to what is termed #13 Pest Shot or "Dust". There are no buck nor bird shot equivalents for the apertures of the 23 and 5 DTC DS plates. There are a further four buck shot, #0000, #00 #0, 'T', and one bird shot, 'B', pellet sizes which have no DTC DS equivalents.

The 21 DTC DS does not match any buck or bird shot sizes. The #1 and #2 buck shot sizes fall between the 21 and 19 DTC DS but the 20 DTC DS does not exist. Despite many further enquiries it has not been possible to discover the reason(s) for the current non-existence of the 22, 20, 18 and 16 DTC DS and also if they ever existed.

The correlation between buck and bird shot sizes and the DTC DS was enhanced by a statement that because buck/bird shot sizes had been standardized for many years in the United Kingdom, and were then readily available, manufacture of DS plates with consistent apertures could be achieved using these pellets.

Table 1 illustrates the various 'matches' which are colour-coded with explanatory 'Notes' below the table.

| Table 1 | | | | | | | | | | |
|---------|-----------|---------------|---|--------------|------------|------------|---------------|---------|-------------|------------------|
| DTC | DTC | DTC | DTC | DTC | BUCK or | DTC | BUCK or | BUCK or | BUCK or | Low er Critical |
| DIAMOND | "Missing" | DIAMOND | DIAMOND | "Missing" | BIRD | DIAMOND | BIRD | BIRD | BIRD | Stone Size |
| SIEVE | DIAMOND | SIEVE | SIEVE | DIAMOND | Shot | SIEVE | Shot | Shot | Shot | per Diamond |
| CLASS | SIEVE | ROUND | ROUND | SIEVE | Pellet | Aperture | Pellet | Pellet | Pellet | Sieve Class |
| | CLASSES | APERTURE | APERTURE | ROUND | diameter | permitted | diameter | Label | Type | southern African |
| | | as per tables | actual | APERTURE | permitted | tolerances | compiled | | | Primary |
| | | normal use | as per tables | Interpolated | tolerances | + / -- | from Internet | | | Kimberlites |
| | | mm | inches | inches | inches | inches | inches | | | carats/ stone |
| +23 | | 10.312 | 0.406 | | 0.002 | | | | | 8.0360 |
| | | | | | 0.002 | | 0.380 | 0000 | buck shot # | |
| | | | | | 0.002 | | 0.370 | 0001/2 | buck shot # | |
| | ? +22 | | | 0.356 | 0.002 | 0.002 | 0.360 | 000 | buck shot # | 5.4506 |
| | | | | | 0.002 | | 0.340 | 001/2 | buck shot # | |
| | | | | | 0.002 | | 0.330 | 00 | buck shot # | |
| | | | | | 0.002 | | 0.320 | 0 | buck shot # | |
| +21 | | 7.925 | 0.312 | | 0.002 | 0.002 | 0.310 | 1 1/2 | buck shot# | 3.6910 |
| | | | | | 0.002 | | 0.300 | 1 | buck shot # | |
| | | | | | 0.002 | | 0.290 | 2 1/2 | buck shot # | |
| | ? +20 | | 0.279 | 0.279 | 0.002 | | 0.270 | 2 | buck shot # | 2.6681 |
| | | | | | 0.002 | | 0.260 | 3 1/2 | buck shot # | |
| +19 | | 6.350 | 0.250 | | 0.002 | 0.002 | 0.250 | 3 | buck shot # | 1.9180 |
| | ? +18 | | 0.238 | 0.238 | 0.002 | 0.240 | 0.240 | 4 | buck shot # | 1.6591 |
| +17 | | 5.740 | 0.226 | | 0.002 | 0.228 | 0.230 | FF | buck shot # | 1.4230 |
| | ? +16 | | 0.219 | 0.219 | | | 0.220 | F | buck shot # | 1.3104 |
| +15 | | 5.410 | 0.213 | | 0.001 | 0.212 | 0.210 | TT | buck shot # | 1.1950 |
| | | | | | | | 0.200 | T | Bird shot # | |
| +14 | | 4.750 | 0.187 | | 0.001 | 0.188 | 0.190 | BBB | Bird shot # | 0.8184 |
| +13 | | 4.521 | 0.178 | | 0.001 | 0.179 | 0.180 | BB | Bird shot # | 0.7030 |
| | | | | | | | 0.170 | B | Bird shot # | |
| +12 | | 4.089 | 0.161 | | 0.001 | 0.160 | 0.160 | 1 | Bird shot # | 0.5230 |
| | | | | | | | 0.150 | 2 | Bird shot # | |
| +11 | | 3.454 | 0.136 | | 0.001 | 0.137 | 0.140 | 3 | Bird shot # | 0.3170 |
| +10 | | 3.277 | 0.129 | | 0.001 | 0.130 | 0.130 | 4 | Bird shot # | 0.2741 |
| | | | | | | | 0.125 | 4 1/2 | Bird Shot # | |
| | | | | | | | 0.120 | 5 | Bird shot # | |
| + 9 | | 2.845 | 0.112 | | 0.001 | 0.111 | 0.110 | 6 | Bird shot # | 0.1790 |
| + 8 | | 2.515 | 0.099 | | 0.0005 | 0.100 | 0.099 | 6 1/2 | Bird shot # | 0.1257 |
| | | | | | | | | 7 | Bird shot # | |
| + 7 | | 2.464 | 0.097 | | 0.0005 | 0.096 | 0.095 | 7 1/2 | Bird shot # | 0.1165 |
| | | | | | | | 0.090 | 8 | Bird shot # | |
| + 6 | | 2.159 | 0.085 | | 0.0005 | 0.084 | 0.085 | 8 1/2 | Bird shot # | 0.0792 |
| | | | | | | | 0.080 | 9 | Bird shot # | |
| + 5 | | 1.829 | 0.072 | | | | | | | 0.0485 |
| + 4 | | 1.753 | 0.069 | | 0.0005 | 0.070 | 0.070 | 10 | Bird shot # | 0.0443 |
| + 3 | | 1.473 | 0.058 | | 0.0005 | 0.059 | 0.060 | 11 | Bird shot # | 0.0256 |
| + 2 | | 1.321 | 0.052 | | 0.0005 | 0.051 | 0.050 | 12 | Bird shot # | 0.0186 |
| + 1 | | 1.092 | 0.043 | | 0.0005 | 0.044 | 0.040 | 13 | Pest Shot# | 0.0106 |
| Totals | | 19 | 23 | | | | 36 | | | |
| Notes | | 19 | Actual DTC Diamond Sieves | | | | | | | |
| | | 23 | Possible DTC Diamond Sieves includes 'missing' DS 22, 20, 18, 16 | | | | | | | |
| | | 37 | Shot Sizes = 16 Buck, 20 Bird & 1 Pest | | | | | | | |
| | | 13 | double matches to within 0.002 inches | | | | | | | |
| | | 4 | possible more double matches to within 0.004 inches | | | | | | | |
| | | 2 | possible more matches to 0.004 ins but DS does not exist, i.e. Missing DS 18 & 16 | | | | | | | |
| | | 10 | Larger Buck Shot sizes exist with no DS equivalent, but could be 22 or 20 DS | | | | | | | |
| | | 7 | Bird Shot sizes exist with no DS equivalent, | | | | | | | |
| | | 2 | DS +23 & +05 match no shot sizes | | | | | | | |

Figures 1 and 2 show the correlations between the buck and bird shot sizes and the DTC Diamond Sieves.

Figure 1 shows the buck and bird shot size labels on the horizontal axis.

Figure 1

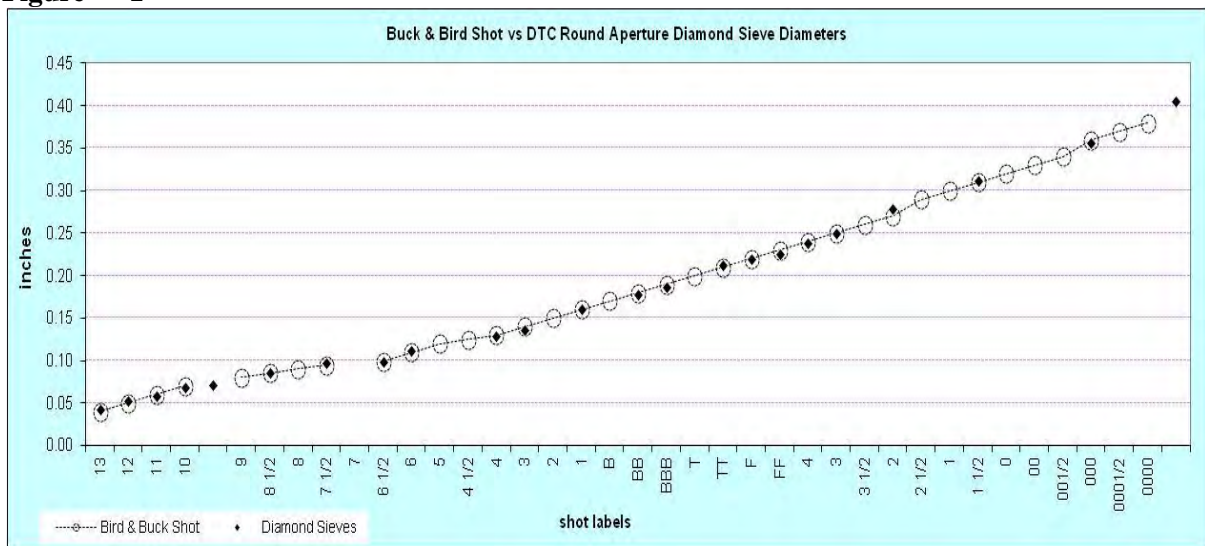
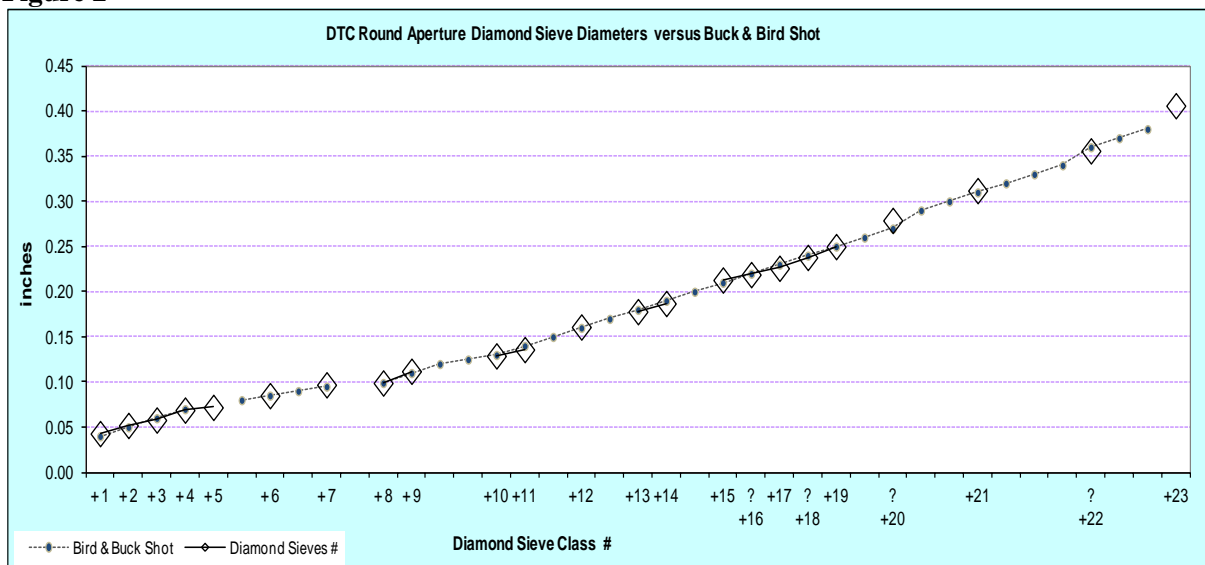


Figure 2 displays the DTC Diamond Sieve class numbers on the horizontal axis.

Figure 2



Inspection of Table 1 with Figures 1 and 2, on the balance of probabilities, substantiate, although do not ‘prove’, the allegation that the round apertures of the DTC Diamond Sieves were based on buck and bird shot pellets sizes.

References

DTC Reference Sheets

Endecotts: http://www.endecotts.com/dltmp/www/56607c62-8044-4b33-ba08-2482bc282b86-400f14323e75/brochure_endecotts_general_en.pdf

Numerous from Wikipedia particularly

[https://en.wikipedia.org/wiki/Shot_\(pellet\)#Comparison_chart](https://en.wikipedia.org/wiki/Shot_(pellet)#Comparison_chart)



New constraints on the origin of carbonates in kimberlites integrating petrography, mineral chemistry and *in situ* stable isotope analysis

Montgarri Castillo-Oliver¹, Andrea Giuliani^{1,2}, William L. Griffin¹, Suzanne Y. O'Reilly¹, Emilie Thomassot³ and Russell N. Drysdale⁴

¹ ARC Centre of Excellence for Core to Crust Fluid Systems and GEMOC, Department of Earth and Planetary Sciences, Macquarie University, NSW, Australia

² School of Earth Sciences, The University of Melbourne, Parkville, 3010 Victoria, Australia^{SEP}

³ Centre de Recherches Pétrographiques et Géochimiques, CNRS, Nancy, France

⁴ School of Geography, The University of Melbourne, Parkville, 3010 Victoria, Australia

Introduction

The composition of kimberlite parental melts and their evolution remains a controversial topic because of the heterogeneous nature of kimberlites and volatile loss or addition during and after eruption. The original composition of these magmas can be significantly modified by a wide variety of processes that take place during, or subsequent to, kimberlite emplacement. These processes may include mantle and crustal assimilation, degassing, deuteric and hydrothermal alteration and/or weathering. Carbonates in kimberlites are the main site for CO₂, and include calcite and dolomite, and very rare alkali-rich carbonates (e.g., Mitchell 1994; Kamenetsky et al. 2007). Despite being major components in hypabyssal kimberlites (Skinner and Clement, 1979), very few studies have included quantitative major- and minor-element analyses of kimberlitic carbonates and detailed petrographic observations. However, the few studies already suggest that carbonate petrogenesis in kimberlites is very complex and involves multiple sources in their formation (e.g., Armstrong et al. 2004; Giuliani et al. 2014). Understanding the origin of carbonates in kimberlites is thus essential to determine the CO₂ composition of parental melts. In this study carbonates in fresh hypabyssal kimberlites (macrocrystic and aphanitic types) from worldwide localities (South Africa, Canada, Finland, Australia, Antarctica, Brazil) are characterised by detailed petrography, as well as by major- and minor-element, bulk-carbonate and *in situ* secondary ion mass spectrometry (SIMS) O-isotope analyses.

Carbonate petrogenesis in kimberlites

Detailed petrographic characterisation of these kimberlites was carried out using optical microscopy, cold cathodoluminescence and SEM. This detailed examination emphasises the complexity of kimberlites and identifies multiple generations of carbonates within each sample.

Groundmass carbonates in most samples occur as fine-grained interstitial calcite between other non-altered groundmass crystals such as olivine, monticellite, apatite and/or perovskite. However, some kimberlites (e.g., De Beers kimberlite), also contain randomly oriented laths (80x1500 μm) of calcite, with inclusions of the same groundmass minerals. Similar laths have been previously interpreted as being of primary (i.e. magmatic) origin (e.g., Kopylova et al. 2007). Likewise, the euhedral Ba-, Na-, Ce- and Nb-rich carbonates, found here either as individual grains or as part of complex segregations (in the Koala kimberlite), may be comparable to the high-temperature, primary carbonates described in other kimberlites of the Lac de Gras field (Armstrong et al., 2004). The work presented here also includes other well-known examples of primary carbonate, such as the Benfontein carbonate sills and diapirs (e.g., Dawson and Hawthorne, 1973). Most of these primary carbonates have a moderate cathodoluminescence response, resulting in brown to dark orange CL colours (fig.1). However, there are also remarkable exceptions, such as the segregations in the Koala kimberlite and the diapirs in the Benfontein kimberlite, which have a strong CL response.

Secondary (non-magmatic) carbonates may also occur in the studied kimberlites either replacing the original groundmass phases, as segregations or as crosscutting veins. Some of the secondary carbonates

(calcite and, less commonly, dolomite) are characterised by abundant inclusions, such as barite, apatite, halides or fluorite. These secondary carbonates are typically characterised either by bright yellow and orange CL colours or, less commonly, by no CL response.

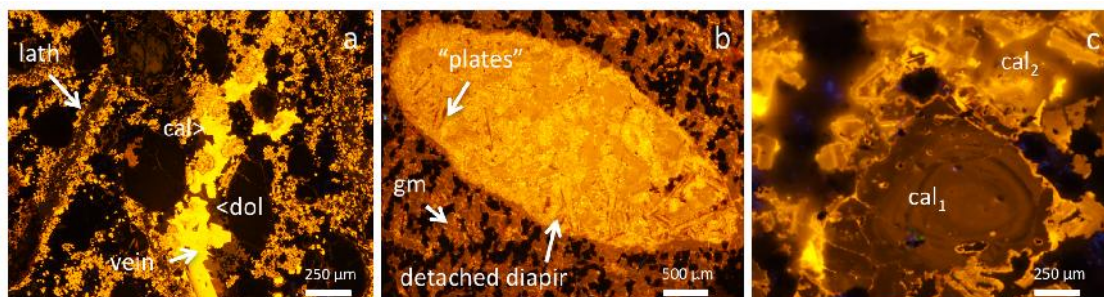


Figure 1: Cold CL images of selected kimberlites. a) De Beers kimberlite, with primary carbonate laths (brown) and secondary veins of calcite (bright yellow) and dolomite (dark red). b) A “detached diapir” of the lower sill at Benfontein; note the different CL response of groundmass carbonates (gm) in the kimberlite matrix, rare dark “plates” and yellow-orange coarser (sparry) calcite in the “detached diapir”. c) A second generation of calcite (cal_2) replacing an earlier, concentrically zoned, calcite (cal_1) in the Premier kimberlites.

Electron microprobe analyses reveal that early-crystallising carbonates are typically Sr-rich calcite (0.6–2.1 wt % SrO), sometimes coupled with slight enrichment in Ba, Mg, Fe and Na (<0.2 wt.% oxides). Although this Sr enrichment is a characteristic feature in all the studied kimberlites, minor compositional variations can be correlated with different kimberlite fields. For example, very high Sr contents are found in the groundmass carbonates of the Lac de Gras kimberlites, contrasting with the lower values typical of the South African kimberlites. The composition of the secondary carbonates clearly differs from that of the early carbonates (Sr contents are either negligible or very high (> 3wt% SrO)) and varies significantly between kimberlites. Although dolomite commonly has significant amounts of Mn and Fe (0.20–0.85 wt % MnO and up to 2.6 wt % FeO), the values for Sr, Ba, REE and Na are usually lower than that in the groundmass.

O isotope analysis in kimberlitic carbonates

Different carbonate generations have clearly distinct ^{18}O composition. As shown in Fig. 2a, primary carbonates typically show values within the mantle range ($^{18}\text{O} = 6\text{--}9\text{‰}$), whereas secondary carbonates commonly have higher values ($^{18}\text{O} = 12\text{--}23\text{‰}$). A remarkable exception was found in the ~1200 Ma Premier kimberlite, where texturally secondary calcite yields an oxygen isotope signature typical of mantle-derived carbonates ($^{18}\text{O} = 7\text{--}9\text{‰}$). Moreover, our results demonstrate that bulk-carbonate ^{18}O data commonly differ from the values obtained from *in situ* analyses (Fig. 2a).

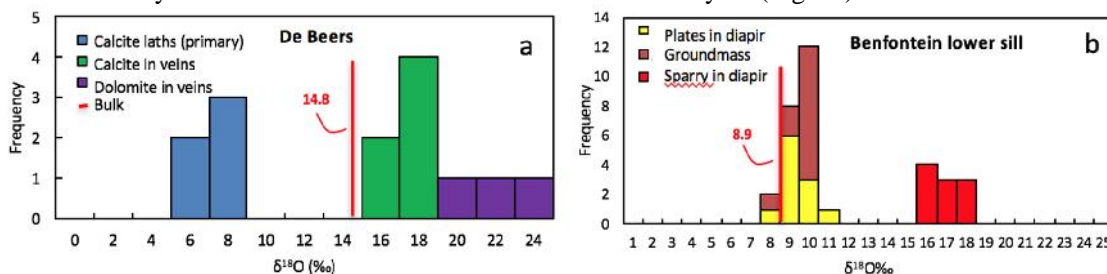


Figure 2: ^{18}O histograms for carbonate grains in the De Beers kimberlite and Benfontein lower sill. The ^{18}O values of primary and secondary carbonates differs from the bulk carbonate analyses.

In situ analyses also revealed an unexpected complexity in the processes that led to the formation of magmatic carbonates and “diapirs” in the lower sill of the Benfontein sill complex (Fig. 2b). The groundmass carbonate in this sill shows a characteristic and homogeneous mantle-like signature ($^{18}\text{O} = 8.3 \pm 0.6 \text{‰}$), which overlaps with the isotopic composition of the Sr-rich calcite plates (Fig. 1b)

found in the “diapirs” ($^{18}\text{O} = 7\text{-}9\text{‰}$). However, the sparry calcite accounting for the bulk of the carbonate diapirs has significantly heavier O isotope values ($^{18}\text{O} = 14.5\text{-}16.5\text{‰}$), which would explain the wide range of values ($^{18}\text{O} = 8.73$ and 14.34‰) previously reported by Dawson and Hawthorne (1973). Secondary dolomite in veins has higher O isotope values than the calcite crystallising in the same vein (e.g. $^{18}\text{O} = 20\text{-}23\text{‰}$ vs $^{18}\text{O} = 16\text{-}18\text{‰}$).

Discussion and conclusions

Carbonate petrogenesis in kimberlites is complex and can only be understood by integrating detailed textural characterisation and *in situ* geochemical measurements. The composition of primary carbonates (groundmass, laths, magmatic segregations and in sills) is strikingly homogeneous in all kimberlites worldwide (calcite with 0.6-2.1 wt % SrO), although minor variations occur between different kimberlite fields. However, the composition of secondary carbonates (replacing early groundmass phases, as segregations or as crosscutting veins) clearly varies between different localities. This is consistent with crystallisation from late fluids strongly influenced by local conditions, including wall rock composition, temperature and/or latitude. *In situ* isotopic analysis have shown that primary kimberlitic carbonates commonly preserve their mantle signature ($^{18}\text{O} = 6\text{-}9\text{‰}$), whereas secondary carbonates commonly have heavier ^{18}O values. The mantle-like values ($^{18}\text{O} = 7\text{-}9\text{‰}$) of texturally secondary carbonates in the Premier kimberlite could be related to deuteritic (i.e. late-stage magmatic) kimberlitic fluids. Alternatively, such isotopic signature may have been imprinted later by melt-related fluids of a large gabbro intrusion (Bartlett 1994).

The significant ^{18}O difference between primary carbonates and bulk kimberlite rocks undoubtedly shows that bulk compositions are not representative of the composition of the parental kimberlitic melt, even for the least altered kimberlites. Therefore this work highlights the necessity of *in situ* characterisation of each carbonate type in order to identify its origin and ultimately define the isotopic composition of magmatic carbonates. This study provides a robust foundation for our ongoing project, which will combine the present O isotope data with additional *in situ* C- and Sr-isotope analysis to better constrain the composition and volatile concentrations of kimberlitic melts.

References

- Armstrong JP, Wilson M, Barnett RL, et al (2004) Mineralogy of primary carbonate-bearing hypabyssal kimberlite, Lac de Gras, Slave Province, Northwest Territories, Canada. *Lithos* 76:415–433. doi: 10.1016/j.lithos.2004.03.025
- Bartlett PJ (1994) Geology of the Premier diamond pipe. In: XVth CMMI Congress. Johannesburg, pp 201–213
- Dawson JB, Hawthorne JB (1973) Magmatic sedimentation and carbonatitic differentiation in kimberlite sills at Benfontein, South Africa. *J Geol Soc London* 12:61–85.
- Giuliani A, Phillips D, Kamenetsky VS, et al (2014) Stable isotope (C, O, S) compositions of volatile-rich minerals in kimberlites: A review. *Chem Geol* 374–375:61–83. doi: 10.1016/j.chemgeo.2014.03.003
- Kamenetsky VS, Kamenetsky MB, Sharygin V V., et al (2007) Chloride and carbonate immiscible liquids at the closure of the kimberlite magma evolution (Udachnaya-East kimberlite, Siberia). *Chem Geol* 237:384–400. doi: 10.1016/j.chemgeo.2006.07.010
- Kopylova MG, Matveev S, Raudsepp M (2007) Searching for parental kimberlite melt. *Geochim Cosmochim Acta* 71:3616–3629. doi: 10.1016/j.gca.2007.05.009
- Mitchell RH (1994) Accessory rare earth, strontium, barium and zirconium minerals in the Benfontein and Wesselton calcite kimberlites, South Africa. In: Meyer HOA, Leonardos OH (eds) *Kimberlites, related rocks and mantle xenoliths*. 5th International Kimberlite Conference. CPRM Special Publication, Araxa, Brazil, pp 115–128
- Skinner EMW, Clement CR (1979) Mineralogical classification of southern African kimberlites. In: Boyd FR, Meyer HOA (eds) *The Mantle Sample*. 2nd International Kimberlite Conference. American Geophysical Union, Washington, D. C., pp 129–139



Metasomatic evolution of the SCLM beneath the Lunda Norte province (NE Angola)

Montgarri Castillo-Oliver¹, William L. Griffin¹, Joan Carles Melgarejo², Salvador Galí², Norman J. Pearson¹, Vladimir Pervov³ and Suzanne Y. O'Reilly¹

¹ ARC Centre of Excellence for Core to Crust Fluid Systems and GEMOC, Department of Earth and Planetary Sciences, Macquarie University, NSW, Australia

² Departament de Mineralogia, Petrologia i Geologia Aplicada, Facultat de Ciències de la Terra, Universitat de Barcelona, Barcelona, Spain, joan.carles.melgarejo.draper@ub.edu

³ Sociedade Mineira de Catoca, Catoca, Lunda Sul, Angola

Introduction

The subcontinental lithospheric mantle (SCLM) is dynamic, continuously modified by partial melting, mantle metasomatism and asthenosphere upwelling. These depletion and refertilisation processes result in a heterogeneous and geochemically complex SCLM, composed of mantle domains differing in composition and thermal state. They also play a major role in the generation of diamond and its preservation in the lithospheric mantle prior to entrainment in the kimberlite, which makes it essential to understand these processes when assessing the diamond potential of a kimberlitic province.

In striking contrast with other cratons worldwide, the lithospheric mantle beneath Central Africa, and in particular the Congo Craton, is still poorly understood. The few studies carried out in the Congo Craton have shown that it is thicker and cooler than other cratons in Africa (O'Reilly et al. 2009; e.g. Begg et al. 2009; Robles-Cruz et al. 2012). Moreover, they suggest that the composition of the SCLM beneath the Congo Craton differs from other African cratons (Batumike et al. 2009; Robles-Cruz et al. 2012; Ashchepkov et al. 2012). Unfortunately, most of these works are based on the study of xenocrysts and megacrysts derived from mineral concentrates, resulting in a lack of petrographic information.

However, improving our current knowledge about the SCLM in the southwestern part of the Congo craton has become essential, since it contains one of the main diamondiferous kimberlite clusters in Africa. This work aims to provide a first insight into the metasomatic evolution of the SCLM beneath the Lunda Sul kimberlitic province (NE Angola), based on the petrographic and compositional characterisation of mantle xenoliths and large clinopyroxene megacrysts brought to the surface by the Catoca and Cat115 pipes.

Petrography and composition of the mantle xenoliths

Both coarse and porphyroblastic (sheared) garnet peridotites were sampled by these two kimberlites. As shown in fig. 1, sheared garnet peridotites are characterised by strong deformation of their pyroxenes, as well as by the occurrence of olivine and orthopyroxene neoblasts, with interstitial, fine-grained clinopyroxene. This clinopyroxene is enriched in incompatible elements (Zr, Hf, LREE) with regards to the coarse Cr-rich diopside found in these xenoliths. These two garnet peridotite suites also differ in the major- and trace-element composition of their rock-forming minerals. The garnet in sheared peridotites is richer in Cr, Zr and Ti, while their olivine has lower #Mg. Such compositional variations, as well as the Zr/Ga and Zr/Y ratios in garnet, are similar to patterns seen in most cratons worldwide (Griffin et al. 1999). However, the mineral modes of the studied xenoliths significantly differ from those described in the Kaapvaal craton and are more comparable to those reported in the Slave craton or in oceanic peridotites.

The eclogites sampled by the Catoca kimberlite have textural and compositional features typical of both type I and type II eclogites as defined by McCandless and Gurney (1989) and Gréau et al. (2011), which suggests that this classification may not be applicable to the mantle eclogites of the Lunda Sul province. Two groups of eclogites (i.e., high- and low-Mg) were identified, which is consistent with previously published studies of eclogites from this kimberlite cluster (Nikitina et al. 2014).

Typical metasomatic phases (phlogopite, Cr-diopside, ilmenite, amphibole) have been identified in several of these xenoliths. Highly-metasomatised xenoliths typically include larger amounts of these minerals, which are accompanied by amphibole, apatite, chromite and rutile. Supergene alteration of some of these xenoliths resulted in the occurrence of phases typical of oxidising environments (barite, celestine and calcite).

Geothermobarometric calculations reveal that the SCLM beneath the Lundas kimberlitic province is composed of two clearly distinct garnet-peridotite layers: a shallow, low-T, coarse peridotite layer (820-1080°C at 30-40 kbar) and a deep, high-T, porphyroclastic (sheared) peridotite layer (1160-1220°C at 46-52 kbar). An intermediate layer dominantly composed of low-Mg eclogites (1040-1140°C, 43-49 kbar) is located between the two garnet-peridotite suites. Unfortunately, our current data are still insufficient to explain the origin of this structure, which could be either explained by subduction stacking or by upwelling and intrusion of mafic magmas.

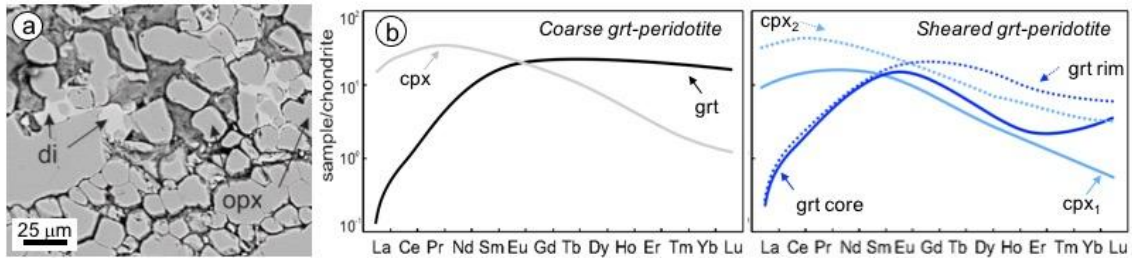


Fig.1. a) BSE image of a sheared garnet-peridotite showing the occurrence of a second generation of interstitial diopside (di) between the orthopyroxene neoblasts (opx). b) Chondrite-normalised REE patterns for garnet (grt) and clinopyroxene (cpx) in coarse and sheared garnet-peridotites. Only one generation of clinopyroxene and garnet is found in the coarse peridotites, whereas compositional differences between the core and the rim of garnets, and the coarse- and fine-grained clinopyroxenes, are a characteristic feature of the sheared peridotites.

Mantle metasomatism in the SCLM in Lunda Sul: a multi-stage process

Complex, multi-stage metasomatic processes were identified in the SCLM beneath the Lunda Sul kimberlitic province, which involved both modal and cryptic/stealth metasomatism. The study of the trace element composition of garnet and clinopyroxene revealed that the low-T and high-T garnet peridotite suites were modified by compositionally different metasomatic melts that percolated through the lithospheric mantle at different times (Fig.1b). Although there is only a limited number of xenoliths available, a possible model of the metasomatic evolution of the SCLM in NE Angola could be proposed.

Our data suggest that the upper SCLM was first metasomatised by silicate melts related to the ascent of asthenospheric melts. This first metasomatic episode could thus be linked either to subduction of oceanic lithosphere or to the ascent of a mantle plume that led to the current layered SCLM. It resulted in the introduction of garnet (\pm cpx) into the originally depleted Archean lithosphere.

Subsequently, a high-T metasomatic event modified the composition of the garnet peridotites located close to the new lithosphere-asthenosphere boundary. The melts involved in this process were of a mixed nature (carbonatite-silicate) and were responsible for the refertilisation of this layer with both clinopyroxene and garnet.

Percolative fractional crystallisation of these carbonate-silicate melts would explain the late formation of clinopyroxene with a carbonatitic trace-element signature and phlogopite in the upper layer of the SCLM. The differences in the calculated melts in equilibrium with garnet and clinopyroxene in the coarse garnet peridotites is consistent with different metasomatic events for both phases. This carbonatite-related metasomatism took place shortly prior to kimberlite eruption. Alternatively, if clinopyroxene was previously present, cryptic carbonatitic metasomatism could be responsible for its current composition.

The latest metasomatic episode is defined by the crystallisation of fine-grained pyroxene along fractures and grain boundaries in eclogites, clinopyroxene megacrysts and deep garnet-peridotites. The new clinopyroxene is typically more enriched in Ti, Ca, REE and Nb, but commonly depleted in Na, and crystallised together with a second generation of phlogopite. This metasomatism has been linked to kimberlite eruption.

Conclusions

A detailed petrographic and compositional characterisation of 25 mantle xenoliths revealed a complex metasomatic evolution of the SCLM beneath the Lundas kimberlitic province (NE Angola). The shallow and the deeper parts of the lithospheric mantle were modified by different metasomatic processes at different times. The model proposed here includes several episodes of mantle refertilisation after the early Archean depletion, involving silicate, carbonate-silicate and carbonatite-related fluids, as well as late kimberlite-related metasomatism. All these processes significantly modified the composition of the diamond indicator minerals (i.e., garnet and clinopyroxene) and caution should be taken when using them to assess the diamond grade of a kimberlite.

References

- Ashchepkov IV, Rotman a. Y, Somov SV, et al (2012) Composition and thermal structure of the lithospheric mantle beneath kimberlite pipes from the Catoca cluster, Angola. *Tectonophysics* 530–531:128–151. doi: 10.1016/j.tecto.2011.12.007
- Batumike JM, Griffin WL, O'Reilly SY (2009) Lithospheric mantle structure and the diamond potential of kimberlites in southern D.R. Congo. *Lithos* 112:166–176. doi: 10.1016/j.lithos.2009.04.020
- Begg GC, Griffin WL, Natapov LM, et al (2009) The lithospheric architecture of Africa: Seismic tomography, mantle petrology, and tectonic evolution. *Geosphere* 5:23–50. doi: 10.1130/GES00179.1
- Gréau Y, Huang J-X, Griffin WL, et al (2011) Type I eclogites from Roberts Victor kimberlites: Products of extensive mantle metasomatism. *Geochim Cosmochim Acta* 75:6927–6954. doi: 10.1016/j.gca.2011.08.035
- Griffin WL, Fisher NI, Friedman J, et al (1999) Cr-Pyrope Garnets in the Lithospheric Mantle. I. Compositional Systematics and Relations to Tectonic Setting. *J Petrol* 40:679–704. doi: 10.1093/petroj/40.5.679
- McCandless TE, Gurney JJ (1989) Sodium in garnet and potassium in clinopyroxene: criteria for classifying mantle eclogites. In: Ross J, Jacques AL, Ferguson J, Green DH (eds) *Kimberlites and Related rocks*. pp 827–832
- Nikitina LP, Korolev NM, Zinchenko VN, Felix JT (2014) Eclogites from the upper mantle beneath the Kasai Craton (Western Africa): Petrography, whole-rock geochemistry and UPb zircon age. *Precambrian Res* 249:13–32. doi: 10.1016/j.precamres.2014.04.014
- O'Reilly SY, Zhang M, Griffin WL, et al (2009) Ultradeep continental roots and their oceanic remnants: A solution to the geochemical “mantle reservoir” problem? *Lithos* 112:1043–1054. doi: 10.1016/j.lithos.2009.04.028
- Robles-Cruz S, Melgarejo J, Galí S, Escayola M (2012) Major- and Trace-Element Compositions of Indicator Minerals that Occur as Macro- and Megacrysts, and of Xenoliths, from Kimberlites in Northeastern Angola. *Minerals* 2:318–337. doi: 10.3390/min2040318



The principal role of silicic crustal xenolith assimilation in the formation of Kimberley-type pyroclastic kimberlites – a petrographic study of the Renard 65 kimberlite pipe, Canada

Gaudet, M.¹, Kopylova, M.¹, Zhuk, V.²

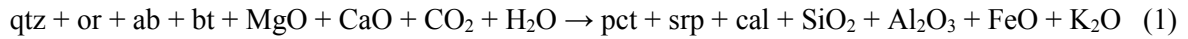
¹ Department of Earth, Ocean and Atmospheric Sciences, University of British Columbia,
mgaudet@eoas.ubc.ca, mkopylova@eoas.ubc.ca

² Stornoway Diamond Corporation, vzhuk@stornowaydiamonds.com

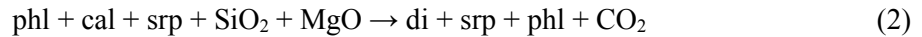
Controversial issues regarding the emplacement processes for Kimberley type pyroclastic kimberlite (KPK) deposits have been 1) whether the pyroclastic textures in KPK rock types reflect the sole effects of magmatic exsolution during emplacement; and 2) whether the characteristic microlitic interclast matrix assemblage of diopside + phlogopite + serpentine in KPK rock types is the product of primary crystallization from the kimberlite magma and associated fluids, or a result of secondary hydrothermal metamorphism of the kimberlite deposit. Solutions to these problems are consequential to an improved understanding of the emplacement-related processes of kimberlite magmas and to the economic modelling of kimberlite deposits. Our extensive petrographic characterization of over 700 m of drill core from four drill hole intersections through the Renard 65 pipe, Quebec, Canada, provides new evidence on the principal role of silicic crustal xenolith assimilation in the formation of KPK deposits.

The Renard 65 pipe is infilled with two distinct phases of kimberlite encompassing rock types ranging in texture from hypabyssal kimberlite (HK) to Kimberley type pyroclastic kimberlite, including a complete suite of rock types with petrographic features intermediate between hypabyssal and Kimberley type pyroclastic kimberlite (HKt/KPKt). Kimb65A is a vertical and roughly cylindrical body of Kimberley type pyroclastic kimberlite containing 40-90 % modal abundance of crustal xenoliths, 5-15 % anhedral calcite-pseudomorphed olivine macrocrysts, and 10-20% spherical magmaclasts containing calcite-pseudomorphed olivine phenocrysts in a groundmass of phlogopite + perovskite + spinel + apatite + titanite + calcite + serpentine; these components are set in a very-fine grained matrix of microlitic diopside + phlogopite + interstitial serpentine, along with heterogeneous distributions of primary perovskite + spinel + apatite. These KPK rock types have a massive and matrix-supported texture, with crustal xenoliths generally appearing sub-angular and weakly reacted. Kimb65B is also a vertical and roughly cylindrical body of kimberlite displaying a sharp, near-vertical contact with Kimb65A. Kimb65B consists of hypabyssal kimberlite in the center of the body, transitioning gradationally into rock types with textures intermediate between coherent kimberlite and Kimberley type pyroclastic kimberlite, towards the outer margins of the body. HK rock types in Kimb65B contain 15-30 % modal abundance of crustal xenoliths, 20-25 % modal abundance of anhedral and partially serpentinized olivine macrocrysts, and 15-20 % modal abundance of subhedral to euhedral serpentinized olivine phenocrysts, all set in a primary groundmass of homogeneously distributed phlogopite + spinel + perovskite + apatite + calcite + serpentine. Crustal xenoliths hosted in HK rock types are of either a dominantly gneissic or granitic composition (representing clasts of a larger, banded, leucocratic granite-gneiss), and are always strongly reacted; they display 1-4 cm thick recrystallized zones composed of anhedral and fine-grained mixtures of calcite + serpentine + pectolite, and very thin sub-millimeter outer monomineralic coronas of diopside (zoned to aegirine), and phlogopite. Over a scale of meters to tens of meters in drill core towards the outer portions of the body of Kimb65B, the texture of the kimberlite changes gradationally towards a rock type in which the groundmass is defined by two distinct assemblages: 1) phlogopite + calcite + serpentine, and 2) microlitic diopside + phlogopite + serpentine. The diopside-rich assemblage forms a patchy texture on a cm-scale and is most pronounced proximal to reacted crustal xenoliths (Figure 1A); these rock types are referred to as HKt rock types. This diopside-rich groundmass assemblage becomes the more dominant assemblage as crustal xenoliths become more abundant towards the outer margins of the body of Kimb65b; these are referred to as KPKt rock types. This change in the mineralogy of the kimberlite groundmass from phlogopite + serpentine + calcite in HK rock types, to diopside + phlogopite + serpentine in transitional HK and KPK rock types, is interpreted to be a consequence of assimilation of silicic xenoliths and

addition of SiO₂, Al₂O₃, FeO, K₂O to the kimberlite magma during emplacement. The recrystallization of granitic xenoliths composed of quartz + orthoclase + albite + biotite to an assemblage of pectolite + serpentine + calcite required the addition of the components CO₂, H₂O, MgO and CaO, all of which would have been readily available in the kimberlite magma (Figure 1B); the components SiO₂, Al₂O₃, FeO and K₂O were produced during this recrystallization reaction (Reaction 1) (Figure 1B).



The consumption of CO₂ and production of SiO₂ during *Reaction 1*, and the reduction in the solubility of CO₂ that would result from an increase in wt% SiO₂ in the magma, stabilizes the crystallization of the diopside-rich assemblage over the diopside-free assemblage as illustrated by *Reaction 2* after (Skinner & Marsh, 2004):



These reactions are interpreted to have been initiated at magmatic temperatures, persisting into subsolidus temperatures, involving significant proportions of crustal xenoliths. The reactions demonstrate that the assimilation of crustal xenoliths and contamination of the kimberlite magmas primarily by Si may have resulted in the enhanced degassing of magmatic volatiles during emplacement. We modelled the effects of crustal xenolith assimilation on kimberlite melt composition and volatile exsolution using geologically constrained abundances of xenoliths in Renard 65 kimberlite and whole rock composition for granitic and gneissic in-situ country rock at Renard. The modelling indicates that SiO₂ content may have increased by 4-9 wt% for KPKt rock types, and 6-13 wt% for HK/HKt rock types. Based on an established negative correlation between the SiO₂ content in melt and CO₂ solubility (Moussallam et al., 2015), this translates into exsolution of 1.4-2 wt% CO₂ at a pressure equivalent depth of 3 km. Therefore, a significant amount (4-20 rel. %) of the CO₂ exsolved during the final 3 km of emplacement may be in response to the assimilation of crustal xenoliths.

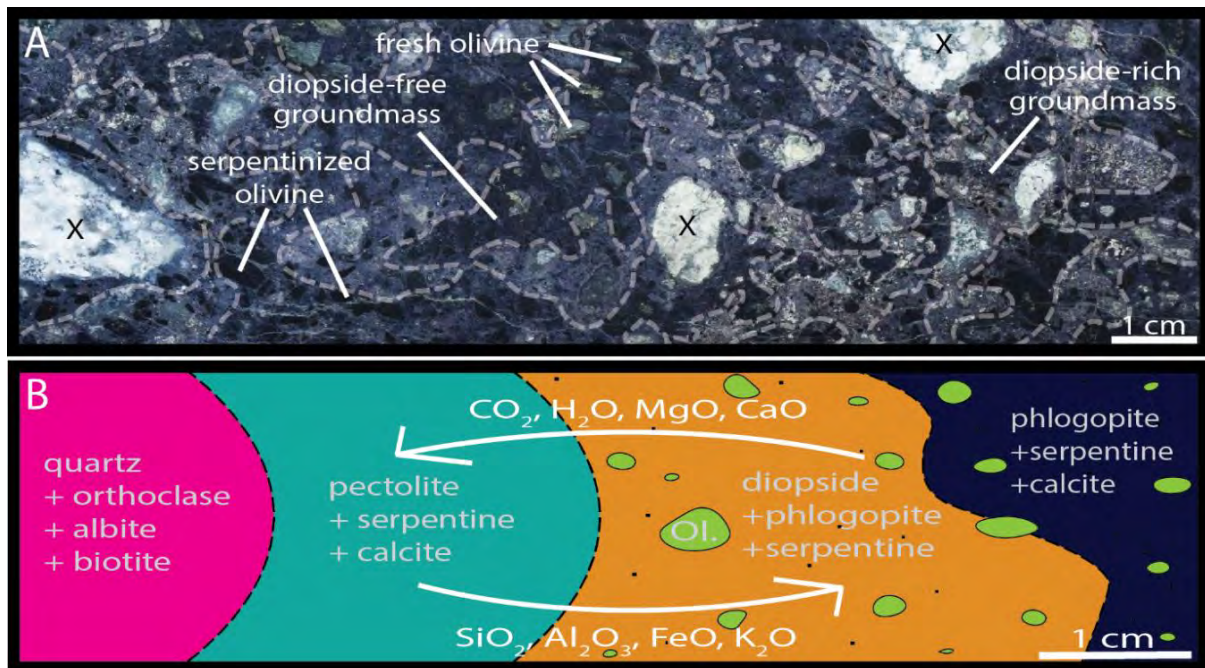


Figure 1 – (A) Transitional coherent kimberlite in polished slab viewed under a binocular microscope showing the patchy distribution of diopside-rich and diopside-free groundmass assemblages; crustal xenoliths are marked with an “x”. (B) The granitic xenolith assemblage of quartz + orthoclase + albite + biotite reacts with oxides MgO, CaO, H₂O and CO₂ in the kimberlite magma, recrystallizing the xenoliths to an assemblage of pectolite + serpentine + calcite and producing oxides SiO₂, Al₂O₃, FeO and K₂O which are assimilated by the kimberlite magma (Reaction 1). The increased activity of SiO₂ in the kimberlite magma results in further exsolution of CO₂ and crystallization of the hybrid groundmass assemblage diopside + phlogopite + serpentine (Reaction 2). Green grains labeled “Ol” are serpentinized olivine macrocrysts.

The formation of KPK rock types in Renard 65 and associated rock types with textures intermediate between hypabyssal and Kimberley type pyroclastic kimberlite reflects the spatial distribution of silicic crustal xenoliths within the magma during emplacement and crystallization. The existing models attributing the formation of KPK rock types to structurally controlled magmatic degassing and fluidization processes, or to hydrothermal alteration of pyroclastic material are inadequate in accounting for both 1) continuous pyroclastic KPK textures to an estimated 1.5 km below the original surface of Renard 65 in Kimb65A, and 2) continuous lateral gradations in rock texture from coherent kimberlite in the center of the body to KPKt towards the margins of Kimb65B. Our alternative model attributing magmatic devolatilization at least in part to the assimilation of silicic crustal xenoliths not only accounts for the distinct mineralogy and textures of Kimberley-type pyroclastic kimberlite rock types, but also for the spatial distribution of these rock types in Renard 65 and other similar kimberlite pipes at Renard and Gahcho Kue. These results further indicate that the differences in the diagnostic mineralogies and textures of Fort-à-la-Corne type and Kimberley type pyroclastic kimberlites may be influenced by the extent of assimilation of silicic crustal xenoliths driving the behavior of the kimberlite magma and magmatic volatiles during emplacement.

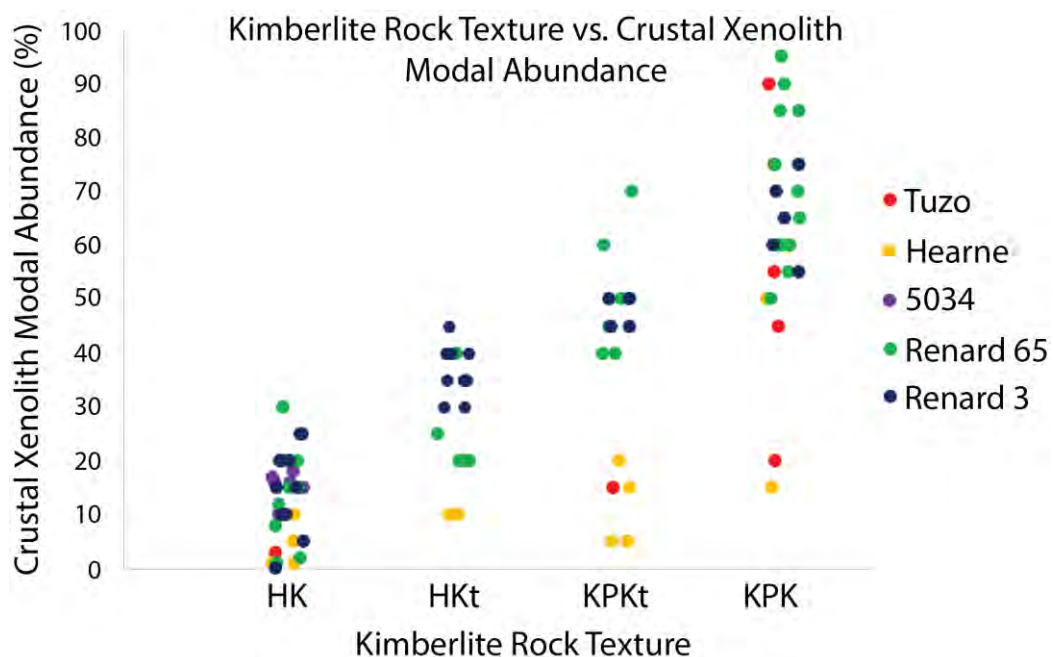


Figure 2 – Correlations between crustal xenolith modal abundances and kimberlite rock textures for kimberlites in multiple pipes from Gahcho Kue (Tuzo, Hearne, 5034) and Renard (Renard 2 & Renard 65). Rock types with transitional to KPK textures in all pipes are associated with increased crustal xenolith modal abundances. Data for the Gahcho Kue pipes Tuzo, Hearne and 5034 are from drill hole summaries in Hetman et al. (2004), and data for the Renard pipes are from drill hole summaries in this research (Renard 65) and geological unit summaries (Renard 3) in Muntener & Scott Smith (2013).

References

- Hetman, C.M., Scott Smith, B.H., Paul, J.L., Winter, F.W., 2004. Geology of the Gahcho Kue kimberlite pipes, NWT, Canada: root to diatreme magmatic transition zones. *Proceedings of the 8th International Kimberlite Conference. Lithos.* 76, pp. 51-74.
- Muntener, C., Scott Smith, B.H., 2013. Economic Geology of Renard 3, Quebec, Canada: A diamondiferous, multi-phase pipe, infilled with hypabyssal and Tuffisitic kimberlite. *Proceedings of the 10th International Kimberlite Conference.* 2, pp. 241-256.
- Moussallam, Y., Morizet, Y., Gaillard, F., 2016. H₂O-CO₂ solubility in low SiO₂-melts and the unique mode of kimberlite degassing and emplacement. *Earth and Planetary Science Letters.* 447, pp. 151-160.
- Skinner, E.M.W., Marsh, S.J., 2004. Distinct kimberlite pipe classes with contrasting eruption processes. *Lithos.* 76, pp. 183-200.

Tracing Lithosphere Melt Compositions using Polymict Peridotites

Lisa Morfi¹, Ben Harte¹, John J. Gurney²

1) School of GeoSciences, University of Edinburgh, Scotland, Great Britain, morfi_lisa@hotmail.com

1) School of GeoSciences, University of Edinburgh, Edinburgh, Scotland, Great Britain, ben.harte@ed.ac.uk

2) Geological Sciences, University of Cape Town, Rondebosch, South Africa, john.gurney@minserv.co.za

Introduction to Polymict Peridotites and related rocks

Polymict peridotites are an exceptional suite of mantle xenoliths recovered from kimberlites in the Kimberley area of South Africa. The xenoliths have breccia-like characteristics and contain rock and mineral fragments (collectively referred to as clasts) usually consisting dominantly of olivine and orthopyroxene. The clasts are embedded in matrix rich in phlogopite together with other silicates, ilmenite, rutile and sulphides. Polymict xenoliths were first described by Lawless et al. (1979, Proc. Int. Kimb. Conf. 2), who considered the matrix to represent a metasomatic fluid. In this submission we will show that this fluid appears to be in equilibrium with silicate and oxide minerals, and was most probably a melt showing similarities to other mantle metasomatic melts (e.g. Harte et al., 1993, Phil. Trans. R. Soc. Lond. A).

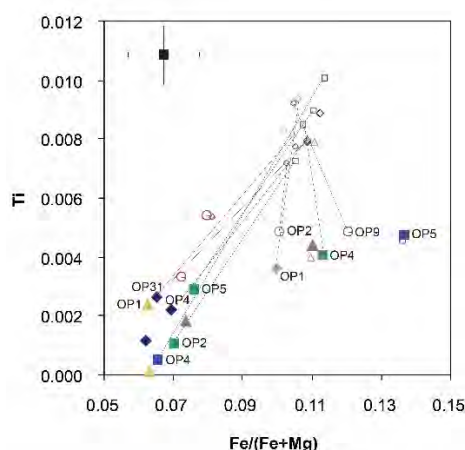


Figure 1: Compositional variations in cations between cores (solid symbols) and rims (open symbols) of orthopyroxene in Polymict Peridotites; tie-lines connect cores and rims of the same grain.

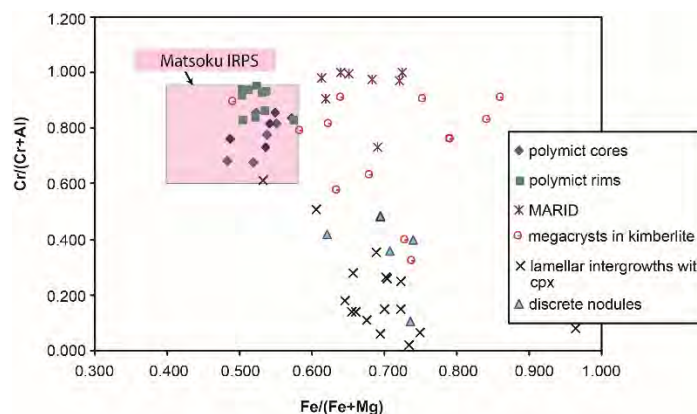


Figure 2: Ilmenite compositions, Cr/(Cr+Al) vs Fe/(Fe+Mg), for Polymict Peridotites and other ilmenite suites. The Matsoku box encompasses ilmenite compositions for Matsoku suite xenoliths.

A detailed electron microprobe and ion microprobe (SIMS) study has been made of eleven polymict xenoliths. The clastic grains are very dominantly minerals related to peridotitic and megacrystic xenolith/xenocryst suites, though a rare eclogite fragment has been identified. The clasts have variable compositions, and many show rims with chemical zoning in major-minor-trace elements. These rims sometimes show complex and oscillatory zoning, but overall the rim compositions of phlogopite, orthopyroxene and garnet show a convergence towards the compositions of these phases in the matrix in each xenolith, and the matrix compositions are believed to indicate the nature of metasomatic infiltrating melt. In one polymict xenolith (BD2394), showing a substantial pool of matrix with orthopyroxene +phlogopite+garnet+ilmenite, there is a close consistency of mineral compositions, and similar compositions are found in the matrix of other polymict xenoliths. In addition these matrix compositions are also closely similar to those found in xenoliths showing intrusive veins and sheets of Matsoku type with the IRPS (ilmenite-rutile-phlogopite sulphide) metasomatic suite (Harte et al. 1993).

These features suggest the possibility that the rim compositions and matrix compositions of the polymict peridotites crystallised from melts similar in composition to those forming veins and sheets in the Matsoku xenoliths. Furthermore, the IRPS minerals in the Matsoku rocks appear to be in equilibrium

with abundant clinopyroxene, garnet, orthopyroxene and olivine (Harte et al., 1987, 1993). The abundance of all these minerals occurring in the Matsoku xenoliths in apparent textural and compositional equilibrium provides an excellent opportunity for determining a wide set of mineral compositions in equilibrium with melt within the lithosphere. Simultaneously, it provides an opportunity for estimating the composition of actual melts involved with the formation of the polymict peridotites and the Matsoku type metasomatic rocks.

Determination of Mineral/Mineral and Melt/Mineral Partition Coefficients.

A set of five xenoliths belonging to the Matsoku IRPS were selected for detailed electron microprobe and ion microprobe analysis at the NERC/Edinburgh University Ion Microprobe Facility (see Burgess and Harte, 2004, for details of analytical techniques). Emphasis was placed upon the Matsoku rocks, rather than the Polymict xenoliths, because of their closer approach to widespread textural and chemical equilibrium. These data were then used to determine melt compositions in the following steps:

a) Trace element compositions were analysed for all phases (clinopyroxene, garnet, orthopyroxene, phlogopite and olivine) in the five selected xenoliths.

b) The partition coefficients of trace elements between different phases were calculated from the analysed mineral compositions (e.g. clinopyroxene ppm/garnet ppm).

c) The average experimental data determined for trace element partitioning between clinopyroxenes and melts by Grutzeck et al. (1974), and Hart and Dunn (1993) were adopted, and the compositions of melts in equilibrium with the clinopyroxene compositions of (a) above calculated.

d) Using the mineral/mineral partition coefficients of (b) in conjunction with the melt compositions determined in (c), a complete set of melt/mineral partition coefficients were obtained for all phases (clinopyroxene, garnet, orthopyroxene, phlogopite and olivine).

e) With an analysis of any one phase, the melt composition in equilibrium with that phase could be calculated. Applying this to several phases in one xenolith, and examining the similarity of melt compositions obtained, also gave a test of the extent to which equilibrium existed between the phases and the validity of the partition coefficients used.

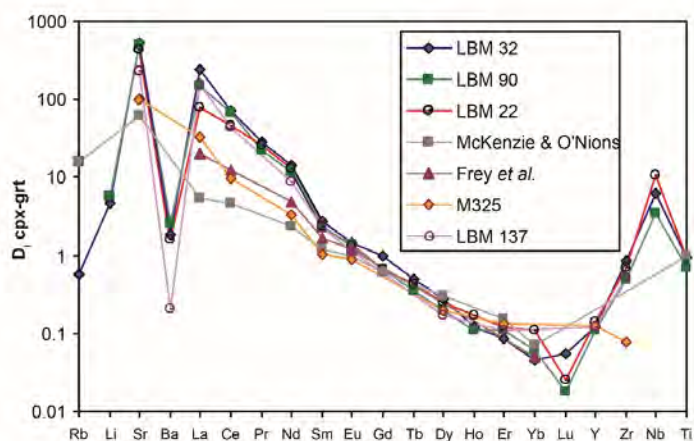


Figure 4: Clinopyroxene-garnet partition coefficients. The LBM data are for Matsoku xenoliths; The data from McKenzie and O'Nions 1991) and Frey et al. (1978) are calculated from their cpx/melt and garnet/melt partition coefficients.

As an example, Figure 4 shows the cpx/garnet partition coefficients

calculated for four Matsoku xenoliths, and the same partition coefficients implied by cpx/melt and garnet/melt data in the publications of McKenzie and O'Nions (1991), and Frey et al. (1978). The consistency of the Matsoku data is apparent. The difference between the Matsoku data and McKenzie and O'Nions data may be attributed to the adoption of data from Shimizu and Kushiro (1975) and the over-estimation of LILE data for garnets at that time (see also Burgess and Harte, 2004).

The newly derived sets of melt/mineral trace element partition coefficients derived from steps (a) to (e) above, have then been used to determine the compositions of the melts associated with the range of polymict xenoliths and IRPS suite xenoliths of Matsoku. Considerable similarities of melt compositions are found using all melt mineral partition coefficients for each xenolith, and between both the Polymict and Matsoku sets of xenoliths.

An extract of this data is shown in Figure 5 using average melt compositions determined using the calculated melt/garnet partition coefficients for the average matrix garnet in polymict BD2394 and Matsoku garnets. As may be seen (Figure 5) the average melt compositions for the BD2394 polymict and the Matsoku suite show considerable similarities to one another. They are also very similar to compositions shown by Type II kimberlites (Tainton 1992). Thus close similarities of melt composition are shown for all these rocks.

Harte et al. (1993) and Burgess and Harte (2004) have

previously suggested that the melts responsible for diverse metasomatic phenomena in Matsoku and Jagersfontein mantle xenoliths, may have been derived by differentiation from the melts giving rise to megacryst suite minerals, which also show similarities to low-percentage melts of the MORB source (Figure 5). In Figure 5, the compositions of melts based on garnet megacrysts and the MORB source show considerable similarities; they also similarities to the BD2394Polymict/Matsoku/Type II kimberlite melts for the heavy REE and Y-Zr-Nb elements. For the LREE and LILE elements, the Polymict/Matsoku/Type II kimberlite compositions show gradually increasing concentrations compared to those seen in the Megacryst and MORB-source melt compositions (Figure 5). This trend to increasing LREE and LILE might be explained by garnet fractionation from Megacryst and MORB-source melts as the percolate upwards through the lithosphere, in a manner similar to that suggested for Jagersfontein percolating melts (Burgess and Harte, 2004).

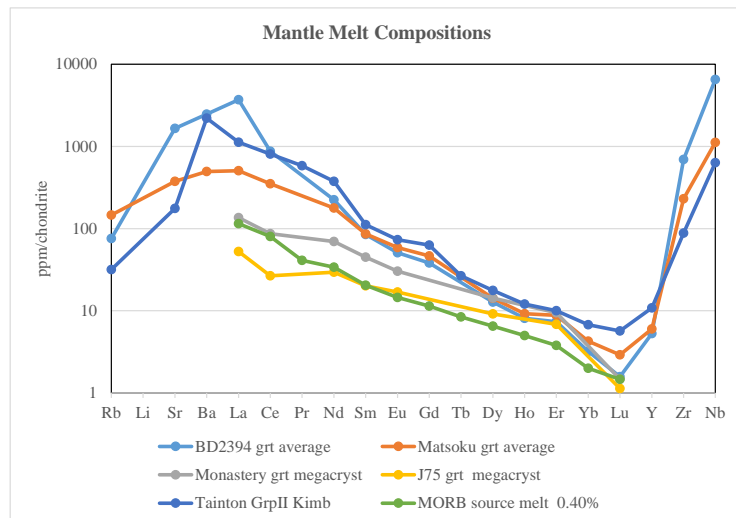


Figure 5. Melt compositions calculated to be in equilibrium with Polymict 2394, Matsoku, and Monastery and Jagersfontein (J75) megacrysts using average garnet compositions. The composition of the 0.4% MORB melt is from Tainton and McKenzie (1994).

References

- Burgess, S.R. & Harte, B. (submitted) Tracing lithosphere evolution through the analysis of heterogeneous G9/G10 garnet in peridotite xenoliths, II: REE chemistry. *J Pet* 45:609-634
- Frey, F.E., Green, D.H., Roy, S.D. (1978) Integrated models of basalt petrogenesis: *J Pet* 19: 463-513.
- Grutzeck M, Kridelbough ., Weill, D. (1974) The distribution of Sr and REE between diopside and silicate liquid. *Geophys Res Lett* 1: 273-275.
- Hart SR, Dunn T (1993) Experimental cpx/melt partitioning of 24 trace elements. *Contrib Min Pet* 113:1-18
- Harte B, Gurney JJ (1975) Ore mineral and phlogopite mineralisation within ultramafic nodules from the Matsoku kimberlite pipe, Lesotho. *Yrbook Carn Inst Wash* 74: 528-536
- Harte B, Hunter RH, Kinny PD (1993) Melt geometry, movement and crystallisation, in relation to mantle dykes, veins and metasomatism. *Phil Trans Roy Soc Lond A* 342:1-21.
- Harte, B., Winterburn, P.A., Gurney, J.J. (1987) Metasomatic phenomena in garnet peridotite facies mantle xenoliths from the Matsoku kimberlite pipe, Lesotho. In: *Mantle Metasomatism*, Acad Press, Lond pp 145-220
- Lawless, P.J., Gurney, J.J., Dawson, J.B. (1979) Polymict peridotites from the Bultfontein and De Beers mines, Kimberley, S. Africa. In: Boyd FR and Meyer HOA (eds) *The mantle sample.*, AGU Washington pp 145-155
- McKenzie D, O’Nions RK (1991) Partial melt distributions from inversion of rare earth element concentrations. *J Pet* 32: 1021-1091
- Shimizu N, Kushiro I (1975) The partitioning of REE between garnet and liquid at high pressure: preliminary experiments. *Geophys Res Letts* 2: 413-416
- Tainton, K.M. (1992) The petrogenesis of Group-2 kimberlites and lamproites from the Northern Cape Province, South Africa. Ph.D. Thesis, Cambridge University of Cambridge



The Petrology of the Kaapvaal Craton Mantle Lithosphere – a synopsis based on Xenolith Field Counts

Ben Harte¹, J. Barry Dawson¹, John J. Gurney², Tim Ivanic³, Steve Richardson²

1) School of GeoSciences, University of Edinburgh, Edinburgh, Scotland, Great Britain, ben.harte@ed.ac.uk

2) Geological Sciences, University of Cape Town, Rondebosch, South Africa, john.gurney@minserv.co.za

2) Geological Sciences, University of Cape Town, Rondebosch, South Africa, steve.richardson@uct.ac.za

3) Department of Mines and Petroleum, Perth, Western Australia, Australia, tim.ivanic@dmp.wa.gov.au.

Introduction

The dumps of rock material from the mining operations of kimberlite pipes in the Northern Cape and Free State (South Africa) towards the end of the 19th century, have provided an invaluable source of mantle xenoliths/nodules for over 100 years. Sampling of these nodules, particularly in the second half of the 20th century, led to selective collecting of the less common rocks (e.g. clinopyroxene-rich samples, deformed peridotites), with the result that the dump exposures became unrepresentative of the original rock proportions. Reworking of the dumps for diamonds around the beginning of the 21st century, led to the exposure of new material. To take advantage of these ‘fresh’ exposures we spent several days on the ground (Figure 1) in November 2004 counting xenolith proportions under the guidance of Jock Robey of De Beers Consolidated mines. At the same time a xenolith count was made at the Letseng La Terae mine in Lesotho. The data collected in 2004 are presented in conjunction with a field count (1979) on the Jagersfontein ‘floors’, and observations on the natural exposures at Matsoku (Lesotho).

Old South African Mine dumps

Xenolith counts were made on areas of reworked dump material at Boshof Road (mainly from the Bultfontein mine), Kenilworth (De Beers mine) and Roberts Victor mine.

The data on xenolith proportions for these three localities are summarised in Figure 2 (the data shown is only for the reworked areas). In addition, data are given on xenolith proportions counted on the old Jagersfontein ‘floors’ in 1979 (by John Gurney, Barry Dawson, Craig Smith and Ben Harte). As expected the most abundant mantle xenoliths at all localities were olivine- and orthopyroxene-rich harzburgites and lherzolites of reasonably coarse grain size, and commonly containing limited amounts (typically estimated at <10 modal %) of garnet and clinopyroxene. Essentially each type of xenolith (harzburgite, lherzolite, and their garnet-bearing varieties) was named according to the presence or absence of clinopyroxene and garnet.

However, rare and small grains of possible clinopyroxene were ignored in many harzburgites. At each locality the common harzburgites, lherzolites, garnet harzburgites and garnet lherzolites appeared to form a continuum with only small variations in mode distinguishing them. Nonetheless, there were some variations from locality to locality in grain size and the overall abundance of clinopyroxene and garnet. Overall the grain sizes were commonly in the range of 1.5 to 7mm; with orthopyroxene tending to be the largest and clinopyroxene the smallest crystals.

The common coarse peridotites described above clearly appear to dominate the lithospheric mantle on the basis of many studies of their temperatures and pressures of formation. They also show modal and bulk compositions indicating depletion in basaltic major-minor elements. Such depletion is evidently



Figure 1: Tim Ivanic, Barry Dawson, Steve Richardson and John Gurney with xenoliths collected on the reworked Kenilworth Flats.

partly offset by the occurrence of injection phenomena in the form of intrusive sheets or veins, or in some cases more pervasive metasomatic infiltration. Such injections are seen in the second major group of peridotitic xenoliths found at Bultfontein and De Beers mines; namely the modal metasomatic and MARID rock group (Figure 2). In the field, the typical minerals of these injection and metasomatic phenomena are: phlogopite, amphiboles, opaque minerals, and clinopyroxene. Elongate crystals, probably of richteritic amphibole, were common in these rocks and presumed to indicate MARID suite xenoliths (Dawson 1987, Erlank et al. 1987). Glimmerites, rich in mica, were included in this grouping.

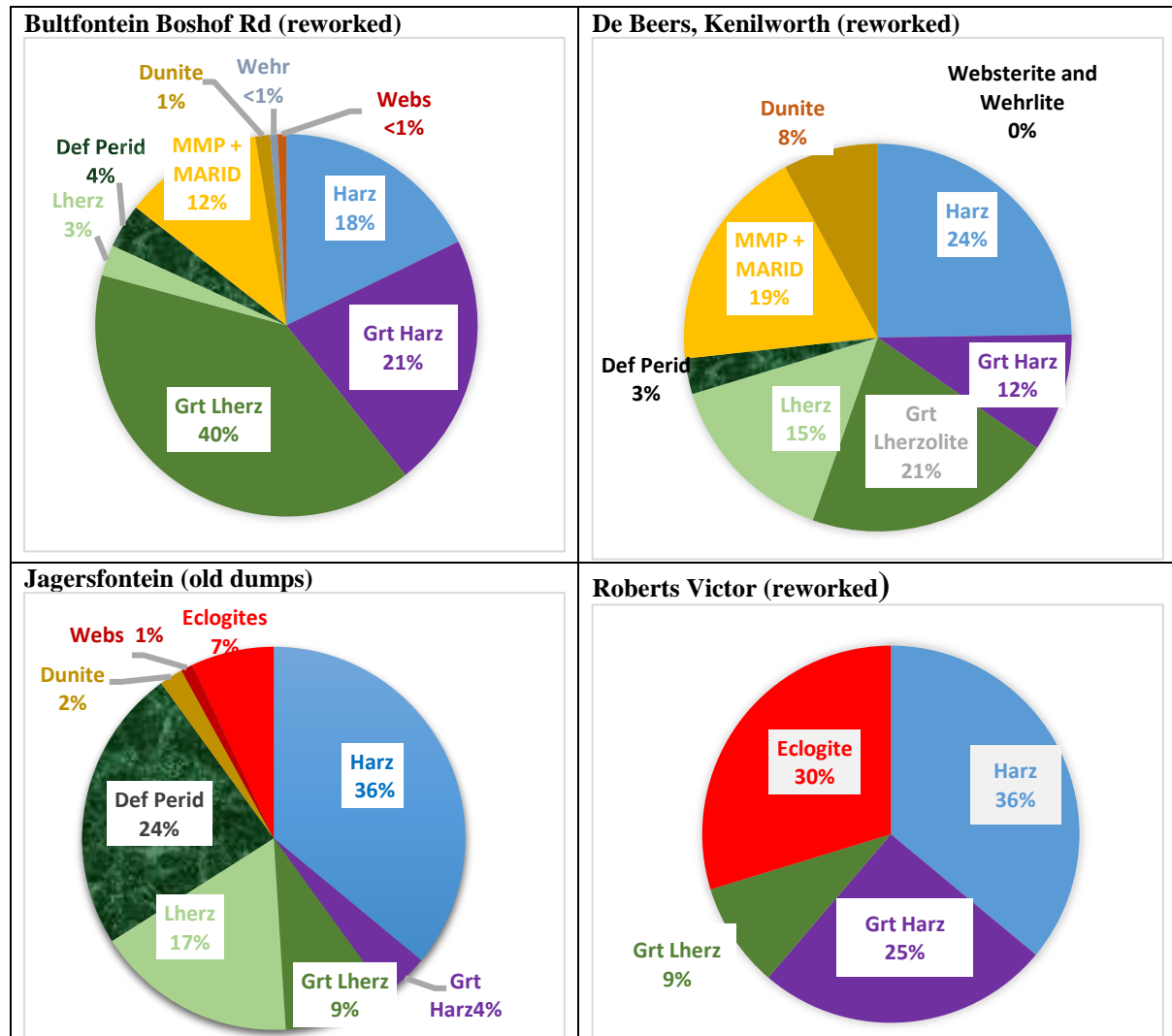


Figure 2: Field counts of xenolith proportions at old diamond mine localities in South Africa. Data based on counts of 804 xenoliths at Boshof Road, 352 at Kenilworth, 355 at Jagersfontein, 111 at Roberts Victor. [harz – coarse harzburgite; lherz – coarse lherzolite; .Def Perid – deformed peridotites; MMP & MARID – Modal Metasomatic & MARID xenoliths; Wehr – wehlite; Webs – websterite; garnet – garnet]

Veined and metasomatised mantle material was not generally recognised at Jagersfontein, where metasomatism involves the presence of an edenitic amphibole (e.g. Johnston 1973; Winterburn et al. 1990). This amphibole is difficult to distinguish from pyroxene in the field and amphibole-bearing xenoliths were not recorded separately from lherzolites. At Roberts Victor the peridotite xenoliths seen in November 2004 were generally very altered (phlogopitised) and mantle metasomatic phenomena were not distinguished, though they have been recorded in the literature.

Deformed peridotites, typically with a foliated character and porphyroclasts of garnet and pyroxene set in a fine-grained matrix of olivine, were a small but regular occurrence at the Bultfontein, De Beers and Jagersfontein localities (Figure 2). Jagersfontein and Roberts Victor were also distinguished by the

presence of eclogites (including kyanite eclogites). The eclogite to peridotite proportions we found at Roberts Victor were well below the >95% eclogite abundance given by Hatton and Gurney (1987).

Lesotho Localities

Unlike the South African localities, the material examined at Letseng La Terae, in November 2004, was discarded and concentrated from the crushing plant (rather than the smooth nodules of the Kimberley dumps, seen in Figure 1). The samples being relatively small were not so readily identified. However, the results of the count were similar to those of Bultfontein and De Beers, except that harzburgites formed a much higher proportion of the coarse peridotites. Dunites and/or deformed and recrystallised megacrysts were also relatively conspicuous.

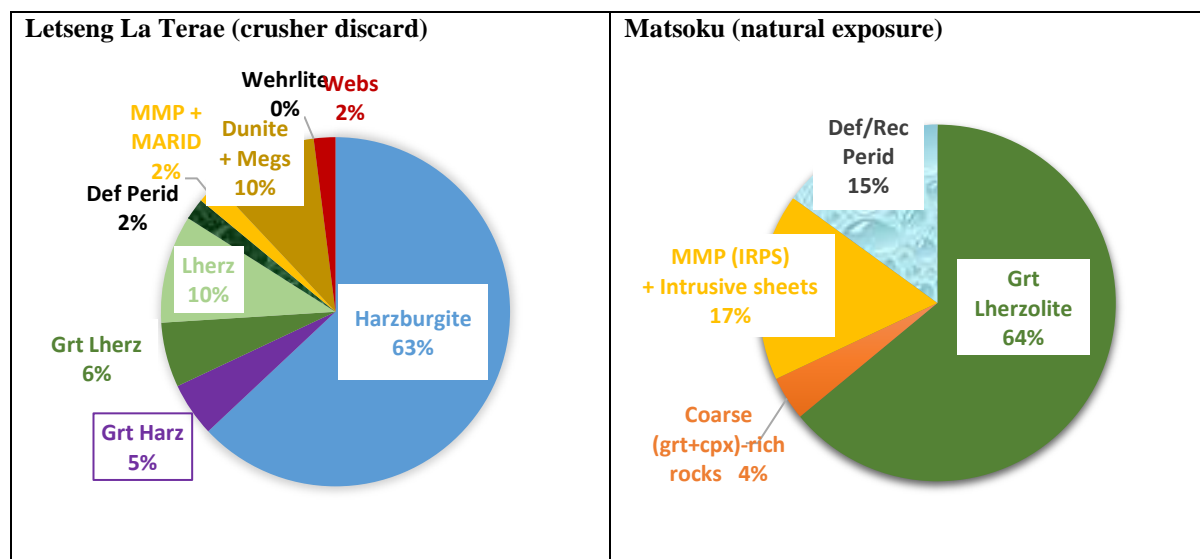


Figure 3: Field counts of Xenolith types at Letseng la Terae and Matsoku, Lesotho. [Abbrevs. as Figure 2]

The Matsoku field count given in Figure 3 is based upon data collected in 1968 and 1973, but is given here to highlight evident variations in the Kaapvaal mantle lithosphere. The Matsoku kimberlite has not been extensively mined, and the mantle xenoliths occur naturally as rocks partly buried in the kimberlitic soil. Coarse peridotites are typically garnet lherzolites, and there is a small group of xenoliths rich in clinopyroxene and garnet (Cox et al. 1973; Harte et al., 1987). Unlike the smooth South African nodules (Figure 1), the xenoliths are frequently angular and may reach sizes of around 0.7m. Many of the larger xenoliths show intrusive sheets or veins, most commonly rich in clinopyroxene, or ilmenite, or phlogopite, but sometimes orthopyroxene and garnet. Amphibole is lacking and they are referred to as the IRPS metasomatic association (Harte et al. 1987). Many peridotites show some evidence of deformation, but such xenoliths show more recrystallisation and grain growth than the Kimberley deformed peridotites; and are referred to as ‘deformed and recovered peridotites’ (Figure 3).

References

- Cox KG, Gurney JJ Harte B (1973) Xenoliths from the Matsoku Pipe. In: Nixon PH (ed) Lesotho Kimberlites, Lesotho national Development Corp., Maseru, pp 76-99
- Dawson JB (1987) The MARID suite of xenoliths in kimberlite: relationship to veined and metasomatised peridotite xenoliths. In: Nixon PH (ed) Mantle Xenoliths, John Wiley & Sons Ltd., Chichester, pp 465-473
- Erlank AJ et al. (1987) Evidence for mantle metasomatism in peridotite nodules from Kimberley pipes, South Africa, In: Menzies MA & Hawkesworth CJ (eds) Mantle metasomatism, Academic Press, London, pp 221-311
- Harte B, Winterburn PA, Gurney JJ (1987) Metasomatic and enrichment phenomena in garnet peridotite facies mantle xenoliths from the Matsoku kimberlite pipe, Lesotho. In: Menzies MA & Hawkesworth CJ (eds) Mantle metasomatism, Academic Press, London, pp 145-220
- Hatton CJ Gurney JJ (1987) Roberts Victor eclogites and their relation to the mantle. In: Nixon PH (ed) Mantle Xenoliths, John Wiley & Sons Ltd., Chichester, pp 465-473
- Johnston JL (1973) Petrology and geochemistry of ultramafic xenoliths from the Jagersfontein Mine, OFS, South Africa. In: Extended Abstracts of the Int. Conf. on Kimberlites, University of Cape Town, pp 181-183
- Winterburn PA, Harte B, Gurney, JJ (1984) Peridotite xenoliths from the Jagersfontein kimberlite pipe. I Primary and primary-metasomatic mineralogy. *Geochim Cosmchim Acta* 54:329-341



Building a Geometallurgical Model for Orapa Diamond Mine, Botswana

Matthew Field¹, Oupa Gilika² Kganetso Maphane², Rebaone Letchuti-Tlawera³ and

¹Amec Foster Wheeler, matthew.field@amecfw.com

²Debswana, Orapa Mine, ogilika@debswana.bw

²Debswana, Orapa Mine, kmaphane2@debswana.bw

³Debswana Corporate Centre, RLetchuti-Tlhalerwa@debswana.bw

⁴Anglo American plc, martin.roberts@angloamerican.com

Introduction

Geometallurgical models have become a major component of the management of ore reserves in many metalliferous mining operations. These models have at their core the mineralogy and other rock characteristics that affect the efficient liberation of the desired metals. For kimberlite ore bodies, the requirements are somewhat different because the optimal extraction of diamonds require a somewhat different approach that focusses on different parts of a typical diamond recovery process plant flow sheet, namely comminution, the removal of fine-grained materials below the economic bottom cut-off size of diamonds (so-called slurry and slimes), dense-media separation (DMS) concentration processes and the final recovery of diamonds from the concentrate. The challenge for building a geometallurgical model for a diamond mine is to identify, quantify and model suitable characteristics in the in-situ ore. This model can then be used to estimate the efficiency of these four main areas of the production plant during ore processing.

At Orapa a great wealth of data has been collected during the most recently completed resource extension project (OREP), but this data was not collected with a geometallurgical fore-thought as an end product. These data include standard geological and geotechnical logging procedures, wet- and dry- bulk density measurements, internal dilution measurements, geotechnical rock hardness measurements, drop-weight testing for comminution parameters, slurry and slimes fraction mineralogy determination by XRD and geochemical analysis of made-up slurry mixtures.

In addition monthly production records from the ore processing plant for the last decade were made available together with the monthly mining blends of ore sourced from different positions in the open pit and from a variety of lithologically controlled stockpiles. These data were used to assess the lithological effects of variable ore on the performance of the process plant over the last decade, and provide confirmation of how the varying characteristics impact plant performance.

Geoscientific Data Acquisition

The following data were selected for modelling for each of the processing areas:

Rock hardness: Rock quality designation (RQD), uniaxial compressive strength (UCS), Brazilain tensile strength, the t_{10} and t_a parameters from drop-weight tests.

DMS Yield: DMS yield percentages obtained by processing large-diameter (24-inch) drill (LDD) product through a DMS bulk sample plant, but adjusting the yields back to insitu mass per sample.

Slurry/Slimes: Mineralogy determined by X-ray diffraction analysis of two size fractions, $-300 \mu\text{m}$ and $-5 \mu\text{m}$. The latter being performed using the glycolation process to ensure accurate identification of clay-mineral species. Also geochemical analyses conducted on slurries made from mixing clay-fraction sample rock powders with samples of Orapa process water. These analyses provided exchange cation concentrations (Na^+ , K^+ , Ca^{2+} and Mg^{2+}) that are used to calculate the sodium-

exchange capacity (ESP) of the slurry, which affects whether clay minerals settle or are dispersed in the slurry.

Final recovery: Specific tests were conducted to determine the percentage of x-ray luminescent gangue minerals in the DMS concentrates of the LDD samples.

Modelling Procedures

After standard exploratory data analysis was completed, each of the datasets were examined to remove extreme outliers where appropriate, and this data was captured in Datamine Studio 3 software where geostatistical analysis was undertaken.

The different variables require different approaches to modelling, since some are considered linear and additive e.g DMS Yield and mineralogy percentages, whilst others are non-additive, e.g the various rock hardness variables. For the former, ordinary kriging can be used for estimation purposes, whilst for the latter multiple indicator kriging was employed, where various threshold values were used and probabilities estimated for each block exceeding those thresholds.

The most recent update of the geological model for Orapa A/K1 (see Maphane et al., this volume) was used for domain control of the estimation process.

Validation of the estimates was conducted using multiple estimation techniques such as nearest neighbour, local average, inverse distance squared and kriging (ordinary or multiple indicator where appropriate). The estimates were compared against each other and against original sample data. In all cases the kriged estimates produced the most satisfactory results that best represent the sample data.

Results

Examples of the outcomes for DMS Yield (an example of a simple additive variable) and uniaxial compressive strength (or UCS – a non-additive variable) are shown in Figure 1 and Figure 2 respectively.

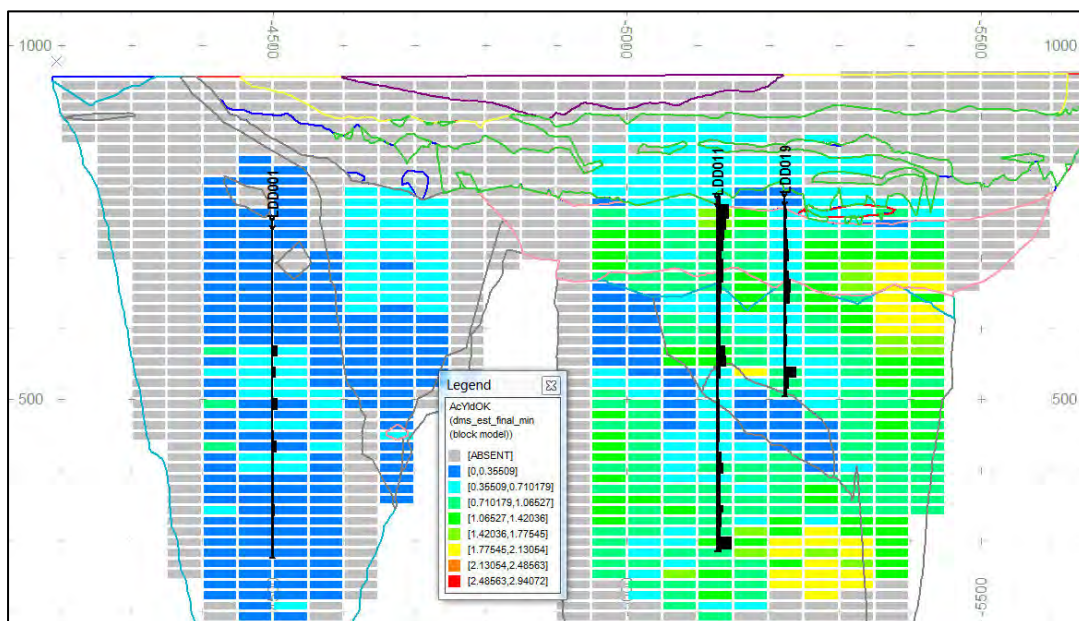


Figure 1: North-south vertical section through Orapa A/K1 with estimated DMS Yield values per block. LDD holes on the section are shown in black. Grid nodes are 100 m x 100 m,

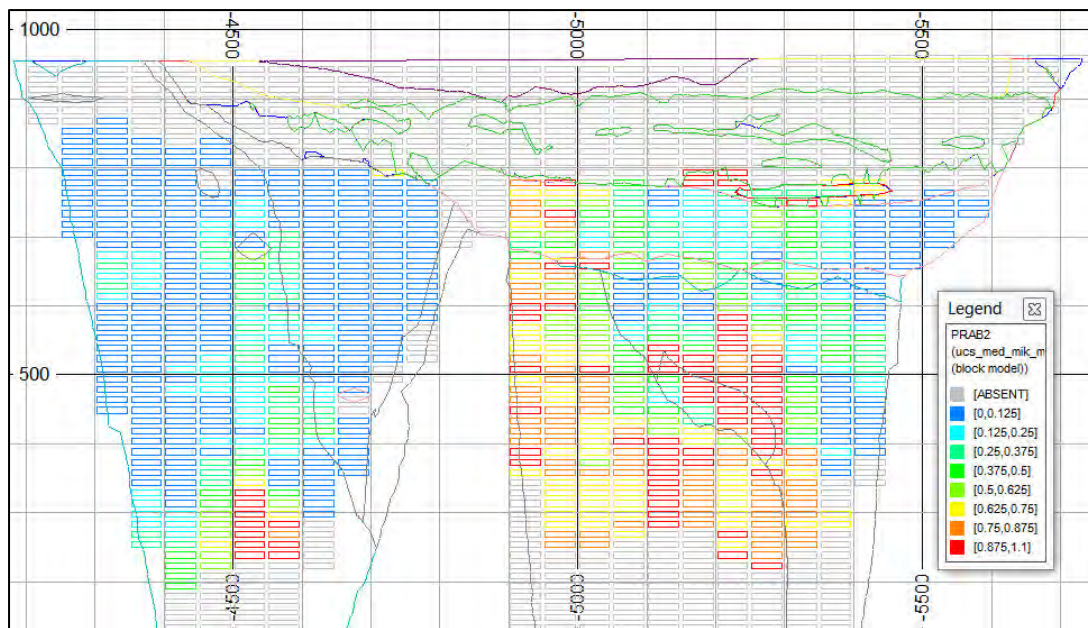


Figure 2: North-south section of Orapa A/K1 with estimated block values of rock hardness here expressed as the probability of UCS exceeding 40 MPa in each block. Grid is 100 m x 100 m.

Production Data Analysis

Production at Orapa is from many different discrete sources (up to 17 in any one month) that include the different lithological domains, but also a variety of stockpiles most of which have a specific lithological source.

The complex relationship between the variety of sources and aggregated monthly measurements taken in the plant, requires specialised statistical analysis. Here cumulative sum and recursive partitioning methods have been applied, and these provide quantitative evidence of the influence of various rock parameters on plant performance. A good example is that the percentage of basalt breccias influences power consumption, but also the quantity of material that does not crush below 25 mm during primary crushing.

All of the parameters measured point to a major change in plant operating conditions when mining transition from the SVK_U and through to the SVK_M geological domain.

Conclusion

All of the data gathered and modelled have been successfully integrated into a geometallurgical model, that not only validates the geological model, but also provides Orapa mine planners with a tool to evaluate future production scenario regarding plant throughput efficiencies. This has been achieved through using standard geological and geotechnical measurements on drill cores obtained during the resource extension project, supplemented with specific metallurgical sampling campaigns on core that remained once all other sampling had been completed.

References

Maphane, K, 2017, Evolution of the Orapa A/K1 Geology Model – Insights from Analysis of Multi-Disciplinary Datasets

Geochemistry of peridotitic clinopyroxene from the diamondiferous Mbuji-Mayi and Tshibwe kimberlites (DRC): Insight into the compositional and thermal State of the SCLM beneath the northeastern Kasai Craton

B. Jaziel Nkere^{1*}, Philip E. Janney¹

¹Department of Geological Sciences, University of Cape Town, Rondebosch 7701, South Africa

Introduction and major element systematics

The composition of clinopyroxenes from heavy mineral concentrates of the diamondiferous Mbuji-Mayi and Tshibwe kimberlites in the DRC have been studied to constrain the thermal and compositional state of the lithospheric mantle underlying the northeastern section of the Archaean Kasai craton of central Africa. Clinopyroxenes from Mbuji-Mayi fall into two populations, a larger subcalcic group (group 1; with Ca# between 41 and 45) and a smaller calcic group (group 2; with Ca# between 45 and 47) with group 2 cpx showing overall lower Al₂O₃ values and a trend of decreasing Al₂O₃ with increasing Ca# (Fig. 1). The group 1 cpx show an increase in Al₂O₃ contents with increasing Ca#. Both groups are relatively Cr-rich (Cr# ranging between 17.7 and 69.1) with group 1 having higher Cr contents, but they both show a broad increase of Cr# with increasing Mg#, and both groups display a broad range of Mg# (from 88.5 to 94 with group 2 cpx having higher Mg# on average than group 1). Both groups have high Na₂O contents (ranging between 1.5 to 3.6 wt %) with group 1 extending to higher Na₂O contents. Contents of TiO₂ and Na₂O decrease with increasing Ca# in group 2 while no correlation is observed in group 1.

Clinopyroxenes from the Tshibwe kimberlite are very similar to the Mbuji-Mayi group 2 clinopyroxenes in terms of their major element compositions. However, they extend to slightly higher Ca# values (44 – 48) and lower Al₂O₃, lower TiO₂ (0.22 – 0.05 wt.%) and lower Na₂O (1.7 – 1.18 wt.%) than Mbuji-Mayi clinopyroxenes.

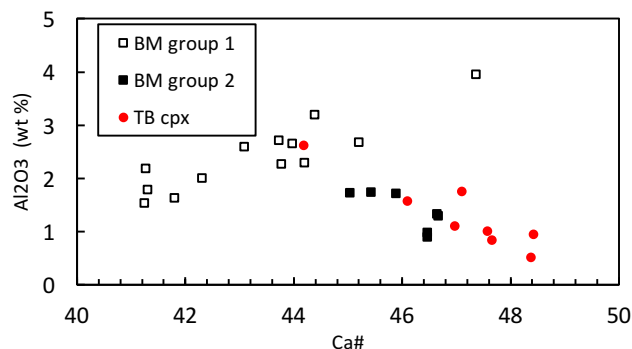


Figure 1: Ca# (Ca/(Ca+Mg) in atomic units) plotted versus wt.% Al₂O₃ in peridotitic clinopyroxenes from concentrate from Mbuji-Mayi (BM groups 1 and 2) and Tshibwe (TB). Note the distinct trends formed by the BM group 1 and TB data.

Trace element and Sr isotope systematics

Trace element patterns of Mbuji-Mayi group 1 and group 2 clinopyroxenes are similar. They show fairly uniform convex upward and LREE enriched REE patterns with group 1 cpx extending to greater extents of LREE enrichment than group 2 cpx ((Nd/Yb)_N = 22.1 – 100.1 and 22.5 – 55.1 for group 1 and group 2, respectively). Both group 1 and 2 cpx show relative depletions in Ba, Pb, Zr and Ti relative to elements of similar incompatibility, but the depletions in Group 1 are stronger (Fig. 2c).

Trace element patterns of Tshibwe clinopyroxenes are very similar to Mbuji-Mayi group 2 clinopyroxenes, but with slightly less LREE-enrichment on average (most Tshibwe cpx have (Nd/Yb)_N ratios between 30.5 and 38.7). However one Tshibwe cpx grains have anomalously high (Nd/Yb)_N value of 150.5 with (Sc/V)_N ratios lower than unity (0.87; Fig. 2a).

Clinopyroxenes from Mbuji-Mayi and Tshibwe span nearly identical ranges of measured ⁸⁷Sr/⁸⁶Sr (with ranges of 0.7031 – 0.7052 and 0.7035 – 0.7053, respectively), falling within the range of Group I kimberlites (including Mbuji-Mayi; Weis & Demaiffe, 1985) and PIC rocks (as summarised by Grégoire, 2002).

Thermobarometry

The P–T equilibration conditions of peridotitic concentrate clinopyroxenes from the Mbuji-Mayi and Tshibwe kimberlites were estimated using the clinopyroxene thermobarometer of Nimis and Taylor (2000). Based on these P – T estimates, clinopyroxenes from Mbuji-Mayi and Tshibwe define a compositional and thermal profile through the northeastern Kasai craton to depths as great as 220 km, a depth consistent with previous thermobarometry and geophysical studies (Batumike et al., 2009; Crosby et al., 2010). The two kimberlites sampled and entrained clinopyroxenes from a pressure and temperature interval between 26 and 72 kbar and 967 to 1264 °C. However, the continental lithospheric mantle beneath Tshibwe, on average, was cooler (with an average thermal gradient of 20°C per kb) than at Mbuji-Mayi (with an average thermal gradient of 26°C per kb) (Fig. 2b)

Origin of clinopyroxenes

Clinopyroxenes from Mbuji-Mayi and Tshibwe show typical peridotitic major element compositions, with high Mg# and with Cr₂O₃ and Al₂O₃ concentrations that plot in the field associated with garnet-bearing lherzolites (Nimis, 1998). Moreover, the REE concentrations and profiles of Mbuji-Mayi and Tshibwe clinopyroxenes are also similar to those reported for diopsides from “type 1” metasomatised garnet lherzolites (Grégoire et al., 2003) from some Kaapvaal kimberlites.

Group 1 clinopyroxenes from Mbuji-Mayi have (Sc/V)_N ratios lower than unity (0.41 – 0.99), typical of clinopyroxenes from garnet lherzolites (Glaser et al., 1999; Barth et al., 2001). Therefore, the group 1 clinopyroxenes likely originated from metasomatised garnet lherzolite. Group 2 cpx from Mbuji-Mayi and Tshibwe cpx have (Sc/V)_N ratios greater than unity (with ranges of 1.01 – 2.19 and 1.14 – 2.56, respectively), suggesting derivation from a mantle lithology with little to no garnet present. This could indicate a highly infertile garnet lherzolitic or possibly a garnet-free peridotitic or pyroxenitic source.

Peridotitic garnets occur, though not abundantly, in the concentrate from these kimberlites. It is therefore likely that garnet lherzolite is the main lithology beneath the northeastern section of the Congo-Kasai Craton. The SCLM beneath Mbuji-Mayi appears to have a higher proportion of garnet lherzolite while the SCLM beneath Tshibwe appears to have a more garnet-depleted lithological character.

Metasomatism

Primitive mantle-normalised incompatible element patterns both in Tshibwe and Mbuji-Mayi clinopyroxenes show evidence of kimberlite-related metasomatism, which is supported by the large degree of Sr isotopic overlap between the clinopyroxenes and whole-rock ⁸⁷Sr/⁸⁶Sr values for Mbuji-Mayi kimberlites (Weis & Demaiffe, 1985). However, it appears that Mbuji-Mayi clinopyroxenes have undergone more extensive metasomatism (stronger LREE enrichment, higher overall incompatible element contents) than at Tshibwe. Therefore, the mantle sampled by the Mbuji-Mayi kimberlites appears to have been warmer and metasomatically more disturbed compared to the cooler and more depleted lithosphere sampled by the Tshibwe kimberlite cluster. The occurrence of different thermal and metasomatic states in mantle located in close proximity (within 35 km) suggests that the Tshibwe cluster kimberlites may have been emplaced prior to Mbuji-Mayi (70 Ma) (Schärer et al., 1997) and prior to major thermal and metasomatic disturbance of the SCLM.

Acknowledgements

Support for this work was generously provided by the South African National Research Foundation to BJN and PEJ, and by the Society for Economic Geologists through a grant to BJN.

References

- Barth, M.G., Rudnick, R.L., Horn, I., McDonough, W.F., Spicuzza, M.J., Valley, J.W., Haggerty, S.E., 2001. Geochemistry of xenolithic eclogites from West Africa, part I: a link between low MgO eclogites and Archean crust formation. *Geochimica et Cosmochimica Acta* **65**, 1499–1527.
- Batumike, J.M., Griffin, W.L., O'Reilly, S.Y., 2009. Lithospheric mantle structure and the diamond potential of kimberlites in southern D.R. Congo. *Lithos* **112** (S1), 166–176.
- Crosby AG, Fishwick S, White N (2010). Structure and evolution of the intracratonic Congo Basin. *Geochemistry Geophysics Geosystems* **11**: Q06010.
- Glaser, S.M., Foley, S.F., Günther, D., 1999. Trace element compositions of minerals in garnet and spinel peridotite xenoliths from the Vitim volcanic field, Transbaikalia, eastern Siberia. *Lithos* **48**, 263–285.
- Grégoire, M., Bell, D.R., Le Roex, A.P., 2002. Trace element geochemistry of phlogopite- rich mantle xenoliths: their classification and their relationship to phlogopite- bearing peridotites and kimberlites revisited. *Contributions to Mineralogy and Petrology* **142**, 603–625.
- Grégoire, M., Bell, D.R., Le Roex, A.P., 2003. Garnet lherzolites from the Kaapvaal craton (South Africa): trace element evidence for a metasomatic history. *Journal of Petrology* **44**, 629–657.
- Nimis, P., 1998. Evaluation of diamond potential from the composition of peridotitic chromian diopside. *European Journal of Mineralogy* **10**, 505 – 519.
- Nimis, P., Taylor, W.R., 2000. Single clinopyroxene thermobarometry for garnet peridotites. Part I. Calibration and testing of a Cr-in-Cpx barometer and an enstatite-in-Cpx thermometer. *Contributions to Mineralogy and Petrology* **139**, 541–554.
- Schärer, U., Corfu, F., Demaiffe, D., 1997. U–Pb and Lu–Hf isotopes in baddeleyite and zircon megacrysts from the Mbuji-Mayi kimberlite: constraints on the subcontinental mantle. *Chemical Geology* **143**, 1–16.
- Weis, D., Demaiffe, D., 1985. A depleted mantle source for kimberlites from Zaire: Nd, Sr and Pb isotopic evidence. *Earth and Planetary Science Letters* **73**, 269–277.

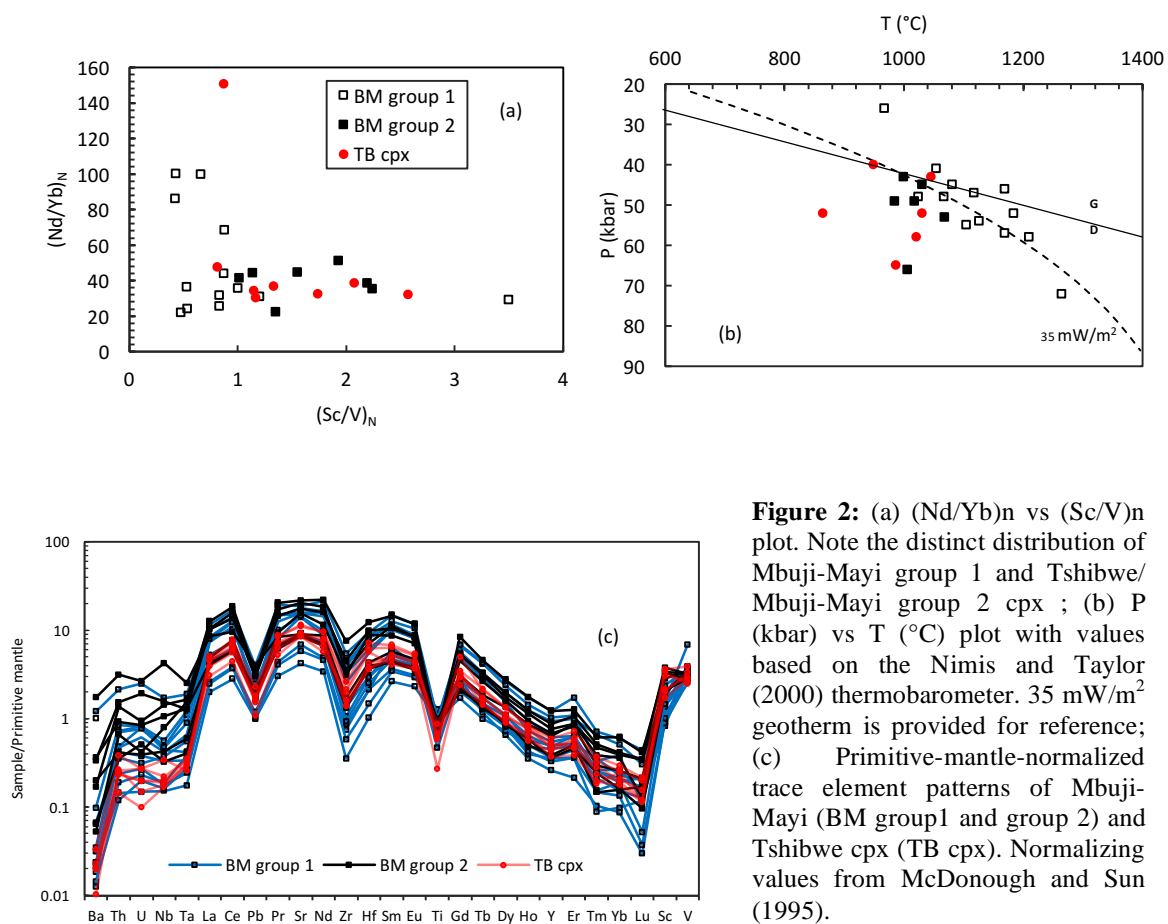


Figure 2: (a) $(\text{Nd}/\text{Yb})_n$ vs $(\text{Sc}/\text{V})_n$ plot. Note the distinct distribution of Mbuji-Mayi group 1 and Tshibwe/Mbuji-Mayi group 2 cpx ; (b) P (kbar) vs T (°C) plot with values based on the Nimis and Taylor (2000) thermobarometer. $35 \text{ mW}/\text{m}^2$ geotherm is provided for reference; (c) Primitive-mantle-normalized trace element patterns of Mbuji-Mayi (BM group1 and group 2) and Tshibwe cpx (TB cpx). Normalizing values from McDonough and Sun (1995).



Ages and sources of mantle eclogites: ID-TIMS U-Pb-Sr isotope systematics of clinopyroxene

Larry M. Heaman¹, Sonja Aulbach², Dorrit Jacob³, K.S. Viljoen⁴

¹University of Alberta, Edmonton AB, Canada, lheaman@ualberta.ca

²Goethe University, Frankfurt am Main, Germany, s.aulbach@em.uni-frankfurt.de

³Macquarie University, North Ryde, Australia, dorrit.jacob@mq.edu.au

⁴University of Johannesburg, Johannesburg, South Africa, fanusv@uj.ac.za

Background and motivation

Mantle eclogites form an integral, in cases dominant, part of most kimberlite-borne xenolith suites. They have been variously interpreted as representing the metamorphosed equivalents of underplated high-pressure melts or of subducted oceanic crust (Jacob 2004). However, it has proven notoriously difficult to extract meaningful age information from the radiogenic isotope systematics of mantle eclogites. In addition, clinopyroxene (cpx), a major carrier of incompatible lithophile elements, including the parent elements of most commonly used radioactive decay systems, is frequently altered. This can preclude separation of enough pristine material for accurate and precise analysis by common mass spectrometric techniques and hinders efforts to unravel the origins and evolution of mantle eclogites and to link their formation to regional or global tectonothermal events.

The advent of highly sensitive inductively coupled plasma mass spectrometers (ICPMS) combined with laser ablation (LA) devices has in recent years led to radical advances in *in situ* dating techniques, among them the acquisition of Pb isotopic compositions of cpx in eclogites (Schmidberger et al. 2007). Such data have yielded valuable model Pb isotope age constraints, but their interpretation is difficult as it is sensitive to both the choice of model Pb evolution curve and the assumption that cpx is essentially U-free. A survey of the literature, however, indicates that eclogitic cpx contains median U and Pb concentrations of 0.01 and 0.5 ppm, respectively, with U/Pb of 0.02, which can generate measurable amounts of radiogenic Pb over the typically billion-year histories of mantle eclogites. In order to further test the veracity of *in situ* cpx Pb and Sr isotope measurements, we determined the U-Pb, Pb-Pb and Sr isotope compositions of cpx from three African eclogite suites by both LA-ICPMS and isotope dilution thermal ionisation mass spectrometry (ID-TIMS).

Samples and Methods

The samples form part of three well-characterised mantle eclogite suites. Two suites from southern African kimberlites (Lace and Orapa) have major- and trace-element relationships indicative of oceanic crustal protoliths (Aulbach and Viljoen 2015; unpubl. data). Some of the Lace eclogites formed in the Archaean, given highly unradiogenic Pb in two samples (Aulbach and Viljoen 2015), but multiple formation and/or modification ages from Proterozoic to Archaean are indicated for Orapa, based on Re-Os dating of sulphide inclusions in eclogitic diamonds (Shirey et al. 2008). Eclogites from Koidu (West African Craton) comprise two distinct suites, with low-Mg eclogites (ca. 3.4 Ga Re-Os whole rock age array) interpreted as subducted oceanic crust and high-Mg eclogites as continental cumulates that foundered into the underlying lithospheric mantle (Barth et al. 2001, 2002).

In situ Pb isotope compositions were determined by LA-ICPMS using a NuPlasma 1 multi-collector ICPMS coupled to a 213 nm New Wave Nd:YAG laser system in the Canadian Center for Isotopic Microanalysis (CCIM), University of Alberta, following the procedure previously described for cpx in mantle eclogites (Schmidberger et al., 2007). *In situ* Sr isotope ratios were acquired in static collection mode with Faraday cups at Goethe-University Frankfurt, using the RESolution (Resonetics) 193nm ArF Excimer Laser (CompexPro 102, Coherent) linked to a Thermo Finnigan Neptune multi-collector ICPMS, following methods outlined in Aulbach et al. (2016). Optically clean cpx separates (typically 1-2 mg) were leached 24h in ~6M HCl and another 24h in Millipore or MQ H₂O. Dry samples were weighed and spiked with a mixed ²⁰⁵Pb-²³⁵U spike, followed by column chromatography to produce

purified Sr, Pb and U fractions. All ID-TIMS analyses were conducted at CCIM. The isotopic compositions of U and Pb were measured using a VG354 (Daly photomultiplier detector mode) and Thermo Triton Plus (single SEM) TIMS. Purified Sr fractions were run on a Sector 54 TIMS operating in static multi-Faraday detector mode.

Preliminary Results and Discussion

We have obtained ID-TIMS (solution) and LA-ICPMS (*in situ*) Pb isotopic data for most eclogite cpx samples (total of 25 xenoliths). For most xenoliths (n=21), at least two multi-grain (n~10 grains) cpx fractions were analysed by ID-TIMS to evaluate repeatability; for the majority of these (14/21) the Pb isotopic compositions agree within analytical uncertainty. Those that have variable Pb isotopic compositions outside analytical uncertainty reflect a multi-component Pb record within a single cpx population. ID-TIMS results for acid-leached eclogitic cpx in this study indicate a moderate range in uranium (0.004-0.369 ppm) and model Th (0.006-5.845 ppm) contents. We have evaluated the effect of an HCl acid-leaching treatment on the Pb isotopic composition of two eclogitic cpx samples. In one case the unleached cpx has U and Th contents and $^{238}\text{U}/^{204}\text{Pb}$ values that are a factor of 10 higher than leached cpx, indicating the presence of labile U and Th. In contrast, the effect of leaching on cpx Pb contents and Pb isotopic ratios is negligible (<1% change in compositions). Leached eclogitic cpx typically have relatively low $^{238}\text{U}/^{204}\text{Pb}$ values (<40; n=41/46), however for ancient xenoliths this corresponds to a significant correction for in-growth of radiogenic Pb in Pb-Pb dating studies. In some cases, variable U concentrations at relatively homogeneous Th and Pb contents of multiple leached aliquots suggests that some labile U can remain after the HCl-leaching treatment.

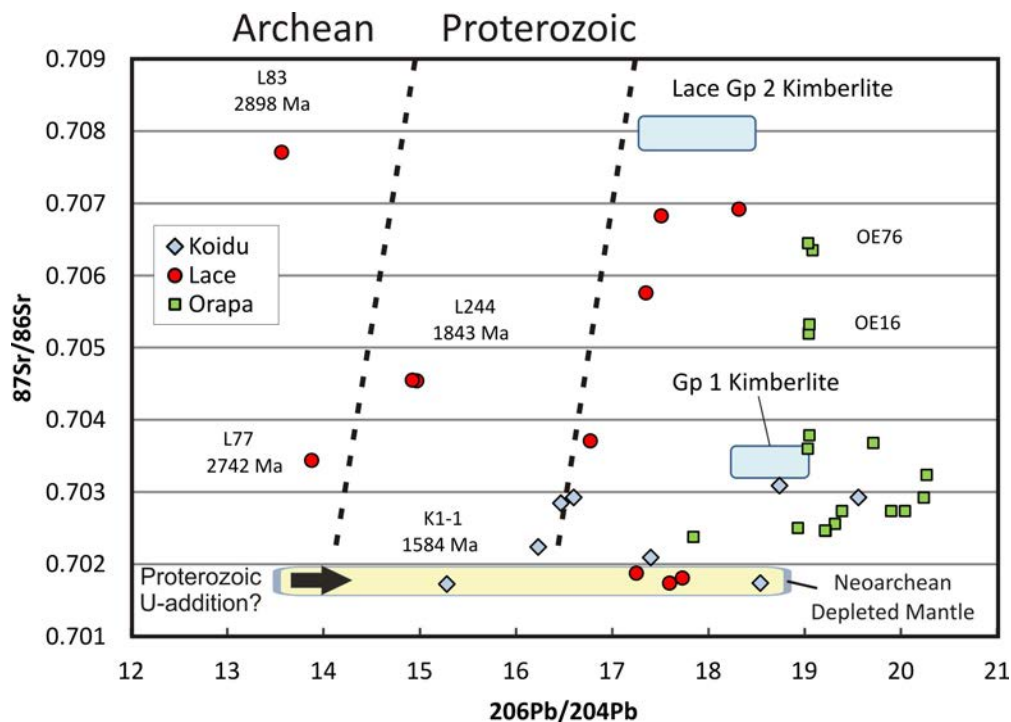


Figure 1. Measured $^{87}\text{Sr}/^{86}\text{Sr}$ versus $^{206}\text{Pb}/^{204}\text{Pb}$ obtained by ID-TIMS for cpx in three eclogite xenolith suites.

Preliminary results show that acid-leached eclogitic cpx with low U contents and matching *in situ* and solution Pb isotope ratios can contain a significant component of radiogenic Pb (up to 10%); hence *in situ* Pb-Pb cpx analyses commonly do not reflect their initial Pb isotopic compositions, resulting in underestimated/inaccurate Pb-Pb model ages. The ID-TIMS cpx data for Lace ($^{206}\text{Pb}/^{204}\text{Pb}$ =13.54-18.32), Koidu (16.25-19.56), and Orapa (17.92-20.27) eclogites define crude linear arrays on Pb-Pb plots with Paleoproterozoic secondary isochron dates (2.15, 2.24 and 1.80 Ga, respectively). Two cpx fractions from Lace eclogite L83, which have high Pb contents (~6 ppm), unradiogenic Pb isotopic

compositions ($^{206}\text{Pb}/^{204}\text{Pb}=13.57\text{-}13.52$), the lowest $^{238}\text{U}/^{204}\text{Pb}$ values (1.0-1.5), and ancient single-stage model Pb dates (2.90-2.84 Ga; minimum estimates for their formation) support an Archaean formation age.

All eclogite suites display a large range in $^{87}\text{Sr}/^{86}\text{Sr}$ values (Figure 1; total range is 0.7017-0.7077) and there is general agreement for most samples between *in situ* and solution results. Several eclogites, representing examples from each suite, have Neoproterozoic depleted mantle-like $^{87}\text{Sr}/^{86}\text{Sr}$ values (0.7017-0.7025), consistent with a subducted oceanic lithosphere protolith. The origin of cpx with radiogenic strontium isotopic compositions is less clear. In some instances there may be cryptic metasomatism caused by the host kimberlite, some Lace eclogites have cpx compositions approaching that of the Lace kimberlite ($^{87}\text{Sr}/^{86}\text{Sr}=0.7072\text{-}0.7084$; Howarth et al. 2011). In others the compositions are more radiogenic than the host kimberlite so likely reflect metasomatic processes influencing the xenoliths prior to entrainment in kimberlite magma. An interesting feature of this study is that Sr and Pb isotopes do not always show coherent behaviour in eclogite cpx; radiogenic Pb (>> Depleted Mantle) is observed in samples with restricted depleted mantle-like $^{87}\text{Sr}/^{86}\text{Sr}$, perhaps due to heterogeneous contributions from various slab components, as previously suggested (Aulbach et al. 2016). Taken together, two pieces of isotopic evidence indicate that some Lace and Koidu eclogites are Archaean: 1) Unradiogenic Pb as described above and 2) very low $^{87}\text{Sr}/^{86}\text{Sr}$ in some xenoliths. In this scenario, the secondary isochrons recorded by Lace and Koidu xenoliths are interpreted as Palaeoproterozoic metasomatic overprint events.

Although this must be regarded as work in progress, our preliminary results confirm that the conclusions arrived at based on both the cpx Pb and Sr LA-ICPMS and ID-TIMS isotopic techniques are the same. *In situ* LA-ICPMS Pb-Pb isotope acquisition is a high-throughput method that provides guidance for sample targeting for the more precise yet highly time-intensive solution work. Together with *in situ* Sr isotope determination it further serves as a valuable check on the purity of the separated cpx with respect to kimberlite contamination. Finally, this study highlights that a ID-TIMS U-Pb study of cpx has the potential to provide geologically meaningful minimum formation ages for mantle eclogites, as well as their source compositions and evolution.

References

- Aulbach S, Gerdes A, Viljoen KS (2016) Formation of diamondiferous kyanite-eclogite in a subduction melange. *Geochim Cosmochim Acta* 179:156-176
- Aulbach S, Viljoen KS (2015) Eclogite xenoliths from the Lace kimberlite, Kaapvaal craton: From convecting mantle source to palaeo-ocean floor and back. *Earth Planet Sci Lett* 431:274-286
- Barth MG, Rudnick RL, Carlson RW, Horn I, McDonough WF (2002) Re-Os and U-Pb geochronological constraints on the eclogite-tonalite connection in the Archaean Man Shield, West Africa. *Precamb Res* 118:267-283
- Barth MG, Rudnick RL, Horn I, McDonough WF, Spicuzza MJ, Valley JW, Haggerty SE (2001) Geochemistry of xenolithic eclogites from West Africa, Part I: A link between low MgO eclogites and Archaean crust formation. *Geochim Cosmochim Acta* 65(9):1499-1527
- Howarth GH, Michael E, Skinner W, Prevec SA (2011) Petrology of the hypabyssal kimberlite of the Kroonstad group II kimberlite (orangeite) cluster, South Africa: Evolution of the magma within the cluster. *Lithos* 125:795-808
- Jacob DE (2004) Nature and origin of eclogite xenoliths from kimberlites. *Lithos* 77(1-4):295-316
- Schmidberger SS, Simonetti A, Heaman LM, Creaser RA, Whiteford S (2007) Lu-Hf, in-situ Sr and Pb isotope and trace element systematics for mantle eclogites from the Diavik diamond mine: Evidence for Paleoproterozoic subduction beneath the Slave craton, Canada. *Earth Planet Sci Lett* 254(1-2):55-68
- Shirey SB, Richardson SH, Harris JW (2008) Mesoarchean to Mesoproterozoic Re-Os ages for sulfide inclusions in Orapa diamonds and implications for Kaapvaal-Zimbabwe craton development. In: 9th Int Kimb Conf, Frankfurt, Germany, Ext Abstr No. 9IKC-A-00365, 02008



Mineralogy of Kimberley-type Pyroclastic Kimberlite and the Transition to Hypabyssal Kimberlite

Roger H. Mitchell¹ and Barbara H. Scott Smith²

¹ Lakehead University, Thunder Bay, Canada, rmitchel@lakeheadu.ca

² Scott-Smith Petrology Inc., North Vancouver, Canada, barbara@scottsmithpetrology.com

Introduction

Kimberley-type pyroclastic kimberlite (KPK; formerly tuffisitic kimberlite) is one of two classes of pyroclastic kimberlite. KPK is unique to kimberlites and distinctly different from the other class, Fort à la Corne-type pyroclastic kimberlite (FPK) which displays features comparable to subaerial basaltic pyroclastic rocks (Scott Smith et al. 2013). KPKs are best known as the diatreme-fill of many pipes in southern Africa. Optical and back-scattered electron petrographic data were obtained for a variety of KPK localities and the associated hypabyssal kimberlite (HK) to provide constraints on their emplacement. The KPK and the, as yet, not well-characterised HK-KPK transition zone in the 530-545 Ma., Kennady Lake cluster, NWT, Canada are emphasised. These bodies exhibit features identical to KPKs occurring at the type locality in Kimberley, South Africa (~90 Ma.; Mitchell et al. 2009), as well as other southern African mines (~90 Ma. Orapa Botswana; ~1100 Ma. Premier, South Africa; ~90 Ma. Letseng, Lesotho) and the ~230 Ma. Pimento Bueno cluster, Brazil.

Kennady Lake Kimberlite Cluster, NWT, Canada

These kimberlites were emplaced into basement granitoids and are eroded bodies with diverse shapes that subcrop below surficial sediments and lakes. Tuzo (1.2ha.) is a typical vertical pipe (Hetman et al. 2004). In contrast, new data show that Faraday 2 and Kelvin are unconventional irregular-shaped inclined pipe-like bodies (Faraday 2: 20-40° dip, >400m long, 20-90m wide; Kelvin: 12-20° dip, >700m long, 30-200m wide, Fig. 1; Barnett et al., Nelson et al., Bezzola et al., this volume).

Tuzo, Gahcho Kuè Mine: The main pipe-fill kimberlite is dominated by typical KPK (Fig. 2a) in which the magmaclast selvages are composed of primary phlogopite, Mg-amphibole, Mg-Cr-spinel, apatite and Nb-rutile. The intermagmaclast matrix consists of Mg-rich Ca-poor amphibole and Al-chlorite which differs from the serpentines and chlorites replacing the olivines. These new data confirm and enhance the results of Hetman et al. (2004) especially with regard to the presence of a continuous but inhomogeneous HK-HKt-KPKt-KPK textural transition with depth.

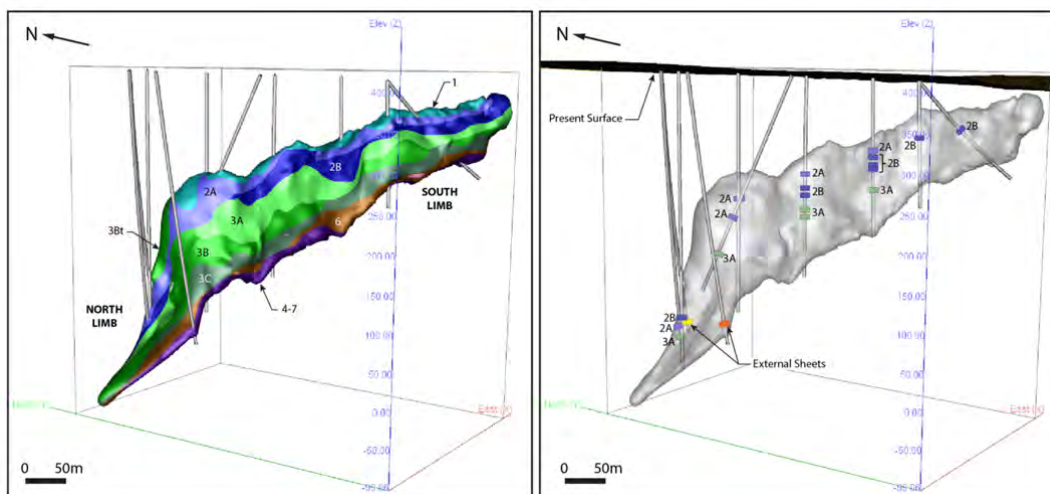


Figure 1: Oblique view of the Kelvin 3D geological model showing the investigated drillholes, and in (a) the “layer cake” internal geology (2A = KIMB2A etc.) and in (b) the sample locations.

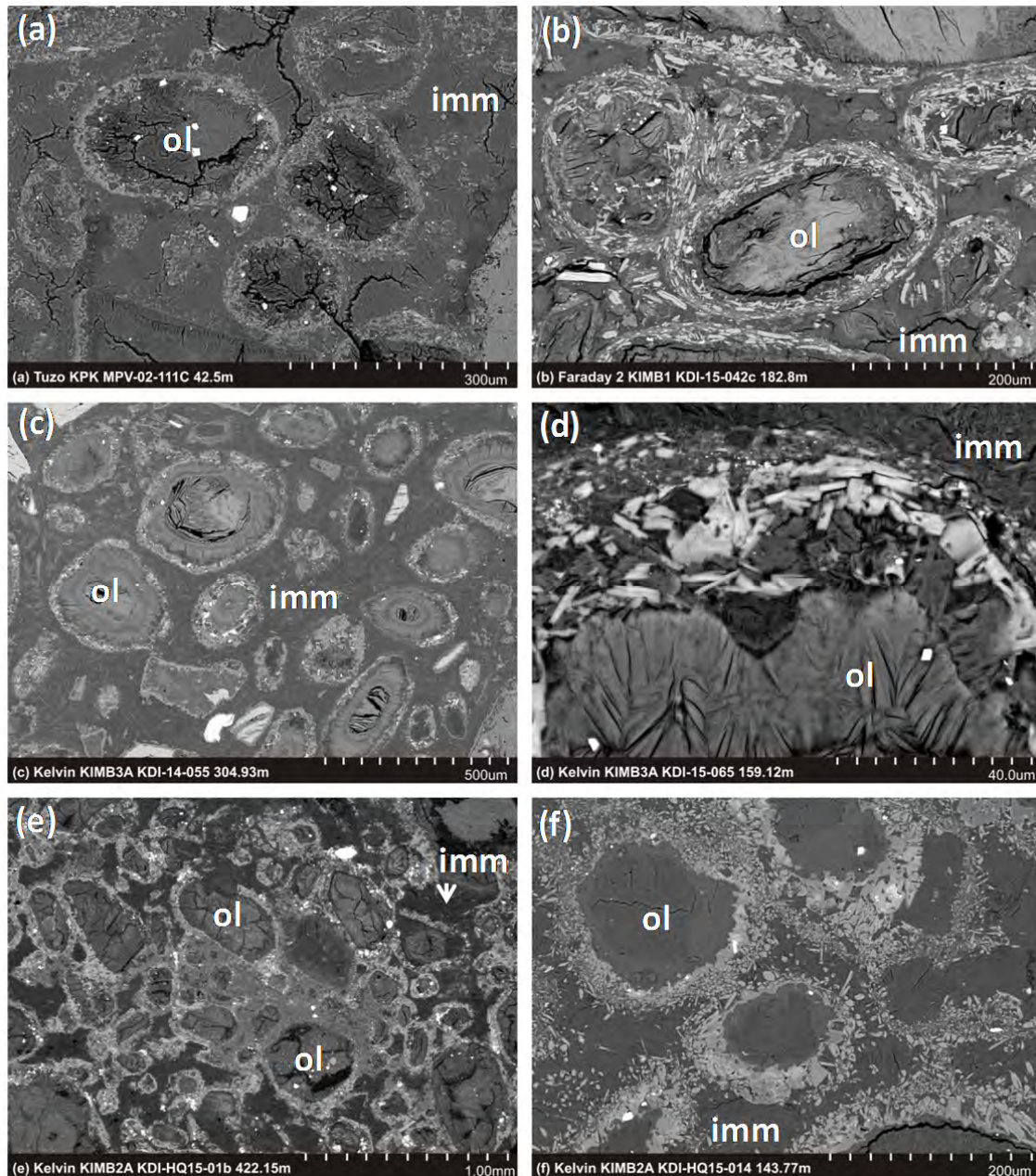


Figure 2: Back-scattered electron images of Tuzo, Faraday and Kelvin kimberlites. (a)-(d) are characteristic KPK: matrix-supported subspherical magmaclasts (formerly pelletal lapilli) with pseudomorphed olivine kernels (ol) and complete thin melt selvages composed of primary minerals including phlogopite and amphibole set in a different intermagmaclast matrix (imm). (e)-(d) illustrate HK-KPK transitional textures.

Faraday 2: The dominant kimberlite phase is KPK (Fig. 2b) with magmaclast selvages consisting of phlogopite, apatite and spinel set in a base of fibrous Mg-amphibole. The tangential orientation of the phlogopite laths confirms their formation is coeval with the magmaclasts. The occurrence of similar phlogopite in the intermagmaclast matrix indicates formation from the same magmatic crystallisation event. Deformation of juxtaposed magmaclasts suggests they were plastic at the time of solidification.

Kelvin: The three dominant and overall uniform juxtaposed phases of kimberlites (Fig. 1a) are each characterised by different textures. KIMB3 is typical KPK with increasing proportions of xenoliths and alteration from KIMB3A to KIMB3C. It is composed of matrix-supported discrete magmaclasts

(Fig. 2c). The chlorites replacing the olivine within the magmaclasts are different in composition to the chlorite-smectite+/-amphibole of the intermagmaclast matrix (Figs. 2c,d). The unaltered groundmass amphibole and phlogopite in the magmaclast selvages (light coloured grains, Fig 2d) must have formed between the two or more separate chlorite events indicating sequential magmatic crystallisation and not external alteration. The adjacent KIMB2B is mainly HK to HKt in which most of the features are comparable to the external intrusive sheets except for the overall finer and more variable grain sizes as well as the development of diopside selvages on pseudomorphed olivines by assimilation of granitoid xenoliths. KIMB2A displays intermediate KPKt-HKt textures in which the incipient magmaclasts are not fully separate (Figs. 2e, f) and there are remnants of the original melt (central area enclosing both 'ol' in Fig 2e). Also, the grain size of the primary phlogopite/amphibole is intermediate between HK and KPK (Fig. 2f) suggesting more rapid crystallisation than HK.

Conclusions

The KPKs investigated all display similar features and are derived from three continents/cratons with emplacement ages ranging from 90 to 1100 Ma.. Thus, KPK is a texture that has been repeated in time and space. The development of different textures within the KPK-HK spectrum (Fig. 2) in juxtaposed phases of kimberlite at Kelvin (Fig. 1a) indicates that *none* of the textures result from pervasive post-emplacement alteration in response to external non-kimberlitic fluids. The HK to KPK transition is characterised by increasing local country rock xenolith content, deuteritic olivine replacement and magmaclast development. The fluidal magmaclasts form from the melt by the nucleation of primary minerals on olivine pseudomorphs. The unaltered amphibole and tangential phlogopite in the magmaclast selvages (Fig. 2b,d) must have formed between distinct magmatic chlorite-forming events, both primary and deuteritic. The occurrence of the same primary minerals in the intermagmaclast matrix indicates it represents the end of a continuum of magmatic crystallisation involving increasingly rapid cooling. The occurrence of significant amounts of amphibole (cummingtonite/anthophyllite with overgrowths of richterite) at Kennady Lake as opposed to diopside which is common elsewhere (e.g. Mitchell et al. 2009) reflects magma contamination resulting from the influx of granitoid xenoliths. The late-stage volatile-rich residual magmatic fluids cause extensive deuteritic hydrothermal replacement of earlier-formed minerals by chlorite-smectite group minerals.

The occurrence of KPK-KPKt-HKt-HK textures in the essentially subsurface bodies at Kelvin (Fig. 1) and Faraday confirms that they did not form by deposition from subaerial pyroclastic eruption columns. This conclusion is supported by: (i) the absence of evidence for any such processes; and (ii) the similarity of pipe-fill HKs to intrusive sheets indicating they represent well crystallised subsurface magma (not welded pyroclastics). The degree of development of the KPK textures is different in each phase of kimberlite. Thus, the textures represent variable degrees of textural modification during the subsurface crystallisation of separate intrusive magmatic systems. The textures are also not uniform within each phase of kimberlite and the different transitional textures coexist on all scales. This indicates the transition is a dynamic process with profound changes in the liquidus and volatile phases over relatively small distances resulting from melt contamination, melt-fluid segregation and rapid sequential crystallisation processes.

References

- Hetman CM, Scott Smith BH, Paul JL, Winter FW (2004) Geology of the Gahcho Kué kimberlite pipes, NWT, Canada: Root to diatreme magmatic transition zones. Proceedings of the 8th International Kimberlite Conference. Lithos 76, 51-74.
- Mitchell RH, Skinner EMW, Scott Smith BH (2009) Tuffisitic kimberlites from the Wesselton Mine, South Africa: Mineralogical characteristics relevant to their formation. Proceedings of the 9th International Kimberlite Conference. Lithos 112 Supplement 1, 452-464.
- Scott Smith BH, Nowicki TE, Russell JK, Webb KJ, Mitchell RH, Hetman CM, Harder M, Skinner EMW, Robey JV (2013) Kimberlite Terminology and Classification. Proceedings of the 10th International Kimberlite Conference. Special Issue of the Journal of the Geological Society of India, Volume 2, 1-17. Springer India.



Re-Os isotope systematics of sulphide inclusions in diamonds from Victor (Superior craton) document mobilisation of volatiles and Os during Rodinia break-up

Sonja Aulbach^{1,2}, Robert A. Creaser¹, Thomas Stachel¹, Ingrid Chinn³, Julie Kong⁴

¹University of Alberta, Edmonton AB, Canada, s.aulbach@em.uni-frankfurt.de, rcreaser@ualberta.ca, tstachel@ualberta.ca

²Goethe University, Frankfurt am Main, Germany.

³De Beers Exploration, Southdale, South Africa, Ingrid.Chinn@debeersgroup.com

⁴De Beers Canada, Toronto, Canada, Julie.Kong@debeersgroup.com

Introduction

The James Bay area on the Superior Craton hosts both Mesoproterozoic kimberlites (~1.1 Ga; Kyle Lake) and Jurassic kimberlites (~180-170 Ma; Attawapiskat, including Victor; Januszczak et al. 2013) in close proximity (separated by ~100 km). A major thermal event related to the development of the Midcontinent Rift at ca. 1.1 Ga induced an elevated regional geothermal gradient that led to partial diamond destruction (Smit et al. 2014a,b). The Victor kimberlite is characterised by an inclusion suite that, contrary to the current paradigm, formed in a moderately depleted lherzolitic mantle and produces diamonds of exceptional value (Stachel et al., this volume). This raises the question of when, and how, the diamond inventory at this locality was formed. Based on a comparison of N aggregation and carbon isotope systematics of diamonds from the two kimberlite age groups, it was hypothesised that the Victor kimberlite sampled a young generation of diamonds which formed after dissipation of the heat associated with the Midcontinent Rift (Smit et al. 2014a). Given that the lherzolite-dominated Victor suite represents an unconventional diamond deposit (Stachel et al., this volume), age dating is required to confirm the timing of this inferred young diamond-formation event. This not only allows us to establish a link to regional tectonothermal evolution, but also to explore broader implications for models of diamond formation and the associated carbon redistribution in the lithospheric mantle as part of the deep carbon cycle.

Sulfides are known to be the main hosts to highly siderophile elements, among them Re (including the radionuclide ¹⁸⁷Re) and Os (including the radiogenic isotope ¹⁸⁷Os), and therefore lend themselves to the determination of single-sulfide Re-Os isotope systematics (Pearson et al. 1998). During strong melt depletion, the mildly incompatible element Re preferentially partitions into the melt, whereas the compatible element Os remains in the residue (Shirey and Walker 1998). Thus, the Re-Os isotope system is particularly well-suited to date the cratonic lithospheric mantle, which formed by extraction of high degrees of melt. We studied a suite of peridotitic sulphide inclusions in diamonds from the Victor Main and Victor South kimberlites for major elements, by Scanning Electron Microprobe (SEM), and Re-Os isotope systematics, by Isotope Dilution Negative Thermal Ionisation Mass Spectrometry (ID-NTIMS), in order to obtain constraints on the nature of their source rocks and formation ages.

Geological Background and Prior Work

The Jurassic (~180-170 Ma) Attawapiskat kimberlites, including Victor, erupted in the Superior craton, near the boundary between the Palaeoarchaeoan Northern Superior and the Mesoarchaeoan North Caribou superterrane. Following cratonisation at ca. 2.7 Ga, the area was affected by a major thermal event related to the Midcontinent Rift to the south. Refertilisation in the course of rifting has been suggested (Smit et al. 2014b), although its timing remains unknown. Rifting, however, led to destruction of older generation(s) of diamond. This is evidenced by (1) an elevated geothermal gradient recorded in mantle xenocrysts from the nearby ca. 1.1 Ga Kyle Lake kimberlites (corresponding to a surface heat flow of 40-41 mW/m²), and (2) the presence at that time of lithospheric diamonds with highly aggregated N, which are largely absent from the younger

kimberlites (Smit et al. 2014a,b). The latter record a return to cooler conditions (39 mW/m²) and a widening of the diamond window from 140-180 km depth to 120-200 km depth (Smit et al. 2014a).

Samples and Analytical Techniques

To constrain the timing of diamond formation beneath Victor, 20 visually crack-free diamonds were broken to retrieve 20 sulphide inclusions in the De Beers Lab at the University of Alberta. Semi-quantitative analysis by SEM was used to assign a paragenesis based on Ni/Fe, showing that 19 stones contained one to two Peridotitic-type sulfide inclusions and one contained multiple Eclogitic-type sulfide inclusions. Of these, the best specimens in terms of size and/or completeness were selected for processing, which included addition of a mixed Re-Os spike, dissolution, purification of Os by distillation and of Re by anion microcolumn chromatography. Purified Re and Os fractions were analysed by negative TIMS on a Micromass Sector 54 mass spectrometer, operated by single collector peak-hopping using an ETP electron multiplier (pulse counting mode) at the Radiogenic Isotope Facility (University of Alberta). Osmium and Re blanks were very low, averaging 6±3 fg and 200±50 fg, respectively. A 1 pg load of the in-house Os standard (AB-2) yielded an accurate ¹⁸⁷Os/¹⁸⁸Os ratio, indistinguishable from larger loads measured with Faraday collectors.

Results and Age Dating

Peridotitic sulphides have Ni/Fe ratios ranging from 0.37 to 0.77, Re contents from ~19 ppb to ~18 ppm and Os contents from 360 ppb to ~860 ppm. This translates into ¹⁸⁷Re/¹⁸⁸Os from 0.0014 to 8.7 (compared to 0.422 for Primitive Upper Mantle, PUM), while ¹⁸⁷Os/¹⁸⁸Os range from 0.1171 to 0.2255 (unradiogenic relative to PUM, with present-day ¹⁸⁷Os/¹⁸⁸Os of 0.1283, to radiogenic).

Given evidence for the formation of diamond in peridotite substrates with non-primitive initial ¹⁸⁷Os/¹⁸⁸Os, combined with the fertile nature of lithospheric mantle beneath Attawapiskat at the time of Victor kimberlite emplacement, which indicates a multi-stage evolution of the mantle source, Re-depletion or mantle model ages are likely to be meaningless (Aulbach et al. 2016). Indeed, mantle model ages (T_{MA}), calculated assuming formation from a primitive mantle source (PUM), range from ca. 3.2 Ga to future ages. Rhenium depletion ages, which are minimum ages, may be calculated from samples with unradiogenic Os. They, too, rely on assumptions about the mantle source, and range from 1.2 to 1.7 Ga. A regression through all data shows a good correlation (r² = 0.96), but also some scatter. Excluding two obvious outliers, the correlation is improved to r² = 0.99. Regression through these data (n=14) yields a 718 ± 49 Ma model 3 isochron (MSWD 6.1), with an initial ¹⁸⁷Os/¹⁸⁸Os of 0.1177 ± 0.0016, i.e. unradiogenic (depleted) at the time of formation.

Discussion and implications

To our knowledge, this is the first model 3 isochron obtained from cratonic peridotitic material that yields an unradiogenic initial Os isotopic composition, pointing to formation or rehomogenisation in a depleted mantle source. The ca. 720 Ma diamond formation age corresponds to rifting at the craton margin during Rodinia break-up and suggests remobilisation of volatile-rich components due to attendant mantle stretching. Such components may have been emplaced during earlier metasomatism, e.g., related to the ca. 1.1 Ga Midcontinent rift. Olivine separates from peridotite xenoliths reveal the mantle beneath Victor to contain regions with both highly unradiogenic and radiogenic Os (0.1012 to 0.1821), reflecting various degrees of melt extraction during cratonic lithosphere formation and subsequent metasomatic enrichment (Smit et al. 2014b). In this light, we interpret the quasi-isochronous behaviour of sulphides in the peridotitic Victor diamond suite to reflect mobilisation of fluid during continental break-up, in amounts sufficient to largely re-homogenise the – by that time – isotopically highly variable Os. The presence of two outliers and scatter in the remaining samples (indicated by the MSWD of ~6) indicates that re-homogenisation was incomplete.

The diamond-forming metasomatic event may have prompted co-precipitation of sulphides and their host diamonds, for example from an H₂S-bearing melt reaching sulphide saturation. Alternatively, the

fluids catalysed recrystallisation - accompanied by isotopic rehomogenisation - of protogenetic sulphides that were reintroduced into the depleted lithosphere during ca. 1.1 Ga refertilisation postulated by Smit et al. (2014b), and which served as a reduction agent for initial diamond crystallisation from a carbonated fluid (Palyanov et al. 2007). This latter interpretation appears consistent with evidence for the oxidising nature of metasomatic fluids (Woodland and Koch 2003), in particular in association with rifting and lithosphere rejuvenation (Foley 2011). In addition, involvement of a carbonated melt seems possible, based on the shallow cratonic lithosphere depth (~150-160 km; Stachel et al., this volume) from which silicate-included Victor diamonds were derived, where relatively high oxygen fugacities permit the coexistence of carbonate-rich melts with diamond (Stagno et al. 2015). Such oxidising fluids would be able to scavenge more Re than Os (Aulbach et al. 2016), leading to crystallisation of sulphides with comparatively high Re/Os that, following encapsulation in diamond, evolved to correspondingly high measured $^{187}\text{Os}/^{188}\text{Os}$, as observed for the Victor sulphide inclusion suite.

Peridotitic sulphide-included diamond formation beneath Victor at ca. 720 Ma demonstrates that volatile remobilisation has taken place in the context of supercontinent reorganisation. Thus, incipient rift settings not only are prospective with respect to diamond formation, but they are also important sites of volatile focusing and redistribution.

References

- Aulbach S, Mungall JE, Pearson DG (2016) Distribution and Processing of Highly Siderophile Elements in Cratonic Mantle Lithosphere. In: Harvey J, Day JMD (eds) *Highly Siderophile and Strongly Chalcophile Elements in High-Temperature Geochemistry and Cosmochemistry*, vol 81. pp 239-304
- Foley SF (2011) A Reappraisal of Redox Melting in the Earth's Mantle as a Function of Tectonic Setting and Time. *J Petrol* 52(7-8):1363-1391
- Januszczak N, Seller MH, Kurszlaukis S, Murphy C, Delgaty J, Tappe S, Ali K, Zhu J, Ellemers P (2013) A Multidisciplinary Approach to the Attawapiskat Kimberlite Field, Canada: Accelerating the Discovery-to-Production Pipeline. *Proceedings of the 10th International Kimberlite Conference*, vol 2:157-171
- Palyanov YN, Borzdov YM, Bataleva YV, Sokol AG, Palyanova GA, Kupriyanov IN (2007) Reducing role of sulfides and diamond formation in the Earth's mantle. *Earth Planet Sci Lett* 260:242-256
- Pearson DG, Shirey SB, Harris JW, Carlson RW (1998) Sulphide inclusions in diamonds from the Koffiefontein kimberlite, S Africa: constraints on diamond ages and mantle Re-Os systematics. *Earth Planet Sci Lett* 160:311-326
- Shirey SB, Walker RJ (1998) The Re-Os isotope system in cosmochemistry and high-temperature geochemistry. *Ann Rev Earth Planet Sci* 26:423-500
- Smit KV, Stachel T, Stern RA (2014a) Diamonds in the Attawapiskat area of the Superior craton (Canada): evidence for a major diamond-forming event younger than 1.1 Ga. *Contrib Mineral Petrol* 167(1)
- Smit KV, Pearson DG, Stachel T, Seller M (2014b) Peridotites from Attawapiskat, Canada: Mesoproterozoic Reworking of Palaeoarchaeoan Lithospheric Mantle beneath the Northern Superior Superterrane. *J Petrol* 55(9):1829-1863
- Stachel T, Banas A, Aulbach S, Smit KV, Wescott P, Chinn I, Fisher D, Kong J (2017) The Victor Diamond Mine (Superior Craton, Canada) - A new paradigm for exploration in unconventional settings. In: *11th International Kimberlite Conference*, vol., Gaborone, Botswana
- Stagno V, Ojwang DO, McCammon CA, Frost DJ (2013) The oxidation state of the mantle and the extraction of carbon from Earth's interior. *Nature* 493:84-88
- Tappe S, Foley SF, Stracke A, Romer RL, Kjarsgaard BA, Heaman LM, Joyce N (2007) Craton reactivation on the Labrador Sea margins: Ar-40/Ar-39 age and Sr-Nd-Hf-Pb isotope constraints from alkaline and carbonatite intrusives. *Earth Planet Sci Lett* 256:433-454
- Woodland AB, Koch M (2003) Variation in oxygen fugacity with depth in the upper mantle beneath the Kaapvaal craton, Southern Africa. *Earth Planet Sci Lett* 214:295-310

Co-magmatic sulfides and sulfates in the Udachnaya-East pipe (Siberia) : sulfur speciation and isotopic composition in kimberlites and their mantle sources

Y. Kitayama¹, E. Thomassot¹, A. Galy¹, A. Golovin², A. Korsakov², Elisabeth d'Eyrames¹, Nelly Assayag³, Nordine Bouden¹, D. Ionov³

¹ Centre de Recherches Pétrographiques et Géochimiques, Vandoeuvre-les-Nancy, France

² Sobolev Institute of Geology and Mineralogy, Novosibirsk, Russia

³ Institut de Physique du Globe, Paris, France.

⁴ Géosciences Montpellier, Montpellier, France

Introduction

Kimberlite magmas travel at high speed through the lithospheric mantle and crust, propelled by their high volatile contents. The origin of volatiles in kimberlite magma, however, is still debated. The loss of volatiles during eruption, the composite nature of kimberlites and their common hydrous alteration make the primary kimberlitic melt composition difficult to infer. Volatiles in the mantle source of kimberlites may come from the recycling of Archean oceanic crust into the lithospheric mantle, as suggested by the finding of Archean ages for eclogite xenoliths from the Udachnaya-East kimberlite (Siberia), thought to represent remnants of early oceanic crust (Pearson et al. 1995; Jacob & Foley 1999). However, a single Archean formation age for the Siberian lithospheric mantle has been challenged by recent publications (Doucet et al. 2015; Ionov et al. 2015 and Moyen et al. 2017) that propose a major rejuvenation of the Archean lithosphere during the paleoproterozoic (ca 1.9 Ga). Here we present new insights from multiple S-isotopes (³²S, ³⁴S, ³³S, ³⁶S), to test whether a surface-derived Archean component is present in the mantle source of the Udachnaya-East kimberlite. Photolytic reactions in the ozone-free atmosphere of the early Earth, produced mass-independent fractionation of sulfur (corresponding to a deviation from the mass-dependent fractionation line). These anomalies were efficiently transferred to sediments such as Archean sedimentary sulfides that carry positive $\Delta^{33}\text{S}$ anomalies (and negative $\Delta^{36}\text{S}$ anomalies) and Archean sulfates that carry negative $\Delta^{33}\text{S}$ (with positive $\Delta^{36}\text{S}$). Accordingly, the presence of these anomalies in igneous rocks may allow to identify Archean surface material recycled into the mantle. If found in kimberlites samples, mass-independent fractionation of sulfur would indicate unambiguously that recycling of Archean supracrustal material was involved in the source of the Udachnaya-East kimberlite.

Methodology

Sulfur isotopic values are reported in the notation δ with respect to V-CDT (Vienna-Canon Diablo Troilite) defined as: $\delta^{3x}\text{S}$ (in ‰) = $1000 * [(^{3x}\text{S}/^{32}\text{S})_{\text{sample}} / (^{3x}\text{S}/^{32}\text{S})_{\text{V-CDT}} - 1]$, where ^{3x}S corresponds to one of the minor stable S isotopes ³³S, ³⁴S or ³⁶S. Furthermore, $\Delta^{33}\text{S}$ and $\Delta^{36}\text{S}$ are defined as: $\Delta^{3x}\text{S}$ (in ‰) = $1000 * [(^{3x}\text{S}/^{32}\text{S})_{\text{sample}} - \lambda * (^{34}\text{S}/^{32}\text{S})_{\text{sample}}]$, where λ is a coefficient directly related to the mass differences between ^{3x}S, ³⁴S and ³²S (0.515 for ³³S and 1.89 for ³⁶S).

Sulfur contained in bulk samples was extracted as Ag₂S by a wet chemistry procedure described in Kitayama et al. (In Press). The extraction was done sequentially in kimberlite samples: first from sulfides, then from sulfates in the same aliquot of sample. After fluorination of Ag₂S to SF₆ gas and purification of SF₆, bulk isotope ratios were measured using a ThermoFinnigan MAT 253 dual-inlet gas-source mass spectrometer.

We studied samples of salty kimberlite, an associated salt-free kimberlite and a serpentinized kimberlitic breccia (also salt-free) and compared them to other sulfur bearing lithologies in the area (hydrothermal minerals, country-rock sediment and brine).

Results and discussion

Except for one outlier with very low sulfide concentration, $\Delta^{33}\text{S}$ and $\Delta^{36}\text{S}$ signatures of sulfides and sulfates in both salty and non-salty kimberlite samples are undistinguishable within uncertainty (Fig. 1). Homogeneous $\Delta^{33}\text{S}$ and $\Delta^{36}\text{S}$ signatures are consistent with isotopic equilibrium and support a cogenetic link between groundmass sulfides and sulfates in the salty kimberlite.

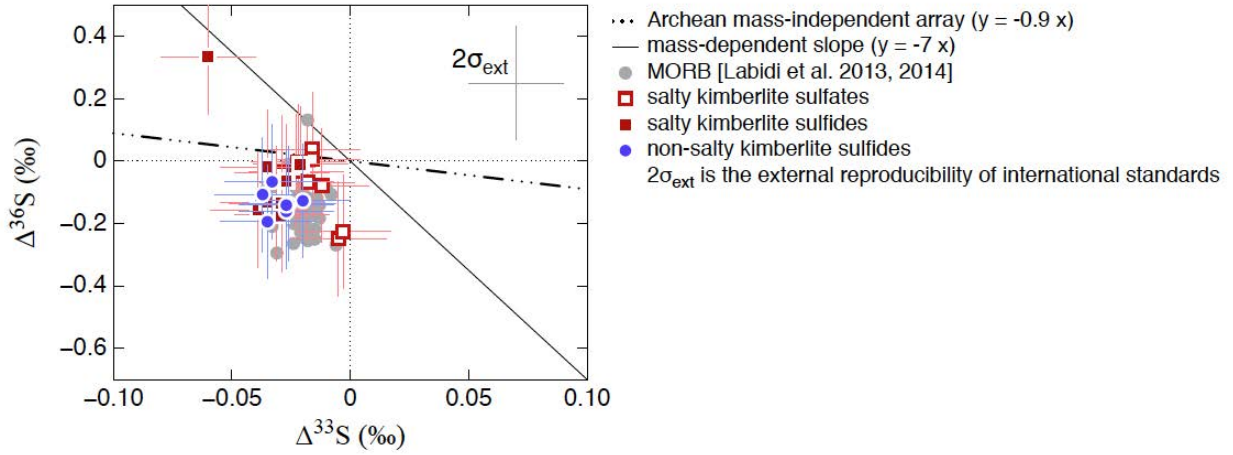


Fig. 1: $\Delta^{36}\text{S}$ vs $\Delta^{33}\text{S}$ (‰) diagram showing that sulfides and sulfates from salty and non-salty kimberlites are homogeneous and overlap with the range of MORB.

Overall, sulfates and sulfides of the salty and non-salty kimberlites display small but systematically negative signatures in both $\Delta^{33}\text{S}$ and $\Delta^{36}\text{S}$ falling in the range of the Canonical mantle value. They are within uncertainty of the V-CDT, and in fact overlap with the compositional range of mid-ocean ridge basalts (MORB) reported by Labidi et al. (2013, 2014). They differs from the Archean mass-independent array and the slightly negative $\Delta^{33}\text{S}$ and $\Delta^{36}\text{S}$ values are too small to unambiguously determine a contribution from Archean sediments to the source of the Udachnaya-East kimberlite. The data thus show no evidence for mass-independent fractionation and therefore no evidence for the involvement of Archean surface material in the source of the kimberlites. We can infer that either: (1) subducted oceanic crust does not contribute significantly to the source of kimberlite melt; or (2) the subducted oceanic crust in the source does not carry mass-independent fractionation of sulfur or is not Archean in age. The homogeneity of $\Delta^{33}\text{S}$ and $\Delta^{36}\text{S}$ in the kimberlite samples suggest that they have not been altered by secondary processes.

There is in fact a larger range of variations in $\Delta^{33}\text{S}$ and $\Delta^{36}\text{S}$ when considering hydrothermal sulfur mineralization, country rock sediment or brine samples (Fig. 2). Hydrothermal processes can generate a significant range in $\Delta^{33}\text{S}$ and $\Delta^{36}\text{S}$ but spread along a slope characteristic of mass-dependent processes (~ -7). Furthermore, the brine and country rock sediment are also aligned along a mass-dependent slope. The brine and this sulfate-rich sediment are thus likely related by processes involving Rayleigh fractionation, such as the dissolution or precipitation of sulfate-rich beds.

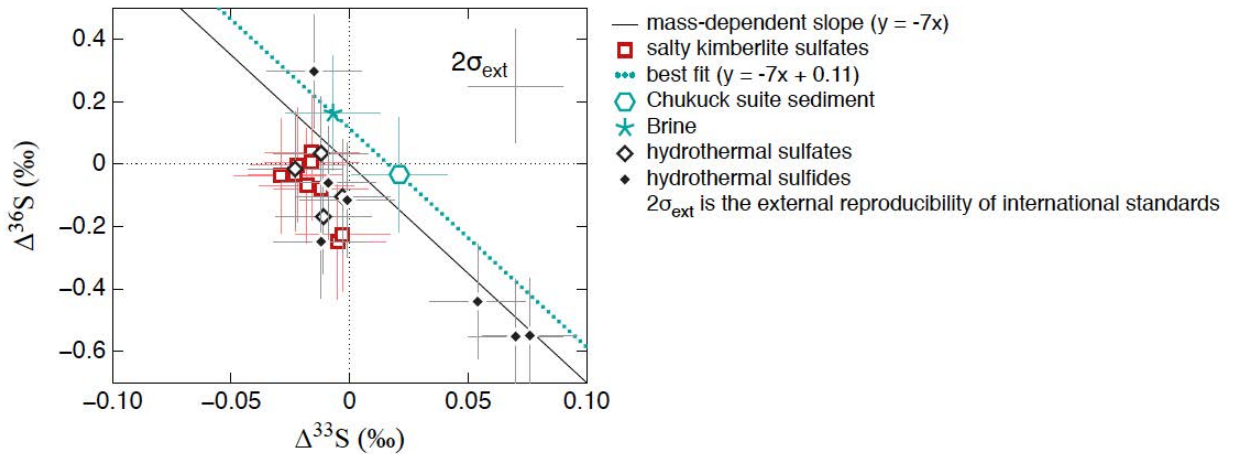


Fig. 2: $\Delta^{36}\text{S}$ vs $\Delta^{33}\text{S}$ (‰) diagram, comparing the range of salty kimberlite sulfates with that of hydrothermal sulfur, brine and country rock sediments.

It is interesting to note that sulfates of the salty kimberlites define a trend with a slope of -9 ± 3 (1σ), also consistent with mass-dependent processes such as a Rayleigh fractionation but with a y-intercept different from the mass-dependent trend defined by the brine and sulfate-rich sediment (Fig. 3). Thus, the brine and

the country rock sediment both clearly differ from the salty kimberlite sulfates in terms of their multiple sulfur isotopic compositions.

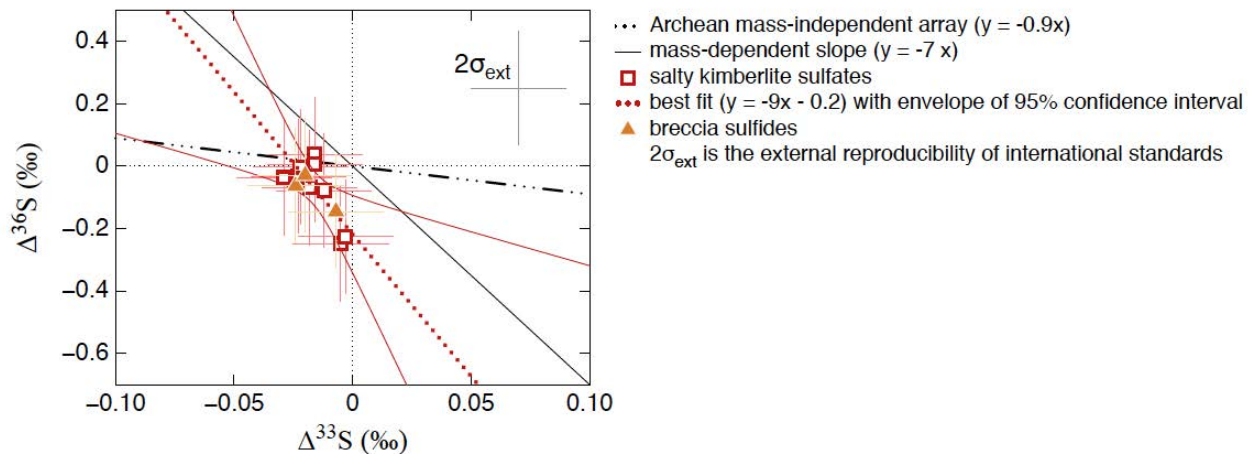


Fig. 3: $\Delta^{36}\text{S}$ vs $\Delta^{33}\text{S}$ (‰) diagram showing that the salty kimberlite sulfates and the breccia sulfides overlap along a trend consistent with that of mass-dependent processes.

This is consistent with the idea that sulfates from the salty kimberlite are, indeed, of mantle origin and that they may have been partly reduced, resulting in the production of secondary sulfides (Kitayama et al. In Press). The observation that sulfides of the breccia fall along the same trend as the salty kimberlite sulfates also confirms the hypothesis that sulfides from the breccia are derived from the reduction of primary kimberlitic sulfates.

References

- Doucet, L. S., Ionov, D. a., & Golovin, A. V. (2015). Paleoproterozoic formation age for the Siberian cratonic mantle: Hf and Nd isotope data on refractory peridotite xenoliths from the Udachnaya kimberlite. *Chemical Geology*, 391, 42–55. <http://doi.org/10.1016/j.chemgeo.2014.10.018>
- Dmitri A. Ionov, Richard W. Carlson, Luc S. Doucet, Alexander V. Golovin, O. B. O. (2015). The age and history of the lithospheric mantle of the Siberian craton : Re – Os and PGE study of peridotite xenoliths from the Obnazhennaya kimberlite. *Earth and Planetary Science Letters*, (August). <http://doi.org/10.1016/j.epsl.2015.07.007>
- Jacob, D. E., & Foley, S. F. (1999). Evidence for Archean ocean crust with low high field strength element signature from diamondiferous eclogite xenoliths. *Developments in Geotectonics*, 24(C), 317–336. [http://doi.org/10.1016/S0419-0254\(99\)80017-2](http://doi.org/10.1016/S0419-0254(99)80017-2)
- Kitayama, Y., Thomassot, E., Galy, A., Golovin, A., Korsakov, A., D'Eyrames, E., Assayag, N., Bouden, N., & Ionov, D. (In Press). Co-magmatic sulfides and sulfates in the Udachnaya-East pipe (Siberia) : A record of the redox state and isotopic composition of sulfur in kimberlites and their mantle sources. <http://doi.org/10.1016/j.chemgeo.2016.10.037>
- Labidi, J., Cartigny, P., Hamelin, C., Moreira, M., & Dosso, L. (2014). Sulfur isotope budget (^{32}S , ^{33}S , ^{34}S and ^{36}S) in Pacific-Antarctic ridge basalts: A record of mantle source heterogeneity and hydrothermal sulfide assimilation. *Geochimica et Cosmochimica Acta*, 133, 47–67. <http://doi.org/10.1016/j.gca.2014.02.023>
- Labidi, J., Cartigny, P., & Moreira, M. (2013). Non-chondritic sulphur isotope composition of the terrestrial mantle. *Nature*, 501(7466), 208–11. <http://doi.org/10.1038/nature12490>
- Moyen, J., Paquette, J., Ionov, D. A., Gannoun, A., Korsakov, A. V, Golovin, A. V, & Moine, B. N. (2017). Paleoproterozoic rejuvenation and replacement of Archaean lithosphere : Evidence from zircon U – Pb dating and Hf isotopes in crustal xenoliths at Udachnaya, Siberian craton. *Earth and Planetary Science Letters*, 457, 149–159. <http://doi.org/10.1016/j.epsl.2016.09.046>
- Ono, S., Beukes, N. J., Rumble, D., & Fogel, M. L. (2006). Early evolution of atmospheric oxygen from multiple-sulfur and carbon isotope records of the 2.9 Ga Mozaan Group of the Pongola Supergroup, Southern Africa. *South African Journal of Geology*. <http://doi.org/10.2113/gssaajg.109.1-2.97>
- Pearson, D. G., Snyder, G. A., Shirey, S. B., Taylor, L. A., Carlson, R. W., & Sobolev, N. V. (1995). Archaean Re–Os age for Siberian eclogites and constraints on Archaean tectonics. *Nature*, 374(6524), 711–713. <http://doi.org/10.1038/374711a0>



Tracking continental-scale modification of the Earth's mantle using zircon megacrysts

J.D. Woodhead¹, J.M. Hergt¹, A. Giuliani^{1,2}, D. Phillips¹, R. Maas¹

¹*School of Earth Sciences, The University of Melbourne, VIC 3010, Australia*

²*Department of Earth and Planetary Sciences, Macquarie University, North Ryde, NSW 2019, Australia*

Introduction

Metasomatism is an important process generating regions of mantle enriched in volatile and incompatible elements that may subsequently melt, giving rise to a range of magma types. The spatial extent of metasomatic processes is poorly understood because geographically extensive studies of relevant metasomatic minerals with known ages are rare. Zircon megacrysts, an uncommon, large (cm-sized) and somewhat unusual mineral occurrence, recovered during the processing of kimberlites to extract diamonds, may fill this gap. Their trace element patterns (e.g., Belousova *et al.*, 2002) and low $\delta^{18}\text{O}$ (Page *et al.*, 2007) indicate that they are not of crustal origin, but crystallised within the mantle and experienced only minimal chemical interaction with the host magmas that transported them to the surface. While details of their petrogenesis (and the origin of megacryst suites more broadly) remain a subject of active research, there is agreement that zircon megacrysts are produced by metasomatic melts in some way related to kimberlite magmas (e.g., Kinny *et al.*, 1989; Nowell *et al.*, 2004; Page *et al.*, 2004). They record precise U-Pb ages and initial $^{176}\text{Hf}/^{177}\text{Hf}$ isotope ratios providing important constraints on the age and nature of the metasomatic events occurring in their mantle sources. We present the first geographically-extensive survey of Hf-isotope and U-Pb age distributions for zircon megacrysts in southern African kimberlites, representing widely spaced intrusions spanning both cratonic (Kaalvaal, Zimbabwe) and non-cratonic settings.

Results and Discussion

Zircons have very low Lu/Hf ratios and thus preserve the initial $^{176}\text{Hf}/^{177}\text{Hf}$ of their source metasomatic melts. Our results reveal an entirely unexpected first order observation; that is, remarkable large-scale isotopic homogeneity among southern African zircon megacrysts across lithospheric domains with widely differing ages. Although a restricted isotopic range in Hf-isotopes has been noted previously in a much smaller dataset of kimberlite megacrysts from this area (Griffin *et al.*, 2000), our analyses show near identical isotopic compositions in samples derived from numerous intrusions distributed across a region of >1 million km².

The data form two homogeneous yet distinct compositional groups, which we term A and B (Fig. 1a); a distinction also mirrored in Nd-isotope data. Some kimberlite pipes contain both zircon groups (e.g., Wesselton, Koffiefontein), as previously reported for the Orapa and Jwaneng kimberlites (Kinny *et al.*, 1989, Griffin *et al.*, 2000). Remarkably, the subtle variations in $^{176}\text{Hf}/^{177}\text{Hf}$ and $^{143}\text{Nd}/^{144}\text{Nd}$ in zircons of the larger Group A correlate with age and may reflect radiogenic ingrowth in the source of the metasomatic zircon parent melts (Fig 1b,c). Although the $^{176}\text{Hf}/^{177}\text{Hf}$ – age correlation is largely defined by the off-craton samples that show the greatest range of ages, it remains true that the cluster of on-craton samples also lies along this array. All results from this study plot below the Nd-Hf isotope mantle array.

Group A zircons yield precise and concordant U-Pb ages which generally approximate the (usually less precise) age estimates of their kimberlite hosts. In contrast, U-Pb systematics for Group B zircons are disturbed, precluding accurate dating, and suggesting a more protracted history.

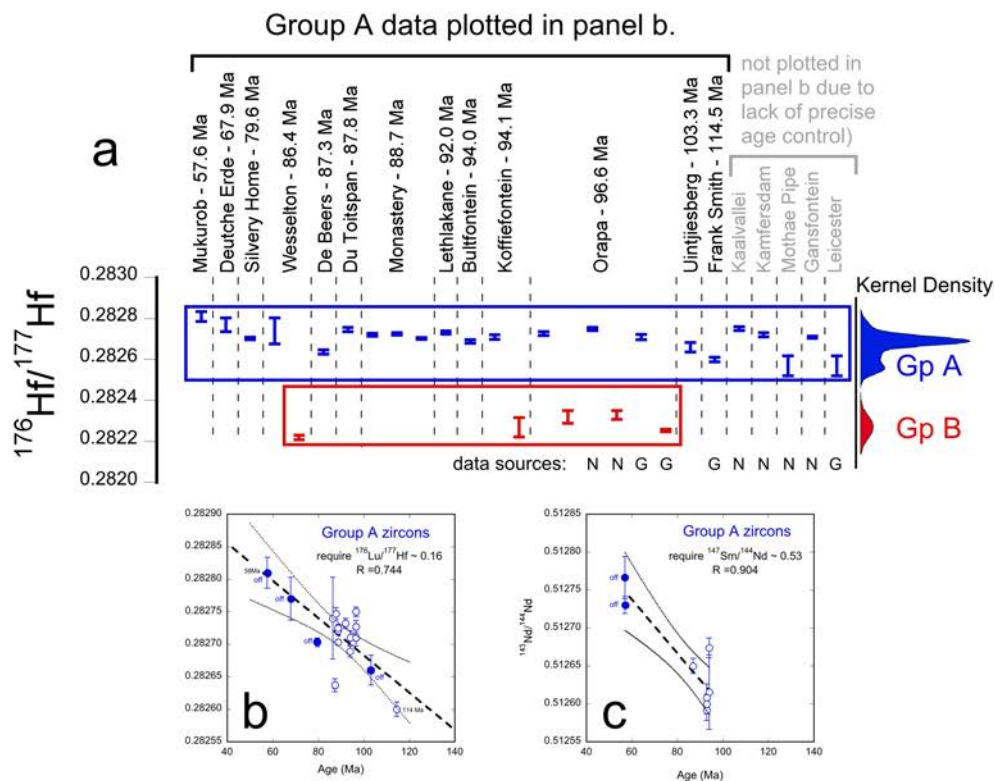


Figure 1 Age and isotopic composition data for zircon megacrysts.

(a) Zircon Hf-isotope data showing a natural compositional subdivision into two distinct groups, further illustrated by Kernel Density estimates. Note the remarkable isotopic homogeneity within each group despite large variations in geographic location and age. All data from this study unless marked: N = Nowell *et al.* (2004), G = Griffin *et al.* (2000).

(b) Inset showing a statistically significant correlation between zircon $^{176}\text{Hf}/^{177}\text{Hf}$ composition and age. Only zircons for which precise U-Pb Concordia ages are available are used to construct this plot. Literature data with less precise age determinations (greyed out in 1a) are excluded.

(c) An equivalent plot to 1b for $^{143}\text{Nd}/^{144}\text{Nd}$ isotope variations.

Our results provide a consistent picture of megacryst parental melts which tapped an isotopically homogeneous source extending over hundreds of kilometres, and encompassing a time interval of nearly 70 Myr, the range of U-Pb ages (114-56 Ma) recorded by the zircons. The apparent $^{176}\text{Hf}/^{177}\text{Hf}$ – age relationship defined by the Group A zircons places important constraints on the nature and evolution of their mantle source(s). To produce such a correlation these source rocks must have been relatively homogeneous initially and subsequently evolved rapidly with a strongly super-chondritic $^{176}\text{Lu}/^{177}\text{Hf}$ ratio (~ 0.16 , Fig. 1b). The initial $^{143}\text{Nd}/^{144}\text{Nd}$ values for Group A zircon megacrysts also correlate with age (Fig. 1c), consistent with a source that evolved with a moderate-high $^{147}\text{Sm}/^{144}\text{Nd}$ ratio of ~ 0.53 (although both parent-daughter ratios are poorly defined, based on the paucity of the data). Importantly, prior to rapid radiogenic ingrowth, the initial source rock composition must have been located off the mantle-array, displaced to lower $^{176}\text{Hf}/^{177}\text{Hf}$ for a given $^{143}\text{Nd}/^{144}\text{Nd}$. This also provides important insights into both the nature of the original mantle source rocks and the metasomatic fluid that modified them.

We postulate that the mantle source rocks originally had a protracted history of unusually low Lu/Hf and Sm/Nd and developed initial $^{176}\text{Hf}/^{177}\text{Hf}$ and $^{143}\text{Nd}/^{144}\text{Nd}$ that are low relative to MORB mantle (i.e., ‘enriched mantle’). Subsequent metasomatism of these source rocks not only drastically raised Lu/Hf to drive rapid ^{176}Hf ingrowth for at least ~ 70 Ma (Fig. 1b) but must also have had a) low Hf contents to preserve the original unradiogenic $^{176}\text{Hf}/^{177}\text{Hf}$ signature of the protolith but b) sufficient Nd

to modify the $^{143}\text{Nd}/^{144}\text{Nd}$ to values more typical of OIB. Metasomatism therefore decoupled Hf from Nd (and presumably Sr) isotope compositions to generate source rocks, and ultimately zircon megacrysts, with compositions to the right of the Nd-Hf mantle array.

The occurrence of near-homogeneous $^{176}\text{Hf}/^{177}\text{Hf}$ in megacryst zircons across two cratons (Kaapvaal and Zimbabwe) and the surrounding Proterozoic requires the inferred metasomatic processes to postdate final tectonic assembly of these crustal domains. This suggests the source of Group A zircons postdates the ~1300 Ma amalgamation of the Kaapvaal craton and the Namaqua-Natal belt (Eglington, 2006), the youngest terrane with Cretaceous kimberlites; a younger limit is provided by the age of the oldest host kimberlite, the 114 Ma Frank Smith pipe. Importantly, the rapid isotopic evolution of the modified mantle source required by the zircon data, make it unlikely that the metasomatic event occurred more than a few hundred million years ago.

Concluding remarks

Our new Hf-isotope data provide clear evidence for a discrete metasomatic event in the southern Africa mantle operating at a continent-wide scale between 114 Ma and several hundred million years ago, and subsequently sampled by separate kimberlite eruptions over a period of at least 70 Ma. The possibility of a link between such large-scale mantle metasomatism and formation of the Karoo large igneous province has previously been suggested (Konzett *et al.*, 1998; Ernst and Bell 2010), and would be consistent with the very large thermal and magmatic perturbation resulting from Karoo activity. New geochronological data for metasomatised mantle xenoliths from the Kimberley kimberlites also suggest a direct association of these events (Giuliani *et al.*, 2014). A link between widespread Karoo magmatism, modification of the southern African continental mantle, initiation of kimberlite magmatism, and megacryst formation therefore appears an intriguing possibility worthy of further study. A more disturbed and less sampled suite of zircon megacrysts supports the occurrence of a similar but older event.

References

- Belousova, E. A., Griffin, W. L., O'Reilly, S.Y., Fischer, N. I. (2002) Igneous zircon: trace element composition as an indicator of source rock type. *Contrib. Mineral. Petrol.* 143: 602-622.
- Eglington, B. M. (2006) Evolution of the Namaqua-Natal Belt, southern Africa – a geochronological and isotope geochemical review. *J. African Earth Sci.* 46: 93-111.
- Ernst, R. E., Bell, K. (2010) Large igneous provinces (LIPs) and carbonatites. *Mineralogy and Petrology* 98: 55-76.
- Giuliani, A., Kamenetsky, V.S., Phillips, D., Kendrick, M.A., Wyatt, B.A., Goemann, K. (2014) LIMA U-Pb ages link lithospheric mantle metasomatism to Karoo magmatism beneath the Kimberley region, South Africa. *Earth Planetary Sci. Lett.* 401: 132-147.
- Griffin, W. L., Pearson, N.J., Belousova, E., Jackson, S.E., van Achterburgh, E., O'Reilly, S.Y., Shee, S.R. (2000) The Hf isotope composition of cratonic mantle: LAM-MC-ICPMS analysis of zircon megacrysts in kimberlites. *Geochim. Cosmochim. Acta* 64: 133-147.
- Kinny, P. D., Compston, W., Bristow, J. W., Williams, I. S. (1989) Archean mantle xenocrysts in a Permian kimberlite: two generations of kimberlitic zircon in Jwaneng DK2, southern Botswana. *Geol. Soc. Aust. Spec. Publ.* 14: 833-842.
- Konzett, J., Armstrong, R.A., Sweeney, R.J., Compston, W. (1998) The timing of MARID metasomatism in the Kaapvaal mantle: an ion microprobe study of zircons from MARID xenoliths. *Earth Planet. Sci. Lett.* 160: 133-145.
- Nowell, G. M., Pearson, D.G., Bell, D.R., Carlson, R.W., Smith, C.B., Kempton, P.D., Noble, S.R. (2004) Hf isotope systematics of kimberlites and their megacrysts: new constraints on their source regions. *J. Petrol.* 45: 1583-1612.
- Page, F. Z., Fu, B., Kita, N.T., Fournelle, J., Spicuzza, M.J., Schultz, D.J., Vijoer, F., Basei, M.A.S., Valley, J.W. (2007). Zircons from kimberlite: new insights from oxygen isotopes, trace elements, and Ti in zircon thermometry. *Geochim. Cosmochim. Acta* 71: 3887-3903.



Trace elements in Gem-Quality Diamonds from De Beers' Victor Mine, Ontario, Canada

Mandy Y. Krebs,¹ D. Graham Pearson,¹ Thomas Stachel,¹ Sarah Woodland,¹ Ingrid Chinn,² and Julie Kong³

¹University of Alberta, Edmonton, Canada, krebs@ualberta.ca, gdpearso@ualberta.ca, tstachel@ualberta.ca

²De Beers Group Exploration, South Africa, Ingrid.Chinn@debeersgroup.com

³De Beers Canada, Julie.Kong@debeersgroup.com

Introduction

In the same way that melt inclusions in phenocrysts have expanded our idea of melt formation and evolution in basalts, studying fluids trapped in diamonds is providing important new constraints on the nature of diamond-forming fluids. Fibrous and cloudy diamonds trap a high but variable density of so-called high-density fluid (HDF) inclusions and, therefore, have been extensively studied, with much progress being made recently in determining the nature of these HDFs using major and trace element compositions (e.g., Schrauder et al., 1996; Zedgenizov et al., 2007; Smith et al., 2012; Weiss et al., 2013, 2015; Klein-BenDavid et al., 2010; Klein-BenDavid et al., 2014 and references therein). In particular, two “endmember” mantle-normalised trace element patterns have been established (Fig. 1; Weiss et al., 2013); ribbed (highly fractionated inter-element ratios) and “planed” (less fractionated inter-element ratios). The “planed” patterns can clearly be related to asthenospherically derived melts whereas the “ribbed” patterns are proposed to represent increased interaction with the sub-continental lithospheric mantle. A key question is whether the same processes also drive the formation of gem diamonds. Constraining the nature of the diamond-forming fluid or melt for high purity gem-quality diamonds, however, is hampered by the sparsity of available high quality trace element data, mainly due to the extremely low concentrations of impurities that these diamonds contain. The recent discovery of fluids in gem diamonds showing similar major element chemistry to fluid-rich diamonds suggest that many diamonds may share a common spectrum of parental fluids (Jablon and Navon, 2016). Here we test this idea further using new trace element data from gem diamonds.

Trace Elements in high purity gem diamonds from the Victor Mine

We present trace element data from gem-quality diamonds originating from De Beers' Victor Mine, Ontario, Canada whose paragenesis can be constrained from the solid macro-inclusions that they contain. Sixteen P-type diamonds - eight bearing silicate inclusions and eight with sulphide inclusions - were analyzed using a novel ‘off-line’ LA-ICP-MS sampling technique followed by sector-field ICPMS (McNeill et al., 2009). This method utilizes a closed-system laser ablation cell in which a diamond is ablated and the products trapped, allowing the accumulation of higher volumes of analyte, thus greatly increasing the chance of producing quantitative data by improving the “signal to noise ratio” many times over ‘on-line’ laser ablation. Solutions are analysed against matrix-matched standard solutions for calibration. The analysed area of each diamond was optically free of solid inclusions or other impurities at the 10 micron scale.

The concentrations of a wide range of elements for all analyzed high quality gem diamonds from the Victor diamond mine are very low, with medians for Sr (9 ppb), Rb (8 ppb), Ba (20 ppb), U (0.3 ppb) and Y (2 ppb), and REE abundances varying from 0.1 to 0.0001 x chondrite. Consistent with their inclusion content (silicates or sulphides), the Victor diamonds can be divided into two compositional groups: Silicate inclusion-bearing diamonds have more fractionated REE_N patterns (median Ce_N/Yb_N ~ 40) than sulphide inclusions-bearing diamonds (median Ce_N/Yb_N ~ 8). In addition, sulphide inclusion-bearing diamonds have more widely varying and generally higher siderophile element concentrations (e.g., Ni, Fe and Co). A select few ratios (such as Sm/Hf) are significantly more fractionated in the silicate-bearing diamonds at Victor, although overall these differences are not striking and also not

consistent across all key trace element ratios. It, therefore, seems likely that the silicate and sulphide-bearing diamonds formed by gradations of the same processes.

Comparison with other gem diamonds

The very low trace element concentrations for the analysed Victor diamonds are significantly lower than values reported for fibrous stones but consistent with “closed-cell” ablation data previously reported for high quality gem diamonds from the Cullinan and Kimberley Pool mines in South Africa, and the Udachnaya Mine in Siberia (McNeill et al., 2009; Melton et al., 2012). Overall, the multi-element patterns for high-purity gem diamonds analysed from these locations compare well with Victor diamonds (Fig. 1). Somewhat less pure “gem” diamonds from the Newlands and Finsch kimberlites (W Kaapvaal craton), also analysed by “closed-cell” ablation, show significantly higher and more fractionated trace element concentrations, correlating broadly with their lower clarity.

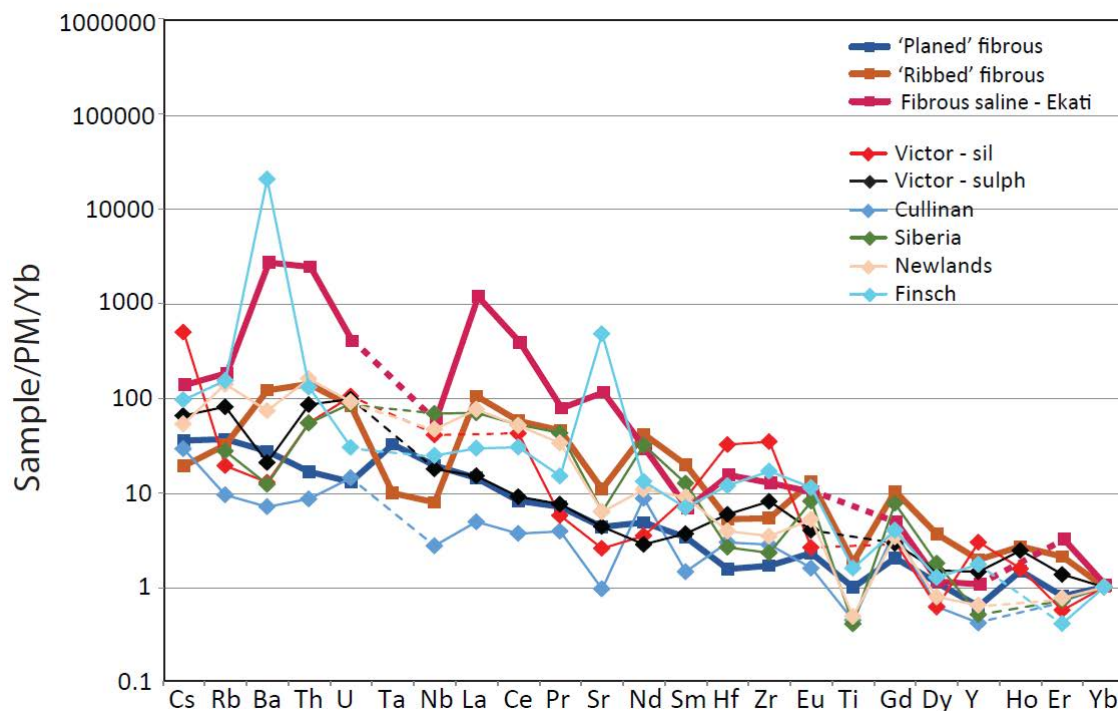


Figure 1: Double-normalised trace element patterns for gem quality diamonds from Victor (Canada; sulphide and silicate paragenesis), S. Africa (Cullinan, Newlands & Finsch) and Siberia (Mir and Udachnaya) (this study and McNeill et al., 2009), for two common patterns, ‘planed’ and ‘ribbed’, of HDFs in fibrous diamond (Weiss et al., 2013) and for saline HDFs in fibrous diamond from the Fox kimberlite (Weiss et al., 2015). Samples are normalised to Primitive Upper Mantle and to a Yb value of 1x PUM to equalise variations in abundance levels caused largely by differences in fluid inclusion abundance.

Normalized first to primitive mantle and then to a Yb_N value of 1, the multi-element data reveal many similarities between the trace element characteristics of the gem diamonds (this study) and of fibrous, fluid-rich diamonds. Multi-element patterns for the high quality gem diamonds from Victor, Cullinan and Siberia resemble the less fractionated “planed” trace element pattern, while the Newlands diamond suite more closely resembles the ‘ribbed’ trace-element pattern, characterized by pronounced peaks and troughs. The Finsch diamonds, derived from a G10 garnet-bearing harzburgite, show striking positive anomalies in Ba and Sr that strongly resemble the patterns of fibrous diamonds containing “saline” inclusions (Fig. 1; e.g., Weiss et al., 2015).

Discussion

Depending on the element, trace element abundances in Victor gem quality diamonds are among the lowest or the lowest measured in gem diamonds. This is conforming with the very high quality and value of the Victor production. Consistent with the major element determinations of Jablon and Navon (2016), we show clear similarities in the trace element patterns of fibrous and gem diamonds, indicating the presence of micro- to nanometer scale, highly dispersed fluid inclusions. While there are subtle differences between some sulphide and silicate-bearing diamonds at Victor, we view the fluids trapped within them as having broadly the same origin and having experienced similar petrogenetic processes, although varying in extent. The quantitative nature of the data produced in this study and that of McNeill et al. (2009) establishes clearly that “planed” trace element patterns characterise the parental fluids of both gem and fibrous diamonds. This fluid likely is a small-degree hydrous melt of carbonated peridotite and from our data, appears to invade both peridotitic and eclogitic diamond substrates. Our data also document the first direct link between some gem diamonds, sampled from a Finsch harzburgite, and highly saline fluids that have been proposed to originate from subducted slabs (Weiss et al., 2015). Overall, we see the same spectrum of fluids in gem diamonds that was previously documented in fibrous diamonds, consistent with similar compositions of diamond-forming fluids (at least in terms of major and trace elements) over billions of years (Smith et al., 2012).

References

- Jablon BM, Navon O (2016) Most diamonds were created equal. *Earth and Planetary Science Letters* 443: 41-47.
- Klein-BenDavid O, Pearson DG, Nowell GM, Ottley CJ, McNeill JCR, Cartigny P (2010) Mixed fluid sources involved in diamond growth constrained by Sr–Nd–Pb–C–N isotopes and trace elements. *Earth and Planetary Science Letters* 289: 123-133.
- Klein BenDavid O, Pearson DG, Nowell GM, Ottley CJ, McNeill JCR, Logvinova A, Sobolev NV (2014) The sources and time-integrated evolution of diamond-forming fluids - trace elements and Sr isotopic evidence. *Geochimica Cosmochimica Acta, Geochimica et Cosmochimica Acta* 125: 146-169.
- Melton GL, McNeill J, Stachel T, Pearson DG, Harris JW (2012) Trace elements in gem diamond from Akwatia, Ghana and DeBeers Pool, South Africa. *Chemical Geology* 314-317: 1-8.
- McNeill JCR, Pearson DG, Klein-BenDavid O, Nowell GM, Ottley CJ, Chinn I (2009) Quantitative trace element analysis of gem quality diamonds. *Journal of Physics: Condensed Matter* 21: 364207, 13 pp.
- Schrauder M, Koeberl C, Navon O, (1996) Trace element analyses of fluidbearing diamonds from Jwaneng, Botswana: *Geochimica et Cosmochimica Acta* 60: 4711-4724.
- Smith EM, Kopylova MG, Nowell GM, Pearson DG, Ryder J (2012) Archean mantle fluids preserved in fibrous diamonds from Wawa, Superior craton. *Geology* 40: 1071–1074.
- Weiss Y, Griffin WL, Navon O (2013) Diamond-forming fluids in fibrous diamonds: The trace-element perspective. *Earth and Planetary Science Letters* 376: 110-125.
- Weiss Y, McNeill J, Pearson DG, Nowell GM, Ottley CJ (2015) Highly saline fluids from a subducting slab as the source for fluid-rich diamonds. *Nature* 524: 339–342.
- Zedgenizov DA, Rege S, Griffin WL, Kagi H, Shatsky VS (2007) Composition of trapped fluids in cuboid fibrous diamonds from the Udachnaya kimberlite: LAM-ICPMS analysis. *Chemical Geology* 240, 151-162.

Peridotite xenoliths of the Chidliak kimberlite province (NE Canada): The North Atlantic cratonic mantle with recent thermal and Ti-Na metasomatic disturbance

M. G. Kopylova^{1,2}, E. Tso¹, F. Ma¹, J. Liu^{2,3}, D. G. Pearson²

1 - University of British Columbia, Vancouver, Canada; mkopylov@eos.ubc.ca, etso@eos.ubc.ca; FrankMa92@hotmail.com

2 - University of Alberta, Edmonton, Canada; jingao@cugb.edu.cn, gdpearso@ualberta.ca

3 - China University of Geosciences, Beijing, China

We studied the petrography, mineralogy, thermobarometry and whole rock chemistry of 120 peridotite and pyroxenite xenoliths collected from the 156-138 Ma Chidliak kimberlite province (Southern Baffin Island). Xenoliths from pipes CH-1, -6, -7, and -44 are divided into two garnet-bearing series, peridotites and wehrlites – olivine pyroxenites. The peridotites may contain spinel (37-62 wt% Cr₂O₃), while wehrlites may contain microilmenite. Peridotites and wehrlites show widely varying textures, from coarse to sheared. Xenoliths from the CH-6 pipe differ from xenoliths in other pipes in terms of their petrography and relative abundances of rock types. Textures indicating the late formation of garnet and clinopyroxene are present in all xenolith series, with the most common texture being garnet mantled by clinopyroxene. Pyroxenes are invariably rimmed by secondary calcic minerals, which appear as dark coronas. SEM observations identify these as 3-15 micron thick mantles of clinopyroxene (on orthopyroxene) and monticellite (on clinopyroxene).

Olivine is more magnesian in coarse peridotites with spinel (Mg#=91-93) than in garnet-bearing coarse and sheared peridotites (Mg#=89-94) or wehrlites (Mg#=85-92). Enstatites in CH-6 peridotites are on average lower in CaO, Cr₂O₃, Al₂O₃, TiO₂, and Na₂O than those in peridotites from CH-1, -7, and -44. Cr-diopsides in all rock types from CH-6 are less titaniferous than Cr-diopsides from other pipes. Garnets are predominantly chromian pyropes from the lherzolitic CaO - Cr₂O₃ field.

Chidliak xenoliths yield equilibration temperatures between 600 and 1300°C and pressures between 20 and 74 kb (Fig. 1). The CH-6 pipe samples shallow to deep mantle spanning the entire P-T range, while pipes CH-1, -7, -44 exclusively sample deeper mantle at P>50 kb. The pressure-temperature array in shallow (P<50 kb) Chidliak mantle falls on conductive geotherms with 33-35 mW/m² surface heat flow. There is a sharp change of the thermal state at P~50 kb, where a cold, shallow mantle is underlain by a hotter, thermally heterogeneous, disturbed mantle with temperatures between 1000 and 1300°C. In the mantle beneath the CH-6 pipe, coarse peridotites occupy shallower depths than sheared peridotites. The deepest samples (P>64 kb) are represented by coarse wehrlites and sheared peridotites. The mantle sampled by CH-1, -7, and -44 pipes also demonstrates a change from marginally shallower coarse peridotites to deeper (54-65 kb) sheared peridotites. Wehrlites from CH-1, -7, and -44 pipes are derived from the shallow mantle where they were not accompanied by any coexisting rock types, but also occur deeper, together with coarse and sheared peridotites. The thermal state of Chidliak's shallow mantle (P<50 kb) resembles that of the Slave and Siberian cratons, and is distinctly colder than the Kaapvaal mantle, but hotter than the shallow mantle in Fennoscandia. The cool shallow geotherm and very high proportion of thermally disturbed deeper samples suggest that the Chidliak mantle is analogous to the Udachnaya cratonic mantle section.

The whole rock major element chemistry of the Chidliak xenoliths reflects initial high levels of melt depletion typical of cratonic mantle, and subsequent refertilization in Ca and Al. Chidliak samples have higher CaO contents relative to Al₂O₃ compared to other cratonic peridotites. Almost half of the Chidliak samples fall off the global Mg/Si-Al trend due to excess Al for a given Mg/Si ratio; this pattern matches the observed late development of Al-rich minerals such as garnet and clinopyroxene. The peridotites and wehrlites, on average, have 83±9 vol.% Ol, 7±7 vol.% Opx, 4±4 vol.% Cpx, and 6±4 vol.% Gar as determined by computer-assisted modal analysis of 120 scanned thin section images. The Chidliak mantle plots close to the "shallow oceanic melt extraction" trend (Fig. 2), being rich in

forsteritic olivine; these compositional traits resemble the North Atlantic Craton (NAC) rather than the more orthopyroxene-rich mantle of other cratons. We assign the more complex Ca-Al systematics of the Chidliak peridotites to repeated episodes of Ca-rich, Si-poor metasomatism, which introduced clinopyroxene and garnet, and later replaced orthopyroxene and clinopyroxene with secondary clinopyroxene and monticellite. The calcic metasomatism was most likely carbonatitic by nature and is manifest in its greatest extent by the formation of wehrlites and “diffuse” veins of pyroxenites. The carbonatitic metasomatism was accompanied by an influx of Fe, which lowered the olivine Mg-numbers in wehrlites (Fig. 2). The metasomatism acted upon the entire sampled mantle depth, from 35 to 70 kb, where clinopyroxene and garnet modes are uniformly and heterogeneously high in the ~110 km deep mantle segment. Equally wide-ranging are Mg-numbers of olivine, defining spans of 4 units at each given pressure.

The Chidliak lithospheric mantle is Archean in age (Liu et al., 2017). It demonstrates strong compositional similarity with only one adjacent block of the cratonic mantle, the North Atlantic Craton (NAC). It is distinctly different from the mantle samples studied so far from the equally proximal Rae and Superior cratons. The Chidliak mantle resembles the NAC in its bulk composition (e.g., Wittig et al., 2008), by the dominance of carbonatitic rather than silicic metasomatism, as well as by its mineral chemistry and the Sr-Nd characteristics of the mantle reservoirs for kimberlites (Heaman et al., 2015). We interpret these features as representing the former contiguous nature of the mantle beneath Chidliak and the NAC extant on W. Greenland, prior to the subsequent rifting into separate continental fragments. The carbonatitic metasomatism and introduction of calcic minerals affected cratonic blocks on a regional scale including the proximal blocks of the NAC and the Chidliak mantle. The identical Sr-Nd systematics of the West Greenland Proterozoic kimberlites and Jurassic Chidliak kimberlites suggests that this unique geochemical reservoir must have developed during Neoproterozoic mantle metasomatic activity. The area may have been in a single Archean NAC that incorporated the Chidliak block, or may have developed in the northeastern part of Laurentia after its 1.8 Ga amalgamation.

Another, more recent type of mantle metasomatism, which affected the Chidliak mantle, is characterised by Ti-Na enrichment. It is expressed as elevated Ti in clinopyroxene and elevated Na and Ti in garnet, typical of Chidliak sheared peridotites from CH-1, -7, and -44. The CH-6 xenolith suite largely excludes such samples. The metasomatized deep mantle shows 1) a high ratio of sheared to coarse samples; 2) a high proportion of mosaic-porphycroclastic samples among sheared peridotites; and 3) temperatures varying isobarically by up to 200°C, indicative of a higher convective heat flow. As represented by the xenolith suite, the Ti-Na metasomatic imprint extends across depths from 55 to 65 kbar. The horizontal scale of the imprint is more ambiguous and could be as regionally extensive as 10's of kms, or as local as < 1 km. The latter scale is constrained by the varied abundance of Ti-enriched garnets within a single kimberlite, which may reflect differential depth sampling of a metasomatically stratified mantle, or different intensities of Ti-Na metasomatism at the scale of individual kimberlites. We postulate that the Ti-Na (megacryst-like) style of metasomatism is genetically related to textural modification and/or thermal transients that affected the deep Chidliak mantle. The time-scale of such transient events relates to a conductive length-scale and could be between 10's Kyr and 1-2 Myr. A highly localized influx of hot hydrous proto-kimberlite fluids rich in Ti, Na and other magmaphile elements weakened the mantle, and triggered formation of sheared peridotites.

References:

- Heaman LA, Pell J, Grütter HS, Creaser RA (2015) U-Pb geochronology and Sr/Nd isotope compositions of groundmass perovskite from the newly discovered Jurassic Chidliak kimberlite fields, Baffin Island, Canada. *Earth Planet Sci Letters* 415: 183-199
- Liu J, Pearson DG, Harris GA, Kopylova MG, Tso E (2017). Age and evolution of the lithospheric mantle beneath southern Baffin Island, Nunavut, Canada. 11th IKC Extended Abstract 11IKC-4584
- Nimis P, Grütter H (2010) Internally consistent geothermometers for garnet peridotites and pyroxenites. *Contrib Miner Petrol* 159 (3): 411-427

Wittig N, Pearson DG, Webb M, Ottley CJ, Irvine GJ, Kopylova M, Jensen SM, Nowell GM (2008)
Origin of cratonic lithospheric mantle roots: A geochemical study of peridotites from the North
Atlantic Craton, West Greenland. *Earth Planet Sci Letters* 274 (1-2): 24-33

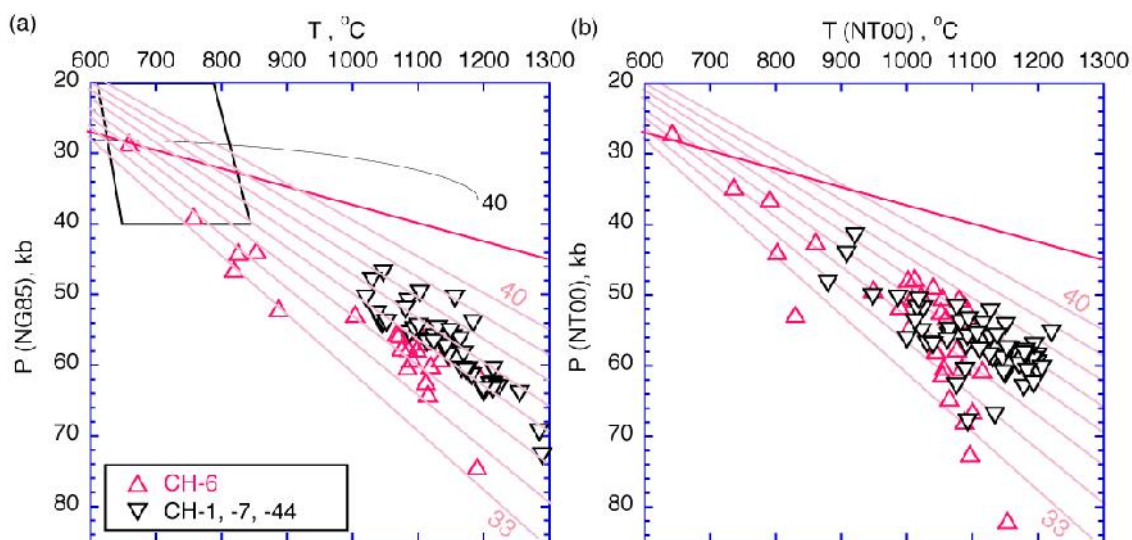


Fig. 1. Pressure-temperature plots for Chidliak peridotites. (a): Taylor (1998) thermometer for lherzolites and the Nimis & Grütter (2010) thermometer for harzburgites combined with the Nickel & Green (1985) barometer; (b): Nimis & Taylor (2000) thermobarometry, only samples that passed all tests for inter-mineral equilibrium are plotted. The open rhombic field on panel (a) corresponds to a possible range of temperatures for spinel-bearing lherzolites at assumed pressures from 20 to 40 kb. Black curve marked “40” in (a) shows the pressure of equilibration of a single spinel-garnet harzburgite (O’Neill, 1981) with Cr_2O_3 in spinel = 40 wt.% and $X_{\text{Fe}^{3+}} = 0-0.1$ for peridotite containing olivine F92. All references for thermobarometers are in Nimis & Grütter (2010). Model conductive geotherms labeled 33-40 mW/m^2 are from Hasterok & Chapman (2011). The red line is the graphite-diamond transition curve (Day, 2012).

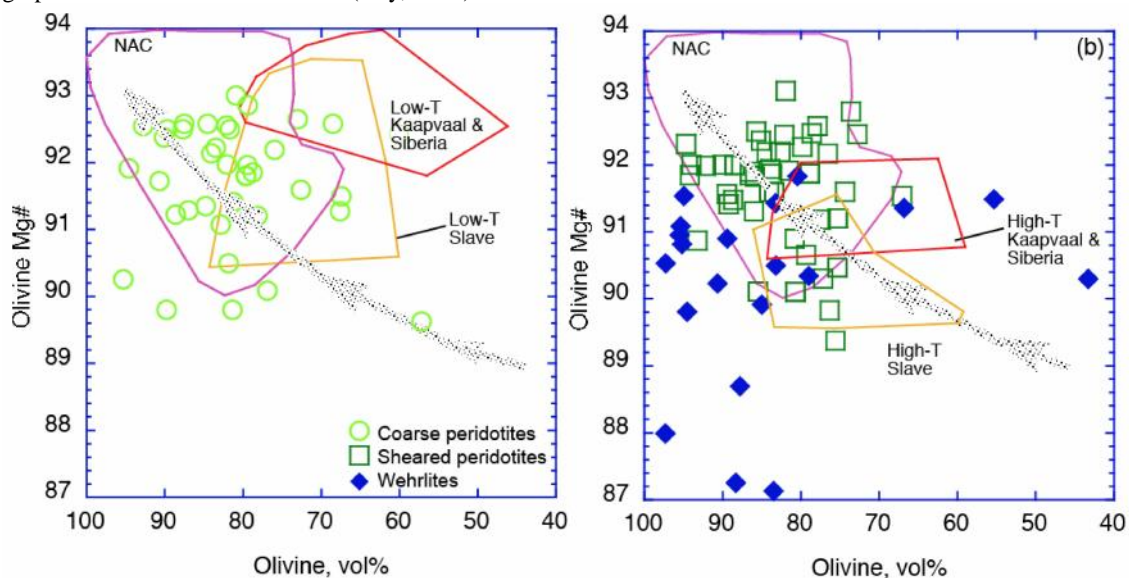


Fig. 2. Olivine mode vs. olivine Mg-number ($\text{Mg}/(\text{Mg}+\text{Fe})$, mol.%) for Chidliak xenoliths in comparison with the Kaapvaal, Slave and North Atlantic Cratons (NAC). (a): Coarse Chidliak peridotites with fields for low-T Kaapvaal & Siberia (red field) and Slave (yellow field) (Kopylova and Russell, 2000). The latter field includes spinel and garnet peridotites. (b): Sheared Chidliak peridotites and wehrlites with fields for high-T Kaapvaal & Siberia (red outline) and Slave (yellow outline) (Kopylova and Russell, 2000). The North Atlantic Craton data are from Pearson and Wittig (2008). Grey patterned arrows are the “shallow oceanic trend” of Boyd (1989).



The mineral chemistry of the megacryst suite from the Schuller and Premier kimberlites.

Deon De Bruin ^{1,2}

¹ *Diamond Indicator Minerals Pty. Ltd., Perth, Australia deondebruin@iinet.net.au*

² *CET, School of Earth and Environment, The University of Western Australia, Australia*

Introduction

The Schuller and Premier kimberlites are situated approximately 30 km east-northeast of Pretoria, South Africa and occur in a cluster of eleven kimberlites of ca. 1180 Ma age (Allsopp et al., 1989).

Clinopyroxene, orthopyroxene and garnet megacrysts from the Schuller and Premier kimberlites were analysed for major elements by electron microprobe. The megacrysts phases from Schuller and Premier Kimberlites define unusually large compositional ranges and can be subdivided into a number of distinct chemical groups. The overall compositional range encompass and expand the range for both Cr-poor and Cr-rich clinopyroxene megacrysts from kimberlite localities world-wide (De Bruin, 1993).

The main groups were classified on the basis of clinopyroxene chemistry (Mg#, Ca# and Cr₂O₃) as: sub-calcic low-Mg# (group 1), sub-calcic intermediate to high Mg# (group 2), calcic low-Mg# (group 3) and calcic high-Mg # (group 4) varieties (De Bruin, 1993). The garnet and orthopyroxene megacrysts were also found to fall in distinct compositional groups but could not be linked to the clinopyroxene groups with confidence. In this study the additional analyses were obtained for orthopyroxene and garnet megacrysts from the Schuller and Premier Kimberlites.

The expanded data sets from Schuller were used to link the clinopyroxene and orthopyroxene groups on basis of similarities in the Ca#, Mg# and Cr₂O₃ distributions as shown in Fig. 1. The Mg# vs. Ca# plot for clinopyroxene and orthopyroxene megacrysts show a remarkably similar in distribution of the different compositional groups relative to the trend shown for Monastery megacrysts. A sample with co-existing group 3 clinopyroxene and orthopyroxene could be used to establish a direct link between these mineral groups. Three orthopyroxene megacrysts from Schuller, with the lowest Mg# compositions were assigned to the group 1 population. Two co-existing group 4 orthopyroxenes and garnet were used to identify the corresponding group 4 garnet population. The garnet megacryst data set for Premier contained a low Mg#, low Cr₂O₃ content population that has the relative similar chemistry and characteristic to the Schuller group 1 clinopyroxene population. A single sample from Schuller fall within this garnet population Premier and thus establishes the presence of co-existing garnet with the group1 clinopyroxene megacrysts at Schuller.

At Schuller corresponding orthopyroxene and garnet populations exist that matches the four clinopyroxene megacrysts populations while at Premier three equivalent megacryst populations are present with corresponding garnet and clinopyroxene group 1 and 4 and corresponding garnet and orthopyroxene with group 2 clinopyroxene.

Single crystal clinopyroxene pressure temperature estimates show that the main groups have formed at different depth levels with groups 1 and 2 at deeper levels and higher temperatures and groups 3 and 4 at shallower depths and at lower temperatures (Fig. 2).

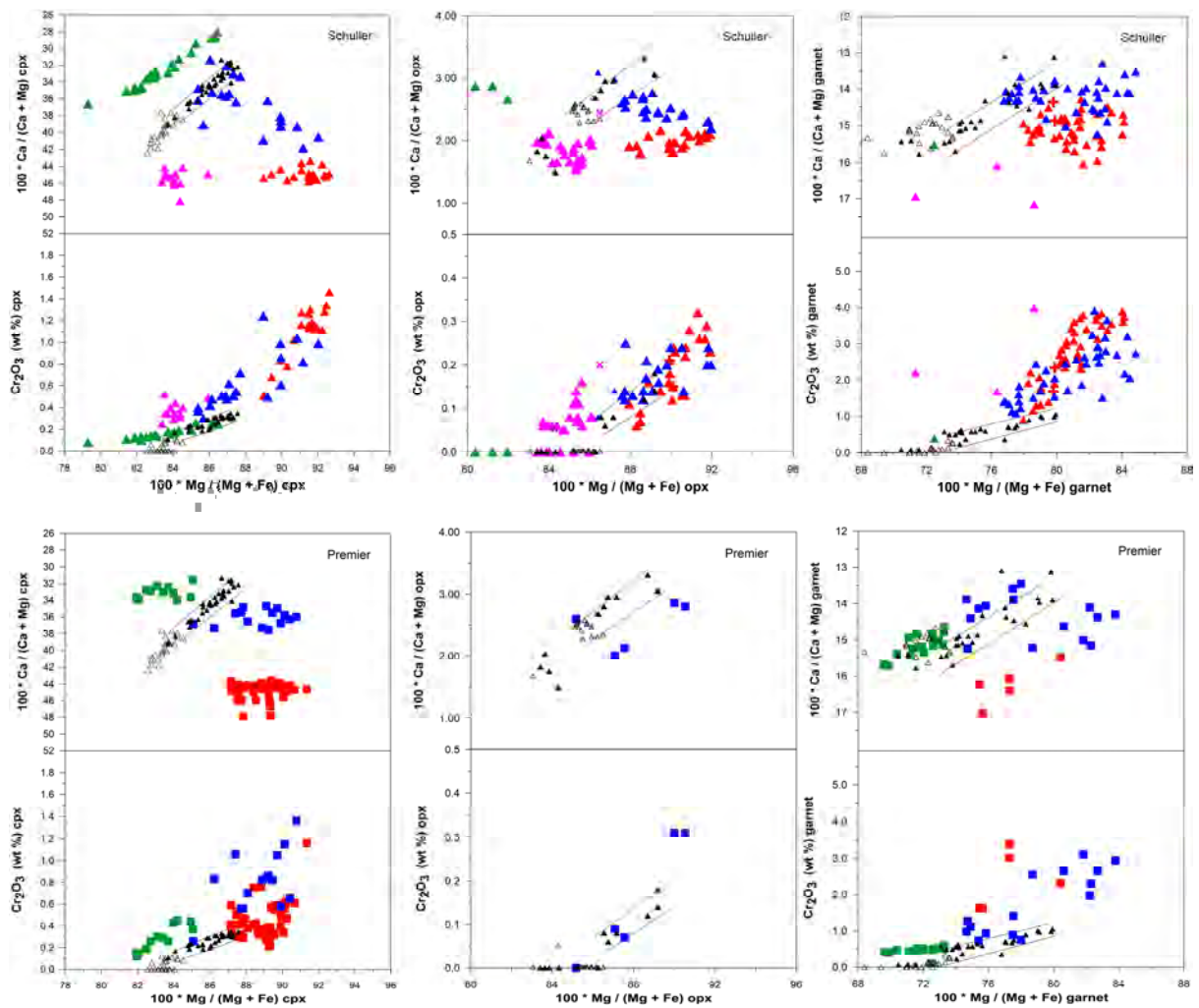


Figure 1. Ca# and Cr₂O₃ vs. Mg# for clinopyroxene, orthopyroxene and garnet megacrysts from Schuller and Premier. Symbols: Schuller (triangles) and Premier (squares). Megacrysts group 1 (green), group 2 (blue), group 3 (purple) and group 4 (red). The black symbols and boundary lines show the compositional spread of clinopyroxene megacrysts from Monastery (data from Jakob, 1977) where solid and open symbols represent the discrete and ilmenite associations, respectively.

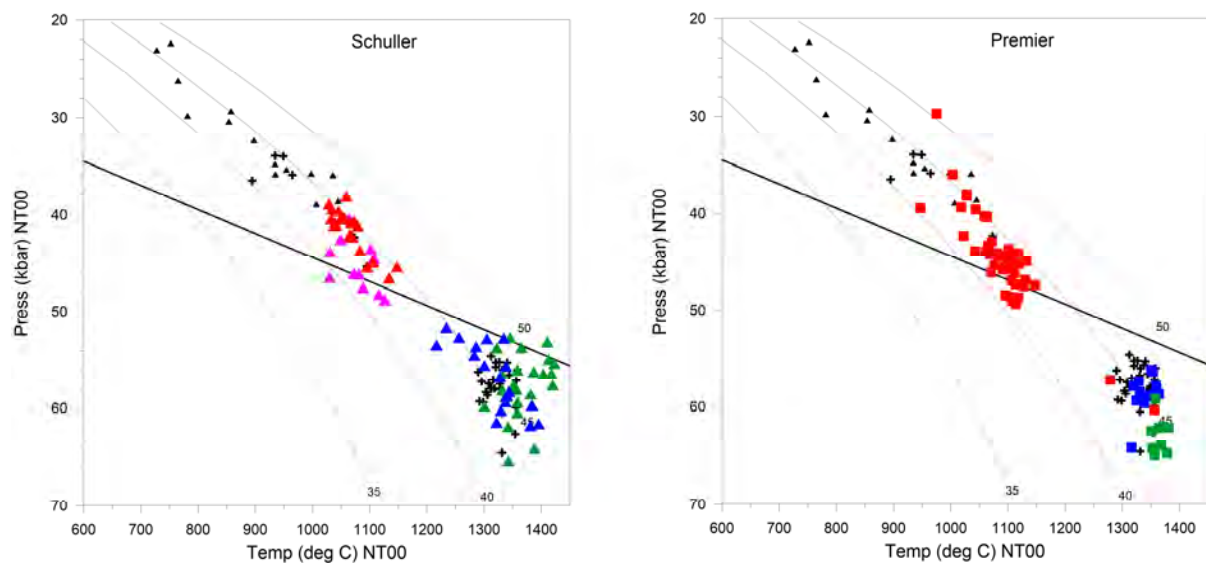


Figure 2. Pressure-temperature estimates for clinopyroxene megacrysts from the Schuller and Premier kimberlites using the single clinopyroxene thermobarometer of Nimis and Taylor (2000). Symbols as for Fig. 1 with black triangles and crosses representing values for lherzolite clinopyroxene for xenoliths from Schuller and Premier respectively. Reference conductive model geotherms with surface heatflows of 35, 40, 45 and 50 mW/m² are those of Pollack and Chapman (1977). Graphite=diamond from Kennedy and Kennedy (1976).

References

- Allsopp HL, Bristow, JW, Smith CB, Brown R, Gleadow AJW, Kramers JD, Garvie O (1989) A summary of radiometric dating methods applicable to kimberlites and related rocks. *Kimberlites and Related Rocks*, vol. 1, Their composition, occurrence, origin and emplacement. Spec. Publ.-Geol. Soc. Aust., vol. 14, pp. 343– 357.
- De Bruin D (1993) The megacryst suite from the Schuller kimberlite, South Africa. *Geological Survey of South Africa Bulletin*, 114, 17 pp
- Jakob WRO (1977) Geochemical aspects of the megacryst suite from the Monastery kimberlite pipe, Unpublished M.Sc. thesis, University of Cape Town, South Africa, 81pp
- Nimis P, and Taylor WR (2000) Single clinopyroxene thermobarometry for garnet peridotites. Part I. Calibration and testing of a Cr-in-Orthopyroxene barometer and an enstatite-in-Orthopyroxene thermometer. *Contributions to Mineralogy and Petrology*, 139, 541-554
- Kennedy CS, Kennedy GC (1976) The equilibrium boundary between graphite and diamond. *Journal of Geophysical Research* 81, 2467–2470
- Pollack HN, Chapman, DS (1977) On the regional variations of heat flow, geotherms and lithosphere thickness. *Tectonophysics* 38, 279–296.



Three styles of diamond resorption in a single kimberlite: Does crustal xenolith assimilation play a role?

Yana Fedortchouk¹, Ingrid L. Chinn², Maya G. Kopylova³

¹Dalhousie University, Halifax, Canada, yana@dal.ca

²De Beers Exploration, Johannesburg, South Africa, Ingrid.Chinn@debeersgroup.com

³University of British Columbia, Vancouver, Canada, mkopylov@eos.ubc.ca

Introduction

Many features of kimberlites indicate explosive eruptions and high content of volatiles. Theoretical modelling and experimental estimates of volatile solubility in kimberlite-like melts are the two main approaches used to constrain exsolution of fluid during kimberlite ascent. Both approaches are hampered by the unknown composition of kimberlite melts. Here, we present a new method for investigating the kimberlitic fluid by using direct evidence from diamond resorption features. Experiments show that diamond interaction with H₂O-rich or CO₂-rich fluids, and with volatile-undersaturated melts produce contrasting resorption features on diamonds. We use 802 diamonds (> 0.5 mm) collected in restricted depth intervals in three drillholes from BK1 kimberlite and one drillhole in AK15 coherent kimberlite (Orapa cluster, Botswana). The diamond data and depth ranges can be found in Table 1 and Fig. 1. In BK1 kimberlite, the drillholes sampled three kimberlite lithologies: coherent kimberlite CK-A, coherent kimberlite CK-B, and a volcanoclastic kimberlite (MVK). We also examined 70 thin-sections from the same drillholes to compare the fluid record in diamond resorption features with the kimberlite textures. The robust geological control on the diamond samples provides a unique opportunity to reconstruct the composition and the parameters of exsolution for magmatic fluid in these kimberlite lithologies.

| Kimberlite | BK1 | BK1 | BK1 | AK15 | TOTAL |
|-------------------------------|-------|-------|-------|-------|--------------|
| Drillhole | H005 | H007 | H008 | H001 | |
| Depth interval (m) | 0-164 | 0-200 | 0-200 | 0-163 | |
| Kimberlite facies | CK-A | MVK | CK-B | CK | |
| Diamonds total | 169 | 294 | 192 | 357 | 1,012 |
| Diamonds studied | 169 | 190 | 168 | 275 | 802 |
| Resorption: | | | | | |
| Kimberlite-induced resorption | 28 | 37 | 90 | 78 | 233 |
| Kimberlitic - mantle combined | 34 | 7 | 18 | 40 | 99 |
| Mantle-derived resorption | 61 | 30 | 14 | 59 | 164 |
| Undefined morphology | 46 | 116 | 46 | 98 | 306 |

Table 1: Macro-diamond samples from four drillholes in BK1 and AK15 kimberlites showing the proportion of diamonds with different origin of resorption (CK-coherent kimberlite, MVK-massive volcanoclastic kimberlite).

Diamond resorption in kimberlite magma and inherited from the mantle

Each of the studied diamond parcels from the four lithologies has one unique resorption style that is 1) the most common for this parcel, 2) present on all rounded tetrahedral (THH) diamonds, 3) present on the rounded sides of pseudohemimorphic diamonds, 4) shown by diamonds attached to kimberlite, and 4) developed along the edges of diamonds with combination of two resorption styles. We can confidently conclude that this specific resorption style represents kimberlite-induced resorption, while any other resorption style in the same parcel is inherited from the mantle. Diamonds with only kimberlitic resorption comprise ~25% in CK-A lithology, ~50% in MVK and AK15 samples, and ~75% in CK-B lithology (Fig. 1). All parcels show an increase in the intensity of kimberlite-induced resorption with drill hole depth (Fig. 1), and this is especially evident in the MVK and AK15 parcels.

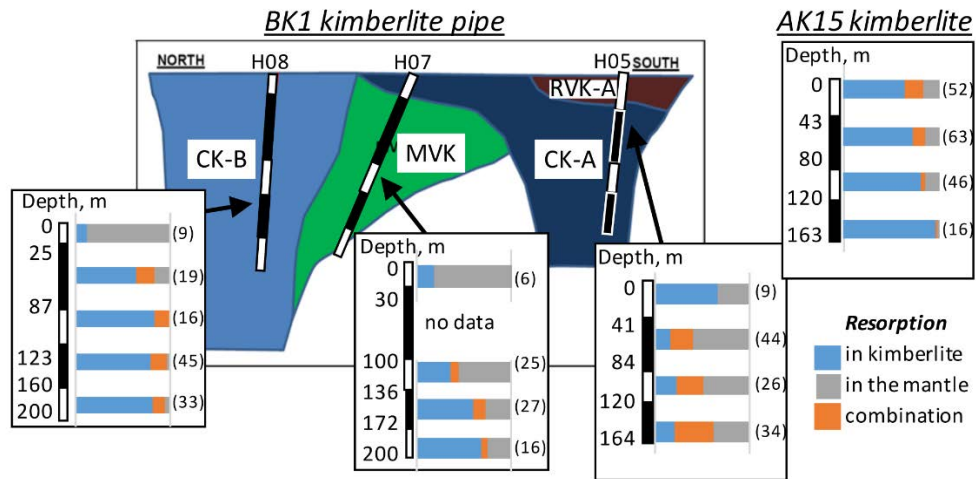


Figure 1: Cross-section of BK1 pipe and position of drill holes in the two lobes filled with coherent CK-A and coherent CK-B kimberlites, and in a pyroclastic kimberlite (MVK) between these lobes. AK15 has one coherent lithology. The inserts show the proportions of diamonds with kimberlite-induced and mantle-derived resorption, and with a combination of both resorption styles with depth in each lithology. The number of diamonds studied in each depth interval is given in brackets.

Three styles of kimberlite-induced resorption in BK1 pipe

Kimberlite-induced resorption is different in the three lithologies from BK1 kimberlite (Fig. 2). MVK diamonds developed glossy well rounded surfaces (Fig. 2A), which are similar to the diamonds from volcanoclastic kimberlites in other localities and resemble experimental products of diamond dissolution in H₂O-rich fluid (Fedortchouk et al., 2010). Very similar kimberlitic resorption is observed in CK-A lithology, but these diamonds exhibit chains of micro-cavities with a diameter of 5-15 μ m (Fig. 2B). Most distinctive is the kimberlite-induced resorption on CK-B diamonds, which yielded severely corroded rounded crystals (Fig. 2C) resembling experimental products of diamond dissolution in carbonate melt (Zhang et al., 2015). SEM imaging revealed similarities between the corroded surfaces of CK-B diamonds and micro-cavities on CK-A diamonds, implying that these cavities represent an initial stage of the same resorption event that affected CK-B diamonds. Surprisingly, resorption in the coherent AK15 kimberlite is identical to that of the MVK samples from BK1 in style and intensity.

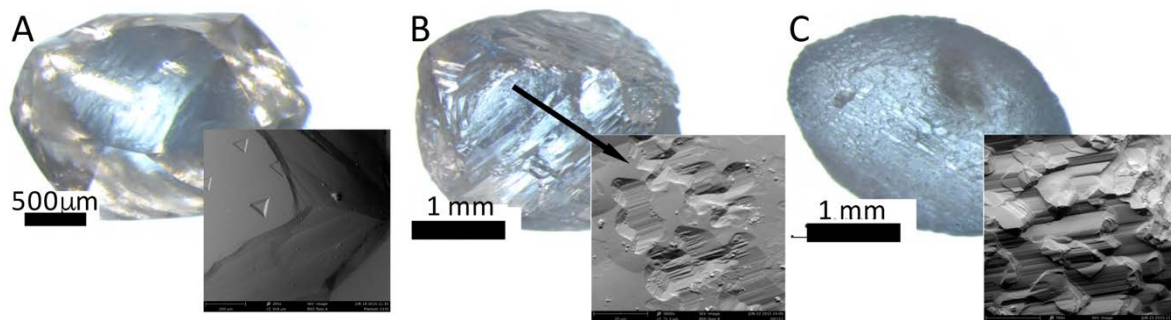


Figure 2: Microphotographs and secondary electron (SEM) images of kimberlite-induced resorption: A - glossy or frosted THH with thin striations, and negatively oriented trigons in BK1 MVK and in AK15; B - similar glossy THH with “chains” of micron-size cavities in CK-A; C - THH with extremely rough corroded surfaces in CK-B.

Kimberlite textures

The kimberlite textures show contrasting features in BK1 lithologies. CK-B is the only lithology with no segregations in the groundmass, no magmaclasts or other indicators of fragmentation. In contrast, CK-A is a coherent macrocrystic kimberlite showing segregatory groundmass formed via fluid exsolution and local development of diffuse magmaclasts. MVK and AK15 also demonstrate textures indicative of fluid exsolution, i.e. magmaclastic texture in MVK with classic “pelletal lapilli” and

segregationary groundmass in AK15. Crustal xenoliths (mostly Karoo basalts) are common in MVK (~30%) and in AK-15 where they increase in abundance with drill hole depth from 5% to 60%. All xenoliths/xenocrysts are mantled by rims of fibrous clinopyroxene. CK-B contains 1-3% of totally digested Karoo xenoliths appearing as patches of serpentine. CK-A contains no crustal xenoliths.

The role of fluid

The different role of volatiles in the three BK1 lithologies is supported by both diamond resorption and kimberlite petrography. The CK-B unit reached the surface as a volatile-undersaturated melt (confirmed by the corrosive diamond resorption and the absence of segregationary groundmass textures). Its slow ascent in the absence of fluid phase explains the intensive kimberlite-induced resorption (Fig. 1). MVK magma reached the surface fragmented as seen in the presence of magmaclasts, with abundant free fluid as evidenced by glossy diamond resorption. Exsolution of fluid in CK-A unit is also confirmed by the glossy diamond resorption and segregationary groundmass textures, while the diamonds also record the second resorption event in volatile-undersaturated melt. The similarity of diamond resorption and groundmass textures in pyroclastic MVK and coherent CK-A units suggests that CK-A represents either a reconstituted (welded or cindered) clastogenic lava (Hayman et al., 2008) or a frozen volcanic degassing front (Hetman et al., 2004). The petrography of CK-A does not support reconstitution model but is compatible with the origin of CK-A and MVK units from a single batch of fluid-oversaturated magma which experienced local degassing. The CK-B unit was formed from a different fluid-undersaturated magma batch. In AK15 groundmass textures contradict reconstitution of extrusive magma and glossy diamond resorption must have been caused by magmatic fluid insufficient for fragmentation.

H₂O and CO₂ reach saturation in kimberlite magma only within the last 2.5 km of ascent (Moussallam et al., 2016). The high proportion of rounded THH diamonds and the character of resorption on BK1 and AK15 diamonds require fluid presence at a much greater depth (> 1 GPa) (Zhang et al., 2015). CO₂ degassing can be triggered by dissolution of silicate-rich material in carbonate-rich magma. Reaction between mantle orthopyroxene and kimberlite melt can start as deep as at 2.5 – 3.5 GPa (Stone et al., 2016). Reaction of kimberlite magma with silicic crustal xenoliths through the tens of kilometers of crust would depend on the volume of crustal xenoliths entrained and assimilated by different portions of the rising kimberlite. Indeed, both units with glossy diamonds, BK1 MVK and AK15, demonstrate significant assimilation of Karoo basalts. CK-A and CK-B lithologies in BK1 have diamonds with corrosive (melt) features and very few assimilated xenoliths. Our work shows that diamond resorption morphology provides a robust record of fluid exsolution during magma emplacement. Reactions of kimberlite melt with mantle orthopyroxene, crustal xenoliths, and decompressional degassing provide three mechanisms for fluid exsolution at progressively shallower depths. We propose that the depth of fluid exsolution and its retention by the melt plays an important role in diamond preservation.

References

- Fedortchouk Y, Matveev S, Carlson JA (2010) H₂O and CO₂ in kimberlitic fluid as recorded by diamonds and olivines in several Ekati diamond mine kimberlites, NWT, Canada. *Earth Plan Sci Let* 289:549-559.
- Hayman PC, Cas RAF, Johnson M (2008) Difficulties in distinguishing coherent from fragmental kimberlite: a case study of the Muskox pipe (Northern Slave Province, Nunavut, Canada): *J. Volcanol. Geotherm. Res.* 174:139–151.
- Hetman CM, Scott Smith BH, Paul JL, Winter FW (2004) Geology of the Gahcho Kue kimberlite pipes, NWT, Canada: root to diatreme magmatic transition zones. *Lithos* 76:51-74
- Moussallam Y, Morizet Y, Gaillard F (2016) H₂O–CO₂ solubility in low SiO₂-melts and the unique mode of kimberlite degassing and emplacement: *Earth Plan Sci Let* 447:151–160.
- Stone RS, Luth RW (2016) Orthopyroxene survival in deep carbonatite melts: implications for kimberlites. *Contrib Mineral Petrol*:171:63
- Zhang Z, Fedortchouk Y, Hanley JJ (2015) Evolution of diamond resorption in a silicic aqueous fluid at 1-3 GPa; application to kimberlite emplacement and mantle metasomatism: *Lithos* 227:179-193.

Diamond surface features and metasomatic processes in subcratonic mantle

Yana Fedortchouk¹, Samantha Perritt², Ingrid L. Chinn²

¹Dalhousie University, Halifax, Canada, yana@dal.ca

²De Beers Exploration, Johannesburg, South Africa, Samantha.Perritt@debeersgroup.com, Ingrid.Chinn@debeersgroup.com

Introduction

Natural diamonds show a large diversity of surface dissolution features, some of which develop in the kimberlite magma during ascent whereas others are inherited from the mantle and are preserved due to diamond enclosure within xenoliths. Such mantle-derived dissolution features reflect conditions associated with diamond-destructive metasomatism and help to shed light on metasomatic processes in the subcratonic mantle. Experiments show that the presence and composition of fluid in kimberlite magmas can also radically change diamond surface features. In this study we examine the distribution of mantle-derived resorption features in four diamond parcels from four different lithologies in the BK1 and AK15 kimberlites (Orapa cluster, Botswana). We apply the results of dissolution experiments conducted at mantle conditions, to predict the nature of metasomatic processes in the subcratonic mantle responsible for diamond growth and partial dissolution. The content and nature of nitrogen defects determined by Fourier transform infrared spectroscopy (FTIR) is used to compare the mantle residence conditions of morphologically different diamond groups.

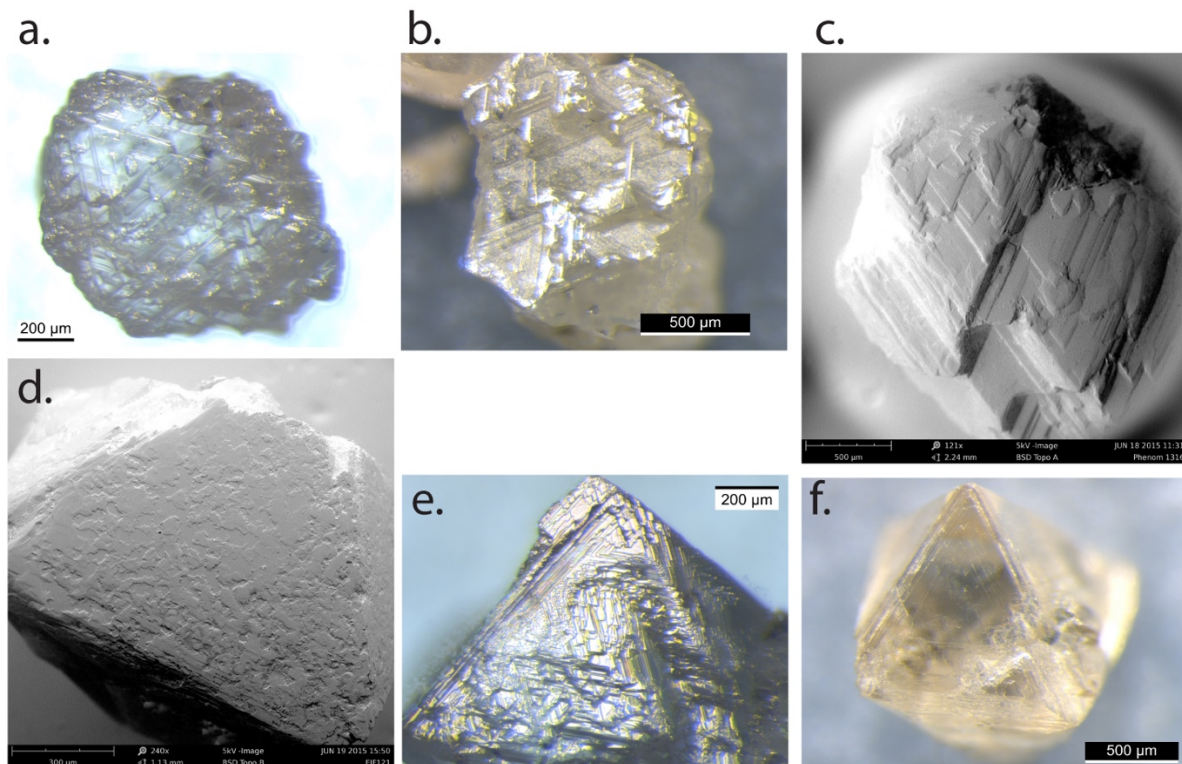


Figure 1: Most common morphological types of mantle-derived resorption on diamonds from BK1 and AK15 kimberlites. a. “complex surface” (MCOM), b. “deep pits”, c. step-faced with protrusions (MSF6), d. “islands”, e. laminae (MLAM), f. step-faced with laminae (MSF4).

Diamond samples and mantle resorption groups

The study uses 802 diamonds (> 0.5 mm) from three kimberlite lithologies in the BK1 pipe and one lithology from the AK15 intrusion (see details in the abstract 11IKC-4582). Diamonds were obtained from reverse circulation drill holes (depths to 160 – 200 m) in each kimberlite lithology and diamonds from each 2 – 13 m interval were studied separately. We discriminate diamonds with 1) kimberlite-induced resorption, 2) mantle-derived resorption, 3) mantle resorption overprinted by resorption in kimberlite magma (see abstract 11IKC-4582). Mantle-derived surface features are identified on 263 diamonds, of which 182 diamonds were assigned to a specific morphological group (Fig. 1). While kimberlite-induced resorption styles are uniform in each lithology and unique to this lithology, mantle-derived resorption in diamonds from each lithology comprises ~12 different types (Fig. 1) in similar proportions for the four diamond parcels (Fig. 2). In each parcel, 30-50% of all diamonds with mantle-derived resorption exhibit the same resorption style with deep stepped etch pits (Fig. 1a). Furthermore, this resorption style shows similarities with resorption styles shown in Figs. 1b,c, which may reflect their common origin. Two other resorption types present in each parcel, MSF4 and “laminae” (Fig. 1e,f), formed by thin layering possibly represent another resorption event. The other seven resorption types, including unresorbed octahedral diamonds, represent a very small fraction of the studied diamonds (Fig. 2).

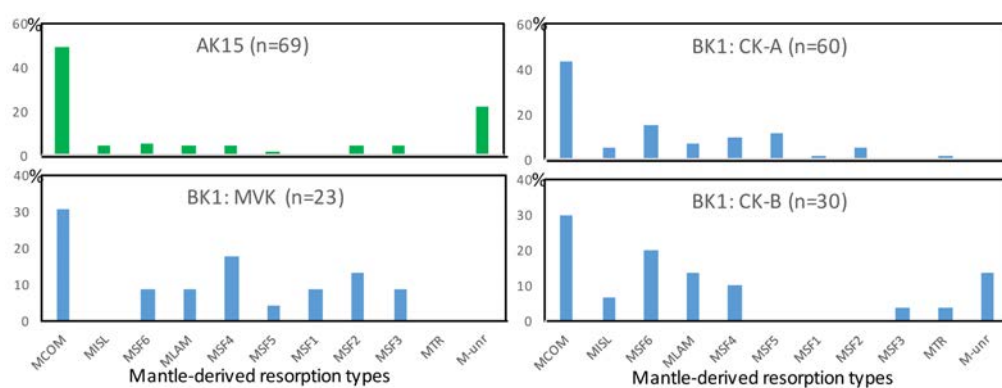


Figure 2: a) Distribution of diamonds between different mantle-resorption groups in AK15 kimberlite and three lithologies from BK1 kimberlite.

Nitrogen content and aggregation state were determined for 636 and 198 diamonds from BK1 and AK15 kimberlites respectively. Our data showed no difference in nitrogen content and aggregation state between diamonds with kimberlite-induced and mantle-derived resorption, or between diamonds with different mantle-derived resorption types (Fig. 3). This may imply a similar degree of disintegration of mantle xenoliths derived from mantle regions with different thermal regimes. Furthermore, different mantle resorption morphologies were developed on diamonds residing in mantle clusters with different thermal regimes. On the contrary, different kimberlite lithologies seem to sample diamonds from different mantle clusters both in terms of thermal regime and nitrogen defects in diamond. Fig. 3 shows a difference in distribution of nitrogen defects in diamonds from the CK-B unit and CK-A and MVK units of BK1. The distribution of nitrogen defects in BK1 and AK15 diamonds is also different.

Diamond-destructive media in the mantle

We compared the mantle-resorption features of diamonds from BK1 and AK15 to the results of diamond dissolution experiments at mantle pressures and temperatures in C-O-H fluids, SiO₂-saturated C-O-H fluids, silica-carbonate melts, and carbonate melts. No mantle-derived dissolution features in our study resemble reaction with subsolidus C-O-H fluids. The resorption style with deep etch pits (Fig. 1a), which characterises 30-50% of the studied diamonds with mantle-derived resorption best corresponds to dissolution in carbonate melt at temperatures above 1450°C and could represent mantle metasomatism by proto-kimberlite magma of carbonatitic composition. Instead, the whole range of observed dissolution morphologies could be produced by diamond reaction with silica-carbonate and

carbonate melts of variable SiO₂ content and temperature. Thus, our data show that at mantle conditions metasomatism by C-O-H fluid is not reactive to diamond, while melt-driven metasomatism causes diamond resorption. Our data support the recent proposal that diamond growth in harzburgitic mantle happens from subsolidus C-O-H fluid saturated in carbon (Stachel and Luth, 2015). The associated metasomatism by such a fluid would transform harzburgite into lherzolite as recorded in mantle garnets (Stachel et al. 2004, Griffin et al. 1999) depressing the temperature of the wet solidus (e.g. Wyllie, 1977). This could result in partial melting producing carbonate-rich melts. If carbon solubility in melts is higher than in C-O-H fluid, diamonds would start to dissolve and would develop resorption features. The depletion of the host mantle lithologies due to partial melting may then raise the solidus temperature and prevent further diamond dissolution. Repeating processes of fluid and melt metasomatism in the same mantle domain could explain the complex growth-dissolution patterns of mantle diamonds (Bulanova 1995). Thus, differences in carbon solubility in C-O-H fluid and carbonate-rich melts could control the balance between diamond growth vs. dissolution processes.

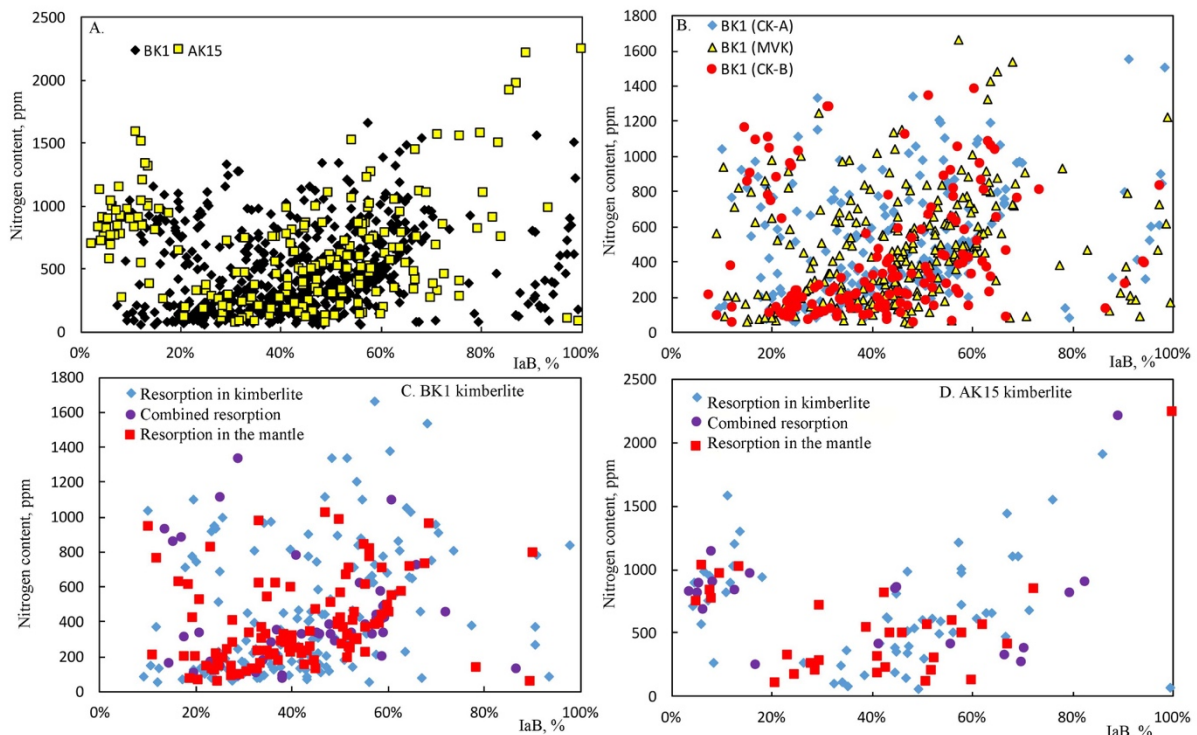


Figure 3: Nitrogen content vs aggregation state in diamonds A) from BK1 and AK15 kimberlites, B) from different lithologies of BK1 pipe, C, D) in diamonds with kimberlite-induced, mantle-derived and combined resorption.

References

- Bulanova GP (1995) The formation of diamond. *J. Geochem. Explor* 53:1–23
- Fedortchouk Y, Chinn IL, Kopylova MG (2017) Three styles of diamond resorption in a single kimberlite: Does crustal xenolith assimilation play a role? Abstract this volume No. 11IKC-4582
- Griffin WL, Shee SR, Ryan CG, Win TT, Wyatt BA (1999) Harzburgite to lherzolite and back again: metasomatic processes in ultramafic xenoliths from the Wesselton kimberlite, Kimberley, South Africa. *Contrib Mineral Petrol* 134:232–250
- Stachel T, Aulbach S, Brey GP, Harris JW, Leost I, Tappert R, Viljoen KS (2004) The trace element composition of silicate inclusions in diamonds: a review. *Lithos* 77:1–19
- Stachel T, Luth RW (2015) Diamond formation — Where, when and how? *Lithos* 220–223:200–220
- Wyllie PJ (1977) Mantle fluid compositions buffered by carbonates in peridotite-CO₂-H₂O. *Jour. Geology* 85(2):187–207

Age and evolution of the lithospheric mantle beneath southern Baffin Island, Nunavut, Canada

Jingao Liu^{1,2}, D. Graham Pearson², Garrett A. Harris², Maya G. Kopylova³, Erica Tso³

¹ China University of Geosciences, Beijing, China, jingao@cugb.edu.cn

² University of Alberta, Edmonton, Canada, dgpearso@ualberta.ca, gaharris@ualberta.ca

³ University of British Columbia, Vancouver, Canada, mkopylov@eos.ubc.ca, etso@eos.ubc.ca

Introduction

In southern Baffin Island, Canada, the terrane known as the “Hall Peninsula Block” (HPB; **Fig. 1**) has an equivocal tectonic origin, poorly constrained from studies of crustal rocks (e.g., Scott, 1999; Connelly et al., 2006; Berman et al., 2013). Little is known about the age and composition of the deep mantle lithosphere beneath this area and such knowledge could help in terms of unravelling the origin of this terrane. The newly discovered diamondiferous Chidliak kimberlite province that was emplaced into the HPB (**Fig. 1**) in the Jurassic carried with the abundant mantle xenoliths. To help unravel the puzzling provenance of the Hall Peninsula Block, we undertook a Re-Os isotope and PGE study of these mantle xenoliths.

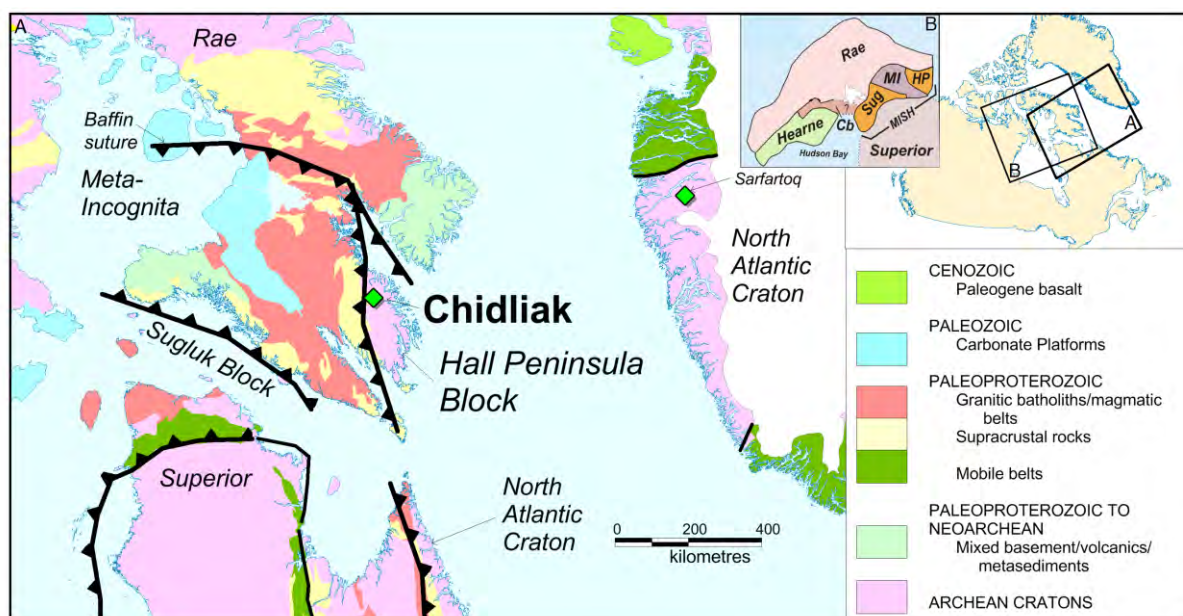


Fig. 1: Simplified geological map of the Canadian Shield and Western Greenland (from **11IKC-4578**; Kopylova et al., 2017), modified from Chorlton (2007). Inset A, heavy black lines are faults with “teeth” showing the direction dip; Green diamonds mark the location of the Chidliak and Sarfartoq kimberlites, respectively. Inset B, Cb – Committee Bay belt, see text for other abbreviations.

Samples and results

The petrography, mineralogy, thermobarometry and whole rock chemistry of 120 peridotite and pyroxenite xenoliths from Chidliak kimberlites (pipes CH-1, -6, -7, and -44) were comprehensively reported in **11IKC-4578** by Kopylova et al. (2017). A subset of 32 peridotite xenoliths were selected for Re-Os dating and PGE analysis in this study. The sample suite spans a range of compositions that typically reflect melt depletion and potential subsequent re-fertilization (e.g., olivine Fo = 88 to 92.7 (**Fig. 2**) and 0.1 to 3.9 wt% bulk rock Al₂O₃ content (**Fig. 3**)). Most of these samples show PGE concentrations that are typical of cratonic peridotites (e.g., Ir = 1 to 6.6 ppb, average = 3.3 ppb) with patterns ranging from P-PGE (Pd and Pt) depletion to slight enrichment relative to I-PGE (Os, Ir and Ru) (**Fig. 4**). The peridotites studied show variable Os isotopic compositions (¹⁸⁷Os/¹⁸⁸Os = 0.1090 to 0.2124) corresponding to Re depletion model ages (T_{RD} at the time of eruption) ranging from 2.94 Ga to present with a main mode in the Meso- the Neoproterozoic.

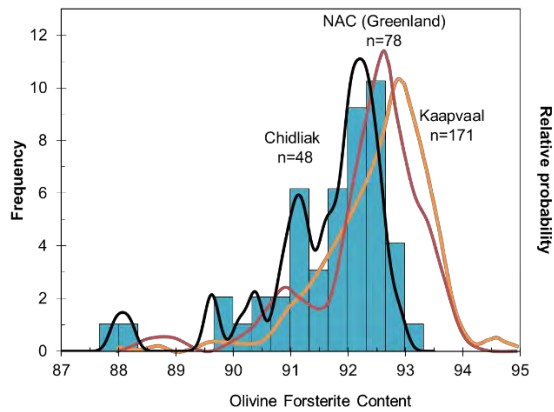


Fig. 2: Histogram of olivine forsterite content from the Chidliak peridotites. Also shown are the relative probability curves for olivine from Kaapvaal and NAC cratons (Pearson and Wittig, 2014).

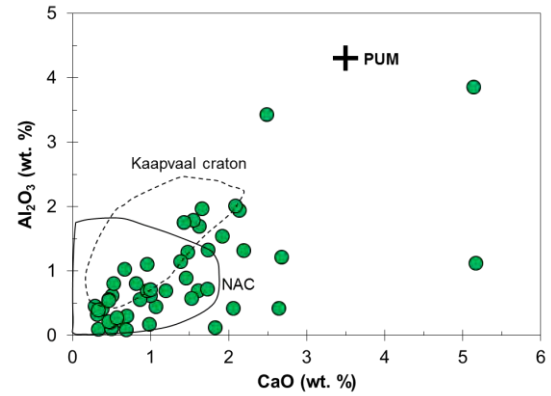


Fig. 3: Whole rock CaO vs Al₂O₃ contents of the Chidliak peridotites. Primitive Upper Mantle (PUM), Kaapvaal and NAC peridotite fields are shown for comparison.

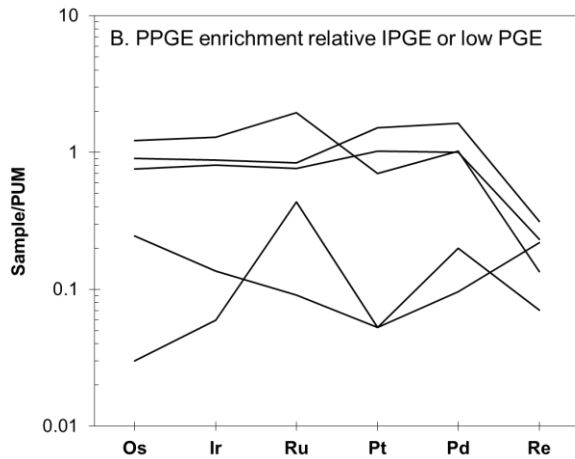
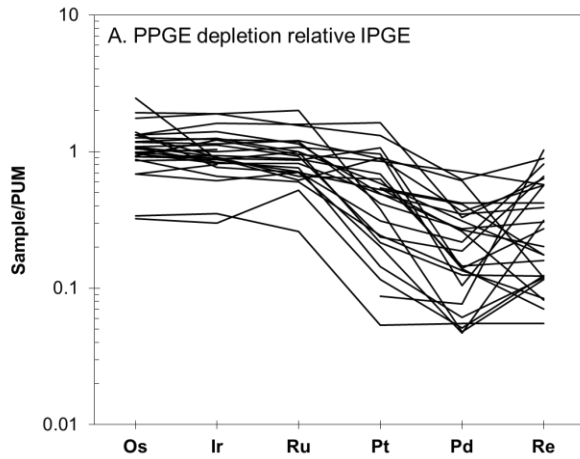


Fig. 4: PUM-normalized PGE patterns of the Chidliak peridotites. A. Main group showing PPGE (Pt & Pd) depletion relative to IPGE (Os, Ir and Ru), often with Re enrichment; B. Sub-group showing PPGE enrichment relative to IPGE or low PGE contents.

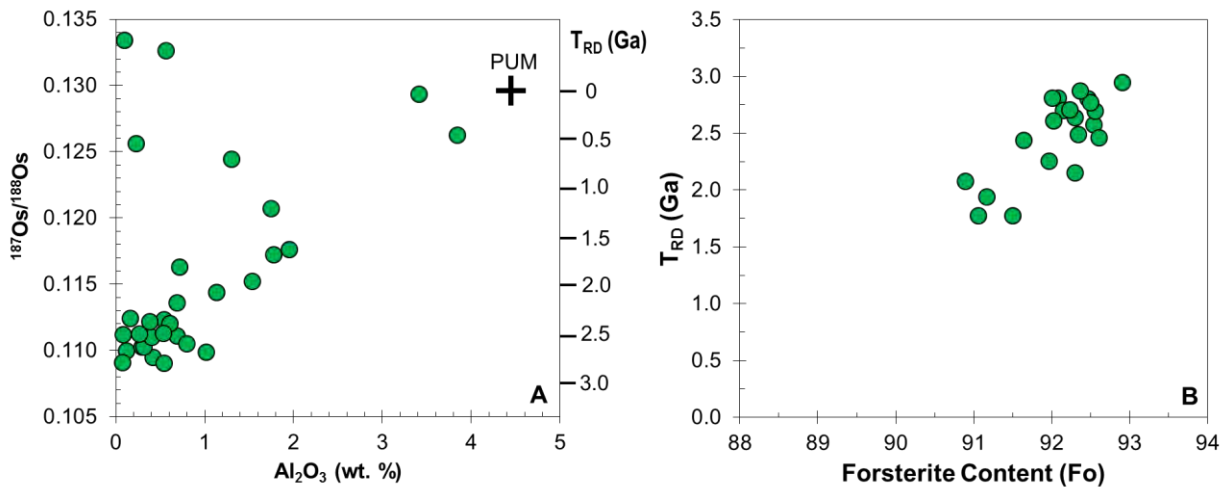


Fig. 5: A. Whole rock Al₂O₃ vs ¹⁸⁷Os/¹⁸⁸Os of Chidliak peridotites. B. Correlation between olivine forsterite content and T_{RD} ages for samples with T_{RD} greater than 1.7 Ga.



Discussion

Among the 32 samples analyzed, 23 peridotites possessing variable P-PGE depletion patterns and T_{RD} ages greater than 1.7 Ga show strong correlations between T_{RD} ages (or $^{187}\text{Os}/^{188}\text{Os}$) and melt depletion indicators (such as Fo, Al_2O_3 , Pd/Ir and Mg/Si; **Fig. 5**), suggesting a common ancient melt depletion event of variable extent that produced depleted peridotite residues at ca. 3 Ga. The oldest T_{RD} ages match the magmatic zircon ages of the oldest crust on the Hall Peninsula (e.g., From et al., 2016).

Given the absence of correlation between Fo or melt depletion indicators and depth (P) of equilibration (Kopylova et al., 2017), there is no general vertical depletion profile preserved in the Chidliak lithospheric mantle root. Osmium model ages remain close to ~3 Ga throughout the depth range of our samples (**Fig. 5**), and appear unaffected by the variety of fertility with depth. Given the lack of correlation between $^{187}\text{Os}/^{188}\text{Os}$ and metasomatic indicators (Ca/Al, or TiO_2 in garnet), the metasomatic event(s) appear to be recent. This is supported by the presence of elevated Re/Os ratios and P-PGE enriched patterns in samples still keeping ancient T_{RD} ages, indicating low Os concentrations in the metasomatic agents, which may have stripped Os from, instead of adding Os to, the mantle lithosphere.

A few samples, derived predominantly from the deepest section of lithosphere (>50 kb) of the CH-1, -7 and -44 mantle domains, have very variable PGE patterns, with $^{187}\text{Os}/^{188}\text{Os}$ ratios close to, or significantly greater than, modern mantle. These ratios are found only in Opx-free, Cpx-enriched samples or in sheared samples. The samples may represent cratonic lithosphere that was heavily overprinted by a high-Os agent, which may be related to varied types of metasomatism observed in Chidliak (Kopylova et al., 2017).

We conclude that the lithosphere beneath southern Baffin Island is cratonic in origin, with a broadly similar age spectrum and composition to that beneath western Greenland (Wittig et al., 2010). These observations support the view that the lithospheric mantle sampled by Chidliak kimberlites represents a portion of the North Atlantic cratonic mantle, with its distinct composition reflecting carbonatitic rather than silicic metasomatism (Kopylova et al., 2017).

References

- Berman, R. G., Sanborn-Barrie, M., Rayner, N. & Whalen, J. (2013). The tectonometamorphic evolution of Southampton Island, Nunavut: Insight from petrologic modeling and in situ SHRIMP geochronology of multiple episodes of monazite growth. *Precambrian Research* 232, 140–166.
- Chorlton, L. (2007). Generalized geology of the world: bedrock domains and major faults in GIS format, Geological Survey of Canada Open File 5529.
- Connelly, J. N., Thrane, K., Krawiec, A. W. & Garde, A. A. (2006). Linking the Palaeoproterozoic Nagsugtoqidian and Rinkian orogens through the Disko Bugt region of West Greenland, *Journal of The Geological Society* 163, 2, 319–335.
- From, R.E., Pearson, D. G., Luo, Y., (2016). U-Pb and Lu-Hf isotopes in complex zircon grains from eastern Hall Peninsula, Baffin Iland uisng laser ablation split stream inductively coupled mass spectroscopy (LASS-ICP MS).
- Kopylova, M., Tso, E., Ma, F., Liu, J., Pearson, D. G. (2017). Peridotite xenoliths of the Chidliak kimberlite province (NE Canada): The thermally disturbed mantle of North Atlantic craton with local Ti-Na metasomatism. To be submitted for *Journal of Petrology*.
- Pearson, D.G., Wittig, N. (2014). The formation and evolution of the subcontinental mantle lithosphere - evidence from mantle xenoliths. *Treatise of Geochemistry, Volume 3: The Mantle and Core, Chapter 3.6*, 255–292.
- Scott, D. J. (1999). U–Pb geochronology of the eastern Hall Peninsula, southern Baffin Island, Canada: a northern link between the Archean of West Greenland and the Paleoproterozoic Torngat Orogen of northern Labrador. *Precambrian Research* 93, 5–26.
- Wittig, N., Webb, M., Pearson, D.G., Dale, C.W., Ottley, C.J., Hutchison, M., Jensen, S.M., Luguét, A. (2010). Formation of the North Atlantic Craton: Timing and mechanisms constrained from Re-Os isotope and PGE data of peridotite xenoliths from SW Greenland. *Chemical Geology* 276, 166–187.



Tracing Mg-rich fluids by Mg-O isotopes at slab-mantle interface in continental subduction zones: insights from the Mg-metasomatic rocks in both Western and Eastern Alps

Yi-Xiang Chen¹, Hans-Peter Schertl², Attila Demény³, Yong-Fei Zheng¹, Fang Huang¹, Kun Zhou¹, Ying-Zeng Gong¹

¹ CAS Key Laboratory of Crust-Mantle Materials and Environments, School of Earth and Space Sciences, University of Science and Technology of China, Hefei 230026, China (yxchen07@ustc.edu.cn)

² Institut für Geologie, Mineralogie und Geophysik, Ruhr-Universität Bochum, 44780 Bochum, Germany

³ Institute for Geological and Geochemical Research, Research Centre for Astronomy and Earth Sciences, Hungarian Academy of Sciences

Introduction

The Mg-metasomatic rocks in both Western Alps (coesite-bearing whiteschist) and Eastern Alps (high pressure leucophyllite) are intriguing for their extreme Mg enrichment (e.g., Demény et al., 1997; Schertl and Schreyer, 2008; Ferrando, 2012). However, the origin of such Mg enrichment still remains to be resolved. If the Mg enrichment is caused by metasomatism of Mg-rich fluids, such samples are important to elucidate the fluid-rock interaction in continental subduction zones. To shed new light on this issue, we choose the typical samples of whiteschist from the Dora-Maira Massif in Western Alps, and leucophyllite from Rabenwald and Miesenbachtal in Austrian Eastern Alps as well as those from the Sopron-Fertorakos area in Hungarian Eastern Alps (Demény et al., 1997; Schertl and Schreyer, 2008). The country rocks of metagranite were also analyzed for comparison.

We performed a combined study of SIMS zircon U-Pb ages and O isotopes, and whole-rock Mg-O isotopes for the whiteschist and leucophyllite in Western Alps and Eastern Alps, respectively. The microbeam zircon U-Pb age and O isotope data confirmed the protolith of the Mg-metasomatic rocks are similar to the country rock, i.e., metagranite. However, the Mg-O isotope compositions suggest two sources of Mg-rich fluids: one is extremely heavy in Mg isotopes, and the other is extremely low in Mg isotopes. Considering the Mg isotope systematics of terrestrial reservoirs, the former fluids were proposed to be derived from talc-rich serpentinites (Chen et al., 2016), whereas the latter fluids can be that has dissolved lots of magnesite. Therefore, this study shows that the fluids at slab-mantle interface can be complex, but can be traced with Mg-O isotopes combined with other petrological and geochemical constraints. Such fluids can greatly influence the geochemistry of crustal rocks in the subduction zones.

Analytical results

Zircon U-Pb dating for whiteschist in Western Alps yields two groups of ages at ~262 Ma and ~34 Ma, respectively (Fig. 1). The Permian ages occur in relict magmatic domains and are consistent with the protolith age of the country rock (metagranite). The Tertiary ages occur in coesite-bearing domains, consistent with the known ultrahigh-pressure metamorphic age. Whereas the relict magmatic domains show higher $\delta^{18}\text{O}$ values of ~9-11‰, the metamorphic domains exhibit lower $\delta^{18}\text{O}$ values of 5.8 to 6.8‰ (Fig. 1). The significant O isotope difference between the two types of domains suggests that the protolith of whiteschist underwent metasomatism by metamorphic fluids with relatively low $\delta^{18}\text{O}$ values. The $\delta^{26}\text{Mg}$ values for the whiteschist are mostly -0.07 to 0.72‰ (except two samples that are -0.46‰ and -0.26‰), considerably higher than the country rock with $\delta^{26}\text{Mg}$ of -0.54 to -0.11‰ (Fig. 2).

For the leucophyllites in Hungarian Eastern Alps, the metagranite to leucophyllite profile shows two trends of Mg isotope variations (Fig. 2): (1) the Mg isotopes become heavier toward the leucophyllite, from -1.30 ~ -0.64‰ in metagranite to -0.09 ~ 0.14‰ in leucophyllite; (2) the Mg isotopes become lighter toward the leucophyllite, from -0.29‰ in metagranite to -0.88‰ in leucophyllite. Similar features were found in Austrian Eastern Alps (Fig. 2).

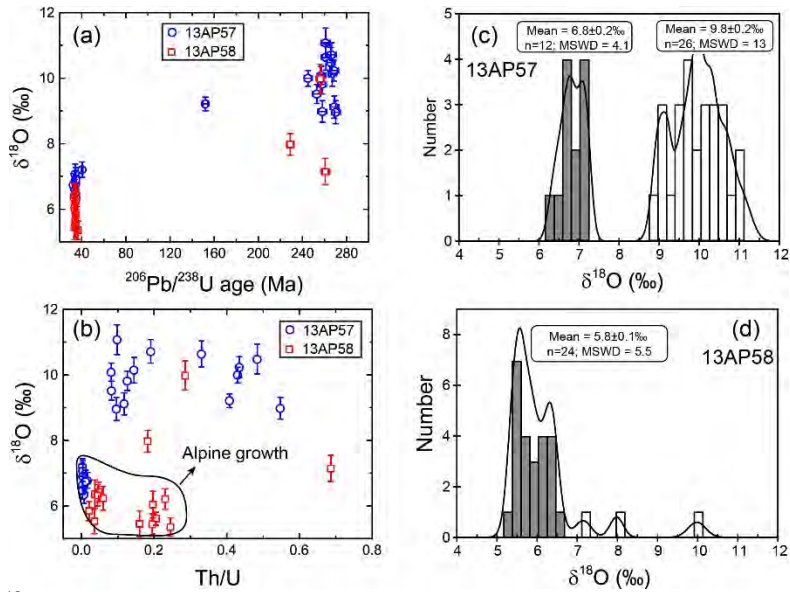


Figure 1: Zircon $\delta^{18}\text{O}$ values and their relations to U-Pb ages for whiteschist from Western Alps. The gray bars in panels c and d are metamorphic domains, others are relict magmatic domains. Data from Chen et al. (2016).

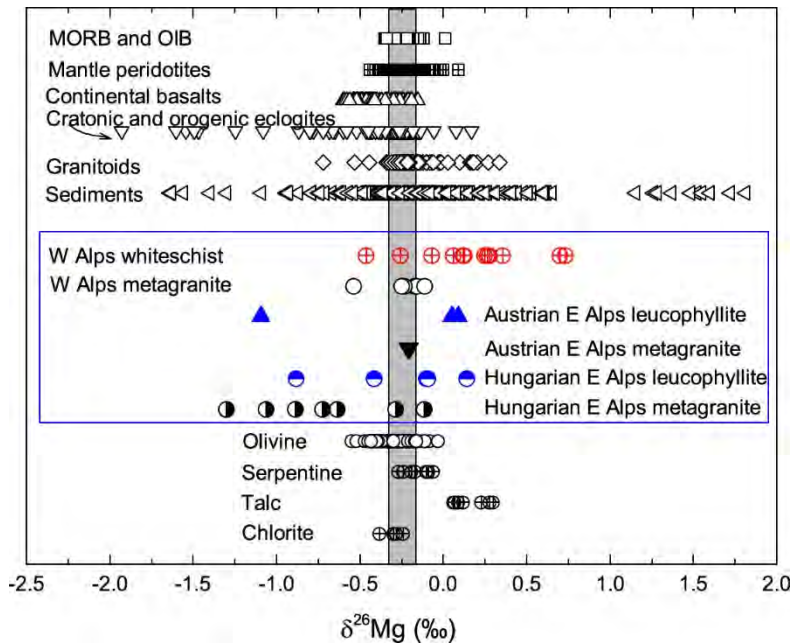


Figure 2: $\delta^{26}\text{Mg}$ values for whiteschist in Western Alps (Chen et al., 2016) and leucophyllite in Eastern Alps. The data for various reservoirs are summarized in Chen et al. (2016).

Discussion and conclusion

The similar zircon U-Pb age of ~ 262 Ma in both whiteschist and the country rock metagranite and the high $\delta^{18}\text{O}$ values of ~ 9 - 11% in such zircons, combined with previous petrological and geochemical studies, lend strong support that the protoliths of the whiteschist in Western Alps are similar to the country rocks of metagranite. The extremely heavy Mg isotopes in the whiteschist can not be interpreted by diffusion process (Chen et al., 2016). Although chemical weathering can result in variably heavy Mg isotopes for the residues, such a process is hard to explain the significantly lower $\delta^{18}\text{O}$ values in the metamorphic zircons, the extremely Mg-rich composition and the highly heterogeneous $\delta^{26}\text{Mg}$ values in the whiteschist. Considering previously reported mineral H-O isotopes and petrological results, we propose that the protolith rocks experienced the metasomatism by a kind of Mg-rich fluids with

heterogeneous but primarily heavy Mg isotope compositions during probably continental subduction. According to available Mg isotope data of rocks and minerals (Fig. 2), the fluids were possibly produced by devolatilization of talc-rich serpentinites at the slab-mantle interface in a subduction channel (Chen et al., 2016). This means the serpentinite dehydration in subduction zones may greatly affect the geochemistry of the deeply subducted continental crust.

The leucophyllite in Eastern Alps has been documented to have a granitic protolith similar to the country rock (e.g., Demény et al., 1997). However, such a protolith have extremely low $\delta^{26}\text{Mg}$ values down to -1.30‰ (Fig. 2). Due to the insignificant Mg isotope change during silicate magma differentiation, and the only reservoir with such low $\delta^{26}\text{Mg}$ values are the carbonates (Teng, 2017), the protolith was possibly derived from partial melting of metasediments containing significant amounts of Mg-rich carbonates. The metagranite to leucophyllite profile shows two trends of Mg isotope variations. Two profiles in Hungarian Eastern Alps show that the Mg isotopes become heavier toward the leucophyllite, from -1.30 ~ -0.64‰ in metagranite to -0.09 ~ 0.14‰ in leucophyllite. This can be interpreted in a similar way to the whiteschist in Western Alps, i.e., the protolith experienced metasomatism by fluids with heavy Mg isotopes, probably derived from the talc-rich serpentinites. However, another profile in Hungarian Eastern Alps shows that the Mg isotopes become much lighter toward the leucophyllite, from -0.29‰ in metagranite to -0.88‰ in leucophyllite. In Austrian Eastern Alps, there is also one leucophyllite sample that shows an extremely low $\delta^{26}\text{Mg}$ value of -1.09‰ (Fig. 2). Whereas the Mg-enrichment in the leucophyllite suggests metasomatism by Mg-rich fluids, the extremely low $\delta^{26}\text{Mg}$ values of the leucophyllite require such fluids with extremely low $\delta^{26}\text{Mg}$ values. Considering the Mg isotope systematics in various reservoirs and the geological context for leucophyllite formation, it is possible that the metasomatic fluids have dissolved amounts of Mg-rich carbonates, probably magnesite, which can occur by carbonation of serpentinites (Beinlich et al., 2014). This metasomatic process can also occur at the slab-mantle interface in a continental subduction channel.

By Mg-O isotope analysis of Mg-metasomatic rocks metamorphosed at different ages and P-T conditions in Western Alps and Eastern Alps, we find extremely heavy and light Mg isotope compositions in such rocks. We propose that they reflect two types of Mg-rich fluids occurred at the slab-mantle interface in continental subduction channel: (a) derived from dehydration of talc-rich serpentinites; (b) derived from dissolution of magnesite produced by carbonation of serpentinites. This study shows that the fluid-rock interaction in the subduction channel can greatly influence the geochemical composition of crustal rocks within the channel.

References

- Beinlich, A., Mavromatis, V., Austrheim, H., Oelkers, E.H., 2014. Inter-mineral Mg isotope fractionation during hydrothermal ultramafic rock alteration-Implications for the global Mg-cycle. *Earth and Planetary Science Letters* 392, 166-176.
- Chen, Y.-X., Schertl, H.-P., Zheng, Y.-F., Huang, F., Zhou, K., Gong, Y.-Z., 2016. Mg-O isotopes trace the origin of Mg-rich fluids in the deeply subducted continental crust of Western Alps. *Earth and Planetary Science Letters* 456, 157-167.
- Demény, A., Sharp, D.Z., Pfeifer, H.-R., 1997. Mg-metasomatism and formation conditions of Mg-chlorite-muscovite-quartzphyllites (leucophyllites) of the Eastern Alps (W. Hungary) and their relations to Alpine whiteschists. *Contributions to Mineralogy and Petrology* 128, 247-260.
- Ferrando, S., 2012. Mg-metasomatism of metagranitoids from the Alps: genesis and possible tectonic scenarios. *Terra Nova* 24, 423-436.
- Schertl, H.-P., Schreyer, W., 2008. Geochemistry of coesite-bearing "pyrope quartzite" and related rocks from the Dora-Maira Massif, Western Alps. *European Journal of Mineralogy* 20, 791-809.
- Teng, F.-Z., 2017. Magnesium isotope geochemistry. *Reviews in Mineralogy and Geochemistry* 82, 219-287.



The Geology of the Faraday 3 kimberlite, Kennady Lake, NWT Canada.

Dan Gainer¹, Casey Hetman², Michael Diering³

¹ Aurora Geosciences Ltd., Yellowknife, Canada, dan.gainer@aurorageosciences.com

² SRK Consulting, Vancouver, Canada, chetman@srk.com

³ SRK Consulting, Vancouver, Canada, mdiering@srk.com

Introduction

The diamondiferous Faraday 3 body is one of four pipes identified in the Kelvin- Faraday cluster. It sits three kilometers north of the main Kelvin kimberlite and is 10 km from the recently constructed Gahcho Kué diamond mine within the Archean Slave Craton in northern Canada. Emplaced along the same structural trend as the other kimberlites in the cluster, Faraday 3 intrudes into gneissic basement comprised of metaturbidites of the Yellowknife Supergroup with minor amphibolite and narrow diabase dikes. Archean granitoids occur immediately to the west of the kimberlite cluster. Similar to the other kimberlite bodies in the Kelvin-Faraday cluster, Faraday 3 is described as a tubular, sub-horizontal, inclined pipe dominantly infilled with volcanoclastic kimberlite. It contains multiple kimberlite phases resulting from various emplacement events. Presently it is drill defined as 300 meters long, 30 meters in height and 70 meters wide.

Evaluation

Extensive geophysical surveys, 59 diamond drill holes and 42, 11-inch diameter reverse circulation (RC) drill holes have defined the external shape of the body. Microdiamond sampling of drill core has revealed that the body is significantly diamondiferous. Detailed logging and clast abundance measurements on the drill core have revealed a complex internal geology. This work is reinforced by a petrological investigation of 163 kimberlite thin sections and 44 country rock thin sections from 16 diamond drill holes selected across the body. Following this investigation a 3D model was generated in Leapfrog (Figure 1). A total of 3.16 tonnes of kimberlite recovered by core drilling was processed for microdiamonds by caustic fusion at the Geoanalytical Laboratories Diamond Services of the Saskatchewan Research Council (“SRC”) to return a sample grade of 2.18 carats per tonne. The diamond recoveries are presented in Table 1 below.

| Unit | Sample Weight (dry tonnes) | Number of Diamonds According to Sieve Size Fraction (mm) | | | | | | | | | | | | Total Stones | Total Carats (+0.85 mm) |
|-------|----------------------------|--|-----------------|------------------|-----------------------|-----------------------|-----------------------|-----------------------|-----------------------|-----------------------|-----------------------|-----------------------|-----------------------|--------------|-------------------------|
| | | +0.106 -0.150 | +0.150 0.212 | +0.212 -0.300 | +0.30 0 - 0.425 | +0.42 5 - 0.600 | +0.60 0 - 0.850 | +0.85 0 - 1.180 | +1.18 0 - 1.700 | +1.70 0 - 2.360 | +2.36 0 - 3.350 | +3.35 0 - 4.750 | +4.75 0 - 6.700 | | |
| KDYKE | 0.0512 | 222 | 154 | 80 | 41 | 25 | 17 | 8 | 3 | - | - | - | - | 550 | 0.1347 |
| KIMB1 | 0.1965 | 531 | 365 | 212 | 145 | 65 | 39 | 16 | 10 | 8 | - | - | - | 1,391 | 1.0764 |
| KIMB2 | 0.1484 | 206 | 165 | 82 | 45 | 24 | 15 | 11 | 6 | 1 | - | - | - | 555 | 0.4009 |
| KIMB3 | 0.0822 | 47 | 31 | 21 | 13 | 8 | 2 | 2 | - | - | - | - | - | 124 | 0.0243 |
| KIMB4 | 2.4712 | 1,456 | 964 | 555 | 332 | 178 | 94 | 51 | 23 | 10 | 9 | 1 | - | 3,673 | 4.6461 |
| MB | 0.0885 | 22 | 18 | 11 | 8 | 1 | 1 | 1 | 1 | - | - | - | - | 63 | 0.0259 |

Table 1: Diamond results by phase for the main pipe infills. Minor phases are not listed.

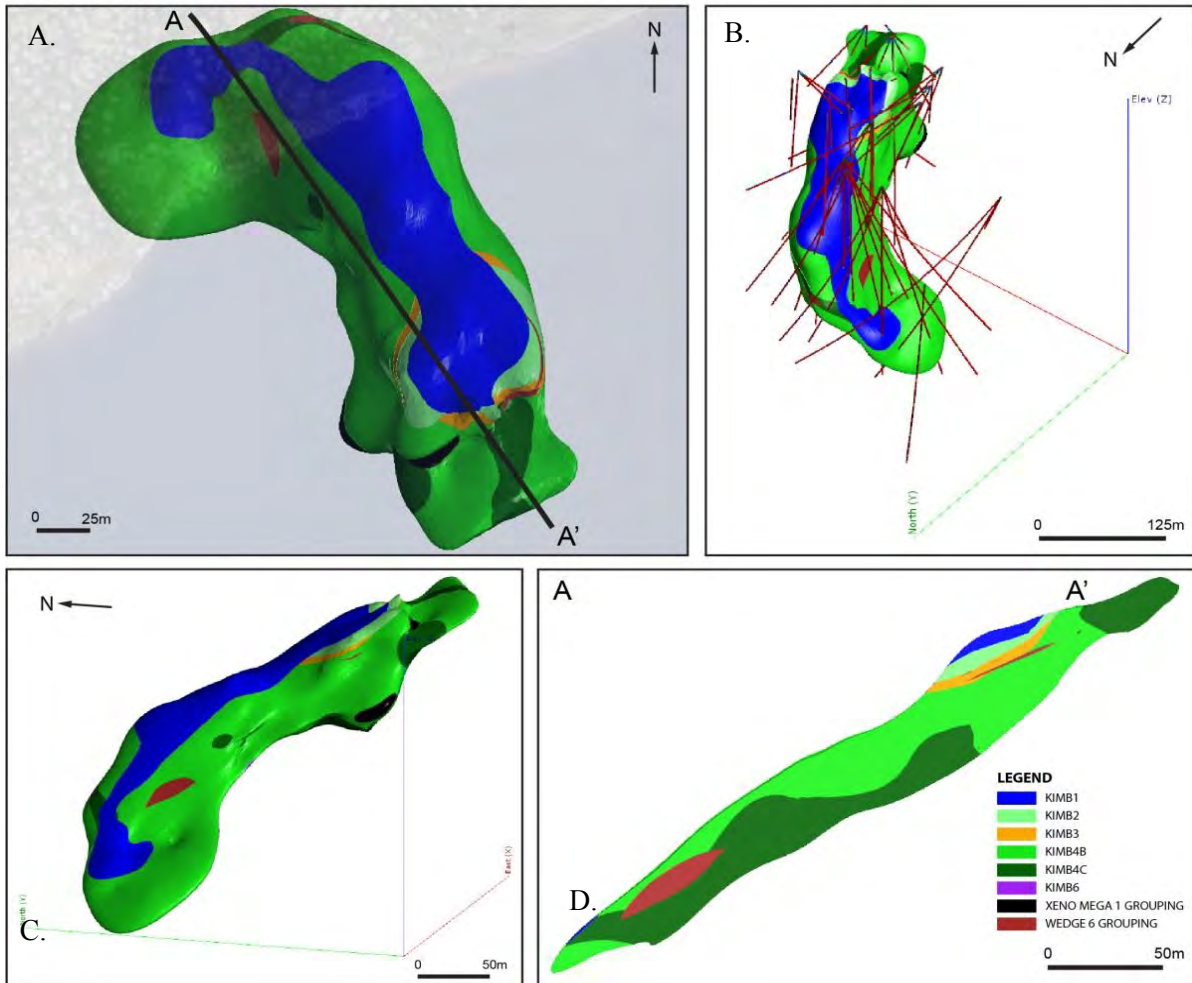


Figure 1: 3D model of the Faraday 3 kimberlite pipe. (A) Plan view; (B) Oblique view of the Faraday 3, looking southeast, with the traces of diamond drill; (C) Detailed geology model of Faraday 3 looking northeast; KIMB1, a hypabyssal kimberlite (HK); KIMB2, a uniform volcanoclastic kimberlite (VK); KIMB3, a well sorted volcanoclastic kimberlite (VK); In-situ gneissic wedges; and KIMB4, a highly variable VK with respect to country rock dilution. KIMB4 has been subdivided into KIMB4A (<25% dilution) not modelled, KIMB4B (25-75% dilution) and KIMB4C (>75% dilution). (D) Long section of Faraday 3 looking northeast.

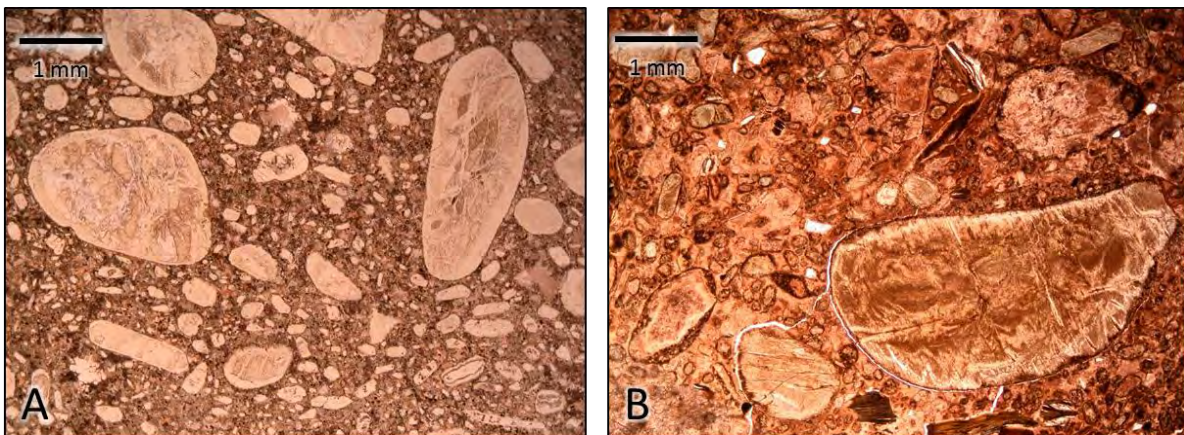


Figure 2: Photomicrographs of the two textural end-members present at Faraday 3. A) Coherent phlogopite kimberlite (KIMB1); note the uniform distribution of olivines altered to serpentine and carbonate set within a groundmass of monticellite> phlogopite> carbonate> spinel> perovskite. B) Volcanoclastic phlogopite kimberlite (KIMB2); olivine rich with thin melt selvages and common fresh country rock xenoliths set within an altered microlitic matrix with abundant serpentine.

Geology

Four kimberlite domains have been modeled in the body: KIMB1, a HK comprised of at least 2 unique phases of kimberlite, one is dominated by a phlogopite groundmass while the other phase contains conspicuous monticellite in the groundmass; KIMB2, a uniform VK; KIMB3, a well sorted VK associated with in-situ gneissic wedges which displays flow features; and KIMB4, a highly variable VK with respect to country rock dilution. KIMB4 has been subdivided into KIMB4A (<25% dilution), KIMB4B (25-75% dilution) and KIMB4C (>75% dilution). The individual phases of kimberlite are related to separate emplacement events and occur in conformable layers. Discrete, unique intervals of volcanoclastic kimberlite, HK sheets and marginal breccias also surround the body. Based on the current drilling, the main pipe infills that occupy the majority of the pipe are KIMB4B, followed by KIMB4C and then KIMB1. The VK infill is characterized by thin skinned pelletal shaped magmaclasts (formally termed pelletal lapilli) set within a serpentine and microlite dominated interclast matrix with common fresh to variably altered locally derived country rock xenoliths and xenocrysts. Mantle derived indicator minerals are rarely encountered within the drill cores and include peridotitic and less common eclogitic garnets and no ilmenite has been identified.

Conclusions

Following detailed petrography, KIMB2 and KIMB4 are further classified as Kimberley type pyroclastic kimberlite (KPK), formerly called tuffisitic kimberlite breccia (TKB) (Smith et al., 2013). KIMB3 has not been classified as such due to the presence of layering. This material is interpreted to represent a zone of flow or a volatile escape feature associated with a contact against in-situ wedges of country rock.

The textures, general geology and preliminary diamond results obtained from Faraday 3 are similar to those published from the Gahcho Kué mine to the south (Hetman et al., 2004). Only the inclined nature of Faraday 3 differs from the emplacement of the Gahcho Kué kimberlites

It is presently unclear if Faraday 1 and 3 volcanoclastic rocks are connected at depth; they share many similarities however further work is required before the relationship (if any) between these rocks can be determined.

Faraday 3 has an average grade of 2.18 carats per tonne based on microdiamond analysis, however in 2017, 42 11-inch large diamond RC drill holes were completed and a 262 tonne bulk sample was collected for the purpose of obtaining a macrodiamond parcel for preliminary grade and diamond value estimates. The macrodiamond results from the 2017 program will be combined with previous data to support a possible resource classification for Faraday 3.

References

- Hetman, C. M., Smith, B. S., Paul, J. L., & Winter, F. (2004). Geology of the Gahcho Kue kimberlite pipes, NWT, Canada: root to diatreme magmatic transition zones. *Lithos*, 76(1), 51-74.
- Smith, B. S., Nowicki, T. E., Russell, J. K., Webb, K. J., Mitchell, R. H., Hetman, C. M., and Robey, J. A. (2013). Kimberlite terminology and classification. In *Proceedings of 10th International Kimberlite Conference* (pp. 1-17). Springer India

Barium and titanium enrichment of zoned phlogopite xenocrysts and phenocrysts in the Adamantin kimberlites, Québec, Canada.

R.L Barnett¹ and C. Laroulandie²

1) R.L. Barnett Geoscientific Ltd, London, ON, Canada, Bob Barnett, rbarnett@odyssey.on.ca

2) Stornoway Diamond Corporation, North Vancouver, BC, Canada, claroulandie@stornowaydiamonds.com

Introduction

The Adamantin kimberlites are located in north central Québec, Canada, approximately 700 km north of Montreal, and 100 km south of the newly commissioned Renard Diamond Mine (Figure 1A). A till sampling program in 2015 highlighted the presence of kimberlite indicator minerals on the property. A reverse circulation (RC) drill program conducted in early 2016 resulted in the discovery of multiple kimberlite occurrences. These kimberlites are emplaced into Archean gneiss and granodiorite of the Epervanche Complex within the south-eastern portion of the Superior Craton (Dubé et al, 1976; Figure 1A). Petrological, petrographic and microprobe work indicates there are three mineralogically distinct groups of coherent kimberlites present, all containing compositionally-zoned phlogopite xenocrysts and phenocrysts (Figure 1B). Individual phlogopite crystals contain up to five distinct and successive compositional growth zones, with each grain containing a characteristic barium and titanium-rich zone near the margins of the grain. Results clearly indicate that significant chemical changes occurred in the chemical environment of the phlogopite crystals during formation and emplacement of the Adamantin kimberlites. Our data also provides strong evidence for the mobility of titanium, chrome and barium in fluids in the mantle, and mobility of titanium and barium during kimberlite ascent and emplacement.

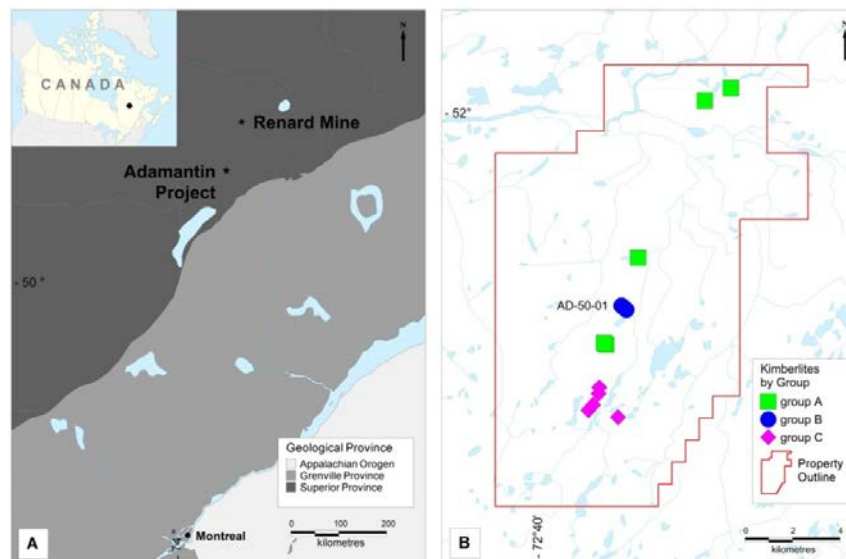


Figure 1: A) Location and regional geology of the Adamantin Project in relation to the Renard Diamond Mine B) Kimberlite occurrences separated into three mineralogically distinct groups as identified through petrological and microprobe work. Group A are perovskite-bearing carbonate phlogopite kimberlites; Group B are monticellite-bearing carbonate phlogopite kimberlites; and Group C are phlogopite carbonate kimberlites. Each group also contains different abundances of mantle-derived macrocrysts.

Kimberlite Types

Petrographic observation of kimberlite chips from the RC drilling reveals an average olivine macrocryst and phenocryst abundance of 30-50 modal % set within a fine-grained crystalline

groundmass of varying amounts of carbonate, serpentine, phlogopite, clinopyroxene, perovskite, spinel and apatite, with little to no country rock xenoliths. Phlogopite generally makes up 20-45 modal % of the rock. These coherent kimberlites can be divided into three distinct mineralogical groups (Figure 1B). Group A is classified as a perovskite-bearing carbonate phlogopite kimberlite, where eclogite, pyrope and ilmenite are the main mantle-derived indicator minerals. Group B is classified as a monticellite-bearing carbonate phlogopite kimberlite, with chromite and chrome diopside, as well as lesser eclogite, pyrope and ilmenite. Finally, Group C is classified as a phlogopite carbonate kimberlite, with no mantle-derived indicator minerals other than olivine.

Phlogopite Growth Zones

Samples of kimberlite were examined petrographically and analyzed using a JEOL Model 733 Electron Microprobe at the laboratory facilities of R.L. Barnett Geoanalytical Ltd in London, Ontario, for the purpose of detailing mantle-derived indicator mineral compositions. Large mm-scale phlogopite crystals and clusters, commonly broken, all have core to margin compositional growth zones. Individual phlogopite crystals commonly display up to five successive, discrete compositional zones. Central core regions are magnesium-rich phlogopite with moderate titanium and little to no chrome, akin to mantle-derived phlogopites reported elsewhere (for example: Mitchell, 1986; see Zone 1 in Table 1 below) and can therefore be classified as phlogopite xenocrysts. A second zone with elevated titanium, chrome and with trace barium precedes a third and important growth zone that appears as a ‘bright’ ring in back scatter imaging, and is consistently enriched in barium, titanium and aluminum, but essentially without chrome (Table 1, Zone 3; Figure 2). A succeeding narrow outer growth zone is commonly magnesium-rich phlogopite with a low titanium and barium content. Smaller, zoned phlogopite crystals are also observed, sharing only the third characteristic ‘bright ring’, containing barium up to 6.50 wt % BaO, and the fourth magnesium-rich, low barium and titanium growth zones (Table 1; Figure 2A) and classified as phlogopite groundmass phenocrysts. The xenocrysts, and more commonly phenocrysts, are mantled by a fifth, low-aluminum, iron-rich, red tetraferriphlogopite rim. In poikilitic phenocrystic phlogopite crystals, the barium and titanium-enriched growth zone (Zone 3) commonly include minute grains of perovskite and zoned oxide atolls.

| Zone | Grain Type | Description | Al ₂ O ₃ | TiO ₂ | Cr ₂ O ₃ | FeO | MgO | BaO |
|------|--------------------------|--|--------------------------------|------------------|--------------------------------|-------|-------|------|
| 1 | Xenocryst | Central core region of mantle-derived xenocrysts | 13.20 | 1.67 | 0.03 | 5.46 | 23.90 | 0.00 |
| 2 | Xenocryst | Increasing titanium, chrome and barium | 15.56 | 4.54 | 1.24 | 4.83 | 21.22 | 0.38 |
| 3 | Xenocryst and Phenocryst | Elevated barium and titanium, and low chrome | 19.41 | 2.53 | 0.04 | 5.04 | 21.82 | 3.31 |
| 4 | Xenocryst and Phenocryst | Magnesium-rich, with a low titanium and barium content | 15.85 | 1.95 | 0.02 | 6.32 | 23.22 | 0.39 |
| 5 | Xenocryst and Phenocryst | Tetraferriphlogopite rim | 1.08 | 0.17 | 0.00 | 18.21 | 24.75 | 0.08 |

Table 1: Typical chemistry of the five successive phlogopite growth zones for both xenocrysts and phenocrysts from drill hole AD-51-01 (Figure 1B and Figure 2A). Oxide analyses in wt%.

Discussion

Phlogopite in kimberlite is generally characterized by high chrome, high magnesium and elevated titanium contents (Mitchell, 1995). An interesting and important feature of the characteristic titanium and barium rings observed in both the xenocrysts and phenocrysts at Adamantin, is that they also plot within the ‘kimberlite groundmass micas’ region on Al-Ti and Al-Fe plots (Mitchell, 1995). These overall chemical evolution trends do not show, however, the important and significant variations in chrome and barium. In Figure 3 we present an Al-Ti plot which demonstrates this relationship. The compositional correlation of elevated barium and aluminum is indicative of a coupled substitution in phlogopite, which also includes titanium.

Experimental studies indicate that the substitution of titanium into the phlogopite structure increases with temperature at any pressure (Tronnes et al, 1985). We propose that in the upper-lower mantle transition, under conditions of high temperature and pressure, titanium is preferentially incorporated into phlogopite over barium regardless of the overall barium content, and hence the barium content of the primitive xenocryst cores are characteristically low. It is suggested that only upon decompression

in the earliest stages of kimberlite genesis, that barium is allowed, in significant amounts, into the phlogopite structure and accordingly forms the characteristic barian-titanian growth zone on 1) the xenocrysts, in a very short-lived, transitory and evolving chemical environment with decreasing temperature and pressure during ascent, and 2) the phenocryst crystals upon rapid cooling of the kimberlite melt. The interpretation of this relationship is that these groundmass phenocrysts nucleated in a scenario of rapid cooling, and that all available barium in the chemical environment immediately fractionated into the phlogopite structure in the near surface environment. The implication is that the characteristic barian-titanian growth zones on the xenocrysts also formed during ascent and in the near surface environment as did the phenocrysts. These phlogopites and the barium-titanium ring zone are important to understanding the overall genesis of the Adamantin kimberlites, and may prove to be useful to the understanding of other kimberlites, orangeites and related rocks as phlogopite is not only stable in the mantle but can also record changing geochemical conditions during emplacement.

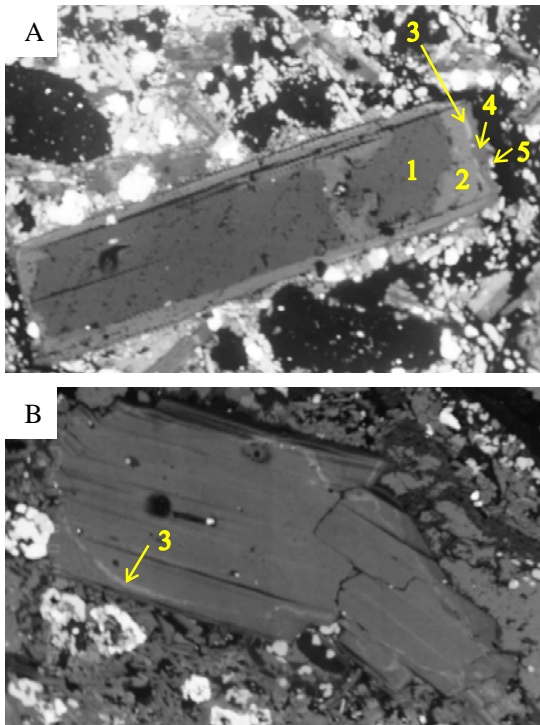


Figure 2: Back scatter images of A) a phlogopite phenocryst displaying the five growth zones listed in Table 1 by number, and B) a composite, multigranular phlogopite xenocryst, where the bright Ba-Ti zone actually encloses both grains of the fragment in a continuous fashion (2.52 wt% BaO, 2.24 wt% TiO₂).

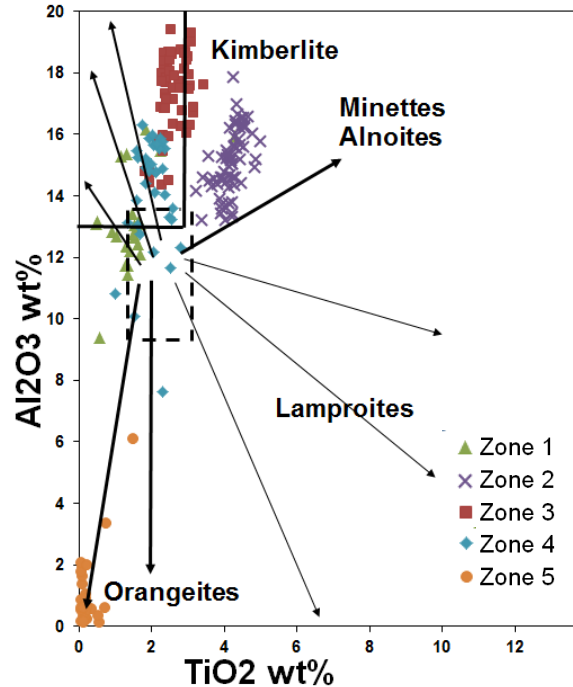


Figure 3: Chemistry of phlogopite crystals from kimberlite AD-51-01 (Figure 1B) classified by Zone # (Table 1). Of note, the barium-titanium rich Zone 3 compositions clearly plot within the trend of kimberlite groundmass micas (after Mitchell, 1995).

References

- Dubé C, Franconi A, Hocq M, Remick JH, Sharma KNM, Avramtchev L and Ducrot C (1976) Compilation géologique de territoire de la baie James. Ministère des Richesse Naturelles, Québec. Services de la documentation Technique, DP 358
- Mitchell RH (1995) Kimberlites, orangeites, and related rocks, Plenum Press, New York 410 pp
- Tronnes RG, Edgar AD, and Arima M (1985) A high pressure-high temperature study of TiO₂ solubility in Mg-rich phlogopite: Implications to phlogopite chemistry. *Geochimica et Cosmochimica Acta*, 49, 2323–2329

Complex zoning of olivine in archetypal kimberlites provides new insights into the evolution of kimberlite magmas

Emilie Lim¹, Andrea Giuliani^{1,2} and David Phillips¹

¹ *KiDs (Kimberlites and Diamonds), School of Earth Sciences, The University of Melbourne, Parkville, VIC, Australia, emilielc@student.unimelb.edu.au*

² *ARC Centre of Excellence for Core to Crust Fluid Systems (CCFS) and GEMOC, Department of Earth and Planetary Sciences, Macquarie University, North Ryde, NSW, Australia*

Introduction

Kimberlites are rare, hybrid igneous rocks consisting of primary magmatic components, and mantle and crustal-derived xenoliths. During ascent, kimberlite magmas transport, assimilate and metasomatise material along the magma conduit. The combination of these processes contributes to generate the peculiar hybrid character of kimberlites (e.g., Giuliani et al. 2016). The degree to which assimilation influences kimberlite melts has been difficult to constrain from the composition of magmatic minerals alone. Olivine is the most abundant phase in kimberlites and, therefore, its composition can provide valuable information about the evolution of kimberlite magmas. In kimberlites, olivine is typically zoned with a mantle-derived, xenocrystic core, and an overgrowth (rim) that crystallises from the kimberlite melt (e.g., Brett et al. 2009; Pilbeam et al. 2013).

In this study, fresh olivine grains from five kimberlites, from different localities in Brazil (Limpeza-18), Canada (Grizzly and Koala from the Ekati property) and South Africa (Samada and New Robinson from the Kaalvallei cluster), were selected for major and trace element analysis. The olivine grains include macrocrysts (0.5 – 10 mm), phenocrysts (> 0.5 mm) and microphenocrysts (0.1-0.5 mm).

Results

BSE-SEM images (Figure 1) and EMP analyses (Figure 2 and 3) show that olivine includes a core, rim and internal layer between the core and rim.

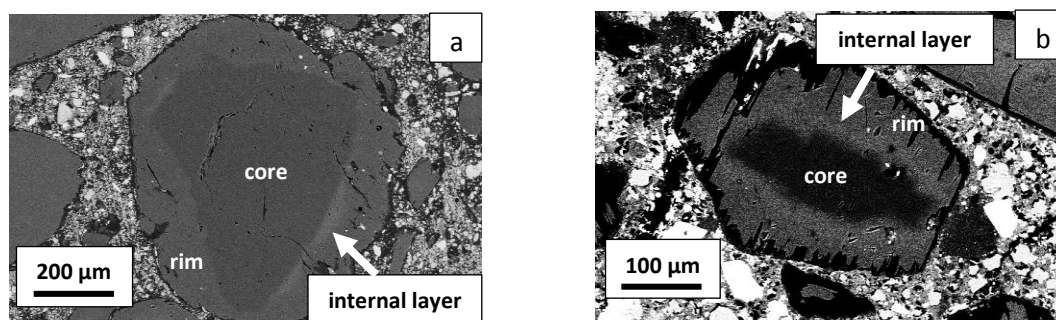


Figure 1. BSE-SEM images of a) a zoned olivine macrocryst from the Grizzly kimberlite; and b) a zoned olivine microphenocrysts from the Limpeza-18 kimberlite.

Olivine grains have cores with varying proportions of Mg-rich ('mantle') and Fe-rich ('megacrystic') components (Figure 2). 'Mantle' cores are characterised by Mg# of 89-95, high NiO (> 0.20 wt.%) and low CaO (typically < 0.11 wt.%) contents. 'Megacrystic' cores comprise compositions with Mg# of 78-88, decreasing NiO contents from 0.36 to 0.03 wt.% and higher CaO concentrations (< 0.19 wt.%) than the 'mantle' cores.

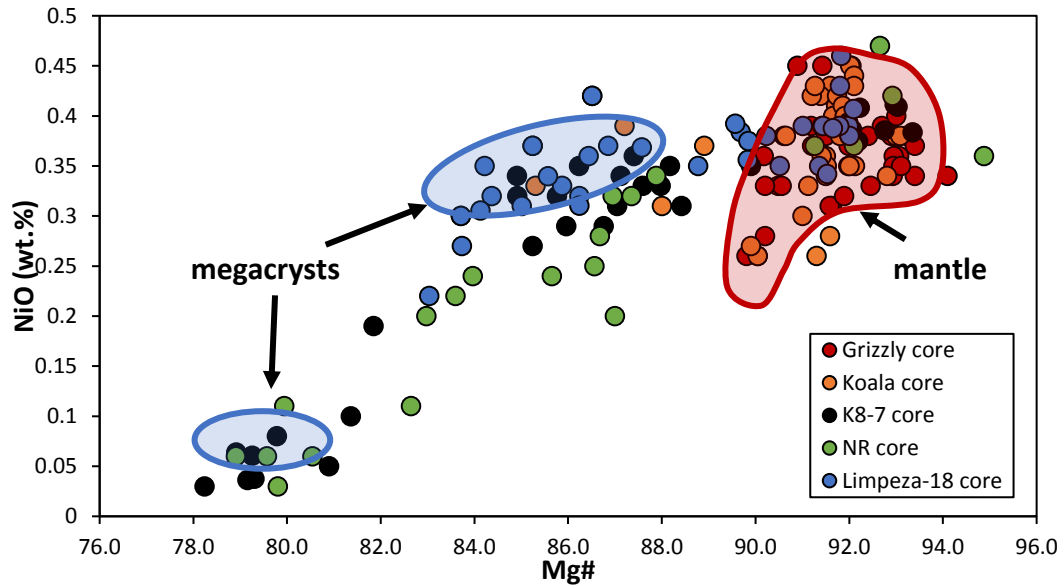


Figure 2. NiO (wt.%) vs. Mg# plot of olivine cores from Grizzly, Koala, Samada (K8-7), New Robinson (NR), and Limpeza-18 kimberlites, with representative compositional fields of olivine from mantle-derived rocks, i.e., ‘mantle’ peridotites (red field; Bussweiler et al. 2015) and ‘megacrysts’ (blue fields; Gurney et al. 1979) which may be genetically related to the olivine cores.

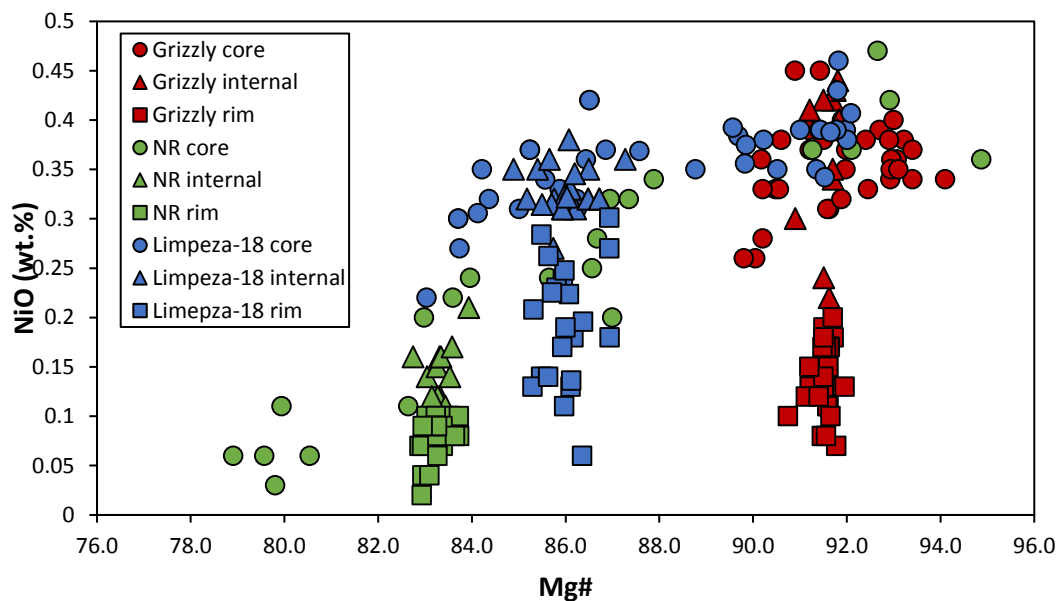


Figure 3. NiO (wt.%) vs. Mg# plot showing the compositions of cores, internal layers and rims of olivine in three studied kimberlites. NR = New Robinson; internal = internal layer.

The internal layers of olivine exhibit higher concentrations of NiO (e.g., 0.11-0.21 wt.% for New Robinson and 0.27-0.38 wt.% for Limpeza-18) than their respective rims. They also have low CaO (< 0.13 wt.%) contents, with restricted Mg# ranges (e.g., 91-92 for Grizzly and 85-87 for Limpeza-18). Olivine rims in all studied kimberlites show decreasing NiO concentrations typically from 0.30 wt.% to values as low as 0.02 wt.%, increasing CaO contents (0.07- 0.30 wt.%) and constant Mg# (e.g., 91- 92 for Grizzly and 85-87 for Limpeza-18). It is noteworthy that in each kimberlite, olivine rims and internal layers show overlapping Mg# values.

In kimberlites containing higher proportions of olivine with ‘megacrystic’ (i.e., Fe-rich) core compositions, the olivine internal layers and rims are richer in Fe (Mg# < 85) than those of olivine grains whose cores are dominated by ‘mantle’ (i.e., Mg-rich) core compositions (Figure 3).

Discussion

The overlapping compositions of ‘mantle’ cores and olivine in peridotites from the underlying lithospheric mantle suggest that these cores probably derive from disaggregated peridotites (e.g., Bussweiler et al. 2015; Dawson et al. 1980). ‘Megacrystic’ cores with Mg# of 82-88, present in different abundances at Koala, Limpeza-18, Samada and New Robinson, significantly overlap with the high Ni (0.30-0.40 wt.% NiO) and Mg (Mg# 84-88) group of olivine megacrysts from the Monastery kimberlite (Gurney et al. 1979). ‘Megacrystic’ cores with Mg# of 78-81, present in the Samada and New Robinson kimberlites, overlap with the second group of Monastery megacrysts (i.e., Mg# 78-81; NiO = < 0.11 wt.%). Therefore, it can be inferred that olivine ‘megacrystic’ cores may be genetically linked to the megacryst suite of xenoliths found in kimberlites worldwide (see also Moore and Costin 2016). The two distinct types of olivine cores were entrained by the ascending kimberlite magma, which then overgrew new olivine around these cores. Similar Mg# compositions of internal layers and rims suggest that the internal layers were produced by the same kimberlite melt(s) that crystallised the rim. We speculate that the internal layer represents the point at which olivine first starts to crystallise in kimberlites, due to the high NiO and low CaO contents. Subsequent crystallisation then results in the formation of olivine rims with lower NiO and higher CaO concentrations.

Assimilation of mostly mantle peridotitic material (e.g., Grizzly and Koala where the cores are dominantly Mg-rich) drives the kimberlite melt towards a Mg-rich composition with formation of high-Mg# internal layers and rims. Conversely, assimilation of more megacrystic component (e.g., Samada and New Robinson where the cores are dominantly Fe-rich), enriches the kimberlite melt in Fe with crystallisation of low-Mg# internal layers and rims. The Limpeza-18 kimberlite provides an intermediate case between the Ekati and Kaalvallei kimberlites. This study therefore provides strong evidence that assimilation of different types of mantle-derived material can generate kimberlites with highly variable compositions, and underlines the extent to which assimilation contributes in making each kimberlite *unique*.

References

- Brett RC, Russell JK, Moss S (2009) Origin of olivine in kimberlite: Phenocryst or impostor? *Lithos* 112:201-212
- Bussweiler Y, Foley SF, Prelević D, Jacob DE (2015) The olivine macrocryst problem: New insights from minor and trace element compositions of olivine from Lac de Gras kimberlites, Canada. *Lithos* 220–223:238-252
- Dawson JB, Smith JV, Hervig RL (1980) Heterogeneity in Upper-mantle Lherzolites and Harzburgites. *Philosophical Transactions of the Royal Society of London Series A, Mathematical and Physical Sciences* 297(1431):323-332
- Giuliani A, Phillips D, Kamenetsky VS, Goemann K (2016) Constraints on kimberlite ascent mechanisms revealed by phlogopite compositions in kimberlites and mantle xenoliths. *Lithos* 240–243:189-201
- Gurney JJ, Jakob WRO, Dawson JB (1979) Megacrysts from the Monastery kimberlite pipe. In: Boyd FR, Meyer HOA (eds) *The mantle sample 2nd International Kimberlite Conference*, vol. American Geophysical Union, Washington, DC, pp 227-243
- Moore A, Costin G (2016) Kimberlitic olivines derived from the Cr-poor and Cr-rich megacryst suites. *Lithos* 258:215-227
- Pilbeam LH, Nielsen TFD, Waight TE (2013) Digestion Fractional Crystallization (DFC): an Important Process in the Genesis of Kimberlites. Evidence from Olivine in the Majuagaa Kimberlite, Southern West Greenland. *Journal of Petrology* 54(7):1399-1425



Kelvin and Faraday Kimberlite Emplacement Geometries and Implications for Subterranean Magmatic Processes

Wayne Barnett¹, Michael Stublely², Casey Hetman¹, Ron Uken¹, Chris Hrkac³ and Tom McCandless⁴

¹ SRK Consulting (Canada) Inc., Vancouver, Canada, wbarnett@srk.com

² Stublely Geoscience, Cochrane, Canada, mike@stublely.ca

³ Aurora Geosciences, Yellowknife, Canada, yellowknife@aurorageosciences.com

⁴ Kennady Diamonds, Toronto, Canada, investors@kennadydiamonds.com

Introduction

The Kennady North Project kimberlites are located approximately 280 kilometres east-northeast of Yellowknife, in the Northwest Territories of Canada. The unusual geometry and extent of the kimberlite magmatic system is revealed by renewed exploration drilling by Kennady Diamonds since 2012. The system comprises multiple intrusive kimberlite dykes and several volcanoclastic bodies, all within 11 kilometres of the Gahcho Kué kimberlite cluster and diamond mine. The detailed exploration of the entire system provides unique evidence for subterranean volcanic conduit emplacement and/or growth processes that may have scientific and practical exploration benefits.

Kimberlite Geometries

The identified Kennady North Project volcanoclastic bodies are named Kelvin, Faraday 1, Faraday 2 and Faraday 3, and have complex geometries atypical of the more common subvertical kimberlite pipes. Rather, these pipe-like bodies are generally inclined between 7° and 41° towards the northwest (Figure 1), with some notable exceptions discussed below. Pipes are contained within a shallow 20° to 27° northwest dipping kimberlite sheeted dyke system. The entire system represents a kimberlite fluid corridor aligned fairly precisely along a N210°E trend over at least 3 km. Locally around Faraday 1 and 2, some deeper dykes have shallower 11° to 15° dips.

The pipes could be described as tubular in shape, in contrast to the spatially associated sheeted dykes. Kelvin and Faraday 2 (and possibly Faraday 1) also have a subvertical elongated profile perpendicular to the tubular shaped NW plunge. The tubular shapes are similar to chonolith geometries described from Ni-Cu-PGE sulphide deposits in ultramafic intrusions (Barnes et al., 2016). Chonoliths are interpreted to have developed their tubular shape from thermo-mechanical erosive processes and channeling of magma flow in the dyke system. On-going detailed petrographic studies at Kennady North have shown that the pipes contain layers of complex volcanoclastic units with variable volumes of xenolithic fragments, as well as coherent magmatic layers. The pipe textures include evidence for high energy magma and country rock fragmentation processes typically observed in open volcanic systems. However, at least a significant component of the fragmentation process must have occurred at depth within the pipe system, similar to that described in ultramafic chonoliths (Barnes et al., 2016).

The sheeted kimberlite dykes have been 3-D modelled along with the pipes. Three possible renditions of the dykes have been created, based on different interpretations of dyke segment continuity. These have been labelled “Optimistic”, “Realistic” and “Pessimistic”. The assumptions made significantly impact interpreted kimberlite continuity and illustrate the importance of understanding continuity and segmentation when developing dyke-type mineral resources.

The Realistic dyke model defines sheeted dyke segments that intersect the Kelvin and Faraday pipes, and those intersections correspond to geometric trends and irregularities in the pipe shapes. In the Faraday pipes, the most prominent dykes appear to define the basal geometry of the pipes. A similar spatial preference of dykes towards the stepped base of the Kelvin pipe is also evident, although the sheeted dykes are not as continuous along the length of the pipe. The coincidental geometries strongly imply that the pipe development interacted with a penecontemporaneous dyke system. It is also

plausible that the pipe shapes developed the upward-elongated profile over time by chonolith type erosive growth processes, either from an original sheeted dyke system or independent chonolith.

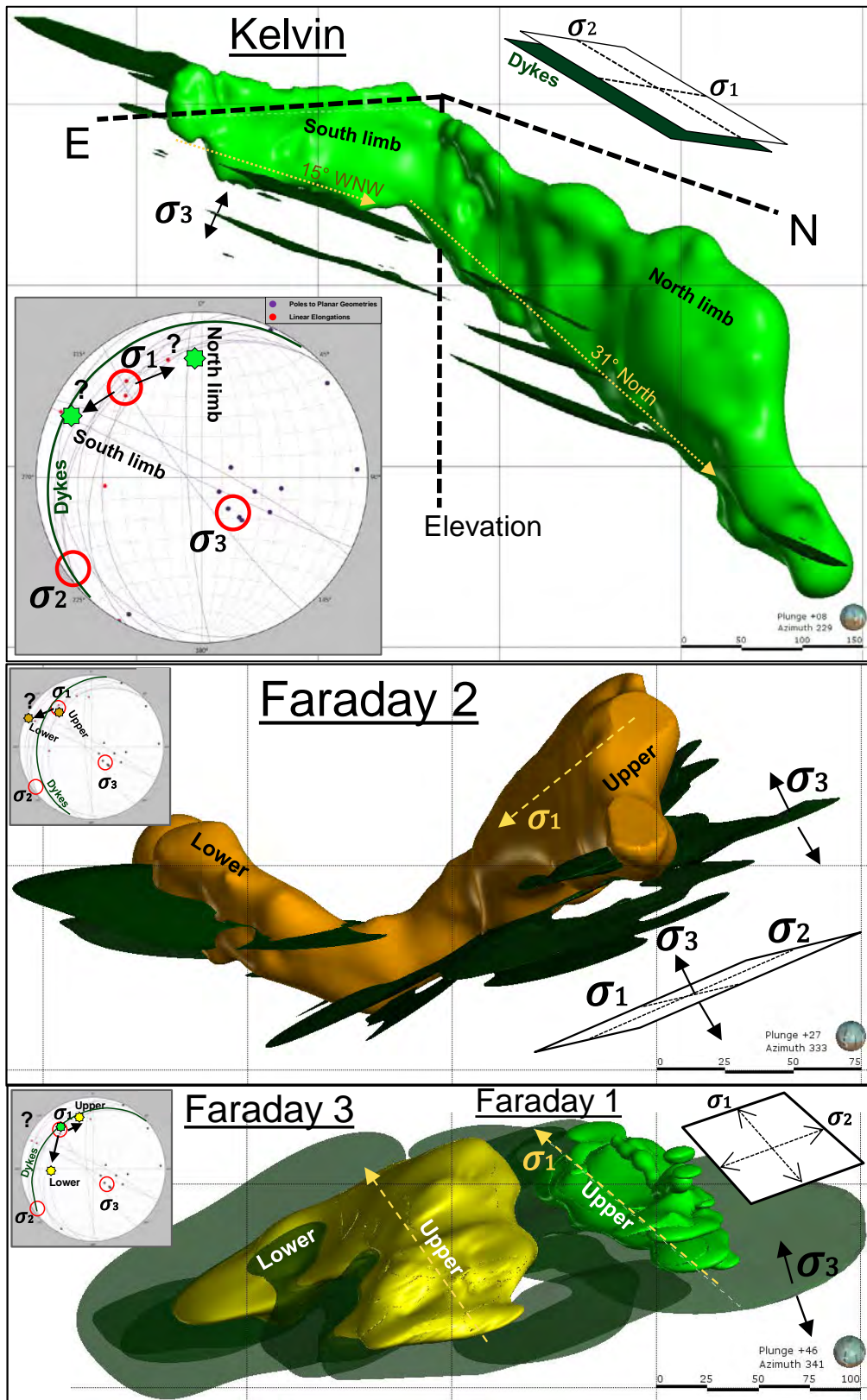


Figure 1: Images showing the 3-D geometries of each Kennady North kimberlite body (labelled). In general, the dykes and chonolith-like bodies dip northwest, but there are some significant deviations. All measured planar and linear elongations in the shapes are represented on insert stereonets, along with the interpreted stress tensor.

The 3-D interpreted kimberlite tubular pipe shape plunges, elongations and planar geometries, as well as sheeted dyke planes were measured. The 3-D interpretation is well constrained by drilling in most areas, except towards depth along the down-plunge extensions of the pipes. The measurements are represented on Figure 1, and are used in combination with our understanding of dyke emplacement mechanics to interpret the property-scale stress tensor orientation at the time of emplacement. In summary, the sheeted dykes are interpreted to occupy the σ_1 - σ_2 plane, with northwest plunging Faraday pipes parallel to σ_1 .

Emplacement Complexities

Detailed structural geology studies, using fault observations in oriented and unoriented drill core, have identified at least two important fault-fracture trends. The first fault-fracture system is parallel to the sheeted dyke segments, and likely related to the intrusion of the dykes and the regional stress tensor during emplacement. The second fault system is subvertical and north-south striking, parallel to the lithological layering within the metasedimentary country rock. Kelvin has a sharp angular change in trend. The Kelvin northern limb plunges 31° towards the north, effectively within the north-south fault system, and this suggests the magma has exploited the faults (oriented approximately 45° to the model σ_1) and allowed a magma conduit to develop. The Kelvin southern limb plunges 15° west-northwest (approximately 20° west of the model σ_1) and this may be due to a local σ_1 stress reorientation; one explanation would be a rotation of σ_1 subparallel to locally west-northwest striking faults (as per Barnett et al., 2013) observed in oriented drill core.

Faraday 2 pipe has a pronounced change in orientation at a depth of 150 m below current surface. It swings in trend towards the west with a change in plunge to 7°, and then curves back towards the northwest. There is also a corresponding change in the dip of the adjacent sheeted dykes from 27° to 11°. This curve is interpreted as a linkage zone (common in dyke systems) that possibly developed between two *en echelon* magma feeder systems. As the system evolved and underwent thermo-mechanical erosion, the linkage zone could have expanded and merged as part of the overall kimberlite pipe system. Faraday 3 has a similar change in pipe trend and dyke dip, also starting at a similar depth. Faraday 1 and 3 pipes, as currently modelled, are within 30 m of each other and connected via the same sheeted dyke system, and may also be connected via a short linkage zone at depth where there are currently inadequate drill holes to define the pipe boundaries. We interpret a spatially and temporally complex interactive system of sheeted and tubular intrusive bodies to depth.

Conclusions

We conclude that the Kennady North subterranean kimberlite development, and its internal textures and resultant geometries are governed by a combination of stress, structure and magmatic fluids, in a system that evolves over a prolonged period of time. There seem to be significant similarities to chonolith-type Ni-Cu-PGE sulphide ultramafic intrusive deposits. We consider the initial intrusive geometry of each pipe to have either evolved from an initial single chonolith-like tubular body or from the linkage zone (or other similar irregularities) of segmented, sheeted dyke systems, with pipe expansion driven by magmatic fluid brecciation and thermo-mechanical erosion processes and channelled flow of magma-xenoliths, fluids and volatiles.

References

- Barnes SJ, Cruden AR, Arndt N, Saumur BM (2016) The mineral system approach applied to magmatic Ni-Cu-PGE sulphide deposits. *Ore Geology Reviews* 76:296-316
- Barnett W, Jelsma H, Watkeys M, Freeman L, and Bloem A (2013) How Structure and Stress Influence Kimberlite Emplacement. In: Pearson et al. (eds.), *Proceedings of 10th International Kimberlite Conference, Volume 2*, Springer India 2013, Special Issue of the *Journal of the Geological Society of India*, pp. 51-65



The role of sulphur during partial melting of eclogite in the cratonic mantle: constraints from experiments and mantle xenoliths

Sara Burness¹, Katie A. Smart¹, Gary Stevens², Sebastian Tappe³

¹ School of Geosciences, University of the Witwatersrand, Johannesburg, South Africa; sara.burness1@gmail.com, katie.smart2@wits.ac.za

² Centre for Crustal Petrology, Stellenbosch University, Stellenbosch, South Africa, gs@sun.ac.za

³ University of Johannesburg, Auckland Park, South Africa, sebastian@uj.ac.za

Introduction

Sulphide- and carbon-bearing melts play an important role as metasomatic agents within the cratonic mantle lithosphere, and may be linked to processes including diamond formation (Griffin et al., 2003), metal transport (Arndt et al., 2005) and the deep carbon cycle (Tappe et al., 2017). While the influence of C-bearing fluids on the lithospheric mantle is under continuous investigation (e.g. Dasgupta et al., 2004), the activity of S-bearing fluids and their role in diamond formation is less well constrained (Mungall and Brenan 2014). Sulphide minerals are key to the mantle S cycle. They control the platinum group element (PGE), siderophile and chalcophile element budgets, and their behaviour during partial melting controls the movement of these economically important metals. Here we present a case study of eclogite metasomatism by S+C-bearing fluids, by comparing new experimental work with geochemical investigations of sulphide-bearing eclogite xenoliths from several kimberlite occurrences on the Kaapvaal craton, South Africa. The focus of this study is to delineate the activity of S on the melting behaviour of eclogite and the relationship between sulphide-melt formation relative to carbonate±silicate melt formation. Our findings add to the knowledge of volatile-bearing solidii in the upper mantle, the partitioning nature of various major and trace elements between the silicate residuum, possible sulphide residuum, and miscible or immiscible silicate±carbonate melts and S-melts. A complementary investigation of sulphide-bearing eclogite xenoliths may serve as a benchmark for the processes of volatile-bearing metasomatism studied here.

Melting of C+S-bearing MORB at upper mantle conditions

In order to investigate the influence of C-O-H-S bearing fluids on mantle processes, we present results from partial melting experiments that constrain the near-solidus phase relations of S- and C-bearing eclogite from 2.0 to 3.5 GPa and 1050 to 1300°C. A synthetic MORB-like composition created from reagent grade silicate and carbonate powders was fired into a glass at 1400°C before being doped with 5wt.% synthetic pentlandite (Fe_{0.93} Ni_{0.17} Cu_{0.03} S_{1.10}; Metal/Sulphur = 1.12; Ni/(Fe+Ni) = 0.15) and, to foster melt detection, various proportions of CO₂ (0.5 and 15wt.%) in the form of CaCO₃. The starting compositions were placed in graphite-lined PdAg capsules and experiments were conducted using non-end loaded piston cylinder apparatus with a run time of 24 hours. The silicate experimental products consist of euhedral to subhedral garnet and omphacitic cpx ±coesite, ±zircon and ±anorthite (Fig. 1), typically ≤15µm in size. Both sulphide liquid (e.g., Fe_{1.0} Ni_{0.1} Cu_{0.006} S_{1.12}; Metal/Sulfur = 0.93; Ni/(Fe+Ni) = 0.09) and MSS (e.g., Fe_{0.78} Ni_{0.22} Cu_{0.05} S_{1.26}; Metal/Sulphur = 0.84; Ni/(Fe+Ni) = 0.22) are precipitated during the partial melting of eclogite. Phase relationships (Fig. 1) show distinct rounded globules of sulphide melt (L_S) which are texturally immiscible to both silica and silica± dominated melts. MSS form discrete sub-angular grains that are usually ≥15µm in size. The location of the sulphide solidus is plotted in Fig. 2 along with carbonated eclogite solidii (1 and 2), a CO₂-free eclogite solidus and the near-solidus phase assemblages. CO₂-rich vapour is inferred as the main medium of carbon at low pressure in experiments with 5wt.% CO₂.

Links to mantle metasomatism in the presence of C+S- bearing fluids/melts

Our study shows that S melts+MSS are the first to appear upon melting of a S+C-bearing high-pressure MORB (Fig. 2). There is a small temperature difference between the S and S+C solidii at the pressures investigated, but this temperature difference may not easily be distinguished during incipient melting. The experimental S-melts and solid MSS are enriched in siderophile and chalcophile elements and likely PGEs (Bockrath et al., 2004), show a striking similarity to sulphide inclusions in E-type diamonds (Fig. 3; Deines and Harris, 1995) and texturally and compositionally resemble the sulphides in our studied eclogite xenoliths. The experimental S-melts and MSS also appear to form high-angle contacts with silicates and Si+C melts, or discrete globules within highly polymerised silicate melt (Fig. 1), such that the immiscible nature of our experimental MSS supports the 'nugget effect' of sulphides observed in mantle eclogite nodules. In summary, our study suggests that S-melts alone may not be effective metasomatic agents in the cratonic mantle. However, since S+C melts are likely produced together during mantle melting, carbonatitic melts with appreciable S may instead be effective ways to concentrate and mobilize PGE minerals within the CLM, and due to the overlap of sulphide DIs and our experiments, S+C melts may be effective diamond-growth media.

References

- Arndt N, Leshar CM, Czamanske GK (2005) Mantle-derived magmas and magmatic Ni-Cu-(PGE) deposits: 5-24
- Bockrath C, Ballhaus C, Holzheid A, (2004) Fractionation of the platinum-group elements during mantle melting. *Science* 305 (5692): 1951-1953
- Dasgupta R, Hirschmann MM, Withers AC, (2004) Deep global cycling of carbon constrained by the solidus of anhydrous, carbonated eclogite under upper mantle conditions. *Earth and Planetary Science Letters* 227(1); 73-85
- Deines P, Harris JW (1995) Sulfide inclusion chemistry and carbon isotopes of African diamonds. *Geochimica et Cosmochimica Acta* 59(15): 3173-3188
- Griffin WL, O'Reilly SY, Abe N, Aulbach S, Davies RM, Pearson NJ, Doyle BJ, Kivi K (2003) The origin and evolution of Archean lithospheric mantle. *Precambrian Research* 127(1): 19-41
- Litasov K, Ohtani E (2010) The solidus of carbonated eclogite in the system CaO–Al₂O₃–MgO–SiO₂–Na₂O–CO₂ to 32GPa and carbonatite liquid in the deep mantle. *Earth and Planetary Science Letters* 295(1): 115-126.
- Mungall JE, Brenan JM (2014) Partitioning of platinum-group elements and Au between sulfide liquid and basalt and the origins of mantle-crust fractionation of the chalcophile elements. *Geochimica et Cosmochimica Acta* 125: 265-289
- Pertermann M, Hirschmann MM (2003) Partial melting experiments on a MORB-like pyroxenite between 2 and 3 GPa: Constraints on the presence of pyroxenite in basalt source regions from solidus location and melting rate. *Journal of Geophysical Research: Solid Earth* 108(B2)
- Schrauder M, Navon O (1994) Hydrous and carbonatitic mantle fluids in fibrous diamonds from Jwaneng, Botswana. *Geochimica et Cosmochimica Acta* 58(2): 761-771
- Tappe S, Romer RL, Stracke A, Steinfeldt A, Smart KA, Muehlenbachs K, Torsvik TH (2017) Sources and mobility of carbonate melts beneath cratons, with implications for deep carbon cycling, metasomatism and rift initiation. *Earth and Planetary Science Letters* 466:152-167
- Yaxley GM, Brey GP (2004) Phase relations of carbonate-bearing eclogite assemblages from 2.5 to 5.5 GPa: implications for petrogenesis of carbonatites. *Contributions to Mineralogy and Petrology* 146(5): 606-619

Kimberlite intrusions, kimberlitic ash dispersal, diamond transport and diamond deposition: The potential role of Earth Systems Modelling in diamond exploration.

R. Crossley¹, J. Harris¹, J. Watson¹, A. Ashley¹, K. Lamb¹, M. Goodrich¹, P. Valdes², J. Hill³ and A. Avdis³

¹ CGG Geoconsulting, Llandudno, Conwy, Great Britain, rob.crossley@cgg.com

² University of Bristol, Bristol, Great Britain

³ Imperial College, London, Great Britain

Introduction

Our Plate Kinematics model can be used to help predict the locations and orientations of kimberlitic intrusions (using intra-plate palaeostress in relation to geological structure). Our Palaeo-Earth Systems Models can be used to predict transport directions of volcanic ash carrying kimberlitic indicators (by modelling palaeowinds) and potential distribution of alluvial diamonds (by quantifying runoff and sediment flux in successive paleogeographic contexts through modelling rainfall, rainfall intensity, evapotranspiration and vegetation). In marine settings, modelling of potential diamond sand distributions includes predictions based on palaeotidal currents, palaeowind-driven currents and gravitational resedimentation of sands on steep slopes.

Plate Model

The Robertson Plate Kinematics model classifies continental crust into areas which have responded rigidly to intraplate stress throughout the Phanerozoic, and into deformable areas which have suffered extension and/or shortening within that period. The deformable areas play an important role in controlling the way in which far-field stress from global-scale plate motions is transmitted into the rigid plates. The plate model incorporates the changing deformation states in these continental areas and so provides a basis for predicting the direction and timing of intraplate stress within Archaean and Proterozoic crust throughout the Phanerozoic. The plate model is also used as the basis for palaeogeographic mapping from which digital elevation models (DEMs) are constructed. An explanation of the Plate Kinematics model, the palaeogeographic mapping and the Earth Systems Modelling are included in Harris *et al.*, (in press).

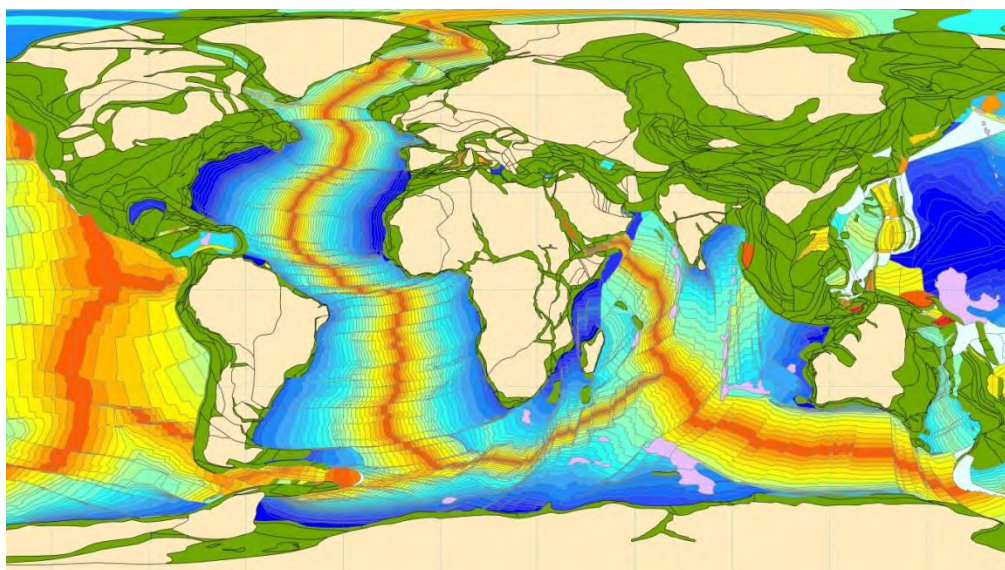


Figure 1: Plates which have shown rigid (pale buff) or deformable (green) behaviour during the Phanerozoic, in relation to oceanic plateau (pink) and oceanic crust age data, which help constrain plate kinematics.

Earth System Models

A series of 18 and Recent Earth System Models have been run, together with a series of sensitivity tests. The ages have been chosen by clients to target time slices of interest for petroleum exploration. The DEMs are coupled with state-of-the-art palaeo-Earth systems models (UK Met Office HadCM3 palaeoclimate model) and an unstructured mesh model to simulate palaeotides (Imperial College, UK, ICOM tide model). The resulting palaeoclimate results fit well with globally distributed geological proxies for palaeoclimatide indicators at these ages. This gives confidence in the palaeogeographies constructed and in the Earth System Model results.

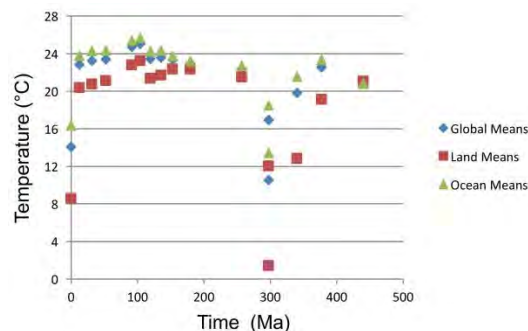
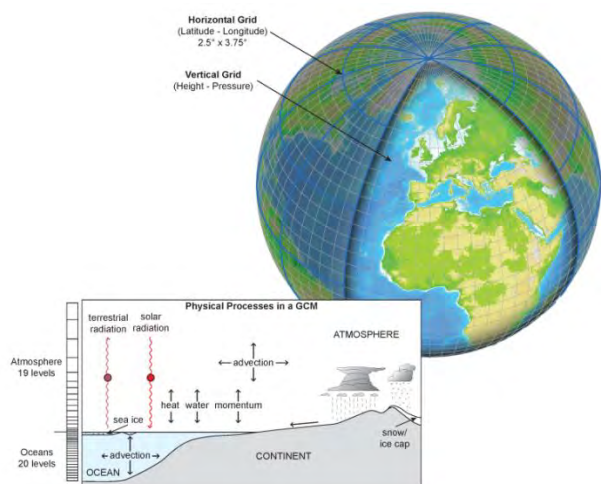


Figure 2: The coupled ocean-atmosphere palaeoclimate model links the physics of oceanic and atmospheric grids.

Figure 3: The palaeoclimate results fit well with “hot house” and “ice house” worlds.

These Earth System Models are run on paleogeographic and palaeotopographic DEMs created using an approach which relates topography and bathymetry to plate tectonic context and depositional environments.

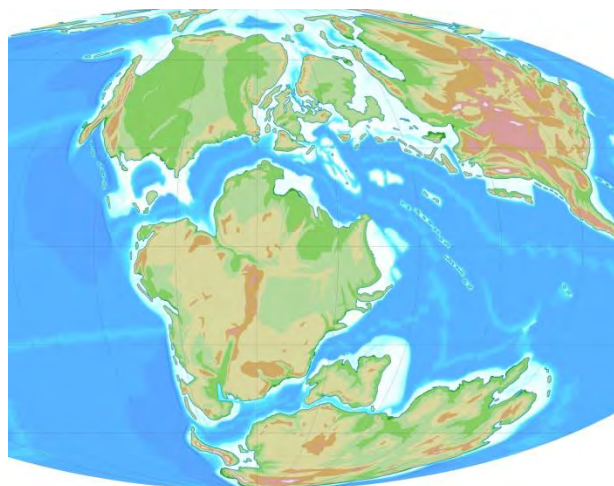
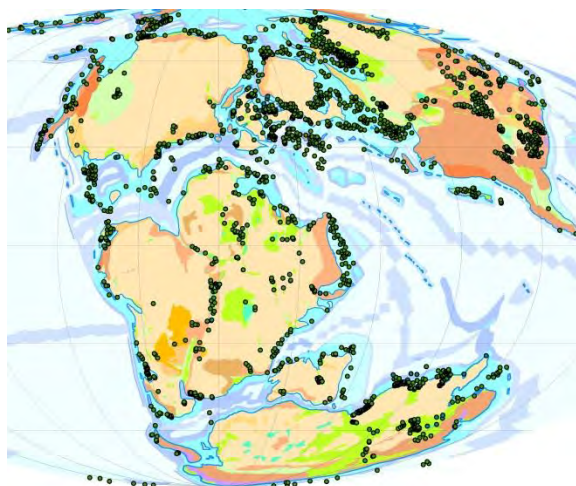


Figure 4: Plate tectonic context polygons and palaeoenvironment control points.

Figure 5: Resulting palaeotopographic and palaeobathymetric digital elevation model.

The palaeogeographies are constrained by legacy data representing over 35 years of petroleum geological studies. The predictions of palaeoclimate and sediment distributions are tested against

thousands of control points collated from the public domain and from confidential oil industry exploration wells. This approach provides an understanding of regional palaeogeographic change and palaeoclimatic geohistory that includes drainage basin evolution and the quantification of clastic sediment flux. These models are run on the entire Earth, and for this conference we will present a series of case studies illustrating operation of these Earth System models on a series of time slices.

Over the last 20 years we have used this methodology to help our oil company partners explore for marine oil-prone source facies and reservoir rocks. We believe the methodology could, with minimal re-tuning, also have applications in exploration for diamonds.

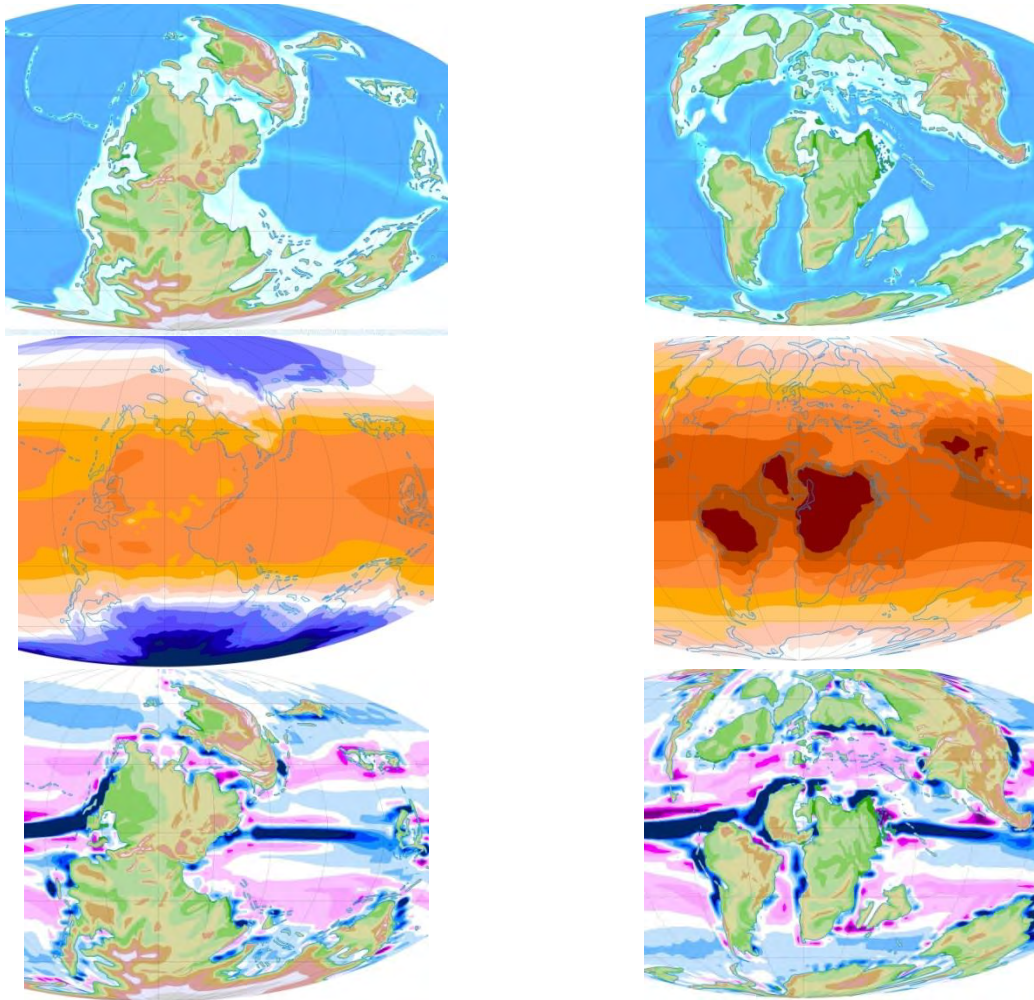


Figure 8: Early Permian palaeogeography, showing surface air temperature (blue: cold) and oceanic upwelling (dark blue) modelled from palaeowind data.

Figure 9: Turonian palaeogeography, showing surface air temperature (red: hot) and oceanic upwelling (dark blue) modelled from palaeowind data.

For example, the palaeowind data, which is compiled on a monthly, seasonal and annual basis, could be used to predict dispersion directions for kimberlitic ash, and hence help track kimberlitic indicators back to undiscovered kimberlite pipes.

Reference

Harris, J., Ashley, A., Otto, S., Valdes, P., Crossley, R., Preston, R., Watson, J., Goodrich, M., and the Merlin+ Project Team (in press). Paleogeography and Paleo-Earth Systems in the Modeling of Marine Paleoproductivity: A Prerequisite for the Prediction of Petroleum Source Rocks, in M. AbuAli and I. Moretti, eds., Petroleum System Case Studies: AAPG Memoir 114, p. 37–60.

Kimberlite fields of Angola: structural control and diamond presence

V. Ustinov¹, A. Feijo², A. Zagainy¹, S. Mityukhin¹, F. Tunga³, I. Mikoev¹,
Yu. Stegnitskiy¹, L. Lobkova¹, E. Nikolaeva¹

¹ ALROSA, Saint-Petersburg, Russia, UstinovVN@alrosa.ru, ZagainyAK@alrosa.ru

² ENDIAMA, Luanda, Angola, Anafiejo.feijo181@gmail.com

³ CATOCA, Luanda, Angola, Felix@catoca.com

About one thousand kimberlite pipes have been discovered on the territory of Angola to date. This makes the country unique in the scale of manifestation of kimberlite magmatism. The pipes are combined into 11 regions and 36 fields (Figure 1). Macrodiamonds were discovered in kimberlites of seven fields. As a rule, each of them has a pipe-leader, characterized by higher grades and diamond reserves. Kimberlite magmatism on the territory of Angola is related to several periods of tectonic and magmatic activity: Proterozoic-Early-Paleozoic (?), Triassic and Early Cretaceous. Majority of kimberlite bodies, including diamond mines, are Cretaceous.

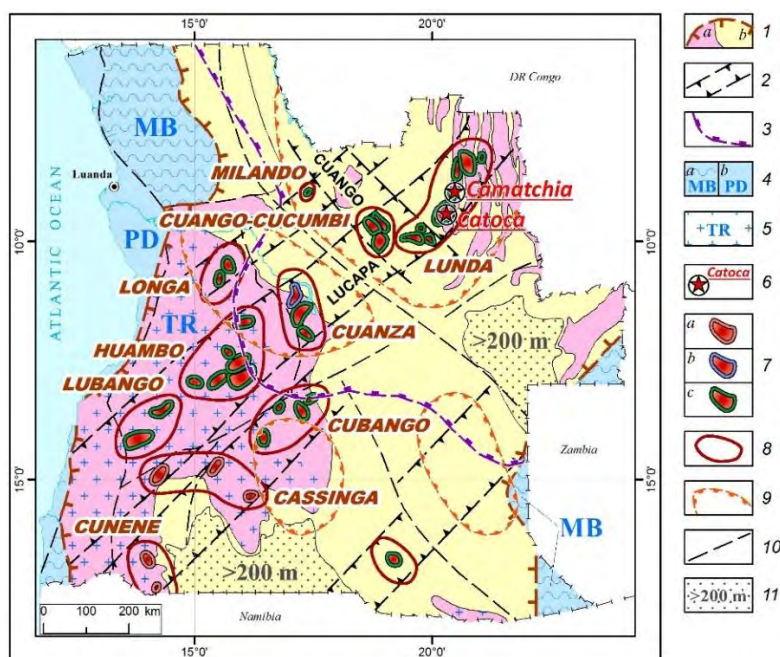


Figure 1: Kimberlite fields and regions in tectonic structure of Angola.

1-5 – main structural and tectonic factors of distribution of kimberlite fields: positive (1 – Archean craton Congo (a – territories with exposed, b – buried kimberlites), 2 – zones of tectonic and magmatic activity, 3 – area of favourable deep structures), negative (4 – mobile belts (a), pericontinental depression (b), 5 – areas of tectonic and thermal reworking); 6-9 – diamond presence: 6 – kimberlite diamond mines, 7 – kimberlite fields (a – Proterozoic-Early Paleozoic (?), b – Triassic, c – Early Cretaceous), 8 – kimberlite regions, 9 – areas of dispersion of diamonds in terrigenous rocks; 10 – major deep-seated faults; 11 – depressions with overburden of >200 m.

Kimberlite pipe sizes vary from 0,3 ha to 100 ha and 150 ha. Six most rich pipes with diamond grades of 0,5-1,0 carats per tonne (cts/t). were discovered in NE of Angola in Camatchia field (Camagico pipe) and five pipes in Catoca field (Catoca, Tchiuzo, CatE42, Luax071 and Luax072). The number of bodies with grades from 0,1 to 0,5 cts/t is around twenty. A typical diamond-bearing

kimberlite pipe in Angola consists of crater, diatreme and root channel zone. The thickness of crater formations reaches 270 m.

Diamond-bearing rocks are characterized by similar compositions of kimberlite indicator minerals (KIMs). Picroilmenites and garnets prevail in all pipes. Comparative analysis of diamonds in kimberlite bodies with different grades showed that stones are characterized by an individual morphogenetic features. The higher diamond grades, the higher the contents of laminar octahedrons. For example, diamonds of Catoca pipe (0,8 cts/t) in the comparison to other bodies are characterized by a relatively high content of octahedrons (up to 40 %) and 40 % of round crystals. Diamonds of Tchiuzo pipe (0,4 cts/t), are represented by round diamonds (85 %) and less amount of octahedrons (7 %). This is evidence of unfavorable physical and chemical conditions of diamond preservation which resulted in dissolution of stones in Tchiuzo pipe. In general, the content of octahedrons in pipes is relatively low: 5-45 %. In all the known pipes rounded crystals (dodecahedroids) prevail.

The conclusion about dissolution of diamonds in kimberlite melts can be supported by analysis of chemical composition of pyropes. For the majority of the pipes the number of pyropes of diamond association and G10 has a direct correlation with diamond presence and the amount of garnets, formed within a diamond window with temperatures from 900 to 1100 °C and pressures around 40-50 kbar (Figure 2). Another group of kimberlite pipes (Txicoa is an example) contains rather high (up to 5 % and more) content of pyropes of diamond association and G10, but does not contain diamonds. One can see on diagram that no one pyrope is in area of diamond window. This indicates sharp changes of temperature conditions in mantle reservoir and shows dissolution of diamonds. This is one of the reasons why many pipes in Angola do not contain diamonds.

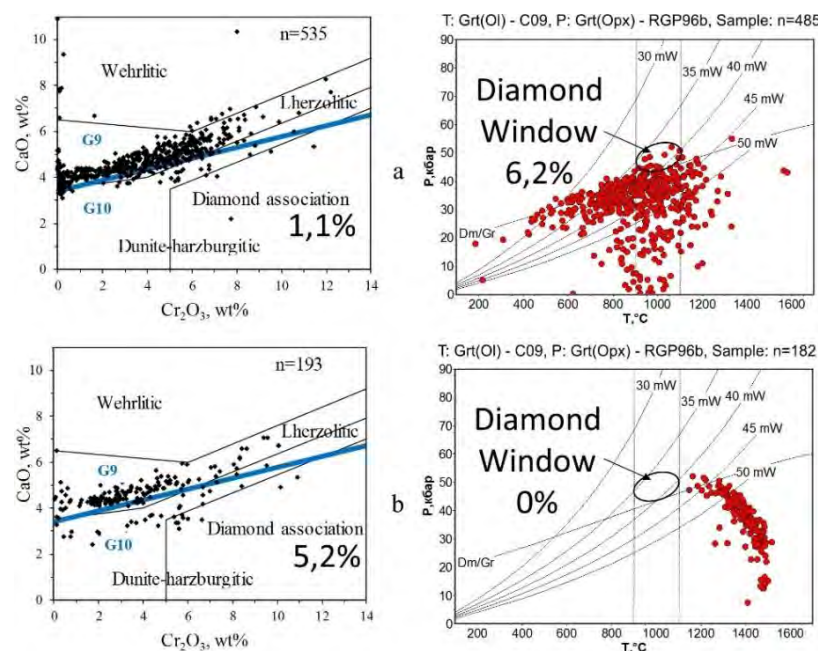


Figure 2: CaO-Cr₂O₃ diagrams of pyropes (fields by N.V. Sobolev, 1974, J.J. Gurney, 1973) in diamondiferous Catoca pipe, 0,8 cts/t (a) and non diamondiferous Txicoa pipe (b) and P-T conditions of garnets formation.

Analysis of conditions of formation of mantle melts (depth of formation, temperature, pressure), morphology of pipes, the number of bodies, diamond potential and other features of 90 % of the pipes shows that the territory of Angola can be divided into four types of the areas (Figure 3). The depth of kimberlite magmatism and diamond potential of pipes increase from the Atlantic coast (SW part) into the continent in the north-eastern direction. Their values have direct correlation with tectonic position of kimberlites and deep structure of the territory.

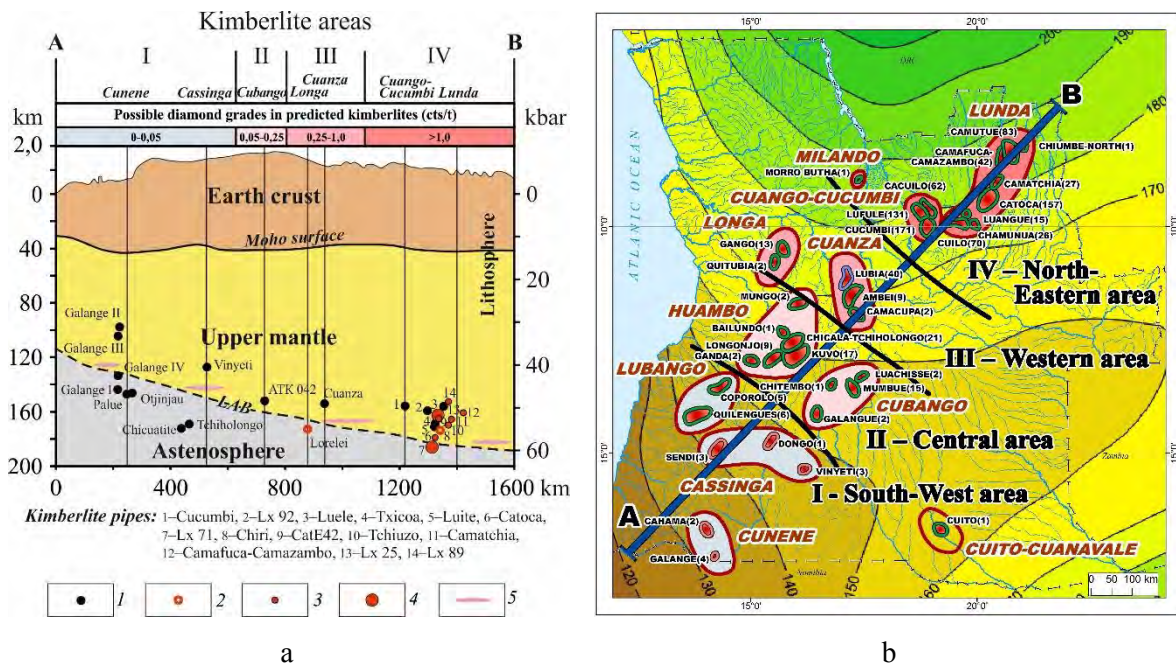


Figure 3: The depth of formation of kimberlitic melts in the section AB of the upper mantle (a) and kimberlite areas on the map of thickness of lithosphere (b).

1-4 – diamond grades in known pipes (cts/t): 1 – 0-0,05; 2 – 0,05-0,25; 3 – 0,25-1,0; 4 – >1,0; 5 – eclogitic lenses.

Structural and tectonic factors of controlling distribution of the known kimberlite fields in Angola were revealed (see Figure 1). The main ones are: 1) confinement to the blocks of Archean stabilization – cratons and within their territories to the areas without tectonic and thermal reworking in Paleoproterozoic (Eburnean) time; 2) connection with paleo-elevations in crystalline basement; 3) presence of positive structures (elevations) in Platform sedimentary cover; 4) confinement to trans-block linear zones of tectonic and magmatic activities. The most important diamond controlling structure of Angola is Lunda zone. The most favorable features of the deep structure for distribution of the known kimberlite fields of Angola are: 1) a significant thickness of the lithosphere (more than 150 km); 2) depressions and its slopes in relief of the Moho surface; 3) areas of decompaction of the Earth's crust; 4) areas of high velocities of seismic waves; and 5) low heat flow.

Based on a comprehensive analysis of kimberlite pipes of Angola (tectonic position, deep structure, morphology, age, conditions of formation of mantle melts, mineralogical and petrographic features at al.) the territories with different diamond potential were distinguished.

Deep Delineation Evaluation Drilling Methods, Jwaneng Mine, Botswana.

F.T. McKinlay¹, Dr. M. Roberts²

1) Debswana, Jwaneng, Botswana, (tmckinlay@debswana.bw),

2) Debswana, Gaborone, Botswana, (mroberts@debswana.bw)

Introduction

Anticipated future mining options at Jwaneng seek to exploit ore to depths of 1000m and beyond. In order to support future mining studies and investment option selection, successful evaluation of geoscientific properties (geological and geotechnical) of the kimberlites at depth are required. Solutions include drilling to intersect the kimberlite ore bodies at depth in the 850 to 1,000 meter zone mining zone and beyond. To date the geological model has been developed with high confidence to 850 meter depth and to 1,000 meters depth with medium confidence. A second option includes developing an underground drift from surface to intercept the kimberlites at depth followed by underground drilling and bulk sampling. The latter option will not be reviewed in this document.

There are several methodologies of drilling from surface that can be considered. They include the following; wireline core drilling with conventional drill sizes (PQ and HQ core sizes); rotary or percussion drilling from surface to a specified depth followed by core drilling; core drilling using larger SK size core drilling equipment producing core sizes of 100mm and 80 mm; drilling from surface using down hole directional drilling equipment to a specified depth followed by wireline core drilling.

Key requirements for successful drilling solutions include a high level of drilling accuracy and recovery of good quality core samples for geotechnical testing and analysis. The three Jwaneng kimberlites (North, Center and South) are composed mainly of volcanoclastic kimberlite (VK), with the North pipe containing a central core of pyroclastic kimberlite (PK). They are hosted within a sequence of quartzitic shales to 500 meters depth underlain by silicified dolomite to a depth beyond 1,000 meters. Developing an accurate method of drilling from surface is critical in order to evaluate individual mining blocks within the kimberlite ore bodies. Geological and geotechnical information is required from evaluation drilling to inform optimized future mine design. The Jwaneng Mine currently is an open pit approximately 400 meters depth. The open pit has been planned to extend to approximately 836 meters depth which defines the bottom of the Cut 9 mining shell. The post Cut 9 zone is that which is defined in the 850 to 1,000 meters depth. Future mining options include consideration for Cut 10 open pit mining or to develop an underground mine.

There are several challenges to drill the kimberlite pipes from surface successfully. Drill rods tend to deviate with increased depth and therefore can miss the planned target. The Jwaneng VK units are typically soft with abundant clay content that cause excessive drill cuttings. A significant percentage of the clay is Na-smectite variety which has properties that cause it to swell when exposed to water. This typically increases resistance and torque on the drill rods and leads to common hole failures at depth. In order to overcome the challenges presented by the clay-rich kimberlite drilling methods need to be developed to enable the drill

cuttings to be lifted out of the deep bore holes efficiently and effectively. Effective management of drill fluid specific gravity is important to ensure that the cuttings are lifted from depth and cleared effectively from the bore hole. Drill additives must be used to supplement the circulating fluids to inhibit or prevent the clay-rich kimberlite from swelling and causing the above mentioned drill failures. Specific chemicals have been developed by various supply companies to reduce torque on the drill rods, to minimize water contact with freshly drilled kimberlite and to build a sturdy filter cake that will stabilize the borehole walls. Strict management of the use of chemical additives while drilling kimberlite intersections is critical to ensure that their designs are effective.

Several methods of drilling deep evaluation holes have been recently tested at Jwaneng to overcome the challenges. Specially designed large diameter drill rods that resist shearing due to increased torque have been successful. This refers to the above mentioned SK drill equipment which produces larger core sizes than conventional drill systems. Top drive drills with appropriate hydraulic pullback capacity to overcome deep drill systems have been utilized. The required pullback power of the drilling system can be determined by the calculating the weight of the drill string plus the bottom hole assembly. Added to this will be the resistance of friction caused by the drill rods resting on the bottom of an inclined drill hole and the pressure that the rock formations exert on the drill string. The clay-rich kimberlite tends to swell and attempts to close the borehole diameter when drilled at depth due to deep confining pressures. Testing large diameter drill holes of 162 mm in diameter have been rotary (tricone) drilled from surface to 900 meters depth followed by large diameter (100mm core size) core drilling. The large diameter core system provides the ability to reduce to a smaller core size to overcome increased torque built up on the rods at depth, and act as casing for the smaller diameter drill systems. The large diameter core systems also provide the ability to utilize larger drill bit sizes (oversize) where the annular space between the drill rods and the borehole wall is proportionally greater than smaller conventional drill sizes and as a result allows drill cuttings to be cleared more effectively. This then allows less chance of cuttings remaining in the hole binding the drill rods and bottom hole assembly.

Accuracy of the planned drill path remains a priority. However rotary drilling was found to deviate significantly away from the drill planned path. The planned inclination of the rotary system dropped by up to 10 degrees beyond the end of the casing. Casing was install to depths up to 120 meters. During testing the rotary drilling continued to 400 meters depth and beyond. It was found that deviation of the drill rods increased beyond acceptable limits past 400 meters depth. Relatively severe directional correction curves in the drill hole create additional challenges as the hole is deepened. When used correctly down hole directionally controlled drill motors (MWD-measure while drilling) were successful to correct the deviated drill path back to the planned target. The experience and skill of the drill operator is also critical for success to prevent additional challenges down the hole.

Appropriate chemicals, as noted above, have also been successfully demonstrated to inhibit the reactive clay-rich kimberlite from swelling (which increases torque on the drill rods). It is important to continue to circulate the designed chemical mixture in the hole especially when intersecting kimberlite. If left unattended the chemicals will break down over time and become less effective in their ability to stabilize the hole and prevent the clay-rich kimberlite from swelling. A majority of the chemicals are biodegradable and will break down if not continually refreshed. It was also found that raw water used to make the drilling fluid mixture could provide additional conditions which could contribute reduced effectiveness of the chemical additives if left unattended. Successful use of drilling additives is also achieved by utilizing technical experts with knowledge of chemicals developed to optimize clay-rich kimberlite drilling.

Technical experts provide knowledge gained from a host of projects. Establishing a dedicated drill-site resource to monitor and maintain drilling fluid composition is also a key to success. Geological structures intersected while drilling can add or remove water from the fluid system upsetting the balance proportions of chemicals. A dedicated “mud manager” will ensure the fluid mixtures are maintained in the correct balance. External consultants from chemical supply companies or those who specialize in drilling fluids add significant value to train personnel to become the in-house on-site mud manager to ensure that chemicals are used properly. Dedicated drill fluid management will significantly increase the ability to recover good quality kimberlite core samples and advance the drill depth through difficult conditions.

The limits of conventional PQ/HQ coring have also been tested and demonstrate the potential to supplement the more expensive but highly accurate directional drilling methods. Small diameter conventional wireline drilling was planned to intersect the kimberlite at a designed pierce point, recover good quality kimberlite core and drill through the kimberlite pipe to intersect a second kimberlite pierce point. PQ size core was drilled to 931 meters depth followed by HQ size core drilled to 1,184 meters depth. VK kimberlite was intersected at 996 meters depth, and 184 meters of good quality core was recovered. While success was achieved by recovering a significant intersection of good quality kimberlite core the hole was stopped due to increased pressures and torque exerted on the rods and bottom hole assembly. Only one kimberlite pierce point was intersected. Minimal deviation of the drill path was observed to approximately 800 meters depth after which the hole swung increasingly to the right as the hole advanced beyond this point. The initial planned point of intersection was not achieved accurately. Therefore while small conventional size core drilling will provide important information to obtain geological and geotechnical information to date has not demonstrated the ability to drill at depth with accuracy without the use of a down hole directional motor.

Continued testing of deep drilling methods (core and LDD) are currently underway in order to test the technical ability to develop integrated geoscience models through drilling methods alone in hole lengths in excess of 1500m (core) and 700m (LDD). Technical specifications for deep drill systems have been established for future kimberlite evaluation drill projects at Jwaneng mine. International consultants have been involved to assist in the development of these technical requirements. They have experience in various types of drill programs and geological conditions operating in several countries. Inclusion of the external experts to help design future drill programs has added considerable value to Jwaneng kimberlite drill projects. Knowledge and training from external technical experts to in-site project management teams has added considerable value to the Jwaneng projects to design future drill programs.



Evolution of the Orapa A/K1 Geology Model – Insights from Analysis of Multi-Disciplinary Datasets

Kganetso Maphane

Debswana, Orapa Mine, kmaphane2@debswana.bw

Introduction

The Cretaceous Orapa A/K1 is exposed as a bilobate kimberlite pipe with preserved crater lithofacies. The pipe is currently the biggest of all known kimberlite bodies within the Orapa Kimberlite Cluster (OKC), covering a surface area of ~118 hectares. A number of these kimberlite bodies are currently being economically exploited (e.g. Orapa A/K1, Damtshaa B/K9 & B/K11, and Letlhakane D/K1 & D/K2) or at advanced evaluation stage (e.g. A/K20). Mining activities in the Orapa area started in 1971 after discovery of the A/K1 kimberlite in 1967.

Following discovery, a number of resource evaluations were conducted and subsequently five geological models generated (Table 1). These models improved with time as the geology of the pipe is exposed through mining, and as more drilling targeting deeper levels were completed. The purpose of this document is to summarise the evolution of the geological models including data input informing the models.

Historical Work

The initial stage of evaluation included shallow pitting to a depth of 30m for grade determination, and a limited core drilling to define the pipe shape. This work focused on the sedimentology of the preserved crater in-fill exposed in the pit and intersected by pitting and core drilling. The result of the pitting exercise was the generation of the first model for planning purposes in the late 1970's and later updated after additional drilling and mapping in 1991. Since much of the mining was in the crater, an extensive work on the preserved fossils in the fossil shale basin was completed. This work included description and dating of the fossils by Rayner and McKay (1987) where they interpreted the paleo Orapa climate as strongly seasonal, with a warm wet summer and dry cold winter. It was during this early work that a strong correlation between lithofacies type and diamond grade was established in the Orapa A/K1 (e.g. Minter, 1978; Dobbs, 1980).

Table 1: Evolution of the Orapa A/K1 Geological Model

| | 1967-1980 | 1982-1993 | 1993-1997 | 2006-2007 | 2006-2009 | 2010-2014 |
|---------------------------|---|---|--|--|--|---|
| <i>Evaluation Program</i> | 250Ft grid pit sampling to 120Ft 50 core drill, <100m depth | 526 LDD jumper holes on 50m grid, Max depth of 260 mbgl | Deep contact & geotech drilling, 66 core holes, Max depth of 600mbgl | Special project commissioned to update A/K1 geological model (no new drilling) | OREP Phase 1 Contact drilling, 99 holes (~38000m). Max depth of 900 mbgl | OREP Phase 2 Grade Sampling (215 core holes at 50*50m grid - 72000m) and Revenue sampling (20 LDD holes - 9100m) Max depth 475 mbgl |
| <i>Geology Model</i> | First A/K1 ore reserve (0-30 mbgl) Dobbs (1978) | Shaw (1991) | 1 st Digital detailed 3-D model (Field 1997) | 2 nd 3-D Model (Maccelari & Farrow 2007) | 3 rd (Letsatle 2009 & Tait 2010) | 4 th & 5 th (Sejoe 2012 & 2013) |

Recent Work

Between the year 1982 and 1997, another core drilling project was initiated targeting the resource at depth. It was after this project that the first digital geological model for A/K1 was developed by Field (1997), incorporating all historical data and information from resource evaluations, geotechnical drilling and mapping. Field (1997) proposed an update of classification scheme during this work which modified the existing schemes used during the course of evaluation and mining of the A/K1. Field (1997) was able to produce an extremely detailed lithofacies analysis of the various rock-types present in A/K1, subdividing lithofacies on the basis of internal structure, composition (mineralogy) and texture. Much of this work became instrumental in devising the kimberlite nomenclature scheme of

Field and Scott-Smith (1999), highlighting the relevance and quality of this work. This model is currently considered comprehensive and accepted as the basis for the A/K1 conceptual model.

More additional drill core and large diameter sampling was later completed between 2006 and 2014 (e.g. OREP1 and 2), and following this work, a series of updated three dimensional geological models were produced (see Table 1). Detailed geological description of the model based on massive semi-quantitative data generated from (e.g. geochemistry-bulk rock XRF, spinel mineral chemistry, micro-diamonds, internal lithic content, lithic size, mantle xenocrysts and ore dressing studies) to augment physical observations was documented. Comments on the emplacement mechanism were also updated in light of recent advancements in kimberlite volcanology. In the A/K1 North Pipe, two new lithofacies (MVK2 and NPK_GG) were added into the internal geology of the pipe. In the A/K1 South Pipe, a new pyroclastic kimberlite (SPK) was added.

It was during the OREP sampling program that extensive geochemical and spinels groundmass analysis (Stiefenhofer 2011 and Field 2015) were conducted for the major rock types in the A/K1. The geochemical analysis completed by Stiefenhofer (2009) concluded that the North and South Pipe major units geochemical signatures were distinct, potentially suggesting different magma sources for the two pipes. This conclusion was tested in Stiefenhofer (2011), and later updated by Field (2015) through spinel groundmass sampling analysis (e.g. $Fe^{2+}/(Fe^{2+}+Mg)$, $Cr/(Cr+Al)$, $Ti/(Ti+Cr+Al)$ and $Fe^{3+}/(Fe^{3+}+Cr+Al)$) where it was further concluded that the South Pipe have near identical compositions and differs from the North Pipe lithologies. The spinel data for North Pipe, although overlapping across the three main geological lithologies, are statistically different suggesting different magma source. Concurrent with analysis of the geochemistry, continuous country-rock xenoliths dilution (+5mm), type and size were analysed and subsequently a 3-D dilution model generated from the data. This data was crucial in identification of individual units and gradational contacts across geological units (Figure 1).

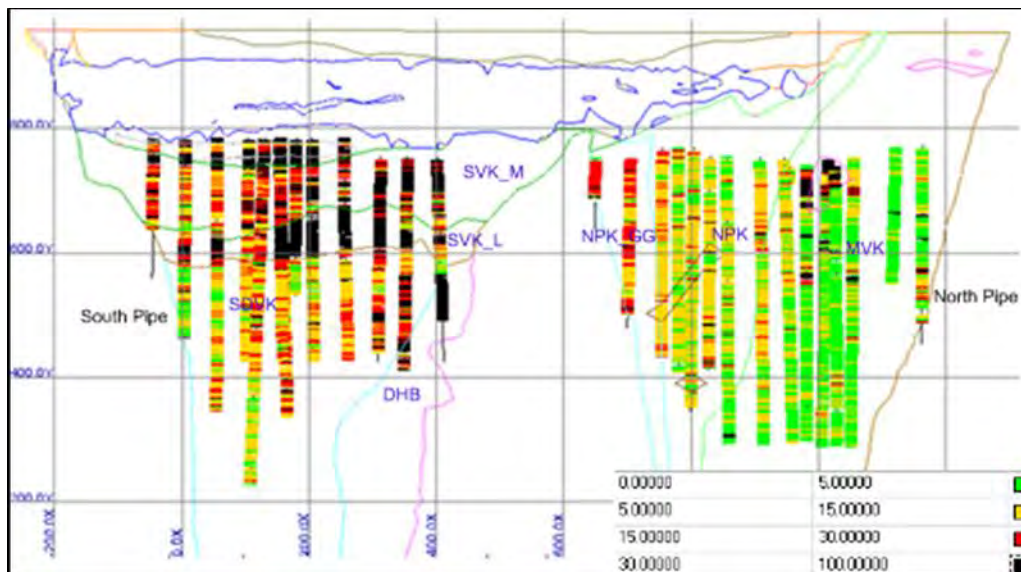


Figure 1: A section showing the crustal dilution distribution across the A/K1 Pipe.

Apart from the above internal studies, De Beers collaborated with external institutions to study and understand the geology of the A/K1. In 2009, Gernon et al. (2009a) applied field mapping data to reconstruct the internal stratigraphy of the A/K1 crater. Additional work by Gernon et al. (2009b) summarized the occurrence of a pyroclastic flow deposit in the A/K1 South Pipe which was suggested to be an infill deposits from another nearby kimberlite eruption. Fontana et al. (2008) collected numerous lithic clasts from within the A/K1 deposits to assess the variations in emplacement temperature of various internal units, by measuring the thermo-remnant magnetism within clasts. This study has demonstrated the vast difference in emplacement temperatures within deposits of A/K1.

Conclusion

An understanding of the geology of the A/K1 kimberlite has improved significantly since the first model was produced, particularly at depth, where additional drill holes have permitted a far better constraint on the stratigraphy of the deposits. The application of continuous downhole dilution effectively distinguished the complex geology of the pipe and has formed the basis for the current model of Sejoe (2013).

References

- Dobbs, P.N., 1980. The relationship between diamond grade and sedimentary facies at Orapa. Internal De Beers (Botswana) Mining Company Report
- Field, M., 1997. A geological model of 2125/AK1. Internal Debswana Company Report
- Field, M., Scott Smith, B.H., 1999. Textural and genetic classification schemes for kimberlites: a new perspective. 7th International Kimberlite Conference, Cape Town, South Africa, Extended Abstracts, pp 214-216
- Field, M., 2015. Groundmass spinel- Orapa North Pipe constrains on geological model OREPII – Botswana
- Fontana G, Mac Niocaill C, Brown RJ, Sparks RSJ, Field M., 2011. Emplacement temperatures of pyroclastic and volcanoclastic deposits in kimberlite pipes in southern Africa. *Bull Volcanol* 73:1063–1083
- Gernon, T.M., Field, M. Sparks, R.S.J. 2009a. Depositional processes in a kimberlite crater: The Upper Cretaceous Orapa South Pipe (Botswana)
- Gernon, T.M., Fontana, G., Field, M., Sparks, R.S.J., Brown, R.J., Mac Niocaill, C., 2009b. Pyroclastic flow deposits from a kimberlite eruption: The Orapa South Crater, Botswana
- Minter, W.E.L., 1978. The nature and economic significance of sediments in the Orapa Crater, DEBOT Report, Record Number: 5124
- Rayner, R.J., Mckay, I. J., 1987. The treasure chest of the Orapa Diamond Mine
- Sejoe, T., 2014. 3-Dimensional Geological Model of the A/K1 Kimberlite Resource. Orapa: Debswana Orapa and Letlhakane Mines.
- Stiefenhofer, J., 2009. Analysis of the geochemical, crustal dilution and clast size data from the Orapa Resource Extension Project (OREP), Botswana. Internal DBGS_MRM report prepared for Debswana
- Stiefenhofer, J., 2011. Analysis of the spinel groundmass data from the Orapa Resource Extension Project (OREP), Botswana-implication for the South Lobe Geological model update



Multiphase solid inclusions in UHP eclogite from the Dabie orogen: constraints on anatectic melts during continental collision

Xiao-Ying Gao

CAS Key Laboratory of Crust-Mantle Materials and Environments, School of Earth and Space Science, University of Science and Technology of China, Hefei, China, gaoying@ustc.edu.cn

Introduction

By definition, MS inclusions are a kind of mineral inclusions that consist of more than one solid mineral phases, with or without a vapor or fluid phase. They generally occur at a microscale and thus are observable under a microscope. Philippot and Selverstone (1991) reported for the first time the occurrence of MS inclusions in pyrope from coesite-bearing whiteschist at Dora-Maira in Western Alps. Subsequently, many kinds of MS inclusions have been reported in high-pressure (HP) to UHP metamorphic rocks worldwide. The study of MS inclusions provide important records of crustal anatexis and melt evolution in collisional orogens. Furthermore, more studies have been carried out for MS inclusions in migmatites and granulites (e.g., Cesare et al., 2011; Bartoli et al., 2013), the products of crustal anatexis at medium to high pressures.

The microstructure and chemical composition of MS inclusions

The MS inclusions may be small droplets of anatectic melts trapped in pritectic minerals, which were then crystallized to polycrystalline aggregates. Usually, the average size of MS inclusion is <25 μm , but exceptionally large inclusions may reach up to ~400 μm in peritectic minerals (such as garnet, omphacite, kyanite, zircon). Most of inclusion exhibit polygonal to negative crystal shapes, depending on the crystallographic control of the host mineral (Fig. 1). The abundance of negative crystal shapes and the occurrence of "necking-down" phenomena (Acosta-Vigil et al., 2007) indicates that solution/precipitation processes were efficient in modifying the shape of inclusion in order to diminish the surface free energy (Roedder, 1984). Different phases in MS inclusions mostly occur in different forms. For micro-inclusions with palisade texture, K-feldspar tends to be concentrated within the palisade or at the contact between the palisade and the core (Fig. 1a). Light grey large crystals occur as interstitials between K-feldspar (dark grey) grains, frequently resembling that of a holly leaf. In the edge of some inclusions, they exhibit the wedge-shaped off-shoot structure (Fig. 1), suggesting reequilibration between the inclusion and its host mineral. They typically contain a great and variable number of solids and lack a visible fluid phase (i.e. H_2O , N_2 , CO_2). The former presence of a fluid phase may be assumed, because of the regular presence of one or more deformed cavities (voids) within inclusions.

The major and trace element compositions of MS inclusions can provide important clues to their origin (e.g., Gao et al., 2012, 2013; Korsakov and Hermann, 2006; Zeng et al., 2009). However, the MS inclusions commonly exhibit varying lithochemical compositions from felsic to mafic, but primarily felsic. Generally, silicate MS inclusions are the most common ones in UHP metamorphic rocks. Felsic MS inclusions are primarily composed of quartz, K-feldspar and/or plagioclase. Generally, these felsic MS inclusions found in UHP eclogites from the Dabie-Sulu orogenic belt exhibit highly heterogeneous major element compositions (Fig. 2). These MS inclusions can be categorized into three types in terms of their mineral paragenesis: (1) feldspar (K-feldspar or albite) + quartz; (2) feldspar + quartz \pm barite; (3) calcite + feldspar + quartz.

Zeng et al. (2009) observed MS inclusions of K-feldspar + albite + quartz + epidote with textures similar to the other K-feldspar + quartz inclusions in omphacite grains of eclogite from the Sulu orogen. Gao et al. (2012, 2013) observed various types of K-bearing MS inclusions in garnet of the UHP eclogite in the Dabie orogen, which are composed of not only felsic minerals such as quartz, K-feldspar, albite and plagioclase, but also minor amounts of mafic minerals (epidote) and sulfate minerals (barite). Chen et al. (2014) also found similar MS inclusions in both garnet and omphacite for zoisite-bearing eclogite from the UHP metamorphic zone in the Sulu orogen. However, these types of MS inclusions found by Chen et al. (2014) are primarily composed of Na-bearing plagioclase.

In general, the MS inclusions found in UHP eclogites from the Dabie-Sulu orogenic belt exhibit very heterogeneous bulk compositions (Zeng et al., 2009; Gao et al., 2009; Chen et al., 2014). The bulk composition of major elements in MS inclusions was estimated by high resolution BSE images, on the assumption that the mineral modal contents estimated from BSE for the MS inclusions exposed on host surface can represent the bulk MS inclusions. Although this assumption can potentially introduce further uncertainty for estimate of the bulk composition of MS inclusions (Cesare et al., 2011), it may only account for the large scatter but do not change the general feature of the data. It is illustrated in the Qz-An-Ab normative diagram (Fig. 2). Obviously, the Qz + Pl + Kfs inclusions show a wide range of SiO₂ and Al₂O₃ values, whereas the Na-bearing inclusions of Qz + Pl generally exhibits lower SiO₂ values and higher Al₂O₃ values. The Kfs + Qz inclusions are essentially composed of SiO₂ (63.8-91.9 wt%), Al₂O₃ values (3.34-19.0 wt%) and K₂O (2.1-15.1 wt%). The variable concentrations of SiO₂, Al₂O₃, K₂O and Na₂O reflect variable amounts of the major phases such as plagioclase, K-feldspar and quartz within the different MS inclusions in the host minerals. The Kfs-bearing inclusions have much lower Ca and Al contents, and remarkably higher K₂O and SiO₂ contents (some larger than 80 wt%) than the quenched melts in the experimental studies of natural eclogites and the crystallized melt inclusions hosted in peritectic garnet of migmatites and granulite that are formed at different P-T-X(H₂O) conditions and by mineralogical reaction of dehydration melting (Cesare et al., 2011; Bartoli et al., 2013).

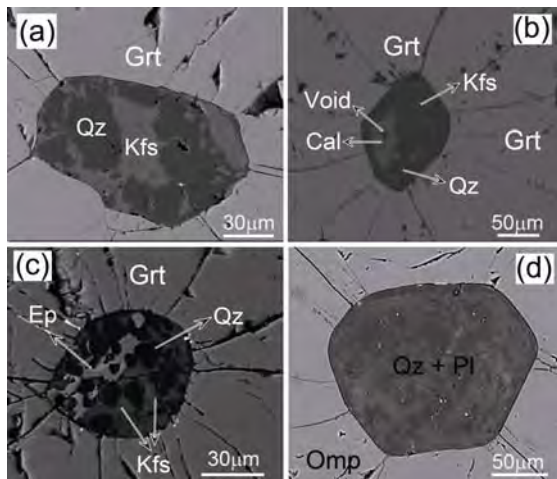


Figure 1: BSE images of MS inclusions in garnet and omphacite from UHP metamorphic rocks.

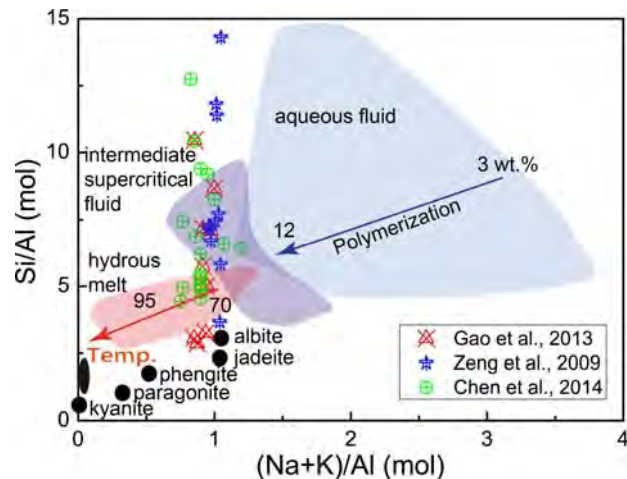


Figure 2: The An-Ab-Or triangular diagram for the major element compositions of bulk MS inclusions.

It is important to determine the trace element composition of silicate MS inclusions despite possible limitations in analytical techniques. In order to estimate the trace element composition of silicate MS inclusions in detail, two different approaches of laser sampling were utilized by Gao et al. (2013). As a consequence, the two approaches yield relatively consistent results of major and trace element compositions. The trace elements analysis of Kfs-bearing MS inclusions by Gao et al. (2014) exhibit enrichment in LILE, Sr and Pb but depletion in HFSE in the primitive mantle-normalized spidergram. However, Chen et al. (2014) found that trace elements in Na-bearing MS inclusions generally show very low concentrations except LILE such as Sr, Ba and Rb. These features suggest different origins for the different types of MS inclusions. Many MS inclusions show variably high K, Rb and Sr abundances, suggesting that the breakdown of hydrous minerals as phengite or paragonite is a basic cause for partial melting of UHP eclogites. These MS inclusions also exhibit consistently low HFSE and Y contents, suggesting that partial melting of the UHP eclogite takes place in the stability fields of rutile and garnet. Consequently, the trace element composition of MS inclusions provides a proxy for that of hydrous silicate melts derived from dehydration melting of the UHP eclogite during the continental collision. An integrated study of petrology, mineralogy and geochemistry indicates that MS inclusions represent the anatexic products of UHP eclogites during continental collision, with possible immiscibility between aqueous solutions and hydrous melts (Zeng et al., 2009a; Gao et al., 2012, 2013; Chen et al., 2014). The K-bearing MS inclusions are generally interpreted as crystallizing from felsic melts due to the dehydration melting of K-bearing hydrous

minerals like phengite in the eclogites (e.g., Gao et al., 2012, 2013). On the other hand, some MS inclusions show remarkably higher Na contents, and they would be primarily derived from dehydration melting of paragonite (Chen et al., 2014).

Beside silicate MS inclusions, carbonate MS inclusions were also found not only in UHP marbles (Korsakov and Hermann, 2006) and eclogites (Gao et al., 2014) but also in low-to-medium pressure migmatites (Ferrero et al., 2016). Gao et al. (2014) found calcite and polyphase carbonate-silicate inclusions in garnet from UHP eclogite from the Daibe orogen, where MS inclusions are primarily composed of variable proportions of carbonate and silicate minerals such as calcite, quartz, K-feldspar and plagioclase with occasional occurrences of magnetite, zircon and barite. Two groups of MS inclusions are categorized according to the proportions of carbonate and silicate phases. Group I is carbonate-dominated with variable proportions of silicate minerals, and Group II is silicate-dominated with small proportions of carbonates. Group I inclusions exhibit remarkably lower REE contents than Group II inclusions, with significant LREE enrichment and large fractionation between LREE and HREE in the chondrite-normalized REE diagram. In contrast, Group II inclusions show rather flat REE patterns with insignificant fractionation between LREE and HREE. In the primitive mantle-normalized spidergram, Group I inclusions exhibit positive anomalies of Zr and Hf, whereas Group II inclusions show negative anomalies of Zr and Hf. Nevertheless, both groups exhibit positive anomalies in Ba, U, Pb and Sr, but negative anomalies in Nb and Ta, resembling the composition of common continental crust. Group I inclusions have higher Ba and U contents than Group II inclusions. Combined with petrological observations, the two groups of MS inclusions are interpreted as having crystallized from composite silicate and carbonate melts during continental collision. The differences in trace element composition between the two groups are primarily attributed to the proportions of carbonate and silicate phases in the MS inclusions. The occurrence of carbonate and silicate MS inclusions in the UHP domain garnet and clinopyroxene indicates the presence of both carbonate and silicate melts during mineral growth (Gao et al., 2014; Korsakov and Hermann, 2006). The MS inclusions would have crystallized from such silicate-carbonate melts at mantle depths. The similar immiscibility between carbonatitic and granitic melts is preserved as polycrystalline inclusions with a characteristic enrichment in Ba, Sr and LREE in the lower crust (Ferrero et al., 2016). The identification and characterization of these MS inclusions in peritectic minerals provides new insights into the anatexis conditions and time of UHP metamorphic rocks, which has great bearing on the chemical geodynamics of subduction zones.

References

- Cesare, B., Acosta-Vigil, A., Ferrero, S., Bartoli, O., 2011. Melt inclusions in migmatites and granulites. *Journal of the Virtual Explorer* 38, paper 2; doi: 10.3809/jvirtex.2011.00268.
- Chen, Y.-X., Zheng, Y.-F., Gao, X.Y., Hu, Z.C., 2014. Multiphase solid inclusions in zoisite-bearing eclogite: evidence for partial melting of ultrahigh-pressure metamorphic rocks during continental collision. *Lithos* 200-201, 1-21.
- Ferrero, S., Wunder, B., Ziemann, M.A., Wälle, M., O'Brien, P.J., 2016. Carbonatitic and granitic melts produced under conditions of primary immiscibility during anatexis in the lower crust. *Earth and Planetary Science Letters* 454, 121-131.
- Gao, X.-Y., Zheng, Y.-F., Chen, Y.-X., 2012. Dehydration melting of ultrahigh-pressure eclogite in the Dabie orogen: evidence from multiphase solid inclusions in garnet. *Journal of Metamorphic Geology* 30, 193-212.
- Gao, X.-Y., Zheng, Y.-F., Chen, Y.-X., Hu, Z.C., 2013. Trace element composition of continentally subducted slab-derived melt: insight from multiphase solid inclusions in ultrahigh-pressure eclogite in the Dabie orogen. *Journal of Metamorphic Geology* 31, 453-468.
- Gao, X.Y., Zheng, Y.F., Chen, Y.X., Hu, Z.C., 2014. Composite carbonate and silicate multiphase solid inclusions in metamorphic garnet from ultrahigh-P eclogite in the Dabie orogen. *Journal of Metamorphic Geology* 32, 961-980.
- Korsakov, A.V., Hermann, J., 2006. Silicate and carbonate melt inclusions associated with diamonds in deeply subducted carbonate rocks. *Earth and Planetary Science Letters* 241, 104-118.
- Zeng, L.S., Liang, F.H., Asimow, P., Chen, F.Y., Chen, J., 2009. Partial melting of deeply subducted continental crust and the formation of quartzofeldspathic polyphase inclusions in the Sulu UHP eclogites. *Chinese Science Bulletin* 54, 2580-2594.



DIAMOND-BEARING IN THE NORTH OF EUROPEAN RUSSIA AND PROSPECTS OF NEW DIAMOND DEPOSITS DISCOVERY

V.S. Shchukin*, V.N. Nesis**, S.I.Trushin**, S.L. Roslyakov**, K.V. Efimov**, A.I. Osetskiy**, E.V. Shchukina***.

*Proex Service Ltd, Arkhangelsk, Russia, vlad.shchukin@mail.ru

**Polymetal International Plc, St. Petersburg, Russia, , VNesis@polymetal.ru, trushin@polymetal.ru, roslyakov@polymetal.ru, efimov@polymetal.ru, osetskiy@polymetal.ru.

***V. S. Sobolev Institute of Geology and Mineralogy SB RAS, Novosibirsk, Russia, helenashchukina@gmail.com

Introduction

According to archival data the first diamond crystal within Russia territories was found in 1730 by a twelve-year old boy on the bank of the North Dvina river near Orletsy fortress in Arkhangelsk Region. It is most likely that the diamond was rather large as it was cut and sent to tsar court. Mikhail Lomonosov knew about this finding as he wrote in his famous treatise “About Earth Layers” the following: “...Orletsy mountains are able to bear diamonds” [5]. Almost 100 years later on July 4th 1829 the second diamond crystal was found in the Urals gold placer deposits. While the diamond finding on the bank of the North Dvina was very soon forgotten and Lomonosov’s ideas were not heard by the scientific world diamond findings in gold placers of Ural became regular which finally led to discovery of numerous placer diamond deposits. The first kimberlite rocks in the North of European Russia were found on the river Mela in Wintercoast diamondiferous area of Arkhangelsk Region in 1975. Furthermore, in 1980 the first diamondiferous kimberlite pipe Pomorskaya was discovered. These discoveries gave a start to the present stage of diamond exploration in the European North of Russia.

Prospecting work in Ural in the second half of the 20th century led to the discovery of a few dozen of placer deposits of diamonds. Round shape (Ural or Brazilian diamond type) and high quality of crystals are the main distinguishing features of Ural diamonds. Success in prospecting work in Ural stimulated diamond search in Timan being for a long time considered as the Ural’s branch. The first diamonds of the Northern Timan were found in alluvial sediments by geologist M. Apenko in 1953. By now diamonds and mineral indicators of kimberlites are identified in the Northern Timan in sediments of early Silurian, middle Devonian and modern alluvium. Fine crystals of diamond are found in dikes of lamprophyres[6]. In middle Timan three non-diamondiferous pipes were found while the diamonds were discovered in middle-late Devonian sediments and modern alluvium. Polymineral placer in Ichet-Yu (diamonds, gold, platinum, tantalum, niobates) in Devonian sediments was explored as well as single crystals of diamonds that were found in South Timan as well.

In 1975 kimberlite sills were detected on the river Mela on Belomoro-Kuloyskoe plateau (Wintercoast diamondiferous area) which led to prospecting work in this area followed by discovery of the first diamondiferous kimberlite pipe in 1980. Currently more than 70 pipes of different composition are discovered in Belomoro-Kuloyskoe plateau, 25 pipes among them are more or less diamondiferous and 6 pipes have industrial significance. Five pipes of Zolotitsa group form Lomonosov diamond deposit and one pipe makes up Grib diamond deposit. Both of these deposits are involved into the industrial development.

Significant increase of diamond prospecting in the North of the East-European platform caused the discovery of Ermakovsky field of low-grade diamondiferous kimberlites at the Kola Peninsula, kimberlites at Kimozero and numerous low-grade diamondiferous bodies of lamproites in Karelia [7].

Four fields of weakly diamondiferous kimberlites and lamproites are found in neighboring Finland[1,2,3,4] Almost all territory of Northern European part of Russia from Finland boundary to Ural has findings of single crystals of diamonds in intermediate collectors and modern alluvium. (Figure 2). Analysis of diamond findings allocation on the area and section sedimentary cover of the platform indicates to multiplicity and wide age range of their original sources and points to high probability of new findings of diamondiferous areas and diamond deposits in the North of Russia.

It is well known that tectonic structure of a territory is crucial for possibilities of diamondiferous magmatism occurrence as well as for allocation of kimberlite fields and separate kimberlite pipes in the area. Therefore the more specific our knowledge about tectonic structure of a territory is especially its crystalline basement the more confident is our prognosis. Peculiar properties of crystalline basement of ancient platforms are very well reflected in magnetic fields, thus interpretation of magnetics susceptibility is very important for understanding of platform foundation structure.

650 maps sheets of 1:200 000 scale of aeromagnetic survey done in various years had been digitized, all sheets united in one project, mapped anomalous magnetic field (ΔT) and visualized the data. On the map obtained all main geological structures of crystalline basement including ancient cores of foundation – cratons and their moving belts are very well displayed. Besides, series of linear combined structures of North-Eastern, sub- meridional and sub-latitudinal spreadings are allocated. Linear structures of sub- meridional spreading controlling the location of diamondiferous magmatism of middle-late Devonian age are of the particular interest. While processing of large-scale survey data it is evident that such structures penetrate nearly all Northern part of the Russian plate (Figure 1).

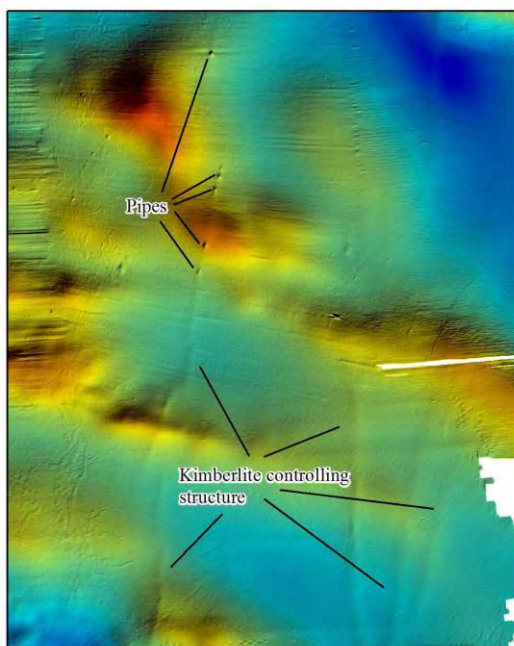


Figure 1. Example of kimberlite controlling structure based on large-scale airborne magnetic survey data.

Tectonic structure scheme of crystalline basement platform of the Northern European part of Russia was made up on basis of map of anomalous magnetic field (ΔT) with the usage of gravimeter and seismology data. Areas of kimberlite and associated magmatism, findings of diamonds and aggregations of mineral indicators of kimberlite in most cases refer to ancient cratons and median masses (Figure 2). Zones of dissection of ancient cratons and median masses by linear structures are of the greatest interest for further exploration of new diamondiferous areas and diamond deposits.

Thus, diamond exploration should be executed with careful consideration of wide age range of diamondiferous magmatism and must be focused within the bounds of ancient cratons and median masses. Findings of new diamondiferous magmatites aged from early Proterozoic to Mesozoic are possible within Murmansk and Karelian cratons. Exploration within Shenkursk, Sysolsky and Volga-Ural cratons should be focused on magmatites of Permian-Triassic

age and younger. Murmansk and Karelian cratons are the most promising areas for discoveries of new diamond deposits of kimberlite and lamproite type at the moment. Moreover opportunities of Wintercoast diamondiferous area are not exhausted at all and our discovery of two new kimberlite pipes in 2016 can justify our concept. Eastern part of Arkhangelsk median mass where the diamond findings are allocated, fragments of kimberlite rocks and numerous mineral indicators of kimberlites have not been examined yet as well as original sources of Ural and Timan placer deposits. Thereby,

all above mentioned facts demonstrate great opportunities to discover new diamondiferous areas and diamond deposits in the European North of Russia.

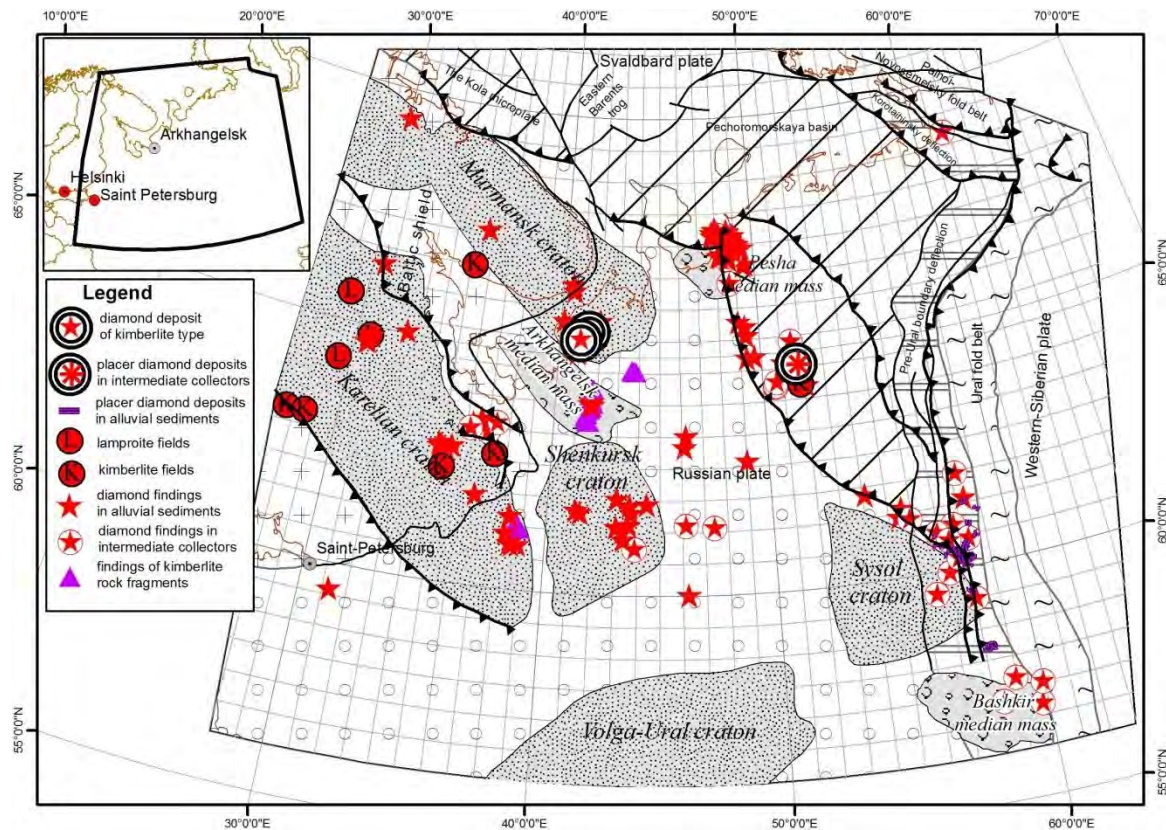


Figure 2. Tectonic scheme and diamond-bearing of the North European part of the East-European platform

References

- 1.H.E. O'Brien and M.Tuni. Mineralogy and geochemistry of kimberlites and related rocks from Finland. Proceedings of the VII International Kimberlite Conference . Volume 2. Cape Town. 1999. p.625-636
- 2.Hugh O'Brien, Marja Lehtonen, Roy Spencer and Andrew Birnie. " Lithospheric mantle in eastern Finland: a 250 km 3D transect" 8th IKC, 2003.
- 3.O'Brien H., Bradley J. " New kimberlite discoveries in Kuusamo, northern Finland. 9th IKC. 2008. Extended Abstract A-0346.
- 4.Marja Lehtonen, Hugh O'Brien, Petri Peltonen, Bo Johanson and Lassi Parranen "Layered mantle at the EDGE of the Karelian craton: P-T of mantle xenocrysts and xenoliths from eastern Finland kimberlites" 8th International Kimberlite Conference Long Abstract, 2003.
- 5.Lomonosov M. V. "About Earth Layers", St. Petersburg, 1763
- 6.Smironov M. U. «Diamondiferous alkaline lamprophyres of Northern Timan». Documents of all-Russian meeting «Diamonds. Diamond-bearing of Timan-Ural region», Syktyvkar, 2001, pages 50-54.
- 7.Vladimir V. Ushkov, Victor N. Ustinov, Chris B. Smith, Galina P. Bulanova, Ludmila I. Lukyanova, Daphne de Vries, D.Graham Pearson. "Kimozero, Karelia; a diamondiferous Paleoproterozoic metamorphosed volcanoclastic kimberlite". 9th International Kimberlite Conference Extended Abstract No 9IKC- A-00199, 2008.

THE RELATIONSHIP AMONG VARIOUS MORPHOLOGICAL TYPES OF DIAMONDS WITHIN DIAMOND DEPOSITS IN RUSSIA: GENESIS, GROWTH, DISSOLUTION AND REAL DIAMOND GRADE

V.K. Garanin¹, A.V. Bovkun¹, K.V. Garanin², G.Yu. Kriulina¹, I.V. Serov²

¹Geological Faculty M.V.Lomonosov Moscow State University, Moscow, Russia, vgaranin@mail.ru, bovkun2004@mail.ru, galinadiamond@gmail.com

²PJSC ALROSA, Mirnyi, Sakha (Yakutia) Republic, Russia, GaraninKV@alrosa.ru, SerovIV@alrosa.ru

Introduction

Russia is the biggest diamond producer all over the World. There are more than 1500 kimberlites and related-rocks occurrences, 15 primary diamonds industrial deposits among them: Internatsionalnaya, Mir, Udachnaya, Aikhal, Nurbinskaya pipes, M.V. Lomonosov deposit and others. All of these deposits differ in diamond grade and quality.

The diamond content in industrial deposits is varying: between 0.25 (Zarnitsa pipe) and 8.71 (Internatsiyonalnaya pipe) ct/t in Yakutia, between 0.5 (M.V. Lomonosova pipe) and 1.72 (Karpinskogo-1 pipe). There is a largest diamond deposit – Udachnaya pipe with total weight of diamonds – 212591 ct. There are also numerous of placer diamond deposits in Russia, include unique placers in the Northern (Ebelyakh, Molodo, Morgogor, Talaktakh and others) and Central (Vodorazdelnye galechniki, Irelyakh, Gornoe, Solur-Vostochnaya, Ruchei Piropovyi, Nurbinskaya and others). The price per carat is also different for deposits: from 45 (Aikhal pipe) to >200 (Komsomolskaya pipe) \$/ct, with forecast (2016-2030) average 135\$/t (Micon, 2016). Fantasy colored high-value diamonds (reddish, green, yellow and others) are also presented in Russian diamond deposits. Every years several large crystals (>50 ct/stone) recovered from kimberlitic pipes and placers in Russia including the biggest diamond 888.06 ct from Yubileynaya pipe (in 2013) (Fig. 1).



Figure 1: The largest Russian diamond (888.06 ct) recovered from Yubileynaya pipe in 2013. (K. Garanin photo)

Generally diamonds in kimberlites located as xenocrysts with size from microns to several centimeters, and also rarely in mantle xenoliths (peridotites and eclogites) within kimberlites.

Additionally diamonds of each deposit are characterized by own gradation, morphology, color characteristics, physical features, etc. These characteristics correlate with mineralogical indicating features: content of main diamond indicator minerals (garnet, clinopyroxene, chromite and ilmenite), its proportion and presence among these minerals grains of diamond paragenesis association. Kimberlites of industrial deposits contain also significant assemble own kimberlitic indicator minerals: high-chromium and low-titanium spinellids, picroilmenites, and low content of perovskite and rutile.

Scope of study

Mineralogical data on diamonds, kimberlitic indicator minerals and own kimberlitic minerals for kimberlitic occurrences and 15 diamond deposits in Russia was combined in united database. The database provides opportunity to solve numerous scientific, exploration and technological problems. This database is a technique for identification potential and real diamond grade in kimberlites. The architecture of analytical system for diamond is presented in Fig. 2.

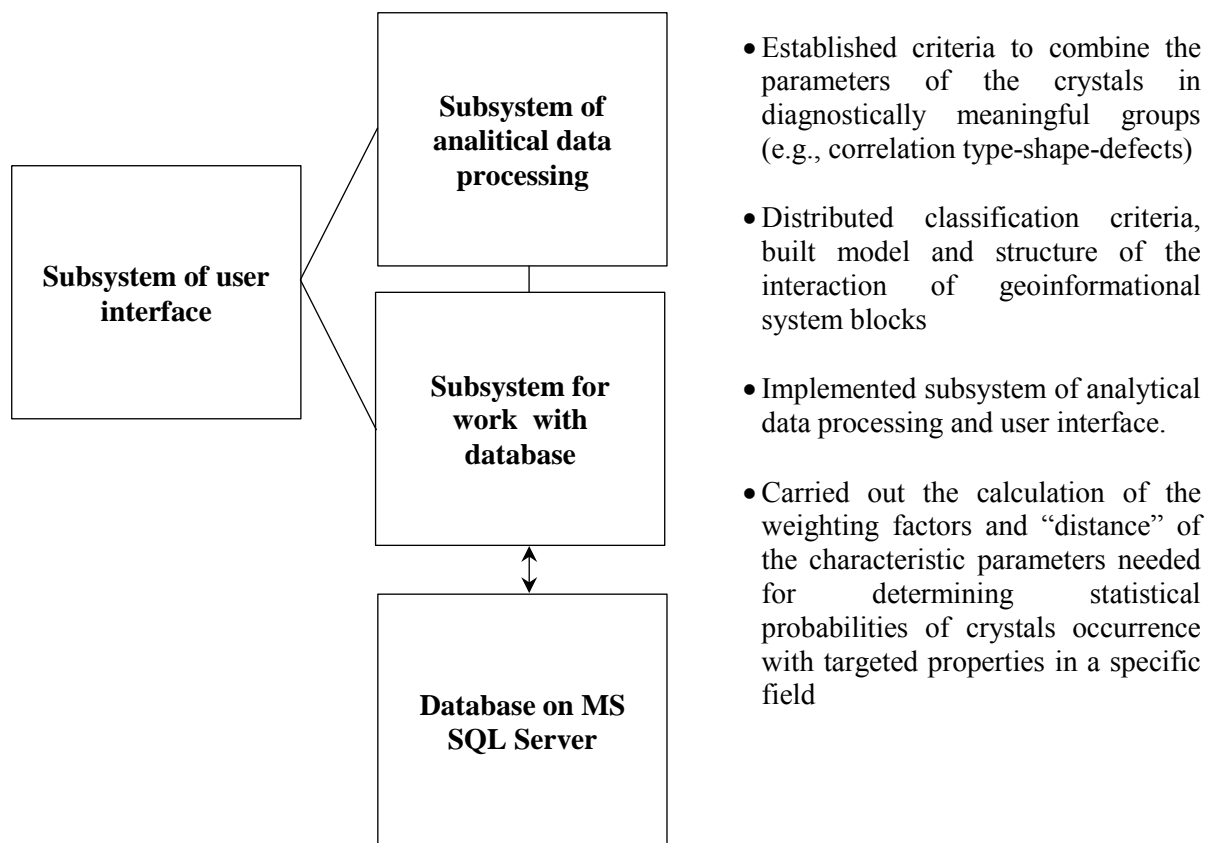


Figure 2: General scheme of analytical system architecture for diamond

Study results

Three petrochemical types of kimberlites were suggested and each of these types have been characterized by indicative parameters: TiO₂ and other rock-forming oxides content, LREE, HREE, CHUR, rock-forming minerals characteristics, groundmass mineralogy, diamond indicator minerals, source of titanium, mantle source (Table 1).

| Parameter | Low-titanium | Moderate-titanium | Highly-titanium |
|-------------------------------|--|--|--|
| TiO ₂ , wt. %, | <1 | 1 – 2.5 | >2.5 |
| LREE (La, Ce, Sm, Nd) | Moderate (fluid metasomatism) | Low | High, La/Yb ratio ~70-130 |
| HREE (Nb, Zr, Ta, Hf, Th,U) | Low | Moderate | High |
| CHUR ε _{Nd} | ~ -6 up to +2 | -0.4 +1.0 | +1.7, +1.2 (Kepinskoe Field) - +3,+4 (Olenekskaya Area) |
| Main rock-forming minerals | Olivine, calcite, phlogopite | Olivine, calcite, phlogopite | Olivine, calcite, phlogopite |
| Rock matrix | Cr-spinellid | Cr-spinellids+ilmenite, perovskite, rutile | Altered: Ti-chromite, Ti-magnetite, rutile, ilmenite |
| HFM/diamond assemble minerals | ↓Cr-spinel, Cr-pyrope-almandine, Cr-diopside, Mg-olivine | ↑Picroilmenite, pyrope-almandine, Cr-diopside, Mg-olivine | Picroilmenite, Cr-spinel, Cr-pyrope, Cr-diopside |
| HFM weight, kg/t | 0.1– 9.7 | 20–50 | <14 |
| Ti | Ti-garnet (0.4-1.5 wt. % TiO ₂) | FeTiO ₃ , CaTiO ₃ , TiO ₂ | FeTiO ₃ , CaTiO ₃ , TiO ₂ |
| Mantle | Enriched ancient mantle type I (EMI) | Close to BSE, depleted, metasomatized, Pb-enriched | Depleted |

Table 1: Petrochemical types of kimberlites in Russia

According to integrated data processing through database it was indicated – there are several populations (generations) of diamonds within every kimberlite body. Each deposit has own features of diamond crystallization in mantle, evolution of diamond matter in metasomatized mantle, complex processes of growth and dissolution of diamond in mantle and further environments within kimberlitic-generated and kimberlite-bearing melts. It was identified the conditions of diamond genesis, growth and dissolution are rather complex, sometimes with long variable crystallization processes in heterogeneous environments. All of these processes directly and indirectly have an impact on crystallization of mantle and kimberlitic minerals. For this reason, based on these minerals investigation, it is possible to detect signs of high or relatively low diamond content of diamonds in the deposit and its quality. It certainly gives every reason for effective production of diamonds with advanced planning at low cost mining.

Conclusion

The developed system is a set of database, original software, and technological schemes of processing newly received data on the diamond, diamond indicator minerals (DIM) and indicator minerals of kimberlites (IMK). That solves a lot of research and industrial problems associated with qualitative and quantitative evaluation of diamond deposit. In addition, collected data provide unique exploration tools for discovery new diamond deposits not only in Russia, but also in other regions of the World.

References

Micon Int Co Ltd (2016) Independent experts report on reserves and resources of ALROSA Group diamond deposits in Russia, 471 p. *In Russian*

FEATURES OF DIAMOND AND ITS INDICATOR MINERALS OF KIMBERLITES OF THE M.V. LOMONOSOV DEPOSIT, ARKHANGELSK REGION, RUSSIA

A.V. Bovkun¹, G.Yu. Kriulina¹, V.K. Garanin², V.V. Tretyachenko³

¹M.V. Lomonosov Moscow State University, Moscow, Russia, bovkun2004@mail.ru, galinadiamond@gmail.com

²A.E. Fersman Mineralogical Museum of RAS, Moscow, Russia, vgaranin@mail.ru

³PJSC ALROSA, Archangelsk, Russia, TretyachenkoVV@severalmaz.ru

Introduction

The M.V. Lomonosov diamond deposit, Arkhangelsk region, NW Russia consists of six kimberlite pipes, forming 9.5 km length cluster within the Zolotitskoe Kimberlitic Field. These pipes are composed of the same type petrography varieties of kimberlitic rocks, but based on a number of geological and diamond features this cluster divided into Northern (M.V. Lomonosova, Pomorskaya, Pionerskaya and Karpinskogo-2 pipes) and Southern (Karpinskogo-1, Archangelskaya) Groups (Fig. 1a). The diamond grade in main types of ore – tuffisitic (autolithic) kimberlites of the Southern Group kimberlite pipes is higher (1.2-1.5 ct/t) than in the Northern Group (0.4-0.7 ct/t). Pomorskaya pipe reserves with low diamond grade ores (<0.1 ct/t) estimated as resources presently, because the mining of this pipe is unecomical presently.

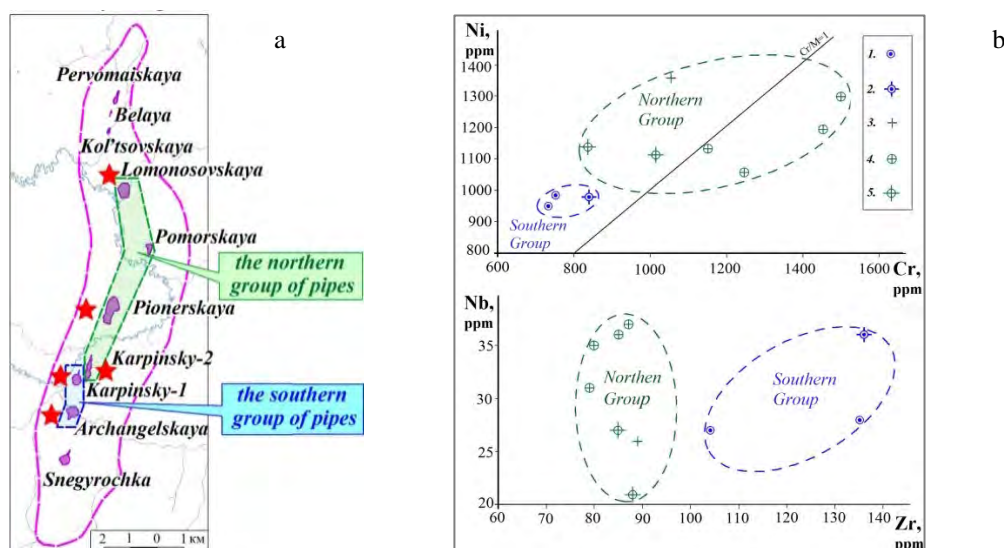


Figure 1: Zolotitskoe Field and M.V. Lomonosov diamond Deposit scheme (a); Cr–Ni и Zr–Nb contents for tuffisitic (autolithic) kimberlites of the Southern (1 - Archangelskaya, 2 - Karpinskogo-1) and Northern (3 - Karpinskogo-2, 4 - Pionerskaya, 5 - Lomonosova) Groups' pipes of the M.V. Lomonosov deposit (Parsadanyan et al., 1996).

The results of present study revealed differences in the chemical composition of diamond indicator minerals (DIMs), morphology, optical properties, internal structure, defect-impurity composition and diamond quality of the Northern and Southern Groups' pipes. The relationship between the diamond characteristics and matter features, diamond grade of main types of diamond-bearing kimberlitic ores was indicated.

Analytical Results

Autolithic kimberlites (AK) of the Southern Group pipes with higher diamond grade are characterized by lower chromium and nickel contents (Fig. 1b) and higher zirconium, strontium, thorium, hafnium contents in comparison with similar rocks of the Northern Group pipes (Parsadanyan et al., 1996).

There are sharply low DIMs (pyrope, chromite and clinopyroxene) content in the Northern Group pipes. In AK of the Southern Group pipes the total number of DIMs is 0.097-0.133 kg/t, and in AK of the Northern Group pipes is 0.035-0.079 kg/t.

DIMs (pyrope, chromite and clinopyroxene) of Northern Group pipes presented by higher chromium varieties corresponding to high-pressure depth subfacies compare to kimberlites of the Southern Group pipes. Pyropes (>5 wt.% Cr₂O₃) are mostly identified in the Pionerskaya (86%) and Karpinskogo-2 (74%) pipes (Northern Group pipes), with lower presence in the Archangelskaya (30%) and Karpinskogo-1 (16%) pipes (Southern Group). Chromite content (60 wt.% Cr₂O₃) in the Pionerskaya (40%) and Karpinskogo-2 (34%) pipes is sharply higher than in Archangelskaya (<11%) and Karpinskogo-1 (17%) pipes, where chromite with 55-60 wt.% Cr₂O₃ is mostly presented (30-33% of total).

However, there is higher content of Cr-spinels and pyropes with higher Ti-content in Northern Group kimberlites in compare with the Southern Group. Chromites with TiO₂> 3 wt.% distributed in the Pionerskaya (14%), Karpinskogo-2 (9%), Pomorskaya (11%) pipes (Northern Group), with lower presence (~5%) in Southern Group pipes. The shares of pyrope with TiO₂>0,4 wt.% for Pionerskaya and Karpinskogo-2 pipes are 24% and 10,5% respectively, but only 4-5% for the Southern Group pipes.

A significant proportion of the pyropes from Northern Group kimberlites also have higher content of Zr (62% grains with Zr>30 ppm), Y and Ga (Sablukov et al., 2009). The collection obtained and published data indicates: the lower diamondiferous kimberlites of the Northern Group related with intensive exposure to the lithospheric mantle by melting metasomatic processes, which caused the destruction of a large part of diamonds in the process of dissolution and a significant increase of the dodecahedrons proportion, especially in large classes.

Despite the low diamond content in the Northern Group pipes, qualitative characteristics of diamond ores are significantly higher in many indicators than for Southern Group pipes. Ultrabasic paragenesis colorless diamonds with high degree of transparency and fiber growth mechanism are dominated in the Pionerskaya and Pomorskaya pipes. Dodecahedrons with high etching and corrosion degree are prevailing. Diamonds have a low content of hydrogen impurity with a large values range. The distribution maximum of CH-centers is identified at 0-5 cm⁻¹, and for the diamonds of the Southern Group pipes at 3-10 cm⁻¹ (Fig. 2b). The Northern Group pipes' diamonds characterized by high presence of nitrogen impurities concentrations (Fig. 2a), and structural centers associated with plastic deformation. Unlike the Southern Group pipes' diamonds, the structural nitrogen is considerably higher aggregated (two maximum allocation %N_B = 10-14 and %N_B = 40-55 according to IR-spectroscopy data; centers P2 and N2 are presented according to EPR), indicating more prolonged exposure in high temperature conditions contributing to oxidative dissolution. Generally, near gem diamonds prevalent (65-70%) in the Pionerskaya pipe. The quality of the Pomorskaya pipe diamonds is significantly lower because of widespread intergrowths and individuals with a low degree of safety, deep etched channels and numerous graphite inclusions.

According to received data, there is lower quality of diamonds in the Southern Group pipes, which is due to inherently defective structure of crystals. The dominant share (60%) of diamonds in the Archangelskaya and Karpinskogo-1 pipes is presented by industrial diamonds. The share of gem-quality diamonds is about 25%. There are mostly dodecahedral and tetrahedral diamonds with zonal-sectorial structure and high degree of internal tension with lots of cracks, graphite and fluid inclusions. The tetrahedral content in all size-classes is 14-27%, but only 5-13% in the Northern Group pipes. Upon that, diamonds of high-nitrogen groups (Fig. 2a) with low degree of defects aggregation are mostly presented there. It is evidence of lower temperatures at genesis of crystals majority and short time post-crystallization annealing. According to FTIR data a large proportion of the Archangelskaya and Karpinskogo-1 pipes diamonds belong to eclogitic paragenesis.

There is a sharp increase in the octahedrons concentration in a small size-class (-1+0.5 mm) identified: 20% for the Northern Group pipes, and 15-17% for the Southern Group pipes (Makhin et al., 1990).

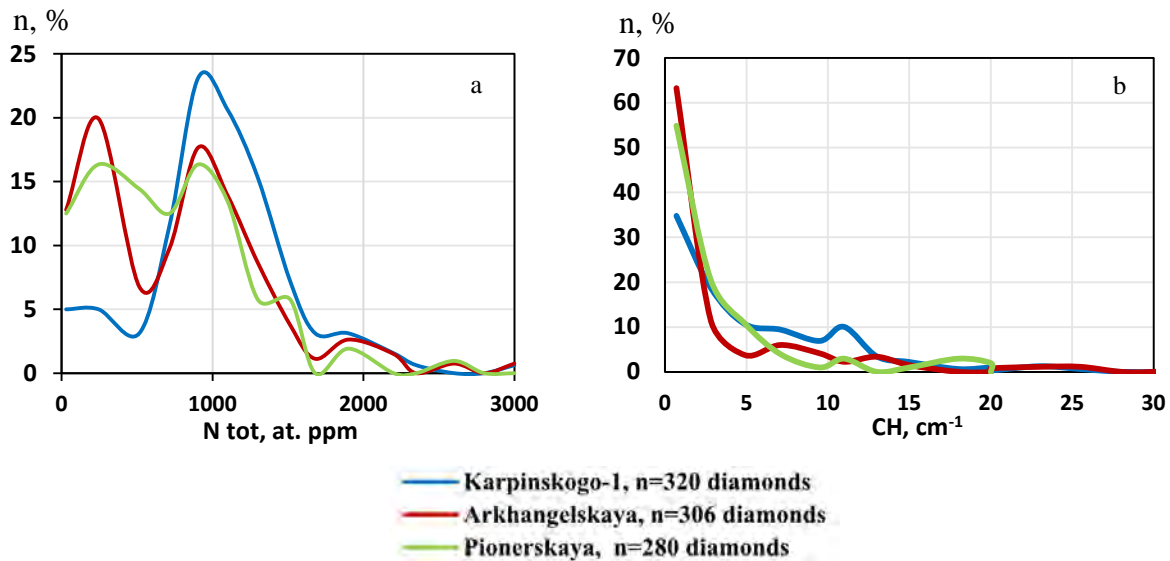


Figure 2: Distribution of diamonds with different total concentration of the defective-impurity centers of nitrogen (Ntot) (a), and with different ratio of the absorption of impurity hydrogen centers CH (3107 cm⁻¹) (b) in the South (Karpinskogo-1 and Arkhangelskaya) and Northern (Pionerskaya) Group pipes of the M.V. Lomonosov diamond deposit

Conclusion

Thus, a significantly higher degree of diamond grade in main types of ore – tuffisitic (autolithic) kimberlites of the Arkhangelskaya and Karpinskogo-1 pipe in connection with the kimberlitic rocks of the Karpinskogo-2 and Pionerskaya pipe is due to lower degree of impact processes of melt of mantle metasomatism, which mostly processed in relation to Northern Group kimberlites. In addition, there is significant higher proportion of eclogitic paragenesis diamonds in most productive Southern Group kimberlites. The common lower diamond quality in the Southern Group pipes is mainly due to more defective crystal structure, which is probably associated with deeper degree differentiation of the initial hypogene substance.

References

- Makhin AI, Bartoshinsky ZV, Bekesha SN, Vinnichenko TG, Voloshinovskiy AS, Vesilov VV (1990) Technical report: to study of main typomorphic features of diamonds from Zolotitskoe Field kimberlites for the purposes of classification, to develop and implement a methodology for integrated study of diamonds in terms of the expedition. Archangelsk. *In Russian*
- Parsadanyan KS, Kononova VA, Bogatikov OA (1996) Sources of the heterogeneous magmatism of the Arkhangelsk diamond-bearing province. *Petrology*, 4 (5): pp. 496-517. *In Russian*
- Sablukov SM, Sablukova LI, Griffin WL (2009) Distribution of rare elements in deep kimberlitic minerals as a feature of plume processes in the North part of the Russian Platform. In: Proc. IX Int. Conf. on Deep-seated magmatism, its sources and plumes, Miass, pp. 135-170. *In Russian*

Main mineralogical-petrological features of early-hercynian volcanic complexes of Archangelsk kimberlite-picrite region, NW Russia

Tretyachenko V.V.¹, Garanin K.V.¹, Garanin V.K.², Bovkun A.V.³

¹PJSC ALROSA, Russia, TretyachenkoVV@severalmaz.ru, GaraninKV@alrosa.ru

²A.E. Fersman Mineralogical Museum of RAS, Moscow, Russia, VGaranin@mail.ru

³M.V.Lomonosov Moscow State University, Moscow, Russia, Bovkun2004@mail.ru

Archangelsk kimberlite-picrite Region is world-class source of diamonds, where two large diamond deposits in mining stage presently, with total reserves more than 300 mln carats. Besides that, there is more than a hundred occurrences of non-diamondiferous kimberlites, its convergent rocks and tholeiitic basalts (Fig.1) (Bogatikov et al., 1999; Garanin, 2006). Within this region based on main petrological characteristics, the largest regional formational taxons have been distinguished: (1) Zimniberezhny Mega-Complex of kimberlites-non-pyroxene alkaline picrites, (2) Nenokso-Chidvinsky Mega-Complex of feldspathic picrites-olivine melilitites (Fig. 2) and (3) Soyana-Pinezhsy dolerite-basalt Complex (Tretyachenko 2008; 2015).

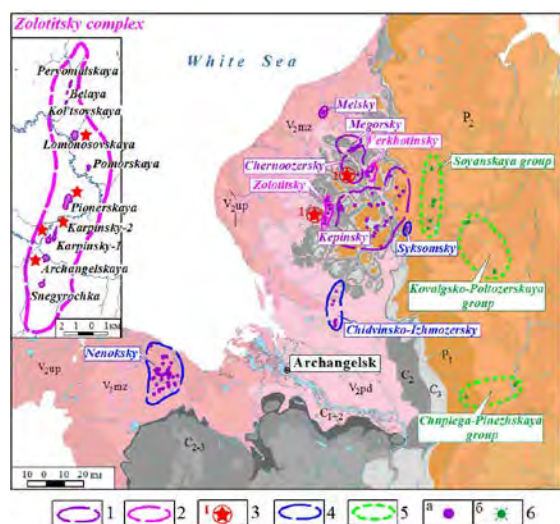


Figure 1: The location of kimberlites of Early-Hercynian volcanic complexes in Archangelsk kimberlite-picrite region.

1-3 – Zimniberezhny Mega-Complex: 1 – Fe-Ti-type (Kepinsky, Megorsy, Melsky, Chernoozersky Complexes); 2 – Mg-Al-type (Zolotitsky, Verkhotinsky Complexes); 3 – Diamond deposits (1 – M.V. Lomonosov, 2 – V. Grib); 4 – Nenokso-Chidvinsky Megacoplex (Nenoksky, Chidvinsko-Izhmozersky, Suksomsky Complexes); 5 – Soyana-Pinezhsy basaltic Complex pipes groups (Soyanskaya, Kovalgsko-Poltozerskaya, Chuplega-Pinezhsкая); 6 – Diatremes: a – kimberlites, picrites, olivine melilitites, b – tholeiitic basalts

1. Diamond-bearing kimberlites of Zimniberezhny Mega-Complex presented by magnesia-aluminous (Al) Zolotitsky Complex (with M.V. Lomonosov diamond deposit) and ferrum-titanium (Fe-Ti) Chernoozersky Complex (with V. Grib diamond deposit). Typomorphic features of these Complexes are associations of high-barophilic accessories: Cr-diopside-pyrope-chromite (Zolotitsky Complex) and essentially pyrope-picroilmenite (Chernoozersky Complex). Diamondiferous kimberlites are characterized petrochemically by high magnesium, low alumina and very low silica lime concentrations, and potassium-sodium hydroxide alkalinity (Bogatikov et al., 1999). Zolotitsky Complex kimberlites are low-titanium - type I and Chernoozersky Complex kimberlites are moderate-titanium - type II (Bogatikov et al., 2007).

With explicit domination of olivine-I phenocrysts, a very important feature of diamondiferous kimberlites is a typomorphism of microcrystalline oxides within groundmass: chromite for Zolotitsky Complex kimberlites and chromite-picroilmenite for Chernoozersky Complex kimberlites (Garanin et al., 2009).

In general, on a basis of petrological characteristics, Zolotitsky Complex diamondiferous kimberlites conform to Nakynskoe Area kimberlites (Yakutian Province, Russia) and Chernoozersky Complex diamondiferous kimberlites resemble to Malobotuobinsky and Daldyno-Alakitsy Areas (Yakutian Province, Russia), rather than.

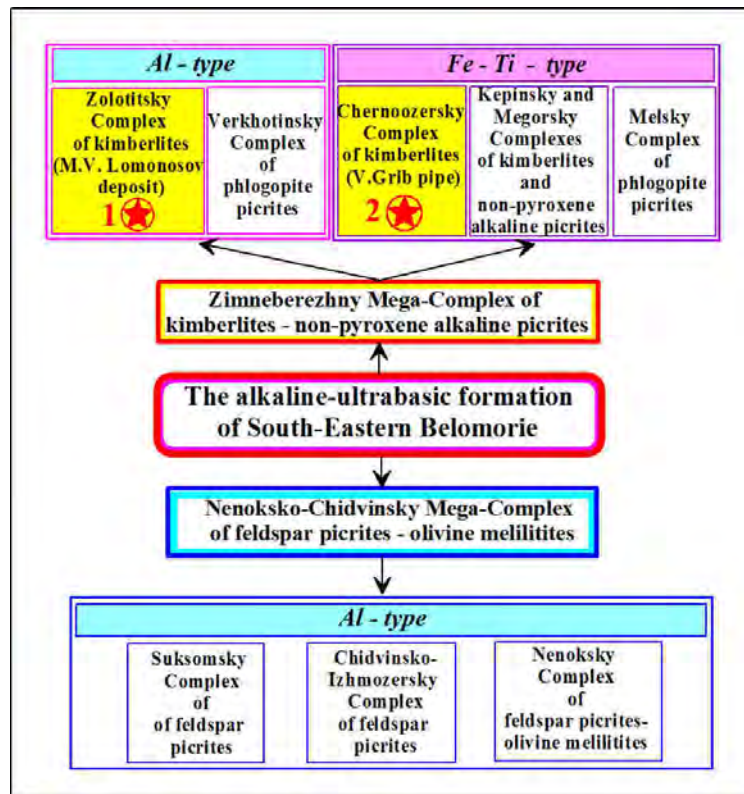


Figure 2: Scheme of structure of alkaline-ultrabasic formation of the Archangelsk kimberlite-picrite region.

2. Non-diamondiferous and poor-diamondiferous kimberlites, non-pyroxene alkaline picrites and feldspathic picrites-olivine melilitites unlike diamond-bearing rock types characterized by a clear predominance of olivine-II phenocrysts. Nenoksky pipes enriched by clinopyroxene I. Phenocrysts phlogopite diffuse in Verkhotina picrites and Mela sills.

In general, significant number of microliths of melilite, clinopyroxene and nepheline, as well as monticellite, richterite in some pipes is very typical for rocks of Nenokso-Chidvinsky mega-complex.

Fe-Ti Non-diamondiferous and poor-diamondiferous kimberlites and picrites Zimnerezhny Mega-Complex characterized by higher and high concentrations of total iron and titanium (Type III of high-titanium kimberlites (Bogatikov et al., 2007). Typochemism of Nenoksko-Chidvinsky Mega-Complex characterized by sharply high alumina, silica lime and the amount of alkali content with stable predominance of potassium over sodium.

There are significant differences for high-barophilic accessories. Thus, Kepinsky kimberlites characterized by significant preponderance of picroilmenites concentrations overpyropes, but low-chromium chromite dominates in Nenokso-Chidvinsky pipes.

An important feature of non-diamondiferous volcanic rocks is typomorphism of microcrystalline oxides within groundmass: Ti-magnetite-rutile for Fe-Ti type and chromite-Ti-magnetite for Al-type rockskimberlites (Garaninet al., 2009).

In general, non-diamondiferous kimberlites of mentioned Complexes are similar to non-diamondiferous kimberlites of the Northern part of Yakutian Province.

Kimberlites of Zolotitsky and Chernoozersky Complexes are greatly differ from non-diamondiferous kimberlites of Archangelsk Region by geochemical characteristics, and located between Group I and II of South African kimberlites, according to Nb- and Zr-content, Sm-Nd and Rb-Sr systems' parameters (Fig. 3). Therefore, it is possible to emphasize unique Zimnerezhny type kimberlites (Bogatikov et al., 2007).

3. Soyana-Pinezhsky-dolerite-basalt Complex comprises three groups of pipes in the eastern part of the region, which are comparable to the petrological characteristics with intraplate tholeiitic basalts of continental environments, that allows to consider them as a part of Early-Hercynian dolerite-basalt formations of the East European platform (Tretyachenko 2008; 2015).

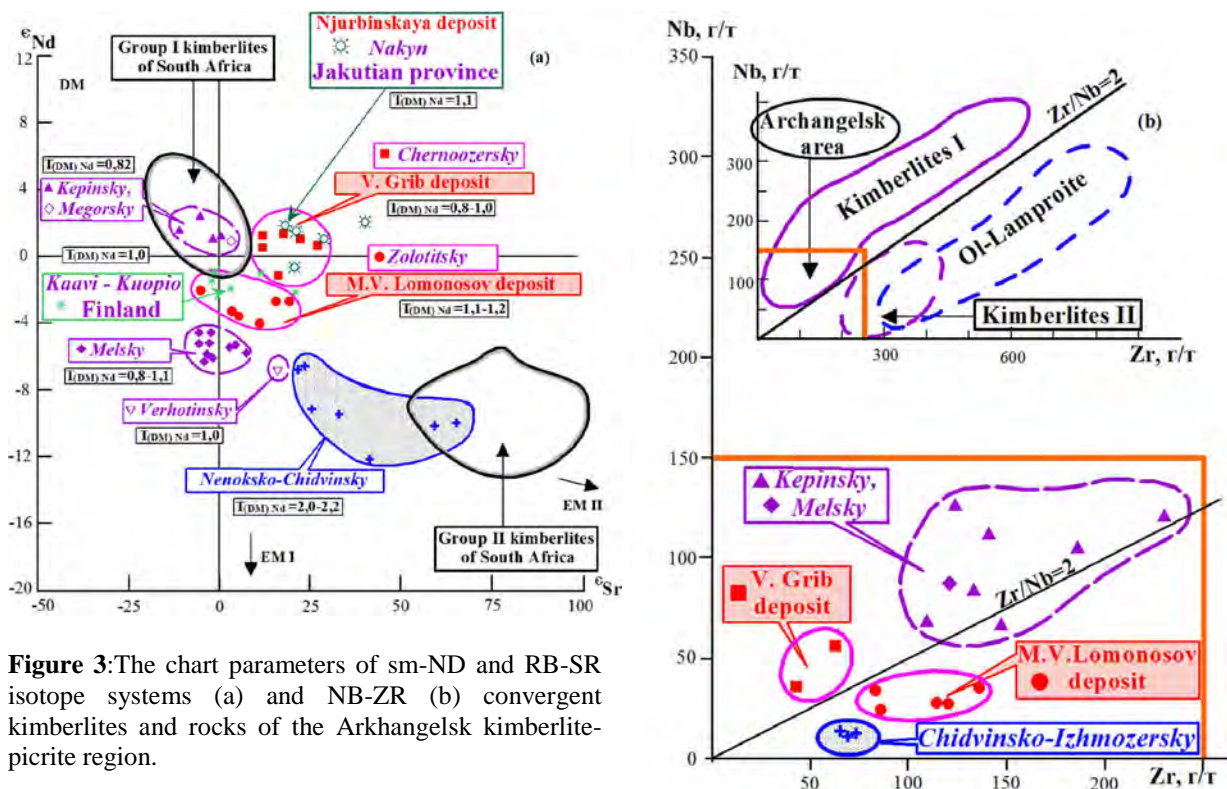


Figure 3: The chart parameters of sm-ND and RB-SR isotope systems (a) and NB-ZR (b) convergent kimberlites and rocks of the Arkhangelsk kimberlite-pirite region.

Is according to: Bogatikov, 1999, 2007; Garanin, 2006; Sablukov, 2010

It should be pointed that diamondiferous kimberlites of Zolotitsky and Chernoozersky Complexes have been formed during Late Devonian-Early Carboniferous Eras (Frasnian -Viséan Age, 375-340 ma), similar to kimberlites of Malo-Botuobinsky, Daldyno-Alakitsky and Verkhnemunsky districts (Yakutian Diamondiferous Province). The other bodies of kimberlites, its converged rocks and tholeiitic basalts have been formed earlier: Pragian-Eifelian Age, 410-390 ma (Kepinsky, Megorsky, and Melsky Complexes), Eifelian -Frasnian Age, 390-380 ma (pipes of Nenoksko-Chidvinsky Mega-Complex and Soyana-Pinezhsky Complex) (Tretyachenko, 2008; 2015).

References:

- Bogatikov, O.A., Garanin, V.K., Kononova, V.A., Kuryavtseva, G.P. et al. Archangelsk Diamondiferous Province. Moscow. 1999. 524 p. In Russian
- Bogatikov, O.A., Kononova, V.A., Nosova, A.A., et al. Kimberlites and lamproites of Eastern-European platform//Petrology. 2007. № 4, V. 15. 339-360 pp. In Russian
- Garanin, K.V. Alkaline ultramafic magmatic rocks of Zimny Bereg (Archangelsk Diamondiferous Province): geology, genesis, diamondiferous, prospecting and prospects of development. – Moscow: Moscow State University, 2006. – 371 p. In Russian
- Garanin, K.V., Bovkun A.V. Garanin K.V., Rotman A.Y., Serov I.V. Microcrystalline oxides from Russian kimberlites and related rocks. – Moscow: GEOS, 2009. – 498 p. In Russian
- Sablukov S.M. Sablukova L.I. et al. Magmatism of Nakyn kimberlite field and geodynamics of Siberian Craton. Proceedings of XXXII International Science Conference dedicated to the 100th anniversary of academician Smirnov V.I. Vol. 2. – Moscow: Moscow State University, 2010. P. 227-251
- Tretyachenko, V.V. Mineragenetic zonation of kimberlitic region of Southern-Eastern Belomorie. PhD. Thesis. Moscow, MSU. 2008. 28 p. In Russian
- Tretyachenko V.V., Garanin V.K., Bovkun A.V., Garanin K.V. // Alkaline Magmatism of the Earth and Related Strategic Metal Deposits. Proceedings of XXXII International Conference edit by L.N. Kogarko. GEOKHI RAS Moscow. Apatity 2015. P. 133-135



ZARYA DIAMOND DEPOSIT, YAKUTIAN PROVINCE, RUSSIA

**V.V. Polyanichko, R.F. Salikhov, V.P. Serov, F.F. Tyurin, K.V. Garanin, Z.V. Spetsyus,
O.V. Tarskikh, M.Yu. Zezekalo**
PJSC ALROSA, GaraninKV@alrosa.ru

Introduction

Zarya pipe is located on the southeast flank of Alakit-Markhinskoe Kimberlite Field, Daldyno-Alakitsky Diamondiferous, Yakutian Diamondiferous Province, Russia. The pipe is on the territory of activity Aikhal mining and concentration complex (MCC) of OJSC ALROSA, being located 2 km south-east of the Aikhal pipe and 3 km south-southeast of the mining and beneficiation plant (MBP) №8, which produced kimberlitic ores refining of Aikhal and Komsomolskaya pipes.

The pipe structure

Permian-Triassic age trap complex rocks (basalts) and Carboniferous age terrigenous layers, totally 103 m thickness, overlap Zarya pipe. The pipe was discovered in 1973, after exploration drilling (500×500 m). Initially the pipe was explored by diamond small-diameter drilling boreholes (160×80 and 80×80 m), at low depth (50 m). According to a non-representative sampling of core (core diameter 90 mm, total weight of 4.5 tons, the weight of core samples averaged 93 kg), poor diamond grade was identified (0.09 ct/t). At the same time, diamond grade reached 0.9 ct/t for individual samples, and 0.23 ct/t for individual boreholes, and high quality diamonds were recovered. Thus, there was the chance of detecting high diamond grade fascia within the pipe, which could be additional source of kimberlitic ore for the MBP № 8.

In recent years, Zarya pipe was re-explored by complex of estimation and exploration works including vertical and directional large-diameter boreholes (net 80×40 and 40×40 m) with total depth 500 m (at absolute level +100 m). It was possible to increase the weight of the individual 10-m core samples – up to 260-450 kg for ordinary boreholes and 1000 kg for cluster boreholes. After last phase of exploration it was identified: the pipe size is 480×260 m, and the size of the central ore column is 350×(180-60) m. Industrial mining is proposed for is the central ore column formed by phase II kimberlite (autolithic kimberlites). The average content of diamonds is 0.25 ct/t (phase II autolithic kimberlites), while the flanks of the deposit (porphyry kimberlites phase I) have grade 0.10 ct/t.

Geology and mineral composition

The geological structure, mineral composition, diamond features, permafrost-hydrogeological, geological and engineering characteristics of the pipes were studied. Two main kimberlite types compose the pipe: porphyry kimberlites (intrusion phase I) and autolithic kimberlite (intrusion phase II), sharply differing in the diamond grade and heavy fraction content. Autolithic kimberlite forms the central ore column, but porphyry kimberlites perform flanks of the pipe.

Porphyry kimberlites (PK) with low-grade of diamonds form North-West, South-East and South-West flanks of the pipe. These kimberlites are gray, light-gray, sometimes with insignificant shades: pale bluish or reddish-brown. The structure is mostly fine- and medium-porphyry, the texture is massive. Olivine excretions are completely serpentinized, their content varies from 13.54 to 30.52%, 22.99% average. There are low content of xenogeneic clasts represented by single fragments of sedimentary (on average 3.64%) and mantle rocks (0.25%). The average content of xenoliths of metamorphic rocks in porphyry kimberlites is 0.93%.

Autolithic kimberlites (AK) are gray rocks with a content of 9.55% xenoliths of sedimentary rocks. The texture of the rock as a whole is brecciated, and the kimberlitic groundmass is fine-medium-porphyry. The spherical texture of the kimberlite is clearly defined. The spherotoxic (spherical) zone is located along the periphery of the pseudomorphs and xenoliths of the sedimentary rocks in the form of small spherical separations of the micrograined structure and variable thickness. The zone is darker than the kimberlite at whole and includes pseudomorphs of olivine. The pseudomorph of olivine in the breccia is less in comparison with the porphyry kimberlite (19.31% average).

The groundmass of kimberlites have serpentine-calcite composition.

There are not statistically significant differences of the contents of main rock-forming oxides in PK and AK. The kimberlites of both phases belong to moderate-titanium ($\text{TiO}_2 = 1.5-1.55$ wt.%) and moderate-magnesium (PK – 26.4 wt.%, AK – 21.8 wt.%) rocks. The content of CaO varies in samples from 5.28 to 26.78 wt.%, depend on varying grade of rocks carbonatization.

The average weight of the heavy minerals fraction is: PK – 52.17 kg/t (16.58-101.80 kg/t), AK – 59.02 kg/t (3.80-307.40 kg/t). Variations in the contents of the heavy fraction depend on secondary magnetite. Content of such magnetite in some samples reaches to 83.4% of the total weight of the heavy fraction. Generally, the content of heavy fraction minerals in AK is more above 13% than in PK. A characteristic feature of indicator minerals in both rock types is sharp prevalence of picroilmenite (average content 2.76 kg/t) on pyrope (0.43 kg/t). There is the almost complete absence of unaltered olivine, an isolated finds of diopside and chrome spinel in both PK and AK.

Garnets mostly presented by widespread raspberry-colored grains, with lower content of orange, orange-red, purple, red and pink grains. The frequency of garnets occurrence with relics of the reaction rims is 50.4%. PK garnets are some larger in size than AK garnets and characterized by high thickness of kelyphitic reaction rims. Orange grains are dominated among PK garnets (69%), while such garnets are not widely presented in AK (29%). Raspberry varieties of garnets are more dominated in AK (47%), than in PK (23%). In our opinion, for this reason, the AK diamond grade is several times above, than in the PK.

Lherzolite paragenesis garnets are dominated (69,2%). There are mostly low- (0.2-2 wt.% Cr_2O_3) – 23%, and moderate-chromium garnets (2-4 wt.%) – 24.3%, with lower amounts of medium- (4-8%) – 14.1%, and high chromium (>8 wt.%) – 7.6% grains. Dunite-harzburgite paragenesis garnets present 10,97% of the total number studied, where diamond association diamonds of dunite-harzburgite paragenesis are 7.74%, and presented by low-calcium chromium pyropes. Low-calcium chromium pyropes of the Zarya pipes are characterized by higher contents of titanium, chromium, relatively lower contents of iron and calcium compare with similar garnets from ultra-high and high diamondiferous kimberlites of Yakutian Diamondiferous Province.

Eclogitic paragenesis garnets (17.42% of total) presented by: the magnesian almandine (16.12%), calcic pyrope-almandines (0.65%) and titanium pyropes (0.65%). A number of diamond association garnet of the eclogite paragenesis is 1.29%, where garnets presented by calcic pyrope-almandines and titanium pyropes.

Werlitic garnets are most rarely presented – 1.94%. There are titanium pyropes, chromium pyropes and uvarovite-pyropes.

Ilmenites of the Zarya pipe characterized by the widest presence of grains with reaction rims compare with ilmenites from other kimberlites of the Yakutian diamondiferous province. Rim zones are characterized by different thickness and mineral composition. Microprobe analysis established that ilmenite presented by picroilmenite (MgO 7.85-of 12.52 wt.%), with wide variations of Cr_2O_3 contents (0.19-5.05 wt.%).

Diamond crystals in Zarya pipe presented by types I, IV, VIII according to the Yu.L. Orlov classification. There are mostly type-I diamonds, a single discovery of coated cube (type-IV) and low proportion of polycrystalline intergrowths (type-VIII). Type-I diamonds presented by octahedrons (15.7%), laminar rhombic-dodecahedrons (22.8%), crystals of the transition habitus (14.1%) and typical rounded diamonds (18.2%). The type-VIII diamonds are presented by gray and black polycrystalline aggregates of octahedrons or transitional forms, with numerous inclusions of graphite and various photoluminescence. Crystals with evidence of natural etching are widely presented (41.2%). Such diamonds represented mostly by the crystals with etching channels, “scars”, the triangular hollows and plastic deformation bands. The total content of diamonds with ultramafic assemblage inclusions is 2.4, while the share of diamonds with eclogite assemblage inclusions (omphacite and orange garnet) is only 0.2%. This, along with the features of garnet, ilmenite and pyroxene, indicates the predominance of ultrabasic rocks on eclogitic in the upper mantle under the pipe.

The majority of the diamonds (82.5%) characterized by medium transparency, with lower quantity of diamonds (6.6%) with high transparency. Colored diamonds share is 34.0%. Different shades of brown diamonds (22,2%) and grey crystals (10.0%) dominate among the colored diamonds. There is also low quantity of “sea wave” color diamonds.

The quantities diamonds with the blue and pink-lilac photoluminescence are the same (35% for each variety). There are lower contents of diamonds with yellow-green, yellow, orange (totally 17.8%) photoluminescence. Generally, Zarya pipe diamonds presented by low-nitrogen varieties.

Resources and development

Total resources of the deposit are following: ore – 39.7 mln t, diamond – 7.1 mln ct, where ore reserves of the central ore column: ore – 20.8 mln t, diamonds – 5.25 mln ct. Economical mining is effective to the absolute level +300 m, with diamonds cut-off grade 0.221 (size size +0.5 mm) according to the Prefeasibility Study.

In June 2016 quarry construction was started in Zarya mine. In 2019 initial bulk sample (100,000 t) is planned. Pilot mining will provide technological characteristics of ores, recovery of 2,000-2,500 carats of diamonds, estimation of diamond quality, carat price, and the profitability of the overall Project.

Carbonate inclusions in Cr-pyropes derived from the mantle beneath Central Aldan superterrane of Siberian craton

Igor S. Sharygin¹, Evgeny I. Nikolenko¹, Konstantin V. Lobov¹

¹*Sobolev Institute of Geology and Mineralogy, Siberian Branch of Russian Academy of Science, Koptyuga ave. 3, Novosibirsk 630090, Russian Federation, isharygin@igm.ncs.ru, nevgeny@igm.nsc.ru, kost_1j@mail.ru*

Introduction

Here we present preliminary results of the micro-Raman spectroscopy, SEM-EDS and EPMA studies of carbonate-bearing mineral inclusions in mantle-derived xenocrysts of lherzolitic Cr-pyropes from magmatic rocks of Chompolo field located at the Central Aldan superterrane of the Siberian craton (Fig. 1). There are ten dikes (e.g., Aldan dike), pipes (e.g., Ogonek pipe) and vein bodies within the Chompolo field. The magmatic rocks of the Chompolo field were previously interpreted as kimberlites, however, recent studies re-classified their as lamprophyres (Kornilova, 1997).

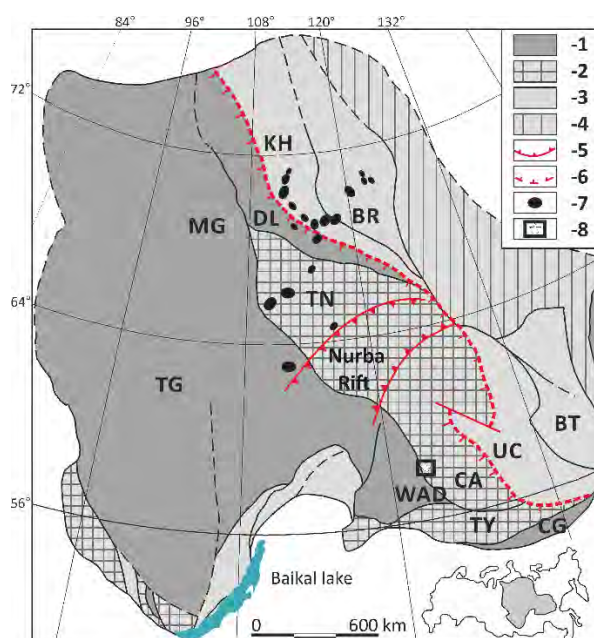


Figure 1: Tectonic structure of the Siberian craton (modified after Smelov and Timofeev, 2007). [1] Archean terranes; [2] Archean-Paleoproterozoic terranes (CA = Central Aldan superterrane); [3] Paleoproterozoic terranes; [4] Mesoproterozoic terranes; [5] Mesoproterozoic rift [1.2-1.0 Ga]; [6] Bilyakh-Fedorovskaya subduction zone [2.3-1.9 Ga]; [7] Kimberlite fields; [8] Location of the Chompolo field.

Results

The chemistry of the studied garnets, namely their high Cr₂O₃ contents and Mg#, clearly points to their mantle origin (Sobolev et al., 1973, Schulze, 2003). The host garnets are Cr-rich (0.4-6.9 wt%) pyropes with Mg# = 73.3-84.2, Ca# = [100·Ca/(Ca+Mg+Fe+Mn)] = 10.9-16.4 and TiO₂ contents below 0.4 wt%. They belong to lherzolitic paragenesis in terms of their CaO and Cr₂O₃ contents. The inclusions of olivine, clinopyroxene and Cr-spinel in Cr-pyropes (Table 1) also suggest the mantle origin of the parent peridotites.

Among studied samples seven garnet grains contain dolomite inclusions, ten – magnesite ones, and three – calcite ones (Table 1). All Cr-pyrope crystals contain from one to several individual, both single and/or composite (Fig. 1), mineral inclusions. Other minerals found along with carbonates within inclusions in the Chompolo garnets are olivine, clinopyroxene, Cr-spinel, phlogopite, amphibole, talc, rutile, Mg-ilmenite, minerals of crichtonite group, apatite, barite, graphite, and sulphides (Table 1).

Thermobarometric calculations yield PT conditions of residence of the garnets with carbonate-bearing mineral inclusions in the mantle as 2.9-3.6 GPa and 700-800 °C. The residual pressure up to 2.1 GPa was inferred for graphite inclusions assuming pressure dependence of the graphite G-band upshift (Nikolenko et al., 2017).

| Sample No. | Magmatic body | Inclusion mineralogy |
|------------|---------------|--|
| s21 | AD | Magnesite + Graphite + Olivine + Clinopyroxene + Phlogopite + CGM |
| ln11 | AD | Magnesite + Graphite + Olivine + Clinopyroxene + Phlogopite + Amphibole + Rutile + Mg-Ilmenite + Rutile + Apatite + CGM + Chalcopyrite |
| s163 | AD | Magnesite + BorniteSS + Chalcopyrite + Pentlandite |
| 2n4 | AD | Magnesite + Phlogopite + Rutile + Apatite + CGM |
| s258 | OP | Magnesite + Phlogopite + Rutile |
| s291 | OP | Magnesite + Olivine + Cr-spinel + Phlogopite + CGM + Amphibole + Mss + Pentlandite + Chalcopyrite |
| s317 | OP | Magnesite + Cr-spinel + Phlogopite + Rutile + CGM + BorniteSS |
| s124 | AD | Dolomite + Graphite + Clinopyroxene + Phlogopite + Cr-spinel |
| s139 | AD | Dolomite + Rutile + Mg-Ilmenite + Talc+ Unidentified mineral |
| s206 | AD | Dolomite + Talc |
| s61 | AD | Dolomite + Talc + Unidentified mineral |
| s182 | AD | Dolomite + Mg-Ilmenite + Phlogopite+ Unidentified mineral |
| s26 | AD | Dolomite + Cr-Spinel + Rutile + Clinopyroxene + Unidentified mineral |
| s113 | AD | Dolomite + Phlogopite + Chalcopyrite + Mss |
| s213 | AD | Dolomite + Cr-Spinel + Chalcopyrite + Mss |
| s256 | OP | Dolomite + Cr-Spinel + Unidentified mineral |
| s261 | OP | Dolomite + Cr-Spinel + Unidentified mineral |
| s275 | OP | Calcite + Cr-Spinel + Barite + Unidentified mineral |
| s337 | OP | Calcite + Cr-Spinel + Rutile + Amphibole + Apatite + CGM + Unidentified mineral |
| S300 | OP | Calcite + Unidentified mineral |

Table 1: Carbonate-bearing mineral inclusion assemblages in mantle-derived garnets from Central Aldan superterrane of Siberian craton. AD – Aldanskaya dike, OP – Ogonek pipe, BorniteSS – bornite solid solution, Mss – monosulphide solid solution, CGM – mineral of crichtonite group.

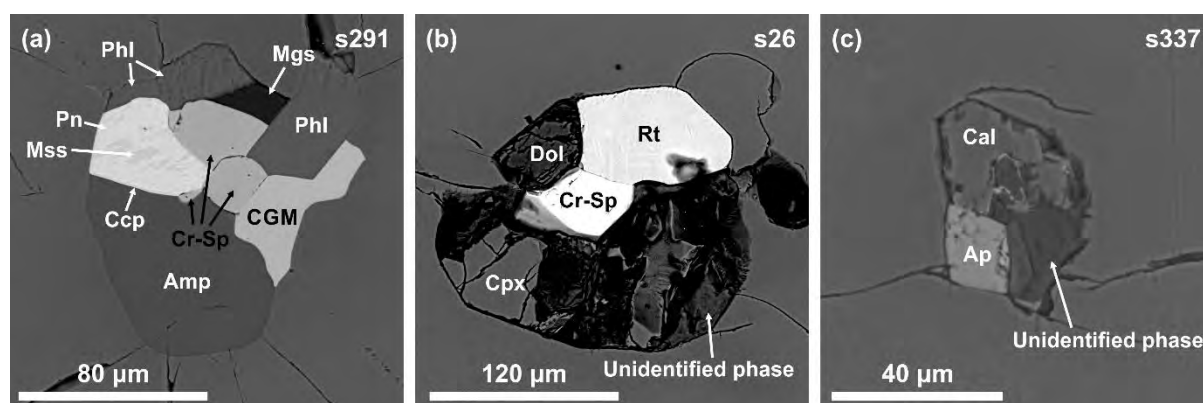


Figure 1: Back-scattered electron images of carbonate-bearing inclusions in mantle-derived garnets from Central Aldan superterrane of Siberian craton. Mgs – magnesite, Dol – dolomite, Cal – calcite, CGM – mineral of crichtonite group, Ap – apatite, Phl – phlogopite, Amp – amphibole, Rt – rutile, Cr-Sp – Cr-spinel, Cpx – clinopyroxene, Mss – monosulphide solid solution, Pn – pentlandite, Ccp – chalcopyrite.

Discussion

We interpreted the shape, composition, and distribution of carbonate-bearing mineral inclusions as evidence of their syngenetic origin with host garnets. For volatile-bearing minerals (mica, amphibole, and apatite) together with titanium-rich phases such as ilmenite, rutile, and minerals of crichtonite group in mantle rocks, there is a consensus for an origin by mantle metasomatism (Haggerty, 1991; Wang et al., 1999; Pearson et al., 2003; Konzett et al., 2013; Malkovets et al., 2016; Rezvukhin et al., 2016). Therefore, studied mineral inclusion assemblages suggest an episode(s) of metasomatism in the lithospheric mantle of the Central Aldan superterrane of the Siberian craton, contemporaneous with the formation of host Cr-pyropes crystals. The presence of carbonate and graphite within inclusions in Cr-pyropes indicates that metasomatic agent(s) was CO₂-rich melt (i.e., carbonatitic melt) or supercritical COH fluid.

Acknowledgements

This work was supported by the grants Nos. 16-35-60052 mol_a_dk and 15-05-04885 from the Russian Foundation for Basic Research and the state assignment project No. 0330-2016-0006.

References

- Haggerty SE (1991) Oxide mineralogy of the upper mantle. *Reviews in Mineralogy and Geochemistry* 25:355-416
- Konzett J, Wirth R, Hauzenberger C, Whitehouse M (2013) Two episodes of fluid migration in the Kaapvaal Craton lithospheric mantle associated with Cretaceous kimberlite activity: evidence from a harzburgite containing a unique assemblage of metasomatic zirconium-phases. *Lithos* 182:165-184
- Kornilova VP (1997) Petrography and mineralogy of the calc-alkaline lamprophyres and eruptive breccias at the basin of Chomppolo river. *Otechestvennaya Geologiya* 9: 6-9
- Malkovets VG, Rezvukhin DI, Belousova EA, Griffin WL, Sharygin IS, Tretiakova IG, Gibsher AA, O'Reilly SY, Kuzmin DV, Litasov KD, Loginova AM, Pokhilenko NP, Sobolev NV (2016) Cr-rich rutile: A powerful tool for diamond exploration. *Lithos* 265:304-311
- Nikolenko EI, Sharygin IS, Alifirova TA, Korsakov AV, Zelenovskiy PS, Shur VY (2017) Graphite-bearing mineral assemblages in the mantle beneath Central Aldan superterrane of North Asian craton: combined confocal micro-Raman and electron microprobe characterization. *Journal of Raman Spectroscopy*:10.1002/jrs.5163
- Pearson DG, Shirey SB, Canil D (2003) Mantle samples included in volcanic rocks: xenoliths and diamonds. In: Carlson RW, Holland HD, Turekian KK (eds) *Treatise on Geochemistry, Vol 2: Geochemistry of the Mantle and Core, vol 2*. Elsevier, Amsterdam, pp 171–275
- Rezvukhin DI, Malkovets VG, Sharygin IS, Kuzmin DV, Gibsher AA, Litasov KD, Pokhilenko NP, Sobolev NV (2016) Inclusions of crichtonite group minerals in pyropes from the Internatsionalnaya kimberlite pipe, Yakutia. *Dokl Earth Sci* 466:206-209
- Schulze DJ (2003) A classification scheme for mantle-derived garnets in kimberlite: a tool for investigating the mantle and exploring for diamonds. *Lithos* 71:195-213
- Smelov AP, Timofeev VF (2007) The age of the North Asian Cratonic basement: an overview. *Gondwana Res* 12:279-288
- Sobolev NV, Lavrent'ev YG, Pokhilenko NP, Usova LV (1973) Chrome-rich garnets from the kimberlites of Yakutia and their parageneses. *Contrib Mineral Petrol* 40:39-52
- Wang L, Essene EJ, Zhang Y (1999) Mineral inclusions in pyrope crystals from Garnet Ridge, Arizona, USA: implications for processes in the upper mantle. *Contrib Mineral Petrol* 135:164-178

In the sheared peridotites, we have found interstitial mineral assemblages, which include olivine (F₀₉₃₋₉₄), clinopyroxene, monticellite, mica, humite, clinohumite, sodalite, zoned spinel, perovskite, apatite, calcite, pentlandite, pyrrhotite and djerfisherite K₆(Fe,Ni,Cu)₂₅S₂₆Cl (Fig. 1). These late interstitial minerals are mostly localized in triple-junctions between both porphyroclasts and neoblasts of rock-forming minerals; less frequently they occur along grain boundaries. Djerfisherite was also observed as rims around blebs of primary Fe-Ni-Cu sulphides. Interstitial olivine and clinopyroxene notably differ in composition from primary ones. Spinel is usually zoned; the core is chromite and the rim is magnetite. Interstitial mica is represented by phlogopite and tetraferriphlogopite.

Discussion

The interpretation of deformation features suggests that porphyroclastic texture of sheared peridotites results from the recrystallization of granular peridotites under a very high-stress and high strain-rate deformation; the preservation of deformation features implies that recrystallization was essentially contemporaneous with the entrainment of xenoliths by kimberlite magma (O'Reilly and Griffin, 2010). The presence of the studied interstitial minerals between both porphyroclasts and neoblasts of rock-forming minerals indicates their close connection with kimberlite magmatism. Mineralogy of the interstitial assemblages, except some minerals, resembles the groundmass of host kimberlites (Sharygin et al., 2007; Kamenetsky et al., 2012). Moreover, composition of some minerals from the interstitial assemblages are similar to those of the kimberlite groundmass of the Udachnaya-East pipe. These facts suggest that the origin of the studied interstitial mineral assemblages in the sheared peridotite is the result of infiltration of transporting kimberlite melt into xenoliths during magma ascent. The majority of interstitial minerals crystallized directly from interstitial kimberlite melt, but djerfisherite rimming primary Fe-Ni-Cu sulphides is the product of their reaction with kimberlite melt.

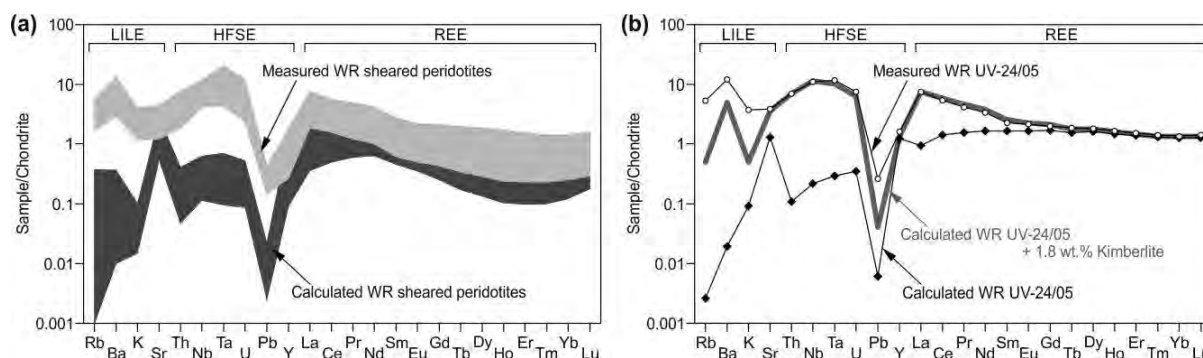


Figure 2: (a) Comparison between chondrite-normalized trace element patterns of measured and calculated whole-rock compositions of the sheared peridotites from the Udachnaya-East kimberlite pipe. (b) Illustration of the effect of transporting kimberlite melt contamination of whole-rock geochemistry of sheared peridotites. Chondrite-normalized trace element patterns of calculated, calculated with the addition of 1.8 wt.% of host kimberlite (Kamenetsky et al., 2012) and measured whole-rock compositions for sample UV-24/05. LILE – large ion lithophile elements, HFSE – high field strength elements, REE – rare earth elements. Chondrite values after McDonough and Sun (1995).

Among rock-forming minerals of peridotites, clinopyroxene and garnet have high amounts of trace elements whereas olivine and orthopyroxene are very poor in trace elements and their contribution to the whole-rock trace elements budget is negligible (Schmidberger and Francis, 2001; Agashev et al., 2013). Therefore, whole-rock trace elements composition of peridotites can be calculated using modal abundances and trace elements contents of clinopyroxene and garnet. The results of such calculations for studied samples indicate that calculated whole-rock trace elements contents are much lower than those measured (Fig. 2). In particular, calculated whole-rock LILE and HFSE abundances are an order(s) of magnitudes lower than those analysed (Fig. 2). Previous studies of mantle xenoliths in kimberlites from other regions demonstrated the same problem (Schmidberger and Francis, 2001; Gregoire et al., 2003). Such large discrepancy for trace elements between the calculated and measured whole-rock compositions can be explained by the presence of tiny accessory phases that contribute significantly to the whole-rock trace elements budget of peridotites.

We identified at least 16 interstitial minerals, which are related to infiltration of transporting kimberlite melt. Among them, perovskite and apatite are the main storage of REE, Nb and Ta, calcite – Sr, djerfisherite – K, mica – K, Rb and Ba. We modeled infiltration of kimberlite melt into the xenoliths of the sheared peridotites by the addition of up to 2 wt% of host kimberlite to the calculated whole-rock compositions. The results yielded trace elements patterns that are remarkably similar to those of the analysed bulk rocks (Fig. 2b). This coincidence supports the conclusion that interstitial mineral assemblages in the sheared peridotite is the result of infiltration of transporting kimberlite melt into xenoliths.

Conclusions

The xenoliths of the sheared peridotites from the Udachnaya-East kimberlite pipe contain interstitial mineral assemblages, which include olivine, clinopyroxene, monticellite, mica, humite, clinohumite, sodalite, zoned spinel, perovskite, apatite, calcite, pentlandite, pyrrhotite and djerfisherite. These minerals crystallized from interstitial kimberlite melt that infiltrated into xenoliths during magma ascent.

The presence of kimberlite-related interstitial minerals (such as perovskite, apatite, carbonate, mica, and djerfisherite) may have an essential influence on the whole-rock trace elements composition of mantle xenoliths. The sheared peridotites had depleted trace elements patterns before contamination by transporting kimberlite melt. This fact should be considered when we use measured bulk geochemical characteristics of mantle xenoliths (even only the central parts of the large xenoliths) for the interpretation of the ancient mantle processes in CLM.

Acknowledgements

This work was supported by the grant No. 16-35-60052 mol_a_dk from the Russian Foundation for Basic Research, the grant No. MK-4534.2016.5 from the President of the Russian Federation and the state assignment project No. 0330-2016-0006.

References

- Agashev AM, Ionov DA, Pokhilenko NP, Golovin AV, Cherepanova Y, Sharygin IS (2013) Metasomatism in lithospheric mantle roots: Constraints from whole-rock and mineral chemical composition of deformed peridotite xenoliths from kimberlite pipe Udachnaya. *Lithos* 160-161:201-215
- Gregoire M, Bell DR, Le Roex AP (2003) Garnet lherzolites from the Kaapvaal craton (South Africa): Trace element evidence for a metasomatic history. *J Petrol* 44:629-657
- Kamenetsky VS, Kamenetsky MB, Golovin AV, Sharygin VV, Maas R (2012) Ultrafresh salty kimberlite of the Udachnaya-East pipe (Yakutia, Russia): A petrological oddity or fortuitous discovery? *Lithos* 152:173-186
- McDonough WF, Sun SS (1995) The composition of the Earth. *Chem Geol* 120:223-253
- O'Reilly SY, Griffin WL (2010) The continental lithosphere-asthenosphere boundary: Can we sample it? *Lithos* 120:1-13
- Schmidberger SS, Francis D (2001) Constraints on the trace element composition of the Archean mantle root beneath Somerset Island, Arctic Canada. *J Petrol* 42:1095-1117
- Sharygin IS, Golovin AV, Pokhilenko NP (2012) Djerfisherite in xenoliths of sheared peridotite in the Udachnaya-East pipe (Yakutia): origin and relationship with kimberlitic magmatism. *Russian Geology and Geophysics* 53:247-261



The 812-Carat Pure Type IaB Constellation Diamond from Karowe – Part of an Even Larger Rough?

Ulrika F.S. D’Haenens-Johansson, Evan M. Smith, Karen V. Smit,
Wuyi Wang, Thomas M. Moses

Gemological Institute of America, New York City, NY, USA,
ujohansson@gia.edu, evan.smith@gia.edu, ksmit@gia.edu, wwang@gia.edu, tmoses@gia.edu

Introduction

Lucara Diamond extracted an 812-carat colorless diamond from the AK6 pipe at Karowe mine (Botswana) in November 2015. Named “The Constellation,” it is recognized as the sixth-largest gem-quality rough diamond ever discovered. The Constellation attained the highest price for a rough diamond to date, selling in May 2016 to Dubai-based Nemesis International DMCC for \$63.1 million (\$77,649 per carat) (Graff 2016). Interestingly, several very large diamonds were recovered at Karowe within the same week. This group includes the second-largest gem-quality rough diamond ever found, the 1,109-carat colorless Lesedi La Rona, as well as other colorless diamonds weighing 374, 296, and 183 carats (Lucara Diamond 2016; Graff 2016; Shor 2016). The Constellation and the 296-carat and 183-carat diamonds were investigated at GIA using a combination of gemological and spectroscopic techniques to analyze the diamonds’ point defect content. Evidence will be presented demonstrating that these diamonds are not unrelated, but stem from a single rough diamond that was shattered into multiple pieces.

Sample and Experimental Details

The Constellation and the 296-carat and 183-carat rough diamonds were separately submitted to our laboratory for scientific examination in 2016, prior to any cutting or polishing (see Figure 1). Their external morphologies and internal features were studied under magnification using Gem Instruments and Nikon SMZ1500 binocular microscopes using dark field and fiber optic illumination.

The diamonds’ fluorescence behavior to ultraviolet (UV) illumination was tested using a combination gem lamp (365 nm and 254 nm emission) commonly used by the diamond industry. UV fluorescence imaging is a useful tool to reveal growth zones, which typically contain different concentrations of impurities reflecting growth fluid changes. A DiamondView fluorescence instrument (< 230 nm) was used to image portions of the 183-carat and 296-carat stones – the large sizes restricted the possible viewing orientations in the chamber. The Constellation was imaged using a GIA-built system under illumination from a deuterium lamp (185 – 400 nm).



Figure 1: (a) The 812-carat Constellation (812.77 ct, 64 × 39 × 34 mm), the (b) 296-carat (183.41 ct, 38 × 23 × 23 mm), and (c) 183-carat diamonds originating from Karowe. Both (b) and (c) show ink markings in preparation for cutting. Photographs by Jiaxin (Jae) Liao.

Impurity concentrations were analyzed using room temperature Fourier Transform Infrared (FTIR) spectroscopy (Thermo Nicolet Nexus 6700 spectrometer) and photoluminescence (PL) at 77 K using a range of excitation sources (Renishaw confocal microspectrometer with laser excitation wavelengths of 488.0, 514.5, 632.5, and 830.0 nm).

Results and Discussion

Diamonds are commonly classified according to their nitrogen content measured by FTIR spectroscopy: Type I diamonds contain nitrogen in either isolated (Ib) or aggregated (IaAB) forms, while Type II diamonds do not contain detectable nitrogen concentrations (IIa), but may contain boron (IIb). Over the past five years at GIA, however, spectroscopic analyses of thousands of Type IaB, IIa, and IIb colorless diamonds have revealed trends that demonstrate that a defect content transition can often be detected between diamond types, rather than being clearly separate groups, with Type IIb and pure IaB bracketing Type IIa diamonds. Based on inclusions, many Type IIa as well as some IaB diamonds originate from the sublithospheric mantle, in association with metallic liquid (Smith et al. 2016). Inclusions also indicate a “superdeep,” sublithospheric mantle origin for Type IIb diamonds (Smith and Wang, 11IKC-4502).

All three diamonds in this study are pure Type IaB, containing 20 ± 4 ppm B-centers (N_4V). The diamonds studied here are notable for being the largest pure Type IaB samples reported, whereas large colorless diamonds are often highlighted as Type IIa. To emphasize the rarity of Type IaB diamonds, we analyzed 5,060 colorless to faintly colored (D–Z) faceted diamonds weighing between 10.0 and 228.3 carats that were submitted for grading services at GIA. As expected, the most common diamond type was Type IaAB (73.8%). However, only 1.2% of diamonds were pure Type IaB, significantly rarer than Type IIa diamonds (24.6%).

PL spectroscopy detected emission from H4 (496 nm, thought to be N_4V_2), H3 (503.2 nm, NVN^0) and GR1 (741 nm, V^0) centers, consistent with natural Type IaB diamonds. Remarkably similar peak characteristics were observed among the suite, with comparable peak intensities and full-width half-maxima (FWHM), as shown in Figure 2. Typically natural diamonds show highly variable PL peak characteristics and combinations, such that the distinctively similar FTIR and PL results in these three diamonds provide compelling evidence that they were once part of a single diamond.

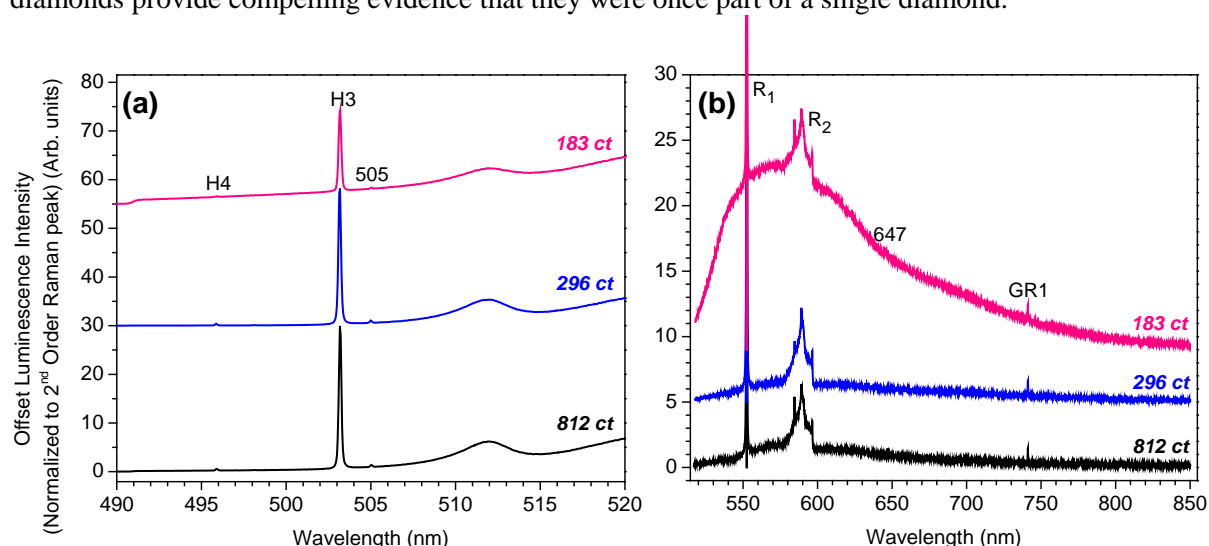


Figure 2: PL spectra collected at 77 K using (a) 488.0 nm and (b) 514.2 nm laser excitations. Data have been normalized to the corresponding 2nd-order diamond Raman peaks and offset for clarity. Spectra indicate low concentrations of luminescent defects, compared to the majority of diamonds investigated by GIA. Consistent emission from H4 (496 nm), H3 (503.2 nm) and GR1 (741 nm) centers were detected for all three diamonds. PL spectra obtained using 632.5 nm and 830.0 nm lasers (not shown) did not reveal any additional defect centers. In (b) R₁ and R₂ indicate the 1st- and 2nd-order Raman peaks. FWHM for the H3 and GR1 emission peaks were calculated for each data set, and were found to be 0.181 ± 0.006 nm and 0.36 ± 0.02 nm, respectively.

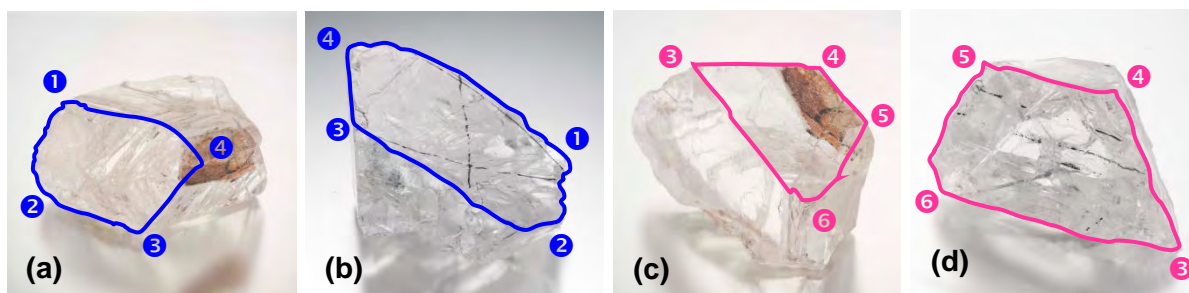


Figure 3: Images illustrating the common cleavage faces for (a, c) The Constellation and the (b) 296-carat and (c) 183-carat diamonds, with corners numbered to facilitate orientation. Outlines for the matching fractured surfaces are color-coded, with blue lines used for The Constellation and the 296-carat diamonds (a–b), and pink used for The Constellation and the 183-carat diamonds (c–d). The edge spanning labels 3 and 4 is common to all three stones. Photographs by Jiaxin (Jae) Liao.

The diamonds showed identical responses when exposed to the gem lamp: weak blue fluorescence, followed by weak blue phosphorescence to short-wave UV, and medium blue fluorescence to long-wave UV. Fluorescence imaging revealed that each sample contained at least two distinct growth zones.

The external morphologies of the stones showed primary octahedral, resorbed, and fractured faces, with both The Constellation and 296-carat diamonds featuring distinct fractures containing metallic inclusions and secondary iron-oxide staining. Minor iron-oxide staining was also observed in the 183-carat stone. The specimens were generally inclusion-free, with only a few small black or reddish-orange inclusions spanning 200–500 μm in size being observed close to fractured surfaces. Detailed inspection of their surfaces revealed shared cleavage planes between The Constellation and the 296-carat and 183-carat stones. Outlines for the matching fractured surfaces are highlighted in Figure 3. Significantly, the iron-oxide stained fractures in The Constellation and the 296-carat diamonds converge to a paired corner (labeled 4). Furthermore, the intrinsic growth structures revealed by UV-fluorescence for these specific surfaces were consistent for the two diamonds. The visual observations further support the conclusion that these three specimens originate from the same rough, which may have broken either during kimberlite eruption or mining processes.

With a combined weight of 1,291 carats, the composite of the studied diamonds would have surpassed the Lesedi La Rona. In fact, due to the similar visual characteristics and extraction dates, it is possible that all five large Karowe diamonds originated from the same rough, 2774 carats combined, although this cannot be confirmed without further inspection. Nevertheless, even without considering the unexamined Lesedi La Rona and 374-carat diamonds, this report shows how multi-technique analyses of point defects and their distributions can link multiple rough diamonds comprising a single diamond of remarkable historic and scientific significance.

References

- Graff M (2016) Lucara sells 812-carat diamond for \$63M. National Jeweler website. <http://www.nationaljeweler.com/diamonds-gems/pricing/4220-lucara-sells-812-carat-diamond-for-63m>. Accessed 20 December 2016
- Lucara Diamond (2016) April 2016 Exceptional Stone Tender Catalogue, Karowe Mine, Botswana Production. Lucara Diamond website. <https://www.lucaradiamond.com/assets/docs/catalogues/lucara-bonas-sdt9-apr132016-1476742115.pdf>. Accessed 23 December 2016
- Shor R (2016) Is another 1,000 (or 3,000) carat diamond around the corner? GIA website. <https://www.gia.edu/gia-news-research/is-another-1000-carat-diamond-around-corner>. Accessed 20 December 2016
- Smith EM, Shirey SB, Nestola F, Bullock ES, Wang J, Richardson SH, Wang W (2016) Large gem diamonds from metallic liquid in Earth's deep mantle. *Science* 354(6318):1403–1405 doi:10.1126/science.aal1303



The P3 kimberlite, Wajrakarur Kimberlite Field, India: Mineralogy, and major and trace element compositions of olivines as records of their magmatic versus xenocrystic origin

Azhar M. Shaikh¹, *, S. C. Patel¹, E.V.S.S.K. Babu², S. Ravi³

¹ Department of Earth Sciences, I.I.T. Bombay, Mumbai 400076, India,

azher.shaikh115@gmail.com, scpatel@iitb.ac.in

² National Geophysical Research Institute, Uppal Road, Hyderabad 500007, India, evsskbabu@gmail.com

³ Geological Survey of India, Bandlaguda, Hyderabad 500068, India, svaiivers@gmail.com

Introduction

We report the mineralogy and high precision microprobe trace element data of olivine from the Mesoproterozoic, diamondiferous P3 kimberlite in the Wajrakarur Kimberlite Field (WKF), southern India. Olivine macrocrysts in the kimberlite exhibit a core-rim structure which offers an opportunity to examine the variation in their minor and trace element (Ni, Ca, Al, Ti, Mn, Cr and Na) contents in order to differentiate melt-derived olivines from mantle olivines and also to distinguish multiple populations of mantle olivines.

Petrography

P3 kimberlite is inequigranular textured with macro- and microcrysts of olivine and phlogopite set in a groundmass dominated by phlogopite and monticellite with subordinate amounts of spinel, perovskite, ilmenite, apatite, serpentine, and calcite and rare baddeleyite. The groundmass is mostly uniform textured with occasional segregations. The rock additionally contains discrete xenocrysts of Cr-pyrope, diopside, and ilmenite; and highly altered microxenoliths. The microxenoliths contain relicts of Cr-diopside within a secondary mass of andradite \pm titanite \pm ferropargasite \pm kumtyubeite ($\text{Ca}_7(\text{SiO}_4)_3\text{F}_2$) \pm zircon. The occurrence of kumtyubeite (F-analogue of humite) in microxenolith is reported for the first time from an Indian kimberlite.

Mineral chemistry

Although compositional zoning in olivine is masked by serpentinization, some olivine macrocrysts preserve a core-rim structure, where the rims represent chemically distinct overgrowths resulting from heterogeneous crystallization onto pre-existing cores. Two macrocryst core populations (olivine I and II) and one rim population (olivine III) are distinguished based on forsterite content and trace element concentrations. Olivine I cores are marked by higher Fo (90–93), Ni (2344–2816 ppm), and Cr (148–595 ppm) relative to olivine II cores (Fo 84–87, Ni 1601–2235 ppm, and Cr 107–261 ppm). Ca concentration is 162–610 ppm in olivine I cores and 262–599 ppm in olivine II cores. Olivine III rims which mantle either olivine I or II cores have intermediate Fo (88–89) and exhibit oscillatory zoning with variations in Ca (306–532 ppm), Ni (1132–2387 ppm), and Cr (175–397 ppm). The rims also exhibit elevated Ti contents (117–179 ppm) compared to olivine I and II cores (35–146 ppm).

Phlogopites of three distinct populations are recognised based on texture and composition: (i) phlogopite I occurs as macrocrysts and in nodules, and is marked by high Cr, low Ti and Ba contents, (ii) phlogopite II forms phenocrysts, microphenocrysts, and overgrowth rims on phlogopite I macrocrysts, and has high Cr and Ti, and moderate Ba contents; and (iii) phlogopite III forms a late generation of phenocrysts, microphenocrysts, and scattered groundmass needles and contains low Ti and Cr and high Ba and F. Spinel grains exhibit atoll structure and are zoned from cores of Cr–Fe–Al–Mg spinel to rims of Mg–Ti magnetite. Groundmass ilmenites are rich in Cr and Mg compared to xenocrystic ilmenites. Two generations of apatite are present, the first generation being richer in F and poorer in Sr than the second generation.

Unlike the nearby P2-west, P5, P12 and P13 intrusions in the WKF which show the lamproitic affinity, P3 intrusion shows mineral characteristics such as phlogopite–kinoshitalite–

eastonite trend of mica, compositional trend-1 of groundmass spinels, and the presence of groundmass monticellite which are typical of worldwide archetypal kimberlites. The intrusion is classified as a phlogopite–monticellite kimberlite.

Discussion

Origin of olivine core and rim

The absence of any groundmass mineral inclusions, the presence of deformation and resorption features in olivine I and II cores are indicative of their mantle origin. This is supported by their wide range of Fo and high Ni contents relative to olivine III rims. The high Fo and Ni contents of olivine I cores are similar to those of olivine in xenoliths of garnet lherzolite and garnet harzburgite reported from P3 and P4 intrusions (Nehru and Reddy, 1989) (Fig. 1a). Therefore, olivine I cores are interpreted to be inherited from such mantle xenoliths. In contrast, the relatively Fe-rich composition of olivine II cores falls outside the field of xenocrystic olivines from most of the worldwide kimberlites. Some workers have attributed the origin of such Fe-rich olivines to a proto-kimberlite melt, whereas others have linked it to some megacryst suites. The Fo and Ni contents of olivine II cores in P3 overlap with those of olivine megacrysts from P4 lamproite in the WKF (authors' unpublished data), and Monastery and Jagersfontein kimberlites in South Africa (Gurney et al., 1979; Hops et al., 1992) (Fig. 1a). Equilibration temperatures calculated for olivine I and II cores using the Al-in olivine thermometer of De Hoog et al. (2010), intersect the xenolith geotherm beneath the WKF at assumed pressures of 40–60 kbar and the P–T stability field of mantle xenoliths from the WKF. This indicates that the olivine cores are not related to a proto-kimberlite melt because otherwise, their equilibration temperatures would have been higher than that indicated by xenolith geotherm at any given depth. Similar Fe-rich olivine cores are known from two lamproite intrusions in the WKF: TK1 (Shaikh et al., 2016) and P4 (authors' unpublished data), whose parental melt compositions are likely to have been different from that of P3 kimberlite. The occurrence of Fe-rich olivines of similar composition in two contrasting magma types (kimberlite and lamproite) indicates that Fe-rich olivines are not related to a proto-kimberlite or proto-lamproite melt, but are derived from a megacryst suite produced by a distinct metasomatic event.

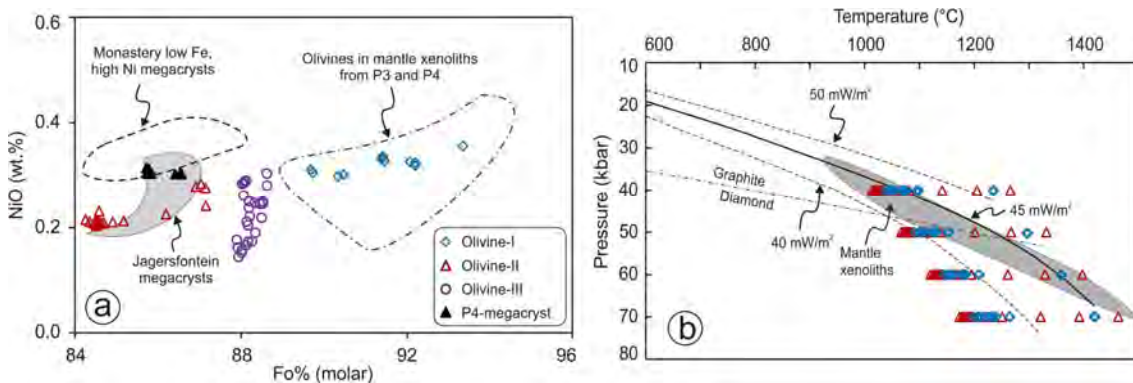


Figure 1: (a) Fo vs NiO plot of P3 olivines. Field of olivine megacrysts from Monastery and Jagerafontein kimberlites from Gurney et al. (1979) and Hops et al. (1992) respectively; (b) P–T plot showing intersection of the calculated temperatures for olivine I and II cores with xenolith geotherm beneath the WKF (thick line) and stability field of mantle xenoliths from the WKF. Data of mantle xenoliths in (a) and (b) from Nehru and Reddy (1989).

Olivine III rim, with oscillatory zoning in Ca, Cr, and Ni, is of magmatic origin; the oscillatory zoning may be produced by rapid growth of crystal faces relative to slow diffusion of ions through the melt. Although it is widely believed that olivine crystallisation is linked to orthopyroxene assimilation in the melt, the relative timing of the two processes and the depth at which they occur are debatable. Based on the recent work of Stone and Luth (2017) it is possible that olivine crystallisation

occurred concomitantly with orthopyroxene dissolution at depths shallower than 3.5 GPa during kimberlite ascent.

Origin of phlogopites

Phlogopite I macrocrysts and nodules show evidences of deformation and locally contain vermicular shaped inclusions of Cr-rich spinel. Their high Cr–low Ti composition is similar to that of phlogopite cores from a variety of metasomatised mantle xenoliths and megacryst suites reported from South African kimberlites, and therefore, these phlogopites are considered to be xenocrysts. Phlogopite II grains occasionally contain inclusions of groundmass minerals indicating their magmatic origin, while their high Cr–high Ti composition and deformed nature suggest crystallization at mantle depths. However, it is uncertain whether phlogopite II crystallized from the same magma from which phlogopite III crystallized or from a separate early magma pulse. The enrichment of Cr and Ti in phlogopite II and also in olivine III can be attributed to the crystallization of these phases from kimberlite magma prior to spinel crystallization.

Conclusions

Fe-rich macrocrystic olivine cores in P3 kimberlite are not related to a proto-kimberlite melt, but are derived from a megacryst suite produced by a distinct metasomatic event in the mantle. This contrasts with the suggestion of several workers on southern African and Russian kimberlites that Fe-rich olivines are cognate phenocrysts related to an early stage of kimberlite magmatism. The crystallisation of oscillatory-zoned olivine rim is interpreted to have occurred during kimberlite ascent.

References

- De Hoog JCM, Gall L, Cornell DH (2010) Trace-element geochemistry of mantle olivine and application to mantle petrogenesis and geothermobarometry. *Chemical Geology* 270:196–215. doi: 10.1016/j.chemgeo.2009.11.017
- Gurney JJ, Jakob WRO, Dawson JB (1979) The Mantle Sample: Inclusion in Kimberlites and Other Volcanics. American Geophysical Union, Washington, D. C., 227-243. doi: 10.1029/SP016p0227
- Hops JJ, Gurney JJ, Harte B (1992) The Jagersfontein Cr-poor megacryst suite: towards a model for megacryst petrogenesis. *Journal of Volcanology and Geothermal Research* 50, 143–160.
- Nehru CE, Reddy AK (1989) Ultramafic xenoliths from Wajrakarur kimberlites, India. In: J. Ross, et al. (Eds.), *Kimberlites and Related Rocks*, Proceedings of the Fourth International Kimberlite Conference, Vol. 2. Geol. Soc. Australia Spl. Pub. 745–759.
- Shaikh AM, Patel SC, Ravi S, Behra D, Pruseth KL (2016) Mineralogy of the TK1 and TK4 “kimberlites” in the Timmasamudram cluster, Wajrakarur Kimberlite Field, India: Implications for lamproite magmatism in a field of kimberlites and ultramafic lamprophyres. *Chemical Geology*. doi: 10.1016/j.chemgeo.2016.10.030.
- Stone RS, Luth RW (2016) Orthopyroxene survival in deep carbonatite melts: implications for kimberlites. *Contributions to Mineralogy and Petrology* 171, 1–9. doi:10.1007/s00410-016-1276-2



The Geology of the Faraday 1 Kimberlite, NWT, Canada

Lindsay Nelson¹, Casey Hetman², Michael Diering³

¹ Aurora Geosciences Ltd., Yellowknife, Canada, lindsay.nelson@aurorageosciences.com

² SRK Consulting, Vancouver, Canada, chetman@srk.com

³ SRK Consulting, Vancouver, Canada, mdiering@srk.com

Introduction

The Faraday 1 kimberlite is located in the southeastern Slave Craton, approximately 10 km northeast of the Gahcho Kué Diamond Mine. The diamondiferous Faraday 1 body is part of the Kelvin-Faraday kimberlite cluster. Preliminary age-dating of the Kelvin kimberlite indicates a late Proterozoic to early Cambrian age of emplacement; it is probable that the Faraday kimberlites are contemporaneous, though no age-dating has been completed. Faraday 1 is the furthest towards the northeast of the pipes in the cluster and adjacent to the Faraday 3 kimberlite. The kimberlite subcrops below a shallow lake and is covered by a thin layer of lake-bottom sediments and glacial till. The host rock consists of metaturbidites of the Yellowknife Supergroup with minor amphibolite and narrow diabase dikes. Archean granitoids occur immediately to the west of the kimberlite cluster. Coherent kimberlite was first discovered in the Faraday 1 area by De Beers Canada in 2001. Since 2012, Kennady Diamonds Inc. has completed geophysical surveying and extensive drilling programs resulting in the discovery of volcanoclastic kimberlite and the delineation of the kimberlite complex. Faraday 1 has a tube-like shape that is inclined at 25° towards the northwest; the central kimberlite body is over 190 m long and varies in width between 30 and 60 m. The other kimberlites in the Kelvin-Faraday cluster also display non-typical inclined pipe morphologies with similar orientations and are dominantly infilled with volcanoclastic kimberlite. All of these pipes are associated with extensive hypabyssal kimberlite sheet systems, some of which have strike lengths exceeding 1000 m. Faraday 1 is the smallest of the kimberlite pipes in the cluster, and it has the highest proportion of hypabyssal kimberlite associated with sheets.

Evaluation

Detailed logging of drill core, petrography, and microdiamond sampling were used to define the complex internal geology of Faraday 1 and produce a 3D model of the kimberlite (Figure 1). A total of 42 core holes and four 11-inch diameter reverse circulation (RC) holes were completed at Faraday 1. Drill core and RC samples were logged in detail using a binocular microscope. Representative samples from 20 holes across the body were selected for a petrographic investigation comprising 137 kimberlite thin sections and 54 country rock and marginal breccia thin sections. A total of 2,228 kg of kimberlite drill core was processed by caustic fusion at the Geoanalytical Laboratories Diamond Services of the Saskatchewan Research Council (SRC); the diamond recoveries are summarized in Table 1.

| Unit | Sample Weight (dry tonnes) | Number of Diamonds According to Sieve Size Fraction (mm) | | | | | | | | | | | | Total Stones | Total Carats (+0.85 mm) |
|-------|----------------------------|--|------------------|------------------|------------------|------------------|------------------|------------------|------------------|------------------|------------------|------------------|------------------|--------------|-------------------------|
| | | +0.106 -0.150 | +0.150 -0.212 | +0.212 -0.300 | +0.300 -0.425 | +0.425 -0.600 | +0.600 -0.850 | +0.850 -1.180 | +1.180 -1.700 | +1.700 -2.360 | +2.360 -3.350 | +3.350 -4.750 | +4.750 -6.700 | | |
| KDYKE | 0.2694 | 688 | 419 | 248 | 146 | 87 | 44 | 20 | 13 | 1 | - | - | 1 | 1,667 | 2.1567 |
| KIMB1 | 1.0049 | 1,006 | 671 | 368 | 211 | 113 | 57 | 37 | 20 | 8 | 6 | - | - | 2,497 | 3.2036 |
| KIMB2 | 0.1128 | 236 | 155 | 95 | 56 | 27 | 23 | 12 | 5 | 3 | 1 | - | - | 613 | 1.1692 |
| KIMB3 | 0.2809 | 940 | 547 | 309 | 188 | 101 | 67 | 29 | 13 | - | - | - | - | 2,194 | 0.6536 |
| KIMB4 | 0.0838 | 124 | 75 | 56 | 27 | 15 | 8 | 4 | 3 | 1 | - | - | - | 313 | 0.2021 |
| KIMB5 | 0.1781 | 245 | 164 | 85 | 71 | 38 | 25 | 13 | 5 | 1 | 1 | - | - | 648 | 0.6518 |
| MB | 0.2977 | 82 | 55 | 27 | 10 | 3 | 1 | 2 | - | - | - | - | - | 180 | 0.0162 |

Table 1: Summary of diamond recovery results by unit.

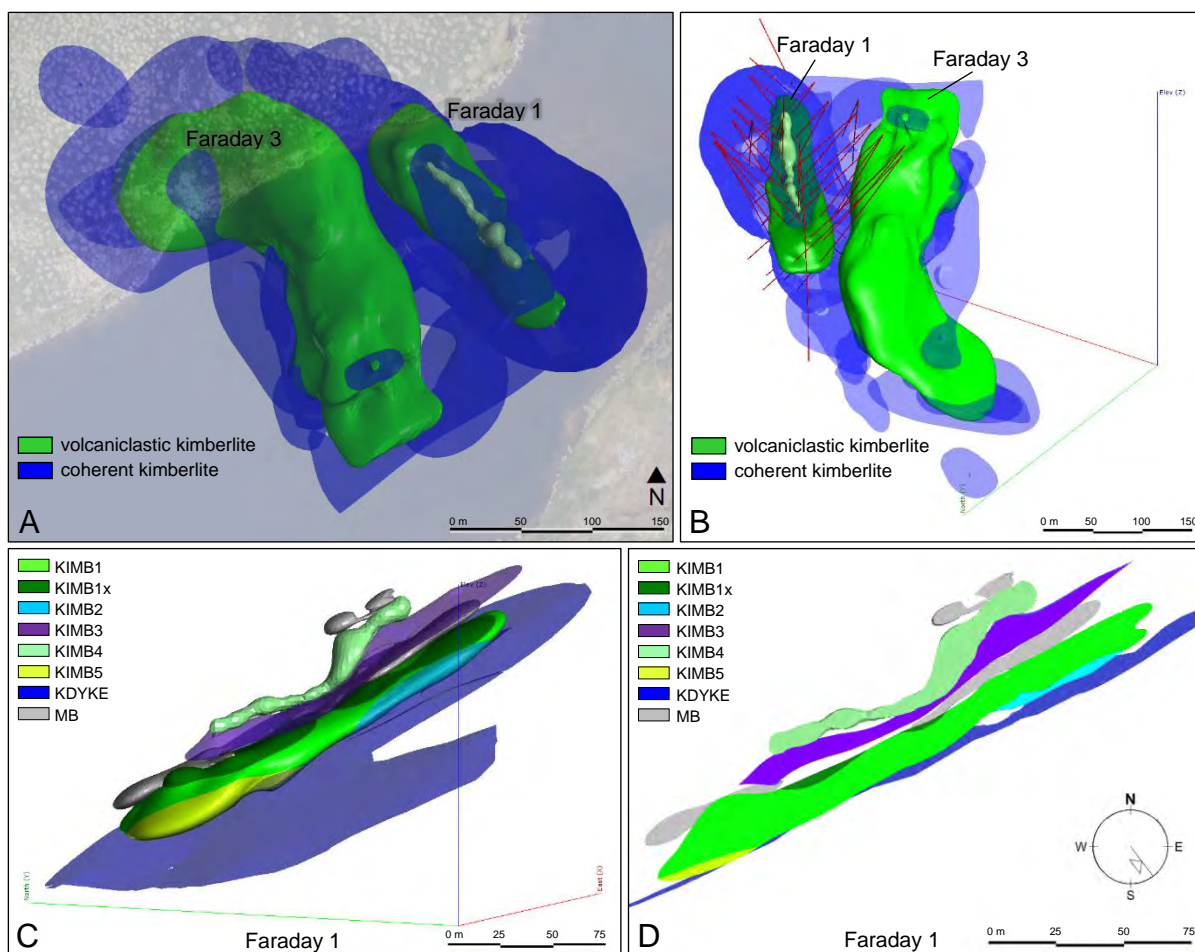


Figure 1: 3D model of the Faraday 1 kimberlite and associated Faraday 3 pipe. (A) Plan view with the surrounding hypabyssal sheet complex; (B) Oblique view of the Faraday 1 and 3 kimberlites, looking southeast, with the traces of diamond drill holes on the Faraday 1 kimberlite; (C) Detailed geology model of Faraday 1 looking northeast; KIMB1: volcaniclastic phlogopite kimberlite, KIMB1x: variation of KIMB1 with high country rock dilution, KIMB2: coherent phlogopite kimberlite with coherent kimberlite autoliths and 3-10% country rock, KIMB3: coherent phlogopite-monticellite kimberlite, KIMB4: volcaniclastic to transitional phlogopite kimberlite, KIMB5: volcaniclastic to transitional phlogopite kimberlite with coherent kimberlite autoliths, KDYKE: hypabyssal kimberlite sheet, MB: marginal breccia. (D) Long section of Faraday 1 looking northeast.

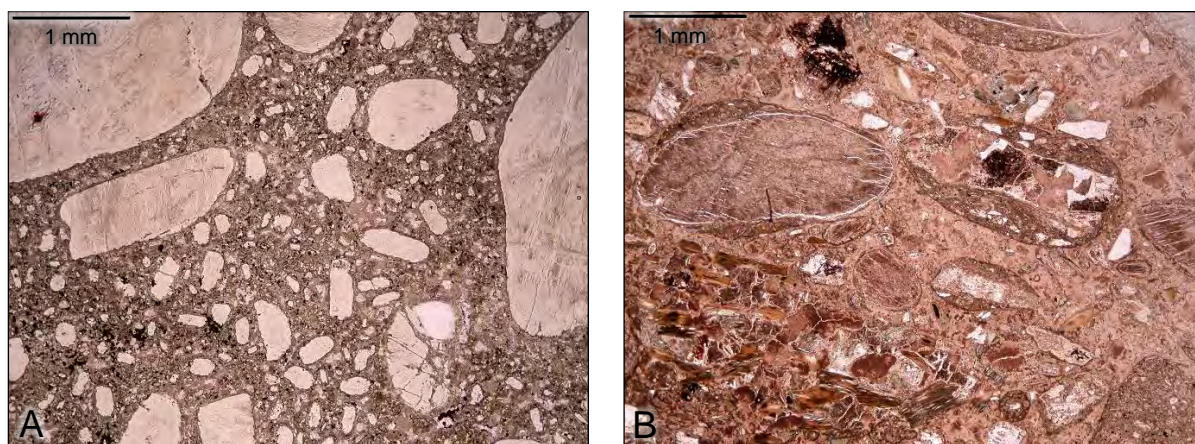


Figure 2: Photomicrographs of the two textural end-members at Faraday 1. (A) Coherent phlogopite-monticellite kimberlite (KIMB3); olivine-rich with a crystalline groundmass containing segregations of serpentine and carbonate. (B) Volcaniclastic phlogopite kimberlite (KIMB1); olivine-rich with abundant country rock shards and well-developed pelletal-shaped magmaclasts.

Geology

Faraday 1 is a complex volcanic system containing both coherent rocks and rocks formed by explosive fragmentation processes. The dominant rock types are a fine- to coarse-grained olivine-rich phlogopite-monticellite hypabyssal kimberlite (KIMB3) and a fine- to medium-grained olivine-rich volcanoclastic phlogopite kimberlite (KIMB1). KIMB3 is characterized by a uniform olivine distribution and well-developed crystalline groundmass containing phlogopite, spinel, and monticellite with irregular segregations of serpentine and carbonate. Country rock dilution is visually estimated at 0-5%. Mantle-derived indicator minerals are rare and primarily consist of peridotitic garnet. KIMB1 contains distinctive pelletal-shaped magmaclasts with well-formed elongate phlogopite laths in the melt selvages; the rock is massive and unsorted with 30-60% dilution by country-rock xenoliths. Country rock xenoliths consist of locally-derived metaturbidite and amphibolite with rare diabase and granitoid. A number of minor kimberlite units have also been identified (Figure 1: KIMB2, KIMB4, KIMB5). These units encompass a range of textures from coherent to transitional and volcanoclastic. There is also a marginal breccia (MB) composed of angular locally-derived xenoliths set within a fine-grained, variably-sorted matrix of pulverized country rock with trace amounts of kimberlitic material.

The spatial relationships between the rock units of Faraday 1 are complicated. KIMB1, KIMB2, and KIMB5 infill the central tube-shaped pipe, which is surrounded by layers of shallowly-dipping hypabyssal kimberlite sheets and a small external volcanoclastic body (Figure 1). Sharp contacts and cross-cutting relationships exist between kimberlite units, indicating the presence of multiple phases of kimberlite related to distinct emplacement events.

Conclusions

Following detailed petrography, volcanoclastic rocks at Faraday 1 are further classified as Kimberley-type pyroclastic kimberlite (KPK), formerly called tuffisitic kimberlite breccia (TKB) (Smith et al., 2013). The association of hypabyssal kimberlite sheets with volcanoclastic pipes is typical of KPK systems worldwide. However, the inclined orientation of the Faraday 1 pipe is unusual outside of the Kelvin-Faraday cluster.

The textures, mineralogy, and significantly diamondiferous nature of the kimberlite units at Faraday 1 are similar to the other bodies in the Kelvin-Faraday cluster and the Gahcho Kué kimberlite cluster (Hetman et al. 2004).

Faraday 1 is the least volcanically mature of the kimberlite pipes in the cluster discovered to date. It is dominated by thick hypabyssal kimberlite sheets and irregular intrusions layered with thin volcanoclastic units, and marginal breccia. Intervals of intact country rock are present between kimberlite units; in some cases, it cannot be determined if these intervals are in-situ or represent xenoliths.

Faraday 1 is open at depth, and additional drilling is required to establish the full extent of the kimberlite. The first bulk sample from Faraday 1 was completed in 2017, with the collection of 25 tonnes of kimberlite by 11-inch reverse circulation drilling. The macrodiamond results from this sample will provide further information about the grade and preliminary diamond value that will be used to support a possible resource classification.

References

- Hetman, C. M., Smith, B. S., Paul, J. L., & Winter, F. (2004). Geology of the Gahcho Kue kimberlite pipes, NWT, Canada: root to diatreme magmatic transition zones. *Lithos*, 76(1), 51-74.
- Smith, B. S., Nowicki, T. E., Russell, J. K., Webb, K. J., Mitchell, R. H., Hetman, C. M., and Robey, J. A. (2013). Kimberlite terminology and classification. In *Proceedings of 10th International Kimberlite Conference* (pp. 1-17). Springer India.



Microinclusions in diamonds from deposits of different genetic kimberlite types

Kriulina G.Yu., Garanin V.K., Vasiliev E.A., Zedgenizov D.A., Bobrov A.V., Vasiliev R.V., Vyatkin S.V.

¹*M.V. Lomonosov Moscow State University, Moscow, Russia;* ²*Saint-Petersburg Mining University, Saint-Petersburg, Russia;* ³*V.S. Sobolev Institute of Geology and Mineralogy of the Russian Academy of Sciences, Russia*
galinadiamond@gmail.com

Kimberlitic rocks represent the complex heterogeneous system including both mantle and crustal substrates in various proportions. Researchers of magmatic rocks widely apply and detail the different mineralogical and petrogeochemical classification schemes in dependence of the region studied. Traditionally, Al and Mg–Fe mineralogical types of kimberlites are distinguished.

The analyzed petrochemical types of kimberlites included the low-titanium ($\text{TiO}_2 < 1\%$, Al-type kimberlite) and mid-titanium ($1 < \text{TiO}_2 < 2,5\%$, Mg–Fe-type kimberlite) varieties. The analysis of the content of defect-structural centers in diamonds from different petrochemical types of kimberlites was performed in this study [Kriulina et al, 2011, 2012; Zedgenizov et al 2004, 2007, 2009, 2015, 2016].

Geochemical studies of syngenetic mineral and crystal/fluid inclusions in diamonds provide evidence for existence of multicomponent diamond-forming substrate in the Earth's mantle. Long-term complex studies of natural diamonds and experiments in this field allowed researchers to conclude that the mantle environment of diamond crystallization is represented by volatile-rich melts or fluids [Logvinova et al., 2008; Anand et al, 2004; Boyd, Gurney, 1986; Bulanova 1995]. In recent years, fluid and fluid-bearing inclusions have been studied in diamonds of different genesis [Israeli et al, 2011; Klein-BenDavid et al 2004 and others].

We suggested that the presence of microinclusions was controlled by the character of crystal growth being determined by the diamond formation depth. The classic mineralogy of diamond [Orlov, 1984; Sobolev, 1978 and others] assumes that layered growth of diamond crystals is supported by high temperatures and long occurrence of crystals under the favorable conditions.

Analyzing the results of our studies and numerous published data, we can make some conclusions. The deepest crystals of octahedral and dodecahedral habit with layered and layered-zoned internal structure are characterized by chloride and chloride-carbonate inclusions of high alkalinity (SEM data), as well as by enrichment in H_2O (the data of IR spectroscopy).

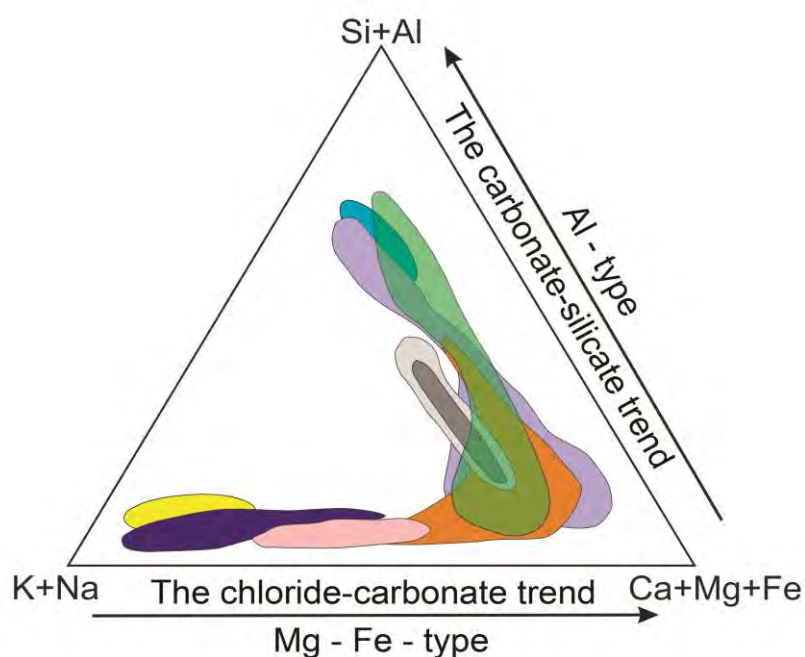
Octahedral diamonds with cloudy inclusions demonstrating change in mechanisms of growth and predomination of octahedral sectors at the final stage have silicate and aluminosilicate compositional trends of microinclusions (i.e. are less deep than the group of diamonds with chloride inclusions).

Crystals of cubic habit (cuboids, tetrahedroids, and dodecahedroids) are the most shallow, have microfibrinous structure and carbonate composition of microinclusions in all studied pipes. These are yellow cuboids with fibrous structure and colorless or gray cube with zoned-sectorial structure.

Marginal areas of coated diamond contains both carbonate and aluminosilicate inclusions (the carbonate-silicate trend).

Significant overlap in the carbonate-rich compositional area shows that carbonate melt is an important environment of the diamond formation in deep zones of the continental lithosphere [Bogysh et al, 2016; Zedgenizov et al 2004, 2007, 2009, 2015, 2016; Bobrov et al, 2011].

Fig. 1 shows the composition of microinclusions in diamonds from kimberlites of the different genetic types.



Fields of the composition of microinclusions in diamonds from different pipes:

Internatsional'naya, violet; Udachnaya, orange;

Komsomol'skaya, yellow; Mir, blue; Arkhangelskaya and Karpinsky, green, semi-transparent; Diavik (Canada), blue; Jwaneng (Botswana), light-gray; Coffiefontain (South Africa), rose; Brazil, gray.

Fig. 1. Compositional fields of melt/fluid microinclusions in diamonds from the different deposits worldwide. The fields are shown according to the results of original studies of Russian diamonds [Bogysh et al, 2016; Zedgenizov et al 2004, 2007, 2009, 2015, 2016; Bobrov et al, 2011] and data on foreign deposits.

Diamonds from kimberlite of the Al-type are characterized by the presence of nanosized inclusions of the carbonate-silicate composition. Increase in the silicate component content indicates increase in the depth of diamond formation.

Diamonds from kimberlite of the Mg-Fe type contain microinclusions of the chloride-carbonate composition and hydrous fluid inclusions. Since these are the deepest diamonds, mostly of the octahedral and dodecahedral habits, they are characterized by the layered growth and sometimes by thin rim overgrowing an octahedral crystal. Diamonds with layered growth mechanism contain single inclusions, almost indistinguishable because of small sizes. Among the daughter phases of microinclusions are phlogopite, biotite; IR spectra contain molecular water and OH groups.

Continuous transitions between the parameters of the composition of water and silicate and carbonate inclusions confirm – “melts” with increased carbonate component are the most effective host-environment for diamonds crystallization and growth. Significant

overlap in composition range enriched by carbonates does not permit a reliable conclusion about the specific diamondiferous deposit (field).

References

1. *Anand M., Taylor L.A., Misra K.C. et al.* (2004) Nature of diamonds in Yakutian eclogites: views from eclogite tomography and mineral inclusions in diamond // *Lithos*. 77. P. 333-348.
2. *Bobrov A.V., Litvin Yu.A., Dimshic A.M.* (2011) Experimental studies of carbonate-silicate mantle systems in connection with the problem of diamond formation. M.:GEOS, 208 c.
3. *Bogush I.N., Specius Z.V., Kovalchuk O.E., Pomazanskiy B.S.* Distribution of structural impurities and fluid microinclusions in crystals of cubic habitus and coated diamond from Yubileynaya pipe (Yakutia) (2016) *Geochemistry* № 8. - P. 708-717.
4. *Boyd F.R., Gurney J.J.* (1986) Diamonds and the African lithosphere // *Science*. 232. P. 472-477.
5. *Bulanova G.P.* (1995) The formation of diamond // *J. Geochem. Explor.* 53. P. 1-23
6. *Izraeli E.S., Harris J.W., Navon O.* Fluid and mineral inclusions in cloudy diamonds from Koffiefontein, South Africa // *Geochim. Cosmochim. Acta*. 2004. V. 68. P. 2561-2575.
7. *Kriulina, G.Yu., Garanin, V.K., Vasilyev, E.A., Kyazimov, V.O., Matveeva, O.P., and Ivannikov, P.V.* (2012). New Data on the structure of diamond crystals of cubic habitus from the Lomonosov deposit. *Moscow University Geological Bulletin*, 67, Issue 5, 282-288.
8. *Kriulina G.Yu., Garanin V.K., Rotman A.Ya., Koval'chuk O.E.* (2011) Peculiarities of Diamonds from the Commercial Deposits of Russia// *Moscow University Geology Bulletin*, том 66, № 3, c. 171-183
9. *Klein-Ben David O., Izraeli E.S., Hauri E., Navon O.* (2004) Mantle fluid evolution – a tale of one diamond // *Lithos*. V. 77. P. 243-253.
10. *Logvinova A.M., Wirth R., Fedorova E.N., Sobolev N.V.* Nanometre-sized mineral and fluid inclusions in cloudy Siberian diamonds: new insights on diamond formation // *Eur. J. Mineral.* 2008. V. 20. P. 317-331.
11. *Orlov Y.L.* (1984) *Mineralogy of the diamond*. Nauka, 263c.
12. *Sobolev E.V.* (1978) Nitrogen centers and growth of natural diamond crystals// *Problems in the petrology of the earth's crust and upper mantle*. Novosibirsk. C. 245-255.
13. *Zedgenizov D., Rubatto D., Shatsky V., Ragozin A., Kalinina V.* (2016) // Eclogitic diamonds from variable crustal protoliths in the northeastern Siberian craton: Trace elements and coupled $\delta^{13}\text{C}$ – $\delta^{18}\text{O}$ signatures in diamonds and garnet inclusions // *Chemical Geology*. v. 422, pp. 46-59.
14. *Zedgenizov D.A., Kagi H., Shatsky V.S., Sobolev N.V.* (2004) Carbonatitic melts in cuboid diamonds from Udachnayakimberlite pipe (Yakutia): evidence from vibrational spectroscopy // *Mineral. Mag.* V. 68 (1). P. 61-73.
15. *Zedgenizov D.A., Ragozin A.L., Shatsky V.S., Araujo D., Griffin W.L., Kagi H.* (2009) Mg and Fe-rich carbonate-silicate high-density fluids in cuboid diamonds from the Internationalnayakimberlite pipe (Yakutia) // *Lithos*, v. 112S, pp. 638-647.
16. *Zedgenizov D.A., Rege S., Griffin W.L., Kagi H., Shatsky V.S.* (2007) Composition of trapped fluids in cuboid fibrous diamonds from the Udachnaya kimberlite: LAM-ICPMS analysis // *Chem. Geol.* V. 240. P. 151-162.
17. *Zedgenizov D.A., Shatsky V.S., Panin A.V., Evtushenco O.V., Ragozin A.L., Kagi H.* (2015) Evidence for phase transitions in mineral inclusions in superdeep diamonds of the São Luiz deposit (Brazil) // *Russian Geology and Geophysics*, v. 56, pp. 296-305.
18. *Zedgenizov D.A., Yefimova E.S., Logvinova A.M., Shatsky V.S., Sobolev N.V.* (2001) Ferropericlae inclusions in a diamond microcrystal from the Udachnayakimberlite pipe, Yakutia // *Doklady Earth Sciences*, Vol. 377a, No 3, pp. 319-321.



Forecast diamond quality in the deposit

Kriulina G. Yu., Garanin V. K.,

M.V. Lomonosov Moscow State University, Moscow, Russia; galinadiamond@gmail.com

Comparative analysis of diamond features and the host kimberlite rocks from the mines of Arkhangelsk and Yakutia diamond provinces enabled to establish the relationship between typomorphic groups of diamond and certain petrochemical type of kimberlite rocks. The most similar parameters have diamonds from the same field and same petrochemical type of kimberlite rocks. The kimberlite productiveness decreases depending on titanium oxide content in the rocks; with that the content of diamonds with high grade of nitrogen aggregation into the B-form and platelets concentration increases. The relationship between features and quality of diamonds and host rocks is understood.

INTRODUCTION

The diamond raw quality is determined upon the popular “4C” system (carat, color, clarity, cut (habit)) base, describe these parameters from mineralogical and gemological view. Analyze the economic based deposit work off on the diamond quantity and quality knowledge base.

OBJECTS and INVESTIGATION METHODS

The research object is diamond raw probes from diamondbearing provinces: Arhangel (ADP, Arkhangelskaya, Karpinskovo-1, n.a. Grib pipes) and Yakutsk (YDP, Botuobinskaya, Nyurbinskaya, Internationalnaya, Mir, Udachnaya, Yubileinaya, Komsomolskaya pipes). The diamond weight is from 0,15 until 1,00 ct. The investigations were held for the ten thousands diamond crystals.

The methods: optic and scanning electron microscopy (SEM), colored cathodoluminescence, optic spectroscopy in infrared (FTIR), ultraviolet and visible range, photoluminescence spectroscopy under xenon lamp light energization within 250-600 nm waves range and electron paramagnetic resonance (EPR).

The crystals infrared spectra registration are held with Furie spectrometer VERRTEX-70 by Bruker company with Hyperion 1000 microscope help in 400-5000 cm^{-1} range. The automatic program provides 2.8 cm^{-1} spectrum split width. The absorption peaks re-count upon quantity content are held according [Boyd et al, 1994, 1995; Khachatryan, 2010]. The platelets (P) and hydrogen centres relative content within diamonds is estimated according absorption band coefficients upon 1370-1365 and 3107 cm^{-1} . The P size is determined according band maximum position on 1370-1365 cm^{-1} [Kvaskov et al, 1997].

THE RESULTS AND THEIR DISCUSSION

The modern investigators (Bogatikov et al 2010; Vasilenko et al 1997 and others) prefer the TiO_2 indicator role for marking kimberlite types, because its low content reflects high pressure during kimberlite origin [Garanin et al 2009]. The common classification based on dividing kimberlite into three petrogeochemical types was suggested [Bogatikov et al 2010]: low-titanium ($\text{TiO}_2 < 1.0$ mas.%) (LTT), medium-titanium ($1.0 < \text{TiO}_2 < 2.5$ mas.%) (MTT) and high-titanium ($\text{TiO}_2 > 2.5$ mas.%).

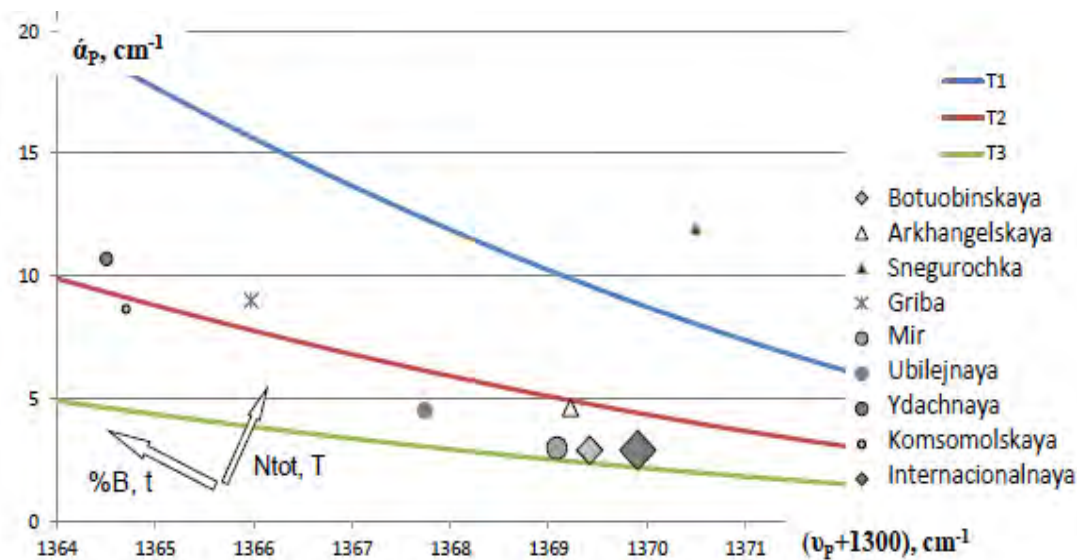
COLOR. The LTT kimberlite diamonds are characterized by the most color spectrum and the more colored diamonds occurrence frequency with octahedron-dodecahedron habit. The yellow, grey, smoky-brown colored crystals are prevailed. It is important to emphasize that one can find the fancy colored samples: pink-violet, light blue, orange (red-brown), yellow. The colorless stones proportion is minimum (less than 10%), together with slightly colored diamonds is amounted 20-25%. The yellow crystals with different intensity dominate (30-54%) [Zinchuk, Koptil, 2003; Kriulina et al, 2011]. Colorless and slightly colored

overload (dominate) among octahedron and dodecahedron habit diamond crystals within MTT kimberlites (33-60%). Yellow-colored samples with noticeable tone proportion is minor (9-19%). Smoky-brown colored stones are widely spread with plastic deformation upon dislocation vanish mechanism [Synthesis of minerals, 2000].

HABIT. It is necessary in case diamond quantity estimation within pipe to take into consideration I type diamonds because they are potentially jewelry raw-stuff. Jewelry yellow rough cubic is rare. The I type diamonds are 77-88% within LTT kimberlites, except Internationalnaya pipe 98%. The typomorphic characteristic Zolotitskaya field diamonds is a cubic habit diamonds significant spreading. Existing to 10% coated diamond is typomorphic to the Nakinskii field pipes.

THE KIMBERLITE BODIES SHAPING. THE DEFECTIVE-ADMIXTURE DIAMOND CONTENT

The diamonds from each petrochemical types deposits, inspite of nitrogen gross content wide variation, are characterized by the close value %B and playlets. The defects transformation occurs at high temperature (in B and P) [Synthesis of minerals, 2000; Taylor, Milledge,1995] and are accompanied by diamond oxide dissolution which (diamond) was in maternal rocks before kimberlite source forming(shaping). The diamonds from low-titanium type kimberlites ($TiO_2 < 1.0$ mas.%. LTT) and medium-titanium type ($1.0 < TiO_2 < 2.5$ mas.%. MTT) are detached into two area on diagram (pic.1). The infrared spectroscopy data were taken into consideration only from octahedron to dodecahedron habit crystals because they are dominate in all pipes that's why fully characterize the deposit.



Pic.1. Diagram of diamonds from low-titanium type kimberlites ($TiO_2 < 1.0$ mas.%) and medium-titanium type ($1.0 < TiO_2 < 2.5$ mas.%) are detached into two area on diagram. $T1 < T2 < T3$.

The diamonds with the most playlets absorption coefficient which is in proportion to this defect content within crystal and the absorption band maximum position is in longwave range grew during the most high temperature conditions. They are the diamonds from Udachnaya, Komsomolskaya, n.a. Grib pipes. The crystals from Internacionalnaya, Mir, Botuobinskaya, Arkhangelskaya, n.a. Karpinskogo-1 grew in less temperature conditions. The epigenetic diamond evolution process is manifested in structure defects transformation, cryastalmorphology changing and sometimes colors, these proceses are connected to each other but can be detached.

CONCLUSION

The kimberlite peridotite and eclogite enrichment most ancient calculated age correlate with short-lasting diamonds after crystallization annealing during which the defects transformation is possible, and low grade nitrogen defects aggregation. The pipes with the most ancient enrichment age are characterized by the certain diamonds morphogenetic groups prevalence depending on kimberlite type of rocks: nitrogenless and with high nitrogen for the LTT bodies [Kriulina et al, 2013]. The kimberlite bodies potential mantle diamondbearing is determined by phisic-chemistry criteria which suggested by Sobolev V.S., Sobolev N.V., Marakuhev and others.

One can forecast in pipes with low titanium content $TiO_2 < 1$ mas.% within kimberlite and enrichment age more than 1 billion years [Bogatikov et al, 2010] the more diamond amount with yellowish nadre and tone. The pink-lilac, lilac (M2 defect) colored diamonds occurance possibility increase [Mineeva et al, 2007]. If the enrichment age is reduced until 0.6 billion years the colorless (with defects in complex A.B.P-forms) and smoky-brown stones (N2, W7 defects) is increased. During the longlasting elevation diamond material to the earth surface the conditions for its oxidation are created, i.e. the habit transformation into dodecahedron with weight loss until its full dissolving and recrystallization also and growth cubic and coated diamonds.

The real kimberlite productivity (i.e. the possible mantle diamondbearing decrease) depends on time of influence high-temperature mantle and the most low-temperature inside-pipe metasomatic proceses. These proceses appear in kimberlite rocks matrix according diversity, spinel trend extention, the reaction minerals development, in diamond – according the nitrogen aggregation grade and curve-facets habits spreading.

By styidiing the kimberlite rocks petrochemical content, the oxide mineralization feature we can forecast kimberlite bodies diamondbearing and come close to undirect estimate the pay working off perspective with considering the diamond raw quality.

References

1. Bogatikov OA, Kovalenko VI, Sharkov EV Magmatism, tectonics, geodynamics of the Earth: connection in time and space M.: Nauka, 2010. 606p.
2. Boyd S. R., Kiflawi I., Woods G. S. The relationship between infrared absorption and the A defect concentration in diamond // *Phil. Mag.*, B. 1994. V. 69. P. 1149–1153.
3. Boyd. S. R., Kiflawi I., Woods G. S. Infrared absorption by the B nitrogen aggregate in diamond // *Phil. Mag.*, B. 1995. V. 72. P. 351–361.
4. Garanin VK Bovkun AV, Garanin KV, Rothman AYa., Serov IV. Microcrystalline oxides from kimberlites and related rocks of Russia. M.: MSU, 2009. 498 p.
5. Kvaskov VB, Vecherin PP Zhuravlyov V.V. Natural diamonds of Russia. M.: Polaron. 1997. 230 p.
6. Khachatryan G.K. Typification of diamonds from kimberlites and lamproites in the distribution of nitrogen centers in crystals // *Ores and minerals*, 2010. No. 2. P. 46-60.
7. Kriulina G.Yu, Garanin V.K., Rotman A.Ya, Koval'chuk O.E. (2011) Peculiarities of Diamonds from the Commercial Deposits of Russia// *Moscow University Geology Bulletin*, том 66, № 3, с. 171-183
8. Kriulina G.Yu, Garanin V.K., Samosorov G.G. Forecasting the quality of diamond in deposits of different petrochemical type. *News of higher educational institutions. Geology and exploration*. M. № 6.
9. Mineeva R.M., Speransky A.V., Titkov S.V., Zudin N.G. The ordered creation of paramagnetic defects at plastic deformation of natural diamonds // *Physics and Chemistry of Minerals*. 2007. V. 34. № 2. P. 53-58.
10. *Synthesis of minerals*. Tom.3 Aleksandrov: VNIISIMS, 2000. 345p.
11. Taylor W.R., Milledge H.J. Nitrogen aggregation character, thermal history and stable isotope composition of some xenolith-derived diamonds from Roberts Victor and Finch // *Extended Abstr. of the 6-th Int. Kimberlite Conf. Novosibirsk*, 1995. P. 620–622.
12. Vasilenko VB, Zinchuk NN, Kuznetsova LG Petrochemical models of diamond deposits in Yakutia. M.: Nauka, 1997. 575p.
13. Zinchuk NN, Koptil VI Typomorphism of diamonds of the Siberian platform. M.: OOO «Nedra-Bisnescentre». 2003. 603 p.

Formation of dunite xenoliths in kimberlites and ailikites; petrographic and mineral compositions from a deformed xenolith in the Majuagaa kimberlite dike, Greenland

Nicholas Arndt¹, Carole Cordier¹, Troels Nielsen², Valentina Batanova¹, Anne-Marie Boullier¹, Igor Ashchepkov³

1- ISTERre, Univ. Grenoble Alpes, F-38400 Grenoble, France; nicholas.arndt@univ-grenoble-alpes.fr; 2 – GEUS, Øster Voldgade 10, DK-1350 Copenhagen, Denmark; tfn@geus.dk; 3 - Institute of Geology and Mineralogy SD RAS, Koptyug ave 3, Novosibirsk, Russian Federation; igor.ashchepkov@igm.nsc.ru

Metasomatism accompanying deformation produces dunite

Kimberlites carry a dense cargo of olivine. Although normally referred to as "macrocrysts", much of this olivine is present in the form of intact or disaggregated multi-grain xenoliths of dunite. Within individual xenoliths, compositions are very constant, but the population as a whole displays a large variation in Fo content accompanied by lesser variation in Ni and other minor elements. The compositions of dunite xenoliths in kimberlites differ from those of normal mantle peridotites because, in the latter, a decline in Fo content is normally accompanied by an increase in the abundance of opx, cpx and an Al-phase. We propose that the dunite xenoliths in kimberlites result from interaction between mantle peridotite and CO₂-rich fluid from the asthenosphere, a process that removed silicate minerals other than olivine produced a silica-bearing carbonate melt (bonafide kimberlite) or CO₂-rich silicate melt (ailikites).

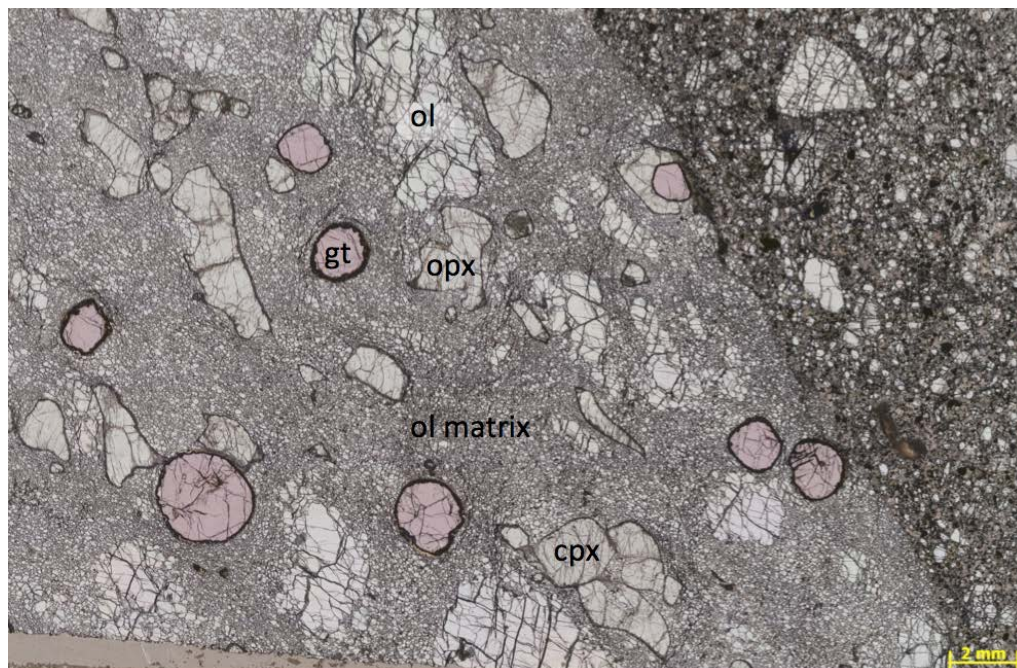


Figure 1: Image of a garnet-lherzolite xenolith in sample 491719, a kimberlite from the Maniitsoq region, in southern West Greenland.

PT conditions

A garnet-lherzolite xenolith in a kimberlite from the Maniitsoq region, in southern West Greenland, catches the process in the act. The xenolith is strongly deformed and olivine (85%) has been transformed into large porphyroclastic relicts (1-5 mm) which lie in a mosaic of much smaller olivine crystals (50-200 microns). Garnets (6%) are isolated almost spherical; orthopyroxene (8%) and rare

clinopyroxene (1%) are blade-shaped with common embayments. The matrix consists entirely of olivine and has a dunitic composition.

Electron microprobe analyses in the studied sample reveal that porphyroclastic and matrix olivine has the same composition ($Fo = 91.3 \pm 0.03$, $n=67$), a composition in equilibrium with opx ($Mg\# = 92.3 \pm 0.001$, $n = 16$) and the other minerals. Geothermometry and geobarometry using all four phases defines the PT conditions between these phases: $T = 1221-1281^\circ\text{C}$, $P = 53-60$ kbar. These conditions correspond to those in the lower part of the lithosphere, with temperatures slightly above a normal craton geotherm (43mw/m^2). This shows that the digestion of orthopyroxene occurred within the mantle rather than during the transport of the xenolith in the kimberlite melt en route to the surface.

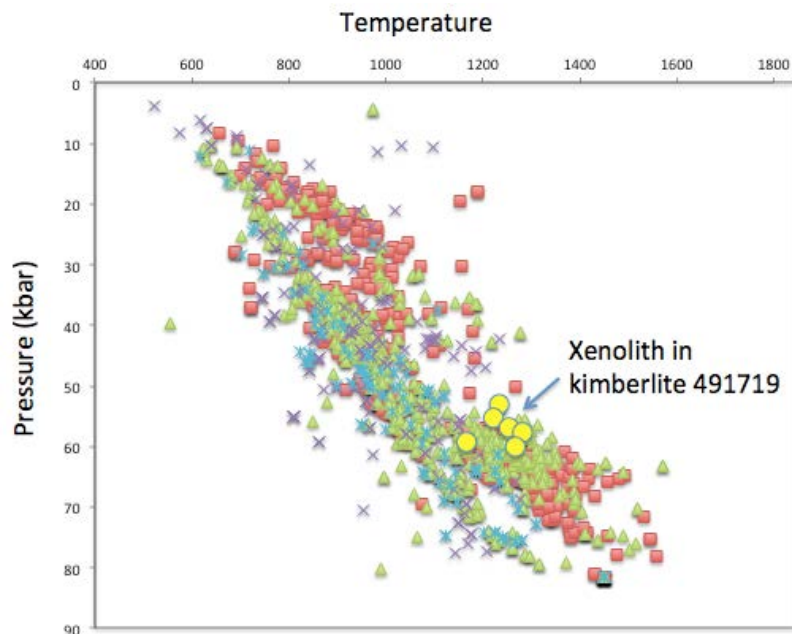


Figure 2: Pressure temperature diagram showing calculated equilibrium conditions for minerals in the kimberlite sample 491719 and in xenoliths from other locations (data from I. Ashchepkov, unpublished.)

Marginal zones

In another kimberlite from the same area, thin marginal zones in which the Ni content plummets as Fo content remains nearly constant surround microxenoliths of dunite and isolated olivine grains. These olivine margins are believed to have crystallized directly from the kimberlite melt. If a high Ni partition coefficient is adopted ($D_{Ni} > 20$), crystallization of olivine alone, without orthopyroxene dissolution, can explain the trends (Cordier et al., 2015).

Conclusion

From these results we propose that almost all olivine in kimberlites, with the exception of the marginal zones, are fragments of dunite that was produced during interaction between mantle peridotite and CO_2 -rich fluid and that this interaction occurred immediately before or during deformation, near the base of the lithosphere.

References

Cordier, C., Sauziat, L., Arndt, N.T., Boullier, A.-M., Batanova, V., Barou, F. (2015) Metasomatism of the lithospheric mantle immediately precedes kimberlite eruption: new evidence from olivine composition and microstructures. *Journal of Petrology* 56, 1775-1796

The emplacement of Voorspoed pipe, South Africa: a tale of incremental pipe growth, tephra jets, mixing, and a shallow crater

Alexandrina Fulop¹, Stephan Kurszlauskis¹, Ricardo Rodrigues², Johann Stiefenhofer³

- ¹ De Beers Canada; 300-1601 Airport Rd., Calgary, Alberta, T2E 6Z8;
Alexandrina.Fulop@debeersgroup.com; Stephan.Kurszlauskis@debeersgroup.com
- ² De Beers Consolidated Mines (Pty) Ltd; Voorspoed Mine; PO Box 1964, Kroonstad, 9500
Ricardo.Rodrigues@debeersgroup.com
- ³ MinRes, Corporate Division, Anglo American Operations Ltd, Johannesburg, South Africa;
Johann.Stiefenhofer@debeersgroup.com

Introduction

The Lower Cretaceous Voorspoed kimberlite pipe is one of the six pipes which comprise the Kroonstad Kimberlite Cluster located in the central region of the Kaapvaal Craton (South Africa). The pipe was initially described as a typical South African tuffisitic kimberlite (Skinner, Marsh, 2004) and later on as a pipe with a 2 km deep crater filled by pyroclastic sedimentation and resedimentation of kimberlite and country rock debris (Howarth, Skinner, 2012) due to the presence of bedded volcanoclastics at a depth of 2 km from the original land surface.

In 2013-2014, a volcanological and petrological study was carried out at Voorspoed mine, following onsite detailed drill core logging and pit mapping. The distribution of the main rock types (Fig. 1) and their spatial relationships investigated in the open pit and drill core revealed a complex facies architecture reflecting a not less complex pipe growth history.

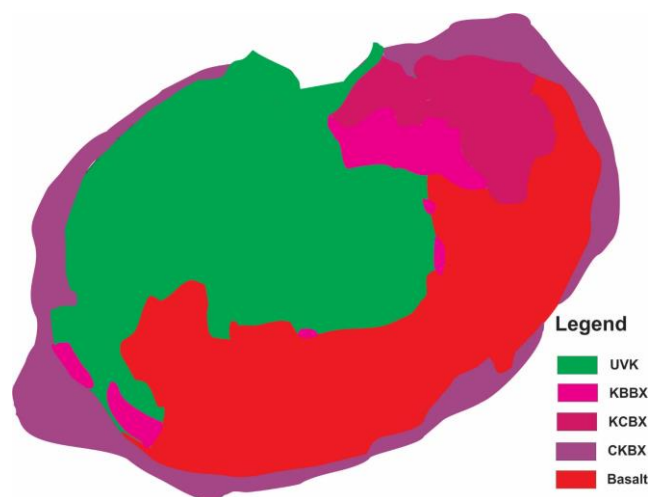


Figure 1: Map of the Voorspoed mine pit with the location of the main rock types

Key findings

Petrography and whole rock chemistry confirm the main volcanoclastic rock types previously identified in Voorspoed pipe: UVK, RXVK, OVK, KCBX and CKBX. Under the microscope, the rocks indicate mixing of different types and abundances of magmatic components (juvenile and cognate pyroclasts)

and country rock xenoliths. Two main types of magmatic components are described in the Voorspoed volcanoclastics, their discrimination being based on olivine and phlogopite abundance ratios (Fig. 2a, b).

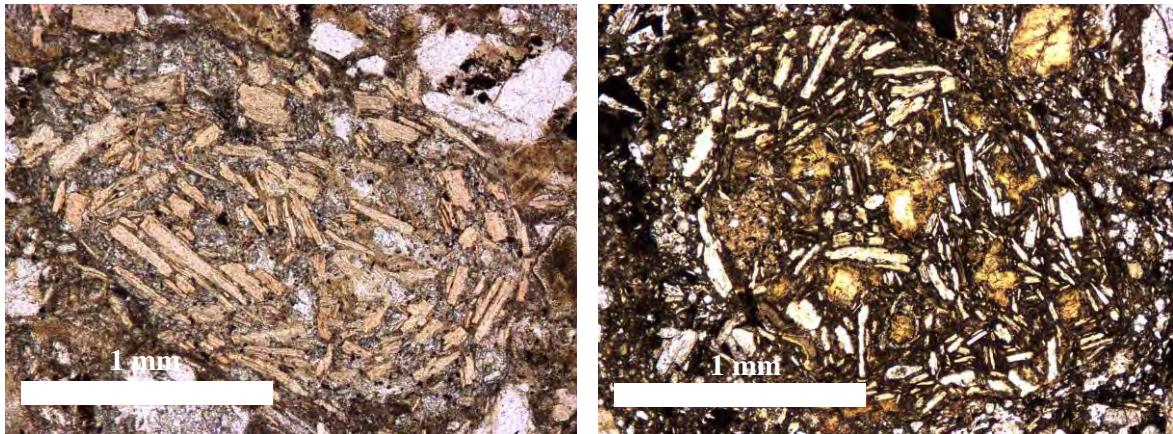


Figure 2: a) Type 1 juvenile pyroclast typical for UVK; b) type 2 juvenile pyroclast, typical for RXVK and OVK.

The type 1 magmatic components are defined by juvenile and cognate pyroclasts which are enriched in phlogopite compared to olivine, and are typically dominant in UVK (Fig. 2a). The type 2 magmatic components are defined by juvenile and cognate pyroclasts which are enriched in olivine compared to phlogopite, and are typically dominant in both RXVK and OVK (Fig. 2b). Although the predominance of magmatic components discriminates sometimes between the UVK and RXVK/ OVK samples, samples of UVK and RXVK/OVK which show similar abundances of type 1 and type 2 magmatic components cannot be discriminated based on this criterion alone. Hence, additional discriminants need to be used to separate the rock types, such as: the frequent presence of a certain type of country rock xenolith like basalt and dolerite, mudstone or black shale; the dominant phlogopite v. olivine component ratio in the matrix, which separates the UVK from the RXVK or OVK, and the grain size and abundance of magmatic components which separate the OVK from the RXVK.

The KBBX and CKBX are interpreted as the more diluted facies of UVK and RXVK. In general, the crustal contamination increases progressively from the OVK and RXVK to UVK, KBBX and CKBX. Whole rock chemistry data discriminate the UVK, RXVK, OVK, KBBX and CKBX rock types. The chemistry of the rock types is controlled by olivine and phlogopite abundance, as well as dilution type and abundance.

The UVK, RXVK and OVK are characterized as “typical” kimberlite varieties if they are dominated by magmatic components of either type 1 or 2, respectively. These rock types commonly occur along the margins of the pipe. Towards the center of the pipe and at depth, the UVK, RXVK and OVK become progressively enriched in the alternating type of magmatic components. These rocks are classified as “hybrid” varieties, and are volumetrically much more abundant than the “typical” kimberlite varieties. The complex petrography suggests sequential eruptions of different magma batches, as indicated by texturally different types of juvenile pyroclasts that were often subsequently mixed and recycled, the latter testified by composite types. End member juvenile pyroclast textures can be traced in all model codes along the margins of the pipe, while the central part is characterized by mixing and recycling of a wide range of textures. This arrangement is best explained by the injection of tephra jets and the consequent collapse of their feeder conduits causing the thorough mixing of several singular and complex composite textured juvenile pyroclasts. In addition, the geometry of the different model codes and their spatial relationships suggest a combination of pyroclastic sedimentation and resedimentation. The UVK occupies the largest portion of the pipe and it is thickest in the central western area of the pipe (Fig. 1). RXVK/OVK is thickest in the NE and shows a wedge geometry which thins towards the SW (Fig. 1). In the central part of the pipe, RXVK/OVK is interlayered with UVK at depth. Pyroclastic sedimentation and resedimentation in the UVK from the central-western part of the pipe, interrupted by

a RXVK/OVK resedimentation event from the NE towards the SW added complexity in the distribution of the different model codes.

The incremental pipe emplacement records several eruptive events separated by hiatuses and the presence of a constantly rather shallow crater. Root zone processes typically include explosive fragmentation but also non-explosive intrusion of magma and, during hiatuses, its consolidation and subsequent fragmentation in later eruptions, as testified by abundant cognate xenoliths with textures similar to the juvenile pyroclasts. Hiatuses are also characterized by passive crater widening through gravitational collapse of unstable crater walls and their overlying tephra rings. This is shown by abundant talus deposits with variable resedimented kimberlite/country rock debris ratio. The country rock componentry identified in the KBBX and CKBX talus deposits varies, and the prevalence of a certain lithology can be linked with a specific source area in the country rock stratigraphy exposed in the maar crater collar suggesting a step-wise crater widening in rather small events. Hiatuses in pyroclastic sedimentation are also implied by ashy mud layers with ductile deformation that suggest at least the temporary presence of a water body in the crater.

The widening of the crater in rather small-volume depositional events and their point source from specific basalt and shale strata suggest that the crater was rather shallow (probably only a few hundred meters). Such a shallow crater was maintained by tephra jets moving material from the root zone to the surface, deposition of pyroclastic and resedimented material onto the crater floor, and subsidence of the diatreme infill into the root zone. Strong evidence for this “conveyor-belt” recycling process can also be seen in Voorspoed pipe by abundant and well developed shear zones along the margin of the pipe.

Conclusions

Our investigation confirms and enhances the rock classification at the mine. Rock discrimination applying petrography tools like the visual estimation of olivine grain size and abundance in the magmatic components and matrix, as well as the identification and estimation of the abundance of country rock xenoliths in all model codes, and the pXRF analysis of blast pattern cuttings are tools that can be used to discriminate the rock types in the mine. The high complexity revealed by our study is reflected in grade distribution. The diamond distribution within the pipe is controlled by the emplacement of several magma batches in the form of feeder conduits, as well as primary pyroclastic and resedimented tephra deposits from the maar crater collar onto the crater floor. Cross-cutting tephra jets have homogenized, mixed and redistributed tephra and consequently the diamonds from pre-existing deposits.

The understanding of emplacement processes is essential for the development of a robust geological model. In addition, grade information from LDD’s correlated with pilot hole data, a systematic sampling protocol and quantitative, complementary data sets are critical to understand the grade distribution in a kimberlite pipe.

References

- Howarth G.H., Skinner E.M. (2012) The geology and emplacement of the volcanoclastic infill at the Voorspoed Group II kimberlite (orangeite) pipe, Kroonstad Cluster, South Africa
J. Volcanol. Geoth. Res. 231-232: 24-38
- Skinner E.M.W., Marsh J.S. (2004) Distinct kimberlite classes with contrasting eruption processes
Lithos 76: 183-200

First identification of molybdenite in diamond-hosted sulphide inclusions and possible implications for Re-Os dating of diamonds

Lotta I.M. Kemppinen¹, Simon C. Kohn¹, Ian J. Parkinson¹, Galina P. Bulanova¹,
Daniel H. Howell¹ and Chris B. Smith¹

¹ University of Bristol, United Kingdom, lk15127@bristol.ac.uk, simon.kohn@bristol.ac.uk,
ian.parkinson@bristol.ac.uk, galina_bulanova@hotmail.com, daniel.howell@bristol.ac.uk
chris_b_smith@btopenworld.com

Introduction

Sulphide inclusions in natural diamonds provide information about sulphides originating at depth during reactions involved in diamond growth. Although their role in the formation of diamonds is unclear, sulphides control the highly-siderophile element budget of the mantle and Re-Os isotopic systematics can be applied to syngenetic sulphide inclusions to date diamond growth and related mantle processes (Pearson et al. 1998, Harvey et al. 2016). Sulphide inclusions in diamonds typically have heterogeneous Fe, Ni and Cu distributions because of mineral unmixing from a former melt or monosulphide solid solution, during their ascent to the surface (Harris 1972, Taylor and Liu 2009). Rosette-shaped fractures which are characteristic of sulphide inclusions, form upon decompression and/or cooling. Here, we report the discovery of a molybdenite phase in sulphide inclusions in eclogitic diamonds from Mir (Yakutia, Russia). Molybdenite is the main host of Re on Earth and its presence in sulphide inclusions and decompression fractures could significantly affect the partitioning of Re inside the inclusions, potentially leading to inaccurate radiometric ages.

Samples and methods

Sulphide inclusions in 7 Mir eclogitic diamonds have been studied with a Thermo Scientific DXR Raman microscope using 455 and 532 nm lasers and a 50× LWD objective. The diamonds are colourless and range in size (3-6 mm) and shape. The samples were previously prepared for sulphide inclusion study at the Diamond and Precious Metal Institute (Siberian Branch RAS, Russia) but still contain many intact inclusions including sulphides, omphacite, pyrope-almandine garnet and coesite (Bulanova et al. 1999). The sulphide inclusions have varying shapes, sizes and decompression fractures (1B).

Raman results

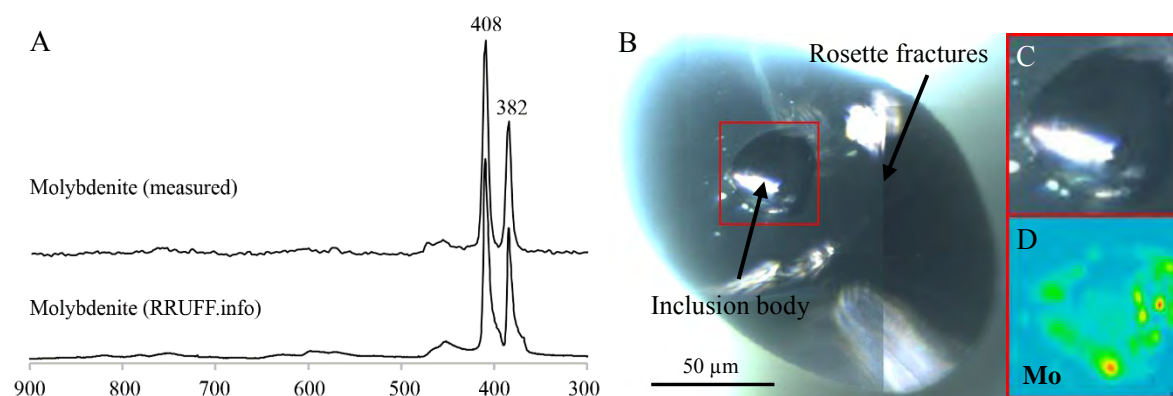


Figure 1: A) Raman spectra of molybdenite measured in a sulphide inclusion compared with the reference spectrum available from the RRUFF database (Lafuente et al. 2015). B) Photomicrograph of an inclusion in a Mir eclogitic diamond containing a sub-euhedral body and rosette-shaped fractures. C) enlargement of the photomicrograph. D) a Raman peak height map shows in red where the molybdenite signal is most intense (yellow and green colours show where the signal is present but weaker).

Raman suggests molybdenite (Fig. 1A) occurs inside at least 75 sulphide inclusions in 7 diamonds. Raman maps show that molybdenite forms as sub- μm sized disseminations or an irregular rim near the edges of the inclusions (Fig. 1D), and sometimes is concentrated in one point. Molybdenite is commonly found intergrown with, or adjacent to, chalcopyrite and both sometimes seen as a film or in points inside the decompression fractures surrounding the inclusions.

To consider whether the occurrence of molybdenite was restricted to Mir or is a more general phenomenon, we conducted preliminary Raman studies of sulphide inclusions from other localities. We have observed molybdenite in sulphide inclusions in eclogitic diamonds from Argyle (NW Australia) and Dachine (French Guiana), as well as peridotitic diamonds from Murowa (Zimbabwe) and Udachnaya (Sakha Republic, Russia).

Application to Re/Os ages

The strong partitioning of Re (relative to Os) into molybdenite implies that radiogenic ^{187}Os could remain in the sampled part of the inclusion but some parent ^{187}Re could be “hidden” in inaccessible, and therefore not dissolved molybdenite. The apparent overabundance of ^{187}Os relative to ^{187}Re would incorrectly imply that a longer time had elapsed in order to generate the measured ^{187}Os concentrations. The details of how Re/Os dates would be affected by missing the molybdenite phase depend on various factors including; a) the abundance of molybdenite in the inclusion, b) the proportion of molybdenite missed (e.g. in decompression fractures) during the extraction of the inclusion, c) the bulk Re and $^{187}\text{Re}/^{188}\text{Os}$ ratio of the inclusion, d) the method of age determination (i.e. model age or isochron age), e) the timing of molybdenite exsolution (i.e. shortly after trapping of the inclusion, or during exhumation by kimberlite), and f) the partition-coefficient (D) of Re between molybdenite and the residual sulphide inclusion. The batch melting equation was used to explore the behaviour of Re between molybdenite and coexisting Fe-Ni-Cu sulphides (termed MSS) (Fig. 2A). Published concentrations of Re in molybdenite relative to Fe- and Cu-sulphides were used to estimate the partition coefficients used in our calculations (Mathur et al. 2002, Lawley et al. 2013). To estimate how much molybdenite could form from a sulphide melt trapped in diamond, we consider sulphide inclusions trapped as a homogeneous phase with mean molybdenum (Mo) content (ppm) forming molybdenite upon eruption. In our model, the amount of molybdenite present ranges from 10^{-5} -0.005 wt. % of the whole inclusion (larger amounts seem unreasonable requiring > 3000 ppm Mo to be dissolved in the sulphide melt/MSS prior to exsolution).

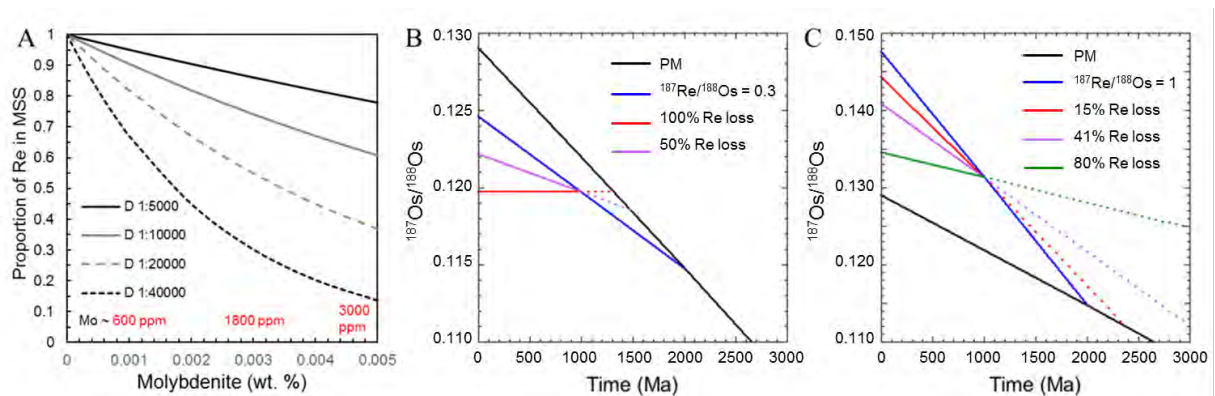


Figure 2: A) The relationship between the amount of molybdenite present (wt.% and ppm) and the proportion of Re remaining in monosulphide solid solution (MSS) for different partition-coefficient (D) values. B) ^{187}Os evolution diagram shows 2 Ga age sulphide with Re loss (in different proportions) at 1 Ga event for sub-chondritic evolution (relative to the Primitive Mantle PM), and C) supra-chondritic evolution.

To model the effects molybdenite could have on the age systematics of host inclusions, we consider hypothetical sulphide inclusions of sub-chondritic (Fig. 2B) and supra-chondritic (Fig. 2C) Re/Os

compositions trapped in diamond in molten form at ~2Ga. In both scenarios, Re has segregated in different proportions into molybdenite at 1 Ga. Figure 2B shows that losing all of the Re from the sampled part of a “sub-chondritic” inclusion would produce a minimum modal age ($T_{RD} = T_{MA}$). 50% Re loss would produce ages older T_{MA} but Re loss (T_{RD}) will always give modal ages. Figure 2C shows that for a supra-chondritic inclusion, 15% Re loss would yield an older age (~2.3 Ga). 41% is the maximum loss giving an age the same as the age of the Earth. Losing more Re would produce ages older than the Earth, until the slope becomes parallel with that of the primitive mantle line, before giving future ages (i.e. like the 80% Re loss curve illustrated in fig. 2C).

Discussion

Molybdenite occurs at the outermost edge of sulphide inclusions and along thermal decompression fractures, implying that it could be missed when extracting the inclusions from diamonds, prior to dissolution and chemical separations of Re and Os. The implications of this for radiometric dating are obscured by uncertainties about the sub-solidus behaviour of Re and Os between different sulphides, and the timing of sulphide exsolution. However, depending on the Re/Os ratio of the inclusions, and the method used in dating, omitting molybdenite could potentially induce errors on the ages of the inclusions, for example by producing ages older than the Earth or future ages. Although the origin and significance of this molybdenite is still unknown, the presence of molybdenite in inclusions inside both peridotitic and eclogitic diamonds implies that something other than bulk Mo availability (increased by subduction for example) may control molybdenite exsolution. Other influences may also play a role, such as different source materials for sulphide and silicate inclusions or variations in oxygen fugacity. Because diamond inclusions are such valuable samples, we suggest that Raman investigation to identify the presence of molybdenite and its location within a diamond inclusion, should precede Re-Os dating procedures or the use of any other destructive techniques.

References

- Mathur R, Marschik R, Ruiz J, Munizaga F, Leveille RA and Martin W (2002) Age of mineralization of the Candelaria Fe oxide Cu-Au deposit and the origin of the Chilean iron belt, based on Re-Os isotopes. *Econ Geol* 97(1):59-71
- Bulanova GP, Shelkov D, Milledge HJ, Hauri EH and Smith CB (1999) Nature of eclogitic diamonds from Yakutian kimberlites: evidence from isotopic composition and chemistry of inclusions. In *Proc 7th Int Kimb Conf* 57-65
- Harris JW (1972) Black material on mineral inclusions and in internal fracture planes in diamond. *Contrib Mineral Petrol* 35:22-33
- Harvey J, Warren JM and Shirey SB (2016) Mantle Sulfides and their Role in Re-Os and Pb Isotope Geochronology. *Rev Mineral Geochem* 81:579-649
- Lafuente B, Downs R T, Yang H and Stone N (2015) The power of databases: the RRUFF project. In: Armbruster T and Danisi RM (eds) *Highlights in Mineralogical Crystallography*, W. De Gruyter, Berlin, Germany, pp 1-30
- Lawley C, Selby D and Imber J (2013) Re-Os molybdenite, pyrite, and chalcopyrite geochronology, lupa goldfield, southwestern Tanzania: tracing metallogenic time scales at midcrustal shear zones hosting orogenic Au deposits. *Econ Geol* 108(7):1591-1613
- Pearson DG, Shirey SB, Harris JW and Carlson RW (1998) Sulphide inclusions in diamonds from the Koffiefontein kimberlite, S Africa: Constraints on diamond ages and mantle Re-Os systematics *Earth Planet Sci Lett* 160:311-326
- Taylor LA and Liu Y (2009) Sulfide inclusions in diamonds: not monosulfide solid solution. *Russ Geol Geophys* 50:1201-1211



The chemical and isotopic composition of Diavik fibrous diamonds and their microinclusions

Oded Navon¹, Brooke Matat Jablon¹, Richard Stern² and Thomas Stachel²

1) Institute of Earth Sciences, The Hebrew University, Jerusalem, Israel, oded.navon@mail.huji.ac.il,

bmjablon@gmail.com

2) Department of Earth and Atmospheric Sciences, University of Alberta, Edmonton, AB, Canada. rstern@ualberta.ca

tstachel@ualberta.ca

We investigate a suite of fibrous diamonds (fibrous coats surrounding a monocrystalline octahedral core and cubes that are fully fibrous) from the Diavik Mine in Canada. The diamonds are opaque due to the presence of many microinclusions. They are 4-6 mm in size and weigh 49-134 mg with average of 104 mg (0.52 carat).

FTIR spectra reveal that the cores carry both A and B centers. In cases where it was possible to record pure spectra of the coats, we detected only A centers.

Electron probe micro analysis (EPMA) of the inclusions in 17 diamonds found saline high-density fluids (HDFs) in ten; one diamond carries high-Mg carbonatitic HDFs; two extend from the saline towards the high-Mg carbonatitic composition and four lie on the low-Mg carbonatitic to silicic array. The saline HDFs are rich in potassium, with average molar K/(Na+K) of 0.6. Their Cl/(Na+K) ratio is ~1. The average composition of the saline HDF (in wt%) is: 34.5% Cl, 27.7% K₂O, 11.0% Na₂O, 8.2% BaO, 7.5% CaO, 7.2% FeO, 5.7% MgO, 2.8% SiO₂, 1.4% Al₂O₃ and 1.3% P₂O₅. The average Mg# of the saline fluids is 58 and it increases with decreasing Cl and increasing Mg and Ca, pointing towards the Mg# of the high-Mg carbonatitic HDF (82). Ba is enriched in the saline HDFs and BaO concentration in the saline fluids grows with increasing Cl.

The carbon and nitrogen isotopic composition of the coats and the fibrous cubes falls within the values of fibrous diamonds ($\delta^{13}\text{C}$: -4 to -10‰, $\delta^{15}\text{N}$: 0 to -10‰, Cartigny et al., 2014). Most of the diamonds reported here fall in a tighter range: $\delta^{13}\text{C}$ of -6.5 to -9.0‰ and $\delta^{15}\text{N}$ between -2 and -4‰. One saline diamond falls at $\delta^{13}\text{C}$ and $\delta^{15}\text{N}$ between -2 and -4‰ and a low-Mg carbonatitic diamond has the same range in $\delta^{13}\text{C}$, but more negative $\delta^{15}\text{N}$ (-4 to -5.5). Even the cores of the coated diamond span a narrow range in $\delta^{13}\text{C}$ (most fall between -4.2 to -5.2), but their $\delta^{15}\text{N}$ covers a wide range (+0.3 to -16).

Nitrogen concentrations vary between 700 and 1900 ppm and exhibit a broad correlation with the isotopic ratios, with the higher nitrogen concentrations are associated with heavy carbon and heavy nitrogen compositions.

The composition of the HDF and the isotopic ratios of carbon and nitrogen fall in the range spanned by other Lac de Gras diamonds. We hope that the high resolution data we acquired and the accurate determination of their location relative to the growth zones of the diamond will allow us to follow covariations in fluid chemistry and isotopic composition and to follow the evolution of the fluids and their host diamonds.



Ilmenite as a recorder of the kimberlite history from mantle to surface: examples from Indian kimberlites

J. Xu¹, J. C. Melgarejo² and M. Castillo-Oliver³

¹ *Departament de Mineralogia, Petrologia i Geologia Aplicada, Facultat de Ciències de la Terra, Universitat de Barcelona, Barcelona, Spain, jingyao.xu@ub.edu*

² *Departament de Mineralogia, Petrologia i Geologia Aplicada, Facultat de Ciències de la Terra, Universitat de Barcelona, Barcelona, Spain, joan.carles.melgarejo.draper@ub.edu*

³ *ARC Centre of Excellence for Core to Crust Fluid Systems and GEMOC, Department of Earth and Planetary Sciences, Macquarie University, NSW, Australia, montgarri.castillo-oliver@mq.edu.au*

Introduction

Indian kimberlites occur in the Bastar craton (Central India) and in the Eastern Dharwar craton (EDC) Southern India. Nearly 100 kimberlite pipes have been discovered in the Eastern Dharwar craton of southern India, and they are distributed in three distinct fields: 1) the southern Wajrakarur kimberlite field (WKF); 2) the northern Narayanpet kimberlite field (NKF); and 3) the Raichur kimberlite field (RKF) (Chalapathi Rao et al, 2013). Nine kimberlites have been selected for this study: three came from the Siddanpalli cluster of RKF (SK-1, SK-2 and SK-3); other six kimberlites came from WKF, from Chigicherla (CC-4 and CC-5), Kalyandurg (KL-3 and KL-4), Lattavaram (P-3) and Mulligripally (P-5). The kimberlite emplacement took place during the Mesoproterozoic, around 1.1 Ga (Chalapathi Rao et al., 2013). Ilmenite is one of the classic diamond indicator minerals (DIMs) and for long it has been used as a guide for kimberlite exploration. The aim of this study is to evaluate the petrogenetic information that can be provided from the textural and geochemical study of the different ilmenite generations present in the Indian kimberlites studied in this work.

Petrography of ilmenite

Ilmenite crystals from the Indian kimberlites are not formed in a single process, and many ilmenite populations can be distinguished. The next textural-compositional types of ilmenite are defined based on petrographic and compositional studies using optical petrography and SEM-EDS: 1) Mg-rich polycrystalline ilmenite xenoliths scattered in the kimberlite groundmass, with compositions in the ilmenite s.s. field; 2) rounded macro-microcrysts of ilmenite scattered in kimberlite groundmass with similar compositions to those indicated above; 3) Mg-very rich ilmenite replacing chromite and other Ti-bearing xenocrysts and type 1 and 2 ilmenite xenocrysts, with compositions in the geikielite field; 4) Mg-rich ilmenite as subhedral thin platelets restricted to fully bastitized pyroxene macrocrysts; 5) late anhedral Mn-rich ilmenite replacing either rutile xenocrysts or type 2 ilmenite and being replaced by perovskite and ulvöspinel; and 6) very late euhedral tabular to anhedral Mn-rich ilmenite associated with calcite and chlorite replacing perovskite and ulvöspinel.

Composition of ilmenite

The classification of the ilmenite types, in terms of the modal proportions of the end members of the ilmenite-hematite-geikielite-pyrophanite series, shows that most of them are ilmenite s.s., except for the type 3 ilmenite, which plots in the geikielite domain (Fig. 1A). The hematite component is never higher than 15%, and in most cases it remains below 10%. The pyrophanite component is enriched in types 5 and 6. However, the Mn content in these late ilmenite types is lower than 0.3 apfu. The compositional ranges of type 1 and type 2 are very similar in terms of their Fe²⁺/Mg ratio, with Mg apfu values between 0.2 and 0.45, within the ilmenite s.s. field. Their Mn and Fe³⁺ contents remain low (less than 0,1 apfu) (Fig. 1B).

Correlations between the major components in different types ilmenites are presented in figure 2. As expected, there is a good negative correlation between Ti and Fe³⁺. The highest Fe³⁺ values are found in the primary ilmenite generations (types 1 and 2) and the lowest ones in the late generations (types 5

and 6, Fig. 2A). These younger ilmenite generations have the lowest contents in MgO in all the field (Fig. 2B). There is a positive correlation between TiO₂ and MgO (type 1, 2 and 3 Fig. 2B). As shown in figure 2B, most Mn-rich ilmenite crystals plot outside the classic kimberlite domain in the TiO₂-MgO diagram of Wyatt et al. (2004). The Fe³⁺ contents in Mn-rich ilmenite (type 5 and 6) are relatively low (less than 0.15 apfu), while Mg-rich ilmenite and geikielite (types 1 to 4) have Fe³⁺ content between 0 and 0.4 apfu. Mn-ilmenite (type 5 and 6) has higher Fe²⁺ content than Mg-ilmenite (type 1 to 4); they also tend to decrease in Fe²⁺ owing to the substitution of Fe²⁺ by Mn²⁺.

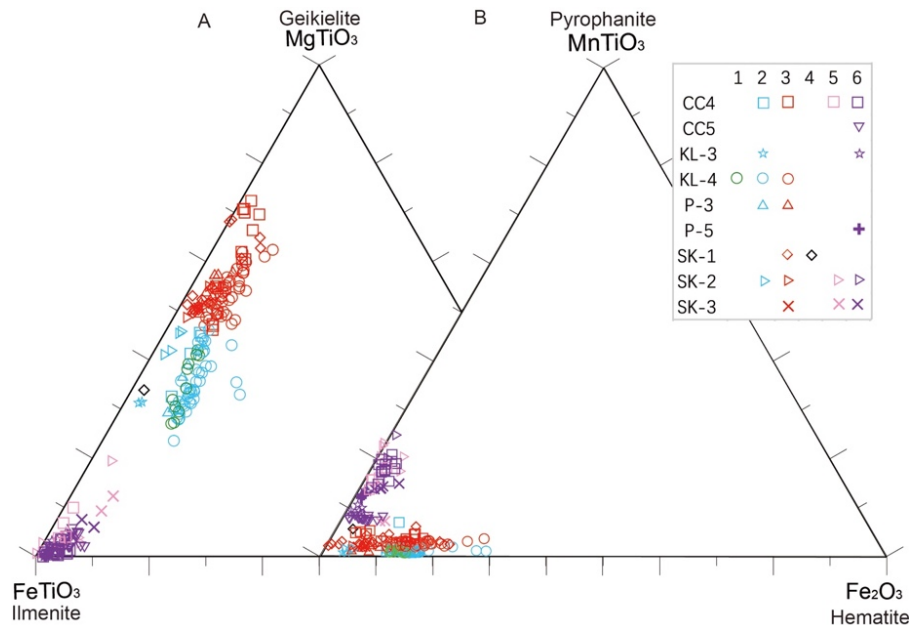


Figure 1: Compositions of the different textural types (type 1 to 6) of ilmenite from different Indian kimberlites: (A) in terms of the geikielite (MgTiO₃)–ilmenite (FeTiO₃)–hematite (Fe₂O₃); (B) in terms of the pyrophanite (MnTiO₃)–ilmenite (FeTiO₃)–hematite (Fe₂O₃) endmembers.

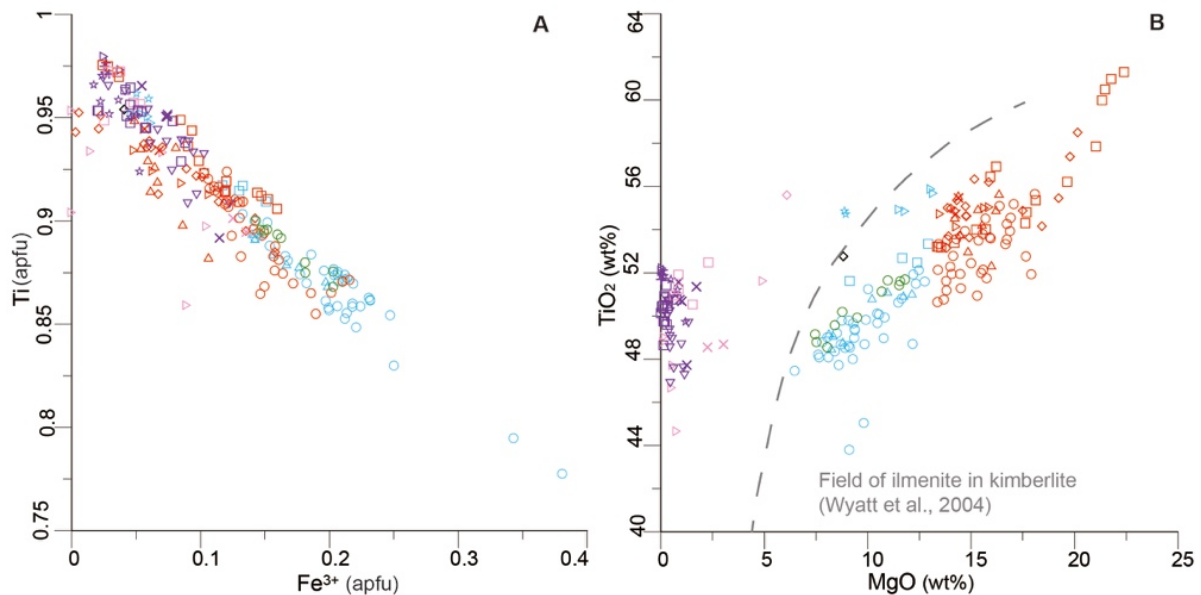


Figure 2: Correlation between major elements for the different types of ilmenite. Legend is indicated in the figure 1.

Significant differences in the Nb content are found among the different textural types. Very low Nb values are common in the older ilmenite generations (types 1 and 2), with only slight Nb enrichment in some type 3, 4, 5 and 6 ilmenites. However, both type 5 and type 6 Mn-rich ilmenite are enriched in Nb when they replace Nb-rich rutile and Nb-rich perovskite, respectively. Type 1 and 2 ilmenite have very

low contents in Cr, and type 3 ilmenite is also poor in this element when it replaces previous ilmenite crystals. However, type 3 ilmenite is enriched in Cr when it replaces chromite and other Cr-rich minerals.

Discussion

Up to 6 compositional-textural types of ilmenite can be distinguished in the Indian kimberlites studied in this work. These ilmenite generations record different processes in the kimberlite history, from mantle to surface. A first generation of polycrystalline Mg-rich ilmenite (type 1 ilmenite) was produced by metasomatic processes in the mantle before the emplacement of the kimberlite. Type 2 ilmenite was produced by disaggregation of these polycrystalline aggregations, resulting in rounded megacrysts (type 2 ilmenite) with a composition similar to the the first generation. Interaction with evolved supercritical fluids produced the replacement of the pre-existing ilmenite megacrysts and aggregates by a new generation of geikielite (type 3 ilmenite) along grain boundaries and cracks. Type 3 ilmenite may also replace other oxides, and the composition of this ilmenite generation is highly dependent on the composition of the replaced minerals. Hence, ilmenite replacing other ilmenite crystals is not much enriched in minor elements, but when ilmenite is replacing Cr-rich minerals it becomes distinctly enriched in Cr. Another generation of Mg-rich ilmenite could be produced by exsolution processes (type 4 ilmenite) but the nature of the host crystals remains obscure, although they are likely enstatite. The late ilmenite generations are characterized by an enrichment in Mn, but two generations can be distinguished based on their stage of formation. Type 5 ilmenite is produced before the crystallization of perovskite and ulvöspinel from the groundmass, and it usually mantles ilmenite and other Ti-rich minerals. Again, the contents of minor elements depend on the replaced mineral; when it is ilmenite, the newly formed ilmenite has no significant contents of minor elements. However, when ilmenite replaces Nb-rutile, it becomes enriched in Nb. Finally, type 6 ilmenite is produced after the crystallization of the groundmass minerals and it replaces them. This ultimate ilmenite has similar behaviour in terms of enrichment in minor elements as in the above examples. Hence, when type 6 ilmenite replaces ulvöspinel it does not have enrichment in minor elements; in contrast, when type 6 ilmenite replaces Nb-rich perovskite it is enriched in Nb.

The composition of the primary ilmenite generations is different to those found as inclusions in kimberlite diamonds from Yakutia (Sobolev et al., 1997). The higher contents in Mg are recorded in metasomatic ilmenite which is produced during kimberlite emplacement, and cannot be associated with the diamond formation. The higher Mn contents are linked to late processes clearly produced after the crystallization of the kimberlite groundmass, and therefore the Mn enrichments cannot be used to establish the diamond grade of the kimberlite.

Acknowledgments

This research was supported the AGAUR 2014SGR01661 of the Generalitat de Catalunya and a FI grant to J. Xu (coded FI_B 00904) sponsored by the Departament d'Educació i Universitats de la Generalitat de Catalunya. The authors also acknowledge the Servei de Làmina Prima (thin section preparation laboratory) and the Centres Científics i Tecnològics de la Universitat de Barcelona (CCiT-UB) for the assistance with SEM-BSE-EDS study (Dr. F. J. García-Veigas, D. Artiaga) and EMP analyses (Dr. Xavier Llovet).

References

- Chalapathi Rao NV, Wu FY, Mitchell RH, Li QL, Lehmann B (2013) Mesoproterozoic U–Pb ages, trace element and Sr–Nd isotopic composition of perovskite from kimberlites of the Eastern Dharwar craton, southern India: distinct mantle sources and a widespread 1.1 Ga tectonomagmatic event. *Chem. Geol.* 353: 48–64
- Wyatt BA, Mike B, Anckar E, Grütter H (2004) Compositional classification of “kimberlitic” and “non-kimberlitic” ilmenite. *Lithos* 77: 819–840
- Sobolev NV, Kaminsky FV, Griffin WL, Yefimova ES, Win TT, Ryan CG, Botkunov AI (1997) Mineral inclusions in diamonds from the Sputnik kimberlite pipe, Yakutia. *Lithos* 39: 135-157



Magma mingling at the Menominee pipe, USA? Contributions from texture and mineral chemistry

Jingyao Xu¹, Joan Carles Melgarejo², Lisard Torró i Abat³, Montgarri Castillo-Oliver⁴

1 Departament de Mineralogia, Petrologia i Geologia Aplicada, Facultat de Ciències de la Terra, Universitat de Barcelona, Barcelona, Spain, jingyao.xu@ub.edu

2 Departament de Mineralogia, Petrologia i Geologia Aplicada, Facultat de Ciències de la Terra, Universitat de Barcelona, Barcelona, Spain, joan.carles.melgarejo.draper@ub.edu

3 Departament de Mineralogia, Petrologia i Geologia Aplicada, Facultat de Ciències de la Terra, Universitat de Barcelona, Barcelona, Spain, lisardtorro@hotmail.com

4 ARC Centre of Excellence for Core to Crust Fluid Systems and GEMOC, Department of Earth and Planetary Sciences, Macquarie University, NSW, Australia, montgarri.castillo-oliver@mq.edu.au

Introduction

Kimberlites and related rocks are petrographically complex. They are hybrid rocks consisting of crystals derived from xenolith disaggregation and direct growth from the magma (Mitchell, 1986). There is a lack of knowledge about the magmatic processes that occur before and during the emplacement. Furthermore, hydrothermal and supergene alterations during and post emplacement difficult the study of these processes. An additional complication is the occurrence of magma mingling in kimberlites (Castillo-Oliver et al., 2016). This work presents a case of mineral sequence in a pipe from Hermansville, Menominee County (Michigan, USA) with the original composition partly preserved, thus allowing to discriminate among primary and secondary minerals.

Textural patterns

The samples studied in this work belong to the hypabyssal facies. Ilmenite and phlogopite mega- and macrocrysts are set in a groundmass made up of olivine phenocrysts, carbonates, several ilmenite generations, spinel group minerals and djerfisherite.

Euhedral olivine phenocrysts are fresh and have complex zoning. The original rounded olivine core (ol₁) has a first euhedral olivine rim (ol₂) enriched in Fe. On its turn, this rim is overgrown by an outermost rim (ol₃) which has lower Fe contents. Fine-grained rounded sulphide inclusions (pentlandite, pyrrhotite) are common in the olivine core.

Two different types of unzoned spinel group minerals were identified in the groundmass. Spinel *sensu strictu* typically occurs as euhedral to anhedral crystals; although it is also found as inclusions in the outer part of the first rim of the olivine phenocrysts. This spinel is sometimes pseudomorphized by meixnerite (Mg₆Al₂(OH)₁₈ · 4H₂O). The second spinel-group mineral has compositions close to qandilite-magnetite fields and it is euhedral. However, it is also found as the last phase replacing Mg-rich ilmenite macrocrysts.

Five textural types of ilmenite-group minerals are present in the Menominee pipe: 1) homogeneous macro- to microcrystic Mg-rich ilmenite, not replaced by other minerals; 2) macro- to microcryst Mg-rich ilmenite replaced along veinlets and grain borders by a sequence of rutile, geikielite and qandilite; 3) euhedral geikielite as very common inclusions in the outer part of the first olivine rim; 4) geikielite replacing Mg-rich ilmenite (type 4a), rutile microphenocryst (type 4b) and rutile included in olivine (type 4c); 5) Mg-rich ilmenite as inclusion in groundmass qandilite.

Rutile has 3 textural types: 1) euhedral rutile as very common inclusions in olivine, at the contact between the olivine core and its first rim, 2) rutile microphenocrysts (about 200 μm) which are replaced by geikielite along their margins and fractures; 3) rutile replacing macro- to microcrysts of Mg-rich ilmenite. On its turn, this third type of rutile is replaced by geikielite and qandilite.

Groundmass carbonates are mainly calcite, which might be replaced by dolomite and barite. Djerfisherite ($K_6(Fe,Cu,Ni)_{25}S_{26}Cl$) occurs in the groundmass as anhedral grains up to 400 μm in diameter. It is partly pseudomorphosed by a sequence of valleriite ($2[(Fe,Cu)S]_{1.53}[(Mg,Al)(OH)_2]$) and galena, followed by magnetite and cronstedtite ($(Fe^{2+},Fe^{3+})_3(Si,Fe^{3+})_2O_5(OH)_4$).

Mineral chemistry

The composition of the rounded olivine core (ol_1) is typically Fo_{90} , with ~0,4 wt % NiO; whereas the first euhedral rim (ol_2) is both poorer in Fe and Ni (Fe_{89} and ~0,2 wt.% NiO). The average composition of the outermost rim (ol_3) is characterised by higher Fe contents, but lower Ni values (Fe_{91} and ~ 0,1 wt.% NiO).

There are two different spinel-group minerals in the groundmass. The first is spinel s.s. (82-90% $MgAl_2O_4$, less than 0.08 Cr apfu) with average structural formula: $[Mg_{0,84}Fe^{2+}_{0,17}][Al_{1,76}Fe^{3+}_{0,1}Cr_{0,08}Ti_{0,02}]O_4$. The spinel s.s. included in olivine phenocrysts has similar composition to the groundmass spinel s.s. The other spinel-group mineral has compositions of Cr-poor qandilite-ulvöspinel-magnetite series with significant contents of qandilite (29-55% Mg_2TiO_4 , 20-46% Fe_2O_3 , 5-19% $MgAl_2O_4$, 3-14% Fe_2TiO_4 , less than 0.19 Cr apfu), corresponding with the next average structural formula: $[Mg_{0,83}Fe^{2+}_{0,16}Mn_{0,01}][Fe^{3+}_{0,76}Ti_{0,43}Fe^{2+}_{0,42}Al_{0,34}Cr_{0,02}V_{0,01}]O_4$. Both spinel s.s. and qandilite plot out of the kimberlite spinel fields established by Mitchell (1986) or Barnes and Roeder (2001). Qandilite is more enriched in Mg than the typical spinels from kimberlite fields, and those replacing ilmenite 4a and 4b are more enriched in Mg than those from the groundmass.

Type 1 and type 2 ilmenite have the same composition, with lower Mg (0,43-0,47 apfu Mg) content than other types of ilmenite as well as low Cr content (0,7-1,4 wt.% Cr_2O_3). Type 3 and type 4 ilmenite have very high Mg contents (0,5- 0,8 apfu Mg), so they must be classified as geikielite. Type 3 ilmenite has 0,53-0,55 apfu Mg, 1,9-3,0 wt.% Cr_2O_3 . Type 4a has 0,55-0,60 apfu Mg and 0,8-1,2 wt.% Cr_2O_3 , while type 4b and 4c have higher contents of Mg (0,66-0,81 apfu) and Cr (1,6-5,7 wt.% Cr_2O_3). Compositions of type 5 ilmenite are similar to those of type 4b and type 4c ilmenite.

The three types of rutile have similar composition, they have 0,9-2,0 wt.% Nb_2O_5 , 0,8-4,5 wt.% Cr_2O_3 and 0,6-0,9 wt.% V_2O_3 .

Djerfisherite has the next average structural formula: $[K_{5,86}Na_{0,03}Ca_{0,03}][Fe_{17,46}Ni_{6,64}Cu_{0,80}Co_{0,15}]S_{26}Cl_{1,00}$. This djerfisherite is Ni-rich (5,5-7,9 apfu Ni) and Cu-poor (0,4-1,2 apfu Cu).

Discussion and conclusions

Zoning in the olivine phenocrysts is interpreted as the result of an epitaxial overgrowth of corroded mantle xenocrysts (ol_1), developed under non-equilibrium conditions. Rutile co-crystallized with the early stages of the first forsterite rim, whereas geikielite and spinel s.s. started to crystallize during the late stages of this rim. The last olivine overgrowth (ol_3) would co-crystallize with qandilite.

Rutile in kimberlitic rocks is commonly interpreted as a xenocryst resulting from disaggregation of a wide variety of rocks, which may have either a crustal or a mantle origin (eclogites, MARID, pyroxenites, metasomatized peridotites). However, it has also been found as diamond inclusions and/or as intergrowths with diamond (Meinhold, 2010). Its composition has been used to constrain its source rock. Like this, while Cr-poor rutile could be derived from both crustal and off-cratonic or cratonic mantle rocks; Cr-rich rutile (>1,7 wt.% Cr_2O_3) is thought to be exclusively related to the cratonic mantle (Malkovets et al., 2016). However, the rutile crystals found as inclusions in olivine or disseminated in the groundmass of the Menominee pipe cannot be xenocrysts. Instead they formed during the early stages of magma crystallization, immediately followed by geikielite and spinel s.s., well before the crystallization of the first olivine rim.

Occurrence of two different spinels (spinel s.s. and qandilite-rich spinels) in the same groundmass can be interpreted as an evidence of magma mingling. Despite both spinels are not exactly contemporaneous, both were formed during groundmass crystallization. Both spinels are unzoned, and therefore they do not follow any of the typical kimberlitic trends. The early crystallization of aluminian spinels has been explained as a result of the cessation of the phlogopite crystallization (Pasteris, 1983), but in this case the development of spinel could be favoured by an increase in the fO_2 . The occurrence of qandilite-rich spinels in the last stages of crystallization could suggest the existence of a very evolved kimberlitic magma, as those mentioned in the Jos and Benfontein kimberlites (Mitchell, 1986).

Finally, djerfisherite is a Cl-bearing potassium sulfide found in meteorites, alkaline ultramafic rocks and carbonatites. Sharygin et al. (2007) suggest a late magmatic origin of djerfisherite in the Udachnaya-East kimberlite groundmass, formed at shallow depths and at $T \leq 800^\circ\text{C}$. Djerfisherite was found also in mantle xenoliths as interstitial rims around Fe–Ni–Cu sulfides and around sulfide globules (Sharygin et al., 2007) and as xenocrysts/megacrysts around primary sulfide globules and as daughter phase in melt inclusions (Kamenetsky et al., 2009). Djerfisherite was also found as inclusions in diamonds (Zedgenizov et al., 1998). However, the experimental data indicated that djerfisherite is not stable at pressure greater than 3Gpa (Minin et al., 2015). Therefore, djerfisherite included in diamond and mantle xenoliths formed by interaction between xenoliths and kimberlitic melts, and the presence of djerfisherite can be an indicator of Cl enrichment of kimberlite melt (Sharygin et al., 2007; Minin et al., 2015). The common occurrence of djerfisherite at the Menominee pipe indicates a high activity of volatiles (S and Cl) and alkalis during melt crystallization, and could be favoured by the fractionation of K to the melt instead of being used to crystallize phlogopite.

Acknowledgments

This research is supported by the AGAUR 2014SGR01661 project (Generalitat de Catalunya) and a FI grant to J. Xu (FI_B 00904) sponsored by the Dept. d'Educació i Universitats de la Generalitat de Catalunya. The authors also acknowledge the Servei de Làmina Prima and the CCT-UB for the assistance with SEM-BSE-EDS study (Dr. García-Veigas, D. Artiaga) and EMP analyses (Dr. Llovet).

References

- Castillo-Oliver M, Galí S, Melgarejo JC, Griffin WL, Belousova E, Pearson NJ, Watangua M, O'Reilly SY (2016) Trace-element geochemistry and U–Pb dating of perovskite in kimberlites of the Lunda Norte province (NE Angola): petrogenetic and tectonic implications. *Chem. Geol.* 426: 118–134
- Barnes SJ, Roeder PL (2001). The range of spinel compositions in terrestrial mafic and ultramafic rocks. *J. Petrol.* 42: 2279–2302
- Kamenetsky VS, Maas R, Kamenetsky MB, Paton C, Phillips D, Golovin AV, Gornova MA (2009) Chlorine from the mantle: Magmatic halides in the Udachnaya-East kimberlite, Siberia. *Earth Planet. Sci. Lett.* 285: 96–104
- Malkovets VG, Rezvukhin DI, Belousova EA, Griffin WL, Sharygin IS, Tretiakova IG, Gibsher AA, O'Reilly SY, Kuzmin DV, Litasov KD, Logvinova AM, Pokhilenko NP, Sobolev NV (2016) Cr-rich rutile: A powerful tool for diamond exploration. *Lithos* 265: 304–311
- Meinhold G (2010) Rutile and its applications in earth sciences. *Earth-Science Reviews* 102: 1–28
- Minin DA, Sharygin IS, Litasov KD, Sharygin VV, Shatskiy A, Ohtani E (2015) High-pressure stability of djerfisherite: Implication for its origin in diamonds and mantle xenoliths. *Advances in high Pressure Research II: Deepest Understanding – 2015*: 14
- Mitchell (1986) *Kimberlites: mineralogy, geochemistry and geology*. Plenum Press, New York. 442pp.
- Pasteris, J.D. (1983): Spinel zonation in the De Beers kimberlite, South Africa: possible role of phlogopite. *Can. Mineral.* 21: 41–58
- Sharygin VV, Golovin AV, Pokhilenko NP, Kamenetsky VS (2007) Djerfisherite in the Udachnaya-East pipe kimberlites (Sakha-Yakutia, Russia): paragenesis, composition and origin. *Eur. J. Mineral.* 19: 51–63
- Zedgenizov DA, Logvinova AM, Shatskii VS, Sobolev NV (1998) Inclusions in microdiamonds from some kimberlite diatremes of Yakutia. *Dokl. Akad. Nauk* 359: 204–208

Transport and eruption of mantle xenoliths: A lagging problem

Kelly Russell¹, Thomas Jones², Graham Andrews³, Ben Edwards⁴ & Jennifer Pell⁵

¹Department of Earth, Ocean & Atmospheric Sciences, University of British Columbia, krussell@eos.ubc.ca

²Department of Earth Sciences, Durham University, UK, tomjj7@gmail.com

³Department of Geology & Geography, West Virginia University, USA, gda0005@mail.wvu.edu

⁴Department of Earth Sciences, Dickinson College, USA, edwardsb@dickinson.edu

⁵Peregrine Diamonds Ltd, Vancouver, Canada, jennifer@pdiam.com

Introduction

One of the main characteristics of kimberlite magmas is the nature and abundance of xenolithic cargo they sample, entrain, transport, and erupt. The population of xenoliths hosted by kimberlite commonly represents random sampling from anywhere within the entire (i.e. ~150-200 km) cratonic mantle and crustal lithosphere. Much of our knowledge of the nature and origins of the subcratonic mantle lithosphere derives directly from our petrological, geochemical and geophysical studies of the xenoliths recovered from kimberlite. Furthermore, the diamond content and economic potential of kimberlite bodies relies exclusively on the successful sampling and transport of mantle cargo originating within the diamond window. Magma ascent velocities are rapid; one line of evidence for this is that xenoliths may be thermally equilibrated with the magma but are not chemically equilibrated and record mantle conditions (Mitchell, 1980). The entrainment of dense mantle cargo also constrains magma rise rates (e.g., Sparks et al. 1977; Mercier, 1979; Spera, 1984; Sparks et al. 2006).

Current models for xenolith sampling and transport are commonly based on the Stokes settling rates determined by the size and density of the mantle cargo relative to the properties of the kimberlite melt. Despite the flaws in these relatively simple calculations, they accentuate the fact that the dense mantle cargo is continually settling through the less dense, low viscosity melt as the kimberlite magma ascends. This implies that xenoliths are potentially being decoupled from the magma that actually sampled them and suggests that a substantial *lag time* exists between eruption of the magma that sampled the xenoliths and eruption of the lagging xenolithic cargo. Here, we explore the implications of these concepts for the distribution of xenoliths within kimberlite deposits and, in particular, for the distribution of mantle xenoliths derived from within the diamond window.

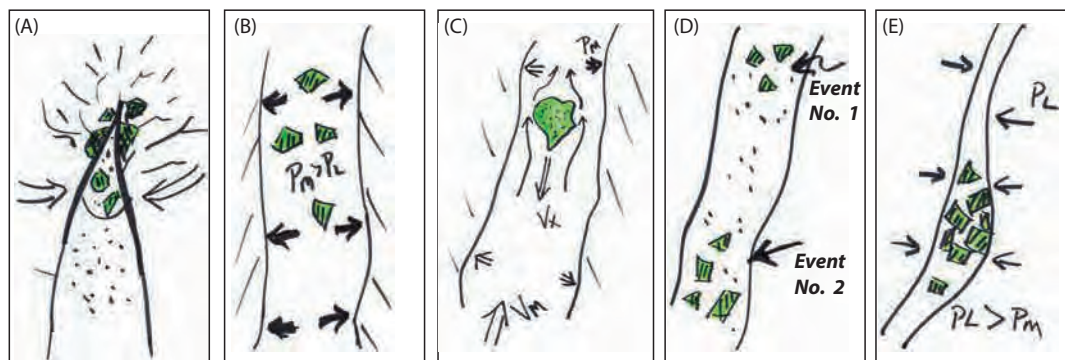


Figure 1. Schematic representation of events attending sampling and transport of mantle xenoliths. (A) Fluid-filled crack tip at head of kimberlite dyke causes brittle damage of mantle providing fragmented material for entrainment. (B) During peak flow, magma pressure (P_M) in the kimberlite dyke exceeds lithostatic pressure (P_L) sustaining magma ascent and xenolith entrainment. (C) Kimberlite ascent velocities (V_M) need to be high enough to compensate for settling of denser mantle cargo (V_X). (D) Xenolith clusters maintain their initial positions relative to other clusters under laminar flow conditions. (E) Field observations of xenolith-bearing dykes are compromised because of dyke relaxation.

Factoids on Xenolith Transport

Mantle xenoliths are extracted by brittle deformation of the surrounding lithosphere by buoyant kimberlite magmas where the stresses imposed by the crack tip at the head the buoyant magma exceed the tensile strength of the wall rocks at depth (e.g., Spera, 1984; Lensky et al. 2006; Wilson and Head, 2007). Dyke propagation through the damaged mantle lithosphere samples and entrains xenoliths (Fig.

1A). Xenoliths continue to sink in the magma as it ascends (Fig. 1C) and require ascent velocities in excess of the settling velocities to reach the surface (Sparks et al. 1977; Spera, 1984; Sparks et al. 2006).

The majority of xenoliths derive from sequential dyke propagation events wherein the damage zones surrounding the dyke's crack tip are sampled (Fig. 1D; Lensky et al. 2006; Brett et al. 2012). Theoretically, after each sampling event, xenoliths should remain clustered together and should preserve their position within the rising magma relative to other clusters of xenoliths (Fig. 1D). However, mixing by turbulent flow could disseminate clusters. Sorting of mantle xenoliths by size (densities are essentially equivalent) is a relatively inefficient process given the average ascent rates of kimberlite. When magma pressure decreases during the waning of ascent, widths of dykes decrease as the system relaxes thereby compromising field observations (i.e. Kavanagh and Sparks, 2011). However, in some instances, dykes closing during the waning stages of an eruption trap clusters of xenoliths and preserve evidence for the minimum dyke thicknesses during transport (Fig. 1E).

Basic Stokes Velocities

The terminal settling velocities (V_x) of dense solids (xenoliths) in viscous melts are predicted with Stokes law for spherical particles under laminar flow as a function of melt viscosity (η), particle radius (r) and the density contrast between melt and xenolith ($\Delta\rho$) (e.g., Spera, 1984):

$$V_x \cong \frac{2g\Delta\rho r^2}{9\eta} \quad (1)$$

One implication of mantle xenoliths being erupted is that the host magma must ascend at rates (V_m) faster than the xenoliths are sinking (i.e. V_x ; Eq. 1; Sparks et al. 1977; Spera 1984). During ascent, the xenoliths are sinking through the rising magma producing a lag time (Δt) given by:

$$\Delta t = \frac{D_x(V_m - V_x)}{V_m V_x} \quad (2)$$

where D_x is the source depth of the xenolith. For example, a differential rise velocity of 1 m s^{-1} between the kimberlite melt ($+4 \text{ m s}^{-1}$) and a mantle xenolith (-3 m s^{-1}) sampled at a depth of 150 km implies a time lag of ~ 3.5 hours (Fig. 2).

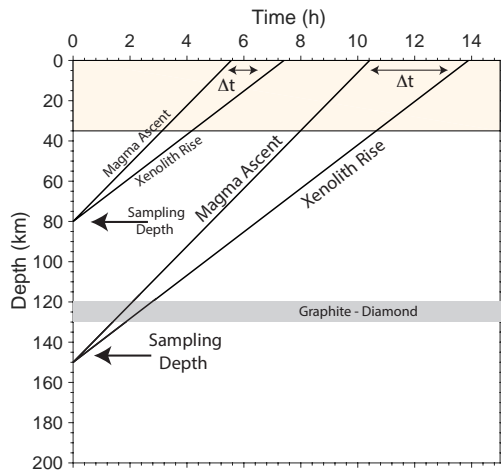


Figure 2. Model lag times for mantle xenoliths having a differential velocity of 1 m s^{-1} and depending on source depth.

In general, the deepest sourced mantle xenoliths will have the greatest lag times, as well as the greatest transport times. Shallow sampled mantle xenoliths will tend to be more strongly coupled the magma and have shorter lag times. Crustal xenoliths are likely to be more or less fully coupled to the kimberlite magma and be erupted continuously throughout the eruption and by the same magma that sampled them. In contrast, deeply sourced xenoliths from within the diamond window are likely to erupt hours after the magma that actually caused the original sampling. These xenoliths are at risk of being left behind if eruption durations are short or magma volumes

are small. Xenoliths sampled at depths of D_x will commonly be inherited and erupted by deeper/later magma (D_m) as described by:

$$D_m = \frac{D_x V_m}{V_x} \quad (3)$$

such that the pairing between kimberlite magma and erupted xenoliths is dependent on the sampling depth and the relative rise velocities of magma and xenolith.

Other Considerations

The concepts developed above derive from the assumption that Stokes law for settling of spherical particles is an adequate representation of the behavior of mantle xenoliths entrained by

kimberlite magma. Whilst silicate melts are Newtonian under normal shear strain rates, magmas can become non-Newtonian (Bingham) if crystal contents are high and develop a yield strength (σ_0 ; Sparks et al. 1977; Spera, 1984). Yield strengths will reduce the critical rise velocity required for the magma to successfully carry the mantle cargo. Indeed, small xenoliths can be fully coupled to the magma where the shear stress of the settling particle (σ_x) is $< \sigma_0$. However, the concept of a lag time between the magma and xenolith is preserved for all xenoliths having $\sigma_x > \sigma_0$.

Crystals in silicate magmas can enhance nucleation of bubbles of H₂O/CO₂ and xenolith entrainment represents another means of enhancing bubble nucleation. Experiments with carbonated liquids and rough-surfaced solids (e.g. 'MentosTM' candies) demonstrate the importance of surfaces for causing rapid, heterogeneous nucleation of bubbles. Xenolith roughened by attrition processes (Campbell et al. 2012; Jones et al., 2014) provide ideal surfaces for inducing vesiculation (i.e. Mentos effect; Edwards and Russell, 2009) thereby facilitating xenolith transport in 3 ways. The addition of bubbles will also introduce a non-Newtonian rheology and lead to shear-thinning characteristics and possibly viscoelastic behavior. Bubbles can lower the density of xenoliths by adhering to and coating xenolith surfaces (Edwards and Russell, 2009), as well as, hinder settling. Thirdly, a decrease in volatile content of the melt will increase melt viscosity. The 'Mentos' effect could also be driven by deep-seated assimilation-driven vesiculation of CO₂ (Russell et al. 2012).

Conclusions

Differential velocities between a rising kimberlite magma and the mantle xenoliths it samples leads to substantial lag times between the eruption of magma and xenolith cargo. These lag times have important implications for the total volume of magma rising, the duration of kimberlite eruptions, the length (depth) of dyke that is open at depth during the eruption, and, ultimately, the distribution of diamonds within kimberlite eruption products.

References

- Brett, RC, Russell, JK, Andrews, GDM & Jones, TJ (2015) The ascent of kimberlite: Insights from olivine. *Earth & Planet Sci Lett* 424, 119-131.
- Campbell, M Russell, JK & Porritt LA (2013) Thermomechanical milling of accessory lithics in volcanic conduits. *Earth & Planet Sci Lett* 377-378, 276-286.
- Edwards, BR & Russell, JK (2009) Xenoliths as magmatic 'menthos'. GAC-MAC & AGU Joint Annual Spring Meeting with Abstracts, Toronto, Canada.
- Jones TJ Russell JK Porritt LA & Brown RJ (2014) The morphology and surface features of olivine in kimberlite lava: implications for ascent and emplacement mechanisms, *Solid Earth* 5, 2283-2312.
- Kavanagh, JL & Sparks, RSJ (2011) Insights of dyke emplacement mechanics from detailed 3D dyke thickness datasets. *J Geol Soc* 168, 965-978.
- Lensky, NG, Niebo, RW, Holloway, JR, Lyakhovskiy, V & Navon, O (2006) Bubble nucleation as a trigger for xenolith entrapment in mantle melts. *Earth & Planet Sci Lett* 245, 278-288.
- Mercier, JC 1979. Peridotite xenoliths and the dynamics of kimberlite intrusion. *The Mantle Sample: Inclusion in Kimberlites and Other Volcanics*, 197-212.
- Mitchell, RH, Carswell, DA & Clarke, DB (1980) Geological implications and validity of calculated equilibration conditions for ultramafic xenoliths from the pipe 200 kimberlite, northern Lesotho. *Contrib Mineral Petrol* 72, 205-217.
- Russell, JK, Porritt, L, Lavalley, Y & Dingwell, D (2012) Kimberlite ascent by assimilation-fuelled buoyancy. *Nature* 481, 352-356.
- Sparks, RSJ, Baker, L, Brown, RJ, Field, M, Schumacher, J, Stripp, G & Walters, A (2006) Dynamical constraints on kimberlite volcanism. *J Volc Geotherm Res* 155, 18.
- Sparks, RSJ, Pinkerton, H & Macdonald, R (1977) The transport of xenoliths in magmas. *Earth & Planet Sci Lett* 35, 234-238.
- Spera, FK (1984) Carbon dioxide in petrogenesis III: role of volatiles in the ascent of alkaline magma with special reference to xenolith-bearing mafic lavas. *Contrib Mineral Petrol* 88, 217-232.
- Wilson, L & Head, JW (2007) Integrated model of kimberlite ascent and eruption. *Nature* 447, 53-57.



The Archean sedimentary sulfur recycling under the Kaapvaal craton revisited from 4S-isotopic compositions in sulfide inclusions in diamonds from Kimberley Pool (South Africa) Jwaneng and Orapa (Botswana)

E Thomassot^{1,2}, J Farquhar³, N Bouden¹, J.W Harris⁴, K. McKeegan⁵, J Cliff⁶
B Wing⁷, P Piccoli³

⁷ CRPG-CNRS and Université de Lorraine, 54501 Vandœuvre-Lès-Nancy, France

² Institut de Physique du Globe de Paris, 1 Rue Jussieu, 75 005 Paris, France.

³ University of Maryland, Washington, United States.

⁴ University of Glasgow, Glasgow, Scotland, UK.

⁵ UCLA, Los Angeles, United States.

⁶ Pacific Northwest National Lab, Richland, United States.

⁷ University of Colorado, Boulder, United States.

Introduction

The sulfur isotope composition of sulfide inclusions in diamond (SID) provides evidence for recycling of sulfur in the diamond stability field. Variations of $\delta^{34}\text{S}$ (Chaussidon 1987; Rudnick 1993) and mass-independent fractionation (S-MIF, Farquhar 2002; Thomassot 2009) are not readily explained by mantle processes and are better attributed to recycling of sulfur with surface $\delta^{34}\text{S}$ and S-MIF signatures. Variations of $\delta^{34}\text{S}$ are large in sedimentary rocks principally because of the role played by microbially-mediated sulfur metabolisms. On the other hand, S-MIF signatures result from photochemical reactions involving ultra-violet (UV) light and were produced in the atmosphere before the Great Oxygenation Event (GOE). Consequently, the presence of S-MIF is diagnostic of Archæan sedimentary sulfur and as such, is one of the most robust geochemical tools for tracking the possible recycling of Archæan surficial sulfur transported to deep-seated rocks.

In sediments, the relative abundance of the minor isotope of sulfur, ^{36}S , is also affected by both mass-dependent reactions (related to microbial cycling, e.g. Ono et al., 2006) and mass-independent atmospheric reactions that lead to variations of $\delta^{34}\text{S}$ and $\Delta^{33}\text{S}$. Accordingly, studying covariations of $\Delta^{33}\text{S}$ and $\Delta^{36}\text{S}$ helps in deciphering peculiar fractionation processes.

Here we use the 4S-isotope signatures in SID *i*) to test the robustness of S-MIF array of specific exospheric sulfur pools along their journey from the surface to the mantle and *ii*) to provide a more complete assessment of the recycled sulfur pools and map the sedimentary ingredients recycled from the surface to the diamond growth-environment.

Samples and Methods

We have selected 40 SID originating from three distinct kimberlite pipes (Jwaneng and Orapa in Botswana, and Kimberley Pool in South Africa) located along the Colesberg Lineament (Kaapvaal craton). This N-S magnetic anomaly represents the suture zone between the eastern and western blocks of the craton, and the cratonic keels below this area likely preserve subducted surficial lithologies as attested by the large proportion of eclogitic xenoliths carried to the surface by kimberlites (Shirey et al., 2003). Among the entire collection, three samples have a peridotitic affinity whereas the other are clearly eclogitic. Samples from Orapa (n=18) and Jwaneng (n= 18) have been analyzed earlier for $\delta^{34}\text{S}$ and $\Delta^{33}\text{S}$ (Farquhar et al., 2002; Thomassot et al., 2009).

We examine the $\Delta^{36}\text{S}$ in addition to $\delta^{34}\text{S}$ and $\Delta^{33}\text{S}$ signatures measured in-situ with secondary ion mass spectrometers (CAMECA 1280 at UCLA and UWA and 1280 HR at CRPG Nancy). The same measurement protocol (Cs^+ primary source, multicollection mode with 3 faraday cups and one electron multiplier for ^{36}S) has been used in all three laboratories. However, instrumental fractionation

correction differs from one laboratory to the other (Laflamme et al., 2017 for UWA and Delavault et al., 2016 for CRPG). Results of the interlaboratory measurement comparison are in good agreement and will be presented at the conference. Two sigma external uncertainties are better than ± 0.15 ‰ for single $\Delta^{33}\text{S}$ measurements and ± 0.35 ‰ for single $\Delta^{36}\text{S}$ measurement.

Results

The sulfur isotopic composition in SID from Jwaneng ($\delta^{34}\text{S}$ from -6.7 ‰ to 3.14 ‰, $\delta^{34}\text{S}_{\text{mean}} = -1.04$ ‰), Kimberley Pool ($\delta^{34}\text{S}$ from -8.9 ‰ to 1.9 ‰, $\delta^{34}\text{S}_{\text{mean}} = -1.07$ ‰) displays a wide range centered around the canonical mantle value ($\delta^{34}\text{S} = -1 \pm 2$ ‰, Labidi et al., 2014) whereas Orapa samples are statistically enriched in ^{34}S ($\delta^{34}\text{S}$ from -8.4 ‰ to 1.7 ‰, $\delta^{34}\text{S}_{\text{mean}} = 0.3$ ‰).

Significant mass-independent sulfur isotopic fractionations have been detected in the three localities with differences in amplitude and $\Delta^{36}\text{S}/\Delta^{33}\text{S}$ (Fig. 1). In Jwaneng samples, significant and (mostly) positive $\Delta^{33}\text{S}$ (ranging from -0.25 to 1.65 ‰) associated with negative $\Delta^{36}\text{S}$ (ranging from -1.67 to 0.29 ‰) match a global negative trend ($\Delta^{36}\text{S}/\Delta^{33}\text{S} = -1.1 \pm 0.23$). In Kimberley Pool, these anomalies are smaller with negative $\Delta^{33}\text{S}$ (from -0.28 to -0.04 ‰) and negative $\Delta^{36}\text{S}$ from $(-1.4$ to -0.3 ‰), defining a weak positive correlation ($\Delta^{36}\text{S}/\Delta^{33}\text{S} = +0.8$). Finally, five samples from Orapa possess positive $\Delta^{33}\text{S}$ (up to 1.3 ‰). The remaining Orapa samples, which are devoid of large $\Delta^{33}\text{S}$ anomalies, are interestingly enriched in ^{36}S (i.e. $\Delta^{36}\text{S}$ ranging from 0 to 1 ‰) and define a trend such as $\Delta^{36}\text{S}/\Delta^{33}\text{S} = -8$.

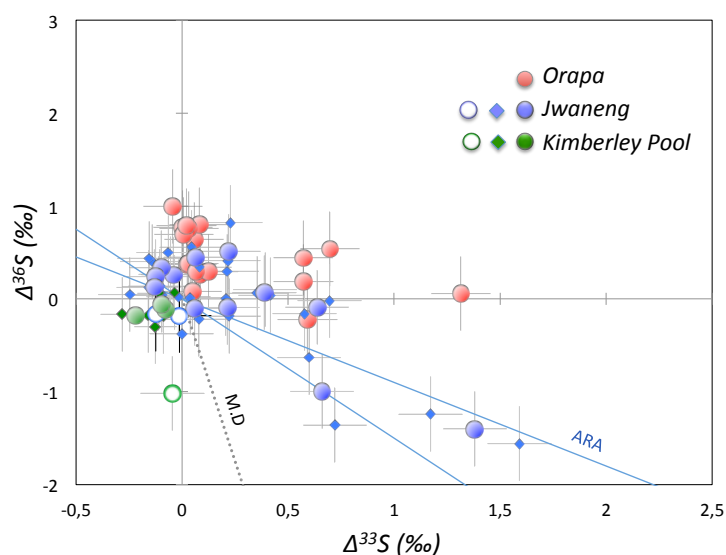


Figure 1 :

Plot of $\Delta^{36}\text{S}$ versus $\Delta^{33}\text{S}$ values determined in situ for sulfides inclusions in diamonds from Jwaneng (blue symbols), Kimberley Pool (green symbols) and Orapa (red symbols).

Plain symbols: E-type specimens

Open symbols: P-type specimens

Diamonds symbols refer to individual measurements. Dot symbols refer to averaged values for a single inclusion.

The blue lines represent the array found in most of Archean sediments ($\Delta^{36}\text{S}/\Delta^{33}\text{S}$ ranging from -0.9 to -1.5). The dotted line represents the mass-dependent fractionation ($\Delta^{36}\text{S}/\Delta^{33}\text{S} = -7$)

Discussion

Re/Os studies in SID originating from the Kaapvaal craton revealed two main groups of ages. A large number of inclusions from the Jwaneng, Kimberley Pool and Orapa plot on a 2.9 Ga isochron with the remainder displaying weaker isochron ages ranging from 1.9 to 1 Ga (Richardson 2001; Shirey et al. 2008). Comparing our results with the isotopic record in sediments from comparable ages, reveals some similarities.

The general isotopic trend found in Jwaneng SID matches the ARA (Fig 2a) and provides a robust confirmation of the recycling of neo-Archæan sediments (Thomassot et al., 2009).

Multiple S-isotopic signatures in Kimberley Pool samples clearly differ from Jwaneng implying a distinct source of sulfur. S-MIF covariations in this location are more elusive as the amplitude of both $\Delta^{33}\text{S}$ and $\Delta^{36}\text{S}$ are small. However Kimberley Pool SID match the composition of some meso-Archæan sediments (Fig 2b), in good agreement with the meso-Archæan isochron age reported in the literature. Finally, Orapa samples can be divided into two subpopulations. A small group of samples is consistent with an Archæan S-MIF signature comparable with Jwaneng samples. The remaining samples, without clearly anomalous $\Delta^{33}\text{S}$ and $\delta^{34}\text{S}$, carry significant variations for $\Delta^{36}\text{S}$ which are

consistent with isotopic fractionation accompanying microbial sulfate reduction (Ono et al., 2006). It is worth noting that the S-MIF trend in Orapa matches the composition of sedimentary sulfur deposited at the surface of the Earth 1.9 ± 0.2 Ga corresponding to one Re/Os isochron age determined for this locality (Shirey et al., 2008).

This study confirms that surficial sulfur has been efficiently transferred to the lithospheric mantle. More interestingly, it shows that S-MIF isotopic signatures (i.e. $\Delta^{36}\text{S}/\Delta^{33}\text{S}$) are preserved during the recycling of sediment. Complementary to radiogenic isotope data, 4S- isotope measurements are thus robust probes for spotting different sedimentary pools (e.g. deposited at different periods of time, or corresponding to different environmental conditions) in mantle rocks.

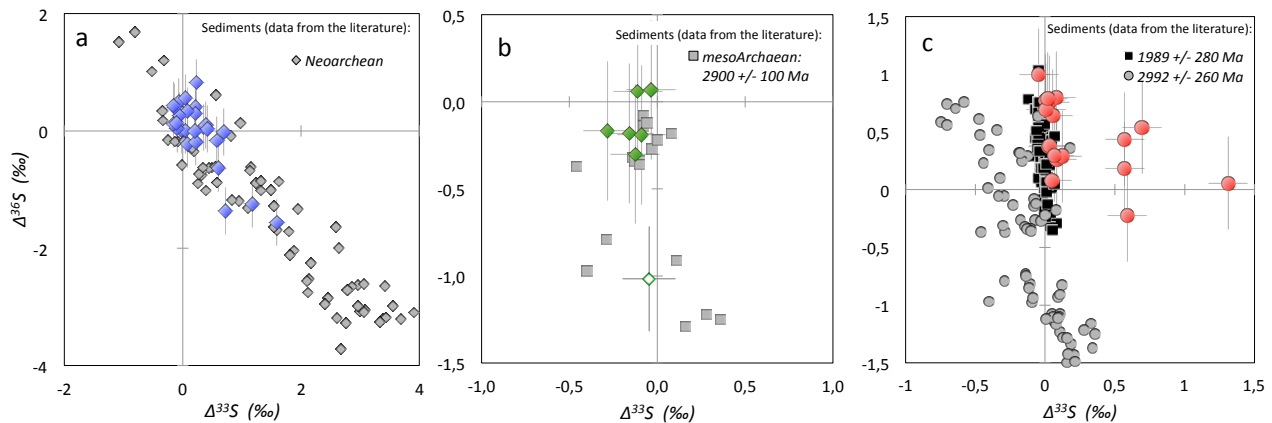


Figure 2 : Plots of $\Delta^{36}\text{S}$ versus $\Delta^{33}\text{S}$ values measured in SID from a) Jwaneng, b) Kimberley Pool and c) Orapa (see Fig 1 for symbol description). The grey symbols are shown for comparison and represent multiple sulfur isotope compositions in sediments from different period of time (data from the literature).

References:

- Chaussidon M., et al. (1987). Sulphur isotope heterogeneity in the mantle from ion microprobe measurements of sulphide inclusions in diamonds. *Nature*, 330(6145), 242-244.
- Delavault, H. et al. (2016). Sulfur and lead isotopic evidence of relic Archean sediments in the Pitcairn mantle plume. *Proceedings of the National Academy of Sciences*, 113(46), 12952-12956.
- Farquhar, J., Bao, H., & Thiemens, M. (2000). Atmospheric influence of Earth's earliest sulfur cycle. *Science*, 289(5480), 756-758.
- Farquhar, J. et al. (2002). Mass-independent sulfur of inclusions in diamond and sulfur recycling on early Earth. *Science*, 298(5602), 2369-2372.
- Izon, G. et al. (2017). Biological regulation of atmospheric chemistry en route to planetary oxygenation. *Proceedings of the National Academy of Sciences*, 114(13), E2571-E2579.
- Ono, S., et al. (2006). Mass-dependent fractionation of quadruple stable sulfur isotope system as a new tracer of sulfur biogeochemical cycles. *Geochimica et Cosmochimica Acta*, 70(9), 2238-2252.
- Labidi, J. et al. (2014). Sulfur isotope budget (^{32}S , ^{33}S , ^{34}S and ^{36}S) in Pacific-Antarctic ridge basalts: A record of mantle source heterogeneity and hydrothermal sulfide assimilation. *Geochimica et Cosmochimica Acta*, 133, 47-67.
- LaFlamme, C. et al. (2016). In situ multiple sulfur isotope analysis by SIMS of pyrite, chalcopyrite, pyrrhotite, and pentlandite to refine magmatic ore genetic models. *Chemical Geology*, 444, 1-15.
- Rudnick, R. L. et al. (1993). Diamond growth history from in situ measurement of Pb and S isotopic compositions of sulfide inclusions. *Geology*, 21(1), 13-16.
- Shirey, S. B., et al., (2008). A review of the isotopic and trace element evidence for mantle and crustal processes in the Hadean and Archean: Implications for the onset of plate tectonic subduction. *Geological Society of America Special Papers*, 440, 1-29.
- Thomassot, E., et al. (2009). Metasomatic diamond growth: A multi-isotope study (^{13}C , ^{15}N , ^{33}S , ^{34}S) of sulphide inclusions and their host diamonds from Jwaneng (Botswana). *Earth and Planetary Science Letters*, 282(1), 79-90.
- Thomassot, E., et al. (2015). Atmospheric record in the Hadean Eon from multiple sulfur isotope measurements in Nuvvuagittuq Greenstone Belt (Nunavik, Quebec). *Proceedings of the National Academy of Sciences*, 112(3), 707-712.



Ilmenite generations in orangeite from Banankoro, Guinea: implications for exploration

Jingyao Xu¹, Joan Carles Melgarejo², Montgarri Castillo-Oliver³, Laia Arqués⁴, Joan Santamaria⁵

(1) Departament de Mineralogia, Petrologia i Geologia Aplicada, Facultat de Ciències de la Terra, Universitat de Barcelona, C/Martí i Franquès s/n, 08028 Barcelona, Spain. jingyao.xu@ub.edu

(2) Departament de Mineralogia, Petrologia i Geologia Aplicada, Facultat de Ciències de la Terra, Universitat de Barcelona, C/Martí i Franquès s/n, 08028 Barcelona, Spain. joan.carles.melgarejo.draper@ub.edu

(3) ARC Centre of Excellence for Core to Crust Fluid Systems and GEMOC, Department of Earth and Planetary Sciences, Macquarie University, NSW 2019, Australia. montgarri.castillo-oliver@mq.edu.au

(4) Departament d'Energia Solar, Institut de Recerca en Energia de Catalunya. Jardins de les Dones de Negre 1, 2n pis. 08930 Sant Adrià del Besòs, Spain. larques@irec.cat

(5) Consultant Geologist, Sabadell, Spain. joan.guinea.casanovas@gmail.com

Introduction

Ilmenite is one of the classic diamond indicator minerals (DIMs) and for long it has been used as a guide for kimberlite exploration. Mg-rich ilmenite is commonly found either as a xenocryst or as a replacement product of ilmenite xenocrysts. However, ilmenite is not present in all kimberlites worldwide, and Mg-ilmenite is rarely documented as a euhedral crystal component of the kimberlite groundmass (Boctor and Boyd, 1980; Haggerty, 1975). The discovery of euhedral Mg-ilmenite crystals in the groundmass of a pipe in the Banankoro area (Guinea) offers a good opportunity to study the textural relations between the different ilmenite generations and the rest of the minerals.

The kimberlites from Banankoro (Guinea) are found in the Man craton, West Africa. The Banankoro kimberlite age was obtained by $^{40}\text{Ar}/^{39}\text{Ar}$ for phlogopite about 139 ± 3 Ma (Skinner et al., 2004). Most of the Man craton kimberlites were classified as phlogopite kimberlites, although K contents are relatively low (Skinner et al., 2004).

Petrography

The samples studied here are hypabyssal, and they consist of corroded xenocrysts of olivine (30% modal), phlogopite (<1% modal) and geikielite (<1% modal) settled in a groundmass (68% modal). On its turn, the groundmass is made up of olivine microphenocrysts altered to serpentine group minerals (40%), phlogopite (38%), calcite (16%), spinel-group minerals (6%) and lesser amounts of perovskite, apatite and ilmenite.

Phlogopite macrocrysts (about 2mm, phlogopite 1) show a reaction rim (phlogopite 2), and they are replaced by a second rim (phlogopite 3). Similarly, groundmass phlogopite has a rounded core of Ti-rich phlogopite (phlogopite 4) replaced by a tetraferriphlogopite rim (phlogopite 5).

Many textural populations of the spinel-group minerals occur in the groundmass. The first one is hemihedral, atoll-shaped and frequently zoned, with a chromite core (spinel 1). It is replaced by another euhedral chromite (spinel 2). Another chromite with different composition (spinel 3) is found together with the spinel 2 included in phlogopite 3. Both spinels may also be mantled by a zoned titanomagnetite rim (spinel 4 and 5). Titanomagnetite (spinel 6) replaces geikielite xenocrysts. Euhedral unzoned titanomagnetite (spinel 7) occurs in rounded massive cloudy aggregates, along with phlogopite.

Four compositional-textural ilmenite types are discriminated. Type 1 Mg-rich ilmenite is anhedral and it is replaced by spinel 6. Type 2 ilmenite is Mg-rich, it occurs as euhedral tabular crystals (about 200 μm), which grew in small cavities along with earlier calcite. This ilmenite may replace spinel and it is replaced by a late generation of Mn-rich ilmenite (type 3) along the borders and fractures. Type 4 ilmenite is Mn-rich ilmenite and it replaces the perovskite margins.

Perovskite in groundmass is euhedral to hemihedral and it is slightly zoned. It is replaced by type 4 Mn-rich ilmenite.

Mineral chemistry

Spinel 1 do not follow the typical spinel trends, and it has lower Al (0,13-0,15 apfu), Mg (0,40-0,43 apfu), and Ti (0,05-0,07) but higher Fe^{2+} (0,59-0,64 apfu) and Fe^{3+} (0,46-0,54 apfu) contents than spinel 2 (0,16-0,32 apfu Al, 0,57-0,61 apfu Mg and 0,12-0,19 apfu Ti; 0,49-0,58 apfu Fe^{2+} and 0,22-0,42 apfu Fe^{3+}). Spinel 2 is magnesiochromite with 0,79-0,89 Cr#. There is an increase in $\text{Ti}/(\text{Ti}+\text{Al}+\text{Cr})$, $\text{Fe}^{2+}/(\text{Fe}^{2+}+\text{Mg})$ and $\text{Fe}^{3+}/(\text{Fe}^{3+}+\text{Al}+\text{Cr})$ from spinel 2 to spinel 5. This compositional trend crosses the T1 and T2 fields established by Mitchell (1986), as well as the kimberlite trend and Fe-Ti trend defined by Barnes and Roeder (2001). Titanomagnetite (spinel 6) replaces Mg-rich ilmenite and hence it is enriched in Mg. The euhedral titanomagnetite (spinel 7) has a composition between spinel 3 and spinel 4.

Type 1 Mg-rich ilmenite is classified as geikielite (0,52-0,58 apfu Mg), it has higher Cr than the other ilmenite types (up to 2,7 wt.% Cr_2O_3), and very low Mn and Nb contents (0,5-0,8 wt.% MnO and ~0,1 wt.% Nb_2O_5). Type 2 euhedral tabular ilmenite is Mg-rich (0,30-0,48 Mg apfu), with low Mn and Nb contents (1,5-2,4 wt. % MnO and 0,4-1,4 wt.% Nb_2O_5). Type 3 ilmenite is slightly enriched in Mn (2,57-4,5 wt. % MnO) but it has low Mg and Cr contents (0,5-2,7wt.% MgO and 0-0,4 wt.% Cr_2O_3). It has enrichment in Nb (0,7-2,5 wt. % Nb_2O_5), with high Fe^{2+} (0,8-0,9 apfu) and low Fe^{3+} (< 0,1 apfu). Type 4 ilmenite is poor in Mg and Cr but it is slightly enriched in Mn (3,2-4,9 wt.% MnO) and Nb. Type 1 ilmenite compositions plot in the kimberlitic domain (Wyatt et al., 2004), while types 2, 3 and 4 plot outside. However, it shows a Mn enrichment from type 2 to type 4 ilmenite. Type 1 has the highest Fe^{3+} and Mg contents.

The phlogopite macrocrysts (type 1) are Al-rich (1,95-1,98 apfu) and Ti-poor (0,02-0,03 apfu). Phlogopite 2 is Al-rich (about 2,42 apfu) and Ti-rich (0,40-0,41 apfu). Phlogopite 3 (outer rim) has the same composition as the core of groundmass phlogopite (phlogopite 4), which is Ti-rich (0,14-0,20 apfu) and Al-rich (1,58-1,80 apfu). These evolve to Al-free (0-0,07 apfu) and Ti-poor (0,02-0,04 apfu) tetraferriphlogopite, thus following the orangeite trend defined by Mitchell (1995). They have 1,49-1,70 apfu Fe^{3+} in the tetrahedral position.

Perovskite in groundmass is slightly zoned, the cores having higher LREE content (5,0- 5,7 wt.% Σ LREE $_2\text{O}_3$) than the borders (up to 1,2-3,9 wt.% Σ LREE $_2\text{O}_3$). Nb contents are quite constant and low (0,8-1,8 wt.% Nb_2O_5).

Discussion and conclusions

The high modal phlogopite and the tetraferriphlogopite trend (Tappe et al., 2005) are indicative of an orangeite affinity for this pipe. However, the occurrence of an early generation of phlogopite with an "alnoite or minette" trend would indicate the existence of an early different magma.

The diversity of spinel and ilmenite generations also records a very complex evolution of this magma. The origin of the type 1 spinel remains obscure, but since it is replaced by the younger chromite generations it could be produced by an early magma of unclear composition. However, the coexistence of type 2 and type 3 spinels (as demonstrated by their occurrence in same growth band of phlogopite) suggests the coexistence of two separate magmas (a possible magma mingling) in this intrusion. At the least, the chemical evolution of the zoned spinels (types 2, 4, 5) can fit the evolution of an orangeite magma, but the higher Mg compositions of the type 3 could also suggest the existence of a more kimberlitic magma. However, one must take into account that the composition of spinel 6 can be interpreted as produced by the same magma as type 4 spinel, but enriched in Mg because it replaces geikielite. Moreover, the occurrence of dense spinel aggregates with a distinct composition (type 7 spinel) can be indicative of another Fe-rich magma of nelsonitic affinity.

Mg-rich ilmenite is commonly found as macro- and megacryst in kimberlite, and it is interpreted as produced by primary magmatic crystallization (Moore, 1987) or as xenocrysts (Armstrong et al., 2004). However, it is found in most of the cases as a replacement product of oxidized ilmenite xenocrysts (Robles-Cruz et al., 2009). Hence, type 1 ilmenite (geikielitic) from Banankoro could be produced by a similar mechanism, because its composition is typically within the kimberlitic domain of Wyatt et al. (2004). This process took place clearly before the crystallization of the groundmass spinel. However, euhedral Mg-rich ilmenite is very different to the other ilmenite generation, also in compositions. Firstly, type 2 euhedral tabular ilmenite from Banankoro plots out of the kimberlite domain in the compositional diagram of Wyatt et al. (2004), and it has a higher Mn contents. Moreover, type 2 ilmenite crystallised as a late product in association with calcite and serpentines, mantling spinels and other groundmass minerals. Therefore, it cannot have any relation with the metasomatic processes in the mantle producing the diamond growth.

Finally, although type 3 Mn-ilmenite has been suggested as a guide for diamond exploration, in Banankoro is clearly a late product replacing Mg-rich euhedral ilmenite and all the spinel minerals. Therefore, its formation is most likely linked to hydrothermal fluids given its systematic association with serpentines.

Acknowledgments

This research was supported the AGAUR 2014SGR01661 of the Generalitat de Catalunya and a FI grant to J. Xu (coded FI_B 00904) sponsored by the Departament d'Educació i Universitats de la Generalitat de Catalunya. The authors also acknowledge the Servei de Làmina Prima and the Centres Científics i Tecnològics de la Universitat de Barcelona (CCiT-UB) for the assistance with SEM-BSE-EDS study (Dr. F. J. García-Veigas, D. Artiaga) and EMP analyses (Dr. Xavier Llovet).

References

- Armstrong KA, Nowicki TE, Read GH (2004) Kimberlite AT-56: a mantle sample from the north central Superior craton, Canada. *Lithos* 77: 695–704
- Barnes SJ, Roeder PL, (2001) The range of spinel compositions in terrestrial mafic and ultramafic rocks. *J. Petrol.* 42: 2279–2302
- Boctor N, Boyd F (1980) Oxide minerals in the Liphobong kimberlite, Lesotho. *Am. Min.* 65: 631–638
- Haggerty SE, (1975) The chemistry and genesis of opaque minerals in kimberlites: Physics and Chemistry of the Earth 9: 295- 307
- Mitchell RH (1995) Kimberlites, Orangeites, and Related Rocks. Plenum Press. New York, 410 pp
- Moore AE (1987) A model for the origin of ilmenite in kimberlite and diamond: implications for the genesis of the discrete nodule (megacryst) suite. *Contrib Mineral. Petrol.* 95: 245–253
- Robles-Cruz SE, Watangua M, Isidoro L, Melgarejo JC, Galí A, Olimpio A (2009) Contrasting compositions and textures of ilmenite in the Catoca kimberlite, Angola, and implications in exploration for diamond. *Lithos* 112: 966–975
- Skinner EMW, Apter DB, Morelli C, Smithson NK. (2004) Kimberlites of the Man Craton, West Africa. *Lithos* 76: 233–259
- Tappe S, Foley SF, Jenner GA, Kjarsgaard BA (2005) Integrating ultramafic lamprophyres into the IUGS classification of igneous rocks: rationale and implications. *J. Petrol.* 46: 1893–1900
- Wyatt BA, Mike B, Anckar E, Grütter H (2004) Compositional classification of “kimberlitic” and “non-kimberlitic” ilmenite. *Lithos* 77: 819–840



Styles of alteration of Ti oxides of the kimberlite groundmass: implications on the petrogenesis and classification of kimberlites and similar rocks

Jingyao Xu¹, Joan Carles Melgarejo², Montgarri Castillo-Oliver³

¹ *Departament de Mineralogia, Petrologia i Geologia Aplicada, Facultat de Ciències de la Terra, Universitat de Barcelona, Barcelona, Spain, jingyao.xu@ub.edu*

² *Departament de Mineralogia, Petrologia i Geologia Aplicada, Facultat de Ciències de la Terra, Universitat de Barcelona, Barcelona, Spain, joan.carles.melgarejo.draper@ub.edu*

³ *ARC Centre of Excellence for Core to Crust Fluid Systems and GEMOC, Department of Earth and Planetary Sciences, Macquarie University, NSW, Australia, montgarri.castillo-oliver@mq.edu.au*

Introduction

Ti-minerals as ilmenite, spinels and perovskite are diamond indicator minerals and are important carriers of petrogenetic information. However, in many cases these minerals suffer complex alteration processes during the hydrothermal or supergene late stages of the kimberlite crystallization sequence.

Altered kimberlites occur in the Bastar craton (central India) and the Eastern Dharwar craton (EDC, Southern India) in India. Kimberlite pipes and dikes (around 100 intrusions) from the EDC of southern India are distributed in three distinct fields: 1) the southern Wajrakarur kimberlite field; 2) the northern Narayanpet kimberlite field; and 3) the Raichur kimberlite field (Chalapathi Rao et al, 2013). This study compares the sequences of alteration in samples from two nearby pipes (SK-1 and SK-2, about 1100 m of distance) from Siddanpalli, Raichur Kimberlite field, EDC, southern India. The emplacement of these kimberlites is assumed to have taken place during the Mesoproterozoic, around 1,1 Ga (Chalapathi Rao et al., 2013).

Mineral textures

Both kimberlites have similar xenocrysts, mainly consisting of Ti oxides as rutile and ilmenite, scattered in a fine-grained groundmass.

Textures of the primary minerals of the groundmass are also similar in both fields, and *grosso modo* comprise calcite, apatite, perovskite and altered atoll-shaped spinel group minerals. The abundance of minerals of the serpentine group in the groundmass suggests that members of the olivine group were also common in this in these kimberlites.

Groundmass perovskite (type 1 perovskite) from SK-1 is euhedral, zoned and slightly replaced by anatase following grain borders and small cracks. Identity of anatase was confirmed by microRaman spectroscopy, and its spectrum was compared with that of anatase altering perovskite in carbonatites (Pereira et al., 2005). Spinel group minerals in groundmass are strongly altered to serpentine, calcite, magnetite and cryptocrystalline Ti-rich hydrogarnets.

Groundmass perovskite (type 1 perovskite) from SK-2 is euhedral to subhedral and it has oscillatory zoning. In addition, a second perovskite generation (type 2 perovskite, euhedral) replaces the atoll spinel of groundmass along with Ti-rich hydrogarnets, calcite and serpentine.

Type 1 perovskite from SK-2 is partially or nearly totally replaced by kassite [CaTi₂O₄(OH)₂] accompanied by abundant aeschynite-(Ce), ideally [(Ce,Ca,Fe,Th)(Ti,Nb)₂(O,OH)₆]. Identity of kassite instead of cafetite (CaTi₂O₅ H₂O) was confirmed by comparing the kassite Raman spectrum from the SK-2 kimberlite with the kassite spectrum published by Martins et al. (2014). SK-2 perovskite may also be replaced by Mn-rich ilmenite along small cracks. Ilmenite and magnetite xenocrysts from SK-2 may be replaced by a sequence of typical groundmass minerals, as ulvöspinel and type 2 perovskite; on its turn, this perovskite may be replaced by anatase.

Mineral chemistry

Spinel-group minerals from groundmass of both kimberlites have compositions in the ulvöspinel-titanomagnetite domain. However, they are strongly altered and the restitic cores may be seldom enriched in Zn (0,1-2,0 wt.% ZnO in SK-1 and 0-7,5 wt.% ZnO in SK-2).

The composition of type 1 groundmass perovskite is similar for both kimberlites. Cores are slightly enriched in REE (4,9-6,2 wt.% Σ REE₂O₃ in the cores vs 1,9-2,8 wt.% Σ REE₂O₃ in the rims in SK-1; 5,1- 5,5 wt.% Σ REE₂O₃ in the centers and 0,9-2,6 wt.% Σ REE₂O₃ in the borders in SK-2). Nb is also slightly enriched in the cores compared to the rims (0,6-1,1 wt % Nb₂O₅ in the cores and 0,4-0,6 wt.% Nb₂O₅ in the rims in SK-1; 0,5-0,8 % Nb₂O₅ in the cores and 0,4 -0,6 wt.% Nb₂O₅ in the rims in SK-2). Perovskite 1 in both kimberlites has FeO contents ranging 0,9-1,6 wt.%.

Type 2 perovskite from the SK-2 kimberlite has different composition than the type 1 perovskite. It is poor in REE (<1 wt.% Σ REE₂O₃) and Nb (<0,1 wt.% Nb₂O₅), but it has higher Fe contents (2,4-3,5 wt.% FeO) than type 1 perovskite.

Kassite replacing type 1 perovskite has a stoichiometric composition, whereas the associated aeschynite tends to concentrate LREE and, to a lesser extent, Nb.

The aeschynite-(Ce) produces the next average structural formula: (Ca_{0,39}Ce_{0,33}La_{0,13}Nd_{0,12}Pr_{0,04}) Σ _{1,01}(Ti_{1,82}Nb_{0,07}Fe³⁺_{0,02}Zr_{0,02}) Σ _{1,93}(O,OH)₆. Therefore, the aeschynite group minerals from SK-2 kimberlite are extremely poor in Nb, U and Th when compared to similar minerals typically occurring as metamictic phases in carbonatites and granitic pegmatites. However, their compositions are similar to those of the late Ti-REE minerals described in the Iron Mountain kimberlite field (Mitchell and Chakhmouradian, 1998).

Ti-rich hydrogarnets from the SK-2 kimberlite were analyzed by EMP while those from the SK-1 pipe are too small to be analyzed. The Ti-rich hydrogarnets replacing Ti-rich spinels from the SK-2 have intermediate compositions between morimotoite, “hydroschorlomite” and Ti-rich “hydroandradite”.

Discussion and conclusion

Perovskite is a principal host of LREE in undersaturated ultramafic and alkaline rocks. However, perovskite may be unstable in CO₂-rich fluid environments characteristic of some carbonatites and kimberlites worldwide (Mitchell and Chakhmouradian, 1998). Perovskite replacement in kimberlites is not common, but may include kassite, anatase and titanite along with calcite, ilmenite and unidentified LREE-Ti oxides (Mitchell and Chakhmouradian, 1998; Martins et al., 2014).

The subsolidus history of the studied Indian kimberlites has important differences, and in particular the alteration of perovskite is more developed in SK-2. The alteration process took place under different fluid/rock ratios in each kimberlite, in a relatively closed system. Under these conditions, Ti-rich minerals are unstable and, in particular, Ti-rich spinels are easily replaced in both kimberlites by mixtures of Ti-rich hydrogarnets, calcite and serpentine. A relatively low SiO₂ and high water activities were necessary to both avoid the crystallization of titanite and favour the crystallization of hydrogarnets. Slight replacement of perovskite by anatase in SK-1 could be indicative of a decrease of temperature under conditions of medium to high f (CO₂), following the experimental data by Martins et al. (2014). However, the same experimental data suggest that the strong replacement of perovskite by kassite in SK-2 needs a high f (H₂O) and a low activity in alkalis. The LREE-rich perovskite is more unstable during these processes than pure end-member perovskite. Therefore, aeschynite-(Ce) inherits the composition of the replaced LREE-bearing perovskite cores, and it is as Nb-poor as are these cores.

The occurrence of abundant Ti-rich garnets in the groundmass of the rock could suggest an aillikitic affinity during a preliminary examination, based on the IUGS rock classification (Tappe et al., 2005). Similar occurrences in Indian pipes have been used to classify the rocks as orangeites (Dogre et al., 2016). However, the Ti-rich hydrogarnets studied in the present work are produced by very late hydrothermal processes and therefore they cannot be representative of the magma composition. Therefore, attention must be paid to the position of Ca-Ti-garnet in the mineral sequence before using it to classify the rock based on its occurrence.

Perovskite commonly crystallizes directly from the kimberlite magma (Mitchell, 1986) and therefore it is one of the most used minerals for U-Pb dating of kimberlites and carbonatites (Cox and Wilton, 2006; Castillo-Oliver et al., 2016). However, our petrographic studies demonstrate the limitations of the use of groundmass perovskite for such purpose. Our data shows that two types of perovskite occur in the studied Indian kimberlites, being the first crystallized directly from the kimberlite magma, but the second from hydrothermal origin. Furthermore, primary perovskite may be strongly altered to secondary minerals that may redistribute REE and potentially, U, Pb and Th. Therefore, accurated petrographic analyses are necessary before proceeding to sort geochronological data with perovskite.

Acknowledgments

This research was supported the AGAUR 2014SGR01661 of the Generalitat de Catalunya and a FI grant to J. Xu (coded FI_B 00904) sponsored by the Departament d'Educació i Universitats de la Generalitat de Catalunya. The authors also acknowledge the Servei de Làmina Prima (thin section preparation laboratory) and the Centres Científics i Tecnològics de la Universitat de Barcelona (CCiT-UB) for the assistance with SEM-BSE-EDS study (Dr. F. J. García-Veigas, D. Artiaga) and EMP analyses (Dr. Xavier Llovet).

References

- Castillo-Oliver M, Galí S, Melgarejo JC, Griffin WL, Belousova E, Pearson NJ, Watangua M, O'Reilly SY (2016) Trace-element geochemistry and U–Pb dating of perovskite in kimberlites of the Lunda Norte province (NE Angola): petrogenetic and tectonic implications. *Chem. Geol.* 426: 118–134
- Chalapathi Rao NV, Wu FY, Mitchell RH, Li QL, Lehmann B (2013) Mesoproterozoic U–Pb ages, trace element and Sr–Nd isotopic composition of perovskite from kimberlites of the Eastern Dharwar craton, southern India: distinct mantle sources and a widespread 1.1 Ga tectonomagmatic event. *Chem Geol.* 353:48–64
- Cox RA, Wilton, DHC (2006) U-Pb dating of perovskite by LA-ICP-MS: An example from the Oka carbonatite, Quebec, Canada. *Chemical Geology* 235: 21-32
- Dongre AN, Viljoen KS, Chalapathi Rao NV, Gucsik A (2016) Origin of Ti-rich garnets in the groundmass of Wajrakarur field kimberlites, southern India: insights from EPMA and Raman spectroscopy. *Mineralogy and Petrology* 110: 295-307
- Martins T, Chakhmouradian AR, Medici L (2014) Perovskite alteration in kimberlites and carbonatites: the role of kassite, $\text{CaTi}_2\text{O}_4(\text{OH})_2$. *Phys Chem Minerals* 41: 473-484
- Mitchell RH (1986) *Kimberlites: Mineralogy, Geochemistry, and Petrology*. Plenum Press, New York. 442pp
- Mitchell RH, Chakhmouradian AR (1998) Instability of perovskite in a CO_2 -rich environment: examples from carbonatite and kimberlite. *Can. Mineral.* 36:939-952
- Pereira VP, Conceição RV, Formoso MLL, Pires AC (2005) Alteration of perovskite to anatase in silica-undersaturated rocks of the Catalão-1 carbonatite complex, Brazil: a raman study. *Rev. Brasil. Geociências* 35: 239-244
- Tappe S, Foley SF, Jenner GA, Kjarsgaard BA (2005) Integrating ultramafic lamprophyres into the IUGS classification of igneous rocks: rationale and implications. *J. Petrol.* 46: 1893–1900

Hidden reservoirs in the continental lithosphere? Evidence from Hf-Sr-Nd-Pb isotopes in southern African kimberlite megacrysts

Philip E. Janney^{1*} & David R. Bell²

¹Department of Geological Sciences, University of Cape Town, Rondebosch 7701, South Africa

²AEON-ESSRI, Nelson Mandela Metropolitan University, Summerstrand 6031, South Africa

Introduction

Hidden mantle reservoirs with anomalous isotopic compositions have been proposed to explain apparent differences between the isotopic composition of the upper mantle as inferred from oceanic basalts and estimates of bulk silicate earth (BSE) composition based on chondrite meteorites (e.g., $^{142}\text{Nd}/^{144}\text{Nd}$). In particular, the displacement of the Nd-Hf isotopic oceanic basalt array away from the BSE composition toward slightly more radiogenic $^{176}\text{Hf}/^{177}\text{Hf}$ values has prompted speculation that a hidden mantle reservoir exists that has relatively unradiogenic ϵ_{Hf} for a given ϵ_{Nd} value (Bizzarro et al., 2002). The presence of anomalously unradiogenic ϵ_{Hf} relative to ϵ_{Nd} in kimberlites and their megacrysts has been explained as the signature of ancient subducted oceanic crust (MORB and/or OIB) segregated at a deep mantle boundary layer, such as the transition zone or core-mantle boundary, constituting a hidden reservoir in the deep mantle (Nowell et al., 2004). Moreover, the presence of such isotopic signatures, which lie outside the range of modern oceanic basalts, has been used to argue for a deep mantle plume origin for kimberlites (Tappe et al., 2013). More recent refinement of chondrite Nd-Hf isotopic compositions (Bouvier et al., 2008) has removed the necessity for a hidden reservoir to reconcile the composition of oceanic basalts with a chondritic mantle, but the unusual Hf-Nd isotopic compositions of kimberlites and megacrysts still requires explanation.

We present Hf-Sr-Nd-Pb isotopic and trace element evidence from clinopyroxene megacrysts from seven Cretaceous southern African kimberlites that (1) requires the presence of a component having anomalously unradiogenic Hf and “enriched mantle” characteristics (unradiogenic ϵ_{Nd} and $^{206}\text{Pb}/^{204}\text{Pb}$, radiogenic $^{87}\text{Sr}/^{86}\text{Sr}$) within the continental lithospheric mantle and (2) suggests the ubiquitous presence of a strong HIMU mantle source with a chemical signature of carbonatite metasomatism in the deep lithosphere or asthenosphere beneath southern Africa.

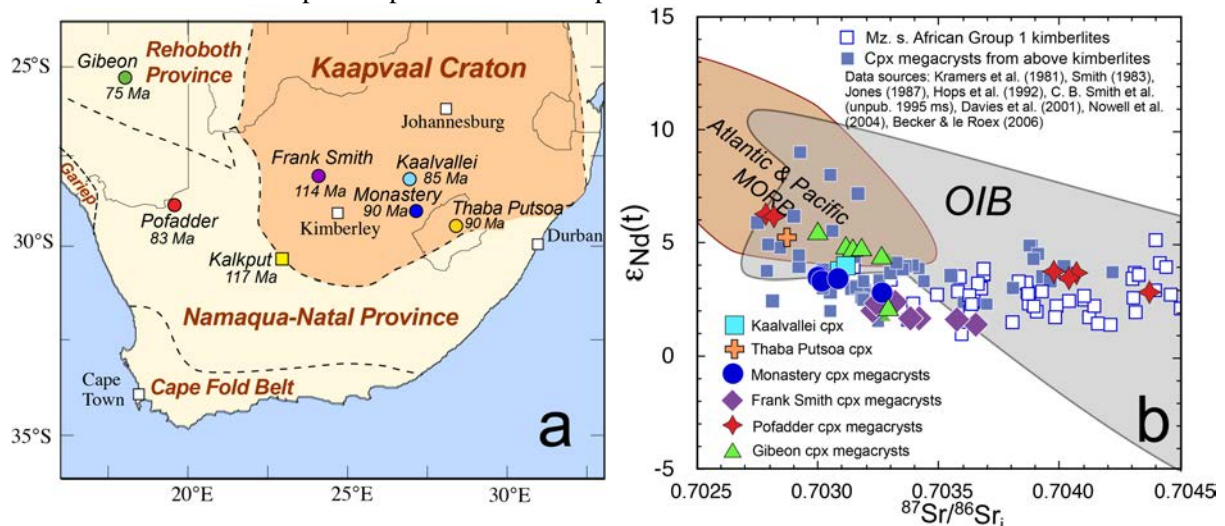


Figure 1. (a) Map of kimberlites from which clinopyroxene megacrysts in this study were analysed. (b) $^{87}\text{Sr}/^{86}\text{Sr}$ vs. $\epsilon_{\text{Nd}}(t)$ plot for the studied Group 1 kimberlite megacrysts along with literature data.

Approach and Results

Approximately 30 clinopyroxene megacrysts from seven Cretaceous southern African kimberlites/clusters (Fig. 1; six Group 1 and one Group 2) were analysed for trace elements and Hf-Sr-Nd-Pb isotope compositions using ultra-low blank methods, mainly at Arizona State University. For four of these (Monastery, Frank Smith, Gibeon and Pofadder, all Group I), six or more

megacrysts were analysed from each so as to cover a range of compositions (Cr-poor to Cr-rich) and crystallization temperatures (based on $\text{Ca}\# = 100 \cdot \text{Ca}/(\text{Ca} + \text{Mg})$ in atomic %). For each of these megacryst suites, the sample with the highest crystallization temperature (lowest Ca#) has the lowest $^{87}\text{Sr}/^{86}\text{Sr}_i$ (0.7027-0.7032), highest $\epsilon_{\text{Nd}}(t)$ (+3.5 to +6.5) and highest $^{206}\text{Pb}/^{204}\text{Pb}_i$ ratios (19.6-20.7), similar to the ‘HIMU’ or ‘FOZO’ source components of ocean island basalts, and has $\epsilon_{\text{Nd}} - \epsilon_{\text{Hf}}$ values that fall only slightly below the global Nd-Hf oceanic basalt array. As crystallization temperatures decrease, the $^{87}\text{Sr}/^{86}\text{Sr}$ values of the megacrysts increase and ϵ_{Nd} , ϵ_{Hf} and $^{206}\text{Pb}/^{204}\text{Pb}$ values all decrease. The samples crystallizing at the lowest temperatures typically fall furthest (up to 8.5 eHf units) below the Nd-Hf oceanic basalt array. This pattern is most easily explained by assimilation of a lithospheric component that has anomalously low ϵ_{Hf} compared to ϵ_{Nd} , combined with high $^{87}\text{Sr}/^{86}\text{Sr}$ and low ϵ_{Nd} and $^{206}\text{Pb}/^{204}\text{Pb}$ values. The above isotopic variations are also accompanied by increases in Zr and Hf concentrations and decreases in $(\text{Lu}/\text{Hf})_N$ ratios.

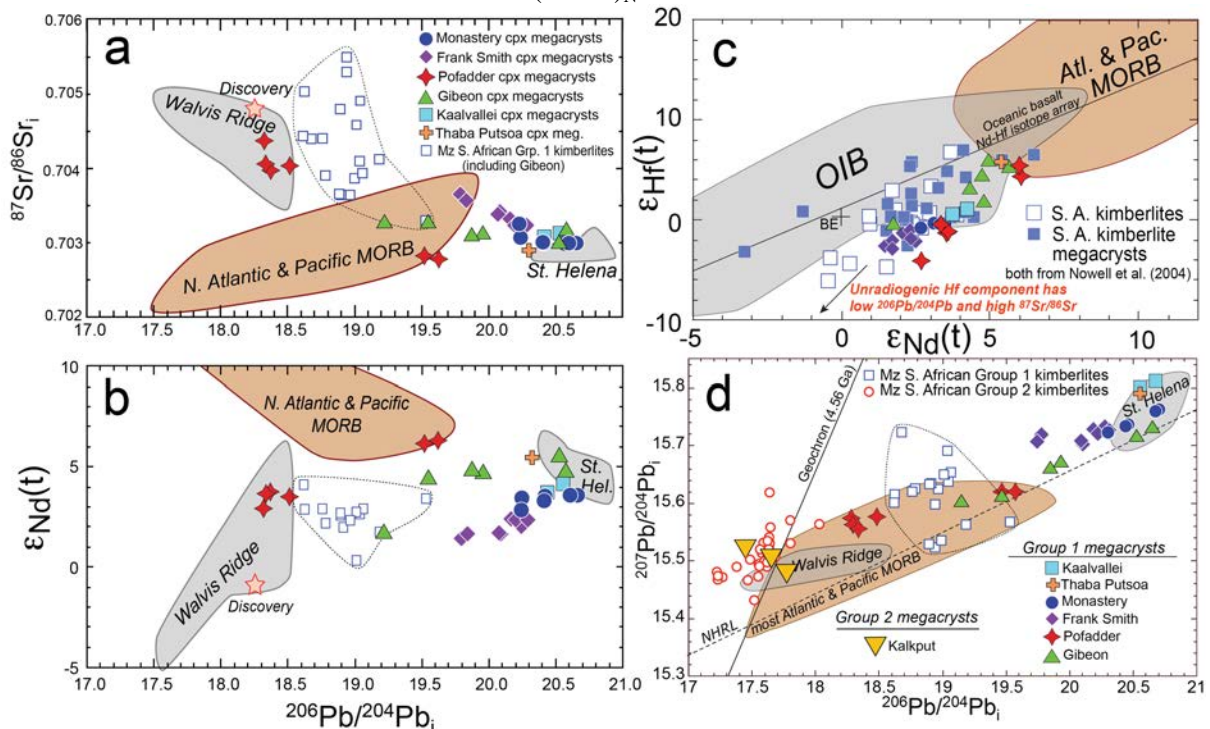


Figure 2. Isotope ratios plots for clinopyroxene megacrysts: (a) $^{206}\text{Pb}/^{204}\text{Pb}$ vs $^{87}\text{Sr}/^{86}\text{Sr}_i$, (b) $^{206}\text{Pb}/^{204}\text{Pb}$ vs. $\epsilon_{\text{Nd}}(t)$, (c) $\epsilon_{\text{Nd}}(t)$ vs $\epsilon_{\text{Hf}}(t)$ and (d) $^{206}\text{Pb}/^{204}\text{Pb}$ vs. $^{207}\text{Pb}/^{204}\text{Pb}$. Kimberlite data are from Figure 1 plus Fraser and Hawkesworth (1992).

Discussion

We propose that southern African Group 1 and Group 2 kimberlites preferentially assimilate metasomatic vein components in the lithospheric mantle analogous to the phlogopite-ilmenite-clinopyroxene (PIC) and MARID xenolith suites, respectively. Chemical data suggest that PIC and MARID xenoliths have low and moderate Lu/Hf ratios, respectively, relative to Sm/Nd (Gregoire et al., 2002), and over time could evolve appropriately unradiogenic Hf and Nd isotopic compositions lying below and on the Hf-Nd isotopic array, respectively.

The prevalence of the strong HIMU isotopic signature in Cr-poor clinopyroxenes from all Cretaceous Group 1 kimberlite megacryst suites investigated, whether on on-craton or off-craton, is intriguing and suggests that this mantle source composition is not derived from localised, deep-seated mantle plumes. The Group 1 megacryst suite that shows the weakest HIMU signature (Pofadder) is strongly dominated by Cr-rich megacryst compositions, suggesting that its HIMU signature may have been diluted at shallow levels. Further, the fact that the Cr-poor megacrysts tend to show strong negative anomalies in Zr and Hf (and often Ti) appears to support the possibility that this HIMU signature could have developed in the deep lithosphere in-situ by a metasomatic process involving recycled carbonatitic material, in a scenario similar to that envisioned by Weiss et al. (2016).

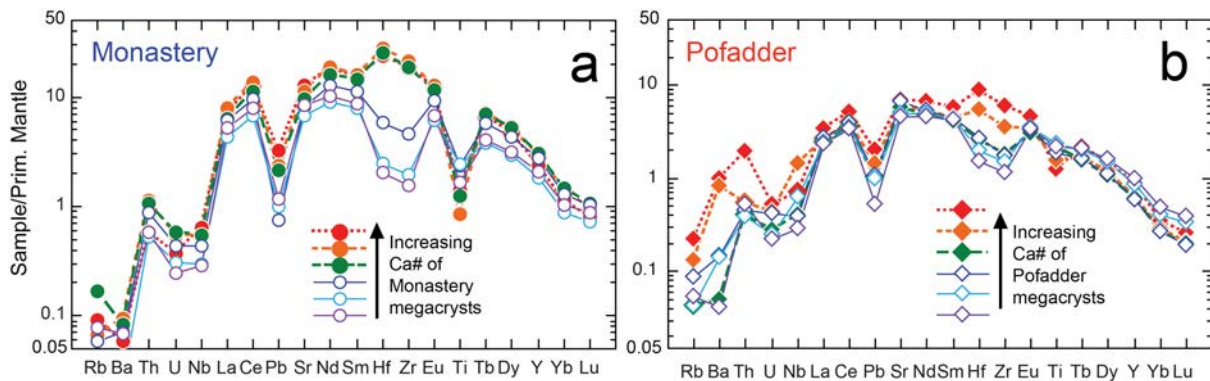


Figure 3. Primitive mantle-normalised incompatible element diagrams for (a) Monastery and (b) Pofadder clinopyroxene megacrysts. Note the depletion in Zr & Hf and the change in these elements with decreasing crystallization temperature (i.e., increasing Ca#). Normalising values from McDonough & Sun (1995)

Acknowledgements

Generous support for this project was provided by the U.S. National Science Foundation (to PEJ and DRB) and the South African National Research Foundation and the UCT Science Faculty to PEJ.

References

- Becker, M. & le Roex, A. P. (2006). Geochemistry of South African on- and off-craton, Group I and Group II kimberlites: Petrogenesis and source region evolution. *Journal of Petrology* **47**, 673-703.
- Bizzarro, M., Simonetti, A., Stevenson, R. K. & David, J. (2002). Hf isotope evidence for a hidden mantle reservoir. *Geology* **30**, 771-774.
- Bouvier, A., Vervoort, J. D. & Patchett, J. D. (2008). The Lu–Hf and Sm–Nd isotopic composition of CHUR: constraints from unequilibrated chondrites and implications for the bulk composition of terrestrial planets. *Earth and Planetary Science Letters* **273**, 48-57.
- Davies, G. R., Spriggs, A. J. & Nixon, P. H. (2001). A non-cognate origin for the Gibeon kimberlite megacryst suite, Namibia: Implications for the origin of Namibian Kimberlites. *Journal of Petrology* **42**, 159-172.
- Davis, G., Krogh, T. & Erlank, A. J. (1976). The ages of zircons from kimberlites from South Africa. *Carnegie Institution Yearbook* **75**, 821-824.
- Fraser, K.J. & Hawkesworth, C.J. (1992). The petrogenesis of group 2 ultrapotassic kimberlites from Finsch Mine, South Africa. *Lithos* **28**, 327-345.
- Gregoire, M., Bell, D. R. & le Roex, A. P. (2002). Trace element geochemistry of phlogopite-rich mafic mantle xenoliths: their classification and their relationship to phlogopite-bearing peridotites and kimberlites revisited. *Contributions to Mineralogy and Petrology* **142**, 602-625.
- Griffin, W. L., Batumike, J. M., Greau, Y., Pearson, N. J., Shee, S. R. & O'Reilly, S. Y. (2014). Emplacement ages and sources of kimberlites in southern Africa: U-Pb ages and Sr-Nd isotopes of groundmass perovskite. *Contributions to Mineralogy and Petrology* **168**, paper 1032.
- Hops, J. J., Gurney, J. J. & Harte, B. (1992). The Jagersfontein Cr-poor megacryst suite - towards a model for megacryst petrogenesis. *Journal of Volcanology and Geothermal Research* **50**, 143-160.
- Jones, R. A. (1987). Strontium and neodymium isotopic and rare earth element evidence for the genesis of megacrysts in kimberlites of southern Africa. In: Nixon, P. H. (ed.) *Mantle Xenoliths*. London: John Wiley & Sons, 711-724.
- Kramers, J. D., Smith, C. B., Lock, N. P., Harmon, R. S. & Boyd, F. R. (1981). Can kimberlites be generated from an ordinary mantle? *Nature* **291**, 53-56.
- McDonough, W. F. & Sun, S. S. (1995). The composition of the Earth. *Chemical Geology* **120**, 223-253.
- Nowell, G. M., Pearson, D. G., Bell, D. R., Carlson, R. W., Smith, C. B., Kempton, P. D. & Noble, S. R. (2004). Hf isotope systematics of kimberlites and their megacrysts: New constraints on their source regions. *Journal of Petrology* **45**, 1583-1612.
- Smith, C. B. (1983). Pb, Sr and Nd isotopic evidence for sources of southern African Cretaceous kimberlites. *Nature* **304**, 51-54.
- Tappe, S., Pearson, D. G., Kjarsgaard, B. A., Nowell, G., & Dowall, D. (2013). Mantle transition zone input to kimberlite magmatism near a subduction zone: origin of anomalous Nd–Hf isotope systematics at Lac de Gras, Canada. *Earth and Planetary Science Letters*, 371, 235-251.
- Weiss, Y., Class, C., Goldstein, S. L. & Hanyu, T. (2016). Key new pieces of the HIMU puzzle from olivines and diamond inclusions. *Nature* **537**, 666-670.

Deciphering the composition and structure of Wyoming craton mantle lithosphere: insights from peridotite xenoliths

Benjamin Parks¹, Emily J. Chin², Alberto Saal¹, Greg Hirth¹, Carter Hearn³, Jean-Louis Bodinier⁴

¹*Brown University, Providence, USA, benjamin_parks@brown.edu, alberto_saal@brown.edu, greg_hirth@brown.edu*

²*Scripps Institution of Oceanography, La Jolla, USA, e8chin@ucsd.edu*

³*USGS, Reston, USA, chearn@usgs.gov*

⁴*Université de Montpellier, Montpellier, France*

Introduction

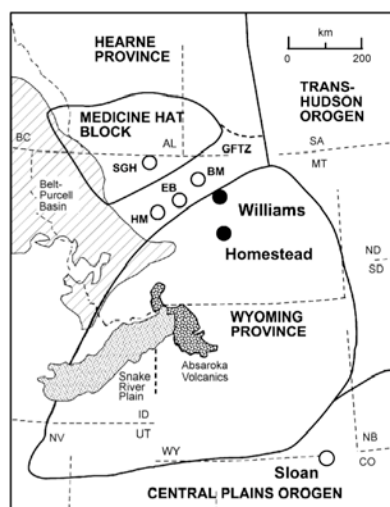


Figure 1: Tectonic map of the Homestead and Williams sample locations with respect to the Wyoming craton and other neighboring basement geologic terranes. Modified from Carlson et al. (2004).

The Wyoming craton stands out among Archean cratons as one that underwent widespread, thick-skinned deformation relatively recently, specifically during the Laramide orogeny. If this deformation occurred within the lithospheric mantle of the Wyoming craton, the thermal, compositional, and rheological effects of this tectonism should be documented by the xenoliths subsequently transported to the surface. A large portion of the mantle xenolith-bearing magmatism occurred in the Eocene-aged Montana high-potassium igneous province at the end of the Laramide (Hearn Jr. 1989; O'Brien, et al. 1991). The xenoliths in this region span the northwestern margin of the Wyoming craton (Figure 1A). In particular, two kimberlite diatremes bear an abundance of garnet and garnet-spinel peridotites: the Homestead diatreme, located toward the interior of the craton, and the Williams diatreme, located near the Proterozoic-aged Great Falls Tectonic Zone. To elucidate how Wyoming cratonic mantle has been modified prior to and during the Laramide, we present the first integrated investigation of mineral major and trace element compositions and deformation microstructures of peridotite xenoliths from the Homestead and Williams kimberlites.

Xenolith Suites & Petrography

Garnet and garnet-spinel peridotite xenoliths sampled from the Homestead and Williams kimberlites can be divided into three groups. The Williams xenoliths comprise one low-temperature group (group LTW) and one high-temperature group (group HTW), as previously categorized (Carlson, et al. 1999). The third group consists of the Homestead xenoliths (group HS). Among all groups, the xenoliths are predominantly harzburgites, while less than 15% of the samples are lherzolites.

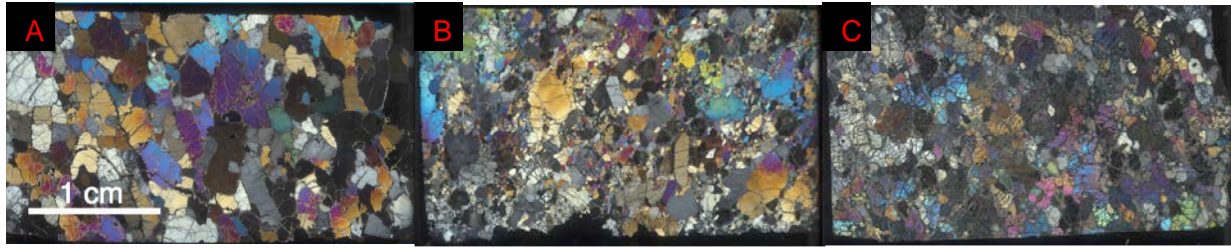


Figure 2: Photomicrographs in cross-polarized light of samples from each of the three xenolith groups: group LTW sample H68-16B (A), group HTW sample H81-26 (B), and group HS sample H00-11-16 (C).

LTW xenoliths yield inter-mineral major element equilibrium temperatures of 850-1050°C and ~3-4.2 GPa, which fall along a 38 mW/m² shield geotherm (Hearn Jr. 2004). This group exhibits a coarse tabular texture with weak foliation relative to group HTW, and predominantly isolated garnet and clinopyroxene grains (Figure 2A). Group HTW is hotter than this shield geotherm, yielding temperatures of 1100-1450°C and pressures of 4-5.5 GPa, and exhibit coarse porphyroclastic to mosaic porphyroclastic textures (Figure 2B). Olivine grains in HTW samples appear as mm-scale porphyroclasts, smaller anhedral neoblasts, and in polygonal tablets that overprint porphyroblasts and neoblasts, which suggests the occurrence of post-deformation annealing. Group HS yields similar P-T estimates to group HTW, with temperatures of 1100-1400°C and pressures of 3.6-4.8 GPa (Hearn Jr. 2004). Group HS xenoliths exhibit predominantly coarse grained to coarse-porphyroclastic textures, including a subset of samples exhibiting coarse grained textures with intimately associated garnet and clinopyroxene (Figure 2C). Re-depletion model ages of group LTW (1.77-2.55 Ga, Carlson, et al. 1999) and group HS (2.30-2.77 Ga, Carlson, et al. 2004) are significantly older than the ages of group HTW (<0.83 Ga, Carlson, et al. 1999). However, the highly variable and unreliable garnet and clinopyroxene tie-line ages given by Rb-Sr, Lu-Hf, and Sm-Nd isotopes for Williams and Homestead peridotite xenoliths (Carlson et al. 2004) suggest that significant, more recent melt-rock interaction occurred.

Mineral Chemistry

Mineral compositions of the sampled xenoliths are generally depleted with respect to major elements. Most olivine Mg# values range from 0.91 to 0.93, falling within the expected range for cratonic peridotites (Bernstein, et al. 2007). The exceptions are two HS samples (one of which is sample H00-11-16, Figure 2C), both with olivine Mg# = 0.90. In clinopyroxenes, molar Cr/Al ratios correlate positively with Mg#; H00-11-16 clinopyroxenes yield the lowest Cr/Al (<0.3), which indicates relatively low depletion, while grains from LTW sample H68-16B yield the highest (~0.6), indicating high depletion. Among all samples, H68-16B yields the largest range in garnet Cr₂O₃ concentrations, such that rims have lower range in Cr₂O₃ (4.0-5.7 wt.%) than cores (4.2-6.4 wt.%).

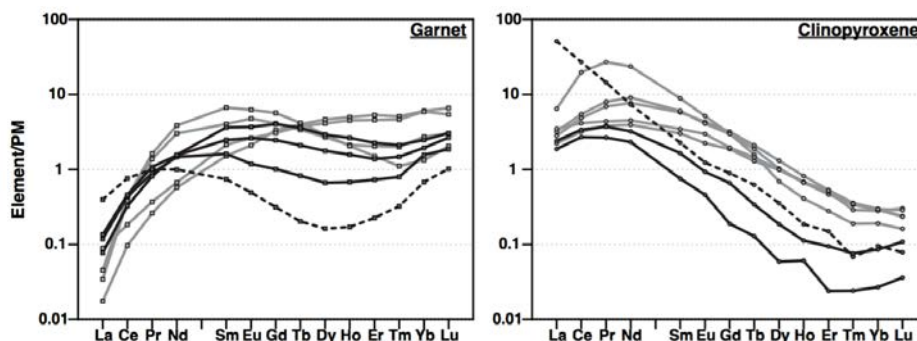


Figure 3: Primitive mantle- normalized REE concentrations in garnet (left) and clinopyroxene (right) for groups HS (solid grey lines), LTW (dashed black lines), and HTW (solid black lines). Normalizing concentrations from McDonough and Sun (1995).

Trace element compositions of garnet and clinopyroxene show significant systematic variations in enrichment, indicating varying degrees and styles of metasomatism among the analyzed sample suite (Figure 3). Primitive-mantle normalized REE patterns in clinopyroxenes range from MREE-enriched (i.e., $(La/Nd)_N < 1$) for groups HTW and HS to LREE-enriched (i.e., $(La/Nd)_N > 1$) for group LTW. For most of the observed samples, garnets have sinusoidal REE patterns. The two HS samples with low olivine Mg# and low cpx Cr/Al have monotonic garnet REE patterns. The low level of depletion in the HS samples that have monotonic REE patterns suggests that parts of the Wyoming craton lithosphere beneath Homestead interacted with an infiltrating melt/fluid at a high melt/fluid-to-rock ratio, while the garnet, cpx and melt/fluid approach chemical equilibrium. In contrast, group LTW, represented by sample H68-16B, shows significant chemical disequilibrium, based on between- and within-grain variation in major element and REE concentrations.

Crystallographic-preferred orientations

The crystallographic-preferred orientations (CPO) of olivines, measured using EBSD, indicate that these peridotites record different fabrics. CPO patterns, shown in Figure 4 for LTW sample H68-16B and HS sample H00-11-16. In the HS sample, opx and olivine align in the [001] direction, parallel to lineation and parallel to the (100) plane, which indicates a B-type fabric. Though few were measured, opx CPOs in both samples appear aligned with olivine CPO perpendicular to foliation in the (010) plane. The significantly different CPO for H00-11-16 may signify that the deformation conditions reflected by mineral CPOs may relate to its relatively undepleted, well-equilibrated chemical composition. Such traits suggest that prior to the ascent of these xenoliths to the surface, considerable removal and (or) reworking of the base of the Wyoming craton mantle lithosphere occurred, potentially related to the Laramide orogeny.

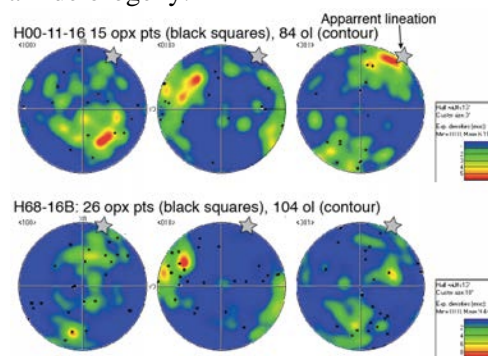


Figure 4: Olivine and orthopyroxene CPO patterns, plotted as lower hemisphere, equal-area projections.

References

- Bernstein S, Kelemen PB, Hangerhøj K (2007) Consistent olivine Mg# in cratonic mantle reflects Archean mantle melting to the exhaustion of orthopyroxene. *Geology* 35(5):459-462
- Carlson R, Irving A, Hearn Jr. B (1999) Chemical and isotopic systematics of peridotite xenoliths from the Williams kimberlite, Montana: clues to processes of lithosphere formation, modification and destruction. In: *Proceedings of the VIIth International Kimberlite Conference*, vol 1. pp 90-98
- Carlson RW, Irving AJ, Schulze DJ, Hearn Jr. BC (2004) Timing of Precambrian melt depletion and Phanerozoic refertilization events in the lithospheric mantle of the Wyoming Craton and adjacent Central Plains Orogen. *Lithos* 77(1):453-472
- Hearn Jr. BC (1989) Introduction: T346 Montana High-Potassium Igneous Province. *Montana High-Potassium Igneous Province: Crazy Mountains to Jordan, Montana*:1-5
- Hearn Jr. BC (2004) The Homestead kimberlite, central Montana, USA: mineralogy, xenocrysts, and upper-mantle xenoliths. *Lithos* 77(1):473-491
- McDonough WF, Sun SS (1995) The composition of the Earth. *Chemical geology* 120(3):223-253
- O'Brien HE, Irving AJ, McCallum IS (1991) Eocene potassic magmatism in the Highwood Mountains, Montana: petrology, geochemistry, and tectonic implications. *Journal of Geophysical Research: Solid Earth* 96(B8):13237-13260



A mantle metasomatic injection event linked to Permo-Carboniferous lamprophyre magmatism and associated rare metal ore deposition (Sn-W-Mo-Li-Sc-In / Ag(-Au)-In-base metal) in the eastern European Variscides

Thomas Seifert¹

¹ *TU Bergakademie Freiberg, Freiberg, Germany, thomas.seifert@mineral.tu-freiberg.de*

Introduction

Lamprophyres which are of mantle origin in subduction zones and continental rift settings are reported as components of bimodal dike suites in a number of hydrothermal Au-polymetallic, Au-Cu, Ag-base metal, Ag(-Au)-Sb, Sb-Hg and fluorite deposits (Rock 1991; Seifert 2007, 2010; Geißler and Seifert 2009). Significant is the association of Sn-W, Sn-sulfide, Sn-In-polymetallic and Ag(-Au)-In-Sb-base metal deposits with Paleozoic and Mesozoic magmatism in the Erzgebirge, Central Asia, and Yakutia which includes granitoids and abundant mafic dikes (Seifert 2008; Seifert et al. 2011, Štemprok and Seifert 2011).

The traditional model for the genesis of late-Variscan deposition of Sn-W-Mo ores in the eastern Variscides favored a crustal-derived, syn- to late-collision granite magmatism (Tischendorf 1986). An alternative model suggests a mantle-related magmatic pulses and associated high-temperature and rare metal-enriched fluids as a source of late-Variscan Sn-, In-, and Ag-polymetallic mineralization in the Erzgebirge-Vogtland metallogenic province (Seifert 2008, 2015). Calc-alkaline lamprophyres (CAL) of the present study crop out in rock quarries, outcrops at roads and railway lines, and often in underground mines of old mining districts (15th to 20th century).

Geology of late-Variscan lamprophyric intrusions

The calc-alkaline lamprophyric dikes and sills (CAL) in the Erzgebirge-Vogtland region are typically 0.5 – 5 m wide, rarely exceeding 30 m. The most CAL occur in areas of crosscutting deep fault zones and lineaments which also act as conduits for post-collisional, F-enriched granitic/rhyolitic intrusions and host post-magmatic Sn-W-Mo-Li-Sc-In, Sn-In-base metal, Ag(-Au)-Sb-base metal, and U deposits (e.g., crosscutting area of the NW-SE Gera-Jáchymov fault zone and the NE-SW Saxonian Lineament; cf. Seifert 2008). CAL took place in the Erzgebirge/Krušné hory-Fichtelgebirge anticlinorium (cf. Seifert 2008 and references therein) and Fichtelgebirge/Smčiny pluton (Gümbel 1874) in different host rocks (ortho- and paragneisses, mica-schists, phyllites, meta-basalts, meta-carbonates, meta-black shales and late-Variscan granites/rhyolites) in NW-SE, NE-SW/NE-SSW, and ENE-WSW trending dikes.

Petrology and relatively age relationships

The calc-alkaline lamprophyric intrusions in the Erzgebirge are divided by Seifert (1997, 2008, this study) using criteria of relatively age relationships to different late-Variscan granite intrusions and associated aplites, rhyolitic and lamprophyric dikes, and late-Variscan rare metal mineralization stages as well as petrographic and geochemically criteria (LD1 - LD3, Fig. 1):

(1) The late-collisional LD1-type lamprophyres (330 Ma) are intruded by late-collisional granites (e.g., Ehrenfriedersdorf Sn-W district, Schlema-Schneeberg U-Ag district) and are characterized by transitional type kersantitic/spessartitic dike intrusions. They predate all Permo-Carboniferous mineralization stages in the Erzgebirge-Vogtland area and are possibly unrelated to late-Variscan ore deposition processes. LD1 show similarities to lamprophyric dikes in the Elbe Zone with K-Ar ages of c. 330 Ma (Kurze et al. 1998).

(2) LD2-type lamprophyres (320-300 Ma) postdate the late-collisional (“Eibenstock type”) granite intrusions and occur widely in the Sn-W-U district Gottesberg-Mühlleithen, U-Ag district Schlema-Schneeberg, Sn-In-Ag-U districts Marienberg-Pobershau and Annaberg, and probably in the Ag-In-Sn-

base metal district Freiberg. LD2 are dominated by mica-minette dike intrusions with strike lengths up to 7 km and a thickness up to 10 m. They are crosscut by Sn-polymetallic, Ag(-Au)-In-Sb-base metal, U, fluorite-barite, and Bi-Co-Ni-As-Ag(-U) mineralization.

(3) LD3-type lamprophyres (310-300? Ma) are identified in the Pobershau Sn-W-Ag ore field and represented by feldspar-phyric kersantitic lamprophyres. LD3 in the Pobershau ore field show post-Sn mineralization age and are crosscut by barite-Bi-Co-Ni-Ag veins

The texture of the LD2-type lamprophyres is partly richly porphyric (phlogopite), with a fine-grained grey-black groundmass. In some LD2-samples from the Marienberg and Freiberg districts a F-enriched phlogopite is the dominated mineral. LD2 in the Tannenberg-Mühlleiten district show low phyric textures and nearly glassy groundmass. Typically for LD1-type lamprophyres are mica-, amphibole-, and feldspar-microphyric textures. The contact between the lamprophyre dikes and host rocks is always sharp and c. 2 – 20 mm chilled margins are often present. The most lamprophyres are characterized by early-magmatic (micro)phenocrysts of Mg-biotites/phlogopites with typical zonation and/or amphibole (micro)phenocrysts. They mostly contain clinopyroxene (diopside, augite) and, locally, olivine. Olivine may enclose Cr-spinel, but is often pseudomorphosed of secondary carbonate, chlorite, amphibole, and talc. Mica-minettes (LD2) have higher modal abundances of alkali feldspar, phlogopite and apatite than LD1 and LD3. This characterization is similar to mafic volcanics of the Sub-Erzgebirge basin (MVSEB). Fluor-apatite is the most common accessory mineral in LD2 and MVSEB.

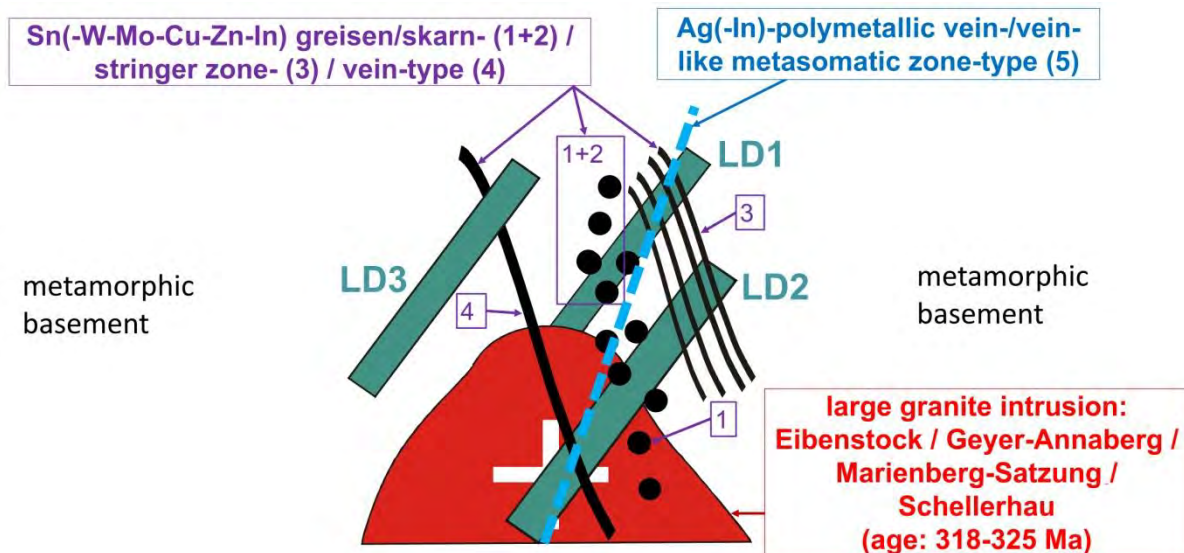


Figure 1: Relatively age relationships of late-Variscan large granite intrusions (western Erzgebirge: Eibenstock; central Erzgebirge: Ehrenfriedersdorf-Geyer-Annaberg / Marienberg-Pobershau-Satzung; eastern Erzgebirge: Schellerhau) and lamprophyric dike intrusions (LD1, LD2, LD3) and rare metal mineralization (1 to 5) in the Erzgebirge-Vogtland region (modified from Seifert 2010, 2015).

Geochemistry

Geochemically LD2 (phlogopite-phyric minette and transitional type kersantite/minette) show a typically ultrapotassic composition similar to the majority of MVSEB. The high concentration of LILE (up to 8.74 wt.% K₂O, 1,100 ppm Rb, 100 ppm Cs, 5,020 ppm Ba, 2,030 ppm Sr) and HFSE (up to 3.7 wt.% TiO₂, 1.3 wt.% P₂O₅, 30 ppm Sc, 1,070 ppm Zr, 35 ppm Hf, 115 ppm Nb, 95 ppm Th, 75 ppm Y, 700 ppm LREE) and the enriched radiogenic isotope composition of LD2 and MVSEB (⁸⁷Sr/⁸⁶Sr_i = 0.70401 to 0.71038; εNd_i = -6.4 to -0.2) indicate melting of a metasomatically enriched mantle. High concentrations of LILE and HFSE, and the ‘primitive’ bulk geochemistry indicated by high mg# (76 – 88) and Cr (up to 890 ppm), Ni (up to 470 ppm), and Co contents (up to 55 ppm) exclude significant crustal contamination as the cause of their enrichment. High volatile contents (CO₂ up to 7.3 wt.%, H₂O⁺ up to 7.92 wt.%, F up to 4,600 ppm, Cl up to 1,700 ppm, S up to 3,160 ppm, P₂O₅ up to 1.33

wt.%) in whole rock samples and high H₂O⁺, F and Cl contents of early magmatic phlogopites and apatites are typical for post-collisional lamprophyres in the Erzgebirge (especially LD2) and shoshonitic/ultrapotassic mafic volcanics in the Sub-Erzgebirge basin.

A carbonate-rich mica-lamprophyre from the nearby Berga anticlinorium (drill hole 4215-76 of SDAG Wismut) is characterized by extremely high CO₂ (12.20 wt.%), P₂O₅ (2.28 wt.%), F (3,200 ppm), Sr (2,940 ppm), Th (135 ppm), and Σ REE (1,400 ppm) contents (Seifert 2008) and show in the Sm-Ce/Yb and Sm-La/Yb diagram (Rock 1991; Mitchell and Bergmann 1991) a clear tendency to the lamproite field.

Bimodal post-collisional magmatism and metallogenic importance for rare metal mineralization

The bimodal lamprophyre-rhyolite assemblage in the Erzgebirge/Sub-Erzgebirge basin area was formed during intracontinental rifting in a 'Fast Extension' setting by melting of a metasomatic enriched mantle source. The emplacement of fluid-enriched lamprophyric and rhyolitic intrusions at the same time is possibly associated with decompression melting of updoming asthenosphere and a mantle plume with a peak magmatic activity from 300 to 280 Ma (cf. Seifert 2009). The metallogenic importance of post-collisional lamprophyres (especially type LD2) and MVSEB is indicated by their high volatile concentrations and relationships to post-collisional high-F granitic intrusions and high-F (partly high-Sn) subalkaline rhyolites/rhyolitic ignimbrites and late-Variscan rare metal ore deposition.

References

- Geißler L, Seifert T (2009) Geology, Mineralogy and Geochemistry of Gold-bearing Polymetallic Sulfide-Quartz Veins and Associated Intrusions in the French Gulch-Deadwood District, California. Freiburger Forschungshefte C 533
- Gümbel CW (1874) Die paläolithischen Eruptivgesteine des Fichtelgebirges. Franz, München
- Kurze M, Seifert T, Weber H, Henjes-Kunst F (1998) Petrographie, Geochemie und Altersstellung der Lamprophyr-Gänge des Elbtalschiefergebirges (Sachsen). Z. Geol. Wiss. 26: 193-202
- Mitchell RH, Bergman SC (1991) Petrology of lamproites. Plenum Press, New York, London
- Rock NMS (1991) Lamprophyres. Blackie, Van Nostrand Reinhold, Glasgow, New York
- Seifert T (1997) Mantle metasomatism and associated late Variscan Sn and base metal mineralization in the Erzgebirge (Germany). In: Hatton CJ (ed) Plumes, Plates and Mineralisation, proceedings volume, University of Pretoria, pp 89-90
- Seifert T (2007) Metallogenetische Bedeutung von Kalkalkali-(CA-)Lamprophyren – Beitrag zur Genese und Exploration von Sn-W-Mo-, Ag-Polymetal- und U-Lagerstätten am NW-Rand des Böhmisches Massivs (DE, CZ). Habilitation, TU Bergakademie Freiberg
- Seifert T (2008) Metallogeny and Petrogenesis of Lamprophyres in the Mid-European Variscides. IOS Press BV, Amsterdam
- Seifert T (2009) Late-Variscan polymetallic ore deposits in central Europe and their relationships to large igneous provinces (LIP) and mantle plume magmatism. Large Igneous Provinces Commission of IAVCEI. <http://largeigneousprovinces.org/09oct>. Accessed October 2009
- Seifert T (2010) Contributions to the metallogenic importance of lamprophyres – examples from polymetallic Au-, Sn-W-Mo-Li-In-, As-Zn-Sn-Cu-In-Pb-Ag- / Ag-Sb-, and U-ore clusters. MINERALOGIA – SPECIAL PAPERS 37: 55-58
- Seifert T (2015) Paragenesis, geochemistry and age of late-Variscan Sn, In and Ag mineralization in the Marienberg district and its relationship to mafic and acidic magmatic events, Erzgebirge. In: André-Meyer AS et al (ed) 13th SGA Biennial Meeting 2015, France, Proceedings, Volume 2, pp 843-846
- Seifert T, Pavlova GG, Borisenko AS (2011) Types of Ag-polymetallic/Ag-Sb vein-type mineralization in the European Variscides, Yakutia, Altai, Tien Shan, and Pamir. In: Geology, Tectonics and Minerogeny of Central Asia, VSEGEI, St. Petersburg, Russia, conference CD
- Štemprok M, Seifert T (2011) An overview of the association between lamprophyric intrusions and rare-metal mineralization. MINERALOGIA 42: 121-162
- Tischendorf G (1986) Variscan ensialic magmatism and metallogenesis in the Ore Mountains - Modelling of the process. Chemie der Erde 45: 75-104



Sodium-bearing phases in the transition zone and uppermost lower mantle: Experimental and natural data

Andrey V. Bobrov^{1,2,3}, Anastasiya P. Tamarova¹, Ekaterina A. Sirotkina^{1,2,3}, Luca Bindi⁴ and Tetsuo Irifune⁵

¹Moscow State University, Moscow, Russia, archi@geol.msu.ru, dragon.of.rainbow@yandex.ru

²Vernadsky Institute of Geochemistry and Analytical Chemistry of Russian Academy of Sciences, Moscow, Russia, skatty.ea@gmail.com

³Institute of Experimental Mineralogy of Russian Academy of Sciences, Chernogolovka, Russia

⁴Dipartimento di Scienze della Terra, Università di Firenze, Firenze, Italy, luca.bindi@unifi.it

⁵Geodynamics Research Center, Ehime University, Matsuyama, Japan, irifune@dpc.ehime-u.ac.jp

Introduction

Na is an incompatible element in the Earth's mantle and among the main hosts for sodium beneath the 410-km boundary are majoritic garnet (transition zone and upper part of the lower mantle), CaSiO₃-perovskite and NaAl-phase (NaAlSiO₄) with the Ca ferrite-type structure (lower mantle).

Na-bearing majoritic garnets (up to 5.89 wt % Na₂O; Kaminsky 2012) were discovered as inclusions in diamonds of the eclogitic assemblage in many regions worldwide including Kankan area in Guinea, West Africa, where majorite with the high sodium content (1.37 wt % Na₂O) associated with potassium-rich clinopyroxene (1.44 wt % K₂O) (Stachel 2001). As is evident from the experimental data (Akaogi 2007), majorite may be stable under pressures of up to 28 GPa (i.e., in the uppermost horizons of the lower mantle), and the concentrations of Na and Si in such garnets may be used for pressure estimation. In addition, Na-bearing majoritic garnet is compatible with sodium-rich alkaline silicate and carbonate-silicate melts produced by partial melting of the mantle material within the diamond depth facies (Bobrov et al. 2008).

Accessory lower mantle phases like CaSiO₃-perovskite or NaAl-phase can contain appreciable amounts of alkalis, but the mantle depleted from crust-extraction is expected to contain very low portions of these phases. This opens the question, how can Na be transferred back into the lower mantle. Only 'refertilization' of mantle by subduction processes can provide these elements for lower mantle phases and form high-Na phases. Recently, nyerereite (Na₂Ca(CO₃)₂) and nahcolite (NaHCO₃) have been identified in a specific lower mantle carbonatitic association (Juina area, Brazil) in association with typical lower mantle minerals, such as CaSi-perovskite and ferropericlaase (Kaminsky 2012).

Experimental techniques

To study the crystal-chemical behavior of sodium in the deep Earth, we performed experiments on a simplified chemical system involving Na-rich carbonated melt and mantle silicate at 24 GPa and 1100–1700°C, thus representing the conditions at the border between the transition zone and lower mantle.

Experiments were performed using a 2000 ton split-sphere press installed at the Ehime University (Matsuyama, Japan). A Co (17 wt%)-doped MgO octahedral pressure medium of 8 mm edge length was compressed using eight cubic tungsten carbide anvils with 3 mm truncation edge lengths. Pyrophyllite gaskets, 4 mm in width, were used to seal the compressed volume and support the anvil flanks. Heating of the sample was performed by a cylindrical LaCrO₃ heater, 3.2/2.0 mm in outer/inner diameter and 4 mm in length. Approximate sample volumes after experiments were 1.0 mm³. Starting mixtures of oxides and carbonate were dried for a few days at a temperature of 105 °C and kept in a dessicator. Temperature during the experiment was controlled by a W₉₇Re₃-W₇₅Re₂₅ thermocouple, 0.1 mm in diameter. The pressure was calibrated at room temperature using the semiconductor-metal transitions of Bi, ZnS, and GaAs (Irifune et al. 2004). The effect of temperature on pressure was further corrected using the α-β and β-γ phase transitions of olivine (Katsura and Ito 1989). The run durations were 15-60 min.

Results

In all samples, partial melting was registered: crystals of Na-bearing Al,Fe³⁺-bridgmanite occurred in microcrystalline carbonate-silicate quenched matrix; at 1300°C, grains of Na₂Mg(CO₃)₂ and (Mg,Fe)O grains were observed. With decreasing temperature melt composition evolved from silicate-carbonate to alkaline-carbonate. Bridgmanite contained Al₂O₃ (0.6-2.7 wt.%), Fe₂O₃ (1.6-3.5 wt.%), and up to 1.6 wt % Na₂O (at 1700°C). There is a positive correlation between the concentration of sodium in bridgmanite and temperature (Figure 1).

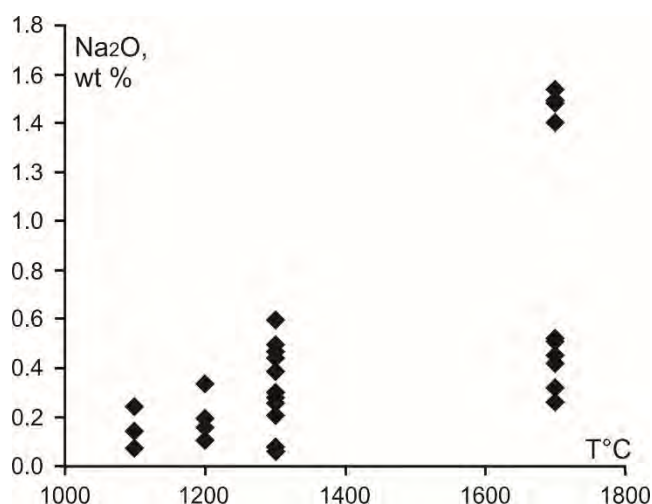


Figure 1: Na₂O concentration in synthetic bridgmanites depending on temperature.

The unit-cell volume observed for Na-bearing bridgmanite (166(1) Å³) is larger than that observed for pure MgSiO₃ (162.53(1) Å³, Dobson and Jacobsen 2004), due to the presence of the large Na cation. However, the mechanisms of Na incorporation in this structure remain unknown and require additional studies. As the chemical compositions obtained are not charge balanced, a probable solution could be a partial oxygen vacancy, as commonly observed in O-deficient perovskites (Akaogi 2007).

High-Na ringwoodite (up to 4.4 wt% Na₂O) was obtained at 24 GPa and 1700°C (Bindi et al 2016). The effect of Na in the ringwoodite structure is also apparent in the unit-cell parameter, which increases to 8.0952(3) in Na-ringwoodite with respect to 8.0816 in pure Mg₂SiO₄ (Ye et al. 2012).

Implications

Our results have implications for transport of alkalis into the lower mantle of the Earth. Although the concentration of alkalis in the Earth's transition zone and lower mantle is low and Na remains incompatible in most of the high-pressure solid phases, it is expected that some mantle phases could act as important hosts for Na, and perhaps K, in the deep transition zone and lower mantle. In the model of Walter et al. (2008), melting occurs as slabs descend and stagnate in the transition zone, and heat up to the carbonated eclogite solidus where they release a low-degree melt. Such low-degree carbonatitic melts from eclogite are expected to be mobile and rich in alkali, and so may act as effective metasomatizing agents. The presence of such melts in the deep mantle is supported by inclusions of Na-carbonates [nyerereite (Na,K)₂Ca(CO₃)₂ and eitelite Na₂Mg(CO₃)₂] in lower mantle diamonds (Kaminsky et al. 2016) and incorporation of sodium in major mantle silicates, such as majoritic garnet ringwoodite, and bridgmanite.

In contrast, proper Na-Mg silicates have not been registered as inclusions in diamonds or in mantle rocks, although they were obtained as products of experiments in many Na-rich model systems (Yang et al. 2009). This is explained by the fact that all natural lithologies are characterized by an excess of Al with respect to Na. However, the finding of an inclusion in diamond with the composition (Na_{0.16}Mg_{0.84})(Mg_{0.92}Si_{0.08})Si₂O₆ in a Chinese kimberlite (Wang and Sueno, 1996) suggests that some local areas of the Earth's deep mantle previously involved in the mantle-crust interaction may be

significantly enriched in Na. In this relation, study of Na-rich Mg-silicates will increase our knowledge on the composition and properties of the deep mantle.

Acknowledgment

This study was supported by the Russian Science Foundation (project no. 17-17-01169).

References

- Akaogi M (2007) Phase transitions of minerals in the transition zone and upper part of the lower mantle, in Ohtani E, ed, *Advances in high-pressure mineralogy: Geol Soc Amer Spec Paper 421:1–13*
- Bindi L, Tamarova A, Bobrov AV, Sirotkina EA, Tschauner O, Walter MJ, Irifune T (2016) Incorporation of high amounts of Na in ringwoodite: possible implications for transport of alkali into lower mantle. *Am Miner* 101:483–486
- Bobrov AV, Litvin YuA, Bindi L, Dymshits AM (2008) Phase relations and formation of sodium-rich majoritic garnet in the system $Mg_3Al_2Si_3O_{12}$ – $Na_2MgSi_5O_{12}$ at 7.0 and 8.5 GPa. *Contrib Mineral Petrol* 156:243–257
- Dobson DP and Jacobsen SD (2004) The flux growth of magnesium silicate perovskite single crystals. *Am Miner* 89:807–811
- Kaminsky F (2012) Mineralogy of the lower mantle: A review of ‘super-deep’ mineral inclusions in diamond. *Earth-Sci Rev* 110:127–147
- Stachel T (2001) Diamonds from the asthenosphere and the transition zone. *Eur J Mineral* 13:883–892
- Walter MJ, Bulanova GP, Armstrong LS, Keshav S, Blundy JD, Gudfinnsson G, Gobbo L (2008) Primary carbonatite melt from deeply subducted oceanic crust. *Nature* 454:622–625
- Wang W, Sueno S (1996) Discovery of a NaPx-En inclusion in diamond: Possible transition zone origin. *Min Journal* 18:9–16
- Ye Y, Brown DA, Smyth JR, Panero WR, Jacobsen SD, Chang YY, Townsend JP, Thomas SM, Hauri EH, Dera P, Frost DJ (2012) Compressibility and thermal expansion of hydrous ringwoodite with 2.5(3) wt% H₂O. *Am Miner* 97:573–582



Estimation of commercial diamond grades based on microdiamonds: a case study of the Koidu diamond mine, Sierra Leone

Tom Nowicki¹; Gareth Garlick¹; Kimberley Webb¹; Miles Van Eeden²

¹Mineral Services Canada Inc., Vancouver, Canada, tomn@mineralservices.com;

gareth@mineralservices.com; kimberley.webb@mineralservices.com

² Koidu Ltd, Freetown, Sierra Leone, MVanEeden@octeagroup.com

Introduction

Given the diversity of natural diamond populations, the relationships between microdiamonds (mostly < 0.5 mm diameter) and commercially relevant larger diamonds (macrodiamonds; mostly > 1 mm diameter) are likely complex and variable. Nonetheless, microdiamonds have been used for more than four decades as a basis for evaluating the grade of primary diamond deposits (Deakin and Boxer, 1989; Steifenhoffer et al, 2016). This has largely demonstrated that, under appropriate conditions, for any given kimberlite unit a systematic relationship can typically be defined between the concentration (number of stones per unit mass of kimberlite) of microdiamonds and the grade (weight of diamond per unit mass) of macrodiamonds. This reflects the fact that, on scales relevant to mining, many kimberlite units are homogeneous with respect to their juvenile components (i.e. those present in the kimberlite magma prior to emplacement). Thus the diamond size frequency distribution (SFD), representing the proportions of diamonds in different size fractions, is broadly constant within a given unit. Diamond size frequency relationships do however vary considerably between different kimberlite units and in many cases are not predictable from microdiamond data alone. Therefore, reliable application of microdiamond-based approaches for quantitative estimation of macrodiamond grade requires: accurate definition of the nature and extent of kimberlite units present; representative microdiamond and macrodiamond data for a portion of each unit being estimated; and confirmation that the SFD of diamonds is constant within each unit. If these conditions are satisfied, macrodiamond grade can be estimated based on microdiamond data combined with the calibrated ratio of microdiamond to macrodiamond content.

This contribution documents application of a microdiamond-based approach to estimation of the grade of the Pipe 1 kimberlite at the Koidu mine in Sierra Leone. Pipe 1 has been mined on and off since 1962 with the majority of the mining taking place between 2005 and 2007 and between 2012 and the present day. The resource estimate documented here was completed in 2014 and applies to the portion of the deposit between the bottom of the open pit at the time (~ 180 masl) and an elevation of -250 masl.

Geology

Pipe 1 is a small (<0.5 ha), irregular pipe-like body comprised of five main kimberlite units, including pipe-fill coherent kimberlite, three varieties of Kimberley Type Pyroclastic Kimberlite (KPK) and volumetrically minor late-stage intrusions of coherent kimberlite. The four volumetrically dominant kimberlite units are: KIMB1, olivine macrocryst- and granitoid xenolith-rich, coherent kimberlite; KIMB2B, very olivine macrocryst-poor, granitoid xenolith-rich KPK; KIMB3, KPK similar to KIMB2B but characterised by the presence of dolerite xenoliths, and autoliths of coherent kimberlite (possible KIMB1) and KIMB4; and KIMB4, medium-grained olivine macrocryst-poor to olivine macrocryst-rich, dolerite microxenolith-rich volcanoclastic to coherent phlogopite kimberlite. The distribution of these units provided the basis for a geological model comprising four domains (Fig. 1). The proportion of country-rock xenoliths varies between and within domains; hence the amount of dilution is a dominant factor controlling diamond grade variability. Petrography and microdiamond results indicate that the diamond SFD is constant within each domain. Furthermore, the massive character of the rocks and results of microdiamond analysis and bulk sampling indicate that, within the four volumetrically dominant pipe kimberlite units, the grade of undiluted kimberlite is constant.

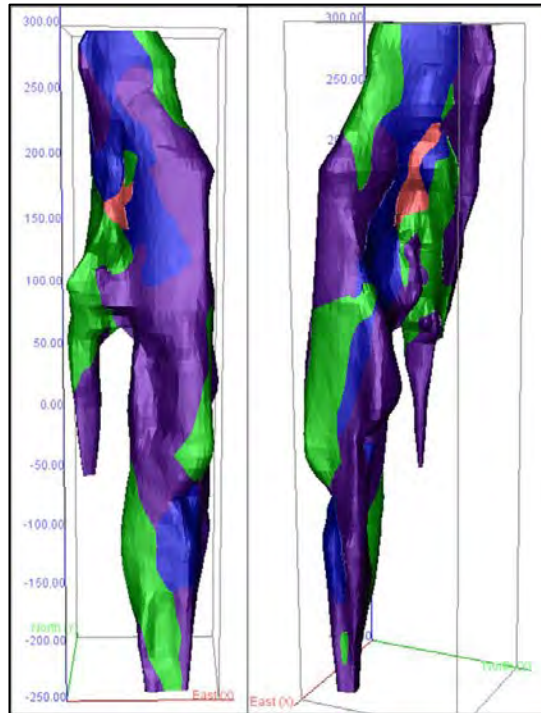


Figure 1. Model of Koidu Pipe 1 kimberlite below 300 masl, looking north (left) and southwest (right). Kimberlite domains are shown in different colours. Purple: K1, dominated by KIMB1; green: K2 dominated by KIMB2B; blue: K3, dominated by KIMB3; red = K4, mixture of KIMB3 and KIMB4.

Methods and evaluation approach

Practical considerations associated with active mining precluded grade estimation using the traditional approach of direct macrodiamond sampling through large diameter drilling. A microdiamond-based approach was therefore applied. The approach is based on: the geological model described above; macrodiamond data from four bulk samples (853 to 1726 tonnes per sample) excavated from each of the main kimberlite units; microdiamond data generated by caustic fusion analysis of 683 well-distributed drill core samples (~8 kg each); and quantitative estimates of the percentage of country-rock dilution, determined by continuous line-scan measurements undertaken on 29 of the 35 core drill holes intersecting the kimberlite in the zone of interest. Macrodiamonds were recovered from the bulk samples by crushing, dense media separation and X-ray diamond recovery using the Koidu production processing plant (1.2 mm bottom cut off). The estimation approach involved calibration of the micro-/macrodiamond relationship using macrodiamond data from the bulk samples paired with representative microdiamond samples of the same material. This relationship was applied to microdiamond stone frequency data (stones per kg) from drill core samples to derive estimates of the average undiluted grade per kimberlite domain. A block model representing the spatial variation in diluted grade was generated from these average domain grades by incorporating an interpolated model of the percentage of country-rock dilution based on the line-scan data.

Results

The results obtained using the above-described approach are summarised in Table 1 which provides an indication of the variability in grade on a bench (10 m mining level) scale within each of the modelled domains. The overall accuracy of the grade estimates has been assessed based on reconciliation with production data obtained subsequent to the definition of the resource (Fig. 2). The production data are derived from mine records of material processed through the Koidu production diamond processing plant, including total, total stones and carats recovered, source of ore (Pipe 1) and the mining level (bench) from which the material was derived. At the time of writing, reliable records (i.e. representing material sourced almost exclusively from Pipe 1) were available for the portion of

the pipe between 160 and 110 masl. From production records, the overall tonnage of material produced from this interval was 620 k tonnes, corresponding with an estimated resource of 561 k tonnes. Possible reasons for the 10% tonnage discrepancy between production records and the resource estimate include minor discrepancies between the modelled and actual kimberlite volume and inclusion of material from the levels immediately overlying and/or underlying the benches to which the production was assigned. The results shown in Figure 2 indicate a very close match between predicted and actual grades on the scale of 10 m benches, indicating that, when supported by a sound geological model and suitable microdiamond and macrodiamond data, the microdiamond-based estimation approach can provide reliable constraints on macrodiamond grade, even in the case of geologically complex bodies such as Koidu Pipe 1.

Table 1. Minimum, mean and maximum bench grades and percentage dilution estimates for each of the Pipe 1 kimberlite domains. The data represent 43 benches (10 m each) between 180 and -250 masl.

| Domain | Dilution (%) | | | Grade (cpt) | | |
|--------|--------------|------|-----|-------------|------|------|
| | Min | Mean | Max | Min | Mean | Max |
| K1 | 17 | 27 | 47 | 0.41 | 0.56 | 0.69 |
| K2 | 22 | 45 | 65 | 0.16 | 0.25 | 0.35 |
| K3 | 19 | 27 | 40 | 0.32 | 0.45 | 0.55 |
| K4 | 15 | 26 | 34 | 0.47 | 0.60 | 0.82 |

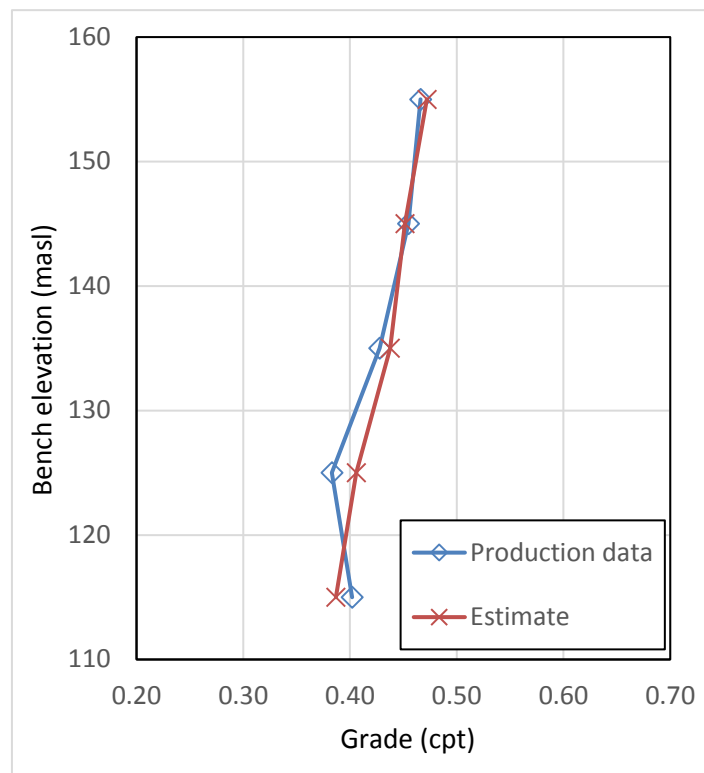


Figure 2. Comparison of bench grades based on production data with those derived from the mineral resource estimate. The comparison applies to the portion of the pipe between 160 and 110 masl.

References

- Deakin, A. S., Boxer, G. L. (1989) Argyle AK1 diamond size distribution: The use of fine diamonds to predict the occurrence of commercial sized diamonds. In: Proceedings of the 4th Int. Kimb. Conf., Geol. Soc. Australia Sp. Publ., 14(2), 1117–11226.
- Stiefenhofer, J., Thurston, M.L., Rose, D.M., Chinn, I.L., Ferreira, J.J. (2016) Principles of using microdiamonds for resource estimation: 1—The impact of mantle and kimberlite processes. CIM Journal, 7:216-238.



Geochemistry of the Namaqualand, Bushmanland and Warmbad melilitite and kimberlite provinces of South Africa and Namibia: the southern extension of the African kimberlitic megalineament

P. E. Janney^{1*}, M.D. Kirchner¹, P.I. Ogungbuyi¹, C. Harris¹, D.R. Bell²

¹Department of Geological Sciences, University of Cape Town, Rondebosch 7701, South Africa

²AEON-ESSRI, Nelson Mandela Metropolitan University, Summerstrand 6031, South Africa

Introduction

The ultimate origin of kimberlites and related igneous rocks, and their potential genetic relationships to deep mantle processes and lithospheric deformation, remains a highly controversial topic of active research (e.g., Nowell et al., 2004; Moore et al., 2008; Jelsma et al., 2009; Torsvik et al., 2010). Globally, most kimberlitic rocks occur as localised clusters that do not show clear age progressions over long distances or form nearly continuous linear zones of volcanism aligned with plate motions analogous to that seen in linear volcanic chains in the ocean basins. A marked exception to this is a remarkable linear zone of NE-SW oriented, largely age-progressive (Early Mesozoic to Early Cenozoic) alkaline magmatism, consisting mainly of diatremes and pipe-like intrusions of kimberlite, carbonatite, melilitite and ultramafic potassic igneous rocks extending from the west coast of South Africa to eastern Zambia (Moore et al., 2008). This lineament extends nearly 2500 km in length and \approx 120 km in width across southern Africa, nearly to the southern end of the East African Rift system. Here we present geochemical results for mafic and ultramafic alkaline igneous rocks from the Namaqualand-Bushmanland Warmbad (NBW) province, in western South Africa and southeastern Namibia, which represents the youngest and densest portion of the megalineament.

Age constraints on the Namaqualand-Bushmanland-Warmbad province

Mafic/ultramafic alkaline igneous magmatism in the NBW province is concentrated in three dense clusters (Figure 1a): *Namaqualand* (consisting of roughly 25 pipes, 38-56 Ma; Moore et al. 2008 and references therein, containing olivine nephelinite and melilitite, with minor carbonatite and ultramafic lamprophyre); *Bushmanland* (consisting of 200-300 pipes, 59 to 80 Ma; Moore et al., 2008; Davis et al., 1976; Griffin et al., 2014; fewer than 100 of which are composed of rocks such as olivine melilitite or rare ultramafic lamprophyre, the others being filled with volcanoclastic breccias or sediments) and *Warmbad* (consisting of approximately 50 Group 1 kimberlite pipes; mainly 60 to 83 Ma; Davis et al., 1976; Griffin et al, 2014; although a few older kimberlites occur in this area).

Age constraints for the NBW province are sparse and in many cases are based on likely unreliable whole-rock K-Ar ages. There are also disagreements in age determinations, most notably for the Rietfontein kimberlite (N. Cape, northernmost in Warmbad cluster) based on U-Pb measurements of kimberlitic zircon (72 ± 1 Ma; Davis et al., 1976) and perovskite (134 ± 9 Ma; Griffin et al., 2014). Northeast of the Warmbad kimberlite province, the age progression largely disappears, with most rocks in the megalineament having ages between 77 and 113 Ma (ages from compilation of Moore et al., 2008), including the Tsabong-Malopo and Orapa kimberlite provinces in Botswana and the Katete and Kaluwe carbonatites in Zimbabwe and Zambia, respectively.

Geochemistry and petrogenesis

Fresh, precisely located igneous rock samples have been obtained from 10 Namaqualand melilitite pipes, 13 Bushmanland melilitite pipes and 5 Warmbad lamprophyre/kimberlite pipes extending the length of the NBW province. Whereas the Bushmanland melilitites and Warmbad kimberlites are all near-primary (with Mg# ranges of 69 to 77 and 78 to 91, respectively), rocks of the Namaqualand cluster (collectively called melilitites, although some do not contain melilitite) are mildly to moderately differentiated (with Mg# between 71 and 45), requiring up to 50% olivine crystallization. The highly SiO₂-undersaturated compositions of the parental magmas result in both SiO₂ and MgO decreasing with increasing fractionation in the Namaqualand melilitites. Although there is no evidence from their chemical or radiogenic isotopic compositions for crustal assimilation,

olivine separates from some of the Namaqualand melilitites emplaced through the Early Cretaceous Koegelfontein intrusive complex have $\delta^{18}\text{O}$ values as low as +4.2‰ (compared to values of +4.9 to +5.6‰ for the other Namaqualand and Bushmanland melilitites; Day et al., 2014). Koegelfontein is a ≈ 30 km diameter igneous complex in southern Namaqualand composed of felsic-intermediate intrusive rocks that were emplaced shortly before opening of the South Atlantic and is notable for containing igneous rocks with remarkably low $\delta^{18}\text{O}$ values (as low as -4‰). This indicates that minor crustal assimilation must have occurred in the genesis of at least some Namaqualand melilitites.

Across the three clusters of the NBW province, there are systematic variations in incompatible element contents from the coastal region to the continental interior, most robustly demonstrated by the relative abundances of Th, U and Nb. Namaqualand melilitites are relatively enriched in U and Nb compared to elements of similar incompatibility and therefore have low Th/Nb and Th/U ratios relative to primitive mantle (Fig. 1b). However, both of these ratios increase markedly in the Bushmanland melilitites and appear to increase further, though more subtly, in the Warmbad kimberlites. Similarly, there is a systematic progression in terms of radiogenic isotope ratios along the length of the lineament. This is most clearly shown in Pb isotope ratios, which are highest in Namaqualand ($^{206}\text{Pb}/^{204}\text{Pb}_i = 19.5$ to 21.1; Fig. 2), showing a fairly strong HIMU source affinity, and somewhat lower in Bushmanland ($^{206}\text{Pb}/^{204}\text{Pb}_i = 18.9$ to 20.3). Sr and Nd isotope ratios in the Namaqualand and Bushmanland clusters are similar ($^{87}\text{Sr}/^{86}\text{Sr}_i = 0.7031$ -0.7036 (for leached samples), $\epsilon_{\text{Nd}}(t) = +2.0$ to +5.5). The Warmbad kimberlites (carefully picked (and leached for Sr isotopes) to avoid alteration & contamination) largely overlap with the Bushmanland melilitites in terms of Nd and Pb isotope composition (e.g., $^{206}\text{Pb}/^{204}\text{Pb}_i = 18.6$ to 19.9), but extend to somewhat higher $^{87}\text{Sr}/^{86}\text{Sr}_i$ ratios (0.7034-0.7044). Cr-poor and Cr-rich clinopyroxene megacrysts from the Pofadder kimberlites (for which there are no fresh whole-rock samples) span a wide range of isotopic compositions overlapping with the melilitites and kimberlites, though at the lower end of the $^{206}\text{Pb}/^{204}\text{Pb}_i$ range.

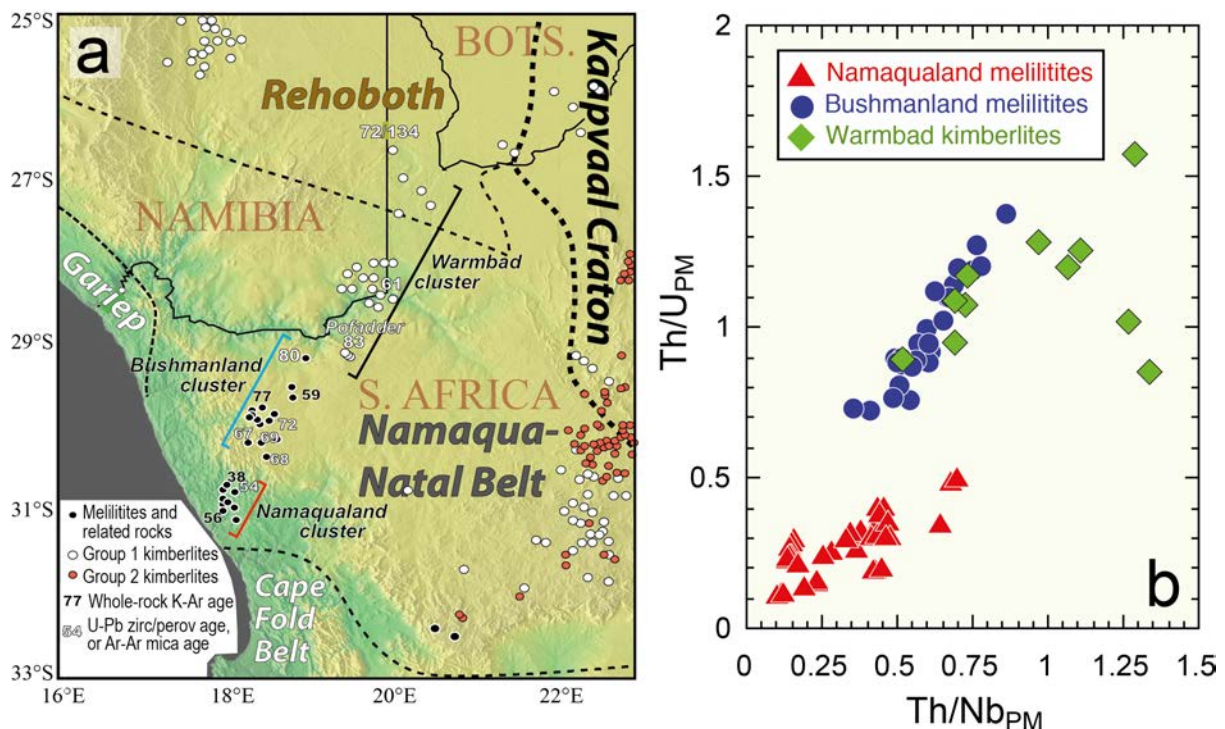


Figure 1. (a) Map of kimberlites and related rocks in southwestern Africa showing location of the NBW province and crustal terrane boundaries. Ages from compilation of Moore et al. (2008), Davis (1976) and Griffin et al. (2014). (b) Primitive mantle-normalised Th/Nb vs. Th/U ratios in the NBW province rocks.

Discussion

The geochemical data display a shift in mantle source compositions indicating that the magmas on the thinnest lithosphere in the coastal region (Namaqualand) have the strongest HIMU affinity (extending to exceptionally high $^{238}\text{U}/^{204}\text{Pb}$ (to more than 500) and low Th/U values (of less than

0.8)), whereas those emplaced on thicker lithosphere toward the continental interior appear to reflect a greater degree of assimilation of ancient metasomatised lithospheric mantle, with sources having lower time-integrated U/Pb ratios, and thus lower $^{206}\text{Pb}/^{204}\text{Pb}$. This finding is consistent with the pattern expected for southwestern Africa passing over a weak HIMU-type mantle plume. However, the poorly defined age-progression within the megalineament and the lack of evidence for young intraplate volcanism in the southeastern Atlantic Ocean that could be related to it do not offer strong support for a plume origin. Therefore origins for the megalineament relating to lithospheric deformation (e.g., extension or shearing) or lithosphere-asthenosphere interactions cannot be ruled out. Further, recent evidence from megacrysts for the prevalence of strong HIMU signatures in the sources of many Cretaceous southern African kimberlites (Janney and Bell, abs. 4630, this volume) suggests that such HIMU signatures do not necessarily require a mantle plume and could possibly be lithospheric in origin.

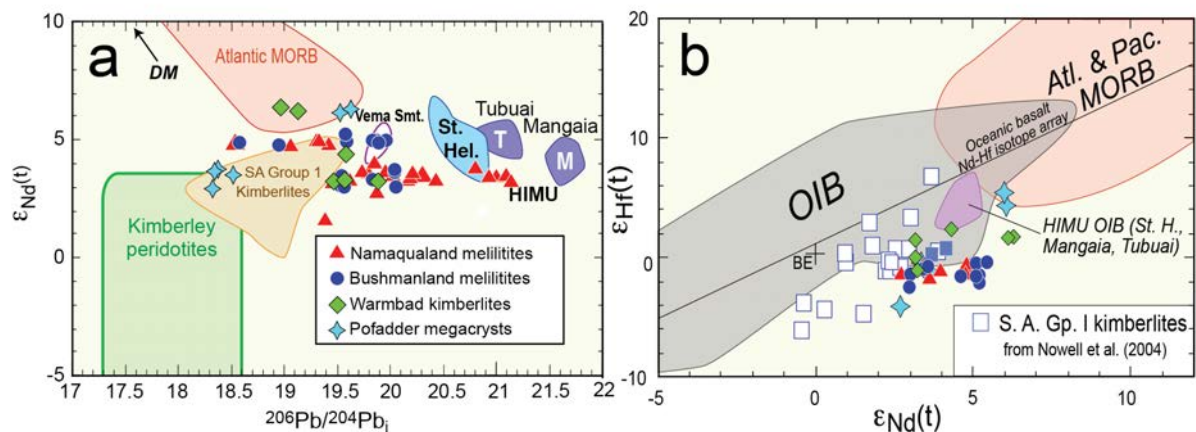


Figure 2. (a) $^{206}\text{Pb}/^{204}\text{Pb}_i$ versus $\epsilon_{\text{Nd}}(t)$ and (b) $\epsilon_{\text{Nd}}(t)$ versus $\epsilon_{\text{Hf}}(t)$ for the NBW melilitites and kimberlites, showing fields for MORB, HIMU OIB and other relevant rock types. Data for Grp. I kimberlites from Smith, (1983); Davies et al. (2001) and Nowell et al. (2004). MORB and OIB data from PETDB and GEOROC.

Acknowledgements

Generous support for this project was provided by the South African National Research Foundation and the UCT Science Faculty to PEJ, and a Council for Geoscience bursary to MDK.

References

- Davies, G. R., Spriggs, A. J. & Nixon, P. H. (2001). A non-cognate origin for the Gibeon kimberlite megacryst suite, Namibia: Implications for the origin of Namibian Kimberlites. *Journal of Petrology* **42**, 159-172.
- Davis, G., Krogh, T. & Erlank, A. J. (1976). The ages of zircons from kimberlites from South Africa. *Carnegie Institution Yearbook* **75**, 821-824.
- Day, J. M. D., Peters, B. J. & Janney, P. E. (2014). Oxygen isotope systematics of South African olivine melilitites and implications for HIMU mantle reservoirs. *Lithos* **202**, 76-84.
- Griffin, W. L., Batumike, J. M., Greau, Y., Pearson, N. J., Shee, S. R. & O'Reilly, S. Y. (2014). Emplacement ages and sources of kimberlites and related rocks in southern Africa: U-Pb ages and Sr-Nd isotopes of groundmass perovskite. *Contributions to Mineralogy and Petrology* **168**, 1032.
- Jelsma, H., Barnett, W., Richards, S. & Lister, G. (2009). Tectonic setting of kimberlites. *Lithos* **112S**, 155-165.
- Moore, A. E., Blenkinsop, T. & Cotterill, F. (2008). Controls on post-Gondwana alkaline volcanism in southern Africa. *Earth and Planetary Science Letters* **268**, 151-164.
- Nowell, G. M., Pearson, D. G., Bell, D. R., Carlson, R. W., Smith, C. B., Kempton, P. D. & Noble, S. R. (2004). Hf isotope systematics of kimberlites and their megacrysts: New constraints on their source regions. *Journal of Petrology* **45**, 1583-1612.
- Smith, C. B. (1983). Pb, Sr and Nd isotopic evidence for sources of southern African Cretaceous kimberlites. *Nature* **304**, 51-54.
- Torsvik, T. H., Burke, K., Steinberger, B., Webb, S. J. & Ashwal, L. D. (2010). Diamonds sampled by plumes from the lower mantle. *Nature* **466**, 352-355.



Geology of the K6-252 Complex, Alberta

Tom McCandless¹, Brian DesGagnes², Mark Shimell² and George Read²

¹*Canterra Minerals Corp., Vancouver, Canada temccandless@gmail.com*

²*Shore Gold Inc., Saskatoon, Canada*

Introduction

The Buffalo Head Hills (BHH) kimberlites comprise the third largest district of diamond-bearing kimberlites in Canada, with 41 kimberlites distributed over 6,000km², of which 27 are diamondiferous. Discovery has been largely through drilling of magnetic targets, and extensive erosion prior to burial under thick glacial made it difficult to correctly model their geology. In 2010 the BHH Joint Venture consisting of Canterra Minerals Corp., Shore Gold Inc. and Encana Corp. undertook systematic grid drilling and detailed logging with emphasis on the modal abundance of macrocrysts, lapilli, xenoliths and matrix. This led to the modeling of several of the kimberlites as larger kimberlite complexes. The most conclusive modeling is for the K6 and K252 kimberlites, hereafter referred to as the K6-252 kimberlite complex.

Geological Setting

The BHH kimberlites are emplaced through the ~2.31.9Ga Buffalo Head Terrane that is notably younger than >2.5Ga lithosphere that hosts diamondiferous kimberlites worldwide. This atypical setting is expressed in mantle indicator chemistry with a near-absence of G10 pyrope. For pyrope as well as the other indicators, neither composition nor abundance correlates with diamond content (Hood and McCandless, 2004). Two kimberlite age groups are present; the ~85Ma Group and the ~60Ma Group. The 85Ma kimberlites were emplaced coevally with deposition of the late Cretaceous Dunvegan and Kaskapau Formations, and then partially eroded in the Tertiary and buried under Quaternary glacial cover.

The K6-252 Complex

At K6 there are two depositional centers (vents) identified by gravity, with the northern vent forming a topographic high. The K252 kimberlite is 300 meters northwest of K6 with a single vent buried under 50 meters of glacial cover (Figure 1). Connecting the two vents is the earliest interbedded unit, an olivine-rich volcanoclastic kimberlite (OLRVK) whose upper contact occurs at the contact of the Dunvegan and Kaskapau Formations. Juvenile lapilli-rich VK (JLRVK) kimberlite rests stratigraphically above the OLRVK and within the Kaskapau Formation. Both units increase in thickness toward K252 and appear to be apron deposits of K252, similar to those observed at some FALC kimberlites (Zonneveld et al., 2004). Both the main vent facies at K6 (MVK) and the matrix-supported vent facies at K252 (MSVK) rest unconformably on the upper Kaskapau Formation and cross-cut the lower marine strata. The MVK at K6 is distinguished by abundant crystalline basement xenoliths, which are relatively rare in the MSVK at K252. When projected at 1:1 scale and correlated to a single datum, the interbedded units stratigraphically align, further supporting the interpretation of K6-252 as a single kimberlite complex (Figure 1).

Subsequent to emplacement in the Cretaceous, the K6-252 complex (and several other BHH complexes) were exposed to weathering and erosion in the Tertiary. Weathering in the Tertiary is believed to have formed a carapace of magnetic minerals near the top of each vent, which was later removed from K252 by glacial erosion in the Quaternary. This model explains why K6 has a strong magnetic signature, whereas K252 is magnetically-transparent and identified as an EM-anomaly prior to drilling (Skelton et al., 2003).

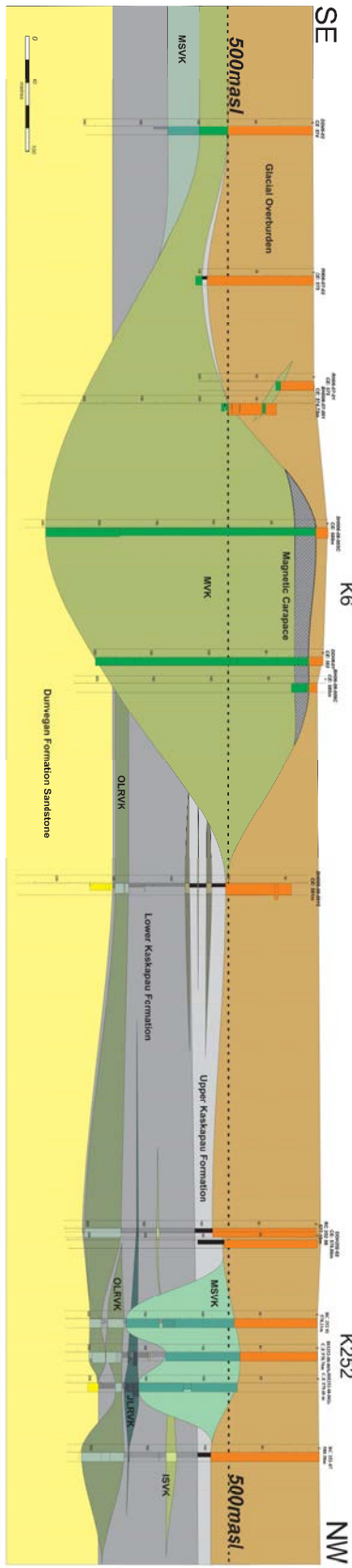


Figure 1. Longitudinal fence diagram for K6-252 referenced to 500masl (dashed line). See text for discussion.

Diamond Characteristics

Diamonds from the K6-252 complex are dominantly tetrahexahdroida, which is typical for the BHH kimberlites (Banas et al., 2007). The K252 vent has the highest diamond content in the BHH at 0.55 carats per tonne (cpt) from 28 tonnes, with grades approaching 1cpt from some interbedded units. Though lower in grade at 0.07cpt (from 232 tonnes), K6 has the largest diamonds reported from the BHH including a 1.77ct colorless and a 0.77ct fancy yellow diamond. Along with the 1.77 carat diamond, three diamonds exceeding one carat and of similar quality were recovered from a ~16 carat sample, suggesting a coarse diamond distribution for this part of the complex (Canterra, 2016).

Conclusions

Systematic drilling and detailed logging of the K6-252 kimberlite complex indicates that it is a multiple eruptive kimberlite with kimberlite units defining both within-vent as well as interbedded lithologies. The complex was emplaced during deposition of late Cretaceous sedimentary rocks in a marine setting. Neither the geology nor the diamond characteristics of K6-252 complex are likely to be unique, and the application of these latest findings could have significant implications for the future exploration and economics of other BHH kimberlites.

References

- Banas, A., Stachel, T., Muehlenbachs, K., McCandless, T.E. 2007. Diamonds from the Buffalo Head Hills, Alberta: formation in a non-conventional setting. *Lithos*, 93, 199-213.
- Canterra. 2016. Canterra provides update for Buffalo Hills Project, Alberta. Canterra Minerals Corp., News Release, March 30, 2016.
- Hood, C.T. and McCandless, T.E. 2004. Systematic variations in xenocryst mineral composition at the province scale, Buffalo Hills kimberlites, Alberta, Canada. *Lithos*, 77, 733-747.
- Scott-Smith, B.H. 2008. The Fort a la Corne kimberlites, Saskatchewan, Canada: geology, emplacement and economics. *J. Geol. Soc. India* 71, 11-55.
- Skelton, D.N., Clements, B., McCandless, T.E., Hood, C., Aulbach, S., Davies, R. and Boyer, L.P. 2003. The Buffalo Head Hills kimberlite province, Alberta. In Kjarsgaard, B.A. (editor) *Slave Province and northern Alberta Field Trip Guidebook*. Geological Survey of Canada, CD-ROM, pp.11-20.
- Zonneveld, J-P. Kjarsgaard, B.A., Harvey, S.E., Heaman, L.M., McNeil, D.H. and Marcia, K.Y. 2004. Sedimentologic and stratigraphic constraints on emplacement of the Star Kimberlite, east-central Saskatchewan. *Lithos* 76, 115-138.



Revitalising exploration in a key diamond district: A case study in the Northwest Territories, Canada

B. Elliott¹, M. Ross², S. Kelley², D. Cummings³, P. Winterburn⁴, B. Ward⁵, A. Mirza¹, P. Normandeau¹, S. Cairns¹

1) Northwest Territories Geological Survey, Yellowknife, Canada, Barrett_Elliott@gov.nt.ca, Asif_Mirza@gov.nt.ca, Phillippe_Normandeau@gov.nt.ca, Scott_Cairns@gov.nt.ca

2) University of Waterloo, Waterloo, Canada, maross@uwaterloo.ca, samuel.kelley@uwaterloo.ca

3) DCGeo Applied Sedimentary Geology Consulting, Aylmer, Canada, cummings1000@gmail.com

4) MDRU - EOAS - The University of British Columbia, Vancouver, Canada, dr.peter.winterburn.geochemist@gmail.com

5) Simon Fraser University, Vancouver, British Columbia, Canada, bward@sfu.ca

Introduction

In 2014 and 2015 the Northwest Territories Geological Survey (NTGS) carried out the Slave Province Surficial Materials and Permafrost Study (SPSMPS), a two-year collaborative government–industry–academic research program in the Lac de Gras region, Northwest Territories, Canada. The overall goals of the project were to advance our understanding of glacial history, develop innovative exploration techniques for glaciated terrain and update surficial maps in targeted areas. The project was funded through the Strategic Investments in Northern Economic Development program of the Canadian Northern Economic Development Agency.

Our industry partners included Dominion Diamond Ekati Corp, Diavik Diamonds Mines Inc., North Arrow Minerals Inc., Peregrine Exploration Ltd., Artic Star Exploration Corp., New Nadina Explorations Limited, and TNT Mineral Science. Our research partners included the Canadian Mining Institute Research Organization, Palmer Environmental Consulting Group Inc., GGL Resources Corporation, DCGeo Applied Sedimentary Geology Consulting, the University of Waterloo, Simon Fraser University, Carleton University and the University of British Columbia. Much of this work was carried out by or with assistance from Aurora Geosciences Ltd.

Highlights include a new database of indicator mineral counts, indicator mineral chemistry and till geochemistry, new three dimensional (3D) models of kimberlite indicator mineral (KIM) trains, a study on the application of surficial geochemistry to the detection of kimberlites, a study on esker transport distance, updated surficial mapping products and a case study in the application of ground penetrating radar (GPR) and Ohm Mapper, a Capacitively Coupled Resistivity (CCR) system, to determine depth to bedrock in permafrost rich environments. To accomplish these objectives, 1131 sediment samples (primarily till) were collected from 235 boreholes. Over 1500 square kilometres of field mapping and approximately 150 line-kilometres of ground geophysics complement the drill data. Logistical support, large proprietary indicator mineral, remote sensing, and mapping datasets were generously provided by our industry partners.

New 3D Indicator mineral datasets

A 3D database of surface and subsurface indicator mineral counts, indicator mineral chemistry and till geochemistry from 174 boreholes has been published by the NTGS (Elliott and Normandeau, 2017, Elliott and Normandeau, 2016, Normandeau, et al. 2016). These reports document several instances of anomalous concentrations of indicator minerals at depth that are not reflected in surficial samples. A more in-depth assessment of this data is currently underway, but this data clearly implies that traditional

indicator mineral sampling may not be sufficient to assess the mineral potential of areas with complex or poorly understood surficial geology.

New 3D Indicator Mineral Entrainment Models

Based on the concepts of glacial dynamics, glacial sediment production, transport and deposition, drift prospecting has been used to trace indicator mineral grains back to a buried bedrock source. Here, 94 reverse circulation (RC) boreholes were drilled, to collect 254 till samples and generate a subsurface model of the dispersal train from the DO-27 / DO-18 kimberlite pipes. The effect of changing ice flow on the composition of till has been well-studied in both map-view, as well as longitudinally in cross section (i.e., dispersal curves). Through a combination of borehole data, field work, and modelling, we are able to compare three-dimensional dispersal patterns in the subsurface with local ice flow records, measured from erosional ice flow indicators in the field.

This dataset allows us to evaluate the role that changing ice flow, as well as local bedrock surface topography, play in controlling dispersal and deposition of clastic sediment by past ice sheets. Our modelling documents buried palimpsest terrains along older ice flow trajectories, demonstrating lateral and vertical variability within a single, relatively thin and discontinuous till sheet. Furthermore, we observe relationships between local indicator mineral concentrations and bedrock topography, with indicator mineral dispersal concentrated along a bedrock-controlled topographic low. This work demonstrates the benefit of more complete mapping and visualisation of a dispersal plume, even in areas of relatively thin and discontinuous till cover, highlighting the role basal topography and shifting ice flow play in shaping the surface expression of a dispersal train.

Determination of Depth to Bedrock in Permafrost Rich Overburden

To develop a method of rapidly determining the depth to bedrock in areas covered with permafrost-rich overburden, GPR and CCR geophysical surveys were carried out in the vicinity of the DO-27 / DO-18 kimberlites and their associated indicator-mineral trains. This work used the high-density drilling from the 3D indicator mineral entrainment study to provide control for the geophysical data. The most reliable depths to the bedrock were obtained by interpreting the CCR and GPR data together. Based on the results of both geophysical surveys, the top of the bedrock can be reliably interpreted from surface to >20 metres in the surveyed area.

Applying Surface Geochemistry Models for the Detection of Kimberlites

One hundred and fifty soil samples were taken from the oxidised upper B-horizon in a 50 x 60 metre grid crossing the DO-18 kimberlite to assess the potential of various geochemical techniques, to detect the presence of a kimberlite concealed by 5-20 metres of till. In conjunction with surface materials mapping and landscape evolution models, four-acid and aqua regia digestions successfully detect the kimberlite, displaying a dispersal of Cr, Mg, Nb and Ni, from directly above the kimberlite in the northern region, to the edge of the sampling grid, in the down-ice direction. Fundamental Parameters X-ray fluorescence analysis repeat the pattern in all elements except Mg, where the concentrations are too low for reliable detection, though a low-level Zn anomaly was detected. A similar pattern was also observed in the Soil Gas Hydrocarbon data, particularly in the light benzenes. Sequential leach on selected samples was undertaken to identify which phases within the soil are host to the aforementioned anomalous elements. Surficial mapping included soil type, topographic variation, landforms, environment and vegetation, giving insight to the surface controls on the geochemistry.

The observed soil geochemical anomaly is hypothesised to have been generated by clastic dispersion of these elements in the direction of glacial movement with geomorphological processes exhibiting a strong influence on surface geochemistry. Part of the study area is interpreted to have been inundated with water, generating lower topography and subduing the soil geochemical responses.

Esker Transport Distance

Eskers are commonly sampled for KIMs during the early stages of diamond exploration, with the understanding that they likely function as "regional dipsticks", much like large streams do in non-glacial settings. Esker sampling was integral to the discovery of the Lac de Gras kimberlite field. During the SPSMPS, a large integrated dataset consisting of Light Detection and Ranging (LiDAR) data, GPR data, grain-size samples, and surficial mapping observations was collected from the Exeter Lake esker, Canada's longest esker. The results suggest that the esker was deposited in short segments, each several kilometres in length, as the ice front retreated, and not as a single, long segment beneath the ice as has commonly been assumed. Segmental Deposition may explain why previously reported esker dispersal trains tend not to considerably overshoot underlying till trains from which they were sourced. If the results of this study are proven representative, eskers may commonly provide similar information as the nearby till, and the "regional dipstick" model of esker-exploration may require reinterpretation.

Updated Surficial Maps

Approximately 60,000 square kilometres of 1:50,000 scale surficial mapping products in the southern Slave Craton have been graciously provided by GGL Resources Corporation. The maps emphasised the role of melt water and enabled the first publicly available comprehensive geographic reconstruction of the paleo-lakes present over the Slave Craton. These lakes reconstructions help explain the presence of distinct surficial materials and landforms across geomorphologic elevation zones, such as washed bedrock field hosting vestiges of esker complexes, disrupted esker complexes hosted by moderately reworked till, and esker complexes with well-defined esker corridors hosted by till.

The nature of these esker corridors and the sediments they contain is the subject of a related study drawing on LiDAR, 3D surficial sediment mapping, sediment composition and granulometry analysis, and geomorphic analysis. This study highlighted the presence of melt water erosive corridors not containing eskers, as well as the ubiquitous presence of sediment mounds in all melt water corridors. The mound composition differs from that of the regional till, and are now interpreted to result from episodic drainage events during late deglaciation. Recognising these features may modify the design and the interpretation of drift prospecting sampling campaign.

References

- Elliott, B. and Normandeau, P.X. (2016) Slave Province Surficial Materials and Permafrost Study – Kimberlite Indicator Mineral Counts and Grain Morphology from the 2015 Reverse Circulation Drilling Program. NWT Open Report 2016-018, Northwest Territories Geological Survey, Yellowknife, NT, 6 p.
- Normandeau, P.X., Elliott, B., and Gervais, S.D. (2016) Slave Province Surficial Materials and Permafrost Study – Geochemical and textural data from the 2015 reverse circulation drilling program. NWT Open Report 2016-012, Northwest Territories Geological Survey, Yellowknife, NT, 12 p.
- Elliott, B., Normandeau, P.X. (2017) Slave Province Surficial Material and Permafrost Study – Kimberlite Indicator Mineral Chemistry from the 2015 reverse circulation drilling program. NWT Open Report 2017-011, Northwest Territories Geological Survey, Yellowknife, NT, 7 p.



Discrimination of Whiskey kimberlite eruptive phases utilizing portable XRF spectrometry data

Bruce A. Kjarsgaard¹, Eric C. Grunsky², Stephan Kurszlaukis³ and Mike Seller⁴

¹University of Alberta, Edmonton, Canada; bakjarsgaard@gmail.com

University of Waterloo, Waterloo, Canada

De Beers Canada, Calgary, Canada

De Beers Canada Exploration, Toronto, Canada

Introduction

The purpose of this study was to examine the viability of using a hand-held portable X-ray fluorescence (pXRF) spectrometer to rapidly obtain geochemical data on kimberlite samples, and thus enable discrimination of different kimberlite phases. Potential applications range from augmenting core logging at the exploration stage, to ore grade control during mining. The use of whole rock geochemistry to distinguish different phases of kimberlite within an individual body is well established (e.g. Star kimberlite: Grunsky and Kjarsgaard, 2008; Orion South kimberlite: Kjarsgaard et al., 2009). The samples for this study are from the Whiskey kimberlite, located in the Attawapiskat field, James Bay Lowlands, northern Ontario, Canada (Januszczak et al., 2013).

Analytical Results

A suite of whole rock geochemical analyses (laboratory fusion ICP-ES/MS) were obtained from a selection of Whiskey kimberlite drill core samples; all the raw geochemical data were subdivided into three distinct kimberlite phases (U1VK, U2VK, U3VK) based on core logging and petrographic studies by De Beers geologists. The three phases are easily distinguished on a geochemical basis, e.g. on simple downhole depth versus concentration plots, or x-y plots such as TiO₂ vs Y (Fig. 1a). The whole rock dataset employed provides a sound statistical training set, which consisted of 189 samples (U1VK = 78; U2VK = 75, U3VK = 36). An analysis of variance (AOV) was undertaken to determine elements with the greatest power to discriminate the three phases, in order to examine the potential of using a pXRF, i.e. can a pXRF obtain viable data for the discriminating elements of interest. Note that pXRF spectrometers typically can only provide reliable data for ten to twenty elements, which are concentration dependant.

Based on the AOV for 44 elements from the training set, a subset of 22 elements from the whole rock data set were selected for statistical treatment, with Ti, Ta, Al, Yb, Y and Cr having the greatest discriminating power, and U, Ca and Na the least discriminating power. A principal component analysis (PCA) was applied to the log-centred transformed (Aitchison, 1986) data for 22 elements. The first three eigenvalues account for the majority (71%) of the variance of data. A linear discriminant analysis was carried out (on 22 elements) and a LD1-LD2 plot of the data demonstrates good group separation and the overall accuracy is 99.1%. The discriminating elements of interest (based on the AOV) can be analysed for by pXRF spectrometry.

A sub-set of kimberlite sample powders (previously analysed by laboratory fusion ICP-ES/MS) were analysed with a Niton pXRF in 'Mining Mode' with He gas, and in 'Soil Mode', both using an 8 mm window. An AOV was undertaken on both pXRF data sets. For 'Mining Mode', the best elements to discriminate the 3 kimberlite phases are Ti, Nb, Ba, Al. A bi-variate plot of Al versus Ti distinctly separates the three kimberlite phases (Fig. 1b). In 'Soil Mode', the best elements to discriminate the 3 kimberlite phases are Ti, Cr, Zr. A more comprehensive statistical treatment via principal component and linear discriminant analyses utilizing only 3 (or 4) elements separates out the 3 kimberlite phases into discrete clusters, as summarized by Grunsky et al. (2013).

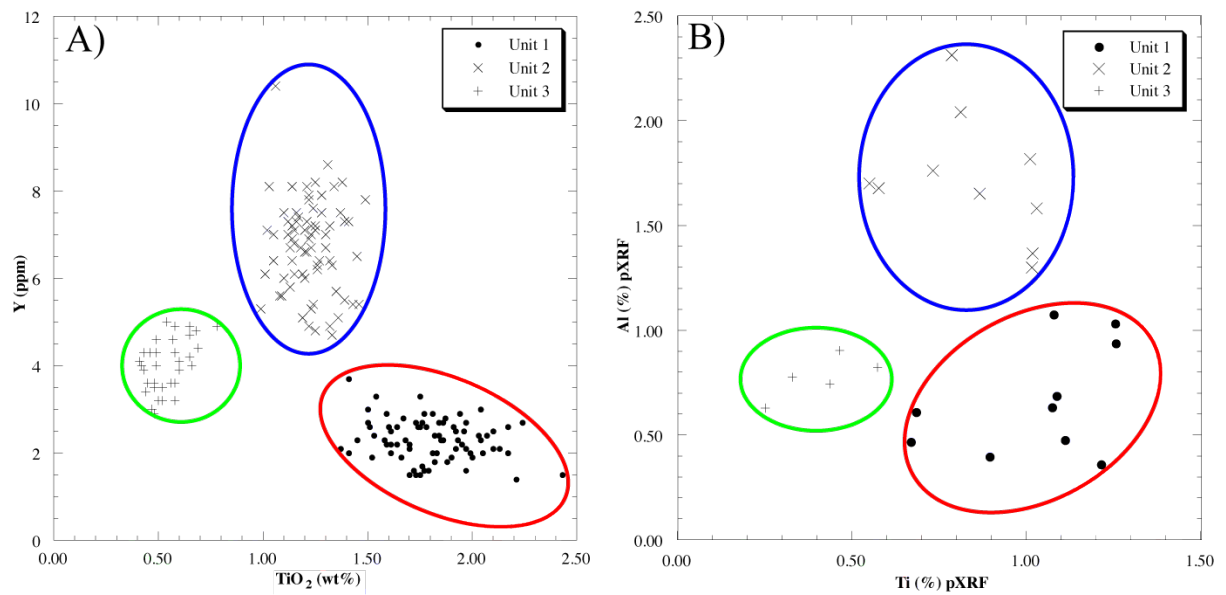


Figure 1: Geochemical separation of the three Whiskey kimberlite phases (A) TiO_2 versus Y from fusion ICP-ES/MS on whole rocks (B) Ti versus Al from hand-held pXRF on kimberlite whole rock powders.

After the successful application of the pXRF on the powders, thirteen cut kimberlite slabs were analysed by pXRF in 'Mining Mode' with He gas, and in 'Soil Mode'. The kimberlite matrix was targeted, avoiding xenoliths and megacrysts, with 5 analyses per slab (Fig. 2). Based on an analysis of variance, K, Rb, Fe, Mg, Al, Cu, Zr are the better discriminants, and the three kimberlite phases form distinct clusters on LD1-LD2 plots using these elements (Fig. 3a). Importantly, note that the best discriminating elements from slab matrices are different than from the wholerock powders.

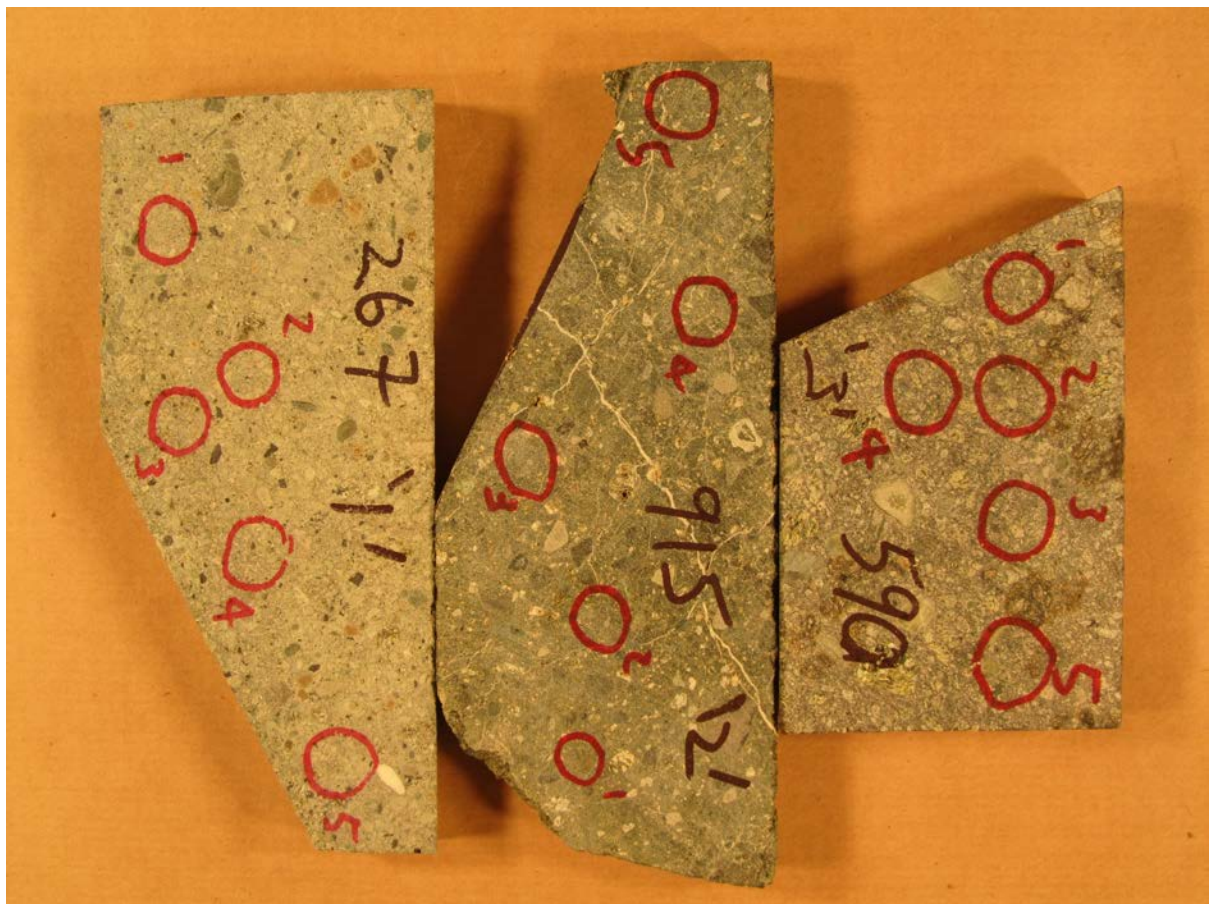


Figure 2: Example of three different phases of the Whiskey kimberlite, with pXRF analysis areas outlined (red).

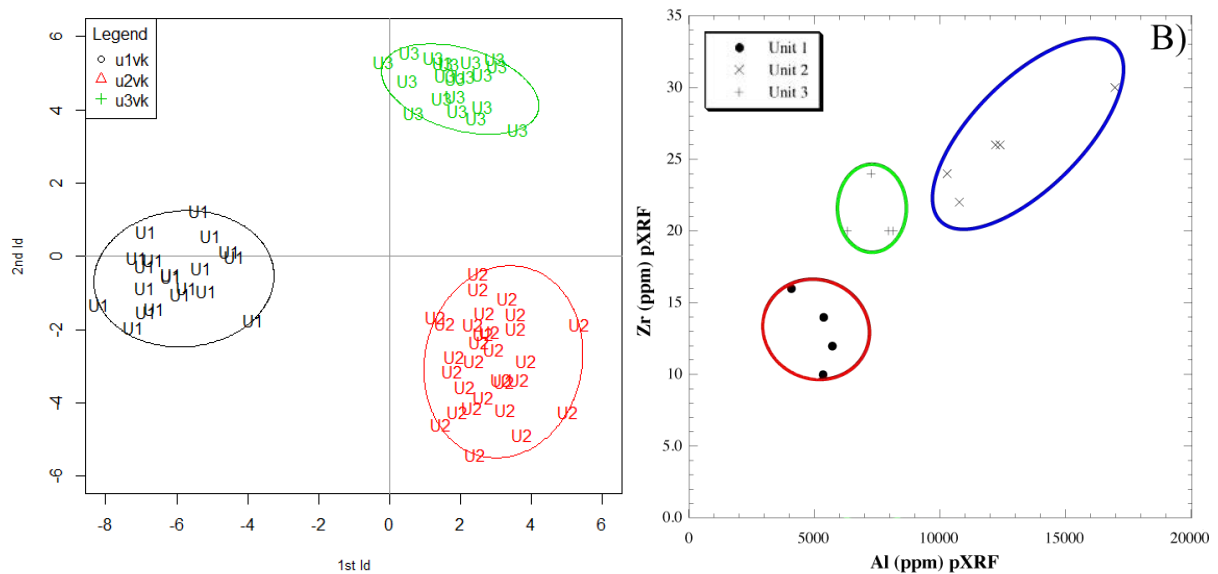


Figure 3: (A) Four element linear discriminant analysis (Fe, Cu, Mg, Al from mining mode), all individual pXRF cut slab analyses plotted: (B) Al versus Zr from pXRF mining mode, average of 5 analyses per cut slab.

Summary

We summarize that hand-held pXRF spectrometry can be an effective tool for discriminating kimberlite phases, with pXRF on cut slabs potentially useful to assist in exploration core logging, and pXRF on whole rock powders providing better quality data that would be best applied for ore grade control situations.

References

- Aitchison, J., 1986, *The Statistical Analysis of Compositional Data*. Chapman and Hall, New York, 416 p.
- Grunsky EC, Kjarsgaard BA, Kurszlauskis S, Seller M, Knight R, Moroz M (2013) Classification of whole-rock geochemistry based on statistical treatment of whole-rock geochemical analyses and portable XRF analyses at the Attawapiskat kimberlite field, Ontario. Geological Survey of Canada, Scientific Presentation #15, 1 sheet.
- Grunsky EC, Kjarsgaard BA (2008) Classification of eruptive phases of the Star Kimberlite, Saskatchewan, Canada based on statistical treatment of whole-rock geochemical analyses. *Applied Geochemistry* 23: 3321-3336.
- Januszczak N, Seller MH, Kurszlauskis S, Murphy C, Delgaty J, Tappe S, Ali K, Zhu J, and Ellemers P. (2013) A multidisciplinary approach to the Attawapiskat kimberlite field: Accelerating the discovery to production pipeline. In: *Proc. 10th Int Kimb Conf, India*: 157-172.
- Kjarsgaard BA, Harvey S, Du Plessis P, McClintock M, Zonneveld J-P, Heaman L, and McNeil D (2009) Geology of the Orion South Kimberlite, Fort à la Corne, Canada. *Lithos* 112: 600 – 617.



Metasomatism of Cratonic Lithosphere by Hydrous, Silica-rich, Fluids Derived from Recycled Sediment: Experimental Insights at 5-7 GPa

R. P. Rapp, S. Timmerman, J. Lowczak and A.L. Jaques

The Australian National University, Canberra, Australia, robert.rapp@anu.edu.au, suzette.timmerman@anu.edu.au, jessica.lowczak@anu.edu.au, lynton.jaques@anu.edu.au

Introduction

It is generally accepted that diamond formation in the sub-cratonic lithospheric mantle (SCLM) was associated with the influx of solute-rich, mixed C-O-H fluids (Shirey et al., 2013) that also acted as transformative metasomatic agents, chemically re-fertilizing the SCLM, and representing an important part of cratonic stabilization in the Archean. Understanding the nature and origin of these fluids and how they might have interacted with the lithospheric mantle is therefore a crucial part of models for both craton evolution and diamond genesis. Terrigenous crustal material (e.g., “continental sediment”) that has been “recycled” in some manner into the base of a developing cratonic root during continent formation could serve as an important source of such fluids. The high-density fluid’ micro-inclusions (HDFs) found in fibrous diamonds provide some constraints on the composition of these fluids, although they may not be directly relevant to metasomatism of the oldest SCLM (Shirey et al., 2013). Mineral inclusions in gem diamonds, presumably syngenetic with their hosts (Stachel and Harris, 2008), also provide clues to how these fluids may have interacted with the depleted peridotite residues of melting (Walter, 1999) that comprised the cratonic root or “keel” of the Archean lithospheric mantle. Where did these fluids originate, how did their influx affect the chemical composition and mineralogy of the SCLM, and what role did they play in diamond formation?

Experimental Approach

The idea that fluids derived from tectonically-recycled “continental” sediments are important to both diamond formation and metasomatism of the SCLM has been explored through a series of laboratory experiments in the multi-anvil apparatus at pressures of 5-7 GPa and ~900-1200°C. Multi-capsule experiments allow us to simultaneously (1) determine the geochemical characteristics of “pristine” fluids derived from water- and carbonate-bearing “terrigenous” metasediments, representing recycled crustal material in the SCLM, through phase equilibria experiments on natural sediment starting materials, and (2) observe how such fluids react with and chemically enrich surrounding peridotite, through fluid ‘infiltration-and-metasomatism’ experiments in which a crustal fluid source (“sediment”) is overlain by a layer of peridotite (“lithospheric mantle”). Fluids produced in the first type of experiment can be directly assessed as diamond-forming fluids, given that they form under P-T conditions appropriate to the diamond stability field (900-1200°C, 5-7 GPa), along a typical cratonic geotherm (32-37 mW/m²). And the compositions of metasomatic minerals produced by reaction between these same crustal fluids and mantle peridotite in the second type of experiment can be directly compared with those of the same phases occurring as presumably ‘syngenetic’ inclusions in diamonds. The terrigenous sediment component in the first type of experiments is represented by (1) a water-rich, carbonate-poor starting material (MAG-1 USGS marine mud), (2) a carbonate-rich, water-poor starting material from the western Alps (Saas-Fee metapelite, SFMP), and (3) a third starting material comprised of a 1:1 mechanical mixture of the first two. A peridotite from the Kamchatkan sub-arc mantle represents the depleted Archean SCLM in the second type of experiment.

Composition of sediment-derived fluids and comparison with HDF inclusions in diamonds

The amount of fluid produced in the phase-equilibria experiments ranges from ~10% to more than 50% by volume, depending upon the bulk composition and temperature. Fluids derived from water-

rich terrigenous sediments at 5-7 GPa are in equilibrium with a kyanite eclogite (gt+cpx+kyanite) phase assemblage that also contains phengite, (Fe-Ni) sulfide and coesite below ~1050°C; co-existing fluids contain between 20 and 40 wt% mixed H₂O-CO₂ component, possess high K₂O/Na₂O (>10), are high in normative quartz and orthoclase and are peralkaline (Na+K>Al). When compared with high-density fluids (HDFs) found in fibrous diamonds, the experimental fluids from the water-rich sediment source show a striking similarity, both in compositional range and major-element chemistry, to the hydrous silicic end-member calculated by Klein-Ben David et al (2009) for Yakutian diamonds, the calculated and measured compositions of HDF inclusions in fibrous diamonds from Congo (Navon et al, 1988; Schrauder and Navon, 1994), and to the fluid composition measured in diamond Z4 from Zaire (Navon et al, 1988) as one specific example that is particularly well correlated with the experimental results. The compositions of “pristine” sediment-derived fluids produced in our experiments are plotted in terms of molar (K+Na), (Si+Al) and (Ca+Fe+Mg) components on Figure 1, where they are compared with HDFs in fibrous diamonds from a number of localities worldwide.

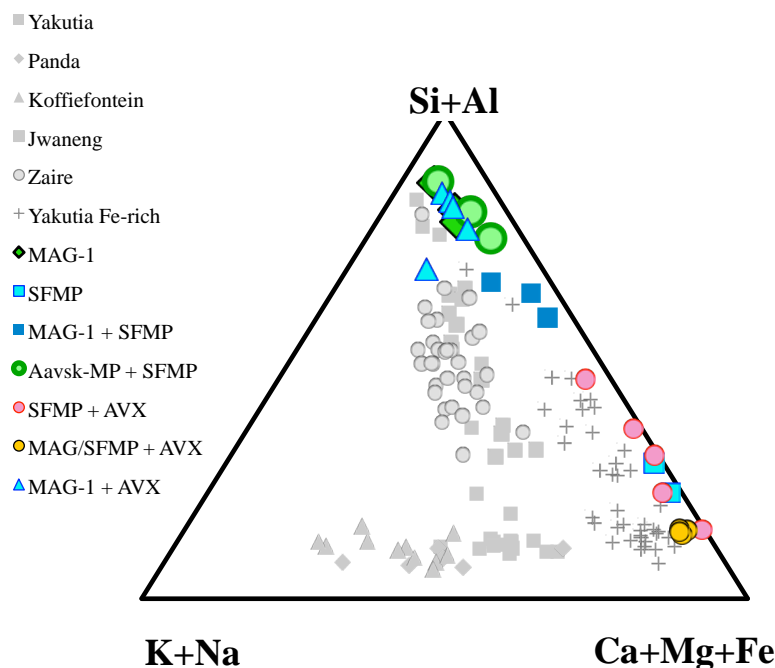


Figure 1. Ternary diagram of K+Na, Si+Al, and Ca+Mg+Fe showing the composition of “pristine”, sediment-derived fluids produced in experiments with: water-rich pelite (MAG-1), carbonate-rich pelite (SFMP), and 1:1 mixes of carbonate-rich and water-rich pelite (MAG-1+SFMP) and carbonate-rich and water-poor pelite (Aask-MP+ SFMP). Shown relative to compositions of high density fluid inclusions in diamonds from Yakutia (Klein-BenDavid et al., 2009), Panda (Tomlinson et al., 2006), Koffiefontein (Israeli et al., 2001, 2004), Jwaneng (Schrauder and Navon, 1994), Zaire (Navon et al., 1988; Kopylova et al., 2010), and Yakutia (Fe-rich compositions; Zedgenizov et al., 2009). Also shown for comparison are mantle-hybridized fluids formed by reaction between pristine, sediment-derived fluids and depleted peridotite AVX.

The effect of the initial reaction between the hydrous fluids derived from water-rich sediments and the overlying peridotite layer in the “infiltration-and-metasomatic reaction” experiments is to consume most of the fluid in metasomatic reactions of the form:



that increase modal orthopyroxene at the expense of (consumed) olivine, dramatically reducing the amount of SiO₂ in the fluid whilst also enriching the “residual” fluids in K₂O (up to 20 wt%) and Cl

(up to 14 wt%). This is manifested in the peridotite as a relatively narrow zone of modal metasomatism, characterized by an orthopyroxene-rich reaction front, beyond the sediment-peridotite interface, that also contains Na-amphibole and phlogopite at lower temperatures ($\leq 1000^{\circ}\text{C}$). Beyond this lies a region of more “cryptic” metasomatism, marked by isolated pockets of residual (saline?) fluids, highly enriched in K and Cl components concentrated from the original fluid. This implies that continued reaction between hydrous, SiO_2 -rich crustal fluids and peridotitic mantle will drive residual fluids from silicic towards increasingly more carbonatitic/saline compositions. Klein-BenDavid et al (2009) observed that decreasing Si (65 to 10 wt%) and Al (13 to 2 wt%) contents in HDFs in fibrous diamonds from Yakutia, Russia were correlated with an increase in K (10 to 22 wt%) and Cl (0.7 to 3 wt%), similar to the trends observed in our experiments.

The ubiquitous presence of Cr-rich, Ca-poor (G-10) garnets in depleted peridotite that has been infiltrated, reacted with, and metasomatized by hydrous, sediment-derived silicic fluids in the second-type of experiment is an important manifestation of the type of reactions that would take place between sediment-derived fluids and cratonic peridotite, and strongly suggests that such water- and silica-rich crustal fluids play a key role in both the chemical evolution of the SCLM, and the origin of diamonds.

References

- Izraeli, E.S., Harris, J.W. and O. Navon (2001) Brine inclusions in diamonds: a new upper mantle fluid. *Earth Planet. Sci. Lett.* 187, 323-443.
- Izraeli, E.S., Harris, J.W. and O. Navon (2004) Fluid and mineral inclusions in cloudy diamonds from Koffiefontein, South Africa. *Geochim. Cosmochim. Acta* 68, 2561–2575
- Klein-BenDavid, O. Izraeli, E.S., Hauri, E. and O. Navon (2007) Fluid inclusions in diamonds from the Diavik mine, Canada and the evolution of diamond-forming fluids. *Geochim. Cosmochim. Acta* 71, 723-744.
- Kopylova, M., Navon, O., Dubrovinsky, L., and G. Khachatryan (2010) Carbonatitic mineralogy of natural diamond-forming fluids. *Earth Planet. Sci. Lett.* 291, 126-137.
- Navon, O., Hutcheon, I.D., Rossman, G.R. and G.J. Wasserburg (1988) Mantle-derived fluids in diamond micro-inclusions. *Nature* 335, 784-789.
- Schrauder, M. and O. Navon (1994) Hydrous and carbonatitic mantle fluids in fibrous diamonds from Jwaneng, Botswana. *Geochim. Cosmochim. Acta* 58, 761-771.
- Shirey, S.B., Cartigny, P., Frost, D.J., Keshav, S., Nestola, F., Nimis, P., Pearson, D.G. and M.J. Walter (2013) Diamonds and the geology of mantle carbon. *Reviews in Mineralogy & Geochemistry* Vol. 75 pp. 355-421.
- Stachel, T. and J.W. Harris (2008) The origin of cratonic diamonds — Constraints from mineral inclusions. *Ore Geology Reviews* 34, 5-32.
- Tomlinson, E.L., Jones, A.P. and J.W. Harris (2006) Co-existing fluid and silicate inclusions in mantle diamond. *Earth Planet. Sci. Lett.* 250, 481-595.
- Walter, M. J. (1999), Melting residues of fertile peridotite and the origin of cratonic lithosphere, in *Mantle Petrology: Field Observations and High-Pressure Experimentation: A Tribute to Francis R. (Joe) Boyd*, edited by Y. Fei, C. M. Bertka, and B. O. Mysen, *Spec. Publ. Geochem. Soc.*, 6, 225–239.
- Zedgenizov, D.A., Ragozin, A.L., Shatsky, V.S., Araujo, D., Griffin, W.L., Kagi, H., 2009. Mg and Fe-rich carbonate-silicate high-density fluids in cuboid diamonds from the Internationalnaya kimberlite pipe (Yakutia). *Lithos* 112 (Supplement 2), 638–647.



Eclogites and garnet pyroxenites from Kimberley, W. Kaapvaal craton, South Africa: severe metasomatism of basaltic cumulates

Q. Shu^{1*}, G.P. Brey², D.G. Pearson¹

¹Dept. of Earth and Atmospheric Sciences, University of Alberta, Edmonton, Canada T6G 2E3.

²Institut für Geowissenschaften, Goethe-Universität, Frankfurt, Germany

*qshu1@ualberta.ca

Introduction

In contrast to the great abundance of peridotite xenoliths erupted by the Kimberley pipes, eclogites from this mantle section are very scarce, being only reported by Jacob et al. (2009). The reworking of the Boshof Road dump allowed the collection of 16 new eclogite and garnet pyroxenites with dimensions of 3-6 cm from the coarse concentrate of the diamond recovery plant established at the former DeBeers mine. Depending on composition, these xenoliths consist of orangey to brown garnets and pale to dark green clinopyroxenes. Half of them have 2-4% phlogopite and two are opx-bearing.

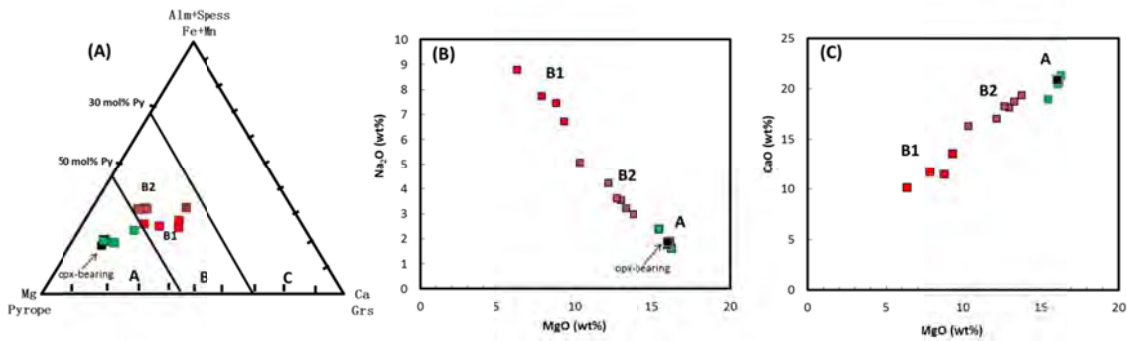


Fig.1 Major element compositions of garnets and clinopyroxenes. The square symbols with various colours present samples from this study divided into 3 groups: A, B1 and B2. (A) Trilateral garnet composition diagram after Coleman et al., 1965; (B) MgO (%) vs. Na₂O (%) variation of clinopyroxenes; (C) MgO (%) vs. CaO (%) variation in clinopyroxenes

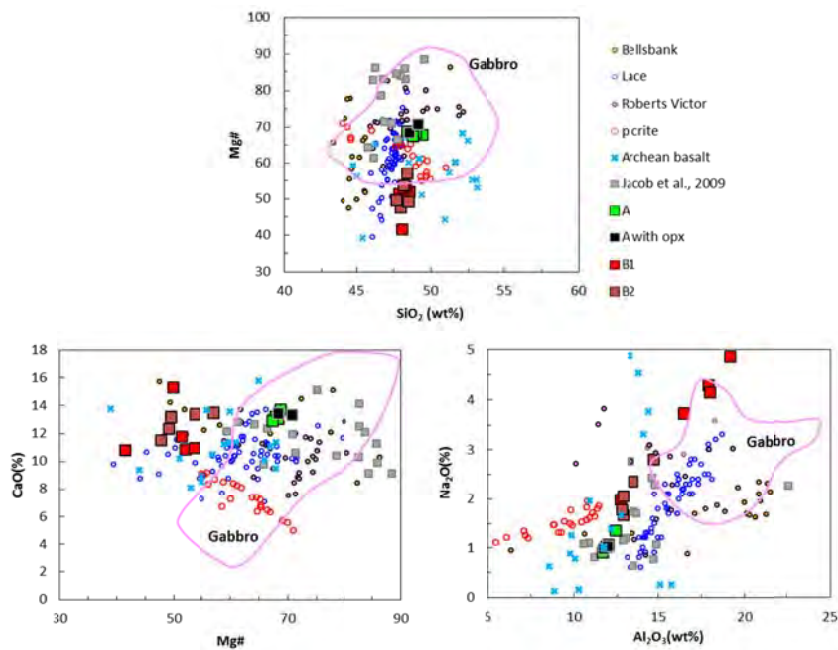


Fig.2 (A) Calculated major element bulk-rock compositions of eclogites from Kimberley mine (this study) and data from Jacob et al., 2009 for eclogites from Kimberley and other locations on the Kaapvaal craton shown in Mg# vs. SiO₂ (A), Mg# vs. CaO (B) and Al₂O₃ vs. Na₂O (C) diagrams. Also shown are fields for Archean basalts (Polat et al., 2003), Hawaiian picritic basalts (Norman and Garcia 1999) and modern gabbroic rocks (SE Indian Ridge, Hart et al., 1999; Bach et al., 2001).

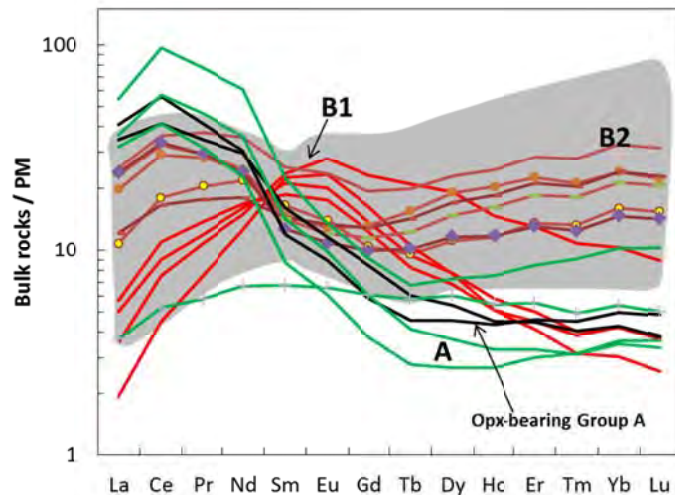


Fig.3 Spidergram for recalculated bulk rock compositions using mineral modal abundances of garnet: clinopyroxene = 45%:55% normalized to values for primitive mantle (McDonough, Sun 1995). The bulk-rock compositional range of Kimberley eclogites from a previous study are shown for comparison (grey area, Jacob et al., 2009).

F

Results and preliminary conclusion

Kimberley eclogite garnet compositions fall in the A and B fields of the classification scheme of Coleman et al. (1965; Fig.1). They are further divided into groups A, B1 and B2 according to the major and trace element characteristics of the garnets and their coexisting clinopyroxenes. The suite of xenoliths in this study shows considerably wider compositional range than the suite reported by Jacob et al. (2009). Group A xenoliths contain pyrope-rich garnet (mostly around Py₇₀Alm₁₀Gr₂₀) associated with jadeite-poor clinopyroxenes that qualifies them as garnet pyroxenites. Two have coexisting orthopyroxene. Their reconstructed bulk-rock major element compositions resemble modern-day gabbroic rocks (Fig.2). The HREE abundances of the calculated bulk rocks are 3 to 8 times that of the primitive mantle (PM) while the lighter REE steeply increase up to 100x PM for Ce (Fig.3). This group of Kimberley xenoliths may have an origin as high-pressure, high-temperature clinopyroxene cumulates in the lower oceanic crust (e.g. Barth et al., 2001; Schmickler et al., 2004) or within the shallow mantle (Bodinier and Godard, 2005). They were heavily metasomatized in incompatible elements after metamorphism. Group B2 xenoliths have garnets ranging from Py₄₈Alm₃₄Gr₁₈ to Py₅₇Alm₂₅Gr₁₈ and omphacites with 3-5 % Na₂O, 10-14% MgO and 10-14% CaO (Fig.1). Their reconstructed bulk-rock major element compositions are comparable to Archean basalts (Fig.2). The MREE and HREE mantle-normalised profiles of the calculated bulk rocks are positively sloped with abundances between 12 to 20 times PM, indicating some degree of partial melting in the garnet stability field while the strongly increased LREE indicate subsequent metasomatism. Group B1 xenoliths are more like eclogites *sensu stricto*. They possess more Ca-rich garnets ranging from Py₃₅Alm₃₄Gr₃₁ to Py₅₂Alm₂₈Gr₂₀ associated with jadeite-rich clinopyroxenes with low Mg#. The REE patterns of the calculated bulk rocks are unique for eclogites. They slope from a hump at ~ 10 to 20 x PM Eu down to 2x PM for La and 3x PM for Lu. They may have been plagioclase rich cumulates that were subsequently severely overprinted by metasomatism after subduction.

Temperatures of last equilibration before kimberlite eruption were determined with the Fe²⁺-Mg garnet-clinopyroxene exchange thermometer of Krogh et al. (1988) and extrapolated to a 40

mW/m² conductive geothermal gradient. Interestingly, the three petrologic groups of eclogites mainly fall into three distinctive pressure-temperature ranges, suggesting that they occupy spatially distinct depths in the lithospheric mantle: Group A samples yield temperatures between 930 and 970°C and pressures between 3.9 to 4.1 GPa, Group B2 samples range from 1038 to 1110°C and 4.6 to 5.1 GPa and group B1 eclogites have highest temperatures and pressures, from 1175 to 1236 °C and 5.6 to 6.2 GPa, sitting at the base of the Kimberley lithospheric mantle. This range in equilibration temperatures and depths indicates a distribution of these lithologies throughout the lithospheric mantle, in contrast to the suggestion by Huang et al., (2012).

In summary, a new expanded eclogite suite from Kimberley shows a much wider bulk and mineral chemical compositional range compared to the initial study of Kimberley eclogites performed by of Jacob et al (2009). Metasomatism is a dominant feature in the eclogites from Kimberley, in keeping with the highly metasomatized nature of the garnet peridotites from Kimberley (REFERENCES, e.g., Simon et al., 2003). Despite of various levels of overprinting, especially on the highly incompatible trace elements, major elements and less incompatible to compatible trace elements still reflect, to a large extent, the protoliths of these rocks. The wide range of depths of derivation indicates a distribution of mafic lithologies through the Kimberley lithospheric mantle column. The distinctive trace element compositions among different eclogite/pyroxenite groups at Kimberley allow us to investigate the metasomatic profile in the cratonic mantle and to reconstruct the metasomatic history via radiometric systems – work currently in progress.

References

- Bach W, Alt JC, Niu YL, Humphries SE, Erzinger JA, Dick HJB (2001) The geochemical consequences of late-stage low-grade alteration of lower ocean crust at the SW Indian Ridge: Results from ODP Hole 735B (Leg 176), *Geochimica Et Cosmochimica Acta* 65(19): 3267-3287.
- Barth M, Rudnick RL, Horn I, McDonough WF, Spicuzza M, Valley JW, Haggerty SE (2001) Geochemistry of xenolithic eclogites from West Africa, part I: a link between low MgO eclogites and Archean crust formation, *Geochimica Et Cosmochimica Acta* 65: 1499 – 1527.
- Bodinier, J-L Godard M (2005) Orogenic, ophiolitic, and abyssal peridotites. In: Carlson RW, Holland HD, Turekian KK (Eds.), *Treatise on Geochemistry. The Mantle and Core*, vol. 2. Elsevier, pp. 103–170.
- Coleman RG, Lee DE, Beatty LB, Brannock WW (1965) Eclogites and eclogites; their differences and similarities, *Geol Soc. Am. Bull* 76: 483-508.
- Hart SR, Blusztajn J, Dick H.J.B., Meyer P.S. and Muehlenbachs K, (1999) The fingerprint of seawater circulation in a 500-meter section of ocean crust gabbros, *Geochimica et Cosmochimica Acta* 63, 4059–4080.
- Huang JX, Gréau Y, Griffin W L, O'Reilly YS, Pearson JN, (2012) Multi-stage origin of Roberts Victor eclogites: Progressive metasomatism and its isotopic effects, *Lithos* 142-143: 161-181.
- Jacob DE, Viljoen KS, Grassineau NV (2009) Eclogite xenoliths from Kimberley, South Africa - a case study of mantle metasomatism in eclogites, *Lithos* 112(S): 1002–1013.
- Krogh EJ (1988) The garnet-clinopyroxene Fe-Mg geothermometer – A reinterpretation of existing experimental data, *Contrib. Mineral. Petrol.* 99: 44-48.
- McDonough WF, Sun SS (1995) The composition of the Earth, *Chem Geol* 120: 223-253.
- Norman MD, Garcia MO (1999) Primitive magmas and source characteristics of the Hawaiian plume: petrology and geochemistry of shield picrites, *Earth Planet.Sci. Lett*, 168: 27–44.
- Polat A, Hofmann AW (2003) Alteration and geochemical patterns in the 3.7–3.8 Ga Isua greenstone belt, West Greenland, *Precambrian Research* 126: 197–218.
- Schmickler B, Jacob DE, Foley SF (2004) Eclogite xenoliths from the Kuruman kimberlites, South Africa: geochemical fingerprinting of deep subduction and cumulate processes, *Lithos* 75(1–2): 173–207.



Diamond ages: what they mean and how they can be interpreted

Steven B. Shirey¹ and D. Graham Pearson²

¹Department of Terrestrial Magnetism, Carnegie Institution for Science, Washington DC 20015 USA

²Department of Earth and Atmospheric Sciences, University of Alberta, Edmonton AB T6G 2E3 Canada

Introduction

In the 32 years since the landmark paper reporting the first Paleoproterozoic Sm-Nd ages on garnet inclusions in lithospheric diamonds (Richardson et al., 1984), the understanding of diamond ages has evolved. The advent of single mineral inclusion dating of sulfide with Re-Os (Pearson et al., 1998) and now of garnet and clinopyroxene with Sm-Nd (Timmerman et al., 2016) has provided improved resolution on individual diamond-forming events and has led to the need for a new formalism to interpret mineral inclusion ages and diamond growth. The textural classification of inclusions as protogenetic, syngenetic, or epigenetic simply fails to provide an adequate framework to handle the typical geological variability. Advances in analytical sensitivity, spatial resolution, on the spectral and isotopic composition of diamond itself, and in the geological understanding of cratonic keel evolution now allow us to go beyond the simple textural classification to propose a practical formalism for diamond ages and their uncertainties.

Geochronological types of age determination

The radiogenic isotopic systems that have been used for diamond age determination have been reviewed by Pearson and Shirey (1999) and Shirey et al. (2013). Although the Ar-Ar method has been applied with some success, the chief methods have relied on the Sm-Nd decay scheme augmented by Rb-Sr and the Re-Os system. The most widely applied diamond age determination approach has been the *isochron or age array on multiple diamonds* from a single mine or alluvial locality. Although with this method there is the potential to combine unrelated diamonds on an isochron that might lead to spurious ages, with enough specimens, multiple generations of diamonds in a single locality can be resolved. The Re-Os system has always permitted single diamond work. The Sm-Nd system, which initially required the combination of groups of inclusions with similar optical properties and/or composition has now moved to the phase where single silicate inclusions can be analyzed (Timmerman et al., 2016).

Single diamonds can be dated in four basic ways: 1) model ages, 2) radiogenic Os ages (common-Os-free), 3) single diamond mineral isochrons, and 4) growth ages. *Model ages* are produced by the intersection of the evolution line for the inclusion with a reference reservoir such as the mantle. These ages can have large uncertainties (e.g. hundreds of myr) due to uncertainties in the reference reservoir and the lack of the systematic check available from other inclusions (as in the case of isochron ages). These ages are most useful when applied to peridotitic inclusions, although they have been used effectively for very high Re/Os eclogitic inclusions. For instance, occasionally sulfide inclusions have occurred with nothing but radiogenic Os derived from the decay of Re. These are rare, *common-Os-free sulfides* that yield a highly accurate absolute age in some ways equivalent to a model age (Richardson et al. 2001). The most accurate single diamond age is determined on a diamonds with multiple inclusions. In this case an *internal isochron* can be obtained that not only establishes equilibrium among the multiple grains but unequivocally dates the time of diamond growth (e.g., Pearson et al., 1998; Westerlund et al., 2006, Smit et al., 2016, Gress et al., 2017). With extreme luck in obtaining the right diamond, *growth ages* can be obtained from inclusions in concentric diamond growth zones visible in UV fluorescence or cathodoluminescence whose ages decrease outward. These single grains can be extracted to give a minimum growth time for the diamond. Time scales for diamond growth can range from geologically instantaneous (Westerlund et al., 2006) to billions of years (Pearson, 1999; Wiggers deVries et al., 2013). In optimal situations, multiple inclusions are present within single growth zones, in single diamonds, allowing internal isochrons to be constructed for individual growth zones in single diamonds (e.g., Gress et al., 2017).

Geological or mineralogical uncertainties to diamond geochronology

Due to excessively low trace element concentrations (McNeill et al., 2009), diamond itself can not be dated directly. A gem diamond retains little of the fluid from which it has crystallized -therefore compositional information related to its encapsulated inclusion is lacking. All mineral inclusions in diamonds are miniscule compared to normal mantle xenoliths yielding a small sample that is poorly

representative of mantle mineralogy. Nestola et al (2014) found that the majority of olivines included in diamonds have no systematic crystallographic relationship with their host. Furthermore, textures alone usually do not permit discrimination between an origin from either the recrystallization of a pre-existing mineral in the presence of a fluid (syngenetic) or simple growth around a pre-existing mineral, with likely extensive dissolution of that mineral to reduce the grain size to that of the inclusion (protogenetic). Thus a primary source of geological/mineralogical uncertainty on diamond ages is any process affecting protogenetic mineral inclusions before encapsulation in the diamond, especially if it occurred substantially before diamond formation.

Good examples of inclusion history prior to incorporation exist in the literature. Mineral inclusions such as sulfides situated in *metasomatic veins* (Liu et al., 2009) are texturally clearly younger than the host rock and document pathways for younger diamond forming fluids. Silicate inclusions such as garnets may display *complex trace element patterns* indicative of multiple-stage processes of melting and enrichment (Stachel and Harris, 2008). Minerals such as harzburgitic garnet can display *low Nd and high Sr isotopic compositions* that are antithetical to the typical trace element depletion associated with extreme melting of the subcontinental lithospheric mantle (Richardson, 1984). Multiple sulfide inclusions in one diamond can display different and *mass independent sulfur isotopic compositions* indicative of unequilibrated solid/liquid phase incorporation (Thomassot et al. 2009), in agreement with the finding of large differences in age between different diamond growth zones (Wiggers de Vries, 2013). Sulfide inclusions can *lose Re to fluid or melt* at the time of diamond formation leading to strongly unsupported radiogenic Os (Smit et al., 2016). *Regional patterns of mineral paragenesis* related to large-scale lithospheric structure and crustal magmatism can be established well before diamond growth (Shirey et al., 2002). The new formalism for documenting a diamond age is designed to account for these uncertainties.

Systematic and analytical uncertainties associated with diamond geochronology

In practical application, the isotopic systems discussed above also carry with them inherent systematic uncertainties. The Re-Os system has a *low blocking temperature* (~400°C; Brenan et al. 2000) and its resistance to resetting in the lithospheric mantle depends chiefly on extreme partitioning of Os into sulfide and metal hosts. Discrete sulfides and mono-sulfide solid solutions will exsolve pentlandite and chalcopyrite upon eruption to the surface and *exsolution will fractionate parent (Re) from daughter (Os)*. This necessitates complete grain recovery from the diamond; partial analysis will induce error. Single grain analysis for both silicate (Sm-Nd) and sulfide (Re-Os) can only produce meaningful results if the *sample-to-blank ratios* are high enough and may set a practical limit to the minimum size of grain that can be processed. As all diamonds are xenocrysts in their kimberlite hosts, most isochrons or age arrays, whether composed of inclusion composites from multiple diamonds or single inclusions from one diamond, have *potentially unrelated diamonds on the isochron*. This and the large range in initial Os isotope ratios within the cratonic mantle, prior to diamond formation emphasizes the desirability of analyzing diamonds from single diamond growth zones (as above) or from diamonds that can be shown to have likely formed from the same fluid (e.g., Wiggers de Vries et al., 2013; Smit et al., 2016; Gress et al, this volume).

Practical formalism for diamond ages

Isotopic equilibrium is the essential condition required for the generation of a statistically robust isochron. Thus, isochron ages from multiple diamonds will record a valid and accurate age when the diamond-forming fluid promotes a large degree of isotopic equilibrium across grain scales, even for pre-existing (protogenetic) minerals. This clearly can and does occur. Furthermore, it can be analytically tested for, and has multiple analogues in the field of dating metamorphic rocks. In cases where an age is suspect, due to any combination of the uncertainties discussed above, an age will be valid if its regression uncertainties can encompass a known and plausible geological event (especially one for which an association exists between that event and the source of diamond-forming fluids) and petrogenetic links can be established between inclusions on the isochron. Numerous examples exist (Jwaneng, Orapa, Kimberley Pool, Ellendale), from individual mines/localities where the age arrays can be associated with a known geological event determined by independent study of crustal magmatism or plate tectonic/geodynamic reconstruction, such as subduction or continental collision. On the larger scale of a terrane or craton, the pattern of age distribution, provinciality, or paragenetic variation relative to large-scale differences in the composition of the lithospheric mantle serves to establish age veracity. These features allow diamond ages to be interpreted using realistic diamond

growth models that relate to actual geologic events, in the same way that we are able to date metamorphic events in earth's crust.

References

- Brenan, J., Cherniak, D., & Rose, L. A. (2000). Diffusion of osmium in pyrrhotite and pyrite: implications for closure of the Re-Os isotopic system. *Earth Planet. Sci. Lett.*, 180, 399–413.
- Gress MU, Pearson DG, Timmerman S, Chinn IL, Koornneef JM, & Davies GR (this volume) Three phases of diamond growth spanning >2.0 Ga beneath Letlhakane established by Re-Os and Sm-Nd systematics of individual eclogitic sulphide, garnet and clinopyroxene inclusions. 11th International Kimberlite Conference Extended Abstract No. 11IKC-4508
- McNeill JCR, Pearson, DG, Klein-BenDavid, O, G.M. Nowell, C.J. Ottley & I. Chinn (2009). Quantitative trace element analysis of gem quality diamonds. *J. Physics: Condensed Matter*. 21, 364207, 13 pp.
- Nestola, F., Nimis, P., Agel, R., Milani, S, Bruno, M, Pricipe, M & Harris, JW (2014) Olivine with diamond-imposed morphology included in diamonds. Syngensis or protogenesis? *International Geology Review*, 56, 1658-1667.
- Pearson DG, Shirey SB, Harris JW, & Carlson RW (1998) Sulphide inclusions in diamonds from the Koffiefontein kimberlite, S Africa: constraints on diamond ages and mantle Re-Os systematics. *Earth Planet Sci Lett*, 160, 311–326.
- Pearson DG, & Shirey SB (1999) Isotopic dating of diamonds. In, Application of radiogenic isotopes to ore deposit research and exploration. *Economic Geology Special Volume 12*, 143–171.
- Richardson SH, Gurney J, Erlank AJ, & Harris JW (1984) Origin of diamonds in old enriched mantle. *Nature*, 310, 198–202.
- Richardson SH, Shirey SB, Harris JW, & Carlson RW (2001). Archean subduction recorded by Re-Os isotopes in eclogitic sulfide inclusions in Kimberley diamonds. *Earth Planet. Sci. Lett.*, 191, 257–266.
- Liu Y, Taylor LA, Sarbadhikari AB, Valley JW, Ushikubo T, Spicuzza MJ, et al. (2009) Metasomatic origin of diamonds in the world's largest diamondiferous eclogite, *Lithos* 112, 1014–1024.
- Shirey SB, Cartigny P, Frost DJ, Keshav S, Nestola F, Nimis P, Pearson DG, Sobolev NV, Walter MJ (2013) Diamonds and the Geology of Mantle Carbon. *Reviews in Mineralogy and Geochemistry*, 75, 355–421.
- Shirey SB, Harris JW, Richardson SH, Fouch MJ, James DE, Cartigny P, Dienes P, Viljoen F (2002) Diamond Genesis, Seismic Structure, and Evolution of the Kaapvaal-Zimbabwe Craton. *Science*, 297, 1683–1686.
- Smit KV, Shirey SB, & Wang W (2016) Type Ib diamond formation and preservation in the West African lithospheric mantle: Re-Os age constraints from sulphide inclusions in Zimmi diamonds. *Precamb. Res.*, 286, 152–166.
- Stachel T & Harris JW (2008) The origin of cratonic diamonds—constraints from mineral inclusions. *Ore Geol. Rev.*, 34, 5–32.
- Thomassot, E., Cartigny, P., Harris, J. W., Lorand, J.-P., Rollion-Bard, C., & Chaussidon, M. (2009). Metasomatic diamond growth: A multi-isotope study (C-13, N-15, S-33, S-34) of sulphide inclusions and their host diamonds from Jwaneng (Botswana). *Earth and Planetary Science Letters* 282, 79–90.
- Timmerman S, Koornneef JM, Chinn IL, & Davies GR (2017) Dated eclogitic diamond growth zones reveal variable recycling of crustal carbon through time. *Earth and Planetary Science Letters*, 463, 178–188.
- Westerlund K, Shirey SB, Richardson SH, Carlson RW, Gurney JG, & Harris, JW (2006) A subduction origin for Early Archean peridotitic diamonds and harzburgites from the Panda kimberlite, Slave craton: Implications from Re-Os isotope systematics. *Contrib. Min. Pet.*, 152, 275–294.
- Wiggers de Vries DF, Pearson DG, Bulanova GP, Smelov AP, Pavlushin AD, & Davies GR (2013) Re-Os dating of sulphide inclusions zonally distributed in single Yakutian diamonds: Evidence for multiple episodes of Proterozoic formation and protracted timescales of diamond growth. *Geochim. Cosmochim Acta*, 120, 363–394.



Geology and resource development of the Kelvin kimberlite pipe, NWT, Canada

**Martina Bezzola¹, Casey Hetman², Gareth Garlick³, Robert Creaser⁴,
Chris Hrkac¹, Gary Vivian¹, Mike Diering², Tom Nowicki³**

¹*Aurora Geosciences Ltd, Yellowknife, Canada, martina.bezzola@aurorageosciences.com*

²*SRK Consulting, Vancouver, Canada, chetman@srk.com*

³*Mineral Services Canada Inc., Vancouver, Canada*

⁴*University of Alberta, Edmonton, Canada*

Introduction

The Kelvin kimberlite pipe is located in the southeast of the Archean Slave Craton in northern Canada, 8 km northeast of the recently opened Gahcho Kué diamond mine. Kelvin was initially discovered in 2000 by De Beers Canada, through glacial till sampling and subsequent drill testing of a horizontal-loop electromagnetic (HLEM) anomaly situated under a shallow lake. Further exploration by Kennady Diamonds Inc. (KDI) resulted in the discovery of significant thicknesses of volcanoclastic kimberlite that had not previously been identified. Exploration and evaluation work carried out by KDI during the period 2012 to 2016 has progressed the project rapidly to the point at which a well-constrained geological model has been developed. In combination with comprehensive microdiamond and commercial-sized diamond sampling this has supported the declaration of a maiden Indicated Mineral Resource of 13.62 million carats at Kelvin.

Methods

The geology and evaluation of the Kelvin kimberlite pipe are based on data generated from extensive delineation core and large diameter reverse circulation (RC) bulk sample drilling programs carried out between 2012 and 2016. The data collected includes logging observation of core from 71 NQ and 104 HQ diameter holes. Detailed logging of over 11,500 metres of kimberlite has been carried out and further verified by petrographic analysis of 730 representative thin sections and polished slabs. Drill cores have been subjected to comprehensive spatially-distributed sampling for bulk density (3,652 samples) and microdiamonds (2,524 samples comprising almost 20 tonnes). A total of 79 RC bulk sample holes provide representative sample coverage of the entire strike length of the body. Bulk sampling has yielded 2,198 ct of diamond (+0.85 mm) from 1,067 tonnes of kimberlite. Surface bedrock mapping, age dating, mantle-derived indicator mineral abundance and composition studies and 3-D modeling have also been completed.

Geology

Hosted in metaturbidites of the Yellowknife Supergroup, the Kelvin kimberlite pipe is an atypical, steep-sided inclined L-shaped pipe with a surface expression of only 0.08 ha. The pipe dips at approximately 15° towards the northwest before turning north and dipping at 20°. The Kelvin pipe is the largest of four pipes in an extensive pipe-sheet complex striking 4.5 km within the Kelvin-Faraday cluster that includes several inclined volcanoclastic pipes along a gently dipping hypabyssal kimberlite sheet system. The pipes represent a spectrum of volcanic maturity with Kelvin being the most well developed pipe. The Kelvin pipe has been defined to a current overall strike length of 700 m with vertical thickness varying 70 to 200 m and width from 30 to 70 m. The pipe infill comprises several units of sub-horizontally layered kimberlite resulting from multiple emplacement events. Infill is dominated by volcanoclastic kimberlite with less common coherent kimberlite and minor units with textures transitional between these end-members. The main volcanoclastic infill within Kelvin, KIMB3, is a massive, fine to medium plus coarse-grained olivine-rich to very olivine-poor, volcanoclastic phlogopite kimberlite. The country rock dilution is dominated by locally

derived gneissic and granitic xenoliths and has been is classified as a ‘Kimberley-type’ pyroclastic kimberlite (KPK) (Smith et al. 2013), historically referred to as a tuffisitic kimberlite breccia (TKB). KIMB3 has been sub-divided based on the abundance of locally derived country rock dilution into KIMB3A, KIMB3B and KIMB3C due to the horizontally consistent layered zones of the dilution and the distinct vertical gradational changes observed within this phase of kimberlite. The second most common infill, KIMB2, is a massive, fine to coarse-grained olivine macrocryst-rich, phlogopite kimberlite that is texturally variable between hypabyssal and volcanoclastic. KIMB2 has been sub-divided into KIMB2A and KIMB2B, where KIMB2A is a massive, fine to coarse-grained olivine macrocryst-rich, xenolith-poor to -rich, transitional phlogopite kimberlite. KIMB2B is a massive, fine to coarse olivine macrocryst-rich, xenolith-poor, hypabyssal phlogopite kimberlite. Several other minor kimberlites (KIMB1, KIMB4, KIMB5, KIMB6 and KIMB7) have been identified and make up less than 20% of the overall pipe infill and will not be described here. In addition to the kimberlite infill, marginal breccias with trace amounts of kimberlite are present above the south limb of the pipe as well as the transition into the north limb.

The emplacement history of Kelvin is believed to have been initiated by the intrusion of HK phases as part of an early kimberlite sheet system. This was followed by the main pipe forming volcanoclastic event, during which the main KPK pipe infill, KIMB3, was emplaced. The pipe was formed along structural weaknesses into the host rock above thickened zones of the pre-existing sheet. The emplacement sequence concluded with a late stage emplacement of hypabyssal and transitional phases along the upper contact of the pipe, cross-cutting the main KPK infill at depth. Dating of phlogopite using Rb-Sr methods have established ages of 531 ± 8 Ma and 546 ± 8 Ma.

Evaluation in Support of Resource Classification

A 3-D geological model of Kelvin was developed from detailed drill core logging and petrography data. The geological model provides constraints on the volume of kimberlite present, and in combination with a spatial (block) model of bulk density, provides estimates of the tonnes of kimberlite present. Microdiamond and commercial-size diamond results from corresponding kimberlite material in each domain were used to define the total content diamond size frequency distribution (SFD) in each domain. In conjunction with appropriate recovery correction factors these SFD models establish a ratio between microdiamond stone frequency (+212 micron stones per kilogram) and commercially recoverable grade (+1 mm carats per tonne). Average diamond values per domain (in US Dollars per carat) are based on a value distribution model (representing the value of diamonds per carat in each sieve size class) combined with the recoverable SFD models for each domain. A maiden Indicated Mineral Resource for the Kelvin kimberlite has been established at 8.5 million tonnes of kimberlite at an average grade of 1.6 carats per tonne with an average value of US\$63 per carat. The Kelvin kimberlite remains open at depth.

Conclusion

The textures, diamond grade, and emplacement age of Kelvin are very similar to those documented at the Gahcho Kué mine immediately to the south (Hetman et al. 2004). The geology of the Kelvin kimberlite is texturally and mineralogically like other KPK systems globally, however, the external pipe morphology and specifically the sub-horizontal inclination of the pipe are unique. The morphology displayed by Kelvin and the other kimberlites discovered within the Kelvin-Faraday cluster have defined a new type of exploration target; and one that is likely not unique to this project. Due to the extremely small surface expression of Kelvin (0.08ha), this pipe as well as others within the cluster are almost blind and therefore traditional exploration methods applied by previous operators on the project were unsuccessful in determining the full extent of the pipe. Our understanding of the emplacement, and deep geology of the Kelvin pipe is still developing and further drilling and sampling are required as Kelvin is open at depth.

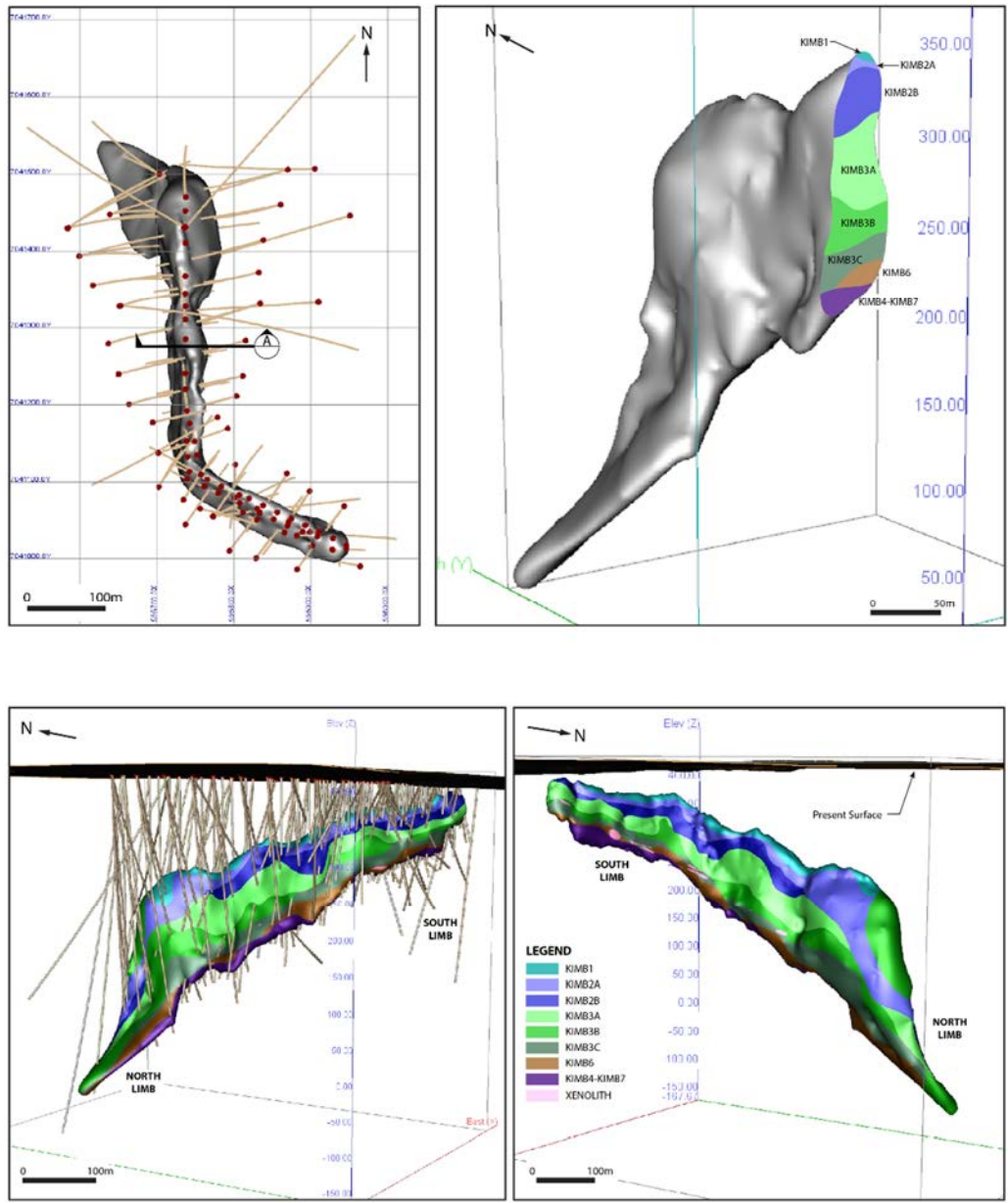


Figure 1. Top Left: Plan view of the Kelvin kimberlite pipe projected to surface with diamond drill holes. Top Right: Cross section view through the north limb pipe showing the horizontal layering of the different kimberlite infills found within the pipe. Bottom Left: Side view of the Kelvin kimberlite pipe looking northeast with all exploration and delineation diamond drill holes. Bottom Right: View of the Kelvin kimberlite pipe looking southwest.

References

Smith, B. S., Nowicki, T. E., Russell, J. K., Webb, K. J., Mitchell, R. H., Hetman, C. M., Harder, M., Skinner, E. M. W. & Robey, J. A. (2013). Kimberlite terminology and classification. In Proceedings of 10th International Kimberlite Conference (pp. 1-17). Springer India.

Hetman, C. M., Smith, B. S., Paul, J. L., & Winter, F. (2004). Geology of the Gahcho Kue kimberlite pipes, NWT, Canada: root to diatreme magmatic transition zones. *Lithos*, 76(1), 51-74.



Old unradiogenic Os in deep mantle metallic liquid from large gem IIA diamonds

Evan M. Smith¹, Stephen H. Richardson², Steven B. Shirey³ and Wuyi Wang¹

¹Gemological Institute of America, New York City, NY, USA

²Department of Geological Sciences, University of Cape Town, Rondebosch 7700, South Africa

³Department of Terrestrial Magnetism, Carnegie Institution for Science, Washington, DC USA

Introduction

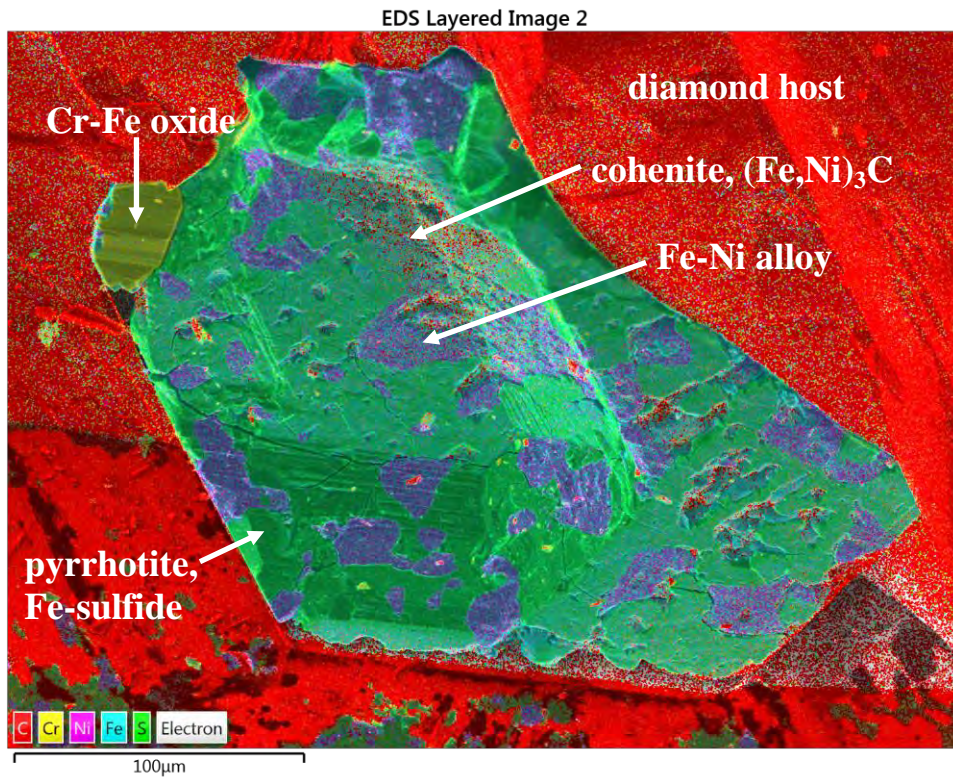
Many of the world's largest and most valuable diamonds such as the *Cullinan*, *Lesotho Promise*, *Constellation* and *Koh-i-Noor* share an unusual set of physical characteristics, suggesting they form by a common mechanism. The most noted characteristic is their nitrogen-deficient character, classifying them as Type IIA. The paragenesis of such diamonds is enigmatic in that they have not been connected to the processes forming more common Type I diamonds or other varieties of Type II diamonds. Research on their geological origin has been scant as these Cullinan-like Type II diamonds are especially valuable as gemstones and rarely contain inclusions.

Inclusion phases

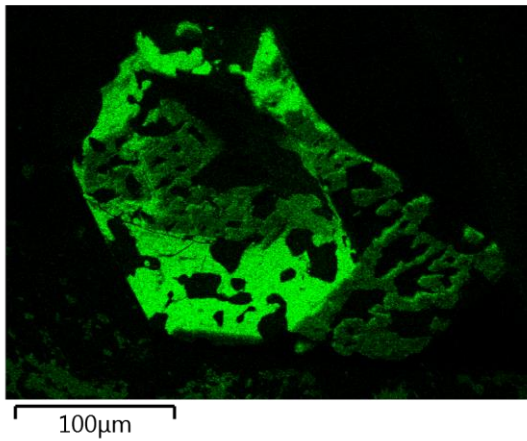
Recent findings have demonstrated a recurring set of inclusions in large, high-quality Type IIA diamonds, distinct from those of more familiar lithospheric/sublithospheric diamonds (Smith et al., 2016). The most abundant inclusion is a metallic, Fe-Ni-C-S multi-phase (cohenite + Fe-Ni alloy + pyrrhotite) assemblage with a surrounding fluid jacket of H₂ and CH₄. The second most abundant inclusion is former CaSiO₃ perovskite, now retrogressed to lower-pressure minerals but also associated with metal, H₂, and CH₄. Trapping CaSiO₃ perovskite inclusions constrains the minimum depth of formation to ~360 km. Two additional Cullinan-like Type IIA diamonds were found to have inclusions of low-Cr majoritic garnet, also indicative of a sublithospheric origin. Overall, the inclusions suggest that these diamonds originate in reduced regions of the mantle where they crystallize from Fe-Ni-C-S metallic liquids. Such regions have long been thought to exist based on experiment and theory but have never before been sampled. An estimated metal content on the order of 1 wt% can be calculated assuming equilibrium with pyrolytic rocks, on the basis of the average composition of the Fe-Ni-C-S inclusions and partitioning of Ni and Fe between olivine (or wadsleyite/ringwoodite) and metallic liquid.

Osmium Isotope Analysis

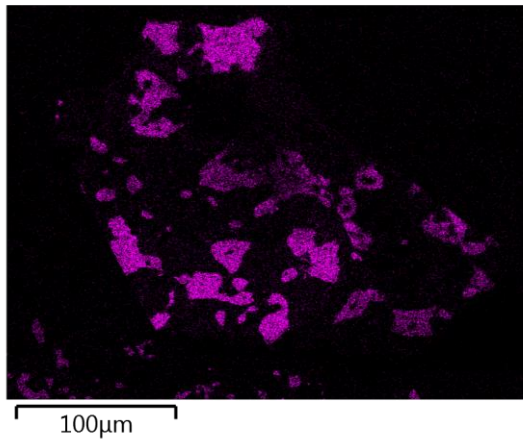
In order to assess the age of the metallic inclusions, their host diamonds, and further constrain the petrogenesis of the metallic phases, an Os isotopic study was initiated on one diamond from Letseng, Lesotho, containing two favorable inclusions. The metallic inclusions were accessed by cleaving polished diamond plates. The multi-phase assemblage of each partly-exposed inclusion was then characterized by qualitative EDS analysis (Figure 1). To facilitate handling of these 50–100 micron magnetic grains, Os was distilled while the metallic grains were still attached to the cleaved surface. Re and Os concentrations are not reported because dissolution by chromic-sulfuric preferentially attacks the pyrrhotite and its dissolution efficacy on Fe-Ni metal, cohenite and other accessory phases such as Cr-Fe-oxide is not known. Furthermore, exsolution of the homogeneous Fe-Ni-C-S liquid on exhumation will fractionate Re from Os. Aside from minor corrections for differential ingrowth of radiogenic Os since kimberlite emplacement at 90 Ma, neither of these factors will affect the Os isotopic compositions of the digested pyrrhotite. The pyrrhotite gives surprisingly low ¹⁸⁷Os/¹⁸⁸Os values of 0.1115±2 and 0.1109±2 relative to Earth's present day convecting mantle (~0.124 to 0.132), which yields Neoproterozoic rhenium depletion model ages (T_{RD}) of about 2.5 Ga.



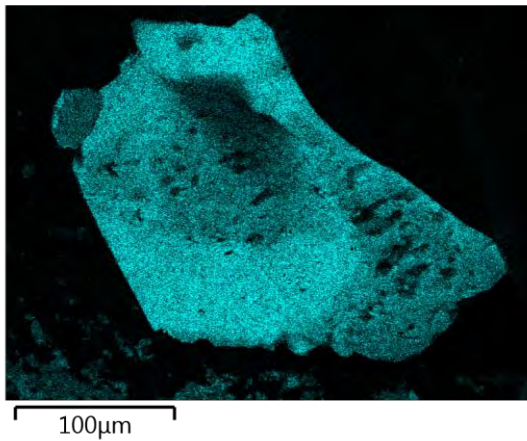
S Kα1



Ni Kα1



Fe Kα1



Cr Kα1

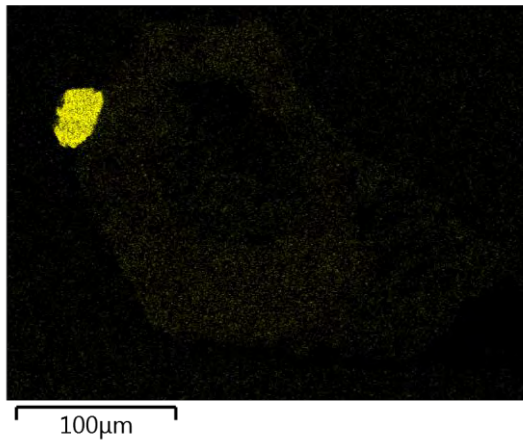


Figure 1: False color SEM X-ray element map of an exposed multi-phase Fe-Ni-C-S inclusion.

Implications

While silicate inclusions found in these diamonds point to an eclogitic host rock (Smith et al., 2016), it appears unlikely that the metallic liquid formed originally from basaltic oceanic crust. Any basalt has a high Re/Os, making it unable to sustain such a low $^{187}\text{Os}/^{188}\text{Os}$ ratio. Furthermore, the metallic inclusions have Ni/(Ni+Fe) ratios (Smith et al., 2016) more in line with peridotitic rocks (Zhang Z et al., unpublished). The old age and implicitly low time-averaged Re/Os indicated by the low $^{187}\text{Os}/^{188}\text{Os}$ suggests that metallic liquid initially forms in peridotite, perhaps recycled together with eclogite to the mantle transition zone by Archean plate tectonics. In this scenario, migration of the metallic liquid from the peridotitic precursor to the eclogitic host could lead to further carbon (and sulfur) scavenging, supersaturation and ultimately Cullinan-like Type IIa diamond crystallization.

The metallic liquid trapped in this Letseng diamond carries a signature that is at least 2.5 Ga old meaning that either the diamond grew at that time or it grew at a later time and incorporated an old metallic liquid. In either case, the evidence that such metallic liquids exist and that they can be old has implications for the processes by which ancient heterogeneities related to the presence of metallic liquid, such as in ^{182}W , can be preserved since soon after the formation of Earth (e.g. Mundl et al., 2017). Such metals would be expected to have an extremely high partition coefficient for W, which could preserve an ancient W signature against later re-equilibration.

References

- Smith EM, Shirey SB, Nestola F, Bullock ES, Wang J, Richardson SH, Wang W (2016) Large gem diamonds from metallic liquid in Earth's deep mantle. *Science* 354: 1403-1405.
- Mundl A, Touboul M, Jackson MG, Day JMD, Kurz MD, Lekic V, Helz RT, Walker RJ (2017) Tungsten-182 heterogeneity in modern ocean island basalts. *Science* 356: 66–69.
- Zhang Z, Davis FA and Hirschmann MM (unpublished) A role for peridotite in the origin of CLIPPIR diamonds?

Karowe Diamond Mine: A World-class source of large exceptional diamonds

John P. Armstrong

Lucara Diamond, Vancouver, CA, John.Armstrong@lucaradiamonds.com

Introduction

The Karowe Mine (AK6 kimberlite), owned and operated by Lucara Diamond, located in the Republic of Botswana, achieved commercial diamond production in July 2012 (Figure 1). Between July 2012 and December 2016 over 1.8 million carats have been mined and sold generating in excess of US\$1 billion dollars in revenue. The AK06 kimberlite within the Orapa Kimberlite field is a roughly north-south elongate kimberlite body with a near surface expression of ~3.3 hectares and a maximum area of approximately 7 hectares at approximately 120 m below surface. The body comprises three geologically distinct, coalescing lobes that taper with depth. These are referred to as the North Lobe, Centre Lobe, and South Lobe.

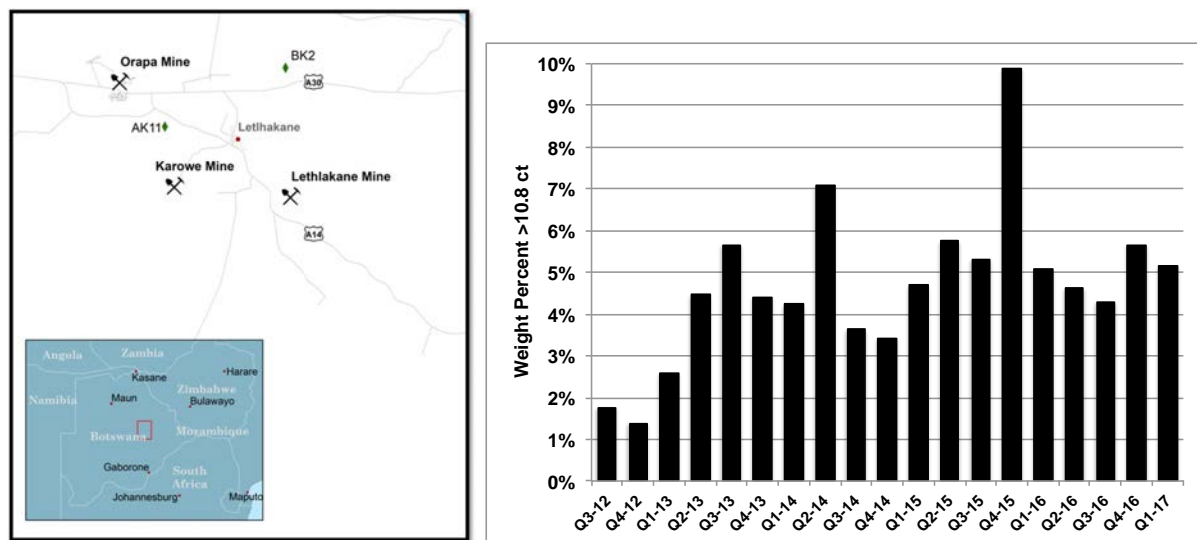


Figure 1 (left). Location of Karowe Mine, AK06 kimberlite, Orapa District Botswana

Figure 2 (right). Weight percent of +10.8 carat diamonds on quarterly carat production Karowe Mine Q3 2012 to end of March 2017.

Kimberlite Geology

The AK6 kimberlite is an opaque-mineral-rich monticellite kimberlite, texturally classified primarily as fragmental volcanoclastic kimberlite with lesser macrocrystic hypabyssal facies kimberlite of the Group 1 variety. The nature of the kimberlite differs between each lobe with distinctions apparent in the textural characteristics. The South Lobe is considered to be distinctly different from the North and Centre Lobes. The North and Centre Lobes exhibit internal textural complexity whereas the bulk of the South Lobe is more massive and internally homogeneous. The South lobe forms the majority of the resource and displays the coarsest diamond size distribution of the three lobes. The proportion of +10.8 carat diamonds increases from approximately 1.8 weight percent in the North Lobe to in excess of 4 weight percent within the South Lobe. Early mining focused on the higher grade North Lobe (Q3 2012 to Q1 2013, Figure 2), as production shifted into the Centre and South Lobes the size distribution became coarser in nature.

The AK6 kimberlite has established a continuing production of large, high value diamonds (Figures 2 and 3). In March 2013 a 239 carat gem quality diamond was recovered which marked the first in a continuing population of large high value Type IIa diamonds recovered from the Centre Lobe and more importantly the South Lobe of the AK6 kimberlite. Recognition of a coarse diamond size

distribution supported through size distribution analysis, breakage studies, and optimization of processing circuits has maintained and enhanced the recovery of large diamonds. Large diamonds >50 carats in size are spatially distributed horizontally and vertically within the South Lobe. Continuity of large diamond recovery is shown for yearly +10.8 carat diamond production normalized to annual total carat production (Figure 3a) and as total volume of +10.8 carat diamonds produced (Figure 3b).

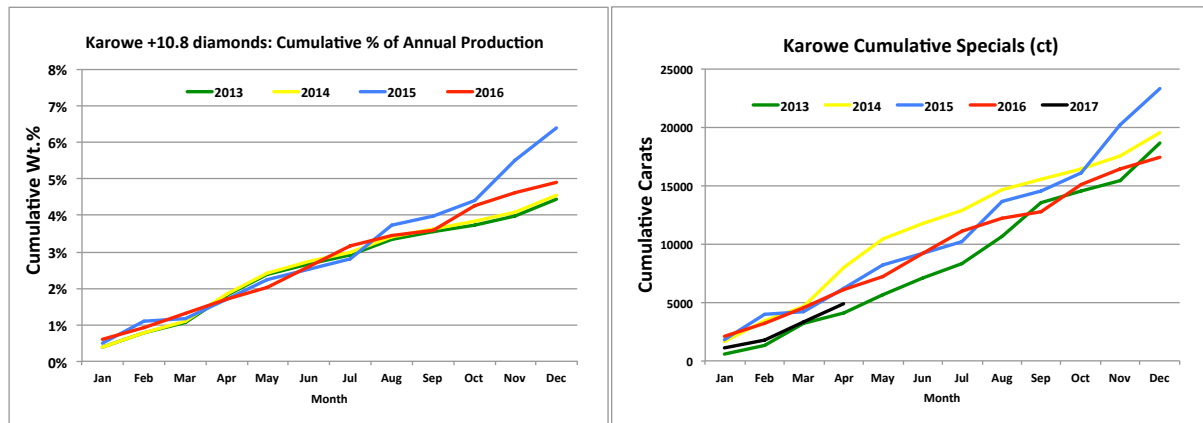


Figure 3a/b. Cumulative +10.8 carat production on a monthly basis normalized to total annual production. Overlap in yearly trends demonstrates stability in large stone recovery. Anomalous uptick noted in November 2015 related to the recovery of above average +10.8 carat production including the 1109 Lesedi La Rona and the 813 carat Constellation. Figure 3b, cumulative +10.8 carat diamond annual production by month for life of mine to end of Q1 2017.

Process plant optimization, including incorporation of sensor-based bulk sorting (X-Ray Transmission), was undertaken to allow treatment of harder, high yielding kimberlite at depth within the South Lobe, and allow the recovery of large diamonds from primary ROM feed pre-concentration. In late 2015 the Karowe Mine recovered an 813 carat stone and the World's second largest gem quality diamond in over 100 years weighing 1,109 carats. Diamonds greater than 10.8ct in weight represent approximately 4.8% by weight of all diamond production over the life of mine to date. Life of Mine average stone size for the +10.8ct production is 28.9 ct/stone.

Log-Log probability plots (carats) of the +10.8 carat recovered diamond population, comprised of in excess of 90,000 carats and over 3200 individual diamonds display evidence for diamond damage/loss in the +100 diamond sizes (Figure 4). Reconstruction of large broken diamonds results in a coarser size distribution model, however, there is still evidence that the diamond population is impacted by the non-recovery of large +100 carat diamonds. This non-recovery of large diamonds may be the result of breakage and/or the host kimberlite has not been processed. Assessment of the size frequency distribution suggests the AK6 kimberlite will continue to produce large and exceptional diamonds.

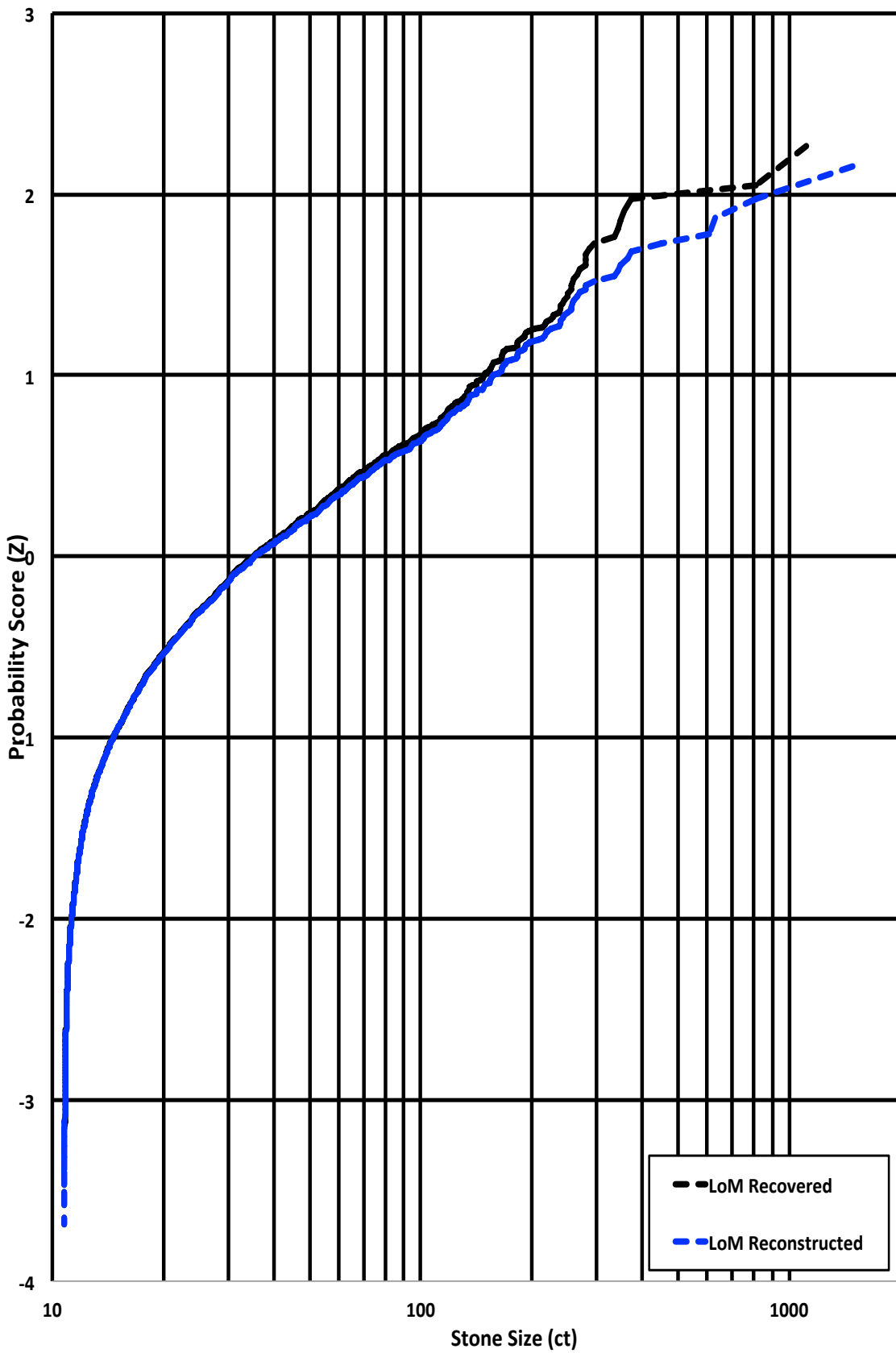


Figure 4. Log-Log Probability diagram for AK6 Life of Mine +10.8 carat diamonds on an as recovered and reconstructed basis.



Lamprophyres, F-Sn-rhyolites and -explosive breccia pipes and their relationship to Sn-polymetallic mineralization in the Muehleithen-Gottesberg district (Germany) - indications for late-Variscan mantle-derived rare metal-enriched fluid pulses

Thomas Seifert¹

¹ TU Bergakademie Freiberg, Freiberg, Germany, thomas.seifert@mineral.tu-freiberg.de

Introduction

An important part of the rare metal resources (Sn, W, Mo, In, Sc, Li) in the Saxo-Thuringian Zone is related to the Permo-Carboniferous Sn-W-Li-F-polymetallic association in the Erzgebirge-Slavkovský les-Vogtland metallogenic province (Bolduan 1972; Baumann et al. 2000). There are still about 1 million metric tons Sn metal related to Sn-polymetallic mineralization in greisen-, stringer zone- and skarn-type ore bodies @ 0.15 - 1 wt.% Sn with significant quantities of W, Mo, Bi, In, and Li as byproduct. One of the most important Sn ore fields in the Variscides is the Muehleithen-Gottesberg old mining district (Sn, U, W, Ba, Ag) which is located at the western contact of the Eibenstock-Nejdek granite massif in the SE part of the Vogtland region. Characteristic are subvolcanic, postgranitic pipe- and dike-shaped felsic intrusions, explosive breccia pipes and lamprophyre dikes which are hosted by the Eibenstock granite and contact metamorphic schists (Kaemmel 1961; Baumann and Gorny 1964; Gottesmann and Kruse 1981; Wasternack et al. 1995; Seifert 2008).

Subeconomic resources of about 47 million metric tons greisen ore of the Gottesberg deposit with an average grade of 0.26 wt.% Sn, 0.015 wt.% Bi, and 0.015 wt.% WO₃ are concentrated in pipe-shaped greisen bodies (with impregnative cassiterite mineralization) with a maximum known size of about 150 m in diameter and about 900 m at depth (Sippel et al. 1983; Gottesmann and Kruse 1991). The cassiterite-bearing greisen orebodies of the Muehleithen Sn(-W) deposit were mined from c. 1500 to 1964. The greisen bodies are located in the main intrusive phase of the Eibenstock granite and are structurally controlled by the granite / phyllite (hornfels) contact (Donath 1964; Kaemmel 1961).

Geology and geochemistry of post-collisional lamprophyric and rhyolitic/microgranitic intrusions with post-Eibenstock granite age

The post-collisional evolution shows an increase of mantle influence which is indicated by NW-SE, ENE-WSW and N-S striking lamprophyric dikes which crosscut the Eibenstock granite and the Ordovician schists. Two distinct episodes of lamprophyric intrusions have been documented: a pre- and post-granitic type in relation to the main intrusion stage of the Eibenstock granite. The pre-granitic lamprophyres (LD1) show exclusively a kersantitic composition, whereas the post-granitic lamprophyres (LD2) are predominantly mica-minettes to mica-kersantites (Ačejev and Harlass 1968; Kramer 1974; Seifert 2008). The studied ENE-WSW striking lamprophyre dike (type LD2) is located in the +835 m level (Tannenberg adit) of the Muehleithen Sn mine at the endocontact zone of the Eibenstock granite and crosscut the porphyric medium-grained monzogranite of the main stage. Significant contents of mantle-compatible elements (275 ppm Cr, 145 ppm V, 20 ppm Sc) and a mg# of 67 measured from dike LDT1a verify a mantle-related magmatism corresponding with worldwide data from Rock (1991) and data from the Mid-European Variscides (Seifert 2008). The relatively low contents of Ni (39 ppm) and Co (17 ppm) are caused by the replacement of phlogopites and olivines by greisen fluids. Chromium-spinel is stable, explaining that the high Cr-content (Fig. 1) is consistent with the Cr-contents of the 'primary magmas' field from Rock (1991). High contents of incompatible LILE and HFSE and $\epsilon\text{Ndi} = -0.2$ indicate mantle metasomatic processes similar to those found in earlier studies of different lamprophyre intrusions in the Saxo-Thuringian (Kramer 1988; Seifert 2008) and a world-wide database from Rock (1991).

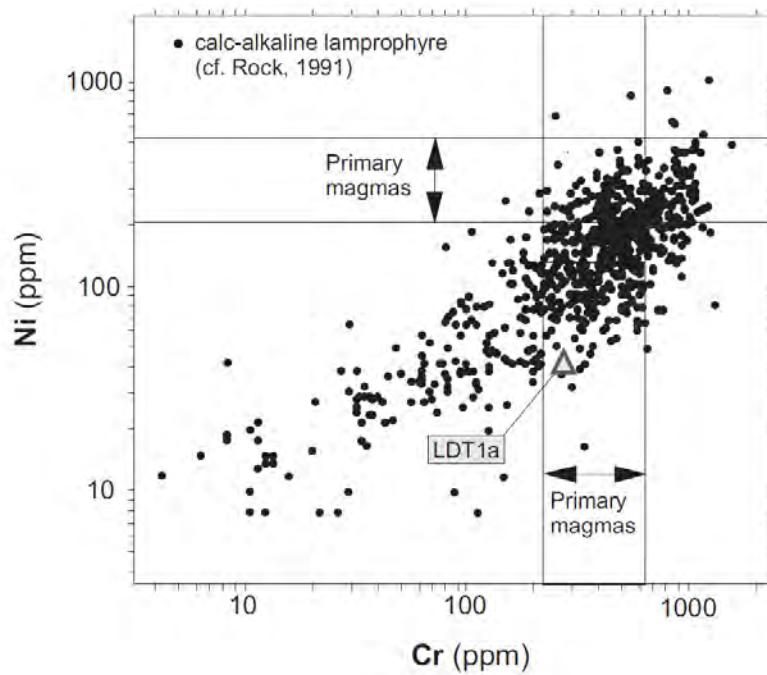


Figure 1: Cr-Ni ratios of lamprophyre dike LDT1a (highlighted by triangle) in comparison to primary Ni and Cr contents of calc-alkaline lamprophyres worldwide compiled by Rock (1991)

Two groups of felsic (sub)volcanic rocks are described in Wasternack et al. (1995): porphyritic rhyolites and serialporphyritic microgranites. Accessories are apatite, fluorite, topaz, zircon, and sulfides. These (sub)volcanic felsic rocks increase in size and abundance with depth. Their shapes change from dike- to tube- and stock-like intrusions at depth. A representative microgranitic dike from the Sn deposit Gottesberg (sample GRGOT, drill hole TAH 4/77, 1171.5 m - 1174 m depth) was analyzed. Accessory minerals are xenotime-(Y), monazite-(Ce), zircon, thorite, and columbite (Fig. 2). Non-primary albite micro-phenocrysts represent post-microgranitic albitization processes with pre-greisen age. Sample GRGOT shows very high Nb (40 ppm), Th (60 ppm), Y (70 ppm), Zr (150 ppm), F (1050 ppm), and LREE (175 ppm) contents and $\epsilon_{\text{Ndi}} = -2.1$. Younger sericite in the microgranite (GRGOT) indicates greisenization.

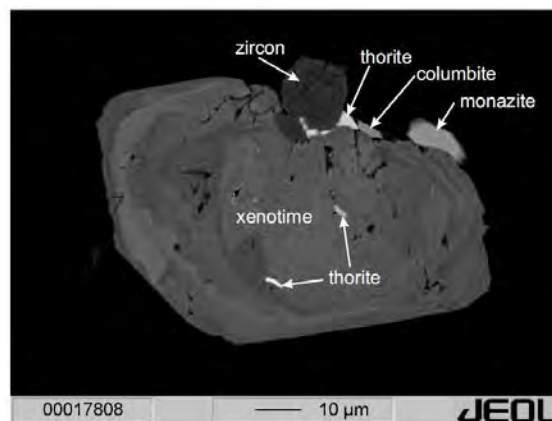


Figure 2: Backscattered electron image of xenotime (Y,U,Th)(Gd-Lu)[PO₄] intergrowth with zircon, monazite, thorite, and columbite grains in microgranitic dike sample GRGOT. drill hole TAH 4/77, 1171.5 m - 1174 m

Late-Variscan magmatic stages and related Sn-polymetallic mineralization of the Muehleithen-Gottesberg Sn-W-U-Ag-Ba district

The important Sn-ore deposition in the Muehleithen-Gottesberg district is spatially and temporal related to an intrusion center of the lamprophyric and rhyolitic (sub)volcanic magmatism which is

controlled by the intersection of NW-SE, N-S, and NE-SW to ENE-WSW deep-rooted regional fault zones. Based on about 17,000 m of drilling (e.g., bore hole Tah 4/77 with a depth of 1,200 m), and intensive fieldwork, exploration geologists proposed that the pipe-like greisen bodies are controlled by older explosive breccia pipes (Donath 1964; Gottesmann and Kruse 1981; Wasternack et al. 1995). The impregnative cassiterite mineralization (meta-monzogranite Sn-greisen) extended to a depth of 900 m and show a significant positive correlation to the F contents (cassiterite-rich topaz and quartz-topaz greisen).

The Sn-polymetallic mineralization of the Muehlleithen-Gottesberg district is spatial and possibly temporal associated with LD2 (Pb-Pb zircon age: 316 ± 2.7 Ma) and subvolcanic pipe- and dike-shaped felsic intrusions (Pb-Pb zircon age: 312 ± 4.6 Ma) and explosive breccia pipes hosted by 318 – 320 Ma age monzogranites of the Eibenstock massiv (cf. Seifert 2008) and by contact metamorphic schists. The extreme F-enrichment of fluids during the emplacement of explosive breccia pipes is represented by intensive topazization (e.g., schist-quartz-topaz breccia pipe “Schneckenstein mountain”). The lamprophyre dikes show extreme high F (20,450 ppm), Rb (1,100 ppm), Cs (100 ppm), Li (230 ppm), and Sn contents (1,350 ppm), and high W (25 ppm) and In contents (5 ppm) as well as cassiterite-arsenopyrite-sphalerite-quartz-topaz mineralization which clearly show the influence of Sn-polymetallic mineralization and consequently the pre-Sn-polymetallic age of LD2.

The emplacement of lamprophyric melts at the base of the lower crust in the Erzgebirge-Vogtland area and Sub-Erzgebirge basin is probably associated with asthenospheric doming. F-Sn-enriched rhyolitic melts and Sn-polymetallic mineralization were probably produced by small amounts of partial melting of the lower crust and mantle-fluids, resulting from underplating of fluid-enriched proto-lamprophyric melts. Genetic relationships to a mantle plume are in discussion (Seifert 2014).

References

- Ačejev BN and Harlass E (1968) Zum Problem der Altersstellung von Lamprophyren im westlichen Erzgebirge. *Geologie* 17: 1178-1194
- Baumann L and Gorny S (1964) Neue tektonische und petrographische Untersuchungsergebnisse in der Zinnerzlagertstätte Tannenberg-Muehlleithen: Freiburger Forschungshefte C 181
- Baumann L, Kuschka E, Seifert T (2000) Lagerstätten des Erzgebirges. Enke im Georg Thieme Verlag, Stuttgart, New York
- Bolduan H (1972) Die Zinnmineralisationen im Erzgebirge - Typen und Verteilung. *Geologie* 21: 677-692.
- Donath E (1964) Das Zinnbergbaugebiet von Gottesberg und Muehlleithen i. V.: Freiburger Forschungshefte C 181, pp 119-133
- Gottesmann B and Kruse B (1981) Bericht über die petrographisch-geochemischen Untersuchungen an der Forschungsbohrung Tah 4/77 (Lagerstätte Gottesberg, Vogtland). Unpublished report, Zentrales Geologisches Institut Berlin
- Kaemmel T (1961) Geologie, Petrographie und Geochemie der Zinnerzlagertstätte “Tannenberg” (Vogtl.). *Geologie, Beihefte* 10: 1-105
- Kramer W (1988) Geochemisch-petrologische Untersuchung basaltoider variszischer Gesteinsformationen sowie mafischer und ultramafischer Xenolithe im nordöstlichen Zentraleuropa. *Schriftenreihe Geologische Wissenschaften* 26, Akademie-Verlag Berlin
- Rock NMS (1991) Lamprophyres. Blackie, Van Nostrand Reinhold, Glasgow, New York
- Seifert T (2008) Metallogeny and Petrogenesis of Lamprophyres in the Mid-European Variscides. IOS Press BV, Amsterdam
- Seifert T (2014) Late-Variscan rare metal ore deposition and plume-related magmatism in the eastern European Variscides (D, CZ). *Geophysical Research Abstracts* 16, EGU2014-11974.
- Sippel H, Märten S, Schiemenz F et al. (1983) Ergebnisbericht Zinn Gottesberg. Unpublished report, VEB Geologische Forschung und Erkundung Freiberg
- Wasternack J, Märten S, Gottesmann B (1995) Field and petrographic study of brecciation and greisenization phenomena in the Gottesberg tin deposit (Saxony, Germany). *Zeitschrift für geologische Wissenschaften* 23: 619-642

Sound velocity of carbonate melts under high pressure and temperature conditions and the origin of mid-lithosphere discontinuity

Kenji Mibe¹ and Yoshio Kono²

¹Earthquake Research Institute, University of Tokyo, Tokyo, Japan, mibe@eri.u-tokyo.ac.jp

²HPCAT, Geophysical Laboratory, Carnegie Institution of Washington, Argonne, Illinois, USA, ykono@ciw.edu

Introduction

CO₂-rich magmas, such as kimberlites and carbonatites, have been reported from all of the Earth's continents including Antarctica. Because both kimberlites and carbonatites are considered to be originated from upper mantle, it is, therefore, reasonable to assume that CO₂-rich magmas are ubiquitously distributed somewhere in the upper mantle beneath the continental crusts. In order to understand the origin and distribution of CO₂-rich magmas in the upper mantle beneath the continents, we have measured the compressional wave velocity (V_p) of carbonate melts under high pressure and temperature conditions.

Experimental method

High pressure and temperature experiments were carried out using a Paris-Edinburgh cell at Beamline 16 BM-B, HPCAT of the Advanced Photon Source, USA. A Si₃N₄ buffer rod was used for transmitting elastic waves between WC anvil and sample. A LiNbO₃ transducer, which generates and receives V_p , was attached to the top WC anvil. Because melt phase only 25 MHz electrical sine waves were used to determine V_p . The details on ultrasonic measurement setup are described in Kono et al. (2012). The starting materials were prepared by mixing reagent grade carbonate powders in appropriate ratios. The compositions of starting materials thus prepared are Na₂Mg(CO₃)₂, Na₂Ca(CO₃)₂, K₂Mg(CO₃)₂, and K₂Ca(CO₃)₂. The measurements were done up to about 2.2 GPa and 1200°C.

Experimental results

The compressible wave velocity in carbonate melts decrease with increasing temperature. The slopes, dV_p/dT , at high pressures obtained in the present study are almost the same as those obtained by the previous study at 1 atmosphere. The V_p in carbonate melts increases with increasing pressure (Fig. 1).

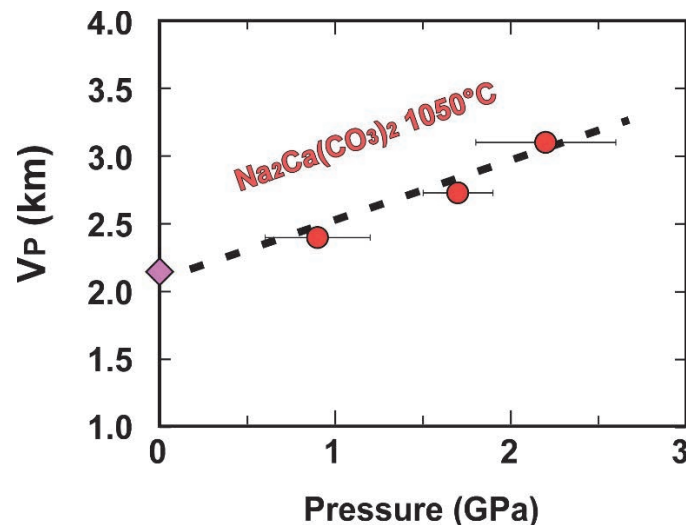


Figure 1: The compressible wave velocity (V_p) in carbonate melt as a function of pressure.

The V_p in carbonate melt, $\text{Na}_2\text{Ca}(\text{CO}_3)_2$, is faster than pure H_2O and slower than basaltic melt within the pressure and temperature conditions investigated. The V_p in carbonate melts decrease with increasing mean atomic weight.

Origin of the mid-lithosphere discontinuity in the continents

It has been reported that seismic body wave velocity drops by 2 to 6% at the mid-lithospheric depths of about 60 to 150 km in almost of all the continents (Karato et al., 2015). However, the origin of this reduction in seismic wave velocity has not been understood yet. According to our experimental results, those drops in seismic wave velocity can be explained by the presence of about 1 to 3 vol% of alkaline carbonate melts in peridotites. The presence of alkaline carbonate melts are often reported as the melt inclusions trapped in mineral grains in mantle xenoliths from sub-continental lithospheric mantle (Giuliani et al., 2012), which is considered to be the direct and natural evidence of the presence of alkaline carbonate melts at the mid-lithospheric depths in continental mantles.

References

- Giuliani A, Kamenetsky V.S., Phillips D, Kendrick M.A., Wyatt B.A, Goemann K (2012) Nature of alkali-carbonate fluids in the sub-continental lithospheric mantle. *Geology*, 40(11):967–970
- Karato S (2015) Mechanisms and geologic significance of the mid-lithosphere discontinuity in the continents. *Nature geoscience* 8:509-514
- Kono Y, Park C, Sakamaki T, Kenny-Benson C, Shen G, Wang Y (2012) Simultaneous structure and elastic wave velocity measurement of SiO_2 glass at high pressures and high temperatures in a Paris-Edinburgh cell. *Rev. Sci. Instrum.* 83:033905

New surprises at old discoveries: Exploration and Sampling of the AK11 Kimberlite, Orapa Kimberlite Field, Botswana

George Q.J. Pybus, Kabelo Tiyedze, John Armstrong

Lucara Diamonds Pty Ltd., GPybus@BotetiMining.co.bw

The AK11 kimberlite was first discovered in 1970 within what is now known as the Orapa Kimberlite Field. Historical work consisted of a single pit excavation with no records of drilling having been identified.

The AK11 geophysical anomaly is comprised of a circular intense magnetic high (~200nT above the local background; >0.008 SI units in the 3d inversion model) with an approximate surface area of 2.5Ha.

The kimberlite was interpreted as hypabyssal (magmatic) kimberlite and given poor diamond results the pipe was subjected to no further exploration.

In 2014 Lucara Diamond acquired a prospecting license over AK11 and proceeded with a program of ground geophysics and core drilling.

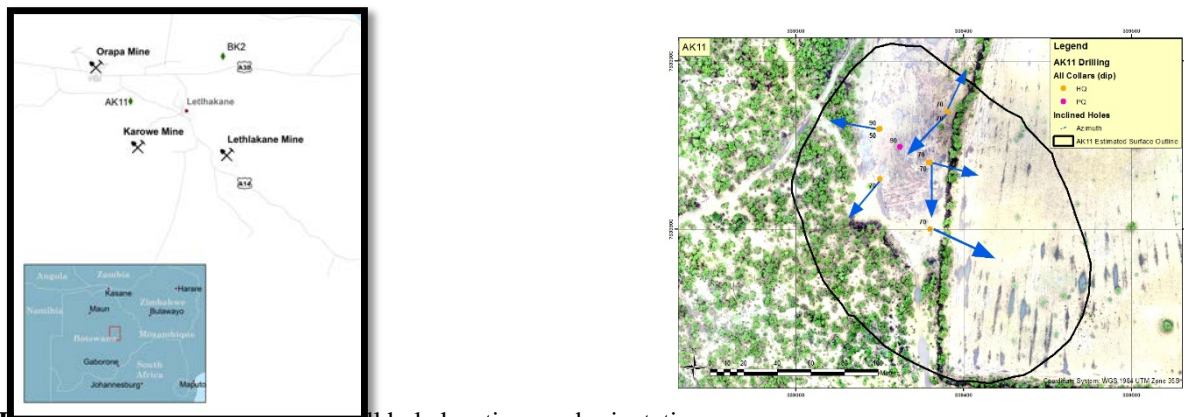


Figure 1. General location and drill hole locations and orientations.

Ground geophysical surveys confirmed the historical work with a circular intense magnetic high feature of approximately 2.5 ha in diameter (**Figure 2**) and a small gravity low, offset slightly to the south east but still within the magnetic anomaly's area. Local geology is comprised of basalts (80 to 100metres thick) overlying sandstones preliminarily identified to be of the Ntane formation.

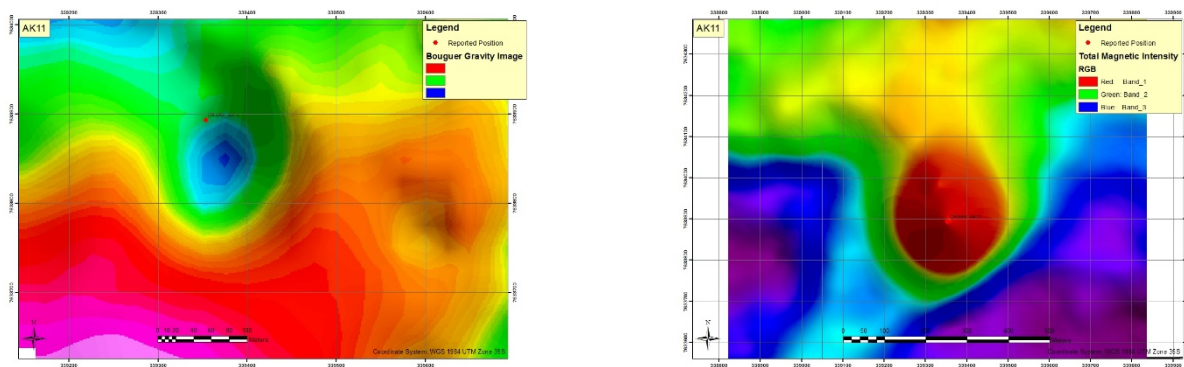
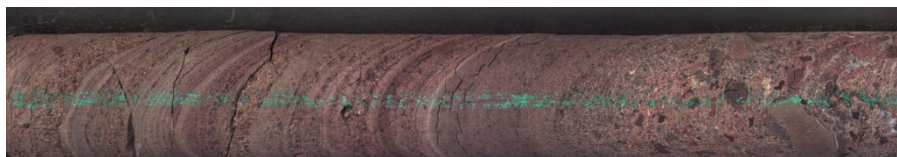


Figure 2: Geophysical data, left: ground gravity at a grid spacing of 50m; right: magnetic data at a line spacing of 20m.

Core drilling of the AK11 kimberlite comprised 9 drill-holes, 2 vertical and 7 inclined at either 50° or 70° (**Figure 1**). All but one of the holes were HQ diameter and all inclined holes were oriented (where recoveries were suitable).

Core drilling of the AK11 anomaly revealed an unexpectedly complex crater infill sequence, some examples are shown in **Figure 3** to **Figure 8**. A sequence of RVK, VK, and debris / collapse features



are observed in the upper 85 meters of the pipe.

Figure 3: AK11_DD007, 71.04m to 71.42m



Figure 4: AK11_DD007, 66.15m to 66.49m.

Graded beds, cross-bedding and variable bed thickness are observed.

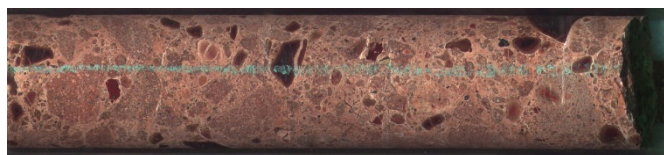


Figure 5: AK11_DD007_57.18m to 57.54m

Variable oxidation states are observed with anoxic and oxidised units observed.



Figure 6: AK11_DD007, 29.04m to 29.91m

This sequence is cut by a more magmatic to pyroclastic sequence with magmaclast development, that is present across at least 60m horizontally through the kimberlite, but shallowing to the south east.



Figure 7: AK11_DD001, 88.55m to 88.75m near pipe center; AK11_DD005, 67.65m to 68.04m in the south east of the pipe.

Both these sequences appear to overlie or are intruded by a competent pyroclastic to magmatic unit that extends from 90metres below present day surface to >200 meters of depth (extent of drilling).



Figure 8: AK11_DD001; Depth 156.1m to 156.57m

The upper units have raised magnetic susceptibility, similar in value to the surrounding basalt, however the deeper unit has significantly higher magnetic susceptibility values associated with it, and is the likely primary cause of the magnetic anomaly (**Figure 9**).

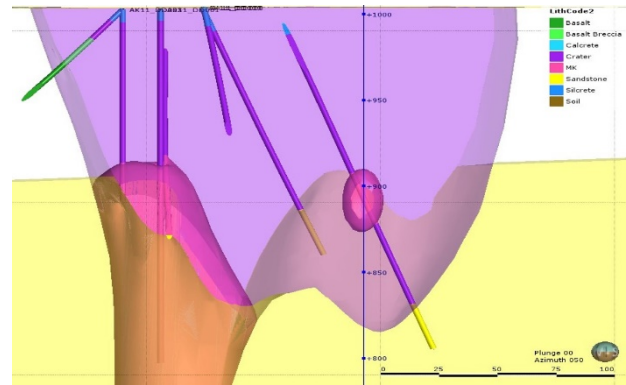
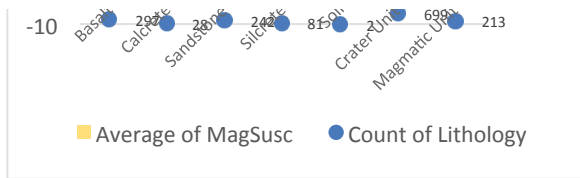
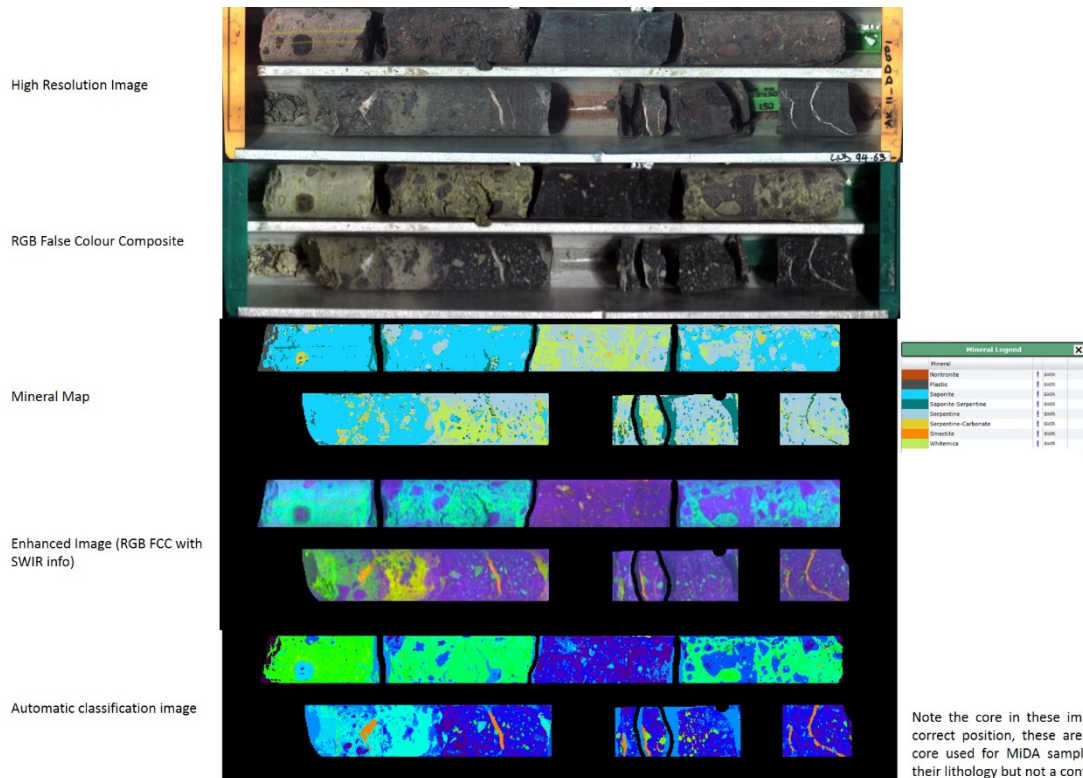


Figure 9: Magnetic susceptibility values per lithology; Right: Section looking NE showing 3d model of pipe based on simplified logs.

Results from microdiamond analysis are still pending.

Hyperspectral imaging of 1482.4 metres of core that was undertaken in Dec 2016 produced spectra including minerals expected in kimberlite, being carbonate, serpentine and saponite. Crustal rocks, (xenoliths and host) are characterised by chlorite and aluminium rich mineral phases (mica group, kaolinites). The textures of different types of kimberlite, including magmaclasts are illustrated in the following pictures. Some magmaclasts have very similar responses in their spectra to the magmatic kimberlite and potentially derive from that unit.

New modern diamond processing, analytical methods and drilling information have enhanced the understanding of the diamond content and intrusive history of the AK11 kimberlite.



Note the core in these images is not in the correct position, these are the exemplars of core used for MIDA sampling and represent their lithology but not a continuous sequence

Figure 10: Examples of data/images available from the core imaging.

References

Mxinwa, T., Apr 2017, Boteti Mine – Karowe 2016 Spectral Processing and Interpretation and Data Product Summary. Consultant Report. Internal Company Document Terracore TCR17173.

Exploration and Sampling of the BK02 Kimberlite, Orapa Kimberlite Field, Botswana

George Q.J. Pybus, Kabelo Tiyedze, John Armstrong

Lucara Diamonds Pty Ltd, GPybus@BotetiMining.co.bw

The BK02 kimberlite was first discovered in the late 1960's. Preliminary work consisted of pit excavation and limited drilling. Subsequent work was conducted in the early to mid-2000's with limited ground geophysics, trenching and drilling. Lucara Diamond acquired a prospecting license in 2014 and proceeded with a program of ground geophysics, surface trenching mini-bulk sampling and core drilling. Previous operator's results indicated the kimberlite was diamondiferous, published results were interpreted by Lucara to suggest the presence of geological similarities to the AK6 kimberlite (Karowe Mine).

The BK02 kimberlite has a surface area of approximately 2.4ha expressed by a high contrast strong magnetic dipole. BK02 is capped by a calcrete layer and since historical works appear to have included significant disturbance of that, there is a slight topographic high marking the central area of the kimberlite. This may be related to the disturbance, rather than a natural feature of the occurrence.

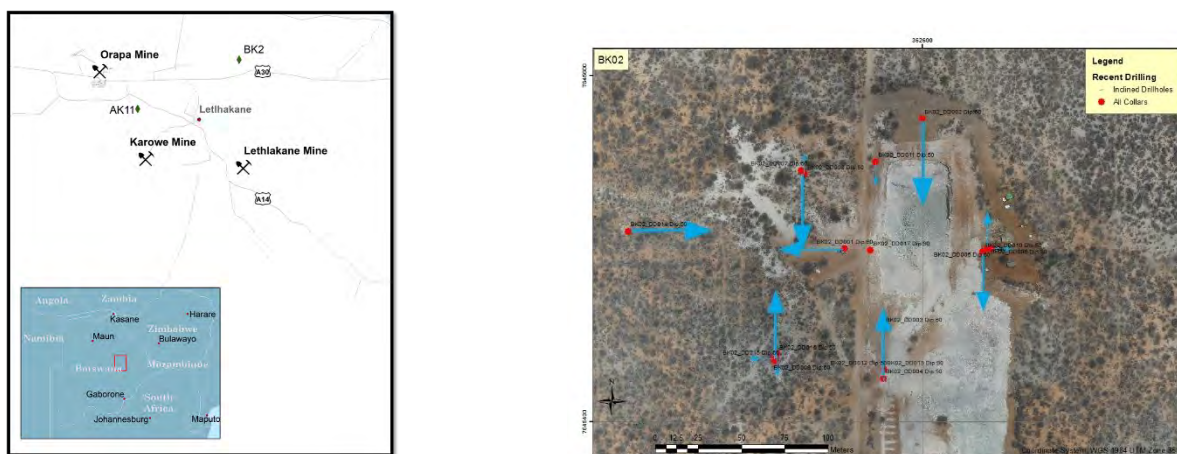


Figure 1: General Location of BK02 and location of drill-holes completed in 2016-2017.

BK02 is described as a magmatic kimberlite intruded into basalts, which are up to 30 meters thick in current drill holes, underlain by sediments (sandstones and deeper siltstones and mudstones, tentatively assigned to the Ntane and Mosolotsane Formations respectively).

A total of ~11,000 tonnes of kimberlite have been processed from BK02 in two samples, confirming a coarse diamond size distribution. The combined results from BK02-1 and BK02-2 samples are presented in Table 1, a total of 584.12 carats have been recovered from 10,937 tonnes of kimberlite for a sample grade of 5.3cpht. A total of 46 diamonds have been recovered greater than 1 carat in weight, including 8 diamonds greater than 2 carats in weight.

Table 1. Combined BK02-1 and BK02-2 Samples

| SAMPLE | SAMPLE TONNES | +21DTC | +19DTC | +17DTC | +15DTC | +13DTC | +11DTC | +9DTC | +7DTC | +5DTC | +3DTC | -3DTC |
|------------|---------------|--------|--------|--------|--------|--------|--------|-------|-------|--------|-------|-------|
| BK02 Total | 10937 | 10.04 | 24.17 | 10.965 | 23.26 | 57.53 | 103.1 | 96.92 | 67.29 | 114.36 | 53.93 | 22.54 |

Three largest diamonds recovered, 5.48, 4.56, 2.71 carats

The diamonds recovered are scheduled to be independently valued early in the second quarter of 2017.

A total of 17 drill holes totalling 1,990 metres were drilled into the BK02 kimberlite during 2016 and Q1 2017. A total of 1059 metres of kimberlite were intersected with the deepest intersection of 201m

in a vertical PQ diamond drill hole, drilled adjacent to the surface mini-bulk sample excavation. The interpreted surface area of BK02 is 2.1 hectares and additional delineation drilling is required to finalise certain parts of the interpretation (data from Lucara Mining Press Release, 6th March 2017)

Observations from drill core suggest that the present-day exposure is close to the basalt/sediment contact with a slightly complicated present day surface expression with basalt breccia/cap on the north and a slightly flaring intrusion to the south. Drilling intersected thicker basalt to the north, slightly thinner to east and west, none to the south. This is currently interpreted to represent a thinning of the basalt in the area and it is proposed that the kimberlite flared along the basalt/sandstone contact toward the south. Additional drilling is required to resolve this geometry. The TMI dipole anomaly is significantly stronger on the eastern side, and this is reflected in raised magnetic susceptibilities observed in drill-holes through this part of the kimberlite.

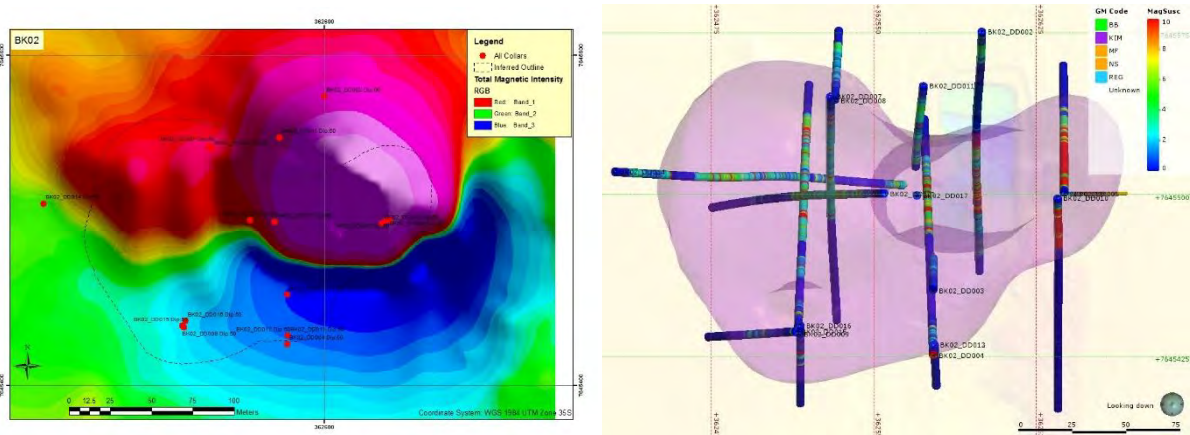


Figure 2: Left: Ground magnetic data total magnetic intensity image with drill hole collars and surface outline from 3d model based on drill-holes. Right: Plan view looking down on the model of the kimberlite, boreholes shown with Magnetic Susceptibility values, note abundance of values greater than 10SI units to the east.

The pipe infill is dominated by a homogenous PK to MK intrusion with minor textural variations and variable extents of weathering, mainly hydration, as indicated by the presence of saponite and montmorillonite (after serpentine, after olivine). The eastern portion (BK02_DD006) appears less weathered, and more coherent than the western portion (BK02_DD001 and BK02_DD007).

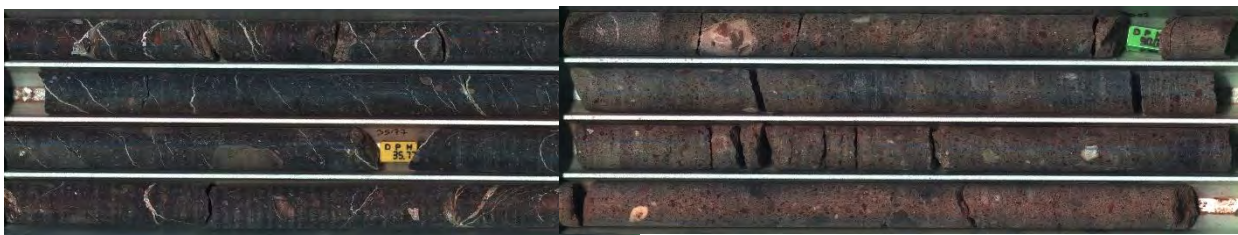
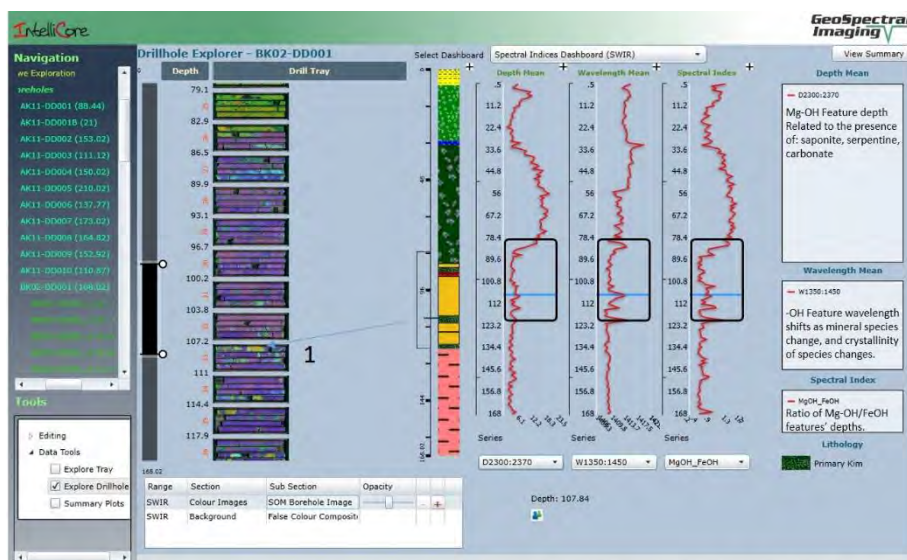


Figure 3: Left: Tray 8 from BK02_DD006 showing eastern kimberlite 33.45m to 36.97m; Right: Tray 27 from BK02 DD007 showing western more weathered less coherent kimberlite, depth 89.19m to 92.79m

The contact between the kimberlite and sediments (sandstones) is complicated in the west and south-west, as seen in BK02_DD001 and BK02_DD009, e.g. **Figure 4**.



1: Thin kimberlite layers within the large sandstone blocks on the margins of the intrusion. Note the logs and trace logs show the whole hole, the tray images show only the length marked by the black boxes. Complex sandstone/kimberlite boundary identified in this borehole.

Figure 4: Core imaging data showing core trays with an automatic classification image showing kimberlite (top and thin layers through the images) and sandstone and shales on the western margin of the kimberlite

Results from a hyperspectral imaging of 1667 metres of core including country rock and kimberlite, that was undertaken in Dec/16 will be presented to enhance the preliminary 3-d model of the BK02 kimberlite, particularly internal geology. This seems to indicate a similar distinction as the magnetic susceptibility, with a variation in the spectral response between the eastern and western parts of the kimberlite (**Figure 5:** depth of OH feature modelled volumes). The imaging was completed in Dec 2016 and therefore excludes 4 holes that were drilled in 2017. The western portion of the kimberlite is therefore data-sparse and modelling has very low confidence.

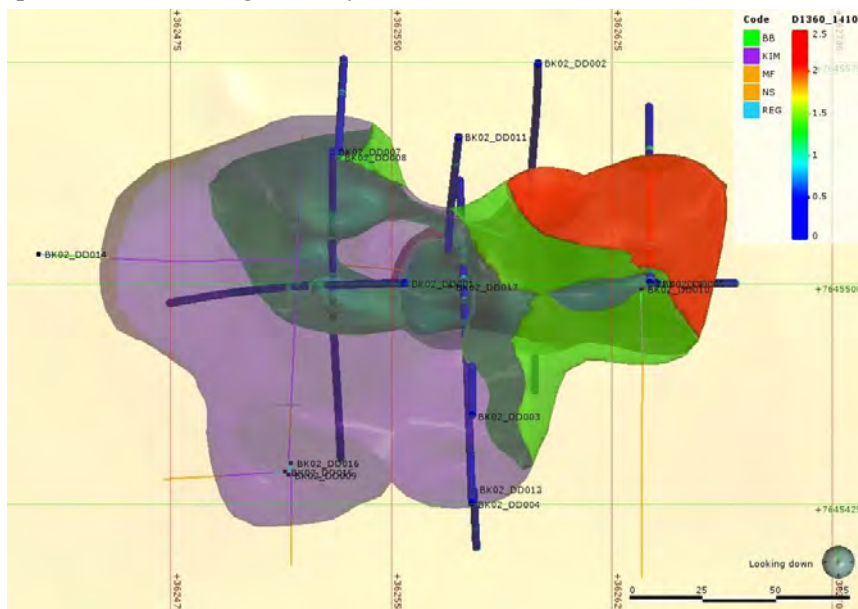


Figure 5: Plan view of 3d model of internal variation of the depth of the hydroxyl absorption feature within BK02. The data is collected on a line by line basis, and calculated to represent a 1m interval by averaging the depth of the feature for all pixels within the selected interval. Holes with no reflectance data are shown with lithology.

New modern diamond processing and drilling information have enhanced the understanding of diamond content and intrusive history of the BK02 kimberlite.

Sulphide inclusions in sub-lithospheric diamonds

Lotta I.M. Kempainen¹, Emilie Thomassot², Simon C. Kohn¹, Galina P. Bulanova¹, Ian J. Parkinson¹ and Chris B. Smith¹

¹ University of Bristol, United Kingdom, lk15127@bristol.ac.uk, simon.kohn@bristol.ac.uk, galina_bulanova@hotmail.com, ian.parkinson@bristol.ac.uk, chris_b_smith@btopenworld.com
² Centre de Recherches Pétrographique et Géochimiques (CRPG-CNRS) et Université de Lorraine, Vandoeuvre-Les-Nancy, France, emilie@crpg.cnrs-nancy.fr

Overview

Sulphide inclusions hosted in sublithospheric (“superdeep”) diamonds from the Juina-5 and Collier-4 kimberlites (Brazil) are being studied by a variety of techniques. Protected from any reequilibration by their host diamond, these samples offer a unique opportunity to investigate the deep sulphur cycle, potentially adding new constraints on recycling of surface material at depths.

Background

Inclusions in diamonds provide a direct insight into the chemistry of diamond-forming domains of the Earth’s mantle, allowing for an understanding of the recycling of volatiles through the Earth’s interior. Diamond formation is often interpreted as the result of redox reactions; diamonds may grow by the interaction of a reduced fluid with oxidised mantle (Thomassot et al., 2007), or by the infiltration of oxidised fluids into reduced ambient mantle (Stachel and Harris 2009; Palot et al. 2014). Sulphide inclusions are abundant in lithospheric diamonds relative to normal mantle sulphur contents (~200 ppm), but their involvement in diamond formation requires further investigation.

The majority of known diamonds have formed in the Earth’s lithospheric upper mantle (<300km) in peridotite (“normal” mantle) or eclogite (of mafic lithology). The major and trace element chemistries of the sulphide inclusions they host are well documented in literature; for example, peridotitic sulphide inclusions are generally characterised by higher Cr and Ni contents compared to eclogitic diamonds, reflecting on the higher degrees of partial melting having affected their source region (Fig. 1A).

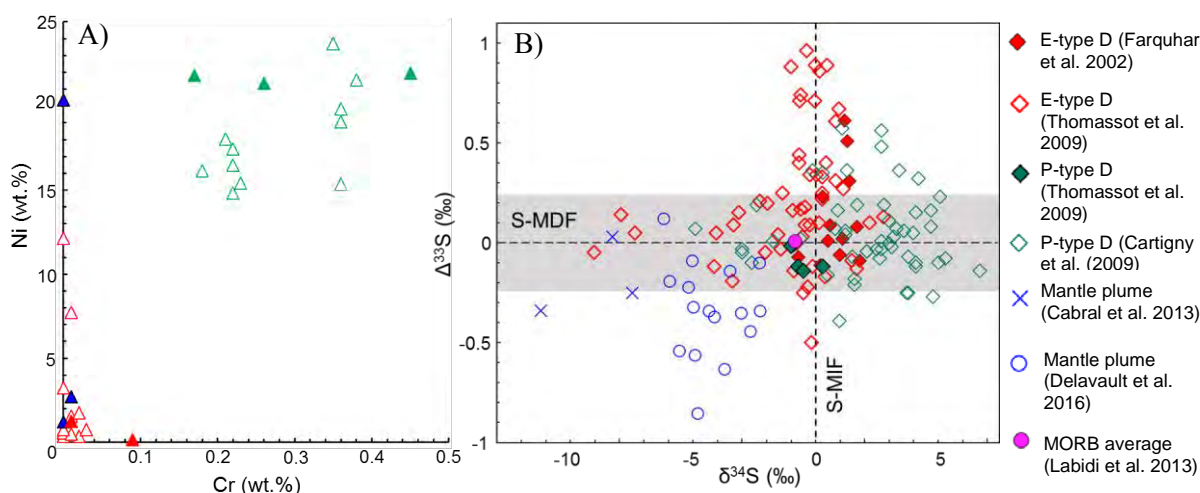


Figure 1: A) Ni versus Cr plot with compositions of eclogitic (red) and peridotitic (green) diamond inclusions from Jwaneng (open symbols from Thomassot et al. 2009) and Mwadui (closed symbols from Stachel et al. 1998) and three inclusions from Machado River (blue symbols from Burnham et al. 2016). B) $\delta^{34}\text{S}$ (mass-dependent fractionation, S-MDF) versus $\Delta^{33}\text{S}$ (mass-independent fractionation, S-MIF) plot showing the compositions of sulphides included in E-type and P-type diamonds, plume material and MORB.

Less is known about the sulphides hosted in sublithospheric diamonds, which make up only a small (<5%) proportion of diamonds studied worldwide, but can sample trapped mantle material at depths >410km (Stachel et al. 2000; Walter et al. 2011). Previous work has shown that superdeep diamonds from Juina-5 and Collier-4 grew by interaction of oxidised oceanic slab-derived carbonate melts with a reduced ambient mantle (Burnham et al. 2015; Thomson et al. 2016). Therefore, one source of sulphur for sulphide inclusions in these diamonds could be a surface-derived sulphate component (e.g. precipitated from a C–O–S–H-rich fluid). Alternatively, sulphide may have been trapped in reduced form, as sulphide included in a subducting slab, or originating from the mantle.

P-type sulphides can preserve mantle-like sulphur isotope signatures, while E-type inclusions can exhibit more scatter in $\delta^{34}\text{S}$ and $\Delta^{33}\text{S}$ compositions due to the heterogeneity of their crustal protoliths (Farquhar et al. 2002; Cartigny et al. 2009; Thomassot et al. 2009) (Fig. 1B). Sulphur mass-independent fractionation (S-MIF, $\Delta^{33}\text{S} \neq 0$) is a signal observed in rocks and diamonds preserving sedimentary material of Archaean age (>2.45 Ga), when photolysis of volcanic SO_2 released into an oxygen-poor atmosphere allowed the formation of sulphates (with negative $\Delta^{33}\text{S}$ anomalies) and elemental sulphur (with positive $\Delta^{33}\text{S}$ signatures) (Farquhar et al. 2000). The latter are preserved in few lithospheric diamonds (Farquhar et al. 2002; Thomassot et al. 2009). Negative $\Delta^{33}\text{S}$ values have been measured in material sampled by mantle plumes (Cabral et al. 2013; Delavault et al. 2016), and the apparent deficit of negative anomalies at the surface could suggest the presence of a negative $\Delta^{33}\text{S}$ reservoir in the lower mantle (Farquhar et al. 2002; Cabral et al. 2013).

Samples, results and discussion

The chemical composition of sulphide inclusions hosted in diamonds from Collier-4 and from Juina-5 is being investigated. The diamonds are 0.5-3 mm in size and octahedral or macle-shaped, often being highly resorbed or broken fragments of originally larger crystals (Fig. 2A and 2B). The inclusions are 5-40 μm in size and consist mainly of iron sulphide ($\text{Fe}_{(1-x)}\text{S}$), although minor exsolutions of chalcopyrite (CuFeS_2) and pentlandite ($(\text{Fe,Ni})_9\text{S}_8$) may also occur. According to electron-microprobe analyses (Thomson et al. 2014) and synchrotron-based x-ray microtomography (SXRTM), sulphides coexist at the edges of inclusions with non-sulphide phases, perhaps suggesting exsolution from a former S-bearing melt (Fig. 2C). The phases coexisting with sulphide have an eclogitic affinity and include Ca-perovskite, Ca-walstromite, spinel, clinopyroxene and coesite (Thomson et al. 2014).



Figure 2: A) Collier-4 diamond polished on two surface contains large polyphase inclusions. B) a resorbed sulphide-bearing diamond from Juina-5. C) Back-scattered electron image of an unmixed Ca-perovskite inclusion in a Juina-5 diamond where sulphide (sul) occurs (Thomson et al. 2014).

The sulphur isotope compositions of superdeep sulphide inclusions will be analysed by secondary ion mass spectrometry (SIMS) using CRPG national facility (Cameca 1280), providing a unique opportunity to investigate the ability of sulphur to preserve recycled signatures during transfer to the Earth's lower mantle. Sulphide inclusions of recycled origin can have mantle-like S isotope compositions, but analysing solely mantle-like $\delta^{34}\text{S}$ values could reflect on the interaction of deep-sourced sulphur, or fluid-hosted SO_4^{2-} with the diamond-forming medium. The S isotope signature can be diluted with mantle-derived sulphur ($\Delta^{33}\text{S} = \sim 0$), especially through interaction with fluids/melts.

However, observing a S-MIF signal would suggest the presence of relatively undisturbed recycled, ancient sediment in the lower mantle diamond-forming region.

Although they can be obscured by mantle mixing and assimilation processes, the compositions and sulphur isotopic signature of sulphide minerals can be used to investigate the nature of the sulphur-bearing phase interacting with the diamond-forming medium. Observing differences in the geochemical or isotopic compositions of sulphides trapped as single phase Fe-sulphide and ones inside polyphase inclusions could suggest different provenances of sulphur in the lower mantle.

References

- Burnham AD, Thomson AR, Bulanova GP, Kohn SC, Smith CB and Walter MJ (2015) Stable isotope evidence for crustal recycling as recorded by superdeep diamonds. *Earth Planet Sci Lett* 432:374-380
- Burnham AD, Bulanova GP, Smith CB, Whitehead SC, Kohn SC, Gobbo L and Walter MJ (2016) Diamonds from the Machado River alluvial deposit, Rondônia, Brazil, derived from both lithospheric and sublithospheric mantle. *Lithos* 265:199-213.
- Cabral RA, Jackson MG, Rose-Koga EF, Koga KT, Whitehouse MJ, Antonelli MA, Farquhar J, Day JM and Hauri EH (2013) Anomalous sulphur isotopes in plume lavas reveal deep mantle storage of Archaean crust. *Nature* 496(7446):490-493
- Cartigny P, Farquhar J, Thomassot E, Harris JW, Wing B, Masterson A, McKeegan K and Stachel T (2009) A mantle origin for Paleoproterozoic peridotitic diamonds from the Panda kimberlite, Slave Craton: evidence from 13 C-, 15 N- and 33, 34 S-stable isotope systematics. *Lithos* 112:852-864
- Cartigny P, Palot M, Thomassot E and Harris JW (2014) Diamond formation: a stable isotope perspective. *Annu Rev Earth Planet Sci* 42:699-732
- Delavault H, Chauvel C, Thomassot E, Devey C and Dazas B (2016) Sulfur and lead isotopic evidence of relic Archean sediments in the Pitcairn mantle plume. *Proc Natl Acad Sci* 113(46):12952-12956
- Farquhar J, Wing BA, McKeegan KD, Harris JW, Cartigny P and Thiemens MH (2002) Mass-independent sulfur of inclusions in diamond and sulfur recycling on early Earth. *Science* 298(5602):2369-2372
- Labidi J, Cartigny P and Moreira M (2013) Non-chondritic sulphur isotope composition of the terrestrial mantle. *Nature* 501(7466):208-211
- Stachel T, Harris JW and Brey GP (1998) Rare and unusual mineral inclusions in diamonds from Mwadui, Tanzania. *Contrib Mineral Petrol* 132(1):34-47.
- Stachel T, Harris JW, Brey GP and Joswig W (2000) Kankan diamonds (Guinea) II: lower mantle inclusion parageneses. *Contrib Mineral Petrol* 140(1):16-27.
- Stachel T and Harris JW (2009) Formation of diamond in the Earth's mantle. *J Phys: Condens Matter* 21(36):364206
- Thomassot E, Cartigny P, Harris JW and Viljoen KF (2007) Methane-related diamond crystallization in the Earth's mantle: stable isotope evidences from a single diamond-bearing xenolith. *Earth Planet Sci Lett* 257(3):362-371
- Thomassot E, Cartigny P, Harris JW, Lorand JP, Rollion-Bard C and Chaussidon M (2009) Metasomatic diamond growth: A multi-isotope study (13 C, 15 N, 33 S, 34 S) of sulphide inclusions and their host diamonds from Jwaneng (Botswana). *Earth Planet Sci Lett* 282(1):79-90
- Thomson AR, Kohn SC, Bulanova GP, Smith CB, Araujo D and Walter MJ (2014) Origin of sublithospheric diamonds from the Juina-5 kimberlite (Brazil): constraints from carbon isotopes and inclusion compositions. *Contrib Mineral Petrol* 168(6):1081
- Thomson AR, Walter MJ, Kohn SC and Brooker RA (2016) Slab melting as a barrier to deep carbon subduction. *Nature* 529(7584):76-79
- Walter MJ, Kohn SC, Araujo D, Bulanova GP, Smith CB, Gaillou E, Wang J, Steele A and Shirey SB (2011) Deep mantle cycling of oceanic crust: evidence from diamonds and their mineral inclusions. *Science* 334(6052):54-57



Magmaclasts in Kimberlite

Kimberley J. Webb¹ and Casey M. Hetman²

¹Mineral Services Canada Inc., North Vancouver, Canada, kimberley.webb@mineralservices.com

²SRK Consulting (Canada) Inc., Vancouver, Canada, chetman@srk.com

Introduction

Despite their widespread occurrence, magmaclasts are perhaps the most enigmatic of kimberlite components; they are diverse in character, usually best or only discerned microscopically and display overlap in characteristics between types, further complicating their identification and interpretation. Yet magmaclasts can serve as powerful tools in kimberlite exploration and evaluation. Here we explain the importance of magmaclasts in economic kimberlite geology and provide an updated set of descriptors (Fig. 1, after Webb 2006) that highlights the features used to identify magmaclasts and to discriminate between magmaclast types, as well as between magmaclasts and other clast types (Fig. 2).

Definition

Magmaclast is a descriptive term for physically-distinct, fluidal-shaped bodies of kimberlite magma (now solidified) formed by any process of magma disruption prior to solidification, typically during near-surface emplacement. It is used as an interim term until further investigation of the magmaclast characteristics and magmaclast-bearing rock allow for interpretation of the magma disruption process, and hence classification of the magmaclasts (Scott Smith et al. 2013) as either:

- 1) *melt segregations* (Fig. 2a), which form non-explosively by magmatic segregation in subvolcanic and non-volcanic hypabyssal intrusions, or
- 2) *melt-bearing pyroclasts* (Fig. 2b,c), which form by fragmentation and rapid cooling of magma during explosive volcanic eruptions and occur in volcanoclastic rocks above and below surface.

The need for a descriptive interim term arises from the potential for either of these types to occur and the common difficulty in discriminating them, especially at initial broad scales of observation, and due to the high degrees of alteration typical of many kimberlites. 'Former' and 'now solidified' are implicit in application of 'magma' to lithified rocks and 'clast' is used in the broadest sense possible. Autoliths, accretionary clasts (Fig. 2d, e) and epiclasts are not magmaclasts, and distinguishing these from magmaclasts is important although not always straightforward. In addition, misleading pseudo-magmaclasts (Fig. 2f) may be produced by pervasive alteration of groundmass in coherent rocks.

Importance of magmaclasts

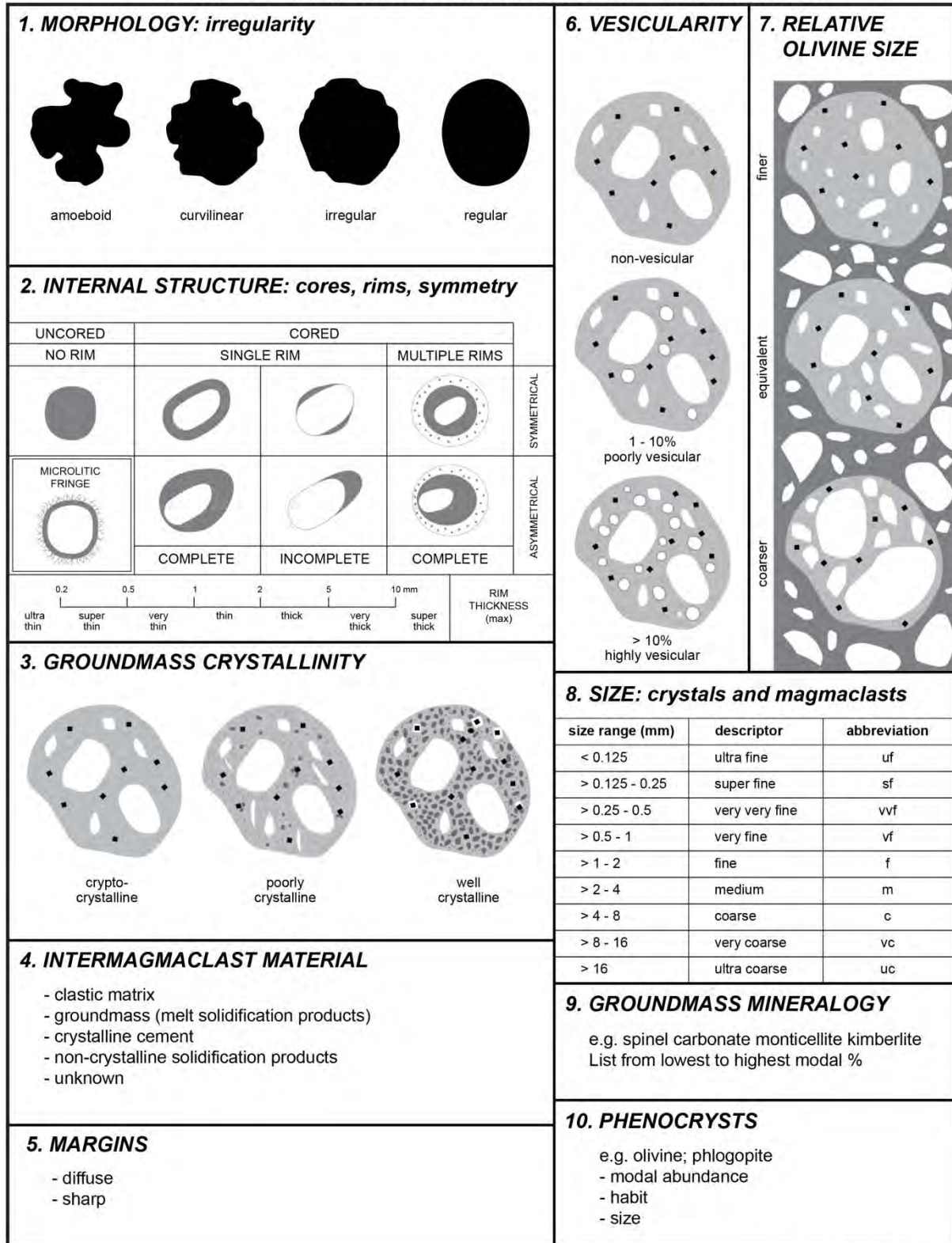
The presence of magmaclasts indicates that a certain degree of modification of the intruded magma has taken place, potentially impacting the inherent diamond content and size frequency distribution. In volcanic environments, the extent of modification and processes involved (e.g. sorting, fines removal) are reflected in part by the distribution, size and physical characteristics of melt-bearing pyroclasts. Magmaclasts are used in the identification of parental magma type, the textural-genetic classification of the infills of kimberlite bodies (and the associated predictions of body size, geometry and internal variability), and in the recognition of and discrimination between different phases of kimberlite in a body. These allow for reconstruction of the emplacement history of a kimberlite and development of valid geological models for resource estimation. Misclassification or lack of attention to magmaclasts, from exploration to mine planning, have resulted in lost dollars and opportunities.

Description and identification

Magmaclasts comprise entrained solids (crystal, lithic) and groundmass (melt solidification products \pm exsolved fluids). They have fluidal shapes resulting from low melt viscosity and surface tension processes. Melt segregations and melt-bearing pyroclasts are distinguished primarily based on shape (especially range thereof), groundmass crystallinity, and nature of the intermagmaclast material, as well as features such as mineral alignment and vesicularity. Distinctive melt-bearing pyroclast

assemblages typically characterise the two main classes of pyroclastic kimberlite, Kimberley-type pyroclastic kimberlite and Fort à la Corne-type pyroclastic kimberlite (KPK and FPK, respectively; Scott Smith et al. 2013), although overlap is observed. They differ in shape, proportion of cored to uncored varieties, thickness of rims, groundmass crystallinity, the nature of margins and vesicularity.

DESCRIPTIVE TERMINOLOGY FOR MAGMACLASTS IN KIMBERLITE



Webb and Hetman (2017)

Figure 1: Descriptive terminology for magmaclasts in kimberlite (after Webb 2006).

Interpretation

Description of the characteristics of magmaclasts represented in Fig. 1, combined with other textural, component and structural aspects of a kimberlite, forms the foundation of valid interpretations of the textural-genetic classification, intrusive or volcanic spatial context and emplacement processes (Scott Smith et al. 2013).

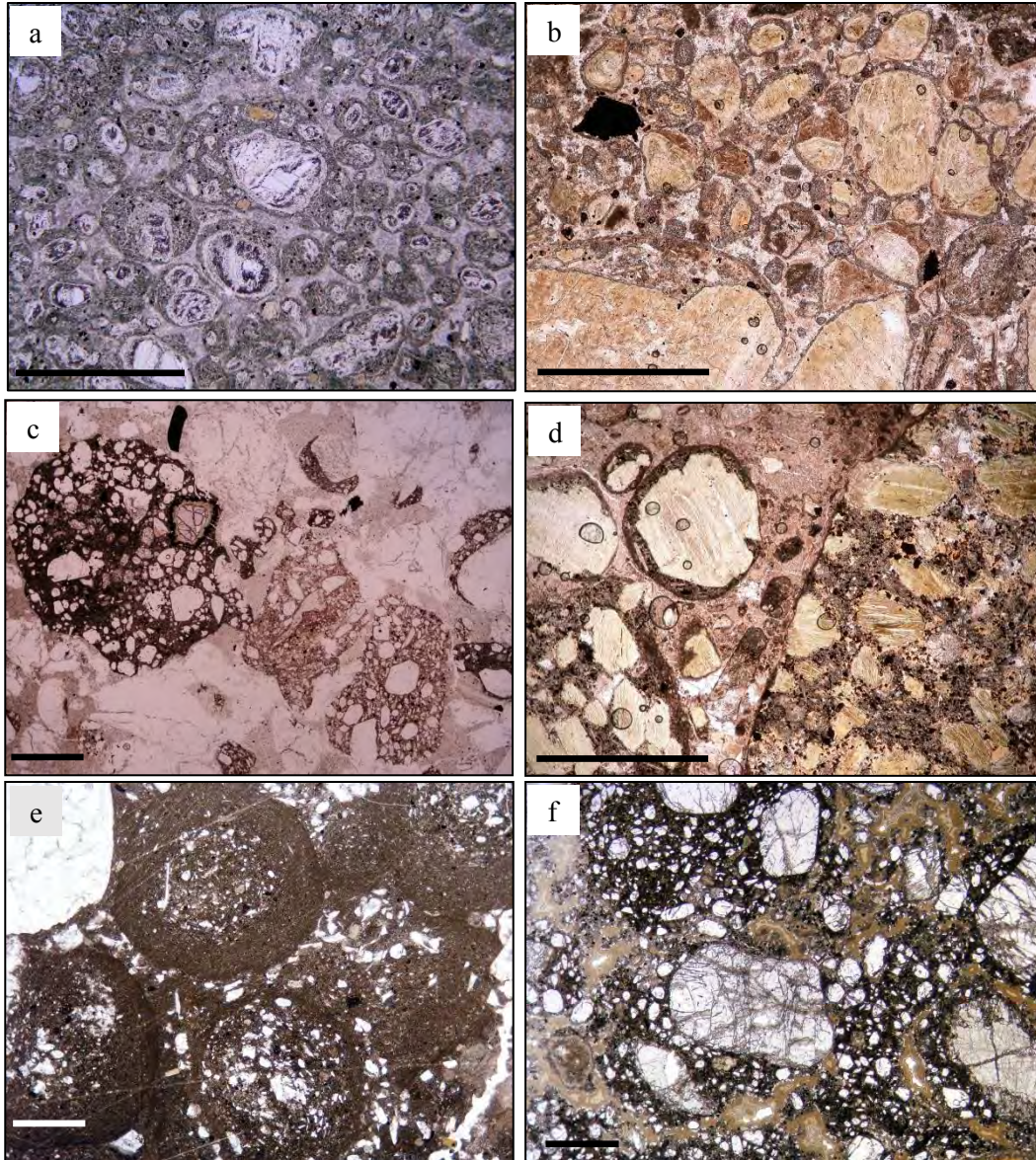


Figure 2: Photomicrographs illustrating diverse characteristics of magmaclasts (a,b,c) and other types of clasts (d,e,f): melt segregations in Wales Island hypabyssal kimberlite (a); melt-bearing pyroclasts in Dutoitspan (Kimberley) KPK (b) and in Fort à la Corne (Body 122) FPK (c); coherent autolith (right) in Letseng KPK (d), accretionary clasts in A418 at Diavik (e) and pseudomagmaclasts in the Rat dyke, Ekati (f). Scale bars = 1 mm.

References

- Scott Smith BH, Nowicki TE, Russell JK, Webb KJ, Mitchell RH, Hetman CM, Harder M, Skinner EMW, Robey JV (2013) Kimberlite terminology and classification. Proceedings of the 10th International Kimberlite Conference. Special Issue J Geol Soc India, 2:1-17. Springer India.
- Webb KJ (2006) Juvenile clasts in kimberlites: standardized comprehensive description towards unraveling emplacement mechanisms. In: Long Abstracts of the 8IKC Kimberlite Emplacement Workshop, Saskatoon, Canada, September 2006.



The carbon cycle in the continental lithosphere and the generation of alkaline mafic melts in cratonic and rift regions

Stephen F. Foley¹ and Tobias P. Fischer²

¹*ARC Centre of Excellence for Core to Crust Fluid Systems and Department of Earth and Planetary Sciences, Macquarie University, North Ryde, New South Wales, Australia*

²*Department of Earth and Planetary Sciences, University of New Mexico, Albuquerque, New Mexico, U.S.A.*

The generation of many continental alkaline magmas, including kimberlites, carbonatites, ultramafic lamprophyres, nephelinites and melilitites requires the presence of CO₂ or carbonates in the source region. These rocks are strongly associated with cratonic lithosphere and particularly with continental rifts in proximity to cratons, where high concentrations of carbonatites occur. However, the origin of the large amounts of CO₂ needed to explain these occurrences remains largely unexplained. Here, we consider the question of where these huge concentrations of carbon come from, and how they are reactivated to result in the generation of strongly alkaline, silica-undersaturated magmas.

In recent years, great strides have been made in understanding the deep carbon cycle, but this has concentrated on the behaviour of carbon during release at the surface as CO₂ degassing through mid ocean ridges and ocean islands, and on the complex mechanisms of the return of carbon to the mantle at subduction zones (Dasgupta and Hirschmann, 2010; Kelemen and Manning, 2015). The time-integrated storage and re-release of carbon from the continental lithosphere has not been adequately quantified in global models. Recent work on outgassing at rifts has found that enormous amounts of CO₂ are passively released, much of it along faults. Extrapolations from the Natron-Magadi basin close to the Kenya-Tanzania border, where carbonate-rich magmatism is abundant, to the whole rift results in an estimate of around 52 Mt C/yr (Lee et al., 2016), higher than most estimates for mid ocean ridges (8-53) and island arcs (18-43) (Dasgupta and Hirschmann, 2010; Kelemen and Manning, 2015; Kagoshima et al., 2015). Later measurements at rift volcanoes as far north as Ethiopia (Hutchison et al., 2016) indicate that this value may be too low, as degassing close to volcanoes may be much higher than previously thought. He and C isotope studies indicate that much of the CO₂ degassed along faults originates in the mantle.

Carbonate in continental alkaline igneous rocks

Carbon in continental rifts is not restricted to passive CO₂ release: large concentrations of carbonate-rich magmas solidify as carbonatites, kimberlites, ultramafic lamprophyres (UML), nephelinites, melilitites, basanites, and their plutonic equivalents. The high volume of these magmas in rifts and their rarity elsewhere attests to a large reservoir of carbon beneath rifts. Although carbonatites at localities such as Oldoinyo Lengai probably originate by liquid immiscibility at upper crustal pressures from melilitite or nephelinite, the extreme CO₂ release at Nyiragongo (Burton et al., 2013) demonstrates that nephelinites also preferentially tap CO₂-rich sources. Furthermore, melilitites and nephelinites are characteristically concentrated at the propagating tips of rifts and along their flanks where the lithosphere is thickest (Foley et al., 2012), and are replaced by voluminous basaltic magmatism in the rift axes as the rift matures.

In the East African Rift, ultramafic, potassium- and carbonate-rich melts including kimberlites, kamafugites and carbonatites are associated with the Tanzanian craton lithosphere, which is consistent with experiments showing that low-degree melts range from carbonatite to UML at depths of 130-200km (Foley et al., 2009). The kamafugites are closely related to UML (aillikites and alnöites) found in similar positions on other continents (Foley et al., 2002; Tappe et al., 2008). Beneath the thick cratons, melts are also characterised by high K/Na because of the abundance of phlogopite in rocks such as carbonated phlogopite pyroxenite in addition to peridotite (Tappe et al., 2008).

These carbon-rich sources are repeatedly tapped: most carbonatites in East Africa were emplaced in the last 40Ma (Woolley and Kjarsgaard, 2008), but earlier episodes at 123-133Ma and 1040Ma

indicate a recurrence of CO₂-rich magmatism, which is also seen in Labrador/Greenland and South Africa (Boyd and Gurney, 1986; Tappe et al., 2007).

Mechanisms of carbon storage and release and the magnitude of their effects

The incorporation of carbon into, and its later release from, the continental lithosphere involves its incorporation during lithosphere formation, accumulation from degassing of the deeper mantle over time, and the remobilization of carbon *within* the lithosphere by the movement of incipient melts.

Despite its relatively restricted areal extent, the great thickness of the cratonic mantle means that it makes up slightly more than half of the continental mantle lithosphere. The formation mechanisms of cratonic lithosphere are debated, with possibilities including accumulation at subduction zones, lateral accretion, and vertical accretion from plumes beneath thick volcanic plateaux (Lee 2006). The age of continental crust and the size of cratonic blocks at different times in the Archean is also controversial. If two thirds of the current crust existed by the end of the Archean and this was underlain and stabilised by strongly depleted lithosphere, then the preferred picture of the cratonic lithosphere is blocks of deep, depleted lithosphere in which magmatism is associated with reactivation along margins and deep fault zones (Foley, 2008; Griffin et al., 2013). This picture is compatible with the long-known association of kimberlites and deep fault zones known as Clifford's Rule. An important corollary of this model is that strongly depleted, deep lithosphere provides a strongly reduced environment that forms a redox trap for diamonds (Foley, 2011; Rohrbach and Schmidt, 2011) during later melt movements. We estimate that a lithospheric carbon content of 0.25 Mt C km⁻³ would result from subduction wedge accretion, whereas ten times this figure could result from vertical accretion of plumes. These values are poorly constrained because of uncertainties surrounding the oxidation state of the atmosphere and near-surface processes, the probably more limited volume of organic material and carbonate sediments in the Archean, and the amount of recycled material in plumes. However, all estimates are insignificant relative to the carbon introduced during later enrichment processes.

Carbon introduced into the lithosphere by gradual, continuous enrichment is estimated based on methods used for CO₂ output at mid-ocean ridges, modified for an incipient melting zone between 300 and 200km depth and an average lithosphere age of 2809 Ma for the cratons. Restricting the accumulation of this carbon to the lowest 5-10% of the lithosphere, and allowing for 50% removal of the lithosphere base by later small-scale convective erosion, this results in 14-28 Mt C/km⁻³. We estimate the amount of carbon scavenged from plumes by assuming passage of a plume every 675 million years, based on the average periodicity of alkaline magmatism in incipient rifts, and using the model for the volatile content of plumes of Sobolev et al. (2011). This results in three phases of enrichment by plumes for average cratonic lithosphere, adding 40-45 Mt C km⁻³ to the basal layers of the lithosphere. After the overprinting of the original carbon content by both gradual degassing and plume enrichment, the lower cratonic lithosphere contains 57-71 Mt C km⁻³, or 1.6-3.2 wt% CO₂.

Carbon is sequestered in the lower lithosphere as diamonds and dyke assemblages; only a small amount probably exists as carbonated peridotite. It is initially trapped by redox freezing, because the deep cratonic mantle is initially extremely reduced due to extreme depletion and to the pressure effect on oxygen fugacity (Foley, 2011; Rohrbach and Schmidt, 2011). However, the influx of later melts oxidises the lithosphere by up to 4 orders of magnitude fO_2 (Yaxley et al., 2017). Remobilisation is initially by redox melting, as the oxidation process remobilises carbon as dissolved carbonate in incipient melts that are carbonatitic to aillikitic with higher CO₂ contents than kimberlites. It is notable here that aillikites and carbonatites are associated with rifts, unlike kimberlites, which may be derived largely from the asthenosphere. These low-SiO₂ incipient melts are very mobile and are effective in the redistribution of carbon long before decompression melting becomes more important at later stages of rifting when the lithosphere is thinned and blocks become delaminated. Repeated plume-triggered melt incursions identify structural weaknesses that focus later melts, eventually forming enriched zones that reach high into the lithosphere beneath later rift locations. Lithosphere blocks may weaken and founder, breaking off blocks and eroding the lithosphere. However, carbon in delaminated blocks will re-melt and migrate upwards as carbonate, forming assemblages that are less

dense (2.95-3.2 g cm⁻³) than peridotite and so contribute to later magmatism. Re-melting of the sub-rift enriched zone produces melts charged with carbonate, bringing sufficient CO₂ towards the surface to feed volcanoes and fault zones that emit 28-34 Mt C/year along the length of the East African Rift for the entire 40 Myr lifespan of a continental rift. Given the uncertainties in many input parameters for these calculations, the value of 28-34 Mt C/year is remarkably similar to the 52 Mt C/yr estimated from passive degassing for the East African rift (Lee et al., 2016).

References

- Boyd FR, Gurney JJ (1986) Diamonds and the African lithosphere. *Science* 272: 472-477
- Burton MR, Sawyer GM, Granieri D (2013) Deep carbon emissions from volcanoes. *Rev. Mineral. Geochem.* 75: 323-354
- Dasgupta R, Hirschmann MM (2010) The deep carbon cycle and melting in Earth's interior. *Earth Planet. Sci. Lett.* 298: 1-13
- Foley SF (2008) Rejuvenation and erosion of the cratonic lithosphere. *Nature Geosci.* 1: 503-510
- Foley SF (2011) A reappraisal of redox melting in the Earth's mantle as a function of tectonic setting and time. *J. Petrol.* 52: 1363-1391
- Foley SF, Andronikov AV, Melzer S (2002) Petrology, geochemistry and mineral chemistry of ultramafic lamprophyres from the Jetty Peninsula area of the Lambert-Amery Rift, Eastern Antarctica. *Mineral. Petrol.* 74: 361-384
- Foley SF, Yaxley GM, Rosenthal A, Buhre S, Kiseeva ES, Rapp RP, Jacob DE (2009) The composition of near-solidus melts of peridotite in the presence of CO₂ and H₂O at 40 – 60 kbar. *Lithos* 112S: 274-283
- Foley SF, Link K, Tiberindwa JV, Barifaijo E (2012) Patterns and origin of igneous activity around the Tanzanian craton. *J. Afr. Earth Sci.* 62: 1-18
- Griffin WL, Begg GC, O'Reilly SY (2013) Continental-root control on the genesis of magmatic ore deposits. *Nature Geosci.* 6: 905-910
- Hutchison W, Biggs J, Mather TA, Pyle DM, Lewi E, Yirgu G, Caliro S, Chiodini G, Clor LE, Fischer TP (2016) Causes of unrest at silicic calderas in the East African Rift: new constraints from InSAR and soil-gas chemistry at Aluto volcano, Ethiopia. *Geochem. Geophys. Geosys.* 17: doi: 10.1002/2015GC006395
- Kagoshima T, Sano Y, Takahata N, Maruoka T, Fischer TP, Hattori K (2017) Sulphur geodynamic cycle. *Scientific Reports* 5:8330
- Kelemen PB, Manning CR (2015) Reevaluating carbon fluxes in subduction zones, what goes down, mostly comes up. *Proc. Nat. Acad. Sci.* 112: E3997-E4006
- Lee C-TA (2006) Geochemical/petrologic constraints on the origin of cratonic mantle. *Geophys. Monograph Series* 164: 89-114
- Lee H, Muirhead JD, Fischer TP, Ebinger CJ, Kattenhorn SA, Sharp ZD, Kianji G (2016) Massive and prolonged deep carbon emissions associated with continental rifting. *Nat. Geosci.* 9: 145-149
- Rohrbach A, Schmidt MW (2011) Redox freezing and melting in the Earth's deep mantle resulting from carbon-iron redox coupling. *Nature* 472: 209-212.
- Sobolev SV, Sobolev AV, Kuzmin DV, Krivolutskaya NA, Petrunin AG, Arndt NT, Radko VA, Vasiliev YR (2011) Linking mantle plumes, large igneous provinces and environmental catastrophes. *Nature* 477: 312-316
- Tappe S, Foley SF, Stracke A, Romer RL, Heaman LM, Kjarsgaard BA, Joyce N (2007) Craton reactivation on the Labrador Sea margins: ⁴⁰Ar/³⁹Ar age and Sr-Nd-Hf-Pb isotope constraints from alkaline and carbonatite intrusives. *Earth Planet. Sci. Lett.* 256: 433-454.
- Tappe S, Foley SF, Kjarsgaard BA, Romer RL, Heaman LM, Stracke A, Jenner GA (2008) Between carbonatite and lamproite – diamondiferous Torngat ultramafic lamprophyres formed by carbonate fusion melting of cratonic MARID-type metasomes. *Geochim. Cosmochim. Acta* 72: 3258-3286.
- Woolley AR, Kjarsgaard BA (2008) Carbonatite occurrences of the world: map and database. *Geological Survey of Canada Open File* 5796
- Yaxley GM, Berry AJ, Rosenthal A, Woodland AB, Paterson D (2017) Redox preconditioning deep cratonic lithosphere for kimberlite genesis – evidence from the central Slave Craton. *Scientific Reports* 7: 30

Kimberlite exploration under thick cover using the new powerful SPECTREM^{PLUS} AEM system

David Khoza¹, Nirocca Devkurran¹, Louis Polome¹, Shawn Letts²

¹Spectrem Air PTY LTD, davidk@spectrem.co.za

²De Beers Group Exploration

Introduction

The challenge in modern kimberlite exploration (and indeed all minerals exploration) is locating economic kimberlite deposits under thick sedimentary cover. In places such as Botswana, South Africa, Angola and Australia, the sedimentary cover sequences can be over 400 m thick. This makes geological exploration and in particular geochemical sampling and mapping extremely difficult.

Geophysical exploration, particularly airborne electromagnetic (AEM), magnetic and gravity techniques, provide an alternative tools that can be deployed in such terrains. These methods also have specific limitations in that some kimberlites are, for example known to be devoid of magnetic or gravity signature. For AEM, the challenge is that the sedimentary cover is not only thick but tends to be conductive. This limits the penetration and the detection of primary and secondary EM fields respectively. In order to overcome the latter challenge, SPECTREM AIR PTY LTD (henceforth called SPECTREM AIR), has upgraded its AEM system (SPECTREM²⁰⁰⁰) to the latest generation SPECTREM^{PLUS}, where the dipole moment has effectively being doubled and the processing improved (Leggatt, 2015) to image geology and possible minerals deposits below thick conductive cover (Pare, 2012).

SPECTREM^{PLUS} AEM system

The SPECTREM^{PLUS} system (Figure 1) is the world most powerful AEM system on a fixed-wing platform. The system is mounted on a modified Basler DC3 twin-turbo prop engine aircraft, and collects EM, magnetic and radiometric data simulatenously. The main advantages of the SPECTREM^{PLUS} system are (1) increased power, which results in high-resolution mapping geology and conductive mineral deposits under thick conductive cover, (2) real-time (on board) processing, which means the data are virtually ready to be modelled as soon as the sortie completed (i.e., fast turn around of data), (3) cost effective mapping of large areas, as the sytem can aquire over 500 line-kilometers of data per sortie. Table 1 shows more system specifications.

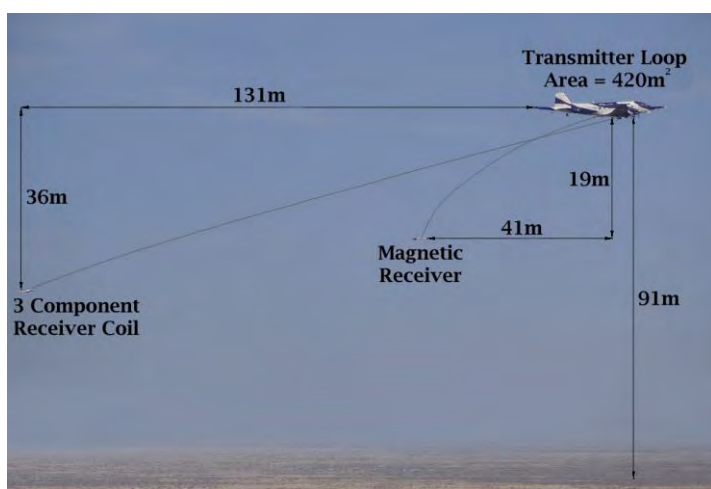


Figure 1: The SPECTREM^{PLUS} AEM system configuration specifications

| Parameter | SPECTREM PLUS (25Hz) |
|---------------------------------|--|
| Transmitter height above ground | 91 m |
| Tx - Rx vertical separation | 36 m (nominal value) |
| Tx - Rx horizontal separation | 131 m (nominal value) |
| Transmitter coil axis | Vertical |
| Receiver coil axes | X : horizontal, parallel to flight direction; Y : horizontal, perpendicular to flight direction, Z: vertical |
| Data units | Parts per million (PPM) of the primary field |
| Current waveform | 100% duty cycle square wave |
| Base frequencies | 25 Hz |
| Transmitter loop area | 420 m ² |
| RMS current | 1800 Amperes |
| RMS dipole moment | 756 000 A.m ² |
| Digitising rate @ 25Hz | 76 800 Hz / component |
| Recording Rate | 5 Hz |
| Number of windows | 10 per component (real-time processing) or 39 post-processing |

Table 1 SPECTREM system

The SPECTREM^{PLUS} system employs a 100% duty cycle transmitter that that transmitter an near square-waveform (Figure 2). A square transmitter waveform has more than double the low frequency spectral content compared to the “pulse” or ”rectangular ramp” type transmitter systems, which gives considerably better depth of penetration for good conductors in conductive environments.



Figure 2: SPECTREM^{PLUS} transmitter waveform

Kimberlite modelling

In order to assess the efficiency of the new SPECTREM^{PLUS} a forward modelling exercise was conducted to investigate how the system would map kimberlite in a geology similar to that in Botswana. For a kimberlite that lies at the base of the Karoo, Figure 3 shows the resulting model. For display purposes, note only the latest EM channels (depicting deeper geology) are shown against the system noise levels derived from data measured at higher altitudes of 3 000 feet.

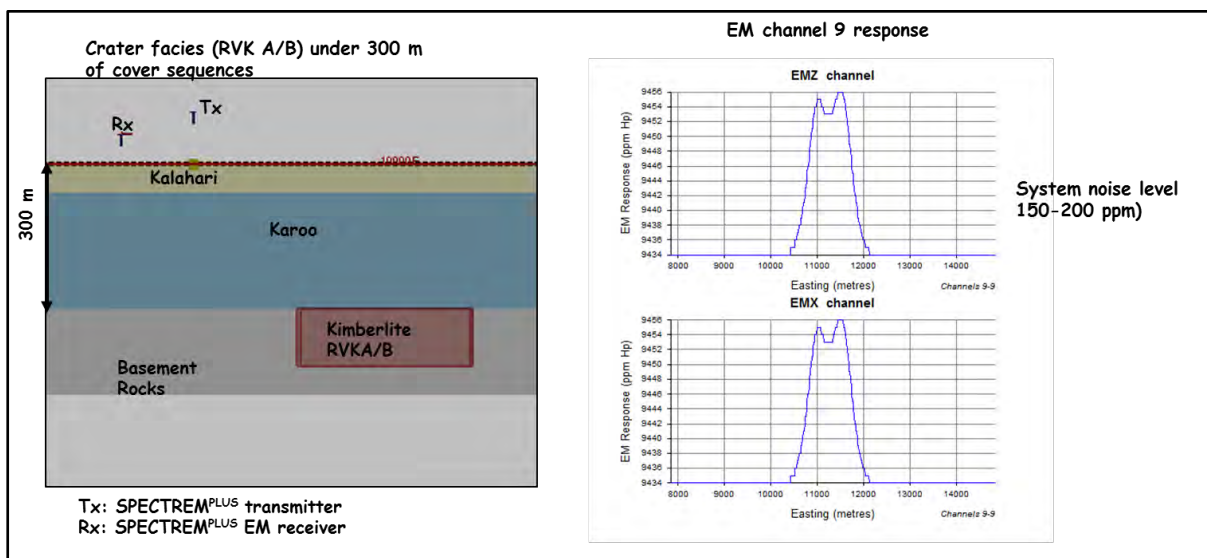


Figure 3 A model depicting a typical geological model where kimberlite RVK-A facies intrudes into the base of the Karoo and the resulting late time EM responses (channel 9). Note these channel 9 amplitudes are above the the system noise level

The model above illustrates the difference that having a higher system power makes in detecting kimberlites under cover.

This next example is based on a typical Orapa type kimberlite which does not have thick cover sediments sequences. It can be readily seen that the kimberlite is clear delineated at late channels, therefore the system will be able to map targets in this setting.

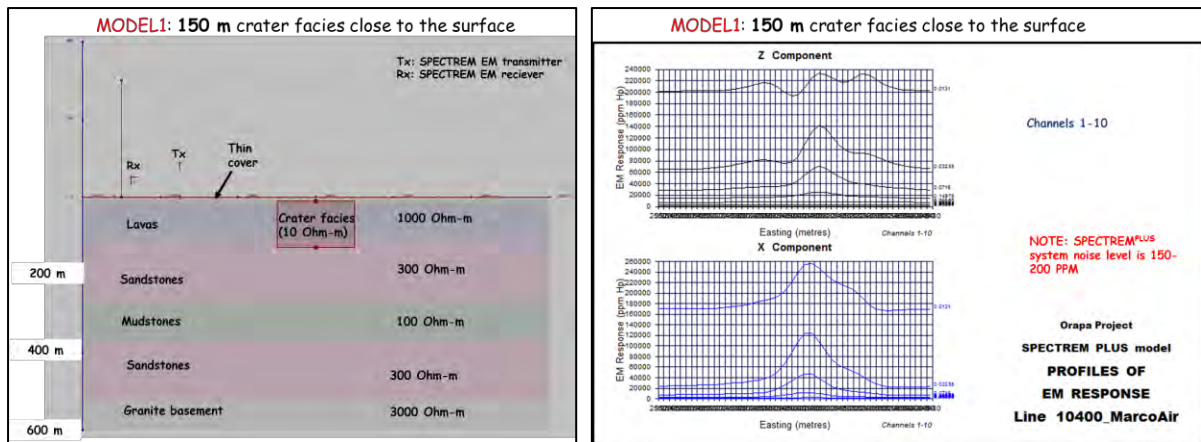


Figure 4 Typical Orapa-type kimberlite setting and the resulting SPECTREM PLUS EM responses, clearly showing that the target will be mapped

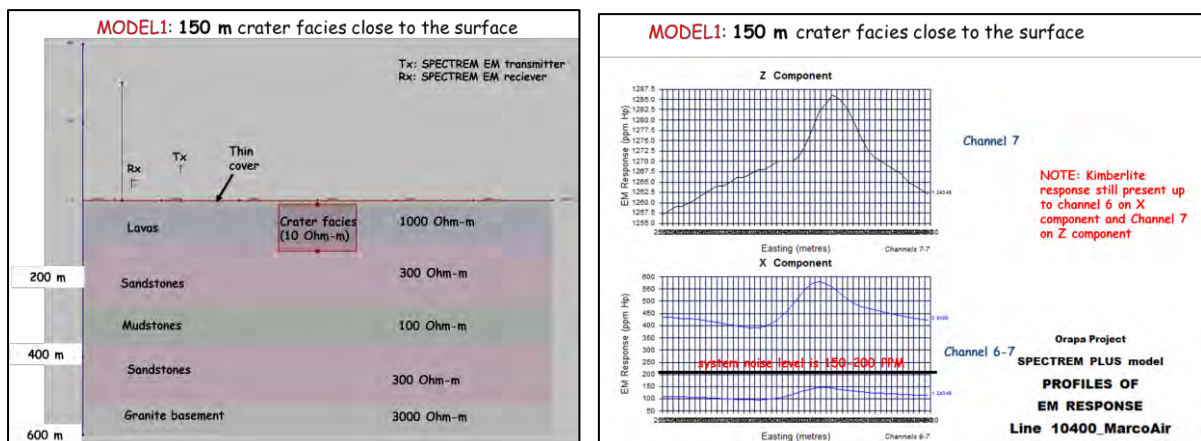


Figure 5 Typical Orapa-type kimberlite setting and the resulting SPECTREM PLUS EM responses, clearly showing that the target will be mapped at late channels

Discussion

The main results of the modelling is that the SPECTREM^{PLUS} system can be used to map kimberlite targets under Kalahari and Karoo cover at 300 m depth. The crater facies (RVK-A/B) has to be significantly more conductive than the Karoo sediments, which in many cases is the case.

Given that some kimberlite can exhibit non-magnetic signature, the results above indicate that AEM can be used to map those kimberlites that otherwise could be missed with AEM.

The results will be presented where SPECTREM^{PLUS} system is flown over an area in Botswana for kimberlite mapping. The non-magnetic targets are mapped relatively well where airborne magnetic could not.

References

- Leggatt, P (2015), Extending the range of conductivities recorded by the SPECTREM AEM system, Exploration Geophysics, 46, 136-139
- Ley-Copper, Munday T J (2012), Inversion of SPECTREM airborne electromagnetic data for groundwater assessment in outback Australia, American Geophysical Union Fall Meeting
- Pare, et al (2012), 3D inversion of SPECTREM and ZTEM airborne electromagnetic data from the Pebble Cu-Au-Mo porphyry deposit, Alaska, Exploration Geophysics, 43, 104-115



Letšeng Diamond Mine, Lesotho: Recent Advances in the Open Pit Geology of the Main Kimberlite Pipe

Mohapi Mohapi¹, Casey Hetman², Jock Robey³, Barbara Scott Smith⁴ and Teboho Nkotsi¹

¹ Letšeng Diamonds (Pty) Ltd., Letšeng-la-Terae, Lesotho, mohapim@letseng.co.ls

² SRK Consulting, Vancouver, BC, Canada, chetman@srk.com

³ Rockwise Consulting, Kimberley, South Africa, jjrobey@telkomsa.net

⁴ Scott-Smith Petrology Inc., North Vancouver, BC, Canada, barbara@scottsmithpetrology.com

¹ Letšeng Diamonds (Pty) Ltd., Letšeng-la-Terae, Lesotho, nkotsit@letseng.co.ls

Introduction

The Letšeng Diamond Mine comprises two adjacent steep-sided kimberlite pipes; Main and Satellite. The results of the recent geological evaluation work undertaken by Letšeng Diamonds within the open pit of the Main Pipe have revealed more complex geology than was previously recognised. The in-pit investigations included geological mapping of recent mining exposures, logging of ahead-of-face percussion drill chips and petrography of pit floor samples. The results of these investigations have been integrated with macrodiamond production data and drill core information to establish an updated geological model of the pipe that will be used for ongoing mining (Fig.1). Different phases of kimberlite within the pit floor exposures have been identified based on features such as contrasting textures, olivine populations, groundmass mineralogies, country rock xenolith contents, degree of xenolith to kimberlite reaction as well as mantle-derived indicator mineral abundances.

General Pipe Geology and History

The ~90 Ma Main Pipe has a surface expression of approximately 17.2 ha and was emplaced into ~1800-2000 m of Karoo basalts. These basalts dominate the observed xenolith population within the Main Pipe. The majority of the pipe infill is classified as Kimberley-type pyroclastic kimberlite (KPK) formerly referred to as tuffisitic kimberlite breccia (TKB; Scott Smith et al. 2013). Recent mapping has revealed the occurrence of resedimented volcanoclastic kimberlite (RVK) extending to the present pit floor at approximately 180 m below the original surface of the pipe. Historic mapping of surface exposures and underground tunnels as well as drill core logging during early evaluation activities undertaken by Rio Tinto Exploration (1967-1972) suggested eight kimberlite “varieties” (K1-K8; Nixon and Bloomer 1973). Mining by De Beers from 1977 to 1982 focused on the single phase of kimberlite called “K6” that forms only a small part of the Main Pipe. Letšeng Diamonds is currently mining all kimberlite phases within the Main Pipe.

Main Kimberlite Rock Types

The Main Pipe (Fig.1) is dominated by one phase of kimberlite, K1 (previously referred to as KMAIN), with the other significant pipe infills: K6, RVK-A, RVK-B and K4.

K1 comprises a relatively uniform KPK containing large megaxenoliths of basalt and a minor but distinctive population of small white garnet-bearing basement xenoliths as well as less common conspicuous mantle-derived garnet peridotite and MARID xenoliths. The country rock xenolith content of K1 is visually estimated as 30%. The pseudomorphed olivine macrocrysts typically range in size from 1-4 mm and display irregular shapes indicative of resorption. Other mantle-derived macrocrysts (indicator minerals) are absent to extremely rare. The olivine phenocrysts are characterised by complex growth aggregate shapes. Magmaclasts are conspicuous throughout K1; they are spherical and can have kernels of an olivine grain or a country-rock xenolith. Basalt megaxenoliths (BB) occur in the north and south of the pipe and, in some cases, are characterised by extensive brecciation and related carbonate and/or kimberlite veins (up to 2-5%).

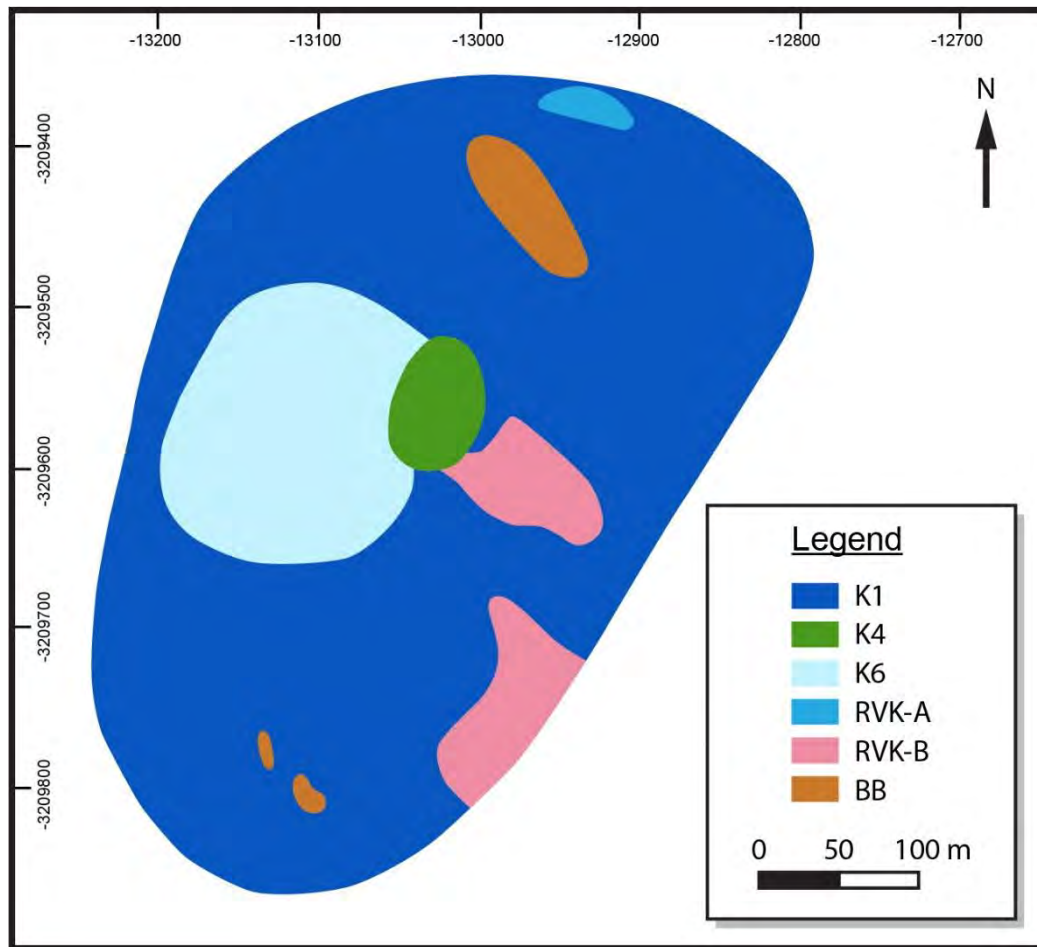


Figure 1: Schematic map of the Main Pipe geology (based on mining levels 3004 to 2864 masl).

Within areas previously considered to be K1, two new kimberlite units have been identified. Significant and apparently related remnants of diverse types of resedimented volcanoclastic kimberlite (RVK-A) occur along much of the pipe margin within the open pit. RVK-A pre-dates K1 indicating an earlier, and presumably initial, major pipe formation event. This pipe must have included an upper crater that remained open for a considerable period to allow gradual infilling by resedimentation of previously-erupted crater rim material. Different depositional processes resulted in contrasting varieties of RVK-A, some of which are well-bedded.

Another less well-defined RVK unit termed “RVK-B” is present in the 2017 pit floor and sidewalls. RVK-B contains conspicuous fresh basalt xenoliths that comprise about 30%-60% of the kimberlite as well as blocks of consolidated K1, indicating RVK-B postdates K1. The matrix is highly altered, very friable and pale brown in colour, with pseudomorphed olivine macrocrysts that are typically 1-4 mm in size. Although other mantle-derived macrocrysts are extremely rare, garnet peridotite and MARID xenoliths are observed. Magmaclasts are present but can be difficult to discern in hand specimen. The juvenile constituents in the matrix of RVK-B are similar to those in K1 and are presumed to be related.

K6 (Fig.2) is internally variable with textures ranging from segregationary coherent kimberlite to more pyroclastic textures. The occurrence of common conspicuous, fine to medium-grained mantle derived garnets clearly distinguishes K6 from other kimberlites within the Main Pipe. The garnets are dominated by peridotitic varieties often with thick kelyphite rims and orange eclogitic and megacrystic garnets are also abundant. Peridotite xenoliths are common. K6 contains 35% of country rock basalt xenoliths (visual estimate).

K4 (Fig.2) is volumetrically the least significant pipe infill of the Main Pipe and occurs as late stage irregular intrusions and thin sheets of hypabyssal kimberlite which cross cut both K6 and K1. Mantle-derived garnets are common as found in K6 but, in contrast, are usually completely kelyphitised.

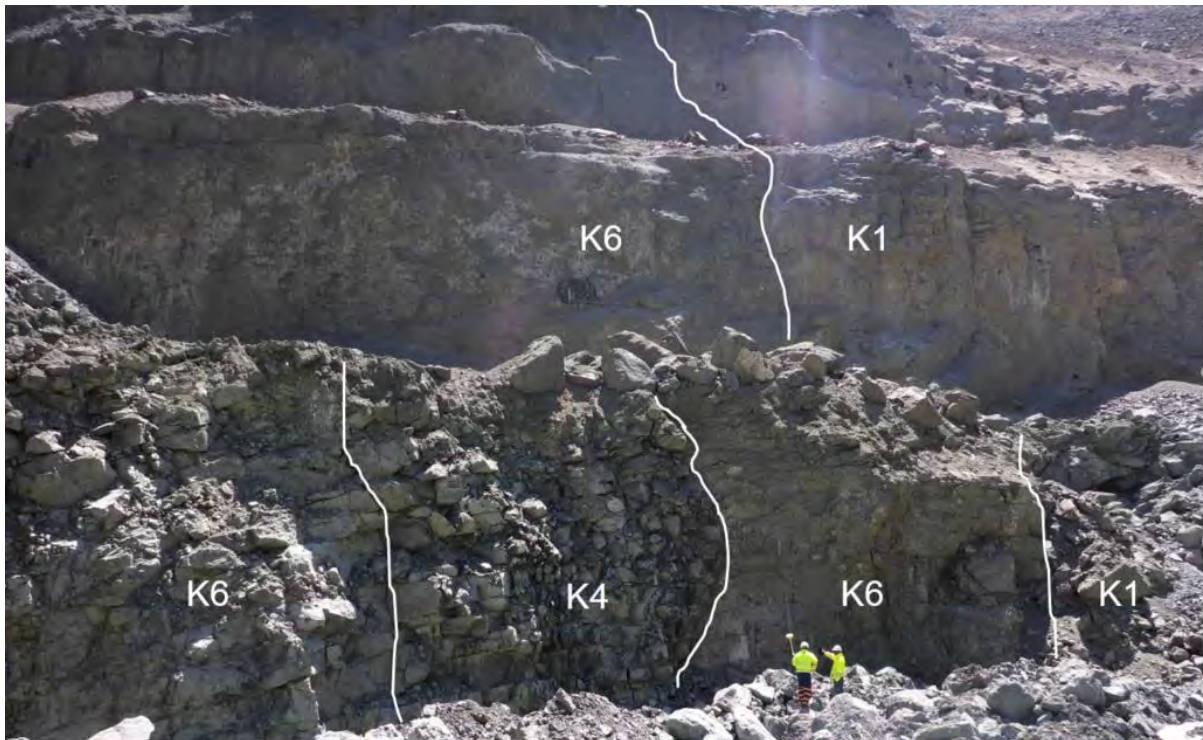


Figure 2: Main Pipe open pit exposures (east wall, 2864 masl) showing the relationship between K1, K6 and K4.

Conclusions

Mapping and petrography of the Main Pipe open pit has established an emplacement sequence that includes multiple episodes of volcanic eruption, intrusion and resedimentation. The first volcanic eruption formed a major pipe which must have included an upper crater that remained open for a considerable period during which infilling by resedimentation formed RVK-A. The latter occurs only as remnants along the upper pipe margins because it was cross-cut by K1, a massive homogeneous KPK resulting from a second major eruption. RVK-B postdates and overlies at least part of K1 and appears to be crater-fill composed of resedimented K1-derived material. Subsequently, K6 was emplaced as a smaller central pipe nested within K1 and infilled with inhomogeneous coherent to more pyroclastic kimberlite. Finally, small intrusion(s) of hypabyssal kimberlite, K4, cross cut both K6 and K1. Together, this shows that the Letšeng Main Pipe was formed by the emplacement of at least four distinct phases of kimberlite: pre-K1, K1, K6 and K4, apparently representing a progression of decreasing explosivity. The first two eruptions each had open craters that were infilled with RVK before subsequent events. The occurrence of KPK and crater-fill RVK is consistent with the estimated erosion at Letseng of 300-500 m and the southern African Hawthorne KPK-pipe model.

References

- Bloomer AG, Nixon PH (1973) The geology of Letšeng-la-terae kimberlite pipes. In: Lesotho Kimberlites (Ed. P.H. Nixon), Lesotho National Development Corporation. p.20-38.
- Scott Smith BH, Nowicki TE, Russell JK, Webb KJ, Mitchell RH, Hetman CM, Harder M, Skinner EMW, Robey JvA (2013) Kimberlite Terminology and Classification. Proceedings of 10th International Kimberlite Conference, Volume Two, Special Issue of the Journal of the Geological Society of India, Volume 2, 1-17. Springer India.

Oxidation of lithospheric mantle beneath Tanzania by melt reaction

Shao-Bing Zhang¹, Roberta Rudnick², Catherine McCammon³

1 CAS Key Laboratory of Crust-Mantle Materials and Environments, School of Earth and Space Sciences, University of Science and Technology of China, Hefei 230026, China

2 Department of Earth Science, University of California at Santa Barbara, Santa Barbara, CA 93106-9630, USA

3 Bayerisches Geoinstitut, Universität Bayreuth, D-95440 Bayreuth, Germany

Introduction

The oxidation state of the mantle is a key parameter in controlling the speciation of fluids and melt and can influence the mantle solidus and resulting melt properties. The variation of mantle oxygen fugacity has important influence on magma genesis, magma degassing, mantle metasomatic processes and the production of diamonds.

The existing data shows that most of the spinel peridotites at the top of the upper mantle yield oxygen fugacity within ± 2 log units relative FMQ buffer. The garnet peridotites from cratonic lithosphere reveal a general decrease in f_{O_2} with depth, which appears to result from the effect of pressure on the controlling Fe^{3+}/Fe^{2+} equilibria. This has been confirmed by a series of studies (e.g., McCammon and Kopylova, 2004; Lazarov et al., 2009; Stagno et al., 2013). On the other hand, the oxidation state of cratonic mantle is readily to be modified by fluid infiltration and melt reaction (e.g., Creighton et al., 2009; 2010). Both geophysical and geochemical evidence shows that the base of the Tanzania Craton has been modified by mantle plume. To understand how the oxygen fugacity of cratonic mantle has been affected by mantle plumes, we collected some garnet and spinel peridotites from the Tanzania Craton to study their oxidation state. The peridotite xenoliths were collected from the Labait volcano, which lies on the border between the Archean Tanzanian Craton and the Neoproterozoic Mozambique Belt.

Mineral chemistry and P-T calibration

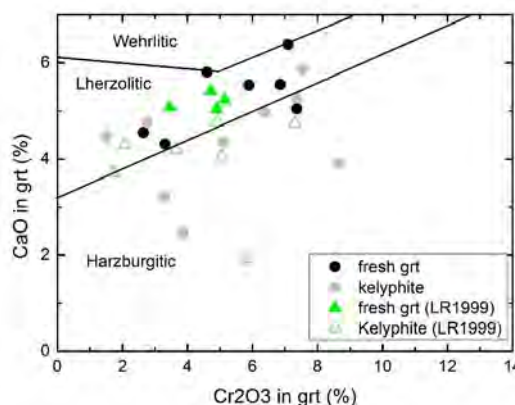


Fig. 1 CaO versus Cr_2O_3 in fresh garnet and kelyphite of peridotites from Labait, Tanzania.

There are both lherzilitic and harzburgitic in the collected xenolith peridotites. Many peridotites preserve the evidence of melt reaction or fluid infiltration: coarsening of clinopyroxene, reaction rims around clinopyroxene, veins with spinel or phlogopite, small patches enriched in clinopyroxene, phlogopite and/or rutile. Among the xenoliths, seven contain fresh garnet and another four contain kelyphite or completely decomposed garnet. Most of the fresh garnet grains are homogeneous in composition. Some garnet is replaced by kelyphite, fine-grained symplectic corona consists of spinel and orthopyroxene. The kelyphite rims around the fresh garnet has identical compositions with the fresh garnet except a few kelyphites have higher MgO and Cr_2O_3 but lower CaO. All the fresh garnet have

high CaO contents of 4.32-6.39 and high Cr₂O₃ contents of 2.64-7.36. They mainly fall into the lherzolitic garnet area (Fig. 1) although most of the host peridotite are actually harzburgite. The Mg# of fresh garnet range from 83.1 to 87.0. The Fo number of olivines from the garnet-bearing peridotites range from 89.2 to 92.0. The Mg numbers of orthopyroxene and clinopyroxene from the garnet-bearing peridotites are 89.9-92.4 and 88.5-91.4, respectively. Some olivines have rims with lower Mg# than the cores and adjacent orthopyroxene.

The six spinel-bearing peridotites have generally heterogenous spinel with Cr# ranging from 46.8 to 90.1. The orthopyroxenes in the spinel peridotites have lower CaO and Al₂O₃ than those in the garnet peridotites. The Mg numbers of orthopyroxene and clinopyroxene from the spinel peridotites are 90.8-93.3 and 90.4-93.2, respectively. The Fo number of olivines from the spinel peridotites range from 90.4 to 92.7.

The 11 garnet peridotites have equilibration temperatures of 1270-1400 °C and pressures of 4.1-5.8 GPa according to the barometer and thermometer of Brey and Kohler (1990). Most of the P-T data are similar with previous results of Lee and Rudnick (1999) except two samples with significantly higher pressure at 5.8 GPa (Fig. 2). They form an adiabatic decomposing trend. The 9 spinel peridotites gave Ca-in-opx temperatures (Brey and Kohler, 1990) of 930-1170 °C assuming a pressure of 4.5 GPa.

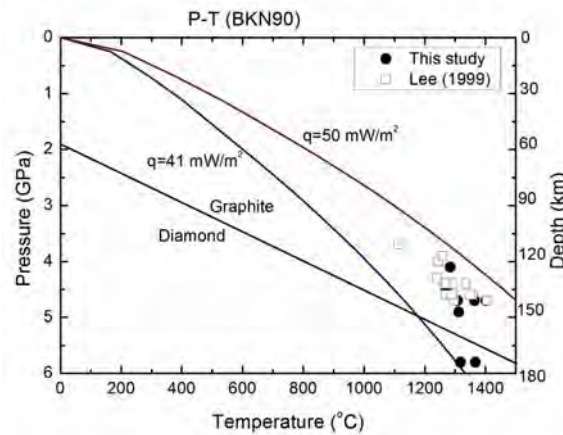


Fig. 2 Pressure and temperature estimates of Labait garnet-bearing peridotites calculated from barometer and thermometer of Brey and Kohler (1990). The results of Lee and Rudnick (1999) are also shown for comparison.

Garnet and spinel fO₂

Nine fresh garnets (six from this study and three from Lee and Rudnick, 1999) were analyzed by Mössbauer spectroscopy, yielding Fe³⁺/total Fe of 0.08±0.02 to 0.16±0.02. The corresponding oxygen fugacity range is -2.1±0.5 to -0.2±0.2 relative to the FMQ buffer, using the calibration of Stagno et al. (2013). Five spinels/chromites (one from this study and four from Lee and Rudnick, 1999) gave Fe³⁺/total Fe values of 0.32±0.04 to 0.9±0.04. The fO₂s obtained from these spinels are -1.8 to -0.2 relative to the FMQ buffer according to O'Neill and Wall (1987), or -0.5 to 0.4 relative to the FMQ buffer according to the calibration of Ballhaus et al. (1991). Generally, the spinel peridotites have oxygen fugacities that are consistent with those from the garnet peridotites. As shown in Fig. 3, these data show that the mantle lithosphere of the Tanzania craton is significantly more oxidized than that of the Kaapvaal craton and the Siberian craton at similar pressure (Stagno et al. 2013 and references therein). However, the Labait samples have similar oxygen fugacity to those of metasomatised xenoliths from the Slave craton (Creighton et al. 2010).

Garnet trace elements

LA-ICPMS trace element analyses on the garnets show variable REE patterns. Some are characterized by depletion in LREE, slow enrichment from MREE to HREE, which is similar to normal garnet REE patterns equilibrated with melt. Some garnets are depleted in LREE and flat from Sm to Lu. Some

garnets have sinusoidal or humped sinusoidal REE patterns with humps at Nd, Sm or Eu, following by a decreasing in MREE with or without a concave up in Yb and Lu. This can be interpreted by reaction of peridotites with melt with different compositions, or in different degrees (Stachel et al., 2004; le Roex and Class, 2016). We hypothesize that the oxidation of the Labait peridotites may result from melt reaction, where the melt is likely derived from the plume of the East African Rift. Although the cratonic mantle has not (yet) been destroyed by the mantle plume, the oxidation state of the entire lithospheric mantle beneath the Tanzania craton may have been reset by the plume-derived magmatism.

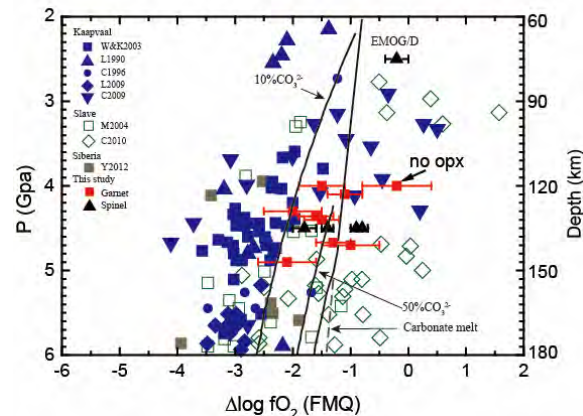


Fig. 3 $\log(f_{O_2})$ (relative to the FMQ buffer) calculated for garnet-bearing and spinel-bearing peridotites from Labait according to the calibration of Stagno et al. (2013). The results from Kaapvaal, Slave and Siberia are shown for comparison.

References

- Ballhaus C, Berry RF, Green DH (1991) High pressure experimental calibration of the olivine-orthopyroxene-spinel oxygen geobarometer: implications for the oxidation state of the upper mantle. *Contrib Mineral Petrol* 107(1):27-40
- BREY GP, KÖHLER T (1990) Geothermobarometry in Four-phase Lherzolites II. New Thermobarometers, and Practical Assessment of Existing Thermobarometers. *J Petrol* 31(6):1353-1378
- Creighton S, Stachel T, Eichenberg D, Luth RW (2010) Oxidation state of the lithospheric mantle beneath Diavik diamond mine, central Slave craton, NWT, Canada. *Contrib Mineral Petrol* 159(5):645-657
- Creighton S, Stachel T, Matveev S, Höfer H, McCammon C, Luth R (2009) Oxidation of the Kaapvaal lithospheric mantle driven by metasomatism. *Contrib Mineral Petrol* 157(4):491-504
- Frost DJ, McCammon CA (2008) The Redox State of Earth's Mantle. *Annu Rev Earth Planet Sci* 36(1):389-420
- Lazarov M, Woodland AB, Brey GP (2009) Thermal state and redox conditions of the Kaapvaal mantle: A study of xenoliths from the Finsch mine, South Africa. *Lithos* 112, Supplement 2(0):913-923
- le Roex A, Class C (2016) Metasomatic enrichment of Proterozoic mantle south of the Kaapvaal Craton, South Africa: origin of sinusoidal REE patterns in clinopyroxene and garnet. *Contrib Mineral Petrol* 171(2):14
- Lee C, Rudnick R (1999) Compositionally stratified cratonic lithosphere: petrology and geochemistry of peridotite xenoliths from the Labait tuff cone, Tanzania. In: *Proceedings of the 7th international Kimberlite conference*, vol., pp 503-521
- McCammon C, Kopylova MG (2004) A redox profile of the Slave mantle and oxygen fugacity control in the cratonic mantle. *Contrib Mineral Petrol* 148(1):55-68
- O'Neil HSC, Wall VJ (1987) The Olivine-Orthopyroxene-Spinel Oxygen Geobarometer, the Nickel Precipitation Curve, and the Oxygen Fugacity of the Earth's Upper Mantle. *J Petrol* 28:1169-1191
- Stachel T, Aulbach S, Brey GP, Harris JW, Leost I, Tappert R, Viljoen KS (2004) The trace element composition of silicate inclusions in diamonds: a review. *Lithos* 77(1-4):1-19
- Stagno V, Ojwang DO, McCammon CA, Frost DJ (2013) The oxidation state of the mantle and the extraction of carbon from Earth's interior. *Nature* 493(7430):84-88

New and revised Crustal and Upper mantle terraine boundaries in Southern Africa: Implications for kimberlite exploration and emplacement

David Khoza¹

¹*Spectrem Air PTY LTD, davidk@spectrem.co.za*

Introduction

It is well appreciated that crustal and lithospheric structures affect the emplacement of diamondiferous kimberlites. Certainly in Southern Africa, the majority of kimberlite clusters appear to be located in close proximity to crustal structures defined from regional magnetic data and deep probing electromagnetic data.

In this work, a new crustal and upper mantle lithospheric structure map beneath Archean and Proterozoic terraines is presented. We use deep probing magnetotelluric data to map the electrical lithosphere up to depths of over 300 km. The new map reveals previously unknown lithosphere in places such as the Limpopo, Kaapvaal and Zimbabwe terrains and provides a targeting tool in these enigmatic terraines.

While the presence of hydrous minerals, which affect the strength of the lithosphere, was not the primary focus of the current study the presence of thick, resistive, cratonic material in some of the terraines point to rigid lithosphere that was not previously documented. A combination of paleomagnetic data, electrical structures and ages from kimberlite xenoliths could be used to provide constraints in placing the mapped terranes in the geo-tectonic framework.

SAMTEX MT data for lithospheric mapping

The magnetotelluric method is an electromagnetic (EM) sounding technique that has evolved rapidly since its first theoretical description in the 1950s. By measuring the time variations on the surface, of the horizontal electric (E_x , E_y) and horizontal and vertical magnetic (H_x , H_y and H_z) fields induced in the subsurface, we can derive the lateral and vertical subsurface variations of electrical resistivity.

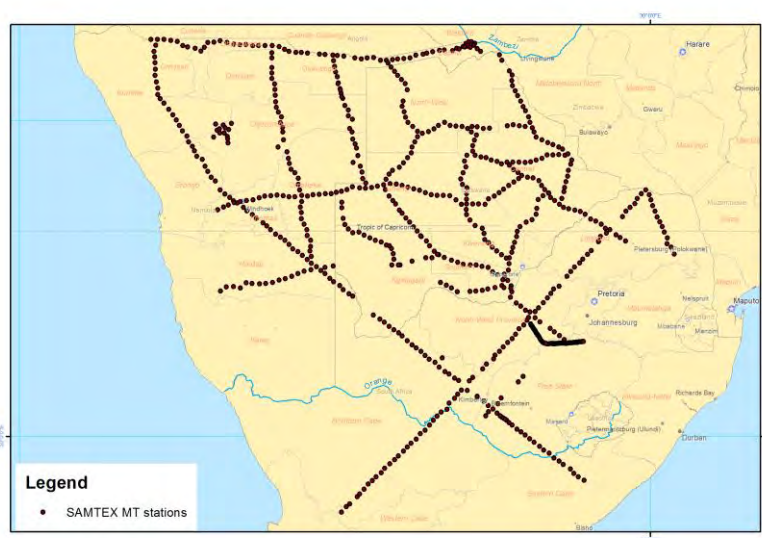


Figure 1 The location of the SAMTEX magnetotelluric station where broadband MT data were collected in Botswana, Namibia and South Africa

In Southern Africa, we have acquired broadband (periods from 0.001 s to 8000 s) and long period (15 s to over 10,000 s) magnetotelluric data as part of the SAMTEX project (Figure 1). More than 750 stations of data were collected in Namibia, Botswana and South Africa over four field seasons along

various profiles from 2003 to 2008, with station spacings of approximately 20 km and 60 km for broadband and long period data, respectively. The orientations of the profiles were chosen to transect over specific geological features of interest.

Crustal mapping (Limpopo and Orapa kimberlite field)

The data over Limpopo belt and Kaapvaal craton were processed and modelled and the result are summarised in the 3D block below (Figure 2). The crust in the southern part of the model is dominated by resistive features in the South Marginal Zone of the Limpopo belt and the Kaapvaal craton. There is a significant resistivity break, up to 20 km in lateral distance, in the model that correlates spatially with the Soutpansberg basin. The location of the crustal PTSZ is characterized by a conductive signature.

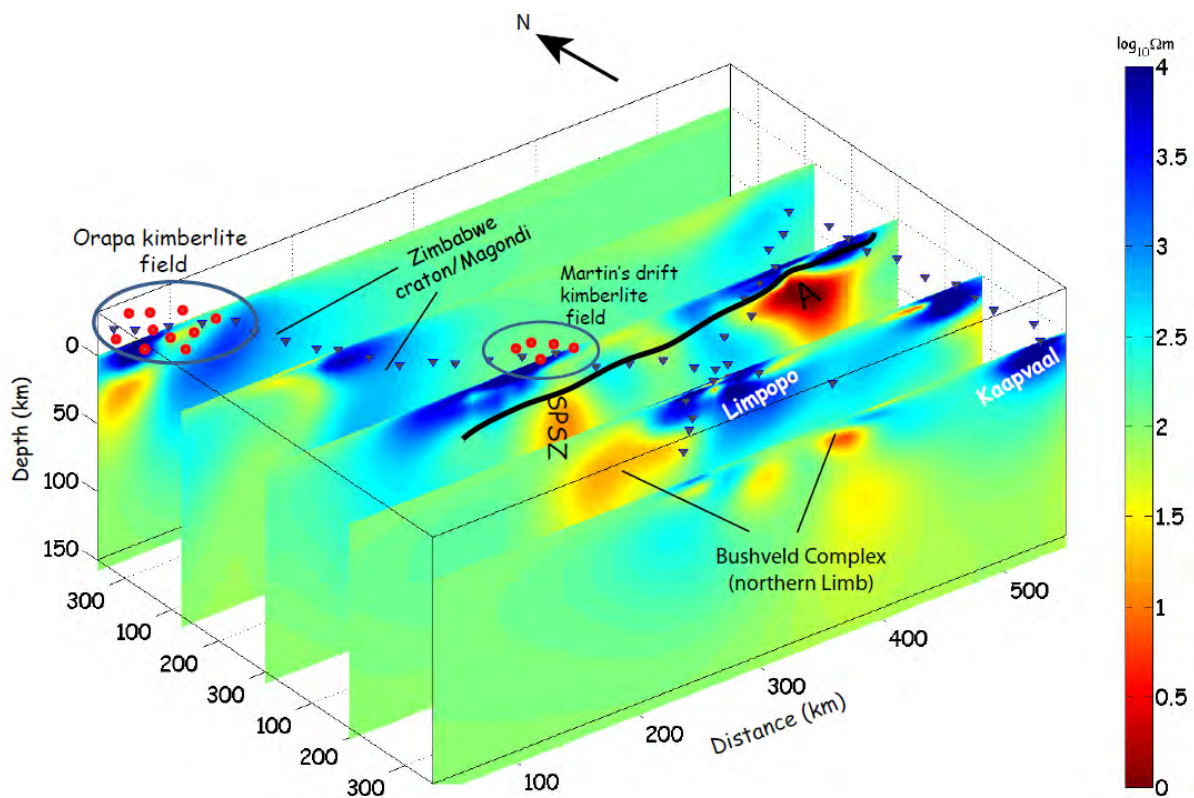


Figure 2 3D E-W perspective view showing the variation in resistivity laterally and depth across the Limpopo belt. The location of the Orapa and Martin's Drift kimberlite fields are projected. The dark solid line shows the approximate trace of the Palala-Tshipise-Sunnyside Shear system. SPSZ: Sunnyside-Palala Shear Zone.

The locations of the Martin's drift and Orapa kimberlite clusters are projected on the model and the lithosphere beneath it is characteristically resistive and thick (Figure 3). This perhaps explains the locations of these clusters being on the margins of deep crustal structures.

These data support the overriding model that diamondiferous kimberlite intrusions tend to occur on the margins of cratons.

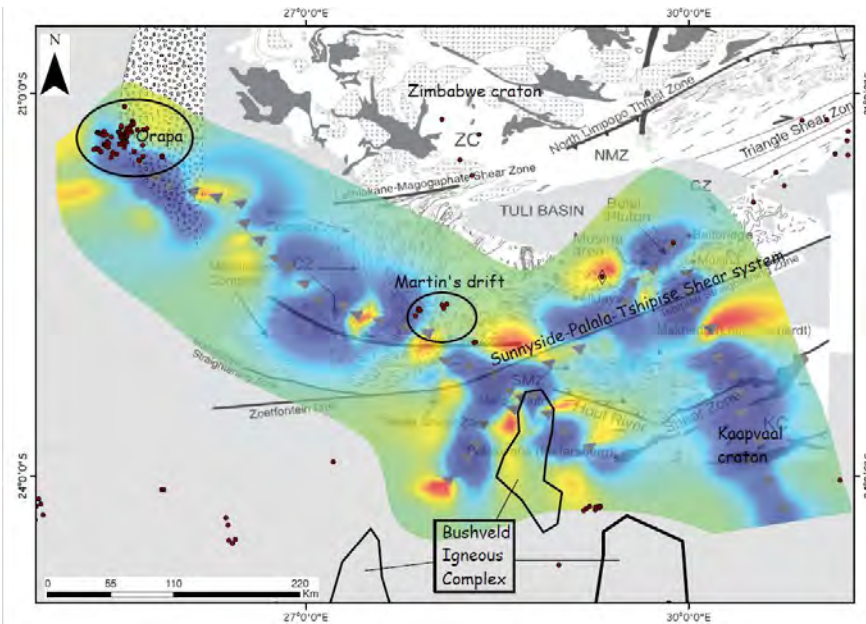


Figure 3 Crustal depth section (10 km) derived from 3D inversion model. The section is overlain on the geological map of the Limpopo belt (after Kramers et al., 2011). The main features are highlighted, including the locations of the Orapa and Martin's drift kimberlite fields.

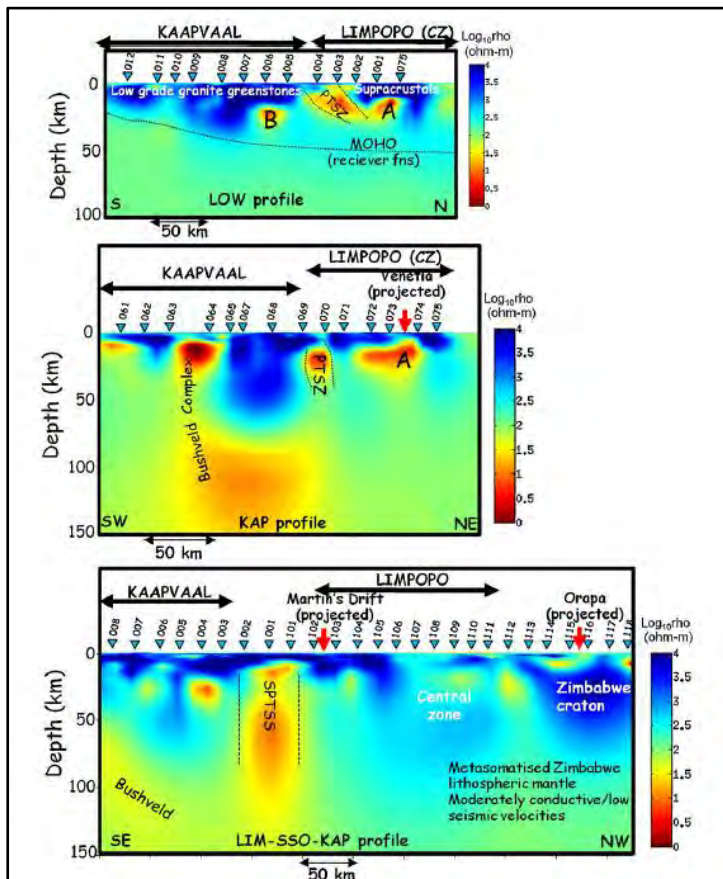


Figure 4 Three MT profiles derived from 3D inversion model. The Moho depth was derived from the seismic receiver function study of Gore et al. (2010) (note the profile depth is 100 km). The location of Venetia kimberlite is projected on the KAP profile and is shown as red arrow. Similarly, the Orapa and Martin's Drift kimberlite clusters are shown on the LIM-SSO profile PTSZ: Palala-Tshipise Shear Zone, SPTSS: Sunnyside-Palala-Tshipise Shear System.

References

Gore, J., James, D.E., Zengeni, T.G., Gwavava, O., 2010. Crustal structure of the Zimbabwe craton and the Limpopo belt of Southern Africa: new constraints from seismic data and implications for its evolution. *South African Journal of Geology* 112, 213–228.

Kramers, J.D., McCourt, S., Roering, C., Smit, C.A., van Reenen, D.D., 2011. Origin and evolution of Precambrian high-grade Gneiss terranes, with special emphasis on the Limpopo Complex of Southern Africa. In: van Reenen, D.D., Kramers, J.D., McCourt, S., Perchuk, L.L (Eds.), *Geological Society of America Memoirs*, vol. 207. Geological Society of America, pp. 311–324

Khoza, D.T., Jones, A.G., Muller, M.R., Webb, S.J., 2011. The electrical lithosphere in Archean cratons: examples from Southern Africa. In: *AGU Fall Meeting Abstracts*, p. 2101.

Geology of KX36 Kimberlite, Central Botswana

S. Lobatlamang, and M. T. Mokgaotsane,
Petra Diamonds Botswana (Pty) Ltd

sebanka.lobatlamang@petradiamonds.com, maureen.mokgaotsane@petradiamonds.com

Introduction

KX36 kimberlite pipe is situated in the southeastern part of Central Kalahari Game Reserve (CKGR), Botswana, at least 60 km from the known Gope and Kikao kimberlite fields (Figure 1). The kimberlite appears to be the only one in the area, a very unusual scenario as most kimberlites occur in clusters. KX36 kimberlite is a single lobed pipe with a surface area of approximately 5ha with circular – subcircular plan views and steep margins. The kimberlite was emplaced into the Karoo Supergroup, which comprised the older sedimentary rocks (300 – 185 Ma) overlain by the flood basalts (185Ma). The Karoo Supergroup rocks are overlain by approximately 80m of Kalahari Group sediments.

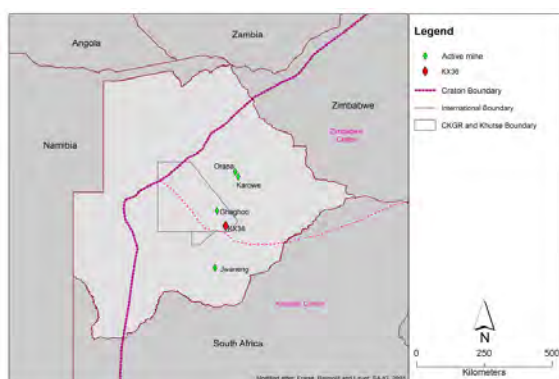


Figure 1: Location Map showing the position of KX36 kimberlite in the Central Kalahari Game Reserve, Botswana.

General Kimberlite Geology

KX36 pipe is dominated by three main facies/units of kimberlite, which have been interpreted as (a) Black 1 Coherent Kimberlite (Black 1 CK), (b) Black 2 Coherent Kimberlite (Black 2 CK) and (c) Green Coherent Kimberlite (Green CK). In general, the difference between the different units

within the kimberlite is very subtle. All the three units have the same type of mantle peridotites (constituting less than 1% in each unit) and crustal xenoliths, with the latter averaging 10% across all the units (in hand specimen).

Black 1 Coherent Kimberlite (Black 1 CK)

Black 1 coherent kimberlite is described as a greyish black, coherent, macrocrystic kimberlite with distinctive red, altered olivine macrocrysts. The kimberlite is also characterised by pervasive secondary sub-horizontal calcite veining which tends to break into thin discs along these veins (see figure 2 below). Downhole geophysical logging shows this unit to be relatively magnetic and highly conductive.

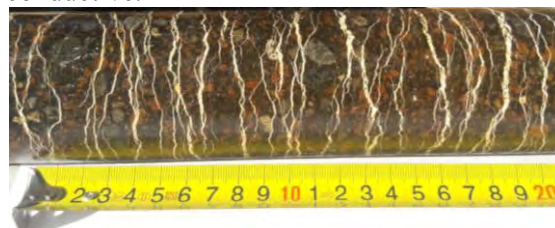


Figure 2: Core picture showing Black 1 coherent kimberlite from KX36 Kimberlite.

Black 2 Coherent Kimberlite (Black 2 CK)

Black 2 coherent kimberlite is also a greyish black, highly olivine macrocrystic kimberlite with the olivines showing a relatively lower degree of alteration compared to Black 1 coherent kimberlite (see figure 3 below). This unit is more competent than Black 1 coherent kimberlite and does not seem to break into thin discs even when intensely veined by secondary calcite. Downhole geophysical logging shows Black 2 coherent kimberlite to be relatively magnetic and has a higher density (similar to that of basalt) than the Black 1

coherent kimberlite. Black 2 and Black 1 coherent kimberlites are generally similar and may actually be one and the same thing except for the subtle differences that may be attributed to secondary features.

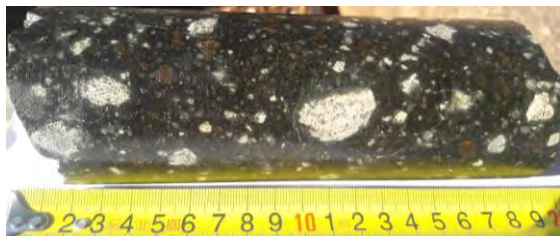


Figure 3: Core picture Showing Black 2 coherent kimberlite from KX36 Kimberlite.

Green Coherent Kimberlite (Green CK)

Green coherent kimberlite is a green grey competent, highly macrocrystic coherent kimberlite with a distinctive green matrix and large brown olivines (see figure 4 below). This unit is generally conductive and less magnetic than Black 1 and Black 2 coherent kimberlites .

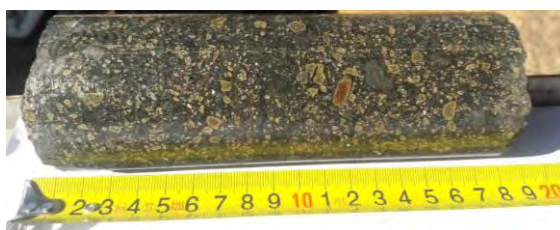


Figure 4: Core picture Showing Green coherent kimberlite from KX36 Kimberlite.

Mantle Xenoliths

Peridotite mantle xenoliths, mainly garnet lherzolite and garnet harzburgite (see figure 5) can be observed in all types kimberlite facies with the latter slightly more abundant. In general peridotite mantle xenoliths constitute not more than 1% in each kimberlite type.

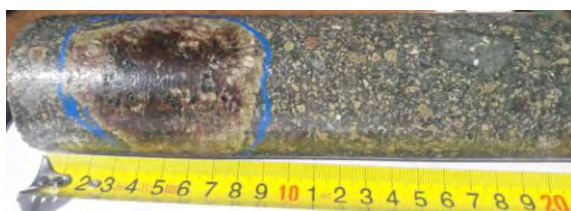


Figure 5: Core picture showing garnet harzburgite in Green coherent kimberlite from KX36 Kimberlite.

Crustal Xenoliths

Crustal xenoliths comprise basement

granitoids, rare feldspar porphyry, marid and basalt, which is the most common crustal xenolith within KX36 kimberlite. Crustal xenoliths abundance as counted on total core is generally not more than 10% with an average size of about 5cm. Basalt xenoliths of up to 1metre have been observed in places. It is worth noting that there is no correlation between crustal xenolith abundance, type or size between the different kimberlite facies.

KX36 Petrography

A total of 55 core samples from KX36 kimberlite were sent to Dr. Mike Skinner for petrographic analysis between 2008 and 2012. KX36 kimberlite can generally be described as an ilmenite- deficient Group 1, macrocrystic hypabyssal phlogopite - montecellite kimberlite. The kimberlite comprises numerous and highly complex textures on a microscopic scale, as is typical of hypabyssal kimberlites. It is also crosscut by secondary carbonate veins. The country rock xenoliths are usually altered to varying degrees. Typically, the macrocrystic olivine is completely altered, but the serpentinized pseudomorphs after olivine clearly preserve the original macrocrystic texture. The groundmass of the kimberlite is typically fine-grained, crystalline, and invariably micaceous (phlogopite). Based on the grain size of the groundmass (euhedral opaque spinels up to 0.07 mm), this kimberlite was petrographically rated as high interest with respect to diamond potential.

Petrographic analysis revealed the existence of two principal types of kimberlite facies that can be classified as coherent (hypabyssal) macrocrystic kimberlite and coherent (transitional) macrocrystic kimberlite. The matrix varies from uniform to segregation-textured and comprises mainly of calcite and serpentine, with minor chlorite.

Hypabyssal kimberlite (Black 1 and Black 2 CK)

The most common type of the hypabyssal facies is a variably altered monticellite-phlogopite kimberlite with variable proportions of country rock xenoliths ranging from 8 to 20 vol.%, far more than what is observed in hand specimen, indicating that

there are abundant very small (1mm) crustal xenoliths.

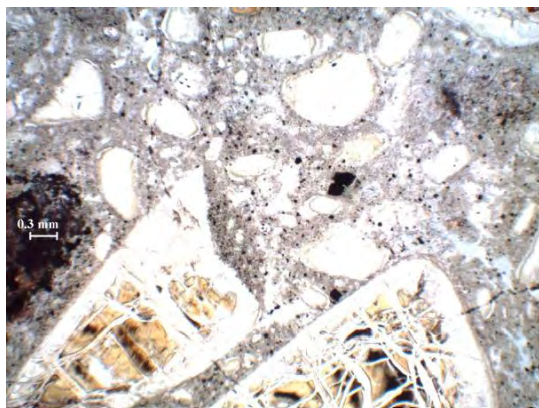


Figure 6: photomicrograph – serpentized olivine grains and dark basalt xenoliths set in a uniform groundmass consisting of fine green monticellite pseudomorphs, opaque spinels and serpentine (white).

Transitional Kimberlite (Green CK)

Two subtypes of transitional hypabyssal kimberlite have been identified in KX36. The one type, which is dominant, is characterized by segregatory structures, the presence of common to abundant microlitic diopside, and relatively abundant country rock xenoliths (from 16 to 28 vol.%) (see figure 7). The other transitional type is characterized by prominent, larger sized, globular segregatory structures, with no microlitic diopside, and few country rock xenoliths (see figure 8).

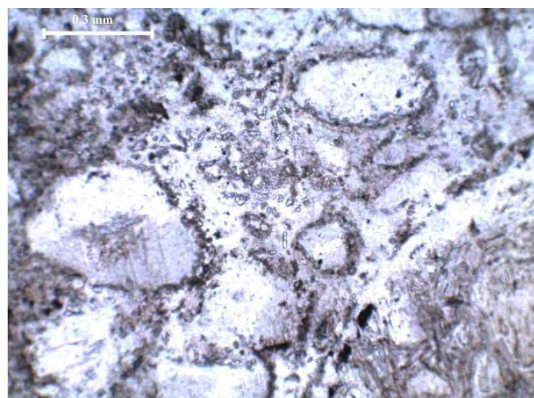


Figure 7: Altered olivine grains mantled by very

fine grained microlitic diopside that also occurs within the general groundmass.

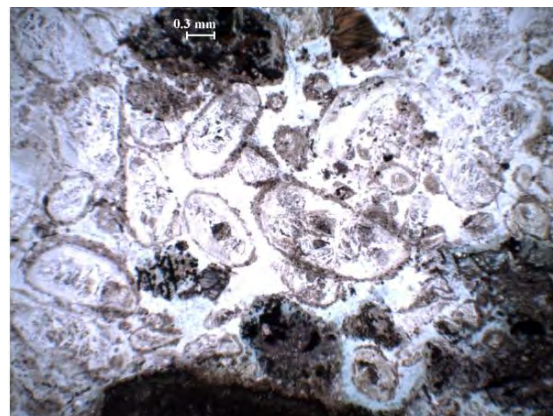


Figure 8: “Globules” of altered olivine grains and dark basalt xenoliths mantled by fine groundmass segregated by fine clear serpentine – Globular segregatory texture.

Conclusions

Petrographic analysis reveals that KX36 comprises two major kimberlite types. The first major type is the Black Coherent hypabyssal type that is essentially a montecellite-phlogopite kimberlite. In hand specimen, Black coherent kimberlite is further subdivided into two subtypes - Black 1 coherent kimberlite and Black 2 coherent kimberlite, where Black 2 coherent kimberlite is the less altered type. The second major type is the transitional Green coherent kimberlite, distinguished in thin section by having a segregatory texture with common to abundant microlitic diopside.

Black 1 coherent kimberlite appears to be mostly restricted to the top part of the kimberlite and seems to be volumetrically small compared to Black 2 and Green coherent kimberlite. It is also evident that Green coherent kimberlite is a later phase as it appears to cut through Black 2 coherent kimberlite.

REFERENCES

- Carney, J.N., Aldiss, D.T., and Lock, N.P. (1994). The geology of Botswana. *Bulletin 37*. Geological Survey of Botswana.
- Robey, J (2014). *KX36 – Logging and petrography: Final Report*.
- Skinner, E.M.W. (2013). *Petrography of drill core from KX36. Grahamstown. South Africa*.



Geochemical evidence for carbonated metasomatite as the mantle source of Cenozoic alkali basalts in western Qinling, China

Li-Qun Dai, Fei Zheng, Zi-Fu Zhao, Yong-Fei Zheng

University of Science and Technology of China, Hefei, China, lqdai@ustc.edu.cn

Introduction

Mantle peridotite was considered as the source lithology of alkali basalts. However, experimental petrology indicates that partial melting of peridotite produces different basaltic melts from natural alkali basalts in some major elements. For example, the experimental products show significantly lower CaO and higher Al₂O₃ contents than natural alkali basalts (e.g., Hirschmann et al., 2003; Dasgupta et al., 2007). Instead of the normal peridotite, three major metasomatic lithologies such as carbonated peridotite, pyroxenite and hornblendite have been suggested as the mantle source of alkali basalts (e.g., Hirschmann et al., 2003; Dasgupta et al., 2007; Pilet et al., 2008). Nevertheless, experimentally produced basaltic melts from these metasomatic lithologies also fail to match all the features of natural alkali basalts. The mantle lithology for alkali basalts still remains enigmatic. In addition, the origin of these metasomatic lithologies for alkali basalts also remains controversial.

During the subduction of oceanic crust, the recycling of carbonate-bearing sediment at convergent plate margins has played an important role in carbonatitic metasomatism and possible global carbon cycling. In particular, carbonated peridotite has received increasing attention due to its petrogenetic link to alkali basalts. Alkali basalts above ancient subduction zones provide us with an excellent opportunity to investigate the recycling of the subducted crustal materials, and the petrogenesis of alkali basalts. In this study, a combined study of whole-rock major-trace elements and Sr-Nd-Hf isotopes was carried out for Cenozoic alkali basalts in western Qinling orogen of China, which are associated with carbonatite. The results provide insights not only into the slab-mantle interaction in the ancient subduction zone, but also into the mantle lithology for the alkali basalts.

Geochemical results

Alkali basalts from Qinling orogen are all silica-undersaturated alkali basalts. They have low contents of SiO₂ (36.9-40.8 wt.%) and Al₂O₃ (7.3-10.2 wt.%) but high CaO (13.5-14.5 wt.%), with high CaO/Al₂O₃ ratios of 1.42 to 2.19. In the chondrite-normalized REE diagram (Fig. 1a), all the basalts show enrichment in LREE with (La/Yb)_N ratios of 37.9 to 53.0, and without profound Eu anomalies. In the primitive mantle-normalized spidergram (Fig. 1b), they exhibit enrichment in Ba, Nb and Ta but depletion in Rb, K, Pb, Zr and Hf, resembling mafic melts derived from partial melting of hornblendite and hornblendite + peridotite to some extent (Pilet, et al., 2008). The significant depletion in Rb, K, Pb, Zr, Hf and Ti is similar to the trace element patterns of oceanic and continental carbonatites derived from partial melting of carbonated mantle sources. The alkali basalts show low whole-rock (⁸⁷Sr/⁸⁶Sr)_i ratios of 0.7041 to 0.7060, and positive ε_{Nd}(t) values of 3.4 to 4.2 and ε_{Hf}(t) values of 5.8 to 7.2.

Discussion

For the study of basalt petrogenesis, field and petrographic observations must be combined with major-trace element and stable-radiogenic isotope compositions to make an integrated interpretation. The studied alkali basalts are associated with carbonatite lava in the field. Carbonate globules and irregular patches are also observed under a microscope. These features suggest the role of a carbonated mantle source in generating the West Qinling alkali basalts. For major elements, the alkali basalts exhibit low SiO₂, but high MgO and CaO with high CaO/Al₂O₃ ratios, requiring their derivation from partial melting of fertile ultramafic rocks. For trace elements, the alkali basalts are enriched in incompatible elements such as LREE, Ba and Sr, but depleted in Rb, K, Zr, Hf, and Ti. Such trace element features are significantly different from normal MORB, but similar to carbonatite to some extent (Figs. 1a and 1b).

Thus, these features probably indicate the involvement of carbonate-bearing crustal material in their source region. For radiogenic isotope compositions, they generally exhibit low $(^{87}\text{Sr}/^{86}\text{Sr})_i$ ratios, and positive $\epsilon_{\text{Nd}}(t)$ and $\epsilon_{\text{Hf}}(t)$ values, suggesting contribution from juvenile crustal components. Taken together, all these geochemical features indicate that the alkali basalts would be originated from a kind of ultramafic lithologies, which is fertile in lithochemistry, enriched in carbonate composition and melt-mobile incompatible trace elements, but depleted in radiogenic isotopes.

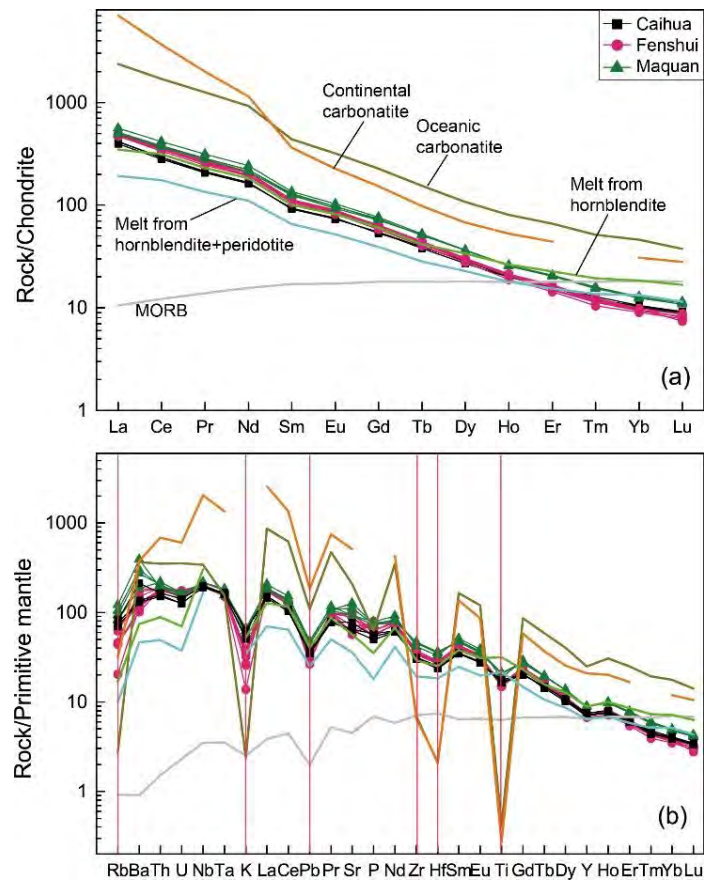


Figure 1: Chondrite-normalized REE patterns (a) and primitive mantle-normalized trace element distribution patterns (b) for alkali basalts from West Qinling. Also compared are the average oceanic and continental carbonatites compositions (Hoernle et al., 2002; Bizimis et al., 2003); melts from hornblende and hornblende + peridotite (Pilet et al., 2008).

Because carbonatitic metasomatism would increase the $(\text{La}/\text{Yb})_N$ ratios of mantle sources and leads to strong depletion in high field strength elements (Coltorti et al., 1999). $(\text{La}/\text{Yb})_N$ together with Ti/Eu ratios can be taken as useful indicators of carbonatitic metasomatism. As shown in Fig. 2a, the West Qinling alkali basalts show significantly higher $(\text{La}/\text{Yb})_N$ ratios and lower Ti/Eu ratios than normal MORB, suggesting the carbonatitic metasomatism of their source region. The carbonatitic metasomatism also increases the CaO contents and $\text{CaO}/\text{Al}_2\text{O}_3$ ratios of mantle peridotite, and thus those of its derived basaltic magma. The high $\text{CaO}/\text{Al}_2\text{O}_3$ ratios, and the positive correlation between $\text{CaO}/\text{Al}_2\text{O}_3$ and $(\text{La}/\text{Yb})_N$ ratios (Fig. 2b), also suggest significant contribution of carbonatitic component to their origin.

The carbonate melts are also characterized by high Zr/Hf , Nb/Ta and Ce/Pb ratios, but low Hf/Sm ratios. As illustrated in Figs. 2c-2f, the West Qinling alkali basalts show significantly higher Zr/Hf , Ce/Pb and Nb/Ta ratios but lower Hf/Sm ratios than normal MORB, and plot toward the average oceanic and continental carbonatites (Hoernle et al., 2002; Bizimis et al., 2003). There are also correlations between $(\text{La}/\text{Yb})_N$ versus Zr/Hf and Ce/Pb ratios, and $\text{CaO}/\text{Al}_2\text{O}_3$ versus Hf/Sm and Nb/Ta ratios. These features suggest that the alkali basalts record the carbonatitic metasomatism.

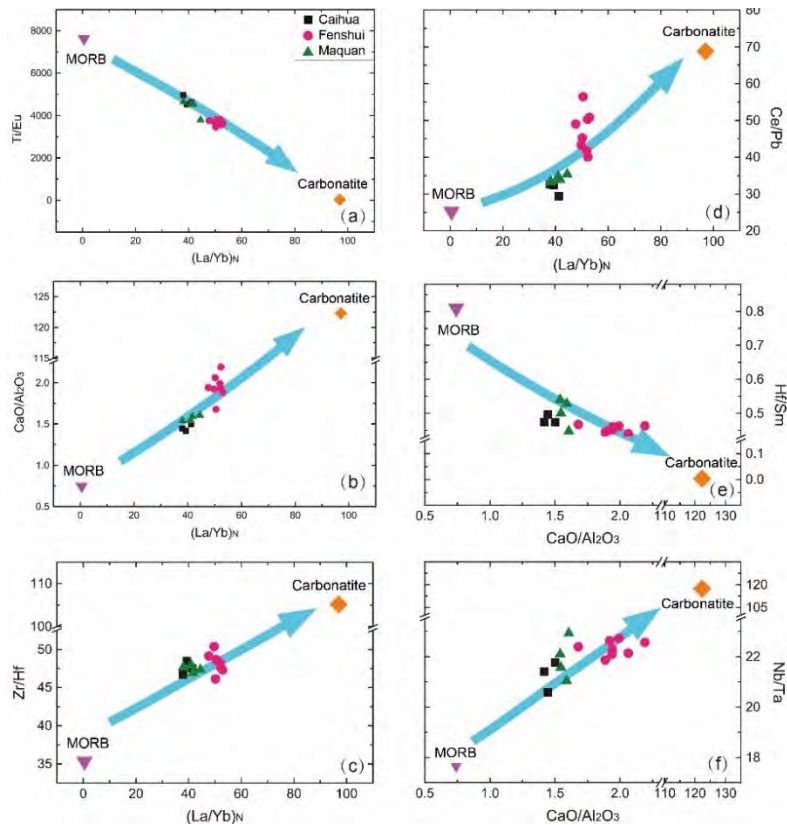


Figure 2: Plots of $(La/Yb)_N$ versus Ti/Eu (a), CaO/Al_2O_3 (b), Zr/Hf (c) and Ce/Pb ratios (d) ratios, as well as CaO/Al_2O_3 versus Hf/Sm (e) and Nb/Ta ratios (f) for alkali basalts from West Qinling, showing carbonatitic metasomatism.

In summary, the West Qinling alkali basalts were originated from carbonated mantle source. A comparison of major-trace elements in the basalts with some representative mantle melts confirms that their mantle lithologies are composed of the carbonated peridotite and hornblendite. Such ultramafic metasomatites would be generated by reaction of the depleted mantle peridotite with anatectic melts, locally rich or poor in carbonate, that originated from the Palaeotethyan oceanic crust in a subduction channel. As carbonation significantly depresses the solidus of mantle lithology, these ultramafic metasomatites are more susceptible to partial melting for the production of alkali basalts.

References

- Bizimis, M., Salters, V.J.M., Dawson, J.B., 2003. The brevity of carbonatite sources in the mantle: evidence from Hf isotopes. *Contributions to Mineralogy and Petrology* 145, 281-300.
- Coltorti, M., Bonadiman, C., Hinton, R.W., Siena, F., Upton, B.G.J., 1999. Carbonatite metasomatism of the oceanic upper mantle: evidence from clinopyroxenes and glasses in ultramafic xenoliths of Grande Comore, Indian Ocean. *Journal of Petrology* 40, 133-165.
- Dasgupta, R., and Hirschmann, M. M., 2010. The deep carbon cycle and melting in Earth's interior. *Earth and Planetary Science Letters* 298, 1-13.
- Hirschmann, M.M., Kogiso, T., Baker, M.B. and Stolper, E.M., 2003. Alkalic magmas generated by partial melting of garnet pyroxenite. *Geology* 31, 481-484.
- Hoernle, K., Tilton, G., Le Bas, M.J., Duggen, S., Garbe-Schonberg, D., 2002. Geochemistry of oceanic carbonatites compared with continental carbonatites: mantle recycling of oceanic crustal carbonate. *Contributions to Mineralogy and Petrology* 142, 520-542.
- Pilet, S., Baker, M.B. and Stolper, E.M., 2008. Metasomatized lithosphere and the origin of alkaline lavas. *Science* 320, 916-919.



Generation of 3D Kimberlite Pipe Models for Resource Classification and Mine Planning: Procedures, Data Sources and Guidelines.

C.M. Hetman, M.D. Diering and W. Barnett

SRK Consulting, Canada: chetman@srk.com, mdiering@srk.com, wbarnett@srk.com

Introduction

Traditional sampling, data handling and 3D geological modelling procedures favored by professionals for various mineral commodities in most cases do not apply to primary diamond deposits. Kimberlite pipes, even within small clusters may be characterized by contrasting external pipe morphologies, different pipe infills and a variable distribution of the mineralization. Many pipes include zones that do not contain economic quantities of diamonds. The unique and highly variable geology displayed by most kimberlites, combined with very low diamond contents even within the highest-grade deposits makes kimberlite evaluation challenging. Structured and systematic geology development combined with representative sampling for diamonds is required in order to establish reliable 3D models that may be used for resource classification and mine planning purposes.

This contribution is intended to serve as a practical guideline for the development of 3D models used for the evaluation of a primary diamond deposit within a pipe. Geological development, sampling and modelling procedures are very different for kimberlite sheet systems and will not be addressed here. The procedures and guidelines presented by the authors encapsulate the methodology and procedures followed for the development of 3D models used in support of multiple kimberlite resource classifications and mine plans globally over the last two decades. It must be appreciated that each volcanic complex is different and therefore flexibility with the application of the geological development, sampling and modelling principles applied can be expected.

Geology Development Approach

The foundation of any 3D pipe model is the geology. Initially the determination of the external pipe shell which contains the mineralization is established. Following this, the internal geology of the pipe is developed, which involves the detailed description and classification of rocks typically examined from drillcores for the purpose of identifying the main pipe infills. This is achieved by establishing the primary mineralogy, textures and xenolith contents within each main phase of kimberlite present. Once the external pipe shell and internal geology have been established then representative sampling for microdiamonds and macrodiamonds can be undertaken in support of resource classification and mine planning. Before 3D modelling is initiated, geological observations and interpretations must be coded in a manner which allows detailed geological information to be uploaded and viewed within a 3D modelling package (Table 1).

Creation of 3D Models

The development of a 3D geology model involves the generation of 3D solids (using various possible software applications, e.g. Gems / Leapfrog / Vulcan / Minesite) which represent the distribution of specific rock types in space, and includes both the pipe infills and often the enclosing country rock. An external pipe shell model (Fig.1a) represents the divide between the potentially mineralized kimberlite and the surrounding country rock or waste. Development of such a model is not a straightforward process as it can be very difficult within many pipes to determine if drillcore intervals of country rock are in fact in situ or xenoliths within a pipe. Another common factor may be the presence of marginal or contact breccias that complicate the determination of the position of the pipe wall. Marginal breccias are often associated with with KPK pipes particularly within volcanically immature systems.

| Hole ID | From (m) | To (m) | Length (m) | Litho | Total Dilution Visual Estimate | KIMB Texture | PIPE Zone Geology | 3D Model Code (phase) | 3D Geology Domain |
|-----------|----------|--------|------------|--------|-----------------------------------|--------------|----------------------|--------------------------|----------------------|
| FX-17-097 | 0.00 | 15.00 | 15.00 | OVb | 100 | NA | OVb | OVb | OVb |
| FX-17-097 | 15.00 | 88.61 | 73.61 | KIMB | 12 | VK | PIPE | KIMB5 | KIMB5 |
| FX-17-097 | 88.61 | 92.65 | 4.04 | KIMB | 15 | VK | PIPE | RFW | RFW |
| FX-17-097 | 92.65 | 132.15 | 39.50 | KIMB | 10 | RFW | PIPE | KIMB5 | KIMB5 |
| FX-17-097 | 132.15 | 137.41 | 5.26 | KIMB | 5 | RFW | PIPE | KIMB1 | KIMB5 |
| FX-17-097 | 137.41 | 152.43 | 15.02 | KIMB | 12 | RFW | PIPE | KIMB5 | KIMB5 |
| FX-17-097 | 152.43 | 154.34 | 1.91 | GRAN | 100 | NA | XENO | XENO-GRAN | KIMB5 |
| FX-17-097 | 154.34 | 159.50 | 5.16 | KIMB | 20 | RFW | PIPE | KIMB5x | KIMB5x |
| FX-17-097 | 159.50 | 160.82 | 1.32 | GRAN | 99 | NA | XENO | XENO-GRAN | KIMB5x |
| FX-17-097 | 160.82 | 175.75 | 14.93 | GRAN | 100 | NA | EXT-PIPE | GRAN-HOST | EXT-PIPE |
| FX-17-097 | 175.75 | 187.84 | 12.09 | KIMB | 10 | HK | PIPE | KIMB1 | KIMB1 |
| FX-17-097 | 187.84 | 188.84 | 1.00 | GRAN | 100 | NA | XENO | XENO-GRAN | KIMB1 |
| FX-17-097 | 188.84 | 194.53 | 5.69 | KIMB | 10 | HK | PIPE | KIMB1 | KIMB1 |
| FX-17-097 | 194.53 | 196.90 | 2.37 | KIMB | 1 | HK | PIPE | KDYKE-INT | KDYKE-INT |
| FX-17-097 | 196.90 | 199.19 | 2.29 | KIMB | 15 | HK | PIPE | KIMB1 | KIMB1 |
| FX-17-097 | 199.19 | 201.56 | 2.37 | GRAN | 90 | NA | XENO | XENO-GRAN | KIMB1 |
| FX-17-097 | 201.56 | 203.29 | 1.73 | KIMB | RFW | RFW | PIPE | RFW | RFW |
| FX-17-097 | 203.29 | 210.22 | 6.93 | GRAN | 100 | NA | EXT-PIPE | GRAN-HOST | EXT-PIPE |
| FX-17-097 | 210.22 | 216.83 | 6.61 | GRAN | 100 | NA | EXT-PIPE | GRAN-HOST | EXT-PIPE |
| FX-17-097 | 216.83 | 218.70 | 1.87 | KIMB | 35 | KPK | PIPE | KIMB6 | KIMB6 |
| FX-17-097 | 218.70 | 357.33 | 138.63 | GRAN | 97 | NA | XENO | XENO-GRAN | KIMB6 |
| FX-17-097 | 357.33 | 369.33 | 12.00 | KIMB | 35 | KPK | PIPE | KIMB6 | KIMB6 |
| FX-17-097 | 369.33 | 371.77 | 2.44 | GRAN | 100 | NA | XENO | XENO-GRAN | KIMB6 |
| FX-17-097 | 371.77 | 387.80 | 16.03 | KIMB | 2 | HK | PIPE | RFW | RFW |
| FX-17-097 | 387.80 | 406.47 | 18.67 | KIMB | 40 | KPK | PIPE | KIMB6x | KIMB6x |
| FX-17-097 | 406.47 | 469.77 | 63.30 | KIMB | 45 | KPK | PIPE | KIMB6x | KIMB6x |
| FX-17-097 | 469.77 | 471.58 | 1.81 | KIMB | 10 | HK | PIPE | KIMB4 | KIMB4 |
| FX-17-097 | 471.58 | 473.50 | 1.92 | GRAN | 100 | NA | XENO | XENO-GRAN | KIMB4 |
| FX-17-097 | 473.50 | 477.40 | 3.90 | KIMB | RFW | HK | PIPE | KIMB4 | KIMB4 |
| FX-17-097 | 477.40 | 479.43 | 2.03 | GRAN | 100 | NA | XENO | XENO-GRAN | KIMB4 |
| FX-17-097 | 479.43 | 483.17 | 3.74 | KIMB | 10 | HK | PIPE | KIMB4 | KIMB4 |
| FX-17-097 | 483.17 | 525.00 | 41.83 | FENITE | 100 | NA | FENITE | FENITE | FENITE |
| FX-17-097 | 525.00 | 528.63 | 3.63 | GRAN | 100 | NA | EXT-PIPE | GRAN-HOST | EXT-PIPE |
| FX-17-097 | 528.63 | 534.01 | 5.38 | KIMB | 1 | HK | KDYKE-EXT | KDYKE-EXT | KDYKE-EXT |
| FX-17-097 | 534.01 | 537.24 | 3.23 | FENITE | 100 | NA | FENITE | FENITE | FENITE |
| FX-17-097 | 537.24 | 547.81 | 10.57 | GRAN | 100 | NA | EXT-PIPE | GRAN-HOST | EXT-PIPE |
| FX-17-097 | 547.81 | 549.32 | 1.51 | KIMB | 2 | HK | KDYKE-EXT | KDYKE-EXT | KDYKE-EXT |
| FX-17-097 | 549.32 | 575.00 | 25.68 | GRAN | 100 | NA | EXT-PIPE | GRAN-HOST | EXT-PIPE |

Table 1: Sample of a geological coding table developed from core logging and petrography.

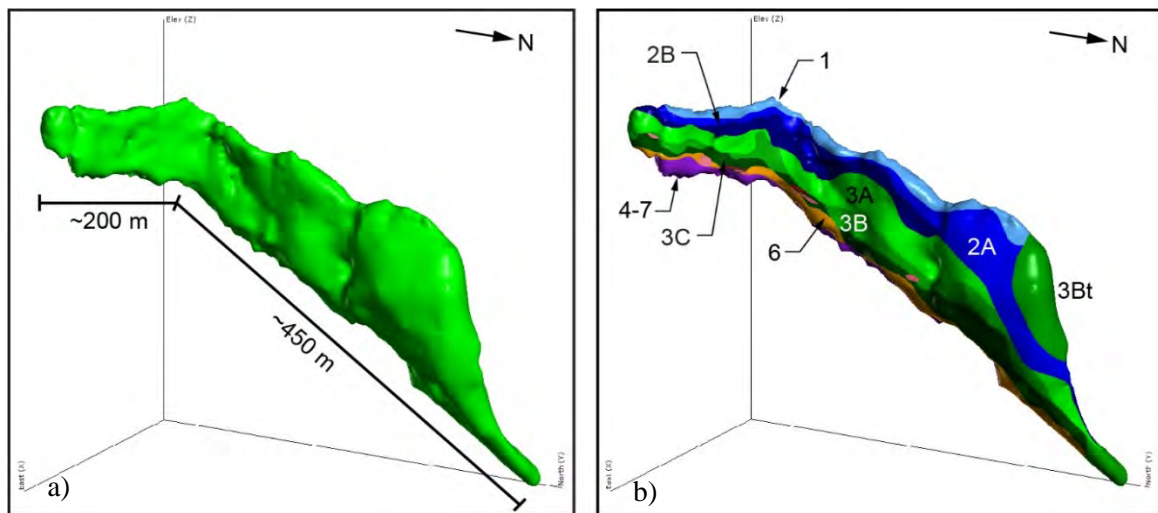




Figure 1: 3D geology models of the Kelvin kimberlite pipe, NWT, Canada. a) external pipe shell, b) internal geology with different phases highlighted by the different coloured solids, with corresponding 3D geology domain codes.

The external shell model or “pipe shell” is developed by the investigation of the “Pipe Zone” data (Table 1) and then by developing a geologically reasonable interpretation for the external shape. This involves not only an understanding of the textural varieties of kimberlite that have been intersected (VK vs. HK), but also an understanding of the possible volcanic or depositional processes (i.e. explosive fragmentation / effusive / intrusive / resedimentation) responsible for the development of specific textures present. Each of these processes and the nature of the host rock geology are associated with different styles of emplacement and resultant pipe shapes. Also critical to the development of a reliable pipe shell, is a good understanding of the host rock geology and xenoliths within the kimberlite.

Following the development of the external shell, the internal geology is developed by the interpretation of the “3D Model Code” data (Table 1). Like the external shell, the internal distribution of the phases of kimberlite are controlled by the volcanic history of the pipe as well as the geological processes responsible for the development of the different textural varieties of kimberlite present. The identification of the “phases” of kimberlite requires not only detailed logging of drillcores and supporting petrographic investigation, but is supported by multiple data sets including microdiamond and macrodiamond results, mantle derived indicator mineral studies, olivine line scans, and dilution line scans. Other studies supporting the definition of the internal kimberlite phases may be applied, including groundmass compositional studies, whole rock geochemistry or spectral scanning and geophysical properties.

Once the kimberlite phases have been established and the “3D Model Codes” have been assigned to all intervals, they are reviewed in 3D. The development of the 3D internal geology model actually represents a reconstruction of the volcanic history of the pipe (Fig.1b). The actual internal geometry of the pipe is determined by the distribution, orientation and nature of the internal contacts between the various phases present. Because the pipes are filled by multiple phases of kimberlite that are emplaced by a number of volcanic events over time, mixing may occur and displaced blocks of earlier phases can be found within younger phases. To cater for these complications the final internal geology model is developed by the use of the “3D Domain Code” (Table 1.) which allows the geologist to group intervals, classified by a particular “3D Model Code” into a geological domain. Each geological domain is dominated (75% or greater volume) by a single phase of kimberlite but may contain blocks of other kimberlite phases. The most challenging part of the 3D modelling process is the extrapolation of geology and grade into undrilled and unsampled portions of a pipe. This is achieved by interpretation constrained by adequate technical understanding of relevant volcanological processes, consistent with the textures and controlling structures identified within each phase of kimberlite

Conclusions

The quality of any 3D geology model produced is a function of the complexity of the geology of a particular pipe being investigated. Also the number and distribution of drillholes or mining exposures available for examination and thin sections available, as well as the amount of time completed on the investigation are critical factors. The experience of the geology team will have a significant impact on the quality of the model generated. The preservation state of the rocks being investigated impact the amount of information that may be revealed; rocks that are extensively altered or weathered may mask important textural and mineralogical information required for accurate classification. Finally the grade of a particular pipe and the types of macrodiamonds present will impact the amount of drilling and sampling required to facilitate the development of a reliable model in support of resource classification and mine planning. All models produced must be considered dynamic as the models will evolve as additional information and investigations are completed through subsequent drilling or mining activities.



The Geology of the Faraday 2 Kimberlite, NWT, Canada

Lindsay Nelson¹, Casey Hetman², Michael Diering³

¹ Aurora Geosciences Ltd., Yellowknife, Canada, lindsay.nelson@aurorageosciences.com

² SRK Consulting, Vancouver, Canada, chetman@srk.com

³ SRK Consulting, Vancouver, Canada, mdiering@srk.com

Introduction

The diamondiferous Faraday 2 kimberlite pipe is located in the southeastern Slave Craton of northern Canada. Faraday 2 is part of the Kelvin-Faraday kimberlite cluster, which consists of at least five irregular pipe-like bodies (Hobbes, Kelvin, Faraday 2, Faraday 3, and Faraday 1; listed from southwest-northeast) and associated kimberlite sheet complexes. The kimberlites subcrop below shallow lakes and their distribution follows a southwest-northeast lineament. The Gahcho Kué Diamond Mine also lies along this regional trend, approximately 10 km to the southwest of Faraday 2. Faraday 2 was first targeted as a result of kimberlite indicator mineral anomalies in glacial till and magnetic and gravity anomalies from geophysical surveying. De Beers Canada intersected kimberlite at Faraday 2 in 2001. Kennady Diamonds Inc. re-initiated exploration in the area in 2012 and has since completed extensive drilling and sampling programs. Faraday 2 has an irregular morphology and non-typical inclined orientation. To date, the pipe has been delineated over 450 m; it varies in width between 20 and 60 m and between 60 and 90 m in vertical thickness. The pipe is inclined towards the northwest, turning further towards the west with increasing depth. The southeastern section of the kimberlite is inclined at 30°, steepening to 40° as the kimberlite turns towards the west, and shallowing to between 0 and 20° in the most northwesterly portion of the body. Several kimberlite units resulting from multiple emplacement events are present within Faraday 2. Volcaniclastic kimberlite is the dominant pipe infill, with lesser amounts of coherent and texturally transitional kimberlite.

Evaluation

Detailed logging of drill core and chip samples, petrographic studies, and diamond results were used to define the irregular external morphology and the internal geology of Faraday 2 (Figure 1). A total of 85 diamond drill holes were completed at Faraday 2 since 2012. In 2016, a 21-tonne bulk sample was collected using 11-inch diameter reverse circulation (RC) drilling. In 2017, a further 263 tonnes of kimberlite was collected from 29 11-inch diameter RC holes. Multiple petrographic investigations were completed, totaling 295 kimberlite and country rock thin sections from 40 diamond drill holes and 93 kimberlite thin sections from RC chip samples. A total of 6,788 kg of kimberlite drill core was processed by caustic fusion at the Geoanalytical Laboratories Diamond Services of the Saskatchewan Research Council (SRC); the diamond recoveries are presented in Table 1.

| Unit | Sample Weight (dry tonnes) | Number of Diamonds According to Sieve Size Fraction (mm) | | | | | | | | | | | | Total Stones | Total Carats (+0.85 mm) |
|-------|-------------------------------|--|------------------|------------------|------------------|------------------|------------------|------------------|------------------|------------------|------------------|------------------|------------------|-----------------|-------------------------------|
| | | +0.106 -0.150 | +0.150 -0.212 | +0.212 -0.300 | +0.300 -0.425 | +0.425 -0.600 | +0.600 -0.850 | +0.850 -1.180 | +1.180 -1.700 | +1.700 -2.360 | +2.360 -3.350 | +3.350 -4.750 | +4.750 -6.700 | | |
| KDYKE | 0.2788 | 940 | 600 | 371 | 198 | 120 | 65 | 23 | 12 | 3 | 3 | - | - | 2,335 | 1.5916 |
| KIMB1 | 3.2072 | 3,967 | 2,609 | 1,564 | 918 | 466 | 290 | 147 | 61 | 21 | 12 | 3 | - | 10,058 | 10.5379 |
| KIMB2 | 0.2955 | 703 | 480 | 296 | 174 | 87 | 61 | 18 | 9 | 5 | 2 | - | - | 1,835 | 1.6241 |
| KIMB3 | 0.3961 | 753 | 495 | 302 | 174 | 85 | 57 | 35 | 21 | 2 | 1 | - | - | 1,925 | 1.4771 |
| KIMB4 | 0.5208 | 367 | 250 | 134 | 101 | 49 | 30 | 11 | 8 | 5 | 3 | - | - | 958 | 1.4758 |

Table 1. Diamond results by unit. A total of 2,090 kg of kimberlite was processed where only the +0.425 size fraction and above was recovered; these results are not included in this table. An additional minor kimberlite unit has been identified (KIMB5). At present, no material from this unit has been processed for diamond recovery.

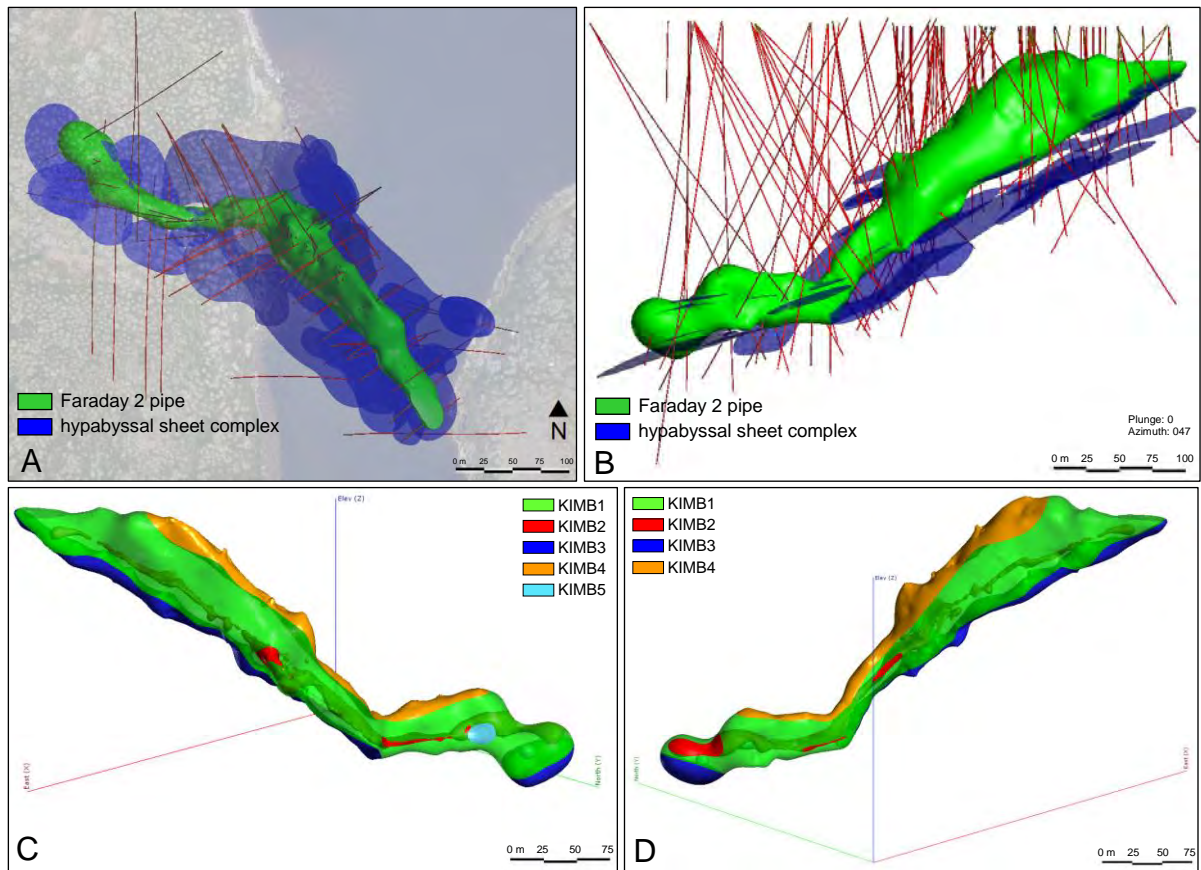


Figure 1. 3D model of the Faraday 2 kimberlite. (A) Plan view of the pipe with the surrounding hypabyssal kimberlite sheet complex and drill hole traces. (B) Oblique view of Faraday 2 looking northeast, with drill hole traces. (C) Internal geology of the pipe, looking southwest. KIMB1: volcanoclastic phlogopite kimberlite, KIMB2: coherent to transitional phlogopite kimberlite, KIMB3: coherent phlogopite kimberlite, KIMB4: volcanoclastic kimberlite with high country rock dilution and localized sorting, KIMB5: transitional phlogopite kimberlite (D) Internal geology of the pipe, looking northeast.

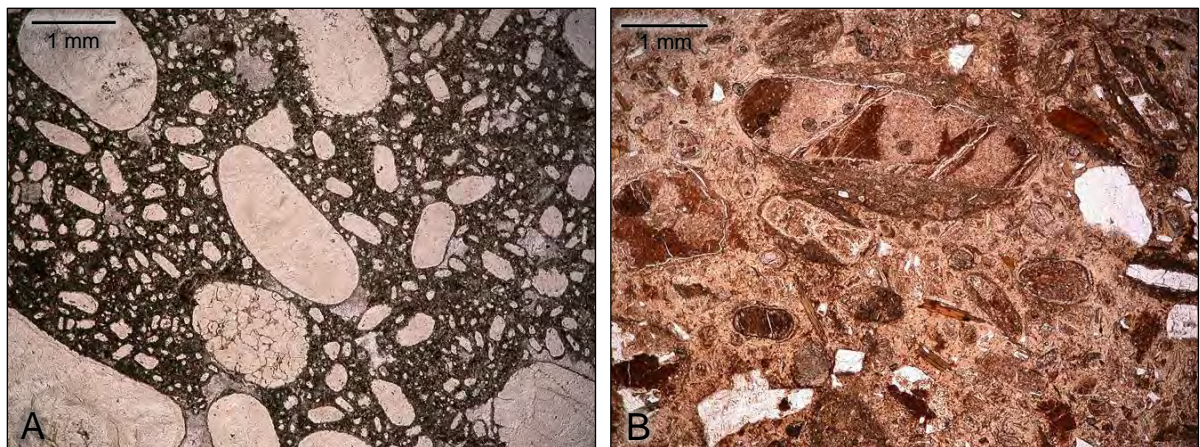


Figure 2. Photomicrographs of the two textural end-members at Faraday 2. (A) Coherent phlogopite kimberlite (KIMB3), olivine-rich with a continuous crystalline groundmass containing irregular segregations of carbonate. (B) Volcanoclastic phlogopite kimberlite (KIMB1) characterized by a loose-packed clast-supported texture with abundant thin-skinned pelletal-shaped magmaclasts and a microlitic serpentine matrix. Angular country rock xenoliths and xenocrysts are common.

Geology

There are five distinct kimberlite units infilling the Faraday 2 pipe, which are differentiated by their textural characteristics, mineralogy, country rock dilution, interpreted emplacement relationships, and diamond grade. The units form layers with contacts that are sub-parallel to the upper and lower edges of the pipe (Figure 1). A marginal breccia (MB) of fractured and pulverized country rock with trace amounts of kimberlitic material occurs above the pipe. Hypabyssal kimberlite sheets (KDYKE) are associated with the pipe and dip towards the northwest.

The dominant pipe infill is volcanoclastic kimberlite (KIMB1 and KIMB4) with lesser amounts of coherent and transitional kimberlite (KIMB2, KIMB3 and KIMB5). KIMB1 comprises over 70% of the pipe volume. It is a massive, olivine-rich phlogopite kimberlite characterized by thin-skinned pelletal-shaped magmaclasts (formerly pelletal lapilli) and country rock xenoliths set within a matrix of serpentine and microlites. Well-formed acicular phlogopite phenocrysts are present in the melt selvages of the magmaclasts. Country rock dilution of KIMB1 ranges between 30 and 40%. Country rock xenoliths are predominantly locally-derived metasediment and amphibolite with rare granitoid and diabase. KIMB4 is a highly-diluted (>70%) volcanoclastic phlogopite kimberlite that exhibits localized sorting. KIMB2 is a texturally variable phlogopite kimberlite with both volcanoclastic and coherent examples. It is characterized by olivine macrocrysts pseudomorphed by pale-coloured serpentine and serpentinized country rock shards set in a poorly-crystalline groundmass or serpentine matrix. KIMB3 is a massive, inequigranular, xenolith-poor, fine to coarse olivine-rich coherent phlogopite kimberlite. KIMB5 is a minor transitional kimberlite unit occurring in the deepest portion of the pipe. Mantle-derived indicator minerals are rare in all units and primarily consist of peridotitic garnet.

Conclusions

The volcanoclastic kimberlite that is the main pipe infill at Faraday 2 (KIMB1) is further classified as a Kimberley-type pyroclastic kimberlite (KPK), formerly referred to as tuffisitic kimberlite breccia (TKB) (Smith et al., 2013). The second volcanoclastic kimberlite (KIMB4) has not been classified as such due to the presence of sorting. KIMB4 was likely formed by gas-escape processes along the pipe margin.

The textures, mineralogy, and significantly diamondiferous nature of the kimberlite units at Faraday 2 are similar to the other bodies in the Kelvin-Faraday cluster and the Gahcho Kué kimberlite cluster (Hetman et al., 2004).

Faraday 2 is characterized by multiple kimberlite units representing multiple phases of kimberlite with separate emplacement events that have formed a non-typical inclined and irregular pipe. The sub-horizontal, inclined orientation of the pipe, internal geology, and close relationship to kimberlite sheets within Faraday 2 are generally similar to the other kimberlites in the Kelvin-Faraday cluster. This inclined pipe orientation is atypical of previously-described KPK systems.

Faraday 2 is open at depth, and additional drilling is required to determine the full extent of the kimberlite. In 2016 and 2017, a total of 284 tonnes of kimberlite was sampled by 11-inch RC drilling. The macrodiamond results from the 2017 program will be combined with previous data to support an inferred resource classification.

References

- Hetman, C. M., Smith, B. S., Paul, J. L., & Winter, F. (2004). Geology of the Gahcho Kue kimberlite pipes, NWT, Canada: root to diatreme magmatic transition zones. *Lithos*, 76(1), 51-74.
- Smith, B. S., Nowicki, T. E., Russell, J. K., Webb, K. J., Mitchell, R. H., Hetman, C. M., and Robey, J. A. (2013). Kimberlite terminology and classification. In *Proceedings of 10th International Kimberlite Conference* (pp. 1-17). Springer India.



Density Measurement of the Kelvin and Faraday Kimberlites in the Northwest Territories of Canada.

A. Bloem¹, C. Hetman¹, G. Arseneau², and C. Hrkac³

¹ SRK Consulting, Vancouver, Canada, abloem@srk.com

¹ SRK Consulting, Vancouver, Canada, chetman@srk.com

² Arseneau Consulting Services, Vancouver, Canada, gillesa@telus.net

³ Aurora Geosciences, Vancouver, Canada, chris.hrkac@aurorageosciences.com

Introduction

Core and reverse-circulation drilling programs have been undertaken on the Kelvin-Faraday kimberlite cluster for exploration, evaluation and resource classification by Kennady Diamonds Inc. All of the pipes and dykes in this cluster are diamondiferous and are located a few kilometres north of the Gahcho Kué mine (operated by De Beers Canada). The country rocks are metaturbidites of the Yellowknife Supergroup with minor amphibolite and narrow diabase dikes, with Archean granitoids occurring immediately to the west of the kimberlite cluster. In support of the resource development work undertaken on the Kelvin and Faraday kimberlites, density data collection were included into the geotechnical data-acquisition program for the project.

The determination of the volume-amount of kimberlite takes precedence in most drilling-delineation programs because it is the basic measure of “how much” material is to be mined and processed. The less understood and more variable parameter is the density of the material to be handled. Mineral resource statements are issued in terms of grades and tonnages, with kimberlite diamond grade reported as either carats per hundred tonnes (cpht), or less commonly, as carats per cubic metre (cts/m³). The significance of the bulk density of the materials to be mined, is that they are used as input parameters for most stages of mine design, including; slope stability analysis, blast design, equipment fleet, comminution and mill design, tailings storage facility design, and waste rock management.

Density Measurement Methods

There are several methods available for determining the bulk density of rocks – some of which are relatively easy (and inexpensive) to implement in-field, while others require open drillholes for geophysical tools or at the extreme, controlled laboratory conditions. The rock mass characterization program of the Kelvin and Faraday kimberlites included the collection of bulk density data using buoyancy, calipered dimensioning, liquid displacement of pulverized rock, and *in situ* gamma-gamma downhole geophysical methods. The reason for testing using multiple density measurement methods, and comparing them to one another, is that there is currently no standard method which describes how this should be done for kimberlites.

Rock Mass Density Data

The drilling and logging program, from 2014 to 2017, included basic geotechnical logging on all holes. All samples in this program were differentiated by rock type, geotechnical (GT) textural classes, intact strength, magnetic and weathering susceptibility, and three-dimensional position within the bodies. The primary in-field classification was done according to major rock type (gneiss or kimberlite), added to which the textural components within these rocks further sub-divided them into five somewhat equal classes with the end-members labelled G1..5 and K1..5 – as illustrated in Figure 1. This formed the start of the geotechnical domain delineation in the absence of a detailed geological model (which has subsequently been constructed).

Xenoliths and country-rock often have densities that are different than those of the kimberlite. This density contrast and ‘blending’ is illustrated in Figure 2. For VK rocks, the xenolith percentages can be estimated using line-counts (of relative percentages of the two components) and then the density of the kimberlite ‘matrix’ adjusted by adding in the density of the xenoliths, to arrive at an overall

density for the rock. This is the ‘cumulative’ method of whole rock density determination. In the case of Kelvin, the country rock is an anisotropic gneiss with varying amounts of platy-minerals which have a relatively consistent range of densities (G1 \approx 2.68 to G5 \approx 2.76) that are, however, sometimes difficult to differentiate in hand-sample – and in this case, using a cumulative-density type of strategy is difficult to implement if the xenoliths are small. We therefore opted for sampling of long-lengths of core and measuring them using calipered dimensioning, and also added the full hole-length gamma-gamma data to reduce the influence of the variable amounts and distribution of xenoliths.

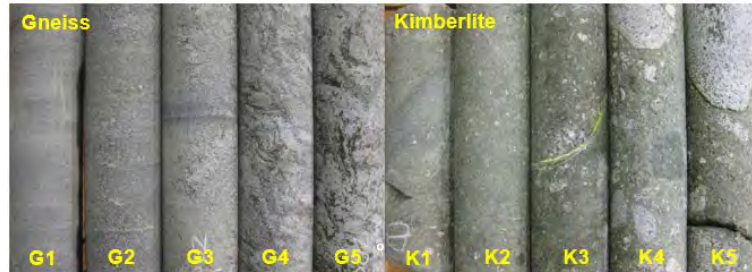


Figure 1: Texture in the host-rock (gneiss) is based on an estimate of the percentage visible platy-minerals (biotite and micas) using a linear scale of approximately 0 - 10% (G1) through to > 40% (G5). In kimberlite, the texture codes are based on an estimate of the xenolith content and uses a linear scale of approximately 0 - 10% mostly fine-grained (K1) through to > 40% xenolithic volcanoclastic (K5) rock.

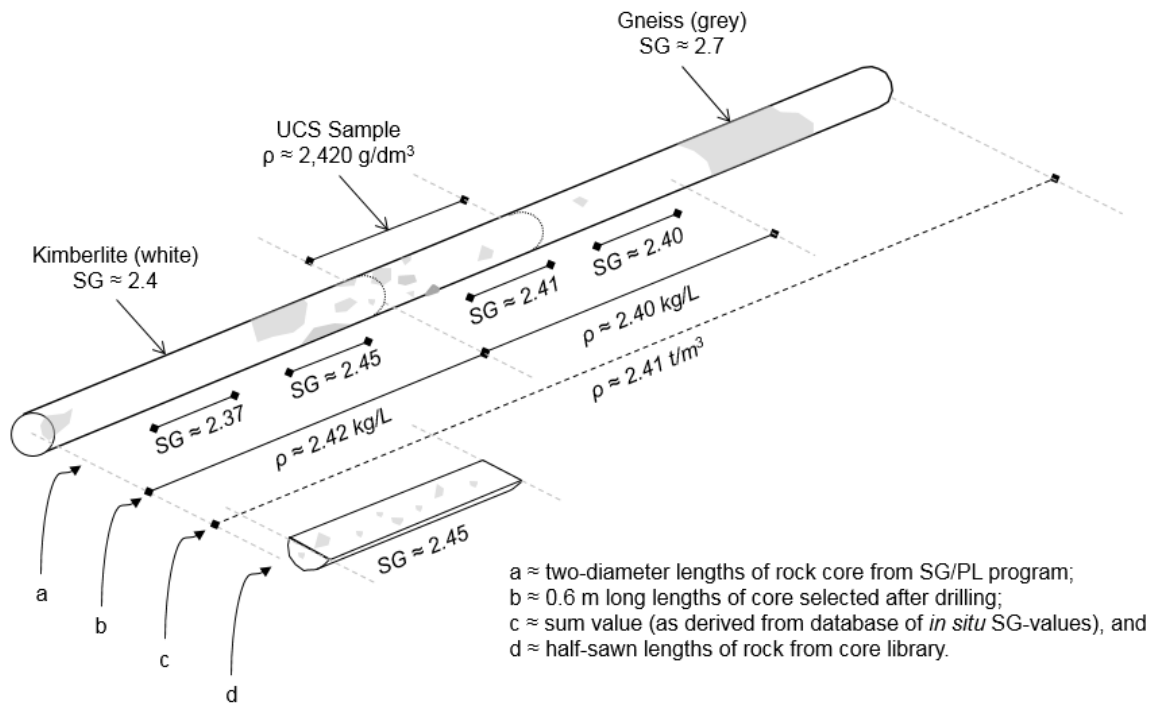


Figure 2: Schematic example of the sampling and testing strategy of rock core; a) is the in situ buoyancy-method measurement of ρ , b) post-drilling checks using a calipered dimensioning for ρ_b , c) an ‘average’ ρ value from within the kimberlite solid, and d) crushed samples for independent verification of ρ_b .

The buoyancy-method data were compared to laboratory and field-based calipered dimensioning, and the geophysical method. An independent check, using pulverized samples in a liquid displacement method, was also done – as illustrated in the table and chart of Figure 3. General agreement was found in the summarized data from each of the methods used; in particular, the trends in the density-data associated with changes in xenolith content are consistent. These overlapping data sets could allow for calibration of the global density model to reflect the required density measurement, dry (for grade and processing) or wet (for mining).

| GT-Texture | Drill rig | | Camp | Laboratory | |
|------------|---------------------|--------------------------|------------------------|------------------------|---------------------------|
| | Buoyancy (ρ) | Gamma-gamma (ρ_e) | C-Caliper (ρ_b) | L-Caliper (ρ_b) | Grain volume (ρ_g) |
| K1 | 2.42 | 2.52 | 2.46 | 2.39 | 2.49 |
| K2 | 2.38 | 2.41 | 2.34 | 2.37 | 2.46 |
| K3 | 2.38 | 2.47 | 2.36 | 2.35 | 2.44 |
| K4 | 2.43 | 2.51 | 2.40 | 2.43 | 2.46 |
| K5 | 2.50 | 2.57 | 2.52 | 2.49 | 2.52 |
| Avg. | 2.41 | 2.46 | 2.41 | 2.40 | 2.46 |
| St.Dev | 0.11 | 0.13 | 0.12 | 0.05 | 0.09 |
| n | 4029 | 157 | 70 | 10 | 90 |
| Wt. (kg) | 3000 | null | 220 | 10 | 60 |

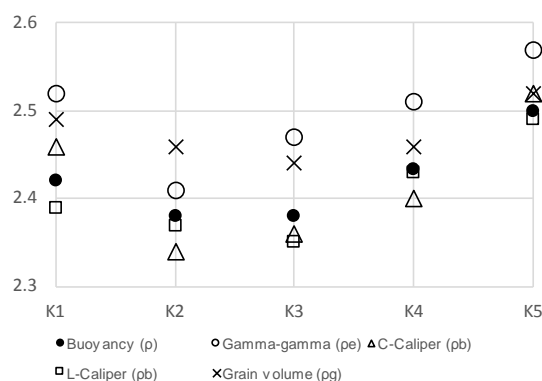


Figure 3: Summarized density data for kimberlite geotechnical textures, tabulated by location and method of data-acquisition for the Kelvin and Faraday kimberlites.

Discussion

The study found that the bulk density contrast between the Kelvin and Faraday kimberlites ($\rho \approx 2.4 \text{ g/cm}^3$) and the gneissic country rock ($\rho \approx 2.7 \text{ g/cm}^3$) is sufficient to differentiate the kimberlites within the country rock based on their density and the point-load strength of the individual hand-sized samples. The increase in xenolith content is reflected in the progressively increasing K3 to K5 GT-textural class densities. These results are in-line with other reported global values of VK (1.4 to 2.2) and CK (2.2 to 3.0) as described by Arnott and Kostlin (2003). The K1 class have densities between 2.4 and 2.5, which is consistent with coherent material (Reed and Witherly, 2007) within the lower diatreme to root zone transition within kimberlites.

A systematic increase in all of the country-rock gneiss densities with depth, from on average 2.72 at surface, to 2.74 at 400 m depth, occurs. This probably reflects increased micro-defects and fracturing near surface which may be a consequence of mechanical unloading of the country rock mass in this post-glacial environment. Using a geotechnical rock-texture classification method based on xenolith abundance and magnetic susceptibility measurements, the kimberlite samples can be separated into cement- (coherent / hypabyssal) and matrix-dominated (volcaniclastic) rocks with varying xenolith populations. In addition, because there are several thousand point samples within the Kelvin kimberlite (measured at a rate of approximately one per 3 m long drill-run) these facilitate 'visualization' of the internal geometry of the main geological zones within the kimberlites.

Conclusions

For pre-production characterization, the use of the buoyancy method with laboratory precision caliper checks is sufficient to characterize the VK and CK infills within Kelvin and Faraday. Because the number of samples was high on this program, it helped demonstrate that the pipes are variable in terms of their internal physical properties and in the spatial arrangement of these properties within the different kimberlite units. A single 'average' density number does not adequately define the *in-situ* densities of these kimberlites or their internal zones – a better approximation is achieved by estimating densities in three dimensional block models. Until such time as there are detailed industry and kimberlite-texture specific density-measurement guidelines, the combined use of volumetric (ct/m³) and weight based (ct/100t) grade statements are a more transparent way of reporting diamond results.

References

1. Arnott, F. and E. Kostlin, 2003, *Petrophysics of Kimberlites*, 8th International Kimberlite Conference, Victoria B.C., Canada.
2. Carmichael, R. S., 1989, *Practical Handbook of Physical Properties of Rocks and Minerals*, CRC Press, Florida USA.
3. Reed, L. E. and K. E. Witherly, 2007, *50 Years of Kimberlite Geophysics, A Review*, in Proceedings of Exploration 07: Fifth Decennial International Conference on Mineral Exploration, edited by B. Milkereit, p. 679-689.

Mining For Diamonds – History and Present

J. Jakubec¹

¹ SRK Consulting, Vancouver, Canada, jjakubec@srk.com

Introduction

Alluvial mining for diamonds started in India and for centuries Alluvial mining was the primary source of diamonds. Hard rock mining of primary kimberlite on an industrial scale had only emerged with diamond discoveries in South Africa in the 19th century. Initially, kimberlite pipes were mined as open cast mines and only within the second half of the 20th century that underground mining was implemented.

The objective of this paper is to provide an overview of modern hard rock mining methods implemented on today's diamond mines worldwide. The focus is to highlight successes and challenges with each method and compare experiences in various geographical, climate, and socioeconomic zones of the world.

World Diamond Mines and Diamond Production

According to www.mining.com and Paul Zimninsky, (1) mined diamond production is estimated to be approximately 142.3 million carats worth some \$15.6 billion. This is a 11.5% increase in carats and 9.9% increase by value from 2016. Majority of the diamonds are being mined from primary deposits (Figure 1), mainly kimberlite and lamproite pipes. Primary mining method is still open cast mining but underground mining is becoming increasingly common.



Figure 1: Main hard rock diamond mines of the world. Note that some are on care and maintenance now.

Mining Methods

Today, out of some 40 diamond hard rock mines mining kimberlite, approximately half are underground and another 20 or so have underground plans or hold the underground mining potential.

Mining methods implemented currently at hard rock diamond mines consist of two main groups: open pit and underground (Figure 2).

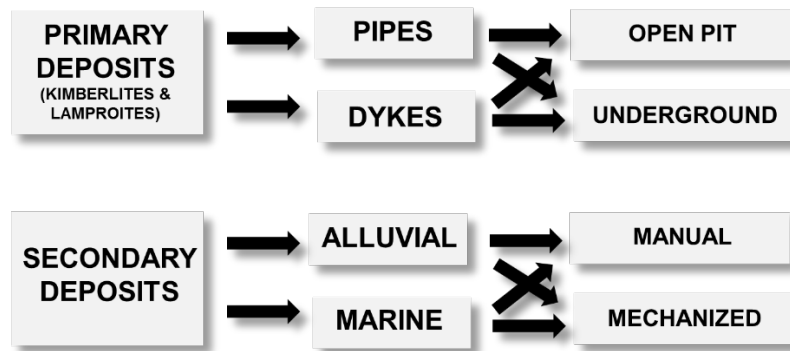


Figure 2: Main mining methods used for primary and secondary diamond deposits

For a mining project to succeed, the mining method must always be appropriate to the context of geology. This is a condition which cannot be changed and if the mining method is in conflict with this context then it will not perform as expected.

In essence, the choice of a mining method depends on the following:

- Orebody size and geometry
- NSR - value per block
- Grade distribution and dilution
- Rock mass competency
- Disturbances (stress, water)
- External constraints (corporate, market, social economic, environmental, etc.)

Open pit mining accounts today for majority of the carats produced but underground mining is playing an increased role. For example, Diavik mine although currently developing open pit A-21 project, is today fully underground. Underground mining introduces increased complexity and operating cost, typically exceeding open pit mining cost while the production rates are significantly reduced. Figure 3 illustrates the ranges of typical mine operating costs in Northern Canada (in Canadian funds).

| | |
|----------------------------------|------------|
| Direct mining cost | |
| Open pit | \$5–10/t |
| Block caving | \$10–20/t |
| Open benching | \$20–35/t |
| Sublevel caving | \$25–40/t |
| Backfill methods | \$60–100/t |
| Processing cost | \$10–20/t |
| Other costs (G&A, Marketing etc) | \$15–35/t |

Figure 3: Northern Canada typical mine operating costs

While total typical operating costs could range from \$30–65/t for open pit mining to well over \$150/t for the backfill underground method, in reality the costs of some recent diamond projects are higher. The estimated open pit operating cost for Diavik Mine is approximately \$80–90/t (2), with \$90–100/t for Jericho Mine (2) and similar values of \$78–88/t reported for Ekati Mine (2). Operating costs for the Diavik underground operation are expected to be approximately \$140/t for backfill method (2), and \$156/t for the Snap Lake underground mine (2).

Cave mining (block, panel or incline caving and sub-level caving) and sub-level retreat accounts for majority underground mining method today.

Mining for diamonds evolved significantly from early days of open cast operations in Kimberley to modern underground operation with fully mechanized and automated mining technology (Figure 4).



Figure 4: Early days of diamond mining in South Africa, Kimberley Diamond Mines c. 1880 (Collection of Cynthia Brantley) on the left and tele-remote operator in modern underground mine (Sandvik Tele-remote Automine)

References

1. www.mining.com/2017-global-natural-diamond-production-forecasted-142m
2. Jakubec, J., "Kimberlite Emplacement Models – The Implications for Mining Projects", Journal of Volcanology and Geothermal Research, 2008 v. 174, iss. 1-3, pp. 20-28.

Underground Diamond Mining at Ekati and Diavik Diamond Mines

J. Jakubec¹, R. Woodward², B. Boggis², L. Clark³, P. Lewis³

¹ SRK Consulting, Vancouver, Canada, jjakubec@srk.com

² Dominion Diamond Corporation, Yellowknife, Canada, rick.woodward@ddcorp.ca

² Dominion Diamond Corporation, Yellowknife, Canada, bill.boggis@ddcorp.ca

³ Rio Tinto – Diavik Diamond Mines, Yellowknife, Canada, lyndon.clark@riotinto.com

⁴ Rio Tinto – Diavik Diamond Mines, Yellowknife, Canada, philip.lewis2@riotinto.com

Introduction

Primary diamond deposits are being mined on an industrial scale only within the past 150 years, mainly as open pit mines. Underground mining of these deposits were implemented only within the second half of the 20th century in South Africa. Over the past 50 years, a relatively large number of underground mining methods were tested, implemented, and evolved mainly in South African mines. In mid 1990s, Alrosa started the development of the first underground diamond mine in Russia, Internationalnaya. Since then, underground mining was implemented on several of their mines including Aikhal, Mir, and Udachny. China had also experimented with underground mining at Nhangma 701 Diamond Mine in the end of the nineties. Today, out of some 40 diamond mines mining kimberlite, approximately half are underground and another 20 have underground plans or the potential to mine underground.

Canadian Underground Diamond Mines Overview

The largest growth of diamond underground mining in the world was experienced in Canada. To date, underground mining was introduced on five kimberlite pipes and one kimberlite sill. Those are Panda, Koala, Koala North at Ekati Mine, A418, A514N, A514S at Diavik Mine and Snap Lake. Although in 2008 De Beers started underground mining on kimberlite sill at Snap Lake, the focus of this paper is to document experiences with underground mining of kimberlite pipes at Ekati and Diavik Mines – see Figure 1.

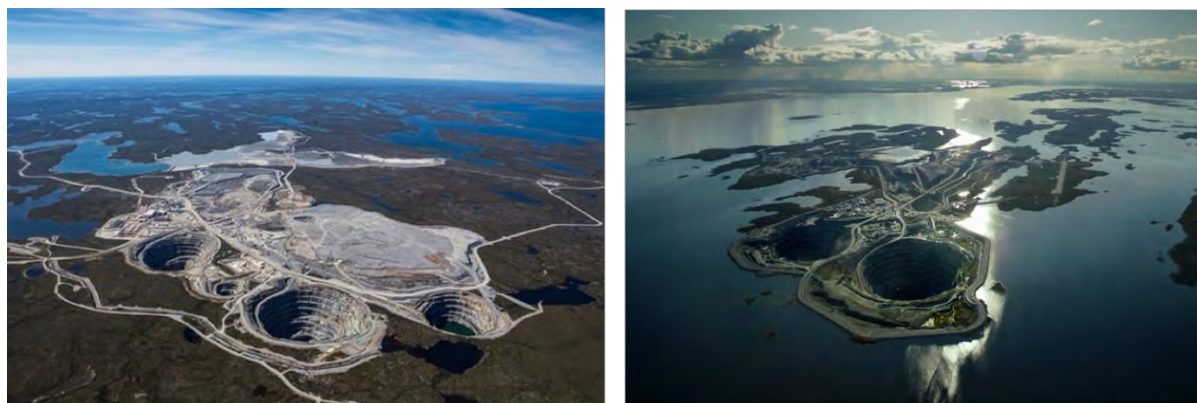


Figure 1: Ekati Mine left and Diavik Mine on the right.

Ekati Diamond Mine was the first diamond mine to be developed near Lac de Gras in the Northwest Territories of Canada and mining commenced as open pit at Panda pipe. Almost concurrently, planning was underway for underground mining at Panda and Koala pipes.

The Koala North pipe has been selected as a trial underground mine for the purposes of testing mining methods and to provide access to the lower elevations of the Panda and Koala pipes. The upper 40 meters of the Koala North pipe was mined in late 2000 as open pit which provided grade and geotechnical information and a prepared surface for the transition to underground mining. The trial mining decision was made primarily because of uncertainty in the several aspects of sub-level retreat (SLR) in the northern Arctic environment. In 2002, Koala North underground was formally opened

and it becomes North America’s first underground diamond mine. Koala North pipe has been successfully mined as mechanized open-benching down to 2115 level (+115 AMSL) and proved that SLR is technically feasible and economically viable mining method for exploiting kimberlite pipes in Arctic. Since then, Panda and Koala pipes were also mined as underground mines after open pits were completed and several other pipes are being investigated for underground mining. At Ekati, three principal underground mining methods were utilized including SLR, sub-level caving (SLC) and incline cave (IC) mining. Table 1 illustrates the production to date from Ekati underground and open pit mines.

| Mining Method | Pipe | Mining Method | Production Rate Mwmt/annum | Tons Produced Mdmmt |
|----------------------|-------------|----------------------|-----------------------------------|------------------------------------|
| Open Pit | Panda | Open Pit | 2.8 | 14.2 |
| | Koala | Open Pit | 3.5 | 9.4 |
| | Beartooth | Open Pit | 0.4 | 1.8 |
| | Misery | Open Pit | 1.4 | 8.7 (includes inferred satellites) |
| | Fox | Open Pit | 3.1 | 24.3 |
| Underground | | | | |
| | Panda | SLR | 1.1 | 4.7 |
| | Koala | SLC, IC | 1.0 | 8.2 IC Still operating |
| | Koala North | SLR | 0.3 | 1.8 |

Table 1: Ekati Underground and Open Pit Mines Production to Date

Diavik Diamond Mine started open pit production in 2003. By 2005, underground development had commenced with plans to mine the A154 and A418 pipes using backfill methods. As geotechnical knowledge was gained, the mining methods were re-evaluated and the sub-level retreat method was chosen for the A154S and A418 pipes, and blasthole stoping (BHS) with cemented rockfill was chosen for the A154N pipe. In 2012, the open pits reached their ultimate depths and Diavik became a fully underground operation. The current mine life is approximately 2024 and mining to date at Diavik is illustrated in Table 2.

| Mining Method | Pipe | Mining Method | Production Rate Mt/anum | Tons Produced t |
|---------------------------------|---------------|----------------------|--------------------------------|------------------------|
| Open Pit (2003-2010) | A154S & A154N | Open Pit | 1.61 (avg) | 12.9 |
| Open Pit (2008-2012) | A418 | Open Pit | 1.10 (avg) | 5.5 |
| Underground (2010 start) | | | | |
| Underground (2010 start) | A154N | BHS | 0.57 (avg), 0.75 (current) | 4.0 |
| Underground (2010 start) | A154S | SLR | 0.40 (avg), 0.49 (current) | 2.8 |
| Underground (2011 start) | A418 | SLR | 0.58 (avg), 1.10 (current) | 3.5 |

Table 2: Diavik Underground and Open Pit Mines Production to Date

Underground Mining Methods

While blasthole stoping with cemented rockfill used at Diavik and SLC used at Ekati are a commonly used method in Canadian underground operations, sub-level retreat was newly introduced to Canada; hence, this paper will focus on SLR, mining method. The decision to select sub-level retreat was made as a result of technical, economical and safety risk consideration. Competent country rocks, favorable geometry, relatively competent kimberlite, and most importantly, the arctic context of the projects

played an important role in the mining method selection process at both Ekati and Diavik Mines. The schematic section illustrating SLR method is shown in Figure 2.

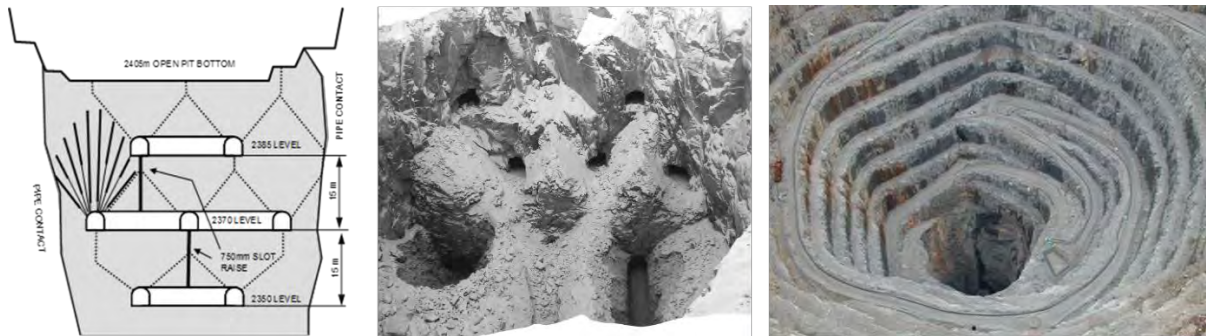


Figure 2: Schematic section through SLR mine (left) and view into Koala North (middle) and Panda (right) mines, both exploited by SLR.

Ekati mine successfully produced from Panda and Koala North pipes approximately 6.5 Mt of ore between 2002-2012 and Diavik produced approximately 6.3 Mt to date and by SLR.

References

Jakubec, J., Long, L., Nowicki, T., Dyck D., "Underground Geotechnical and Geological Investigation at Ekati Diamond Mine – Koala North Case Study", 8th International Kimberlite Conference, Victoria, 2002, Lithos, v. 76, iss. 1-4 [SPECIAL ISSUE], p. 337-345, 2004

Jakubec, J., Page C., Harvey, P., "Mining Method Selection for Diamond Mines - Challenges in the Arctic", MASSMIN 2004, Santiago, Chile, Aug. 2004

Jakubec, J., Long, L., "Open Benching at Ekati Mine – Koala North Case Study", MASSMIN 2004, Santiago, Chile, Aug. 2004



Stability of Fe³⁺-bearing majorite in the Earth's mantle

Yingwei Fei and Renbiao Tao

Geophysical Laboratory, Carnegie Institution of Washington, 5251 Broad Branch Road N.W., Washington, DC 20015, USA; Email: fei@gl.ciw.edu

Introduction

Recent discovery of an oxidized majorite inclusion in a garnet host (Xu *et al.*, 2017) has motivated us to investigate the stability of Fe³⁺-bearing majorite in the mantle. Majorite, characterized by excess Si in octahedral coordination, forms only at pressures higher than 6 GPa, and the majoritic component increases with increasing pressure. Direct recovery of majoritic garnet in mantle rocks has not been observed because of back transformation of majorite to garnet plus pyroxene upon exhumation. The preservation of Fe³⁺-rich majorite inclusions, particularly in a garnet host, requires new high-pressure experiments to understand the mechanism of recovery. It has been shown that ferric iron may play important roles in the mantle and subduction environment because of redox reactions and high intrinsic oxygen fugacity (e.g., McCammon and Ross, 2003; Rohrbach *et al.*, 2007; Stagno *et al.*, 2015). However, there has been very little understanding of the formation and stability of Fe³⁺-rich majorite in the mantle. The effect of Fe³⁺ content on the formation depth of natural majoritic garnets is also not well understood. In this study, we perform a series of experiments to synthesize Fe³⁺-rich majoritic garnets under mantle conditions using high-pressure multi-anvil apparatus. The experimental data are used to understand the role of ferric iron in the stability and formation of majorite under different mantle conditions.

Experimental Procedure

Synthesis experiments of Fe³⁺-bearing majoritic garnets were carried out in the multi-anvil apparatus from 6.5 to 15 GPa. The first set of experiments were designed to examine the effect of the Fe³⁺ content on the majorite geobarometer (Tao *et al.*, 2017), using a starting material with similar chemical composition to that of the natural Fe³⁺-majoritic garnet in eclogite xenolith from Earth's deep upper mantle (Xu *et al.*, 2017). It consists of mixing CaCO₃ and oxides (MgO, Cr₂O₃, Al₂O₃, Fe₂O₃, and SiO₂). All Fe is introduced as Fe₂O₃ in the starting material. We also mixed a second starting material with all Fe²⁺. The chemical composition is analogous to that of the natural garnet host (Xu *et al.*, 2017). The mixture of each starting material was ground under ethanol in an agate mortar for 1 hour and decarbonated twice in a furnace at 1000 °C for 24 hours. The all Fe²⁺ starting material was prepared under controlled oxygen fugacity. The chemical compositions of the two starting materials are listed in Table 1, and compared to the natural mineral compositions.

Table 1. Chemical compositions of starting materials, compared with nature mineral compositions

| | Fe ³⁺ -sm | Fe ²⁺ -sm | Fe ³⁺ -rich Majorite | Garnet-II |
|--------------------------------|----------------------|----------------------|---------------------------------|-------------------------|
| | This study | This study | Xu <i>et al.</i> (2017) | Xu <i>et al.</i> (2017) |
| SiO ₂ | 43.49 | 42.30 | 44.20 | 42.40 |
| TiO ₂ | - | - | 0.10 | 0.10 |
| Al ₂ O ₃ | 6.96 | 22.03 | 7.09 | 22.13 |
| Cr ₂ O ₃ | 1.08 | 1.08 | 1.10 | 1.09 |
| FeO | - | 8.04 | 18.47* | 7.71* |
| Fe ₂ O ₃ | 20.15 | | | |
| MgO | 26.98 | 20.69 | 27.16 | 20.79 |
| CaO | 1.33 | 5.04 | 1.35 | 5.09 |
| MnO | - | - | 0.32 | 0.30 |
| Na ₂ O | - | - | 0.03 | 0.02 |
| Total | 100.00 | 100.00 | 99.82 | 99.60 |

*Total iron oxide

We used the 14/8 assembly (Bertka and Fei, 1997) for all the high-pressure experiments up to 15 GPa. It consists of an MgO octahedron with a ZrO₂ thermal insulator sleeve and a Re heater. The starting material was loaded, sealed into a Pt capsule. The pressure was calibrated using fixed phase transition points in CaGeO₃, SiO₂, and Mg₂SiO₄ (Bennett *et al.*, 2016). The temperature was measured using a Type-C thermocouple, inserted axially to the top of the Pt capsule. The recovered samples were polished and examined with scanning electron microscopy (SEM). The chemical compositions for the coexisting minerals were determined with a JEOL JXA-8530F field-emission electron probe. The Fe³⁺ contents of the majoritic garnets were analyzed using the “Flank method” (Höfer *et al.*, 1994; Höfer and Brey, 2007), that are in general agreement with results based on the charge balance calculations. Figure 1 shows a representative SEM image of a sample quenched from 12 GPa and 1200 °C, that contains majoritic garnet (Maj), olivine (Ol), pyroxene (Px), and magnetite (Mt).

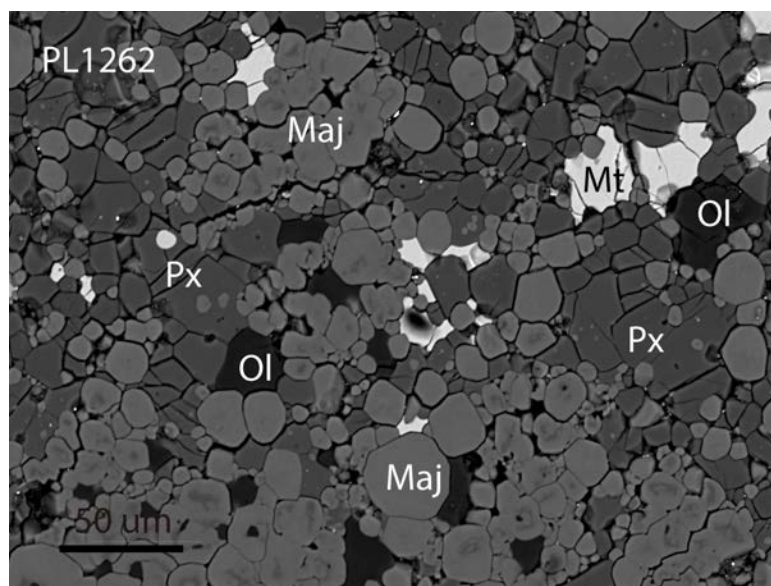


Fig. 1. Backscatter-electron image of recovered sample from high-pressure experiments at 12 GPa and 1200 °C, showing coexisting minerals, majoritic garnet (Maj), olivine (Ol), pyroxene (Px), and magnetite (Mt).

Results and Discussion

We performed a series of experiments from 6.5 to 15 GPa at temperatures up to 1600 °C to develop a new majorite geobarometer for Fe³⁺-bearing majoritic garnets, using the Fe³⁺ starting material. The experiments produced majorites with high Fe³⁺/ΣFe ratios (0.47-0.63) and low Al³⁺ contents. Using the same fitting procedure described by Collerson *et al.* (2010), we found that the synthesis pressure linearly changes with the cation substitution parameter. The linear relationship for Fe³⁺/ΣFe ~ 0.6 has a slope that is 2 times higher than that of the geobarometer defined for Fe³⁺/ΣFe = 0 (Tao *et al.*, 2017).

Fe³⁺-rich majorite in the mantle could form under high oxygen fugacity. However, the maximum Fe³⁺ content in majorite may be limited by the equilibrium element partitioning among the coexisting mineral even at the highest mantle oxygen fugacity. Majorite coexisting with magnetite and olivine/pyroxene has a typical Fe³⁺/ΣFe ratio of 0.48 at 12 GPa and 1200 °C, using both Fe³⁺ and Fe²⁺ starting materials. The alternative to produce high Fe³⁺-bearing majoritic garnets is through the reduction of carbonate accompanied by oxidizing the iron component in silicate. We carried out experiments to investigate redox reactions to form Fe³⁺-rich majorite through the reduction of carbonates including CaCO₃, FeCO₃, and MgCO₃. The starting material used in the experiments contains only Fe²⁺. The reaction with CaCO₃ produced high Fe³⁺/ΣFe ratios in majorite, 0.77-0.94, at 12 GPa and 1200 °C (Fig. 2). The majorite also contains high CaO and low MgO content. On the other hand, the reaction with MgCO₃ and FeCO₃ at the same condition produced majorites with low Fe³⁺/ΣFe ratios, < 0.33 (Fig. 2).

The Fe^{3+} content in majorite produced in carbonate reduction is strongly correlated with the CaO content and anticorrelated with the MgO content because of possible coupled substitutions in the structure. We also investigated the possible back transformation of Fe^{3+} -rich majorite. The Fe^{3+} -rich majorite is exceptionally stable and has a high kinetic barrier for the back transformation at low pressure because the decomposition has to involve an Fe^{3+} phase such magnetite. The experiments provide new insights into the preservation of the Fe^{3+} -bearing majorite inclusion from deep mantle.

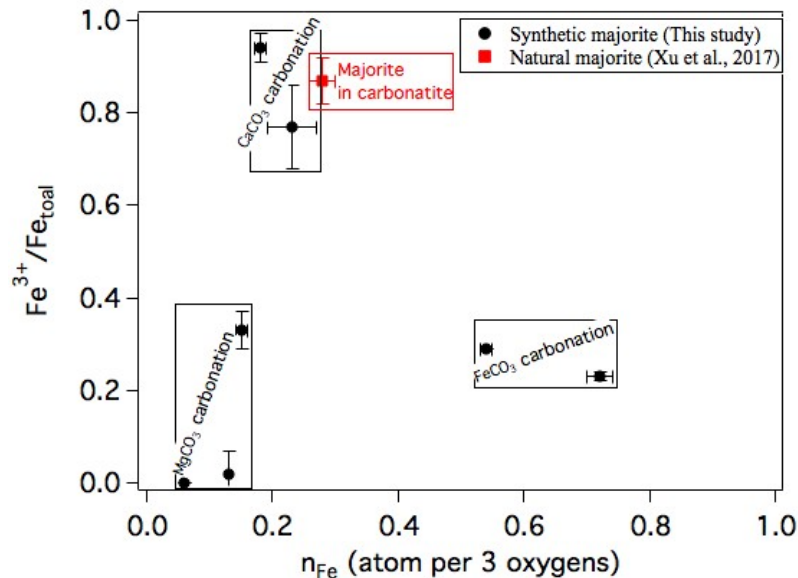


Fig. 2. $\text{Fe}^{3+}/\Sigma\text{Fe}$ ratio v.s. n_{Fe} of the synthetic majorites produced through reaction with different carbonates, CaCO_3 , FeCO_3 , and MgCO_3 . The value for the natural majorite is also plotted for comparison.

References

- Bennett NR, Brenan JM, Fei Y (2016) Thermometry of the magma ocean: Controls on the metal–silicate partitioning of gold. *Geochimica et Cosmochimica Acta* 184: 173-192.
- Bertka CM, Fei Y (1997) Mineralogy of the Martian interior up to core-mantle boundary pressure. *Journal of Geophysical Research* 102: 5251-5264.
- Collerson KD, Williams Q, Kamber BS, Omori S, Arai H, Ohtani E (2010) Majoritic garnet: A new approach to pressure estimation of shock events in meteorites and the encapsulation of sub-lithospheric inclusions in diamond. *Geochimica et Cosmochimica Acta* 74: 5939-5957.
- Höfer HE, Brey GP (2007) The iron oxidation state of garnet by electron microprobe: Its determination with the flank method combined with major-element analysis. *American Mineralogist* 92: 873-885.
- Höfer HE, Brey GP, Schulz-Dobrick B, Oberhänsli R (1994) The determination of the oxidation state of iron by the electron microprobe. *European Journal of Mineralogy* 6: 407-418.
- McCammon CA, Ross NL (2003) Crystal chemistry of ferric iron in $(\text{Mg,Fe})(\text{Si,Al})\text{O}_3$ majorite with implications for the transition zone. *Physics and Chemistry of Minerals* 30: 206-216.
- Rohrbach A, Ballhaus C, Golla-Schindler U, Ulmer P, Kamenetsky VS, Kuzmin DV (2007) Metal saturation in the upper mantle. *Nature* 449: 456-458.
- Stagno V, Frost DJ, McCammon CA, Mohseni H, Fei Y (2015) The oxygen fugacity at which graphite or diamond forms from carbonate-bearing melts in eclogitic rocks. *Contributions to Mineralogy and Petrology* 169: 1-16.
- Tao R, Fei Y, Bullock ES, Xu C, Zhang L (2017) Experimental investigation of Fe^{3+} -rich majoritic garnet and its effect on majorite geobarometer. *Geochimica et Cosmochimica Acta*: in review.
- Xu C, Kynický J, Tao R, Liu X, Zhang L, Pohanka M, Song W, Fei Y (2017) Recovery of an oxidized majorite inclusion from Earth's deep asthenosphere. *Science Advances* 3: e1601589.

Mapping heat flow from a time series of satellite temperature images as a regional exploration tool for kimberlites

Neil Pendock

Terracore

Introduction

Various estimates of the Curie depth point [CDP] for countries and cratons have been made from regional and satellite magnetic surveys, the most recent in March for the whole planet using the Earth Magnetic Anomaly Grid [1]. Such estimates have applications for mineral exploration such as subaqueous hot spring gold deposits and kimberlites.

To be practically useful for exploration, spatial resolution of CDPs needs to be increased. EMAG2 has a spatial resolution of 2 arc minutes while the regional magnetic grid of the Okavango Rift Zone on which a 3D inversion was performed to estimate CDPs [2] had a spatial resolution of 62.5m.

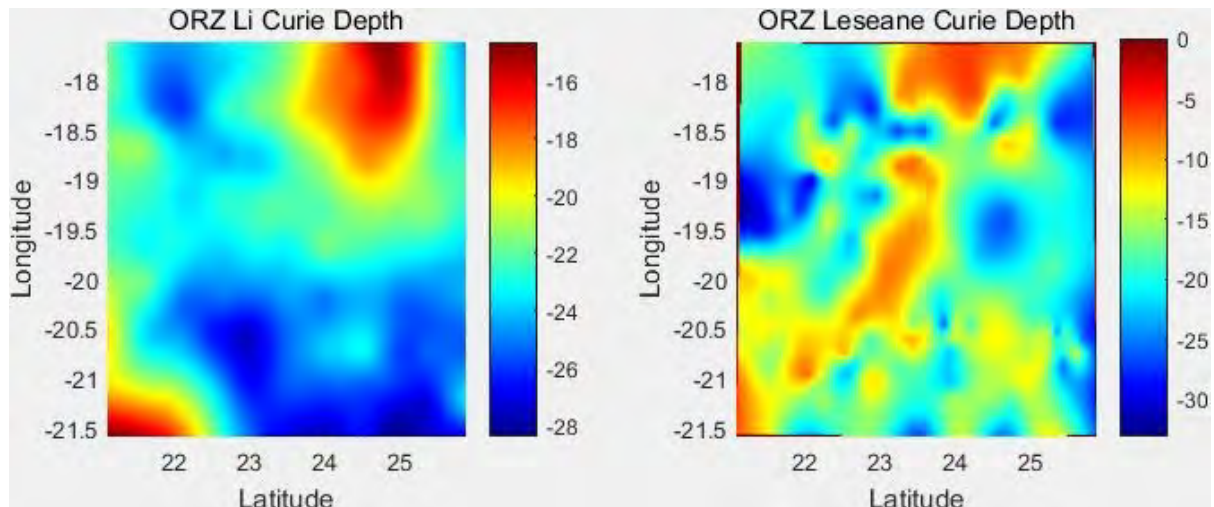


Figure 1: Curie depth estimates from satellite magnetic (left) and airborne magnetic surveys (right)

The ~60 km wide NE-trending zone of shallow CDPs coincident with major rift-related border faults and the boundary between Proterozoic orogenic belts is lost in the EMAG2 inversion. The two CDPs have a correlation of 0.19 and shallow structure is clearly lacking in the satellite derived estimate.

High resolution regional magnetic grids are rare, at least in the public domain, while finer regional magnetic surveys raise issues for 3D inversion techniques as they are computationally demanding.

Less computationally intensive CDP estimators using the slope of the radially averaged power spectrum of the Fourier Transform of the magnetic field have issues with regards to which frequencies to use to compute the slope. The EMAG2 result, a power spectrum estimation, used different ranges of frequencies for different moving windows of data.

A technique to improve CDP spatial resolution is needed for an effective exploration tool.

The temperature of the earth's surface is measured every day and night at various spatial resolutions from kilometers down to 90m by a variety of remote sensing and POES weather satellites. Available

spatial and temporal resolution is about to increase dramatically as proposed microsatellite systems from companies such as Planetary Resources become operational.

If a sufficiently long time series of temperatures is collected, common sense would suggest that the only signal constant over time would be heat flow from the mantle. Transient factors such as weather would be averaged out while thermal emittance from surficial geology could be modelled using day and night time temperature estimates.

Heat flow from temperature times series

We assume a simple linear model:

$$\text{measured temperature} = \text{surface reflection} + \text{surface emittance} + \text{atmospheric/weather related effects} \\ + \text{slope/aspect/elevation effects} + \text{heat flow from the mantle}$$

We are interested in estimating the last factor as an aid to kimberlite exploration as we'd like to flag areas with lithospheric conditions conducive to the production and preservation of carbon in diamond form, which requires relatively low heat flows of 40–45 mW m⁻² [3].

41 8-day and 42 8-night surface temperature averages collected by the MODIS satellite at 1 Km spatial resolution during 2016 over the central Kalahari were downloaded from reverb.echo.nasa.gov. Last year was the peak of the worst drought in Southern Africa for a century so transient surface water effects are minimized. We also included a 1 Km resolution DTM subsampled from Aster satellite stereo pairs from earthexplorer.usgs.gov to account for elevation effects.

Published heat flows for the ORZ [2] are used as the target variable in a multiple linear regression model and the temperature time series and DTM are explanatory variables. We are using magnetic derived heat flows to calibrate our temperature/DTM model. The estimates correlate at 0.74.

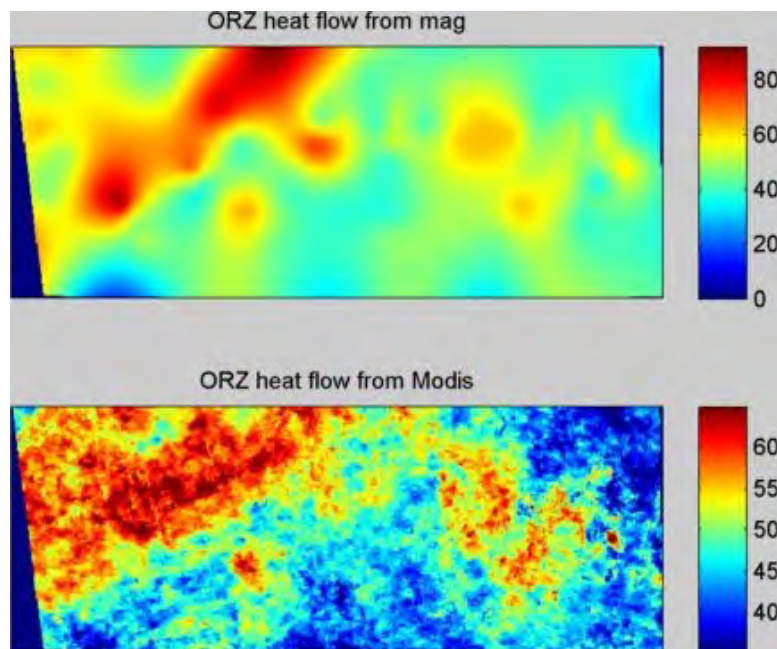


Figure 2: CDP from regional magnetics (top) and Modis temperatures (bottom)

The model is then extended to central Botswana for which no target CDPs are available.

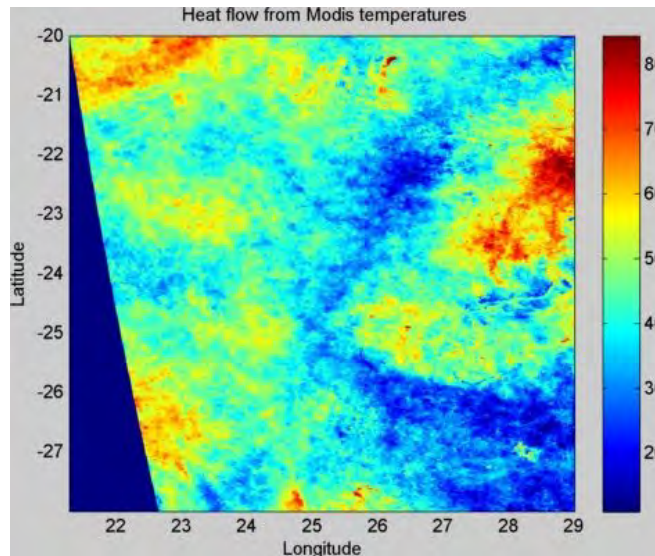


Figure 3: Modis heat flow for central Botswana

Visual inspection of kimberlite locations in the Jwaneng area confirms a spatial correlation with low heat flow regions.

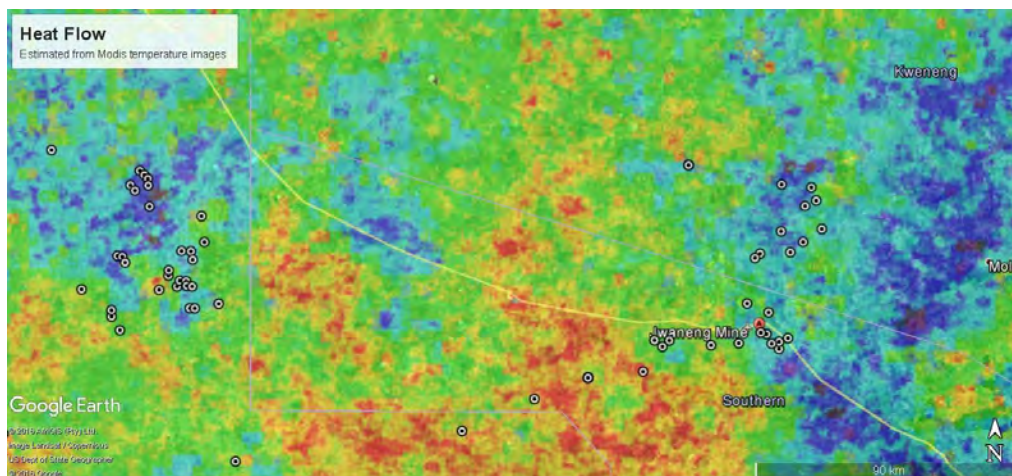


Figure 4: Modis heat flows for Jwaneng region

Heat flows can be used as an inexpensive reconnaissance tool in a regional exploration program.

References

1. Li, C.-F. et al. (2017). A global reference model of Curie-point depths based on EMAG2. *Sci. Rep.* 7, 45129; doi: 10.1038/srep45129.
2. Leseane, K., Atekwana, E. A., Mickus, K. L., Abdelsalam, M. G., Shemang, E. M. and Atekwana, E. A. (2015), Thermal perturbations beneath the incipient Okavango Rift Zone, northwest Botswana. *J. Geophys. Res. Solid Earth*, 120: 1210–1228. doi: [10.1002/2014JB011029](https://doi.org/10.1002/2014JB011029).
3. Bouguern, A., Allek, K., Khalifa M., Bendiab, F. and D. Bouboya (2015), https://www.researchgate.net/publication/282161742_Mapping_curie_point_depth_of_the_west_African_Craton_from_satellite_magnetic_data_and_its_implication_for_diamond_exploration.



Letšeng Diamond Mine, Lesotho: Recent Advances in the Open Pit Geology of the Satellite Kimberlite Pipe

Teboho Nkotsi¹, Casey Hetman², Jock Robey³, Barbara Scott Smith⁴ and Mohapi Mohapi¹

¹ Letšeng Diamonds (Pty) Ltd., Letšeng-la-Terae, Lesotho, nkotsit@letseng.co.ls

² SRK Consulting, Vancouver, BC, Canada, chetman@srk.com

³ Rockwise Consulting, Kimberley, South Africa, jjrobey@telkomsa.net

⁴ Scott-Smith Petrology Inc., North Vancouver, BC, Canada, barbara@scottsmithpetrology.com

¹ Letšeng Diamonds (Pty) Ltd., Letšeng-la-Terae, Lesotho, mohapim@letseng.co.ls

Introduction

The Letšeng Diamond Mine in Lesotho differs from many other mines in southern Africa because it occurs near the margin of the Archaean Kaapvaal Craton, and produces some of the largest and most valuable diamonds from the lowest grade kimberlite mined in the world. The Mine comprises two adjacent steep-sided volcanic kimberlite pipes, Satellite and Main. In the Satellite pipe historic mapping of surface exposures, underground tunnels and drillcore logging during evaluation by Rio Tinto Exploration (1967-1972) reported nine poorly documented phases of kimberlite that were later combined into a single phase during limited mining by De Beers (1977-1982). Subsequently, Letšeng subdivided the pipe into two dominant kimberlite domains: Southern Volcaniclastic Kimberlite (SVK) and Northern Volcaniclastic Kimberlite (NVK). This investigation demonstrated more complex geology (Fig. 1) based on mapping of recent open pit exposures, logging of blast-hole and ahead of face drill chips and petrography. These results have been integrated with macrodiamond production data and drillcore information to update the present 3D geology model used for mine planning purposes.

Pipe Geology

The ~90 Ma Satellite Pipe (Stanley et al. 2015) is a smooth, steep-sided pipe that has an oval surface expression of approximately 5.2 ha. The pipe was emplaced into ~1800-2000 m thick sequence of Karoo basalts, which are partially exposed in the open pits. These basalts dominate the observed xenoliths within the kimberlite and range in size from microxenoliths to large-megaxenoliths with lengths greater than 100 m (Fig. 1). The majority of the pipe-fill is classified as Kimberley-type pyroclastic kimberlite (KPK; formerly tuffisitic kimberlite) broadly comparable to the type area pipes in Kimberley, South Africa (Scott Smith et al. 2013). Other textural types include hypabyssal kimberlite (HK) and rocks with textures transitional between HK and KPK.

Internal Geology

Distinct phases of kimberlite have been identified based on features including variations in kimberlite textures, size and abundance of country rock xenoliths and olivine macrocrysts, as well as the degree of xenolith-kimberlite reaction. This investigation of the current mining levels to ~190 m below surface confirmed that pipe-fill is dominated by SVK and NVK and that they are separated by a steep, sharp cross-cutting internal contact. Internal complexities within the SVK and NVK domains have been established and in addition, two new smaller phases of kimberlite have been identified: the Central Volcaniclastic Kimberlite (CVK) and the Central Coherent Kimberlite (CCK) as shown in Figure 1. All the kimberlites in the Satellite Pipe are characterised by very low abundances of mantle-derived xenocrysts (indicator minerals); however, garnet and spinel bearing peridotite xenoliths may be locally abundant within the NVK.

The dominant pipe-fill within the Satellite pipe is SVK, a uniform KPK with minor layering observed adjacent to the pipe wall and large xenoliths. It is a dark grey to green, altered kimberlite which contains 35 modal % fine-medium grained pseudomorphed olivine. The SVK consists of clast

supported, loosely packed cored and uncored magmaclasts and partly altered to fresh basalt xenoliths set within an altered

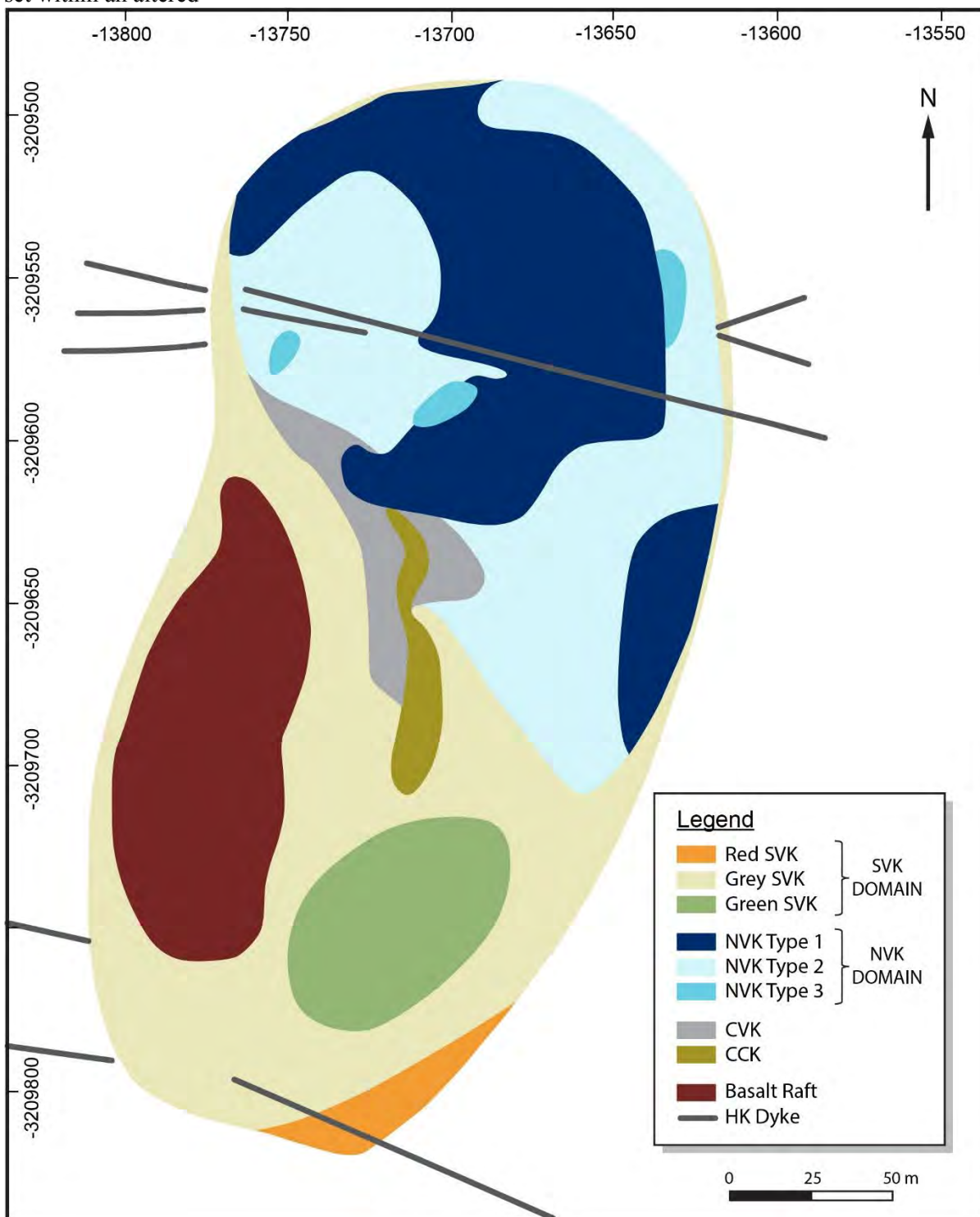


Figure 1: Plan view of the Satellite Pipe showing the internal geology between 3050-2878m above sea level.

interclast matrix. Primary groundmass minerals within the magmaclasts include variable amounts of melilite, phlogopite, spinel and perovskite. The mantle content of the SVK is uniform and three subtypes (green SVK, red SVK, grey SVK; Fig.1) have been mapped based on variations in country rock xenolith abundance and degree of reaction with the host kimberlite.



The second volumetrically significant pipe infill is NVK which is notably inhomogeneous with three subtypes identified in pit exposures and subsurface drillcores. The subtypes display different textures ranging from KPK to HK. Other variations include the size and proportion of basalt xenoliths, the degree of xenolith to kimberlite reaction and the sizes of both the magmaclasts and olivine macrocrysts. Most of the NVK is altered, massive, dark grey to black KPK (Type 2) containing 40-45 modal % pseudomorphed olivine, abundant matrix-supported magmaclasts and common, extensively reacted basalt xenoliths. The magmaclasts are both cored and uncored with selvages containing phlogopite, melilite, spinel and perovskite. The other NVK subtypes include an HK with textures transitional to KPK (Type 1) characterized by a similar modal % of olivine; however, this rock type contains conspicuous olivine macrocrysts larger than 1 cm as well as common magmaclasts larger than 5 cm. Type 3 NVK is considered a minor rock type with 35-45 modal % pseudomorphed olivine and is characterized by distinct layering defined by basalt xenoliths.

The newly established phase of kimberlite termed CVK has been identified in the centre of the pipe close to the NVK/SVK contact. This kimberlite is similar to the SVK and distinctly different from the NVK. It is a grey, massive KPK which contains 30-40 modal % fine to medium grained olivine macrocrysts that are much finer grained compared to both the SVK and NVK rock types.

The Central Coherent Kimberlite (CCK) is late-stage irregular HK intrusion which cross-cuts the SVK and CVK and ranges in thickness from a few centimetres up to 4-5 m. The CCK is a dark brown, massive, homogenous, well crystallized HK containing abundant fresh olivine crystals (55 modal %) characterised by complex morphology.

Several HK dykes are associated with the pipe which both predate pipe emplacement and cross-cut the pipe. The dykes are sub vertical, less than 1 m wide and range from perovskite and spinel-bearing phlogopite to carbonate kimberlites.

Conclusions

The emplacement history of the Satellite pipe can be reconstructed based on spatial relationships of the contrasting phases of kimberlite present within the pit exposures, together with the sharp, sub-vertical, cross-cutting relationships between them. The Satellite pipe was formed along and cross-cuts a pre-existing northeast-southwest kimberlite dyke system. The first of two major pipe forming events was the SVK. A number of thin remnants of SVK present between the NVK and the country rock indicates that the initial SVK event involved formation of the entire Satellite Pipe together with the relatively uniform KPK pipe-infill. This was followed by the emplacement of the NVK as a pipe which dominated the northern part of the Satellite pipe, and was nested within the SVK. The internally complex NVK includes KPK, HK and layered VK. The smaller CVK comprises a finer grained KPK emplaced along the boundary of the NVK and SVK domains. The CCK formed an irregular intrusion cross-cutting both the SVK and CVK. Finally, various cross-cutting HK dykes pass from the country rock into the Satellite pipe.

References

- Scott Smith BH, Nowicki TE, Russell JK, Webb KJ, Mitchell RH, Hetman CM, Harder M, Skinner EMW and Robey JvA (2013) Kimberlite Terminology and Classification. Proceedings of 10th International Kimberlite Conference, Volume Two, Special Issue of the Journal of the Geological Society of India, Volume 2, 1-17. Springer India.
- Stanley JR, Flowers RM, and Bell DR (2015) Erosion patterns and mantle sources of topographic change across the Southern African Plateau derived from the shallow and deep records of kimberlites, *Geochem. Geophys. Geosyst.*, 16, doi:10.1002/. AGU Publications. 2015GC005969.



Vertical Pit Mining-An Alternative to Open Pit Mining for Massive/Shallow Orebodies

P. J. Terbrugge¹, R. Armstrong¹

¹SRK Consulting (South Africa)

Introduction

The concept of vertical pit mining has developed as an alternative mining method for the exploitation from surface of small, vertical or near vertical, massive orebodies to depths of approximately 100m where ore extraction can become uneconomical due to high stripping ratios. Support of the sidewalls is ensured with systematic anchoring depending on the condition of the insitu rock mass together with the installation of mesh and shotcrete in order to prevent small-scale ravelling and spalling which, with the pit at depth, can prove hazardous to operations at the base of the pit.

Hoisting of the ore is carried out either by a vertical A Frame hoist at the crest of the pit, which requires tramping of ore at the base of the pit to the hoist. Alternatively, a Blondin Cableway system, which allows for loading of kibbles at any location within the pit, negating the need for a tram to the hoist located on the side of the pit, can be utilised.

For various reasons the technique has been successfully applied to the mining of a chrome deposit in Zimbabwe to a depth of 95m and a kimberlite pit in West Africa where the pit was terminated at a depth of 85m due to a sidewall failure. Feasibility studies for two further vertical pits were conducted for orebodies in South Africa and Australia, kimberlite and nickel respectively, but due to economic considerations, have not been mined.

Performance Requirements

To receive serious consideration, mining methods must satisfy certain performance requirements with the following points being extremely important: Safety, Technical feasibility, Excavation Stability, Monitoring Capability, Economic Viability, and Acceptable Environmental Impact.

The vertical pits mined to date fundamentally comply with these requirements and possess the advantage that the two main components of the system, lateral support comprising cable anchors and the hoisting systems, are well proven technology and thus provide the required performance with a high level of confidence.

Vertical Pit Design

The vertical pit design for the kimberlite pipe in West Africa was characterised by a unique set of circumstances comprising political, social, geographical and administrative challenges, with the vertical pit established at the base of an existing pit approximately 50m below ground level. Material parameters were obtained from a suite of laboratory tests previously carried out as well as geotechnical mapping of the existing pit walls, including the kimberlite/granodiorite country rock mass. Using the Hoek-Brown failure criteria the design calculations comprised both 2-dimensional and 3-dimensional numerical analyses to define the cable anchor and rock bolt requirements to provide stability to the excavated vertical wall of the pit. The general support was comprised of the following elements:

- 20m long cable anchors with a 5m fixed length tensioned to 40 tons at a 5 x 7m spacing as the primary support,
- 3m fully bonded grouted dowels with an ultimate tensile strength of 14 tons at a 2m spacing.
- 4mm weldmesh with a 150mm aperture fixed to the pit wall with “S” pins, covered with 30MPa shotcrete and a design thickness of 75mm.

During the mining programme, it became necessary to install 40m anchors beneath the headgear to prevent a wedge type failure of the hoist platform. This was achieved with the headgear remaining intact and operational during the life of the vertical pit. The anchor support together with a section through the vertical pit is included as Figure 1.

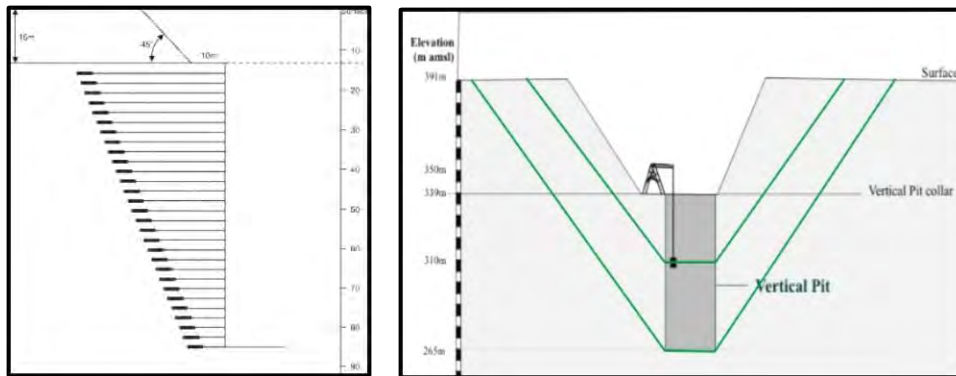


Figure 1: Anchor support with a section through the vertical pit

Implementation

One of the most important aspects of implementation was the restriction on the time and frequency of blasting due to the number of households within the 250m blast envelope, with evacuation of this area required before each blast. With the agreed two blasting cycles per week, coordination of the activities within the pit and adherence to the schedule was of prime importance. The schedule required support installation, including drilling of holes for cable anchors before meshing and shotcrete could be applied, with the cycle having to be completed before the following blast in a particular area of the pit. The cycle time for anchor installation was four days from the time the anchor was installed in the hole, grouted and tensioned. Support and mining production activities therefor have to be carefully synchronised to ensure continuous operations in the pit.

With a limited hoisting capacity and the restricted access at the base of the pit, maintaining ore production targets in order to keep process plants operating at capacity can be a challenge, with downtime necessary for hoist examinations and maintenance on a regular basis. Because of the constricted area at the base of a vertical pit, other factors to be considered, include sump maintenance and drainage in order to maintain a dry operating floor as well as the creation of a free face for optimal blasting results. With the relatively small floor area it is not practically feasible to remove all the mining equipment from the pit bottom for a blast and as such a great deal of emphasis should be put on the blast design. Figure 2 provides a view of the vertical pit and operations at the base of the pit.

In both vertical pits discussed, groundwater played a major role in the design of the operations with vertical wells drilled and pumps installed to lower the groundwater table to acceptable levels. Pore water pressures within the country rock mass were also problematic and where the vertical wells were inadequate, horizontal holes were drilled from within the pit to effect slope drainage.

With the vertical nature of the pit side walls and the potential risk of collapse, slope monitoring played an important part of the slope management programme, with conventional methods being used.



Figure 2: View of the vertical pit with operations at the base of the pit

With respect to the blast design, and a key component being the least damage to the rock mass behind the mine design line, and damage to mining equipment in the confined pit, careful consideration is required in the design. Using the regular open pit “pit limit blast design strategy”, blast layouts should comprise pre-splits, a narrow trim and the production blast. The pre-split should be fired first, followed by the production blast and then the trim. Load out arrangements at the base of the pit and surface are shown in Figure 3.



Figure 3: Load out arrangements at the base of the pit and surface

Conclusions

While vertical pit mining has been shown to be more expensive than conventional open pit mining, the benefit is realised when considering the negligible waste mining required for a return of the same ore tons. The stripping ratio for the West African vertical pit was 0.65 compared to 6.2 on the first cut for a conventional pit and 13.5 on the final cut. Concerning hoisting facilities, a Blondin Cableway System is the preferred option due to its flexibility in that kipples for loading can be placed at any location within the vertical pit, with ore from the blast muck pile loaded directly into the kibble and hoisted to surface. It is considered that vertical pit mining is a viable alternative to conventional open pit mining and can effectively be exploited on small to medium sized kimberlite pipes.

References

Redford M S, Terbrugge P J (2000) Vertical Pit Mining – A novel alternative to open pit or underground methods of mining of appropriate massive shallow orebodies. Massmin 2000, Brisbane, Australia.

Joubert J S C, Freeman L A, Terbrugge P J, Venter J (2008) The Koidu Vertical Pit – Sierra Leone. Surface Mining 2008, Southern African Institute of Mining and Metallurgy, Johannesburg, South Africa.



Letšeng Diamond Mine, Lesotho: A Variant of Kimberley-type Pyroclastic Kimberlite Emplacement

Casey Hetman¹, Barbara Scott Smith² Jock Robey³, Teboho Nkotsi⁴, Mohapi Mohapi⁴, Thabang Mohapi⁴

¹*SRK Consulting, Vancouver, BC, Canada, chetman@srk.com*

²*Scott-Smith Petrology Inc., North Vancouver, BC, Canada, barbara@scottsmithpetrology.com*

³*Rockwise Consulting, Kimberley, South Africa, jjrobey@telkomsa.net*

⁴*Letšeng Diamonds (Pty) Ltd., Letšeng-la-terai, Lesotho, Southern Africa, nkotsit@letseng.co.ls*

⁴*Letšeng Diamonds (Pty) Ltd., Letšeng-la-terai, Lesotho, Southern Africa, mohapim@letseng.co.ls*

⁴*Letšeng Diamonds (Pty) Ltd., Letšeng-la-terai, Lesotho, Southern Africa, mohapit@letseng.co.ls*

Introduction

The Letšeng Diamond Mine comprises two adjacent kimberlites, the Main and Satellite pipes. Very low grade and low frequency of high value stones preclude use of standard evaluation methods, increasing the need for high confidence geology models. New results of drillcore investigations, including core logging, country rock dilution measurements, indicator mineral abundances and petrography are integrated with open pit mapping and macrodiamond production data to present updated 3D geological models of the Main and Satellite pipes (Fig.1).

Letšeng was emplaced ~90 Ma and forms part of a Cretaceous kimberlite province extending across southern Africa. The Letšeng bodies are steep-sided volcanic pipes that are infilled with multiple asymmetric phases of kimberlite separated by near-vertical, sharp, cross-cutting internal contacts. There are associated marginal carbonate-cemented country-rock breccias and sub-vertical kimberlite dykes that can occur within a zone of well-developed carbonate veining adjacent to the pipes. The pipe infills are dominated by kimberlite closely resembling Kimberley-type pyroclastic kimberlite (KPK; formerly tuffisitic kimberlite; Scott Smith et al. 2013) that contains common large megaxenoliths of massive and brecciated country rock basalt. Other textural varieties include hypabyssal kimberlite (HK), transitional HK-KPK and resedimented volcanoclastic kimberlite (RVK). Each phase of kimberlite represents a separate magmatic system. In each KPK there is a continuum of crystallization from the magmaclast selvages to the intermagmaclast matrix. As documented elsewhere, the HK-KPK transition involves an increasing (i) degree of deuteric replacement of olivine, (ii) amount of incorporated country rock xenoliths and (iii) textural modification of the magma prior to solidification subsurface within the diatreme. These conclusions negate some other proposed modes of emplacement.

Internal Pipe Geology

The larger Main pipe (Fig. 1a) was formed by at least five phases of kimberlite emplacement that display decreasing explosivity over time: (i) initial pipe formation now represented by marginal remnants of diverse RVKs deposited into an open crater (RVK-A); (ii) formation of a dominant and relatively uniform KPK-infilled diatreme (K1); (iii) a poorly delineated subsequent RVK-B containing blocks of the latter KPK; (iv) a central nested pipe infilled with inhomogeneous coherent to more pyroclastic kimberlite (K6); and (v) a late cross-cutting irregular intrusive HK pipe-sheet complex (K4). The occurrence of both KPK and RVK is consistent with the estimated erosion of 300-500 m and the southern African composite 'Hawthorne' KPK-pipe model.

The Satellite pipe was formed by at least five phases of kimberlite emplacement: (i) an initial pipe infilled with relatively uniform KPK (Southern Volcanoclastic Kimberlite - SVK); (ii) a nested pipe with variable complex KPK-HK textures (Northern Volcanoclastic Kimberlite - NVK); and (iii) three smaller later diverse cross-cutting kimberlites (CVK, CCK and HK dykes). The apparent absence of RVK in this pipe is consistent with the development of a smaller pipe where the upper crater has been completely eroded.

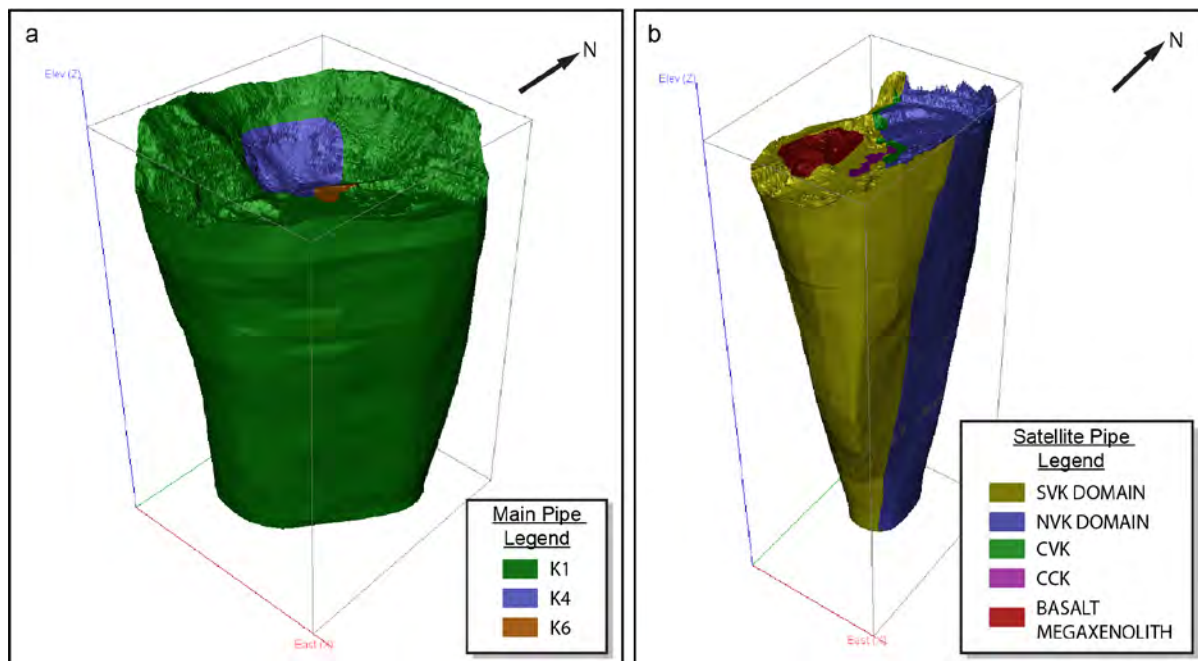


Figure 1: Simplified 3D geological models of the Main (a) and Satellite pipe (b) – looking north west. Note: not all phases of kimberlite are shown.

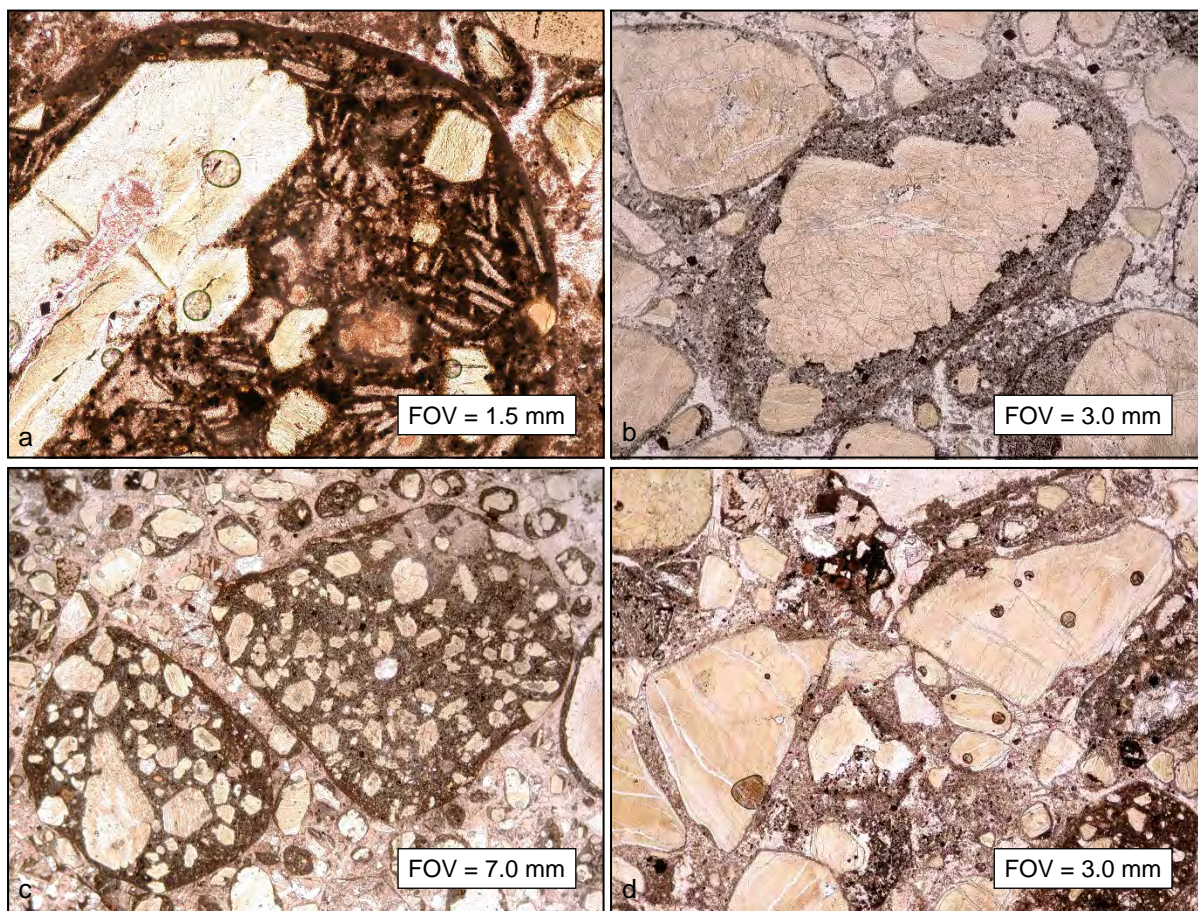




Figure 2: Photomicrographs from the Satellite and Main pipes highlighting some of the key petrographic features from Letšeng KPKs that differ from the type-area KPKs: (a) complex-shaped olivine phenocrysts and common melilite laths within the groundmass of a magmaclast in the SVK, Satellite pipe; (b) the kernel to the central magmaclast is a complex-shaped olivine macrocryst displaying embayed margins interpreted as resulting from resorption in K1, Main pipe; (c) examples of uncored magmaclasts in the SVK with well crystallized groundmass minerals, a feature more typical of Fort à la Corne-type pyroclastic kimberlites (FPK); (d) conspicuous broken olivine macrocrysts from K1 of the Main pipe, another feature more typical of FPK.

Pipe-fill KPK Characteristics

Volumetrically, the most significant rock type within the Satellite pipe is SVK and within the Main pipe it is K1; both of these are classified as KPKs. SVK and K1 display macroscopic and petrographic features consistent with type-area KPKs (Fig.2). These include the overall massive structure with only localized layering adjacent to parts of the pipe wall or within the SVK adjacent to megaxenoliths. Both these KPKs contain abundant locally-derived basalt xenoliths that display limited reaction with the host kimberlite. Olivines are completely pseudomorphed. At Letšeng the KPKs contain atypical olivine phenocrysts that display complex growth features, twinning and may be unusually large (> 1.0 mm). Olivine macrocrysts display extensive embayed margins indicative of resorption. Magmaclasts are abundant with thin groundmass selvages occurring on most olivine crystals and many country rock xenoliths similar to those of typical KPKs (formerly referred to as pelletal lapilli). The magmaclasts at Letšeng also contain abundant uncored examples with well developed groundmass minerals including phlogopite, spinel and perovskite that are atypical of KPKs. Laths of pseudomorphed melilite are widespread, however the size and abundance of these crystals varies. A feature characteristic of type-area KPKs is the presence of microlites (clinopyroxene / phlogopite / amphibole) surrounding all constituents; although present, the microlites are not as well developed at Letšeng.

Conclusions

A significant number of features in the Letšeng kimberlites differ from the type-area KPKs including the following: (i) smaller and more complex-shaped olivine macrocrysts; (ii) abundant groundmass melilite and clinopyroxene indicating a more marginal melnoite-like parental magma; (iii) melt-bearing pyroclasts displaying some characteristics similar to Fort à la Corne-type pyroclastic kimberlites; and (iv) widespread common component breakage. The Letšeng kimberlite pipes therefore appear to represent a variant of KPK emplacement that may be characteristic of the Lesotho Highlands and reflect the different craton margin setting and emplacement into >1500 m of Karoo basalt that form the Lesotho Highlands. The identification of RVK within the present mining levels of the Main pipe indicate that crater development is much deeper than originally recognized. These features are all important for understanding and predicting the distribution of diamonds at Letšeng.

References

Scott Smith BH, Nowicki TE, Russell JK, Webb KJ, Mitchell RH, Hetman CM, Harder M, Skinner EMW, Robey JvA (2013) Kimberlite Terminology and Classification. Proceedings of 10th International Kimberlite Conference, Volume Two, Special Issue of the Journal of the Geological Society of India, Volume 2, 1-17. Springer India.



Geochemical and Petrographical Study of Megacrysts and Mantle Xenoliths from Gemsbok Hollow and Gruendorn Kimberlites in the Warmbad Kimberlite Province, South Africa.

de Klerk, W.¹, Bell, D.R.¹

¹ Africa Earth Observatory Network – Earth Stewardship Science Research Institute (AEON-ESSRI), Nelson Mandela Metropolitan University (NMMU), Port Elizabeth, South Africa, geologistwdk@gmail.com, David.Bell@nmmu.ac.za

Introduction

Kimberlites and their inclusions are unique in their depth of origin, thereby providing insights to mantle lithology and geochemistry. In Southern Africa, with its anomalously high topography, kimberlites are widely distributed across contrasting crustal tectonic terranes, offering the opportunity to compare the composition of the deep lithosphere between these regions, as well as to examine processes of kimberlite genesis. The aim of this study is to characterize the field relations, petrography and geochemistry of two xenolith-bearing Warmbad kimberlites (Gemsbok Hollow (GBH) and Gruendorn (GD)) with a focus on their mantle xenolith suites in order to improve our knowledge of the underlying mantle in this region. In addition this study will further contribute to megacryst formation processes and origin as well as provide further insights, in the context of megacryst analyses from GBH and GD as well as ~50 other Southern African kimberlite suites, to characterize deep lithospheric structure and compositional variation.

Study Area

The Warmbad kimberlite province is part of a larger province known as the Namaqua-Bushmanland-Warmbad (NBW) kimberlite and melilitite province. This study focuses particularly on the Warmbad kimberlite province (WKP) which is a relatively unstudied group of ~30 kimberlite pipes (including the GBH and GD pipes in this study) and dikes that erupted through the Proterozoic Namaqua belt in Southern Namibia and the Northern Cape province of South Africa. The kimberlites in this region have erupted through a complex tectonostratigraphic Proterozoic Namaqua belt crustal tectonic terrane, the various domains (Richetersveld, Bushmanland, Kakamas, Areachap, Kaaien) within Proterozoic Namaqua belt amalgamated in Grenville Orogeny (1-1.3 Ga) (Bial et al., 2016; Hartnady et al., 1985). The Group I kimberlites of GBH (-28.055200°; 20.037710°) and GD (-28.053350°; 20.029230°) are situated approximately 100 km WNW of Upington, South Africa, adjacent to the border between South Africa and Namibia (Figure 1). The dating of these kimberlites has proved somewhat difficult with some as old as 530 Ma (perovskite, U-Pb, Ondermatjie) (Wu et al. 2010) and some as young as 60 Ma e.g. Stolzenfels (perovskite U-Pb) (Griffin et al. 2014). Rietfontein for example has two age determinations that conflict, 72 Ma (zircon, U-Pb) (Davis et al., 1976) and 134 ± 9 Ma (perovskite, U-Pb) (Griffin et al. 2014).

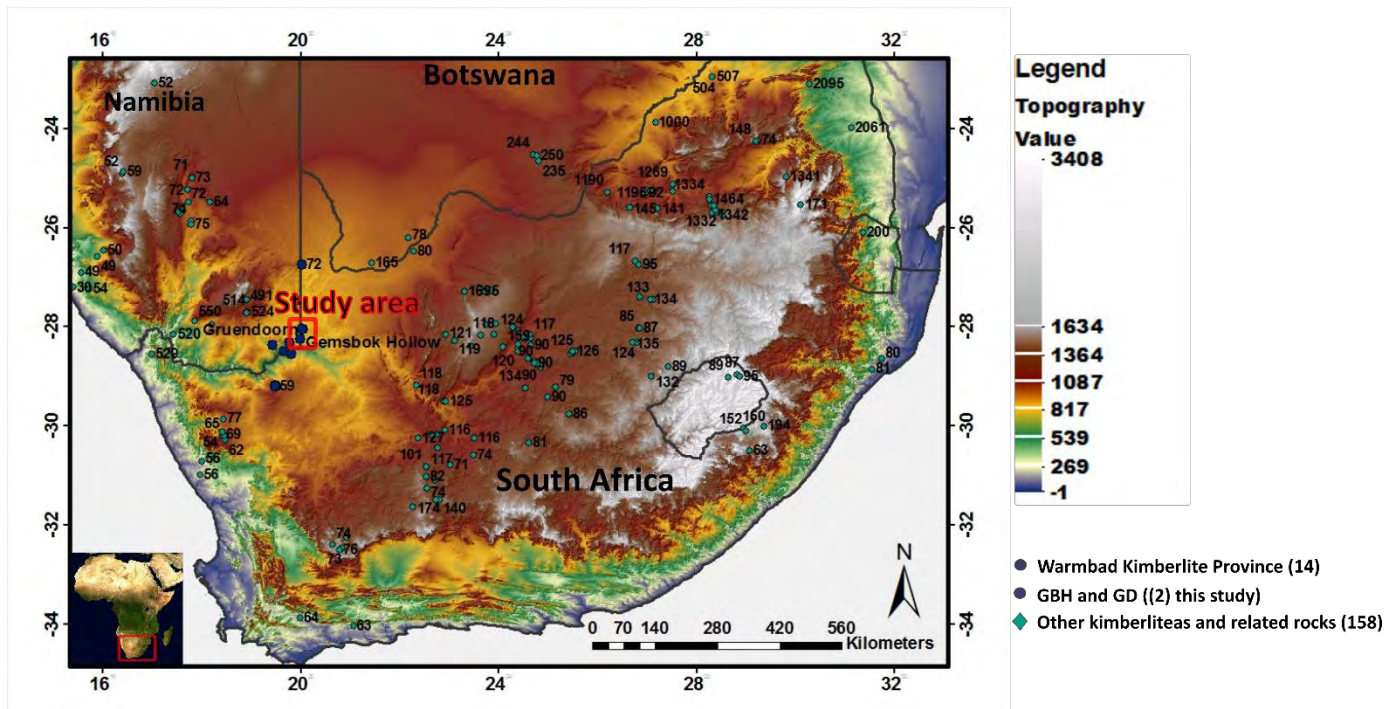


Figure 1: Regional topographic map showing kimberlite and related rock age distributions in relation to some Warmbad kimberlites (dark blue) in the study area (kimberlite data: Jelsma et al., 2009; this study). The few age constraints suggest a late-Cretaceous eruption age (~75 Ma) with some evidence for a possible older (~500 Ma) component for the Warmbad kimberlites of GBH and GD.

Samples and Preliminary Petrographic Results

Reconnaissance field work has revealed two large pipes, approximately 70 m and 400 m in diameter, and associated sills capped by carbonate. These intrude into sediments of the Nama Group at the plateau forming the northern margin of the Orange River drainage system (Figure 2). Kimberlites in the Nama plateau typically present as dome-like depressions and often exhibit a blue to greenish colour depending on the degree of weathering.

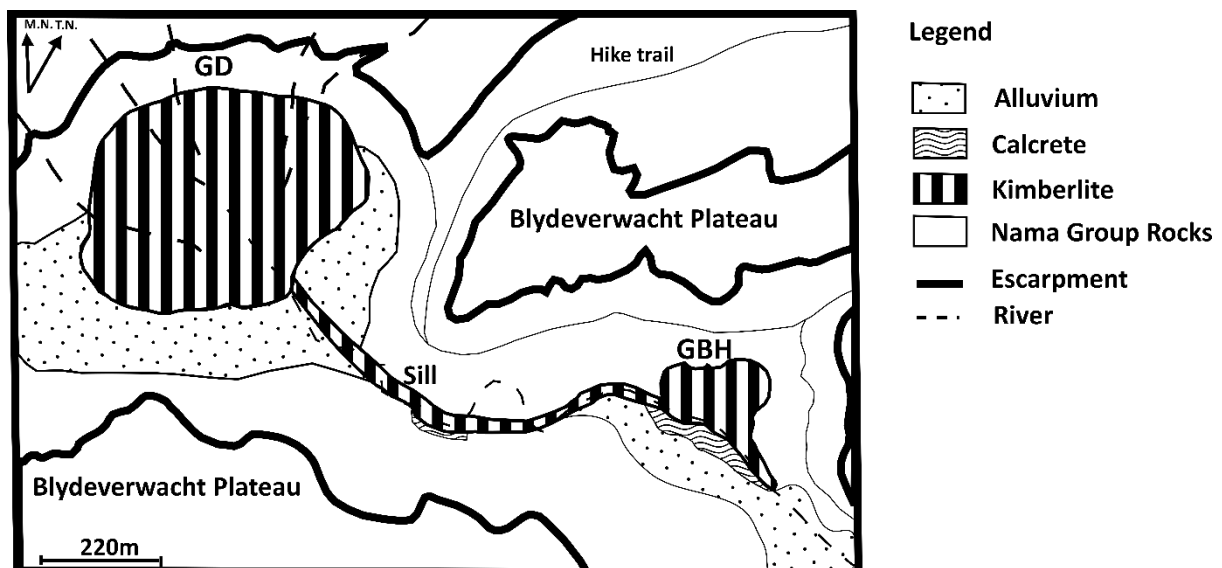


Figure 2: Field sketch of the two diatremes of Gruendorn (GD) and Gembok Hollow (GBH) and associated sill that has intruded in the Pre-Cambrian-Cambrian aged Nama Group rocks at the plateau of the northern margin of the Orange River drainage system.

The mantle-derived inclusion suite consists of peridotites, Cr-poor megacrysts and occasional eclogite and pyroxenite. The megacryst suite is dominated by abundant garnet megacrysts (≤ 6 cm in diameter),

abundant ilmenite (≤ 2 cm), and rarer phlogopite, subcalcic clinopyroxene (≤ 3 cm) and zircon (5-10 mm). Relative abundances of megacryst minerals differ at the two pipes. Several garnet megacrysts are deformed and a few contain inclusions of sub-rounded clinopyroxene and/or subrounded to amoeboidal shaped quenched sulfide melt pockets. Clinopyroxenes with garnet exsolution lamellae are also observed. Peridotites (up to ~ 50 cm) are highly weathered, with fresh olivine and/or orthopyroxene (8%) rarely preserved, and are dominated by garnet lherzolite (80%) with subordinate harzburgite (10%) and dunite (2%). The majority of peridotites have relic coarse granular textures with rounded garnet grains with extensive kelyphite rim development, whilst others have porphyroclastic texture. Preliminary micro-petrographic observations using SEM have revealed low Na content for the garnet megacryst suite, although secondary garnet patches or zones with relatively higher Na content (~ 2 wt%) have been observed in some garnets and seem to be a major coexisting phase inclusion with secondary cpx (~ 2 wt % Na) patches. In both these types of inclusion patches ilmenite is always present as an inclusion. In addition, large primary subrounded, isolated cpx inclusions are also observed. Some non-isolated cpx inclusions have vein-like extensions, suggesting possible introduction as a droplet. Quenched sulphide melt pockets were identified that are polyphased, traces of small sulphide droplets in an aligned row have been observed, suggesting the denser material percolated into partial crystalizing garnet, possibly crystalizing from a melt. Some of these garnets show single grains with differing Ca content, with zig-zag grain boundaries, indicating they were possibly amalgamated and fused together under subtle differing temperature conditions, similarly for some cpx megacrysts. Some ilmenite zoning has been observed. Ilmenite megacrysts themselves do not have cpx inclusion, with dolomite (occurring as percolative droplets or as veins in which the dolomite is zoned), apatite and rutile being the major inclusion phases. Mica megacrysts exhibit a strong mineral inclusion association between xenotime and zircon, with zircons occurring as inclusions within the large xenotime crystals. In addition, there is also a spatial relationship between the occurrence of apatite and zircon as well as a spatial relationship between ilmenite, xenotime (Y-phosphate), zircon and apatite (Ca-phosphate). The major inclusion phase in the mica megacrysts are thus phosphates in association with zircon and apatite.

Ongoing Work

Numerous grains from various samples constituting 50 garnet megacrysts (GBH), 30 garnet megacrysts (GD), 13 Cpx megacrysts (GBH, GD combined), 50 ilmenite megacrysts (50 ilmenite), mica megacryst (10), 30 peridotite garnets (GBH), 30 peridotite cpx (GBH) have been mounted for EPMA-WDS and LA-ICPMS analysis of major and trace – elements, with additional sample preparation for radiogenic isotope analysis. In addition, few zircon megacrysts, and few zircon inclusions in mica megacrysts are prepared in preparation for geochronology. These geochemical results, together with field relations and petrographic observations, will be used to improve our knowledge of the underlying mantle, megacryst petrogenesis and lithospheric structure in the region. Additionally, these results together with ~ 50 other Southern African kimberlite suites, will be used to characterize deep lithospheric structure and compositional variation over crustal tectonic terranes.

References

- Bial J, Büttner S, Appel P (2016) Journal of African Earth Sciences Timing and conditions of regional metamorphism and crustal shearing in the granulite facies basement of south Namibia : Implications for the crustal evolution of the Namaqualand metamorphic basement in the Mesoproterozoic. *J African Earth Sci* 123:145–176.
- Davis, G.L., Krogh, T.E., Erlank AJ (1976) The ages of zircons from kimberlites from South Africa. In: Year Book-Carnegie Institution of Washington, Vol. 75. pp 821–824
- Griffin WL, Batumike JM, Greau Y, et al (2014) Emplacement ages and sources of kimberlites and related rocks in southern Africa: U-Pb ages and Sr-Nd isotopes of groundmass perovskite. *Contrib to Mineral Petrol* 168:1–13.
- Hartnady C, Joubert P, Stowe C (1985) Proterozoic crustal evolution in southwestern Africa. *Episodes* 8:236–244.
- Jelsma H, Barnett W, Richards S, Lister G (2009) Tectonic setting of kimberlites. *Lithos* 112:155–165.
- Wu FY, Yang YH, Mitchell RH, et al (2010) In situ U-Pb age determination and Nd isotopic analysis of perovskites from kimberlites in southern Africa and Somerset Island, Canada. *Lithos* 115:205–222.

Petrology of the White River Diamondiferous Paleoproterozoic Intrusive Rocks

Richard Curtis Brett¹, Samuel Metteer², Warren Riemer³, Samuel Russell⁴, Andrew Faragher⁵, Shannon Zurevinski⁶

¹Rio Tinto Exploration Canada Inc., Vancouver, Canada, curtis.brett@riotinto.com

²Lakehead University, Thunder Bay, Canada, sam.metteer@gmail.com

³Rio Tinto Exploration Canada Inc., Thunder Bay, Canada, warren.riemer@riotinto.com

⁴Rio Tinto Exploration Canada Inc., Thunder Bay, Canada, sam.russell1@riotinto.com

⁵Rio Tinto Exploration Canada Inc., Vancouver, Canada, andrew.faragher@riotinto.com

⁶Lakehead University, Thunder Bay, Ontario, Canada, shay@lakeheadu.ca

Introduction

Diamond-bearing kimberlitic rocks have recently been identified within the Oskabukuta property owned by Rio Tinto Exploration Canada Inc. (RTECI), 15km west of the town of White River, Northwestern Ontario (Figure 1). The property is located in the Abitibi-Wawa island-arc terrane within the Archean Superior Province. The rocks are predominantly hosted within post tectonic granites of the Pukaskwa Complex (2.719-2.688 Ga). The diamond-bearing intrusion has been mapped at surface for over a 900 m, and is referred to as the Rabbit Foot intrusion. We present a description of the mineralogy, mineral chemistry, age dates and geothermobarometry for this occurrence. These data are used to constrain the timing of the destruction of Southern Superior Province's cratonic roots.



Figure 1: Location of the Oskabukuta Project

Petrography and Mineral Chemistry

The Rabbit Foot rocks are divided into several phases based on distinctive textural characteristics, and generally described as an intrusion, 2 to 30 meters in width, containing abundant xenocrysts of serpentized-olivine (2 mm to 2 cm), garnet, ilmenite, chromite, chrome diopside and diamond. These phases are set in a crystalline matrix consisting of a phenocryst assemblage of olivine-phlogopite-clinopyroxene-carbonate-apatite-oxide (spinel-magnetite-perovskite) with a variably serpentized carbonate bearing groundmass (Figure 2). The rock contains mantle derived micro-xenoliths of garnet lherzolite and can contain up to 50 percent of a diverse suite of altered country rock xenoliths.

Phenocrystic olivine range in modal abundance from 0 – 25 %, are <0.5 mm, typically anhedral, and variably serpentised/carbonatised. Forsterite content ranges between 0.85-0.87 and contains variable NiO (0-0.38 wt. %). Mica ranges in size and shape from 1 mm hexagonal oscillatory laths, to anhedral groundmass grains <0.5mm with orange/red mantles. The modal abundance of mica ranges between 10 – 45 %. Mica ranges in composition from Ba-phlogopite to tetraferriphlogopite; the barium content is not high enough (0-4.4 wt. % BaO) to identify the mica as kinoshitalite. Groundmass spinel are subhedral to euhedral, <0.5mm, represents 10-30 percent of the groundmass phases and can display

oscillatory zoning and atoll textures. Cores are typically chromite in composition with titanomagnetite rims. The trend features spinel whose compositions range from aluminous magnesian chromite, to titanian chromite to ulvöspinel-magnetite series. Perovskite are <200µm, subhedral, are relatively pure CaTiO₃, and lack substantive REE concentrations. Clinopyroxene is present, and is typically related to the rims of altered crustal xenoliths (Metteer, 2016). The xenocryst assemblage consists of olivine, pyrope and eclogitic garnet, chrome diopside, orthopyroxene, chromite, ilmenite and diamond. A dominant proportion of chromite contains high Cr₂O₃ and low TiO₂ contents, consistent with chromite inclusions in diamonds worldwide. Garnet compositions are typically harzburgitic and lherzolititic and contain a minor eclogitic garnet component based on mineral chemistry. Macrocrystic olivine compositions average Fo₉₃ and contains Ni contents of ~3300 ppm.

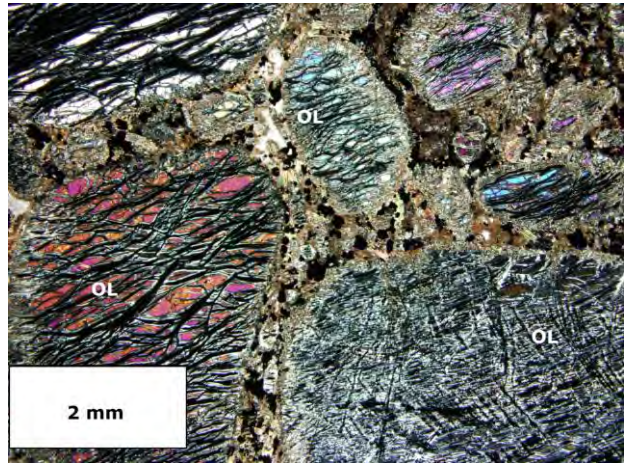


Figure 2: Photomicrograph showing coarse serpentinised olivine in an olivine-phlogopite-calcite-oxide

Geochronology and Age of Emplacement

²⁰⁶Pb/²³⁸U geochronology by ICP-MS was completed on 250 groundmass perovskite grains at the University of Alberta. Results from 250 grains returned a model age of 1945.3 ± 1.9 Ma. Textural evidence suggests the perovskite to be a relatively late stage crystallisation product from the melt as shown by its inter-grown relationship with other phenocrystic phases such as oxides and in olivine rims. For this reason we interpret the 1945.3 Ma date to closely represent the emplacement age.

Geothermobarometry and Paleoheat flow

Clinopyroxene (cpx) and garnet were extracted from heavy mineral concentrates. Major and trace element mineral chemistry was analysed at Rio Tinto's Bundoora Analytical Facility, Australia. We use cpx and garnet mineral chemistry to assess the paleoheat flow of the Southern Superior Province by obtaining P-T estimates from a combination of the single crystal enstatite-in-cpx thermometer, Cr-in-cpx barometer of Nimis and Taylor (2000), garnet geobarometer of Grutter et al. (2006) and Ni-in-Garnet geothermometer of Canil (1999).

Figure 3 shows mineral compositions used in this study and comprise cpx compositions consistent with garnet peridotite (220 grains; Figure 3a), and lherzolititic and harzburgitic compositions for garnet (693 grains; Figure 3b). Figure 3c shows P-T estimates for cpx (closed black circles), and garnet (open purple circles). Model conductive geotherms are shown for 35, 40 and 45 mW/m² for reference. Although significant scatter exist with respect to the cpx data, our best estimate for a conductive heat flow is 38-

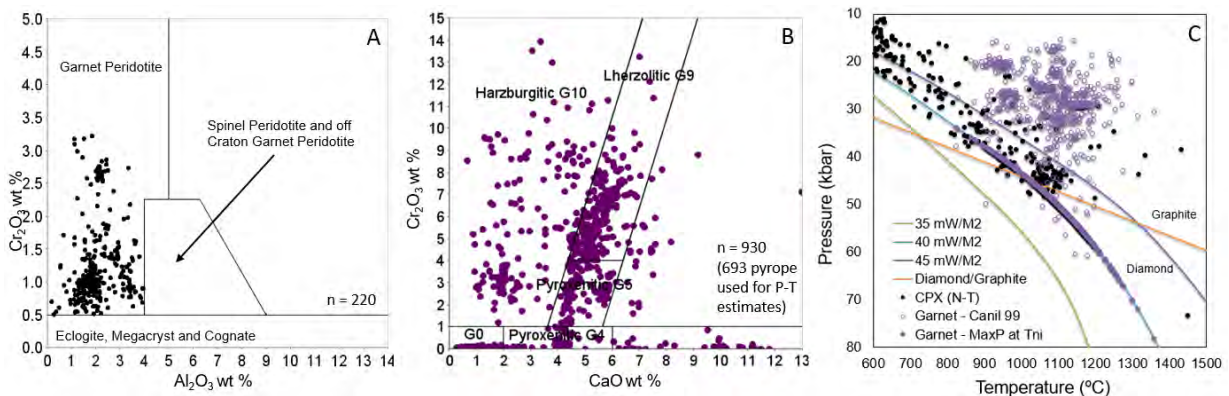


Figure 3: A) Cr₂O₃ vs. Al₂O₃ cpx compositions, B) Cr₂O₃ vs. CaO garnet compositions used in the study, and C) P-T estimates with reference conductive geothermal gradients.

41 mW·m⁻². Systematics of the Cr-in-garnet geobarometer and Ni-in-garnet geothermometer (Canil, 1999) are such that maximum pressures at a given temperature defines the geotherm assuming coexisting chromite and orthopyroxene equilibration (Ryan and Griffin, 1996). Garnet P-T estimates have been projected onto the 40 mW/m² geotherm (closed purple circles) for reference, however maximum pressures are consistent with an interpolated model conductive geotherm of ~39 mW/m², comparable with our cpx P-T estimates.

Discussion

There are many problems related to the classification of alkaline ultramafic rocks under volatile-rich conditions, and it is out of the scope here to definitively classify the Rabbit Foot rocks; however, the abundance of olivine macrocrysts, the macrocrystal suite (i.e. harzburgitic garnet, diamond), the phenocryst mineral suite and compositions (forsterite - Ba-phlogopite - trend-2-spinel- Sr-rich REE-poor apatite and perovskite) and presence of groundmass calcite are all characteristics which are undoubtedly of kimberlitic affinity. In addition to the melt fraction, the system transported diamond-bearing harzburgitic and lherzolitic lithosphere to crustal levels during the Paleo-Proterozoic, approximately 1945 Ma.

Geothermobarometry of the Proterozoic (2.7 Ga) aged diamondiferous metaconglomerate in Wawa (90 km SE) reported a maximum geothermal gradient range between 39 and 41 mW/m² corresponding to a minimum lithospheric thickness of the Superior Craton of 190-220 km (Miller et al., 2012). In contrast, these authors highlight that younger kimberlite (e.g. ~1.1 Ga Wawa kimberlite) within the Southern Superior record a substantially warmer conductive geotherm (46 mW/m²; Kaminsky et al., 2002) and maximum depth of garnet sampled of 150 km. Miller et al. (2012) interpret the apparent heating of the mantle is likely to have resulted from the Midcontinent Rift, which is broadly coeval with the Wawa kimberlite age.

Our data support the interpretation of Miller et al. (2012) and further constrain the presence of a cool and thick Southern Superior keel was still present 1945 Ma. In fact, several of our garnet compositions support a minimum lithosphere-asthenosphere boundary (LAB) of 250 km in depth and suggest (along with the presence of diamond) that the Rabbit Foot intrusion transected and sampled a significant portion of depleted and diamond stable lithospheric mantle at ~1945 Ma. A later thermal event, likely related to the Mid-continental rift, has subsequently heated and thinned the Southern Superior Craton, thereby constraining timing of the cessation of diamond fertile sublithospheric mantle in the region.

Acknowledgments

We would like to thank Alan Kobussen and the entire Project Generation Group in Australia for their technical expertise and input into this project.

References

- Canil, D., 1999. The Ni-in-garnet geothermometer: calibration at natural abundances. *Contribs Min & Pet*, 136, p.240-246.
- Grütter, H., Latti, D. and Menzies, A., 2006. Cr-saturation arrays in concentrate garnet compositions from kimberlite and their use in mantle barometry. *J Pet*, 47 p.801-820.
- Kaminsky, F.V., Sablukov, S.M., Sablukova, L.I., Shchukin, V.S. and Canil, D., 2002. Kimberlites from the Wawa area, Ontario. *Can J of Earth Sci*, 39 p.1819-1838.
- Metteer, S. (2016). Mineralogy and Petrology of the Rabbit Foot Dyke, White River, On. B.Sc. Thesis, Lakehead University.
- Miller, C.E., Kopylova, M.G. and Ryder, J., 2012. Vanished diamondiferous cratonic root beneath the Southern Superior province: evidence from diamond inclusions in the Wawa metaconglomerate. *Contribs to Min & Pet*, 164, p.697-714.
- Nimis, P. and Taylor, W.R., 2000. Single clinopyroxene thermobarometry for garnet peridotites. Part I. Calibration and testing of a Cr-in-Cpx barometer and an enstatite-in-Cpx thermometer. *Contribs to Min & Pet*, 139, p.541-554.
- Griffin, W.L. and Ryan, C.G., 1996. An experimental calibration of the "nickel in garnet" geothermometer with applications. *Contribs to Min & Pet*, 124, p.216-218.



Can microdiamonds be used to predict the distribution of large Type IIa macrodiamonds? A case study at the Letseng Mine

Anetta Banas¹, Thomas Stachel², Richard A. Stern², Andrew Allan^{3*}, Lauren Freeman³

¹ APEX Geoscience Ltd., Edmonton, Canada, abanas@apexgeoscience.com

² University of Alberta, Edmonton, Canada, tstachel@ualberta.ca, rstern@ualberta.ca

³ Gem Diamonds Technical Services, Illovo, South Africa, LFreeman@gemdiamonds.com

* formerly with Gem Diamonds

Introduction

The Letseng Diamond Mine combines relatively low grade ore (1.7 carats per 100 tonne) with large, exceptional quality Type IIa diamonds. The Letseng Diamond Mine is located in the Maloti Mountains of Lesotho and comprises two late Cretaceous kimberlites (Bowen et al., 2009). Since 2006 Letseng has produced four of the 20 largest, white gem quality diamonds ever recovered. Letseng is the highest average dollar per carat kimberlite diamond mine in the world, averaging US\$1695 per carat in 2016. The value at Letseng is driven by the relatively high proportion of Type II stones in the macrodiamond population. Due to the low grade of the deposit and the rareness of large Type IIa macrodiamonds, we evaluated the possibility to employ microdiamonds to predict the distribution of Type IIa diamonds.

Sample Suites and Analytical Techniques

Micro- and macrodiamonds from the Letseng Mine were analysed by FTIR (Fourier Transform Infrared) Spectroscopy and SIMS (Secondary Ion Mass Spectrometry) to assess a genetic relationship between microdiamonds and Type IIa macrodiamonds. The macrodiamond parcel was screened with a ZVI Yehuda Colorimeter, which detects Type IIa stones, and was intended to contain mostly Type IIa diamonds. The microdiamond parcel contained the full spectrum of diamonds recovered from processing. A total of 67 macrodiamonds and 254 microdiamonds were analysed by FTIR to determine their bulk nitrogen content and aggregation state. A total of 67 macrodiamonds and 305 microdiamonds were analysed for nitrogen content and carbon isotope composition by SIMS.

Nitrogen Characteristics

FTIR analysis identified 67% of the (preselected) macrodiamonds as Type IIa. The remaining 33% contained between 8 and 224 atomic ppm nitrogen and their nitrogen aggregation ranged from Type IaA to IaB (Figure 1). The low nitrogen content of the Type Ia macrodiamonds may be a consequence of sampling bias. FTIR and SIMS analyses show a good correlation in the Type classification.

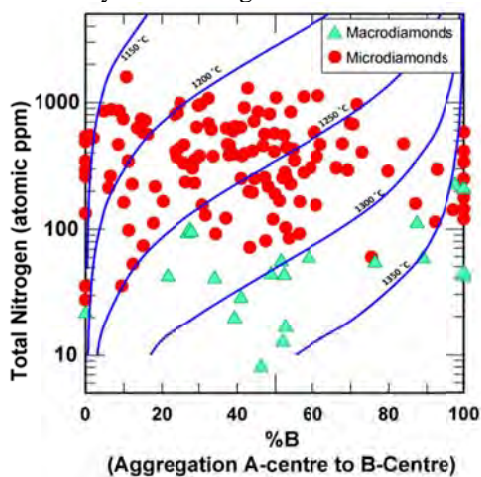


Figure 1. Nitrogen contents and aggregation states (relative proportion of nitrogen in B-centers) for Type I diamonds from Letseng. Solid lines are isotherms (°C) for a mantle residence time of 1 Ga (after Taylor et al., 1990; Leahy and Taylor, 1997).

FTIR analysis identified 46% of the microdiamond parcel as Type IIa, whereas SIMS analysis classified only 19% as Type IIa. This difference is attributed to different spatial resolutions of the techniques and the inhomogeneity of the diamonds themselves. Based on the FTIR analyses, the Type Ia microdiamonds have nitrogen contents of 28 – 1595 atomic ppm, with nitrogen aggregation ranging from Type IaA to Type IaB (Figure 1). SIMS analyses resulted in nitrogen contents of 9 – 2335 atomic ppm.

Diamond Morphology

The morphology of the examined macrodiamonds is dominated by a flattened, elongate resorbed (“dodecahedral”) shape. In the literature, this shape has been referred to as “irregular” or “shapeless”. This is a highly unusual morphology and has been recognized as a common characteristic of Type IIa diamonds from around the world (Wilks and Wilks, 1991). Other shapes exhibited by the macrodiamonds include octahedra, rounded dodecahedra, twin and irregular (Figures 2 and 3a).



Figure 2. Macrodiamond shapes observed within the studied parcel from left to right: Octahedron, rounded dodecahedroid, flattened elongate dodecahedroid, macle, and irregular.

The most common morphology in the microdiamond population are octahedral shapes (36%) with various degrees of resorption. Other shapes observed in the microdiamond population include aggregates (26%), fragments (15%), polycrystalline forms (10%), macles (9%) and irregulars (3%). Rounded dodecahedra, cubes and flattened, elongate dodecahedra are very rare. This morphological distribution is significantly different to that observed in the macrodiamond population (Figure 3b).

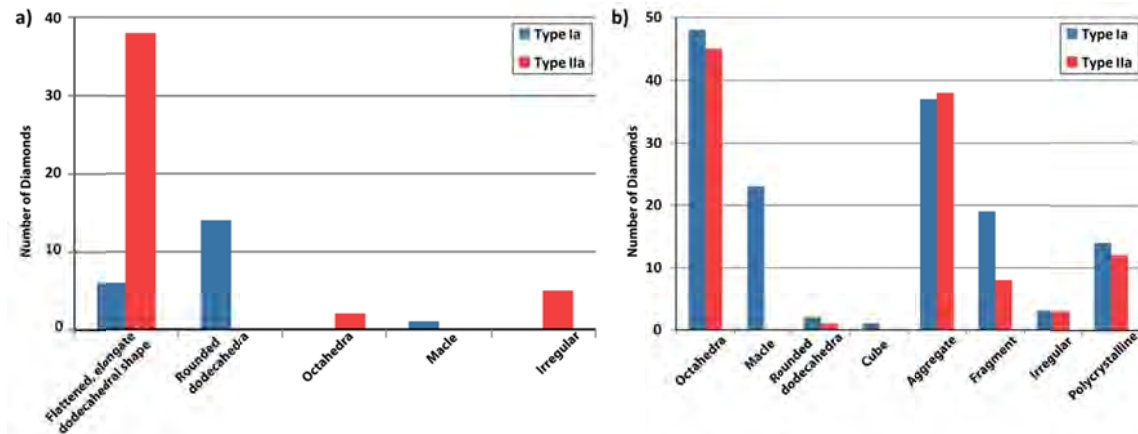


Figure 3. The distribution of **a)** macrodiamond and **b)** microdiamond shapes as function of diamond Type as determined by FTIR.

Carbon Isotope Characteristics

The Type IIa microdiamonds have a narrow range in carbon isotope ($\delta^{13}\text{C}$) values around the mantle value of -5‰ and overlap the carbon isotopic signature of Type Ia micro- and macrodiamonds (Figure 4a). This narrow distribution agrees with previously published data on small macrodiamonds from Letseng (McDade and Harris, 1999). Due to this similarity it is suggested that microdiamonds and Type Ia macrodiamonds likely have similar paragenetic origins: predominantly peridotitic with minor eclogitic and websteritic components.

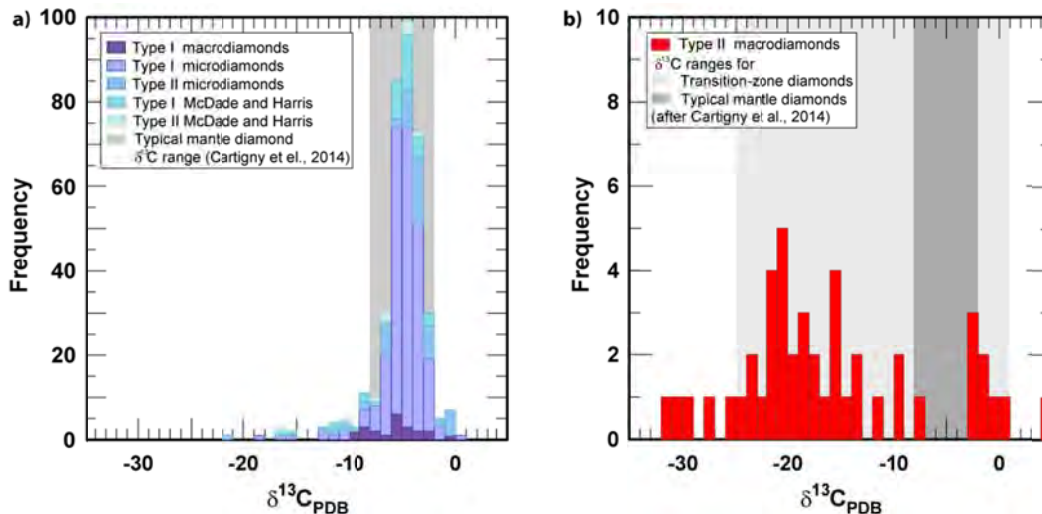


Figure 4. Carbon isotope histograms of a) Type Ia micro- and macrodiamonds and Type IIa microdiamonds, b) Type IIa macrodiamonds.

Type IIa macrodiamonds show a broad range in carbon isotope values from -32 to +4‰ with an absence of values about -5‰ (Figure 4b). This is highly distinct from the microdiamond and Type Ia macrodiamond suites, indicating the Type IIa macrodiamonds have a different paragenetic source altogether. Combining the broad range in carbon isotope values, documenting both strong enrichment and depletion of $\delta^{13}\text{C}$, with the absence of diamonds with mantle-like carbon, Letseng Type IIa diamonds likely formed from carbon sourced from subducted material. Consequently, the Letseng Type IIa macrodiamonds analysed are largely, if not exclusively, of eclogitic and/or websteritic affinity. Smith et al. (2016) provided inclusion-based evidence that large Type IIa diamonds relate to sublithospheric sources, which could link the Letseng Type IIa macrodiamonds to remnant oceanic slabs residing in the transition zone and/or lower mantle.

Conclusions

The broad carbon isotope distribution of Type IIa macrodiamonds is distinct from the Type Ia and Type IIa microdiamond and Type Ia macrodiamond samples analysed, indicating the Type IIa macrodiamonds are derived from distinct carbon sources and, by inference, diamond substrates in the Earth's mantle. The strongly resorbed nature of the supposedly superdeep Type IIa macrodiamonds may be an indication that the microdiamonds have a very low survival potential during ascent through the convecting mantle. Consequently, microdiamonds may not be an appropriate proxy for understanding the Type IIa macrodiamond distribution at Letseng and warrants further investigation. Future work should focus on establishing relationships with associated minerals to definitively constrain the paragenesis and depth of diamond formation of the large Type IIa stones.

References

- Bowen, D.C., Ferraris, R.D., Palmer, C.E., Ward, J.D. (2009). On the unusual characteristics of the diamonds from Letseng-la-Terae kimberlites, Lesotho. *Lithos*, V112, 767-774.
- Cartigny, P., Palot, M., Thomassot, E., Harris, J.W. (2014) Diamond Formation: A stable Isotope Perspective. *Annual Reviews Earth and Planetary Sciences*, V42, 699-732.
- Leahy, K., Taylor, W.R., (1997) The influence of the Glennie domain deep structure on the diamonds in Saskatchewan kimberlites. *Russian Geology and Geophysics* V38, 481–491.
- McDade, P., Harris, J. W. (1999) Syngenetic inclusion bearing diamonds from Letseng-la-Terae, Lesotho. *In* 7th International Kimberlite Conference Proceedings Gurney et al. (eds), V2, 557-565.
- Smith, E., Shirey, S.B., Nestola, F., Bullock, E.S., Wang, J., Richardson, S.H., Wang, W. (2016). Large gem diamonds from metallic liquid in Earth's deep mantle. *Science*, V354, p.1403-1405
- Taylor, W.R., Canil, D., Milledge, H.J. (1996) Kinetics of Ib to IaA nitrogen aggregation in diamond. *Geochimica Cosmochimica Acta* V60, 4725–4733.
- Wilks, E., Wilks, J. (1991) *Properties and Applications of Diamond*. Butterworth Heinemann Ltd., Oxford.



Kimberlites – from Mantle to Mine

Barbara H. Scott Smith

Scott-Smith Petrology Inc., Vancouver Canada, barbara@scottsmithpetrology.com

Introduction

Kimberlite is the term coined in the late 19th century to describe “the matrix to diamond” when it was realised that the second South African diamond rush deposits were not alluvial but of volcanic origin. Today, kimberlite geology is the foundation of diamond mines. It is a descriptive science based on mega-, macro- and micropetrography which is communicated using words; a recent rationalisation of kimberlite terminology provides the words (Scott Smith et al. 2013, 2017). The resulting evidence is summarised here to provide a basis for improving our understanding of kimberlites, from the mantle to a mine, and to enhance the application of the results to diamond mining and research.

Kimberlite

Kimberlite, the main primary source of diamonds, now has a petrographic-based definition: 25 modal % anhedral olivine macrocrysts (>1 mm; Fig. 1) and 25 modal % euhedral olivine microcrysts (<1 mm) set in a fine grained primary groundmass (Scott Smith et al. 2017). The definition is based on non-volcanic intrusive hypabyssal rocks from diamond mines which are the best representation of near surface pre-eruption magmas. Recognising pre-eruption magmas as kimberlites (*sensu stricto*), although not straightforward, is key to focussed exploration and research; including other rock types (e.g. marginal kimberlites and related rocks) clouds our understanding of kimberlites.

From the Mantle

Kimberlites are a petrological clan with a narrow petrographic range (Fig. 1) suggesting the source of the initial melts is asthenospheric mantle (Fig. 2) with a composition persistent through space and time (50-1800 Ma.), a conclusion supported by diamond inclusion data. The olivine macrocrysts (Fig. 1) are xenocrysts incorporated during ascent of the melts through peridotitic subcratonic lithospheric mantle. The constant ~25 modal % abundance of olivine macrocrysts (Fig. 1) indicates the maximum mantle cargo that a kimberlite magma can transport to surface, thus indicating the magmas with the greatest potential to contain macrodiamonds. Lamproites are a separate petrological clan which, in contrast to the kimberlite clan, encompasses a very wide petrographic range (Fig. 1) and derive from metasomatised lithospheric mantle (Fig. 2). The petrographic similarity and common petrogenesis of orangeites led Scott Smith et al. (2017) to propose they be renamed *lamproite* (*var. Kaapvaal*). Only the low proportion of lamproites that are olivine macrocryst-rich (Fig. 1) have the potential to carry macrodiamonds while olivine melnoites have a low potential. The diversity in abundance and type of other mantle xenocrysts including diamond entrained from the non-uniform lithospheric mantle shows that the melts ascend as discrete batches (Fig. 2).

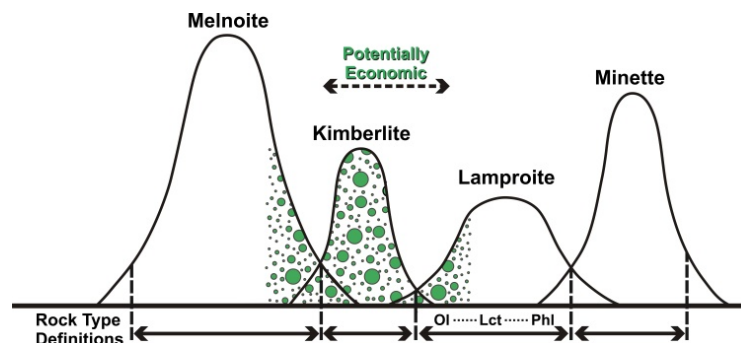


Figure 1: Schematic representation of petrographic-based definitions for kimberlite and related rocks. For each curve: (i) width of base indicates relative petrographic range within each petrological clan (Ol-olivine, Lct-leucite, Phl-phlogopite denotes the wide range in lamproites); (ii) height reflects relative worldwide frequency; (iii) green circles mimic olivine macrocryst content, in particular the characteristic 25% of kimberlites.

Ascent

Kimberlite magmas rise from >200 km reaching surface within ~1 day. Many features are explained by proposals that the starting melt is carbonatite-like and ascent is driven by assimilation of cratonic mantle orthopyroxene and then clinopyroxene which: (i) modifies the melt composition towards kimberlite; (ii) triggers exsolution of a low density volatile phase (CO₂+/-H₂O); (iii) reduces magma density and viscosity and increases buoyancy relative to lithospheric mantle, and (iv) causes rapid ascent of magma as dykes by crack-tip propagation with retention of ~25 modal % mantle cargo.

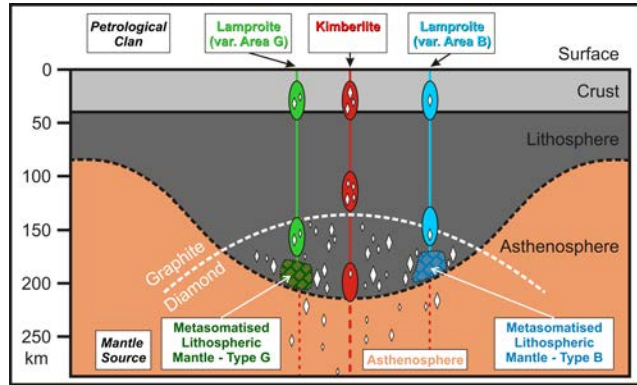


Figure 2: Schematic origin of primary sources of diamond: kimberlite and lamproite. White diamonds = non-uniform distribution of diamonds in the mantle. Red ovals = three separate batches of kimberlite melt ascending to surface with different diamond contents. Green and blue are contrasting types (G and B) of inhomogeneous (denoted by hashes) metasomatised lithospheric mantle that yield different area-specific lamproite melts, e.g. lamproite (var. Area G or B).

Olivine microcrysts form another ~25 modal % of the magma that reaches near surface. Their remarkably uniform size (<0.5-1 mm) and euhedral habit indicate formation by similar melt crystallisation histories in each batch of magma prior to reaching near surface. Crystallisation of the olivine microphenocrysts which includes overgrowths on olivine xenocrysts may start at depths of ~110 km as a consequence of pyroxene assimilation. Early primary Cr-spinel can co-crystallise with olivine and early phlogopite can follow.

To a Mine

A single kimberlite body is formed by the separate emplacement of a number of discrete batches of magma (Fig. 2) in <1-2 Ma.; formation of a province spans <10-30 Ma.. All the emplacement products of a single batch of magma form one phase of kimberlite. Although broadly similar (50 modal % olivine and 50 modal % melt with minor spinel and phlogopite), each batch of kimberlite magma arriving at surface has had a different origin and ascent history resulting in variations in attributes such as the relative abundance of mantle xenoliths and xenocrysts (indicator minerals), groundmass minerals, crustal xenoliths and their reaction products. Such features are used to distinguish different phases of kimberlite within a single body. Applying predictive geology to their distribution is the foundation of the 3D geological models upon which diamond resource estimates are based because each phase of kimberlite has a different diamond content (grade and value). Each batch of magma also has a separate emplacement history during which the diamond content can be modified, sometimes on a scale important to economic assessments. It is important to note that one phase of kimberlite can include several textural types, or facies, resulting from variations within one overall emplacement event and the terms facies and phase are not synonymous.

Emplacement of kimberlite magma near surface forms two main types of body: volcanic pipes and intrusive sheets (Fig. 3). The latter involves the simple solidification of the melt portion of the magma through the crystallisation of fine grained groundmass spinel, perovskite, phlogopite, monticellite, apatite, serpentine and carbonate to form hypabyssal kimberlite (HK). When they reach surface, kimberlite magmas are unusual in that they retain significant amounts of volatiles. Volatile exsolution before and during emplacement can cause deuteric replacement of most components. Separation of an exsolving fluid phase from an ascending batch of magma can produce precursor emplacement events, in particular, the exploitation of pre-existing cracks. The formation of most volcanic pipes involves breakthrough to surface and eruption with volatile exsolution and expansion being important parts of the process. Primary pipe-infills form by magmatic processes; there is little evidence for phreatomagmatic processes being involved.

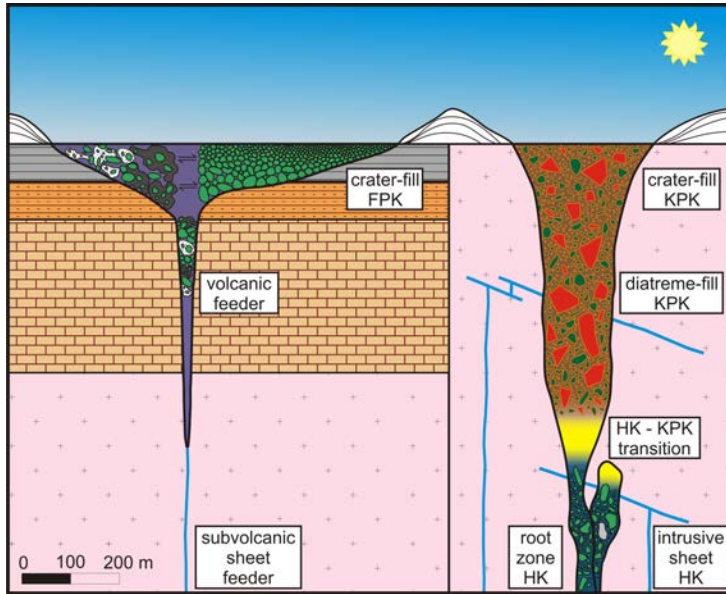


Figure 3: Schematic representation of the geology of the two end member types of pipes, their infills and associated features (after Fig. 4, Scott Smith 2008). Contrasting attributes include: the distribution of olivine (green) and xenoliths (red), the nature of the magmaclasts and intermagmaclast matrix as well as the association with HK. Relative to the pre-eruption magma (HK), changes in the distribution of any macrodiamonds present can be predicted using olivine macrocrysts.

Kimberlites include two distinct types of volcanic pipes and infills: Fort à la Corne-type and Kimberley-type pyroclastic kimberlites (FPK and KPK, respectively; Fig. 3). FPKs are broadly similar to subaerial basaltic pyroclastics. KPKs are unique to kimberlites with the diatreme-fill forming from subsurface intrusive texturally-modified magmatic systems (e.g. Mitchell and Scott Smith, this volume). The near surface country rock appears to control which pipe-type forms. The nature of associated coherent kimberlite also varies with pipe-type. Intrusive HK occurs as sheets and root zones to diatreme-fill KPKs (Fig. 3). In FPKs coherent kimberlite occurs as extrusive lava lakes. Vacant pipes are infilled by diverse crater-rim resedimentation.

Conclusions

With the re-classification of orangeites as lamproites (var. Kaapvaal), primary sources of diamond include only two petrological clans: kimberlite and lamproite (Fig. 1). The relative proportions of olivine macrocrysts in the rocks (Fig. 1) reflects the thickness of cratonic lithospheric traversed during ascent (Fig. 2) and thus their diamond potential. Kimberlites are the main “matrix to diamond” because they are the deepest mantle-derived melts (Fig. 2). The key to interpreting all aspects of kimberlites at surface is understanding the nature of typical pre-emplacment parental magmas described in the petrological definition of kimberlite. Finding new kimberlite mines is based on discovering bodies formed from magmas that match the definition (Fig. 1). Deviations from the definition usually indicate magmas with a lower diamond potential (Fig. 1) whereas minor differences within the definition are used to identify separate phases of kimberlite forming a body. Understanding the nature of pre-emplacment kimberlite magmas also results in more meaningful interpretation of emplacement products and processes (Fig. 3) and the potential to optimise exploration, evaluation and mining strategies. Further, research on kimberlites from mantle-to-mine and the economic implications thereof are most relevant if focussed on the “matrix of diamond”, in other words well constrained kimberlite samples derived from mines with detailed supporting datasets.

References

- Scott Smith BH (2008) Canadian kimberlites: Geological characteristics relevant to emplacement. *Journal of Volcanology and Geothermal Research*, 174, p. 9-19.
- Scott Smith BH, Nowicki TE, Russell JK, Webb KJ, Mitchell RH, Hetman CM, Harder M, Skinner EMW, Robey JV (2013) Kimberlite Terminology and Classification. *Proceedings of the 10th International Kimberlite Conference. Special Issue of the Journal of the Geological Society of India, Volume 2, 1-17.* Springer India.
- Scott Smith BH, Nowicki TE, Russell JK, Webb KJ, Mitchell RH, Hetman CM, Robey JV (2017) A Glossary of Related Terms. Scott-Smith Petrology Inc., Vancouver, Canada.



The birth, growth and ageing of the Kaapvaal subcratonic mantle

Gerhard P. Brey

Institut für Geowissenschaften, Goethe-Universität, Frankfurt, Germany, brey@em.uni-frankfurt.de

Introduction

There is general consensus that the subcratonic lithospheric mantle originated in the Archean by high degrees of partial melting and subsequently suffered metasomatic overprint (e.g. Pearson and Wittig 2008). It consists of two major components, volumetrically dominating ultramafic rocks (peridotites) and a subordinate mafic portion (eclogites and garnet pyroxenites) which are the metamorphic equivalents of seafloor altered basaltic magmas and their low pressure cumulates. Less consensus exists about the melting regime and the geodynamic setting in the Archean. Due to the metasomatized nature of cratonic peridotite, only compatible and moderately incompatible elements like the HREE, V, Sc and Cr are suitable to deduce the melting regime. A strong case can be made that partial melting occurred mainly at low pressures based on abundances of these elements and their ratios. Much fewer samples indicate the presence of residua from higher pressure melting in the garnet stability field. The Archean age of the cratonic mantle has been clearly established with the Re-Os isotope system. However, the concept of Rhenium depletion age (T_{RD}) yields a continuum of mainly Archean ages with broad, prominent modes at 2.7-3.0 Ga for Kaapvaal peridotites in an age density distribution curve (see e.g. summary by Pearson and Wittig 2008). A continuum for mantle melting contrasts with the episodic events recorded in the overlying crust. The discrepancy may be blamed to the disguising effects of ubiquitous metasomatism in cratonic mantle samples. The dilemma for obtaining accurate ages of mantle processes is furthered by the facts that xenoliths are generally contaminated along grain boundaries and reaction rims by the host kimberlite magma and that, consequently, the lithophile element systematics like the Rb-Sr, Sm-Nd and Lu-Hf isotope systems of the bulk rocks are disturbed.

Our approach

We use garnet xenocrysts with low calcium contents (subcalcic garnets) from the older Group II generation of kimberlites from the Kaapvaal craton to evaluate old, Archean processes. This is because samples from the younger Group I kimberlites are likely to be metasomatized by the preceding kimberlite magmatism in addition to previous events. Subcalcic garnets are mostly derived from clinopyroxene-free garnet harzburgites. They are rare as xenoliths but their debris is common in heavy mineral concentrates from diamond mining and best preserved as subcalcic garnet grains. They are the major host for most trace elements of their host rocks including those of the Sm-Nd and Lu-Hf isotope systems (Lazarov et al. 2009; Shu and Brey 2015). Results on these isotope systems from such xenocrysts can be treated as bulk rock compositions. Characterization of source materials may be tested in isochron diagrams, by model age calculations and initial isotope values. We further used clean garnet and clinopyroxene separates from Finsch peridotite xenoliths to reconstruct bulk rock compositions and test for agreement with subcalcic garnets. The Re-Os isotope and PGE data were also determined in the same Finsch peridotite xenoliths from which Lu-Hf and Sm-Nd isotope data were obtained. We also examined the mafic counterparts, eclogite and garnet pyroxenite xenoliths, to obtain further constraints on the formation and development of the Kaapvaal mantle via the Lu-Hf and Sm-Nd isotope systems.

Results and Discussion

Our results on major and trace elements fortify the arguments for a predominance of residua from low pressure melting in the Kaapvaal mantle, evidenced e.g. by high and variable Cr/Al ratios and extremely low HREE abundances. Model calculations indicate that most of the peridotite xenoliths are residues of 25-40% partial melting mainly in the spinel stability field (e.g. Lazarov et al. 2012 a,b). The Lu-Hf isotope system in subcalcic garnets records a series of ancient metasomatic events in the

Kaapvaal craton by a) a 2.64 Ga Lu-Hf isochron for subcalcic garnet xenocryst from the Finsch mine with $\epsilon\text{Hf}(t) = +26$ and a further at 1.9 Ga [$\epsilon\text{Hf}(t) = 0$], b) a 2.95 Ga isochron from the Roberts Victor mine [$\epsilon\text{Hf}(t) = +2.4$] and c) a 3.2 ± 0.5 Ga errorchron from Lace mine (Lazarov et al. 2009 and 2012; Shu et al. 2013). Quantitative model calculations on metasomatic processes demonstrate that the subcalcic garnets were affected by 0.3 to 3% carbonatitic to kimberlitic melts (Shu and Brey 2015). Some garnet xenocrysts yield extraordinary negative $\epsilon\text{Hf}(0)$ and $\epsilon\text{Nd}(0)$ values, one extreme case with $\epsilon\text{Hf}(0)$ at -65 and $\epsilon\text{Nd}(0)$ at -41. The negative ϵHf and ϵNd values correspond to the initial ratios of the metasomatizing agent that most likely was derived from an ancient (early Archean or even Hadean) crustal component. Extremely negative ϵNd values are also characteristic for garnet inclusions in diamonds and are also an argument for an early Archean growth of diamonds (Richardson et al., 1984).

Our new results on the Re-Os isotope system from Finsch together with data of Griffin et al. (2004) yield T_{RD} ages mostly around 2.6 Ga which is in good agreement with the Lu-Hf metasomatic age. The Re-Os isotope system in Finsch peridotites may also record the Archean metasomatic overprint and even the oldest may represent only minimum ages for partial melting. Such an interpretation is further supported by a decent positive correlation between the modal abundances of garnet (and subordinate with cpx and opx) and $^{187}\text{Os}/^{188}\text{Os}$. It indicates that the reintroduction of fertility-indicator mineral(s) and of Re-Os back to a depleted lithosphere result from the same metasomatic process.

Various ways for estimating the age of eclogite xenoliths from cratonic mantle gave mainly late Archean ages (summary by Aulbach and Jacob 2016). A direct measure of a minimum age are extremely low $^{87}\text{Sr}/^{86}\text{Sr}$ ratios (0.7008-0.7009) in clinopyroxenes from eclogite xenoliths in the Kaapvaal craton (Jacob et al. 2005 and Shu et al. 2016). Projection of such low values onto a mantle evolution line yields minimum ages for eclogites of close to 3.2 Ga. Attempts to obtain eclogite ages with reconstructed bulk rock compositions from two-point garnet-clinopyroxene tie-lines are not successful for the Sm-Nd and Lu-Hf isotope systems. The various types of eclogites and garnet pyroxenites generally yield a scatter of data points in isochron diagrams and protolith or metamorphic ages cannot be derived. Nevertheless, the usefulness of garnet-clinopyroxene tie-line ages lies in the possibility to derive cooling rates for the subcratonic mantle (Shu et al. 2014). Plotting the temperatures of last equilibration as derived from Fe-Mg exchange thermometry between garnet and clinopyroxene against the garnet-clinopyroxene two-point isochron ages yields a) a low temperature alignment for both the Sm-Nd and Lu-Hf isotope systems of increasing age with decreasing temperature, and b) an alignment around the kimberlite eruption ages at high temperatures. The intersect between the two temperature limbs gives about 920°C as closure temperature for the Lu-Hf system and about 850°C for the Sm-Nd system. These systematics allow to derive a cooling rate of around 0.1°C/Ma at least since the beginning of the Proterozoic (Shu et al. 2014).

A brief synthesis

Highly depleted peridotitic lithosphere was generated by partial melting at low pressures, possibly in settings analogues to modern mid ocean ridges at least in the mid-Archean as evidenced by: (i) oldest T_{RD} ages from the Kaapvaal craton around 3.3 Ga, (ii) the extremely positive initial ϵHf ratio of the 2.64 Ga metasomatic isochron from Finsch peridotites, (iii) extremely unradiogenic Nd isotope data ($\epsilon\text{Nd}=-41$) in subcalcic garnet xenocrysts and garnet inclusions in diamonds and iv) the minimum age for eclogites of 3.2 Ga. The partial melts and their differentiates cooled in an ocean floor environment. The package of depleted residues (harzburgite), seafloor-altered basalts, picrites, komatiites and sediments was eventually subducted to greater depths from where the xenoliths are derived.

Subduction of this cooler material likely occurred under very low geothermal gradients by a compressional process (Sommer et al. 2017) into a hotter mantle. This created immediate massive thermal and chemical disequilibrium within an early lithospheric keel. Thermal adjustment to a stable geothermal gradient was induced by heat flow between a continental lid containing high abundances of radioactive elements and a deep convecting asthenosphere (Michaut and Jaupart 2007). The resulting gradient would have been significantly higher in the Archean than today. The subducted packages were heated possibly up to 1400 - 1500°C during such a process. Thermal equilibrium could be reached within less than 500 Ma according to the model of Michaut and Jaupart (2007).

Based on the information from radiometric systems, the main stage of metasomatism which is responsible for modifying the lithospheric keel of the Kaapvaal craton, occurred during the time leading up to thermal equilibrium. The cooler, subducted portions of lithosphere with low melting components such as seafloor altered basalts or carbonated and hydrous sediments (e.g. black shales) were heated, hybrid melts from reactions between them and peridotite percolated into surrounding and overlying peridotite to drive prevailing metasomatism in the cratonic mantle. The Lu-Hf isochrons and possibly the mode of the T_{RD} ages mostly record the main stage of this process. After reaching equilibration and except for local disturbances, the subcratonic mantle as a whole has cooled with a rate of about 0.1°C/Ma.

References

- Aulbach S, Viljoen KS (2015) Eclogite xenoliths from the Lace kimberlite, Kaapvaal craton: from convecting mantle source to palaeo-ocean floor and back. *Earth Planet Sci Lett* 431:274–286
- Pearson DG, Wittig N (2008) Formation of Archaean continental lithosphere and its diamonds: the root of the problem. *J Geol Soc* 165: 895–914.
- Griffin WL, Graham S, O'Reilly SY, Pearson NJ (2004) Lithosphere evolution beneath the Kaapvaal Craton: Re–Os systematics of sulfides in mantle-derived peridotites. *Chem Geol* 208: 89–118
- Jacob DE, Bizimis M, Salters VJM (2005) Lu/Hf and geochemical systematics of recycled ancient oceanic crust: evidence from Roberts Victor eclogites. *Contrib Miner Petrol* 148(6):707–720
- Lazarov M, Brey GB, Weyer S (2009) Time steps of depletion and enrichment in the Kaapvaal craton as recorded by subcalcic garnets from Finsch (SA). *Earth Planet Sci Lett* 27: 1–10.
- Lazarov M, Brey GB, Weyer S (2012a) Evolution of the South African mantle — A case study of garnet peridotites from the Finsch diamond mine (Kaapvaal craton); part 1: Inter-mineral trace element and isotopic equilibrium *Lithos* 154: 193–209
- Lazarov M, Brey GB, Weyer S (2012b) Evolution of the South African mantle – a case study of garnet peridotites from the Finsch diamond mine (Kaapvaal craton); Part 2: Multiple depletion and re-enrichment processes. *Lithos* 154: 210–223
- Michaut C Jaupart C (2007) Secular cooling and thermal structure of continental lithosphere. *Earth Planet Sci Lett* 257: 83–96
- Richardson SH, Gurney J, Erlank A, Harris J (1984) Origin of diamonds in old enriched mantle. *Nature* 310: 198–202
- Sommer H, Jacob DE, Stern RA, Petts D, Matthey DP, Pearson DG (2017) Fluid-induced transition from banded kyanite- to bimineralic eclogite and implications for the evolution of cratons *Geochim Cosmochim Acta* doi.org/10.1016/j.gca.2017.03.017
- Shu Q, Brey GP, Gerdes A, Hofer H (2013) Geochronological and geochemical constraints on the formation and evolution of the mantle underneath the Kaapvaal craton: Lu–Hf and Sm–Nd systematics of subcalcic garnets from highly depleted peridotites. *Geochim Cosmochim Acta* 113: 1–20
- Shu Q, Brey GP, Gerdes A, Hofer HE (2014) Mantle eclogites and garnet pyroxenites—the meaning of two-point isochrons, Sm–Nd and Lu–Hf closure temperatures and the cooling of the subcratonic mantle. *Earth Planet Sci Lett* 389:143–154
- Shu Q, and Brey GP (2015) Ancient mantle metasomatism recorded in subcalcic garnet xenocrysts: Temporal links between mantle metasomatism, diamond growth and crustal tectonomagmatism. *Earth Planet Sci Lett* 418: 27–39
- Shu Q, Brey GP, Hofer H, Zhao Z, Pearson DH (2016) Kyanite/corundum eclogites from the Kaapvaal Craton: subducted troctolites and layered gabbros from the Mid- to Early Archean. *Contrib Mineral Petrol* (2016) 171: 11–24



Olivine zoning and the evolution of kimberlite systems

Andrea Giuliani^{1,2}, Ashton Soltys², Emilie Lim², Henrietta Farr², David Phillips²,
Karsten Goemann³, William L. Griffin¹

¹ ARC Centre of Excellence for Core to Crust Fluid Systems (CCFS) and GEMOC, Department of Earth and Planetary Sciences, Macquarie University, Australia
andrea.giuliani@mq.edu.au, andrea.giuliani@unimelb.edu.au

² KiDs (Kimberlites and Diamonds), School of Earth Sciences, The University of Melbourne, Australia

³ Central Science Laboratory, University of Tasmania, Tasmania, Australia

Introduction

Olivine is the most abundant mineral in kimberlite rocks and generally occurs as macrocrysts (i.e. anhedral grains larger than ~1 mm in size), and (micro-)phenocrysts (i.e. subhedral to euhedral crystals commonly less than 1 mm in size). Recent advances in imaging and microanalytical techniques have confirmed that olivine macrocrysts and the vast majority of phenocrysts contain cores and a rims with distinct compositions (e.g., Kamenetsky et al., 2008; Brett et al., 2009; Giuliani et al., 2017), as per the observations of Boyd and Clement (1977) for olivine grains in the De Beers kimberlite (South Africa). The rims of macrocrysts and phenocrysts typically contain primary inclusions of groundmass phases (e.g., chromite, MUM spinel, Mg-ilmenite), and exhibit homogeneous Mg# composition coupled with decreasing Ni and increasing Ca and Mn concentrations. These features are consistent with a magmatic origin for the rims. Conversely, the olivine cores host inclusions of typical mantle phases (e.g., clinopyroxene, garnet, Cr-spinel), which are not stable in kimberlite magmas. The cores show widely variable compositions extending from those of olivine in lithospheric mantle peridotites (i.e. Mg# ~ 91-94) to compositions richer in Fe. Although there is broad consensus that the olivine cores derive from disaggregation of peridotite wall rocks, the following features have been invoked to suggest that some olivine cores originate from mantle wall rocks formed by earlier kimberlite metasomatism (Arndt et al., 2010; Sobolev et al., 2015; Howarth and Taylor, 2016): 1) low-Mg# cores display unusual compositions unlike typical mantle peridotites; 2) clinopyroxene and garnet inclusions with variable compositions occur in individual cores; and 3) the textural features of some macrocrysts indicate deformation and recrystallisation immediately prior to kimberlite entrainment. The occurrence of phlogopite antecrysts in kimberlites and entrainment of mantle polymict breccia xenoliths (which represent failed kimberlite intrusions at mantle depths), are additional indications that earlier pulses of kimberlite melt 'prime' the mantle before kimberlite eruptions (e.g., Giuliani et al., 2016). It is however unclear if there is any relationship between these kimberlite-related metasomatic processes and the composition of kimberlite magmas that are emplaced at surface. Furthermore, as olivine is a liquidus mineral in kimberlite melts and olivine formation can persist throughout most of the kimberlite crystallisation sequence, deciphering the processes that control the compositional evolution of olivine can provide enhanced constraints on kimberlite petrogenesis.

Samples, methods and results

We have examined the zoning (SEM-EDS imaging) and major-element compositions (electron microprobe (EMP) analyses) of olivine in archetypal kimberlites from South Africa, Botswana, Lesotho, Canada and Brazil, and compared these results with new and existing data for kimberlites, orangeites and ultramafic lamprophyres from South Africa, Canada, Russia and Greenland. In addition, we have assessed compositional variations across kimberlite grains from the Bultfontein (Kimberley, South Africa) and Udachnaya-East (Russia) kimberlites using detailed EMP traverses.

Olivine macrocrysts and phenocrysts from the kimberlites examined in this study are typically zoned, with a core, rim and one or more internal zone(s) (i.e. intermediate between cores and rims; Fig. 1). The core is often partly resorbed, particularly when enriched in Fe. The (outermost) internal zone hosts chromite inclusions. The compositional features of cores and rims are consistent with previous studies, e.g., variable core Mg# vs constant rim Mg#. Different kimberlite pipes from individual clusters (e.g., Kimberley in South Africa, Ekati in Canada) contain olivine with very similar compositional features (e.g., restricted range of rim Mg#). However, large compositional variations are evident for olivine grains from kimberlite clusters on the same craton and worldwide.

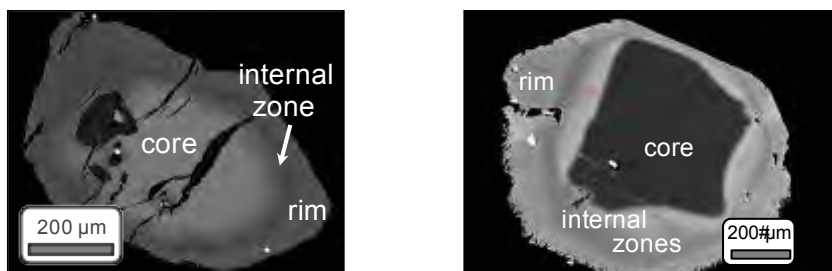


Figure 1. SEM-EDS images of zoned olivine grains from the Bultfontein (left panel) and Udachnaya-East kimberlites (right panel; red line: EMP traverse).

The most remarkable finding of this study is the linear correlation between the compositions of olivine cores and rims in kimberlites worldwide, which extends to South African orangeites and carbonate-rich ultramafic lamprophyres (i.e. aillikites) from Greenland. The correlation between average core Mg# (or NiO concentrations) and average rim Mg# values of olivine in kimberlites (orangeites and aillikites) is statistically significant ($R^2 = 0.85$), despite our dataset including samples from five continents and different carbonate-rich magma types. Conversely, olivine grains from the olivine melilitite sample included in this study (Sutherland, South Africa) plot outside this trend.

Multiple core-to-rim EMP traverses across 10 olivine grains from the Bultfontein kimberlite exhibit very consistent patterns in Mg# vs Ni, Mn, Ca, or Cr charts, despite significantly different core compositions (Mg# = 86.3-93.5; Fig. 2, left panel). The patterns show a moderately to strongly curved segment, which extends from compositions of the core to the individual internal zone, and is present in every measured grain (e.g., Fig. 1). This internal zone shows remarkably consistent composition (Mg# = 89.7 ± 0.3 ; NiO = 0.43 ± 0.02 wt.%; CaO = 0.08 ± 0.01 wt.%; 1sd) across the ~60 grains measured from this kimberlite. The traverses include a second segment, where Mg# initially decreases to values typical of the rims and then becomes constant, while Ni and Cr decrease, and Ca and Mn increase throughout this segment. Olivine Mg# vs Ni, Mn or Ca charts where cores, rims and internal zones were measured by spot analysis only provide the endmembers of the patterns illustrated by the traverses (Fig. 2, right panel).

SEM-EDS images and EMP traverses across 8 representative grains of the Udachnaya-East kimberlite show considerably more complexity than the Bultfontein olivine (e.g., Fig. 1), including up to 3 internal zones. However, similar to Bultfontein, the outermost (or single) internal zone has consistent composition across the sample suite at higher Mg# (89.5-90.0) and NiO contents (0.33-0.35 wt.%) than the rims.

Discussion

Olivine in kimberlites worldwide exhibit remarkably consistent geochemical features, i.e. 1) distinct zoning between core, internal zone(s) and rim (plus Mg-enriched outer rinds preserved in some localities; e.g., Kamenetsky et al., 2008; Howarth and Taylor, 2016); 2) variable core compositions; and 3) rims with very restricted Mg# ranges. Our work demonstrates that all zoned grains contain an internal zone (the outermost when more internal zones occur), where compositions do not vary amongst olivine grains

from the same kimberlite. This feature, coupled with inclusions of magmatic chromite, suggests that the (outermost) internal zone represents the liquidus phase of the host kimberlite magmas. Partial resorption of olivine cores and Ni-Cr enrichment of the internal zones (e.g., Fig. 2) indicate that liquidus olivine crystallises after significant assimilation of wall rock material. The correlation between Mg# of (xenocrystic) cores and magmatic rims also suggests that the composition of wall rocks along the kimberlite magma conduit exerts a fundamental control on the composition of the olivine rims and, therefore, kimberlite magmas. This process also applies to other mantle-derived carbonate-rich magmas (orangeites and aillikites). Low-Mg# olivine cores have compositions resembling olivine belonging to the megacryst suite or sheared peridotites, for which a genetic relationship with early kimberlite metasomatism is commonly advocated. We therefore propose that more intense metasomatism of mantle magma conduits by early kimberlitic fluids results in olivine rims and, therefore, kimberlite magmas more enriched in Fe and Mn, and depleted in Mg and Ni.

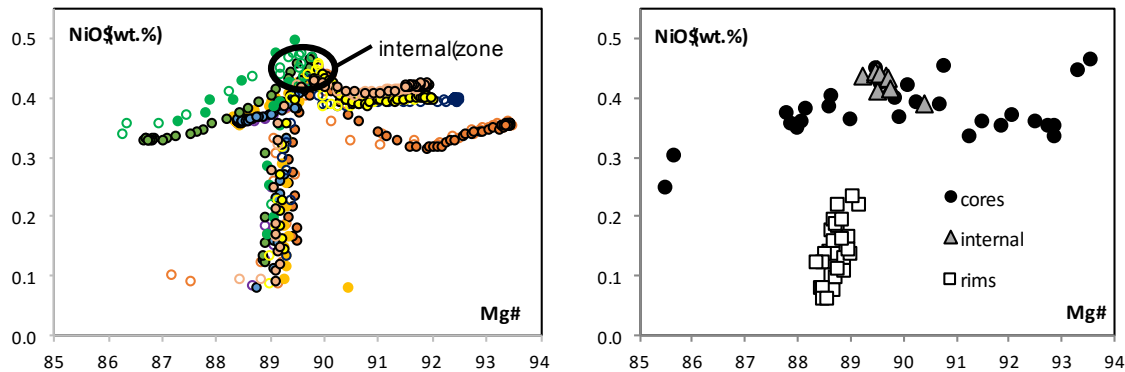


Figure 2. Mg# vs NiO compositions of olivine grains in the Bultfontein kimberlite from electron microprobe traverses (left panel) and spot analyses (right panel). In the left panel, the various traverses are shown using different colours. Internal: internal zones.

References

- Arndt NT, Guitreau M, Boullier AM, le Roex A, Tommasi A, Cordier P, Sobolev A (2010) Olivine, and the Origin of Kimberlite. *Journal of Petrology* 51(3):573-602
- Brett RC, Russell JK, Moss S (2009) Origin of olivine in kimberlite: Phenocryst or impostor? *Lithos* 112S:201-212
- Boyd FR, Clement CR (1977) Compositional zoning of olivines in kimberlites of the De Beers mine, Kimberley, South Africa. *Carnegie Yearbook* 76:485-493
- Giuliani A, Phillips D, Kamenetsky VS, Goemann K (2016) Constraints on kimberlite ascent mechanisms revealed by phlogopite compositions in kimberlites and mantle xenoliths. *Lithos* 240–243:189-201
- Giuliani A, Soltys A, Phillips D, Kamenetsky VS, Maas R, Goemann K, Woodhead JD, Drysdale R, Griffin WL (2017) The final stages of kimberlite petrogenesis: Petrography, mineral chemistry, melt inclusions and Sr-C-O isotope geochemistry of the Bultfontein kimberlite (Kimberley, South Africa). *Chemical Geology*, in press
- Howarth GH, Taylor LA (2016) Multi-stage kimberlite evolution tracked in zoned olivine from the Benfontein sill, South Africa. *Lithos* 262:384-397
- Kamenetsky VS, Kamenetsky MB, Sobolev AV, Golovin AV, Demouchy S, Faure K, Sharygin VV, Kuzmin DV (2008) Olivine in the Udachnaya-East Kimberlite (Yakutia, Russia): Types, Compositions and Origins. *Journal of Petrology* 49(4):823-839
- Sobolev NV, Sobolev AV, Tomilenko AA, Kovyazin SV, Batanova VG, Kuz'min DV (2015) Paragenesis and complex zoning of olivine macrocrysts from unaltered kimberlite of the Udachnaya-East pipe, Yakutia: relationship with the kimberlite formation conditions and evolution. *Russian Geology and Geophysics* 56:260-279



Application of Machine Learning Techniques to Exploration: An Example Using Self-Organising Maps for Garnet Data

Alan F. Kobussen¹, Paul D. Agnew¹, Graeme Broadbent²

¹ Rio Tinto Exploration, Melbourne, Australia, alan.kobussen@riotinto.com, paul.agnew@riotinto.com

² Rio Tinto Exploration, Perth, Australia, graeme.broadbent@riotinto.com

Introduction

The application of machine learning techniques in the earth sciences is relatively rare despite the availability of large, suitable datasets. The chemistry of diamond indicator minerals is one such dataset that has been routinely and consistently collected for the purposes of exploration and research for at least the last 50 years. There are established methodologies for interpreting these data, particularly for garnet (e.g. Gurney, 1984; Grütter et al., 2004), which are in widespread use by diamond explorers today. The existing methodologies are effective at categorising and prioritising garnet chemical data, in most cases by using binary or linear cuts in the data for one or more major-element variables. The self-organising map (SOM) is a variety of machine learning technique which organises data based on all input variables simultaneously. By applying this technique to garnet compositional dataset, relationships emerge which are not apparent in diagrams traditionally used for garnet indicator data interpretation. These relationships can be used as the basis of an exploration tool which more effectively sub-divides and prioritises garnet data from all parageneses.

The SOM Method and Dataset

The SOM is a data analysis and visualisation tool (Kohonen, 2001). It is a vector-based unsupervised clustering technique, meaning no prior knowledge of initial grouping is required. The data are organised by the SOM according to similarity using a competitive, iterative training process. The output of the SOM is a two-dimensional representation (a “map”) of the multi-variate input data. The map is composed of a collection of nodes arranged in a grid. In this map, topology is preserved such that points lying close to one another on the map are more similar in composition than points lying far apart. Toroidal grids can improve results and are commonly used. Each node in the grid represents a particular n -dimensional vector, referred to as the weight vector, where n is the number of variables used to construct the map. The size of the map is determined by the user and can be varied according to task or the size of the input data. Small maps have the effect of clustering the data while large maps are more effective for visualising topology.

For this study 151,044 major-element analyses of garnet were compiled. This includes data from a wide variety of rock types in order to capture a comprehensive picture of garnet major-element compositions. Oxides of the eight major elements of the common garnet series end-members (SiO_2 , TiO_2 , Al_2O_3 , Cr_2O_3 , FeO , MnO , MgO , CaO) were used as input variables. Minor oxides, such as Na_2O , were not included due to incompleteness in the dataset and concerns about the quality and precision of some measurements. A toroidal SOM with 8064 nodes (84 by 96) was then constructed from this data using the SiroSOM software package (Fraser and Dickson, 2007).

Results

A convenient way to visualise the SOM result is by plotting the magnitudes of individual weight vector components in space. The garnet SOM has eight-dimensional weight vectors; one dimension for each of the major-elements. Overlaying these images then gives a picture of the distribution of the elements relative to one another in garnet compositional space. Maps of the Cr_2O_3 and CaO component vectors are shown as an example in Figure 1A and 1B, respectively.

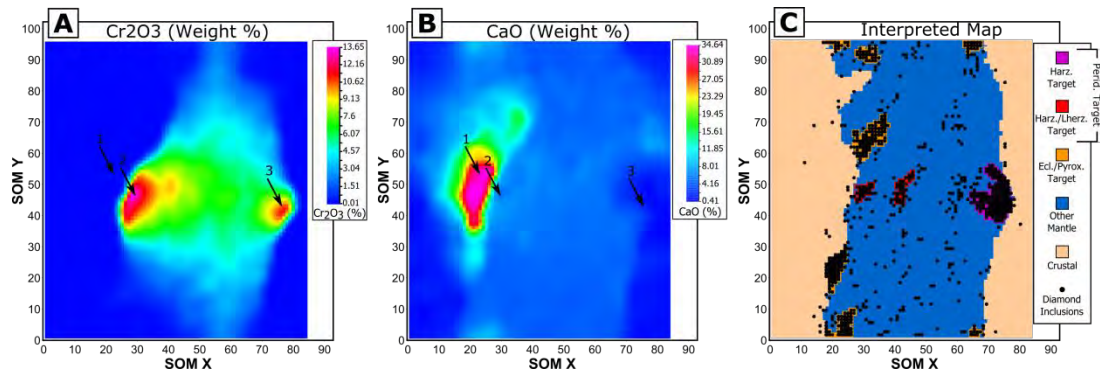


Figure 1: SOM weight vector component plots for garnet Cr_2O_3 and CaO concentrations, in weight percent (A and B), and the interpreted map (C). The garnets highest in CaO (lying in the map area indicated by arrow 1 in A and B) represent the grossular and andradite garnet end-members, nearby nodes on the map rich in Cr_2O_3 with modest CaO (indicated by arrow 2) are garnets dominated by the uvarovite molecule, and garnets poor in CaO , but rich in Cr_2O_3 (indicated by arrow 3; these garnets are also rich in MgO which is not depicted here) are dominated by the knorringite molecule. The distribution of the chemistry of garnet inclusions in diamond (C; black dots) have been used to define target compositional fields for new data (the purple, red and orange outlined areas). Due to the toroidal grid geometry, opposite edges of the map are connected (left-right and top-bottom).

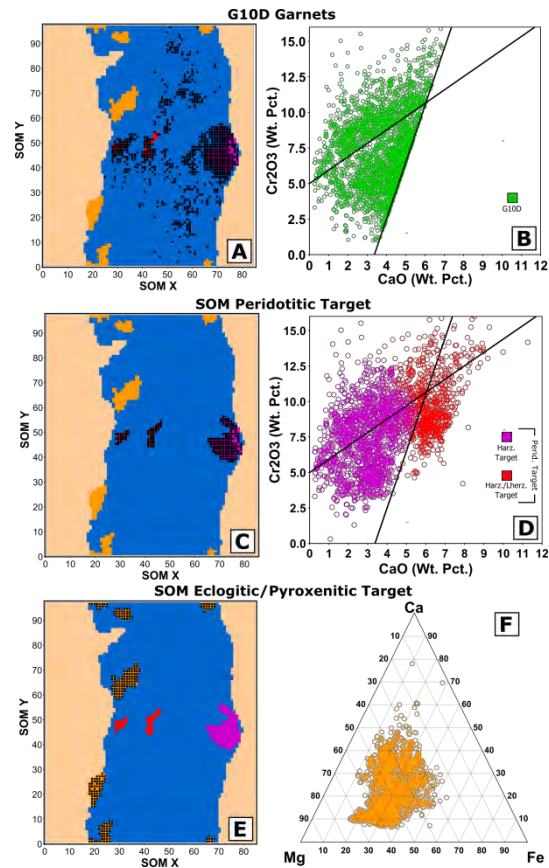
The original 151,044 data points are divided across the 8064 nodes based on their Euclidian distance from the weight vector of each node. The node with the minimum distance between the weight vector and the training vector is referred to as the best matching unit (BMU). Highlighting the BMUs where specific groups of the reference data are present reveals spatial patterns on the SOM related to similarities in garnet composition. The distribution in SOM space of the compiled data for garnet inclusions in diamond is shown in Figure 1C. The diamond inclusions cluster into several coherent compositional groups, separated by zones where diamond inclusions are sparse or completely absent. These clusters have been used to define target compositional fields on the SOM map. Defining the target in this way is based on the observations that: 1) there is a definite association between these garnet compositions and diamond; and 2) coherent clustering of the majority of diamond inclusion data suggests a common process (or processes) is responsible for the formation of most diamond globally, which is reflected in the garnet composition.

To understand how effective the SOM target compositional fields are at identifying a diamondiferous source rock in comparison to existing methods, the reference data have been classified using the scheme of Grütter et al. (2004) and compared against the SOM result in Figure 2, and compiled in Table 1. In this comparison, the diamond inclusion data have been excluded to avoid bias. The proportion of G10D garnets coming from diamondiferous sources is high (84.4%), and similar to the values for the peridotitic SOM target fields (86.3%). Note the SOM target fields contain a significant lherzolitic (G9) component (Fig. 2D). The eclogitic/pyroxenitic SOM target fields define an extremely wide compositional range (Fig. 2F), but despite this the proportion of garnets from diamondiferous sources in the target field remains high (90.2%). Without reliable Na_2O data for a majority of garnet, the comparison to the scheme of Grütter et al. (2004) for eclogitic and pyroxenitic lithologies cannot be evaluated.

| Group of Data | Count of Garnets from Barren Sources (Count of Sources) | Count of Garnets from Diamondiferous Sources (Count of Sources) | Count of Garnets from Sources with Unknown Diamond Content (Count of Sources) | Effectiveness (Count Diamondiferous/(Count Diamondiferous + Count Barren))*100 |
|---|---|---|---|--|
| G10D | 450 (59) | 2,426 (191) | 2 (1) | 84.4% |
| Peridotitic SOM Target | 323 (55) | 2,033 (184) | 8 (2) | 86.3% |
| Eclogitic/Pyroxenitic SOM Target | 297 (50) | 2,722 (141) | 428 (2) | 90.2% |
| All Reference Data | 75,407 (181) | 68,066 (298) | 3,649 (4) | N/A |

Table 1: Effectiveness of classification technique on reference data, exclusive of diamond inclusion data.

Figure 2: A comparison of the distribution of garnet compositions on SOM and Cr₂O₃-CaO plots. A,B) Distribution of G10D garnets in SOM space and Cr₂O₃-CaO space, respectively; C,D) Distribution of peridotitic SOM target garnets in SOM space and Cr₂O₃-CaO space, respectively; E,F) Distribution of eclogitic and pyroxenitic SOM target garnets in SOM space and Ca-Mg-Fe (molar) space, respectively. SOM map colours same as Figure 1. The lines on the Cr₂O₃-CaO plots are the GDC of Grütter et al. (2006) and the G9/G10 dividing line of Gurney (1984).



Discussion and Conclusions

Early work on garnets established the empirical link between host rock and diamond based on Cr₂O₃-CaO relationships. The SOM technique presented here is an extension of this work into eight dimensions, with the same empirical focus on diamond association. The observed clustering of diamond inclusion data has been used to define garnet target composition and results in the ability to predict whether the garnet host rock was diamondiferous with similar accuracy to existing classification schemes for peridotitic lithologies. However, the peridotitic SOM target clusters also capture a lherzolitic (G9) component while maintaining a similar accuracy to the comparison scheme here. This population of garnets may reflect the minor population of lherzolite-associated inclusions found in most diamond-bearing source rocks. It is not possible to directly compare the effectiveness of the eclogitic and pyroxenitic SOM target fields to commonly used techniques based on Na₂O, but the SOM can be shown to correctly predict a diamondiferous source with a high degree of accuracy. These factors make the garnet SOM a powerful tool for the prediction of diamond potential of a host rock without the exploration expense of fusion for microdiamonds or drill testing, particularly for indicator suites dominated by lherzolitic or eclogitic lithologies which are traditionally difficult to evaluate.

The SOM technique is based entirely on data relationships and as a result does not necessarily require the detailed petrological and mineralogical research and understanding that have developed around indicator mineral interpretation. This makes it well suited to application to other minerals with a smaller knowledge base than garnet, such as chromite and ilmenite, which also have large available datasets.

References

- Fraser SJ, Dickson BL (2007) A new method for data integration and integrated data interpretation: Self-organising maps. In: Milkereit B (ed) Proceedings of Exploration 07: Fifth decennial international conference on mineral exploration. Decennial Mineral Exploration Conferences, Toronto, pp 907-910
- Grütter HS, Latti D, Menzies A (2006) Cr-saturation arrays in concentrate garnet compositions from kimberlite and their use in mantle barometry. *J Pet* 47:801-820
- Grütter HS, Gurney JJ, Menzies AH, Winter F (2004) An updated classification scheme for mantle-derived garnet, for use by diamond explorers. *Lithos* 77:841-857
- Gurney JJ (1984) A correlation between garnets and diamonds. In: Glover JE, Harris PG (eds) Kimberlite occurrence and origin: a basis for conceptual models in exploration. Geology Department and University Extension, Publication 8, University of Western Australia, Perth, pp 143-166
- Kohonen T (2001) Self-organizing maps. Springer-Verlag, Berlin



Prospecting History Leading to the Discovery of Botswana's Diamond Mines: From artefacts to Lesedi La Rona

Mike C J de Wit

Tsodilo Resources Ltd, Canada/ University of Pretoria, South Africa, mdewit@tsodiloresources.com

Introduction

Bechuanaland/Botswana has a long and colourful history in exploration and mining, which can be divided into three main phases: pre-historic, historic and modern exploration and mining. The Motloutse drainage for instance was prospected at least four times, twice in historic and twice in modern times, before the area across the watershed to the west was explored, leading to the important discovery of BK01 in 1967. This was followed by the discovery of almost 400 kimberlites in Botswana with the last one around Orapa (AK25) in 2011. This discovery success resulted in 2 Tier-1, 3 Tier-2 and 3 Tier-3 mines, which have cumulatively produced some 755 Mct, worth US\$39.2B, up to the end of 2016.

1. Pre-historic mining

The first evidence of pre-historic mining and local beneficiation is from 'factory' sites at outcrops of siliceous stone, such as along palaeo-lake shore lines of the major pans and along some of the rivers containing Early (2Ma – 280,000 yrs ago) to Middle Stone Age tools (280,000 – 20,000 yrs ago). Minerals, such as specularite, limonite and later graphite were mined c. 2,000 BP in places like Tsodilo Hills and used as pigment for rock paintings and decorative purposes. Copper was mined near Dukwe and on the Matsitama and Tati Greenstone Belts (AD 1,000 – 1,700) in the Francistown region on the Tati Greenstone Belt (1,000-1,300 AD), and the main source of iron was the Tswapong Hills near Palapye with some smelting sites dating back to c. AD 800-1,000. Mining gold started around AD 1,200 in the Tati and Vuma Greenstone belts.

2. Historic mining and exploration (1867 – 1959)

Henry Harley found gold near the lower Tati River in 1867. A gold rush started at the Tati settlement in 1868 and spread across the Tati Greenstone Belt from 1869 until 1872 after which many prospectors left for the diamond fields in Kimberley. Mining resumed in 1881 and led to the establishment of Francistown in 1897, the same year that the Cape to Bulawayo railway line arrived there.

1887 – 1888 Bangwaketsi Native Reserve (Balkis Ltd, A Roberts)

Two concessions over the Bangwaketsi Reserve (Fig. 1), to prospect for precious stones, were acquired by Balkis Ltd. Gravels were noted but much of the area had already been tested for diamonds without any success (Du Toit, 1934). De Beers had also testing gravels of the Metsimotlhaba River within the adjoining Bakwena Reserve (a British South Africa Company -BSAC- concession), but no diamonds were found (Du Toit, 1934).

1896 – 1898 Ngamiland (British West Charterland Ltd, S Passarge)

Siegfried Passarge was part of the Ngami expedition between 1896-1898 which was led by Sir Frederick Lugard, a close friend of Cecil John Rhodes. This mission was carried out by British West Charterland Ltd, on behalf of Rhodes' BSAC to explore for gold and diamonds in northwest Botswana (Fig. 1). The scientific results were published by (Passarge (1904). Du Toit (1931) acknowledged that the area was mapped and examined 'in minute detail', but that the results were however not very encouraging.

1932 – 1934 Bamangwato Reserve (Victoria Prospecting Company Ltd, AL du Toit)

Although the BSAC had secured the rights to prospect in the Bamangwato Reserve in 1893, Khama's son Tshekedi, objected to the terms of this agreement and after lengthy negotiations with the BSAC a much revised agreement was signed in 1932 (Crowder, 1985).

Du Toit (1931), who was Chief Consulting Geologist to De Beers Consolidated Mines Ltd from 1927 to 1941, felt that kimberlites were undoubtedly present in Botswana and that gravels in the larger rivers in the east may well be diamond bearing. He advised De Beers to join Anglo American Corp (AAC) in the exploration of Bamangwato. In May 1932 the board of AAC, a company which held a large

shareholding in BSAC, approved an 18 month program to which De Beers contributed 20% through Victoria Prospecting Co Ltd. Prospecting started in 1932 mainly by traversing lines some 600 m apart mapping geology and mineralisation, looking for pipes and gravels (Du Toit, 1932). Du Toit refers to a report by Bennett (BSAC engineer) that diamonds had been found in the Motloutse area in 1894 while people were digging Phiri's water well (Bennet, 1911). Bennet had apparently located the 70 foot well in 1911, cleaned it out but found no indications of diamonds (Du Toit, 1933).

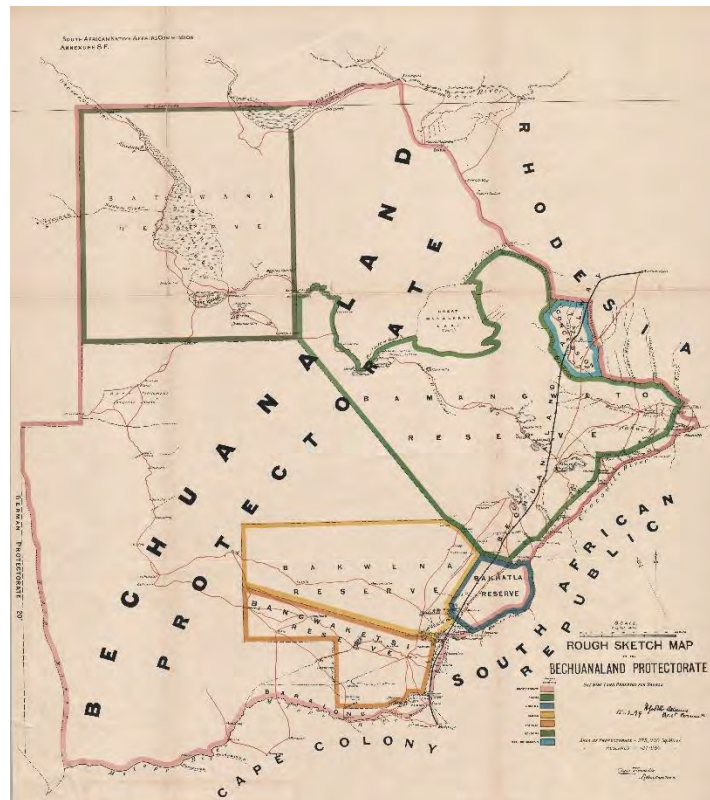


Figure 1. Sketch map of the Bechuanaland Protectorate showing tribal reserves (1899 - UCT archives)

After AAC withdrew from the venture in 1934, Du Toit (1934) convinced De Beers to investigate some of the gravels, and identified the area near the Sisi siding, close to Foley Station, as one of the largest continuous gravel areas in Bamangwato. De Beers washed 200 loads of gravel west of Sisi, close to Phiri's well, but no diamonds and kimberlitic minerals were found.

1930s Other reports of diamonds

The first authenticated diamonds in Botswana were recovered in 1934 at Pitsani along the Ramathlabama spruit, where De Beers had recovered 4 'minute' diamonds from 1163 loads of gravel (Du Toit 1938). Du Toit also refers to Mpayathyutlwa pan, north of Tshabong, where diamondiferous gravel was alleged but the clasts were derived from Dwyka Group tillites. Finally, Du Toit (1939) tried to interest De Beers in returning to Ngamiland as the presence of diamonds and 'rubies' has been reported northwest of Tsau by Colonel Naus. But there is no record that this was ever followed up.

The Geological Survey was established in 1948 with Wayland as the first Director. He felt that there was no geological reason why diamonds would not exist beneath the Kalahari. He suggested that pans form over diamond pipes because claims of diamonds in some of the pans have been strongly maintained, and he proposed a systematic exploration of specific types of pans (Wayland, 1949).

3. Modern exploration and mining

1959 – 1960 Bamangwato Reserve (Consolidated African Selection Trust, JHA Willis)

Tshedeki Khama signed an exploration agreement with Rhodesian Selection Trust Group (RST) in 1959 to mine the copper at Selebi-Phikwe. At the same time Consolidated African Selection Trust Ltd (CAST), part of the Selection Trust Group, obtained a Crown Grant (CG24) valid for a year to explore

the Bamangwato Reserve (Fig. 1) for diamonds. Being familiar with stream sampling, from their West Africa experience, they only covered the eastern part, which had drainage (Willis, 1960). Stream and selected bulk samples were collected from terraces and rivers (Willis, 1960). Only three small diamonds were recovered from the Upper Motloutse River and it was concluded that these were probably derived from Karoo sediments and hence from 'pre-Cambrian' sources (Willis, 1960). Another option considered was that there had been an ancient drainage across the Kalahari connected to the Motloutse, but that 'warping' and erosion had removed any trace. This hinted of kimberlites well to the west but this area was considered unsamplable (Willis, 1960). In 1960 the Geological Survey of Botswana (GSB) carried out a sampling program in the same area to follow-up on CAST's results but also found no kimberlitic minerals and agreed that the diamonds had weathered out of Karoo sediments (Boocock, 1965). Boocock (1965) also reported that pyrope garnet had been found by a mining company carrying out diamond prospecting north-east of Ghanzi and in the Ngwezumba Valley south of Kasane.

1955 – present De Beers Botswana previously Kimberlitic Searches Ltd. (GT Lamont)

In 1955 De Beers was back exploring the Bechuanaland Protectorate with Gavin Lamont. In 1966 they discovered 'para-kimberlites' near Mochudi. Although De Beers had been working in the Motloutse River area since 1962 it was only in 1964 that the idea crystallised, based on Du Toit's (1933) crustal warping, that diamonds may well be sourced from the west. A brief reconnaissance trip to the Letlhakane area in 1966 produced the first positive samples which led to the discovery of the first kimberlite in Botswana - BK01. Jennings, Deputy Director of the GSB, with a background in geophysics, was asked to do ground magnetic surveys at Mochudi and later over AK01 which led to the very first airborne magnetic survey to find kimberlites in 1968. Following the discovery of the Orapa cluster, De Beers found many kimberlites, using mainly soil sampling, of which Jwaneng (1972), the most important kimberlite find of all-times, and Lerala (1991) became mines.

1977 – 1982 Falconbridge (CMH Jennings)

Jennings left the GSB in 1970 and joined Falconbridge Pty. He took charge of Falconbridge's diamond exploration in Botswana in 1974. Drawing on De Beers' heavy mineral results, Falconbridge focussed on applying airborne magnetic surveys and found many kimberlites near Tshabong and Kukong. In 1980 they also completed a heli-borne sampling program in the Central Kalahari Game Reserve (CKGR) and found Gope 25 in 1981, which later became GEM Diamonds's Ghaghoo Mine.

Others

Many companies entered the scene without much success in finding economic kimberlites except Petra Diamonds that discovered KX36, also in the CKGR, presently subjected to a pre-feasibility study. More recently, several companies have re-evaluated some of the early kimberlites discoveries, and turned some of those into mines such as AK06 (Lucara), BK11 (Firestone), BK09 and BK12 (Debswana). With the recovery of the some very large and valuable stones from Karowe Mine (AK06) the industry has turned considerable energy to improved treatment processes to recover such gems as Lesedi La Rona (1,109 ct) without damaging the diamonds, as well as the re-treatment of tailing dumps.

References

- Bennett WE (1911) The prospecting of Khama's country. A report to the resident Mining Engineer of the BSA Co.
- Boocock C (1965) Mineral resources of the Bechuanaland Protectorate. In: Overseas Geology and Mineral Resources, Vol. 9, no.4, 369-417, and Bull. Geol. Surv. Bech., 1
- Crowder M (1985) Tshekedi Khama and Mining in Botswana 1929-1959. African Studies Institute, University of the Witwatersrand, African Studies Seminar Paper, 172, 1-17
- Du Toit AL (1931) Memorandum on the geological investigation of the Bechuanaland Protectorate. Internal memo to the Assisyant General Manager, DBCM Ltd, pp 8
- Du Toit AL (1934) Diamond prospecting operations in the Bechuanaland Protectorate. Note to H Dickinson, Consulting Engineer, Johannesburg, pp 4
- Du Toit AL (1938) Bechuanaland Prospecting. Letter to H Dickinson, Consulting Engineer, JHB 4 pp
- Wayland EJ (1949) Minerals in the Bechuanaland Protectorate. Geol. Surv. Bech. Unpubl. Report
- Willis JHA (1960) Bechuanaland Investigation 1959/1960. Final report, 12 pp



Fluid-rich microinclusions in diamonds open windows to large mantle processes.

Yaakov Weiss

Lamont-Doherty Earth Observatory of Columbia University, New York, United States, yweiss@ldeo.columbia.edu

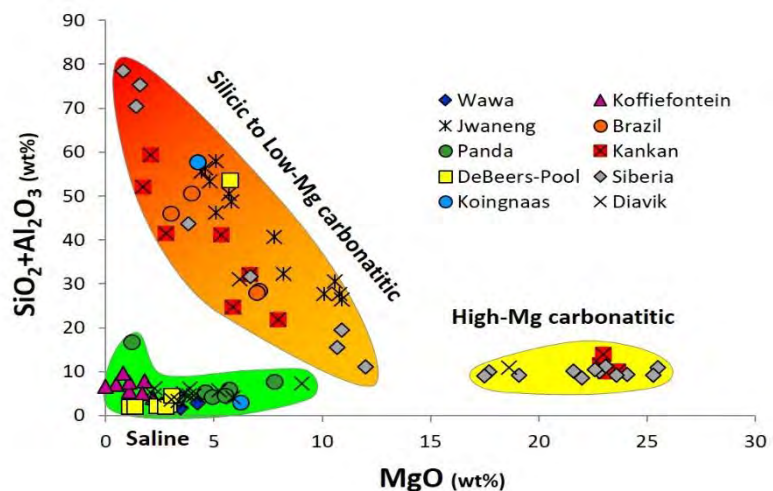
Introduction

Diamond formation in the Earth's mantle is induced by circulating carbon- and water-rich (C-O-H) mantle fluids and melts. This broadly accepted concept is based on (1) the concentric growth patterns of diamonds, as revealed by cathodoluminescence images indicating that they grew undisturbed into surrounding fluids/melts; (2) their association with veins and alteration zones in xenoliths; and (3) evidence that mineral inclusions in diamonds show enrichments in incompatible trace elements from the fluids that also deposited their host diamond. Deep C-O-H mantle fluids are often encapsulated as μm -scale high-density fluid (HDF) inclusions in fast-growing diamonds (i.e. 'hailstone boart', 'sugary', 'fibrous', 'cloudy'). Due to the physical strength and chemically inert nature of their diamond hosts, these inclusions remain pristine for billions of years even when brought to Earth's surface, and represent our only direct samples of deep Earth C-O-H fluids.

The compositions of HDF micro-inclusions in individual diamonds are homogenous. To date, out of ~250 diamonds analyzed by electron microprobe (EMPA) for their individual micro-inclusion major element compositions, HDFs show significant radial (core-to-rim) changes in only 4 diamonds. Thus ~98% of known fluid-rich diamonds are homogenous, and the individual micro-inclusions in a single diamond spans a limited range of compositions from core-to-rim (typically <10-20% 1σ for the major oxides). HDFs in diamonds from 4 continents and 8 cratons vary in major-element compositions between four major types (Fig. 1): a hydrous-silicic end-member rich in Si, Al, K and water; a hydrous-saline fluid end-member rich in Cl, K, Na and varying water and carbonate; and high- and low-Mg carbonatitic end-members rich in Ca, Mg, Fe, K and carbonate (Navon et al., 1988; Weiss et al., 2009 and references therein). Similar HDF compositions appear in diamonds from different lithospheric provenances and ages, and it is common to find more than one HDF type in a suite of diamonds from the same locality and/or kimberlite. The HDF end-members can be distinguished by their variation in MgO vs. $\text{SiO}_2+\text{Al}_2\text{O}_3$ (in wt.%; Figure 1), or by their relative abundances of water-carbonate-silicate-apatite (Extended Abstract No. 11IKC-004457).

Figure 1: $\text{SiO}_2+\text{Al}_2\text{O}_3$ vs. MgO in HDFs (wt% on a water- and carbonate-free basis). The high-Mg carbonatitic compositions are close to experimental near-solidus melts of carbonate-peridotite, while the low-Mg carbonatitic to silicic HDFs form an array close in composition to experimentally produced fluids/melts in the eclogite+carbonate \pm water system (Weiss et al., 2009). Datapoints include HDF compositions from the published literature.

HDFs of different end-member compositions display two main trace-element patterns, one with high field strength element (HFSE) depletions and large ion lithophile element (LILE) enrichments similar to calcalkaline magmas and continental rocks, the other with lower LILE abundances and 'smoother' overall



trace-element patterns similar to oceanic basalts. Radiogenic isotope data from HDFs are very scarce, nevertheless, available data show $^{87}\text{Sr}/^{86}\text{Sr}$ between 0.703-0.723 (Akagi and Masuda, 1988; Klein-BenDavid et al., 2014; Smith et al., 2012), indicating sources ranging from ‘depleted’ oceanic mantle to old continental crust. Thus, HDFs record a large range of compositions and sources for deep C-O-H diamond-forming fluid agents. Their study permits a glimpse back in time to the active role C-O-H fluids play in the global material circulation, deep Earth processes, and their impacts on the sub-continental lithospheric mantle (SCLM).

Deep C-O-H mantle fluids, diamond formation and regional tectonics and volcanism

A strong connection has been established between high-Mg carbonatitic HDFs and carbonated peridotite sources, either lithospheric or asthenospheric in origin, while silicic and low-Mg carbonatitic HDFs have been related to hydrous eclogite (plus or minus carbonate). Recently, Weiss et al. (2015) reported the first conclusive trace-element and Sr isotope evidence for seawater-altered subducting slabs as the source of deep C-O-H-bearing mantle fluids having saline compositions, and that these fluids are parental to carbonatitic and silicic melts in the lithosphere. These authors suggested that the whole spectrum of deep C-O-H fluids observed in diamonds (from saline-to-carbonatitic-to-silicic) is linked to saline fluids derived from seawater-altered subducted oceanic lithospheric slabs, and that carbonatitic and silicic melts develop through fluid-rock interaction of parental saline fluids with peridotitic or eclogitic lithologies in the lithospheric mantle (Fig. 2). Moreover, they linked the chemistry of the parental saline fluids and the timing of host diamond formation to Mesozoic plate subduction under western North America as the source for the saline fluids. These results imply a strong association between subduction, deep C-O-H mantle fluids, metasomatism and fluid-rich diamond formation, emphasizing the importance of subduction-derived fluids in affecting the composition of the deep SCLM.

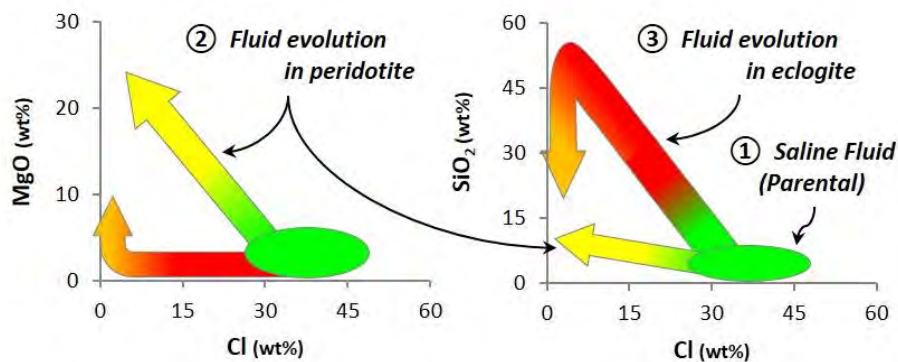


Figure 2: HDF compositional evolution depicted in the inset MgO–Cl and SiO₂–Cl trends. When the parental saline fluids (1) enter the lithosphere they react with local lithology. The melt-depleted nature of cratonic lithospheric peridotite prevents notable melting unless the saline fluids traverse either carbonated-peridotite or

eclogite lenses, leading to *in situ* formation of high-Mg carbonatitic (2) and silicic melts (3), respectively. The presence of carbonate in eclogite may lead to formation of low-Mg carbonatite fluids with increasing melting. Rapid diamond formation occurs during fluid-rock interaction due to the oxidation gradient between the evolving fluids and local lithosphere.

Another example for a connection between deep C-O-H mantle fluids and regional tectonics comes from HDFs encapsulated in a suite of diamonds from the DeBeers-Pool and Finsch kimberlites in the Kaapvaal craton, South Africa (Extended Abstract No. 11IKC-004461 and Weiss et al. unpublished data). New U, Th and He compositional data in these diamonds reveal 3 episodes of chemical changes in the Kaapvaal craton SCLM during the last ~1 Gyr, each by a different metasomatic agent. The youngest episodes indicate direct relationships between highly-saline fluid metasomatism, fluid-rich diamond formation and late-Mesozoic kimberlite eruptions, while the older silicic and carbonatitic metasomatic events may be related to the Namaqua–Natal Orogeny (~1 Gyr), Damara Orogeny (~500 Myr), or Karoo magmatism (~200 Myr) (Extended Abstract No. 11IKC-004460).

The fingerprints of old C-O-H fluid metasomatism in young mantle plumes

HIMU basalts stand out hotspots with the highest Pb isotope ratios, high Os isotope ratios, low Sr isotope ratios slightly higher than depleted MORB, and Nd-Sr isotopes plotting ‘below’ the ‘Nd-Sr mantle array’. Its mantle source is generally considered to be recycled basaltic oceanic crust. However, recent high-precision analyses of olivine phenocrysts in HIMU lavas indicate derivation from peridotite partial melting, rather than pyroxenitic remnants of recycled basalt, and show exceptionally high Ca/Al ratios that are far outside the range previously reported for olivines from MORB and OIB (Weiss et al., 2016). The high Ca/Al ratios indicate a metasomatic enrichment process involving carbonatitic fluid. A key piece to the HIMU puzzle is similarities in trace-element patterns between high-Mg carbonatitic HDFs in diamond, Group I kimberlites, and HIMU lavas, indicating that the mantle sources experienced similar histories of trace-element enrichment and depletion. This “HIMU–diamond-forming fluids connection” indicates that deep C-O-H fluids plays a major role in forming the HIMU OIBs, and provides new support for the involvement of C-O-H-fluid metasomatised SCLM in mantle plumes (Fig. 3).

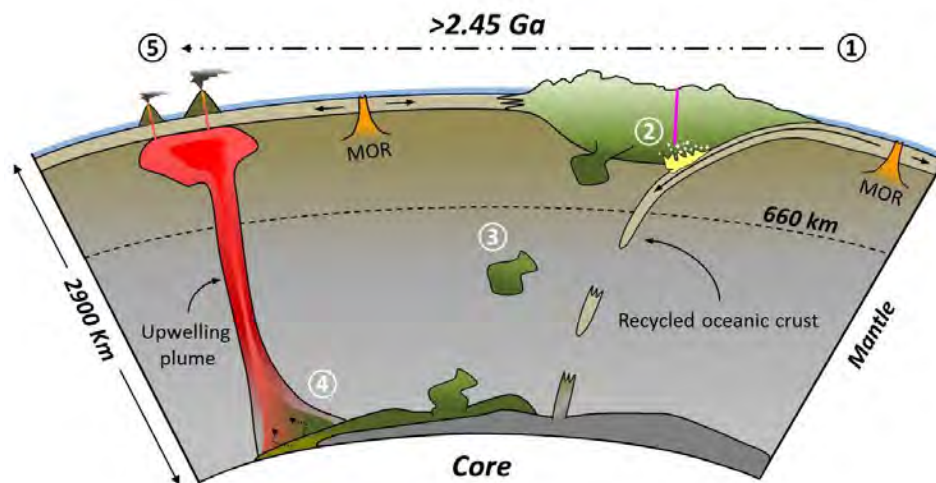


Figure 3: Conceptual model for the formation of the HIMU mantle source: (1) Subduction during the Archean or early Proterozoic. (2) Metasomatism of the melt-depleted SCLM by carbonatite-rich fluids-melts released by the subducting slabs (which can also produce diamonds); the metasomatised SCLM develops high Pb and Os isotopes over time. (3) The SCLM

delaminates and is transported to a mantle boundary layer, likely the core–mantle boundary. (4) Entrainment of recycled SCLM into an upwelling plume. (5) The upwelling plume generates the HIMU OIB.

References

- Akagi T, Masuda A (1988) Isotopic and elemental evidence for a relationship between kimberlite and Zaire cubic diamonds. *Nature* 336:665-667
- Klein BenDavid O, Pearson DG, Nowell GM, Ottley CJ, McNeill JCR, Logvinova A, Sobolev NV (2014) The source and time-integrated evolution of diamond-forming fluids – trace element and Sr isotopic evidence. *Geochimica et Cosmochimica Acta* 125:146–169.
- Navon O, Hutcheon ID, Rossman GR, Wasserburg GJ (1988) Mantle-derived fluids in diamond microinclusions. *Nature* 355:784-789.
- Smith EM, Kopylova MG, Nowell GM, Pearson DG, Ryder J (2012) Archean mantle fluids preserved in fibrous diamonds from Wawa, Superior craton. *Geology* 40:1071-1074
- Weiss Y, Kessel R, Griffin WL, Kiflawi I, Klein-BenDavid O, Bell DR, Harris JW, Navon O (2009) A new model for the evolution of diamond-forming fluids; evidence from microinclusion-bearing diamonds from Kankan, Guinea. *Lithos* 112:660-674.
- Weiss Y, McNeill J, Pearson DG, Nowell GM, Ottley CJ (2015) Highly saline fluids from a subducting slab as the source for fluid-rich diamonds. *Nature* 524:339-342.
- Weiss Y, Class C, Goldstein S, Hanyu T (2016) Key new pieces to the HIMU puzzle from olivines and diamond inclusions. *Nature*, 537:666–670.



Ocean–Continent Transition to Suprasubduction Zone Origin of the Western Yarlung Zangbo Ophiolites in Southwest Tibet, China: Constraints from the Petrology, Mineralogy, and Geochemistry of the Peridotites

Fei Liu^{1,2}, Dongyang Lian^{1,3}, Jingsui Yang¹, Xiaolu Niu¹, Yildirim Dilek^{1,2}, Guangying Feng¹, Hui Zhao^{1,4}, Guanlong Li^{1,4}

1. Institute of Geology, Chinese Academy of Geological Sciences, Beijing, China, lfhy112@126.com, yangjsui@163.com, niuxiaoludx@126.com, fengguangying198@163.com

2. Department of Geology and Environmental Earth Science, Miami University, Oxford, USA, dileky@miamioh.edu

3. Faculty of Earth Sciences, China University of Geosciences, Wuhan, China, 947608482@qq.com

4. Department of Geology and Mineral Resources, China University of Geosciences, Beijing, China, 13717926721@163.com, 240193488@qq.com

Introduction

The ophiolites that crop out discontinuously along the ~2000 km Yarlung Zangbo Suture zone (YZSZ) between the Nanga Parbat and Namche Barwa syntaxes in southern Tibet, China represent the remnants of Neotethyan oceanic lithosphere. We have investigated the internal structure and the geochemical makeup of mafic-ultramafic rock assemblages that are exposed in the westernmost segment of the YZSZ where the suture zone architecture displays two distinct sub-belts of ophiolitic and mélangé units separated by a continental Zhongba terrane. These two sub-belts include the Daba – Xiugugabu in the south (Southern sub-belt, SSB) and the Dajiweng – Saga in the north (Northern sub-belt, NSB). We present new mineralogical and geochemical data from upper mantle peridotites occurring in these two sub-belts and discuss their tectonomagmatic origin.

Results

These ophiolites are composed chiefly of peridotites with minor cumulated gabbros, volcanic and siliceous sedimentary rocks (Liu et al., 2015). No sheeted dikes and pillow lavas have been observed in this area. Harzburgites of the western Yarlung Zangbo ophiolites have prominent LREE-enriched (U-shaped or spoon-shaped) chondrite normalized REE patterns (Figure 1). Such patterns have generally been interpreted as the result of modification by suprasubduction zone (SSZ) melts/fluids. However, the abundance of peridotites sampled from mid-ocean ridge (MOR) with similar LREE-enriched REE patterns suggest that this feature is not unique to SSZ peridotites.

The U shaped REE patterns of the Dajiweng harzburgites in NSB, combined with their low HREE contents and highest partial melting degree of 17% to 22%, indicate that these rocks most likely have been modified by SSZ melts (e.g., boninitic melts) in a forearc setting (Figure 1a). Baer, Cuobuzha, Gongzhu, Kazhan and Zhilai harzburgites in NSB are similar to abyssal peridotites in mineral chemistry and whole-rock geochemistry (Figures 1b-d), most likely have been refertilized in a MOR or backarc setting. Similarly, Dongbo, Xiugugabu, Zhaga and Zhongba harzburgites in SSB shown less than 15% melting degree are consistent with abyssal peridotites (Figures 1d-f), which also have U-shaped REE patterns but are characterized by high HREE contents, high Al₂O₃/SiO₂ ratios, low MgO/SiO₂ ratios, and relatively fertile mineral compositions, have likely been modified in a MOR setting. Whereas, Purang harzburgites with a wider partial melting degree of 6% to 20% fall within the field of abyssal and forearc peridotites (Figure 1f). Furthermore, clinopyroxene-rich harzburgites and lherzolites in Purang contain rare spinel–pyroxene symplectites after garnet. Their clinopyroxenes have low MREE-to-HREE ratios at

relatively high HREE concentrations, and are Na-rich but Nd-poor, the REE patterns of western Yarlung Zangbo peridotites are also mainly comparable to those of sub-continental lithospheric mantle (SCLM) (Figures 1b-f), which suggest an origin from Na-rich SCLMs (Gong et al., 2016). All lines of evidence suggest that these peridotites underwent initial melting in the stability field of garnet-facies peridotites, followed by additional melting in the spinel-facies mantle. Combined with the mafic intrusions from Baer, Cuobuzha, Jianabeng and Purang massifs, we propose that the western Yarlung Zangbo ophiolites represent fragments of Ocean-Continent Transition peridotites altered by fluids in an initial intraoceanic SSZ setting.

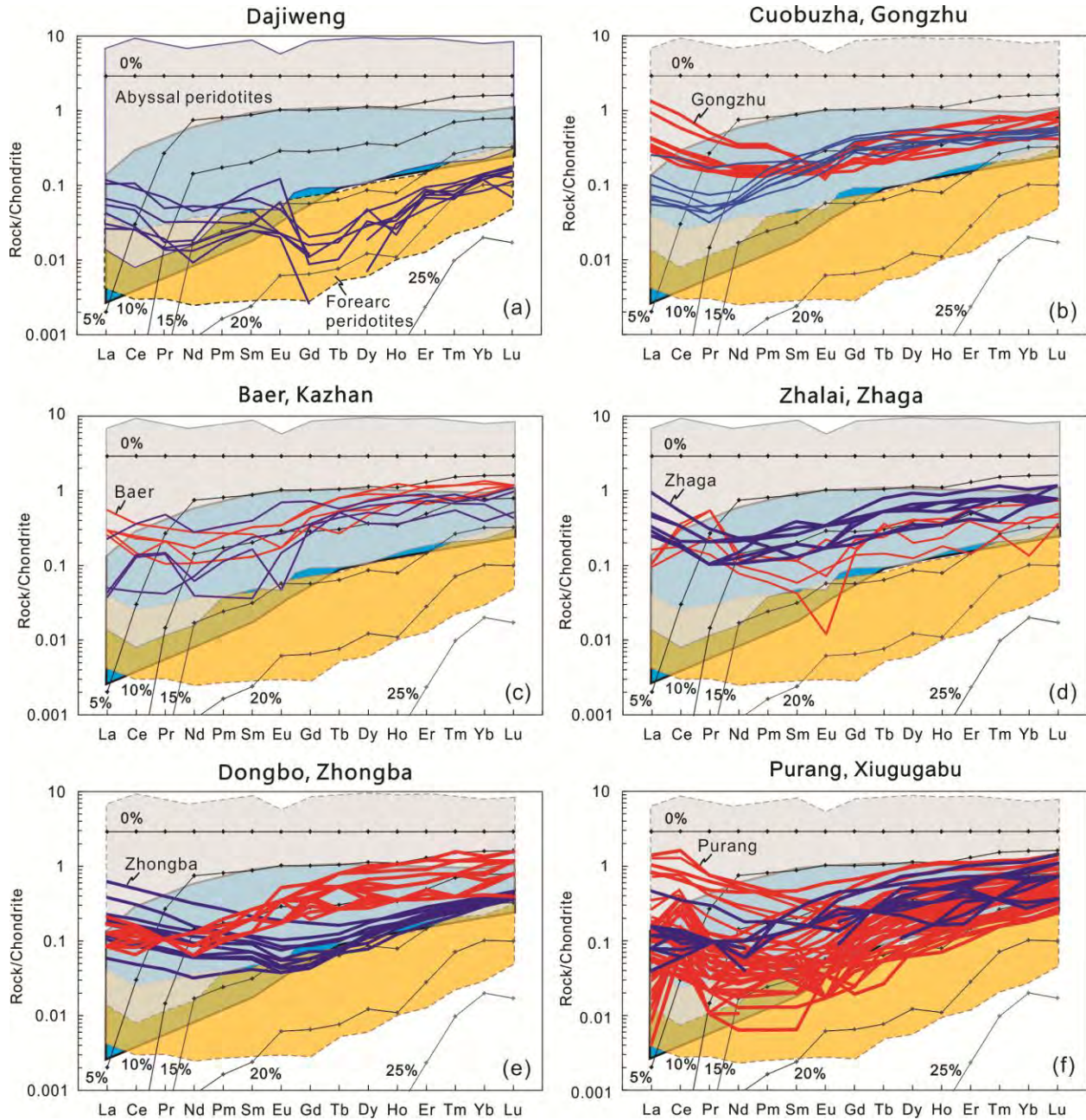


Figure 1: Chondrite-normalized rare earth element patterns for the harzburgites from the western Yarlung Zangbo ophiolites including Dajiweng (Lian, et al., 2016) (a), Cuobuzha (Feng et al., 2017) and Gongzhu (Lian et al., 2017) (b), Baer and Kazhan (c) and Zhalai (d) (Lian et al., 2016) massifs in the NSB; Zhaga (Zhang et al., 2016) (d), Dongbo (Niu et al., 2015) and Zhongba (Dai et al., 2011) (e), Purang (Gong et al., 2016; Su et al., 2015) and

Xiugugabu (Bédard et al., 2009) (f) in the SSB. Abyssal peridotite (Niu, 1997), forearc peridotite (Parkinson and Pearce, 1998), sub-continental Lithospheric mantle peridotite of Lanzhou massif, Italy in blue color (Downes, 2001), Chondrite (Sun and McDonough, 1989).

Acknowledgements

This research was funded by grants from the China Geological Survey (DD20160022-01, DD20160023-01), the National Science Foundation of China (41672063, 41373029, 41303019), and the Basic Outlay of Scientific Research Work from the Ministry of Science and Technology of China (J1321, J1618)

References

- Bédard É, Hébert R, Guilmette C, Lesage G, Wang CS, Dostal J (2009) Petrology and geochemistry of the Saga and Sangsang ophiolitic massifs, Yarlung Zangbo Suture Zone, Southern Tibet: Evidence for an arc-back-arc origin. *Lithos* 113(1–2):48-67
- Dai JG, Wang CS, Hébert R, Santosh M, Li YL, Xu JY (2011) Petrology and geochemistry of peridotites in the Zhongba ophiolite, Yarlung Zangbo Suture Zone: Implications for the Early Cretaceous intra-oceanic subduction zone within the Neo-Tethys. *Chemical Geology* 288(3–4):133-148
- Downes H (2001) Formation and modification of the shallow sub-continental lithospheric mantle: a review of geochemical evidence from ultramafic xenolith suites and tectonically emplaced ultramafic massifs of western and central Europe. *Journal of Petrology* 42(1):233-250
- Feng G, Yang J, Dilek Y, Liu F and Xiong F. 2017. Petrological and Re-Os isotopic constraints on the origin and tectonic setting of the Cuobuzha peridotite, Yarlung Zangbo suture zone, southwest Tibet, China. *Lithosphere*. doi: 10.1130/L590.1
- Gong XH, Shi RD, Griffin WL, Huang Q, Xiong Q, Chen S, Zhang M, O'Reilly SY (2016) Recycling of ancient subduction-modified mantle domains in the Purang ophiolite (southwestern Tibet). *Lithos* 262:11-26
- Lian DY, Yang JS, Liu F, Wu W, Zhang L, Zhao H, Huang J (2017) Geochemistry and tectonic significance of the Gongzhu peridotites in the northern branch of the western Yarlung Zangbo ophiolitic belt, western Tibet. *Mineralogy and Petrology*:1-18
- Lian DY, Yang JS, Robinson PT, Liu F, Xiong F, Zhang L, Gao J, Wu W (2016) Tectonic Evolution of the Western Yarlung Zangbo Ophiolitic Belt, Tibet: Implications from the Petrology, Mineralogy, and Geochemistry of the Peridotites. *The Journal of Geology* 124:353-376
- Liu F, Yang JS, Dilek Y, Xu ZQ, Xu XZ, Liang FH, Chen SY, Lian DY (2015) Geochronology and geochemistry of basaltic lavas in the Dongbo and Purang ophiolites of the Yarlung-Zangbo Suture zone: Plume-influenced continental margin-type oceanic lithosphere in southern Tibet. *Gondwana Research* 27(2):701-718
- Niu XL, Yang JS, Dilek Y, Xu JF, Li J, Chen S, Feng GY, Liu F, Xiong F, Liu Z (2015) Petrological and Os isotopic constraints on the origin of the Dongbo peridotite massif, Yarlung Zangbo Suture Zone, Western Tibet. *Journal of Asian Earth Sciences* 110:72-84
- Niu YL (1997) Mantle Melting and Melt Extraction Processes beneath Ocean Ridges: Evidence from Abyssal Peridotites. *Journal of Petrology* 38(8):1047-1074
- Parkinson IJ, Pearce JA (1998) Peridotites from the Izu-Bonin-Mariana Forearc (ODP Leg 125): Evidence for Mantle Melting and Melt-Mantle Interaction in a Supra-Subduction Zone Setting. *Journal of Petrology* 39(9):1577-1618
- Su BX, Teng FZ, Hu Y, Shi RD, Zhou MF, Zhu B, Liu F, Gong XH, Huang Q, Xiao Y, Chen C, He Y (2015) Iron and magnesium isotope fractionation in oceanic lithosphere and sub-arc mantle: Perspectives from ophiolites. *Earth and Planetary Science Letters* 430:523-532
- Sun SS, McDonough WF (1989) Chemical and isotopic systematics of oceanic basalts: implications for mantle composition and processes. Geological Society, London, Special Publications 42(1):313-345



Mg-metasomatized Fe-rich dunites from the Thaba Putsoa kimberlite, Lesotho: Headstones in a kimberlite graveyard

Victor Toth^{1,2}, and Daniel J. Schulze¹

¹ *Departments of Earth Sciences and Chemical and Physical Sciences, University of Toronto, Mississauga, Ontario, Canada*

² *De Beers - Canada*

Megacrysts of olivine and mosaic-porphyroclastic dunites from the Thaba Putsoa kimberlite in Lesotho represent variably deformed and recrystallized members of the Cr-poor megacryst suite. Olivine compositions are readily divided into two groups, one of which is rich in Mg and Ni (molar Mg/(Mg+Fe) = 0.835-0.882, 0.25-0.39 wt% NiO). In the other, olivine is more Fe-rich (molar Mg/(Mg+Fe) = 0.772-0.820), substantially lower in nickel (0.05-0.13 wt% NiO) and associated with ilmenite. These two groups are equivalent to those of the Cr-poor olivine megacryst population at the nearby Monastery Mine in South Africa. At Thaba Putsoa, olivine neoblasts in several of the samples from the Fe-rich group are significantly enriched in Mg and Ni relative to porphyroclasts and are similar in composition to olivines of the Mg-rich group and to olivines in associated (and genetically related) igneous-textured ilmenite orthopyroxenites. Batches of magma, parent to the Cr-poor megacrysts but in different stages of differentiation (crystallization), must have been closely associated in space and time, allowing more primitive (magnesian) magmas to infiltrate and metasomatize earlier crystallization products (Fe-rich olivines and dunites). Rods and blebs of Ni-bearing sulfides in the most Fe-rich olivine megacrysts of the magnesian group at Monastery are evidence of development of an immiscible sulfide magma that caused Ni to be partitioned into the sulfide phase, resulting in dramatic depletion of Ni in subsequently formed Fe-rich olivines at both Monastery and Thaba Putsoa.